Cover Picture

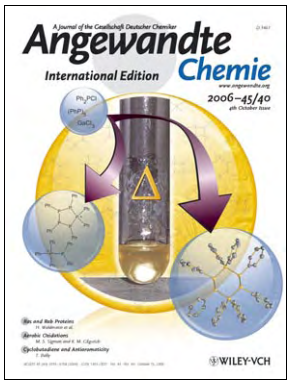

Jan J. Weigand,* Neil Burford,* Michael D. Lumsden, and Andreas Decken

A new melt approach has enabled the synthesis of the first *catena*-hexaphosphorus dications, as described in the Communication by N. Burford, J. J. Weigand, and co-workers on page 6733 ff. The cover picture (by Jared MacPherson) shows a photograph of the reaction melt of $^{4}/_{5}\,(PhP)_5$, $2\,Ph_2PCl$, and $2\,GaCl_3$ at 100 °C, which solidifies to yield $[P_6Ph_8][GaCl_4]_2$ quantitatively upon further heating. Such cations represent a new direction in phosphorus chemistry and promise a parallel to catena-carbon (organic) chemistry.

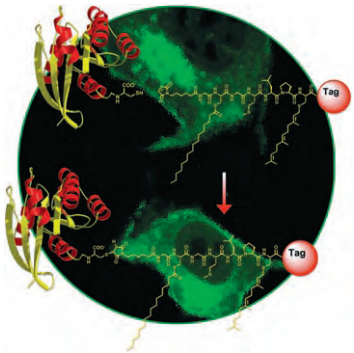

Chemical Biology
Solid-phase synthesis produces lipid-modified peptides that can be chemoselectively ligated onto proteins. In their Review on page 6622 ff., H. Waldmann and co-workers discuss unsolved questions about the Ras-superfamily GTPases.

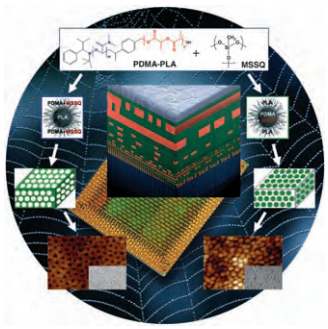

Porous Materials
In their Communication on page 6648 ff., J. L. Hedrick and co-workers describe the preparation of organosilicate monoliths and nanoparticles by solvent-directed self-assembly. By changing the deposition solvent, a single block copolymer/organosilicate mixture can generate widely different nanostructures.

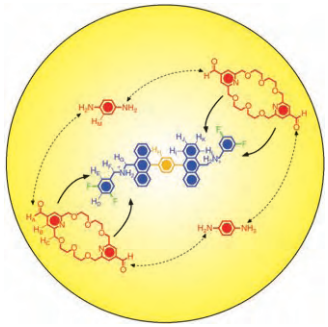

Supramolecular Chemistry
J. F. Stoddart, D. J. Williams, and co-workers introduce a new class of mechanically interlocked molecular compounds called “suitanes” in their Communication on page 6665 ff., and discuss the template-directed synthesis of the simplest member of this series, suit[2]ane.

Contents

The following Communications have been judged by at least two referees to be "very important papers" and will be published online at www.angewandte.org soon:

*C. M. Erben, R. P. Goodman, A. J Turberfield**
Single-Molecule Protein Encapsulation in a Rigid DNA Cage

F. D. Lewis, H. Zhu, P. Daublain, B. Cohen, M. R. Wasielewski**
Hole Mobility in DNA A-Tracts

*S. Sekharan, M. Sugihara, V. Buss**
Origin of Spectral Tuning in Rhodopsin: It is Not the Binding Pocket

*H. Ma, T. P. Spaniol, J. Okuda**
Highly Heteroselective Ring-Opening Polymerization of *rac*-Lactide Initiated by Bis(phenolato) Scandium Complexes

H. Braunschweig, T. Kupfer, M. Lutz, K. Radacki, F. Seeler, R. Sigritz*
Metal-Mediated Diboration of Alkynes with [2]Borametalloarenophanes under Stoichiometric, Homogeneous, and Heterogenous Conditions

*M. E. Chiu, D. J. Watson, G. Kyriakou, M. S. Tikhov, R. M. Lambert**
Tilt the Molecule and Change the Chemistry: Mechanism of S-Promoted Chemoselective Catalytic Hydrogenation of Crotonaldehyde on Cu(111)

News

Organic Chemistry: Nakamura, Bach, and Dupont honored ____ **6608**

Books

Polymorphism in the Pharmaceutical Industry	Rolf Hilfiker	*reviewed by R. K. Harris*	**6609**
High Temperature Superconductor Bulk Materials	Gernot Krabbes, Günter Fuchs Wolf-Rüdiger Canders, Hardo May, Ryszard Palka	*reviewed by O. Eibl*	**6609**

Highlights

Aerobic Oxidations

K. M. Gligorich, M. S. Sigman* ____ **6612 – 6615**

Mechanistic Questions about the Reaction of Molecular Oxygen with Palladium in Oxidase Catalysis

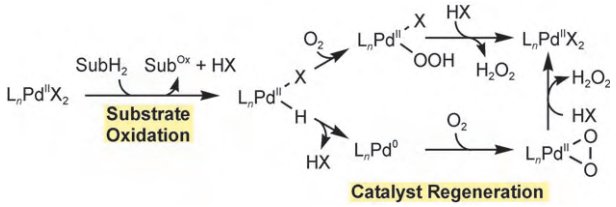

Which pathway? Aerobic Pd-catalyzed oxidation reactions couple organic-substrate oxidation to the reduction of O_2. Two pathways are prevalent for the regeneration of the active Pd^{II} catalyst (see scheme; $SubH_2$ = substrate; Sub^{Ox} = oxidized substrate), and recent studies have provided a deeper fundamental understanding of the interactions of Pd with O_2.

InterScience

© 2006 Wiley-VCH Verlag GmbH & Co. KGaA, Weinheim

The heat of formation of cyclobutadiene has recently been determined by Kass and co-workers. This determination is taken as an occasion to reflect on the difficulty to extract from this number the "antiaromatic destabilization" and the strain energy of this most fundamental species.

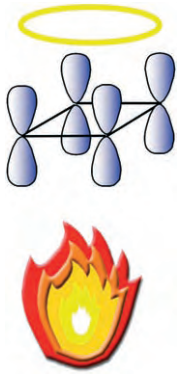

Cyclobutadiene

T. Bally* ——— 6616 – 6619

Cyclobutadiene: The Antiaromatic Paradigm?

Reviews

Chemical biology in action: The progress in the fields of lipidated-peptide synthesis and protein-ligation methods has enabled access to natural and modified Ras GTPases. The generated peptides and proteins have served to elucidate unsolved biological questions in the field of the Ras-superfamily GTPases. Pal = palmitoyl, Far = farnesyl.

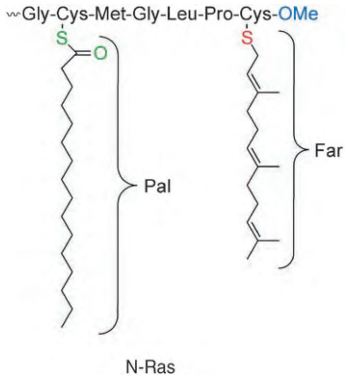

Bioorganic Chemistry

L. Brunsveld, J. Kuhlmann, K. Alexandrov, A. Wittinghofer, R. S. Goody, H. Waldmann* ——— 6622 – 6646

Lipidated Ras and Rab Peptides and Proteins—Synthesis, Structure, and Function

Communications

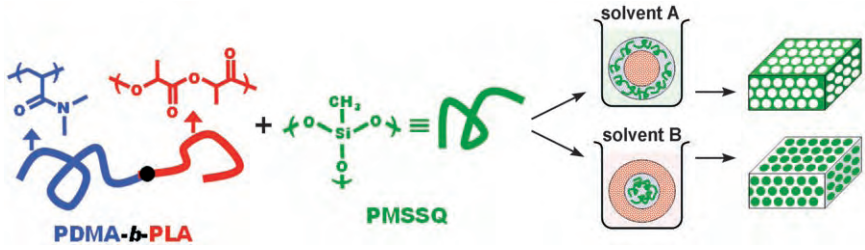

An inverse relationship: Mixtures of poly(dimethylacrylamide)-*block*-polylactide copolymer (PDMA-*b*-PLA) with organosilicate oligomers (PMSSQ) selectively sequestered into the PDMA phase form micelles and inverse micelles in solution depending on the solvent. The micellar structures are imprinted into the resulting cured organosilicate to give monoliths or assemblies of densely packed organosilicate nanoparticles, respectively.

Solvent-Directed Self-Assembly

T. M. Hermans, J. Choi, B. G. G. Lohmeijer, G. Dubois, R. C. Pratt, H.-C. Kim, R. M. Waymouth, J. L. Hedrick* ——— 6648 – 6652

Application of Solvent-Directed Assembly of Block Copolymers to the Synthesis of Nanostructured Materials with Low Dielectric Constants

For the USA and Canada:
ANGEWANDTE CHEMIE International Edition (ISSN 1433-7851) is published weekly by Wiley-VCH PO Box 191161, D 69451 Weinheim, Germany. Air freight and mailing in the USA by Publications Expediting Inc. 200 Meacham Ave., Elmont, NY 11003. Periodicals postage paid at Jamaica NY 11431. US POSTMASTER: send address changes to *Angewandte Chemie*, Wiley-VCH, 111 River Street, Hoboken, NJ 07030. Annual subscription price for institutions: US$ 5685/5168 (valid for print and electronic / print or electronic delivery); for individuals who are personal members of a national chemical society prices are available on request. Postage and handling charges included. All prices are subject to local VAT/sales tax.

© 2006 Wiley-VCH Verlag GmbH & Co. KGaA, Weinheim

The best in chemistry –

for more than a hundred years

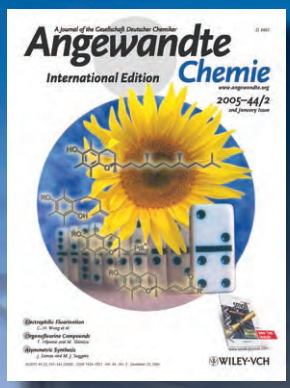

A Journal of the Gesellschaft Deutscher Chemiker

Angewandte
International Edition **Chemie**

www.angewandte.org

1888: ***The beginning of a success story***

Constant Innovations

1962: *First issue of the International Edition*
1976: *Graphical abstracts*
1979: *Cover pictures*
1988: *Centenary of Angewandte*
1989: *Routine use of color*
1991: *New section: Highlights*
1992: *Computerized editorial tracking system*
1995: *Internet service for readers*
1998: *Regular press service; full-text online*
2000: *New section: Essays; EarlyView: Communications available online ahead of the printed version*
2001: *New section: Minireviews*
2002: *Online submission of manuscripts*
2003: *Weekly publication; new section: News; new layout*
2004: *Backfiles (1962-1997); ManuscriptXpress: Online system for authors and referees*

Angewandte's advisors...

Rainer Metternich
Schering AG, Berlin

»***Angewandte Chemie*** *keeps me up to date on the top new developments in chemistry. I am engaged in drug discovery, and this high-quality journal covering breakthrough discoveries in interdisciplinary research, particularly in bioorganic chemistry, is of the highest relevance to me. Each issue of Angewandte provides an outstanding source for innovations.*«

Angewandte Chemie International Edition *is a journal of the German Chemical Society (GDCh)*

GDCh

WILEY InterScience® DISCOVER SOMETHING GREAT

WILEY-VCH

1804502_gu

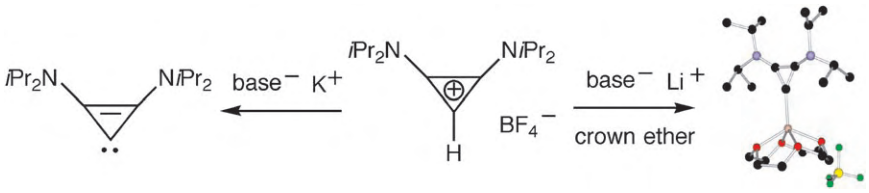

Luck is important: In the 1970s, Yoshida and Weiss both had the right cyclopropenium cation precursor. With the right counteranion, they would have isolated the first carbene–lithium adduct (see scheme; C black, N blue, O red, Li pink, B yellow, F green). With the right base and counteranion combination, they would have isolated the first stable free carbene.

Carbenes

V. Lavallo, Y. Ishida, B. Donnadieu, G. Bertrand* ——— **6652 – 6655**

Isolation of Cyclopropenylidene–Lithium Adducts: The Weiss–Yoshida Reagent

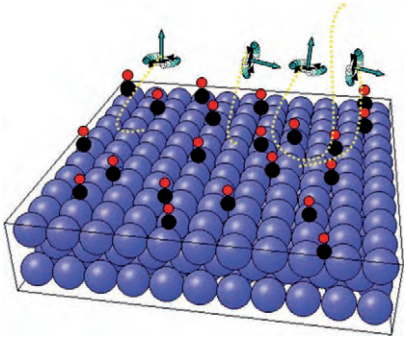

It's all in the spin: The initial sticking probability of O_2 on a CO-precovered Pd(100) surface and the rate of CO_2 production are strongly affected by the alignment of the incoming molecules. Whereas O_2 molecules impinging with cartwheel-like motion can stick in small holes, molecules moving with helicopter-like motion need a large array of free sites (see picture).

Surface Chemistry

A. Gerbi, L. Savio, L. Vattuone,* F. Pirani, D. Cappelletti, M. Rocca ——— **6655 – 6658**

Role of Rotational Alignment in Dissociative Chemisorption and Oxidation: O_2 on Bare and CO-Precovered Pd(100)

Economic power: A robust and low-cost microbial fuel cell has a tungsten carbide anode electrocatalyst, a pyrolyzed iron(III) phthalocyanine cathode catalyst for oxygen reduction, and hydrogen-producing soil bacteria as biocatalysts (see picture). Power and current densities of up to 585 $\mu W cm^{-2}$ and 3 $mA cm^{-2}$, respectively, are achieved.

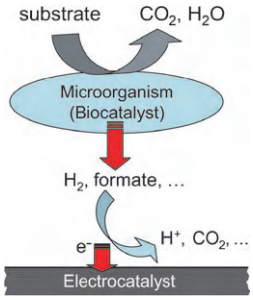

Fuel Cells

M. Rosenbaum, F. Zhao, U. Schröder,* F. Scholz ——— **6658 – 6661**

Interfacing Electrocatalysis and Biocatalysis with Tungsten Carbide: A High-Performance, Noble-Metal-Free Microbial Fuel Cell

Colorimetric guest signaling is effected by a supramolecular approach that uses a mesoporous hybrid solid functionalized with gatelike scaffoldings. When the gate is open, a dye (see scheme; orange dots) embedded in the pore walls of a mesoporous solid is released into the solution giving color. If the appropriate anion (red dots) is present the gate is closed, the dye is locked into the pores, and the solution remains colorless.

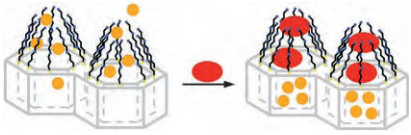

Sensors

R. Casasús, E. Aznar, M. D. Marcos, R. Martínez-Máñez,* F. Sancenón, J. Soto, P. Amorós ——— **6661 – 6664**

New Methods for Anion Recognition and Signaling Using Nanoscopic Gatelike Scaffoldings

© 2006 Wiley-VCH Verlag GmbH & Co. KGaA, Weinheim

Contents

Supramolecular Chemistry

A. R. Williams, B. H. Northrop, T. Chang, J. F. Stoddart,* A. J. P. White, D. J. Williams* ——— **6665 – 6669**

Suitanes

Molecules in suits: Supramolecular assistance leads to the self-assembly of a mechanically interlocked compound called a suit[2]ane (see picture). Two bisformyldipyrido[24]crown-8 rings (red) recognize and encircle two secondary ammonium ion centers on a rigid linear scaffold (blue for the most part in the picture) with a bulky midriff, followed by the dynamic formation of four imine bonds involving two *p*-phenylenediamine molecules as linkers.

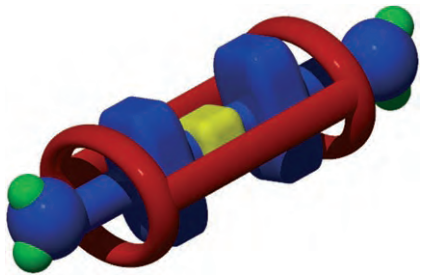

Polyoxometalates

R. P. Bontchev, M. Nyman* ——— **6670 – 6672**

Evolution of Polyoxoniobate Cluster Anions

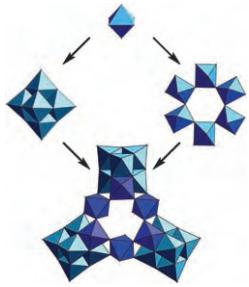

A new geometry for polyoxoniobates is observed in $\{Nb_{24}O_{72}H_9\}^{15-}$, the largest isopolyoxoniobate cluster anion known to date. Its structural evolution from isolated Lindqvist anions $[Nb_6O_{19}]^{8-}$ and the cyclic pyrochlore unit $[Nb_6O_{30}]$ through to the complex dimer $[(\{Nb_{24}O_{72}H_9\}\{Cu(en)_2(H_2O)\}_2\{Cu(en)_2\})_2]^{18-}$ is discussed.

Asymmetric Self-Assembly

I. K. Voets, A. de Keizer, P. de Waard, P. M. Frederik, P. H. H. Bomans, H. Schmalz, A. Walther, S. M. King, F. A. M. Leermakers, M. A. Cohen Stuart* ——— **6673 – 6676**

Double-Faced Micelles from Water-Soluble Polymers

Asymmetric disk-shaped Janus micelles form spontaneously and reversibly when simple water-soluble diblock copolymers in aqueous solutions are mixed. The combination of associative and segregative phase separation within one nanostructure results in a disk-shaped micelle with a complex coacervate core and an asymmetric water-swollen corona which is microphase-separated into two distinct domains or faces.

Carbon Nanotubes

H. Isobe,* T. Tanaka, R. Maeda, E. Noiri, N. Solin, M. Yudasaka, S. Iijima, E. Nakamura* ——— **6676 – 6680**

Preparation, Purification, Characterization, and Cytotoxicity Assessment of Water-Soluble, Transition-Metal-Free Carbon Nanotube Aggregates

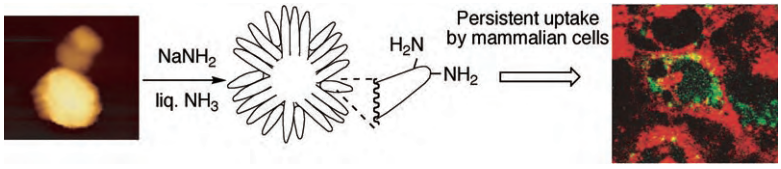

The risk assessment of carbon materials, an important topic in nanomaterials research, has been hampered by the lack of characterizable samples. Transition-metal-free carbon nanohorn aggregates have been prepared that are covalently bonded aggregates of single-walled nanotubes. They were functionalized to give water-soluble derivatives (see picture), which were incubated with cells in cytotoxicity assessments.

© 2006 Wiley-VCH Verlag GmbH & Co. KGaA, Weinheim

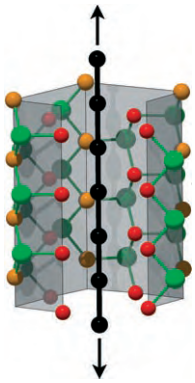

A mixed-valent subnitride host structure with parallel channels ($Ca_3^{2+}Ca_4^{1.5+}N_4^{3-}$) readily accommodates metal guest chains (see picture; Ca^{2+} orange, $Ca^{1.5+}$ red, N green, M black). These incommensurate guests, which comprise linear chains of equidistant metal atoms (M = Ag, Ga) or fragments thereof (M = In, Tl), interact only weakly with their hosts.

Host–Guest Systems

P. Höhn, G. Auffermann, R. Ramlau, H. Rosner, W. Schnelle, R. Kniep* ——— 6681 – 6685

$(Ca_7N_4)[M_x]$ (M = Ag, Ga, In, Tl): Linear Metal Chains as Guests in a Subnitride Host

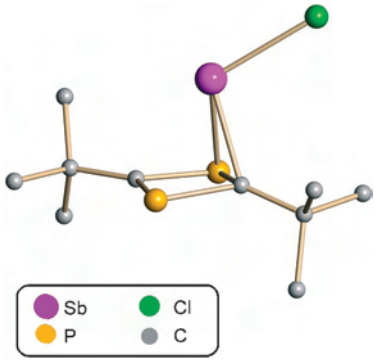

The carbon–phosphorus–antimony cage of $P_2C_2tBu_2SbCl$ (see picture) adopts an envelope-type structure which is quite distinct from its phosphorus analogue, the tricyclic compound $P_2C_2tBu_2PCl$. DFT calculations reveal that subtle changes in electronic structure as a result of the inert-pair effect lead to profound differences in structural and dynamic behavior.

Envelope Clusters

C. Fish, M. Green,* J. C. Jeffery, R. J. Kilby, J. M. Lynam,* J. E. McGrady,* D. A. Pantazis, C. A. Russell,* C. E. Willans ——— 6685 – 6689

A Main-Group Analogue of Housene: The Subtle Influence of the Inert-Pair Effect in Group 15 Clusters

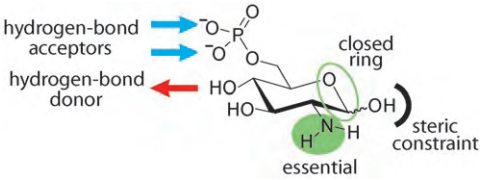

A tweak here, a tweak there: A series of analogues of glucosamine-6-phosphate (GlcN6P, see picture) was used to examine the molecular-recognition characteristics of a *glmS* ribozyme that is activated by this ligand. Although several functional groups on the ligand are critical for binding, there are opportunities to create new analogues that fully trigger ribozyme action.

Riboswitches

J. Lim, B. C. Grove, A. Roth, R. R. Breaker* ——— 6689 – 6693

Characteristics of Ligand Recognition by a *glmS* Self-Cleaving Ribozyme

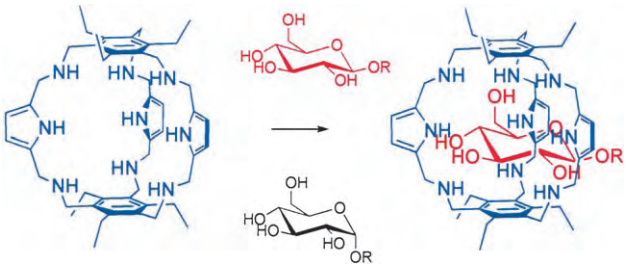

Fishing for β-glucose: Three dialdehydic and two triamino components quantitatively self-assemble into a pyrrolic cage receptor that effectively discriminates D-glucopyranosides among various monosaccharides and recognizes the β anomer exclusively.

Molecular Recognition

O. Francesconi, A. Ienco, G. Moneti, C. Nativi, S. Roelens* ——— 6693 – 6696

A Self-Assembled Pyrrolic Cage Receptor Specifically Recognizes β-Glucopyranosides

© 2006 Wiley-VCH Verlag GmbH & Co. KGaA, Weinheim

Contents

Lead Iron Oxides

A. M. Abakumov,* J. Hadermann, S. Bals, I. V. Nikolaev, E. V. Antipov, G. Van Tendeloo ——— **6697 – 6700**

Crystallographic Shear Structures as a Route to Anion-Deficient Perovskites

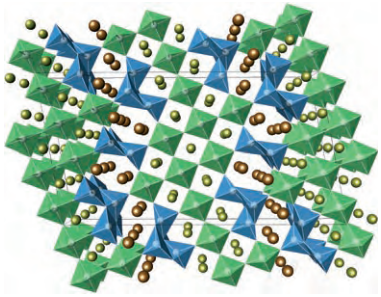

Shear innovation: By analyzing the crystallographic shear (CS) structures of "$Pb_2Fe_2O_5$" (see picture; spheres Pb, polyhedra FeO_6/FeO_5), new building principles are derived for perovskite-based compounds containing cations with a lone electron pair in the A sites of the perovskite structure. The chemical composition can be adjusted by varying the orientation of the CS planes and the thickness of the perovskite slabs between the planes.

Catalytic Isomerization

J. Xu, J. Y. Ying* ——— **6700 – 6704**

A Highly Active and Selective Nanocomposite Catalyst for C_{7+} Paraffin Isomerization

No coking: A $Pt/WO_3/Al\text{-}ZrO_x$ nanocomposite enables the efficient conversion of various hydrocarbons at a temperature as low as 150 °C (see figure, X = conversion) without deep cracking or coking problems. This novel catalyst might potentially be used for the production of high-octane fuel with a low content of aromatics by converting *n*-alkanes into their multibranched isomers with excellent selectivity.

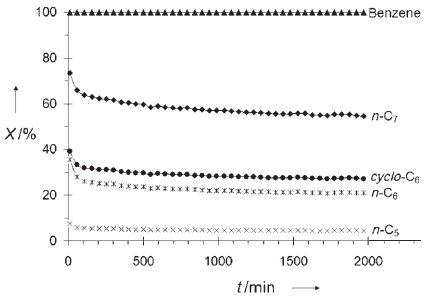

Furan Synthesis

J. Zhang, H.-G. Schmalz* ——— **6704 – 6707**

Gold(I)-Catalyzed Reaction of 1-(1-Alkynyl)-cyclopropyl Ketones with Nucleophiles: A Modular Entry to Highly Substituted Furans

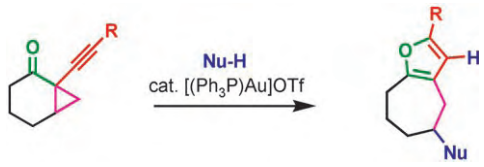

Ring round: 1-Acyl-1-alkynyl-cyclopropanes smoothly react with nucleophiles in the presence of a gold(I) catalyst to afford substituted furans in a fully atom-economical fashion (see scheme; Nu = nucleophile, Tf = trifluoromethanesulfonyl). The reaction tolerates a wide range of substrates.

Iron(III) Compounds

P. J. Alonso,* A. B. Arauzo, J. Forniés, M. A. García-Monforte, A. Martín, J. I. Martínez, B. Menjón,* C. Rillo, J. J. Sáiz-Garitaonandia ——— **6707 – 6711**

A Square-Planar Organoiron(III) Compound with a Spin-Admixed State

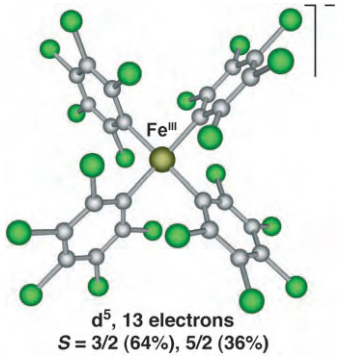

Square-planar iron(III) species bearing no axial ligands can still behave as spin-admixed systems ($S = {}^3/_2, {}^5/_2$). The highly unusual homoleptic σ-organoiron complex $[Li(thf)_4][Fe^{III}(C_6Cl_5)_4]$ (see anion in picture; green Cl, gray C) is an example of such a system.

© 2006 Wiley-VCH Verlag GmbH & Co. KGaA, Weinheim

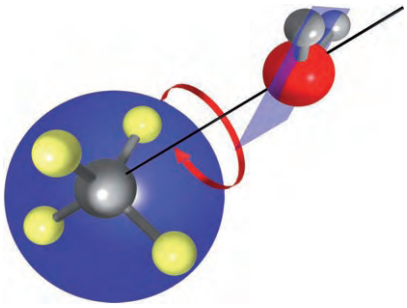

Top stuff: The configuration of tetrafluoromethane–water is driven by dipole–dipole interactions rather than hydrogen bonds. The complex, which consists of a planar and a spherical moiety, is an asymmetric top in its equilibrium conformation, but its effective behavior is that of a symmetric top, owing to its high internal dynamics.

Dipole–Dipole Interactions

W. Caminati,* A. Maris, A. Dell'Erba, P. G. Favero ——— **6711 – 6714**

Dynamical Behavior and Dipole–Dipole Interactions of Tetrafluoromethane–Water

---

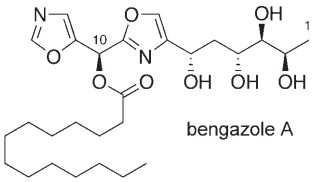

Candidate for *Candida*: A high-yielding and versatile synthesis of bengazole A has been developed; the first to provide access to a single stereoisomer of the natural product. Key steps include the construction of the 2,4-disubstituted oxazole under mild conditions and a diastereoselective 1,3-dipolar cycloaddition.

Total Synthesis

J. A. Bull, E. P. Balskus, R. A. J. Horan, M. Langner, S. V. Ley* ——— **6714 – 6718**

Stereocontrolled Total Synthesis of Bengazole A: A Marine Bisoxazole Natural Product Displaying Potent Antifungal Properties

---

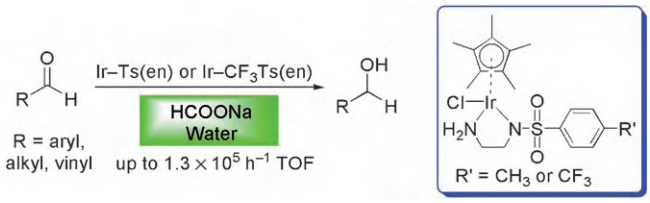

Water as solvent: A fast, selective, and high-yielding transfer hydrogenation of a wide range of aldehydes is achieved using Ir^{III} catalysts containing simple ethylenediamine (en) ligands (see scheme; Ts = *p*-toluenesulfonyl, TOF = turnover frequency). This procedure is suitable for aldehydes with a wide range of functional groups.

Transfer Hydrogenation

X. Wu, J. Liu, X. Li, A. Zanotti-Gerosa, F. Hancock, D. Vinci, J. Ruan, J. Xiao* ——— **6718 – 6722**

On Water and in Air: Fast and Highly Chemoselective Transfer Hydrogenation of Aldehydes with Iridium Catalysts

---

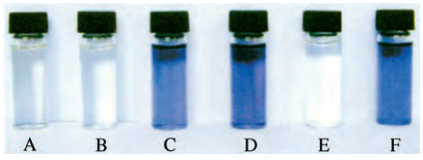

Seeing is believing: Treatment of tryptophan with formic acid and hydrochloric acid generates a violet-blue color. The reaction is very specific, and can be used to identify tryptophan in a mixture of amino acids, or corroborate the existence of tryptophyl groups in peptides or proteins (see picture; A: blank; B: a mixture of 9 representative amino acids; C: tryptophan; D: mixture (B) and tryptophan; E: reduced glutathione; F: egg-white albumin).

Analytical Methods

Z. Bao, S. Sun, J. Li, X. Chen, S. Dong, H. Ma* ——— **6723 – 6725**

Direct Identification of Tryptophan in a Mixture of Amino Acids by the Naked Eye

© 2006 Wiley-VCH Verlag GmbH & Co. KGaA, Weinheim

Contents

Synthetic Methods

S. Couty, C. Meyer, J. Cossy* **6726 – 6730**

Diastereoselective Gold-Catalyzed Cycloisomerizations of Ene-Ynamides

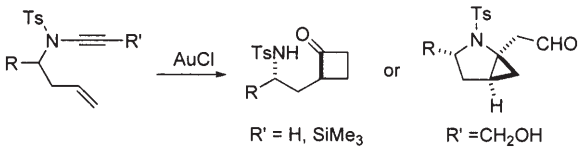

Around they go: 1,6-Ene-ynamides undergo highly diastereoselective gold-catalyzed cycloisomerizations that lead to functionalized cyclobutanones or carbonyl compounds with a 2-azabicyclo-[3.1.0]hexane subunit, depending on the substitution pattern (Ts = *p*-toluenesulfonyl).

Silicon Chemistry

M. Driess,* S. Yao, M. Brym, C. van Wüllen **6730 – 6733**

Low-Valent Silicon Cations with Two-Coordinate Silicon and Aromatic Character

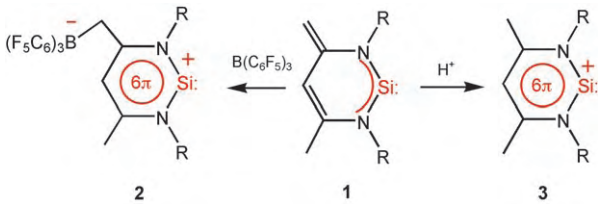

Desperately seeking silyenylium: Electrophilic attack of silylene **1** (R = 2,6-diisopropylphenyl) by $B(C_6F_5)_3$ and H^+ afforded the silylene-like zwitterion **2** and the "free" silyliumylidene cation **3** (in the presence of the noncoordinating $[B(C_6F_5)_4]^-$ anion), respectively. Cations **2** and **3** represent a novel class of low-coordinate silicon cations with promising potential for the synthesis of heteroleptic silylenes.

Homocyclic Phosphorus Compounds

J. J. Weigand,* N. Burford,* M. D. Lumsden, A. Decken **6733 – 6737**

A Melt Approach to the Synthesis of *catena*-Phosphorus Dications To Access Derivatives of $[P_6Ph_4R_4]^{2+}$

P analogues of cyclohexane: The first examples of hexaphosphorus homocyclic dications $[P_6Ph_4R_4]^{2+}$ (R = Ph, Me; see picture, P yellow, C dark gray) were prepared in a melt reaction from readily accessible starting materials in essentially quantitative yield. X-ray analysis of the dications reveals cyclohexane-like twist-boat and chair conformations of the phosphorus homocycle in the solid state.

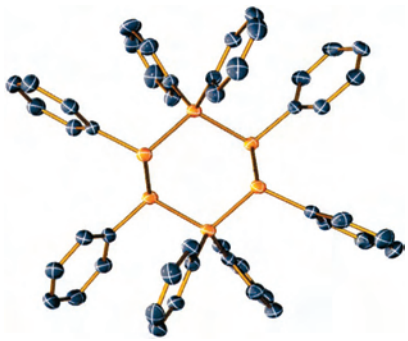

Biaryl Synthesis

B. O. Ashburn, R. G. Carter* **6737 – 6741**

Diels–Alder Approach to Polysubstituted Biaryls: Rapid Entry to Tri- and Tetra-*ortho*-substituted Phosphorus-Containing Biaryls

Rapid construction: A Diels–Alder-based approach to the synthesis of highly functionalized biaryls from readily available precursors is disclosed. The utility of these biaryl templates in palladium-mediated couplings is explored along with subsequent reductions of the nitro and phosphine oxide moieties. Finally, initial application of a synthesized biaryl as a highly active ligand in palladium-mediated coupling is carried out.

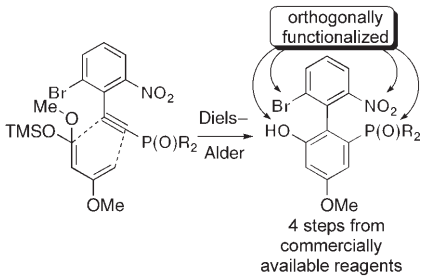

© 2006 Wiley-VCH Verlag GmbH & Co. KGaA, Weinheim

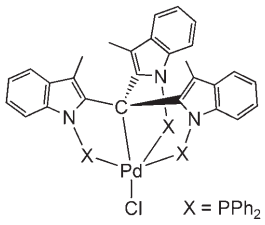

A C_3-symmetric palladium complex formed from a new readily accessible and rigid tripodal phosphorus-based ligand has no chirality in either of its pendent arms but is intrinsically chiral (see picture). The potential of the racemic complex as a catalyst is demonstrated in several Suzuki cross-coupling reactions. The enantiomerically pure compound is also tested for asymmetric catalysis in a model reaction.

Homogeneous Asymmetric Catalysis

M. Ciclosi, J. Lloret, F. Estevan, P. Lahuerta,* M. Sanaú, J. Pérez-Prieto* ——— **6741 – 6744**

A C_3-Symmetric Palladium Catalyst with a Phosphorus-Based Tripodal Ligand

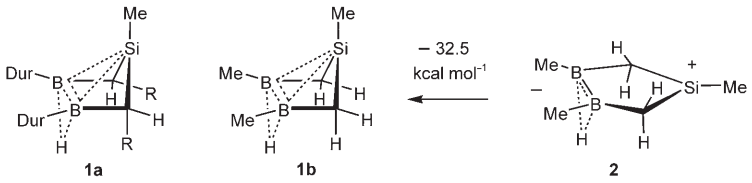

Charge separation in the reference molecules is the main reason for the unusually high aromatic stabilization energies (ASEs) of nonclassical 1-sila-3,4-diboracyclopentanes of type **1**. Compound **1a** was synthesized, and the ASE for its model compound **1b** was computed. In reference molecule **2** the two electrons, which are cyclically delocalized in **1b**, are localized in a B–B bond (R = $SiMe_3$, Dur = 2,3,5,6-tetramethylphenyl).

Homoaromatics

C. Präsang, P. Amseis, D. Scheschkewitz, G. Geiseler, W. Massa, M. Hofmann, A. Berndt* ——— **6745 – 6747**

Strong Neutral Homoaromatics

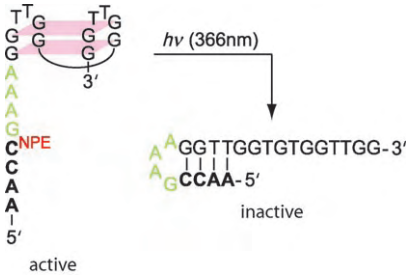

A light remedy to overdosing: Aptamers with an intramolecular "caged" antisense region remain active until they are irradiated. Upon irradiation, the antisense activity is released and the aptamer refolds into an inactive structure (see scheme).

Antisense Agents

A. Heckel,* M. C. R. Buff, M.-S. L. Raddatz, J. Müller, B. Pötzsch, G. Mayer* ——— **6748 – 6750**

An Anticoagulant with Light-Triggered Antidote Activity

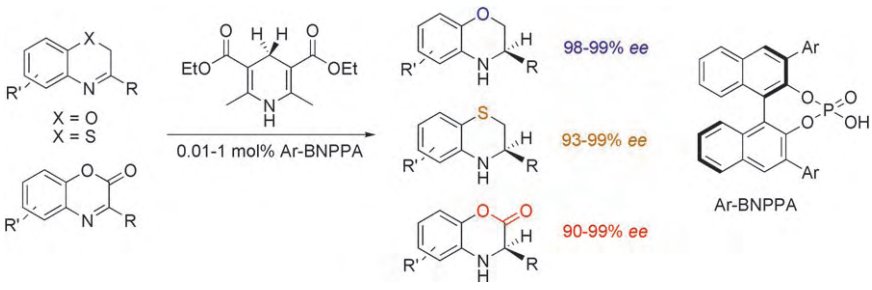

A highly efficient transfer hydrogenation of benzoxazines, benzothiazines, and benzoxazinones with as low as 0.01 mol% binol phosphate catalyst furnishes the dihydro-2*H*-benzoxazines, -benzothiazines, and -benzoxazinones in good yields and with excellent enantioselectivities (see scheme). Particularly noteworthy are the mild reaction conditions and the wide scope of substrates, including sulfur-containing compounds.

Brønsted Acid Catalysis

M. Rueping,* A. P. Antonchick, T. Theissmann ——— **6751 – 6755**

Remarkably Low Catalyst Loading in Brønsted Acid Catalyzed Transfer Hydrogenations: Enantioselective Reduction of Benzoxazines, Benzothiazines, and Benzoxazinones

© 2006 Wiley-VCH Verlag GmbH & Co. KGaA, Weinheim

Contents

Oligosilanes

U. Jäger-Fiedler, M. Köckerling, R. Ludwig, A. Wulf, C. Krempner* ____ **6755 – 6759**

Hydroxy-Substituted Oligosilane Dendrimers: Controlling the Electronic Properties through Hydrogen Bonding

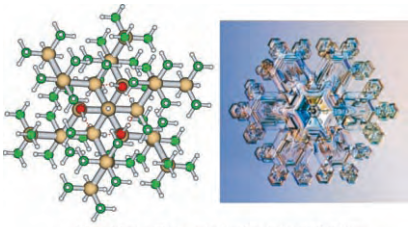

Reprinted with permission from Arash Partow, http://www.partow.net/miscellaneous/snowflakes.html

Reminiscent of a snowflake: The dimer of a hydroxy-substituted oligosilane dendrimer (see picture, left; Si yellow, C green, H white, O red) is remarkably stable according to IR spectroscopy and DFT calculations. Strong intermolecular hydrogen bonds are not only the glue that holds the "silicon snowflake" together, but are also the key to understanding the relationship between the conformation of the oligosilane backbone and its thermochromic behavior.

Antimicrobial Coatings

A. D. Fuchs, J. C. Tiller* ____ **6759 – 6762**

Contact-Active Antimicrobial Coatings Derived from Aqueous Suspensions

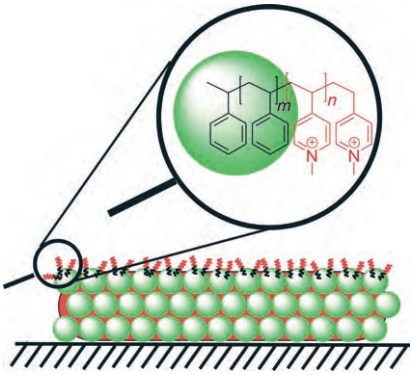

Kills germs on contact! Environmentally friendly aqueous dispersions of polymer nanobeads with a surface-grafted antimicrobial emulsifier were prepared. Coatings prepared from these dispersions (see picture) kill microbes on contact, without releasing a biocide.

WILEY InterScience®
DISCOVER SOMETHING GREAT

"Hot Papers" are chosen by the Editors for their importance in a rapidly evolving field of high current interest. A preview with the graphical abstracts of these articles can be found on the *Angewandte Chemie* homepage in Wiley InterScience at www.angewandte.org.

All articles in *Angewandte Chemie* are published online several weeks ahead of print. They are found under the "EarlyView" link on the journal's homepage in Wiley InterScience.

Service

Keywords ____ *6764*

Authors ____ *6765*

Angewandte's Sister Journals ____ *6763*

Preview ____ *6767*

For more information on ChemMedChem see www.chemmedchem.org

© 2006 Wiley-VCH Verlag GmbH & Co. KGaA, Weinheim

Corrigenda

The authors have recently determined that the structure of the proposed [4+3] oxidative cyclization product **35** (see Scheme 7 in the original Communication) was incorrectly assigned. The previous structure (**35**) as well as the revised structure (**35′**) are shown below. The authors apologize for the error, but point out that the chemistry leading up to the oxidative cyclization reported in Scheme 7 is correct.

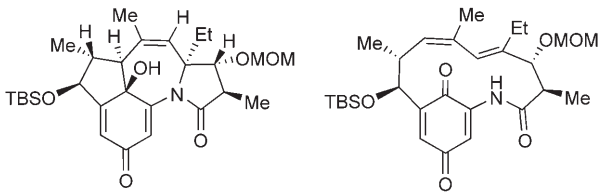

35
(original structure)

35'
(revised structure)

Synthesis of the Tetracyclic Core of the Tetrapetalones through Transannular Oxidative [4+3] Cyclization

X. Wang, J. A. Porco, Jr.* ____ **3067–3071**

Angew. Chem. Int. Ed. **2005**, *44*

DOI 10.1002/anie.200500247

In Figure 1 B of this Communication, the tile labels in the annealing structure scheme appeared incorrectly. The correct numbering is shown below (Figure 1).

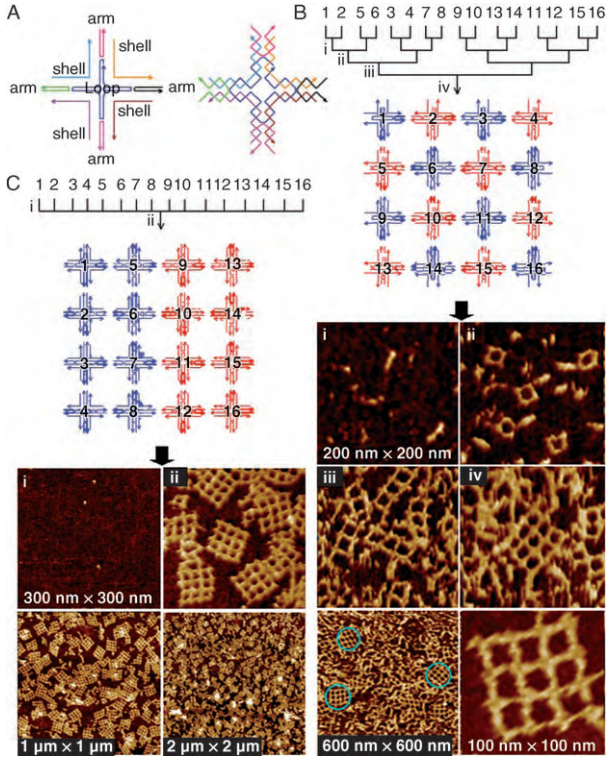

Finite-Size, Fully Addressable DNA Tile Lattices Formed by Hierarchical Assembly Procedures

S. H. Park, C. Pistol, S. J. Ahn, J. H. Reif, A. R. Lebeck, C. Dwyer,* T. H. LaBean* _____ **735–739**

Angew. Chem. Int. Ed. **2006**, *45*

DOI 10.1002/anie.200503797

Figure 1. DNA tile and NA structures and assembly schemes. A) Schematic drawings of the strand trace in cross tiles with strand names marked (arm, shell, and loop). B) MSS strategy and constructs. A converging-stream diagram of the four-step assembly process starting with eight tubes of two tiles each (i) and concluding with one tube containing all 16 tiles (iv). The blue and red diagram shows the placement of tiles (1 through 16) in the NA and the identity of loop strands (A-loops are blue and B-loops are red). The bottom six panels are AFM height images with dimensions as labeled and height scale from 0 to 3 nm. Panels i)–iv) correspond to the same labels as in the annealing scheme above; thus, i) 1×2 NA, ii) 2×2 NA, iii) 2×4 NA, and iv) 4×4 NA. The two bottom AFM images are zoom-out and zoom-in pictures of (iv), with error-free NAs in the zoom-out image circled in turquoise. C) MD strategy and constructs. A converging-stream diagram of the two-step assembly starts with 16 tubes with one tile each (i) and goes directly to one tube of 16 tiles (ii). The blue and red diagram shows the placement of A-loop and B-loop tiles in the final NA. The bottom four panels are AFM height images with i) showing single tiles and ii) showing complete 4×4 NAs. The two bottom panels are zoom-out images to show the increased production yield of defect-free assemblies from the two-step method.

 © 2006 Wiley-VCH Verlag GmbH & Co. KGaA, Weinheim

Awarded...

E. Nakamura receives Humboldt Prize

Eiichi Nakamura (University of Tokyo) will join the groups of J. Okuda and C. Bolm at RWTH Aachen University (Germany) this autumn and next summer to carry out research work thanks to a Humboldt Research Award from the Alexander von Humboldt Foundation. The main research themes of his own group are focused on new organometallic intermediates and catalysis, organometallic mechanisms of important synthetic reactions, carbon cluster complexes in material science, and the nanoscience of custom-made cluster molecules in biology. He recently reported in *Chemistry – An Asian Journal* on gene delivery by aminofullerene with a focus on structural requirements for efficient transfection,[1a] as well as the mechanism of remote conjugate addition of lithium organocuprates to polyconjugated carbonyl compounds.[1b] He serves on the editorial board for *Chemistry – An Asian Journal* as well as the international advisory board of *Angewandte Chemie*.

E. Nakamura

Nakamura completed his undergraduate studies and doctorate (1978; I. Kuwajima) at the Tokyo Institute of Technology, before joining G. Storck at Columbia University (NY, USA) as a postdoctoral researcher. In 1980 he joined the Tokyo Institute of Technology as an assistant professor and became a full professor there in 1993. Since 1995, he has been a professor at the University of Tokyo. Other honors include receiving the Silver Nagoya Medal (2001) and the Chemical Society of Japan's Prize (2003).

Degussa Prize for T. Bach

Thorsten Bach (Technical University Munich, Germany) has received the Award for Chirality in Chemistry from Degussa AG (Düsseldorf, Germany). The award, which has a value of €5000, was established in 2004 to recognize young chemists for their innovative work in chiral chemistry. Bach is recognized in particular for his work in the area of asymmetric catalysis and photochemistry; he recently reported on enantiomerically pure bicyclo[4.2.0]octanes by Cu-catalyzed [2+2] photocycloaddition and enantiotopos-differentiating ring opening in *Angewandte Chemie*.[2] Besides this topic, his research group is interested in heterocylic chemistry and the synthesis of biologically active substances to establish structure–activity relationships of antibiotic and cytotoxic compounds.

T. Bach

Bach carried out his undergraduate studies at the University of Heidelberg and at the University of Southern California (USA) with G. A. Olah (Nobel Prizewinner, 1994). He completed his PhD in 1991 with M. T. Reetz at the University of Marburg and then joined D. A. Evans at Harvard University (Cambridge, MA, USA) as a postdoctoral researcher. He carried out his habilitation studies at the University of Münster (1992–96). Following a visiting professorship in Helsinki, Bach returned to Münster as a professor in 1997. In 2000 he joined the Technical University Munich. Earlier this year, he was elected a Member of the German Academy of Sciences, Leopoldina.

Bessel Prize for J. Dupont

Jairton Dupont (Universidade Federal do Rio Grande do Sul (UFRGS), Porto Alegre, Brazil) has been recognized with a Friedrich Wilhelm Bessel Prize. The prize is awarded by the Alexander von Humboldt Foundation to young scientists from abroad who already are recognized as outstanding researchers in their fields. The award will allow Dupont to spend some time as a collaborative researcher with J. Gladysz at the University of Erlangen-Nürnberg (Germany).

Dupont studied chemistry at the Pontifícia Universidade Católica do Rio Grande do Sul in Porto Alegre (Brazil) and completed his PhD in 1988 under the guidance of M. Pfeffer at the Université Louis Pasteur in Strasbourg (France). Following a postdoctoral fellowship with S. G. Davies at the University of Oxford (UK), he joined the UFRGS at Porto Alegre as a visiting scientist, and in 1992 he was appointed a professor of organic chemistry there. He has since returned as a professor to Strasbourg (2000 and 2004) and also spent time at Erlangen-Nüremberg (2005–2006). The research interests of his group are focused on synthetic organometallic chemistry, with an emphasis on homogeneous and biphasic catalysis in ionic liquids. He recently reported in *Advanced Synthesis & Catalysis* on a copper-free catalytic system for the arylation of alkynes[3a] and on halide-free imidazolium ionic liquids.[3b] He also highlighted the non-innocent nature of 1,3-dialkylimidazolium ionic liquids in *Angewandte Chemie*.[3c]

J. Dupont

[1] a) H. Isobe, W. Nakanishi, N. Tomita, S. Jinno, H. Okayama, E. Nakamura, *Chem. Asian J.* **2006**, *1*, 167; b) N. Yoshikai, T. Yamashita, E. Nakamura, *Chem. Asian J.* **2006**, *1*, 322.

[2] I. Braun, F. Rudroff, M. D. Mihovilovic, T. Bach, *Angew. Chem.* **2006**, *118*, 5667; *Angew. Chem. Int. Ed.* **2006**, *45*, 5541.

[3] a) C. S. Consorti, F. R. Flores, F. Rominger, J. Dupont, *Adv. Synth. Catal.* **2006**, *348*, 133; b) C. C. Cassol, G. Ebeling, B. Ferrera, J. Dupont, *Adv. Synth. Catal.* **2006**, *348*, 243; c) J. Dupont, J. Spencer, *Angew. Chem.* **2004**, *116*, 5408; *Angew. Chem. Int. Ed.* **2004**, *43*, 5296.

DOI: 10.1002/anie.200603737

WILEY InterScience DISCOVER SOMETHING GREAT

© 2006 Wiley-VCH Verlag GmbH & Co. KGaA, Weinheim

Dateiname: G603737E
Seite: 1 te von 1
Status Neusatz
Sprache

Pagina: 6608
Umfang (Seiten): 1
Datum: 41 KW., 9. Oktober 2006 (Montag)
Zeit: 6:10:59 Uhr

Aerobic Oxidations

DOI: 10.1002/anie.200602138

Mechanistic Questions about the Reaction of Molecular Oxygen with Palladium in Oxidase Catalysis**

*Keith M. Gligorich and Matthew S. Sigman**

Keywords:
homogeneous catalysis · molecular oxygen · oxidation · palladium · reaction mechanisms

Oxidation reactions are essential for both manipulation of functional groups and introduction of heteroatoms in target synthesis. Therefore, the development of selective, practical oxidation reactions is a continuing challenge facing chemists in both academia and industry.[1] A key consideration in developing oxidation reactions is selection of the stoichiometric oxidant where versatility, expense, and environmental impact need to be addressed. An attractive approach is the use of metal-catalyzed oxidations coupled to the reduction of a practical terminal oxidant.[2] As an example, Pd-catalyzed oxidations have emerged as a particularly promising reaction type owing to their ability to directly couple O_2 reduction.[3]

An important aspect of Pd-catalyzed oxidation chemistry is that the catalysis can be separated into two distinct half reactions: 1) substrate oxidation using Pd^{II} (generally a dehydrogenation reaction) and 2) O_2-coupled regeneration of the active Pd^{II} catalyst with ultimate formation of H_2O from disproportionation of H_2O_2 (Scheme 1).[3a] Thus, Pd-catalyzed oxidations have been termed "oxidase"-type reactions wherein substrate oxidation does not occur by oxygen-atom transfer from O_2. Oxidase catalysis has broad implications in the development of new reactions, in that nearly all catalyzed oxidative transformations of an organic substrate can be coupled to O_2 reduction. This is highlighted by the diversity of Pd^{II}-catalyzed aerobic oxidative transformations such as oxidative amination,[3,4] alcohol oxidation,[3,5] Wacker-type reactions,[3,6] and oxidative Heck reactions.[3,7]

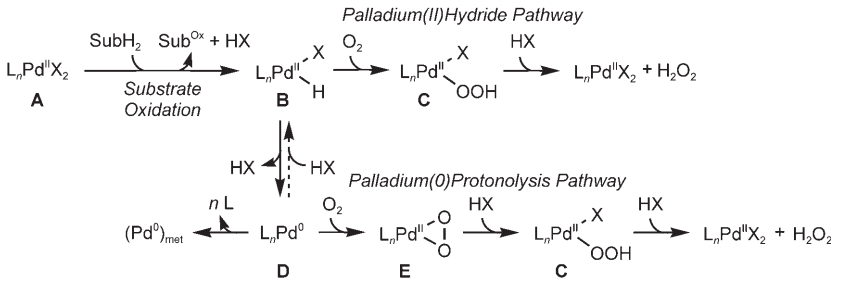

Scheme 1. Two pathways for the regeneration of the active Pd^{II} catalyst from the reaction of Pd complexes with O_2. $SubH_2$ = substrate; Sub^{Ox} = oxidized substrate.

Because substrate oxidation is often rate-limiting in Pd oxidative catalysis,[5c,8] it has been difficult to mechanistically characterize how O_2 interacts with the Pd center in the catalysis. Interestingly, the reaction of triplet-state O_2 with a Pd center is formally a spin-forbidden process,[9] and this leads to the question: how does O_2 readily react with Pd? Insight into this question will be crucial for the development of new and more efficient direct O_2-coupled Pd-catalyzed oxidative transformations. This highlight describes what has been ascertained about the interactions of O_2 with both Pd^{II} and Pd^0 complexes and the implications this has for catalysis.

Two different pathways have been proposed for the reaction of Pd complexes with O_2 (Scheme 1). The first mechanistic possibility is the direct insertion of O_2 into a Pd^{II} hydride **B** to produce a Pd^{II} hydroperoxide species **C**, which upon protonation releases H_2O_2 and reforms the Pd^{II} catalyst (Scheme 1, top pathway).[10] It should be noted that this pathway need not proceed through Pd^0. The other commonly proposed pathway involves formation of Pd^0 species **D** by reductive elimination of HX from complex **B** and subsequent oxygenation of **D** to yield an η^2-peroxido Pd^{II} species **E**.[11] Protonation of **E** leads to formation of a similar Pd^{II} hydroperoxide intermediate **C**, again with a second protonation liberating H_2O_2 and the active Pd^{II} catalyst (Scheme 1, bottom pathway).

In these oxidation reactions, the precipitation of Pd metal is common and most likely stems from the aggregation of Pd^0 centers that are produced in the catalysis. This issue has affected both the development of improved catalysts and characterization of the key intermediates involved in Pd–O_2 interactions. To overcome catalyst-decomposition issues, several groups have recently utilized oxidatively stable mono- and bidentate nitrogen-containing ligands[3–7] and N-heterocyclic carbene (NHC) ligands for these transformations (Figure 1).[3,5c,12] The use of these ligands has allowed for the development

[*] K. M. Gligorich, Prof. M. S. Sigman
Department of Chemistry
University of Utah
315 S. 1400 E.
Salt Lake City, UT 84112 (USA)
Fax: (+1) 801-581-8433
E-mail: sigman@chem.utah.edu

[**] We thank the National Institutes of Health (NIGMS RO1 GM3540) for financial support.

InterScience
© 2006 Wiley-VCH Verlag GmbH & Co. KGaA, Weinheim

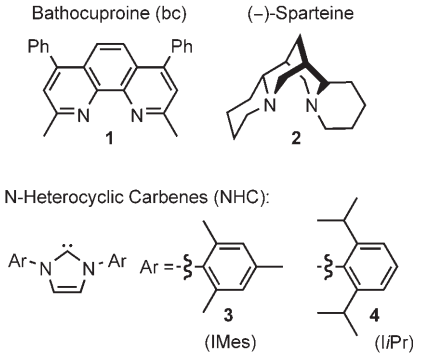

Figure 1. Examples of oxidatively stable ligands employed in aerobic Pd-catalyzed oxidative transformations.

of more reactive and robust catalysts for Pd-catalyzed oxidations capable of high turnover numbers at lower pressures of oxygen.[3,5c,13] Moreover, and of fundamental importance, the use of ligands has also allowed researchers to kinetically and structurally characterize the reactions of both Pd^{II} and Pd^0 complexes with O_2.

Using both bathocuproine (bc)[11a] and NHC ligands,[11b] Stahl and co-workers have studied the stoichiometric reactions of Pd^0 complexes with O_2 to probe the possibility of direct oxygenation of Pd^0 (Scheme 2). Indeed, upon exposure of both the $[Pd^0(bc)(dba)]$ (dba = dibenzylideneacetone) complex and the $[Pd^0(IMes)_2]$ complex **5** to O_2, the expected η^2-peroxido species were isolated. Both Pd^{II} η^2-peroxido complexes were subsequently exposed to acetic acid. Interestingly, only $[Pd^0(IMes)_2]$ produced a Pd^{II} hydroperoxide complex **7**, which was the first example of a dioxygen-derived Pd^{II} hydroperoxide complex. The authors reasoned that rapid *cis–trans* ligand isomerization of complex **7** slows the approach of a second equivalent of acid, which is required to liberate H_2O_2 and complex **9**.

Mechanistic studies on the oxygenation of $[Pd^0(bc)(dba)]$ showed a first-order dependence on $[O_2]$ and no dependence of the reaction rate upon addition of up to 10 equivalents of dba.[11a] Furthermore, activation parameters obtained from a temperature-dependent study revealed a substantial negative entropy of activation, $\Delta S^{\neq} = -43(7)\,cal\,K^{-1}\,mol^{-1}$. Together, these data support an associative oxygenation

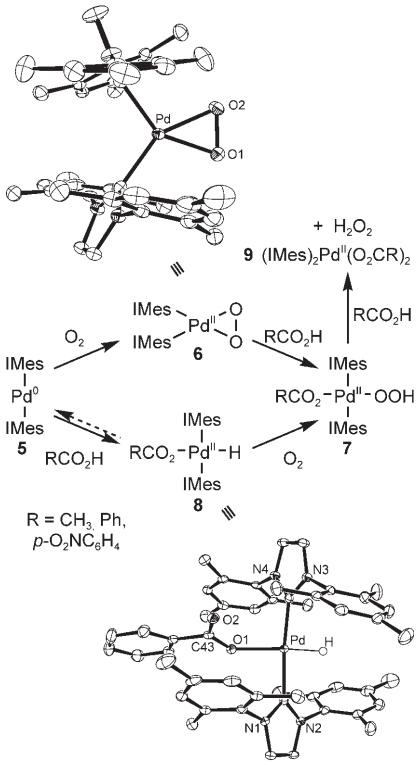

Scheme 2. The reaction of **5** with O_2 and a carboxylic acid.

reaction, which more closely resembles an olefin substitution rather than an oxidative addition. Interestingly, the oxygenation of $[Pd^0(bc)(dba)]$ typically takes 20–30 minutes at room temperature, while the $[Pd^0(IMes)_2]$ complex reacts extremely rapidly with O_2 even at −78 °C. This observation suggests that the oxygenation of $[Pd^0(bc)(dba)]$ could be occurring by an associative olefin substitution (loss of dba), whereas a direct oxygenation pathway may be occurring for the $[Pd^0(IMes)_2]$ complex. It is important to note that under typical catalytic conditions Pd^{II} salts are used and dba would not be present. Therefore, more efficient oxygenation of $[Pd^0(bc)]$ would be expected under catalytic conditions.

Even though there is substantial experimental evidence for the oxygenation of Pd^0, the reaction of triplet-state oxygen and Pd^0 is formally spin-forbidden. Landis, Stahl, and co-workers investigated this question by using spin-unrestricted density functional theory (DFT).[9a] The results of their study indicate an exothermic reaction, which produces a triplet diradical Pd^I η^1-superoxide intermediate, and a triplet-to-singlet surface crossing ultimately yields the Pd^{II} peroxido complex **C** (Scheme 1). The formation of the di radical, with one spin localized on oxygen and one on the Pd center allows for a low kinetic barrier. Crossover to the singlet state is most likely facilitated by the relatively large spin–orbit coupling of the Pd center.

Experimental and theoretical evidence supports the direct oxygenation of Pd^0, but can O_2 insert directly into a Pd^{II} hydride? Stahl and co-workers investigated this possibility by subjecting $[Pd^0(IMes)_2]$ to one equivalent of a carboxylic acid, which produced the Pd^{II} hydride **8** (Scheme 2).[14] Subsequent exposure of **8** to O_2 yielded the Pd^{II} hydroperoxide complex **7**. The formation of the Pd^{II} hydroperoxide supports a direct insertion pathway. An alternate pathway of reductive elimination of HX from **8** to yield $[Pd^0(IMes)_2]$ and subsequent oxygenation and protonation would produce the same species and cannot be ruled out. Kinetic measurements of the reaction revealed a first-order dependence on the concentration of Pd hydride **8**, and the rate of oxygenation with *p*-nitrobenzoate is almost eightfold faster than when benzoate is used as a ligand. The ligand dependence suggests the possibility of rate-limiting carboxylate dissociation followed by oxygenation. However, the current data could support either a direct insertion pathway or a slow reductive elimination followed by fast oxygenation and is therefore insufficient to differentiate the two pathways.

In this system, a linear increase of the rate of oxygenation was observed with respect to the addition of exogenous benzoic acid, which was unexpected owing to the possibility of pre-equilibrium reductive elimination of HX from complex **8**, which would inhibit the formation of $[Pd^0(IMes)_2]$. While the origin of these results is the subject of future studies, these initial data point toward either rate-limiting carboxylate dissociation or the possibility of protonation of the Pd^{II} η^2-peroxido species **6** in the rate-limiting step. Our group has observed a similar dependence upon addition of exogenous acid in the $[Pd^{II}(IiPr)(OAc)_2]$-catalyzed aerobic oxidation of alcohols (Scheme 3).[5c] Kinetic measurements

© 2006 Wiley-VCH Verlag GmbH & Co. KGaA, Weinheim

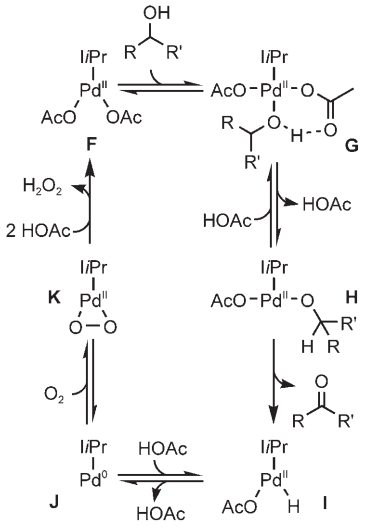

Scheme 3. Proposed mechanism of the [Pd^{II}-(I*i*Pr)$(OAc)_2$]-catalyzed aerobic oxidation of alcohols.

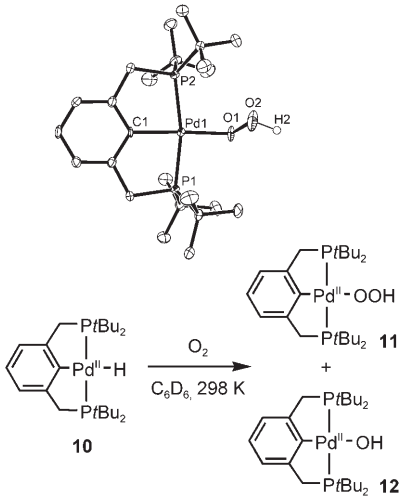

Scheme 4. Insertion of O_2 into a Pd^{II} hydride.

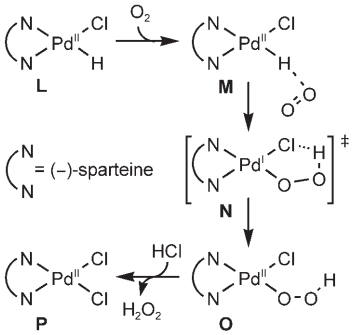

Scheme 5. Mechanism proposed by Goddard et al. for O_2 insertion into [Pd{(−)-sparteine}-H(Cl)] (**L**) in toluene.

of the oxidation reaction with greater than 2 mol% of exogenous acetic acid suggests that β-hydride elimination of the Pd^{II} alkoxide intermediate **H** is rate-limiting. However, at lower concentrations of acetic acid (0–0.62 mol%) competitive turnover-limiting protonation of a Pd^{II} peroxido species **K** is proposed based upon kinetic isotope effect (KIE) measurements and a partial positive order on the concentration of acetic acid. Catalyst decomposition occurs with no added acetic acid and can be attributed to reversible oxygenation of the [Pd^0(I*i*Pr)] complex **J**. Therefore, increasing the concentration of acetic acid enhances the rate of protonation of the Pd^{II} peroxido species **K** while simultaneously decreasing the rate of alcohol oxidation by protonation of the Pd^{II} alkoxide **H** which yields intermediate **G**. These results suggest that the addition of exogenous acid can prevent the formation of metallic palladium by increasing the rate of catalyst turnover in aerobic Pd-catalyzed oxidative transformations.

Because of the potential for a pre-equilibrium reductive elimination of HX from complex **8**, the question of whether O_2 can directly insert into a Pd^{II} hydride remains. Goldberg, Kemp, and co-workers have recently reported the reaction of O_2 with complex **10**, which cannot undergo reductive elimination (Scheme 4).[15] Exposure of **10** to O_2 yielded the expected Pd^{II} hydroperoxide **11** and the Pd^{II} hydroxide **12** in a 25:1 ratio. This is the first example of what is assumed to be a direct insertion of O_2 into a Pd^{II} hydride.

Kinetic measurements of the reaction indicated a first-order dependence on **10** and also a first-order dependence upon oxygen pressure. A large KIE of 5.8(5) was measured for the insertion of O_2 into the Pd^{II}–H(D) bond, which indicates Pd^{II}–hydride bond cleavage in the rate-determining step. In order to rule out the possibility of a radical-chain pathway, the authors performed the reaction in the presence of radical inhibitors 2,6-di-*tert*-butyl-4-hydroxytoluene (BHT) and 2,2,6,6,-tetramethyl-1-piperidinyloxy free radical (TEMPO), whereby no significant change in the rate of the reaction was observed.[16] Additionally, no substantial rate difference was measured for the disappearance of **10** when the reactions were performed in the dark and under ambient light. However, Pd^{II} hydroperoxide **11** in a benzene solution at room temperature slowly converts into the Pd^{II} hydroxide **12**. This reaction was accelerated in the presence of light and suggests a radical pathway similar to the decomposition of organic peroxide analogues like *tert*-butyl hydroperoxide to *tert*-butyl alcohol and O_2.[17]

Together, these data support a mechanism involving either coordination of O_2 to the Pd^{II} hydride and subsequent migratory insertion or direct insertion of O_2 into a Pd^{II}–hydride bond. In support of these hypotheses, Goddard and co-workers have recently disclosed a theoretical study of the direct insertion of O_2 into a [Pd^{II}{(−)-sparteine}H(Cl)] complex **L** and a [Pd^{II}(bipyridine)H(Cl)] complex, which yields the respective Pd^{II} hydroperoxides (Scheme 5).[9b] The results of their DFT study indicate initial hydrogen bonding of triplet O_2 directly to the hydride intermediate **M**. Insertion of O_2 yields a triplet Pd^{I} hydroperoxide complex **N**, in which the proton of the hydroperoxido ligand is hydrogen-bound to the anionic ligand. Subsequent spin transition to the singlet Pd^{II} hydroperoxide yields intermediate **O**, which after protonation leads to the formation of both the active catalyst and H_2O_2.

In conclusion, oxygenation of Pd^0 and direct insertion of O_2 into a Pd^{II}–hydride bond have both been shown to be possible pathways for the reaction between O_2 and Pd complexes. Experimental and theoretical evidence support the viability of both mechanisms, but further experimental work will be required to elucidate the details of these pathways in which ligand and additives will most likely have a profound influence. It should be noted that these studies do not mimic catalytic conditions, and it is anticipated that characterizing the intermediates/pathways under truly catalytic conditions will be quite challenging. However, the insights garnered from these studies showcase why Pd/ligand-catalyzed aerobic oxidation chemistry is a rapidly growing field.

Published online: September 20, 2006

 © 2006 Wiley-VCH Verlag GmbH & Co. KGaA, Weinheim

[1] S. S. Stahl, *Science* **2005**, *309*, 1824 – 1826.

[2] T. Punniyamurthy, S. Velusamy, J. Iqbal, *Chem. Rev.* **2005**, *105*, 2329 – 2364.

[3] a) For a comprehensive review of Pd-catalyzed O_2-coupled oxidations, see: S. S. Stahl, *Angew. Chem.* **2004**, *116*, 3480 – 3501; *Angew. Chem. Int. Ed.* **2004**, *43*, 3400 – 3420; b) for related reviews, see: M. S. Sigman, M. J. Schultz, *Org. Biomol. Chem.* **2004**, *2*, 2551 – 2554; c) T. Nishimura, S. Uemura, *Synlett* **2004**, 201 – 216; d) B. M. Stoltz, *Chem. Lett.* **2004**, 362 – 367.

[4] a) V. I. Timokhin, S. S. Stahl, *J. Am. Chem. Soc.* **2005**, *127*, 17888 – 17893; b) J. L. Brice, J. E. Harang, V. I. Timokhin, N. R. Anastasi, S. S. Stahl, *J. Am. Chem. Soc.* **2005**, *127*, 2868 – 2869.

[5] For recent reviews of Pd-catalyzed alcohol oxidations, see: a) R. A. Sheldon, I. W. C. E. Arends, G.-J. ten Brink, A. Dijksman, *Acc. Chem. Res.* **2002**, *35*, 774 – 781; b) J. Muzart, *Tetrahedron* **2003**, *59*, 5789 – 5816; c) M. S. Sigman, D. R. Jensen, *Acc. Chem. Res.* **2006**, *39*, 221 – 229.

[6] a) For a recent review of Wacker oxidations, see: J. M. Takacs, X.-t. Jiang, *Curr. Org. Chem.* **2003**, *7*, 369 – 396; b) T. Mitsudome, T. Umetani, N. Nosaka, K. Mori, T. Mizugaki, K. Ebitani, K. Kaneda, *Angew. Chem.* **2006**, *118*, 495 – 499; *Angew. Chem. Int. Ed.* **2006**, *45*, 481 – 485; c) D. Yang, B.-F. Zheng, Q. Gao, S. Gu, N.-Y. Zhu, *Angew. Chem.* **2006**, *118*, 261 – 264; *Angew. Chem. Int. Ed.* **2006**, *45*, 255 – 258, and references therein.

[7] For recent examples, see: a) C. H. Yoon, K. S. Yoo, S. W. Yi, R. K. Mishra, K. W. Jung, *Org. Lett.* **2004**, *6*, 4037 – 4039; b) M. M. S. Andappan, P. Nilsson, H. von Schenck, M. Larhed, *J. Org. Chem.* **2004**, *69*, 5212 – 5218.

[8] B. A. Steinhoff, S. S. Stahl, *J. Am. Chem. Soc.* **2006**, *128*, 4348 – 4355, and references therein.

[9] a) C. R. Landis, C. M. Morales, S. S. Stahl, *J. Am. Chem. Soc.* **2004**, *126*, 16302 – 16303; b) J. M. Keith, R. J. Nielsen, J. Oxgaard, W. A. Goddard III, *J. Am. Chem. Soc.* **2005**, *127*, 13172 – 13179.

[10] a) K. Takehira, T. Hayakawa, H. Orita, M. Shimizu, *J. Mol. Catal.* **1989**, *53*, 15 – 21; b) T. Hosokawa, S. Murahashi, *Acc. Chem. Res.* **1990**, *23*, 49 – 54; c) T. Hosokawa, T. Nakahira, M. Takano, S. Murahashi, *J. Mol. Catal.* **1992**, *74*, 489 – 498; d) T. Nishimura, T. Onoue, K. Ohe, S. Uemura, *J. Org. Chem.* **1999**, *64*, 6750 – 6755.

[11] a) S. S. Stahl, J. L. Thorman, R. C. Nelson, M. A. Kozee, *J. Am. Chem. Soc.* **2001**, *123*, 7188 – 7189; b) M. M. Konnick, I. A. Guzei, S. S. Stahl, *J. Am. Chem. Soc.* **2004**, *126*, 10212 – 10213.

[12] a) D. R. Jensen, M. J. Schultz, J. A. Mueller, M. S. Sigman, *Angew. Chem.* **2003**, *115*, 3940 – 3943; *Angew. Chem. Int. Ed.* **2003**, *42*, 3810 – 3813; b) C. C. Scarborough, B. V. Popp, I. A. Guzei, S. S. Stahl, *J. Organomet. Chem.* **2005**, *690*, 6143 – 6155; c) C. C. Scarborough, M. J. W. Grady, I. A. Guzei, B. A. Gandhi, E. E. Bunel, S. S. Stahl, *Angew. Chem.* **2005**, *117*, 5403 – 5406; *Angew. Chem. Int. Ed.* **2005**, *44*, 5269 – 5272; d) M. M. Rogers, J. E. Wendlandt, I. A. Guzei, S. S. Stahl, *Org. Lett.* **2006**, *8*, 2257 – 2260.

[13] T. Iwasawa, M. Tokunaga, Y. Obora, Y. Tsuji, *J. Am. Chem. Soc.* **2004**, *126*, 6554 – 6555.

[14] M. M. Konnick, B. A. Gandhi, I. A. Guzei, S. S. Stahl, *Angew. Chem.* **2006**, *118*, 2970 – 2973; *Angew. Chem. Int. Ed.* **2006**, *45*, 2904 – 2907.

[15] M. C. Denney, N. A. Smythe, K. L. Cetto, R. A. Kemp, K. I. Goldberg, *J. Am. Chem. Soc.* **2006**, *128*, 2508 – 2509.

[16] D. D. Wick, K. I. Goldberg, *J. Am. Chem. Soc.* **1999**, *121*, 11900 – 11901.

[17] R. R. Hiatt, T. Mill, F. R. Mayo, *J. Org. Chem.* **1968**, *33*, 1416 – 1420.

© 2006 Wiley-VCH Verlag GmbH & Co. KGaA, Weinheim

Cyclobutadiene

DOI: 10.1002/anie.200602279

Cyclobutadiene: The Antiaromatic Paradigm?

*Thomas Bally**

Keywords:
antiaromaticity · cyclobutadiene · thermochemistry

In memory of Satoru Masamune (1928–2003)

There is probably no other single molecule that has fascinated experimental and theoretical chemists so consistently over the past 40 years as has cyclobutadiene (CBD). On average, 16 publications which deal, in one form or another, with the parent compound C_4H_4 and 40 which deal with cyclobutdienes in general have appeared in every year of this time span, and there are probably many more on derivatives and metal complexes. There is no sign that interest in CBD is about to wane, as the highest number of papers per year appeared in 2000 and 2002, and in the last five years two entire thematic issues of *Chemical Reviews*, both with many references to CBD, were dedicated to issues of aromaticity/antiaromaticity[1] and localization/delocalization,[2] that is, topics that are central to the debate on CBD.

Recently the first direct and reasonably accurate determination of the enthalpy of formation of CBD has been achieved by the group of Kass.[3,4] Thus they have provided a solid foundation for the discussion on the thermochemical consequences of antiaromaticity, and I take this occasion to reflect on recent developments in this field and to point out the pitfalls with which the resulting discussion is fraught.

In spite of the great activity documented in the opening paragraph, many myths surround this fascinating molecule, most of which relate to the extent of delocalization of its π electrons and/or the degree of antiaromaticity. It is widely accepted (and hardly disputed) that benzene, with its six cyclically delocalized π electrons, represents the paradigm of aromaticity. In view of the famous Hückel $4n/4n+2$ electron rule, one is tempted to rush to the conclusion that CBD, with its four cyclically delocalized π electrons, is therefore the paradigm of antiaromaticity.

However, this conclusion is not as straightforward as it might seem, because in benzene the two Kekulé resonance structures contribute with equal weights to the D_{6h} equilibrium geometry, whereas in CBD, with its rectangular structure having strongly localized single and double bonds, this is obviously not the case. Thus the notion of "bond delocalization" does not have the same meaning in the two compounds, and one of the issues of the continuing debate is to what extent this affects the properties that are associated with (anti)aromaticity. Another issue is of course how exactly one should or should not assess these properties. I will comment herein on some aspects of this debate.

Various criteria have been proposed over time to judge whether a molecule is aromatic or not (it is perhaps worth recalling that the term "aromatic" itself implies that a pleasant odor must at one time have been considered as an important criterion; thus, by the same token, antiaromatic compounds should smell unpleasantly), and it was generally assumed that several of these criteria have to be met for a molecule to qualify for this distinction.

Two types of characteristic traits of aromaticity have emerged as "beacon" features. The first relates to magnetic properties, in particular the anisotropy of the diamagnetic susceptibility and its exaltation, which distinguishes aromatic compounds from polyenes. Following suggestions by Pauling and Londsdale, London proposed in 1937 a very appealing model that accounts for these effects in terms of ring currents that are induced by the external magnetic field in the system of cyclically delocalized π electrons.[5]

There has been a vigorous debate in recent years about whether and to what extent these ring currents contribute to the deshielding or shielding of protons attached to aromatic or antiaromatic rings, respectively,[6–8] as manifested in ^{1}H NMR spectra. At the focus of this debate stand the "nuclear independent chemical shifts" (NICS values)[9] that can be computed at any point in the space surrounding a molecule. It has become clear that the original proposal[9] to calculate NICS values at the center of (anti)aromatic rings does not provide a valid measure of currents induced in the cycle of π electrons. However, it seems that the sign and magnitude of the π component of the magnetic-shielding (or NICS) tensor at some distance (usually 1 Å) above the ring provides a good indication of the direction and size of the ring current, even in systems that have only σ electrons.[10]

However, I will focus herein on the other class of "beacon" properties that are characterictic of (anti)aromaticity, namely thermochemical and/or kinetic ones (the two often being mixed up). Clearly, benzene enjoys a special thermodynamic stability which expresses itself, for example, in the fact that its (mono)hydrogenation is endothermic by 22 kJ mol^{-1} (Scheme 1), in contrast to that of hexatriene, which is exothermic by about 114 kJ mol^{-1} (the exact number depends on the choice of conformations). As there is no evident reason why one or the other of the conjugated dienes that result from these hydrogenations should suffer from any

[*] Prof. T. Bally
Chemistry Department
University of Fribourg
1700 Fribourg (Switzerland)
E-mail: thomas.bally@unifr.ch
Homepage:
http://www-chem.unifr.ch/tb/bally/

InterScience
© 2006 Wiley-VCH Verlag GmbH & Co. KGaA, Weinheim

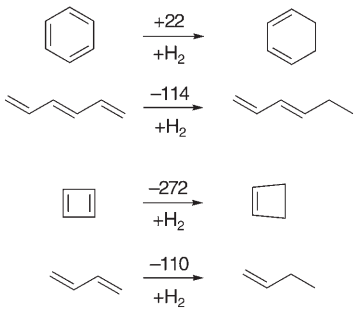

Scheme 1. Heats of hydrogenation of various compounds in kJ mol^{-1}.[11]

special destabilization, and because both compounds may be regarded as essentially strain-free, the 136 kJ mol^{-1} difference must a result of some special stability of benzene compared to hexatriene. By the same token, the high exothermicity of the hydrogenation of CBD is an indication of a similar thermochemical destabilization of this compound (relative to butadiene, for example).

As long as the argument remains on such a semiquantitative level, there is no problem. However, if one wants to quantitate the "(anti)aromatic (de)stabilization energy" more precisely, one invariably hits upon the question of what exactly one should take as a reference, which could be either a real molecule or a theoretical construct.[12] There is an enormous body of literature dealing with this very controversial question, literature which has been reviewed elsewhere.[13] However, an important point is that one should carefully distinguish between the total energy that is gained by putting double bonds into (linear or cyclic) conjugation and the energy gained (or lost) *exclusively by virtue of the conjugation being cyclic*. The difference of these two energies may be termed "conjugation energy" because it accounts for conjugation, but not for cyclic resonance.

The total energy gain corresponds to the original Pauling–Wheland resonance energy,[14] and it is invariably negative (that is, the energy is lowered), irrespective of whether the species under consideration is aromatic, nonaromatic, or antiaromatic. The second, which may be negative or positive, is usually termed Dewar resonance energy.[15,16] It derives from the observation that enthalpies of atomization or formation of polyenes can be composed from experimentally based bond[15] or group increments.[17] Such increments allow one to calculate the energy of a (purely hypothetical) cyclic polyene that benefits from all the conjugation energy but *not* the special contribution resulting from the cyclic arrangements of double bonds that allows for equivalent resonance structures in the case of benzene.

The extra energy gained or lost in this way (that is, the Dewar resonance energy) is then equated with the difference between the experimental enthalpy of atomization or formation of the compound under scrutiny and its hypothetical polyene reference. If one uses the latest version of Benson-type group increments,[18] this energy difference amounts to 87 kJ mol^{-1} in benzene. I believe that this procedure and the resulting Dewar resonance energy represent the best and most transparent way to assess the aromatic resonance stabilization in benzoid hydrocarbons. The results are indeed in good accord with determinations of the same quantity—usually by much more complicated procedures—relative to comparable (experimental or theoretical) standards.

In the case of benzene (or benzenoid hydrocarbons) the assessment of the Dewar resonance energy is greatly facilitated by the fact that this is the only nonadditive effect that needs to be considered, because such compounds are assumed to be free of strain (all bond angles have the ideal value of 120° for sp^2-hybridized carbon atoms, and the separations between nonbonding hydrogen atoms are larger than the sum of their van der Waals radii).

However, this is clearly not the case in CBD. If one compares the recently determined heat of formation of CBD (429 ± 16 kJ mol^{-1})[3] with that obtained by adding four polyenic C_d-(H)(C_d) group increments (113 kJ mol^{-1}),[18] one is left with a whopping destabilization energy of 316 ± 16 kJ mol^{-1}. One then faces the problem of how to figure out which part of this energy results from some form of strain, and which results from antiaromatic destabilization.

It is very important to recognize (as Kass and co-workers did) that *there is no unambiguous way to dissect the above number*. If one wants to quantitate the antiaromatic destabilization energy of CBD, one must make some assumption about its strain energy. The most reasonable such assumption would seem to be that the strain energy increases linearly in the series cyclobutane/cyclobutene/CBD. In this case the antiaromatic destabilization energy is given by the enthalpy change for the isodesmic Reaction (1).[3]

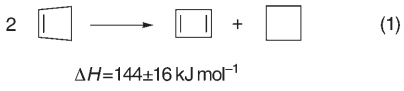

However, the above assumption merits some consideration. The fact that the strain energy increases by a mere 4 kJ mol^{-1} on going from cyclobutane to cyclopropane indicates that the energetic cost of angular deformation (Baeyer strain) cannot account for this property alone. Two different explanations have been advanced to account for this discrepancy. The first argues that the increase in angular strain between the two compounds is largely balanced by an increase in the strength of the C–H bonds, owing to rehybridization of the ring carbon atoms, and that the strain energy of cyclopropane is therefore anomalously low, whereas that of cyclobutane is rather normal.[19] The second explanation refers to the proposal, originally advanced by Dewar,[20] that cyclic delocalization of $4n + 2$ or $4n$ σ electrons in C–C bonds may also lead to aromatic stabilization or destabilization, respectively.[10] Accordingly, cyclopropane is stabilized by this so-called σ aromaticity (which manifests itself, for example, in negative NICS values above the ring plane), whereas cyclobutane is destabilized by σ antiaromaticity (positive NICS values).[10] Although the energetic consequences of this effect cannot be directly assessed, they have been proposed to account for the surprisingly small difference in strain energies between cyclopropane and cyclobutane. Perhaps both of the above explanations need to be invoked to arrive at a complete picture of "strain" in the two compounds.

An additional complication, pointed out originally by Politzer et al.,[21] concerns the observation that in CBD two π bonds are forced into a much more proximate position than in any other polyene. The fact that the C–C bond

 © 2006 Wiley-VCH Verlag GmbH & Co. KGaA, Weinheim

length in CBD (ca. 1.57 Å according to high-level calculations[22]) is nearly 0.1 Å longer than in butadiene, whereas the C=C bond length is similar in the two compounds, may be an expression of a substantial repulsion between the two π bonds. However, it is difficult to quantitate this repulsion, and the pronounced alternation in bond length in CBD may also be attributed to strong vibronic coupling between the ground electronic state and the first excited singlet state.[23]

Two corollaries follow from the above considerations: a) "strain" is a multifaceted property which is composed of several nonadditive effects that were invented by chemists to understand this property, and it cannot be reduced to angular deformation and/or steric repulsion; b) it is therefore not a priori clear why and how this property changes on going from cyclobutane to cyclobutene to CBD. It is unclear whether σ antiaromaticity is the same for puckered (as in cyclobutane) and planar (as in CBD) four-membered rings and how it depends on the size of the ring. If σ antiaromaticity does contribute significantly to the destabilization of CBD, the tantalizing question arises as to whether this should be counted towards antiaromaticity or towards strain.

In view of all the above it is not surprising that recent opinions vary enormously on how much CBD is thermochemically destabilized solely by virtue of the cyclic conjugation of its four π electrons; estimations range from 230 kJ mol^{-1} (Deniz et al.[24]) to 44 kJ mol^{-1} (Mo and Schleyer[13]). If even this lower number is attributed to π repulsion, one is left with the prediction that CBD, in spite of its enormous destabilization, must be considered as essentially nonaromatic, as based on its thermochemical properties. In fact, Schleyer concludes in his above-cited paper[13] that "instead of the conventional interpretation of CBD as the antiaromatic paradigm, it should be regarded as a unique molecule", a view that I tend to share.

What other properties might be associated with antiaromaticity in CBD? The ionization energy of CBD (8.16 eV[25]) is nearly 1 eV lower than that of butadiene (9.08 eV), whereas that of benzene (9.25 eV) is higher than that of hexatriene (8.29 eV) by a similar amount. What this comparison indicates is that the energy of the π HOMO of CBD is raised by cyclic conjugation, while it is lowered in benzene. Of course this trend carries over to the total π energy, which in the case of CBD is the same as that of two ethylene molecules ($4\alpha+4\beta$ in Hückel molecular orbital terms) and nearly 0.5β higher than that of butadiene, whereas the total π energy of benzene is lower than that of three ethylene molecules by 2β (and lower than that of hexatriene by about 1β). In this perspective the ionization potential is an expression of (anti)aromaticity.

As CBD and benzene are alternant hydrocarbons, their HOMO–LUMO gaps should correlate with the HOMO energy (that is, the ionization potential). For that reason, the energies of the lowest singlet states should also be very different in the two compounds. Unfortunately, this comparison is hampered by the fact that, owing to the degeneracies of the frontier MOs, the lowest excited singlet state of benzene cannot be described by simple HOMO–LUMO excitation.[26] However, the real problem is that the absorption spectrum of CBD has not been unambiguously assessed by experiment. An absorption band observed at 300 nm[27] has never been confirmed as such, but cleavage of CBD upon irradiation at 350–420 nm to give acetylene[28] indicates that CBD must absorb in this region, albeit too weakly for a band to be observed.

Thus, we must rely on excited-state calculations, which are surprisingly scarce.[29] According to these calculations, rectangular CBD has two near-UV electric-dipole-forbidden transitions that correspond to the excitation of one ($1\,^1A_g \rightarrow 1\,^1B_{1g}$) or two electrons ($1\,^1A_g \rightarrow 2\,^1A_g$) from the HOMO to the LUMO. The recent coupled-cluster calculations of Levchenko and Krylov[22] predict that these two transitions occur (vertically) at 360 and 285 nm. According to our own CASPT2 calculations,[30] the first allowed transition ($1\,^1A_g \rightarrow 1\,^1B_{3u}$) occurs above 7 eV (< 180 nm), that is, in the vacuum-UV region. Thus, the observed near-UV photocleavage of CBD must indeed involve HOMO–LUMO excitation at around 1.5 eV lower in energy than in benzene.

Finally there is the question of the rate and automerization barrier of the two rectangular structures of CBD. Experiment has so far only provided rough estimates and limits. From trapping studies in solution, Whitman and Carpenter concluded that the barrier must lie between 6.7 and ca 40 kJ mol^{-1},[29] while Orendt et al. deduced from IR and NMR measurements in cryogenic matrices that the rate constant of interconversion must be higher than 10^3 at 25 K,[30] which translates into a free energy of activation of less than 4 kJ mol^{-1}. However, the best high-level ab initio calculations predict the barrier to lie between 27 and 32 kJ mol^{-1}.[31,32] These two facts can only be reconciled if one invokes heavy-atom tunnelling. In 1983 Carpenter had in fact done exactly that to account for the negative entropy of activation which he had deduced from his experiments,[29] and he concluded that the tunnelling mechanism would actually dominate the automerization process at temperatures below 0 °C.[33] Although this proposal originally met with a great deal of scepticism, it has not been dispelled to date.

Thus, cyclobutadiene continues to fascinate chemists and it will certainly continue to serve as a benchmark and testing ground for different theoretical models that chemists come up with to make sense of the sometimes ambivalent manifestations of aromatic or antiaromatic molecules. Now that a well-founded number is available for the heat of formation of CBD, the purported paradigm of antiaromaticity, any speculation about the contributions of various effects to its destabilization rests at least on solid ground.

I am indebted to Profs. Barry Carpenter (Cornell University, now University of Cardiff) and Josef Michl (University of Colorado, Boulder) for critical reading of the manuscript.

Published online: September 20, 2006

[1] *Chem. Rev.* **2001**, *101(5)*, 1115.
[2] *Chem. Rev.* **2005**, *105(10)*, 3433.
[3] A. Fattahi, L. Liz, Z. Tian, S. R. Kass, *Angew. Chem.* **2006**, *118*, 5106; *Angew. Chem. Int. Ed.* **2006**, *45*, 4984.
[4] The enthalpy of formation of cyclobutadiene had been previously derived from

 © 2006 Wiley-VCH Verlag GmbH & Co. KGaA, Weinheim

the heat liberated during the photodecomposition of a polycyclic cyclobutadiene precursor (see reference [24]). However, owing to various assumptions that had to be made with regard to the thermochemical properties of this precursor and side products of this reaction, their resulting estimate of $\Delta_f H°(\mathrm{CBD}) = 477 \pm 46\ \mathrm{kJ\,mol^{-1}}$ turned out to be significantly too high.

[5] F. C. London, *J. Chem. Phys.* **1937**, *5*, 837.

[6] C. S. Wannere, P. von R. Schleyer, *Org. Lett.* **2003**, *5*, 605.

[7] R. Viglione, R. Zanasi, P. Lazzeretti, *Org. Lett.* **2004**, *6*, 2265.

[8] A. Stanger, *J. Org. Chem.* **2005**, *70*, 883.

[9] P. von R. Schleyer, C. Maerker, A. Dransfeld, H. Jiao, N. J. R. van Eikema Hommes, *J. Am. Chem. Soc.* **1996**, *118*, 6317.

[10] D. Moran, M. Manoharan, T. Heine, P. von R. Schleyer, *Org. Lett.* **2003**, *5*, 23.

[11] Based on enthalpies of formation from: H. Y. Afeefy, J. F. Liebman, S. E. Stein in *NIST Chemistry WebBook, NIST Standard Reference Database No 69* (Eds.: P. J. Lonstrom, W. G. Mallard), National Institute of Standards and Technology, Gaithersburg, MD, **2005** (http://webbook.nist.gov/chemistry), and the enthalpy of formation of cyclobutadiene from the recent work of Kass and co-workers.[3]

[12] Notwithstanding repeated and continuing claims to the contrary, especially by theoreticians, it is impossible to measure (anti)aromaticity "absolutely", that is, without recourse to a nonaromatic reference or standard.

[13] Y. Mo, P. von R. Schleyer, *Chem. Eur. J.* **2006**, *12*, 2009 and references cited therein.

[14] L. C. Pauling, G. W. Wheland, *J. Chem. Phys.* **1933**, *1*, 362.

[15] M. J. S. Dewar, C. de Llano, *J. Am. Chem. Soc.* **1969**, *91*, 789.

[16] L. J. Schaad, B. A. Hess, *Chem. Rev.* **2001**, *101*, 1465.

[17] S. W. Benson, *Thermochemical Kinetics*, Wiley, New York, **1976**.

[18] E. S. Domalski, E. S. Hearing, *J. Phys. Chem. Ref. Data* **1993**, *22*, 1963.

[19] R. D. Bach, O. Dmitrenko, *J. Am. Chem. Soc.* **2004**, *126*, 4444. According to calculations, the strength of the C–H bonds (that is, their dissociation enthalpy) increases by about $35\ \mathrm{kJ\,mol^{-1}}$ on going from cyclobutane to cyclopropane. In order to keep the overall strain energies of the two compounds as similar as they are, the increase in angular strain on narrowing the C-C-C bond angles from 90° to 60° would therefore have to be about $70\ \mathrm{kJ\,mol^{-1}}$ per CH_2 group, that is, the angular strain would have to be over $200\ \mathrm{kJ\,mol^{-1}}$ higher in cyclopropane than in cyclobutane! This shows once more that dissecting nonadditive effects is a delicate matter.

[20] M. J. S. Dewar, *J. Am. Chem. Soc.* **1984**, *106*, 669.

[21] P. Politzer, M. E. Grice, J. S. Murray, J. M. Seminario, *Can. J. Chem.* **1993**, *71*, 1123.

[22] S. V. Levchenko, A. I. Krylov, *J. Chem. Phys.* **2004**, *120*, 175.

[23] S. Zilberg, Y. Haas, *J. Phys. Chem. A* **1998**, *102*, 10843.

[24] A. A. Deniz, K. S. Peters, G. J. Snyder, *Science* **1999**, *286*, 1119.

[25] D. W. Kohn, P. Chen, *J. Am. Chem. Soc.* **1993**, *115*, 2844.

[26] L. Salem, *Molecular Orbital Theory of Conjugated Systems*, W. Benjamin, New York, **1966**, chap. 4.

[27] T. Bally, S. Masamune, *Tetrahedron* **1980**, *36*, 343.

[28] B. R. Arnold, J. Michl, *J. Phys. Chem.* **1993**, *97*, 13348.

[29] B. R. Arnold, J. Michl, in *Kinetics and Spectroscopy of Carbenes and Biradicals* (Ed.: M. S. Platz), Plenum Press, New York, **1990**, p. 20.

[30] H. Aboulfadl, T. Bally, unpublished results.

[31] D. W. Whitman, B. Carpenter, *J. Am. Chem. Soc.* **1982**, *104*, 6473.

[32] A. M. Orendt, B. R. Arnold, J. G. Radziszewski, J. C. Facelli, K. D. Malsch, H. Strub, D. M. Grant, J. Michl, *J. Am. Chem. Soc.* **1988**, *110*, 2648.

[33] A. Balkova, R. J. Bartlett, *J. Chem. Phys.* **1994**, *101*, 8972.

[34] S. V. Levchenko, T. Wang, A. I. Krylov, *J. Chem. Phys.* **2005**, *122*, 224106.

[35] B. Carpenter, *J. Am. Chem. Soc.* **1983**, *105*, 1700.

 © 2006 Wiley-VCH Verlag GmbH & Co. KGaA, Weinheim

Bioorganic Chemistry

DOI: 10.1002/anie.200600855

Lipidated Ras and Rab Peptides and Proteins—Synthesis, Structure, and Function

*Luc Brunsveld, Jürgen Kuhlmann, Kirill Alexandrov, Alfred Wittinghofer, Roger S. Goody, and Herbert Waldmann**

Keywords:
bioorganic chemistry · GTPases · lipopeptides · lipoproteins · protein ligation

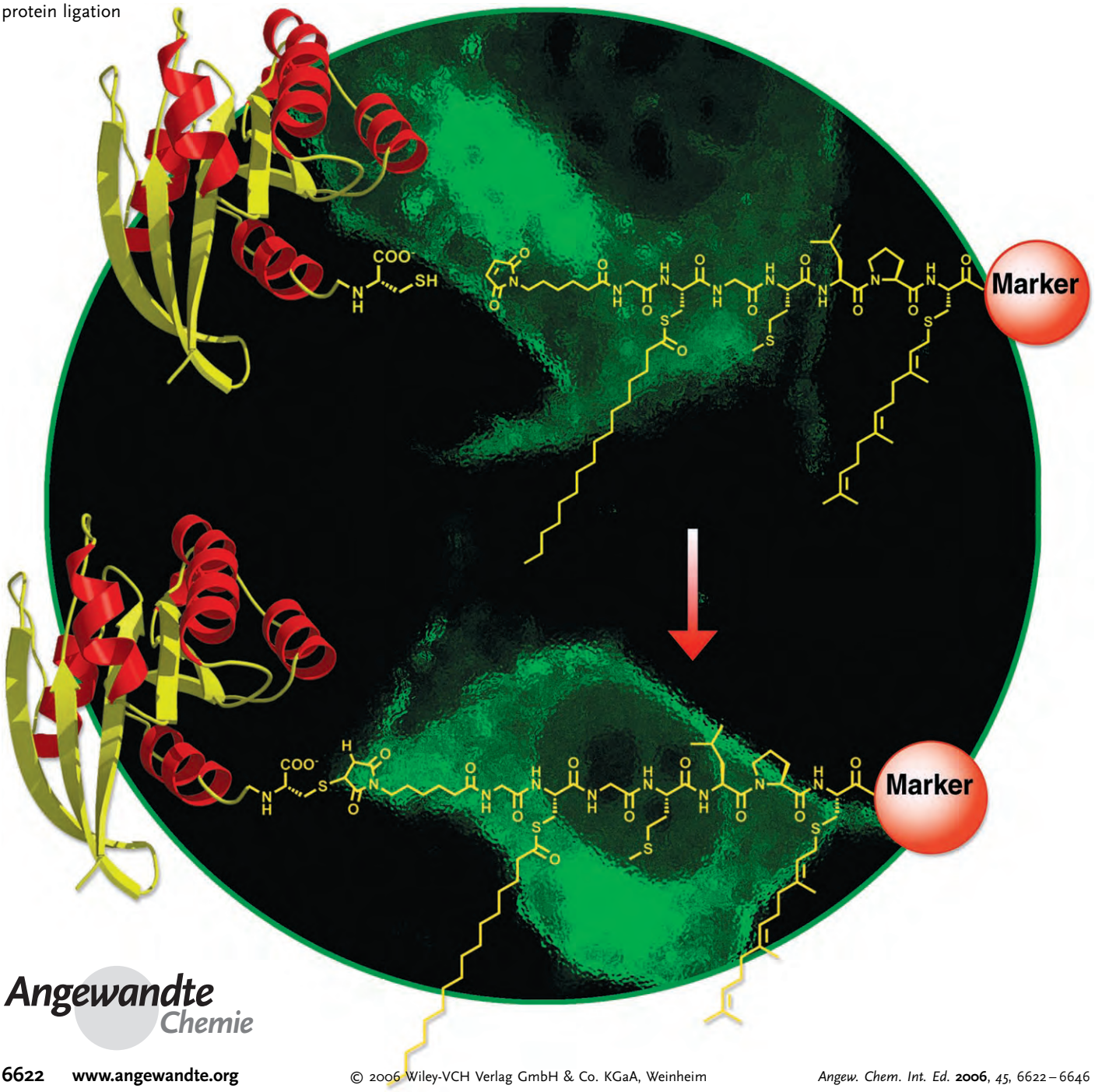

© 2006 Wiley-VCH Verlag GmbH & Co. KGaA, Weinheim

Chemical biology can be defined as the study of biological phenomena from a chemical approach. Based on the analysis of relevant biological phenomena and their structural foundation, unsolved problems are identified and tackled through a combination of chemistry and biology. Thus, new synthetic methods and strategies are developed and employed for the construction of compounds that are used to investigate biological procedures. Solid-phase synthesis has emerged as the preferred method for the synthesis of lipidated peptides, which can be chemoselectively ligated to proteins of the Ras superfamily. The generated peptides and proteins have solved biological questions in the field of the Ras-superfamily GTPases that are not amendable to chemical or biological techniques alone.

From the Contents

1. Introduction 6623
2. Synthesis of Lipidated Ras and Rab Peptides 6625
3. Synthesis of Lipidated Ras and Rab Proteins 6633
4. Biophysical Studies with Lipidated Peptides 6636
5. Structural and Biological Studies of Lipidated Ras and Rab Proteins 6638
6. Ras Proteins as Tools in Cell Biology 6640
7. Conclusions and Outlook 6642

1. Introduction

Ras GTPases belong to the class of monomeric G proteins that are involved in cellular processes such as vesicle transport, the cell cycle, nuclear import, and signal transduction.[1] G proteins adopt their so-called active state by complexation with GTP, whereas binding of GDP stabilizes their inactive state. The active form acts by stimulating or inhibiting cellular processes through interactions with effectors. Owing to the importance of these molecular switches, their faulty regulation often has deleterious consequences. Prominent examples can be found in many cancer cells in which mutated Ras proteins that are "arrested in the GTP-bound state" are often encountered.[2] These Ras proteins are thus continuously in their active form, which results—together with additional disturbances in signal transduction processes—in uncontrolled cell growth.

Members of the Ras superfamily are posttranslationally modified through prenylation and in some cases acylation reactions.[3,4] The Ras proteins are a subgroup of the Ras superfamily and consist of the three isoforms, H-, N-, and K-Ras as well as R-Ras, TC21, Rheb, and the Rap and Ral proteins.[5] When fully posttranslationally modified, the proteins are located at the inner leaflet of the plasma membrane. The differences in amino acid sequence between these Ras proteins are mainly in their C-terminal region. This apparently random-coiled terminal part contains the signal sequence for the posttranslational modifications. The Rho (Ras homologous) family of proteins also belongs to the Ras superfamily and is involved in the organization of the actin cytoskeleton.[6] The Rab (Ras gene from rat brain) proteins are the largest subgroup of the Ras superfamily with over 60 members.[7] The Rab proteins are involved in vesicular transport within the cell, with many of the proteins localized in specific compartments of the secretory and endocytic pathways.[8] The Ran (Ras-related nuclear) proteins are the only so far known members of the Ras superfamily that are not posttranslationally lipid modified. They play a role in the regulation of nuclear import and export.[9,10] A schematic overview of proteins belonging to the Ras superfamily and their function is depicted in Figure 1.

The three most common types of posttranslational lipid modifications encountered in the Ras superfamily are N-myristoylation, S-palmitoylation, and S-isoprenylation.[11–13] Isoprenylation and myristoylation are stable (nonreversible) modifications, whereas palmitoylation is a reversible process.[14,15] Additionally, some of the proteins from the Ras superfamily are posttranslationally converted into C-terminal methyl esters. Some typical posttranslational modifications encountered on the C termini of proteins from the Ras superfamily are shown in Scheme 1.

The lipidation of the C termini of members of the Ras superfamily results in membrane association of the posttranslationally modified proteins. These posttranslational modifications are essential for protein function. However, until recently, the majority of experiments with these proteins, such as structure determination by X-ray diffraction, NMR spectroscopy, and biochemical characterization, were performed on the soluble part of the proteins, that is, the protein

[*] Prof. Dr. H. Waldmann
Max-Planck-Institut für molekulare Physiologie
Otto-Hahn-Str. 11, 44227 Dortmund (Germany)
and
Fachbereich Chemie
Universität Dortmund
Otto-Hahn-Str. 6, 44221 Dortmund (Germany)
Fax: (+49) 231-133-2499
E-mail: herbert.waldmann@mpi-dortmund.mpg.de
Dr. L. Brunsveld
Max-Planck-Institut für molekulare Physiologie
Otto-Hahn-Str. 11, 44227 Dortmund
and
Chemical Genomics Centre
Otto-Hahn-Str. 15 44227 Dortmund (Germany)
Dr. J. Kuhlmann, Dr. K. Alexandrov, Prof. Dr. A. Wittinghofer, Prof. Dr. R. S. Goody
Max-Planck-Institut für molekulare Physiologie
Otto-Hahn-Str. 11, 44227 Dortmund (Germany)

© 2006 Wiley-VCH Verlag GmbH & Co. KGaA, Weinheim

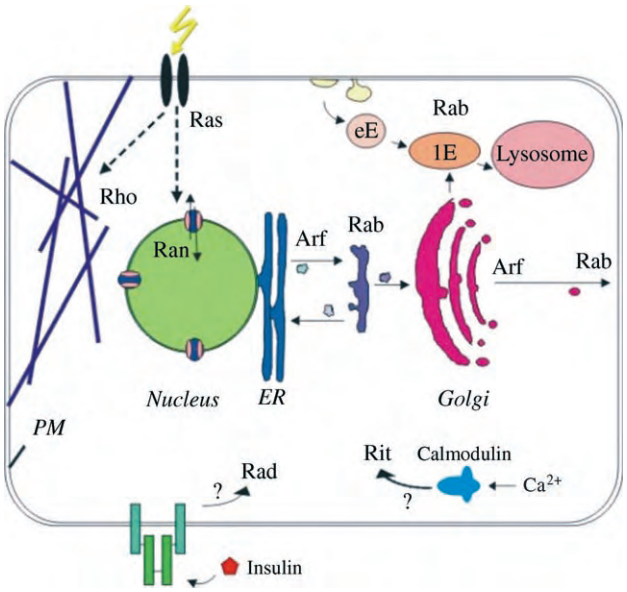

Figure 1. Proteins belonging to the Ras superfamily and their localization and function in the cellular context. eE: early endosome, 1E: late endosome, PM: plasma membrane, ER: endoplasmatic reticulum, Arf: ADP-ribosylation factor, Rit: Ras-like protein in tissues. Rad: Ras-related protein associated with diabetes.

without the C terminus. The results obtained through these approaches can, at best, only give an approximation of the real situation, especially as diversity between the individual members is often encountered in the lipidated C terminus of the protein. The biochemical generation of fully functionalized and modified lipidated proteins is, however, difficult, time consuming, and in the case of S-palmitoylation, leads to heterogeneous mixtures and is therefore in most cases not practical or applicable. In contrast, chemical biological approaches have been developed in the last years, giving access to the fully functional lipidated proteins and additional non-natural modifications, thereby enabling the study of the complete functional proteins.[16,17] This was achieved through two techniques that were developed more or less in parallel: 1) protein ligation and chemical synthesis of proteins (the subject of many reviews[18] and discussed in this review only in relation to proteins of the Ras superfamily) and 2) lipidated-peptide synthesis, both in solution and on solid support. These developments and their application to explain unsolved questions in biochemistry, biophysics, and the biology of proteins of the Ras superfamily are the focus of this review. We will first discuss the progress made in the synthesis of these lipidated peptides. The chemical focus will be on the application of recently developed methods in the solid-phase chemistry of lipidated peptides to the chemical biology of lipidated Ras GTPases. Comprehensive overviews of previous work on solution-phase approaches can be found in the recent literature.[19–24] The review of the peptide synthesis will be followed by the description of how these peptides were used for the generation of fully lipidated or modified proteins of the Ras superfamily. The last part of this review is devoted to some selected examples of biophysical, biological, and structural studies that employ these peptides and semisynthetic proteins. Furthermore, we deal with the use of non-natural elements within these lipidated-protein segments.

Luc Brunsveld was born in 1975 in Culemborg, the Netherlands. He received his PhD in supramolecular chemistry at the Eindhoven University of Technology in 2001 with Bert Meijer. He was a postdoctoral fellow in the group of Herbert Waldmann at the Max Planck Institute (MPI) in Dortmund from 2001 to 2003 and research scientist in the area of medicinal chemistry at Organon from 2003 to 2004. Since 2005 he has been a group leader at the Max Planck Institute of Molecular Physiology in Dortmund. His research interests are in supramolecular chemistry and chemical biology.

Jürgen Kuhlmann, born in 1962 in Schwerte a. d. Ruhr, Germany, studied at the Universität Dortmund and completed his PhD in kinetic and thermodynamic studies on ligand binding of the nicotinic acetylcholine receptor with Alfred Maelicke at the MPI for Nutrition Physiology. After working in an environmental-analysis laboratory, he became manager of the biophysical analysis group in the Department of Structural Biology at the MPI for Molecular Physiology. In 2002 he became a private lecture in Biophysical Chemistry at Ruhr University Bochum where he is still a private lecturer in the faculty of chemistry.

Kirill Alexandrov was born in 1967 in Leningrad, USSR, and studied zoology at the State University of Leningrad (MS 1989). He worked as a technician at the Institute for Cytology in Leningrad and Dana-Farber Cancer Institute in Boston USA untill 1992 when he moved to the European Molecular Biology Laboratory in Heidelberg, Germany, where he complted his PhD in cell biology in 1996. He moved to the MPI for Molecular Physiology, Dortmund, Germany, in 1997 as a postdoctoral fellow where he subsequently became a group leader in 1999.

Alfred Wittinghofer, born 1943 in Goch, Germany, studied in Aachen and completed his diploma thesis and PhD with Prof. H. Zahn at the Deutsche Wollforschungsinstitut, Aachen (synthesis of the insulin A chain). After a postdoctoral fellowship with Dr. R. Hiskey at the University of North Carolina and one at the MPI für medizinische Forschung in Heidelberg, he established his own research group in Heidelberg and began researching Ras and other Ras-like GTP-binding proteins. He was appointed Director at the MPI für molekulare Physiologie in 1992.

© 2006 Wiley-VCH Verlag GmbH & Co. KGaA, Weinheim

2. Synthesis of Lipidated Ras and Rab Peptides

Synthesis strategies that give access to lipidated peptides have been developed during the last 10 years and reviewed both for solution and for solid-support approaches.[19,20,25,26] It is therefore not our aim to provide an all-inclusive review, but rather highlight the different approaches that can be followed for the synthesis of lipidated peptides and to describe and compare their characteristics.

The synthesis of lipidated peptides of the Ras superfamily can follow several different strategies. One can decide between 1) the use of solid-phase techniques compared with solution phase, 2) the use of lipidated building blocks or peptide lipidation after assembly of the peptide, and 3) the application of the Boc or Fmoc strategy. The strategy that is followed generally depends on the types and positions of the lipid groups in the peptides, the length of the peptide, C-terminal functionality, and the presence of additional functional groups, such as fluorescent markers or spin labels. Particularly for the lipids and functional groups, the synthesis strategy has to be fully adapted to the labilities of the modifications. For solid-phase chemistry, the choice of the linker to the resin is an additional criterion to consider in the synthesis planning.

For lipidated peptides some general guidelines are easily formulated: 1) (strong) acid-labile protecting groups or linkers cannot be used in combination with prenyl groups; 2) the same holds true for protecting groups that have to be removed under hydrogenolytic conditions; 3) thioesters, such as palmitoyl (Pal) groups attached to cysteines, are labile towards strong nucleophiles (see Schemes 2 and 4). Additional issues that must be considered include: 4) the characteristics of other functional groups such as fluorophores, photoactivatable groups, and tags for ligation to proteins; 5) diketopiperazine formation of prenylated dipeptide esters upon N-terminal deprotection; and 6) the undesired *S,N*-acyl shift of the palmitoyl group on an N-terminally unmasked cysteine.

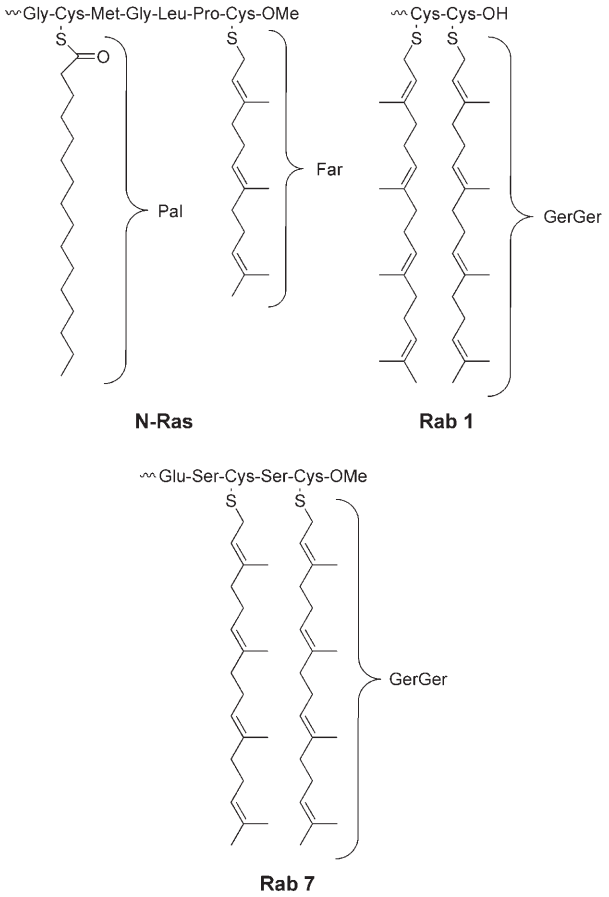

Scheme 1. C-terminal lipidation motifs for N-Ras, Rab1, and Rab7. The C-terminal cysteine is either a carboxylic acid or a methyl ester.

Considering these features and limitations, one might wonder if a general strategy for the synthesis of lipidated peptides of the Ras superfamily can be developed at all. In the following section we will review some of the recent approaches undertaken for the synthesis of these complex lipidated peptides. We will try to guide the reader to some generally validated approaches that meet the restraining demands imposed by the peptides. The main focus of this section will be on solid-phase approaches that offer, in our experience, a faster and more flexible approach to multiply lipidated peptides than methods in the solution phase.

2.1. Solution-Phase Approaches

The synthetic strategies used for solution-phase lipidated-peptide synthesis show parallels to solution-phase syntheses of regular peptides. Seminal studies concerning the lipidated-

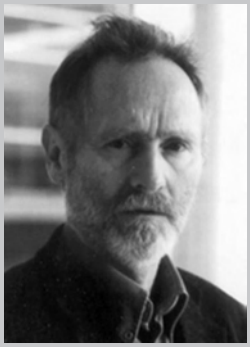

Roger Goody was born in 1944 in Northampton, England, and studied at the University of Birmingham, England. He obtained his BSc in chemistry in 1965 and his PhD in 1968. After two postdoctoral positions, he completed his habilitation in biochemistry/biophysics at the University of Heidelberg, Germany, and was nominated professor in 1990. Since 1993, he has been director at the MPI of Molecular Physiology, Dortmund. In 2004 he became Professor of Biochemistry at Ruhr-University Bochum, Germany. His interests are in the area of phosphate transferring proteins.

Herbert Waldmann received his PhD in 1985 at the University of Mainz under Prof. Kunz in organic chemistry after which he completed a postdoctoral appointment with Prof. G. Whitesides at Harvard University. He was appointed as Professor of Organic Chemistry at the University of Bonn (1991), full Professor of Organic Chemistry at the University of Karlsruhe (1993), and Director at the MPI of Molecular Physiology Dortmund and Professor of Organic Chemistry at the University of Dortmund (1999). His research interests lie in compound libraries, solid-phase synthesis, and Ras proteins.

 © 2006 Wiley-VCH Verlag GmbH & Co. KGaA, Weinheim

peptide synthesis in solution and biological application of the synthesized peptides have been published by Silvius and co-workers.[27–32]

The introduction of the lipid groups can follow two approaches. Either prelipidated amino acids are coupled under regular coupling conditions, or selectively deprotected peptides are lipidated after completion of the backbone synthesis. Peptides that bear only one type of lipid modification can usually be synthesized in a relatively straight forward manner by using established protecting-group techniques in solution. Palmitoyl thioesters are stable under acidic conditions and therefore classical acid-labile protecting groups like the Boc group can be used. Prenyl thioethers are inert at pH > 7, which allows for the use of base-labile protecting groups (e.g. the Fmoc group), highly acid-labile protecting groups (e.g. those based on the trityl (Trt) group), or other orthogonal groups (e.g. enzyme-labile or noble-metal-labile protecting groups). Finally, myristoyl amides tolerate both acidic and basic reaction conditions and therefore do not limit the protecting-group strategy.

Peptides that incorporate two types of lipid modifications or other labile functional groups, however, require a more sophisticated protecting-group strategy, and it is around this aspect that most of the investigations in solution have evolved. A schematic overview of protecting groups that were found to be appropriate for the solution synthesis of multiply functionalized peptides is given in Scheme 2. The combined use of enzyme-labile, noble-metal, or extremely acid-labile protecting groups has turned out to be a profitable approach for the synthesis of these demanding peptides in solution.[21,33,34] However, these synthesis protocols do require a certain amount of experience and can definitely not be regarded as standardized. Generally, it can be stated that every lipidated peptide to be synthesized in solution requires individual synthesis planning and optimization. Concomitantly, these solution-phase peptide syntheses are relatively labor intensive, not only because of the optimization of the reaction conditions and the number of coupling steps, but also because of the time-consuming purification of the intermediates that often feature detergent-like characteristics. Occasionally, the extreme differences in the nature of the coupling partners, for instance with respect to hydrophobicity, can be used to facilitate the separation of product and starting compounds. Considering all the mentioned aspects, it is valid to conclude that the synthesis of fully decorated lipidated peptides through solution-phase approaches is feasible, however, other more-flexible approaches would definitely be preferred, both considering time and the overall yield of the entire synthesis effort.

2.2. Combined Solution/Solid-Phase Approaches

A possible way of overcoming the time-consuming aspect of solution-phase peptide synthesis is to use a combined solution/solid-phase approach. In such an approach, the majority of the peptide sequence is rapidly synthesized on a solid support, cleaved, and coupled with lipidated amino acids in solution or lipidated by alkylation of the free thiol side chains of cysteines. These approaches have been used quite frequently and are especially successful for prenylated peptides as has been shown by the notable contribution of Naider and co-workers,[19,35] Gelb and co-workers,[36–38] Poulter and co-workers,[39] and Waldmann and co-workers.[40–43]

A typical example of a synthesis of such a prenylated peptide is given in Scheme 3.[41] The C-terminal N-Ras peptide features a C-terminal lipidated cysteine, which, in solution, is coupled to the C-terminal part of the peptide that has been assembled on a solid support. The N terminus of the peptide is functionalized with the MIC group for ligation to a cystein on the Ras-GTPase. The cysteine is protected as a *tert*-butyl disulfide as this protecting group allows reductive cleavage under physiological conditions. The use of these protecting and functional groups makes the final segment condensation a relatively straight-forward task. When performing such a segment condensation, it is important to watch for possible racemization; selection of validated coupling techniques, however, usually proves sufficient to avoid or minimize this racemization.

The peptide depicted in Scheme 3 is, however, not too structurally demanding as, apart from the two cysteines, none of the amino acids

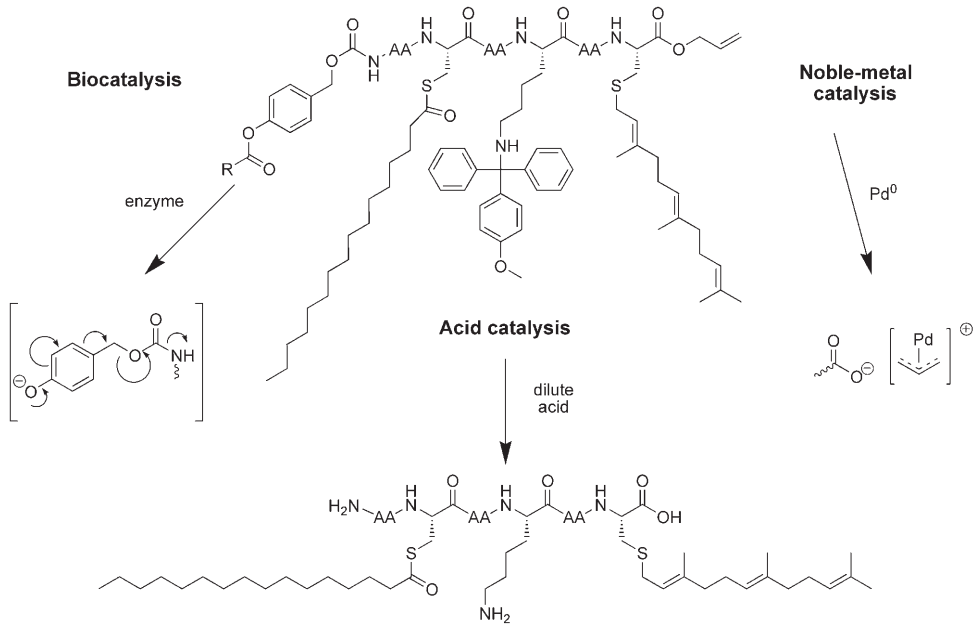

Scheme 2. An overview of the different protecting groups, orthogonal to prenyl and palmitoyl modifications, utilized in solution-phase lipopeptide synthesis of multiply lipidated peptides.

 © 2006 Wiley-VCH Verlag GmbH & Co. KGaA, Weinheim

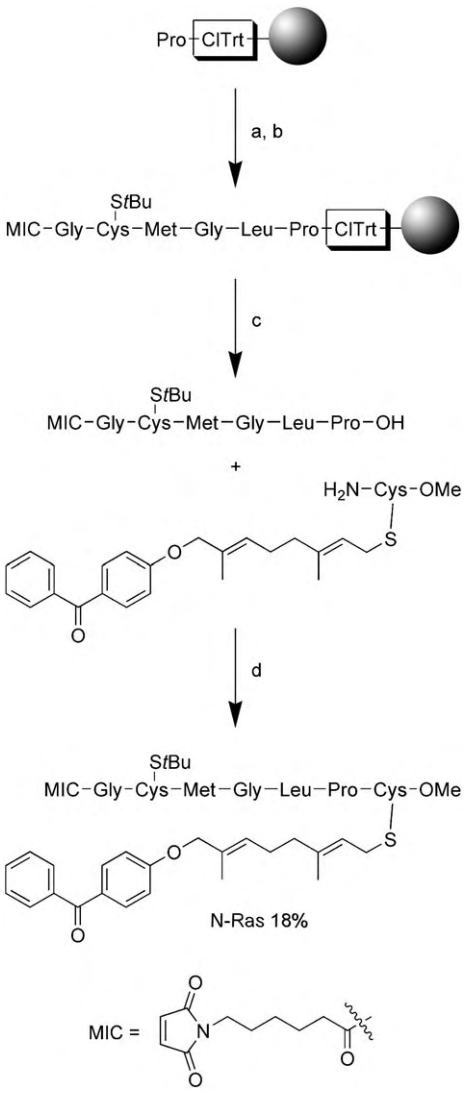

Scheme 3. Combined solution-phase and solid-phase approach for the synthesis of the N-Ras C terminus. a) Repeated couplings of amino acids: Fmoc-AA-OH, HBTU, HOBt, DIPEA, DMF; and repeated removals of Fmoc: piperidine/DMF (1:4); b) MIC-OH, HBTU, HOBt, DIPEA, DMF; c) TFA/CH_2Cl_2 (1:9); d) EDC, HOBt, CH_2Cl_2/TFE (9:1).

feature reactive side chains, nor does it contain an unprotected N-terminal amine. A combined solution/solid-phase approach becomes more challenging when multiple lipid anchors need to be introduced in the peptide or when the peptide features additional amino acids with (reactive) polar side chains. Apart from the need for additional steps in solution, orthogonality of the protecting and functional groups might become problematic and similar issues arise as for the solution-phase approach.

2.3. Solid-Phase Approaches

The recent focus on lipidated-peptide synthesis has shifted to the preparation of peptides completely on solid supports. Critical issues that have been under scrutiny have been, for example, the screening of different linkers, cleavage conditions, and the evaluation of synthesis routes for the introduction of the lipid groups with a suitable orthogonal protecting-group strategy. Like the solution-phase approaches, protecting groups need to be orthogonal to the lipids and other functional groups in the peptides. Additionally, the linker to the resin should be cleavable under conditions that do not interfere with the peptide functionalities. In an ideal setup, the cleavage of the linker would also allow for the introduction of different types of functional groups at the C-terminal carboxy function. The requirements of a solid-phase synthesis approach with respect to the integrity of the functional groups, protecting groups, and linkers are visualized in Scheme 4. The results obtained in the field of lipidated-peptide synthesis on a solid phase are reviewed in the following paragraphs and ordered according to the linker studied and the method for the introduction of the lipid groups.

2.3.1. Linker Strategies

The major challenge to be met in the development of a universal solid-phase synthesis approach for lipidated peptides is the definition of a set of suitable orthogonally stable protecting groups and a linker that allows for the selective introduction of different lipids and other functional groups (Table 1). Typical solid-phase linkers, such as the Wang linker and the Rink amide linker, are not compatible with these requirements, as, for example, the acid required for cleavage of the peptides from these resins is not compatible with prenyl groups. Other linkers, such as those based on the trityl group or the Sasrin resin, allow cleavage under mildly acidic conditions and as such are compatible with prenyl and palmitoyl groups. However, they do not allow for the introduction of chemical diversity at the C terminus.

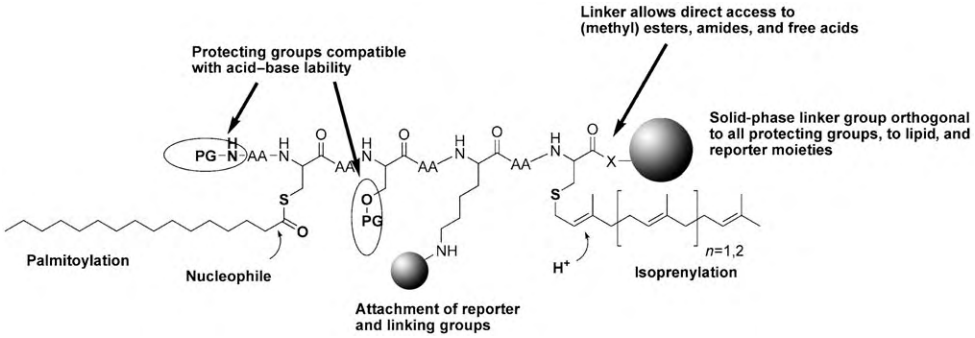

Scheme 4. Overview of the requirements for a generally applicable method of solid-phase synthesis for lipidated peptides of the Ras superfamily, and characteristic reactivities of lipid functionalities. The double bonds of the prenyl lipids are sensitive to acid, and the thioester of palmitoyl groups is attacked and cleaved by nucleophiles. PG = protecting group.

 © 2006 Wiley-VCH Verlag GmbH & Co. KGaA, Weinheim

Table 1: Characteristic properties of some linkers regarding their applicability for lipidated-peptide synthesis of Ras-superfamily peptides.

	Oxime linker	Trityl linker	Hydrazinobenzoyl linker	Ellman sulfonamide linker
structure	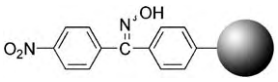	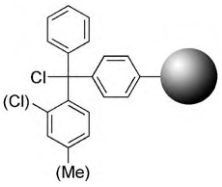	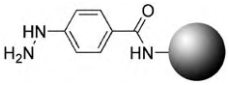	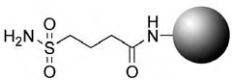
cleavage protocol	amines	weak acid	oxidation and a nucleophile	alkylation of linker and a nucleophile.
C-terminal cleavage products:	amides	acid or esters and amides (if anchored to a peptide through a side chain)	acid, esters, amides.	acid, esters, amides
cleavage orthogonal to:	acid-labile groups (Far, Boc), noble-metal-labile groups (eg. Aloc)	acid-labile groups (Far, Boc), base-labile groups (e.g. Fmoc, Pal), noble-metal-labile groups (e.g. Aloc)	acid-labile groups (e.g. Far, Boc), base-labile groups (e.g. Fmoc, Pal), noble-metal-labile groups (e.g. Aloc)	acid-labile groups (e.g. Far, Boc), base-labile groups (e.g. Fmoc, Pal), noble-metal-labile groups (e.g. Aloc)
linker orthogonal to:	acid	base, noble metal.	acid, base, and noble metal.	acid, base, and noble metal.
disadvantages:	*N*-Boc chemistry allows only for introduction of one prenyl group at N terminus of peptide.	no introduction of C-terminal functionality, unless attachment through the side chain of an amino acid.	linker susceptible to cleavage under nucleophilic aerobic conditions, loss of peptide during cleavage, requirement for protection of amines during cleavage	loading not optimal, requirement for protection of amines during cleavage

2.3.1.1. *Kaiser Benzophenone Oxime Resin*

A resin that has been used for the synthesis of a library of some small Ras C-terminal peptides is the Kaiser benzophenone oxime resin.[44] Tetrapeptides with a N-terminal S-farnesylated cysteine[45] and a similar tetrapeptide with an additional biotin tag[46] were readily synthesized on this resin and cleaved from the resin with L-amino acid benzyl ester tosylates under mildly acidic conditions. The requirement for *N*-Boc chemistry, however, limits the freedom and flexibility with respect to placement of the prenyl groups. As such, the resin can only be used for the synthesis of peptides featuring one prenyl group, which is located at the N-terminus of the peptide.

2.3.1.2. *Trityl Linker*

The trityl linker allows for cleavage of the synthesized peptide under mildly acidic conditions that are compatible with most prenyl groups. When the peptide is connected to the trityl linker through its C terminus, the cleaved product will be the free carboxylic acid. As such, the trityl linker does not allow for the generation of additional functionality at the C terminus. However, when the peptide is anchored to the resin through a side chain of one of the amino acids, for example, the ε-NH_2 group of lysine, the linker can be used for the synthesis of lipidated peptides with functional C termini.[47,48]

This approach has been applied mainly for polybasic lipidated peptides. The synthesis of peptides, such as those corresponding to the C termini of Rho A, K-Ras 4B, and D-Ral, is based on the anchoring of a lysine side chain of the polybasic stretch to a trityl linker. The amino acid that is coupled through its side chain to the resin is best located close to the C terminus of the peptide. In this way, troublesome block condensations on the solid support with concomitant risk of racemization are avoided. The C-terminal farnesylated or geranylgeranylated cysteine of the Ras peptide is then introduced by coupling a prelipidated cysteine to the selectively deprotected carboxyl function of the anchored lysine. After obtaining such a dipeptide on the resin, the additional steps of the synthesis can be performed in the N-terminal direction by using standard protocols and, for example, an Fmoc/Aloc strategy. The Aloc-protected side chains of lysine and arginine can be liberated from the solid support by cleavage with palladium(0) and an appropriate nucleophile. Treatment of the resin with only 1% TFA and a scavenger subsequently releases the peptides while leaving the prenyl group intact. An example for a synthesis of such a polybasic prenylated peptide on a trityl linker is given in Scheme 5.[48]

The characteristics of the trityl linker can thus be summarized as: 1) it is orthogonal to prenyl groups, including geranylgeranyl; and 2) it allows for introduction of functional groups both in the sequence and at the C terminus. A critical requirement for the use of the trityl linker in the above described method is the presence of an anchor group in the C-

 © 2006 Wiley-VCH Verlag GmbH & Co. KGaA, Weinheim

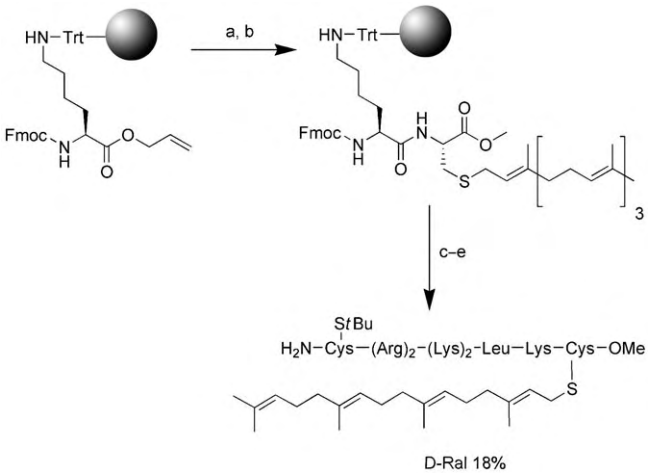

Scheme 5. Solid-phase synthesis of a D-Ral lipopeptide on trityl resin. a) $Pd(PPh_3)_4$, $PhSiH_3$, THF; b) H_2N-Cys(GerGer)-OMe, PyBop, NMM, CH_2Cl_2; c) 1. Fmoc-AA-OH, HATU, HOAt, DIPEA, DMF, 2. piperidine/DMF (1:4); d) $Pd(PPh_3)_4$, DMF/piperidine (1:4); e) TFA (1%) TES (2%) in CH_2Cl_2.

terminal part of the peptide sequence, which allows the linker to be cleaved from the resin afterwards with only 1% TFA. It turned out that 1% TFA is dilute enough not to lead to double-bond isomerization of even geranylgeranyl groups.

Another limitation to the method developed so far is the incompatibility with thioesters, for example, palmitoylated cysteine. The deprotection of the Aloc groups with piperidine as the scavenger is not compatible with the nucleophile-labile thioester. Optimization of the type of nucleophile might provide a solution, but deprotection of a large number of Aloc groups on the solid support is not always a trivial matter. Finally, Aloc deprotection turned out to be incompatible with the maleimide functionality as triphenylphosphin, used as ligand for the palladium catalyst, undergoes a nucleophilic attachment to this function.

The trityl linker/Aloc protecting group combination turned out to be the linker of choice for the synthesis of polybasic sequences and the method proved to be more efficient than other linker strategies that had a significantly lower efficiency.[47,48]

2.3.1.3. *Hydrazide Linker*

Although the trityl linker allows for the solid-phase synthesis of a variety of Ras peptides, it does not allow all types of peptides from the Ras superfamily to be synthesized. The aryl hydrazide linker was therefore investigated for the synthesis of lipidated peptides. This oxidation-sensitive group has been known for more than 30 years,[49] but has only recently been applied in the field of solid-phase peptide synthesis. As a linker, the aryl hydrazide group has been employed for the generation of small-peptide esters and amides[50,51] and cyclic peptides.[52] The linker is cleaved by oxidation to an acyldiazene, which is then attacked by a suitable nucleophile (Scheme 6). The two most utilized methods are a method that uses $Cu(OAc)_2$, O_2, and a nucleophile in situ and a method in which the linker is first oxidized with NBS followed by cleavage in a second step with a nucleophile. The linker is orthogonal to classical urethane protecting groups, such as Boc, Fmoc, and Aloc, and racemization does not occur upon cleavage. Typical nucleophiles that can be used for the cleavage are amines, water, and alcohols.[53] Owing to the oxidation sensitivity of the linker, the coupling reactions and especially the Fmoc-deprotecting reactions need to be performed in the absence of oxygen because of possible oxidation of the linker and subsequent cleavage with nucleophilic reagents that are present.

Although used previously for peptide synthesis, the special utility of the hydrazide linker really came to light when applied to the synthesis of lipidated peptides.[54–58] A typical peptide sequence synthesized on the hydrazide linker is shown in Scheme 7. The target peptide contains a farnesyl (Far) group, a palmitoyl thioester, and a fluorophore that is attached to a lysine side chain as well as a C-terminal methyl ester. Coupling conditions of the amino acids are similar to normal solid-phase peptide syntheses (SPPSs) with other linkers. One important precaution was taken, however, in the synthesis to avoid an *S*,*N* acyl shift of the palmitoyl group after the Fmoc deprotection of palmitoylated cysteine. To this end, it was found that the S-palmitoylated peptides remained stable when the Fmoc deprotection was performed by using a solution of 1% DBU in DMF for 2×30 seconds. The next coupling was performed immediately with preactivated amino acid and HATU as the coupling reagent.[56]

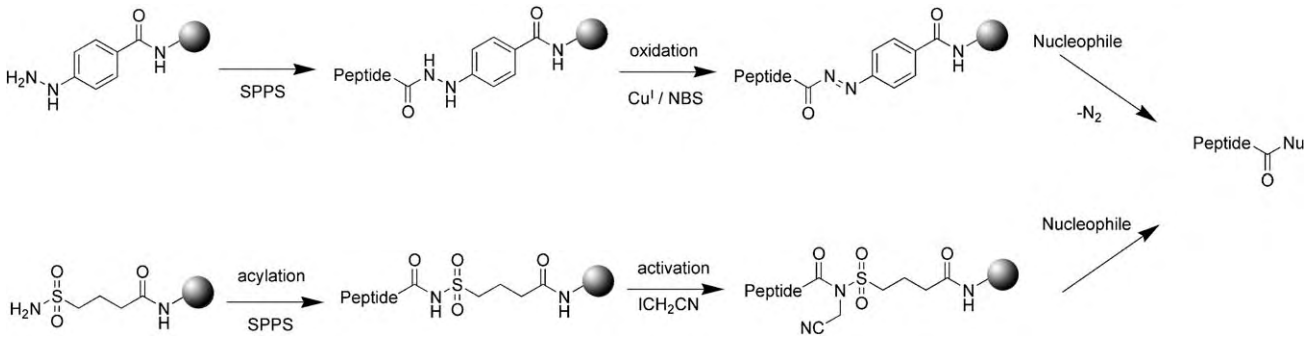

Scheme 6. Overview of the application of the aryl hydrazide and the Ellman sulfonamide linker in peptide synthesis. The hydrazide linker is activated for cleavage with a nucleophile through oxidation, whereas the sulfonamide linker is activated upon N-alkylation.

 © 2006 Wiley-VCH Verlag GmbH & Co. KGaA, Weinheim

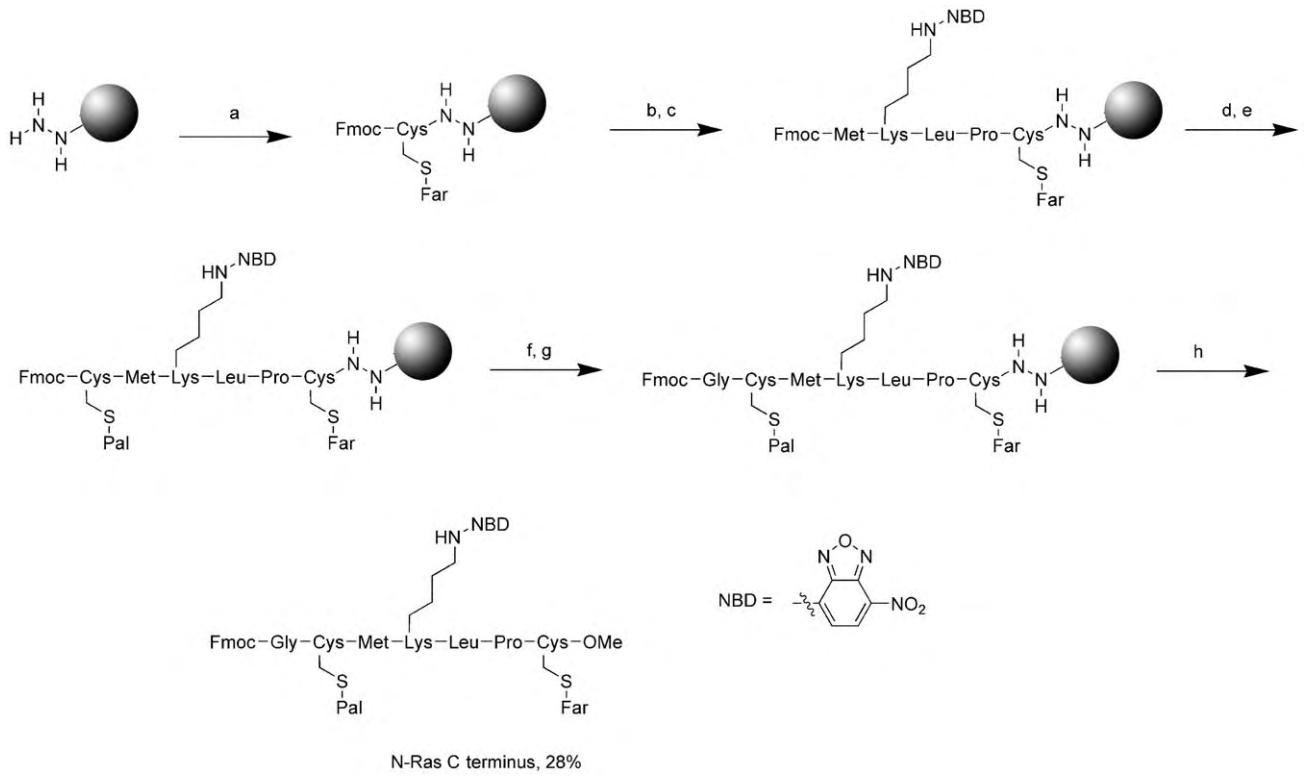

Scheme 7. Solid-phase synthesis of an N-Ras lipopeptide on hydrazide resin. a) Fmoc-Cys(Far)-OH, HBTU, HOBt, TMP, CH_2Cl_2/DMFs (1:1); b) piperidine/DMF (1:4); c) Fmoc-AA-OH, HBTU, HOBt, DIPEA, DMF; d) piperidine/DMF (1:4); e) Fmoc-Cys(Pal)-OH, HBTU, HOBt, TMP, CH_2Cl_2/DMF (1:1); f) DBU (1%) in DMF; g) Fmoc-Gly-OH, HATU (5 equiv), DIPEA (20 equiv) CH_2Cl_2/DMF (7:1); h) $Cu(OAc)_2$ (0.5 equiv), pyridine (30 equiv), acetic acid (50 equiv), methanol (215 equiv) CH_2Cl_2, O_2.

By using similar approaches, many different peptides were synthesized on the hydrazide linker, including those containing farnesyl, geranylgeranyl (GerGer), fluorescent labeled geranyl, and palmitoyl lipids. Fluorescent markers such as nitrobenzoxadiazole and photoactivatable groups like the benzophenone group have been introduced and Ras-superfamily peptides with C-terminal acid, ester, or amide functionalities have been cleaved from the resin.

An orthogonal linker does not diminish the use of protecting groups for the amino acid side-chain functionalities. Therefore, for peptides synthesized on the hydrazide linker, protecting groups were in general used that were either highly acid labile, such as the trityl group for alcohols, base labile, such as the 9-fluorenylmethyl ester group for the protection of carboxylic acids, or labile towards noble metals, such as the Aloc group for amines. These protecting groups can be cleaved from the peptide while still on the resin. However, amines are preferably not deprotected before cleavage as their nucleophilic nature gives rise to side products; the liberated amines attack the oxidized linker and cleave the peptide leading to cyclic peptides or oligomers. The more sterically demanding and less nucleophilic alcohol functions of, for example, the serine side chain feature these problems to a much lesser extent and can generally be deprotected on the resin. Protection of the amine functionalities after cleavage somewhat limits the flexibility in the sense that after cleavage from the solid phase, an additional deprotection step in solution is required.

An additional observation that was made during the course of the development of these solid-phase syntheses was that after oxidative cleavage of the hydrazide linker, fractions of the synthesized lipopeptides remained bound to the solid support by means of an unidentified linkage that could not be cleaved oxidatively or under acidic or basic conditions. As the oxidative cleavage of the hydrazide linker more than likely proceeds through an intermediate acyl radical, this radical may form a covalent bond with the polymeric support.[59,60]

2.1.3.4. Ellman Sulfonamide Linker

The Ellman sulfonamide linker is stable towards acid and base and is activated upon alkylation (nevertheless orthogonal to the methionine thioether). It then releases the target compounds after attack by a nucleophile.[61] These features are intrinsically orthogonal to the lipidated peptides of the Ras superfamily and therefore this sulfonamide linker was studied as a potential linker for their synthesis.[62] The first studies have indicated that this linker is indeed a valuable alternative for the synthesis of lipidated peptides and it even seems to outperform the hydrazide linker substantially in that it allows for the synthesis of peptides longer than 20 amino acids and with multiple lipid motifs, as, for example, shown by the synthesis of a NO-synthase-derived hexacosapeptide (Scheme 8). Additional studies concerning the general applicability of this linker are currently being undertaken (Table 1).

 © 2006 Wiley-VCH Verlag GmbH & Co. KGaA, Weinheim

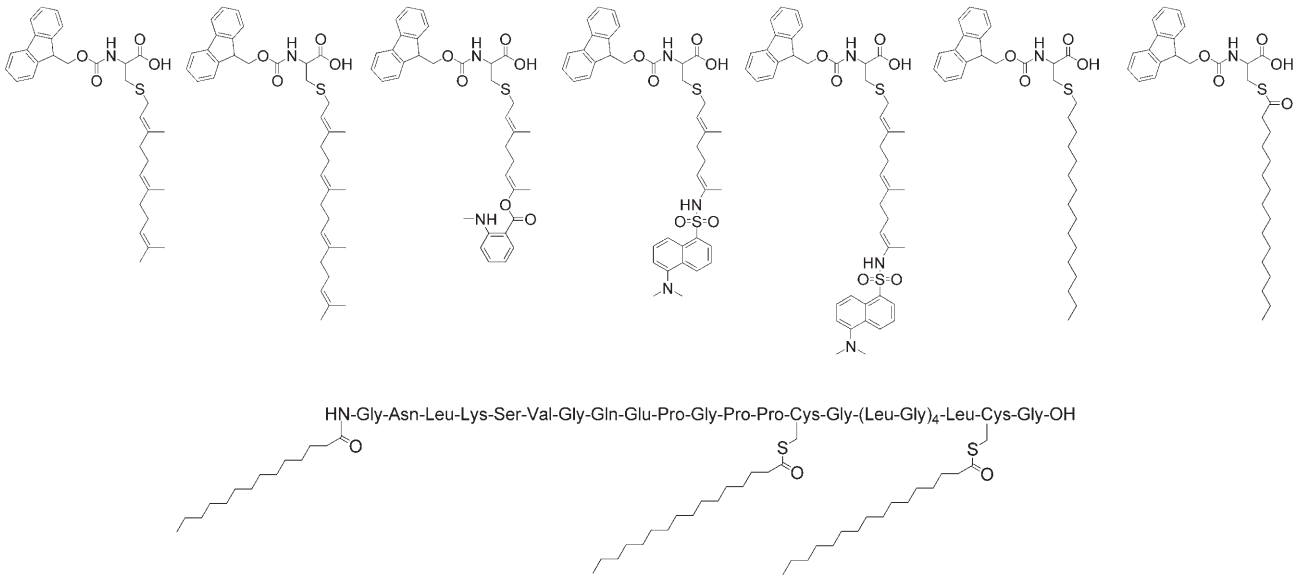

Scheme 8. Top: Lipidated cysteine building blocks for SPPS. Fmoc-Cys(Far)-OH, Fmoc-Cys(GerGer)-OH, Fmoc-Cys(GerMant)-OH, Fmoc-Cys(GerDansyl)-OH, Fmoc-Cys(FarDansyl)-OH, Fmoc-Cys(HD)-OH and Fmoc-Cys(Pal)-OH. Below: NO-synthase-derived hexacosapeptide synthesized by using prelipidated building blocks.

A recently investigated linker for the synthesis of lipidated peptides is the PTMSEL linker, which allows cleavage by using TBAF.[63] Although this linker only allowed for the synthesis of C-terminal carboxylic acid derivatives, its cleavage conditions are fully orthogonal to the lipid functionalities.

2.3.2. *Introduction of the Lipid Groups*

The introduction of the lipid functionalities into the peptide can basically be performed by using two protocols (independent of solid- or solution-phase chemistry). Either the lipid groups are introduced through coupling of prelipidated amino acids or they are introduced through lipidation of a selectively deprotected peptide, that is, a peptide with a free thiol group. Both on-resin lipidation[54,55,64–71] and the use of prelipidated building blocks[56,57] have been investigated for the synthesis of lipidated peptides on a solid support. Initially, the first approach was chosen to synthesize C-terminal Ras-GTPase peptides. An example for this approach is given in Scheme 9. An orthogonal protecting group strategy allowed the stepwise introduction of both a farnesyl and a palmitoyl group in the same peptide.[54,55] This protocol uses a large excess of the lipid groups, which is problematic if the lipid

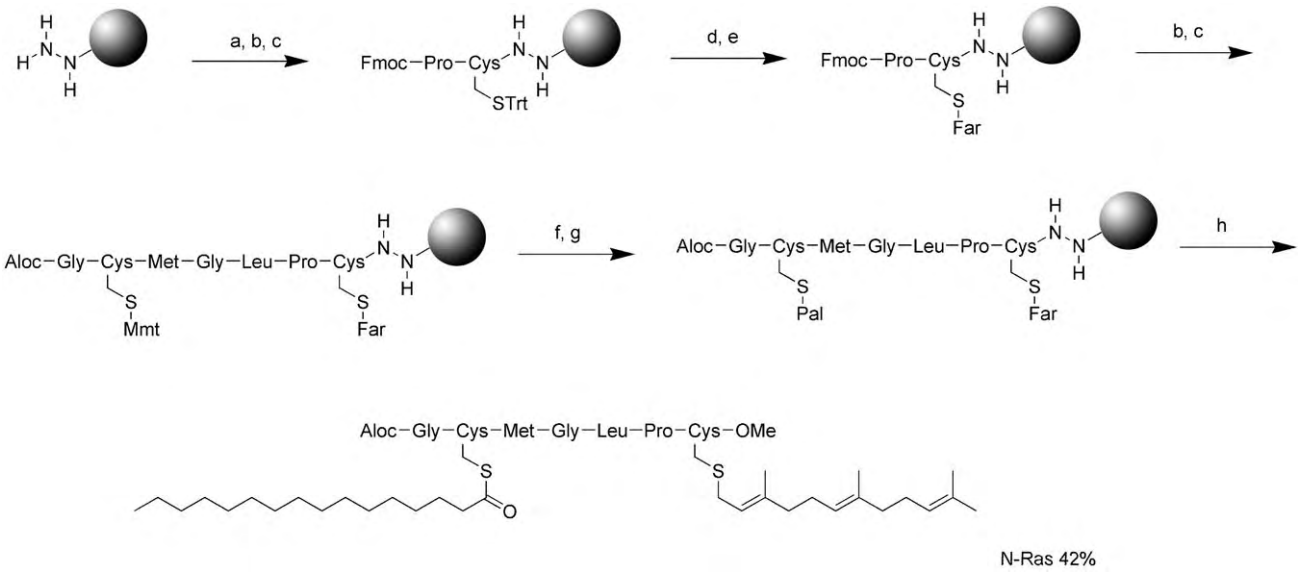

Scheme 9. Synthesis protocol by using on-resin lipidation.[54] a) Fmoc-Cys(Trt)-OH, DIC, HOBt, DMF; b) piperidine/DMF (1:1); c) Fmoc-AA-OH, HBTU, HOBt, DIEA, DMF; d) TFA (50%), TES, CH_2Cl_2; e) Far-Br, DIEA, DMF; f) TFA (1%), TES, CH_2Cl_2; g) Pal-Cl, HOBt, Et_3N, CH_2Cl_2, DMF; h) $Cu(OAc)_2$, acetic acid, pyridine, O_2, CH_2Cl_2, MeOH. Mmt = monomethyloxytrityl.

 © 2006 Wiley-VCH Verlag GmbH & Co. KGaA, Weinheim

groups need to be synthesized, for example, in a modified form, and as a result requires an extensive protecting-group strategy. As such, the introduction of several lipid groups of the same connection type, such as a geranylgeranyl group and a farnesyldansyl group, might become problematic. A possible solution to overcome this problem might be the application of the recently developed reversed approach of S-farnesylation and S-palmitoylation to solid-phase chemistry.[72] In this approach, lipid groups were introduced through S_N2 displacement of bromide by the reaction of a lipid containing a thiol group as the nucleophile with bromoalanine-containing peptides as the electrophile in solution. Another elegant approach to introduce the prenyl thioether into the peptide is the use of a chemoselective conjugate addition of a thiolate nucleophile (e.g. farnesylthiolate) to a dehydroalanine.[73] The absence of stereoselective control in this conjugate addition was nicely solved by using peptides containing aziridine-2-carboxylic acid.[74] This nonproteinogenic amino acid allowed for site- and stereoselective conjugation with various thiol nucleophiles both in solution and on the solid support. These newly developed methods for the incorporation of lipidated amino acids might prove beneficial in future syntheses of peptides of the Ras superfamily.

A further approach that builds on prelipidated cysteine building blocks is a different way to build up lipidated peptides and overcome the issues associated with on-resin prenylation. These prelipidated building blocks (Scheme 8) can be handled as normal amino acids in the coupling sequence and can be inserted anywhere within a sequence without the need to modify the protecting-group strategy. This therefore provides a highly flexible and generic approach that is applicable to other types of prenylated peptides. An example of this second approach is given in Scheme 10.[57] Two different prenyl groups could be introduced into the Rab7 peptides through the use of these prenylated cysteines. To avoid racemization in the cysteine couplings, methods were generally applied that avoided the use of basic conditions and polar solvents.

2.4. Conclusions for Peptide Synthesis

A large number of the peptides discussed in this review have been made both in solution and through solid-phase chemistry. This allows for a good comparison between the two methods. An overview of the critical differences between the solution- and solid-phase synthesis of lipidated peptides of the Ras superfamily can be found in Table 2. In general, both in terms of efficiency and flexibility, the solid-phase method is superior to the solution-phase synthesis in the large majority of cases. It gives purer peptides within a shorter period of time and with superior overall yields. The sequence and characteristics of the peptide have to be taken into consideration with respect to the selection of the linker for solid-phase synthesis. The hydrazide linker and the Ellman sulfonamide linker are, however, the most versatile linkers currently available.

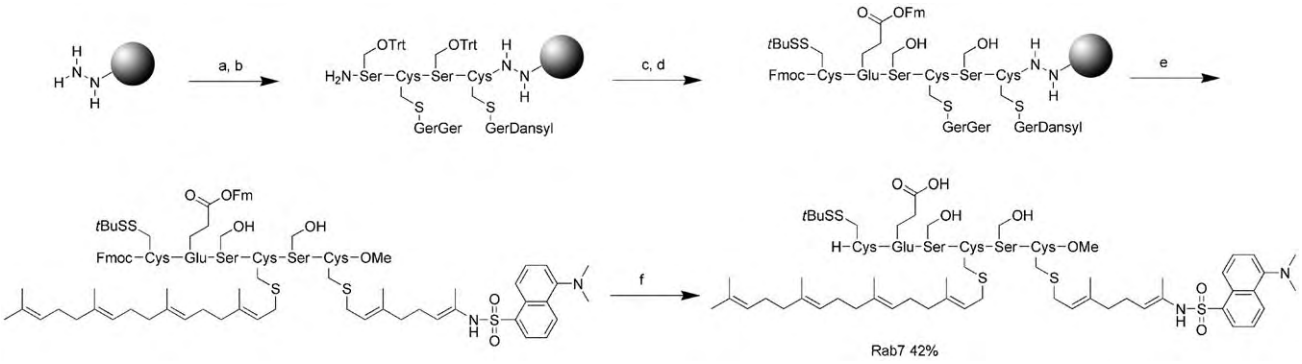

Scheme 10. Synthesis protocol by using lipidated building blocks.[57] a) Fmoc-AA-OH, DIC, HOBt, CH_2Cl_2/DMF (1:1); b) piperidine/DMF (1:2); c) Fmoc-Cys(SS*t*Bu)-Glu(OFm)-OH, DIC, HOBt, CH_2Cl_2/DMF (1:1); d) TFA (1%), TES (2%), CH_2Cl_2; e) $Cu(OAc)_2$, pyridine, O_2, CH_2Cl_2, MeOH; f) Et_2NH, CH_2Cl_2.

Table 2: Comparison of the synthesis characteristics of solution-phase and solid-phase synthesis of lipidated peptides of the Ras superfamily.

	Solution-phase synthesis	Solid-phase synthesis
purification	purification of each individual intermediate required, lower overall yield	only the final product needs to be purified through preparative chromatography
yield of a double lipidated hexamer	individual reactions have moderate to good coupling yields, overall yield: 7–8%	individual reactions go with almost complete conversion, overall yield: 40–50%
building block synthesis	yes	yes
peptide synthesis time (depends on sequence)	≈weeks	≈days
combinatorial aspects	not suited for library synthesis; new synthetic strategies may be required for each desired compound and long synthetic pathway	library synthesis possible; depending on point of divergence, synthetic efforts moderate
areas of cost	geranylgeranyl groups, low yields	resin and prelipidated cysteine building blocks

 © 2006 Wiley-VCH Verlag GmbH & Co. KGaA, Weinheim

By using solid-phase synthesis, a variety of the C termini of Ras-family GTPases have been synthesized, including H-, K-, N-Ras, Rab7, and RhoA peptides. The general methodology is, however, applicable to other types of lipidated peptides and a general length of 10 amino acids is usually readily accessible in multimilligram amounts. However, longer peptides can also be obtained, as illustrated, for example, by the synthesis of the triply lipidated hexacosapeptide of endothelial NO synthase, a 26mer.[62] Additionally, multiple functional groups, such as fluorophores, photoactive linkers, and elements for thiol conjugation, are regularly incorporated. The solid-phase methods are generally reliable and deliver functional peptides on a time scale of 1–2 weeks, including purification.

The developed solid-phase synthesis methods can now be used to make other types of lipidated peptides, peptides bearing non-natural amino acids or D-amino acids and, for example, peptides featuring other possibly biologically relevant lipidation motifs. The replacement of palmitoyl for other fatty acids has been shown to have biological relevance[75] and could be applied to proteins of the Ras family as well to investigate their influence on protein–protein and protein–lipid interactions. Similar to the discussed lipopeptides featuring prenyls modified with, for example, fluorophores, fatty acids like oleate and arachidonate could be introduced instead of the palmitoyl group. The developed chemistry is generally applicable to these functional fatty acids and should not lead to side reactions.

3. Synthesis of Lipidated Ras and Rab Proteins

3.1. Synthesis through Biological Methods and their Limitations

The production of recombinant proteins is a key technology in life sciences. However, progress in the generation of authentic or engineered polypeptides has been more difficult for proteins that undergo posttranslational modifications. This imbalance is primarily due to the intricacy of protein modification pathways as well as the lack of methodologies for their manipulation.[76]

The introduction of posttranslational modifications, such as phosphorylation, glycosylation, isoprenylation, and acylation, is typical for eukaryotic organisms. In prokaryotes, like *E. coli.*, these modifications generally do not occur, although it should be noted that *E. coli.* can be generated to express processing enzymes, like the *N*-myristoyl transferase.[77] This requires the synthesis of posttranslationally modified proteins to be performed almost exclusively in eukaryotic expression systems.[78–80] These production systems are, however, typically much more labor intensive (with respect to, for example, purification of the products) and have low yields and high costs. The situation is even more complex when the protein in question is modified with lipids at multiple sites.[81] The problem becomes particularly difficult when the desired functionalities have to be attached to a protein with a high degree of control in a site-specific manner, for instance, in the proximity of an active center or an interaction surface. These problems are related to the inapplicability of the otherwise powerful methods of organic chemistry to such large and diversely reactive molecules as proteins. The situation becomes even more dramatic when the proteins of interest undergo posttranslational modifications that are incompatible with other desired protein modifications or engineering. This makes the case more difficult as the modified proteins would not be recognizable by natural modification pathways. All these apparently nonorthogonal modifications apply to engineered proteins of the Ras GTPase superfamily.

Studies of Ras-superfamily proteins require methods that provide preparative amounts of lipidated proteins, both with natural and new functionalities, such as fluorescence, photoreactivity, spin-labeled groups, or lipid groups, at non-native positions. The recently developed protein-ligation methods provide the necessary platform for combining large recombinant protein scaffolds with peptides generated by organic synthesis.[82–86]

3.2. Synthesis through Protein-Ligation Methods

Progress in the area of protein-ligation methods has given access to a broad spectrum of methods for the semisynthetic production of posttranslationally modified proteins. These methods yield either native bonds (e.g. prior thiol group capture, native chemical ligation, or expressed protein ligation) or non-native bonds (e.g. imine capture ligation, oxime ligation, maleimidocaproic acid ligation). This combination of organic chemistry and molecular biology gives access to modified proteins (including both natural and non-natural modifications) that are generally not accessible thorugh other, for example, enzymatic, processes.[18]

A variety of methods exist for the introduction of modified lipids and lipopeptides into proteins. Three important approaches have been applied for Ras GTPases (Scheme 11). One approach for the introduction of modified lipids is through attachment in vitro of the modified prenyl lipids by using the corresponding prenyltransferases (Scheme 11C).[87,88] Both Ras[89,90] and Rab[91,92] proteins have been modified by using this approach. For this purpose, the protein is expressed with all amino acids and only the prenyl group(s) is (are) introduced at the later stage. This approach also allows for the incorporation of some non-natural prenyl analogues. Additionally, isoprenoid analogues have proven to be versatile tools for probing the mechanism and structure of prenyltransferases. Fluorescent or photoactive groups have been incorporated into the prenyl moiety, but smaller steric constraints have also been investigated with regard to the binding and subsequent functionality of the prenyltransferases.[87,93–107] Azide-carrying farnesyl groups are an especially promising approach for proteomics strategies.[108]

A second approach that incorporates synthetic lipidated peptides is based on the use of the maleimidocaproyl (MIC)-controlled ligation (Scheme 11B).[109] This ligation requires an accessible, for example, C-terminal free thiol group on the protein (usually from a cysteine,) to connect the N-terminally MIC-modified peptide. The third approach, expressed protein ligation (EPL),[110,111] connects a lipidated peptide with an N-

 © 2006 Wiley-VCH Verlag GmbH & Co. KGaA, Weinheim

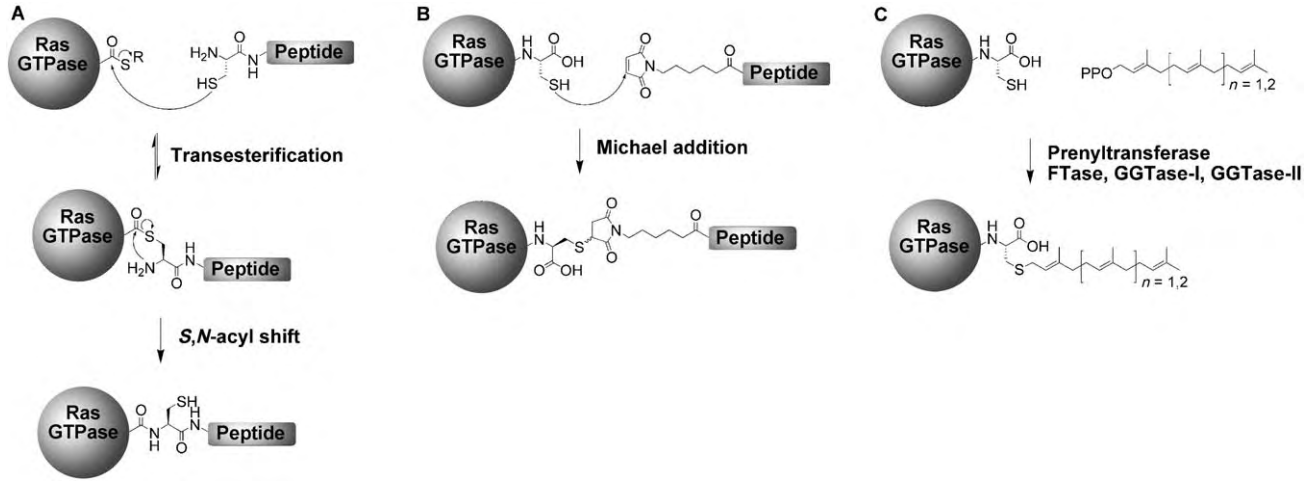

Scheme 11. Methods applied for the introduction of the natural and modified lipidated C terminus on Ras GTPases: A) Expressed protein ligation (EPL); B) Maleimidocaproyl (MIC) ligation; C) Prenylation by using prenyltransferases.

terminal cysteine to the C terminus of a thioester-tagged Ras GTPase through a native peptide bond (Scheme 11 A).

Each of the ligation techniques has its own typical characteristics, which are briefly summarized in Table 3. Illustrative examples of Ras GTPase synthesis through MIC ligation for N-Ras and EPL for Rab are given in the following sections.

3.2.1. *Expressed Protein Ligation of Rab Proteins*

Full-length Rab proteins contain approximately 210 amino acids, with the cysteine residues bearing prenyl groups localized on the last four C-terminal amino acids.[112] Rab proteins, including their C-terminally truncated forms, can be expressed without posttranslational modifications in *E. coli*. This expression system allows the Rab proteins to be expressed fused to an engineered intein, followed by a chitin binding domain (CBD). This enables purification and isolation of the corresponding C-terminal thioesters of the truncated Rab proteins.[113]

The prenylated C-terminal Rab peptides synthesized through organic-synthesis methods are generally only sparingly soluble in aqueous media because of their apolar lipid modifications. The ligation of lipopeptides containing an N-terminal cysteine to Rab proteins was first explored by using a ligation assay.[114] By using C-terminal thioester-tagged Rab7ΔC6 and the test peptide CK(dansyl)C(GG)-OMe, it was found that the otherwise robust native chemical ligation did not proceed for this lipidated peptide in plain buffer solution. To increase the solubility of the peptides, a wide range of detergents was tested of which cetyltrimethylammonium bromide (CTAB) was selected as it appeared to be the most potent facilitator of the prenylation reaction.

To generate preparative amounts of fluorescent Rab7 proteins that bear geranylgeranyl moieties at different positions, preparative ligation reactions were performed in vitro.[57,114–116] The reactions proceed overnight and typically yielded around 85% of coupled (unpurified) Rab protein. The protein usually precipitates after ligation and the noncovalently bound peptide can usually be removed by simple extraction of the ligation mixture with organic solvent. The remaining insoluble pellet, mainly containing the protein, was dissolved in 6 M guanidinium chloride and then refolded by stepwise dilution into CHAPS-containing buffer solution.

Table 3: Comparison of the different protein synthesis methods applied for the synthesis of Ras GTPases.

Synthesis method	Characteristics	Requirements	Applied to
expressed protein ligation	native peptide bond, free thiol group at the connection site in the final product.	protein/peptide with C-terminal thioester. peptide/protein with N-terminal cysteines.	Rab1, Rab7, K-Ras
maleimide ligation	non-natural thioether bond, free carboxylic acid group at the connection site in the final product, selectivity issue.	protein with C-terminal cysteines. Peptide with N-terminal maleimide. only one accessible cysteine allowed.	H-Ras, N-Ras
prenylation in vitro	limited access to proteins with other functional groups. Acceptance of modified prenyl donor.	Protein with CAAX box (FTase/GGTase-I) or with double cysteine motif (GGTase-II). Additional protein factor (e.g. REP). Processing enzymes (aaX protease, carboxylmethyl transferase)	Rab7, H-Ras

 © 2006 Wiley-VCH Verlag GmbH & Co. KGaA, Weinheim

Subsequently, REP-1 (Rab escort protein) or GDI (GDP-dissociation inhibitor) protein was added and the formed complex was further purified by dialysis and gel filtration. The approach yields native, correctly folded Rab7 GTPases and the procedure produces similar results regardless of the number of conjugated prenyl groups. An overview of some of the Rab7 proteins synthesized by using EPL is given in Scheme 12. Similarly, EPL has also been used to obtain a K-Ras construct.[48] For Ras proteins, no chaperone is available to solubilize the lipidated protein. In the case of K-Ras, however, the C-terminal polybasic sequence aids in solubilizing the protein and allows purification.

3.2.2. *Maleimide Ligation with N-Ras Proteins*

All Ras isoforms are prenylated on the C-terminal cysteine in the CaaX box by a cytosolic farnesyltransferase, followed by a cleavage of the last three amino acids (aaX), and conversion of the S-farnesylated cysteine into a methyl ester. The N- and H-isoforms of Ras undergo an additional modification, that is, palmitoylation of one or two other cysteines located at the C-terminus. All these modifications are not easily performed by using biological techniques and therefore lipidated peptides featuring the required functional groups were synthesized and ligated to truncated Ras proteins at the C-terminus.[117,118]

For this purpose, the Ras protein was expressed in a truncated form in bacteria with a free C-terminal cysteine, providing a reactive thiol group for the MIC ligation. This cysteine is highly exposed to the solvent because of the flexibility of the C terminus. This makes the ligation reaction fast and selective. Further cysteines in the protein sequence are buried and therefore less accessible, limiting the extent of side reactions.[119] However, the ratio of peptide to protein has to be limited and generally should not exceed 3:1 to prevent additional MIC ligations. Purification of the neolipoprotein utilizes the additional hydrophobicity of the lipid groups. Extraction with a Triton X-114 saturated solution at a temperature above 30 °C separated the ligated protein from unligated protein. A collection of natural and non-natural lipopeptides have been synthesized and used for the generation of specifically functionalized Ras proteins. Apart from prenyl groups of different lengths and nonhydrolyzable palmitoyl group analogues, fluorescent markers and photoactivatable groups have also been introduced. (Scheme 13)

3.2.3. *Diels–Alder Ligation*

A recently developed protein-ligation method that has shown applicability to Ras GTPases is the Diels–Alder ligation.[120] First results with peptides demonstrated the general applicability of the Diels–Alder ligation. With the exception of cysteines with free thiol functions, all amino acids were tolerated. The incompatibility with free thiol groups can usually be solved by temporarily blocking free thiol functions on proteins. The Diels-Alder ligation was

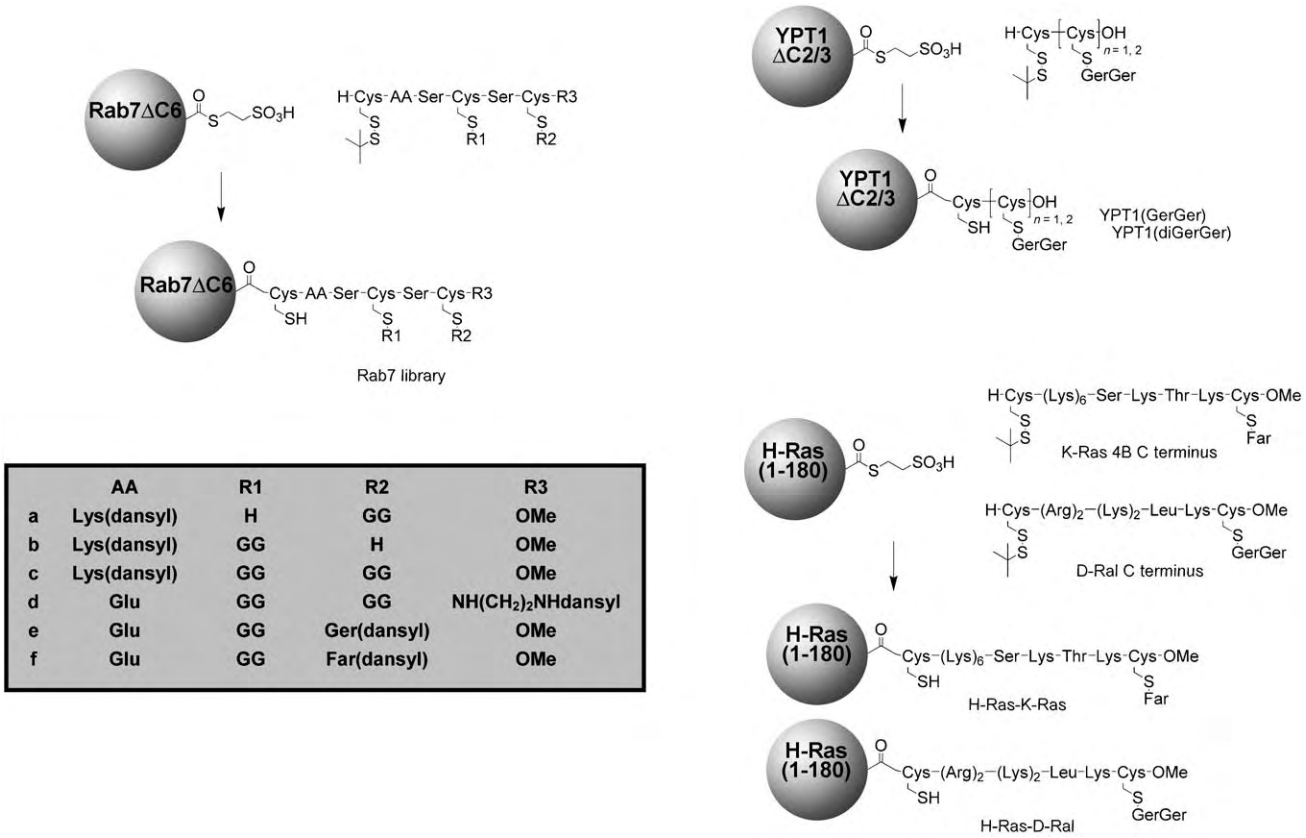

	AA	R1	R2	R3
a	Lys(dansyl)	H	GG	OMe
b	Lys(dansyl)	GG	H	OMe
c	Lys(dansyl)	GG	GG	OMe
d	Glu	GG	GG	$NH(CH_2)_2NH$dansyl
e	Glu	GG	Ger(dansyl)	OMe
f	Glu	GG	Far(dansyl)	OMe

Scheme 12. Synthesis of a collection of Rab and Ras proteins by using EPL.

© 2006 Wiley-VCH Verlag GmbH & Co. KGaA, Weinheim

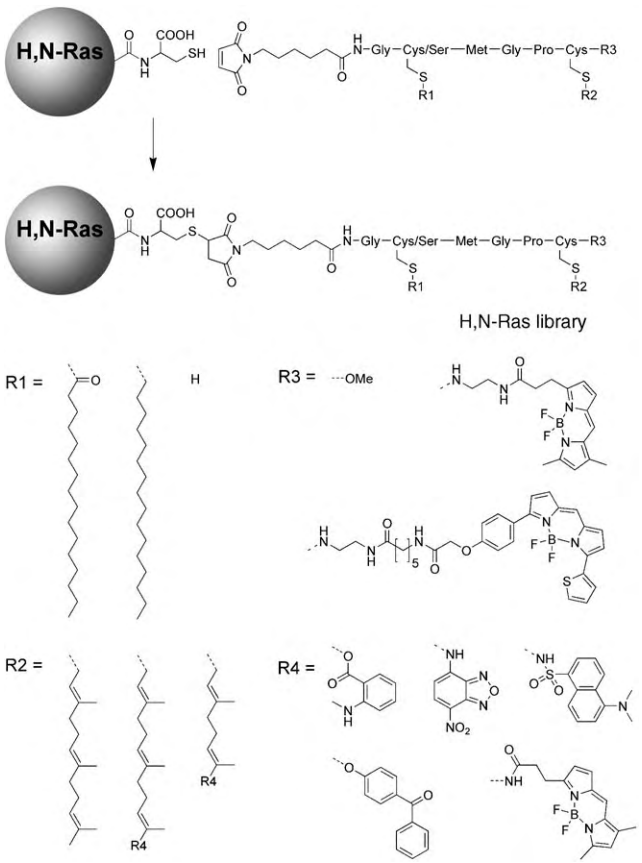

Scheme 13. A collection of semisynthetic neo-Ras proteins, synthesized by using MIC coupling.

applied for the ligation of a lipidated peptide to Rab7ΔC6. The functionality of the GTPase after ligation was demonstrated by its ability to bind the REP-1. The method could also be used to immobilize proteins on glass slides.

4. Biophysical Studies with Lipidated Peptides

4.1. Insertion into Model Membranes

Although the structure of the soluble part of the Ras protein (residues 1–166) was solved by both X-ray diffraction[121,122] and solution NMR spectroscopy,[123] the structure, dynamics, and details of the membrane association of the C terminus were primarily investigated by employing lipidated peptides. Extensive work has been performed in this area,[30] for example, studies were undertaken to investigate the membrane binding of a doubly lipid-modified synthetic heptapeptide that mimics the C terminus of the human N-Ras protein (residues 180–186).[124–126] A variety of biophysical methods (attenuated total reflectance (ATR) FTIR, quantitative ^{1}H MAS NOESY, ^{2}H solid-state NMR spectroscopy, and neutron diffraction) were used to investigate where the peptide backbone and side chains are localized in the membrane, what their dynamic transversal distribution is, and how the lipid chains of the peptide insert into the host phospholipid bilayer.

The C terminus of the human N-Ras protein contains two lipid modifications, a farnesyl chain and a palmitoyl chain, to facilitate biophysical studies. This C terminus was prepared carrying two deuterated lipid modifications. A model summarizing the results of the experiments obtained for the lipidated Ras peptide binding to a membrane is shown in Figure 2. The polypeptide chain of the doubly lipid-modified

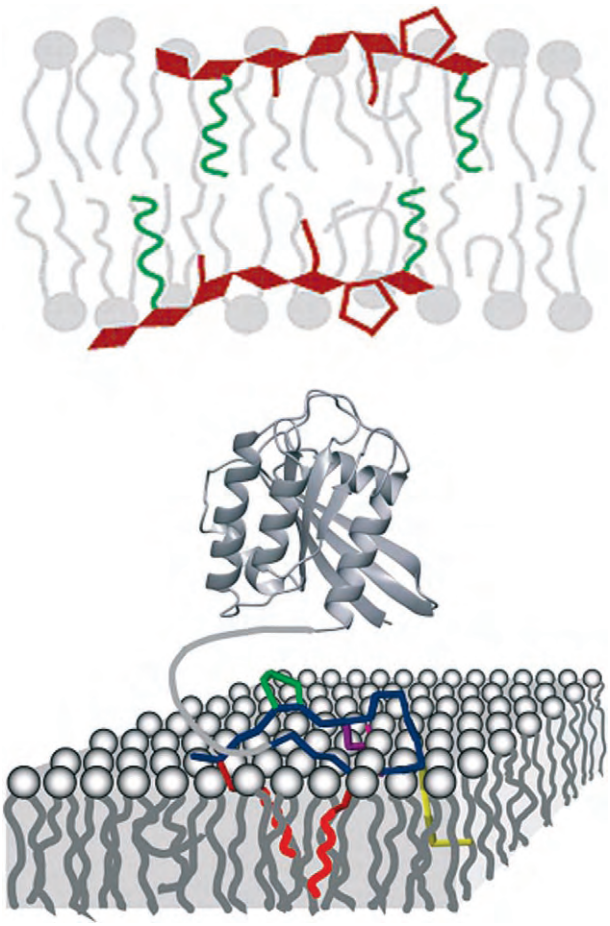

Figure 2. Structural results for membrane insertion of the lipid-modified Ras peptide.[125,127]

N-Ras peptide is located at the lipid–water interface of the membrane (in contrast to polybasic lipidated peptides), and signatures of a defined peptide secondary structure were not found. The peptide lipid chains insert completely into the phospholipid acyl chain region, maximizing the hydrophobic interactions. Additionally, the hydrophobic amino acid side chains also penetrate the middle chain region and contribute to a free-energy minimum of the lipid–peptide complex. Therefore, the peptide is assumed to have a flexible structure in the bilayer and to experience large conformational freedom. Consequently, the location of the peptide segments is described by broad distribution functions to be parallel to the membrane normal. As the C terminus of the Ras protein is unstructured, the described mobile peptide conformation appears to be relevant for the structure of the full-length membrane-bound Ras protein.

 © 2006 Wiley-VCH Verlag GmbH & Co. KGaA, Weinheim

A similar result was recently found for the binding of the completly lipidated N-Ras protein to model membranes.[127] The experimental results obtained for the Ras peptide were in excellent agreement with recent molecular-dynamics studies.[128] The molecular-dynamics simulations for a 10-ns time scale showed that the lipid chains of the peptide are more moble than those of the surrounding phospholipids chains. It was additionally found that the peptide at the membrane is rather rigid, but can bindin different extended conformations. The exact mechanism of insertion of Ras proteins into membranes in vivo might also involve specific farnesyl membrane receptors.[129,130] Proposed candidates for farnesyl-mediated membrane receptors are Sos,[131] PI3K,[132] and PDEδ.[133]

4.2. Membrane Subdomain Binding

The structure and lateral organization of lipids and proteins in biological membranes are issues under heavy scrutiny in the fields of membrane biochemistry and biophysics.[30,134–136] The existence of membrane subdomains with different lipid composition and the relationship between lipid-domain formation and the conformation and functional properties of membrane-associated proteins is one of the central questions in this field. In a chemical biological approach to clarify some of these aspects for membrane-embedded lipidated proteins, the effects of a fluorescent peptide on model membranes consisting of binary and ternary lipid mixtures were explored.[137] The peptide contained a farnesyl and a palmitoyl anchor, thus representing a membrane-recognition model system for N-Ras proteins. Specifically, the influence of the peptide on lipid lateral organization and concentration fluctuations as well as the possibility of molecular sorting of lipids by the embedded peptide was explored.

From these studies, it could be concluded that palmitoyl/farnesyl dual-lipidated peptides do not associate preferentially with liquid-ordered or gel-like domains in phase-separated bilayer membranes. In particular, the study shows the interesting ability of the peptide to induce formation of fluid microdomains at physiologically relevant cholesterol concentrations. This effect very much depends on the concentration of fluid compared with that of ordered lipid molecules. The peptide apparently has a high affinity for a fluid environment. It could also be concluded that, in general, the palmitoyl/farnesyl dual-lipidation motif found in proteins such as Ras may not promote significant association with liquid-ordered or gel-like domains in phase-separated bilayer membranes. Therefore partitioning into biological lipid rafts driven by lipoprotein–lipid interactions only is unlikely (analogous with the results of solely prenylated proteins).[32,138–140] These results seem to concur with the observations made with NMR spectroscopy and neutron diffraction.[125] The membrane association of N-Ras is, however, not analogous to H-Ras, for example, which was found to have a strong affinity for lipid rafts upon GDP loading.[141,142] This is in agreement with the idea that the lipidated C terminus of Ras proteins is one of the regulators of the specific membrane localization of the complete protein.

Recently, the complete lipidated and fluorescently labeled N-Ras protein was produced through a combined chemical and biological approach and was found to have a preference for the liquid-disordered phase over the liquid-ordered and solid-ordered phase.[143] Fluorescence measurements of the lipidated protein gave analogous results to those obtained for the peptide, suggesting that for N-Ras, the membrane localization is probably completely governed by the lipidated C terminus, in contrast to, for example, H-Ras, for which other elements of the polypeptide chain are also involved in its localization.[142]

Analysis of the localization of lipidated N-Ras in lipid microdomains with AFM yielded improved spatial resolution compared with the fluorescence measurements (Figure 3). These AFM measurements revealed that, to a large extent,

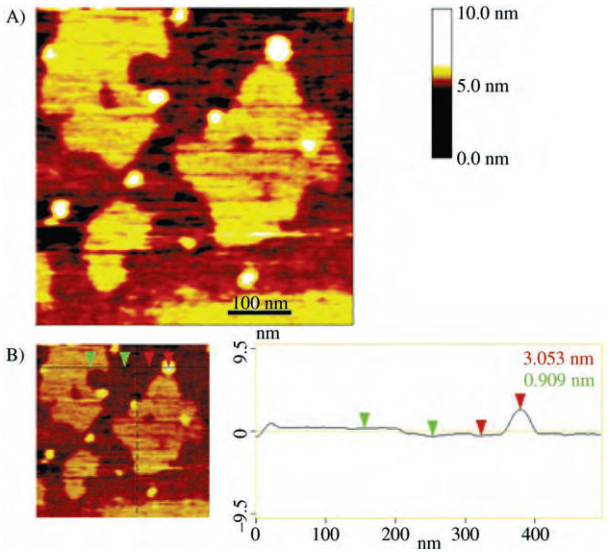

Figure 3. A) AFM images of N-Ras in supported lipid bilayers (POPC/BSM/Chol 2:1:1; $T = 25\,^{\circ}C$). B) Concomitant section profile of the AFM image. The protein can be targeted in l_o raft domains as well as in l_d domains, showing the expected height difference of about 3–4 nm, which roughly corresponds to the linear dimension of N-Ras.

the lipidated protein is located in the boundary region of the domains in mixed-phase liquid-ordered/liquid-disordered bilayers. This might lead to a favorable decrease in line energy (tension), which is associated with the rim of the demixed phases. The specific localization and accumulation of N-Ras proteins on the interfaces of lipid-bilayer domains may favor protein–protein interactions and hence may serve as a vehicle for protein association. Recent studies and calculations on plasma-membrane compartmentalization of GFP-labeled H- and K-Ras constructs indicated that lipidated proteins on the inner plasma membrane are able to drive the formation of nanoclusters.[144–146]

The pamitoyl functionality, though being the most abundant S-acylated fatty acid, is not the only fatty acid found connected to protein cysteines. Different acylation motifs may substantially influence the functionality of the lipidated

© 2006 Wiley-VCH Verlag GmbH & Co. KGaA, Weinheim

protein under scrutiny. It has been shown, for example, that Src-family kinases can be acylated with dietary fatty acids other than myristate and palmitate. This differential fatty acylation with unsaturated fatty acids results in the displacement of these lipidated kinases from membrane rafts.[75] Similar studies might be undertaken for Ras-family proteins to investigate the localization of these proteins and the influence of different lipidation motifs on protein–protein and protein–lipid interactions and their influence on downstream signaling events.

5. Structural and Biological Studies of Lipidated Ras and Rab Proteins

5.1. Structural Biology of Rab Proteins

Knowledge of the structures of Rab/Ypt proteins (Ypt = yeast protein transport, the yeast analogue of the mammalian Rab) and their interacting proteins is essential to understand the mechanism of their action and vesicular transport processes in cells at the molecular level. The structures of many Rab proteins, both in GTP- and in GDP-bound forms, are known.[147–154] However, crystal-structure information of Rabs in complex with effector proteins had, with the exception of the Rab3A–Rabphilin-3A complex,[155] not been obtained. In view of the numerous interactions in which Rab proteins participate, the lack of structural information is striking and required addressing.

An important interaction partner of Rabs is Rab GDI. GDI associates with prenylated Rab proteins and retrieves inactivated Rab protein (i.e. Rab with bound GDP) from the membrane at the end of its functional cycle and delivers it back to the donor membranes. The importance of this protein–protein interaction stimulated intense research of several groups into the structural elucidation of the complex. Initially, the structure of GDI with geranylgeranyl cysteines was solved, which led to the false suggestion that the lipid binding site is located on domain I above the mobile effector loop.[156] This structure, however, lacked the complete fully lipidated Rab. It was therefore decided to generate complexes of mono- and diprenylated Rabs with GDI by using a combination of chemistry and biology.

Crystallization studies of Rab proteins require efficient methods to provide preparative amounts of prenylated Rab proteins. The semisynthesis of prenylated Rab proteins by means of EPL was shown to be generally applicable to different Rabs and peptides and to be capable of producing relatively large amounts of pure and homogeneous protein material (see Section 3.2.1).[114,115] To elucidate the structure of the complex between prenylated Rabs and GDI, a chemical biological approach was selected by employing the synthesis of Rab proteins through EPL. Ypt1, truncated by two residues, was expressed and produced with a C-terminal thioester.[116] To simplify the preparation of suitable amounts of prenylated peptides, a readily accessible monoprenylated dicysteine peptide was made, providing ready access to preparative amounts of prenylated protein after their ligation to Ypt1ΔC2. The ligation of the cysteine-containing dipeptide to Ypt1ΔC2 led to native monoprenylated Ypt1. After the addition of GDI, a 1:1 complex was isolated by gel filtration and then crystallized. The part of the structure of the complex of the monoprenylated Ypt1 and GDI, which displayed binding of the critical C terminus of Ypt1 in a pocket on GDI, is shown in Figure 4.

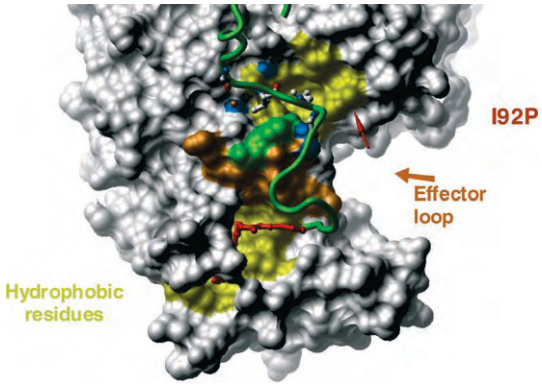

Figure 4. Binding of the monoprenylated Rab1 C terminus to GDI and the molecular basis of familial mental retardation caused by the GDI I92P mutation.

Analysis of the complex showed that the single prenyl group was found to be sufficient to confer binding of Ypt1 to GDI. Ypt1 primarily contacts the highly conserved Rab binding platform of GDI comprising the switch I and II regions, which are sensitive towards the nucleotide-bound state of GTPases, explaining the observed preference of GDI for the GDP-bound conformation of Rab proteins. Interactions of Ypt1 and GDI mainly rely on the contact of the last C-terminal 20 amino acid residues of Ypt1, including the hydrophobic isoprenoid(s). The C-terminal binding region (CBR) induces a 90° turn in the C terminus of Ypt1, enabling the geranylgeranylated C terminus to coordinate to GDI through a hydrophobic patch (upper yellow-colored surface in Figure 4). This is in accordance with observations that mutations in this area, for example, the I92P mutation, lead to erroneous Rab membrane extraction and delivery.[157,158] Recently, the structure of a double-prenylated Ypt1 in complex with GDI, produced through similar chemical biological methods, was also obtained.[159] This structure shows the positioning of the two prenyl groups close to each other in the same hydrophobic area as that of monogeranylgeranylated Ypt1 and provided a general model for the Rab–GDI/REP selectivity and the binding and extraction of prenylated Rabs to membranes.

The results obtained with respect to the structural and kinetic properties of the GDI–Rab interaction have allowed formulation of a simple model for the extraction of Rabs from membranes by both GDI and for the structurally and mechanistically related REP molecule.[159] According to this model, GDI or REP can recognize the GDP-bound form of Rab by an initial interaction that only involves the globular part of the GTPase. Subsequently, docking of the Rab C terminus onto GDI/REP leads to extraction of the prenyl moieties from the membrane, a process that is driven by

 © 2006 Wiley-VCH Verlag GmbH & Co. KGaA, Weinheim

binding of the lipid groups in the highly hydrophobic GDI/REP binding site. The driving force for the overall extraction process is the difference in affinities (and therefore interaction free energies) between the initially bound state (only the globular part involved) and the final bound state (globular part and lipidated C terminus involved). As this difference is much greater for GDI than for REP, it explains the observed greater efficiency of GDI in lipid extraction, which is commensurate with its main biological role. The delivery process, while obviously being a reversal of the extraction process at some level, probably also involves a membrane-bound factor with specificity for specific Rab molecules (GDF; GDI-displacement factor). The extraction/delivery process is reversible as long as GDP is bound to Rab, but is made irreversible by the action of an exchange factor that catalyzes GDP replacement by GTP, thus reducing the affinity of GDI/REP for Rab.

5.2. Biophysics of Ras Proteins

The semisynthesis of Ras lipoproteins has allowed for selective modification of the natural anchors in the Ras C termini as well as binding studies that utilize biosensors equipped with artificial membranes. For N-Ras membrane anchoring, it could be shown that two hydrophobic modifications (isoprenylation and S-acylation) are essential for stable insertion. Under nonhydrolyzing conditions, the exact nature of the alkylchain linkage makes no difference for membrane binding. Both the natural palmitoyl thioester and a stable hexadecylthioester at the same cysteine show the same stability of membrane binding.[119] Furthermore, the biophysical behavior of Ras lipoproteins did not differ from that of streptavidine conjugates with the corresponding biotinylated Ras lipopeptides,[160] indicating that specific structural properties of the protein core are interchangeable in such model experiments as long as this moiety dominates the solubility of the entire lipoprotein complex in aqueous solutions.

To obtain a more-detailed insight into the kinetics of the membrane binding of lipidated proteins, experiments were designed that required the generation of fluorescent and lipid-labeled peptides and proteins. Lipidated peptides containing C-terminal esters of cholesterol and related steroids as membrane anchors and representing the C terminus of the hedgehog protein were synthesized, studied, and ligated to the N-Ras protein.[161] Biophysical and cell biological fluorescence experiments on these Hedgehog peptides and modified N-Ras proteins showed that the membrane characteristics of lipidated peptides and lipidated proteins differ significantly. The experiments showed that, for example, a cholesterol moiety, which is able to incorporate peptides almost irreversibly to membranes, does dissociate with half-lives of about 3 h when attached to a 20 kDa protein.

In two recent studies, the synthesis of Ras lipoproteins with the basic K-Ras4B C terminus was achieved through EPL (see Section 3.2.1),[48] and synthesis of GFP-K-Ras4B was achieved through conjugation of the farnesylated K-Ras4B terminus to GFP by a cysteine iodoacetamide coupling.[38] These protein-synthesis approaches enabled detailed studies on the membrane-insertion process of this Ras isoform, which is driven by both electrostatic and hydrophobic contributions. Results from these studies supported the concept that the cationic charges on the protein C terminus interact strongly with negative charges in the membrane layer, thus enabling efficient binding of the monoprenylated K-Ras4B lipoprotein.[27] The preparation and study of a GFP construct with an all-D-amino acid C terminus confirmed the electrostatic mechanism over a highly specific K-Ras4B membrane receptor.[38]

5.3. Biophysics of Rab Proteins

The prenylation of Ras-GTPase family members occurs through the reaction of soluble phosphoisoprenoids (farnesyl or geranylgeranyl) with one or two C-terminal cysteine residues of the target protein forming a thioether linkage. In the case of Rab proteins, this prenylation is catalyzed by Rab geranylgeranyltransferase (RabGGTase or GGTase-II).[162] This enzyme transfers the geranylgeranyl moieties onto two C-terminal cysteines of the Rab GTPases (wide range amino acid sequences) and requires REP as an additional factor for its activity. Unlike other prenyltransferases, RabGGTase does not recognize a specific cysteine-containing C-terminal sequence, but rather a complex of the RabGTPase with REP. The ensuing diprenylation reaction is a multistep process that was previously proposed to follow a random sequential mechanism in which one cysteine is weakly preferred for the first prenylation.[163] However, owing to the inaccessibility of selectively functionalized Rab proteins, monocysteine mutants of Rab proteins were used in all cases to provide only an approximation of the native situation. Moreover, the available reports have disputed the exact sequence of isoprenoid addition.[163,164] It is also not entirely clear to which extent the monoprenylated Rab–REP complex dissociates from RabGGTase between two rounds of prenylation. Upon diprenylation, the conjugated isoprenoids are removed from the active site in order to bind to a lipid-binding site on REP, inducing a conformational change that leads to dissociation of the complex.[165,166] By using a combination of chemical synthesis and EPL, mono- and digeranylgeranylated fluorescent RabGTPases were synthesized (see Section 3.2.1), allowing the elucidation of these aspects of the Rab proteins.[114,115]

The interactions of the synthesized monoprenylated Rab GTPases with RabGGTase were analyzed by means of Förster resonance energy transfer (FRET) with a dansyl fluorophore positioned at the chemically synthesized C terminus.[114] It was found that the C-terminally prenylated (Cys 207) form interacts with RabGGTase with a several fold higher affinity than Rab7 prenylated on Cys 205. The higher affinity of prenylated Rab proteins appears to arise from a difference in effective association rates. It was proposed that this is due to steric constraints imposed by the active site of RabGGTase on the monoprenylated C terminus. The availability of an environmentally sensitive fluorophore near the prenylation site allowed development of a fluorescence-based Rab prenylation assay. By using this assay, the rates for

© 2006 Wiley-VCH Verlag GmbH & Co. KGaA, Weinheim

conversion of the monoprenylated reaction intermediates into the diprenylated reaction product were determined. The obtained rate is in excellent agreement with values reported previously for the Rab diprenylation reaction as determined by other assays. These data indicate that the more-tightly bound monoprenylated reaction intermediate is also more-rapidly converted to the diprenylated product. It was concluded that the majority of Rab7 proteins proceed to diprenylation by first acquiring prenylation on the C-terminal cysteine, followed by modification of the N-terminal cysteine (Scheme 14).

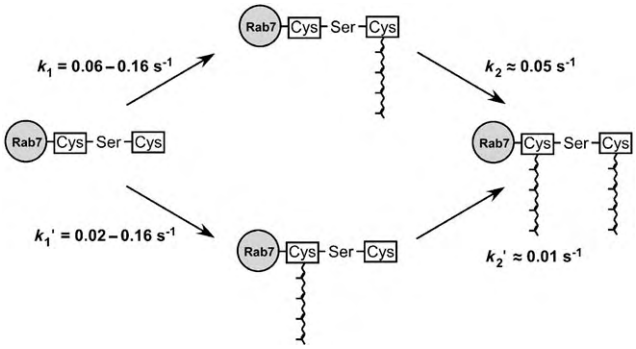

Scheme 14. Rab7 diprenylation reaction by RabGGTase and the associated rate constants.[114]

6. Ras Proteins as Tools in Cell Biology

6.1. Cellular Localization and Trafficking of Ras

Having demonstrated their principal functionality in living cells,[119] semisynthetic production of MIC-coupled Ras lipoproteins has been extended for the introduction of several functional modifications in the C-terminal segment. A first challenge was the placement of fluorescent tracer groups suitable for fluorescence microscopy into the chemically synthesized lipopeptide at locations that do not impair the biological activity of the lipoprotein. These studies revealed that incorporation of a fluorescent group in the isoprenoid moiety could not match both requirements. Either the tracer was sufficiently small and hydrophobic to mimic the size of the farnesyl function but possessed inadequate fluorescence properties for observation in living cells, or it gave suitable fluorescence signals after microinjection but was too large or polar for correct membrane insertion of the isoprenoid chain, leading to a loss of biological activity. Replacement of the C-terminal methyl ester by a strong fluorophore served to overcome the dilemma. This new fluorescent Ras lipoprotein was capable of inducing the Ras signal transduction pathway and gave a fluorescence distribution pattern, after microinjection in several cell lines, that corresponded perfectly with data from corresponding GFP-Ras constructs. Yielding the same quality of the fluorescence detection, the new constructs now allowed for selective manipulation of the posttranslational status of the lipoprotein (Figure 5).[42]

After peptide studies were performed,[167] the possibility of externally defining the modification status of Ras lipoproteins became a key element in the analysis of trafficking of H- and N-Ras lipoproteins between the plasma membrane and intracellular membranes. The use of a fluorescent Ras lipoprotein with a nonhydrolyzable alkyl thioether instead of the native palmitoyl thioester proved that reversible acylation is necessary for the constitutive de- and reacylation cycle of H- and N-Ras in the living cell and that is attributed to the control of Ras activity in the different organelles (Figure 6).[168]

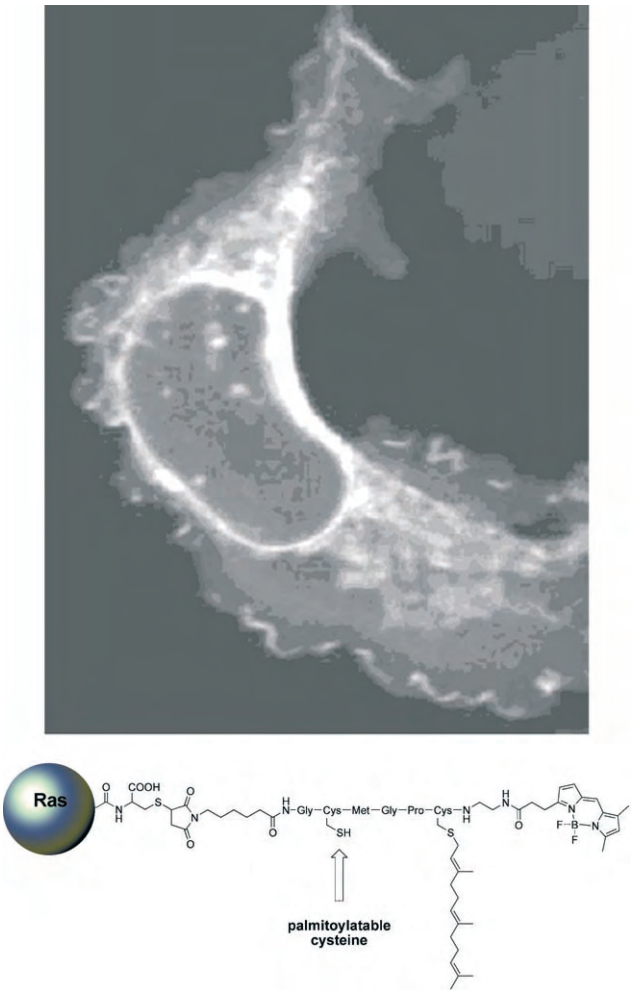

Figure 5. Fluorescent Ras lipoprotein with a BodipyFL group at the C terminus. The lipoprotein shows an identical staining of intracellular membrane structures (Golgi apparatus and plasma membrane) as observed for GFP-Ras constructs.

6.2. Mapping of Isoprenoid-Sensitive Ras Binding Partners

Beside its function in membrane anchoring, there are several hints that the isoprenyl group in posttranslationally modified Ras might be directly involved in the interaction with regulators like the guanine-nucleotide exchange factor Sos,[131] or effectors such as PI3-kinase.[132] To address the role of the farnesyl moiety in such protein–protein and protein–lipid interactions, photoactivatable groups can be introduced into the Ras lipoproteins as a new functional element

 © 2006 Wiley-VCH Verlag GmbH & Co. KGaA, Weinheim

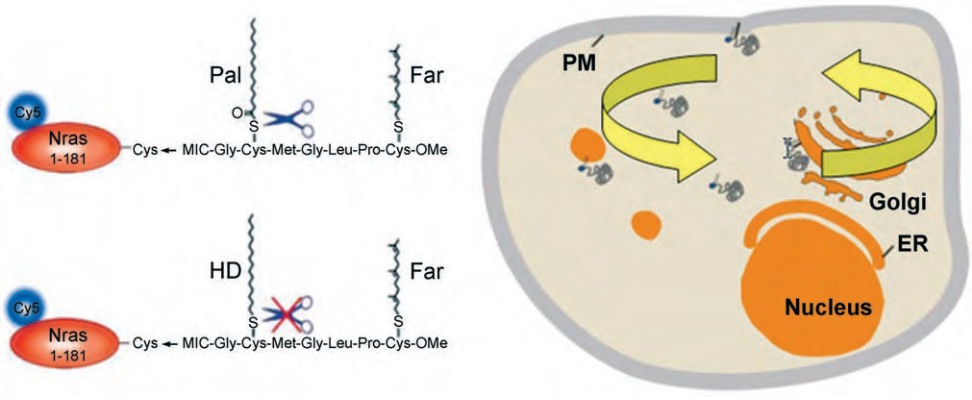

Figure 6. Model for a constitutive de- and reacylation cycle of H- and N-Ras in living cells.[168] S-palmitoylation of the two Ras isoforms occurs at the Golgi apparatus, followed by directed vesicular transport to the plasma membrane where the protein can be released after enzymatic hydrolysis of the thioester. A lipoprotein with a nonhydrolyzable hexadecylthioether impaired this process and caused complete mislocalization of the Ras lipoprotein, arguing for an essential fine tuning of Ras palmitoylation for correct targeting.

(Scheme 15). In this context, substitution of isoprenoid fragments in the farnesyl residue was performed. The modification with benzophenone groups appears not to disturb the isoprenoid function. Accordingly, the biological activity of such benzophenone modified Ras constructs could be demonstrated in a cellular assay in which phaeochromocytoma cells (PC12) differentiated into a neurite-like cell type upon microinjection of oncogenic Ras mutants with a isoprene-benzophenone modification.[40] The benzophenone-

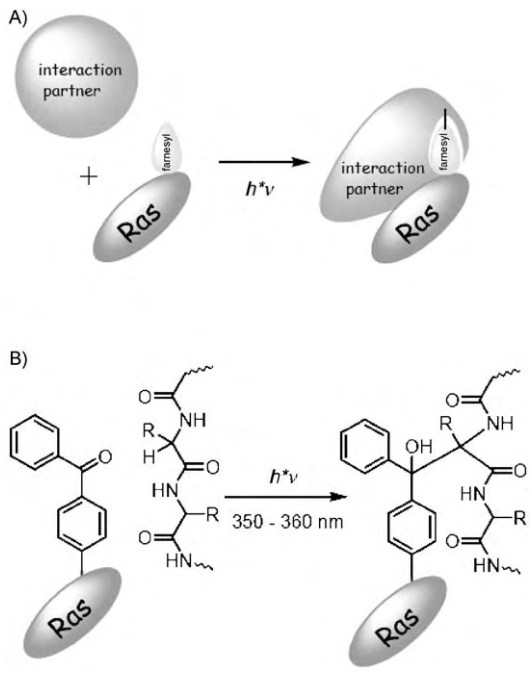

Scheme 15. A) Photolabeling of farnesyl-sensitive binding sites in Ras interaction partners by benzophenone-modified isoprene structures. B) After complex formation, the photoactivatable group is illuminated leading to spontaneous insertion into C–H bonds of the Ras binding partner in the direct proximity of the isoprenoid element.

Ras lipoproteins showed an enhanced nucleotide-exchange activity after stimulation with Sos and gave a specific coupling product after activation of a Ras–Sos mixture with UV light.[41]

The concept of mapping established isoprene-sensitive binding partners of Ras by photoactivatable lipoproteins is now extended to identify so far unknown effectors, regulators, or receptors. In particular, membrane-bound Ras receptors might be responsible for targeting of these small GTPases to the correct membrane substructures and help to explain the spatial–temporal pattern of Ras activity. For this purpose, membrane-permeable benzophenone lipopeptides are developed to open a proteomic access for proteins expressed in eukaryotic cell cultures.

6.3. Chemical Genetic Applications for Ras Lipopeptides and Lipoproteins

Owing to the involvement of oncogenic Ras mutations in the development of cancer diseases, inhibition of Ras activity is a promising approach in the development of new anticancer drugs. On the basis of the indispensable connection between membrane anchoring and biological activity of both natural and mutant Ras proteins, a blockade of the posttranslational modification steps of this protein came to the fore. Several farnesyl transferase inhibitors have been developed by pharmaceutical companies worldwide.[169] The employment of the palmitoylation process would open up a new opportunity to target oncogenic H- and N-Ras. The isoprenylation step of Ras proteins could be addressed by enzymatic assays with bacterially expressed Ras and farnesyl transferase.[170] For the palmitoylation process, two enzyme complexes were recently found that appear to play an important role in the regulation of the palmitoylation state of the proteins: a human protein palmitoyltransferase complex was discovered consisting of DHHC9 (with a DHHC cysteine-rich domain) and GCP16, a palmitoylated membrane protein that is localized on the Golgi[171] and the acylprotein thioesterase 1 (APT1) was analyzed as a protein putatively involved in regulating the status of posttranslational modification of N- and H-Ras.[172]

To employ the palmitoylation process, a chemical genetics approach was studied that utilized semisynthetic lipopeptides and lipoproteins. APT1-inhibitors (Scheme 16) were developed that prevented differentiation of PC12 cells by oncogenic N-Ras if this protein had to be processed within the cell. The biological activity of a N-Ras lipoprotein with a complete membrane anchor was not reduced by the same inhibitor.

 © 2006 Wiley-VCH Verlag GmbH & Co. KGaA, Weinheim

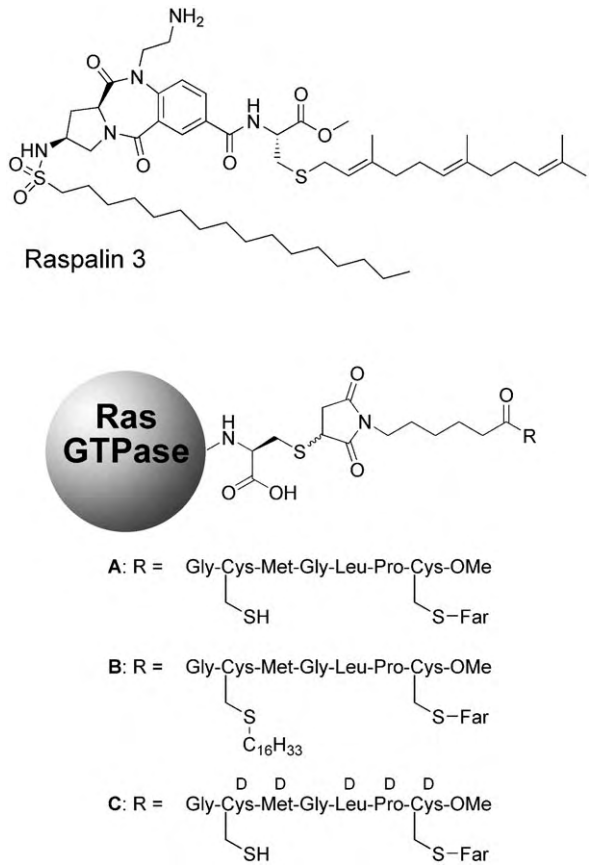

Scheme 16. Top: The benzodiazepinedione Raspalin 3, a 30 nM APT1 inhibitor. Bottom: and a small selection of semisynthetic Ras proteins employed in the study of the validation of APT1 as a Ras palmitoylation enzyme.

Experiments with N-Ras lipopeptides and lipoproteins in vitro revealed that APT1 might function as a bidirectional enzyme, promoting both Ras palmitoylation and depalmitoylation, depending on the local environment and substrate availability. In this investigation, several semisynthetic Ras proteins were employed as indispensable tools without which the whole study would have been impossible (see Scheme 16 for a small selection). By using protein **A** (Scheme 16), it could be shown, for example, that the addition of Raspalin 3 to **A** in PC12 cells reduced the neurite outgrowth rate compared to the absence of Raspalin 3. Raspalin 3 had no effect on the neurite outgrowth induced by protein **B**, which features a hydrolysis-resistant hexadecyl thioether. The stereotolerance of the enzyme catalyzing the S-palmitoylation was investigated by microinjection of protein **C**. Protein **C**, induced a differentiation rate comparable to its natural analogue **A**, thus demonstrating the large substrate tolerance of the enzyme involved. By using additional model peptides, it was shown that APT1 can depalmitoylate and pamitoylate the Ras protein in vitro. Combined with the data obtained from the semisynthetic proteins, this indicates that APT1 most probably has a direct involvement with Ras palmitoylation in vivo.

7. Conclusions and Outlook

The life sciences are molecular. Obtaining information from genomic and proteomic approaches and resolving biological problems therefore require interdisciplinary research that integrates chemistry and biology. This integration has led to the development of the field of chemical biology. The application of approaches originating from chemistry and the subsequent combination of chemistry and biology has allowed the study of biological phenomena previously not possible through chemical or biological approaches alone.[173,174] This approach was illustrated herein by the synthesis and biological evaluation of lipidated peptides and proteins of the Ras superfamily.

For such an integrated research activity, differently modified proteins that carry modifications whose structure can be changed at will through synthesis are invaluable tools. They enable experiments that yield answers in precise molecular detail that are hardly accessible with biological techniques alone. In the first part of this review, we discussed the progress made in the synthesis of the lipidated peptides from the Ras superfamily. Recently developed solid-phase-synthesis methods are the preferred synthesis method for the majority of the required peptides. They give access to native and modified peptides on a scale that allows peptide-consuming studies such as for X-ray crystal-structure determination. These designed peptides have served to elucidate biological questions by using a variety of biophysical studies. The lipidated peptides can also be ligated to proteins and the ways of connecting these lipidated peptides to truncated Ras or Rab proteins by using different chemical biological methods were discussed. This approach has enabled the successful synthesis of previously not available proteins, both labeled and unlabeled forms, in desired quantities. It has also allowed the elucidation of many biological aspects of the Ras-family GTPases.

Prospects for the investigation of Ras-superfamily proteins through chemical biological approaches are blooming. In our view, the research on these proteins in the upcoming years should see a focus on their cellular localization, trafficking, and processing and on the identification and structure determination in complex with interaction partners. The chemical tools to obtain the majority of the required proteins have been developed. From a chemical point of view, the methods developed for the synthesis of Ras lipopeptides and lipoproteins can now be applied and investigated for other proteins with diverse and not readily accessible lipidation motifs.

Abbreviations

AA	amino acid
Aloc	allyloxycarbonyl
Boc	*tert*-butoxycarbonyl
BSM	brain sphingomyelin
CHAPS	3-[(3-cholamidopropyl)dimethylammonio]-propanesulfonic acid
Chol	cholesterol

 © 2006 Wiley-VCH Verlag GmbH & Co. KGaA, Weinheim

DBU	1,8-diazabicyclo[5.4.0]undec-7-ene
DIC	diisopropylcarbodiimide
DIEA	*N*,*N*-diisopropylethylamine
DIPEA	*N*,*N*′-diisopropylethylamine
DMF	*N*,*N*-dimethylformamide
EDC	1-ethyl-3-[3-dimethylaminopropyl]carbodiimide hydrochloride
Far	farnesyl
Fmoc	9-fluorenylmethoxycarbonyl
GDI	GDP-dissociation inhibitor
GDF	GDI-displacement factor
GDP	guanosindiphosphate
GerGer	geranylgeranyl
GTP	guanosintriphosphate
HATU	*O*-(7-azabenzotriazole-1-yl)-*N*,*N*,*N*′,*N*′-tetramethyluroniumhexafluorophosphate
HBTU	*O*-benzotriazole-*N*,*N*,*N*′,*N*′-tetramethyluroniumhexafluorophosphate
HOAt	1-hydroxy-7-azabenzotriazole
HOBt	1-hydroxybenzotriazole
NBS	*N*-bromosuccinimide
NMM	*N*-methylmorpholine
Pal	palmitoyl
POPC	palmitoyloleoyl phosphatidylcholine
PTMSEL	(2-phenyl-2-trimethylsilyl)ethyl
PyBop	benzotriazole-1-yl-oxytripyrrolidinophosphoniumhexafluorophosphate
REP	Rab escort protein
SPPS	solid-phase peptide synthesis
TBAF	tetrabutylammoniumfluoride
TES	triethylsilyl
TFA	trifluoroacetic aicd
TFE	trifluoroethanol
TMP	trimethylpyridine
Trt	trityl group

We are grateful to our colleagues, to those working in our groups, and to those working in the field of the chemical biology of RasGTPases for stimulating discussion. LB would like to thank the Alexander von Humboldt foundation for support through the Sofja Kovalevskaja Award. Our research was generously supported by the Max Planck Gesellschaft, the Deutsche Forschungsgesellschaft, the Volkswagen Stiftung, and the Fonds der Chemischen Industrie.

Received: March 6, 2006

[1] Y. Takai, T. Sasaki, T. Matozaki, *Physiol. Rev.* **2001**, *81*, 153 – 208.
[2] M. Barbacid, *Annu. Rev. Biochem.* **1987**, *56*, 779 – 827.
[3] M. H. Gelb, *Science* **1997**, *275*, 1750 – 1751.
[4] J. Kuhlmann, *Methods Mol. Biol.* **2004**, *283*, 217 – 220 ("Bioconjugation Protocols: Strategies and Methods").
[5] J. L. Bos, *Biochim. Biophys. Acta* **1997**, *1333*, M19 – M31.
[6] D. J. G. Mackay, A. Hall, *J. Biol. Chem.* **1998**, *273*, 20685 – 20688.
[7] M. Zerial, H. McBride, *Nat. Rev. Mol. Cell Biol.* **2001**, *2*, 107 – 117.
[8] J. B. Bock, H. T. Matern, A. A. Peden, R. H. Scheller, *Nature* **2001**, *409*, 839 – 841.
[9] M. S. Moore, *J. Biol. Chem.* **1998**, *273*, 22857 – 22860.
[10] I. R. Vetter, C. Nowak, T. Nishimoto, J. Kuhlmann, A. Wittinghofer, *Nature* **1999**, *398*, 39 – 46.
[11] M. D. Resh, *Biochim. Biophys. Acta* **1999**, *1451*, 1 – 16.
[12] J. T. Dunphy, M. E. Linder, *Biochim. Biophys. Acta* **1998**, *1436*, 245 – 261.
[13] F. L. Zhang, P. J. Casey, *Annu. Rev. Biochem.* **1996**, *65*, 241 – 269.
[14] A. I. Magee, L. Gutierrez, I. A. Mckay, C. J. Marshall, A. Hall, *EMBO J.* **1987**, *6*, 3353 – 3357.
[15] J. A. Duncan, A. G. Gilman, *J. Biol. Chem.* **1996**, *271*, 23594 – 23600.
[16] Y. T. Guo, Y. M. Li, Y. F. Zhao, *Chin. J. Org. Chem.* **2004**, *24*, 722 – 727.
[17] A. Watzke, L. Brunsveld, T. Durek, K. Alexandrov, A. Rak, R. S. Goody, H. Waldmann, *Org. Biomol. Chem.* **2005**, *3*, 1157 – 1164.
[18] B. L. Nilsson, M. B. Soellner, R. T. Raines, *Annu. Rev. Biophys. Biomol. Struct.* **2005**, *34*, 91 – 118.
[19] F. R. Naider, J. M. Becker, *Biopolymers* **1997**, *43*, 3 – 14.
[20] D. Kadereit, H. Waldmann, *Monatsh. Chem.* **2000**, *131*, 571 – 584.
[21] D. Kadereit, J. Kuhlmann, H. Waldmann, *ChemBioChem* **2000**, *1*, 144 – 169.
[22] C. Peters, M. Wagner, M. Volkert, H. Waldmann, *Naturwissenschaften* **2002**, *89*, 381 – 390.
[23] F. Eisele, D. J. Owen, H. Waldmann, *Bioorg. Med. Chem.* **1999**, *7*, 193 – 224.
[24] O. Seitz, I. Heinemann, A. Mattes, H. Waldmann, *Tetrahedron* **2001**, *57*, 2247 – 2277.
[25] I. Heinemann, M. Völkert, H. Waldmann, *Methods Mol. Biol.* **2004**, *283*, 221 – 232 ("Bioconjugation Protocols: Strategies and Methods").
[26] L. Pegoraro, L. Moroder in *Houben-Weyl Methods of Organic Chemistry, Synthesis of Peptides and Peptidomimetics*, *Vol. E 22b* (Eds.: M. Goodman, A. Felix, L. Moroder, C. Toniolo), Thieme, Stuttgart **2003**, pp. 333 – 374.
[27] R. Leventis, J. R. Silvius, *Biochemistry* **1998**, *37*, 7640 – 7648.
[28] S. Quesnel, J. R. Silvius, *Biochemistry* **1994**, *33*, 13340 – 13348.
[29] S. Shahinian, J. R. Silvius, *Biochemistry* **1995**, *34*, 3813 – 3822.
[30] J. R. Silvius, *Prog. Protein-Lipid Interact.* **2002**, *52*, 371 – 395.
[31] J. R. Silvius, F. Lheureux, *Biochemistry* **1994**, *33*, 3014 – 3022.
[32] T. Y. Wang, R. Leventis, J. R. Silvius, *Biophys. J.* **2000**, *79*, 919 – 933.
[33] D. Kadereit, P. Deck, I. Heinemann, H. Waldmann, *Chem. Eur. J.* **2001**, *7*, 1184 – 1193.
[34] D. Kadereit, H. Waldmann, *ChemBioChem* **2000**, *1*, 200 – 203.
[35] C. B. Xue, J. M. Becker, F. Naider, *Tetrahedron Lett.* **1992**, *33*, 1435 – 1438.
[36] L. Liu, G. F. Jang, C. C. Farnsworth, K. Yokoyama, J. A. Glomset, M. H. Gelb, *Methods Enzymol.* **1995**, *250*, 189 – 206 ("Lipid Modifications of Proteins").
[37] F. Ghomashchi, X. H. Zhang, L. Liu, M. H. Gelb, *Biochemistry* **1995**, *34*, 11910 – 11918.
[38] N. M. Okeley, M. H. Gelb, *J. Biol. Chem.* **2004**, *279*, 21833 – 21840.
[39] M. Berezovski, W. P. Li, C. D. Poulter, S. N. Krylov, *Electrophoresis* **2002**, *23*, 3398 – 3403.
[40] J. Kuhlmann, A. Tebbe, M. Volkert, M. Wagner, K. Uwai, H. Waldmann, *Angew. Chem.* **2002**, *114*, 2655 – 2658; *Angew. Chem. Int. Ed.* **2002**, *41*, 2546 – 2550.
[41] M. Volkert, K. Uwai, A. Tebbe, B. Popkirova, M. Wagner, J. Kuhlmann, H. Waldmann, *J. Am. Chem. Soc.* **2003**, *125*, 12749 – 12758.

 © 2006 Wiley-VCH Verlag GmbH & Co. KGaA, Weinheim

[42] R. Reents, M. Wagner, J. Kuhlmann, H. Waldmann, *Angew. Chem.* **2004**, *116*, 2765 – 2768; *Angew. Chem. Int. Ed.* **2004**, *43*, 2711 – 2714.
[43] R. Reents, M. Wagner, S. Schlummer, J. Kuhlmann, H. Waldmann, *ChemBioChem* **2005**, *6*, 86 – 94.
[44] W. F. Degrado, E. T. Kaiser, *J. Org. Chem.* **1980**, *45*, 1295 – 1300.
[45] E. K. Dolence, J. M. Dolence, C. D. Poulter, *J. Comb. Chem.* **2000**, *2*, 522 – 536.
[46] E. K. Dolence, J. M. Dolence, C. D. Poulter, *Bioconjugate Chem.* **2001**, *12*, 35 – 43.
[47] B. Ludolph, F. Eisele, H. Waldmann, *ChemBioChem* **2002**, *3*, 901 – 904.
[48] D. Gottlieb, C. Grunwald, C. Nowak, J. Kuhlmann, H. Waldmann, *Chem. Commun.* **2006**, 260 – 262.
[49] T. Wieland, J. Lewalter, C. Birr, *Justus Liebig Ann. Chem.* **1970**, *740*, 31 – 47.
[50] A. N. Semenov, K. Y. Gordeev, *Int. J. Pept. Protein Res.* **1995**, *45*, 303 – 304.
[51] C. R. Millington, R. Quarrell, G. Lowe, *Tetrahedron Lett.* **1998**, *39*, 7201 – 7204.
[52] C. Rosenbaum, H. Waldmann, *Tetrahedron Lett.* **2001**, *42*, 5677 – 5680.
[53] C. Peters, H. Waldmann, *J. Org. Chem.* **2003**, *68*, 6053 – 6055.
[54] B. Ludolph, H. Waldmann, *Chem. Eur. J.* **2003**, *9*, 3683 – 3691.
[55] B. Ludolph, F. Eisele, H. Waldmann, *J. Am. Chem. Soc.* **2002**, *124*, 5954 – 5955.
[56] G. Kragol, M. Lumbierres, J. M. Palomo, H. Waldmann, *Angew. Chem.* **2004**, *116*, 5963 – 5966; *Angew. Chem. Int. Ed.* **2004**, *43*, 5839 – 5842.
[57] L. Brunsveld, A. Watzke, T. Durek, K. Alexandrov, R. S. Goody, H. Waldmann, *Chem. Eur. J.* **2005**, *11*, 2756 – 2772.
[58] M. Lumbierres, J. M. Palomo, G. Kragol, S. Roehrs, O. Müller, H. Waldmann, *Chem. Eur. J.* **2005**, *11*, 7405 – 7415.
[59] M. Volkert, S. Koul, G. H. Muller, M. Lehnig, H. Waldmann, *J. Org. Chem.* **2002**, *67*, 6902 – 6910.
[60] J. A. Camarero, B. J. Hackel, J. J. de Yoreo, A. R. Mitchell, *J. Org. Chem.* **2004**, *69*, 4145 – 4151.
[61] B. J. Backes, J. A. Ellman, *J. Org. Chem.* **1999**, *64*, 2322 – 2330.
[62] J. M. Palomo, M. Lumbierres, H. Waldmann, *Angew. Chem.* **2006**, *118*, 491 – 495; *Angew. Chem. Int. Ed.* **2006**, *45*, 477 – 481.
[63] M. Lumbierres, J. M. Palomo, G. Kragol, H. Waldmann, *Tetrahedron Lett.* **2006**, *47*, 2671 – 2674.
[64] M. Joseph, R. Nagaraj, *Bioorg. Med. Chem. Lett.* **1993**, *3*, 1025 – 1028.
[65] N. Pfender, E. Guénin, J. M. Greer, E. Trifilieff, *Lett. Pept. Sci.* **2003**, *10*, 581 – 588.
[66] B. Denis, E. Trifilieff, *J. Pept. Sci.* **2000**, *6*, 372 – 377.
[67] D. T. S. Rijkers, J. A. W. Kruijtzer, J. A. Killian, R. M. J. Liskamp, *Tetrahedron Lett.* **2005**, *46*, 3341 – 3345.
[68] A. Harishchandran, B. Pallavi, R. Nagaraj, *Protein Pept. Lett.* **2002**, *9*, 411 – 417.
[69] B. Pallavi, R. Nagaraj, *J. Biol. Chem.* **2003**, *278*, 12737 – 12744.
[70] S. P. Creaser, B. R. Peterson, *J. Am. Chem. Soc.* **2002**, *124*, 2444 – 2445.
[71] P. Mayer-Fligge, J. Volz, U. Kruger, E. Sturm, W. Gernandt, K. P. Schafer, M. Przybylski, *J. Pept. Sci.* **1998**, *4*, 355 – 363.
[72] K. Pachamuthu, X. M. Zhu, R. R. Schmidt, *J. Org. Chem.* **2005**, *70*, 3720 – 3723.
[73] Y. Zhu, W. A. van der Donk, *Org. Lett.* **2001**, *3*, 1189 – 1192.
[74] D. P. Galonic, N. D. Ide, W. A. van der Donk, D. Y. Gin, *J. Am. Chem. Soc.* **2005**, *127*, 7359 – 7369.
[75] X. Q. Liang, A. Nazarian, H. Erdjument-Bromage, W. Bornmann, P. Tempst, M. D. Resh, *J. Biol. Chem.* **2001**, *276*, 30987 – 30994.
[76] R. S. Goody, K. Alexandrov, M. Engelhard, *ChemBioChem* **2002**, *3*, 399 – 403.
[77] L. J. Knoll, J. I. Gordon, *J. Biol. Chem.* **1993**, *268*, 4281 – 4290.
[78] M. J. Page, A. Hall, S. Rhodes, R. H. Skinner, V. Murphy, M. Sydenham, P. N. Lowe, *J. Biol. Chem.* **1989**, *264*, 19147 – 19154.
[79] H. Horiuchi, O. Ullrich, C. Bucci, M. Zerial, *Methods Enzymol.* **1995**, *257*, 9 – 15 ("Small GTPases and Their Regulators Part C: Proteins Involved in Transport").
[80] A. Kikuchi, T. Yamashita, M. Kawata, K. Yamamoto, K. Ikeda, T. Tanimoto, Y. Takai, *J. Biol. Chem.* **1988**, *263*, 2897 – 2904.
[81] T. Magee, M. C. Seabra, *Curr. Opin. Cell Biol.* **2005**, *17*, 190 – 196.
[82] T. W. Muir, D. Sondhi, P. A. Cole, *Proc. Natl. Acad. Sci. USA* **1998**, *95*, 6705 – 6710.
[83] R. M. Hofmann, T. W. Muir, *Curr. Opin. Biotechnol.* **2002**, *13*, 297 – 303.
[84] T. J. Tolbert, C. H. Wong, *J. Am. Chem. Soc.* **2000**, *122*, 5421 – 5428.
[85] J. P. Tam, J. X. Xu, K. D. Eom, *Biopolymers* **2001**, *60*, 194 – 205.
[86] G. G. Kochendoerfer, S. B. H. Kent, *Curr. Opin. Chem. Biol.* **1999**, *3*, 665 – 671.
[87] T. A. Kale, S. J. Hsieh, M. W. Rose, M. D. Distefano, *Curr. Top. Med. Chem.* **2003**, *3*, 1043 – 1074.
[88] A. Kalinin, N. H. Thoma, A. Iakovenko, I. Heinemann, E. Rostkova, A. T. Constantinescu, K. Alexandrov, *Protein Expression Purif.* **2001**, *22*, 84 – 91.
[89] T. Dudler, M. H. Gelb, *Biochemistry* **1997**, *36*, 12434 – 12441.
[90] P. Mcgeady, S. Kuroda, K. Shimizu, Y. Takai, M. H. Gelb, *J. Biol. Chem.* **1995**, *270*, 26347 – 26351.
[91] D. J. Owen, K. Alexandrov, E. Rostkova, A. J. Scheidig, R. S. Goody, H. Waldmann, *Angew. Chem.* **1999**, *111*, 570 – 573; *Angew. Chem. Int. Ed.* **1999**, *38*, 509 – 512.
[92] N. H. Thoma, A. Iakovenko, D. Owen, A. S. Scheidig, H. Waldmann, R. S. Goody, K. Alexandrov, *Biochemistry* **2000**, *39*, 12043 – 12052.
[93] T. C. Turek, I. Gaon, M. D. Distefano, C. L. Strickland, *J. Org. Chem.* **2001**, *66*, 3253 – 3264.
[94] T. C. Turek-Etienne, C. L. Strickland, M. D. Distefano, *Biochemistry* **2003**, *42*, 3716 – 3724.
[95] T. A. Kale, M. D. Distefano, *Org. Lett.* **2003**, *5*, 609 – 612.
[96] T. A. Kale, C. Raab, N. Yu, E. Aquino, D. C. Dean, M. D. Distefano, *J. Labelled Compd. Radiopharm.* **2003**, *46*, 29 – 54.
[97] M. W. Rose, J. H. Xu, T. A. Kale, G. O'Doherty, G. Barany, M. D. Distefano, *Biopolymers* **2005**, *80*, 164 – 171.
[98] X. H. Liu, G. D. Prestwich, *J. Am. Chem. Soc.* **2002**, *124*, 20 – 21.
[99] X. H. Liu, G. D. Prestwich, *Bioorg. Med. Chem. Lett.* **2004**, *14*, 2137 – 2140.
[100] M. K. Kim, T. S. Kleckley, A. J. Wiemer, S. A. Holstein, R. J. Hohl, D. F. Wiemer, *J. Org. Chem.* **2004**, *69*, 8186 – 8193.
[101] R. Shchepin, R. Dumitru, K. W. Nickerson, M. Lund, P. H. Dussault, *Chem. Biol.* **2005**, *12*, 639 – 641.
[102] K. A. H. Chehade, D. A. Andres, H. Morimoto, H. P. Spielmann, *J. Org. Chem.* **2000**, *65*, 3027 – 3033.
[103] K. A. H. Chehade, K. Kiegiel, R. J. Isaacs, J. S. Pickett, K. E. Bowers, C. A. Fierke, D. A. Andres, H. P. Spielmann, *J. Am. Chem. Soc.* **2002**, *124*, 8206 – 8219.
[104] E. Micali, K. A. H. Chehade, R. J. Isaacs, D. A. Andres, H. P. Spielmann, *Biochemistry* **2001**, *40*, 12254 – 12265.
[105] T. Subramanian, Z. W. Wang, J. M. Troutman, D. A. Andres, H. P. Spielmann, *Org. Lett.* **2005**, *7*, 2109 – 2112.
[106] J. M. Troutman, M. J. Roberts, D. A. Andres, H. P. Spielmann, *Bioconjugate Chem.* **2005**, *16*, 1209 – 1217.
[107] J. M. Troutman, K. A. H. Chehade, K. Kiegiel, D. A. Andres, H. P. Spielmann, *Bioorg. Med. Chem. Lett.* **2004**, *14*, 4979 – 4982.
[108] Y. Kho, S. C. Kim, C. Jiang, D. Barma, S. W. Kwon, J. K. Cheng, J. Jaunbergs, C. Weinbaum, F. Tamanoi, J. Falck, Y. M. Zhao, *Proc. Natl. Acad. Sci. USA* **2004**, *101*, 12479 – 12484.
[109] G. T. Hermanson in *Bioconjugate Techniques*, Academic Press, London, **1996**, pp. 297 – 418.

 © 2006 Wiley-VCH Verlag GmbH & Co. KGaA, Weinheim

[110] T. W. Muir, *Annu. Rev. Biochem.* **2003**, *72*, 249 – 289.
[111] S. R. Chong, F. B. Mersha, D. G. Comb, M. E. Scott, D. Landry, L. M. Vence, F. B. Perler, J. Benner, R. B. Kucera, C. A. Hirvonen, J. J. Pelletier, H. Paulus, M. Q. Xu, *Gene* **1997**, *192*, 271 – 281.
[112] O. Martinez, B. Goud, *Biochim. Biophys. Acta* **1998**, *1404*, 101 – 112.
[113] T. Durek, R. S. Goody, K. Alexandrov, *Methods Mol. Biol.* **2004**, *283*, 233 – 244 ("Bioconjugation Protocols: Strategies and Methods").
[114] T. Durek, K. Alexandrov, R. S. Goody, A. Hildebrand, I. Heinemann, H. Waldmann, *J. Am. Chem. Soc.* **2004**, *126*, 16368 – 16378.
[115] K. Alexandrov, I. Heinemann, T. Durek, V. Sidorovitch, R. S. Goody, H. Waldmann, *J. Am. Chem. Soc.* **2002**, *124*, 5648 – 5649.
[116] A. Rak, O. Pylypenko, T. Durek, A. Watzke, S. Kushnir, L. Brunsveld, H. Waldmann, R. S. Goody, K. Alexandrov, *Science* **2003**, *302*, 646 – 650.
[117] A. Wittinghofer, H. Waldmann, *Angew. Chem.* **2000**, *112*, 4360 – 4383; *Angew. Chem. Int. Ed.* **2000**, *39*, 4193 – 4214.
[118] M. Wagner, J. Kuhlmann, *Methods Mol. Biol.* **2004**, *283*, 245 – 254 ("Bioconjugation Protocols: Strategies and Methods").
[119] B. Bader, K. Kuhn, D. J. Owen, H. Waldmann, A. Wittinghofer, J. Kuhlmann, *Nature* **2000**, *403*, 223 – 226.
[120] A. D. de Araujo, J. M. Palomo, J. Cramer, M. Kohn, H. Schroder, R. Wacker, C. Niemeyer, K. Alexandrov, H. Waldmann, *Angew. Chem.* **2006**, *118*, 302 – 307; *Angew. Chem. Int. Ed.* **2006**, *45*, 296 – 301.
[121] E. F. Pai, W. Kabsch, U. Krengel, K. C. Holmes, J. John, A. Wittinghofer, *Nature* **1989**, *341*, 209 – 214.
[122] M. V. Milburn, L. Tong, A. M. Devos, A. Brunger, Z. Yamaizumi, S. Nishimura, S. H. Kim, *Science* **1990**, *247*, 939 – 945.
[123] P. J. Kraulis, P. J. Domaille, S. L. Campbell-Burk, T. Vanaken, E. D. Laue, *Biochemistry* **1994**, *33*, 3515 – 3531.
[124] D. Huster, K. Kuhn, D. Kadereit, H. Waldmann, K. Arnold, *Angew. Chem.* **2001**, *113*, 1083 – 1085; *Angew. Chem. Int. Ed.* **2001**, *40*, 1056 – 1058.
[125] D. Huster, A. Vogel, C. Katzka, H. A. Scheidt, H. Binder, S. Dante, T. Gutberlet, O. Zschornig, H. Waldmann, K. Arnold, *J. Am. Chem. Soc.* **2003**, *125*, 4070 – 4079.
[126] A. Vogel, C. P. Katzka, H. Waldmann, K. Arnold, M. F. Brown, D. Huster, *J. Am. Chem. Soc.* **2005**, *127*, 12263 – 12272.
[127] G. Reuther, K.-T. Tan, J. Köhler, C. Nowak, A. Pampel, K. Arnold, J. Kuhlmann, H. Waldmann, D. Huster, *Angew. Chem.* **2006**, *118*, 5513 – 5517; *Angew. Chem. Int. Ed.* **2006**, *45*, 5387 – 5390.
[128] A. A. Gorfe, R. Pellarin, A. Caflisch, *J. Am. Chem. Soc.* **2004**, *126*, 15277 – 15286.
[129] M. Sinensky, *Biochim. Biophys. Acta* **2000**, *1529*, 203 – 209.
[130] S. J. McTaggart, *Cell. Mol. Life Sci.* **2006**, *63*, 255 – 267.
[131] E. Porfiri, T. Evans, P. Chardin, J. F. Hancock, *J. Biol. Chem.* **1994**, *269*, 22672 – 22677.
[132] I. Rubiol, U. Wittig, C. Meyer, R. Heinze, D. Kadereit, H. Waldmann, L. Downward, R. Wetzker, *Eur. J. Biochem.* **1999**, *266*, 70 – 82.
[133] H. B. Zhang, X. H. Liu, K. Zhang, C. K. Chen, J. M. Frederick, G. D. Prestwich, W. Baehr, *J. Biol. Chem.* **2004**, *279*, 407 – 413.
[134] M. Edidin, *Annu. Rev. Biophys. Biomol. Struct.* **2003**, *32*, 257 – 283.
[135] A. G. Lee, *Mol. Biosyst.* **2005**, *1*, 203 – 212.
[136] R. M. Epand, *Biopolymers* **1997**, *43*, 15 – 24.
[137] S. Janosch, C. Nicolini, B. Ludolph, C. Peters, M. Volkert, T. L. Hazlet, E. Gratton, H. Waldmann, R. Winter, *J. Am. Chem. Soc.* **2004**, *126*, 7496 – 7503.
[138] T. Y. Wang, R. Leventis, J. R. Silvius, *Biochemistry* **2001**, *40*, 13031 – 13040.
[139] K. A. Melkonian, A. G. Ostermeyer, J. Z. Chen, M. G. Roth, D. A. Brown, *J. Biol. Chem.* **1999**, *274*, 3910 – 3917.
[140] S. Moffett, D. A. Brown, M. E. Linder, *J. Biol. Chem.* **2000**, *275*, 2191 – 2198.
[141] I. A. Prior, A. Harding, J. Yan, J. Sluimer, R. G. Parton, J. F. Hancock, *Nat. Cell Biol.* **2001**, *3*, 368 – 375.
[142] B. Rotblat, I. A. Prior, C. Muncke, R. G. Parton, Y. Kloog, Y. I. Henis, J. F. Hancock, *Mol. Cell. Biol.* **2004**, *24*, 6799 – 6810.
[143] C. Nicolini, J. Baranski, S. Schlummer, J. M. Palomo, M. Lumbierres, M. Kahms, J. Kuhlmann, S. Sanchez, E. Gratton, H. Waldmann, R. Winter, *J. Am. Chem. Soc.* **2006**, *128*, 192 – 201.
[144] S. J. Plowman, C. Muncke, R. G. Parton, J. F. Hancock, *Proc. Natl. Acad. Sci. USA* **2005**, *102*, 15500 – 15505.
[145] S. Roy, S. Plowman, B. Rotblat, I. A. Prior, C. Muncke, S. Grainger, R. G. Parton, Y. I. Henis, Y. Kloog, J. F. Hancock, *Mol. Cell. Biol.* **2005**, *25*, 6722 – 6733.
[146] J. F. Hancock, R. G. Parton, *Biochem. J.* **2005**, *389*, 1 – 11.
[147] J. J. Dumas, Z. Y. Zhu, J. L. Connolly, D. G. Lambright, *Structure* **1999**, *7*, 413 – 423.
[148] D. Chattopadhyay, G. Langsley, M. Carson, R. Recacha, L. DeLucas, C. Smith, *Acta Crystallogr. Sect. D* **2000**, *56*, 937 – 944.
[149] C. Stroupe, A. T. Brunger, *J. Mol. Biol.* **2000**, *304*, 585 – 598.
[150] H. Esters, K. Alexandrov, A. T. Constantinescu, R. S. Goody, A. J. Scheidig, *J. Mol. Biol.* **2000**, *298*, 111 – 121.
[151] A. Iakovenko, E. Rostkova, E. Merzlyak, A. M. Hillebrand, N. H. Thoma, R. S. Goody, K. Alexandrov, *FEBS Lett.* **2000**, *468*, 155 – 158.
[152] A. T. Constantinescu, A. Rak, K. Alexandrov, H. Esters, R. S. Goody, A. J. Scheldig, *Structure* **2002**, *10*, 569 – 579.
[153] A. Rak, A. Niculae, A. Kalinin, N. H. Thoma, V. Sidorovitch, R. S. Goody, K. Alexandrov, *Protein Expression Purif.* **2002**, *25*, 23 – 30.
[154] A. Rak, O. Pylypenko, A. Niculae, K. Pyatkov, R. S. Goody, K. Alexandrov, *Cell* **2004**, *117*, 749 – 760.
[155] C. Ostermeier, A. T. Brunger, *Cell* **1999**, *96*, 363 – 374.
[156] Y. An, Y. Shao, C. Alory, J. Matteson, T. Sakisaka, W. Chen, R. A. Gibbs, I. A. Wilson, W. E. Balch, *Structure* **2003**, *11*, 347 – 357.
[157] P. D'Adamo, A. Menegon, C. Lo Nigro, M. Grasso, M. Gulisano, F. Tamanini, T. Bienvenu, A. K. Gedeon, B. Oostra, S. K. Wu, A. Tandon, F. Valtorta, W. E. Balch, J. Chelly, D. Toniolo, *Nat. Gen.* **1998**, *19*, 134 – 139.
[158] P. M. Gilbert, C. G. Burd, *J. Biol. Chem.* **2001**, *276*, 8014 – 8020.
[159] O. Pylypenko, A. Rak, T. Durek, S. Kushnir, B. E. Dursina, N. H. Thomae, A. T. Constantinescu, L. Brunsveld, A. Watzke, H. Waldmann, R. S. Goody, K. Alexandrov, *EMBO J.* **2006**, *25*, 13 – 23.
[160] M. Schelhaas, E. Nagele, N. Kuder, B. Bader, J. Kuhlmann, A. Wittinghofer, H. Waldmann, *Chem. Eur. J.* **1999**, *5*, 1239 – 1252.
[161] C. Peters, A. Wolf, M. Wagner, J. Kuhlmann, H. Waldmann, *Proc. Natl. Acad. Sci. USA* **2004**, *101*, 8531 – 8536.
[162] P. J. Casey, M. C. Seabra, *J. Biol. Chem.* **1996**, *271*, 5289 – 5292.
[163] F. Shen, M. C. Seabra, *J. Biol. Chem.* **1996**, *271*, 3692 – 3698.
[164] N. H. Thoma, A. Niculae, R. S. Goody, K. Alexandrov, *J. Biol. Chem.* **2001**, *276*, 48631 – 48636.
[165] N. H. Thoma, A. Iakovenko, A. Kalinin, H. Waldmann, R. S. Goody, K. Alexandrov, *Biochemistry* **2001**, *40*, 268 – 274.
[166] O. Pylypenko, A. Rak, R. Reents, A. Niculae, V. Sidorovitch, M. D. Vioaca, E. Bessolitsyna, N. H. Thoma, H. Waldmann, I. Schlichting, R. S. Goody, K. Alexandrov, *Mol. Cell* **2003**, *11*, 483 – 494.
[167] H. Schroeder, R. Leventis, S. Rex, M. Schelhaas, E. Nagele, H. Waldmann, J. R. Silvius, *Biochemistry* **1997**, *36*, 13102 – 13109.
[168] O. Rocks, A. Peyker, M. Kahms, P. J. Verveer, C. Koerner, M. Lumbierres, J. Kuhlmann, H. Waldmann, A. Wittinghofer, P. I. H. Bastiaens, *Science* **2005**, *307*, 1746 – 1752.

 © 2006 Wiley-VCH Verlag GmbH & Co. KGaA, Weinheim

[169] A. D. Basso, P. Kirschmeier, W. R. Bishop, *J. Lipid Res.* **2006**, *47*, 15 – 31.
[170] M. Thutewohl, L. Kissau, B. Popkirova, I. M. Karaguni, T. Nowak, M. Bate, J. Kuhlmann, O. Muller, H. Waldmann, *Angew. Chem.* **2002**, *114*, 3768 – 3772; *Angew. Chem. Int. Ed.* **2002**, *41*, 3616 – 3620.
[171] J. T. Swarthout, S. Lobo, L. Farh, M. R. Croke, W. K. Greentree, R. J. Deschenes, M. E. Linder, *J. Biol. Chem.* **2005**, *280*, 31141 – 31148.
[172] P. Deck, D. Pendzialek, M. Biel, M. Wagner, B. Popkirova, B. Ludolph, G. Kragol, J. Kuhlmann, A. Giannis, H. Waldmann, *Angew. Chem.* **2005**, *117*, 5055 – 5060; *Angew. Chem. Int. Ed.* **2005**, *44*, 4975 – 4980.
[173] M. E. Hahn, T. W. Muir, *Trends Biochem. Sci.* **2005**, *30*, 26 – 34.
[174] M. R. Pratt, C. R. Bertozzi, *Chem. Soc. Rev.* **2005**, *34*, 58 – 68.

Life's Simple Pleasures!

No need to waste precious time looking for the right information – Register now for the free **Wiley-VCH Alerting Service.**

It's simple – and it's fast.

To receive regular news per e-mail tailored precisely to your needs and interests, just fill in the registration form at **www.wiley-vch.de/home/pas/**

WILEY-VCH

 © 2006 Wiley-VCH Verlag GmbH & Co. KGaA, Weinheim

Solvent-Directed Self-Assembly

DOI: 10.1002/anie.200601888

Application of Solvent-Directed Assembly of Block Copolymers to the Synthesis of Nanostructured Materials with Low Dielectric Constants**

*Thomas M. Hermans, Jeongsoo Choi, Bas G. G. Lohmeijer, Geraud Dubois, Russell C. Pratt, Ho-Cheol Kim, Robert M. Waymouth, and James L. Hedrick**

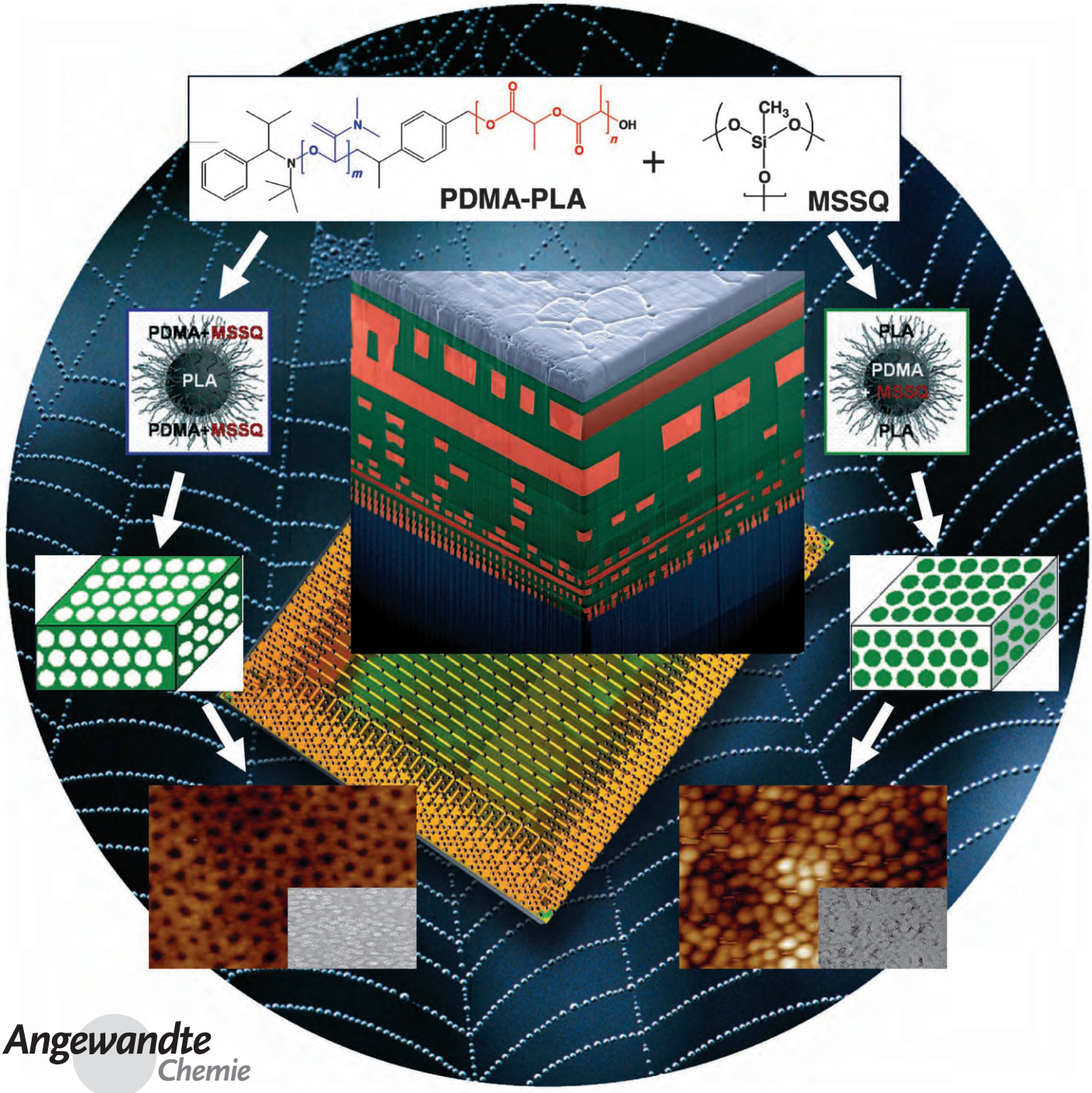

© 2006 Wiley-VCH Verlag GmbH & Co. KGaA, Weinheim

The pursuit of low-dielectric-constant, on-chip insulating media to mitigate both signal delays and power consumption for back-end of the line (BEOL) applications continues to be a challenge in the microelectronics industry.[1] A promising class of low-dielectric-constant materials are methyl silsesquioxanes (MSSQ) or organosilicates, and dielectric extendibility for future technologies (65- and 45-nm lithographic nodes) is through the controlled introduction of porosity. However, interconnectivity between the pores is obtained at a high level of porosity, which results in the contamination of the dielectric materials, including metal migration during processing, and subsequent degradation of the electrical properties.[2] The ability of a porous media to support high levels of porosity without percolation continues to be a grand challenge. In this regard, isolated pores with minimal interconnectivity have been generated through templating of organosilicates using star-shaped block copolymers[3] or dendrimers.[4,5] Nevertheless, the synthesis of these complex architectures is difficult. Another approach is based on the formation of a 3D cubic phase by the self-assembly of a diblock or triblock copolymer with a silica precursor.[6–11]

Here we describe a novel approach to highly porous hydrophobic MSSQ thin films with minimally interconnected porosity based on the co-assembly of organosilicate precursors with poly(*N*,*N*-dimethylacrylamide)-*block*-poly(*rac*-lactide) copolymer (PDMA-PLA). We also demonstrate that the deposition solvent plays a key role in directing the vitrification of the organosilicate, thus significantly expanding the range of accessible morphologies.[12–18] The use of PLA stems from its incompatibility with the organosilicate and thermal instability, as demonstrated by Hillmyer and Rzayev with the use of PLA copolymers to generate porous organic materials.[19,20] The nitrogen substitution in PDMA delivers characteristics commensurate with the formation of miscible blends with organosilicates, that is, polarity, hydrogen-bonding capability, and basicity, which promote strong interactions between the polymeric porogen and the thermosetting organosilicate precursors as described by Chujo and Saegusa.[21] The ability of the thermosetting organosilicate to be sequestered selectively into the PDMA phase allows preserv ation of the supramolecular assembly once cross-linked and results in a contiguous functional film. The utility of selectively cross-linking of the individual components of such self-assembled nanostructures has been shown by Wooley et al.,[22–24] who demonstrated stability, subsequent functionalization, and application in diverse environments. The distinguishing feature here is the use of a single block copolymer/organosilicate mixture that can generate widely different nanostructures simply by changing the deposition solvent.[12–18] A solvent selective for either the PDMA/MSSQ phase or PLA phase generates micellar or inverse micellar structures, respectively, followed by the preservation of the structure through organosilicate vitrification and copolymer burnout to give highly porous films with uniquely defined morphologies.

A series of poly(*N*,*N*-dimethylacrylamide)-*block*-polylactide block copolymers were prepared using Hawker's dual-headed initiator containing an alkoxyamine and a primary hydroxy group (Scheme 1).[25] Four hydroxy-terminated PDMA macroinitiators of various molecular weight were synthesized by nitroxide-mediated polymerization. Subsequent ring-opening of *rac*-lactide was accomplished by using a thiourea tertiary amine catalysts for bifunctional activation of both monomer and alcohol through hydrogen bonding.[26] Separating the tertiary amine functionality from the thiourea catalyst enabled us to increase polymerization rates without loss of control by addition of an auxiliary tertiary amine such as (−)-sparteine.[27] The versatility of this catalytic system is demonstrated through the synthesis of narrowly dispersed PLA blocks with predictable molecular weights (see Supporting Information). An example of the successful chain

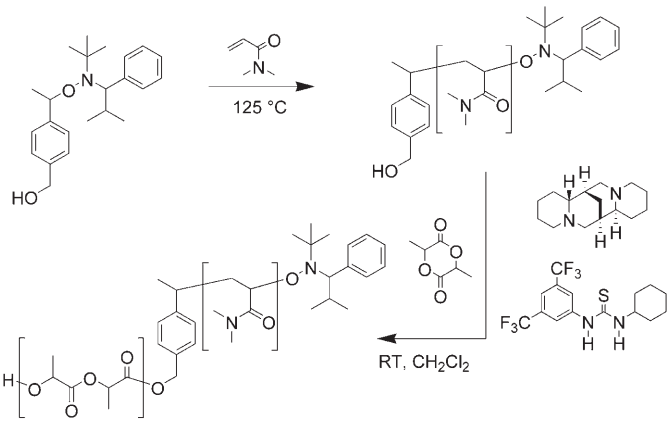

Scheme 1. Synthesis of PDMA-PLA block copolymers by sequential nitroxide-mediated and ring-opening polymerization.

[*] T. M. Hermans,[+] Dr. J. Choi,[+] Dr. B. G. G. Lohmeijer,[+] Dr. G. Dubois, Dr. R. C. Pratt, Dr. H.-C. Kim, Dr. J. L. Hedrick
IBM Almaden Research Center
650 Harry Road, San Jose, CA 95120 (USA)
Fax: (+1) 408-927-3310
E-mail: hedrick@almaden.ibm.com
Prof. R. M. Waymouth
Department of Chemistry
Stanford University
Stanford, CA 94305 (USA)

[+] These authors contributed equally to this work.

[**] The authors acknowledge support from the NSF Center for Polymer Interfaces and Macromolecular Assemblies (CPIMA: NSF-DMR-0213618). This work was also partially supported by the Korea Research Foundation Grant funded by the Korean Government (MOEHRD) (KRF-2005-214-D00273). Part of this research was carried out at the Stanford Synchrotron Radiation Laboratory, a national user facility operated by Stanford University on behalf of the US Department of Energy, Office of Basic Energy Sciences. The SSRL Structural Molecular Biology Program is supported by the Department of Energy, Office of Biological and Environmental Research, and by the National Institutes of Health, National Center for Research Resources, Biomedical Technology Program. We thank M. Toney, H. Tsuruta, and M. Niebuhr for help with the SAXS experiments, and Leslie E. Krupp for the TEM studies. J.C. thanks Byeongdu Lee at Argonne National Laboratory for valuable assistance with the SAXS data analysis.

Supporting information for this article is available on the WWW under http://www.angewandte.org or from the author.

 © 2006 Wiley-VCH Verlag GmbH & Co. KGaA, Weinheim

extension of the PLA block from the PDMA macroinitiator with no trace of homopolymer contamination is also shown in the Supporting Information. The volume fractions of the four PDMA-PLA block copolymers used for this study were very similar ($\phi_{PDMA} \approx 0.25$) and facilitate comparison of structure–property relationships of the obtained organosilicate structures after polymer burnout.

When MSSQ resin and block copolymer **3** ($PDMA_{70}$-PLA_{150}, $M_n = 47\,100\ g\,mol^{-1}$, PDI = 1.11) are dissolved in propylene glycol propyl ether (PGPE), a selective solvent for PDMA and a poor solvent for PLA, the solutions immediately manifest a blue glow, suggesting micelle formation. Using deuterated methanol as a model solvent, ^1H NMR spectroscopy shows that the signals associated with the PLA block are suppressed up to 60 °C, suggesting that PLA comprises the core of the micelle and is collapsed (see Supporting Information). Above 60 °C, the supramolecular structure is disrupted and leads to solvation, as shown by reacquisition of the ^1H NMR signals of the PLA block. Similarly, in the PLA-selective solvent *n*-butyl acetate (BuOAc) copolymers **1**–**4** show a blue glow as an indicator of micelle formation.

Thin films of hybrids containing approximately 60 % (w/w) of a block copolymer, about 40 % (w/w) MSSQ, and roughly 2 % triethylamine (a catalyst for MSSQ condensation) were prepared by spin-coating both PGPE and BuOAc solutions (10 % solids (w/w)) onto silicon wafers. The spin-coated films were annealed at 50 °C for 3 days to accelerate vitrification of the MSSQ while preserving the micellar structure, and then heated to 450 °C to degrade the polymer template out of the thin films.

Transmission electron microscopy (TEM) and field-emission scanning electron microscopy (FESEM) images together with the atomic force microscopy (AFM) image of the top surface of the mixture of MSSQ and copolymer **3** deposited from PGPE and BuOAc solutions are shown in Figure 1. In the case of the PGPE film, discrete, minimally interconnected pores are observed in the bulk of the film with a pore size of approximately 30 nm in diameter, and AFM measurements show analogous porosity on the surface. These structures are consistent with the imprinting of the micellar structure, with silica-free PLA comprising the core and the PDMA-MSSQ phase comprising the corona. The high final cure temperature allows the outer surfaces of the micelles to condense into a contiguous film, but the empty micellar cores are preserved to give a material that is highly porous with minimal interconnectivity. The refractive index and dielectric constant (k) of the porous material are 1.1825 and 1.71, respectively, values that are considerably lower than those for the dense organosilicate (1.3703 and 2.80, respectively). The density of the film material as determined from the critical angle of X-ray reflectivity (XRR) is $0.616\ g\,cm^{-3}$, which provides an estimate of the porosity as 52 % when compared to the bulk material ($1.273\ g\,cm^{-3}$). As the volume fraction of PLA is 45 %, most of the porosity is believed to be derived from the space occupied by the PLA core.[28]

A markedly different morphology is observed for the MSSQ/**3** mixture deposited from BuOAc and subsequently cured under the same conditions (Figure 1). The AFM

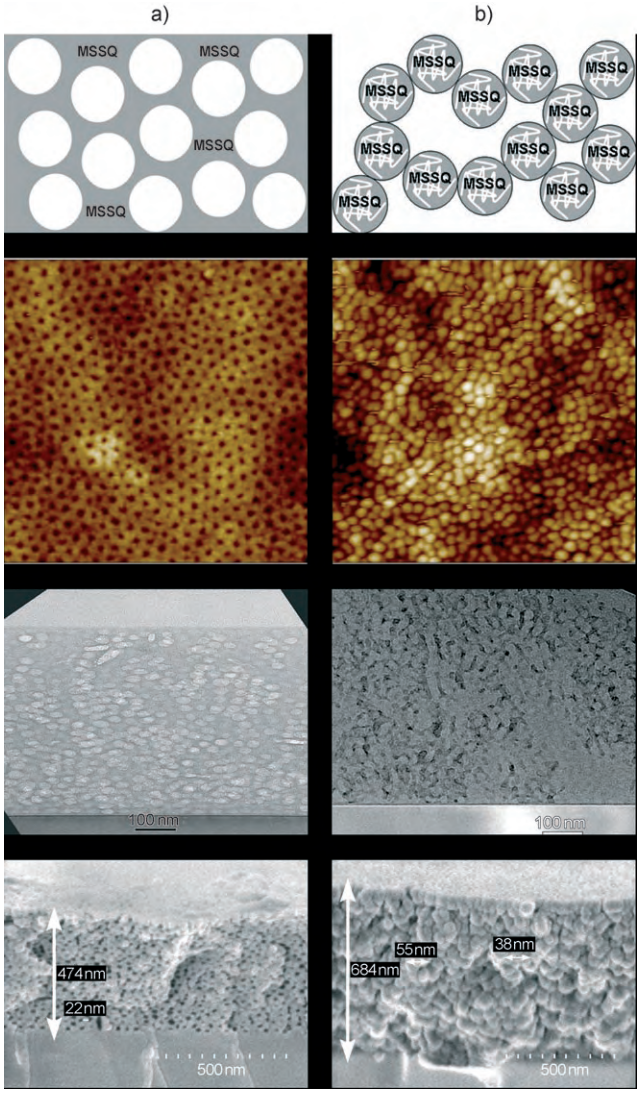

Figure 1. Micrographs of a) micellar and b) inverse micellar nanostructured thin films. Top: AFM images; middle: TEM images; bottom: FESEM images. See text for details.

micrographs show packed silica nanoparticles in both the bulk and on the surface. The exacerbated interstitial sites stem from the PLA phase that forms the corona of the nanoparticle precursors. The porosity was estimated at 64 % (v/v) by XRR measurement (density: $0.456\ g\,cm^{-3}$) which corroborates the decrease in both the dielectric constant and refractive index to 1.65 and 1.13, respectively. The higher porosity implicates roles for both phases of the copolymer when BuOAc is used as the casting solvent. Although PDMA is miscible with MSSQ, curing causes phase separation of the PDMA component and subsequent formation of microporosity in the nanoparticles.[29,30] Pore generation therefore is reflected in both PLA-derived interstitial spaces and PDMA-derived inherent porosity of the nanoparticle matrix.

The microstructure of the porous films was investigated using small-angle X-ray scattering (SAXS). The 2D scattering image was integrated to 1D data after careful removal of background scattering. The reduced data were analyzed using

 © 2006 Wiley-VCH Verlag GmbH & Co. KGaA, Weinheim

the Pederson formalism[31] with a Schultz size distribution (see Supporting Information for details). Figure 2 a and b show the SAXS profiles as well as their fitted lines for thin films of MSSQ/**3** cast from PGPE and BuOAc, respectively. The

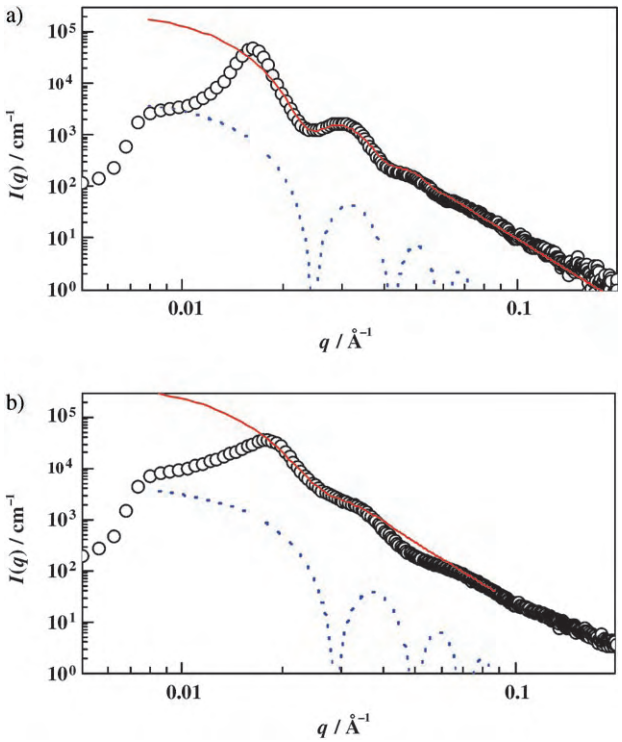

Figure 2. SAXS scattering profiles (symbols) and fits (solid lines) of thin film prepared from a) PGPE and b) BuOAc. Dotted lines show the scattering profiles calculated for monodisperse hard spheres, with the radius of gyration (R_g) being the average value in the distribution.

characteristic SAXS profiles indicate that the pores in the thin films cast from PGPE are well-defined spheres, while the particles in the thin films cast from BuOAc are relatively deformed spheres. SAXS intensity profiles were further analyzed to characterize the structural features of thin films. From the extracted structure factor, $S(qr)$ (see Supporting Information), it was determined that the pores in thin films cast from PGPE form with a relatively ordered structure presumably in the manner of simple cubic (SC) or body-centered cubic (BCC) crystals, while the particles in thin films cast from BuOAc are not assembled into long-range-ordered structures. The deformation of the spheres and destruction of ordered structure in thin films cast from BuOAc may reflect the merging and respacing of the MSSQ particles upon thermolysis of the PLA phase.

In summary, the co-assembly of organosilicate precursors with PDMA-PLA block copolymers deposited from solvents selective for either the PDMA or PLA phases was described. Mixtures deposited from PGPE produced a film with a dielectric constant of $k = 1.71$ and with discrete, minimally interconnected pores, while samples deposited from BuOAc generated contiguous films ($k = 1.47$) of packed, microporous nanoparticles. The simplicity of this strategy makes it attractive for application to future technology nodes.

Received: May 13, 2006
Published online: August 14, 2006

Keywords: block copolymers · micelles · porous materials · self-assembly · silicates

[1] J. L. Hedrick, T. Magbitang, E. F. Connor, T. Glauser, W. Volksen, C. J. Hawker, V. Y. Lee, R. D. Miller, *Chem. Eur. J.* **2002**, *8*, 3308.
[2] M. R. Baklanov, K. Maex, *Philos. Trans. R. Soc. London Ser. A* **2006**, *364*, 201.
[3] E. F. Connor, L. K. Sundberg, H. C. Kim, J. J. Cornelissen, T. Magbitang, P. M. Rice, V. Y. Lee, C. J. Hawker, W. Volksen, J. L. Hedrick, R. D. Miller, *Angew. Chem.* **2003**, *115*, 3915; *Angew. Chem. Int. Ed.* **2003**, *42*, 3785.
[4] B. Lee, Y. H. Park, Y. T. Hwang, W. Oh, J. Yoon, M. Ree, *Nat. Mater.* **2005**, *4*, 147.
[5] B. Lee, I. Park, J. Yoon, S. Park, J. Kim, K. W. Kim, T. Chang, M. Ree, *Macromolecules* **2005**, *38*, 4311.
[6] D. Zhao, P. Yang, N. Melosh, J. Feng, B. F. Chmelka, G. D. Stucky, *Adv. Mater.* **1998**, *10*, 1380.
[7] A. Jain, L. M. Hall, C. B. W. Garcia, S. M. Gruner, U. Wiesner, *Macromolecules* **2005**, *38*, 10095.
[8] A. Jain, G. E. S. Toombes, L. M. Hall, S. Mahajan, C. B. W. Garcia, W. Probst, S. M. Gruner, U. Wiesner, *Angew. Chem.* **2005**, *117*, 1252; *Angew. Chem. Int. Ed.* **2005**, *44*, 1226.
[9] A. Jain, U. Wiesner, *Macromolecules* **2004**, *37*, 5665.
[10] Y. Zhou, J. H. Schattka, M. Antonietti, *Nano Lett.* **2004**, *4*, 477.
[11] D. L. Gin, W. Q. Gu, B. A. Pindzola, W. J. Zhou, *Acc. Chem. Res.* **2001**, *34*, 973.
[12] K. J. Hanley, T. P. Lodge, C. I. Huang, *Macromolecules* **2000**, *33*, 5918.
[13] T. P. Lodge, B. Pudil, K. J. Hanley, *Macromolecules* **2002**, *35*, 4707.
[14] R. Glass, M. Moller, J. P. Spatz, *Nanotechnology* **2003**, *14*, 1153.
[15] J. F. Gohy, E. Khousakoun, N. Willet, S. K. Varshney, R. Jerome, *Macromol. Rapid Commun.* **2004**, *25*, 1536.
[16] J. F. Gohy, N. Willet, S. Varshney, J. X. Zhang, R. Jerome, *Angew. Chem.* **2001**, *113*, 3314; *Angew. Chem. Int. Ed.* **2001**, *40*, 3214.
[17] I. I. Potemkin, M. Moller, *Macromolecules* **2005**, *38*, 2999.
[18] G. Riess, *Prog. Polym. Sci.* **2003**, *28*, 1107.
[19] J. Rzayev, M. A. Hillmyer, *Macromolecules* **2005**, *38*, 3.
[20] J. Rzayev, M. A. Hillmyer, *J. Am. Chem. Soc.* **2005**, *127*, 13373.
[21] Y. Chujo, T. Saegusa, *Adv. Polym. Sci.* **1992**, *100*, 12.
[22] H. Y. Huang, E. E. Remsen, T. Kowalewski, K. L. Wooley, *J. Am. Chem. Soc.* **1999**, *121*, 3805.
[23] Q. G. Ma, E. E. Remsen, T. Kowalewski, K. L. Wooley, *J. Am. Chem. Soc.* **2001**, *123*, 4627.
[24] K. K. Perkin, J. L. Turner, K. L. Wooley, S. Mann, *Nano Lett.* **2005**, *5*, 1457.
[25] C. J. Hawker, A. W. Bosman, E. Harth, *Chem. Rev.* **2001**, *101*, 3661.
[26] A. P. Dove, R. C. Pratt, B. G. G. Lohmeijer, R. M. Waymouth, J. L. Hedrick, *J. Am. Chem. Soc.* **2005**, *127*, 13798.
[27] R. C. Pratt, B. G. G. Lohmeijer, D. A. Long, P. N. P. Lundberg, A. P. Dove, H. Li, C. G. Wade, R. M. Waymouth, J. L. Hedrick, unpublished results.
[28] A total of 55% (v/v) porosity is expected according to an independent experiment using 15% (w/w) PDMA ($M_r = 7000$) wherein 10% (v/v) porosity was obtained.

 © 2006 Wiley-VCH Verlag GmbH & Co. KGaA, Weinheim

[29] D. Mecerreyes, E. Huang, T. Magbitang, W. Volksen, C. J. Hawker, V. Y. Lee, R. D. Miller, J. L. Hedrick, *High Perform. Polym.* **2001**, *13*, S11.
[30] R. D. Miller, W. Volksen, V. Y. Lee, E. Connor, T. Magbitang, R. Zafran, L. Sundberg, C. J. Hawker, J. L. Hedrick, E. Huang, M. Toney, Q. R. Huang, C. W. Frank, H. C. Kim in *Polymers for Microelectronics and Nanoelectronics*, ACS Symposium Series 894, ACS, Washington DC, **2004**, pp. 144.
[31] J. S. Pedersen, *J. Appl. Crystallogr.* **1994**, *27*, 595.

 © 2006 Wiley-VCH Verlag GmbH & Co. KGaA, Weinheim

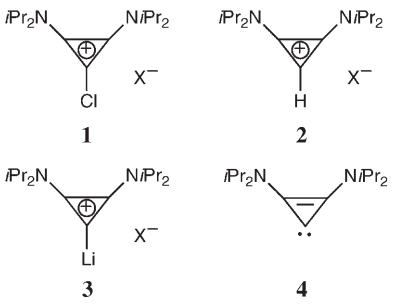

Scheme 1. Schematic representation of bis(diisopropylamino) derivatives of chlorocyclopropenium **1**, cyclopropenium **2**, cyclopropenylidene–lithium adduct **3**, and cyclopropenylidene **4**.

Carbenes

DOI: 10.1002/anie.200602701

Isolation of Cyclopropenylidene–Lithium Adducts: The Weiss–Yoshida Reagent**

*Vincent Lavallo, Yutaka Ishida, Bruno Donnadieu, and Guy Bertrand**

In the 1950s, Breslow[1] and Wanzlick[2] realized that the stability of a carbene could be dramatically enhanced by the presence of amino substituents, but they were unable to isolate a "monomeric" carbene.[3] It was only in 1991, three years after the isolation of a (phosphino)(silyl)carbene,[4] that a bottleable diamino carbene, namely an imidazol-2-ylidene, was prepared.[5] Even more strikingly, in a paper entitled "1,2,3,4-Tetraphenylimidazol-2-ylidene: The Realization of Wanzlick's Dream", Arduengo et al.[6] reported that a modification of the experimental procedure published by Wanzlick's group makes it possible to isolate one of the exact same carbenes that was postulated in 1970.[7]

Wanzlick was not the only one to nearly isolate the first stable carbene. Indeed, in the 1970s, Yoshida[8] and Weiss[9] attempted independently the preparation of the bis(diisopropylamino)cyclopropenylidene **4** (Scheme 1). Recently, we isolated exactly the same carbene after deprotonation of cyclopropenium salt **2** ($X = BPh_4$) with potassium bis(trimethylsilyl)amide.[10] Among the routes used by Yoshida and Weiss were lithium/halogen exchange from **1** ($X = ClO_4$)[9a] and the deprotonation of **2** ($X = ClO_4$),[8a,b] both with *n*BuLi. However, they were not able to isolate the resulting product. Initially, Yoshida claimed the successful synthesis of the free cyclopropenylidene **4**,[8a] but several years later he[8b–e] and Weiss[9a] concluded concurrently that the compound in question was more likely the carbene–lithium adduct **3** ($X = ClO_4$). More recently, Tamm, Hahn, et al.[11] repeated the lithium/halogen exchange reaction of **1** ($X = ClO_4$ and CF_3SO_3) with *n*BuLi and described the product as stable only at low temperatures. It has also been shown that this compound, generated in situ, effectively transfers the cyclopropenylidene moiety **4** to a number of substrates, including transition metals and main-group fragments.[8,9,11,12]

Weiss proposed the formation of the carbene–lithium adduct **3** ($X = ClO_4$), rather than that of the free carbene **4**, based primarily on the observation that no $LiClO_4$ precipitated from the reaction mixture.[9a] The only spectroscopic data that exist for the Weiss–Yoshida (W–Y) reagent is a single report of a lithium NMR chemical shift.[8d] All these experimental observations, including the transfer reactions, do not rule out the possibility that the W–Y reagent could actually be the free carbene **4**. Indeed, carbenes that can be isolated as free species do not generally form stable complexes with simple lithium salts (LiX, X = halogen or more weakly coordinating anion),[13,14] although there are two exceptions.[15]

This analysis prompted us to reinvestigate the exact nature of the W–Y reagent. First, we reproduced the lithium/halogen exchange reaction with *n*BuLi, but to avoid any potential explosive hazards resulting from the perchlorate anion, the chlorocyclopropenium tetrafluoroborate salt **1** ($X = BF_4$) was used as a precursor. After the reaction mixture had been stirred for ten minutes at −78 °C, a very clean reaction occurred and crucially, a ^{13}C NMR signal at $\delta =$ 167 ppm was observed. This signal is shifted to high field compared to that of the carbene carbon nucleus of the free cyclopropenylidene **4** ($\delta = 185$ ppm),[10] exactly as expected for a lithium complex. Indeed, it has been shown for the exceptions mentioned above[15] that such a complexation induces an upfield shift of about 20 ppm. Surprisingly, the ^{13}C NMR spectrum remained unchanged when the solution was warmed to room temperature. After evaporation of the solvent under high vacuum, the residue was washed with hexane to afford a highly air-sensitive white powder, which was recrystallized in diethyl ether at −25 °C. The resulting colorless crystals (m.p. 88–90 °C (decomp), 45 % yield) were subjected to a single-crystal X-ray diffraction study.[16] In the solid state, **3** is a polymeric chain with an overall stoichiom-

[*] V. Lavallo, Dr. Y. Ishida, B. Donnadieu, Prof. G. Bertrand
UCR–CNRS Joint Research Chemistry Laboratory (UMI 2957)
Department of Chemistry
University of California
Riverside, CA 92521-0403 (USA)
Fax: (+1) 951-827-2725
E-mail: gbertran@mail.ucr.edu

[**] We are grateful to the NIH (R01 GM 68825) and Rhodia for financial support of this work, and to the JSPS for a Fellowship to Y.I.

InterScience
© 2006 Wiley-VCH Verlag GmbH & Co. KGaA, Weinheim

etry of five $LiBF_4$ units per four carbene ligands (Figures 1 and 2). Each cyclopropenylidene moiety is bonded to a lithium cation, which is coordinated by three fluorine atoms

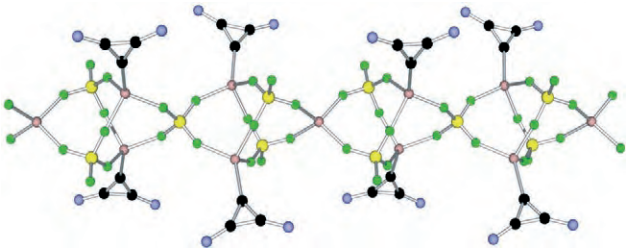

Figure 1. Molecular view of the structure of polymeric **3** in the crystal (C black, N blue, Li pink, B yellow, F green). The isopropyl groups on the nitrogen atoms have been omitted for clarity.

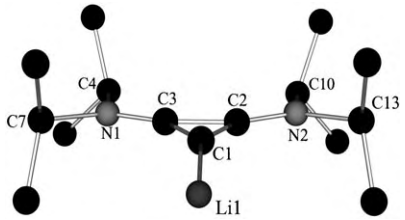

Figure 2. Molecular view of the structure of **3**. Selected bond lengths [Å] and angles [°]: Li1-C1 2.139(7), C1-C2 1.399(5), C1-C3 1.418(5), C2-C3 1.389(5), C2-N2 1.334(4), C3-N1 1.320(5); Li1-C1-C2 150.3(3), Li1-C1-C3 148.9(3), C2-C1-C3 59.1(3), C1-C2-N2 146.8(3), C3-C2-N2 152.0(4), C1-C2-C3 61.2(3), C1-C3-N1 147.5(4), C2-C3-N1 152.8(4), C1-C3-C2 59.8(3), C3-N1-C7 117.1(3), C3-N1-C4 121.0(3), C4-N1-C7 121.4(3), C2-N2-C13 116.9(3), C2-N2-C10 122.3(3), C10-N2-C13 120.7(3).

from three different tetrafluoroborate anions. The lithium cations that are not complexed by a cyclopropenylidene moiety are tetrahedrally coordinated by fluorine atoms from four different BF_4 anions. The carbene–lithium bond length (C1–Li1 2.093 Å) is significantly shorter than those observed in the few other reported carbene–lithium adducts (2.135–2.155 Å).[17]

If we view the conjugate acid (**2**) of the cyclopropenylidene **4** as a proton/carbene complex, there are clearly several structural and spectroscopic trends (Table 1). An elongation of the exocyclic C–N bonds is observed through the series **2** < **3** < **4**, which corresponds to decreased π donation from the amino groups. This trend is confirmed by the observed rotational barriers about the C–N bond, as deduced from variable-temperature NMR experiments. The bond angle about the carbene center contracts along the series **2** > **3** > **4**, which suggests an increase in s character for the exocyclic sp hybrid-type orbital. All of the relevant geometric parameters for **3** are closer to those for the free cyclopropenylidene **4** than its proton complex **2**, thus indicating a certain amount of ionic character in the carbene–lithium bond.

To test the lability of cyclopropenylidene **4** from the Li^+ ion we attempted, unsuccessfully, solvent extraction of the free carbene with several nonpolar solvents. We then tried to sequester the metal ion into a strong complexing agent. Upon addition of an excess of [12]crown-4 to a solution of **3** in diethyl ether, a yellow solid precipitated immediately. After recrystallization from THF/Et_2O, the compound was isolated as yellow crystals (m.p. 105–107 °C (decomp)) in 60 % yield. The ^{13}C NMR spectrum showed signals characteristic of the crown ether. Compared to **3**, the chemical shifts for the carbene carbon atom and the other two ring carbon atoms remained essentially the same ($\Delta\delta = 3$ and $\Delta\delta < 1$ ppm, respectively). These results clearly rule out the presence of the free cyclopropenylidene **4**. A single-crystal X-ray diffraction study showed the formation of tertiary complex **5** (Figure 3). Although the structure's disorder precludes

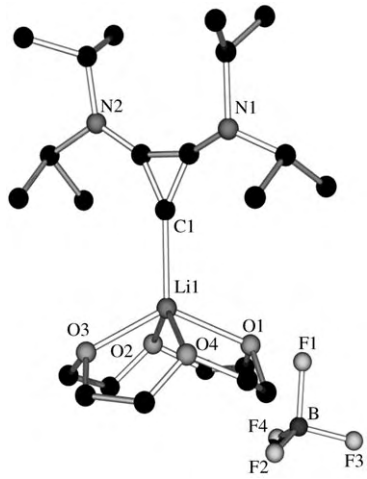

Figure 3. Molecular view of the structure of **5** in the crystal. Owing to thermal disorder, geometric parameters cannot be accurately discussed.

Table 1: Comparison of the geometric parameters, rotational barrier (E_{rot}) about the C_{ring}–N bonds, and spectroscopic data for compounds **2**, **3**, and **4**.

Compound	C_{ring}–N[a] [Å]	Carbene angle [°]	E_{rot}[b] [kJ mol^{-1}]	δ (^{13}C)[c] [ppm]
2[10]	1.306	62.3	75	99
3	1.328	59.1	56	167
4[10]	1.334	57.2	53	185

[a] Average value of the C_{ring}–N bond lengths. [b] Calculated based on variable-temperature NMR experiments. [c] Chemical shift for the carbene carbon atom in **4** and the corresponding carbon atoms in **2** and **3**.

detailed discussion of the geometric parameters, it can be seen that it is a monomeric carbene–lithium complex, a type of compound which has eluded isolation thus far.[17,18] These results are in contrast with Alder's observation[15a] that addition of [12]crown-4 to the *N*,*N*-diisopropyltetrahydropyrimid-2-ylidene $LiBF_4$ complex induces the liberation of the free carbene. This finding suggests that cyclopropenylidene **4** coordinates lithium cations much more strongly than N-heterocyclic carbenes.

We then turned our attention to the deprotonation route. When *n*BuLi was used as a base, as Yoshida et al. did with **2**

 © 2006 Wiley-VCH Verlag GmbH & Co. KGaA, Weinheim

($X = ClO_4$),[8a,b] the reaction with **2** ($X = BF_4$) appeared to be very clean. The ^1H and ^{13}C NMR data of the resulting product are identical to those of the lithium complex **3** that was obtained by the lithium/halogen exchange reaction. Interestingly, when *n*BuLi is replaced by potassium bis(trimethylsilyl)amide, under identical experimental conditions, multinuclear NMR spectroscopy shows the clean formation of the free cyclopropenylidene **4**. After work up, carbene **4** was isolated in 53% yield, which compares advantageously with the 20% yield observed when the cyclopropenium salt **2**, with BPh_4 as a counteranion, was used for the deprotonation reaction.[10]

From these results as a whole, it appears that free cyclopropenylidene **4** cannot be generated by using *n*BuLi or any other lithium-containing bases. In contrast to Li^+, the presence of K^+ ions does not prevent the isolation of the free carbene **4**. Moreover, comparing our results with the previous reports, it seems that the counteranion of the cyclopropenium precursors **1** and **2** has a considerable importance with respect to the stability of the lithium cyclopropenylidene complexes. In fact, in our hands, all attempts to isolate the lithium cyclopropenylidene complex with the BPh_4^- counterion instead of BF_4^- failed.

It can be concluded that Weiss and Yoshida were not lucky. They had the right cyclopropenium cation, but they did not choose the right counteranion to isolate the first carbene–lithium complex. Moreover, had they chosen the right base and counteranion combination, they would have isolated the first stable carbene. The isolation of both the free carbene and its lithium adduct should allow for the proliferation of cyclopropenylidene chemistry.

Experimental Section

1 and **2** ($X = BF_4$) were obtained from **1** and **2** ($X = Cl$) by the reported procedure,[19,10] with the exception that $NaBF_4$ was used for the anion exchange. **1** ($X = BF_4$): 30.0 g, 90%, m.p. 120–121 °C; **2** ($X = BF_4$): 33.5 g, 90%, m.p. 121–122 °C.

3 ($X = BF_4$): *n*BuLi (1 equiv) was added to a suspension of **1** ($X = BF_4$; 3.00 g, 8.36 mmol) or **2** ($X = BF_4$; 3.00 g, 9.25 mmol) in diethyl ether (80 mL) at −78 °C. The reaction was stirred for 15 minutes and then warmed to room temperature. After concentration in a vacuum and washing with hexane (40 mL), a white powder was obtained. The residue was recrystallized from a solution of diethyl ether at −25 °C, and colorless crystals were obtained (yield: 1.59 g (45%) from **1**, 1.88 g (48%) from **2**). M.p. 88–90 °C (decomp); ^1H NMR (C_6D_6, 25 °C, 300 MHz): $\delta = 3.62$ (br m, 4H, CH), 1.21 ppm (br m, 24H, CH_3); ^{13}C NMR ([D_8]THF, 25 °C, 75 MHz): $\delta = 166.8$ (CLi), 154.9 (C_{ring}), 50.4 (br, CH), 21.1 ppm (CH_3); ^7Li NMR ([D_8]THF, 25 °C, 233 MHz): $\delta = 0.27$ ppm (rel. to LiCl in D_2O as external standard).

5: At room temperature, [12]crown-4 (2 equiv) was added to a solution of **3** (2.00 g, 4.72 mmol) in diethyl ether (60 mL), and a precipitate immediately formed. The yellow solid was washed with hexane (40 mL) and dried in a vacuum. The residue was recrystallized from THF/Et_2O (50/50) at −25 °C, and yellow crystals were obtained (yield: 1.43 g, 60%). M.p. 105–107 °C (decomp); ^1H NMR ([D_8]THF, 25 °C, 300 MHz): $\delta = 4.00$ (sept, 4H, CH, $J = 6.7$), 3.57 (s, 16H, CH_2), 1.41 ppm (d, 24H, CH_3, $J = 6.7$); ^{13}C NMR ([D_8]THF, 25 °C, 75 MHz): $\delta = 164.6$ (CLi), 154.6 (C_{ring}), 52.1 (br, CH), 48.8 (br, CH), 20.9 ppm (CH_3); ^7Li NMR ([D_8]THF, 25 °C, 233 MHz): $\delta = -0.10$ ppm (rel. to LiCl in D_2O as external standard).

Received: July 7, 2006
Published online: September 20, 2006

Keywords: carbenes · complexation · cyclopropenylidenes · lithium · structure elucidation

[1] R. Breslow, *J. Am. Chem. Soc.* **1958**, *80*, 3719.
[2] H.-W. Wanzlick, *Angew. Chem.* **1962**, *74*, 129; *Angew. Chem. Int. Ed. Engl.* **1962**, *1*, 75.
[3] a) R. W. Hoffmann, *Angew. Chem.* **1968**, *80*, 823; *Angew. Chem. Int. Ed. Engl.* **1968**, *7*, 754; b) A. J. Arduengo III, R. Krafczyk, *Chem. Unserer Zeit* **1998**, *32*, 6; c) A. J. Arduengo III, *Acc. Chem. Res.* **1999**, *32*, 913.
[4] a) A. Igau, H. Grützmacher, A. Baceiredo, G. Bertrand, *J. Am. Chem. Soc.* **1988**, *110*, 6463; b) A. Igau, A. Baceiredo, G. Trinquier, G. Bertrand, *Angew. Chem.* **1989**, *101*, 617; *Angew. Chem. Int. Ed. Engl.* **1989**, *28*, 621.
[5] A. J. Arduengo III, R. L. Harlow, M. Kline, *J. Am. Chem. Soc.* **1991**, *113*, 361.
[6] A. J. Arduengo III, J. R. Goerlich, R. Krafczyk, W. J. Marshall, *Angew. Chem.* **1998**, *110*, 2062; *Angew. Chem. Int. Ed.* **1998**, *37*, 1963.
[7] H.-J. Schönher, H.-W. Wanzlick, *Justus Liebigs Ann. Chem.* **1970**, *731*, 176.
[8] a) Z. Yoshida, *Abstr. 2nd Int. Symp. Chemistry of Nonbenzenoid Aromatic Compounds*, Lindau **1974**, p. 23; b) Z. Yoshida, H. Konishi, S. Sawada, H. Ogoshi, *J. Chem. Soc. Chem. Commun.* **1977**, 850; c) H. Konishi, S. Matsumoto, Y. Kamitori, H. Ogoshi, Z. Yoshida, *Chem. Lett.* **1978**, 241; d) Z. Yoshida, *Pure Appl. Chem.* **1982**, *54*, 1059; e) S. Miki, T. Ohno, H. Iwasaki, Z. Yoshida, *J. Phys. Org. Chem.* **1988**, *1*, 333.
[9] a) R. Weiss, C. Priesner, H. Wolf, *Angew. Chem.* **1978**, *90*, 486; *Angew. Chem. Int. Ed. Engl.* **1978**, *17*, 446; b) R. Weiss, C. Priesner, H. Wolf, *Angew. Chem.* **1979**, *91*, 505; *Angew. Chem. Int. Ed. Engl.* **1979**, *18*, 472; c) R. Weiss, M. Hertel, H. Wolf, *Angew. Chem.* **1979**, *91*, 506; *Angew. Chem. Int. Ed. Engl.* **1979**, *18*, 473; d) R. Weiss, H. Wolf, *Chem. Ber.* **1980**, *113*, 1746.
[10] V. Lavallo, Y. Canac, B. Donnadieu, W. W. Schoeller, G. Bertrand, *Science* **2006**, *312*, 722.
[11] a) M. Tamm, A. Grzegorzewski, F. E. Hahn, *J. Organomet. Chem.* **1995**, *501*, 309; b) H. Schumann, M. Glanz, F. Girgsdies, F. E. Hahn, M. Tamm, A. Grzegorzewski, *Angew. Chem.* **1997**, *109*, 2328; *Angew. Chem. Int. Ed. Engl.* **1997**, *36*, 2232.
[12] a) R. Gompper, E. Bartmann, *Angew. Chem.* **1978**, *90*, 490; *Angew. Chem. Int. Ed. Engl.* **1978**, *17*, 456; b) R. Gompper, U. Wolf, *Liebigs Ann. Chem.* **1979**, 1406.
[13] One of the most classical methods for the preparation of stable free carbenes is the deprotonation of the conjugate acid; very often lithium salts are present and no complexation occurs.
[14] a) W. A. Herrmann, *Angew. Chem.* **2002**, *114*, 1342; *Angew. Chem. Int. Ed.* **2002**, *41*, 1290; b) D. Bourissou, O. Guerret, F. P. Gabbaï, G. Bertrand, *Chem. Rev.* **2000**, *100*, 39; c) N. Kuhn, A. Al-Sheikh, *Coord. Chem. Rev.* **2005**, *249*, 829.
[15] a) R. W. Alder, M. E. Blake, C. Bortolotti, S. Bufali, C. P. Butts, E. Linehan, J. M. Oliva, A. G. Orpen, M. J. Quayle, *Chem. Commun.* **1999**, 241; b) M. Otto, S. Conejero, Y. Canac, V. D. Romanenko, V. Rudzevitch, G. Bertrand, *J. Am. Chem. Soc.* **2004**, *126*, 1016.
[16] CCDC-613889 (**3**) and CCDC-613890 (**5**) contain the supplementary crystallographic data for this paper. These data can be obtained free of charge from The Cambridge Crystallographic Data Centre via www.ccdc.cam.ac.uk/data_request/cif.

 © 2006 Wiley-VCH Verlag GmbH & Co. KGaA, Weinheim

[17] a) G. Boche, C. Hilfe, K. Harms, M. Marsch, J. C. W. Lohrenz, *Angew. Chem.* **1995**, *107*, 509; *Angew. Chem. Int. Ed. Engl.* **1995**, *34*, 487; b) C. Hilf, F. Bosold, K. Harms, J. C. W. Lohrenz, M. Marsch, M. Schimeczek, G. Boche, *Chem. Ber. Recl.* **1997**, *130*, 1202; c) C. Hilf, F. Bosold, K. Harms, M. Marsch, G. Boche, *Chem. Ber. Recl.* **1997**, *130*, 1213; d) A. J. Arduengo III, M. Tamm, J. C. Calabrese, F. Davidson, W. J. Marshall, *Chem. Lett.* **1999**, 1021; e) R. Fränkel, C. Birg, U. Kernbach, T. Habereder, H. Nöth, W. P. Fehlhammer, *Angew. Chem.* **2001**, *113*, 1961; *Angew. Chem. Int. Ed.* **2001**, *40*, 1907; f) P. L. Arnold, S. A. Mungur, A. J. Blake, C. Wilson, *Angew. Chem.* **2003**, *115*, 6163; *Angew. Chem. Int. Ed.* **2003**, *42*, 5981; g) P. L. Arnold, M. Rodden, K. M. Davis, A. C. Scarisbrick, A. J. Blake, C. Wilson, *Chem. Commun.* **2004**, 1612.

[18] All carbene–lithium complexes isolated so far[17] are dimers or higher-order aggregates.

[19] Z. Yoshida, Y. Tawara, *J. Am. Chem. Soc.* **1971**, *93*, 2574.

 © 2006 Wiley-VCH Verlag GmbH & Co. KGaA, Weinheim

Surface Chemistry

DOI: 10.1002/anie.200602180

Role of Rotational Alignment in Dissociative Chemisorption and Oxidation: O_2 on Bare and CO-Precovered Pd(100)**

Andrea Gerbi, Letizia Savio, Luca Vattuone, Fernando Pirani, David Cappelletti, and Mario Rocca*

The adsorption of gas-phase molecules that approach solid surfaces in well-defined quantum states represents a fundamental step for the understanding of heterogeneous chemical reactions[1] and for better control over the growth of self-assembled layers.[2] This objective has been achieved only in a few cases to date (NO,[3,4] H_2,[5] CH_4[6,7]). Vibrational excitations and conversion of translational to vibrational energy were thereby found to account for strong enhancements in the dissociation probability. Less attention has been devoted to rotations because they involve less energy,[8] and are therefore important only for physisorption.[9,10] We show here that rotations as well as the alignment of the rotational axis play a role in the dissociative chemisorption of O_2 onto a CO–Pd(100) surface. The effect, which arises from the requirements needed to pass through the CO adlayer, leads to different sticking probabilities and average O–CO distances, and has possible general applications for controlling reactions and film growth.

The alignment of rotational angular momentum can be exploited to investigate stereodynamical effects in molecular adsorption processes.[9,11–13] Such an alignment, which consists of a propensity of molecules to populate specific helicity states (defined by the quantum number M, the projection of the rotational angular momentum along the propagation direction) can be naturally induced by collisions in seeded supersonic molecular beams (MBs). Diatomic, linear, and linear-like molecules flying in the MB with $M=0$ behave as cartwheels when impinging on the surface at normal incidence, while when M is maximum they move in a helicopter-like manner. In particular, it has been shown that for the interaction of C_2H_4 with an O_2-precovered Ag(100) surface,[9,11] and for C_3H_6/Ag(100),[12] molecules with helicopter-like motion adsorb more efficiently than cartwheeling ones only at intermediate hydrocarbon coverage. The stereo-insensitivity of the initial sticking probability S_0 and its coverage dependence indicated that the effect is due to the collision between trapped molecules, which still remember about their original alignment, and preadsorbed ones, which lie flat on the surface. Rotational alignment was found to be ineffective for more strongly bound systems such as σ-bonded C_2H_4/Pd(100)[13] and O_2/Ag(100) (interactions mediated via a chemisorbed molecular precursor). This result was attributed to steering forces turning the incoming molecule into the most favorable configuration and causing it to lose memory of its initial state.

For O_2 on CO-precovered Pd(100), however, we find that molecules moving as cartwheels stick better than those with helicopter-like motion and that molecular alignment also affects the initial sticking probability. The system under investigation is important because of the effective rate of CO oxidation on Pd(100) when exposed to molecular oxygen. Herein we focus on stereodynamical effects of O_2 on the S_0 value and on the production of CO_2.

According to Ref. [14], rotational alignment of O_2 is generated by collisions during a supersonic seeded expansion of O_2 diluted in lighter and faster carrier atoms, typically He and Ne. Under these conditions most of the oxygen molecules in the MB are relaxed in the ground rotational level ($K=1$)[15] and cartwheeling motion prevails on average over helicopter-like motion. In addition, as demonstrated[14] by the use of a high-resolution mechanical velocity selector (consisting of eight rotating slotted disks) the angular momentum of the O_2 molecules belonging to the slow tail (ST) of the velocity distribution are nearly randomly oriented (ca. 33 % in $M=0$),

[*] Dr. A. Gerbi, Dr. L. Savio, Dr. L. Vattuone
Dipartimento di Fisica
CNISM Unità di Genova
Università di Genova
Via Dodecaneso 33, 16146 Genova (Italy)
Fax: (+39) 010-314-218
E-mail: vattuone@fisica.unige.it
Homepage: http://www.fisica.unige.it/~vattuone
Prof. F. Pirani
Dipartimento di Chimica
Università di Perugia
Via Elce di Sotto, Perugia (Italy)
Prof. D. Cappelletti
Dipartimento di Ingegneria civile ed ambientale
Università di Perugia (Italy)
Prof. M. Rocca
Dipartimento di Fisica and IMEM del CNR
Università di Genova (Italy)

[**] We acknowledge financial support by MIUR under PRIN projects.

Supporting information for this article is available on the WWW under http://www.angewandte.org or from the author.

 © 2006 Wiley-VCH Verlag GmbH & Co. KGaA, Weinheim

while those in the fast tail (FT) fly mostly with cartwheeling motion (>80%). In the present experiment (see the Experimental Section and the Supporting Information) the fraction moving as cartwheels are approximately 0.4 and 0.7 for the ST and FT regions, respectively.

Figure 1 shows the partial pressure of O_2 in the chamber, measured by a quadrupole mass spectrometer (QMS), during exposure of the Pd(100) sample at 394 K to the ST or FT of the

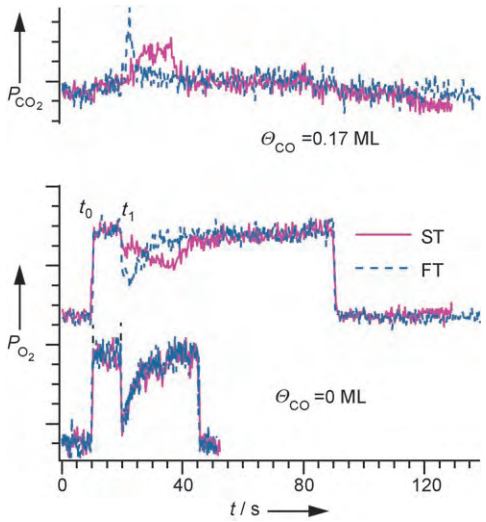

Figure 1. O_2 partial pressure, measured by a QMS not directly in line with the MB, as a function of time for the slow and fast tails of the MB interacting with the bare surface (lower traces) and with Pd(100) precovered with 0.17 ML of CO (middle traces). At time $t_0 \approx 10$ s the supersonic MB enters the UHV chamber but a flag prevents it from striking the sample; at time $t_1 \approx 20$ s the flag in front of the sample is removed and the beam hits the Pd surface. The top set of traces show the partial pressure of CO_2.

O_2 supersonic MB seeded in He at normal incidence. The sample is initially shielded by an inert cover (flag), so that no direct adsorption occurs. The background pressure typically increases by 2×10^{-10} mbar, mostly because of He, so that adsorption from the background over the time scale of an experiment (<100 s) is also negligible. When the flag is removed (t_1) the beam strikes the reactive surface of the sample. The relative decrease in the QMS signal corresponds to the O_2 sticking probability S.[16] The lower traces refer to the interaction with bare Pd(100). No difference is observed between the FT and ST experiments, thus indicating either that steering is efficient in turning the molecule into the most favorable configuration for dissociation or that the interaction between Pd and O_2 is stereo-insensitive within the sensitivity of our experimental system (the error on S amounts to ca. 0.07). The upper O_2 traces correspond to adsorption on a surface precovered with 0.17 monolayer (ML) of CO. Differences in the ST and FT regions are evident both for S_0 and when O atoms accumulate on the surface. The CO_2 traces show that the reactivity is also markedly different for the two tails. The evolution with O_2 exposure is complicated by the formation and desorption of CO_2 which makes new free sites available. Such processes do not, however, affect S_0.

Similar data were recorded for various crystal temperatures T between 250 and 400 K as well as for a lower translational energy (0.26 eV, obtained by seeding O_2 in a He/Ne mixture). No dependence on T and a weak dependence on the translational energy[17] for the ST was found, which is in agreement with the direct and non-activated nature of the chemisorption process. Indeed, chemisorption is dissociative, as confirmed by inspection of vibrational spectra.[18,19] Therefore, we are confident that most of the difference between the results observed with the ST and the FT arises from different adsorption probabilities for molecules moving as helicopters and cartwheels. These findings have been confirmed by a more extensive investigation of the dependence of S_0 on CO precoverage, as measured using the O_2 MB seeded in He at two different temperatures. Experimental data are summarized in Figure 2; the results of a model calculation (discussed

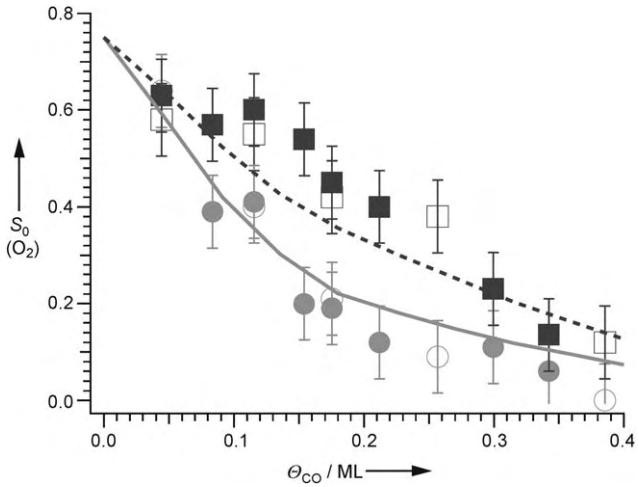

Figure 2. The initial sticking probability S_0 of O_2 as a function of CO precoverage Θ_{CO} (expressed in ML of the Pd(100) surface) for ST (circles) and FT (squares) at $T=313$ K (open symbols) and 394 K (filled symbols). The continuous and dashed lines are the results of a Monte Carlo model calculation of S_0 for ST and FT, respectively, as described in the text.

below) are also shown. We note that for a CO precoverage of 0.20 ML, the value of S_0 reduces by about 30% for the FT with respect to that of the bare surface (mostly cartwheeling molecules) while it drops by more than 80% for the ST (mostly molecules moving in a helicopter-like manner).

The observed steric effect is very different from that reported previously for ethylene and propylene on Ag(100)[11,12] because:

a) O_2 alignment not only affects the coverage dependence of S, it also affects S_0. The magnitude of the reduction of the S_0 value for molecules moving with helicopter-like motion indicates that the effect cannot be explained by the mere blocking of sites by preadsorbed CO;
b) cartwheeling O_2 molecules stick better than ones moving in a helicopter-like fashion, while the opposite holds true for ethylene and propylene;
c) the sticking event takes place directly for O_2, while it is mediated by a precursor for the hydrocarbons.

 © 2006 Wiley-VCH Verlag GmbH & Co. KGaA, Weinheim

To the best of our knowledge, this is the first experimental evidence of an influence of molecular alignment on the initial sticking probability and on the rate of oxidation.

We propose that the steric effect in the initial sticking probability of O_2 on the CO-precovered surface is due to the larger number of free sites required to allow for a molecule with helicopter-like motiom to land between CO molecules (sitting in bridge sites, see Ref. [20]). To support this hypothesis we carried out a Monte Carlo simulation on a lattice model for the investigated system. In particular, we used the same code and parameters for the interaction energy between adsorbed CO already employed by one of us[21] to reproduce the coverage dependence of the heat of adsorption of CO on Pd(100). More details are reported in Figure 3 A.

We set up the model to compute the probability P_{MC} of finding four free (bridge) sites in a square (I), six free sites (II), and a more complicated set of twenty free sites (III). These arrangements are illustrated in Figure 3 B. The results are displayed versus CO coverage in Figure 3 C. Configurations I and II may be adequate for the landing of a molecule in (or close to) an upright position, with the O–O bond (nearly) perpendicular to the surface, provided that CO can be displaced during dissociation of O_2 to allow the oxygen adatoms to occupy next-neighbor sites. This is reasonable since the adsorption energy of oxygen atoms is much larger than that of carbon monoxide.[21] Moreover, in our experimental conditions, oxygen atoms cannot occupy first neighbour sites in the final state, otherwise it would already be possible to reach a local coverage greater than 0.5 ML at low exposure. On the contrary, experiments show that high coverage phases are produced only for a total coverage exceeding 0.45 ML.[20] The much more stringent configuration III corresponds to the eight (fourfold hollow) sites requirement for dissociation of O_2 on oxygen-precovered Pd(100)[22] if it is supposed that all bridge sites belonging to the seven first neighbors of the two oxygen adatoms (green in the figure) are empty. This array is certainly sufficient for the landing and dissociation of oxygen molecules moving with a helicopter-like motion and does not require CO to move. The final results of the model (see Supporting Information) have been obtained assuming a fraction of 0.42 and 0.72 for the cartwheeling molecules in the ST and FT, respectively. The value of S_0 for the bare surface (0.75) is thus multiplied by the probability of having four bridge sites, as in I, for the cartwheeling molecules and a set as in III for molecules with helicopter-like motion. Figure 2 shows that, despite its simplicity, the model provides an acceptable description of the experimental data.

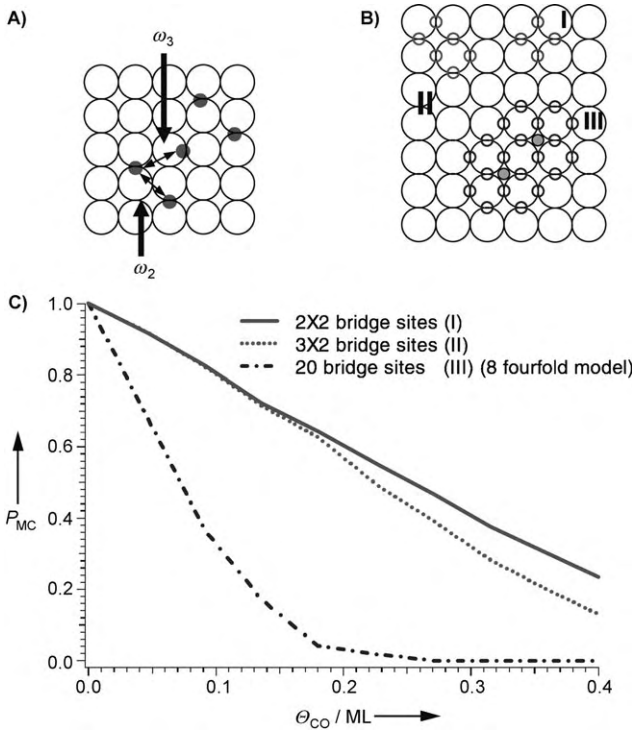

Figure 3. A) Illustration of the interaction between first (ω_2) and second (ω_3) neighbor sites occupied in the $c(2\sqrt{2}\times\sqrt{2})R45°$ structure which corresponds to a CO coverage of 0.5 ML. A strong repulsive interaction is imposed on closer molecules to prevent occupation of neighboring sites, which experimentally does not occur below 0.5 ML. The values of ω_2 (25 KJ mol^{-1}) and ω_3 (2.5 KJ mol^{-1}) are taken from Ref. [21], where they have been used to fit the coverage dependence of the heat of adsorption of CO. The value of the CO–Pd bond is set to the experimental value of 170 kJ mol^{-1}, which corresponds to the heat of adsorption of CO in the low coverage limit. B) Schematic diagram of the configurations I–III corresponding to the squared array of four bridge sites (I), the rectangular shaped set of six free bridge sites (II), and the array of twenty free sites (III; unfilled circles) obtained by eight fourfold hollow sites blocked by two oxygen atoms (filled circles). C) Probability P_{MC} of finding different sets (I–III) of free bridge sites versus CO precoverage as obtained by Monte Carlo simulation.

From Figure 1 we see that CO oxidation proceeds rapidly with the FT and more slowly for the ST regions. Although a detailed analysis of this phenomenon will be presented elsewhere, we point out here that the different behavior corresponds to the rate of reaction in an O–CO layer where the two reactants are in close contact (FT) and in a layer where they are further apart (ST). This effect is due to the lower heat of adsorption of O close to CO which reduces the activation barrier for oxidation,[23] thereby yielding a faster reaction for O resulting from the cartwheeling O_2 molecule. Our study thus discloses a rich reaction dynamics which was hidden to date because of the lack of experimental techniques able to control molecular alignment.

In conclusion we have demonstrated that both the initial sticking probability of O_2 on CO-precovered Pd(100) and the rate of CO_2 production are strongly affected by the alignment of the incoming molecules, being definitively larger for molecules moving in a cartwheeling than a helicopter-like fashion. This result is explained by the more stringent requirements for the landing of the latter species on the CO-precovered surface.

Since O_2 moving in a helicopter-like manner can only stick in larger holes in the CO adlayer, we propose that molecular alignment may be used to prepare mixed CO–O layers with different average distances between the O and CO. We have moreover shown that this largely affects the yield of CO_2 in the prototype Pd-O-CO system. This finding may open up the possibility of employing the deposition of molecules with controlled alignment for the growth[24] of more-ordered layers.

 © 2006 Wiley-VCH Verlag GmbH & Co. KGaA, Weinheim

Experimental Section

Sample preparation: The Pd(100) sample was a 10-mm diameter disk, cut within 0.1° off the nominal surface plane. Its surface was prepared in an ultrahigh vacuum (UHV, base pressure 2×10^{-10} mbar) following the method given in Ref. [20] (see Supporting information). Surface cleanliness was checked by Auger electron spectroscopy and, in a separate set of experiments, also by high-resolution electron energy loss spectroscopy (HREELS). The temperature was measured by a Chromel-Alumel thermocouple, spot-welded to the sample.

Determination of the degree of alignment: A mixture of O_2 (4%) seeded in He was employed and the MB source conditions were kept as close as possible to those of Ref. [14]. The velocity selector consists of only two rotating disks,[25] a setup which allows for easy insertion into the apparatus and for the largest possible transmission. Since the degree of alignment achieved for O_2 molecules cannot be measured in situ, we rely on the experimental observations in Ref. [14] and to the guidelines discussed in Ref. [26]. The control of molecular alignment has therefore been inferred indirectly by explicitly taking into account, through a Monte Carlo simulation (see the Supporting Information), velocity and angular resolution conditions employed both in our sticking probability measurements and in previous experiments.[14]

Received: June 1, 2006
Revised: August 7, 2006
Published online: September 20, 2006

Keywords: adsorption · interfaces · O–O activation · palladium · surface chemistry

[1] R. J. Madix in S *urface Reactions*, Springer, Berlin, **1994**.
[2] L. Casalis, M. F. Danisman, B. Nickel, G. Bracco, T. Toccoli, S. Iannotta, G. Scoles, *Phys. Rev. Lett.* **2003**, *90*, 206101.
[3] E. W. Kuipers, M. G. Tenner, A. W. Kleyn, S. Stolte, *Nature* **1988**, *334*, 420–422.
[4] H. Hou, Y. Huang, C. T. Rettner, D. J. Auerbach, A. M. Wodtke, *Science* **1999**, *284*, 1647–1650.
[5] M. Gostein, G. O. Sitz, *J. Chem. Phys.* **1997**, *106*, 7378–7390.
[6] R. D. Beck, P. Maroni, D. C. Papegeorgopoulos, T. T. Dang, M. P. Schmid, T. R. Rizzo, *Science* **2003**, *302*, 98–100.
[7] R. R. Smith, D. R. Killelea, D. F. Del Sesto, A. L. Utz, *Science* **2004**, *304*, 992–995.
[8] P. Riviere, A. Salin, F. Martin, *J. Chem. Phys.* **2006**, *124*, 084706.
[9] L. Vattuone, A. Gerbi, M. Rocca, U. Valbusa, F. Pirani, D. Cappelletti, F. Vecchiocattivi, *Angew. Chem.* **2004**, *116*, 5312–5315; *Angew. Chem. Int. Ed.* **2004**, *43*, 5200–5204.
[10] L. Vattuone, U. Valbusa, M. Rocca, *Phys. Rev. Lett.* **1999**, *82*, 4878–4881.
[11] A. Gerbi, L. Vattuone, M. Rocca, F. Pirani, U. Valbusa, D. Cappelletti, F. Vecchiocattivi, *J. Chem. Phys.* **2005**, *123*, 224709.
[12] A. Gerbi, L. Vattuone, M. Rocca, F. Pirani, U. Valbusa, D. Cappelletti, F. Vecchiocattivi, *J. Phys. Chem. B* **2005**, *109*, 22884–22889.
[13] D. Cappelletti, A. Gerbi, F. Pirani, M. Rocca, M. Scotoni, L. Vattuone, U. Valbusa, *Phys. Scr.* **2006**, *73*, C20–C24.
[14] V. Aquilanti, D. Ascenzi, D. Cappelletti, F. Pirani, *Nature* **1994**, *371*, 399–402.
[15] In the ground electronic state $^3\Sigma_g^-$ O_2 behaves according to the Hund's case "b", where the rotational angular momentum **K** couples with the electronic spin **S** to give the total angular momentum **J**. Alignment in **K** manifests as nonstatistical distribution in the **J** projections along the molecular beam axis (see Ref. [13]).
[16] D. A. King, M. G. Wells, *Surf. Sci.* **1972**, *29*, 454–482.
[17] At 0.26 eV, for a CO precoverage of 0.17 ML, S_0 is approximately 0.42 in the FT region while it increases from 0.20 (O_2 in He) to about 0.34 (O_2 in He/Ne) in the ST region.
[18] G. W. Simmons, Y. N. Wang, J. Marcos, K. Klier, *J. Phys. Chem.* **1991**, *95*, 4522–4528.
[19] Adsorption is always dissociative at low coverage. In agreement with Ref. [18], HREEL spectra show a loss at 43 meV after an exposure of the bare surface to 0.5 ML O_2 at 0.40 eV for both the ST and FT regions. A precursor mechanism is excluded under the present experimental conditions by the dependence of S on oxygen coverage in the absence of CO (see Figure 1) and by the independence of S_0 on T between 273 and 733 K (here only data at 313 and 393 K are reported).
[20] R. J. Behm, K. Christmann, G. Ertl, M. A. Van Hove, *J. Chem. Phys.* **1980**, *73*, 2984–2995.
[21] Y. Y. Yeo, L. Vattuone, D. A. King, *J. Chem. Phys.* **1997**, *106*, 1990–1996.
[22] J. W. Evans, *J. Chem. Phys.* **1987**, *87*, 3038–3048.
[23] C. J. Zhang, P. Hu, *J. Am. Chem. Soc.* **2001**, *123*, 1166–1172.
[24] a) D, Ramos, H. M. G. Correia, *J. Phys. Condens. Matter* **2006**, *18*, S429–S438; b) H. Fujikake, T. Suzuki, F. Isaka, F. Sato, *Jpn. J. Appl. Phys. Part 2* **2004**, *43*, L536 L539.
[25] F. Pirani et al., *Rev. Sci. Instrum.* **2004**, *75*, 349–354.
[26] V. Aquilanti, D. Ascenzi, M. de Castro Vitores, F. Pirani, D. Cappelletti, *J. Chem. Phys.* **1999**, *111*, 2620–2632.

 © 2006 Wiley-VCH Verlag GmbH & Co. KGaA, Weinheim

Fuel Cells

DOI: 10.1002/anie.200602021

Interfacing Electrocatalysis and Biocatalysis with Tungsten Carbide: A High-Performance, Noble-Metal-Free Microbial Fuel Cell**

Miriam Rosenbaum, Feng Zhao, Uwe Schröder, and Fritz Scholz*

Microbial fuel cells (MFCs) produce electricity by utilizing the metabolism of living microorganisms to catalyze the oxidation of organic or inorganic substrates for electricity generation. Different concepts and mechanisms for electron transfer from the biocatalyst to the anode of the fuel cell have

[*] M. Rosenbaum, F. Zhao, Dr. U. Schröder, Prof. Dr. F. Scholz
Institute of Chemistry and Biochemistry
University of Greifswald
Friedrich-Ludwig-Jahnstrasse 18C, 17487 Greifswald (Germany)
Fax: (+49) 3834-864-451
E-mail: uweschr@uni-greifswald.de
Homepage: http://www.chemie.uni-greifswald.de/~analytik/mfc.html

[**] U.S. thanks the Deutsche Forschungsgemeinschaft (DFG). U.S., M.R., and F.S. acknowledge support by the Fonds der Chemischen Industrie.

WILEY InterScience DISCOVER SOMETHING GREAT
© 2006 Wiley-VCH Verlag GmbH & Co. KGaA, Weinheim

been proposed.[1] Thus, direct electron transfer to the fuel-cell anode via membrane-bound cytochromes (for example, *Geobacter* species,[2] *Rhodoferax ferrireducens*[3]) is possible (Figure 1a); however, this method so far delivers current

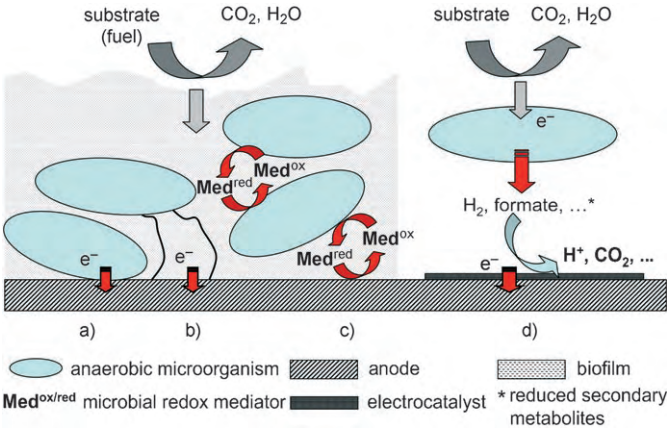

Figure 1. Identified electron-transfer mechanisms in MFCs. Electron transfer via a) cell-membrane-bound cytochromes, b) electrically conductive pili (nanowires), c) microbial redox mediators, and d) oxidation of reduced secondary metabolites.

densities as low as 3 $\mu A\,cm^{-2}$.[3] Alternatively, direct electron transfer can also take place through conductive bacterial pili ("nanowires"), as was recently demonstrated for *Shewanella oneidensis MR-1* (Figure 1b).[4] Electrochemically enriched microbial biofilm consortia show a very promising performance.[5–7] Herein, bacterial redox mediators are assumed to enhance electron transport to the anode and between multiple cell layers[8] (Figure 1c). For high MFC performance, however, selection procedures of over 70 days seem necessary.[9]

We have focused our research on the exploitation of electron-rich microbial metabolites as fuels (electron shuttles) for electricity generation (Figure 1d). For this approach, we have developed robust and yet highly effective electrocatalytic anode catalysts based on platinum–polyaniline[10] and platinum–poly(tetrafluoroaniline)[11] sandwich materials that allow the efficient in situ oxidation of microbial hydrogen, that is, in the microbial cultures. Current densities up to 1.5 $mA\,cm^{-2}$, short lag times, and a great versatility to exploit fermentative,[12,13] photofermentative,[14] and even purely photosynthetic[15] microbial activity set new standards for MFC performance.

So far the expensive electrocatalyst, the lack of suitable oxygen reduction cathodes, and the use of bacterial monocultures have been the main disadvantages of this promising approach. We now present a MFC that overcomes these problems. The major cornerstone is a noble-metal-free and yet highly efficient MFC anode based on tungsten carbide (WC) that allows current densities of presently up to 3 $mA\,cm^{-2}$ to be reached. By combining this electrocatalytic anode with an oxygen reduction cathode based on pyrolyzed Fe^{III} phthalocyanine (pyr-FePc)[16,17] and hydrogen-producing soil bacteria that serve as biocatalysts,[18] we can report herein a fully noble-metal-free high-performance MFC that reaches a maximum power density of 585 $\mu W\,cm^{-2}$ (5.85 $W\,m^{-2}$).

Figure 2a shows the current generation at a WC-modified graphite electrode immersed in a glucose substrate solution freshly inoculated with heat-treated soil. The electrode was potentiostatically poised at a potential of 0.2 V (vs Ag/AgCl) to allow the anode performance to be studied unaffected by the cathode performance. The small size of the anode (0.19 cm^2) in relation to the large volume of the substrate solution (0.25 L) in these experiments guarantees that there is only a negligible feedback of the electrode reaction on the microbiological processes. This condition is important as, in contrast to biofilm-based MFCs, the use of microbial suspensions allows the electrochemical and biocatalytic performances to be separated. In experiments with biofilms on

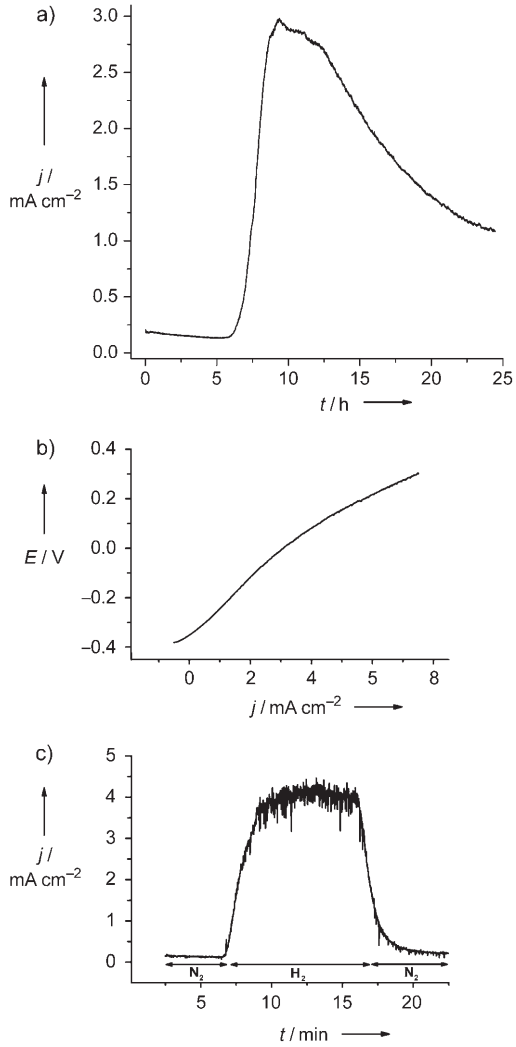

Figure 2. a) Current generation in an anaerobic glucose substrate solution (5 $g\,L^{-1}$) inoculated with heat-treated soil. The working electrode was a WC-modified graphite disk poised at a potential of 0.2 V and the temperature was 37 °C. b) Galvanodynamic experiment performed in the fermenting medium of (a). The scan rate was 10 $\mu A\,s^{-1}$. c) Current–time measurement as in (a), but performed in sterile phosphate buffer (100 mM, pH 7) and hydrogen/nitrogen purged.

 © 2006 Wiley-VCH Verlag GmbH & Co. KGaA, Weinheim

electrodes, the amount of biocatalyst is inextricably dependent on the size of the anode. As can be seen in Figure 2a, the current flow starts after a lag time of only seven hours. The current is caused by the electrocatalytic oxidation of reduced metabolic products (mainly hydrogen and formate) of the commencing fermentation of glucose by the anaerobic culture that develops from the soil inoculum. The current reaches a maximum density of 3 mA cm^{-2} (geometric surface area). Such a large peak current density has never been reported before, and it even exceeds our results with platinum–polyaniline sandwich electrodes.[10,11] After about 12 hours the current density decreases because of substrate exhaustion in the medium. The excellent performance of the WC-modified graphite disk electrode can also be derived from galvanodynamic polarization experiments (see Figure 2b), which show that high current densities are achieved even at rather negative potentials. Thus, at a potential of −0.1 V the current density still exceeds 2 mA cm^{-2}. By feeding hydrogen gas into the medium the measured current density even went up to 4 mA cm^{-2} (Figure 2c). The oxidation of formate (0.2 M) in phosphate buffers yielded current densities of 1.9 mA cm^{-2} (data not shown).

Since the studies of Böhm in the early 1970s,[19] WC has been discussed as a possible replacement for platinum as an electrocatalyst for hydrogen oxidation.[20–22] It has also been shown to possess good electrocatalytic properties toward the oxidation of formate,[23,24] but it could not fulfill the demands of chemical fuel cells. MFCs do not require this high oxidation performance, as the power generation is limited by the rate of bacterial metabolism, but they do require cheap, robust, and biocompatible anode materials. As the results described above indicate, WC fulfills these prerequisites for an excellent MFC anode catalyst. It also possesses the ability to catalyze several different pathways for the oxidation of inorganic and organic metabolites, for example, hydrogen and formate. This is of prime importance for achieving high conversion efficiencies.

MFC polarization experiments confirm the results of the half-cell measurements. In combination with an oxygen reduction cathode based on pyr-FePc,[16,17] an open-circuit potential of 864 mV is achieved (Figure 3). The maximum power point (MPP) of 585 μW cm^{-2} (5.85 W m^{-2}) at a current density of 1.6 mA cm^{-2} represents the highest power density measured in a MFC thus far.

In summary, we have introduced a high-performance, noble-metal-free MFC, and have shown that the cheap and yet effective catalyst WC allows electrocatalysis to be effectively interfaced with biocatalysis. By using a WC anode, pyr-FePc as cathode catalyst (oxygen reduction), and soil-based bacteria as biocatalysts, the performance of MFCs can be significantly increased with concurrently improved robustness and low costs.

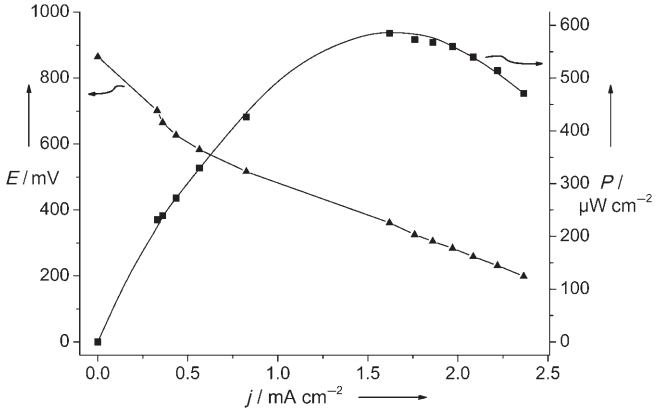

Figure 3. Polarization (■) and power (▲) curves of a MFC experiment using a WC-modified graphite disk as the anode. The substrate was glucose (5 g L^{-1}) and the biocatalyst inoculum was heat-treated soil.

Experimental Section

Catalyst synthesis: WC powder was prepared from $WO_3 \cdot H_2O$ in a tube oven under a CO stream for 10 h at 800 °C.[25] CO was provided by dropping dry HCOOH into hot oleum at a rate of two to three drops per minute.[26]

Electrode preparation: For anode preparation, WC powder was mechanically pressed onto a carbon support (10 mg cm^{-2}; graphite disk electrodes, paraffin impregnated,[27] ∅ 4.9 mm, geometrical surface area 0.19 cm^2, Elektrokohle, Lichtenberg) using 5% Nafion solution as binder. Anodes based on platinum–poly(tetrafluoroaniline) catalyst were prepared by the electrodeposition of platinum black and subsequent polymer coating as described elsewhere.[11] The cathode was prepared by coating graphite foil (geometrical surface area 55 cm^2) with pyrolized iron(III) phthalocyanine[16]/polytetrafluoroethylene (pyr-FePc/PTFE). The catalyst load was 1 mg cm^{-2}.

Biocatalyst: Foliage/dung soil from the botanical garden (University of Greifswald) was pretreated for 2 h at 120 °C to select spore-forming microbes. Sieved soil (2 g) was inoculated into culture medium (250 mL): at the beginning, mineral medium as in reference [18] containing glucose (5 g L^{-1}) was used; later only glucose (5 g), NH_4HCO_3 (2 g), and aqueous KH_2PO_4 (3.6 g L^{-1}) were employed. The culture medium was purged with nitrogen for 15 min prior to inoculation and cultivated anaerobically at 37 °C.

Electrochemical systems: Experiments were conducted in a batch-type two-chamber model fuel cell.[14] The cathode compartment was filled with phosphate buffer (250 mL, 50 mM, pH 4.4) and was purged with air using a fish pump. The anode compartment was filled with the soil bacterial solution. The anode and cathode compartments were separated by a Nafion 117 proton-exchange membrane. The monitoring of redox potentials and currents under different external resistance loads was performed with a data acquisition system (Keithley Integra 2700 digital multimeter) interfaced to a personal computer. The electrochemical (half-cell) characterization of the WC anodes was carried out galvanostatically or potentiostatically in a conventional three-electrode arrangement, with a graphite rod as counter electrode and a Ag/AgCl electrode (saturated KCl, 0.197 V vs normal hydrogen electrode (NHE)) as the reference electrode. All electrode potentials refer to this reference electrode. The experiments were carried out with PSTAT10, PGSTAT20, and PGSTAT30 potentiostats (Ecochemie, Netherlands). The PGSTAT30 was equipped with five array modules that allowed multiple working electrode measurements. The counter electrode was separated from the working electrode(s) by a Nafion 117 perfluorinated membrane.

Received: May 22, 2006
Published online: September 13, 2006

Keywords: biocatalysis · electrocatalysis · energy conversion · fuel cells · tungsten

 © 2006 Wiley-VCH Verlag GmbH & Co. KGaA, Weinheim

[1] B. E. Logan, B. Hamelers, R. Rozendal, U. Schröder, J. Keller, S. Freguia, P. Aelterman, W. Verstraete, K. Rabaey, *Environ. Sci. Technol.*, DOI: 10.1021/es0605016.
[2] D. R. Bond, D. E. Holmes, L. M. Tender, D. R. Lovley, *Science* **2002**, *295*, 483.
[3] S. K. Chaudhuri, D. R. Lovley, *Nat. Biotechnol.* **2003**, *21*, 1229.
[4] Y. A. Gorby, S. Yanina, J. S. McLean, K. M. Rosso, D. Moyles, A. Dohnalkova, T. J. Beveridge, I. S. Chang, B. H. Kim, K. S. Kim, D. E. Culley, S. B. Reed, M. F. Romine, D. A. Saffarini, E. A. Hill, L. Shi, D. A. Elias, D. W. Kennedy, G. Pinchuk, K. Watanabe, S. Ishii, B. Logan, K. H. Nealson, J. K. Fredrickson, *Proc. Natl. Acad. Sci. USA*, **2006**, *103*, 11358–11363.
[5] K. Rabaey, G. Lissens, S. D. Siciliano, W. Verstraete, *Biotechnol. Lett.* **2003**, *25*, 1531.
[6] B. H. Kim, H. S. Park, H. J. Kim, G. T. Kim, I. S. Chang, J. Lee, N. T. Phung, *Appl. Microbiol. Biotechnol.* **2004**, *63*, 672.
[7] H. Liu, B. E. Logan, *Environ. Sci. Technol.* **2004**, *38*, 4040.
[8] K. Rabaey, N. Boon, W. Verstraete, M. Höfte, *Environ. Sci. Technol.* **2005**, *39*, 3401.
[9] K. Rabaey, N. Boon, S. D. Siciliano, M. Verhaege, W. Verstraete, *Appl. Environ. Microbiol.* **2004**, *70*, 5373.
[10] U. Schröder, J. Nießen, F. Scholz, *Angew. Chem.* **2003**, *115*, 2986; *Angew. Chem. Int. Ed.* **2003**, *42*, 2880.
[11] J. Nießen, U. Schröder, M. Rosenbaum, F. Scholz, *Electrochem. Commun.* **2004**, *6*, 571.
[12] J. Nießen, U. Schröder, F. Harnisch, F. Scholz, *Lett. Appl. Microbiol.* **2005**, *41*, 286.
[13] J. Nießen, U. Schröder, F. Scholz, *Electrochem. Commun.* **2004**, *6*, 955.
[14] M. Rosenbaum, U. Schröder, F. Scholz, *Environ. Sci. Technol.* **2005**, *39*, 6328.
[15] M. Rosenbaum, U. Schröder, F. Scholz, *Appl. Microbiol. Biotechnol.* **2005**, *68*, 753.
[16] F. Zhao, F. Harnisch, U. Schröder, F. Scholz, P. Bogdanoff, I. Herrmann, *Electrochem. Commun.* **2005**, *7*, 1405.
[17] F. Zhao, F. Harnisch, U. Schröder, F. Scholz, P. Bogdanoff, I. Herrmann, *Environ. Sci. Technol.*, DOI: 10.1021/es060332p.
[18] J. Nießen, F. Harnisch, M. Rosenbaum, U. Schröder, F. Scholz, *Electrochem. Commun.* **2006**, *8*, 869.
[19] H. Böhm, *Electrochim. Acta* **1970**, *15*, 1273.
[20] G. Bronoel, E. Museux, G. Leclercq, L. Leclercq, N. Tassin, *Electrochim. Acta* **1991**, *36*, 1543.
[21] R. Fleischmann, H. Böhm, *Electrochim. Acta* **1977**, *22*, 1123.
[22] D. R. McIntyre, G. T. Burstein, A. Vossen, *J. Power Sources* **2002**, *107*, 67.
[23] H. Binder, A. Köhling, W. Kuhn, G. Sandstede, *Angew. Chem.* **1969**, *81*, 748; *Angew. Chem. Int. Ed. Engl.* **1969**, *8*, 757.
[24] V. S. Palanker, R. A. Gajyev, D. V. Sokolsky, *Electrochim. Acta* **1977**, *22*, 133.
[25] C. Ma, W. Zhang, D. Chen, B. Zhou, *Trans. Nonferrous Met. Soc. China* **2002**, *12*, 1015.
[26] The average grain size was 14 nm (determined by X-ray powder analysis), which is considerably smaller than that of commercial WC powders.
[27] F. Scholz, U. Schröder, R. Gulaboski, *Electrochemistry of Immobilized Particles and Droplets*, Springer, Berlin, **2005**.

 © 2006 Wiley-VCH Verlag GmbH & Co. KGaA, Weinheim

Sensors

DOI: 10.1002/anie.200602045

New Methods for Anion Recognition and Signaling Using Nanoscopic Gatelike Scaffoldings**

Rosa Casasús, Elena Aznar, M. Dolores Marcos, Ramón Martínez-Máñez, Félix Sancenón, Juan Soto, and Pedro Amorós*

In the last ten years, interest in the molecular recognition of anions has grown.[1] The prominent roles that anions play in biological and environmental processes prompted researchers to investigate the design and synthesis of a number of receptors based on supramolecular concepts.[2] An emerging subdiscipline of the field of anion chemistry is the development of anion signaling protocols. Most of these systems are designed to observe tuned changes in color or fluorescence or both upon anion coordination.[3] Several approaches have been described in the design of anion chemosensors, but most of them are based on the use of suitable binding sites (or reactive sites) and signaling units (i.e., suitable dyes) that are usually covalently attached.[3] The signaling unit is a chromophore, whereas the binding site is designed to selectively coordinate a certain anion. This approach is widely used, but one that harbors certain limitations. For example, many anion-binding sites suffer competition from the strong hydrogen-bonding ability of water and many demand challenging synthetic routes, especially when the aim is the selective recognition of very similar guests.

In addition to this somewhat classical molecular approach, we are interested in seeking new methods for anion recognition and signaling. Some prominent examples involve the blending supramolecular chemistry with concepts derived from materials science.[4] For example, recently it was shown that cooperative signal amplification could be obtained by using functionalized silica nanoparticles with pre-organized fluorescent moieties at the surface.[5] In a different context, we

[*] R. Casasús, E. Aznar, Dr. M. D. Marcos, Prof. R. Martínez-Máñez, Dr. F. Sancenón, Dr. J. Soto
Instituto de Química Molecular Aplicada
Departamento de Química
Universidad Politécnica de Valencia
Camino de Vera s/n, 46022 València (Spain)
Fax: (+34) 963-879-349
E-mail: rmaez@qim.upv.es
Dr. P. Amorós
Institut de Ciència del Materials, ICMUV
Universitat de València
P.O. Box 2085, 46071 València (Spain)

[**] We thank the Ministerio de Ciencia y Tecnología (project MAT2003-08568-C03 and CTQ2006-15456-C04-01/BQU) for support F.S. also thanks the Ministerio de Educación y Ciencia for a Ramón y Cajal contract.

Supporting information for this article is available on the WWW under http://www.angewandte.org or from the author.

© 2006 Wiley-VCH Verlag GmbH & Co. KGaA, Weinheim

believe that the use of hybrid mesoporous solids with nanoscopic cavities might be a promising approach towards the development of novel tunable sensory systems with enhanced recognition abilities. In fact, although mesoporous solids have received much attention because of their potential use in applications such as catalysis and optical devices, they are less-well studied in the context of molecular recognition based on supramolecular concepts.[6] In particular, we were interested in testing the potential use of molecular gatelike systems in hybrid scaffoldings as a new strategy for the chromofluorogenic signaling of target anions. A molecular gate is a device that modulates mass transport at the nanometric level and whose state (open or closed) can be controlled, for example, by the presence of certain chemical species. Several nanoscopic supramolecular gatelike systems, which are formed by coupling molecular systems and mesoporous materials, were reported.[7] These nanoscopic devices were designed as model systems for delivery purposes and use photochemical or electrochemical switching mechanisms. However, as far as we know, such functional gated nanoscaffolding has never been applied to the potential development of molecular-recognition and signaling methods.

The general idea of using molecular gatelike hybrid ensembles for guest-sensing purposes is outlined in Scheme 1 and involves molecular-recognition events coupled with the

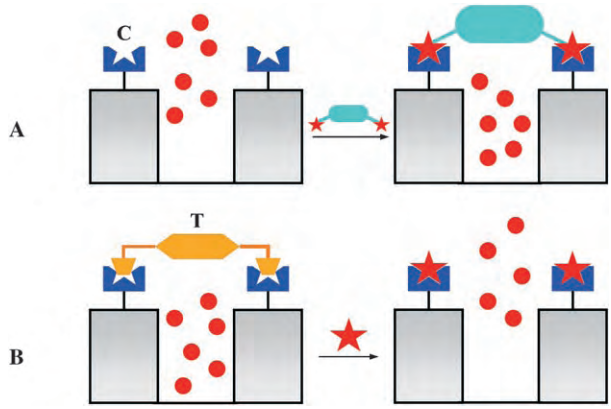

Scheme 1. Anion recognition and signaling by using nanoscopic gatelike scaffoldings through: A) opened-to-closed; B) closed-to-opened anion-induced protocols; see text for full description.

control of dye transport; it entails the use of solids with nanoscopic 3D organized surfaces (e.g., MCM-41-type mesoporous materials) that have been functionalized at the outer surface with certain binding sites (labeled C in Scheme 1). Additionally, the pores have been loaded with a suitable dye (depicted as a red dot in Scheme 1). From this functionalized hybrid system, two basic approaches can be considered: In the first case (Scheme 1 A) there is an open gatelike system that is able to deliver the enclosed dye to the solution. The addition of a target anionic guest capable of forming a suitable complex with the binding site, C, might "close the gate", which would lead to recognition and signaling of the target anion by the inhibition of the mass-delivery process. In the second case, the binding sites are blocked with a large polydentate molecule (T). The interaction of T with C has to be strong enough to avoid liberation of the dye but not be very selective. The addition of a suitable anion able to form strong complexes with C will lead to the displacement of T, the delivery of the dye to the bulk solution, and the signaling of the anion. These two situations (Scheme 1 A and B), based on nanoscopic mass control, are reminiscent of the fluorescence enhancement/quenching or color development/bleaching observed in classical fluorogenic or chromogenic sensors.

In the development of new methods for guest sensing by nanoscopic hybrid supramolecular concepts based on gatelike ensembles and as a proof of the concept, we report herein an example based on Scheme 1 A that involves the use of an MCM-41 mesoporous solid support functionalized on the external surface with polyamines (C in Scheme 1 A) which are suitable receptors for anions. For this purpose the MCM-41 mesoporous solid was prepared from tetraethylorthosilicate (TEOS) as the hydrolytic inorganic precursor and the surfactant hexadecyl trimethylammonium bromide (CTAB) as the porogen species. After removal of the surfactant by calcination, solid MCM-41 (pore diameter 2.5 nm; 1.0 g) was suspended in anhydrous acetonitrile (50 mL) and heated at 110 °C in a Dean–Stark apparatus to remove adsorbed water by azeotropic distillation. The dye tris(2,2′-bipyridyl)ruthenium(II) chloride (0.6 g, 0.8 mmol) was added to the suspension and stirred for 24 h with the aim of loading the pores of the MCM-41 scaffolding to the maximum. Excess 3-[2-(2-aminoethylamino)ethylamino]propyl trimethoxysilane (4.3 mL, 15.0 mmol) was then added and the suspension was stirred for 5.5 h. The final orange solid (S1) was collected by filtration, washed with acetonitrile, and dried at 70 °C for 12 h. After this grafting procedure, the polyamines are preferentially attached to the pore outlets rather than inside the pore walls, which are full of the $[Ru(bipy)_3]^{2+}$ dye.

Figure 1 shows the powder X-ray pattern of solid S1. The expected features of the MCM-41 phase are evident, which

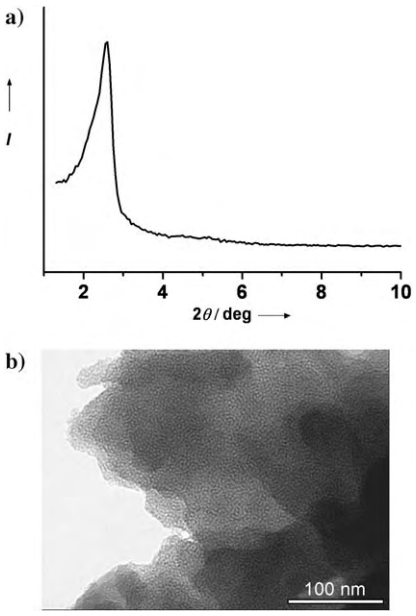

Figure 1. a) X-ray pattern, and b) TEM image of the hybrid solid, S1.

© 2006 Wiley-VCH Verlag GmbH & Co. KGaA, Weinheim

indicates that filling the pores with $[Ru(bipy)_3]^{2+}$ and anchoring the polyamine at the pore outlets do not change the mesoporous structure. Figure 1 also shows a representative TEM image of S1. The final solid contained 7.0 wt% polyamine substituent and the amount of $[Ru(bipy)_3]^{2+}$ in the pores was 10 wt% (both values are derived from elemental analysis and X-ray microanalysis).

The performance of the amine-functionalized dye-containing S1 material as a nanoscopic molecular gatelike system was tested in water. In a typical experiment, solid S1 (10 mg) was suspended in water (25 mL) and the pH value adjusted. The suspension was stirred at 40 °C and the solid isolated by filtration with teflon filters. The delivery of the dye into aqueous solution was easily detected by monitoring the spin-allowed d–π metal-to-ligand charge-transfer (MLCT) transition band of the $[Ru(bipy)_3]^{2+}$ complex centered at 454 nm. A complete description of the dye delivery as a function of pH value in aqueous solution will be described in due course. It is important to state that at acidic pH (acidified with sulfuric acid) the amines are fully protonated, the gate in S1 is closed, and no $[Ru(bipy)_3]^{2+}$ is released. This functional nanoscopic pore blockage is related to the repulsion between protonated polyamines—which are pushed away from each other towards the pore openings—and the cationic $[Ru(bipy)_3]^{2+}$ dye. Furthermore, the interaction of the polyamines with a large number of sulfate counterions at the pore outlet might help to close the path of the dye from the pore voids to the bulk aqueous solution. In contrast, at neutral and slightly basic pH, the attached polyamines are only partially protonated, the effects contributing to pore blockage are much less pronounced, and there is a massive delivery of the $[Ru(bipy)_3]^{2+}$ dye from the pores to the solution.

Solid S1 at neutral pH was used as the starting open-gate system (see Scheme 1), which contains binding sites at the pore openings (amines) and a dye in the pore voids. These partially protonated polyamines in S1 at neutral pH form complexes with anions through hydrogen-bonding interactions and electrostatic attractive forces.[8] Therefore, the ability of solid S1 to deliver the ruthenium(II) dye at neutral pH (pH 7.8, tris(hydroxymethyl)aminomethane (Tris) 10^{-3} mol dm^{-3}) was studied in the presence of the anions fluoride, chloride, bromide, iodide, nitrate, phosphate, sulfate, acetate, and carbonate without noteworthy differences in the delivery process. Even at concentrations up to 0.01 mol dm^{-3} of anions, there was no significant influence in the dye-delivery process and in all cases, virtually identical dye-release kinetics were found. This fact could be ascribed to the relatively poor coordination of the anions tested with the polyamines in the pore openings. Pore blockage was also not observed with larger anions, such as guanosine monophosphate (GMP; see Figure 2).

In contrast, upon adding S1 to neutral aqueous solutions of adenosine triphosphate (ATP) and adenosine diphosphate (ADP; concentration of anions: 1×10^{-4} mol dm^{-3}), the solutions remained essentially colorless, which indicates that the pores of the solid were blocked (Figure 2). A schematic representation is shown in Scheme 2. This selective response—the inhibition of the release of the $[Ru(bipy)_3]^{2+}$ complex—in the presence of these two nucleotides clearly

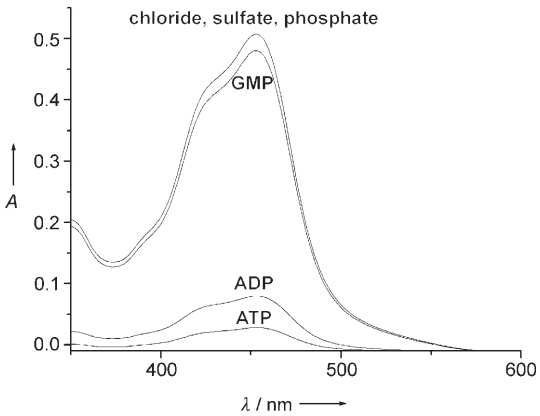

Figure 2. Absorbance of solutions containing solid S1 (10 mg) and different anions in water at pH 7.8 (Tris 10^{-3} mol dm^{-3}). The band centered at 454 nm is due to the delivery of the $[Ru(bipy)_3]^{2+}$ dye from the pores to the aqueous solution. The anions were tested at a concentration of 10^{-4} mol dm^{-3}.

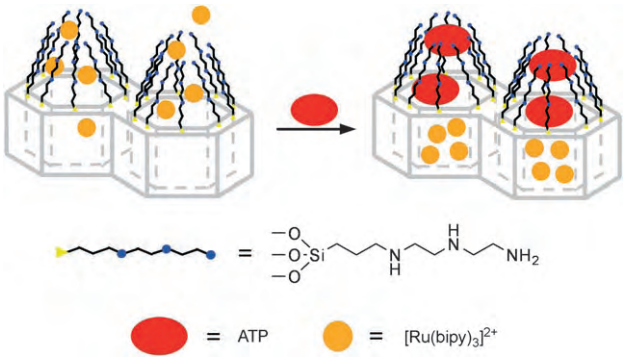

Scheme 2. ATP recognition and signaling by inhibiting dye release with nanoscopic supramolecular gatelike systems on mesoporous MCM-41 supports.

indicates the relevance of this gated solid system in the context of molecular recognition and sensing.

The chromogenic response of S1 is related to the ability of the protonated polyamines to strongly coordinate nucleotides.[9] The extent of this coordination is good enough at neutral pH to block the pores and the strength of the interaction is enhanced by the preorganization effect that arises from grafting the polyamine moieties onto the inorganic supports. As can be seen in Figure 2, this blockage is not dependent on size, as the GMP anion has a similar volume to that of ADP and yet is not able to close the gate of S1. In fact, pore blockage is observed for anions that form strong complexes with polyamines (ATP > ADP > GMP). This colorimetric recognition of ATP and ADP with respect to GMP, based on the switching of a supramolecular functionality (mass transport control), is not unusual and would have been hard to achieve using classical chemosensors.[10]

Coordination in relation to dye transport in mesoporous hybrid solids has been used as a signaling method for anions. This approach has not been used previously and displays potential that cannot be considered for classical receptors. For example, the modulation of the pore size, the nature of the

 © 2006 Wiley-VCH Verlag GmbH & Co. KGaA, Weinheim

appended molecular gate by using some other anion binding sites, and the properties of the loaded signaling dye can be easily modified.

In summary, we have shown herein—for the first time and as a proof of the concept—how nanoscopic molecular gatelike systems (i.e., functionalized mesoporous materials that contain polyamines) can be used for the design and development of new anion-recognition and signaling systems. These findings, along with others recently reported,[11] offer new perspectives in the use of 3D functionalized solid hosts for innovative advanced functional "hetero-supramolecular" methods.

Received: May 23, 2006
Published online: September 20, 2006

Keywords: host–guest systems · mesoporous materials · molecular devices · molecular recognition · sensors

[1] *Supramolecular Chemistry of Anions* (Eds.: E. Bianchi, K. Bowman-James, E. García-España), Wiley-VCH, New-York, **1997**.

[2] P. D. Beer, P. A. Gale, *Angew. Chem.* **2001**, *113*, 502 – 532; *Angew. Chem. Int. Ed.* **2001**, *40*, 486 – 516; ; F. P. Schmidtchen, M. Berger, *Chem. Rev.* **1997**, *97*, 1609 – 1646; C. R. Bondy, S. J. Loeb, *Coord. Chem. Rev.* **2003**, *240*, 77 – 99; J. L. Sessler, S. Camiolo, P. A. Gale, *Coord. Chem. Rev.* **2003**, *240*, 17 – 55.

[3] R. Martínez-Máñez, F. Sancenón, *Chem. Rev.* **2003**, *103*, 4419 – 4476; R. Martínez-Máñez, F. Sancenón, *J. Fluoresc.* **2005**, *15*, 267 – 285.

[4] G. Cooke, *Angew. Chem.* **2003**, *115*, 5008 – 5018; *Angew. Chem. Int. Ed.* **2003**, *42*, 4860 – 4870; ; Y. Umezawa, H. Aoki, *Anal. Chem.* **2004**, *76*, 321A – 326A; E. Katz, I. Willner, *Angew. Chem.* **2004**, *116*, 6166 – 6235; *Angew. Chem. Int. Ed.* **2004**, *43*, 6042 – 6108.

[5] M. Montalti, L. Prodi, N. Zacheronni, G. Falini, *J. Am. Chem. Soc.* **2002**, *124*, 13540 – 13546; M. Montalti, L. Prodi, N. Zaccheroni, *J. Mater. Chem.* **2005**, *15*, 2810 – 2814; E. Brasola, F. Mancin, E. Rampazzo, P. Tecilla, U. Tonellato, *Chem. Commun.* **2003**, 3026 – 3027; E. Rampazzo, E. Brasola, S. Marcuz, F. Mancin, P. Tecilla, U. Tonellato, *J. Mater. Chem.* **2005**, *15*, 2687 – 2696; L. Basabe-Desmonts, J. Beld, R. S. Zimmerman, J. Hernando, P. Mela, M. F. García Parajó, N. F. van Hulst, A. van den Berg, D. N. Reinhoudt, M. Crego-Calama, *J. Am. Chem. Soc.* **2004**, *126*, 7293 – 7299; M. Crego-Calama, D. N. Reinhoudt, *Adv. Mater.* **2001**, *13*, 1171 – 1174.

[6] V. S.-Y. Lin, C.-Y. Lai, J. Huang, S.-A Song, S. Xu, *J. Am. Chem. Soc.* **2001**, *123*, 11510 – 11511; D. R. Radu, C.-Y. Lai, J. W. Wiench, M. Pruski, V. S.-Y. Lin, *J. Am. Chem. Soc.* **2004**, *126*, 1640 – 1641; A. B. Descalzo, K. Rurack, H. Weisshoff, R. Martínez-Máñez, M. D. Marcos, P. Amorós, K. Hoffmann, J. Soto, *J. Am. Chem. Soc.* **2005**, *127*, 184 – 200; M. Comes, M. D. Marcos, R. Martínez-Máñez, F. Sancenón, J. Soto, L. A. Villaescusa, P. Amorós, D. Beltrán, *Adv. Mater.* **2004**, *16*, 1783 – 1786; K. Inumaru, Y. Inoue, S. Kakii, T. Nakano, S. Yamanaka, *Chem. Lett.* **2003**, *32*, 1110 – 1111; K. Inumaru, Y. Inoue, S. Kakii, T. Nakano, S. Yamanaka, *Phys. Chem. Chem. Phys.* **2004**, *6*, 3133 – 3139; M. Comes, G. Rodríguez-López, M. D. Marcos, R. Martínez-Máñez, F. Sancenón, J. Soto, L. A. Villaescusa, P. Amorós, D. Beltrán, *Angew. Chem.* **2005**, *117*, 2978 – 2982; *Angew. Chem. Int. Ed.* **2005**, *44*, 2918 – 2922; A. B. Descalzo, D. Jiménez, M. D. Marcos, R. Martínez-Máñez, J. Soto, J. El Haskouri, C. Guillem, D. Beltrán, P. Amorós, M. V. Borrachero, *Adv. Mater.* **2002**, *14*, 966 – 969; A. B. Descalzo, M. D. Marcos, R. Martínez-Máñez, J. Soto, D. Beltrán, P. Amorós, *J. Mater. Chem.* **2005**, *15*, 2721 – 2731.

[7] R. Casasús, M. D. Marcos, R. Martínez-Máñez, J. V. Ros-Lis, J. Soto, L. A. Villaescusa, P. Amorós, D. Beltrán, C. Guillem, J. Latorre, *J. Am. Chem. Soc.* **2004**, *126*, 8612 – 8613; N. K. Mal, M. Fujiwara, Y. Tanaka, *Nature* **2003**, *421*, 350 – 353; N. K. Mal, M. Fujiwara, Y. Tanaka, T. Taguchi, M. Matsukata, *Chem. Mater.* **2003**, *15*, 3385 – 3394; Q. Yang, S. Wang, P. Fan, L. Wang, Y. Di, K. Lin, F.-S. Xiao, *Chem. Mater.* **2005**, *17*, 5999 – 6003; R. Hernandez, H.-R. Tseng, J. W. Wong, J. F. Stoddart, J. I. Zink, *J. Am. Chem. Soc.* **2004**, *126*, 3370 – 3371; T. D. Nguyen, H. R. Tseng, P. C. Celestre, A. H. Flood, Y. Liu, J. F. Stoddart, J. I. Zink, *Proc. Natl. Acad. Sci. USA* **2005**, *102*, 10029 – 10034; C.-Y. Lai, B. G. Trewyn, D. M. Jeftinija, K. Jeftinija, S. Xu, S. Jeftinija, V. S.-Y. Lin, *J. Am. Chem. Soc.* **2003**, *125*, 4451 – 4459; J. A. Gruenhagen, C. Y. Lai, D. R. Radu, V. S.-Y. Lin, E. S. Yeung, *Appl. Spectrosc.* **2005**, *59*, 424 – 431; S. Giri, B. G. Trewyn, M. P. Stellmaker, V. S.-Y. Lin, *Angew. Chem.* **2005**, *117*, 5166 – 5172; *Angew. Chem. Int. Ed.* **2005**, *44*, 5038 – 5044.

[8] F. Sancenón, A. Benito, J. M. Lloris, R. Martínez-Máñez, T. Pardo, J. Soto, *Helv. Chim. Acta* **2002**, *85*, 1505 – 1516; M. M. G. Antonisse, D. N. Reinhoudt, *Chem. Commun.* **1998**, 443 – 444; M. E. Huston, E. U. Akkaya, A. W. Czarnik, *J. Am. Chem. Soc.* **1989**, *111*, 8735 – 8737; S. Y. Hong, A. W. Czarnik, *J. Am. Chem. Soc.* **1993**, *115*, 3330 – 3331; D. H. Vance, A. W. Czarnik, *J. Am. Chem. Soc.* **1994**, *116*, 9397 – 9398.

[9] M. W. Hosseini, A. J. Blacker, J.-M. Lehn, *J. Chem. Soc. Chem. Commun.* **1988**, 596 – 597; H. Fenniri, M. W. Hosseini, J.-M. Lehn, *Helv. Chim. Acta* **1997**, *80*, 786 – 803; M. T. Albelda, M. A. Bernardo, E. García-España, M. L. Godino-Salido, S. V. Luis, M. J. Melo, F. Pina, C. Soriano, *J. Chem. Soc. Perkin Trans. 2* **1999**, 2545 – 2549; M. T. Albelda, J. Aguilar, S. Alves, R. Aucejo, P. Díaz, C. Lodeiro, J. C. Lima, E. García-España, F. Pina, C. Soriano, *Helv. Chim. Acta* **2003**, *86*, 3118 – 3134.

[10] Selective chemosensors for chromogenic ATP sensing: F. Sancenón, A. B. Descalzo, R. Martínez-Máñez, M. A. Miranda, J. Soto, *Angew. Chem.* **2001**, *113*, 2710 – 2713; *Angew. Chem. Int. Ed.* **2001**, *40*, 2640 – 2643; S. C. McCleskey, M. J. Griffin, S. E. Schneider, J. T. McDevitt, E. V. Anslyn, *J. Am. Chem. Soc.* **2003**, *125*, 1114 – 1115; C. Yin, F. Gao, F. Huo, P. Yang, *Chem. Commun.* **2004**, 934 – 935; C. Li, M. Numata, M. Takeuchi, S. Shinkai, *Angew. Chem.* **2005**, *117*, 6529 – 6532; *Angew. Chem. Int. Ed.* **2005**, *44*, 6371 – 6374.

[11] A. B. Descalzo, R. Martínez-Máñez, F. Sancenón, K. Hoffmann, K. Rurack, *Angew. Chem.* **2006**, *118*, 6068 – 6093; *Angew. Chem. Int. Ed.* **2006**, *45*, 5924 – 5948.

 © 2006 Wiley-VCH Verlag GmbH & Co. KGaA, Weinheim

Supramolecular Chemistry

DOI: 10.1002/anie.200602173

Suitanes**

Avril R. Williams, Brian H. Northrop, Theresa Chang, J. Fraser Stoddart, Andrew J. P. White, and David J. Williams**

The making of mechanically interlocked molecular compounds[1] has evolved from a statistical beginning[2] to the use of molecular-recognition-driven, self-assembly protocols[3] that rely upon the operation of covalent,[4] metal,[5] or noncovalent[6] templates,[7] prior to the formation of the mechanical bond(s) by either kinetically or thermodynamically controlled processes, involving either dative[8] or covalent[9] bond formation. Previously, we have speculated[10] about the existence of another class of interlocked molecule beyond the archetypal catenanes[11] and rotaxanes,[12] which are not all that dissimilar from carceplexes[13] and yet are distinguishable from them.[14] In searching for some simple term for this class of mechanically interlocked molecule (Figure 1), which consists of two separate components—a body with two or more limbs that are rigid and protrude outwards, the torso of which carries a close-fitting, all-in-one suit, such that it encompasses the torso of the body—we have come up with the term suitane, in which a number is inserted between "suit" and "ane" to indicate the number of protruding limbs. Thus, the simplest member of the series would be suit[2]ane, a linear structure in which the suit surrounds the body with limbs protruding outwards in opposite directions (180°; Figure 1 a), such that there is no easy way by which the suit can be removed from the body. Likewise, suit[3]ane (Figure 1 b) and suit[4]ane (Figure 1 c) will consist of bodies with three and four limbs, respectively, that are trigonal (120°) and square (90°) planar and ready to be fitted out with the appropriate suit containing three and four holes, respectively.

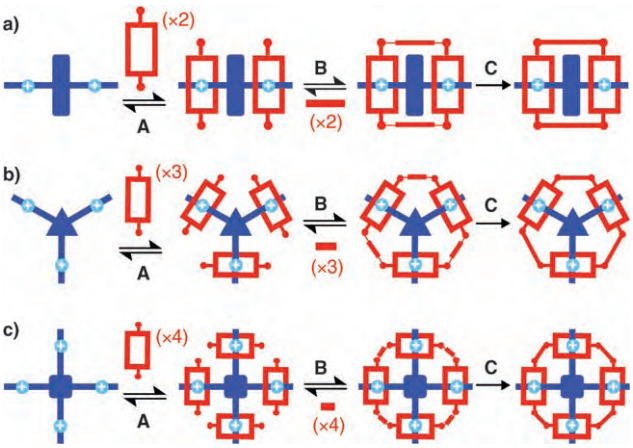

Figure 1. Schematic representations of the approach that is being pursued in the construction of a new class of mechanically interlocked molecular compounds known as suitanes. The construction of a) suit[2]ane, b) suit[3]ane, and c) suit[4]ane. The "+" signs on the protruding limbs of the templates (blue) represent the -NH_2^+- centers on the linear, triangular, and square templates. The (red) rectangles introduced in each case in step A are crown ethers with [24]crown-8 constitutions. In step A, noncovalent bonding leads to complex formation, in which the rectangles are positioned to be covalently linked under thermodynamic control in step B before being kinetically fixed in step C.

A doll dressed up in an all-in-one suit, or a "onesie", provides an analogy with a suit[5]ane (Figure 2).

Let us consider the specific example (Scheme 1) of a linear body template[15] **LBT**-H_2^{2+} carrying two -CH_2-$NH_2^+CH_2$- recognition sites separated from each other by a bulky midriff[16] such that the double linking up of two matching [24]crown-8 rings in the shape of $(CHO)_2$-**DP24C8** units[17] can be achieved reversibly by forming four imine bonds with a diaminobenzene spacer, such as *p*-phenylenediamine (**PPD**). The virtue of employing reversible imine bond formation[18] to clothe the **LBT**-H_2^{2+} dication with two $(CHO)_2$-**DP24C8** units and two **PPD** spacers is that errors can be corrected[19] before the final structure is fixed by

Figure 2. A doll dressed in an all-in-one suit constitutes an example of a suit[5]ane.

[*] Dr. A. R. Williams, B. H. Northrop, Dr. T. Chang, Prof. J. F. Stoddart
California NanoSystems Institute and
Department of Chemistry and Biochemistry
University of California, Los Angeles
405 Hilgard Avenue, Los Angeles, CA 90095-1569 (USA)
Fax: (+1) 310-206-5621
E-mail: stoddart@chem.ucla.edu
Dr. A. J. P. White, Prof. D. J. Williams
Department of Chemistry
Imperial College
South Kensington, London SW7 2AY (UK)
Fax: (+44) 20-7594-5835
E-mail: djw@imperial.ac.uk

[**] This work was supported by the National Science Foundation (CHE-9974928 and CHE-0092036). B.H.N. thanks the ACS Division of Organic Chemistry for a graduate fellowship, sponsored by the Nelson J. Leonard ACS DOC Fellowship, sponsored by Organic Synthesis, Inc.

Supporting information for this article is available on the WWW under http://www.angewandte.org or from the author.

© 2006 Wiley-VCH Verlag GmbH & Co. KGaA, Weinheim

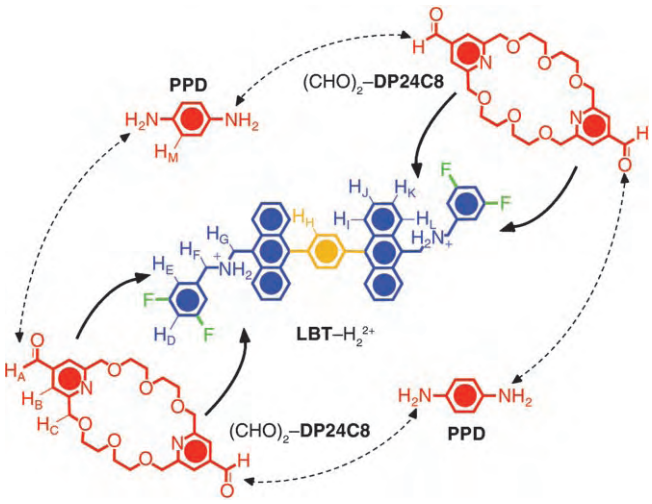

Scheme 1. Synthetic protocol for the construction of suit[2]ane from 1.0 equivalent of **LBT**-H_2^{2+} and 2.0 equivalents each of $(CHO)_2$-**DP24C8** and **PPD**.

reducing the imine functions to amino groups. Herein, we report the efficient self-assembly of a suit[2]ane from five components by using a dynamic covalent synthetic protocol[20] on the back of experimental and computational investigations of the 1:2 complex formed between the **LBT**-H_2^{2+} dication and two equivalents of $(CHO)_2$-**DP24C8** in solution and in the solid state. The tetraimine, which is formed when two equivalents of **PPD** are added to a 2:1 mixture of $(CHO)_2$-**DP24C8** and **LBT**-$H_2{\cdot}2\,PF_6$, is a remarkably stable compound in its own right in solution, from whence it crystallizes. We describe the X-ray crystal (super)structure analysis of both the 1:2 complex and the suit[2]ane.

As a model for the dynamic assembly of a suit[2]ane, the self-assembly of **LBT**-H_2^{2+} and **DP24C8** has been investigated in solution, in the solid state, and by computational methods. When stoichiometric quantities of **DP24C8** were added to **LBT**-$H_2{\cdot}2\,PF_6$ in CD_3NO_2 both the 1:1 and 2:1 (macrocycle/thread) complexes were observed by ^1H NMR spectroscopic analysis. Single crystals, suitable for X-ray analysis, of the [3]pseudorotaxane formed between **LBT**-H_2^{2+} and 2.0 equivalents of **DP24C8** were grown by vapor diffusion of iPr_2O into MeCN. Its solid-state superstructure[21] reveals (Figure 3) the anticipated threading of the dicationic spindle through the centers of the two **DP24C8** rings. Complex stabilization is achieved by pairs of N^+—H···N and N^+—H···O hydrogen bonds, as illustrated in Figure 3a. The 2:1 complex has crystallographic inversion symmetry, and the planes of the terminal 3,5-difluorobenzyl and central phenylene rings are oriented essentially orthogonally to the pair of anthracene ring systems aligned in parallel. The separations of the ring centroids of the two 3,5-difluorobenzyl groups are 22.8 Å, and the distance between the two NH_2^+ centers is 16.0 Å. With a view to constructing the desired macropolycycle in which two **DP24C8** rings are doubly linked through the 4-positions of their pyridyl rings, thus entrapping the central dication, the separations of these 4-positions are important in the context of identifying suitable linking spacer groups. In this 2:1 complex, these distances are approximately 14.5 Å[22].

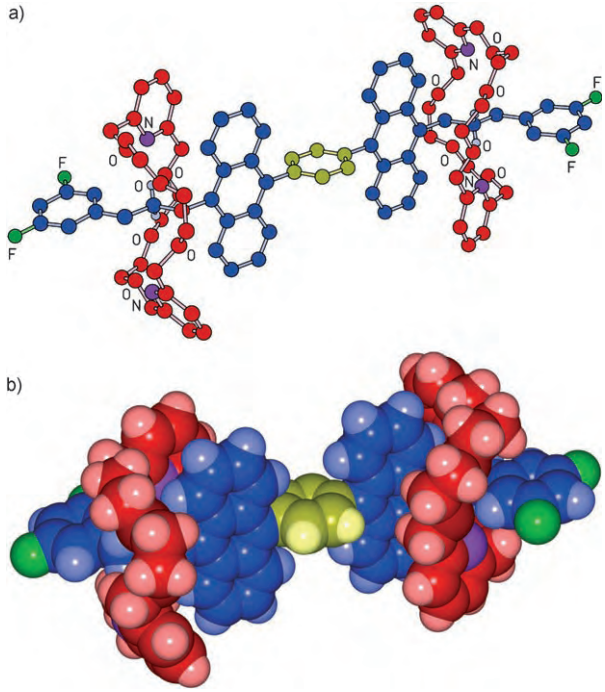

Figure 3. a) Ball-and-stick representation of the solid-state superstructure of the 2:1 complex. The N^+—H···N hydrogen bonds have N^+···N and H···N distances of 2.97 and 2.07 Å, respectively, and N^+—H···N angles of 179°. The N^+—H···O hydrogen bonds have N^+···O and H···O distances of 3.05 and 2.16 Å, respectively, and N^+—H···O angles of 168°. b) Space-filling representation of the same superstructure.

Computational force-field modeling[23] predicts the most stable co-conformation of the [3]pseudorotaxane (Figure 4a) in solution to be that in which the macrocycle pyridine rings are involved in π–π stacking interactions with both of the **LBT**-H_2^{2+} anthracene moieties in a manner similar to molecular clips[24] or molecular tweezers.[25] In the structure obtained from modeling, the separation between the 4-positions of the **DP24C8** rings is 8.8 Å, a full 5.7 Å closer than in the solid-state superstructure. Such proximity is ideally suited to form a suit[2]ane upon functionalizing the 4-positions of each pyridine ring with formyl groups and adding two equivalents of **PPD**. The lowest energy co-conformer obtained from modeling of the fully assembled suit[2]ane (Figure 4b) bears an almost uncanny structural resemblance to the modeled [3]pseudorotaxane. In the case of the fully assembled suit[2]ane, the 4-positions of the **DP24C8** rings are separated by 10.1 Å, only 1.3 Å further apart than in the modeled 2:1 precursor complex. This observation is a strong indication that the noncovalent interactions responsible for the self-assembly of the **LBT**-$H_2{\cdot}2\,PF_6$ and the **DP24C8** macrocycles will be preserved in the dynamically assembled suit[2]ane. It may also be anticipated that the *p*-phenylene ring of **PPD** can impart greater stability to the interlocked suit[2]ane through π–π stacking interactions with the central *p*-phenylene unit of **LBT**-H_2^{2+}. By comparing the lowest energy structures obtained for **DP24C8**, **LBT**-H_2^{2+}, the [3]pseudorotaxane, the suit[2]ane, and the tetraimine host of suit[2]ane, a semiquantitative evaluation of the binding energies between the host/guest pairs in both the [3]pseudo-

 © 2006 Wiley-VCH Verlag GmbH & Co. KGaA, Weinheim

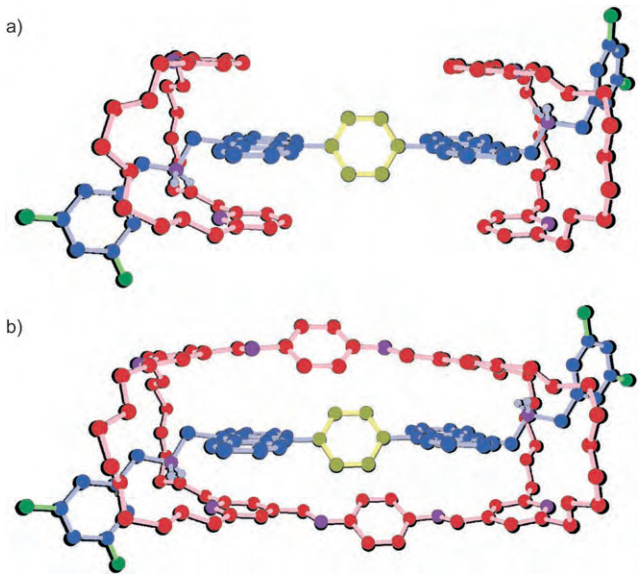

Figure 4. a) Profile representation of the lowest energy co-conformation of the model 2:1 complex obtained from computational modeling. The solution-phase modeling predicts that π–π stacking interactions between the **DP24C8** and anthracene moieties may, upon functionalization of the **DP24C8** rings with formyl groups, facilitate the formation of the fully assembled suit[2]ane on the addition of **PPD**. b) The lowest energy co-conformation of the fully assembled suit[2]ane obtained from modeling bears a striking resemblance to the modeled 2:1 complex.

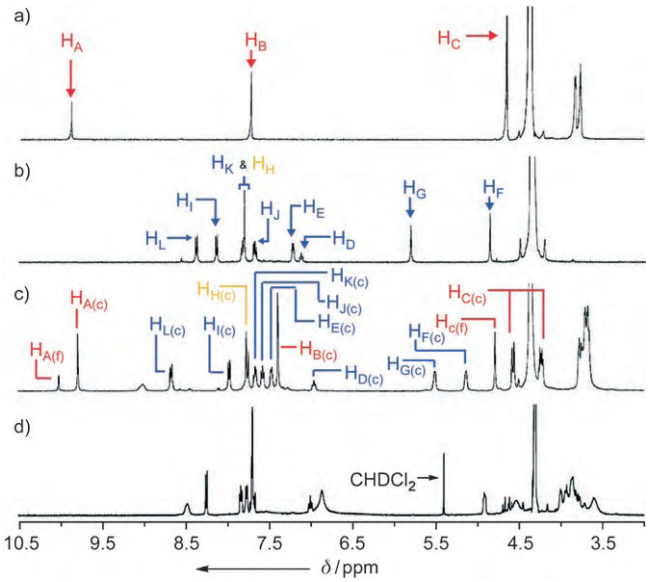

Figure 5. Partial ^{1}H NMR spectra recorded at 500 MHz in CD_3NO_2 showing a) free $(CHO)_2$-**DP24C8**, b) free **LBT**-H_2·2 PF_6, c) [3]pseudorotaxane, and d) suit[2]ane after equilibration. For the proton (H) assignments, see Scheme 1.

rotaxane and the suit[2]ane can be made.[26] Such a comparison leads to the conclusion that the binding of **LBT**-H_2^{2+} by the tetraimine host is 1.1 kcal mol^{-1} more favorable than binding of **LBT**-H_2^{2+} by two equivalents of **DP24C8**. Such a small energy difference is, however, well within the error of these force-field calculations, and the two binding energies of the two compounds should, therefore, be taken to be roughly identical. These modeling results indicate, at the very least, that formation of the suit[2]ane and concomitant co-conformational change in the [3]pseudorotaxane host/guest complex do not disrupt, and perhaps even enhance, the binding of **LBT**-H_2^{2+}.

With these encouraging predictions to hand, the dipyrido[24]crown-8 derivative $(CHO)_2$-**DP24C8** was prepared and added to a solution of **LBT**-H_2^{2+} in CD_3NO_2 in a 2:1 ratio. Nearly quantitative formation of the corresponding [3]pseudorotaxane is observed (Figure 5) by ^{1}H NMR spectroscopy within 5 minutes of mixing. The effects and efficiency of complexation is reflected in shifts of the signals corresponding to protons on both the $(CHO)_2$-**DP24C8** macrocycles as well as on the **LBT**-H_2·2 PF_6 once the latter finds itself threaded through two equivalents of the former. For example, methylene protons H_F and H_G, which are adjacent to the $-CH_2NH_2^+CH_2-$ centers of **LBT**-H_2^{2+}, appear as singlets at $\delta = 4.8$ and 5.8 ppm, respectively, in the free template (Figure 5b). Upon complexation, H_F and H_G appear (Figure 5c) as multiplets and shift to $\delta = 5.1$ and 5.5 ppm, respectively, as they are involved in hydrogen-bonding interactions with the $(CHO)_2$-**DP24C8** macrocycles. The signal for the benzylic methylene protons of $(CHO)_2$-**DP24C8** shifts from being a singlet centered at $\delta = 4.7$ ppm when uncomplexed to two doublets ($\delta = 4.6$ and 4.2 ppm) as a result of their diastereotopic relationship when complexed. Furthermore, the anthracene protons H_I, which point "inward" toward the central *p*-phenylene unit of **LBT**-H_2^{2+}, undergo a downfield shift of $\Delta\delta = 0.4$ ppm upon complexation ($\delta = 8.4$–8.0 ppm). This observation suggests that π–π stacking occurs between the $(CHO)_2$-**DP24C8** pyridine rings and the anthracene units of **LBT**-H_2^{2+}, similar to that predicted by computational modeling (Figure 4a).

The addition of 2 equivalents of **PPD** to the [3]pseudorotaxane formed from a solution of **LBT**-H_2·2 PF_6 and $(CHO)_2$-**DP24C8** (1:2) in CD_3NO_2 results, initially, in a mixture of kinetic products. The ^{1}H NMR spectrum recorded after 29 days (Figure 5d) of equilibration corresponds to the formation of one dominant, highly symmetric, thermodynamic product in solution. No significant spectroscopic changes were observed after 29 days. The disappearance of the aldehyde peak at $\delta = 9.8$ ppm and appearance of a sharp imine peak at $\delta = 8.2$ ppm, which integrates to give four protons, strongly indicate the formation of the suit[2]ane. X-ray-quality single crystals were grown by vapor diffusion of *i*Pr_2O into Me_2CO, and the solid-state structure,[21,27] corresponding to suit[2]ane, was obtained (Figure 6a,b). The similarity between the suit[2]ane structure as predicted by computational modeling (Figure 4b) and that obtained from X-ray crystallographic analysis is quite remarkable. The solid-state structure of the suit[2]ane reveals the desired encapsulation of the central aromatic core, containing the two anthracene rings and their linking phenylene unit, within the macropolycycle. In addition to the mechanical interlocking of the two components, secondary stabilization is achieved by a combination of $N^+-H\cdots N$, $N^+-H\cdots O$, $C-H\cdots O$, and $C-H\cdots\pi$ interactions, as illustrated in Figure 6a. The overall

 © 2006 Wiley-VCH Verlag GmbH & Co. KGaA, Weinheim

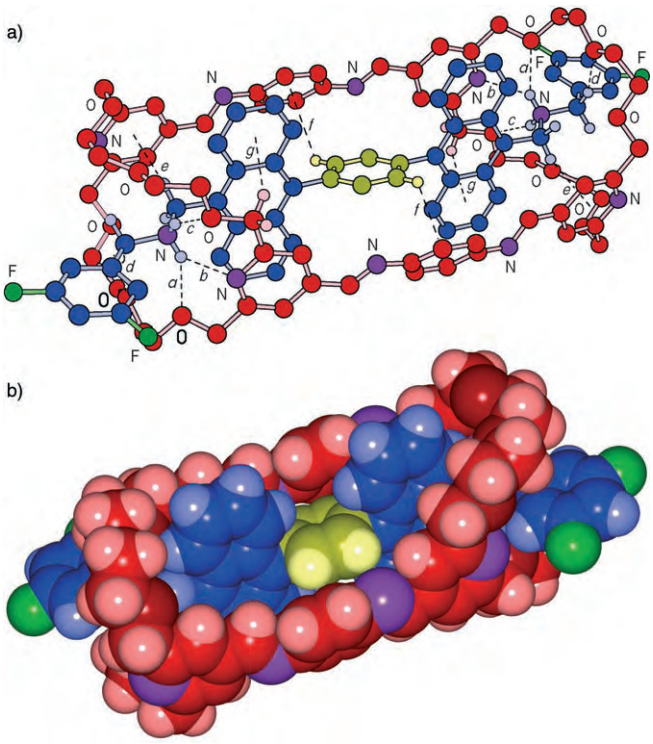

Figure 6. a) Ball-and-stick representation of the solid-state structure of a suit[2]ane. The X^+—H···X and H···X hydrogen bonds labeled *a*–*d* have X^+···N, H···X distances [Å] and X^+—H···X angles [°], respectively, of 2.94, 2.13, 150 (*a*); 2.95, 2.28, 130 (*b*); 2.86, 2.03, 154 (*c*); and 3.27, 2.35, 160 (*d*). The C—H···π interactions labeled as *e*–*g* have H···π [Å] distances and C-H···π angles [°], respectively, of 2.70, 132 (*e*); 2.91, 120 (*f*); and 2.97, 145 (*g*). b) Space-filling representation of the solid-state structure of the suit[2]ane.

dimensions of the dication are changed little from those observed in the 2:1 complex with a centroid–centroid separation of the two terminal 3,5-difluorobenzyl ring systems of 23.2 Å and of the nitrogen centers of 16.2 Å. This linking of the 4-positions of the **DP24C8** rings by **PPD** spacers causes decreases of approximately 4.0 Å in the separations of the two pairs of **DP24C8** rings relative to those observed in the 2:1 complex. The parallel-aligned **PPD** ring systems have an interplanar separation of approximately 8.2 Å.

The successful template-directed synthesis of this suit-[2]ane echoes the painstaking efforts that went into designing its constituent parts with crucial input from computational chemistry. On reflection, **LBT**-H_2^{2+} is a fairly rigid template which becomes trapped as the "guest" inside a relatively flexible "host" built up of a couple of difunctionalized crown ethers $(CHO)_2$-**DP24C8** that can embrace the -CH_2-$NH_2^+CH_2$- recognition sites at both ends of the **LBT**-H_2^{2+} dication. In the final analysis, it is the choice—herein it is **PPD**—of the linker that matters: it must not be too short nor too long so that it dictates a successful outcome for this first stab (Figure 1a) at making suit[2]anes, which employs dynamic covalent and noncovalent chemistries.

Before we can claim that the compound we call suit[2]ane is a molecule, we have to gather evidence that it is truly a mechanically interlocked molecular compound. Although minor changes were observed in the relative intensities of some of the signals in the ^{1}H NMR spectrum when a sample of the compound was heated at 70 °C in CD_3CN for 30 days, the chemical shifts δ remained essentially unchanged. Moreover, there was no evidence, after the 30 days of heating, for the presence of free **LBT**-H_2^{2+} dications, or indeed of the free tetraimine host. These observations demonstrate the integrity and stability of this class of mechanically interlocked molecular compounds.[28]

Our success in the template-directed synthesis of suit-[2]ane holds out hope for being able to self-assemble suit[3]anes (Figure 1b) and suit[4]anes (Figure 1c) around trigonal and square planar templates, respectively. When this "two-dimensional" goal is realized then there is no reason why entering the third dimension with tetrahedral and octahedral scaffolds should not be contemplated. Supramolecular assistance to covalent synthesis, in which the template is consumed stoichiometrically, can be regarded as a forerunner to template-directed reactions[29] in which the template keeps expressing or even copying itself.

Received: June 1, 2006
Published online: September 19, 2006

Keywords: dynamic covalent chemistry · interlocked molecules · mechanical bonds · supramolecular chemistry · template-directed synthesis

[1] a) D. B. Amabilino, J. F. Stoddart, *Chem. Rev.* **1995**, *95*, 2725–2828; b) *Molecular Catenanes, Rotaxanes, and Knots* (Eds.: J.-P. Sauvage, C. Deitrich-Buchecker), Wiley-VCH, Weinheim, **1999**.
[2] a) E. Wasserman, *J. Am. Chem. Soc.* **1960**, *82*, 4433–4434; b) H. L. Frisch, E. Wasserman, *J. Am. Chem. Soc.* **1961**, *83*, 3789–3795.
[3] S. A. Vignon, J. F. Stoddart, *Collect. Czech. Chem. Commun.* **2005**, *70*, 1493–1576.
[4] G. Schill, *Catenanes, Rotaxanes, and Knots*, Academic Press, New York, **1971**.
[5] V. Aucagne, K. D. Hanni, D. A. Leigh, P. J. Lusby, D. B. Walker, *J. Am. Chem. Soc.* **2006**, *128*, 2186–2187.
[6] M. C. T. Fyfe, J. F. Stoddart, *Acc. Chem. Res.* **1997**, *30*, 393–401.
[7] a) D. H. Busch, N. A. Stephenson, *Coord. Chem. Rev.* **1990**, *100*, 119–154; b) S. Anderson, H. L. Anderson, J. K. M. Sanders, *Acc. Chem. Res.* **1993**, *26*, 469–475; c) *Templated Organic Synthesis* (Eds.: F. Diederich, P. J. Stang), Wiley-VCH, Weinheim, **1999**; d) J. F. Stoddart, H.-R. Tseng, *Proc. Natl. Acad. Sci. USA* **2002**, *99*, 4797–4800; e) F. Aricó, J. D. Badjić, S. J. Cantrill, A. H. Flood, K. C.-F. Leung, Y. Liu, J. F. Stoddart, *Top. Curr. Chem.* **2005**, *249*, 203–259.
[8] D. H. Busch, *Top. Curr. Chem.* **2005**, *249*, 1–65.
[9] a) A. G. Kolchinski, N. W. Alcock, R. A. Roesner, D. H. Busch, *Chem. Commun.* **1998**, 1437–1438; b) T. J. Kidd, D. A. Leigh, A. J. Wilson, *J. Am. Chem. Soc.* **1999**, *121*, 1599–1600; c) A. F. M. Kilbinger, S. J. Cantrill, A. W. Waltman, D. W. Day, R. H. Grubbs, *Angew. Chem.* **2003**, *115*, 3403–3407; *Angew. Chem. Int. Ed.* **2003**, *42*, 3281–3285; d) E. Guidry, S. J. Cantrill, J. F. Stoddart, R. H. Grubbs, *Org. Lett.* **2005**, *7*, 2129–2132; e) F. Aricó, T. Chang, S. J. Cantrill, S. I. Khan, J. F. Stoddart, *Chem. Eur. J.* **2005**, *11*, 4655–4666; f) K. C.-F. Leung, F. Aricó, S. J. Cantrill, J. F. Stoddart, *J. Am. Chem. Soc.* **2005**, *127*, 5808–5810.

 © 2006 Wiley-VCH Verlag GmbH & Co. KGaA, Weinheim

[10] T. Chang, A. M. Heiss, S. J. Cantrill, M. C. T. Fyfe, A. R. Pease, S. J. Rowan, J. F. Stoddart, D. J. Williams, *Org. Lett.* **2000**, *2*, 2943 – 2946.

[11] A catenane comprises two or more interlocked rings: a) C. A. Hunter, *J. Am. Chem. Soc.* **1992**, *114*, 5303 – 5311; b) W.-Q. Deng, A. H. Flood, J. F. Stoddart, W. A. Goddard III, *J. Am. Chem. Soc.* **2005**, *127*, 15994 – 15995.

[12] A rotaxane is a molecule that comprises a dumbbell-shaped component on which one or more rings are located because of the bulkiness of the stoppers of the dumbbell: a) P.-L. Anelli, N. Spencer, J. F. Stoddart, *J. Am. Chem. Soc.* **1991**, *113*, 5131 – 5133; b) J. W. Choi, A. H. Flood, D. W. Steuerman, S. Nygaard, A. B. Braunschweig, N. N. P. Moonen, B. W. Laursen, Y. Luo, E. DeIonno, A. J. Peters, J. O. Jeppesen, K. Xe, J. F. Stoddart, J. R. Heath, *Chem. Eur. J.* **2006**, *12*, 261 – 279; c) D. S. Marlin, D. González Cabrera, D. A. Leigh, A. M. Z. Slawin, *Angew. Chem.* **2006**, *118*, 83 – 89; *Angew. Chem. Int. Ed.* **2006**, *45*, 77 – 83.

[13] "Carceplexes are comprised of host and guest components that cannot separate from one another without the breaking of covalent bonds. Their existence does not depend upon host–guest interactions nor on other than gross size complementarity. Rather their existence depends upon physical envelopment of guests during shell closures leading to carceplexes." This quote is taken from D. J. Cram, J. M. Cram in *Container Molecules and Their Guests* (Ed.: J. F. Stoddart), The Royal Society of Chemistry, Cambridge, **1994**, p. 147.

[14] The class of mechanically interlocked molecules we propose to call suitanes differ from carceplexes in so far as their existence is established by host–guest interactions during their template formation. These interactions will normally live on in the molecules afterwards, provided the recognition sites are not switched off by some means or another. Herein, the recognition in the form of noncovalent bonds would have their strength considerably diminished and impaired by the addition of base.

[15] The synthesis of **LBT**-H_2·2 PF_6 is reported in the Supporting Information.

[16] The formation of the 2:1 complexes—or [3]pseudotoraxane—is assisted principally by N^+–H···O hydrogen bonds and C–H···O interactions between the $-CH_2NH_2^+CH_2-$ recognition sites on the **LBT**-H_2^{2+} dication and the matching dipyrido[24]crown-8 rings in $(CHO)_2$-**DP24C8**. For reviews on the use of this particular recognition motif as a template, see: a) P. T. Glink, C. Schiavo, J. F. Stoddart, *Chem. Commun.* **1996**, 1438 – 1490; b) T. J. Hubin, A. G. Kolchinski, A. L. Vance, D. H. Busch, *Adv. Supramol. Chem.* **1999**, *6*, 237 – 357; c) T. J. Hubin, D. H. Busch, *Coord. Chem. Rev.* **2000**, *200–2002*, 5 – 52; d) S. J. Cantrill, A. R. Pease, J. F. Stoddart, *J. Chem. Soc. Dalton Trans.* **2000**, 3715 – 3734.

[17] B. H. Northrop, F. Aricó, N. Tangchiavang, J. D. Badjić, J. F. Stoddart, *Org. Lett.* **2006**, *8*, 3899 – 3902.

[18] a) W. R. Layer, *Chem. Rev.* **1963**, *63*, 489 – 510; b) S. Dayagi, Y. Degani in *The Chemistry of the Carbon–Nitrogen Double Bond* (Ed.: S. Patai) Interscience, New York, **1970**, pp. 64 – 83; c) I. Huc, J.-M. Lehn, *Proc. Natl. Acad. Sci. USA* **1997**, *94*, 2106 – 2110.

[19] S. J. Rowan, S. J. Cantrill, G. R. L. Cousins, J. K. M. Sanders, J. F. Stoddart, *Angew. Chem.* **2002**, *114*, 938 – 993; *Angew. Chem. Int. Ed.* **2002**, *41*, 898 – 952.

[20] This protocol has been honed to near perfection with the almost quantitative self-assembly of nanoscale Borromean ring compounds from 18 components by the template-directed formation of 30 dative bonds and 12 imine bonds; see: a) K. S. Chichak, S. J. Cantrill, A. R. Pease, S.-H. Chui, G. W. V. Cave, J. L. Atwood, J. F. Stoddart, *Science* **2004**, *304*, 1308 – 1312; b) J. S. Siegel, *Science* **2004**, *304*, 1256 – 1258; c) C. A. Schalley, *Angew. Chem.* **2004**, *116*, 4499 – 4501; *Angew. Chem. Int. Ed.* **2004**, *43*, 4399 – 4401; d) K. S. Chichak, A. J. Peters, S. J. Cantrill, J. F. Stoddart, *J. Org. Chem.* **2005**, *70*, 7956 – 7962; e) C. D. Pentecost, A. J. Peters, K. S. Chichak, G. W. V. Cave, S. J. Cantrill, J. F. Stoddart, *Angew. Chem.* **2006**, *118*, 4205 – 4210; *Angew. Chem. Int. Ed.* **2006**, *45*, 4099 – 4104.

[21] Crystal data for [(**DP24C8**)$_2$(**LBT**-H_2)]: $[C_{94}H_{98}F_4N_6O_{12}]$-$(PF_6)_2$·2 MeCN, $M_r = 1951.83$, monoclinic, $P2_1/n$ (no. 14), $a = 12.6367(14)$, $b = 26.388(3)$, $c = 15.594(2)$ Å, $\beta = 111.060(8)°$, $V = 4852.6(11)$ Å^3, $Z = 2$ (C_i symmetry), $\rho_{calcd} = 1.336$ g cm^{-3}, $\mu(Cu_{K\alpha}) = 1.222$ mm^{-1}, $T = 293$ K, colorless prisms; 7207 independent measured reflections, F^2 refinement, $R_1 = 0.133$, $wR_2 = 0.364$, 2730 independent observed reflections ($|F_o| > 4\sigma(|F_o|)$, $2\theta_{max} = 120°$), 659 parameters.

[22] It should be noted that, in the solid-state superstructure, two co-conformations of relative occupancies 0.65:0.35 were observed for the **DP24C8** rings, and the separations of the carbon atoms in the 4-positions of the pyridine rings in the two different co-conformations were 14.3 and 14.6 Å, respectively; Figure 3 depicts the major conformer.

[23] Computations were performed using the program Maestro v 3.0.038 with the AMBER* force-field and GB/SA solvent model for $CHCl_3$. Full details of computational procedures can be found in the Supporting Information.

[24] a) J. N. K. Reek, A. H. Priem, H. Engelkamp, A. E. Rowan, J. A. A. W. Elemans, R. J. M. Nolte, *J. Am. Chem. Soc.* **1997**, *119*, 9956 – 9964; b) J. A. A. W. Elemans, M. B. Claase, P. P. M. Aarts, A. E. Rowan, A. P. H. J. Schenning, R. J. M. Nolte, *J. Org. Chem.* **1999**, *64*, 7009 – 7016.

[25] a) C. W. Chen, H. W. Whitlock, *J. Am. Chem. Soc.* **1978**, *100*, 4921 – 4922; b) S. C. Zimmerman, *Top. Curr. Chem.* **1993**, *165*, 71 – 102; c) F.-G. Klärner, U. Burkert, M. Kamieth, R. Boese, J. Benet-Buchholz, *Chem. Eur. J.* **1999**, *5*, 1700 – 1707.

[26] The [3]pseudorotaxane binding energy was taken as the difference in energy between the fully optimized structures of the [3]pseudorotaxane and that of the fully separated **LBT**-H_2^{2+} and two equivalents of $(CHO)_2$-**DP24C8**. The binding energy of suit[2]ane was taken as the difference in energy between the fully optimized structures of the suit[2]ane and those of the fully separated **LBT**-H_2^{2+} plus the tetraimine host.

[27] Crystal data for suit[2]ane: $[C_{110}H_{106}F_4N_{10}O_{12}](PF_6)_2$·8 Me_2CO, $M_r = 2590.61$, monoclinic, $P2_1/n$ (no. 14), $a = 16.3400(3)$, $b = 21.1680(3)$, $c = 20.7430(4)$ Å, $\beta = 110.5770(6)°$, $V = 6717.0(2)$ Å^3, $Z = 2$, $\rho_{calcd} = 1.281$ g cm^{-3}, $\mu(Mo_{K\alpha}) = 0.123$ mm^{-1}, $T = 123$ K, pale yellow plates; 12156 independent measured reflections, F^2 refinement, $R_1 = 0.083$, $wR_2 = 0.232$, 7171 independent observed absorption-corrected reflections ($|F_o| > 4\sigma(|F_o|)$, $2\theta_{max} = 51°$), 837 parameters. CCDC-608949 ([(**DP24C8**)$_2$(**LBT**-H_2)]) and -608950 (suit[2]ane) contain the supplementary crystallographic data for this paper. These data can be obtained free of charge from The Cambridge Crystallographic Data Centre via www.ccdc.cam.ac.uk/data_request/cif.

[28] The four imine bonds in suit[2]ane constitute a fairly stable entity. In principle, as we have shown with numerous other polyimine macrocycles, it should be possible to reduce them with reagents, such as BH_3–THF or BH_3–lutidine—and, in so doing, fix the structure for all time in a kinetic regime.

[29] a) D. H. Lee, J. R. Granja, J. A. Martinez, K. Severin, M. R. Ghadiri, *Nature* **1996**, *382*, 525 – 528; b) B. Wang, I. O. Sutherland, *Chem. Commun.* **1997**, 1495 – 1496; c) V. C. Allen, D. Philp, N. Spencer, *Org. Lett.* **2001**, *3*, 777 – 780; d) X. Li, J. Chimielewski, *J. Am. Chem. Soc.* **2003**, *125*, 11820 – 11821; e) S. J. Howell, N. Spencer, D. Philp, *Org. Lett.* **2002**, *4*, 273 – 276; f) R. J. Pearson, E. Kassianidis, A. M. Z. Slawin, D. Philp, *Org. Biomol. Chem.* **2004**, *2*, 3434 – 3441; g) E. Kassianidis, R. J. Pearson, D. Philp, *Org. Lett.* **2005**, *7*, 3833 – 3836; h) S. J. Cantrill, R. H. Grubbs, D. Lanari, K. C.-F. Leung, A. Nelson, K. G. Poulin-Kerstein, S. P. Smidt, J. F. Stoddart, D. A. Tirrell, *Org. Lett.* **2005**, *7*, 4213 – 4216.

 © 2006 Wiley-VCH Verlag GmbH & Co. KGaA, Weinheim

Polyoxometalates

DOI: 10.1002/anie.200602200

Evolution of Polyoxoniobate Cluster Anions**

*Ranko P. Bontchev and May Nyman**

Early transition metals such as V, Mo, and W are well known to form complex polyoxoanions over a wide pH range,[1] for example, some exceptionally large ring-shaped oxo–molybdenum clusters that contain up to several hundred metal centers.[2] In contrast, polyoxoniobates can be stabilized only under basic conditions, and their chemistry was initially dominated by the hexaniobate Lindqvist anion $[Nb_6O_{19}]^{8-}$ in solution and by its alkali salts in the solid state.[3] More recently, the dodecaniobate Keggin ion $[TNb_{12}O_{40}]^{16-}$ (T = Si, Ge, P) and its lacunary derivatives were also synthesized by using hydrothermal processing and slightly lower alkalinity.[4] The isolation of alternative polyoxoniobate cluster types in the solid state, especially through nonhydrothermal synthetic routes, has been hindered by the narrow working pH range (10.5–12.5) and the pervasiveness of the oxido–niobium Lindqvist and Keggin ions. The only other polyoxoniobate clusters known to date are $[Nb_{10}O_{28}]^{6-}$,[5a] its structural analogue $[Ti_2Nb_8O_{28}]^{8-}$,[5b] and the dimeric derivative $[Nb_{20}O_{54}]^{8-}$.[5c] The unique characteristics of the polyoxoniobate family (high charge/surface ratio and basicity) justify further exploration of potential practical applications in virology,[6a] nuclear-waste treatment,[4c,6b,c] and the base-catalyzed decomposition of biocontaminants.[6d]

Herein we report the synthesis and crystal structure of a new polyoxoniobate cluster type $\{Nb_{24}O_{72}H_9\}^{15-}$ (**1**). To the best of our knowledge, **1** has no analogues among the known polyoxometalate cluster geometries and is the largest isopolyniobate cluster reported to date. We also show that its structure could be derived from two fundamental structural types (Figure 1) and that **1** may serve as a building block for even larger clusters and extended structures.

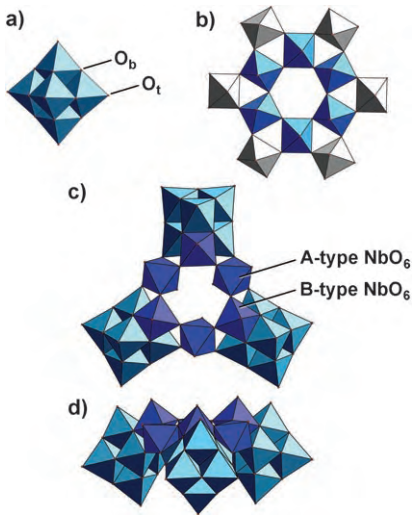

Figure 1. a) The Lindqvist anion $[Nb_6O_{19}]^{8-}$; O_b and O_t depict bridging (Nb–O_b–Nb) and terminal (Nb–O_t) oxygen atoms, respectively; b) the cyclic $\{Nb_6O_{30}\}$ unit (dark blue) in the pyrochlore frameworks $HNbO_3{\cdot}0.5\,H_2O$ and $RbNb_2O_5F$ (gray);[8] c) top view of the cluster anion $\{Nb_{24}O_{72}H_9\}^{15-}$ (**1**) consisting of three Lindqvist $\{Nb_6O_{19}H_x\}$ clusters (light blue) linked by a cyclic $\{Nb_6O_{30}H_{9-x}\}$ cluster (dark blue); d) side view of **1**.

The reaction of rubidium hexaniobate, copper(II) nitrate, ethylenediamine (en), and water at near-ambient temperature yielded crystals of $(H_2en)_6[Cu(en)_2(H_2O)_2]_3[(\{Nb_{24}O_{72}H_9\}\{Cu(en)_2(H_2O)\}_2\{Cu(en)_2\})_2]{\cdot}66\,H_2O$ (**2**).[7] The new cluster anion **1** is shown in Figure 1c. It can be described as three Lindqvist $\{Nb_6O_{19}\}$ clusters linked together by a cyclic $\{Nb_6O_{30}\}$ cluster. The same $\{Nb_6O_{30}\}$ structural motif is found in Nb-based solids of the pyrochlore type, such as $HNbO_3{\cdot}0.5\,H_2O$ and $RbNb_2O_5F$ (Figure 1b).[9] The $\{Nb_6O_{30}\}$ ring consists of six NbO_6 octahedra sharing common (μ_2-O) corners. Three of these NbO_6 octahedra (A-type NbO_6) link two adjacent $\{Nb_6O_{19}\}$ clusters through corner atoms, and the remaining three (B-type) NbO_6 octahedra each share three edges with a Lindqvist cluster (Figure 1c). The B-type NbO_6 octahedron is also bonded to the face of the Lindqvist superoctahedron and hence together may be alternatively described as a heptaniobate cluster.

A number of differentiating structural features of the $\{Nb_6O_{30}\}$ ring in **1** emerge in comparison with the pyrochlore motif ($Nb_6O_{24}F_6$) mentioned above.[9] The NbO_6 octahedra in the pyrochlore motif are only slightly tilted with respect to each other (Figure 1b). In comparison, the A-type NbO_6 octahedra in **1** are considerably more tilted and their O_t–Nb=O_t axes (Nb=$O_t \approx 1.75$ Å, *trans*-Nb–$O_t \approx 2.45$ Å) point almost parallel to the equatorial plane of the ring (Figure 1c,d). Another significant difference is the presence of *trans* terminal (μ_1-O_t) oxygen atoms in each A-type NbO_6 octahedron in **1** (Figure 1c). In contrast, all O/F atoms in the pyrochlore motif are bridging (μ_2-type), all occupy one crystallographically independent position, and the Nb–O(F)

[*] Dr. R. P. Bontchev, Dr. M. Nyman
Sandia National Laboratories
P.O. Box 5800, MS 0754, Albuquerque, NM 87185-0754 (USA)
Fax: (+1) 505-844-7354
E-mail: mdnyman@sandia.gov

[**] Sandia is a multiprogram laboratory operated by Sandia Corporation, a Lockheed Martin Company, for the United States Department of Energy's National Nuclear Security Administration under contract DE-AC04-94AL85000. This work was supported by Sandia National Laboratories' Laboratory Directed Research and Development (LDRD) program. We thank Dr. M. Iliev (Texas Center for Superconductivity and Advanced Materials, Houston, Texas) for the Raman analyses. We thank Reference Metals, Inc. (CBMM, Araxá, Brazil) for the generous gift of hydrous niobium. We cite to the definition of "evolution" from the Merriam-Webster dictionary as "a process of continuous change from a lower, simpler to a higher, more complex state" in reference to the assembly of more-complex structures from simpler building blocks.

Supporting information (table comparing Nb–O bond lengths for **1**, protonated and nonprotonated $\{Nb_6O_{19}\}$ Lindqvist ions, and pyrochlore) for this article is available on the WWW under http://www.angewandte.org or from the author.

InterScience
© 2006 Wiley-VCH Verlag GmbH & Co. KGaA, Weinheim

bond lengths are equal and on the order of 2.0 Å (see the Supporting Information).[9] All six short Nb=O bonds in the $\{Nb_6O_{30}\}$ ring are located on the same side with respect to the equatorial plane of the Nb_6 ring (Figure 1c), and the same is also true for their long *trans*-oriented Nb–O counterparts.

Charge-balance considerations of **2** dictate that there must be nine protons per $\{Nb_{24}O_{72}\}$ unit (i.e., $\{Nb_{24}O_{72}H_9\}^{15-}$). The very high number of crystallographically independent atoms and variable parameters prevented direct location of the protons from the Fourier maps.[7] Bond-valence calculations did not provide an obvious solution as a result of atypical distortions and the relatively wide variation of the Nb–O bond lengths.[10] These bond lengths are summarized and compared with those of protonated $Rb_6[Nb_6O_{19}H_2]\cdot 9H_2O$ and nonprotonated $Rb_8[Nb_6O_{19}]\cdot 14H_2O$ Lindqvist clusters in the Supporting Information.[3c] The typical lengthening of the Nb-μ_2-OH bonds in protonated $\{Nb_6O_{19}\}$ clusters is further masked by additional distortions that result from the linking of the $\{Nb_6O_{19}\}$ and $\{Nb_6O_{30}\}$ units, which makes the unambiguous assignment of the protonated oxygen atoms in **1** challenging. Neutron-diffraction studies have shown that the protons in $HNbO_3\cdot 0.5H_2O$, $HTaWO_6$, and $HTaWO_6\cdot H_2O$ pyrochlores are present as framework hydroxy groups.[9a] The three long Nb–O_t bonds (2.27–2.45 (1) Å) of the A-type NbO_6 octahedra in $\{Nb_6O_{30}\}$ (Figure 1b,c) indicate the most obvious sites for protonation. Bond valence sum (BVS) calculations gave values of 0.2–0.3 for each of these Nb–O_t terminal oxygen atoms.[10] The expected oxygen BVS of 2 could be completed by assuming a hydrogen atom at bonding distance of 0.7–0.8 Å.

In several earlier infrared and Raman studies of $\{Nb_6O_{19}\}$, the bands corresponding to terminal Nb–O_t and bridging Nb–O_b–Nb vibrations were identified and assigned as Nb–O_t > 800 cm^{-1} and 400 < Nb–O_b–Nb < 750 cm^{-1}.[11] In our FTIR and Raman studies on $Rb_8[Nb_6O_{19}]\cdot 14H_2O$, $Rb_6[Nb_6O_{19}H_2]\cdot 9H_2O$, and **2**, we observed systematic and measurable shifts towards higher energies of the same bands in the spectra of the protonated clusters relative to the nonprotonated clusters (see the Experimental Section). This observation indicates that the same types of oxygen atoms (bridging) of the Lindqvist ions in **1** are most probably protonated. This conclusion is also in accordance with recent structural studies on protonated Lindqvist salts such as $Rb_6[Nb_6O_{19}H_2]\cdot 14H_2O$ which showed that the protons are associated with two adjacent bridging (μ_2-O) sites.[3c] Even stronger evidence comes from the structural characterization of several related $\{Cu(en)_2\}^{2+}$-linked $\{Nb_6O_{19}H_2\}$ phases that feature the same doubly protonated cluster faces.[3h] All of the above evidence strongly suggests that six of the nine protons in **1** are located as neighboring μ_2-O_bH pairs on the three Lindqvist units and the other three are on the oxygen atoms of the three long terminal Nb–O_t bonds of the A-type NbO_6 octahedra of the $\{Nb_6O_{30}\}$ ring.

Each $\{Nb_{24}O_{72}H_9\}^{15-}$ cluster is "decorated" by two terminal $\{Cu(en)_2(H_2O)\}$ units with Cu–N bond lengths ranging between 1.90(1) and 2.17(1) Å (Figure 2). One is connected to the O_t oxygen atom of the A-type NbO_6 octahedron with Cu–O_t = 2.30 (1) Å and Cu–OH_2 = 2.71(1) Å. The second $\{Cu(en)_2(H_2O)\}$ unit is connected to a bridging (μ_2-O_b) oxygen atom from the diametrically opposite $[Nb_6O_{19}]$ Lindqvist unit with bond lengths of Cu–O_b = 2.36(1) Å and Cu–OH_2 = 2.71(1) Å (Figure 2). A pair of $\{Nb_{24}O_{72}H_9\}\{Cu(en)_2(H_2O)\}_2$ clusters are linked together by two $\{Cu(en)_2\}$ bridges through one terminal oxygen atom (Cu–O_t = 2.47(1) Å) and one bridging oxygen atom (Cu–O_b = 2.67(1) Å) from Lindqvist units on adjacent clusters of **1** to form dimers $[(\{Nb_{24}O_{72}H_9\}\{Cu(en)_2(H_2O)\}_2\{Cu(en)_2\})_2]^{18-}$ (Figure 2). The remaining overall charge balance is provided by isolated, disordered $[Cu(en)_2(H_2O)_2]^{2+}$ complexes and $(H_2en)^{2+}$ molecules, which, together with water molecules, fill the space between the clusters. An extended network of O–H···O hydrogen bonds between all of the lattice species provides the 3D connectivity in the overall structure.

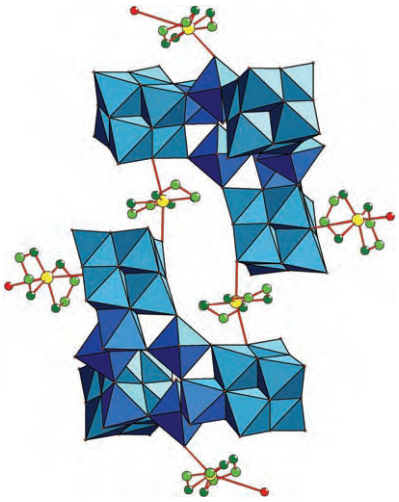

Figure 2. The dimer $[(\{Nb_{24}O_{72}H_9\}\{Cu(en)_2(H_2O)\}_2\{Cu(en)_2\})_2]^{18-}$. The clusters of **1** are shown in blue; copper, oxygen, carbon, and nitrogen atoms are shown as yellow, red, and light- and dark-green spheres, respectively.

Although not unique to polyoxometalates,[12] the fact that the countercations in **2** are charged copper complexes and protonated organic species is quite unusual for polyoxoniobates. All of the structurally characterized Lindqvist-based clusters to date are charge compensated only by alkali cations, which generally have higher charge density than organic cations.[3] It is tempting to assume that in polyoxoniobate chemistry, large cations with relatively low charge density similar to $[CuL_x]^{2+}$ favor the formation of larger clusters such as **1.** Supporting this idea is the fact that the only other structurally characterized polyoxoniobates different from the Lindqvist or Keggin anions, namely $[Nb_{10}O_{28}]^{6-}$ and $[Nb_{20}O_{54}]^{8-}$, have been also isolated by using low-charge-density cations (tetramethyl- and tetrabutylammonium, respectively).[5a,c] All these considerations suggest that the use of organic cations or metal–ligand cations could provide new avenues towards diversification of polyoxoniobate cluster geometries, as well as an insight in their non-aqueous chemistry.

In conclusion, we have followed the structural evolution of the simple NbO_6 octahedron to two basic structural units—the Lindqvist $\{Nb_6O_{19}\}$ and the pyrochlore cyclic $\{Nb_6O_{30}\}$ clusters. We have demonstrated that their combination results

 © 2006 Wiley-VCH Verlag GmbH & Co. KGaA, Weinheim

in the unique polyoxoniobate cluster anion $\{Nb_{24}O_{72}H_9\}^{15-}$ (**1**), the $\{Cu(en)_2(H_2O)\}$-coordinated species, the dimer $[(\{Nb_{24}O_{72}H_9\}\{Cu(en)_2(H_2O)\}_2\{Cu(en)_2\})_2]^{18-}$, and finally the complex overall 3D structure of **2**. Synthetic studies towards related polyoxoniobate-counterion systems are currently under way.

Experimental Section

Synthesis of **2**: Rubidium hexaniobate was synthesized as previously reported.[3c] $Rb_8Nb_6O_{19}\cdot 14H_2O$ (0.95 g, 0.5 mmol), $Cu(NO_3)_2\cdot 2.5H_2O$ (0.48 g, 2.0 mmol), ethylenediamine (10 g, 167 mmol), and water (10 g, 550 mmol) were mixed in a 50-mL beaker by stirring at 60 °C for 30 min. The beaker was covered with parafilm and left at room temperature. Prismatic deep-purple crystals up to 0.5 mm in size began forming at the bottom of the beaker after 3 days. After 5 days, the sample was filtered, and a few crystals were selected for single-crystal X-ray diffraction analysis. Elemental analysis (Galbraith Laboratories, Inc.): expected formula (XRD) $(Cu_{4.5}Nb_{24}C_{24}N_{24}O_{77}H_{151})\cdot 33H_2O$; found $(Cu_{4.34}Nb_{24.29}C_{23.73}N_{23.39}H_{150.91})\cdot 18H_2O$; the difference in the number of water molecules of crystallization is due to prolonged storage. Infrared spectra were recorded on a Perkin Elmer Spectrum One spectrometer within the range 400–4000 cm^{-1} as KBr pellets. Raman spectra were measured by using the Ar^+ laser line (488.0 nm) and a CCD single spectrometer (spot diameter 5–7 μm, 0.6 mW, average laser power density of 1000–2000 $W\,cm^{-2}$). IR: **2**: $\tilde{\nu}$ = 530s, 704s, 751s, 848s cm^{-1}; $Rb_8[Nb_6O_{19}]\cdot 14H_2O$: $\tilde{\nu}$ = 523s, 691s, 736s, 825s cm^{-1}; $Rb_6[Nb_6O_{19}H_2]\cdot 9H_2O$: $\tilde{\nu}$ = 531s, 969s, 749s, 867s cm^{-1}. Raman: **2**: $\tilde{\nu}$ = 480s, 533s, 561s, 816m, 856m, 897vs cm^{-1}; $Rb_8[Nb_6O_{19}]\cdot 14H_2O$: $\tilde{\nu}$ = 463, 536, 828m, 876vs cm^{-1}; $Rb_6[Nb_6O_{19}H_2]\cdot 9H_2O$: $\tilde{\nu}$ = 474s, 536s, 556s, 820m, 848m, 892vs cm^{-1}.

Received: June 2, 2006
Revised: August 8, 2006
Published online: September 20, 2006

Keywords: cluster compounds · niobium · polyoxometalates · solid-state structures

[1] a) M. T. Pope, *Heteropoly and Isopoly Oxometalates*, Springer, New York, **1983**; b) M. T. Pope, A. Müller, *Angew. Chem.* **1991**, *103*, 56; *Angew. Chem. Int. Ed. Engl.* **1991**, *30*, 34; c) W. G. Klemperer, T. A. Marquart, O. M. Yaghi, *Angew. Chem.* **1992**, *104*, 51; *Angew. Chem. Int. Ed. Engl.* **1992**, *31*, 49.

[2] a) A. Müller, E. Krickemeyer, H. Bögge, M. Schmidtmann, C. Beugholt, P. Kögerler, C. Lu, *Angew. Chem.* **1998**, *110*, 1278; *Angew. Chem. Int. Ed.* **1998**, *37*, 1220; b) A. Müller, M. Koop, H. Bögge, M. Schmidtmann, C. Beugholt, *Chem. Commun.* **1998**, 1501; c) C.-C. Jiang, Y.-G. Wei, Q. Liu, S-W. Zhang, M.-C. Shao, Y.-Q. Tang, *Chem. Commun.* **1998**, 1937; d) A. Müller, S. Q. N. Shah, H. Bögge, M. Schmidtman, *Nature* **1999**, *397*, 48; e) A. Müller, P. Kögerler, A. W. M. Dress, *Coord. Chem. Rev.* **2001**, *222*, 193; f) B. Botar, P. Kögerler, C. L. Hill, *J. Am. Chem. Soc.* **2006**, *128*, 5336.

[3] a) I. Lindqvist, *Ark. Kemi* **1953**, *5*, 247; b) A. Goiffon, E. Philippot, M. Maurin, *Rev. Chim. Miner.* **1980**, *17*, 466; c) M. Nyman, T. M. Alam, F. Bonhomme, M. A. Rodriguez, C. S. Frazer, M. E. Welk, *J. Cluster Sci.* **2006**, *17*, 197; d) M. Muller, *Rev. Chim. Miner.* **1970**, *7*, 359; e) G. M. Rozantsev, O. I. Dotsenko, G. V. Taradina, *Russ. J. Coord. Chem.* **2000**, *26*, 247; f) T. M. Alam, M. Nyman, B. R. Cherry, J. M. Segall, L. E. Lybarger, *J. Am. Chem. Soc.* **2004**, *126*, 5610; g) T. Ozeki, T. Yamase, H. Naruke, Y. Sasaki, *Bull. Chem. Soc. Jpn.* **1994**, *67*, 3249; h) R. Bontchev, M. Nyman, unpublished results.

[4] a) M. Nyman, F. Bonhomme, T. M. Alam, M. A. Rodriguez, B. R. Cherry, J. L. Krumhansl, T. M. Nenoff, A. M. Sattler, *Science* **2002**, *297*, 996; b) M. Nyman, F. Bonhomme, T. M. Alam, J. B. Parise, G. M. B. Vaughan, *Angew. Chem.* **2004**, *116*, 2847; *Angew. Chem. Int. Ed.* **2004**, *43*, 2787; c) F. Bonhomme, J. P. Larentzos, T. M. Alam, E. J. Maginn, M. Myman, *Inorg. Chem.* **2005**, *44*, 1774; d) M. Nyman, A. J. Celestian, J. B. Parise, G. P. Holland, T. M. Alam, *Inorg. Chem.* **2006**, *45*, 1043.

[5] a) E. J. Graeber, B. Morosin, *Acta Crystallogr. Sect. B* **1977**, *33*, 2137; b) M. Nyman, L. Criscenti, F. Bonhomme, M. A. Rodriguez, R. T. Cygan, *J. Solid State Chem.* **2003**, *176*, 111; c) M. Maekawa, Y. Ozava, A. Yagasaki, *Inorg. Chem.*, DOI: 10.1021/ic0601788.

[6] a) J. T. Rhule, C. L. Hill, D. A. Judd, *Chem. Rev.* **1998**, *98*, 327; b) M. H. Dickman, M. T. Pope, *Inorg. Chem.* **2001**, *40*, 2582; c) M. H. Cjoamg, C. W. Williams, L. Soderholm, M. R. Antonio, *Eur. J. Inorg. Chem.* **2003**, *14*, 2663; d) A. J. Russell, J. A. Berberich, G. F. Drevon, R. R. Koepsel, *Annu. Rev. Biomed. Eng.* **2003**, *5*, 1.

[7] a) Crystal structure data for **2**: crystal size $0.38\times 0.37\times 0.14\ mm^3$, triclinic, space group $P\bar{1}$ (no. 2), a = 16.7734(10), b = 20.6133(13), c = 26.3179(16) Å, α = 112.520(1), β = 102.932(1), γ = 96.186(1)°, V = 8001.1(8) $Å^3$, Z = 2, ρ_{calcd} = 2.059 $g\,cm^{-1}$; diffractometer: Siemens SMART 1K CCD ($Mo_{K\alpha}$ radiation λ = 0.71073 Å, graphite monochromator), μ = 2.332 mm^{-1}; narrow-frame scan at T = 293 K, $2\theta_{max}$ = 46.00°, 38657 measured reflections, 22126 independent reflections, the program SADABS[8a] was used for the absorption correction; structure solved by direct methods and refined by least-squares methods on F^2 by using SHELXTL;[8b] 1490 free parameters; GOF = 1.004, R values ($I > 2\sigma(I)$): $R1$ = 0.081, $wR2$ = 0.213; max./min. residual electron density: 1.70/−0.55 $e^-\,Å^{-3}$. CCDC 606228 contains the supplementary crystallographic data for this paper. These data can be obtained free of charge from The Cambridge Crystallographic Data Centre via www.ccdc.cam.ac.uk/data_request/cif.

[8] a) G. M. Sheldrick, SADABS, v. 2.10. Program for Empirical Absorption Correction of Area Detector Data, University of Gottingen: Gottingen, Germany, **2003**; b) SHELX97 (Includes SHELXS97, SHELXL97, CIFTAB)—Programs for Crystal Structure Analysis (Release 97-2). Institüt für Anorganische Chemie der Universität, Tammanstrasse 4, 3400 Göttingen, Germany, **1998**.

[9] a) J. T. Lewandowski, I. J. Pickering, A. J. Jacobson, *Mater. Res. Bull.* **1992**, *27*, 981; b) J. L. Fourquet, C. Jacoboni, R. de Pape, *Mater. Res. Bull.* **1973**, *8*, 393.

[10] I. D. Brown and D. Altermatt, *Acta Crystallogr. Sect. A* **1985**, *41*, 244.

[11] a) F. J. Farell, V. A. Maroni, T. G. Spiro, *Inorg. Chem.* **1969**, *8*, 2638; b) M. Von Rainer, H. Bierbusse, J. Fuchs, *Z. Anorg. Allg. Chem.* **1971**, *385*, 230; c) C. Rocchiccioli-Deltcheff, R. Thouvenot, M. Dabbabi, *Spectrochim. Acta Part A* **1977**, *33*, 143.

[12] a) M. I. Khan, *J. Solid State Chem.* **2000**, *152*, 105; b) M. I. Khan, E. Yohannes, D. Powell, *Inorg. Chem.* **1999**, *38*, 212; c) M. I. Khan, E. Yohannes, D. Powell, *Chem. Commun.* **1999**, 23; d) J. Lu, Y. Xu, N. K. Goh, L. S. Chia, *Chem. Commun.* **1999**, 832; e) J. Do, R. P. Bontchev, A. J. Jacobson, *Inorg. Chem.* **2000**, *39*, 4305.

 © 2006 Wiley-VCH Verlag GmbH & Co. KGaA, Weinheim

Asymmetric Self-Assembly

DOI: 10.1002/anie.200601000

Double-Faced Micelles from Water-Soluble Polymers**

*Ilja K. Voets, Arie de Keizer, Pieter de Waard, Peter M. Frederik, Paul H. H. Bomans, Holger Schmalz, Andreas Walther, Stephen M. King, Frans A. M. Leermakers, and Martien A. Cohen Stuart**

Polymer technology finds much of its inspiration in nature, but it lacks the subtle input of millions of years of evolution. Conventional routes to biomimetic architectures involve elaborate syntheses and multistep preparation protocols.[1–4] Indeed, this approach has led to many new solution morphologies, including exotic geometries and multidomain structures (beyond core/shell type). Recently, a wide variety of nonspherical shapes, ranging from vesicles to nanowires,[5] from toroids[6] to hollow icosahedras,[7] as well as internally structured nanoassemblies have been reported (see, for example, literature on "layered" micelles, that is, core–shell–corona or onion-type micelles,[8,9] multicompartment micelles,[1,2] micelles with a phase-segregated corona in block-selective solvents,[4,10] and chemically cross-linked colloidal particles with a corona consisting of two different solvent-swollen polymers[3]). However, only a small percentage of these synthetic analogues to complex biological structures assemble spontaneously and reversibly from their molecular constituents. On the contrary, they are typically frozen-in architectures, dynamically arrested and thus fundamentally different from their biomacromolecular analogues. In order to preserve dynamics and responsiveness of the structure, the driving forces need to be weak and well-balanced, enforcing just the right architecture.

We set out to meet these requirements by combining associative and segregative phase separation. More specifically, electrostatic interaction (complex coacervation) is used to confine two double hydrophilic block copolymers in the same aggregate, while a subtle repulsion between unlike neutral, water-soluble blocks ensures segregation into two distinct phases on a slightly larger length scale but within the same structure. The result is the spontaneous and reversible formation of a disk-shaped micelle having a complex coacervate core and an asymmetric water-swollen corona (Figure 1) which is microphase-separated into two distinct domains or faces, that is, Janus-type.

Figure 1. Representation of a disk-shaped Janus micelle. Complex coacervate core (PAA and P2MVP): orange; coronal hemispheres: green (PEO) and blue (PAAm).

When aqueous solutions of poly(acrylic acid)-*block*-poly(acryl amide), PAA_{42}-*b*-$PAAm_{417}$, and poly(2-methylvinylpyridinium iodide)-*block*-poly(ethylene oxide), $P2MVP_{42}$-*b*-PEO_{446}, were mixed, micelles formed almost instantaneously in a narrow region around a mixing fraction $f_+ = 0.5$ ($f_+ = [P2MVP]/([PAA]+[P2MVP])$). The reversibility and responsive nature of this type of micelle, so-called complex coacervate core micelles (C3Ms),[11–13] polyion complex micelles,[14,15] block ionomer complex micelles[16,17] and interpolyelectrolyte complexes (IPEC),[18] has been extensively documented in previous work.[12,13] PAAm and PEO were chosen as corona blocks on the basis of published compatibility data.[19–21] From these reports, we estimate the Flory–Huggins interaction parameter $\chi_{PAAm,PEO}$ to be about 0.05.

In dynamic light-scattering experiments, we find a very small (linear) angular and concentration dependence for the diffusion coefficient. CONTIN analysis shows one rather narrow mode corresponding to an effective hydrodynamic radius, $R_{h,eff,c\to 0,q\to 0}$, of 18.3 ± 0.5 nm. Three independent methods (a partial Zimm analysis, a Guinier analysis, and a Debye analysis) have been used to analyze the static light-scattering data ($0.5 < C_p < 2\ g\,L^{-1}$, $0.018 < q < 0.032\ nm^{-1}$,

[*] MSc. I. K. Voets, Dr. A. de Keizer, Prof. Dr. F. A. M. Leermakers, Prof. Dr. M. A. Cohen Stuart
Laboratory of Physical Chemistry and Colloid Science
Wageningen University
Dreijenplein 6, 6703 HB Wageningen (The Netherlands)
Fax: (+31) 317-483-777
E-mail: martien.cohenstuart@wur.nl
Dr. P. de Waard
Wageningen NMR Centre
Wageningen University
Dreijenlaan 3, 6703 HA Wageningen (The Netherlands)
Dr. P. M. Frederik, P. H. H. Bomans
EM Unit, Pathologie
Universiteit Maastricht
Universiteitssingel 50, 6229 ER Maastricht (The Netherlands)
Dr. H. Schmalz, MSc. A. Walther
Makromolekulare Chemie II
Universität Bayreuth
95440 Bayreuth (Germany)
Dr. S. M. King
ISIS Facility
Rutherford Appleton Laboratory
Chilton, Didcot, Oxon (England)

[**] We thank ISIS for providing the beam time, R. K. Heenan, A. E. Terry, and D. Visser for help, and NWO and the SONS Eurocores program (Project JA016-SONS-AMPHI) for financial support. We thank B. B. Venne for the creation of the disk schematic in Figure 1. This work was carried out in the framework of the EU Polyamphi/Marie Curie program (FP6-2002, proposal 505027).

Supporting information for this article is available on the WWW under http://www.angewandte.org or from the author.

 © 2006 Wiley-VCH Verlag GmbH & Co. KGaA, Weinheim

where $q = 4\pi n_0/\lambda \sin(\theta/2)$, λ is the wavelength in vacuum, n_0 is the solvent refractive index, θ is the scattering angle, and C_p is the total polymer concentration) resulting in a micellar mass, $M_{micelle}$, of 860 ± 23 kg mol^{-1}, an aggregation number, P_{agg}, of 30.0 ± 0.4, and a radius of gyration, R_g, of 16.9 ± 0.25 nm. Thus we obtain a R_g/R_h value of 0.92 ± 0.04, which is rather high for spherical aggregates ($R_g/R_h = 0.775$ for hard spheres) and indicative of elongated structures, such as ellipsoids, rods, or worms. Using the P_{agg} and R_h values we can roughly estimate the volume fraction of polymer in the corona, φ_{corona}, for which we find values between 5 and 10%. Thus φ_{corona} exceeds $\varphi_{critical}$, which should induce phase separation in the corona.

Cryo-transmission electron microscopy (cryo-TEM) confirms a nonspherical morphology (Figure 2). Both core and

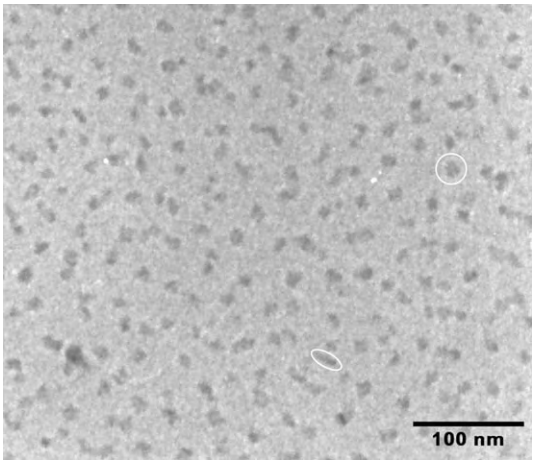

Figure 2. Cryo-TEM image of a 0.1-wt% solution of PAA_{42}-*b*-$PAAm_{417}$ and $P2MVP_{42}$-*b*-PEO_{446}.

corona are highly penetrated by solvent, resulting in a low contrast image in which only the core is visible. These low-polymer-volume fractions are typical for and directly related to the reversible character of C3Ms. A rough estimate for the core dimensions would be 20 ± 2 nm (diameter) by 7 ± 2 nm (thickness).

The small-angle neutron scattering (SANS) curves can be fitted using a form factor for monodisperse disks (Figure 3; $R = 18$ nm ± 1 nm, axial ratio $= 0.14 \pm 0.02$) but not with a monodisperse-sphere model nor with a polydisperse-sphere model, as this leads to physically unrealistically high values of polydispersity, in flagrant conflict with the DLS data and cryo-TEM images.

To the best of our knowledge, C3Ms in solution with a nonspherical morphology have never been reported before. Moreover, disk-shaped micelles are theoretically predicted as a possible morphology in the transition from spheres to lamellae,[22] but they are very rarely experimentally observed.[23] When observed, they are typically polydisperse and found as transients in the transition from (mixed) micelles to vesicles.[23] In this system, disk-shaped micelles of constant dimensions are found over a wide concentration range (0.1–1 wt%), suggesting an alternative mechanism to stabilize the disk-shaped morphology.[24,25]

We propose that this alternative mechanism is the coronal microphase separation of the PAAm and PEO blocks. To test

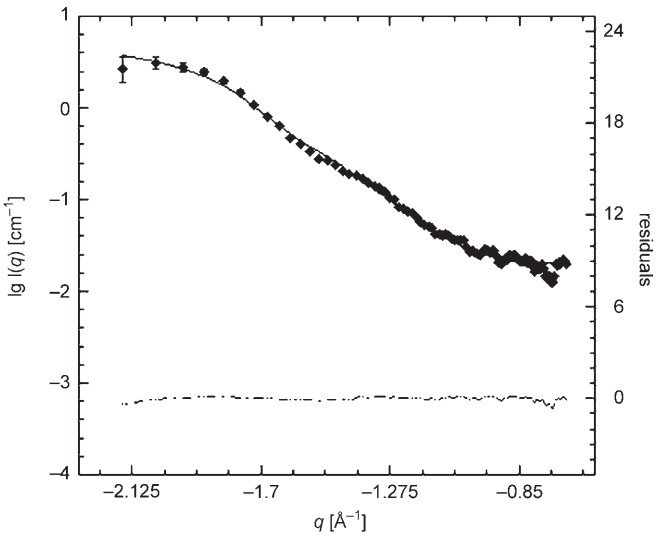

Figure 3. SANS curve of a 1-wt% aqueous solution of PAA_{42}-*b*-$PAAm_{417}$ and $P2MVP_{42}$-*b*-PEO_{446}. Experimental data (◆), form factor fit (solid line) to a uniform, monodisperse oblate ellipsoid, and residuals (dotted line). S(*q*) and core-shell structure are not included in the fit.

this hypothesis, we performed ^{1}H NMR NOESY experiments, in which the 3D spatial correlations of neighboring protons are probed. Cross peaks in the 2D ^{1}H NMR spectrum would indicate close proximity, that is, distances < 0.5 nm. Indeed, no cross peaks are observed between the ^{1}H NMR signals of PEO (3.6 ppm) and PAAm (1.65 (methylene, CH_2), 2.2 ppm (methine, CH)), while cross peaks are observed between the signals of the methylene and methine protons of PAAm and PAA (Figure 4).

As a positive control, we also present a contour plot of a ^{1}H NOESY experiment on C3Ms of $PDMAEMA_{45}$-*b*-$PGMA_{90}$ (poly(*N*,*N*-dimethylaminoethyl methacrylate)-*block*-poly(glyceryl methacrylate)) and PAA_{42}-*b*-$PAAm_{417}$. Figure 5 clearly shows cross peaks between the (fairly compatible) corona blocks PGMA and PAAm. In DLS measurements no angular dependence was found, indicating spherical morphology.

We expect that this strategy of C3Ms undergoing coronal microphase separation in combination with a systematic variation of lengths and solubility/miscibility of the corona blocks (especially towards more asymmetric ratios) will lead to a rich and exotic phase diagram in bulk, solution, and blends. More importantly, the directionality of the Janus micelle can be used in a secondary self-assembly process to produce micellar-like organization on a larger length scale.

Our current findings elegantly illustrate that highly ordered solution architectures can assemble easily and spontaneously when linear, flexible water-soluble diblock copolymers are simply mixed. This indicates a versatile and general route to hierarchical self-assembled structures on multiple length scales.

Experimental Section

Poly(2-methylvinylpyridinium iodide)-*block*-poly(ethylene oxide), $P2MVP_{42}$-*b*-PEO_{446}, and poly(acrylic acid)-*block*-poly(acryl amide),

 © 2006 Wiley-VCH Verlag GmbH & Co. KGaA, Weinheim

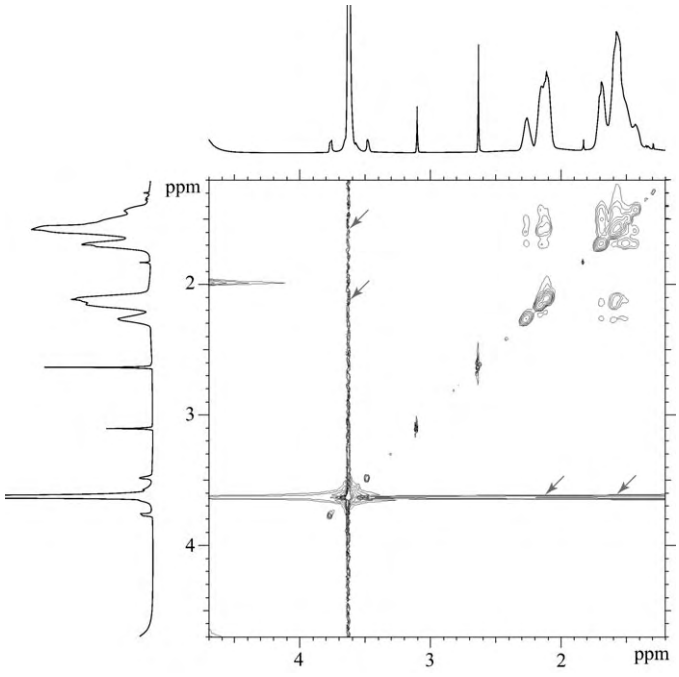

Figure 4. ^{1}H NMR 2D NOESY contour plot of a 1-wt% aqueous solution (1 mM $NaNO_3$, pH 7.73) of PAA_{42}-*b*-$PAAm_{417}$ and $P2MVP_{42}$-*b*-PEO_{446}. Arrows indicate where cross peaks between PAAm and PEO should occur in case of close proximity.

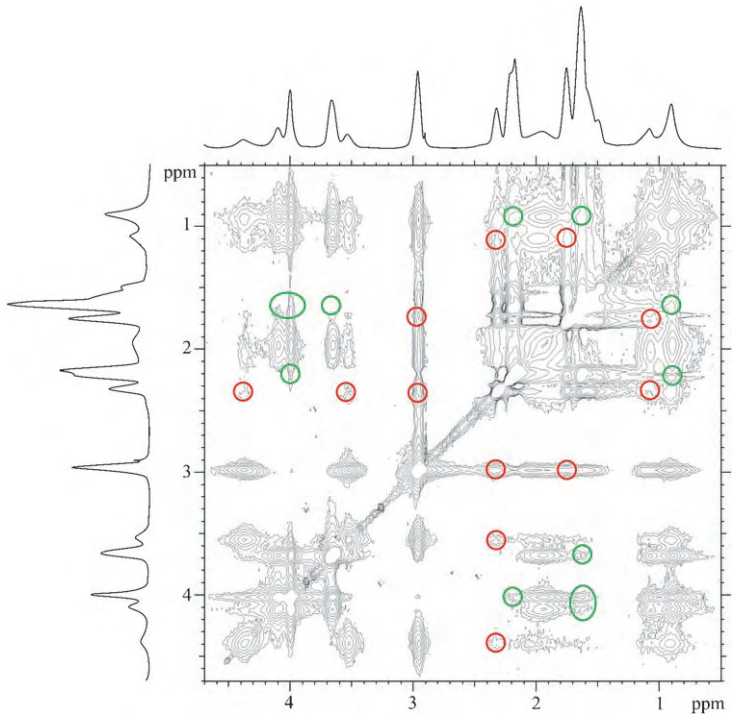

Figure 5. ^{1}H NMR 2D NOESY contour plot of a 1-wt% aqueous solution of PAA_{42}-*b*-$PAAm_{417}$ and $PDMAEMA_{45}$-*b*-$PGMA_{90}$. Circles indicate cross peaks between core (red) and corona (green) blocks. See the Supporting Information for details.

PAA_{42}-*b*-$PAAm_{417}$, were synthesized by sequential anionic polymerization[26] (followed by quaternization with methyl iodide) and the MADIX process,[27] respectively (for details see the Supporting Information). Aqueous solutions of micelles were prepared by mixing diblock copolymer stock solutions. The copolymer solutions were prepared by dissolving known amounts of copolymer into deionized water (or D_2O for SANS and ^{1}H NOESY experiments) followed by pH adjustment using NaOH and HNO_3. All experiments were performed at 1 mM $NaNO_3$, pH 7.73, and 25.0 °C.

For details on light-scattering, cryo-TEM, SANS, and ^{1}H NMR experiments, see the Supporting Information.

Received: March 14, 2006
Revised: July 7, 2006

Keywords: block copolymers · complex coacervation · micelles · self-assembly

[1] Z. B. Li, E. Kesselman, Y. Talmon, M. A. Hillmyer, T. P. Lodge, *Science* **2004**, *306*, 98.
[2] J. F. Lutz, A. Laschewsky, *Macromol. Chem. Phys.* **2005**, *206*, 813.
[3] R. Erhardt, A. Boker, H. Zettl, H. Kaya, W. Pyckhout-Hintzen, G. Krausch, V. Abetz, A. H. E. Mueller, *Macromolecules* **2001**, *34*, 1069.
[4] C. A. Fustin, V. Abetz, J. F. Gohy, *Eur. Phys. J. E* **2005**, *6*, 291.
[5] W. A. Lopes, H. M. Jaeger, *Nature* **2001**, *414*, 735.
[6] D. J. Pochan, Z. Y. Chen, H. G. Cui, K. Hales, K. Qi, K. L. Wooley, *Science* **2004**, *306*, 94.
[7] M. Dubois, B. Deme, T. Gulik-Krzywicki, J. C. Dedieu, C. Vautrin, S. Desert, E. Perez, T. Zemb, *Nature* **2001**, *411*, 672.
[8] E. A. Lysenko, T. K. Bronich, E. V. Slonkina, A. Eisenberg, V. A. Kabanov, A. V. Kabanov, *Macromolecules* **2002**, *35*, 6351.
[9] D. V. Pergushov, E. V. Remizova, M. Gradzielski, P. Lindner, J. Feldthusen, A. B. Zezin, A. H. E. Mueller, V. A. Kabanov, *Polymer* **2004**, *45*, 367.
[10] J. F. Gohy, E. Khousakoun, N. Willet, S. K. Varshney, R. Jerome, *Macromol. Rapid Commun.* **2004**, *25*, 1536.
[11] M. A. Cohen Stuart, N. A. M. Besseling, R. G. Fokkink, *Langmuir* **1998**, *14*, 6846.
[12] S. van der Burgh, A. de Keizer, M. A. Cohen Stuart, *Langmuir* **2004**, *20*, 1073.
[13] M. A. Cohen Stuart, B. Hofs, I. K. Voets, A. de Keizer, *Curr. Opin. Colloid Interface Sci.* **2005**, *10*, 30.
[14] A. Harada, K. Kataoka, *Macromolecules* **1995**, *28*, 5294.
[15] K. Kataoka, A. Harada, Y. Nagasaki, *Adv. Drug Delivery Rev.* **2001**, *47*, 113.
[16] A. V. Kabanov, T. K. Bronich, V. A. Kabanov, K. Yu, A. Eisenberg, *Macromolecules* **1996**, *29*, 6797.
[17] A. V. Kabanov, V. A. Kabanov, *Adv. Drug Delivery Rev.* **1998**, *30*, 49.
[18] J. F. Gohy, S. K. Varshney, R. Jerome, *Macromolecules* **2001**, *34*, 3361.
[19] M. Silva, J. C. Machado, V. Mano, G. G. Silva, *J. Polym. Sci. Part B* **2003**, *41*, 1493.
[20] R. J. Hefford, *Polymer* **1984**, *25*, 979.
[21] M. B. Perrau, I. Iliopoulos, R. Audebert, *Polymer* **1989**, *30*, 2112.
[22] J. C. Eriksson, S. Ljunggren, *Langmuir* **1990**, *6*, 895.
[23] M. Almgren, *Biochim. Biophys. Acta* **2000**, *1508*, 146.
[24] W. F. Edmonds, Z. B. Li, M. A. Hillmyer, T. P. Lodge, *Macromolecules* **2006**, *39*, 4526.
[25] T. Zemb, M. Dubois, B. Deme, T. Gulik-Krzywicki, *Science* **1999**, *283*, 816.
[26] H. Schmalz, M. G. Lanzendoerfer, V. Abetz, A. H. E. Mueller, *Macromol. Chem. Phys.* **2003**, *204*, 1056.

 © 2006 Wiley-VCH Verlag GmbH & Co. KGaA, Weinheim

[27] D. Taton, A. Z. Wilczewska, M. Destarac, *Macromol. Rapid Commun.* **2001**, *22*, 1497.
[28] P. M. Frederik, D. H. W. Hubert, in *Liposomes Part E*, *Vol. 391*, Elsevier Academic, Amsterdam, **2005**, p. 431.
[29] R. K. Heenan, J. Penfold, S. M. King, *J. Appl. Crystallogr.* **1997**, *30*, 1140.
[30] R. K. Heenan in *RAL Technical Reports* **1989**.

 © 2006 Wiley-VCH Verlag GmbH & Co. KGaA, Weinheim

Carbon Nanotubes

DOI: 10.1002/anie.200601718

Preparation, Purification, Characterization, and Cytotoxicity Assessment of Water-Soluble, Transition-Metal-Free Carbon Nanotube Aggregates**

Hiroyuki Isobe, Takatsugu Tanaka, Rui Maeda, Eisei Noiri, Niclas Solin, Masako Yudasaka, Sumio Iijima, and Eiichi Nakamura**

Besides attracting the attention of scientists and engineers because of potential applications, carbon nanotubes (NTs) are also a subject of concern owing to potential medical and environmental problems.[1–5] As the NTs belong to a class of graphite that is not toxic, the concern resides mainly in the effect of their nanometer dimensions and the tubular structure with curved surface and fullerene-like end caps. There have been conflicting reports on the biological effects of NTs, some reporting high[6–11] and others low toxicity.[12–14] Among the issues that complicate the matter are the catalyst metal contaminants in NTs, which have so far been impossible to remove entirely without destroying the structural entity of NTs. A recent report on the genetic response to NTs indicates that risk assessment studies of NTs to date may be viewed as a sum of the effects of NTs and the transition metals,[15] some of which are known to be toxic by themselves.[1] Another issue is the lack of methods to prepare water-soluble NT particles that are homogeneous enough to ensure validity of the studies on the alleged nanosize effects. The uncontrollable aggregation behavior of NTs, for instance, bundle formation, poses an additional problem that hampers risk assessment studies.[4,5] Note that the surfactants used widely for solubilization of NTs[16,17] are toxic by themselves and must therefore be avoided. We report here the preparation of a homogenous aqueous solution of approximately 130-nm-sized structurally stable aggregates of entirely metal-free single-walled (SW) NTs, the evidence of persistent uptake into the cytoplasm of mammalian cells, and the low-level cytotoxicity of these particles. In the present study, physicochemical properties of NT samples—size distribution, agglomeration state, shape, chemical composition, surface area, surface chemistry, surface charge, and porosity[18]—have been characterized for the first time, and the samples conform to the criteria[4,5] specified for nanomaterials samples suitable for toxicological studies. During the studies, we found that NTs disturb the colorimetric bioassays that have been used for risk assessment tests and hence may have affected the reported toxicities of NT materials.

The carbon nanohorn aggregate[19] (NHA; Scheme 1) is unique among the NT varieties, and its properties make it suitable for risk assessment studies. First, it has all of the properties of NTs except the high aspect ratio of a single isolated NT. Second, since NHA is a covalently bonded class of self-aggregated NTs, its local peripheral morphology represents the terminal region of a single NT, and the global morphology represents spherically assembled NT bundles (see Figure 1 f and Supporting Information). For instance, its bulk morphology resembles a spherical aggregate of metal-containing NTs previously studied for biological assay.[10] Third and most importantly, as NHAs are prepared by laser ablation of a carbon rod without using a transition-metal catalyst, they do not contain any metallic impurities. The NHA as it is prepared forms agglomerates (Scheme 1; cf. Figure 1 c) that cannot be separated physically, and hence they are essentially insoluble in water.

In the first step of our study, we devised a simple and effective method to convert the agglomerates into a water-soluble amino NHAs (a-NHA **2** and its derivatives **3** and **4**) (Scheme 1), which, if necessary, can be chromatographically fractionated according to their size. The approximate molecular weight of these particles as well as the number of the

[*] Dr. H. Isobe, T. Tanaka, R. Maeda, Dr. N. Solin, Prof. E. Nakamura
Department of Chemistry and
Center for NanoBio Integration
The University of Tokyo
Hongo, Bunkyo-ku, Tokyo 113-0033 (Japan)
Fax: (+81) 3-5800-6889
E-mail: hisobe@chem.s.u-tokyo.ac.jp
nakamura@chem.s.u-tokyo.ac.jp
Dr. E. Noiri
University Hospital and Center for NanoBio Integration
The University of Tokyo
Hongo, Bunkyo-ku, Tokyo 113-0033 (Japan)
Dr. M. Yudasaka, Prof. S. Iijima
SORST, JST, NEC Corporation
Tsukuba, Ibaraki 305-8501 (Japan)
Dr. H. Isobe
PRESTO, JST (Japan)
Prof. E. Nakamura
ERATO, JST (Japan)
Prof. S. Iijima
Department of Material Science and Engineering
Meijo University
Shiogamaguchi, Tenpaku, Nagoya, Aichi 468-8502 (Japan)

[**] This study was supported in part by Monbukagakusho, Japan (the 21st Century COE Program for Frontiers in Fundamental Chemistry to E.N., grant-in-aid for Scientific Research, Young Scientists (A) to H.I.). We thank Dr. K. Suenaga and Dr. Z. Liu for TEM analysis, Prof. Y. Umezawa and Dr. M. Sato for advice on confocal microscopy, and Dr. J. Miyawaki for Raman spectroscopic measurements. N.S. thanks the Knut och Alice Wallenbergs Stiftelse (Stockholm, Sweden) for a postdoctoral fellowship.

Supporting information for this article is available on the WWW under http://www.angewandte.org or from the author.

WILEY InterScience DISCOVER SOMETHING GREAT
© 2006 Wiley-VCH Verlag GmbH & Co. KGaA, Weinheim

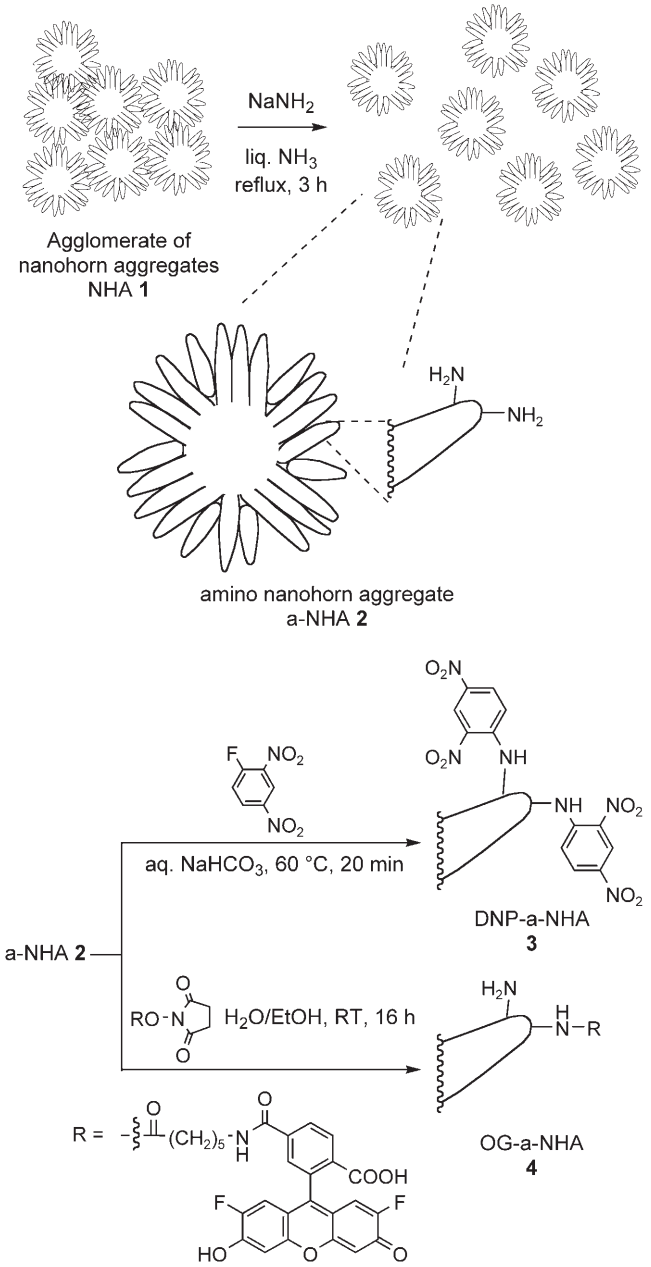

Scheme 1. Chemical transformation of NHA agglomerates into single-particle amino NHA **2** and subsequent derivatization.

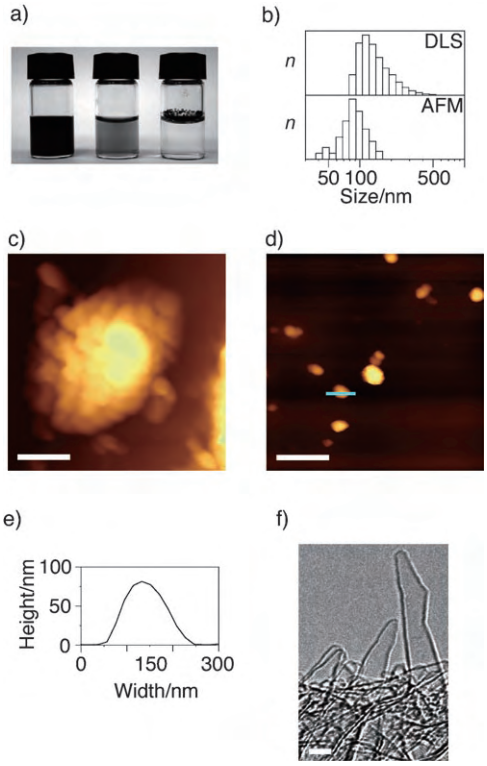

Figure 1. Carbon nanohorn aggregate. a) Photographs of solutions of a-NHA **2** in water at concentrations of 1 mg mL^{-1} (left) and 0.02 mg mL^{-1} (center) and intact NHA (right). b) Size distribution of **2** in water (0.2 mg mL^{-1}) determined by DLS analysis (top) and of a solution of **2** deposited on mica determined by AFM analysis (bottom). The AFM data was obtained by the height analysis of 117 particles in four images. An average dimensional aspect ratio of the particles was measured to be 2.5:1. c) An AFM image of agglomerate of NHA **1** deposited on HOPG. The outline of single NHA particles in the agglomerate can be seen. Scale bar: 500 nm. d) An AFM image of **2** deposited on mica. Scale bar: 500 nm. e) The height profile of an a-NHA particle measured along the blue line in Figure 1 d. f) TEM image of a-NHA **2** showing that no damage was caused by the $NaNH_2$ treatment. Scale bar: 2 nm.

amino groups attached to them has been determined (see below). We found that, upon treatment with $NaNH_2$, the NHA agglomerates can be converted, in their entirety, into water-soluble a-NHA **2** (Scheme 1). Treatment of 1.00 g of NHA with $NaNH_2$ in refluxing liquid NH_3 (−33 °C) for 3 h, followed by evaporative removal of NH_3 and washing with aq. NH_4Cl afforded 1.03 g of a-NHA **2** as a black power. Though the reaction did not cause any obvious change of the powder behavior, the material was now soluble in water. Dilution of **2** in ultrapure water with sonication resulted in a homogeneous black solution with a concentration of up to 1 mg mL^{-1}. This method for solubilization features low-temperature and basic conditions in contrast to the previously reported methods that generally rely on oxidation with nitric acid or hot oxygen gas. Note that liquid NH_3 and $NaNH_2$ can be readily removed at room temperature by evaporation and washing with water.

The bulk properties of the aqueous solution of **2** were characterized by dynamic laser light scattering (DLS), atomic force microscopy (AFM), and ζ potential measurement. Figure 1 a shows homogeneous solutions of **2** with concentrations of 1 mg mL^{-1} and 0.02 mg mL^{-1}, which leave no insoluble materials upon filtration through a 5-μm-pore membrane filter. The vial on the right contains a suspension of the insoluble NHA agglomerate at a concentration of 0.2 mg mL^{-1}. DLS analysis of more dilute solution of **2** (0.2 mg mL^{-1}; Figure 1 b) indicates that the solution contains isolated particles of 134 ± 5 nm (average diameter). The size distribution was found to be stable for several months, and the particles did not show any sign of reagglomerization.

AFM analysis of the solution deposited on mica surface showed spheroidal particles distributed on the surface as in Figure 1 d. The morphology is entirely different from that of

 © 2006 Wiley-VCH Verlag GmbH & Co. KGaA, Weinheim

the NHA agglomerate (Figure 1c). The particles have an average height of 95 nm and an aspect ratio of 2.5:1 (Figure 1d). Such particles would be measured as 122–156 nm by DLS,[20] which agrees with the average DLS value of 134 nm. The data also agree with the size estimated previously by transmission electron microscopy (TEM).[19] The average particle size (based on AFM) corresponds to an approximate volume of $1–3\times10^{-21}$ m^3. This value coupled with the reported density of 1.25 g mL^{-1}[18] leads to an estimated molecular weight of $8–20\times10^8$ Da, which in turn results in an estimate of $3–7\times10^{11}$ particles per mL in a solution of **2** with a concentration of 1 mg mL^{-1}. The ζ potential of **2** in ultrapure water was found to be −28 mV. Such negative potentials have been commonly found for carbonaceous materials such as SWNTs and carbon black.[13,21]

a-NHA **2** can be separated into fractions according to particle size. After chromatographic purification of the solution (0.2 mg mL^{-1}) on a polyacrylamide size-exclusion column 92% of the material was recovered (see the chromatogram in Figure 2a). As evident in the DLS data

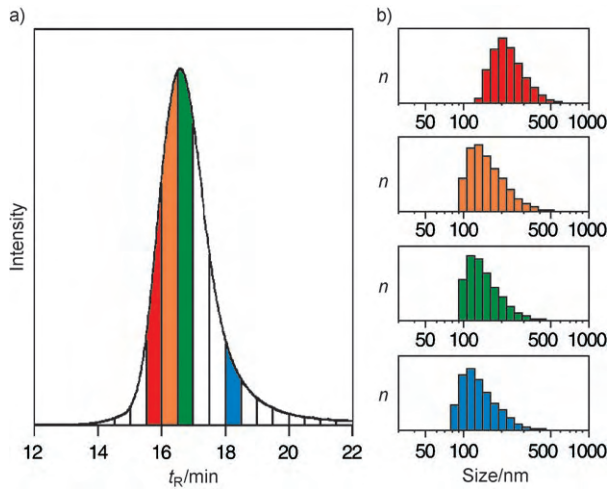

Figure 2. Fractionation of a-NHA **2** by gel permeation column chromatography. a) Chromatogram of **2** (0.2 mg mL^{-1}, 0.5 mL) eluted on Sephacryl 500HR (bed volume: 17 mL, detection: 260 nm). Fractions collected at t_R = 15.5 min (red); t_R = 16.0 min (orange); t_R = 16.5 min (green); t_R = 18.0 min (blue). b) DLS analysis of the representative fractions. Mean sizes of particles in fractions are 198 ± 17, 148 ± 1, 134 ± 6 and 127 ± 7 nm, respectively. The color code of the fractions corresponds to the colored fractions in (a). t_R = time of retention.

measured for four representative fractions (Figure 2b), chromatographic separation of a-NHA of various sizes (127, 134, 148, and 198 nm, mean diameter) has been achieved. We expect that further optimization of the chromatographic conditions will result in better resolution.

Chemical characterization of the water-soluble NHA indicated that $NaNH_2$ treatment has introduced amino groups on the surface of the graphitic structure. Careful TEM observation (Figure 1f and Supporting Information) showed that there has been no change of the gross SWNT structure; that is, neither holes nor added materials were observed. The UV/Vis spectra of **2** in water show a broad absorbance due to the tubular graphite (Supporting Information). Thermal gravimetric analysis (TGA) and Raman spectra suggest that the amination reaction under mild conditions did not cause any significant change of the gross NHA structure.[22,23] The presence and the quantity of the amino groups on **2** were determined by the Sanger method used widely for characterization of amino groups in proteins.[24] Treatment of **2** with 4-fluoro-1,3-dinitrobenzene (Scheme 1) gave a water-soluble black powder that exhibits an absorption at 350 nm (Supporting Information). This is characteristic of the dinitrophenylamino (DNP) group and is not observed for the two starting materials. Neither excess reagent nor longer reaction time led to an increase of the 350-nm absorption, and we conclude that all available amino groups have been dinitrophenylated.

On the basis of the known molar absorption coefficient of the DNP group and the value measured for DNP-a-NHA (**3**), we calculate the amount of the amino group to be 0.22 μmol mg^{-1}. A density of one amino group per 380 carbon atoms can be thus calculated. It is reasonable to assume that the amination reaction took place on the exposed surface, which can be estimated from the surface area available for N_2 absorption. The reported surface area of NHA, 308 m^2 g^{-1}, [18] and the calculated amine density gives an estimated amine density on the surface to be one amino group per 46 carbon atoms. This ratio suggests that the reaction occurred on the reactive cap or bent regions rather than on the smooth surface of the tube.

Similarly, we introduced fluorescent Oregon Green (OG) dye to the a-NHA. To maintain water-solubility, we exposed the fluorescent probe to only 8% of the available amino groups. The presence and the amount of the probe were determined by quantitative absorption and fluorescence spectroscopic analysis (Supporting Information).

With the physicochemical data of the soluble NHAs in hand, we investigated the cell uptake and the toxicity of this material. The soluble labeled OG-a-NHA **4** (Scheme 1, used as such without fractionation of particles) was incubated with growing mammalian cells (3T3 and HeLa cells), and the cell uptake was monitored by flow cytometry (FCM). As shown in Figure 3, the amount of **4** in the cells showed dose- (0.01 mg mL^{-1} vs. 0.05 mg mL^{-1}) and time-dependent increase.[12,13,25] Notably, the uptake per cell increased persistently for 22 h.

The location of OG-a-NHA **4** in the cells after an incubation time of 20 h was determined by microscopy (Figure 3c and d). The black spots several μm in size seen in Figure 3c are agglomerates of **4** located within the cytoplasm.[26] Smaller particles of **4** are seen as green fluorescent particles in Figure 3d. The cell membrane stained by FM4-64 appears red in Figure 3d, and the yellowish area represents the overlap of the red and green colors, thus indicating that **4** is not located in the outer cell membrane but within the cytoplasm.

Having learned that a-NHA readily enters into mammalian cells, we next examined its cytotoxicity. We used quartz particles of 5 μm in size and TiO_2 particles of 25–70 nm in size (primarily anatase) as controls.[4] While both are used widely

 © 2006 Wiley-VCH Verlag GmbH & Co. KGaA, Weinheim

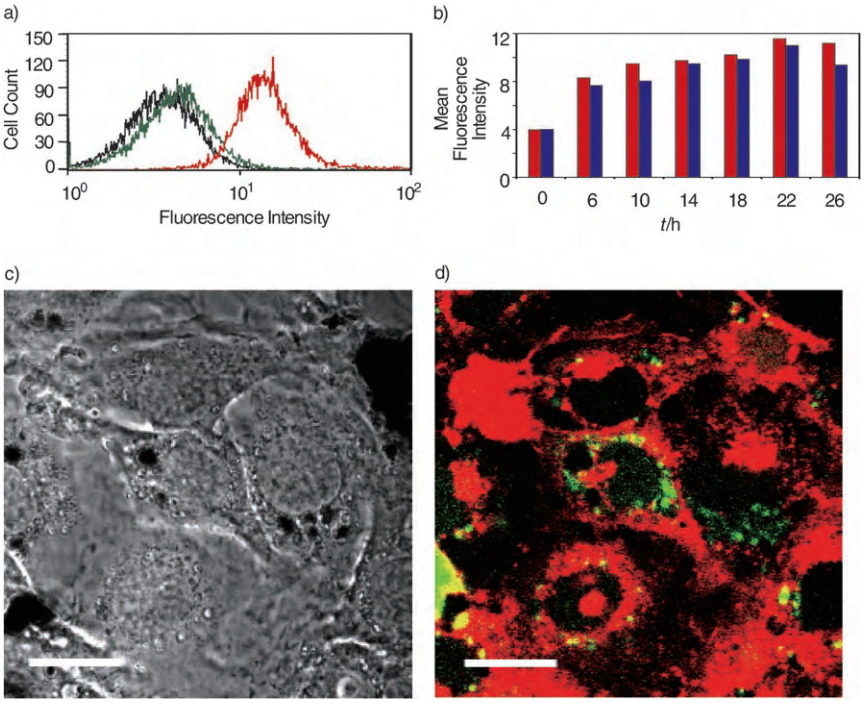

Figure 3. FCM and confocal microscopic analysis of OG-a-NHA **4** taken up by cultured mammalian cells. a) Fluorescence histograms of control cells (black; 3T3 cells) and cells incubated with **4** at concentrations of 0.01 mg mL^{-1} (green) and 0.05 mg mL^{-1} (red). b) Time-dependent fluorescent intensity of cells (3T3: red; HeLa: blue) incubated with **4** (0.05 mg mL^{-1}). c) Phase contrast image of 3T3 cells after incubation with **4** (0.05 mg mL^{-1}) for 20 h. Scale bar: 20 μm. d) Confocal microscope image of the same region as in (c). OG-a-NHA **4** was observed with the fluorescence at 518 nm (green), and the cell membrane was stained with FM4-64 and observed with the fluorescence at 590 nm (red).

in industry, the former shows a certain level of cytotoxicity[7,8] and the latter is considered nontoxic. We examined the cytotoxicity for two standard cell lines (3T3 and HeLa cells) by using quantitative Bradford protein assay,[27] where the protein is freed of the carbon material at the time of analysis (vide infra). In the quartz control experiments for 3T3 cells, 0.1 mg mL^{-1} of the quartz powder dropped the cell activity to 75% and 1 mg mL^{-1} to 28%, but TiO_2 showed no cytotoxicity up to 1 mg mL^{-1}. As shown in Figure 4, a-NHA **2** shows no cytotoxicity up to 0.1 mg mL^{-1}, but at the 1.0-mg dose the cell activity dropped to 78% (3T3) and 74% (HeLa). The cytotoxicity of the a-NHA is therefore one-tenth of that of quartz microparticles by weight.

In conclusion, aminative deagglomerization of NHA agglomerates resulted, for the first time, in the high-yielding preparation of well-characterized NHA, which form homogeneous aqueous solutions of primary particles of uniform size distribution. Unlike the NT materials synthesized under transition-metal catalysis, our samples do not contain any transition-metal impurities. The preparative method is very simple and amenable to large-scale syntheses. The primary particles thus obtained could not be disintegrated further into individual NTs either physically or chemically. Therefore, the amino NHA particle may be regarded as a big macromolecule. The amination method and subsequent chromatographic purification provide transition-metal-free SWNT materials that are available in a variety of sizes ranging from 80 nm to 400 nm; these materials may thus serve as standards for risk assessment of carbon nanoparticles. In a sense, the amino NHA is a congener of water-soluble fullerenes, whose biological activities have been studied since the early 1990s.[28–34]

As expected for water-soluble materials 100 nm in size,[35] the amino NHA is taken up by mammalian cells but does not show significant cytotoxicity; in fact, the cytotoxicity is much lower than that of the quartz microparticles widely used in road-marking paints. Nonetheless, appropriate care must be taken in handling since it would be persistently taken up by growing cells. We argue that the observed level of cytotoxicity may possibly arise from the removal of necessary nutrients by absorption on the surface (see below), chemical effects of the amino groups attached to the NHA surface, or certain profound effects of the nanographitic structure on the crucial mechanism of life. The low toxicity described above stands in contrast to some reports reporting that NTs are much more toxic than quartz microparticles.[8–10] In addition to the problem of the metal impurities discussed above,

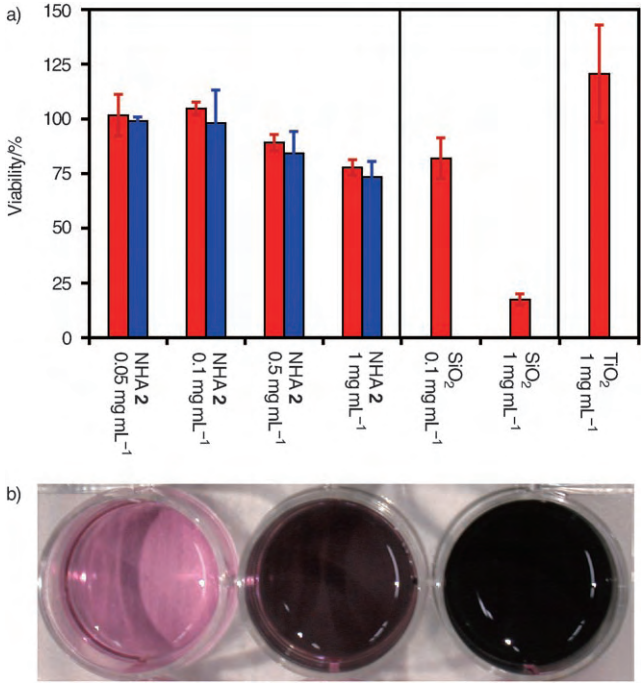

Figure 4. Cytotoxicity assessment of a-NHA. a) Viability of 3T3 (red) and HeLa (blue) cells after incubation with particles for 24 h. Viability was determined by the Bradford assay. b) Photograph of culture dish of 3T3 cells. Control (left, pink color due to phenol red pH indicator) and in the presence of a-NHA **2** at the concentrations of 0.1 mg mL^{-1} (center) and 1 mg mL^{-1} (right).

© 2006 Wiley-VCH Verlag GmbH & Co. KGaA, Weinheim

another caveat of the bioassays of NT-like compounds that we discovered in the present study is that such graphitic materials reduce the coloration of the aromatic dye employed in the assay and hence result in false data. Thus, dye-based assays of cell viability such as the MTT (3-(4,5-dimethylthiazol-2-yl)-2,5-diphenyltetrazolium bromide) assay, the Alamar Blue test, and the propidium iodide test, which have been used in the NT bioassays, uniformly gave us incorrect results unless care was taken to prevent contact of the graphitic materials with the dye (details in the Supporting Information).

Received: May 2, 2006
Revised: July 27, 2006

Keywords: amination · cellular uptake · liquid chromatography · nanotubes · toxicology

[1] V. L. Colvin, *Nat. Biotechnol.* **2003**, *21*, 1166 – 1170.
[2] R. F. Service, *Science* **2004**, *304*, 1732 – 1734.
[3] R. F. Service, *Science* **2005**, *310*, 1609.
[4] G. Oberdörster, A. Maynard, K. Donaldson, V. Castranova, J. Fitzpatrick, K. Ausman, J. Carter, B. Karn, W. Kreyling, D. Lai, S. Olin, N. Monteiro-Riviere, D. Warheit, H. Yang, *Part. Fibre Toxicol.* **2005**, *2*, (http://www.particleandfibretoxicology.com/content/2/1/8/).
[5] R. H. Hurt, M. Monthioux, A. Kane, *Carbon* **2006**, *44*, 1028 – 1033.
[6] D. B. Warheit, B. R. Laurence, K. L. Reed, D. H. Roach, G. A. M. Reynolds, T. R. Webb, *Toxicol. Sci.* **2004**, *47*, 117 – 125.
[7] C.-W. Lam, J. T. James, R. McCluskey, R. L. Hunter, *Toxicol. Sci.* **2004**, *47*, 126 – 134.
[8] G. Jia, H. Wang, L. Yan, X. Wang, R. Pei, T. Yan, Y. Zhao, X. Guo, *Environ. Sci. Technol.* **2005**, *39*, 1378 – 1383.
[9] L. E. Murr, K. M. Garza, K. F. Soto, A. Carrasco, T. G. Powell, D. A. Ramires, P. A. Guerrero, D. A. Lopez, J. Venzor III, *Int. J. Environ. Res. Public Health* **2005**, *2*, 31 – 42.
[10] K. F. Soto, A. Carrosco, T. G. Powell, K. M. Garza, L. E. Murr, *J. Nanopart. Res.* **2005**, *7*, 145 – 169.
[11] S. K. Manna, S. Sarkar, J. Barr, K. Wise, E. V. Berrera, O. Jejelowo, A. C. Rice-Ficht, G. T. Ramesh, *Nano Lett.* **2005**, *5*, 1676 – 1684.
[12] D. Pantarotto, J.-P. Briand, M. Prato, A. Bianco, *Chem. Commun.* **2004**, 16 – 17.
[13] N. W. S. Kam, T. P. Jessop, P. A. Wender, H. Dai, *J. Am. Chem. Soc.* **2004**, *126*, 6850 – 6851.
[14] T. Murakami, K. Ajima, J. Miyawaki, M. Yudasaka, S. Iijima, K. Shiba, *Mol. Pharm.* **2004**, *1*, 399 – 405.
[15] L. Ding, J. Stilwell, T. Zhang, O. Elboudwarej, H. Jiang, J. P. Selegue, P. A. Kooke, J. W. Gray, F. F. Chen, *Nano Lett.* **2005**, *5*, 2448 – 2464.
[16] M. J. O'Connell, S. M. Bachilo, C. B. Huffman, V. C. Moore, M. S. Strano, E. H. Haroz, K. L. Rialon, P. J. Boul, W. H. Noon, C. Kittrell, J. Ma, R. H. Hauge, R. B. Weisman, R. E. Smalley, *Science* **2002**, *297*, 593 – 596.
[17] M. Zhang, M. Yudasaka, J. Miyawaki, J. Fan, S. Iijima, *J. Phys. Chem. B* **2005**, *109*, 22201 – 22204.
[18] K. Murata, K. Kaneko, F. Kokai, K. Takahashi, M. Yudasaka, S. Iijima, *Chem. Phys. Lett.* **2000**, *331*, 14 – 20.
[19] S. Iijima, M. Yudasaka, R. Yamada, S. Bandow, K. Suenaga, F. Kokai, K. Takahashi, *Chem. Phys. Lett.* **1999**, *309*, 165 – 170.
[20] W. Van De Sande, A. J. Persoons, *Phys. Chem.* **1985**, *89*, 404 – 406.
[21] R. Xu, *Particle Characterization: Light Scattering Methods*, Kluwer, Dordrecht, Netherlands, **2000**, pp. 289 – 343.
[22] Weight loss of **2** occurred at 560 °C in TGA, which is slightly lower than that observed for the intact NHA (J. Miyawaki, M. Yudasaka, S. Iijima, *J. Phys. Chem. B* **2004**, *108*, 10732 – 10735).
[23] The intensity ratio of the G-band (1590 cm^{-1}) and the D-band (1350 cm^{-1}) in Raman spectra of **2** and intact NHA were 0.96 and 0.91, respectively.
[24] C. H. W. Hirs, *Methods Enzymol.* **1967**, *11*, 548 – 555.
[25] N. W. S. Kam, Z. Liu, H. Dai, *Angew. Chem.* **2006**, *118*, 591 – 595; *Angew. Chem. Int. Ed.* **2006**, *45*, 577 – 581.
[26] Since the larger particles of the NHA scatter light and are seen as black in the image, the actual amount of **4** in cells would be greater than that determined with FCM.
[27] M. M. Bradford, *Anal. Biochem.* **1976**, *72*, 248 – 254.
[28] S. H. Friedman, D. L. DeCamp, R. P. Sijbesma, G. Srdanov, F. Wudl, G. L. Kenyon, *J. Am. Chem. Soc.* **1993**, *115*, 6506 – 6509.
[29] R. F. Schinazi, R. Sijbesma, G. Srdanov, C. L. Hill, F. Wudl, *Antimicrob. Agents Chemother.* **1993**, *37*, 1707 – 1710.
[30] H. Tokuyama, S. Yamago, E. Nakamura, T. Shiraki, Y. Sugiura, *J. Am. Chem. Soc.* **1993**, *115*, 7918 – 7919.
[31] S. Yamago, H. Tokuyama, E. Nakamura, K. Kikuchi, S. Kananishi, K. Sueki, H. Nakahara, S. Enomoto, F. Ambe, *Chem. Biol.* **1995**, *2*, 385 – 389.
[32] E. Nakamura, H. Isobe, N. Tomita, M. Sawamura, S. Jinno, H. Okayama, *Angew. Chem.* **2000**, *112*, 4424 – 4427; *Angew. Chem. Int. Ed.* **2000**, *39*, 4254 – 4257; .
[33] S. Bosi, T. Da Ros, G. Spalluto, M. Prato, *Eur. J. Med. Chem.* **2003**, *38*, 913 – 923.
[34] E. Nakamura, H. Isobe, *Acc. Chem. Res.* **2003**, *36*, 807 – 815.
[35] H. Isobe, W. Nakanishi, N. Tomita, S. Jinno, H. Okayama, E. Nakamura, Chem. Asian J. **2006**, *1*, 167 – 175.
[36] H. Gao, W. Shi, L. B. Freund, *Proc. Natl. Acad. Sci. USA* **2005**, *102*, 9469 – 9474.

 © 2006 Wiley-VCH Verlag GmbH & Co. KGaA, Weinheim

Host–Guest Systems

DOI: 10.1002/anie.200601726

$(Ca_7N_4)[M_x]$ (M = Ag, Ga, In, Tl): Linear Metal Chains as Guests in a Subnitride Host**

*Peter Höhn, Gudrun Auffermann, Reiner Ramlau, Helge Rosner, Walter Schnelle, and Rüdiger Kniep**

A large number of ternary nitrides of the alkaline-earth metals (EA) with main-group or transition-metal elements contain "isolated" nitride ions, which are in an octahedral coordination environment and surrounded only by EA atoms. Condensation of the coordination polyhedra (EA_6N) through common corners and edges leads to structural patterns of various dimensionalities with different kinds of cavities,[1] which contain main-group and transition-metal species with various homo- or heteronuclear interconnections (e.g., $(Sr_6N)[Ga_5]$,[2] $(Sr_5N)[NbN_4]$,[3] $(Ca_3N)_2[FeN_3]$,[4] $(Ca_4N)[In_2]$,[5] $(Ca_3N)[Au]$[6]). Ternary nitrides with the composition $(Ca_7N_4)[M_x]$ (M = Ag, Ga, In, Tl) were first investigated in the late 1990s.[7,8] As essential details of the crystal structures remained unclear at that time, the data stayed unpublished. The main problems in understanding the chemical bonding in these compounds arose from the assumption that the (Ca_7N_4) partial structure should be positively charged (2+) and from the fact that the $[M_x]$ partial structure, an infinite linear chain, could not be clearly resolved (e.g., the value of x and the question as to whether there are additional N atoms within the chains). Meanwhile, we investigated the redox intercalation of binary EA subnitrides (EA_2N) and the formation of nitride diazenides.[9–11] The reactions are clearly controlled by EA species in a low-valence state (+1.5), which are structurally characterized by atomic positions associated with three condensed EA_6N octahedra ($EA_{6/3}N \triangleq EA_2N$). By taking into account this structural peculiarity of the low-valency EA species and by applying this principle to the $(Ca_7N_4)[M_x]$ series, we see that the Ca/N partial structure immediately appears as an uncharged mixed-valency subnitride ($Ca_3^{2+}Ca_4^{1.5+}N_4^{3-}$). The situation is depicted in Figure 1 and leads to the conclusion that there is no need for further charge balancing, which makes the central (linear) M_x chains an object of special interest.[12]

Single crystals of the highly hygroscopic phases, $(Ca_7N_4)[M_x]$, are obtained by treatment of Ca_3N_2 with M under N_2 or Ar at temperatures of approximately 1000 K.[13] The crystal structures of the orthorhombic phases (*Pbam*) were determined from X-ray data.[14] The (Ca_7N_4) framework consists of 2 × 2 chains of edge- and corner-sharing octahedra connected through common apices to form large channels running along [001]; M atoms are located inside the channels. A precise determination of the positional parameters for M from the diffraction data was virtually impossible.[14] As judged from electron-density calculations, the compositional indices, x, for the in-channel positions depend on the size of the M atoms and decrease with increasing size of the metal atom. The shapes and cross sections of the channels also depend on the M species incorporated, that is, increasing the size of the metal atom causes increasing "orthogonality". In contrast, the rigidity of the octahedral Ca/N building blocks (2 × 2 chains) is clarified by the almost constant c lattice parameter, which is independent of the in-channel M species. Relevant data that characterizes the crystal structures of the series $(Ca_7N_4)[M_x]$, M = Ag, Ga, In, and Tl, are included in Figure 1 and Figure 2 with the given parameter x derived from the crystal-structure refinements. The values of x should be taken as a first approximation and provide a first basis for comparison with the other experimental and theoretical results discussed below.

High-resolution electron microscopy (HREM) and electron diffraction (ED) were performed to obtain more information about the positions of the M atoms within the channels. Unfortunately, all representatives of the $(Ca_7N_4)[M_x]$ family readily hydrolyze when exposed to air, and only specimens of the silver compound, $(Ca_7N_4)[Ag_{1.36}]$, were amenable to ED experiments after preparation and transfer to the electron microscope under a strictly inert-gas atmosphere. High-quality HREM imaging was not possi-

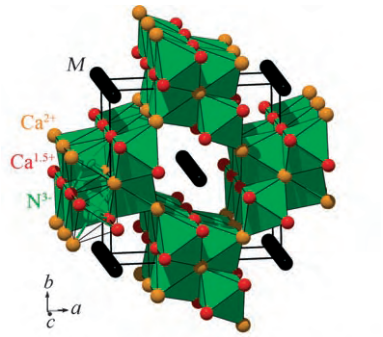

Pbam	Ag	Ga	In	Tl
Color	brass	bronze	bronze	brass
a [pm]	1145[a]	1147[b]	1168[b]	1158[b]
b [pm]	1203[a]	1208[b]	1213[b]	1200[b]
c [pm]	365[a]	364[b]	364[b]	363[b]
x	1.36	1.33	1.02	0.97
d(M-M) [pm]	269	274	356	373

[a] Neutron powder data.
[b] X-ray single crystal data.

Figure 1. Crystal structure of $(Ca_7N_4)[M_x]$. (Ca_7N_4) framework in polyhedral representation; the assignment of Ca^{2+} (orange) and $Ca^{1.5+}$ (red) ions is emphasized. $[M_x]$ is represented by black cylindrical rods inside the channels. Table: lattice parameters (space group *Pbam*) and occupancy x for $(Ca_7N_4)[M_x]$.[14]

[*] Dr. P. Höhn, Dr. G. Auffermann, Dr. R. Ramlau, Dr. H. Rosner, Dr. W. Schnelle, Prof. Dr. R. Kniep
Max-Planck-Institut für Chemische Physik fester Stoffe
Nöthnitzer Strasse 40, 01187 Dresden (Germany)
Fax: (+49) 351-46-46-3002
E-mail: kniep@cpfs.mpg.de

[**] We thank the Fonds der Chemischen Industrie for generous support, Ulrich Schwarz for fruitful discussions, Ulrike Schmidt and Anja Völzke for chemical analyses, Ralf Koban for physical properties measurements, and the BENSC (HMI Berlin) for access to their neutron facilities. H.R. thanks the Emmy Noether-Programm for financial support.

© 2006 Wiley-VCH Verlag GmbH & Co. KGaA, Weinheim

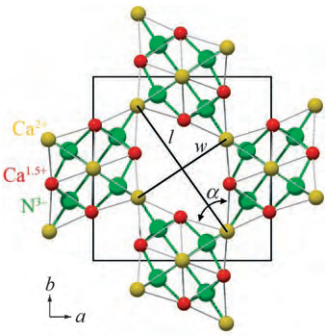

	$Ag_{1.36}$	$Ga_{1.33}$	$In_{1.02}$	$Tl_{0.97}$
l [pm]	1011	994	975	934
w [pm]	678	699	736	761
α [°]	67.7	70.2	74.1	78.3

Figure 2. Projection on the Ca/N partial structure along [001]. The shape of the channel is specified by the aperture angle α and the diagonals l and w of the rhombic cross section. Table: Values for l, w, and α are governed by the type of metal atom.

ble.[16] Selected-area electron diffraction (SAED) patterns of $(Ca_7N_4)[Ag_{1.36}]$ were registered for the [100], [110], and [010] zones (Figure 3). In all three zones, continuous diffuse lines can be discerned in addition to the Bragg reflections of the subnitride (and a product arising from hydrolyzation). Reconstruction in 3D reciprocal space results in sheets of diffuse intensity described by the plane equation $R = G \pm \varepsilon a^* \pm \eta b^* \pm \gamma c^*$, with ε, η being continuous variables and $\gamma = 1.357(25)$, which appear as first-order "satellites" to the subnitride Bragg-reflections $G = [hkl]^*$. Very weak second-order satellite sheets (lines) are also present. Such diffuse sheets are indicative of a 2D disordered (1D ordered) structure or substructure,[17] that is, perfectly periodic, identical, and parallel chains of atoms, which are not arranged regularly with respect to each other. Since two Laue conditions are violated, the scattering is concentrated on a family of parallel sheets (of first and higher order), which are normal to the chains of atoms and show a spacing that corresponds to the translational period along the chains. On the one hand, diffuse sheets of higher than first order are hardly visible. On the other hand, the pair of first-order sheets is multiplied by double (or multiple) diffraction, which is much more prevalent in ED than in X-ray or neutron diffraction.[18] As a result of double diffraction, a first-order pair of diffuse lines accompanies every systematic row of strong Bragg reflections, which extends horizontally, that is, orthogonally to c^* (Figure 3). In summary, the ED experiment shows that 1) the Ag atoms form chains with equidistant d(Ag–Ag) separations of 270(5) pm; 2) the chains are incommensurate with the subnitride structure; 3) there is no correlation between the z coordinates of Ag atoms (chains) in different channels, that is, the Ag chains are arbitrarily shifted along the channels.[17] Although it cannot be completely excluded that the chains might be interrupted by vacancies, thus leading to a loss of correlation even along a single channel, we favor the picture of the infinite chains with d(Ag–Ag) 270(5) pm, which gives $x = 1.36$, a value consistent with that derived from X-ray data ($x = 1.36$, d(Ag–Ag) 269 pm; Figure 1).[14] The incommensurate host–guest arrangement and the missing correlation between the Ag guest chains suggest quasi 1D behavior of these structural elements. Similar linear metal chains are observed in high-pressure modifications of the main-group elements K, Rb, Sr, Ba, As, Sb, and Bi,[19] and the transition metal, Sc.[20] The pairing of atoms within the 1D substructures, which is predicted to result from a Peierls distortion, is still under debate. To investigate the hypothesis of weakly interacting chains in a rigid host framework, electronic-structure calculations by using a full-potential local-orbital (FPLO) code were carried out.[21] To estimate the host–guest interaction, we calculated the band structure and the density of states (DOS) of a series of commensurate approximants. In all cases, only weak hybridization of the guest chains with the host lattice has been obtained. The band structure shows very pronounced 1D bands for the orbitals related to the guest chains, especially for the valence p_z orbitals. In the DOS, the corresponding van Hove singularities are present. Thus, the weak host–guest interaction estimated this way justifies the simulation of the guest chains by free, infinite, 1D chains. The in-chain bond length was optimized by using the total energy (Figure 4). The resulting value d(Ag–Ag) 266 pm is in good agreement with the bond lengths derived from SAED (270 pm) and from X-ray data (269 pm), thereby confirm-

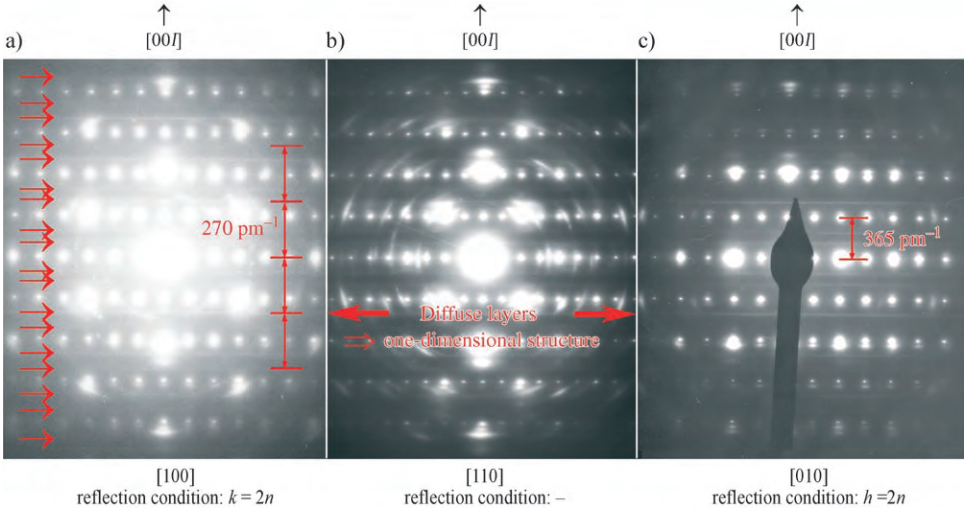

Figure 3. SAED patterns of $(Ca_7N_4)[Ag_x]$ in a) [100], b) [110], and c) [010] orientation taken from different microcrystals. All three patterns show continuous diffuse lines, which extend orthogonally to c^*. They appear as first-order "satellites" to the subnitride Bragg reflections at a distance $|q| = \gamma |c^*|$ with $\gamma = 1.357 \pm 0.025$. For further interpretation see text. The textured rings are attributed to some hydrolyzation product of the hypersensitive compound. The reason for the splitting of Bragg reflections is still unknown.

 © 2006 Wiley-VCH Verlag GmbH & Co. KGaA, Weinheim

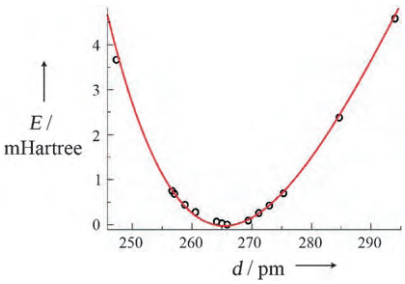

Figure 4. Energy versus bond length for an infinite, equidistant, and linear chain of Ag atoms. The red line is a fourth-order fit to the calculated data. The energy of the minimum at 266 pm is set to zero.

ing the picture of incommensurate metallic, 1D Ag guest chains in the (Ca_7N_4) subnitride host channels (Figure 5). The slightly smaller lattice parameter (about 1%) for the guest chain compared with the experimental data is a well-known systematic error arising from the local density approximation (LDA). We know from previous experience that the good agreement of the band-structure results with the guest chains and the experimental data is a strong indication of the excellent quality of the approximation of non-interacting guest chains in a rigid host. However, the metallic character of the resistivity (see below) for the Ag and the Ga compounds implies that the remaining interaction between the host and guest lattice is strong enough to inhibit a Peierls distortion, which would occur for a purely 1D chain and cause an insulating ground state. A detailed theoretical study of the host–guest interaction and its impact on the electronic structure will be undertaken.

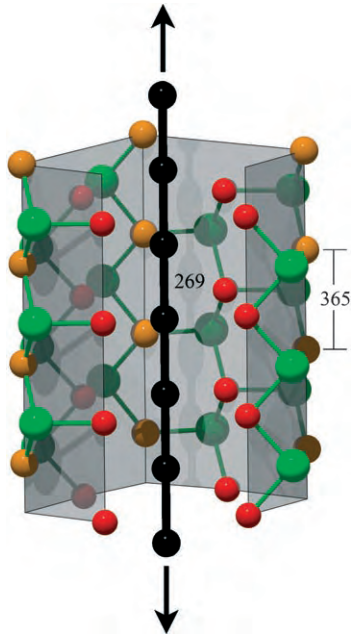

Figure 5. [$Ag_{1.36}$] chain within a channel formed by the subnitride (Ca_7N_4). Front octahedra of the channel are omitted for clarity; Ca^{2+} orange, $Ca^{1.5+}$ red, and N green. Incommensurability is indicated by the given values for c (365 pm) and d(Ag–Ag) (269 pm, from X-ray data).

The optimization of the in-chain bonding distance d(M–M) by using the total energy, which is obtained by the same procedure as that presented in Figure 4, yields 278 pm (M = Ga), 305 pm (In), and 317 pm (Tl). Although the calculated value for the Ga chain is in good agreement with the distance derived from the X-ray investigation ($x = 1.33$, d(Ga–Ga) 274 pm), the calculated distances for In and Tl are much shorter than the respective values based on $x = 1.02$ (d(In–In) 356 pm) and $x = 0.97$ (d(Tl–Tl) 373 pm).[14]

For (Ca_7N_4)[In_x], we were able to prepare a larger amount of single-phase material and a chemical analysis was carried out that gave $x = 1.06(1)$,[22] which is close to the X-ray value ($x = 1.02$) and is unequivocally smaller than the value obtained by calculations based on the assumption that the chains of In atoms are equidistant, $x = 1.19$. This lower value suggests the presence of In–In chain fragments within the host channels with average lengths consistent with the observed composition. The same model holds for the Tl compound. To date, there is no evidence for significant variations in the compositional index, x, for the In and Tl compounds, but this observation has to be investigated in more detail.

From a structural point of view, the (Ca_7N_4)[M_x] family can be divided into two groups: the Ag and Ga compounds with infinite host chains of equidistant metal atoms, and the In and Tl phases, which contain metal-chain fragments. For infinite chains, metallic conductivity can be expected, whereas segments of metallic chains would exhibit activated electronic conduction.

The electrical resistivities, $\rho(T)$, of cold-pressed powder samples of the four compounds were investigated by using the van der auw method (Figure 6). The Ag compound clearly

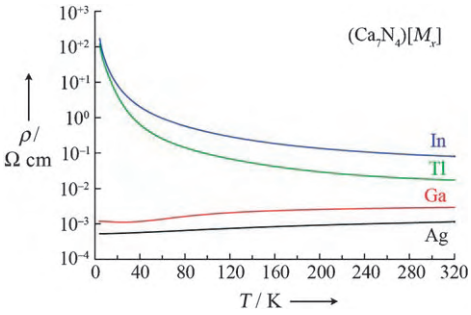

Figure 6. Electrical resistivity, ρ, versus temperature, T, for cold-pressed powder samples of (Ca_7N_4)[M_x]. The measurement was performed by the van der Pauw method in a die cell made of a sapphire crystal.

displays a linear temperature dependence with $\rho(T)$ increasing with T and a room-temperature resistivity around 1 mΩ cm, which indicates a metallic conductor, albeit a poor one. The resistivity of the Ga compound is metallic above about 30 K (increasing with temperature), but shows a weak upturn below this temperature. The In and Tl compounds exhibit a thermally activated conduction mechanism. Note in powder samples, the metallic regions of the crystallites are generally interrupted, thus increasing the overall resistivity. In the In and Tl compounds, the metal chains are assumed to be

 © 2006 Wiley-VCH Verlag GmbH & Co. KGaA, Weinheim

interrupted on the atomic scale. Simple statistics suggest that with the given values of x and the calculated equilibrium distances of the M atoms, average chain lengths for M = In and Tl are 1824 and 1794 pm, respectively. A closer inspection of the temperature dependence of $1/\rho$ of these samples reveals that their conduction mechanism can be well described by 3D variable range hopping with an exponent $\gamma = 1/4$,[23] as could be expected for an ensemble of fragmented conducting, metallic chains. Only the Ag compound behaves like a metal powder a result that is compatible with uninterrupted infinite chains of M.

Powdered samples of $(Ca_7N_4)[M_x]$ (M = Ag, Ga, In, and Tl) show a paramagnetic susceptibility (Figure 7). The susceptibilities are interpreted as the sum of weakly temperature-dependent paramagnetic contributions and low-temperature upturns from Curie-like impurities. Thus, the materials are Pauli-paramagnetic metals with occupied states at the Fermi level, E_F, which confirms the metallic character of the chains or chain segments in all four compounds. The weakly temperature-dependent Pauli-paramagnetic contribution, χ_P, and the diamagnetic core contributions, χ_{dia}, can not be separated easily. However, we estimate $\chi_P \approx 300 \times 10^{-6}$ emu mol^{-1} for the Ag and In compounds. This value corresponds to a density of states, $N(E_F) =$ 9–10 states eV^{-1} f.u.$^{-1}$ (f.u. = formula unit). For the compounds with M = Ga, Tl, about half the density of states is estimated.

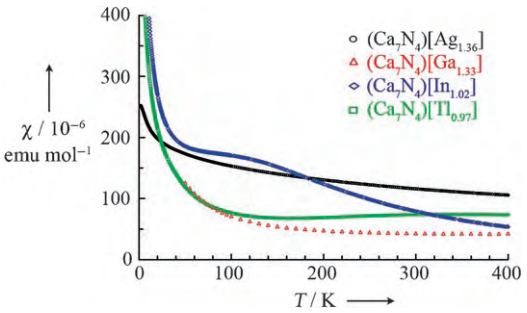

Figure 7. High-field magnetic susceptibility $\chi = M/H$ (M magnetic moment, H magnetic field strength versus T. The data were measured in $\mu_0 H = 7$ T and were corrected for ferromagnetic impurities.

In conclusion, we have presented a series of compounds consisting of a mixed-valent subnitride host structure ($Ca_3^{2+}Ca_4^{1.5+}N_4^{3-}$) containing parallel channels that are incommensurably filled with linear chains of equidistant metal atoms (M = Ag, Ga) or fragments of linear chains of equidistant atoms (M = In, Tl) that interact only weakly with the host lattice. Experimental results and theoretical calculations carried out so far lead to a consistent picture, which will be the basis for future work. Our main focus is to grow and prepare single crystals suitable for the measurement of physical properties in the directions parallel and perpendicular to the metal chains. Further TEM investigations are needed, including HREM imaging, which is dependent on the purity and stability of the samples. The question of a possible homogeneity range for the In and Tl compounds has to be answered and there is a need for further experimental evidence concerning the valence states of the elements involved. Finally, we will investigate whether there are other metal atoms, besides Ag, Ga, In, and Tl, that fit within this type of subnitride structure—altogether a challenging program for the future.

Received: May 2, 2006
Revised: June 19, 2006
Published online: September 15, 2006

Keywords: ab initio calculations · host–guest systems · nitrides · subvalent compounds

[1] P. Höhn, R. Kniep, *Z. Anorg. Allg. Chem.* **2002**, *628*, 2174.
[2] G. Cordier, M. Ludwig, D. Stahl, P. C. Schmidt, R. Kniep, *Angew. Chem.* **1995**, *107*, 1879; *Angew. Chem. Int. Ed. Engl.* **1995**, *34*, 1761.
[3] P. Höhn, R. Kniep, *Z. Anorg. Allg. Chem.* **2002**, *628*, 463.
[4] G. Cordier, P. Höhn, R. Kniep, A. Rabenau, *Z. Anorg. Allg. Chem.* **1990**, *591*, 58.
[5] M. Kirchner, W. Schnelle, F. R. Wagner, R. Kniep, R. Niewa, *Z. Anorg. Allg. Chem.* **2005**, *631*, 1477.
[6] J. Jaeger, D Stahl, P. C. Schmidt, R. Kniep, *Angew. Chem.* **1993**, *105*, 738; *Angew. Chem. Int. Ed. Engl.* **1993**, *32*, 709.
[7] M. Ludwig, Dissertation, TU Darmstadt **1998**.
[8] J. Jäger, Dissertation, TU Darmstadt, **1995**.
[9] G. Auffermann, Y. Prots, R. Kniep, *Angew. Chem.* **2001**, *113*, 565; *Angew. Chem. Int. Ed.* **2001**, *40*, 547.
[10] G. V. Vajenine, G. Auffermann, Y. Prots, W. Schnelle, R. K. Kremer, A. Simon, R. Kniep, *Inorg. Chem.* **2001**, *40*, 4866.
[11] Y. Prots, G. Auffermann, M. Tovar, R. Kniep, *Angew. Chem.* **2002**, *114*, 2392; *Angew. Chem. Int. Ed.* **2002**, *41*, 2288.
[12] P. Höhn, R. Ramlau, H. Rosner, W. Schnelle, R. Kniep, *Z. Anorg. Allg. Chem.* **2004**, *630*, 1704.
[13] Single-phase powder samples of $(Ca_7N_4)[M_x]$ (M = Ag, Ga, In, and Tl) are synthesized by the reaction of appropriate mixtures of Ca_3N_2 [from calcium (Alfa, 99.98 %) loaded in a tungsten crucible in a stream of N_2 (Messer Griesheim, 99.999 %, purified with a Merck BTS catalyst) for 24 h at 1023 K] and the respective metals, M (Alfa, > 99.9 %) in tantalum crucibles at temperatures of 1123 K for 48 h under an Ar atmosphere (Messer Griesheim, 99.999 %, purified with a Merck BTS catalyst). Repeated reactions with intermediate regrinding and reforming of pellets were employed. Small amounts of needlelike single crystals were prepared by using a small excess of Ca in the reaction mixtures.
[14] For single crystal X-ray diffraction experiments, a STOE IPDS diffractometer was used: $(Ca_7N_4)[Ga_{1.33(1)}]/(Ca_7N_4)[In_{1.02(1)}]/(Ca_7N_4)[Tl_{0.97(1)}]$; $Mo_{K\alpha}$, graphite monochromator, $T =$ 298 K; 1256/1220/1229 measured, 660/703/646 unique reflections; $R = 0.044/0.051/0.082$, $R_w = 0.104/0.121/0.218$. Neutron diffraction experiments were carried out on the powder diffractometer E9 at the reactor BER II of the HMI Berlin: $(Ca_7N_4)[Ag_{1.36(2)}]$; $wR_{profile} = 0.0468$, $R_{Bragg} = 0.0723$, 415 observed reflections. The samples were sealed under argon into cylindrical vanadium containers (diameter 8 mm, length 47 mm, wall thickness 0.15 mm), which were closed with caps containing an indium seal. Crystal-structure data derived from neutron diffraction experiments with the wavelength $\lambda = 1.79704(2)$ Å in the range $2° \le \Theta \le 158°$. The refinements were carried out by using the program Fullprof.[15] Structure determination and crystallographic data: $(Ca_7N_4)[Ag_{1.36(2)}]$, $(Ca_7N_4)[Ga_{1.33(1)}]$, $(Ca_7N_4)[In_{1.02(1)}]$, $(Ca_7N_4)[Tl_{0.97(1)}]$; orthorhombic, *Pbam*; $a =$ 1144.8(1)/1147.4(1)/1168.1(2)/1158.3(1) pm, $b = 1202.9(1)/$ 1208.0(1)/1212.9(2)/1199.6(1) pm, $c = 365.2(1)/363.6(1)/$

 © 2006 Wiley-VCH Verlag GmbH & Co. KGaA, Weinheim

364.3(1)/362.8(1) pm; $Z=2$, $\rho_{calc}=3.18/2.84/2.93/3.52\ g\,cm^{-3}$. The x values were determined by adding up the electron density within the channels under the assumption of exclusive occupation by metal. Further details on the crystal-structure investigation may be obtained from the Fachinformationszentrum Karlsruhe, 76344 Eggenstein-Leopoldshafen, Germany (fax: (+49) 7247-808-666; e-mail: crysdata@fiz-karlsruhe.de), on quoting the depository numbers CSD-416506, -416502, -416501, and -416500.

[15] J. Rodriguez-Carvajal, Laboratoire Léon Brillouin, Saclay FULLPROF. 2 K Version 3.40, November **2005**.

[16] The Tecnai G^2F30 electron microscope (spherical aberration constant $C_S=1.2$ mm) with field emission gun was operated at 300 kV. Selected-area electron-diffraction patterns were registered on photographic film and with a Gatan US-CCD camera (2048 × 2048 pixels). Microcrystallites appropriate for ED were prepared in a glove box (argon atmosphere) by finely crushing the polycrystalline compound. The hypersensitive specimens were mounted in standard holders and transferred to the microscope by using an inert gas shuttle system.

[17] a) A. Guinier, *X-ray diffraction in crystals, imperfect crystals, and amorphous bodies*, Dover Publications, **1994**; b) F. Frey, *Acta Crystallogr. Sect. B* **1995**, *51*, 592.

[18] R. L. Withers, *Z. Kristallogr.* **2005**, 220, 1027.

[19] a) U. Schwarz, *Z. Kristallogr.* **2004**, *219*, 376; b) M. McMahon, R. J. Nelmes, *Z. Kristallogr.* **2004**, *219*, 742; and references therein.

[20] a) H. Fujihisa, Y. Akahama, H. Kawamura, Y. Gotoh, H. Yamawaki, M. Sakashita, S. Takeya, K. Honda, *Phys. Rev. B* **2005**, *72*, 132103; b) M. I. McMahon, L. F. Lundegaard, C. Hejny, S. Falconi, R. J. Nelmes, *Phys. Rev. B* **2006**, 73, 134102.

[21] K. Koepernik, H. Eschrig, *Phys. Rev. B* **1999**, *59*, 1743. In the scalar-relativistic calculations, the exchange and correlation potential of Perdew and Wang (J. P. Perdew, Y. Wang, *Phys. Rev. B* **1992** *45*, 13244) was used. As the basis sets, Ga (3s, 3p, 3d, 4s, 4p), Ag and In (4s, 4p, 4d, 5s, 5p), and Tl (5s, 5p, 5d, 6s, 6p) states were employed. The lower lying states were treated fully relativistically as core states. A k mesh of 1056 points (30 intervals along the chain direction) in the irreducible part of the Brillouin zone (12000 in the full zone) was used to ensure accurate total energies, density of states and band-structure information.

[22] The metallic components were analyzed with an inductively coupled plasma optical emission spectrometer (ICP–OES; Varian Vista RL). The nonmetallic components, N, O, H, and C, were quantitatively determined by the carrier-gas hot-extraction or combustion technique (LECO TC 436 DR/5, RH 404, and C200CHLH): $(Ca_7N_4)[In_{1.06}]$ $Ca_{obs/calcd}$ 60.5(4)/61.2 wt.%, $In_{obs/calcd}$ 26.4(2)/26.6 wt.%, $N_{obs/calcd}$ 12.5(1)/12.2 wt.%. Impurities of O, H, and C were not detected (limits of detection: $C\le0.1$; $H\le0.005$; $O\le0.05$ wt%).

[23] N. F. Mott, *Philos. Mag.* **1969**, *19*, 835.

 © 2006 Wiley-VCH Verlag GmbH & Co. KGaA, Weinheim

Envelope Clusters

DOI: 10.1002/anie.200601804

A Main-Group Analogue of Housene: The Subtle Influence of the Inert-Pair Effect in Group 15 Clusters**

Cheryl Fish, Michael Green, John C. Jeffery, Richard J. Kilby, Jason M. Lynam,* John E. McGrady,* Dimitrios A. Pantazis, Christopher A. Russell,* and Charlotte E. Willans*

Dedicated to Professor John F. Nixon

The Binger and Regitz groups have described the reaction of zirconocene 1,3-diphosphabicyclo[1.1.0]butane (**1**) with PCl_3 (*n*-hexane, 110 °C) to give the tricyclic *P*-chloro triphosphacyclopentane **2** (Scheme 1),[1] and we have recently shown

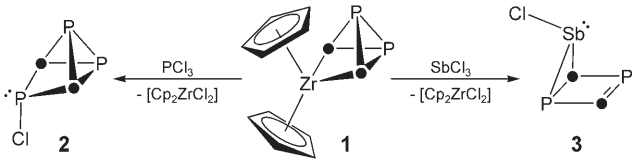

Scheme 1. Syntheses of tricyclic *P*-chloro triphosphacyclopentane **2** and envelope compound **3**. ● = C*t*Bu.

that this compound is a valuable precursor for both *nido*-1,2,4-P_3C_2 cationic species and the cyclic 1,3,4-P_3C_2 anion.[2–4] Against this background it was clearly of interest to attempt the incorporation of other heteroatoms into the P_2C_2 manifold through reactions of **1** with group 15 trihalides, such as

[*] C. Fish, Prof. M. Green, Dr. J. C. Jeffery, Dr. R. J. Kilby, Dr. C. A. Russell
School of Chemistry
University of Bristol
Cantock's Close, Bristol, BS81TS (UK)
Fax: (+44) 117-929-0509
E-mail: michael804902@aol.com
chris.russell@bristol.ac.uk

Dr. J. M. Lynam, C. E. Willans
Department of Chemistry
University of York
Heslington, York, YO105DD (UK)
Fax: (+44) 1904-432-516
E-mail: jml12@york.ac.uk

Prof. J. E. McGrady, Dr. D. A. Pantazis
WestCHEM
University of Glasgow
Joseph Black Building, Glasgow, G128QQ (UK)
Fax: (+44) 141-330-4888
E-mail: j.mcgrady@chem.gla.ac.uk

[**] We thank the Royal Society (University Research Fellowship for C.A.R.), the University of Bristol (M.G., C.A.R., C.F.) and the EPSRC (R.J.K., D.A.P., C.E.W.) for financial support.

Supporting information for this article is available on the WWW under http://www.angewandte.org or from the author.

© 2006 Wiley-VCH Verlag GmbH & Co. KGaA, Weinheim

$SbCl_3$, because this particular reaction could provide selective access to the *nido*-SbP_2C_2 cation[5] and the cyclic 1-Sb-3,4-P_2C_2 anion.[6] In the event the reaction proceeded in an unexpected and interesting way to form the envelope compound **3** (Scheme 1), which exhibited unusual solid-state and solution-phase behavior. Herein, we report the synthesis and structural characterization of **3**, along with its variable-temperature NMR spectra. Density functional theory provides a framework for the interpretation of these results.

Addition of two molar equivalents of $SbCl_3$ to a stirred orange-red solution of **1** in *n*-hexane at room temperature led, after 2 h, to the formation of a gray-white precipitate and a change in color of the solution to bright yellow. Filtration followed by recrystallization (−15 °C) of the hexane-soluble material afforded, in good yield, yellow crystals of the only phosphorus-containing product, **3** (according to $^{31}P\{^1H\}$ NMR spectroscopic analysis). A single-crystal X-ray diffraction study of the extremely air-, moisture-, and temperature-sensitive crystals revealed that, although **3** is related to **2** via replacement of one phosphorus center with antimony, the two species have completely different structures, with **3** adopting the envelope-type topology illustrated in Figure 1.

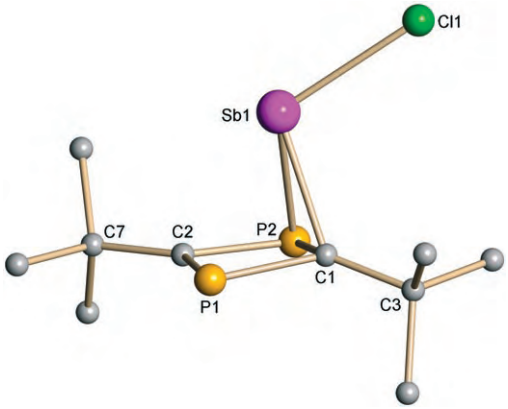

Figure 1. Molecular structure of **3** in the solid state (hydrogen atoms have been omitted for clarity). The molecule is disordered over two sites (relative occupancy 90:10); the disordered units are ostensibly identical and only the major site is shown and discussed. Selected bond lengths [Å] and angles [°]: Sb1–C1 2.241(4), Sb1–P2 2.562(2), Sb1–Cl1 2.511(1), P1–C1 1.844(4), P2–C2 1.807(4), P2–C1 1.831(4), P1–C2 1.725(4); C1-Sb1-P2 44.21(9), Cl1-Sb1-P2 114.92(4), Cl1-Sb1-C1 104.5(1), Sb1-C1-P1 84.8(2), Sb1-P2-C2 74.5(1), P1-C1-P2 94.4(2), C1-P2-C2 81.8(2), P2-C2-P1 99.5(2), C2-P1-C1 83.7(2).

The structure shown in Figure 1 reveals a number of rather unusual features that suggest that the bonding in **3** is more subtle than indicated in the Lewis structure shown in Scheme 1. Most notably, although the Sb–Cl fragment bridges a single carbon–phosphorus bond, the plane defined by the C1-Sb1-P2 triangle is tilted significantly inwards towards the center of the C1-P2-C2-P1 ring, such that the angle between the triangle and the ring is only 80.6°. The Sb1–Cl1 and P1–C2 bonds (2.511(1) and 1.725(4) Å, respectively) are also considerably longer than normal (Sb–Cl is 2.33 Å in $SbCl_3$[7] and P=C bonds in phosphaalkenes range from 1.60 to 1.70 Å).[8] These structural parameters are consistent with the presence of significant interactions between the P=C double bond and the Sb–Cl fragment.

The adoption of completely different structural motifs by the Sb and P analogues has encouraged us to explore the fundamental electronic differences between the two species using density functional theory (DFT). For the two model compounds, $ClP_3(CH)_2$ and $ClSbP_2(CH)_2$, we have located distinct minima corresponding to the envelope and tricyclic structures (Figure 2). The optimized envelope structure for

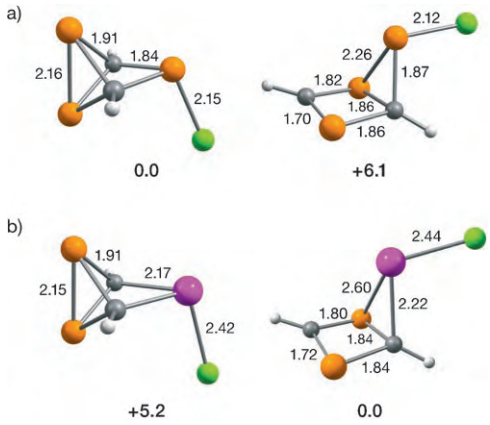

Figure 2. Optimized tricyclic and envelope structures for a) $ClP_3(CH)_2$ and b) $ClSbP_2(CH)_2$. Relative energies in kcal mol^{-1} are given in bold. Sb pink, P orange, Cl green, C gray, H white.

$ClSbP_2(CH)_2$ reproduces the key features of the X-ray structure of **3**, including the inward tilt of the SbCl fragment towards the C2–P1 bond and the rather long Sb–Cl and P=C bonds. Critically, the tricyclic structure is favored by 6.1 kcal mol^{-1} for the phosphorus system, but the order is reversed for the antimony analogue, in which the envelope structure is more stable by 5.2 kcal mol^{-1}.[9]

A natural bond orbital (NBO) analysis[10] reveals the origin of this reversal of stability on moving from phosphorus to antimony. For both $ClSbP_2(CH)_2$ and $ClP_3(CH)_2$, the lone pair at the bridgehead atom (Sb or P) has significantly greater s character in the envelope structure (Sb: 89 %, P: 77 %) than in its tricyclic counterpart (Sb: 79 %, P: 65 %) as a result of the very tight angles (θ) at the bridgehead (envelope: θ = 257°(Sb)/260°(P); tricyclic: 267°(Sb)/284°(P)), which favor greater p orbital participation in the bonding orbitals at the bridgehead atom in the envelope structure. Thus, the reluctance of the antimony center to participate in sp^n hybridization destabilizes the tricyclic structure and drives the switch to the envelope topology. The change in structure is therefore a manifestation of the well-known inert-pair effect.

Although the envelope structure of **3** was unexpected in light of our previous work on the tricyclic compounds $C_2tBu_2P_2ECl$ (E = P, As),[5] it is a relatively well-known structural motif, most notably in the hydrocarbon species bicyclo[2.1.0]pent-2-ene (housene)[11] and its triphospha-derivative, 1,2-$(CH(SiMe_3)_2)$P-1,3-$P_2(CtBu)_2$.[12] Despite the apparent isomorphism of these three compounds, the inward tilt of the apical SbCl fragment noted above is conspicuously

 © 2006 Wiley-VCH Verlag GmbH & Co. KGaA, Weinheim

absent in the other two species. Thus, whereas the angle between the C1-Sb1-P2 and C1-P2-C2 planes is acute (80.6°) in **3**, the corresponding angles in bicyclo[2.1.0]pent-2-ene and 1,2-HP-1,3-$P_2(CH)_2$ are 124.5° and 103.7°, respectively. Furthermore, although the formally bonded (2.562(2) Å) and nonbonded (2.770(2) Å) Sb–P distances in **3** are similar, there is a much sharper distinction in 1,2-HP-1,3-$P_2(CH)_2$ (2.24 and 3.02 Å).

A natural bond orbital (NBO) analysis clearly reveals that the inward tilt of the SbCl group in **3** is a result of two significant donor–acceptor interactions, both of which are intimately connected to the unusual structure of **3**. The first corresponds to a σ→π* donation from the Sb1–P2 bond to the empty π* natural orbital of the P1=C2 double bond (Figure 3a), which lengthens Sb1–P2 and P1=C2 while

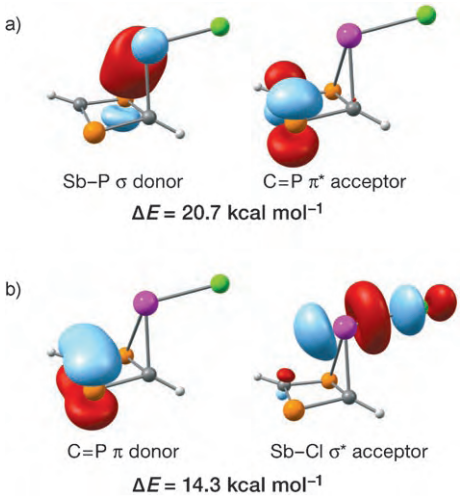

Figure 3. Natural bond orbitals and stabilization energies for the dominant donor–acceptor interactions of 1,2-ClSb-1,3-$P_2(CH)_2$. a) Sb–P σ donor orbital (left) and P=C π* acceptor orbital (right). b) P=C π donor orbital (left) and Sb–Cl σ* acceptor orbital (right). Sb pink, P orange, Cl green, C gray, H white.

reducing the Sb1–P1 distance. The second interaction is a π→σ* donation from the P1=C2 double bond to the Sb–Cl σ* orbital (Figure 3b), which pulls the SbCl fragment towards the double bond while lengthening both Sb1–Cl1 and P1=C2. The associated stabilization energies of 20.7 and 14.3 kcal mol^{-1} indicate a substantial departure from the idealized Lewis structure, in marked contrast to 1,2-HP-1,3-$P_2(CH)_2$. The first of these interactions (donation from P–P σ to C=P π*) is considerably reduced in magnitude (7.1 kcal mol^{-1}), while the second (donation from C=P π to P–H σ*) is almost completely absent (3.0 kcal mol^{-1}), consistent with the much higher energy of the P–H σ* orbital relative to Sb–Cl σ*. Hence, the NBO analysis identifies compact "cluster-like" bonding for $ClSbP_2(CH)_2$ that is quite distinct from the phosphorus analogue, 1,2-HP-1,3-$P_2(CH)_2$.

Despite the presence of phosphorus atoms in two distinct environments in the solid-state structure of **3**, its room-temperature $^{31}P\{^1H\}$ NMR spectrum in CD_2Cl_2 reveals only a single resonance at $\delta = 174.9$ ppm (singlet), which remains sharp even on cooling to 193 K. Similarly, the ^1H NMR spectrum (CD_2Cl_2) shows only a single resonance ($\delta =$ 1.12 ppm), the shape of which is also temperature-invariant, and the signals for the C*t*Bu groups in the ^{13}C NMR spectrum are both triplets as a result of bonding to two P atoms that are equivalent on the NMR timescale. The NMR data therefore indicate the presence of one or more processes that average both the phosphorus and C*t*Bu environments in solution.

We considered several dynamic processes that may account for this fluxionality,[13] and concluded the most likely mechanism was conceptually related to the "walk rearrangement" which has been extensively discussed for both housene and 1,2-HP-1,3-$P_2(CH)_2$. Here, the bridgehead group migrates in a series of 1,3 sigmatropic shifts around the edge of the ring and C_s-symmetric transition states lead to inversion of configuration at the bridgehead atom.[14,15] In the case of housene, the barrier to this 1,3 shift is rather large (31 kcal mol^{-1}) and the transition state has strong biradical character with one unpaired electron on the CH_2 fragment, the other delocalized in the allyl unit of the C_4 ring.[16] In contrast, we calculated barriers for migration of the PH unit over P and C of 10.8 and 31.0 kcal mol^{-1}, respectively, in the model system 1,2-HP-1,3-$P_2(CH)_2$.[15,17,18] The rather low barrier for the first process (**TS_a** in Figure 4) is certainly consistent with the reported presence of only a single resonance in the ^{31}P NMR spectrum of 1,2-[$CH(SiMe_3)_2$]P-1,3-$P_2(CtBu)_2$ down to 163 K.[12] The rather high-lying transition state for the 1,3 shift via the phosphorus center (**TS_b**) should, however, be sufficient to prevent free movement of the PR fragment around the entire C_2P_2 ring, leaving the C*t*Bu

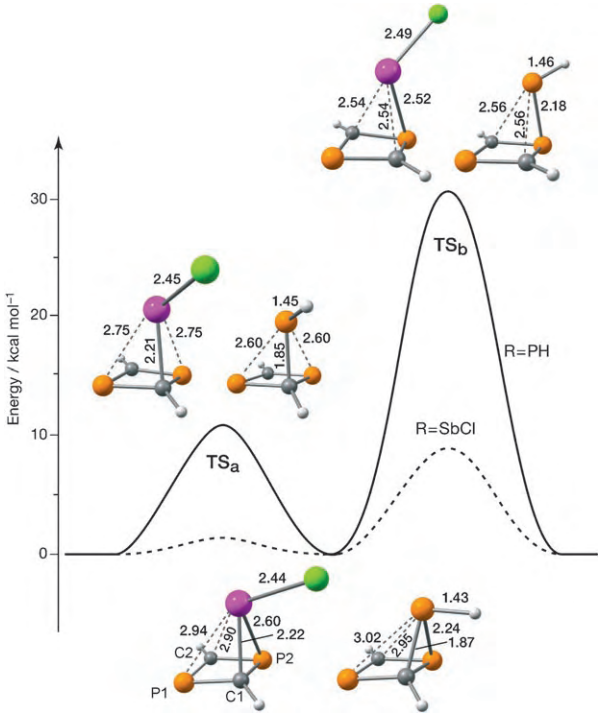

Figure 4. Comparison of the potential-energy surfaces for migration of PH (full line) and SbCl fragments (dashed line) around the C_2P_2 ring. All structures shown were optimized using DFT.

 © 2006 Wiley-VCH Verlag GmbH & Co. KGaA, Weinheim

groups inequivalent on the NMR timescale. The initial communication reports only the ^{31}P NMR spectrum and not the complementary ^{1}H and ^{13}C NMR data, so we are unable to confirm this by comparison to experiment.

In the model antimony species, 1,2-ClSb-1,3-$P_2(CH)_2$, the barrier to migration via a carbon center on the ring is reduced to only 0.6 kcal mol^{-1} (**TS$_a$**), indicating that the SbCl fragment is free to move almost unimpeded around the P-C-P unit. To understand this reduction in the barrier from 10.8 kcal mol^{-1} in 1,2-HP-1,3-$P_2(CH)_2$ to less than 1 kcal mol^{-1} for the antimony analogue, we need look no further than the equilibrium structure of **3**, and in particular its compact cluster-like geometry. As a result of the inward tilt, the two Sb–P bonds are very similar even at equilibrium (Figure 2), and so although the motion can be categorized formally as a 1,3 sigmatropic shift, in reality only a very minor displacement of the Sb center is required to interconvert the two isomers.[19] The more delocalized bonding in the antimony case has an even more profound influence on the alternative migration pathway involving cleavage of the Sb–C bond. The barrier of 28.7 kcal mol^{-1} in 1,2-HP-1,3-$P_2(CH)_2$[17] is reduced to only 8.6 kcal mol^{-1} in 1,2-ClSb-1,3-$P_2(CH)_2$ (**TS$_b$** in Figure 4). The structure of **TS$_b$** is quite distinct from the corresponding stationary state in its phosphorus analogue 1,2-HP-1,3-$P_2(CH)_2$ because the antimony center remains centrally located above the C_2P_2 ring, and so the loss of bonding to one carbon center is significantly compensated by enhanced overlap with the other.

Thus, although the 1,3 sigmatropic shifts in 1,2-HP-1,3-$P_2(CH)_2$ and 1,2-ClSb-1,3-$P_2(CH)_2$ are superficially similar, the nature of the electron redistribution in the two cases is fundamentally different. In the case of 1,2-HP-1,3-$P_2(CH)_2$, the 1,3 sigmatropic shift is probably best considered as localized P–P bond cleavage process, and the rather strong P–C bond prevents free movement of the PH unit around the entirety of the P_2C_2 moiety. In contrast, the corresponding process in 1,2-ClSb-1,3-$P_2(CH)_2$ is more accurately envisaged as the migration of an SbCl unit around a continuous ring of electron density formed by the C_2P_2 unit. In the case of **3**, therefore, the SbCl unit is able to migrate around the whole circumference of the C_2P_2 ring with a maximum barrier of only 9 kcal mol^{-1}, which leads to the equivalence of both phosphorus and C*t*Bu units on the NMR timescale. The observed disorder in the crystal structure of **3** may be an experimental manifestation of this fluxionality.

In summary, the synthesis and structural characterization of **3**, along with a detailed analysis of its electronic structure, has revealed a number of distinct differences in the bonding and topology induced by the replacement of a PH or PCl fragment with isolobal SbCl. The relative weakness of the Sb–P bonds and the electron-deficiency of the Sb center lead to a compact, cage-like structure, and also to facile migration of the bridging SbCl unit.

Experimental Section

All experimental procedures were performed under an atmosphere of nitrogen or argon by using standard Schlenk line and glovebox techniques.

3: Compound **1** (0.21 g, 0.5 mmol)[1] was dissolved in *n*-hexane (10 mL) and reacted with two equivalents of antimony trichloride (0.22 g, 1 mmol) for 2 h. The by-product, [Cp_2ZrCl_2], was separated from the reaction mixture by filtration through Celite, and storage of the resulting yellow solution for 16 h at −15 °C afforded yellow cubic crystals of **3**. The yield was quantitative (according to NMR spectrosopic analysis). These crystals decomposed upon attempted isolation which resulted in limited physical data on the crystalline material. The following data were obtained from solutions of **3** and the single-crystal X-ray diffraction study.

$^{31}P\{^1H\}$ NMR (121.45 MHz, 21 °C, CD_2Cl_2): $\delta = 174.9$ ppm; ^1H NMR (270.16 MHz, 21 °C, CD_2Cl_2): $\delta = 1.12$ ppm (s, $C(CH_3)_3$); $^{13}C\{^1H\}$ NMR (100.54 MHz, 21 °C, CD_2Cl_2): $\delta = 31.8$ (t, $^3J_{CP}$ 4 Hz, $C(CH_3)_3$), 35.9 (t, $^2J_{CP}$ 5 Hz, $C(CH_3)_3$), $C_2tBu_2P_2$ not observed. MS (EI): *m*/*z*: observed 355.9617 [M^+], calculated 355.9610.

Single-crystal X-ray diffraction data for **3**: $C_{10}H_{18}ClP_2Sb$, $M_r = 357.38$ g mol^{-1}, crystal dimensions $0.05 \times 0.05 \times 0.05$ mm^3, triclinic, space group $P\bar{1}$, $a = 6.2063(1)$, $b = 10.1944(2)$, $c = 12.2553(2)$ Å, $\alpha = 73.797(1)$, $\beta = 77.887(1)$, $\gamma = 73.967(1)$°, $V = 708.15(2)$ Å^3, $Z = 2$, $\rho_{calcd} = 1.676$ Mg m^{-3}, $\mu = 19.039$ mm^{-1}, $\theta = 3.80$–69.96°, 5492 measured reflections, 2401 independent reflections, $R_{int} = 0.0386$, $R_1(I > 2\sigma)$ 0.0388, wR_2 (all data) = 0.1132. Diffraction data were collected at 100(2) K on a Bruker PROTEUM CCD three circle diffractometer with $Cu_{K\alpha}$ radiation ($\lambda = 1.54178$ Å). The structure was solved by direct methods and refined by full-matrix least squares using the SHELX suite of programs (v5.1, Sheldrick, 1998).[26] All non-hydrogen atoms were refined anisotropically. Hydrogen atoms were constrained to ideal geometries and refined with fixed isotropic displacement parameters. The two P and the Sb atoms are disordered over two sites which were refined with partial occupancies (90:10). Because the occupation of the minor occupancy site is low, equivalent distances were constrained to be similar to ensure a stable refinement. CCDC-606634 contains the supplementary crystallographic data for this paper. These data can be obtained free of charge from The Cambridge Crystallographic Data Centre via www.ccdc.cam.ac.uk/data_request/cif.

Computational methods: Full geometry optimizations were performed with the B3LYP functional[20] using flexible polarized basis sets of the cc-pVTZ family.[21] For Sb we used Peterson's cc-pVTZ-PP basis set that incorporates the small-core MCDHF-adjusted relativistic pseudopotential of Metz, Stoll, and Dolg.[22] Transition states were located with the STQN algorithm,[23] and all stationary points were characterized as minima or first-order saddle points by their harmonic vibrational frequencies. All calculations as well as the NBO analysis[24] were carried out with the Gaussian 03 series of programs.[25]

Received: May 8, 2006
Revised: July 27, 2006
Published online: September 20, 2006

Keywords: antimony · cluster compounds · density functional calculations · phosphorus · structure elucidation

[1] P. Binger, T. Wettling, R. Schneider, F. Zurmühlen, U. Bergsträsser, J. Hoffmann, G. Maas, M. Regitz, *Angew. Chem.* **1991**, *103*, 208; *Angew. Chem. Int. Ed. Engl.* **1991**, *30*, 207.
[2] J. M. Lynam, M. C. Copsey, M. Green, J. C. Jeffery, J. E. McGrady, C. A. Russell, J. M. Slattery, A. C. Swain, *Angew. Chem.* **2003**, *115*, 2884; *Angew. Chem. Int. Ed.* **2003**, *42*, 2778.
[3] D. A. Pantazis, J. E. McGrady, J. M. Lynam, C. A. Russell, M. Green, *Dalton Trans.* **2004**, 2080.
[4] C. Fish, M. Green, J. C. Jeffery, R. J. Kilby, J. M. Lynam, C. A. Russell, C. E. Willans, *Organometallics* **2005**, *24*, 5789.

 © 2006 Wiley-VCH Verlag GmbH & Co. KGaA, Weinheim

[5] C. Fish, M. Green, J. C. Jeffery, R. J. Kilby, J. M. Lynam, J. E. McGrady, D. A. Pantazis, C. A. Russell, C. E. Willans, *Chem. Commun.* **2006**, 1375.
[6] Although the 3,4,1-diphosphastibolyl anion has not been characterized, there have been several reports on the related 2,4,1 isomer—see C. Jones, R. C. Thomas, *J. Organomet. Chem.* **2001**, *622*, 61, and references therein.
[7] N. N. Greenwood, A. Earnshaw, *The Chemistry of the Elements*, 2nd ed., **1997**, Butterworth Heinemann, Oxford, p. 560.
[8] F. Mathey, *Angew. Chem.* **2003**, *115*, 1616; *Angew. Chem. Int. Ed.* **2003**, *42*, 1578.
[9] Neither of these structures corresponds to the global minimum, which is an envelope structure with an isolated C=C double bond and a P-Sb-P or P-P-P triangle. There is, however, no obvious way of accessing this structure through our synthetic route.
[10] F. Weinhold in *Encyclopedia of Computational Chemistry*, *Vol. 3* (Eds.: P. von R. Schleyer et al.), Wiley, Chichester, **1998**, pp. 1792 – 1811.
[11] J. I. Brauman, L. E. Ellis, E. E. van Tamelen, *J. Am. Chem. Soc.* **1966**, *88*, 846; A. H. Andrist, J. E. Baldwin, R. K. Pinschmidt, Jr., *Org. Synth.* **1976**, *55*, 15; S. L. Hsu, A. H. Andrist, T. D. Gierke, R. C. Benson, W. H. Flygare, J. E. Baldwin, *J. Am. Chem. Soc.* **1970**, *92*, 5250.
[12] The triphospha-derivative of bicyclo[2.1.0]pent-2-ene was synthesised by UV irradiation of the corresponding 1,2,4-triphosphole, $P_3C_2tBu_2CH(SiMe_3)_2$ (see V. Caliman, P. B. Hitchcock, J. F. Nixon, *Chem. Commun.* **1998**, 1537); it has not been characterized crystallographically, but the ^{31}P NMR spectroscopic data is consistent with its formulation as an envelope structure, as is the structure of the model compound $P_3C_2H_3$, optimized at the MP2/6-31G* level (see reference [15]). Interestingly, the reaction to form **3** detailed herein proceeds both in the presence and absence of laboratory light.
[13] We have considered other possible dynamic processes, notably autoionization to give the known $[C_2tBu_2P_2Sb]^+$ cation (see reference [5]) and Cl^-, and a "back-flip" mechanism in which the SbCl unit migrates from one side of the C_2P_2 ring to the other. For autoionization, the computed heterolytic Sb–Cl bond dissociation energy in CH_2Cl_2 solution is rather high (+25 kcal mol^{-1}), casting some doubt on the viability of this pathway. For the "back-flip" mechanism, the pyramidal (C_{2v}-symmetric) structure that lies at the midpoint of this pathway is a second-order saddle point, as distinct from a transition state.
[14] See P. N. Skancke, K. Yamashita, K. Morokuma, *J. Am. Chem. Soc.* **1987**, *109*, 4157, and references therein.
[15] S. M. Bachrach, V. Caliman, J. F. Nixon, *J. Chem. Soc. Chem. Commun.* **1995**, 2395.
[16] The biradical nature of the transition state has posed a considerable challenge to theory, as a result of which the precise shape of the potential energy surface has been extensively debated—see Ý. Özkan, A. Kinal, M Balci, *J. Phys. Chem. A* **2004**, *108*, 507, and references therein.
[17] Nixon and co-workers reported very similar barriers of 11.6 kcal mol^{-1} and 28.7 kcal mol^{-1} using the MP4SDTQ/6-31G*//MP2/6-31G* method (see reference [15]).
[18] We find no evidence for the singlet–triplet instabilities that would indicate biradical character analogous to that encountered in housene in either 1,2-HP-1,3-$P_2(CH)_2$ or 1,2-ClSb-1,3-$P_2(CH)_2$; clearly the more diffuse orbitals on phosphorus and antimony atoms prevent the localization of spin density.
[19] The imaginary frequency at the transition state is largely associated with a swinging motion of the Cl atom rather than any significant change in Sb–P bonding.
[20] a) A. D. Becke, *J. Chem. Phys.* **1993**, *98*, 5648; b) C. Lee, W. Yang, R. G. Parr, *Phys. Rev. B* **1988**, *37*, 785; c) P. J. Stephens, F. J. Devlin, C. F. Chabalowski, M. J. Frisch, *J. Phys. Chem.* **1994**, *98*, 11623.
[21] a) T. H. Dunning, Jr., *J. Chem. Phys.* **1989**, *90*, 1007; b) D. E. Woon, T. H. Dunning, Jr., *J. Chem. Phys.* **1993**, *98*, 1358.
[22] a) K. A. Peterson, *J. Chem. Phys.* **2003**, *119*, 11099; b) B. Metz, H. Stoll, M. Dolg, *J. Chem. Phys.* **2000**, *113*, 2563.
[23] C. Peng, P. Y. Ayala, H. B. Schlegel, M. J. Frisch, *J. Comput. Chem.* **1996**, *17*, 49.
[24] E. D. Glendening, A. E. Reed, J. E. Carpenter, F. Weinhold, NBO, Version 3.1, Madison, Wisconsin, USA.
[25] Gaussian 03 (Revision C.01): M. J. Frisch et al., see Supporting Information.
[26] G. M. Sheldrick, SHELXTL V5.1, Bruker AXS, Inc., Madison, USA, **1997**.

 © 2006 Wiley-VCH Verlag GmbH & Co. KGaA, Weinheim

Riboswitches

DOI: 10.1002/anie.200602534

Characteristics of Ligand Recognition by a *glmS* Self-Cleaving Ribozyme**

*Jinsoo Lim, Beth C. Grove, Adam Roth, and Ronald R. Breaker**

The *glmS* ribozyme[1–7] from *Bacillus cereus* is a representative of a unique riboswitch class[8,9] whose members undergo self-cleavage with accelerated rate constants when bound to glucosamine-6-phosphate (GlcN6P). These metabolite-sensing ribozymes are found in numerous Gram-positive bacteria, where they control expression of the *glmS* gene. The *glmS* gene product (glutamine:fructose-6-phosphate amidotransferase) generates GlcN6P,[10,11] which binds to the ribozyme and triggers self-cleavage by internal phosphoester transfer.[1] The ribozyme is embedded within the 5′ untranslated region (UTR) of the *glmS* messenger RNA and self-cleavage prevents production of GlmS protein, thereby decreasing the concentration of GlcN6P. The combination of molecular

[*] Dr. J. Lim, Dr. A. Roth, Prof. R. R. Breaker
Department of Molecular, Cellular and Developmental Biology
Yale University
New Haven, CT 06520 (USA)
Fax: (+1) 203-432-0753
E-mail: ronald.breaker@yale.edu

B. C. Grove
Department of Molecular Biophysics & Biochemistry
Yale University
New Haven, CT 06520 (USA)

[**] We thank Dr. Gail Emilsson and other members of the Breaker group for helpful comments, and Inbal Jona for assisting with several assays. This work was supported by grants from the NIH, the NSF, and DARPA. B.C.G. was supported by a training grant (CMB) to Yale University from the NIH.

Supporting information for this article (including full experimental protocols and characterization data) is available on the WWW under http://www.angewandte.org or from the author.

© 2006 Wiley-VCH Verlag GmbH & Co. KGaA, Weinheim

sensing, self-cleavage, and gene control functions allows this small RNA to operate both as a ribozyme and as a riboswitch.

Previous studies have shown that the *glmS* ribozyme from *B. cereus* and the homologous ribozyme from *Bacillus subtilis* respond to GlcN6P with an apparent dissociation constant (K_D) of approximately 200 μM.[1,3,6] Although this K_D value is greater than those determined for most other natural riboswitches, *glmS* ribozymes exhibit a high level of molecular recognition specificity and are able to reject even close chemical analogues of GlcN6P. For example, glucosamine-6-sulphate can induce ribozyme activation to the same extent as GlcN6P, albeit when present at concentrations that are approximately 100-fold greater. In contrast, glucose-6-phosphate, wherein the 2-amine group of GlcN6P is replaced with a hydroxy group, completely fails to trigger ribozyme action.[1,3]

Riboswitches must be capable of discriminating against compounds related to their natural ligands to prevent undesirable regulation of metabolic genes. However, it is possible to generate analogues that trigger riboswitch function and inhibit bacterial growth, as has been demonstrated for riboswitches that normally respond to lysine[12] and thiamine pyrophosphate.[13] Proper expression of the GlmS protein is critical for bacterial viability,[10,11] and analogues of GlcN6P that could interfere with normal gene expression by triggering *glmS* ribozyme activity might serve as new types of antimicrobial agents. Therefore, we sought an increased understanding of the molecular recognition characteristics of *glmS* ribozymes.

We evaluated the molecular recognition characteristics of the *glmS* ribozyme by determining the effects of GlcN6P and various GlcN6P analogues on the self-cleavage activity of a 200-nucleotide *glmS* ribozyme construct from *B. cereus* (Figure 1). K_D values for each ligand were determined by plotting ribozyme rate constants versus ligand concentrations (see Experimental Section). Previous studies using similar methods revealed that the phosphate moiety of GlcN6P (Figure 1b; **1a**) is necessary for maximal affinity between ligand and *glmS* ribozyme.[1,3] The amine group of the ligand is also known to be essential for ribozyme function.[1,3] However, linear amine-containing compounds can induce modest ribozyme activity,[3] suggesting that acyclic (**1b**) or alternative anomeric forms (**1c**) of GlcN6P might be active. Therefore, we tested a series of analogues (Figure 2) to probe the importance of structural conformation of GlcN6P and of individual functional groups on the pyranose ring.[14]

Under physiological conditions, GlcN6P equilibrates between an acyclic form (**1b**) and two cyclic β-anomer (**1a**) and α-anomer (**1c**) forms (Figure 1b).[15] The relative ratio of **1a** and **1c** in solution is 60:40 at 25 °C as determined by ^{1}H NMR spectroscopy in D_2O (data not shown), with less than 1% in the acyclic form.[15] Each conformer could exhibit differences in RNA binding affinity and ribozyme activity similar to that observed for the GlmS protein.[16]

Small molecules such as serinol and ethanolamine promote ribozyme activity, although they are orders of magnitude less effective than GlcN6P.[3] Similarly, the acyclic analogue **3** has no detectable activity under the assay conditions used in the current study (see Figure 2b and

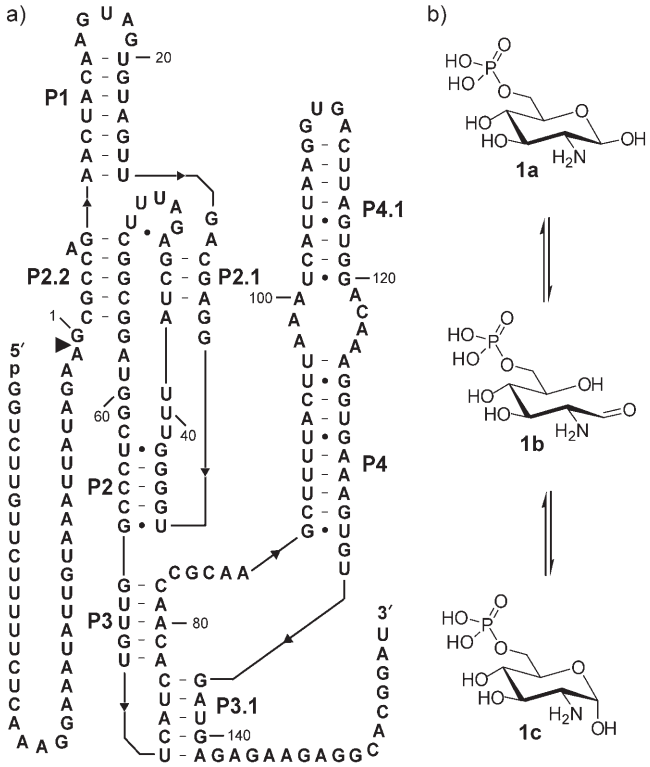

Figure 1. a) Secondary structure model of the *glmS* ribozyme from *B. cereus*. The model was adapted using data from a model for the *glmS* ribozyme from *Thermoanaerobacter tengcongensis* based on X-ray crystal structural data.[23] b) Equilibrium of the β-anomer (**1a**), acyclic form (**1b**), and α-anomer (**1c**) of GlcN6P, the ligand of *glmS* ribozyme.

Experimental Section). In contrast, the cyclic analogue **8**, which lacks the hydroxy group at the 1-position, activates ribozyme self-cleavage to approximately 1/70th of the activity exhibited by GlcN6P (Figure 2c, Figure 3). These results demonstrate that alteration of the chemical structure at the 1-position of the pyranose ring has only a modest effect on ribozyme activity, but opening of the ring at this position (as in **3** and most likely in **1b**) is far more deleterious.

Because **1b** is unlikely to be relevant for normal function of the ribozyme, one or both of the anomers of GlcN6P must serve as the activator. We tested analogues of **1a** (**5**) and **1c** (**6**), in which the stereochemistry of the analogues are maintained by methylation of the oxygen atoms at the 1-position. Unfortunately, neither **5** nor **6** induced ribozyme cleavage, and this result prevents us from establishing the activities of the two anomers by using these analogues. Perhaps a future study might exploit similar analogues in which the methoxy groups are replaced with fluorine. However, the current results suggest the ribozyme forms a tight binding pocket near the 1-position that precludes analogue binding. As **8** can activate ribozyme cleavage substantially, the modification at the 1-position might only modestly disrupt a molecular interaction between the ligand and ribozyme. Alternatively, the influence of the 1-hydroxy group on the pK_a value of the 2-amine group also could be the cause of the reduction in activity of **8**. For example, ethyl-

 © 2006 Wiley-VCH Verlag GmbH & Co. KGaA, Weinheim

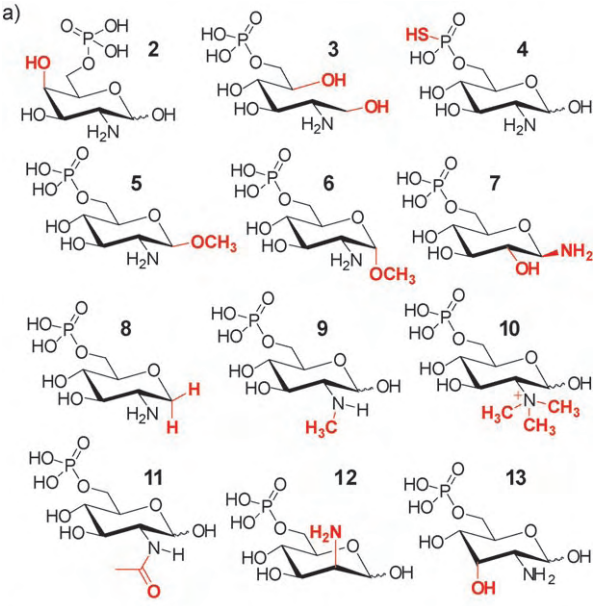

c)

compd	1	4	8	9	12	13
k_{obs} [min^{-1}]	1.26	0.0094	0.018	0.079	0.036	0.36
k_1/k	1	134	70	16	35	3.5

Figure 2. GlcN6P analogues and their influence on *glmS* ribozyme self-cleavage. a) Chemical structures of GlcN6P analogues.[14] Red portions designate differences from GlcN6P. b) Yields of ribozyme cleavage actions using a 200-nucleotide *glmS* RNA construct incubated with GlcN6P (**1**) or with various compounds as indicated. 5′-^{32}P-labeled precursor (Pre)-RNAs were incubated for 30 minutes in the presence of 1 mM effector as noted for each lane. The bar labeled with "–" reveals the extent of RNA cleavage when a reaction containing 1 mM GlcN6P was terminated with loading buffer[6] at time zero. Data for all assays were corrected for the amount of cleaved RNA present in the reaction generating the lowest amount of cleavage (reaction containing **7**). Unshaded bars designate active compounds that were further examined to establish ribozyme rate constants. c) Observed rate constants (k_{obs}) for ribozyme cleavage and the ratio of rate constants (k_1/k) measured using GlcN6P (**1**) versus the most active GlcN6P analogues, each at 100 μM. Rate constants for the remaining compounds are estimated to be less than 0.001 min^{-1}.

amine ($pK_a = 10.7$) has a higher pK_a value than ethanolamine ($pK_a = 9.50$),[17] indicating that an adjacent hydroxy group can reduce the basicity of an amine by more than one unit. Therefore the change in the pK_a value caused by the absence of the 1-hydroxy group in **8** could disrupt either ligand binding or ribozyme catalysis.

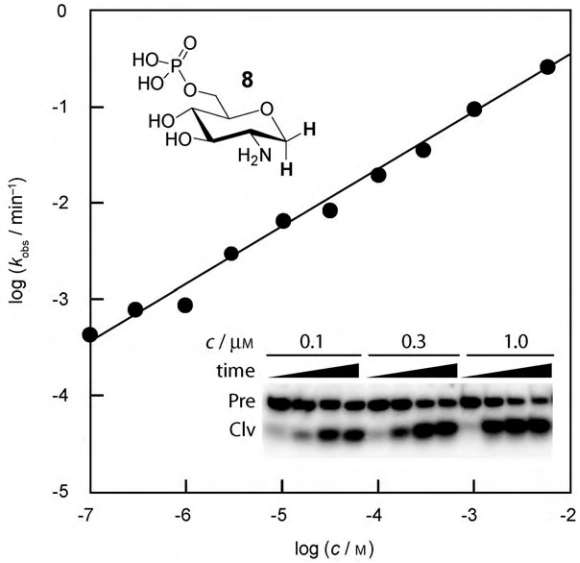

Figure 3. Observed rate constants for ribozyme self-cleavage at different concentrations of **8**.[14] The inset depicts three representative assays in which the radiolabeled precursor (Pre) was incubated for various times with different concentrations (c) of **8** as indicated. Cleaved (Clv) RNAs were separated by polyacrylamide gel electrophoresis (PAGE). Aliquots of ribozyme reactions were removed and terminated at $t = 0$, 4, 15.3, and 19.5 h.

Compounds **2** and **13** were examined to determine the importance of the 3- and 4-hydroxy groups for ribozyme activation. While **13** exhibits activity that is similar to that of GlcN6P, **2** does not induce activity under the assay conditions used (Figure 2b and c). These results imply that the 4-hydroxy group is critical for binding. In contrast, the 3-hydroxy group might have only a modest impact on binding or otherwise might influence reactivity by means of an inductive effect on the 2-amine group.

Replacement of the phosphate group with sulfate reduces affinity for the ligand by about 100-fold.[1] However, removal of the phosphate group (glucosamine) causes an even greater loss of ligand affinity. To further assess the importance of phosphate oxygen atoms, we generated the phosphorothiolate analogue **4**. This change also reduces the rate constant of ribozyme cleavage by approximately two orders of magnitude relative to **1**. However, GlcN6P is bound by the ribozyme about 1000-fold more tightly than is glucosamine.[1,3,18,19] Although the phosphate modifications tested might only disrupt a single interaction between ligand and ribozyme, it is likely that more than one binding interaction is made to this part of the ligand.

The 2-amine group, or an analogous amine, is present in all compounds that induce ribozyme activity.[1,3] Therefore, we tested a series of structural and stereochemical isomers of **1** in which this functional group was altered. The interchange of 1-hydroxy and 2-amine groups in **7** does not support ribozyme cleavage, which suggests that the location of the 2-amine group is critical for activity. The ribozyme is activated by **9** with only a modest reduction in efficiency compared to GlcN6P, despite the steric hindrance that might be caused by the methyl group. In contrast, **10** and **11** are inactive,

 © 2006 Wiley-VCH Verlag GmbH & Co. KGaA, Weinheim

suggesting that the ability of the amine to accept or donate protons for bonding or catalysis is essential.

Compound **12** carries an amine group at the 2-position with opposing stereochemical configuration and surprisingly induces cleavage to 1/35th of that of the natural ligand. It seems possible that **12** could be bound using the same contacts that are used to bind GlcN6P, but the relocation of the amine group in this pocket only slightly detracts from its ability to bind or to participate in proton-transfer-mediated catalysis.

On the basis of our findings, we generated a series of predicted molecular recognition determinants for GlcN6P binding (Figure 4). The 6-phosphate and 4-hydroxy groups

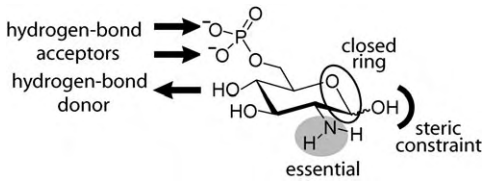

Figure 4. Predicted molecular recognition determinants of *glmS* ribozymes. Confirmation of the precise type or number of molecular contacts for some functional groups requires testing of additional analogues.

are likely to serve as hydrogen-bond donor and acceptor sites. Although the nonbridging oxygen atoms of a phosphate group can interact with metal ions by inner-sphere coordination, this is unlikely for this RNA because the ribozyme can attain full activity when Mg^{2+} ions are replaced with cobalt hexamine.[6] Cobalt hexamine simulates fully hydrated Mg^{2+} ions and can only form hydrogen bonds with an adjacent phosphate.

The exact role of the essential 2-amine group remains unclear. The reduced activity for **8** could be a result of the expected increase in the pK_a value of the amine, which would influence its ability to function in proton-transfer reactions. However, it is not clear whether the loss of activity observed with **8** is due entirely to a shift in pK_a value of the amine or due at least in part to disruption of a molecular recognition contact. We have suggested that GlcN6P could function as a cofactor for RNA cleavage,[1] and nucleic acid enzymes that use small molecules presumably to assist in proton transfer have been identified previously.[20] Both the absence of ligand-induced shape change in the RNA[21] and pH profile changes brought about by the use of various ligand analogues[3] are consistent with the hypothesis that GlcN6P directly participates in the chemical step of the reaction.

If the amine group of GlcN6P is a key moiety in the ribozyme active site, then the simplest explanation for the data is that the ligand serves as a general base catalyst. The logarithm of k_{obs} for ribozyme activity with increasing pH value increases linearly with a slope of 1.[1,3,6] Furthermore, GlcN6P analogues that exhibit higher pK_a values for the amine group are less effective inducers of ribozyme activity (i.e. **8**) or exhibit an increase in the pH required to reach half-maximal ribozyme activity.[3] Although other more complex mechanisms are possible, the ribozyme might use GlcN6P to assist in deprotonation of the 2-hydroxy group at the labile internucleotide linkage.[6]

Previous studies of the molecular recognition characteristics of other riboswitch classes revealed that a high level of molecular discrimination can be achieved by natural ligand-binding RNAs.[22] Although the *glmS* ribozyme also strongly discriminates against many closely related GlcN6P analogues, there appears to be considerable opportunity to design novel analogues that efficiently and selectively trigger *glmS* ribozyme cleavage. Such compounds possibly could be used to reduce the expression of GlmS metabolic enzymes in pathogenic bacteria, which is expected to disrupt their normal cellular function.

Experimental Section

The *glmS* ribozyme from *B. cereus* (Figure 1a) was generated by in vitro transcription as described previously,[6] 5′-^{32}P-radiolabeled,[22] and purified by PAGE. Rate constants were established by using methods and reaction conditions similar to those described previously,[6] with the exception that reaction mixtures contained 50 mM HEPES buffer (pH 7.5 at 23 °C) in place of Tris-HCl buffer. Ligand concentrations and incubation times used are defined for each assay. Ribozyme activity was established by quantifying the amounts of cleaved and uncleaved RNAs using a Typhoon imager (Amersham Biosciences).[14]

Received: June 23, 2006
Published online: September 20, 2006

Keywords: gene expression · molecular recognition · ribozymes · RNA · structure–activity relationships

[1] W. C. Winkler, A. Nahvi, A. Roth, J. A. Collins, R. R. Breaker, *Nature* **2004**, *428*, 281 – 286.
[2] J. E. Barrick, K. A. Corbino, W. C. Winkler, A. Nahvi, M. Mandal, J. Collins, M. Lee, A. Roth, N. Sudarsan, I. Jona, J. K. Wickiser, R. R. Breaker, *Proc. Natl. Acad. Sci. USA* **2004**, *101*, 6421 – 6426.
[3] T. J. McCarthy, M. A. Plog, S. A. Floy, J. A. Jansen, J. K. Soukup, G. A. Soukup, *Chem. Biol.* **2005**, *12*, 1221 – 1226.
[4] S. R. Wilkinson, M. D. Been, *RNA* **2005**, *11*, 1788 – 1794.
[5] G. A. Soukup, *Nucleic Acids Res.* **2006**, *34*, 968 – 975.
[6] A. Roth, A. Nahvi, M. Lee, I. Jona, R. R. Breaker, *RNA* **2006**, *12*, 607 – 619.
[7] J. A. Jansen, T. J. McCarthy, G. A. Soukup, J. K. Soukup, *Nat. Struct. Mol. Biol.* **2006** *13*, 517 – 523.
[8] M. Mandal, R. R. Breaker, *Nat. Rev. Mol. Cell Biol.* **2004**, *5*, 451 – 463.
[9] W. C. Winkler, R. R. Breaker, *Annu. Rev. Microbiol.* **2005**, *59*, 487 – 517.
[10] M.-A. Badet-Denisot, L. René, B. Badet, *Bull. Soc. Chim. Fr.* **1993**, *130*, 249 – 255.
[11] S. Milewski, *Biochim. Biophys. Acta* **2002**, *1597*, 173 – 192.
[12] N. Sudarsan, J. K. Wickiser, S. Nakamura, M. S. Ebert, R. R. Breaker, *Genes Dev.* **2003**, *17*, 2688 – 2697.
[13] N. Sudarsan, S. Cohen-Chalamish, S. Nakamura, G. M. Emilsson, R. R. Breaker, *Chem. Biol.* **2006**, *13*, 1325 – 1335.
[14] See Supporting Information for additional methods, synthetic details and spectral data.
[15] K. J. Schray, S. J. Benkovic, *Acc. Chem. Res.* **1978**, *11*, 136 – 141.
[16] The atomic structure of GlmS bound to GlcN6P reveals a preference for the α-pyranose form; A. Teplyakov, G. Obmo-

 © 2006 Wiley-VCH Verlag GmbH & Co. KGaA, Weinheim

lova, M.-A. Badet-Denisot, B. Badet, I. Polikarpov, *Structure* **1998**, *6*, 1047 – 1055.
[17] D. R. Lide, *CRC Handbook of Chemistry and Physics*, 75th ed., CRC, Boca Raton, FL, **1994**, pp. 8 – 45.
[18] G. Mayer, M. Famulok, *ChemBioChem* **2006**, *7*, 602 – 604.
[19] K. F. Blount, I. Puskarz, R. Penchovsky, R. R. Breaker, *RNA Biol.* **2006**, in press.
[20] A. Roth, R. R. Breaker, *Proc. Natl. Acad. Sci. USA* **1998**, *95*, 6027 – 6031.
[21] K. J. Hampel, M. M. Tinsley, *Biochemistry* **2006**, *45*, 7861 – 7871.
[22] J. Lim, W. C. Winkler, S. Nakamura, V. Scott, R. R. Breaker, *Angew. Chem.* **2006**, *118*, 978 – 982; *Angew. Chem. Int. Ed.* **2006**, *45*, 964 – 968.
[23] J. Cochrane, S. Strobel, personal communication.

 © 2006 Wiley-VCH Verlag GmbH & Co. KGaA, Weinheim

Molecular Recognition

DOI: 10.1002/anie.200602412

A Self-Assembled Pyrrolic Cage Receptor Specifically Recognizes β-Glucopyranosides**

*Oscar Francesconi, Andrea Ienco, Gloriano Moneti, Cristina Nativi, and Stefano Roelens**

The molecular recognition of carbohydrates has been acknowledged as a subject of paramount importance in chemistry and biology.[1] Despite the endeavor dedicated to the research in this field in the last decade,[2] full knowledge of recognition events and control over recognition processes have yet to be achieved. By capitalizing on noncovalent interactions,[3] encouraging results have been obtained, mostly in organic solvents, with synthetic receptors that rely on hydrogen bonding; however, high selectivity remains the most ambitious goal yet to be achieved. Among the plethora of synthetic receptors reported so far,[4] cage structures endowed with various hydrogen-bonding groups have been successfully explored.[5–8] The best results have been obtained with cage receptors that employ a concerted arrangement of amidic hydrogen bonds for the multipoint binding of mono- and oligosaccharides.[5] Alternative hydrogen-bonding groups may be conveniently employed: for example, amino and hydroxy groups have been shown to be complementary hydrogen-bonding partners, both geometrically and coordinatively, thus giving rise to molecular recognition and self-assembly.[9] Likewise, pyrroles are well-established hydrogen-bonding donors, which have been largely employed for anion binding,[10] but appear to be yet unexplored for the recognition of carbohydrates. We thought that combining amino and pyrrole groups in organized architectures may result in effective receptors, provided that steric, geometric, coordinative, and functional requirements for the recognition of carbohydrates could be met through careful structural design. We describe herein the first cage receptor featuring pyrrole residues for the multipoint binding of carbohydrates, which spontaneously forms in quantitative yield by the one-pot self-assembly of five components and exhibits a specificity toward β-D-glucose and its glycosides that marks a significant step ahead in the selective recognition of monosaccharides.

When a 2:3 mixture of 1,3,5-tris(aminomethyl)-2,4,6-triethylbenzene (**1**)[4g] and pyrrole-2,5-dicarboxaldehyde (**2**)[11] in methanol was stirred overnight at room temperature, a single compound was unexpectedly obtained in quantitative yield and unambiguously identified as the hexaimine macrobicyclic cage **3** by NMR spectroscopic as well as ESI and high-resolution (HR) mass spectrometric (MS) analysis (Scheme 1).[12] Reversible imine condensation was driven toward the complete formation of a single product by precipitation, as **3** is very poorly soluble in methanol. Solubility is not, however, the only driving factor, as the corresponding reaction of the triaminoethyl homologue of **1** gave only an intractable polymeric material by precipitation. Clearly, **3** is the thermodynamically favored product that arises from condensation of five reacting molecules, which self-assemble through the concerted formation of six imine bonds.

A one-pot reduction of **3** with $NaBH_4$ gave the corresponding macrobicyclic hexaamine **4** in essentially quantitative yield. In contrast to **3**, compound **4** is freely soluble in lipophilic solvents. The ESI MS and HRMS spectra of **4** confirmed the identity of the cage, whereas the ^1H and ^{13}C NMR spectra displayed signals in agreement with a highly symmetrical structure. The cause of the observed spectroscopic simplicity is evident from the single-crystal X-ray structure of **4** (see Supporting Information), which shows a nearly perfect C_{3h} symmetry of the cage,[13] apparently persistent in solution, with all the amine groups pointing inward, the ethyl groups pointing outward, and the pyrrole rings facing the cavity (Figure 1).

Although the pyrrole rings are somewhat tilted, a roughly spherical cavity is envisaged from the projection: the size of the cavity, whose diameter between the benzene rings is

[*] Dr. O. Francesconi, Prof. C. Nativi, Dr. S. Roelens
Dipartimento di Chimica Organica
CNR and Università di Firenze
Via della Lastruccia, 13
50019 Sesto Fiorentino, Firenze (Italy)
Fax: (+39) 055-457-3570
E-mail: stefano.roelens@unifi.it
Dr. A. Ienco
Istituto di Chimica dei Composti Organometallici
CNR, Via Madonna del Piano
50019 Sesto Fiorentino, Firenze (Italy)
Prof. G. Moneti
Centro Interdipartimentale di Spettrometria di Massa
Università di Firenze, V.le G. Pieraccini, 6
50139 Firenze (Italy)

[**] Financial support by Ente Cassa di Risparmio di Firenze for the acquisition of a 400-MHz NMR spectrometer is gratefully acknowledged. High-field NMR experiments were performed at the Magnetic Resonance Center, University of Florence. M. Lucci is gratefully acknowledged for his kind assistance.

Supporting information for this article is available on the WWW under http://www.angewandte.org or from the author.

 © 2006 Wiley-VCH Verlag GmbH & Co. KGaA, Weinheim

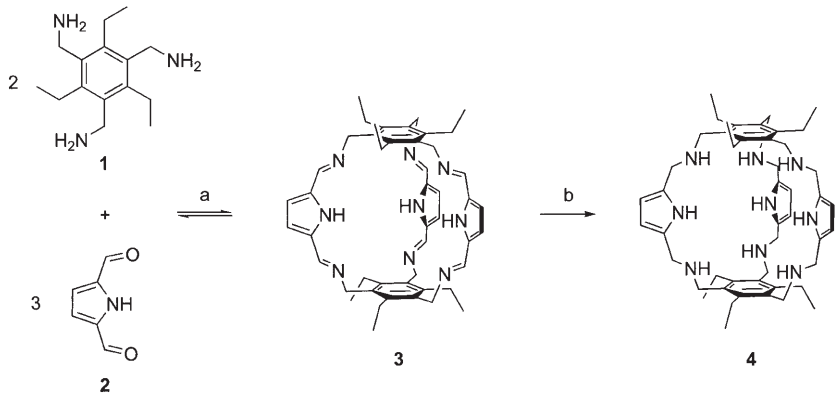

Scheme 1. Synthesis of the macrobicyclic cage **4**. a) MeOH, 12 h, room temperature; b) $NaBH_4$, MeOH/$CHCl_3$ (3:1), 30 min, room temperature.

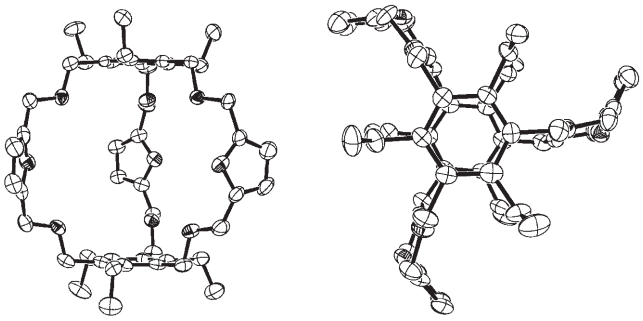

Figure 1. ORTEP projections of the X-ray crystal structure of **4**. Side view (left); top view (right). Ellipsoids are shown at the 50% probability level. Nitrogen atoms are represented as shaded ellipsoids. Solvent molecules and hydrogen atoms are omitted for clarity.

8.4 Å, and the arrangement of the amino groups appear well suited for guest binding.

Binding experiments were thus performed by ^{1}H NMR spectroscopic analysis in $CDCl_3$ with octyl-β-D-glucopyranoside (OctβGlc) as a soluble glycosidic guest. The spectra obtained by varying the **4**/OctβGlc molar ratio at a constant total concentration of reactants are shown in Figure 2.

The disappearance of the signals of **4** and the appearance of a new set of signals testified to the formation of a host–guest complex in a slow-exchange regime with the free species on the NMR timescale. Note that the single signal for the three equivalent pyrrolic NH protons is split into three nonequivalent singlets, whereas the pyrrolic CH signal splits into three strongly coupled nonequivalent signals, which show that the C_{3h} symmetry is lost upon complexation. Both slow exchange and desymmetrization, together with the marked downfield shift of the NH signals, point to the formation of a hydrogen-bonded complex with the glucoside at least partially included in the cavity. Indeed, a separate set of signals is observed for the glucose moiety as well, upfield with respect to that of the free glucoside and consistent with the shielding effect of the benzene rings; the glucose protons H3, H4, and H5 experience the largest shifts, thus suggesting inclusion from the side opposite the glycosidic chain (see Supporting Information). A 1:1 stoichiometry was inferred from complete disappearance of the free host for just over a stoichiometric reactant ratio and from the maximum intensity of the signals of the complex observed for a 1:1 molar ratio; the corresponding association constant (K_a) of $4.83(8)\times10^4\,M^{-1}$, which corresponds to an affinity of 20.7 μM of **4** for OctβGlc, was obtained with excellent agreement from four independent experiments at different reactant concentrations. Quite strikingly, the same experiment performed with the α anomer (OctαGlc) did not show any evidence of binding, thus indicating that **4** is able to bind the β anomer exclusively. Although very high β/α selectivities have been reported,[5d] to our knowledge, exclusive binding of one anomer in the recognition of glycosides is unprecedented for synthetic receptors. We believe that improved performance results from both a precise size fit of the β-glucoside and a closer complementarity of the amino/pyrrole versus the amide group in hydrogen bonding to the glucose moiety.

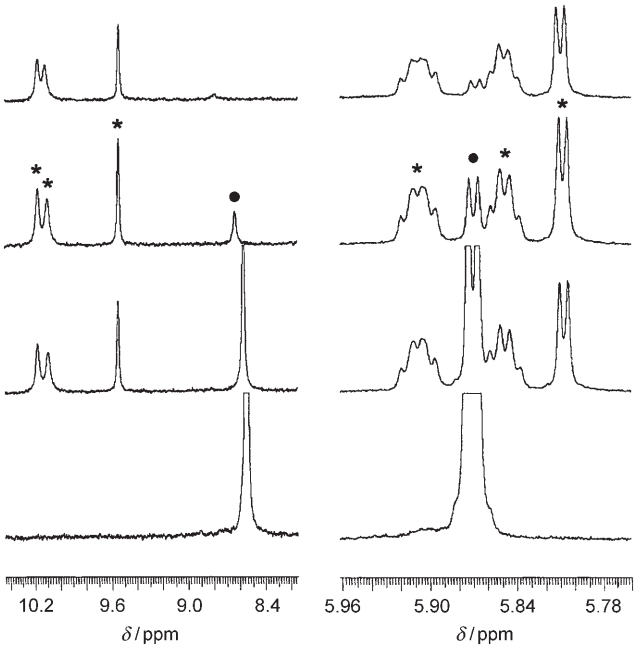

Figure 2. ^{1}H NMR spectra (400 MHz, 25 °C, $CDCl_3$) of mixtures of **4** and OctβGlc for a varying molar ratio (bottom to top: 1:0, 2:1, 1:1, 1:2) at constant total concentration of reactants. Only the pyrrole NH (left) and CH (right) signals of **4** are shown. Asterisks (*) correspond to [**4**·OctβGlc]; circles (●) indicate free **4**.

Further evidence supports the binding ability of **4**. Methyl-β-D-glucopyranoside (MeβGlc) is insoluble in $CDCl_3$. When solid MeβGlc was shaken with a millimolar solution of **4** in $CDCl_3$, the solid partially dissolved and the spectrum of the resulting solution unambiguously showed that over 40% of the cage was present in the complexed form. Bound **4** was increased to 50% in CCl_4 and to 75% when the experiment was performed in C_6D_6, thus proving that the cage receptor is capable of bringing insoluble β-glucosides (but not α-glucosides) into lipophilic solvents of low polarity. Indeed,

 © 2006 Wiley-VCH Verlag GmbH & Co. KGaA, Weinheim

MeαGlc was not appreciably dissolved in any of the above solvents. Most remarkably, β-D-glucose (βGlc) itself could be dissolved in benzene, with up to nearly 20% of bound receptor observed, whereas αGlc could not. Thus, the possibility that the observed β/α selectivity may be steric in origin, caused by the bulky octyl group, can be ruled out.

The behavior of the cage receptor toward α- and β-octylglycosides of biologically relevant monosaccharides, namely, galactopyranosides (Gal) and mannopyranosides (Man; Scheme 2), was further tested in $CDCl_3$. Although

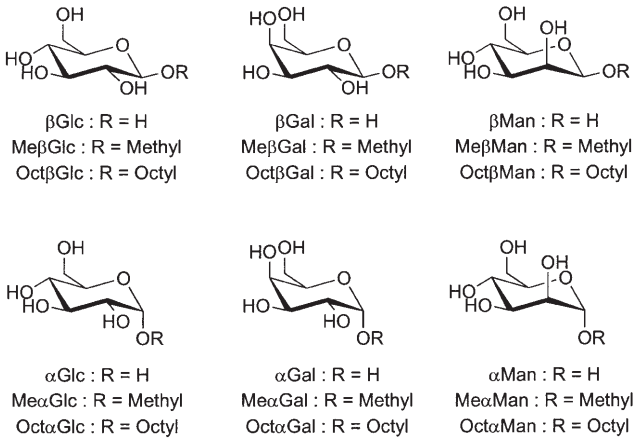

Scheme 2. Monosaccharides used in recognition experiments.

interaction between partners was observed by a shift of some signals of both the host and guest, the presence of a separate set of signals for the complex species was not detected in any case. Competitive experiments feeding **4** with equimolar mixtures of OctβGlc and each of the selected glycosides showed that for a 1:1:1 ratio of reactants, the fraction of **4** bound to OctβGlc decreased, with respect to that observed in the absence of competitors, by significantly less than 10% in the most adverse case. Experimental evidence demonstrated that none of the tested glycosides could effectively compete with OctβGlc for **4**.

Interestingly, the hexaimine cage **3** did not exhibit the same binding ability of **4**. Addition of OctβGlc to a solution of **3** in $CDCl_3$ did not show evidence of complexation, but rather induced slow re-equilibration of the cage to oligomeric products. Likewise, mixing **1** and **2** in the presence of OctβGlc as a template gave substantial amounts of oligomeric iminic products, together with lower yields of **3**. Apparently, the iminic cage does not bind to OctβGlc, and therefore using the latter as a template hampers, rather than assists, the formation of the cage. This contrasting behavior is most likely related to the geometrical restrictions imposed by the iminic double bond, which must lie coplanar to the conjugated pyrrole ring, rather than to the basicity/coordinative properties of the imine nitrogen atom, considering that the cage size is essentially identical.

Independent experimental support was desirable to validate the binding affinity results. Unfortunately, crystals suitable for X-ray analysis could not be obtained for any of the complexes of **4** with glucosides. However, ESI MS analysis provided clear-cut evidence that was in full agreement with the NMR binding studies. Two equimolar solutions of **4** with OctβGlc and OctαGlc, respectively, of the same concentration were submitted to positive-ion-mode ESI MS analysis under the same conditions. Although a peak for the $[\mathbf{4}\cdot\text{Oct}\beta\text{Glc}+\text{H}]^+$ complex was present in the spectrum of the former with comparable abundance with respect to the $[\mathbf{4}+\text{H}]^+$ peak, the peak of the complex could only be detected at the noise level in the spectrum of the latter (Figure 3). The

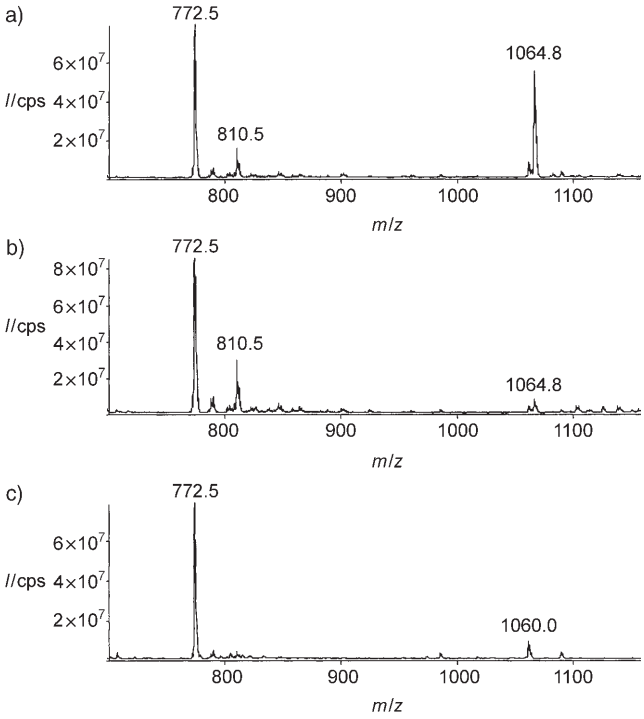

Figure 3. ESI MS spectra of a) **4** + OctβGlc (both 0.2 mM); b) **4** + OctαGlc (both 0.2 mM); and c) **4** + β-D-glucopyranoside pentaacetate (both 0.2 mM). Solvent: $CHCl_3/CH_3CN$ (1:1); ESI voltage: 6 kV; sampling cone potential: 56 V. *m/z*: 772.5 $[\mathbf{4}+\text{H}]^+$, 794.6 $[\mathbf{4}+\text{Na}]^+$, 810.5 $[\mathbf{4}+\text{K}]^+$, 1064.8 $[\mathbf{4}\cdot\text{Oct}\beta(\alpha)\text{Glc}+\text{H}]^+$.

latter spectrum appeared to be unaffected by three subsequent twofold increases of the concentration of the OctαGlc injected. In addition, the spectrum of an equimolar mixture of **4** and β-D-glucopyranoside pentaacetate, run for comparison under the same conditions, revealed a complete absence of the peak of the complex, thus showing that in the absence of free hydroxy groups, binding to the glucose moiety in the gas phase does not occur. Clearly, OctαGlc, which differs from OctβGlc only by the stereochemistry at C1, was not bound to **4** to a significantly larger extent than β-D-glucopyranoside pentaacetate.

Conclusive evidence was obtained by collision-induced dissociation (CID) experiments run on a triple quadrupole mass spectrometer. A scan of the intensity of the $[\mathbf{4}\cdot\text{Oct}\beta\text{Glc}+\text{H}]^+$ and $[\mathbf{4}+\text{H}]^+$ ions that originate from the ion of the complex selected at *m/z* 1065 with increasing potential gave the profiles shown in Figure 4b, which crossed for an energy value of 13.9 eV and corresponds to the energy

 © 2006 Wiley-VCH Verlag GmbH & Co. KGaA, Weinheim

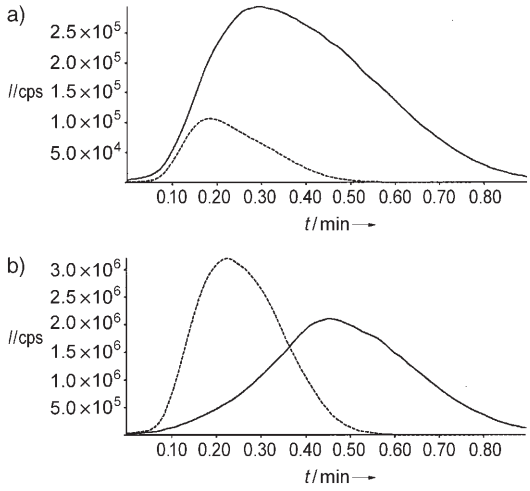

Figure 4. CID MS/MS analysis of the complex detected as the $[M+H]^+$ ion at m/z 1065. Products: 1065 ($[M+H]^+$, dotted line), 772 ($[\mathbf{4}+H]^+$, solid line). Solvent: $CHCl_3/CH_3CN$ (1:1); ESI voltage: 6 kV; sampling cone potential: 56 V; signal acquisition: 0.90 min, 89 scans over collision energies from 6 to 50 eV in 0.5 eV steps; collision-gas pressure: $P = 2.64\times10^{-5}$ torr. a) **4** + OctαGlc (0.2 mM each); b) **4** + OctβGlc (0.2 mM each).

required to dissociate 50% of the complex under the specific experimental conditions. The CID profiles that originated from the $[\mathbf{4}\cdot\text{OctαGlc}+H]^+$ ion under identical conditions (Figure 4a) did not exhibit any crossing point in the whole range of collision energies investigated, thus proving that spontaneous dissociation of the complex is prevalent for [**4**·OctαGlc] and that dissociation as a result of collisions is negligible at all concentrations, as identical results were obtained for four different concentrations of the OctαGlc injected (see Supporting Information). Exclusive recognition of the β anomer, observed in solution, was thus confirmed in the gas phase.

In summary, we have described a new synthetic cage receptor, quantitatively obtained by a one-pot reduction of a spontaneously self-assembled macrobicyclic cage, which forms by condensation of five component molecules through the thermodynamically controlled formation of six imine bonds. The receptor specifically recognizes the β anomer of D-glucose and its alkyl glucosides with complete β/α selectivity and effectively discriminates β monosaccharides of the gluco series from both the α and β anomers of the galacto and manno series. The discovery is bound to have an impact on the understanding of the structural features and the rational design of synthetic receptors for the molecular recognition of carbohydrates.[14]

Received: June 15, 2006
Revised: July 6, 2006

Keywords: cage compounds · carbohydrates · molecular recognition · self-assembly · synthetic receptors

[1] B. Ernst, G. W. Hart, P. Sinaÿ, *Carbohydrates in Chemistry and Biology*, *Part I*, *Vol. 2*, Wiley-VCH, Weinheim, **2000**; B. Ernst, G. W. Hart, P. Sinaÿ, *Carbohydrates in Chemistry and Biology*, *Part II*, *Vol. 4*, Wiley-VCH, Weinheim, **2000**.

[2] a) A. Lutzen in *Highlights in Bioorganic Chemistry* (Eds.: C. Schmuck, H. Wennemers), Wiley-VCH, Weinheim, **2004**, pp. 109–119; b) "Host–Guest Chemistry. Mimetic Approaches to Study Carbohydrate Recognition": *Topics in Current Chemistry*, *Vol. 218* (Ed.: S. Penadés), Springer, Heidelberg, **2001**; c) A. P. Davis, R. S. Wareham, *Angew. Chem.* **1999**, *111*, 3160–3179; *Angew. Chem. Int. Ed.* **1999**, *38*, 2978–2996.

[3] Covalent interactions have also been exploited in the recognition of carbohydrates; see, for example: T. D. James, K. R. A. S. Sandanayake, S. Shinkai, *Angew. Chem.* **1996**, *108*, 2038–2050; *Angew. Chem. Int. Ed. Engl.* **1996**, *35*, 1910–1922.

[4] For some recent examples, see: a) J. Bitta, S. Kubik, *Org. Lett.* **2001**, *3*, 2637–2640; b) S.-i. Tamaru, S. Shinkai, A. B. Khasanov, T. W. Bell, *Proc. Natl. Acad. Sci. USA* **2002**, *99*, 4972–4976; c) K. Ladomenou, R. P. Bonar-Law, *Chem. Commun.* **2002**, 2108–2109; d) Y.-H. Kim, J.-I. Hong, *Angew. Chem.* **2002**, *114*, 3071–3074; *Angew. Chem. Int. Ed.* **2002**, *41*, 2947–2950; e) O. Rusin, K. Lang, V. Kral, *Chem. Eur. J.* **2002**, *8*, 655–663; f) M. Segura, B. Bricoli, A. Casnati, E. M. Munoz, F. Sansone, R. Ungaro, C. Vicent, *J. Org. Chem.* **2003**, *68*, 6296–6303; g) A. Vacca, C. Nativi, M. Cacciarini, R. Pergoli, S. Roelens, *J. Am. Chem. Soc.* **2004**, *126*, 16456–16465; h) M. Mazik, H. Cavga, P. G. Jones, *J. Am. Chem. Soc.* **2005**, *127*, 9045–9052; i) C. Schmuck, M. Schwegmann, *Org. Lett.* **2005**, *7*, 3517–3520; j) H. Abe, Y. Aoyagi, M. Inouye, *Org. Lett.* **2005**, *7*, 59–61.

[5] a) T. Velasco, G. Lecollinet, T. J. Ryan, A. P. Davis, *Org. Biomol. Chem.* **2004**, *2*, 645–647; b) T. J. Ryan, G. Lecollinet, T. Velasco, A. P. Davis, *Proc. Natl. Acad. Sci. USA* **2002**, *99*, 4863–4866; c) G. Lecollinet, A. P. Dominey, T. Velasco, A. P. Davis, *Angew. Chem.* **2002**, *114*, 4267–4270; *Angew. Chem. Int. Ed.* **2002**, *41*, 4093–4096; d) A. P. Davis, R. S. Wareham, *Angew. Chem.* **1998**, *110*, 2397–2401; *Angew. Chem. Int. Ed.* **1998**, *37*, 2270–2273.

[6] a) R. Welti, Y. Abel, V. Gramlich, F. Diederich, *Helv. Chim. Acta* **2003**, *86*, 548–562; b) R. Welti, F. Diederich, *Helv. Chim. Acta* **2003**, *86*, 494–503.

[7] T. Ishi-i, M. A. Mateos-Timoneda, P. Timmerman, M. Crego-Calama, D. N. Reinhoudt, S. Shinkai, *Angew. Chem.* **2003**, *115*, 2402–2407; *Angew. Chem. Int. Ed.* **2003**, *42*, 2300–2305.

[8] R. Liu, W. Clark Still, *Tetrahedron Lett.* **1993**, *34*, 2573–2576.

[9] a) S. Hanessian, M. Simard, S. Roelens, *J. Am. Chem. Soc.* **1995**, *117*, 7630–7645; b) O. Ermer, A. Eling, *J. Chem. Soc. Perkin Trans. 2* **1994**, 925–944.

[10] J. L. Sessler, S. Camiolo, P. A. Gale, *Coord. Chem. Rev.* **2003**, *240*, 17–55.

[11] C. E. Loader, H. J. Anderson, *Synthesis* **1978**, 295–297.

[12] For some recent examples of the efficient assembly of macrocyclic and supramolecular hosts of complex structure by imine formation, see: a) X. Liu, Y. Liu, G. Li, R. Warmuth, *Angew. Chem.* **2006**, *118*, 915–918; *Angew. Chem. Int. Ed.* **2006**, *45*, 901–904; b) M. J. MacLachlan, *Pure Appl. Chem.* **2006**, *78*, 873–888; c) J. Gawronski, K. Gawronska, J. Grajewski, M. Kwit, A. Plutecka, U. Rychlewska, *Chem. Eur. J.* **2006**, *12*, 1807–1817; d) N. Kuhnert, A. Lopez-Periago, G. M. Rossignolo, *Org. Biomol. Chem.* **2005**, *3*, 524–537; e) E. A. Katayev, G. Dan Pantos, M. D. Reshetova, V. N. Khrustalev, V. M. Lynch, Y. A. Ustynyuk, J. L. Sessler, *Angew. Chem.* **2005**, *117*, 7552–7556; *Angew. Chem. Int. Ed.* **2005**, *44*, 7386–7390.

[13] For recent highlight articles on C_3-symmetric receptors and ligands, see: a) C. Moberg, *Angew. Chem.* **2006**, *118*, 4838–4840; *Angew. Chem. Int. Ed.* **2006**, *45*, 4721–4723; b) M. Albrecht, *Angew. Chem.* **1999**, *111*, 3671–3674; *Angew. Chem. Int. Ed.* **1999**, *38*, 3463–3465.

[14] See Supporting Information for general methods and materials, synthetic experimental details, NMR spectra, and CID MS spectra.

 © 2006 Wiley-VCH Verlag GmbH & Co. KGaA, Weinheim

Lead Iron Oxides

DOI: 10.1002/anie.200602480

Crystallographic Shear Structures as a Route to Anion-Deficient Perovskites**

Artem M. Abakumov, Joke Hadermann, Sara Bals, Ivan V. Nikolaev, Evgeny V. Antipov, and Gustaaf Van Tendeloo*

Because of the technological importance of perovskite-based oxides, numerous pathways towards new structures have been developed, including ordering at the A and/or B cation sites of the perovskite (ABO_3) structure, vacancy ordering at the anion site, the intergrowth of perovskite and related structures, and the formation of hexagonal perovskite polytypes. However, it has been generally accepted that crystallographic shear (CS) structures cannot be realized in perovskites.[1] CS planes commonly occur in anion-deficient oxides derived from the ReO_3 or rutile (TiO_2) structures, which are based on metal-centered octahedra. Arrangement of the CS planes at different periodicities generates a homologous series. Some of the well-known examples of CS structures are M_nO_{3n-1}, M_nO_{3n-2} (M = Mo, W), Ti_nO_{2n-1}, and the block structures of Nb_2O_5 and its Ti-containing derivatives.[2–6] The shear operation is such that along the CS plane the octahedra share edges or faces, instead of corners or edges as in the basic structure. The ReO_3 structure is based on the same three-dimensional framework of corner-sharing BO_6 octahedra found in the perovskite structure, but the 12-coordinate A cation sites of the perovskite structure are empty in ReO_3. Usually, the presence of A cations in perovskites favors point defects in the anion sites (in a random or ordered arrangement), leading to a lower coordination number for the B cations, and prevents the elimination of anion point defects by a shear operation.[2] Herein, we report the occurrence of CS structures in perovskite-based "$Pb_2Fe_2O_5$" for the first time. We also describe the general crystallographic mechanism of CS-plane formation in a perovskite framework with the A sites filled by cations bearing a lone $6s^2$ electron pair, which involves the elimination of O vacancies by the shear operation and the relaxation of the structure at the CS plane. We discuss the role of the lone electron pair in directing structure formation, as well as the relationship between the crystallographic orientation of the CS plane and the chemical composition. The discovery of this mechanism opens up new possibilities for the design of novel perovskite-based compounds containing A cations with a lone $6s^2$ electron pair.

"$Pb_2Fe_2O_5$" (or "$PbFeO_{2.5}$") is expected to be an anion-deficient perovskite of the brownmillerite (Ca_2AlFeO_5) type;[7–9] however, its structure has not yet been determined. Because of the complexity of the structure and the prevalence of domain fragmentation, the only road to solving the structure is by transmission electron microscopy (TEM). The brighter reflections in the electron diffraction (ED) patterns of "$Pb_2Fe_2O_5$" (Figure 1a) reveal a perovskite

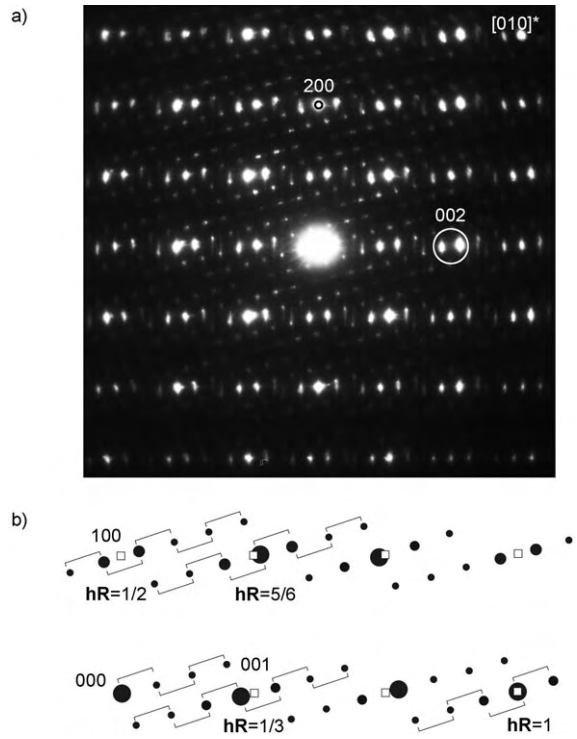

Figure 1. a) [010]* ED pattern of "$Pb_2Fe_2O_5$", indexed in the perovskite subcell. b) Derivation of fractional shifts $\mathbf{hR}$; empty squares indicate the positions of reciprocal lattice nodes of the perovskite subcell; square brackets denote the modulation vector $\boldsymbol{q}$; see text for details.

sublattice with a parameter $a_p \approx 3.9$ Å (p denotes the perovskite subcell). Linear arrays of satellite reflections associated with each basic reciprocal lattice node are typical for periodic CS planes. The displacement vector for the CS planes was deduced from the ED patterns as $\mathbf{R} = 1/2\,[110]_p + 1/3\,[001]_p$ by measuring the fractional shifts $\mathbf{hR}$ for the satellite reflections (Figure 1b).[10,11][+] Closer inspection of the [010]*

[*] Dr. A. M. Abakumov, I. V. Nikolaev, Prof. E. V. Antipov
Department of Chemistry
Moscow State University
119992 Moscow (Russia)
Fax: (+7) 495-939-47-88
E-mail: abakumov@icr.chem.msu.ru
Prof. J. Hadermann, Dr. S. Bals, Prof. G. Van Tendeloo
Centre for Electron Microscopy for Materials Science
University of Antwerp
Groenenborgerlaan 171, 2020 Antwerp (Belgium)

[**] The work was supported in part by the IAP V-1 program of the Belgium government and by the Russian Foundation for Basic Research (RFBR; 05-03-34812, 06-03-90168). The authors acknowledge Pavel S. Chizhov for the ELF calculations. S.B. is grateful to the Fund for Scientific Research, Flanders.

[+] The fractional-shift method describes the positions of the satellite reflections as $\mathbf{H} = \mathbf{h} + [m + \mathbf{hR}]\,\boldsymbol{q}$, where $\mathbf{H}$ and $\mathbf{h}$ are satellite and basic diffraction vectors, $\boldsymbol{q}$ is the modulation vector, m is the order of the satellite reflection, and $\mathbf{R}$ is the displacement vector of the CS planes. The product $\mathbf{hR}$ results in the fractional shift of the array of satellites with respect to the position of the basic reflection.

 © 2006 Wiley-VCH Verlag GmbH & Co. KGaA, Weinheim

ED pattern reveals the incommensurate character of the modulation. The monoclinic unit-cell parameters (denoted by m) for the commensurate approximant are $\mathbf{a}_m = 3\mathbf{a}_p + 7\mathbf{c}_p$, $\mathbf{b}_m = \mathbf{b}_p$, $\mathbf{c}_m = -4\mathbf{a}_p + \mathbf{c}_p$ ($a_m = 29.881$, $b_m = 3.884$, $c_m = 16.062$ Å, $\beta = 98.49°$; space group $C2/m$). The CS planes are parallel to $(100)_m = (104)_p$.

The cation positions in "$Pb_2Fe_2O_5$" were determined using high-angle annular dark field (HAADF) scanning transmission electron microscopy (STEM). In the scanning transmission mode, the intensity related to a column of atoms is proportional to Z^n ($1 < n < 2$), where Z is the average atomic number of the projected column. This relationship often allows a straightforward interpretation of HAADF STEM images. The brighter spots on the unfiltered [010] HAADF STEM image of "$Pb_2Fe_2O_5$" (Figure 2a) are associated with the Pb columns, whereas the weaker spots (difficult to see in Figure 2a) correspond to the projection of the Fe columns. The resulting atomic arrangement of the cations is shown in Figure 2b. The perovskite blocks (outlined by thick dashed lines in Figure 2b) have a length of $4a_p$ and are mutually shifted along c_p by one perovskite unit cell, according to the $(104)_p$ orientation of the CS plane. Between the perovskite blocks, six-sided channels consisting of six Fe columns surrounding two Pb columns are formed (outlined by thin solid lines in Figure 2b). This arrangement is confirmed by simulations of the [010] HAADF STEM image (Figure 2a).

The new structure is derived from the perovskite structure by a periodic insertion of $(104)_p$ CS planes with the displacement vector $\mathbf{R} = \mathbf{R}_0 + \mathbf{R}_1$, where $\mathbf{R}_0 = 1/2[110]_p$ and $\mathbf{R}_1 = 1/3[001]_p$. The $\mathbf{R}_0$ shift applied along the $(\bar{1}01)_p$ plane eliminates the O atoms marked as open squares in Figure 3a. The O atoms at the edges of the perovskite unit cell parallel to c_p (gray square in Figure 3a) are not eliminated by the shear operation, but cannot be retained together with the Pb columns, owing to abnormally short Pb–O separations. The $\mathbf{R}_0$ displacement introduces columns of edge-sharing FeO_5 square pyramids that are bridged through corner sharing with columns of FeO_6 octahedra (Figure 3b). Pb atoms are positioned inside the resulting channels, where space is available for their lone $6s^2$ electron pairs. However, the $\mathbf{R}_0$ shear alone would lead to very short Pb–Pb separations of $a_p/\sqrt{2} \approx 2.76$ Å between the Pb atoms within the channels. The displacement $\mathbf{R}_1$ increases this distance to 3.56 Å (Figure 3c). The $\mathbf{R}_1$ displacement also distorts the FeO_5 square pyramids, making the coordination environment of the Fe atoms closer to a trigonal bipyramid.

CS planes with high $(h0l)$ indices can be considered as composed of short segments of low-index CS planes, such as the $(\bar{1}01)_p$ and $(001)_p$ planes, as the main constituents. The $1/2[110]_p(\bar{1}01)_p$ structure (in which square brackets indicate the displacement vector and parentheses indicate the orientation of the CS plane) contains layers of six-sided channels parallel to $(\bar{1}01)_p$ (Figure 3d), which are separated by n perovskite layers, resulting in a $A_2Fe_2O_4 + n\,AFeO_3$ homologous series.

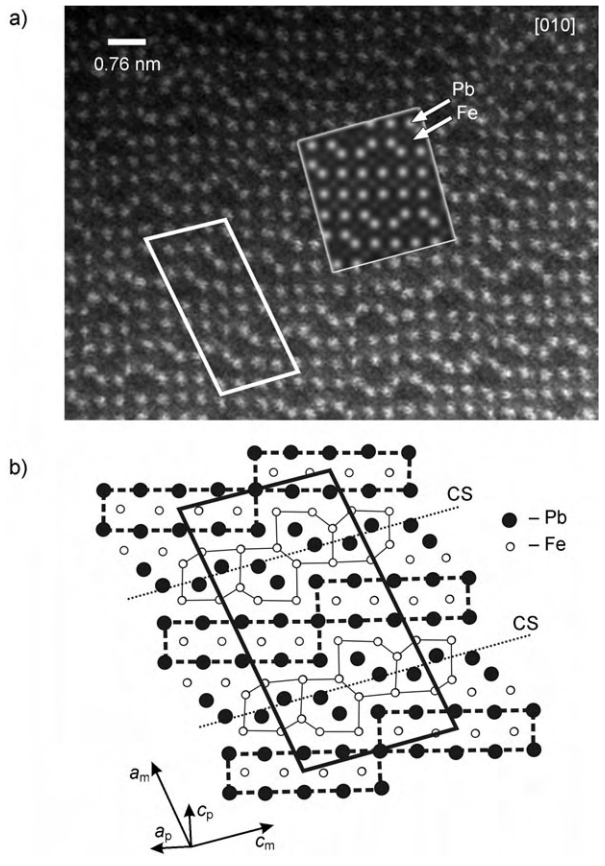

Figure 2. a) [010] HAADF STEM image of "$Pb_2Fe_2O_5$"; the monoclinic unit cell is outlined by thick white lines; a simulation of the image is outlined by thin white lines. b) Arrangement of the columns of Pb and Fe atoms in "$Pb_2Fe_2O_5$"; the monoclinic unit cell is outlined by thick solid lines; the perovskite blocks are outlined by thick dashed lines; the six-sided channels are outlined by thin solid lines; the CS planes are indicated by thin dotted lines.

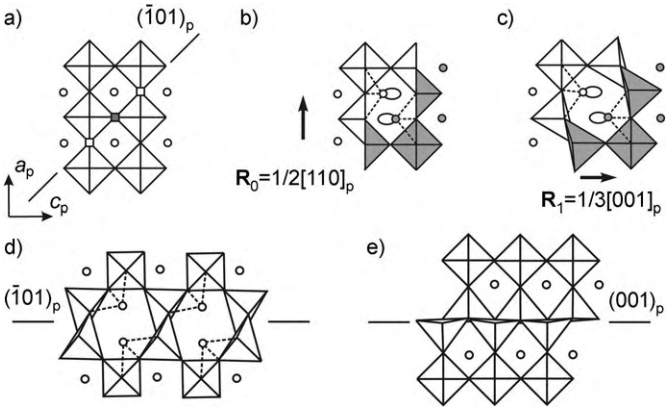

Figure 3. Generation of CS planes in "$Pb_2Fe_2O_5$": a) creation of O vacancies (squares) along the $(\bar{1}01)_p$ plane; b) application of the $\mathbf{R}_0 = 1/2[110]_p$ displacement vector, leading to the formation of FeO_5 square pyramids and six-sided channels; c) application of the $\mathbf{R}_1 = 1/3[001]_p$ displacement vector, leading to an increase in the Pb–Pb separation within the channels; circles Pb (with lone $6s^2$ electron pairs), polyhedra FeO_6/FeO_5; displaced part of the structure is gray. d) Structure of the low-index $1/2[110]_p(\bar{1}01)_p$ CS plane. e) Structure of the low-index $1/2[110]_p(001)_p$ CS plane.

 © 2006 Wiley-VCH Verlag GmbH & Co. KGaA, Weinheim

Despite not having been previously considered as a CS structure, $Pb_{1.33}Sr_{0.67}Fe_2O_5$ ($A_4Fe_4O_{10}$) corresponds to the second member ($n=2$) of this series.[12]

The $1/2[110]_p(001)_p$ operation could be a conservative shear, since the displacement vector is parallel to the interface plane. However, the $1/2[110]_p$ shift along the FeO_2 plane transforms the FeO_6 octahedra into twice as many FeO_5 square pyramids (Figure 3e). Only half of the square pyramidal sites are occupied by Fe atoms; however, filling the vacant sites by extra Fe atoms would result in a composition of Fe_2O_2 for the layer and an excess of Fe with respect to the overall composition. These double layers of edge-sharing FeO_5 pyramids can be separated by perovskite layers, leading to $AFe_2O_3 + n\,AFeO_3$ homologues. Similar alternating double layers of strongly distorted FeO_5 pyramids and perovskite layers of FeO_6 octahedra occur in $Sr_4Fe_6O_{12+\delta}$ ($A_2Fe_3O_6$), which can be considered as the $n=1$ member of the homologous series.[13]

The $1/2[110]_p(104)_p$ CS structure observed for "$Pb_2Fe_2O_5$" can be broken up as $2(101)_p + (\bar{1}01)_p + (001)_p$, resulting in a composition of $3\,Pb_2Fe_2O_4 + PbFe_2O_3 + 8\,PbFeO_3 = Pb_{15}Fe_{16}O_{39}$, since the perpendicular $(101)_p$ and $(\bar{1}01)_p$ planes delimit rectangular perovskite blocks of eight FeO_6 octahedra.

Other CS planes, such as $(\bar{3}05)_p$, were also observed for "$Pb_2Fe_2O_5$" (in the same sample). The corresponding CS structure can be represented as $3(\bar{1}01) + 2(001)$ with a composition of $3\,Pb_2Fe_2O_4 + 2\,PbFe_2O_3 + 10\,PbFeO_3 = Pb_{18}Fe_{20}O_{48}$, because the perovskite layers between the CS planes have an average thickness of two FeO_6 octahedra. The cation composition agrees with the Pb deficiency experimentally determined using energy-dispersive X-ray (EDX) microanalysis (Pb:Fe = 0.90(3):1.00).

The [010] projections of the $Pb_{15}Fe_{16}O_{39}$ and $Pb_{18}Fe_{20}O_{48}$ structures are shown in Figure 4; experimental evidence for the structures is presented in Figure 5. Image simulations based on the structures in Figure 4 (Figure 5, insets) are in excellent agreement with the experimental high resolution electron microscopy (HREM) images.

The CS structures in "$Pb_2Fe_2O_5$" ($1/2[110]_p(\bar{1}04)_p$ and $1/2[110]_p(\bar{3}05)_p$ CS planes), $Pb_{1.33}Sr_{0.67}Fe_2O_5$ ($1/2[110]_p(\bar{1}01)_p$ CS plane),[12] and $PbMnO_{2.75}$ ($1/2[110]_p(704)_p$ CS plane)[14] occur because the B cations are able to adopt coordination numbers of 5 or 6 and because the Pb^{2+} cations, which have a lone electron pair, favor an asymmetric coordination environment. The Pb atoms within the six-sided channels of all three structures are coordinated to O atoms at three short (2.28–2.43 Å) and three long (2.63–2.70 Å) Pb–O distances.[12] The lone $6s^2$ electron pair E completes the coordination polyhedron of the Pb atoms (PbO_6E). We confirmed the localization of the lone electron pairs on the Pb atoms in the six-sided channels by analyzing the electron localization function (ELF) distribution in the $Pb_{1.33}Sr_{0.67}Fe_2O_5$ structure. Typically ionic cations, such as Sr^{2+} prefer the A sites in the perovskite blocks. This result agrees with the experimentally observed Pb and Sr distribution in $Pb_{1.33}Sr_{0.67}Fe_2O_5$, in which the six-sided channels are exclusively filled with Pb^{2+} cations.[12]

It is expected that the building principles derived herein can lead to new perovskite-based compounds, in which the chemical composition is adjusted by varying the orientation of the CS plane and the thickness of the separating perovskite slabs. In the CS structures observed herein, the size of the perovskite slabs between CS planes of a particular orientation is determined by the oxidation state of the Fe cations; thus, a change in the partial O_2 pressure or the synthesis temperature could induce a variety of other possible structures. The power of the new structural principles becomes clear if one considers introducing two types of B cations with different oxidation states and coordination numbers, in addition to an A cation with a lone electron pair, into the perovskite-based structure.

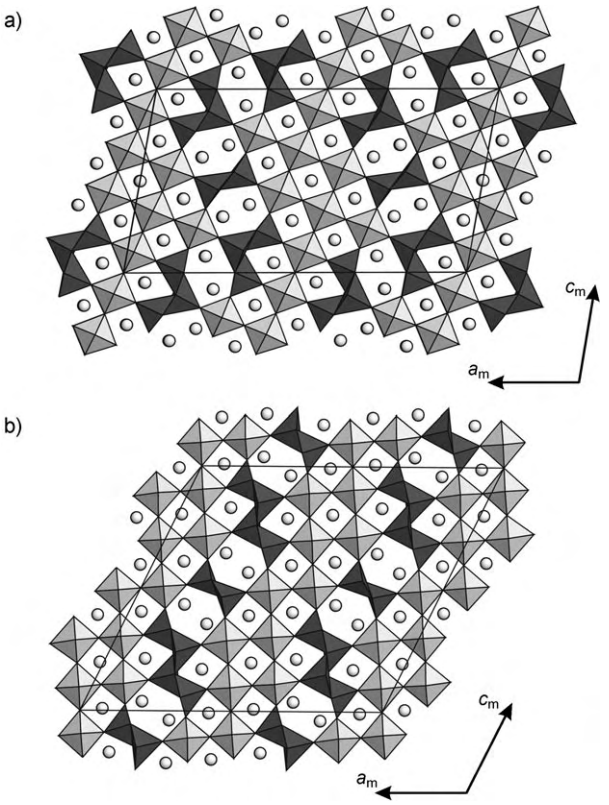

Figure 4. [010] projections of the a) $Pb_{15}Fe_{16}O_{39}$ and b) $Pb_{18}Fe_{20}O_{48}$ CS structures; circles Pb, gray polyhedra FeO_6, black polyhedra FeO_5.

Experimental Section

"$Pb_2Fe_2O_5$" was prepared by annealing PbO and Fe_2O_3 in a 2:1 ratio in air at 800 °C for 210 h. The X-ray diffraction pattern of the product was fit using the Le Bail method, resulting in the parameters $a=3.8879(2)$, $b=3.8838(2)$, $c=3.9386(3)$ Å, $\beta=90.291(6)°$, $\mathbf{q}=0.03760(1)\mathbf{a}^*+0.12981(2)\mathbf{c}^*$ ($\mathbf{q}=1/2\,\boldsymbol{q}$, where $\boldsymbol{q}$ is the modulation vector used for the fractional-shift method) and the $(3+1)$D space group $X2/m(\alpha 0\gamma)$, $X=[1/2,\ 1/2,\ 1/2,\ 1/2]$. The EDX analysis was performed on a JEOL JSM 5510 electron microscope with an INCA attachment. For the electron microscopy, Philips CM20, Jeol 4000EX, and Jeol 3000F instruments were used. Image simulations were carried out with the MacTempas software. The ELF distribution was evaluated for a model compound of composition $PbSrFe_2O_5$, in which the mixed-occupancy ($Pb_{0.33}Sr_{0.67}$) position in the perovskite block of the $Pb_{1.33}Sr_{0.67}Fe_2O_5$ structure is fully occupied by Sr. The ELF was determined from the results of density functional theory (DFT) calculations performed using the TB-LMTO-ASA method and the

 © 2006 Wiley-VCH Verlag GmbH & Co. KGaA, Weinheim

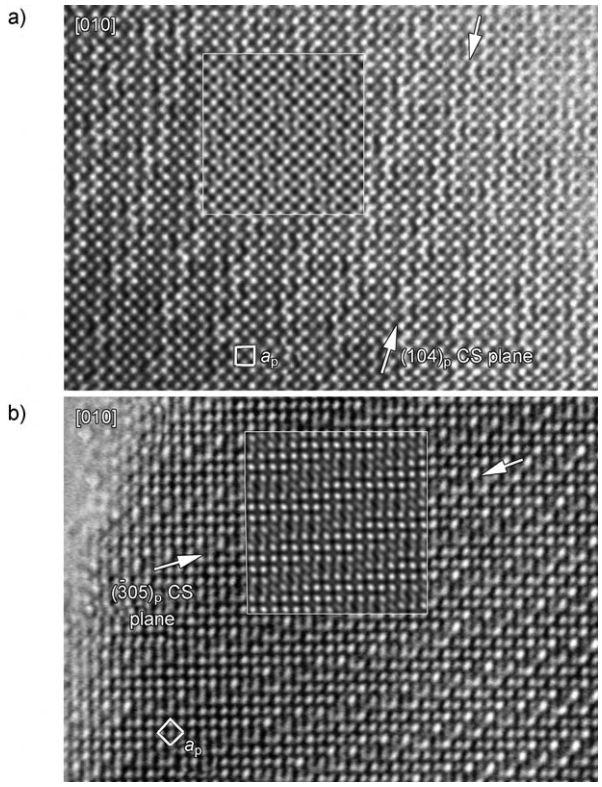

Figure 5. [010] HREM images of the a) $Pb_{15}Fe_{16}O_{39}$ $(1/2[110]_p(104)_p$ CS plane) and b) $Pb_{18}Fe_{20}O_{48}$ $(1/2[110]_p(\bar{3}05)_p$ CS plane) structures; the cubic perovskite unit cell is outlined by thick white lines; simulations of the images ($\Delta f = -275$ Å, $t = 30$ Å (a); $\Delta f = -200$ Å, $t = 30$ Å (b) are outlined by thin white lines. Δf = defocus, t = thickness.

Barth–Hedin exchange-correlation potential,[15] with the LMTO 4.7 program package.[16]

Received: June 20, 2006
Published online: September 13, 2006

Keywords: crystallographic shear · electron microscopy · iron · lead · perovskite phases

[1] R. H. Mitchell, *Perovskites: Modern and Ancient*, Almaz Press, Thunder Bay (Canada), **2002**.
[2] A. Magneli, *Acta Chem. Scand.* **1948**, *2*, 501 – 517.
[3] L. Kihlborg, *Ark. Kemi* **1963**, *21*, 443 – 460.
[4] A. D. Wadsley, *Rev. Pure Appl. Chem.* **1955**, *5*, 165 – 193.
[5] S. Andersson, L. Jahnberg, *Ark. Kemi* **1963**, *21*, 413 – 426.
[6] A. D. Wadsley, *Acta Crystallogr.* **1961**, *14*, 660 – 664; A. D. Wadsley, *Acta Crystallogr.* **1961**, *14*, 664 – 670.
[7] J.-C. Grenier, M. Pouchard, P. Hagenmuller, *Rev. Chim. Miner.* **1977**, *14*, 515 – 522.
[8] J. Mexmain, S.-L. Hivert, *Ann. Chim.* **1978**, *3*, 91 – 97.
[9] F. P. Glasser, *Am. Mineral.* **1967**, *52*, 1085 – 1093.
[10] J. Van Landuyt, R. De Ridder, R. Gevers, S. Amelinckx, *Mater. Res. Bull.* **1970**, *5*, 353 – 362.
[11] D. Van Dyck, D. Broddin, J. Mahy, S. Amelinckx, *Phys. Status Solidi A* **1987**, *103*, 357 – 373.
[12] V. Raynova-Schwarten, W. Massa, D. Z. Babel, *Z. Anorg. Allg. Chem.* **1997**, *623*, 1048 – 1054.
[13] M. D. Rossell, A. M. Abakumov, G. Van Tendeloo, J. A. Pardo, J. Santiso, *Chem. Mater.* **2004**, *16*, 2578 – 2584.
[14] C. Bougerol, M. F. Gorius, I. E. Grey, *J. Solid State Chem.* **2002**, *169*, 131 – 138.
[15] U. Barth, L. Hedin, *J. Phys. C* **1972**, *5*, 1629 – 1642.
[16] O. Jepsen, A. Burkhardt, O. K. Andersen, *The TB-LMTO-ASA Program*, Version 4.7, Max-Planck-Institut für Festkörperforschung, Stuttgart (Germany), **1999**.

 © 2006 Wiley-VCH Verlag GmbH & Co. KGaA, Weinheim

Catalytic Isomerization

DOI: 10.1002/anie.200600377

A Highly Active and Selective Nanocomposite Catalyst for C_{7+} Paraffin Isomerization**

*Jinsuo Xu and Jackie Y. Ying**

Due to the increasingly stringent regulation by the EPA of toxic aromatics in motor fuel, there has been a sharp rise in the demand for processes that can boost the octane value of non-aromatic hydrocarbons.[1] This is particularly true for C_{7+} paraffins (i.e. *n*-C_7 and higher paraffins), whose straight-chain counterparts have very low octane values. Skeletal isomerization of these hydrocarbons into high-octane branched paraffins has been found to be the most effective route to compensate for the octane value loss associated with removal of aromatics.[1–4] However, the isomerization of C_{7+} paraffins is very different from the isomerization of light paraffins (i.e. *n*-C_4 and *n*-C_5) as cracking becomes increasingly competitive with isomerization as the carbon chain length increases.[2,5] Furthermore, the yield of multibranched paraffins is more critical for the economics of the process than the yield of total branched paraffins since the monobranched C_{7+} paraffins do not have high enough octane numbers to be blended directly into the octane pool. Thus, minimizing cracking while achieving high yields of multibranched paraffins has been a

[*] Prof. J. Y. Ying
Institute of Bioengineering and Nanotechnology
31 Biopolis Way
The Nanos, Singapore 138669 (Singapore)
Fax: (+65) 6478-9020
E-mail: jyying@ibn.a-star.edu.sg
Homepage: www.ibn.a-star.edu.sg
Dr. J. Xu, Prof. J. Y. Ying
Department of Chemical Engineering
Massachusetts Institute of Technology
Cambridge, MA 02139-4307 (USA)

[**] We thank Dr. Frits Dautzenberg and Dr. Philip Angevine (ABB Lummus Global, Inc.) for helpful discussions, and Michael Frongillo (MIT-NSF CMSE) for assistance with HR-TEM studies. This work was supported by ABB Lummus Global, Inc.

Supporting Information for this article is available on the WWW under http://www.angewandte.org or from the author.

WILEY InterScience DISCOVER SOMETHING GREAT
© 2006 Wiley-VCH Verlag GmbH & Co. KGaA, Weinheim

major challenge for the development of C_{7+} isomerization catalysts.[2,4,6–12]

Here we report the development of a highly active and selective multicomponent nanocomposite catalyst, $Pt/WO_3/M\text{-}ZrO_x$. This system involves highly dispersed WO_3 domains and Pt clusters supported on heteroatom-substituted ZrO_2 nanocrystals ($M\text{-}ZrO_x$). This nanocomposite material enables the efficient isomerization of C_{7+} paraffins at a remarkably low temperature of 125 °C. This highly active catalyst is very selective for branched paraffins, especially multibranched paraffins, and demonstrates long-term stability and excellent tolerance to feed impurities. Unlike conventional isomerization catalysts, which are designed as strong solid acids, the superior catalytic performance of $Pt/WO_3/M\text{-}ZrO_x$ is associated with an unusually high surface density of spilt-over H_2 and a facile reverse process of H_2 spillover.[13–15]

Nanocomposite processing can be used to develop unique catalysts with superior surface areas, ultrahigh dispersion of components, and excellent stability.[16,17] In this study, an easier method of simultaneously precipitating different metal cations, such as Al^{3+} with Zr^{4+}, under controlled pH conditions is employed to obtain metal hydroxides that are mixed at an atomic level. Ultrahigh dispersions of WO_3 and Pt on the $M\text{-}ZrO_x$ support are then obtained by sequential impregnation. The resulting $Pt/WO_3/M\text{-}ZrO_x$ nanocomposite catalyst exhibits significantly greater activity than the benchmark $Pt/WO_3/ZrO_2$ and Pt/Beta catalysts and is able to successfully convert various paraffins with boiling points close to that of n-C_7 at a relatively low temperature with superb isomerization selectivity.

n-Heptane isomerization was chosen as a model reaction to evaluate the catalyst performance. Figure 1 shows that $Pt/WO_3/Al\text{-}ZrO_x$ is about six times as active as $Pt/WO_3/ZrO_2$ and twice as active as Pt/Beta at 200 °C after about 2 h. The dopant also improves the catalyst's isomerization selectivity substantially. At 80% conversion of n-heptane, an isomerization selectivity of 86% was maintained over $Pt/WO_3/Al\text{-}ZrO_x$, whereas selectivities of 81% and 76% were obtained with $Pt/WO_3/ZrO_2$ and Pt/Beta, respectively.

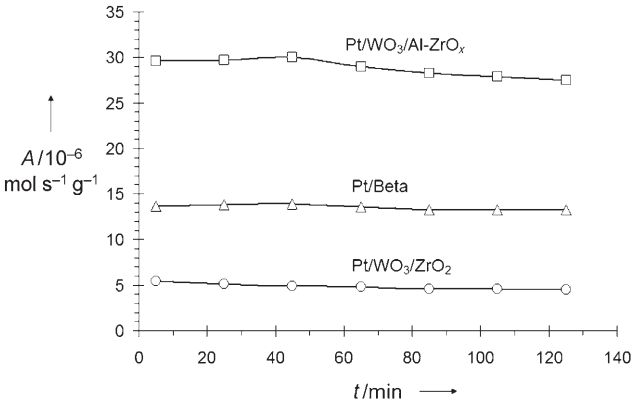

Figure 1. n-Heptane isomerization activities (A) over $Pt/WO_3/Al\text{-}ZrO_x$, Pt/Beta, and $Pt/WO_3/ZrO_2$ at 200 °C and atmospheric pressure; t = reaction time, H_2/n-C_7 feed molar ratio = 16. The contact time was adjusted to obtain n-C_7 conversions of 15–30%.

The superior activity of $Pt/WO_3/Al\text{-}ZrO_x$ allows this nanocomposite catalyst to operate at a lower reaction temperature, which is favorable for greater isomerization selectivity. As shown in Figure 2, an isomerization selectivity

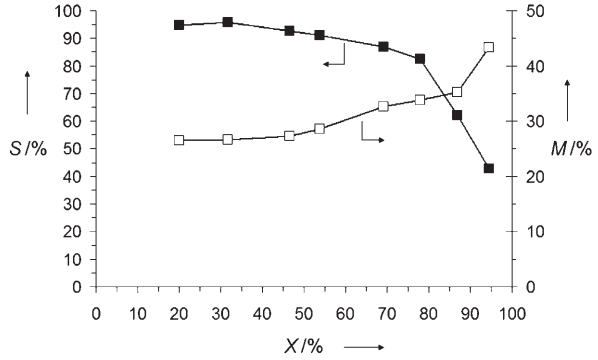

Figure 2. Isomerization selectivity (S; ■) and percentage of multibranched paraffins in total isomers (M; □) versus n-C_7 conversion (X) over $Pt/WO_3/Al\text{-}ZrO_x$ at 150 °C and atmospheric pressure; H_2/n-C_7 feed molar ratio = 16. The contact time was adjusted to obtain the different levels of n-C_7 conversions noted.

of more than 80% is attained even at 90% conversion of n-heptane at 150 °C. Remarkably, multibranched heptanes account for over 45% of the isomers obtained, thus providing an unprecedented boost in octane value. At 150 °C, the $Pt/WO_3/Al\text{-}ZrO_x$ nanocomposite catalyst also efficiently converts other paraffins that are typically present with n-C_7 in the refinery stream, such as n-hexane (0.22 $\mu mol\,s^{-1}\,g^{-1}$) and n-octane (9.9 $\mu mol\,s^{-1}\,g^{-1}$), again with excellent isomerization selectivities. At 80% conversions of n-hexane and n-octane, isomerization selectivities of 98% and 82%, respectively, were attained (see Supporting Information).

The reaction temperature over $Pt/WO_3/Al\text{-}ZrO_x$ could be lowered further at elevated pressures, as commonly practiced in commercial processes. For example, at a total pressure of 100 psig, a H_2/n-C_7 feed molar ratio of 1.0, and a volume hour space velocity of 1 h^{-1}, 30% conversion of n-C_7 with greater than 99% isomerization selectivity was obtained over this nanocomposite catalyst at 125 °C under trickle-bed conditions. Such a low reaction temperature would further boost the formation of highly branched isomers while simultaneously reducing cracking.

$Pt/WO_3/Al\text{-}ZrO_x$ also demonstrates good tolerance against feed impurities and excellent long-term stability. Pt/chlorided-alumina catalysts can be rapidly deactivated by trace amounts of aromatics or cyclohexane in the feedstock due to the strong adsorption of these electron-rich molecules at acidic sites.[5] Pt/zeolite catalysts are also sensitive to aromatics and cyclohexane; additionally, they cannot isomerize n-hexane effectively without significantly cracking the heavier paraffins present in the feed stream.[2] Thus, complicated separation and purification processes are needed for the isomerization of light reformate over traditional bifunctional catalysts. The performance of $Pt/WO_3/Al\text{-}ZrO_x$ under realistic conditions was examined using a simulated feedstock of light reformate, which contained 19.4 mol% of n-pentane,

 © 2006 Wiley-VCH Verlag GmbH & Co. KGaA, Weinheim

28.0 mol% of *n*-hexane, 37.8 mol% of cyclohexane, 13.1 mol% of *n*-heptane, and 1.7 mol% of benzene. The nanocomposite catalyst successfully converted all the different components in a single process at 150°C without substantial deactivation (Figure 3). *n*-Heptane and *n*-hexane

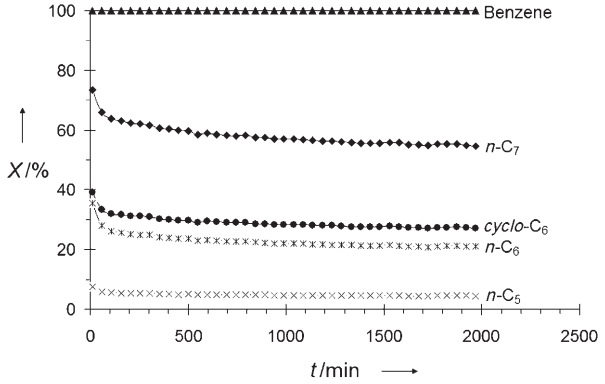

Figure 3. Isomerization of simulated light reformate feedstock over Pt/WO_3/Al-ZrO_x at 150°C and atmospheric pressure; X = conversion, t = time on stream. Reaction conditions: infuse rate of the mixed feed = 0.44 mL h^{-1}; H_2 flow rate = 21.1 mL min^{-1}; WHSV = 3.1 h^{-1}; catalyst loading = 1.0 g.

were efficiently converted into their branched isomers, while a lower conversion of *n*-pentane was obtained. Cyclohexane was isomerized to methylcyclopentane, which has a higher octane value than cyclohexane. Benzene was completely hydrogenated to cyclohexane, followed by partial isomerization to methylcyclopentane. The overall octane number of the light reformate feedstock was increased by about 13 (from 54 to 67), with less than 0.85% mass loss due to cracking. This significant upgrade in octane value is very attractive considering that current premium gasoline with an octane number of 89 is generally US$ 0.10–0.20 more expensive per gallon than regular gasoline with an octane number of 87.

The catalytic performance of Pt/WO_3/M-ZrO_x nanocomposite is critically related to the doping of the support, unlike other doped oxide catalysts, where the support's surface area or crystal phase play a more important role.[11,18,19] In our nanocomposite system, the heteroatom is truly substituted as a dopant for Zr^{4+} in the ZrO_2 crystal lattice instead of forming a separate phase. This was confirmed by changes in the ZrO_2 unit cell volume (Figure 4) produced by the introduction of dopants of different ionic radii. The most significant increases in catalytic activity were observed when Al^{3+} and Ga^{3+} were used as the dopants; these trivalent cations also lead to substantial decreases in the ZrO_2 unit cell volume. In contrast, a lower reduction in the ZrO_2 unit cell volume was observed when Si^{4+} was introduced. This is because only part of the Si^{4+} is incorporated in the ZrO_2 lattice—most of the Si^{4+} introduced is segregated into a separate silica phase on the zirconia surface. This could weaken the interaction between WO_3 and the zirconia support and give rise to the severe reduction in catalyst activity observed in Figure 4.

The method of introducing dopants into ZrO_2 has a significant impact on the successful heteroatom substitution

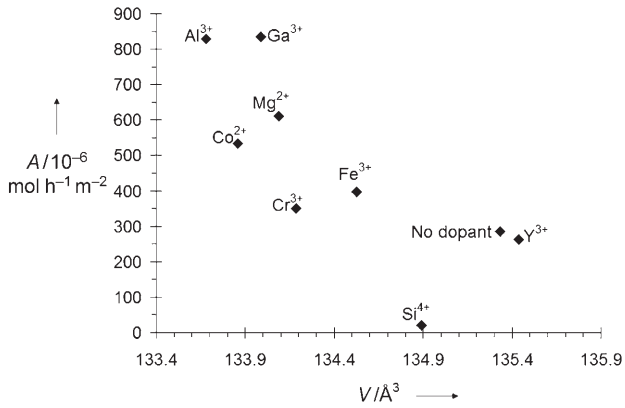

Figure 4. Catalytic activity of Pt/WO_3/M-ZrO_x (A) versus the unit cell volume of M-ZrO_x (V), where M represents the cation introduced (M/Zr cation ratio = 0.05). Reaction conditions: 200°C, 1 atm, H_2/*n*-C_7 feed molar ratio = 16. The contact time was adjusted to obtain *n*-C_7 conversions of 15–30%.

in the ZrO_2 lattice, and consequently on the catalyst performance. Straightforward co-precipitation by adding the base solution to a mixed solution containing both dopant and Zr^{4+} salts has frequently been used in the preparation of doped oxide catalysts.[18,20,21] However, this method has serious drawbacks when an ultrahigh dispersion of dopants is required because the dopant and Zr^{4+} might precipitate at different points and different rates under a variable pH environment. An Al^{3+}-doped catalyst prepared by this direct method also consists of irregularly shaped oxide particles with a broad size distribution of 5–25 nm (see Supporting Information). This limitation of Al^{3+} substitution and the poor control of nanoparticle precipitation lead to an Al^{3+}-doped catalyst that is only slightly more active than the undoped catalyst.[20] In contrast, our Al^{3+}-doped zirconia nanocrystals were prepared at a constant pH of 9, whereby the Zr^{4+} and Al^{3+} cations are simultaneously precipitated from their mixed salt solution. This constant-pH precipitation ensures an ultrahigh dispersion of Al^{3+} and Zr^{4+}, and a high level of Al^{3+} substitution in the ZrO_2 lattice. It also leads to spherical oxide particles with a very narrow size distribution of 10–12 nm (see Supporting Information).

Generally, the increase in activity in conventional isomerization catalysts can be correlated to changes in their acidic properties.[11,18,21] In our case, the distribution of Brønsted and Lewis acid sites in the Pt/WO_3/Al-ZrO_x nanocomposite was found to be very similar to that in Pt/WO_3/ZrO_2, according to the IR spectra of samples subjected to pyridine chemisorption. The total acid amount is actually slightly lower in Pt/WO_3/Al-ZrO_x (0.13 mmol NH_3 per gram) than in Pt/WO_3/ZrO_2 (0.15 mmol NH_3 per gram). Thus, factors other than acidity must be responsible for the superior catalytic performance of Pt/WO_3/Al-ZrO_x. As the H_2 atmosphere is important and necessary for the isomerization reaction, the amount of H_2 adsorbed on the different catalysts under a flowing stream of H_2 was measured by thermogravimetric analysis (TGA). All samples were reduced at 350°C in H_2 prior to H_2 adsorption at room temperature. It was found that the H_2 uptake by Pt/WO_3/Al-ZrO_x is more than twice that of Pt/

 © 2006 Wiley-VCH Verlag GmbH & Co. KGaA, Weinheim

WO_3/ZrO_2 (Figure 5a). The remarkably high H_2/Pt molar ratio over both catalysts indicates that H_2 is adsorbed not only by Pt but also by WO_3 and/or Al-ZrO_x through H_2 spillover.[14] It has been reported that H_2 spillover takes place very readily in the Pt/WO_3 system.[15] However, the large difference in H_2 uptake between Pt/WO_3/Al-ZrO_x and Pt/WO_3/ZrO_2 can be best explained by the role of Al-ZrO_x in H_2 storage, which would typically occur only at very high temperatures in undoped ZrO_2.[22]

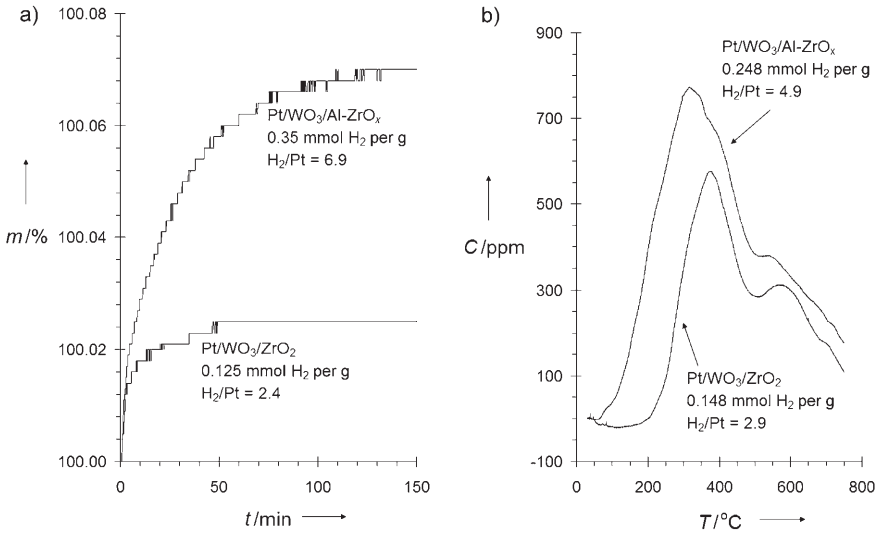

Figure 5. a) Uptake and b) TPD of H_2 over Pt/WO_3/Al-ZrO_x and Pt/WO_3/ZrO_2. m = weight; t = adsorption time; C = H_2 desorbed; T = desorption temperature.

Hydrogen desorption from the catalysts was measured in temperature-programmed desorption (TPD) studies. As shown in Figure 5b, H_2 desorption in Pt/WO_3/Al-ZrO_x occurs at a temperature about 150 °C lower than in Pt/WO_3/ZrO_2, and the amount of H_2 desorbed from Pt/WO_3/Al-ZrO_x is about 69% higher than from Pt/WO_3/ZrO_2. Substitution of Zr^{4+} by a lower valence cation, such as Al^{3+}, would generate oxygen vacancies in the ZrO_2 crystal structure to preserve the electroneutrality. These oxygen vacancies could increase the ionic conductivity of ZrO_2 significantly.[23] As a result, the rate of reverse H_2 spillover could be increased in Pt/WO_3/Al-ZrO_x, thus allowing for a more facile H_2 desorption.[24] In an isomerization reaction, the higher surface density of spilt-over H_2, which might exist in the form of an H^+/H^- pair, and the rapid H^+/H^- migration in the catalyst could substantially facilitate the hydrocarbon conversion and inhibit the cracking of intermediates arising from long residence times at the acidic sites.[4,5]

In conclusion, our Pt/WO_3/Al-ZrO_x nanocomposite allows for the highly efficient and selective conversion of C_{7+} paraffins at a remarkably low temperature of 125 °C. This novel catalyst provides a competitive alternative to traditional zeolites and liquid acids in oil refinery and petrochemical production. The superior catalytic performance of Pt/WO_3/Al-ZrO_x is attributed to the much higher surface density of spilt-over H_2 and a more facile reverse process of H_2 spillover. The significant differences in H_2 adsorption and desorption behavior in Pt/WO_3/Al-ZrO_x compared to Pt/WO_3/ZrO_2 are related to the uniform and successful substitution of Zr^{4+} by Al^{3+} in ZrO_2, which produces a large number of oxygen vacancies and significantly increases the ionic conductivity of ZrO_2. This structure–property relationship might have a broad impact on the rational design of complex oxide catalysts and multifunctional nanocomposites.

Experimental Section

The incorporation of Al^{3+} into ZrO_2 was achieved by co-precipitation of Zr^{4+} and Al^{3+} salts (Al^{3+}/Zr^{4+} atomic ratio = 0.05) at a constant pH value of 9.0 by adding an aqueous solution of ammonium hydroxide. The precipitate was washed thoroughly with deionized water and dried at 120 °C. Ammonium metatungstate hydrate (99.9+%, Strem Chemicals) was then loaded onto the precipitate by the incipient-wetness impregnation technique at a tungsten concentration of 20–25 wt% (based on the hydroxides). The resulting material was calcined at 800 °C for 3 h to yield WO_3/Al-ZrO_x with a surface area of 56 $m^2 g^{-1}$. It was then loaded with 1.0 wt% of Pt by impregnation with $[Pt(NH_3)_4](NO_3)_2$ (99%, Strem Chemicals), and calcined at 450 °C for 1.5 h to yield the Pt/WO_3/Al-ZrO_x nanocomposite.

Pt/WO_3/ZrO_2 (containing 16 wt% W based on zirconium hydroxide) and Pt/Beta were prepared as benchmark catalysts. The former was synthesized according to the literature procedure;[4,10] WO_3/ZrO_2 was obtained with a surface area of 63 $m^2 g^{-1}$. Pt/Beta was obtained by calcining NH_4^+-Beta zeolite (Si/Al = 12.5, Zeolyst International) at 500 °C for 3 h to produce H^+-Beta, followed by loading with 1.0 wt% of Pt.

n-Heptane isomerization was conducted in a tubular reactor at atmospheric pressure. Prior to the reaction, the catalyst was treated in situ at 450 °C in air for 1.5 h to purge its surface, followed by reduction in H_2 at 350 °C for 1.5 h to reduce Pt^{II} to Pt metal. *n*-Heptane was introduced into the feed stream by flowing H_2 through an *n*-heptane saturator at 25 °C, which gave a H_2/*n*-heptane molar ratio of 16. The catalyst was tested at variable weight hour space velocities (WHSV) to obtain the desired *n*-C_7 conversion. For example, to compare the activities of different catalysts, the conversion was controlled from 15% to 30%. In the selectivity versus conversion studies, the conversion of *n*-C_7 was varied from 10% to 90% systematically by changing the WHSV.

H_2 uptake was measured by TGA. The catalyst was treated first in an air stream at 450 °C for 1.5 h, followed by reduction in 5.2% H_2 in helium for 3 h. It was then flushed with pure helium at 450 °C for 12 h to remove the adsorbed H_2 and cooled to room temperature in helium. When the catalyst weight became stable, the gas flow was switched from pure helium to 5.2% H_2 in helium, and the weight gain at room temperature due to H_2 adsorption was recorded as the amount of H_2 uptake.

TPD studies of H_2 was conducted in a tubular reactor. The catalyst was reduced at 350 °C in H_2 for 1.5 h and then cooled to room temperature in H_2. It was then flushed with argon to remove the weakly adsorbed H_2. H_2 desorption upon heating the catalyst bed

 © 2006 Wiley-VCH Verlag GmbH & Co. KGaA, Weinheim

from 30 °C to 750 °C at a rate of 5 K min^{-1} was analyzed with an HP 6890 GC equipped with a thermal conductivity detector (TCD).

Received: January 28, 2006
Revised: June 1, 2006
Published online: September 20, 2006

Keywords: alkanes · heterogeneous catalysis · hydrocarbons · isomerization · nanocomposites

[1] H. Weyda, E. Köhler, *Catal. Today* **2003**, *81*, 51.
[2] A. Chica, A. Corma, *J. Catal.* **1999**, *187*, 167.
[3] Z. B. Wang, A. Kamo, T. Yonedo, T. Komatsu, T. Yashima, *Appl. Catal. A* **1997**, *159*, 119.
[4] E. Iglesia, D. G. Barton, S. L. Soled, S. Miseo, J. E. Baumgartner, W. E. Gates, G. A. Fuentes, G. D. Meitzner, *Stud. Surf. Sci. Catal.* **1996**, *101*, 533.
[5] J. F. Kriz, T. D. Pope, M. Stanciulescu, J. Monnier, *Ind. Eng. Chem. Res.* **1998**, *37*, 4560.
[6] K. J. Chao, H. C. Wu, L. J. Leu, *Appl. Catal. A* **1996**, *143*, 223.
[7] S. Calero, M. Schenk, D. Dubbeldam, T. L. M. Maesen, B. J. Smit, *J. Catal.* **2004**, *228*, 121.
[8] E. A. Blekkan, C. Pham-Huu, M. J. Ledous, J. Guille, *Ind. Eng. Chem. Res.* **1994**, *33*, 1657.
[9] E. Iglesia, S. L. Soled, G. Kramer, *J. Catal.* **1993**, *144*, 238.
[10] M. Hino, K. Arata, *J. Chem. Soc. Chem. Commun.* **1988**, *18*, 1259.
[11] J. G. Santiesteban, J. C. Vartuli, S. Han, R. D. Bastian, C. D. Chang, *J. Catal.* **1997**, *168*, 431.
[12] E. Blomsma, J. A. Martens, P. A. Jacobs, *J. Catal.* **1997**, *165*, 241.
[13] H. Hattori, T. Shishido, *Catal. Surv. Jpn.* **1997**, *1*, 205.
[14] J. G. Santiesteban, D. C. Calabro, W. S. Borghard, C. D. Chang, J. C. Vartuli, Y. P. Tsao, M. A. Natal-Santiago, R. D. Bastian, *J. Catal.* **1999**, *183*, 314.
[15] P. A. Sermon, G. C. Bond, *J. Chem. Soc. Faraday Trans. 1* **1980**, *76*, 889.
[16] J. Y. Ying, T. Sun, *J. Electroceram.* **1997**, *1*, 219.
[17] A. J. Zarur, J. Y. Ying, *Nature* **2000**, *403*, 65.
[18] W. Hua, Y. Xia, Y. Yue, Z. Gao, *J. Catal.* **2000**, *196*, 104.
[19] M. Scheithauer, R. E. Jentoft, B. C. Gates, H. Knözinger, *J. Catal.* **2000**, *191*, 271.
[20] W. Hua, J. Sommer, *Appl. Catal. A* **2002**, *232*, 129.
[21] S. T. Wong, T. Li, S. Cheng, J. F. Lee, C. Y. Mou, *J. Catal.* **2003**, *215*, 45.
[22] D.-L. Hoang, H. Berndt, H. Lieske, *Catal. Lett.* **1995**, *31*, 165.
[23] D. K. Hohnke, *Solid State Ionics* **1981**, *5*, 531.
[24] H. Uchida, H. Yoshikawa, H. Iwahawa, *Solid State Ionics* **1989**, *35*, 229.

 © 2006 Wiley-VCH Verlag GmbH & Co. KGaA, Weinheim

Furan Synthesis

DOI: 10.1002/anie.200601252

Gold(I)-Catalyzed Reaction of 1-(1-Alkynyl)-cyclopropyl Ketones with Nucleophiles: A Modular Entry to Highly Substituted Furans**

*Junliang Zhang and Hans-Günther Schmalz**

Highly substituted furans are found as key structural elements in many bioactive natural products and important pharmaceuticals. They also represent versatile building blocks for the synthesis of more elaborate heterocyclic compounds.[1,2] The search for efficient general routes to substituted furans is an important, continuing goal of organic synthesis. Several studies have focused on metal-catalyzed methods for furan synthesis (Scheme 1). These include the cyclization of allenyl ketones,[3] 3-alkyn-1-ones,[4] or 2-(1-alkynyl)-2-alken-1-ones[5] through nucleophilic attack of the carbonyl oxygen atom to a transition-metal-coordinated C–C double or triple bond (Mode A, Scheme 1). Alternatively, alkylidene cyclopropyl ketones[6] or cyclopropenyl ketones[7] are prone to metal-catalyzed cycloisomerization to afford furans through (regioselective) cleavage of the three-membered ring and subsequent cyclization (Mode B, Scheme 1).

As cyclopropanes are readily accessible and reactive because of their ring strain,[8,9] we designed 1-(1-alkynyl)-cyclopropyl ketones **1** (Scheme 2) that contain both an alkyne and a cyclopropane unit as starting materials for cyclization reactions catalyzed by transition metals. Although both modes A and B (to form 2,3-dihydrofurans[10]) are potentially possible pathways for metal-mediated reactions involving **1**, we envisioned that furan formation through attack of the carbonyl oxygen atom on the alkyne (Mode A) seemed to be particularly feasible.

Herein, we present a mild and efficient method for the synthesis of multiply substituted furans starting from compounds of type **1**. In particular, we show that the atom-economical gold(I)-catalyzed cascade process allows access to condensed ring systems (for example, furo[*b*]cycloheptenes) under ring expansion.

First, we examined the reaction of (racemic) ketone **2a** using different metal catalysts (5 mol%) with MeOH (2 equiv) in CH_2Cl_2 (Table 1). Remarkably, the ring-expanded bicyclic cycloheptafuran **3aa** was formed regiose-

[*] Dr. J. Zhang, Prof. Dr. H.-G. Schmalz
Institut für Organische Chemie
Universität zu Köln
Greinstrasse 4, 50939 Köln (Germany)
Fax: (+49) 221-470-3064
E-mail: schmalz@uni-koeln.de

[**] This work was supported by the Alexander von Humboldt Stiftung (postdoctoral fellowship to J.Z.) and the Fonds der Chemischen Industrie.

Supporting information for this article is available on the WWW under http://www.angewandte.org or from the author.

 WILEY InterScience DISCOVER SOMETHING GREAT

© 2006 Wiley-VCH Verlag GmbH & Co. KGaA, Weinheim

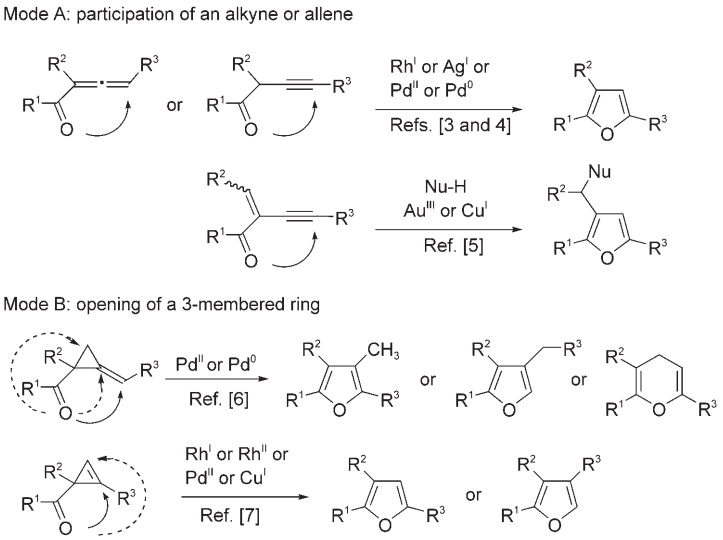

Scheme 1. Transition-metal-catalyzed synthesis of furans. Nu = nucleophile.

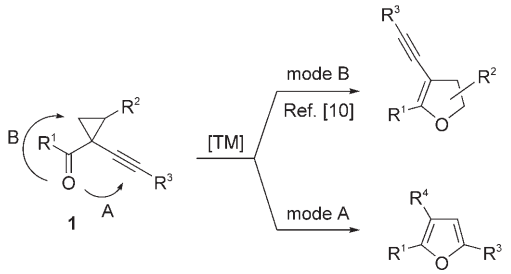

Scheme 2. Two possible modes of reaction for the cyclization of **1**. [TM] = transition metal reagent.

Table 1: Effect of catalyst on the reaction of **2a** to give **3aa**.

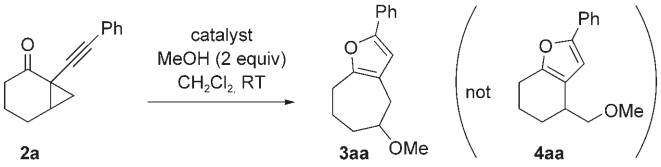

Entry	Catalyst	(Amount)	Time	Yield [%]
1	none	–	24 h	0
2	$Cu(OTf)_2$	(5 mol%)	16 h	74
3	$In(OTf)_3$	(5 mol%)	22 h	41
4	$Ga(OTf)_3$	(5 mol%)	16 h	55
5	$Sc(OTf)_3$	(5 mol%)	18 h	63
6	$Yb(OTf)_3$	(5 mol%)	24 h	70
7	AuCl	(5 mol%)	1 h	66
8	$AuCl_3$	(5 mol%)	1 h	68
9	AgOTf	(5 mol%)	1 h	85
10	$(PPh_3)AuOTf$	(5 mol%)	< 5 min	90
11	$(PPh_3)AuOTf$	(1 mol%)	< 10 min	91

Tf = triflate = trifluoromethanesulfonyl.

lectively in all cases as the only major product. Lewis acids such as $Cu(OTf)_2$, $In(OTf)_3$, $Ga(OTf)_3$, $Sc(OTf)_3$, and $Yb(OTf)_3$ were active, but only modest yields were obtained after long reaction times. Faster reactions were observed using AuCl, $AuCl_3$, and AgOTf as the catalyst;[11] AgOTf afforded the product in a respectable 85% yield after 1 h. Significantly, we found that $(Ph_3P)AuOTf$[12] is a particularly efficient catalyst for this reaction. With only 1 mol% of this catalyst, the cascade ring expansion/furan formation was complete after less than ten minutes at room temperature to afford pure **3aa** in 91% yield (Table 1, entry 11). No trace of the isomeric product (**4aa**) could be detected.

Two plausible mechanisms can be envisioned for this novel Au^I-catalyzed transformation (Scheme 3).[11] In cycle **A** (Scheme 3), a cationic Au^I species first coordinates to the triple bond to generate an intermediate **5**. Nucleophilic attack of the carbonyl oxygen atom on the activated triple bond with concomitant (regioselective) cleavage of the cyclopropane would generate a carbocation **6**, which can be trapped by a nucleophile (MeOH). Protonolysis of the resulting organogold intermediate **7** gives product **3** and regenerates the Au^I catalyst. Alternatively (cycle **B**, Scheme 3), a chelate complex **8** could form as a primary intermediate, which could be attacked by the nucleophile (MeOH) in a regioselective homo-Michael-type addition to generate an Au–enolate **9**, which then undergoes cycloisomerization to afford intermediate **7**.

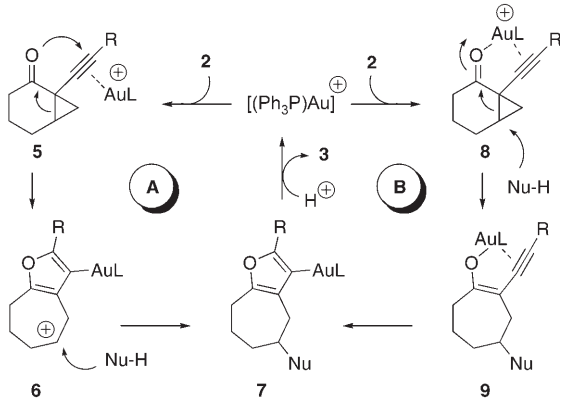

Scheme 3. Possible mechanisms of the Au-catalyzed transformation. L = ligand.

To probe the scope of the reaction, we performed a series of experiments with different ketones of type **2** and also varied the nucleophile (Table 2). While $(Ph_3P)AuOTf$ was used as it was found to be the most effective catalyst, some reactions were also studied using AgOTf for comparative purposes.

A variety of O nucleophiles, such as alcohols (including *tert*-butanol),[13] phenols, or acetic acid, react smoothly to afford the desired products (Table 2). An N-nucleophilic 2-pyrrolidone could also be employed to give the corresponding N-alkylated product (Table 2, entry 10); however, the reaction was slower than those performed using alcohols as the nucleophiles. When indole was used as the nucleophile, the C3 alkylation product was formed selectively in good yield (Table 2, entry 7). The reaction tolerates a wide range of R

 © 2006 Wiley-VCH Verlag GmbH & Co. KGaA, Weinheim

Table 2: Au^{I}-catalyzed ring expansion/cyclization reactions of substrates **2** with different nucleophiles.[a]

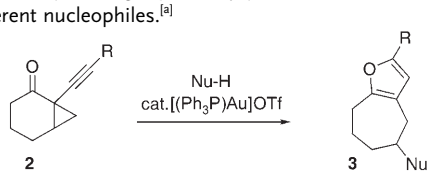

2 3

Entry	Ketone	R	Nu−H	Prod.	Yield [%][b]
1	**2a**	Ph	MeOH	**3aa**	91 (85)
2	**2a**	Ph	*i*PrOH	**3ab**	90 (85)
3	**2a**	Ph	*t*BuOH	**3ac**	85 (77)
4	**2a**	Ph	Ph-C≡C-CH_2OH	**3ad**	77 (88)
5	**2a**	Ph	*p*-MeO-C_6H_4-OH	**3ae**	84
6	**2a**	Ph	AcOH	**3af**	84 (61)
7	**2a**	Ph	indole	**3ag**	73 (31)
8	**2b**	1-cyclohexenyl	MeOH	**3ba**	80
9	**2c**	cyclopropyl	MeOH	**3ca**	82
10	**2c**	cyclopropyl	2-pyrrolidone	**3ch**	68 (59)
11	**2d**	*n*-butyl	MeOH	**3da**	86
12	**2e**	H	MeOH	**3ea**	76
13	**2f**	TMS	MeOH	**3ea**	35

[a] Unless otherwise specified, reactions were carried out as follows: a solution of (racemic) ketone **2** (0.5 mmol), $(Ph_3P)AuOTf$ (1 mol%), and nucleophile (2.0 equiv) in CH_2Cl_2 (2.8 mL) was stirred at RT for 15 min. [b] Yields of isolated products; yield given in parenthesis refer to reactions performed with AgOTf (5 mol%, 1 h). [c] Indole (1.5 equiv). [d] 6 h. TMS = trimethylsilyl.

groups on the alkyne in substrate **2**.[13] Besides phenyl, alkyl, and alkenyl substituents, even a cyclopropyl unit is tolerated (Table 2, entries 9 and 10). This result demonstrates the remarkable chemoselectivity of the reaction.

The generality of the method was also investigated using the cycloheptane derivative **10**, the 2,3-methanochromanone derivative **12**, and the monocyclic 1-(1-alkynyl)cyclopropyl ketones **14** and **16**, all of which afforded the expected products (**11**, **13**, **15**, and **17**) in good yields (Scheme 4). In the case of **16**, nucleophilic addition occurs at the more substituted position of the cyclopropane ring.

Remarkably, no reaction took place when **16** was subjected to the standard reaction conditions (1 mol% of $(Ph_3P)AuOTf$, CH_2Cl_2, RT) in the absence of a nucleophile. Furthermore, no reaction was observed when Et_3SiH was used as a potential hydride source in place of a nucleophile. These facts contradict a mechanism involving a carbocation intermediate; however, further studies are necessary to obtain deeper mechanistic insights.

In conclusion, a gold-catalyzed cascade reaction was developed which provides efficient access to highly substituted furans under mild conditions. The substrates can be readily prepared from the corresponding enones through cyclopropanation.[14] Further studies concerning both the mechanism and possible synthetic applications of the methodology are currently being carried out.

Experimental Section

A solution of cyclopropyl ketone **2a** (105 mg, 0.5 mmol) and methanol (32 mg, 1.0 mmol) in dry CH_2Cl_2 was added to a solution of Ph_3AuOTf (generated by mixing equal equivalents of $(Ph_3P)AuCl$ and AgOTf, with AgCl filtered off) in CH_2Cl_2 (0.00625 M, 0.8 mL, 0.005 mmol). The mixture was stirred for 15 min at room temperature. After evaporation of the solvent, the residue was purified by column chromatography on silica gel (cyclohexane/ethyl acetate 10:1) to afford 110 mg of **3aa** (91%) as a light yellow oil; ^{1}H NMR (300 MHz, $CDCl_3$): $\delta = 7.63$–7.59 (m, 2H), 7.40–7.32 (m, 2H), 7.25–7.18 (m, 1H), 6.48 (s, 1H), 3.41 (s, 3H), 3.35 (tt, $J = 9.3$, 2.7 Hz, 1H), 2.96–2.82 (m, 2H), 2.81–2.70 (m, 1H), 2.61 (dd, $J = 15.6$, 9.6 Hz, 1H), 2.30–2.16 (m, 1H), 2.08–1.96 (m, 1H), 1.82–1.54 ppm (m, 2H); ^{13}C NMR (75.4 MHz, $CDCl_3$): $\delta = 153.12$, 150.23, 131.06, 128.52, 126.58, 123.17, 116.67, 108.90, 79.69, 56.18, 35.76, 31.17, 28.34, 22.77 ppm; IR (neat): $\nu = 2926$, 2850, 1600, 1580, 1551, 1485, 1444, 1091, 757 cm^{-1}; MS (70 eV): *m/z* (%): 242 (100) [M^+]; HRMS calcd for $C_{16}H_{18}O_2$ [M^+]: 242.1307, found: 242.131. For preparative procedures and spectroscopic data for all new compounds, see the Supporting Information.

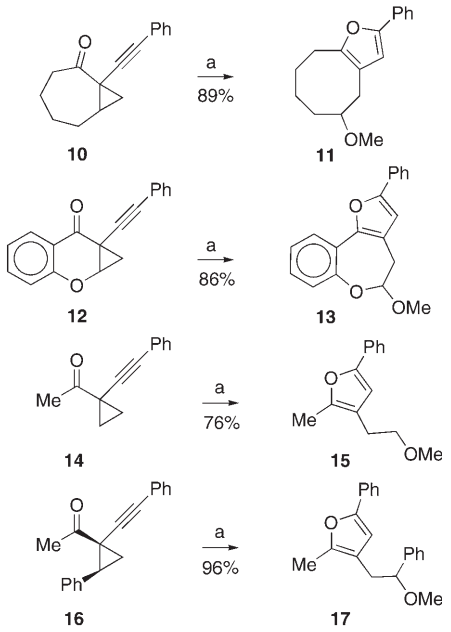

Scheme 4. The generality of the reaction. Conditions: a) $(Ph_3P)AuOTf$ (1 mol%), MeOH (2.0 equiv), CH_2Cl_2, RT.

Received: March 30, 2006
Revised: August 2, 2006
Published online: September 20, 2006

Keywords: cyclopropanes · furans · gold · ring expansion · transition metals

[1] For reviews, see: a) X. L. Hou, H. Y. Cheung, T. Y. Hon, P. L. Kwan, T. H. Lo, S. Y. T. Tong, H. N. C. Wong, *Tetrahedron* **1998**, *54*, 1955; b) B. A. Keay, *Chem. Soc. Rev.* **1999**, *28*, 209; c) X. L. Hou, Z. Yang, H. N. C. Wong in *Progress in Heterocyclic Chemistry*, *Vol. 14* (Eds.: G. W. Gribble, T. L. Gilchrist), Pergamon, Oxford, **2002**, p. 139.

[2] a) R. J. Sundberg in *Comprehensive Heterocyclic Chemistry*, *Vol. 5* (Eds.: A. R. Katrizky, C. W. Rees), Pergamon, New York, **1984**, p. 313; b) H. Heaney in *Natural Products Chemistry* (Ed.: K. Nakanishi), Kodansha, Toyko, **1974**, p. 297; c) B. H. Lipshutz, *Chem. Rev.* **1986**, *86*, 795; d) M. Shipman, *Contemp. Org. Synth.* **1995**, *2*, 1.

[3] a) J. A. Marshall, E. D. Robinson, *J. Org. Chem.* **1990**, *55*, 3450; b) J. A. Marshall, G. S. Bartley, *J. Org. Chem.* **1994**, *59*, 7169;

 © 2006 Wiley-VCH Verlag GmbH & Co. KGaA, Weinheim

c) J. A. Marshall, E. M. Wallace, *J. Org. Chem.* **1995**, *60*, 796; d) A. S. K. Hashmi, *Angew. Chem.* **1995**, *107*, 1749; *Angew. Chem. Int. Ed. Engl.* **1995**, *34*, 1581; e) A. S. K. Hashmi, T. L. Ruppert, T. Knofel, J. W. Bats, *J. Org. Chem.* **1997**, *62*, 7295; f) A. S. K. Hashmi, L. Schwarz, J. H. Choi, T. M. Frost, *Angew. Chem.* **2000**, *112*, 2382; *Angew. Chem. Int. Ed.* **2000**, *39*, 2285; g) S. Ma, L. Li, *Org. Lett.* **2002**, *4*, 941; h) S. Ma, Z. Yu, *Angew. Chem.* **2002**, *114*, 1853; *Angew. Chem. Int. Ed.* **2002**, *41*, 1775; i) S. Ma, J. Zhang, L. Lu, *Chem. Eur. J.* **2003**, *9*, 2447; j) M. H. Suhre, M. Reif, S. F. Kirsch, *Org. Lett.* **2005**, *7*, 3925.

[4] a) Y. Fukuda, H. Shiragami, K. Utimoto, H. Nozaki, *J. Org. Chem.* **1991**, *56*, 5816; b) A. V. Kel'in, V. Gevorgyan, *J. Org. Chem.* **2002**, *67*, 95; c) A. W. Sromek, A. V. Kel'in, V. Gevorgyan, *Angew. Chem.* **2004**, *116*, 2330; *Angew. Chem. Int. Ed.* **2004**, *43*, 2280.

[5] a) T. Yao, X. Zhang, R. C. Larock, *J. Am. Chem. Soc.* **2004**, *126*, 11164; b) N. T. Patil, H. Wu, Y. Yamamoto, *J. Org. Chem.* **2005**, *70*, 4531.

[6] a) S. Ma, J. Zhang, *Angew. Chem.* **2003**, *115*, 193; *Angew. Chem. Int. Ed.* **2003**, *42*, 184; b) S. Ma, L. Lu, J. Zhang, *J. Am. Chem. Soc.* **2004**, *126*, 9645.

[7] a) A. Padwa, J. M. Kassir, S. L. Xu, *J. Org. Chem.* **1991**, *56*, 6971; b) S. Ma, J. Zhang, *J. Am. Chem. Soc.* **2003**, *125*, 12386.

[8] For selected recent examples, see: a) I. S. Young, M. A. Kerr, *Angew. Chem.* **2003**, *115*, 3131; *Angew. Chem. Int. Ed.* **2003**, *42*, 3023; b) M. Yu, B. L. Pagenkopf, *J. Am. Chem. Soc.* **2003**, *125*, 8122; c) M. Lautens, W. Han, J. H.-C. Liu, *J. Am. Chem. Soc.* **2003**, *125*, 4028; d) C. Meyers, E. M. Carreira, *Angew. Chem.* **2003**, *115*, 718; *Angew. Chem. Int. Ed.* **2003**, *42*, 694; e) F. Bertozzi, B. V. Gandersen, M. Gustafsson, R. Olsson, *Org. Lett.* **2003**, *5*, 1551; f) M. Yu, B. L. Pagenkopf, *Org. Lett.* **2003**, *5*, 5099; g) I. S. Young, M. A. Kerr, *Org. Lett.* **2004**, *6*, 139.

[9] For a review, see: H.-U. Reissig, R. Zimmer, *Chem. Rev.* **2003**, *103*, 1151.

[10] a) U. M. Dzhemilev, R. I. Khusnutdinov, N. A. Shchadneva, G. A. Tolstikov, *Izv. Akad. Nauk SSSR Ser. Khim.* **1990**, 1598; *Bull. Acad. Sci. USSR Div. Chem. Sci. (Engl. Transl.)* **1990**, *39*, 1447; b) S. Husbands, W. Fraser, C. J. Suckling, H. C. S. Wood, *Tetrahedron* **1995**, *51*, 865.

[11] For recent reviews on gold-catalyzed reactions, see: a) S. Ma, S. Yu, Z. Gu, *Angew. Chem.* **2006**, *118*, 206; *Angew. Chem. Int. Ed.* **2006**, *45*, 200; b) A. Hoffmann-Röder, N. Krause, *Org. Biomol. Chem.* **2005**, *3*, 387; c) A. S. K. Hashmi, *Angew. Chem.* **2005**, *117*, 7150; *Angew. Chem. Int. Ed.* **2005**, *44*, 6990; d) A. S. K. Hashmi, *Gold Bull.* **2004**, *37*, 51; e) A. Arcadi, S. D. Giuseppe, *Curr. Org. Chem.* **2004**, *8*, 795; f) A. S. K. Hashmi, *Gold Bull.* **2003**, *36*, 3; g) G. Dyker, *Angew. Chem.* **2000**, *112*, 4407; *Angew. Chem. Int. Ed.* **2000**, *39*, 4237; for selected recent examples, see: h) J. Barluenga, A. Diéguez, A. Fernández, F. Rodríguez, F. J. Fañanás, *Angew. Chem.* **2006**, *118*, 3054; *Angew. Chem. Int. Ed.* **2006**, *45*, 2091; i) N. Morita, N. Krause, *Angew. Chem.* **2006**, *118*, 1930; *Angew. Chem. Int. Ed.* **2006**, *45*,1897; j) C. Brouwer, C. He, *Angew. Chem.* **2006**, *118*, 1776; *Angew. Chem. Int. Ed.* **2006**, *45*, 1744; k) X. Han, R. A. Widenhoefer, *Angew. Chem.* **2006**, *118*, 1779; *Angew. Chem. Int. Ed.* **2006**, *45*, 1747; l) C. Ferrer, A. M. Echavarren, *Angew. Chem.* **2006**, *118*, 1123; *Angew. Chem. Int. Ed.* **2006**, *45*, 1105; m) E. Genin, P. Y. Toullec, S. Antoniotti, C. Brancour, J.-P. Genêt, V. Michelet, *J. Am. Chem. Soc.* **2006**, *128*, 3112; n) J. Zhang, C.-G. Yang, C. He, *J. Am. Chem. Soc.* **2006**, *128*, 1798; o) L. Zhang, S. Wang, *J. Am. Chem. Soc.* **2006**, *128*,1442; p) D. J. Gorin, N. R. Davis, F. D. Toste, *J. Am. Chem. Soc.* **2005**, *127*, 11260; q) L. Zhang, S. A. Kozmin, *J. Am. Chem. Soc.* **2005**, *127*, 6962; r) X. Yao, C.-J. Li, *J. Am. Chem. Soc.* **2004**, *126*, 6884.

[12] Phosphane-stabilized Au^I salts with weakly coordinating anions have successfully been used also in other laboratories; see, for example, Ref. [3j], Ref. [11], as well as: a) L. Zhang, *J. Am. Chem. Soc.* **2005**, *127*, 16804; b) X.-Y. Liu, C.-H. Li, C.-M. Che, *Org. Lett.* **2006**, *8*, 2707.

[13] It should be noted that *t*BuOH could not be used as the nucleophile[5a] and the R group on the alkyne could not be alkyl[5b] in a similar transformation, thus indicating that the highly strained cyclopropane in our system may provide the driving force for the reaction.

[14] J. Cossy, N, Furet, S. Bouzbouz, *Tetrahedron* **1995**, *51*, 11751.

 © 2006 Wiley-VCH Verlag GmbH & Co. KGaA, Weinheim

Iron(III) Compounds

DOI: 10.1002/anie.200601774

A Square-Planar Organoiron(III) Compound with a Spin-Admixed State**

Pablo J. Alonso, Ana B. Arauzo, Juan Forniés, M. Angeles García-Monforte, Antonio Martín, Jesús I. Martínez, Babil Menjón,* Conrado Rillo, and José J. Sáiz-Garitaonandia*

Dedicated to Dr. Francisco Martínez-Buenaga on the occasion of his 60th birthday

Iron is an abundant, inexpensive, and essentially nontoxic element that is of central importance in almost every branch of chemistry, materials science and technology, and life

[*] Prof. Dr. P. J. Alonso, Prof. Dr. J. Forniés, Dr. M. A. García-Monforte, Dr. A. Martín, Dr. J. I. Martínez, Dr. B. Menjón, Prof. Dr. C. Rillo
Instituto de Ciencia de Materiales de Aragón
Universidad de Zaragoza and C.S.I.C.
C/Pedro Cerbuna 12, Zaragoza (Spain)
Fax: (+34) 976-761-187
E-mail: alonso@unizar.es
menjon@unizar.es

Dr. J. J. Sáiz-Garitaonandia
Departamento de Física Aplicada II
Facultad de Ciencia y Tecnología
Universidad del País Vasco
Apdo. 644, 48080 Bilbao (Spain)

Dr. A. B. Arauzo
Servicio de Instrumentación Científica, Medidas Físicas
Universidad de Zaragoza
C/Pedro Cerbuna 12, Zaragoza (Spain)

[**] This work was supported by the Spanish MCYT (DGI)/FEDER (projects CTQ2005-08606-C02-01 and BFU2005-07422-C02-02) and the Gobierno de Aragón (Grupo de Excelencia: Química Inorgánica y de los Compuestos Organometálicos). We are indebted to Prof. Dr. S. Alvarez (Universitat de Barcelona) for kindly providing values of continuous-shape measurements as well as for sharing results prior to publication.

Supporting information for this article (Experimental Section, the model developed to explain the physical properties of **1**, and additional Mössbauer and EPR spectra of **1**) is available on the WWW under http://www.angewandte.org or from the author.

© 2006 Wiley-VCH Verlag GmbH & Co. KGaA, Weinheim

science.[1,2] Much effort has been devoted to studying the magnetic properties of several classes of iron derivatives in different oxidation states (especially Fe^{II} and Fe^{III}) because of their relevance to various biological systems.[3] Underlying this intensive research is one of the ultimate goals in chemistry—to understand the relationship between electronic structure, molecular geometry, and as many chemical, magnetic, and spectroscopic properties as possible.[4] Fe^{III} is a d^5 ion that usually adopts tetrahedral (T-4) or octahedral (OC-6) environments when surrounded by four or six substituents, respectively.[1,5] Mononuclear Fe^{III} derivatives in both these coordination environments usually exhibit a high-spin (HS) configuration ($S = {}^5/_2$), and only in the OC-6 case is the action of strong-field ligands able to induce the electron-pairing that gives rise to the low-spin (LS) configuration ($S = {}^1/_2$). Interesting cases of spin crossover between the HS and LS configurations have also been described.[6] A particularly rich magnetic behavior has been observed in six- or five-coordinate Fe^{III} porphyrins, phthalocyanines, and related derivatives bearing macrocyclic ligands, be they synthetic or protein-bound: in addition to the common HS and LS configurations, examples of intermediate-spin ($S = {}^3/_2$), as well as spin-admixed (that is, mixed-spin, $S = {}^3/_2, {}^5/_2$) configurations have been reported.[7] Intermediate-spin states have also been found in square-pyramidal (SPY-5) Fe^{III} complexes.[8] In contrast to all these well-established coordination polyhedra, the square-planar (SP-4) geometry is virtually absent from Fe^{III} chemistry and, hence, little is known with certainty about the magnetic properties associated with the d^5 ion in this coordination environment. Herein, we report on the synthesis and characterization of an unambiguously established SP-4 Fe^{III} compound, as well as the study of its magnetic properties.

Anhydrous $FeCl_3$ was found to react with LiC_6Cl_5 in Et_2O to give the organometallic anion $[Fe^{III}(C_6Cl_5)_4]^-$, which was isolated in reasonable yield as the $[Li(thf)_4]^+$ salt (**1**, Scheme 1).[9] Compound **1** is an extremely rare example of a

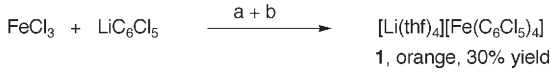

Scheme 1. Experimental procedure to obtain **1**: a) reaction in Et_2O at −78 °C; b) addition of THF.

homoleptic σ-organoiron(III) derivative for which the only precedent could possibly be the alkynyl complex $K_3[Fe^{III}(C{\equiv}CH)_6]$, which was obtained by oxidation of the precursor $K_4[Fe^{II}(C{\equiv}CH)_6]$ with O_2 in liquid ammonia.[10] Unfortunately, however, the high thermal instability of the oxidized alkynyl species, together with its proneness to explode, precluded even a minimally satisfactory characterization of the material. All other σ-organoiron(III) compounds invariably contain ancillary ligands, to enhance the stability of the corresponding organometallic species.[11]

The synthetic method leading to **1** is also noteworthy in that the Fe^{III} ion undergoes full arylation without undergoing any redox process. $FeCl_3$ and other simple Fe^{III} substrates are known to react with organolithium or -magnesium reagents to give organoiron(II) derivatives[12] or lower-valent species of mostly uncertain stoichiometries. Many of these reduced species show interesting reactivity patterns for application in organic synthesis.[13] The ability of $FeCl_3$ to promote C–C coupling reactions was noted very early on.[14] In this context, it is interesting to recall that one of the two original methods for the synthesis of ferrocene was, in fact, intended to give fulvalene by the $FeCl_3$-promoted reductive coupling of C_5H_5MgBr.[15] An exception to this reductive behavior is found in the reaction of $FeCl_3$ with norborn-1-yllithium, which has been reported to proceed with oxidation of the metal center to give $[Fe^{IV}(\text{norborn-1-yl})_4]$.[16] It was suggested by the authors that *"negatively charged complexes probably form"* during this reaction, although these were not detected.

The crystal and molecular structure of **1** was established by single-crystal X-ray diffraction. There are two sets of crystallographically independent $[Li(thf)_4]^+$ and $[Fe^{III}(C_6Cl_5)_4]^-$ ions in the crystal lattice; since they show no significant differences, we will discuss only one of them. The Fe^{III} centers in the lattice are well separated from each other, with the smallest intermetallic distance being greater than 1.1 nm. The $[Li(thf)_4]^+$ ion shows the usual tetrahedral (T-4) arrangement of the thf molecules around the Li^+ ion.[17] The local coordination environment of the Fe^{III} center in the $[Fe^{III}(C_6Cl_5)_4]^-$ ion (Figure 1) can be described as slightly distorted SP-4, in light of the low value of the continuous-shape measure determined for that geometry (0.41 for SP-4 versus 27.96 for T-4).[18] The Fe^{III} ion lies in the best coordination plane (imposed by symmetry), while each pair of *trans*-oriented carbon atoms depart slightly from it in opposite directions (±12 pm), which results in an incipient tetrahedral distortion. The C_6Cl_5 rings are helicoidally arranged around the Fe^{III} center and form angles of 63.6 and 53.4° with the coordination plane. This helicoidal

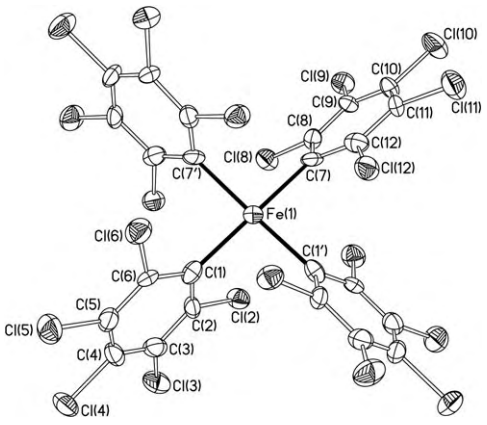

Figure 1. Thermal ellipsoid diagram (50% probability) of one of the two crystallographically independent $[Fe(C_6Cl_5)_4]^-$ ions in **1**. Selected bond lengths [pm] and angles [°] with estimated standard deviations: Fe(1)–C(1) 207.8(10), Fe(1)–C(7) 205.0(9); C(1)–Fe(1)–C(7) 173.2(4), C(1)–Fe(1)–C(1′) 93.5(5), C(1)–Fe(1)–C(7′) 87.5(4), C(7)–Fe(1)–C(7′) 92.2(5), C(2)–C(1)–Fe(1) 116.2(6), C(6)–C(1)–Fe(1) 128.2(7), C(8)–C(7)–Fe(1) 118.4(7), C(12)–C(7)–Fe(1) 126.8(7). Nonbonding distances to *ortho*-chlorine atoms [pm]: Fe(1)···Cl(2) 313.8, Fe(1)···Cl(6) 355.2, Fe(1)···Cl(8) 318.2, Fe(1)···Cl(12) 353.8. The smallest distance between iron centers is 1.109 nm, which corresponds to the Fe(1)···Fe(2) separation.

 © 2006 Wiley-VCH Verlag GmbH & Co. KGaA, Weinheim

arrangement makes the whole anion chiral (the one depicted in Figure 1 is the clockwise (*C*) enantiomer). Moreover, the C_6Cl_5 groups also exhibit a considerable swing about the *ipso*-carbon atoms, which results in different Fe–C^{ipso}–C^{ortho} angles and different Fe···Cl^{ortho} distances within each ring. All the Fe···Cl^{ortho} distances are too long (> 310 pm) to be considered as indicative of any bonding interaction. Moreover, in those cases in which such M···Cl^{ortho} secondary bonding interactions do occur, very distorted coordination polyhedra are observed because of the high strain associated with the small-bite chelating ligand C_6Cl_5-$\kappa C,\kappa^2 Cl$ (compare to the pseudo-octahedral structure found for the isoleptic d^3 species $[Cr^{III}(C_6Cl_5)_4]^-$).[17] The distortions found in the environment of the Fe^{III} center in **1** involve a decrease in the effective symmetry from the ideal D_{4h} to approximately D_2 symmetry.

There has been much interest in obtaining four-coordinate Fe^{III} derivatives with SP-4 geometry, especially those containing macrocyclic-$\kappa^4 N$ ligands because of their relevance to heme systems. That geometry, however, has proven to be highly elusive in Fe^{III} chemistry, since additional axial interactions are generally established that eventually yield five- or six-coordinate species.[7] Even so-called weakly coordinating ligands become involved in such axial interactions. For instance, axial agostic interactions have been suggested to be present between the Fe^{III} center and the remote methyl substituents of the porphyrinogen ring in $[Li(NCMe)_4][Fe^{III}\{LMe_8\text{-}\kappa^4 N\}]$ (H_4LMe_8 = *meso*-octamethylporphyrinogen).[19] The closely related species $[NEt_4][Fe^{III}\{LCy_4\text{-}\kappa^4 N\}]$ (H_4LCy_4 = *meso*-tetracyclohexylporphyrinogen) has also been reported recently, but has not yet been described in detail.[20] The magnetic properties of all these species depend strongly on the relative strengths of the equatorial versus axial iron–ligand bonding interactions. Based on this dependence, a new scale for the σ-donor ability of a ligand has been derived recently: the magnetochemical series.[21] Considering the formal relationship between the aromatic *C*-donor phenyl and *N*-donor pyrrolyl rings, complex **1** can be considered as a model for Fe^{III} heme systems with no axial ligands.[22] Hence, a physical characterization of **1**, including a detailed study of its magnetic behavior, seemed to be of interest.

The ^{57}Fe Mössbauer spectrum of **1** at 77 K is shown in Figure 2a. The dominant contribution[23] is a doublet with an isomer shift of $\delta = 0.20(1)\ mm\,s^{-1}$ and a quadrupolar splitting of $\Delta E_Q = 3.00(1)\ mm\,s^{-1}$, typical of an Fe^{III} entity in an $S = {}^3/_2$ or a spin-admixed state. Spectral features with similar δ and ΔE_Q values are observed for **1** in the temperature range of 14–200 K. Asymmetric broadening of the quadrupolar-doublet components appears at temperatures below 77 K (see Supporting Information for the Mössbauer spectrum of **1** at 14 K).

The X- (Figure 2b) and Q-band (see Supporting Information) EPR spectra of **1** at 10 K can be ascribed to a paramagnetic entity with an effective spin of $S' = {}^1/_2$ and a markedly orthorhombic effective *g* tensor (*g*′) with the principal values given in Table 1. This spectrum is qualitatively similar to that reported for the five-coordinate $S = {}^3/_2$ species $[Fe^{III}\{LR_2R'_2\text{-}\kappa^4 N\}I]$, where $\{LR_2R'_2\}^{2-}$ is the 6,13-bis(ethoxycarbonyl)-5,14-dimethyl-1,4,8,11-tetraazacyclotetradeca-4,6,12,14-tetraenato(2−) ligand.[24] When the temperature is increased, the EPR spectra of **1** broaden and their intensities decrease sharply, becoming undetectable at temperatures above 40 K (see Supporting Information).

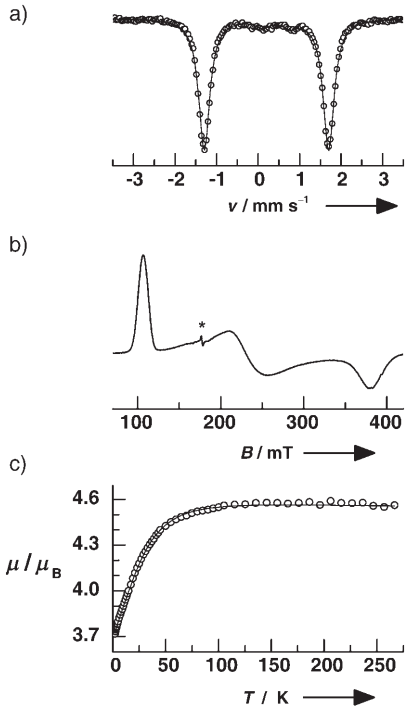

Figure 2. Physical properties of **1** (polycrystalline samples). a) ^{57}Fe Mössbauer spectrum recorded at 77 K in the absence of a magnetic field.[23] b) X-band EPR spectrum recorded at 10 K; the signal marked * at 170 mT is due to the cavity. c) Plot of the effective magnetic moment as a function of temperature; the solid line represents the calculated thermal evolution (see text).

The magnetic susceptibility (χ) of **1** was measured as a function of temperature in the range 1.8–265 K. After correcting for the temperature-independent contribution (χ_{TI}), the magnetic moment (μ) was deduced.[25] Its thermal evolution, $\mu(T)$, is depicted in Figure 2c, and the high- and low-temperature limit values (μ_∞ and μ_0) are given in Table 1.

Table 1: Experimental and calculated parameters associated with the magnetic properties of **1**.

Parameter	Experimental	Calculated
g'_x	2.98(2)	3.01(1)
g'_y	6.52(2)	6.51(1)
g'_z	1.84(2)	1.71(1)
μ_0/μ_B	3.7(1)	3.67(2)
μ_∞/μ_B	4.6(1)	4.52(2)

A value of $\mu_\infty \approx 3.9\ \mu_B$ is expected for a pure intermediate-spin Fe^{III} species with an orbital singlet ground-state. The higher value obtained for **1** ($\mu_\infty = 4.6(1)\ \mu_B$) can be explained by considering a spin-admixed ($S = {}^3/_2, {}^5/_2$) state. These types of systems have been thoroughly studied by Loew (née Harris), and Maltempo and Moss, who developed a useful theoretical framework for electronic structures with axial symmetry.[26] Given the markedly orthorhombic character of

 © 2006 Wiley-VCH Verlag GmbH & Co. KGaA, Weinheim

the electronic structure of the Fe^{III} center in **1**, a new model was needed to account for its magnetic properties. For this purpose, we have developed an ad hoc model that takes into consideration all the following interactions: interelectronic, spin–orbit, ligand-field, and Zeeman.[9]

The total number of possible states in a d^5 configuration is 252, but in accordance with previous results,[27] only the 18 states derived from the $^6A_1$ and $^4T_1$ cubic terms seem to be of major significance. Accordingly, we restricted our calculations to these states. In D_2 symmetry and in the absence of spin–orbit interactions, the orbital triplet $^4T_1$ splits into three singlets, namely $^4B_1$, $^4B_2$, and $^4B_3$, which transform as z, y, and x, respectively ($^4T_0$, ^4T_y, and ^4T_x). The interelectronic and ligand-field contributions are described by the parameters Δ_o, Δ_t, and δ, which are defined as the energy differences between the appropriate terms (Figure 3).

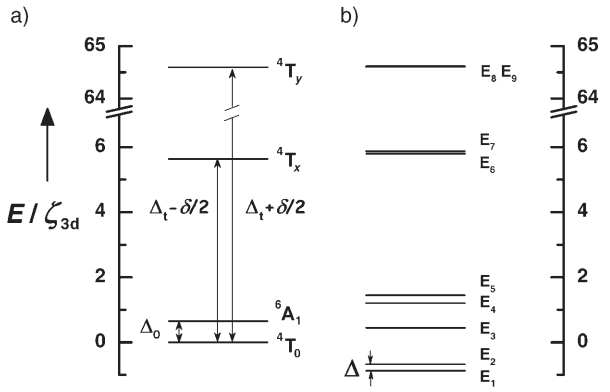

Figure 3. Energy diagrams of the relevant levels of **1** in D_2 symmetry. a) Terms in the absence of spin–orbit coupling; ordering depends on the actual value of Δ_o, Δ_t, and δ, which are defined in the text. b) Structure of the Kramers doublets after inclusion of the spin–orbit interaction.

Introduction of the spin–orbit interaction with a ζ_{3d} monoelectronic coupling coefficient gives a set of nine Kramers doublets (Figure 3). The base function of each of these doublets is obtained as a linear combination of the uncoupled $^4T_1$ and $^6A_1$ wave functions.[9] The coefficients of these linear combinations depend only on the dimensionless parameters u, v, and w, which are related to the aforementioned Δ_o, Δ_t, δ parameters by the expressions in Equation (1).

$$u = \frac{\Delta_t}{\zeta_{3d}}, \quad v = \frac{\delta}{\Delta_t} = \frac{\delta}{\zeta_{3d}}\frac{1}{u}, \quad w = \frac{\Delta_o}{\zeta_{3d}} \tag{1}$$

At a sufficiently low temperature, only the lowest Kramers doublet would be populated. Accordingly, the EPR spectrum of **1** can be assigned to transitions between the states originating from that level by Zeeman interaction. Following our model, the principal effective g values of this $S' = {}^1/_2$ entity depend only on the parameters u, v, and w. An estimate of these coefficients can therefore be made by fitting the calculated g'_x, g'_y, and g'_z values to the experimentally observed ones. The best fitting yields the values $u = 35.1(2.7)$, $v = 1.68(3)$, and $w = 0.65(4)$, which allow us to calculate the energies (Figure 3) and the wave functions (see Supporting Information) of all nine levels involved.[9] For the ground state (E_1) and the first excited state (E_2) the $S = {}^3/_2$ contribution is about 64 %.

Taking into account that ζ_{3d} is approximately 420 cm^{-1} for the free Fe^{III} ion, and considering the energy diagram depicted in Figure 3, only the two lowest-lying energy doublets (E_1 and E_2) need to be considered when calculating the thermal dependence of the magnetic moment, $\mu(T)$ [Eq. (2)].

$$\mu(T) = \mu_B\left[C_1 + C_2\left(\frac{2k_BT}{\Delta}\right)\tanh\left(\frac{\Delta}{2k_BT}\right) + C_3\tanh\left(\frac{\Delta}{2k_BT}\right)\right]^{1/2} \tag{2}$$

The dimensionless coefficients C_1, C_2, and C_3 depend only on the parameters u, v, and w; Δ is the energy difference between the E_1 and E_2 levels (Figure 3). Since the values of C_1, C_2, and C_3 are determined by the EPR data, the magnitude of Δ can be estimated by fitting the expression given in Equation (2) to the experimentally observed $\mu(T)$. The best fitting for the whole thermal evolution (solid line in Figure 2c) is obtained with $\Delta = 78(3)$ cm^{-1}, which yields the calculated μ_0 and μ_∞ values given in Table 1. On the other hand, $\Delta/\zeta_{3d} = 0.20$, as deduced from the u, v, and w values. This means that ζ_{3d} is 390(15) cm^{-1} in our compound, which is a slight decrease with respect to the free ion value, as commonly found in transition-metal chemistry. In addition, the unpaired electronic distribution in the two levels E_1 and E_2 is practically indistinguishable (see Supporting Information), which explains why the quadrupolar splitting is unaffected by temperature. On the other hand, the thermal averaging of E_1 and E_2 with increasing temperature should involve averaging of the "third component" of the spin and orbital moments. This could result in a drastic reduction of the hyperfine coupling and therefore in a narrowing of the Mössbauer quadrupolar lines,[28] as observed experimentally (see Supporting Information and Figure 2a). The thermal dependence of the EPR spectrum noted above, as well as the deviation observed in the g'_z value (Table 1), could also be due to this dynamic process, a detailed study of which is beyond the scope of the present communication. Otherwise, a remarkably good agreement between calculated and experimental values for the relevant parameters, associated with the magnetic properties of **1** (Table 1), is provided by our ad hoc model.

To summarize, the magnetic properties of the SP-4 compound $[Li(thf)_4][Fe^{III}(C_6Cl_5)_4]$ (**1**) reveal that the Fe^{III} center behaves as a spin-admixed species ($S = {}^3/_2, {}^5/_2$). Thus, even in the absence of axial ligands, the sextet state may be sufficiently close in energy to the quartet ground state to enable a significant admixture with it.

Received: May 5, 2006
Published online: September 15, 2006

Keywords: EPR spectroscopy · homoleptic compounds · iron · magnetic properties · Moessbauer spectroscopy

 © 2006 Wiley-VCH Verlag GmbH & Co. KGaA, Weinheim

[1] *Chemistry of Iron* (Ed.: J. Silver), Blackie Academic & Professional, Glasgow, UK, **1993**.

[2] *Metal Sites in Proteins and Models: Iron Centres* (Eds.: H. A. O. Hill, P. J. Sadler, A. J. Thomson), Springer, Berlin, **1999**.

[3] "Bioinorganic Chemistry": A. X. Trautwein, E. Bill, E. L. Bominaar, H. Winkler, *Struct. Bonding (Berlin)* **1991**, *78*, 1.

[4] S. Alvarez, J. Cirera, *Angew. Chem.* **2006**, *118*, 3078; *Angew. Chem. Int. Ed.* **2006**, *45*, 3012.

[5] F. A. Cotton, G. Wilkinson, C. A. Murillo, M. Bochman, *Advanced Inorganic Chemistry*, 6th ed., Wiley, New York, **1999**, chap. 17, Section E, pp. 775–814.

[6] "Spin Crossover in Transition Metal Compounds I": P. J. van Koningsbruggen, Y. Maeda, H. Oshio, *Top. Curr. Chem.* **2004**, *233*, 259.

[7] W. R. Scheidt, M. Gouterman in *Iron Porphyrins*, *Part I* (Eds.: A. B. P. Lever, H. B. Gray), Addison–Wesley, Reading, MA, **1983**, chap. 2, pp. 89–139; W. R. Scheidt, C. A. Reed, *Chem. Rev.* **1981**, *81*, 543.

[8] R. L. Carlin, *Science* **1985**, *227*, 1291.

[9] A more detailed description can be found in the Supporting Information.

[10] R. Nast, F. Urban, *Z. Anorg. Allg. Chem.* **1956**, *287*, 17.

[11] R. B. Kerber in *Comprehensive Organometallic Chemistry II*, *Vol. 7* (Eds.: E. W. Abel, F. G. A. Stone, G. Wilkinson, D. F. Shriver, M. I. Bruce), Elsevier, Oxford, UK, **1995**, chap. 2, pp. 101–229; M. D. Johnson in *Comprehensive Organometallic Chemistry*, *Vol. 4* (Eds.: G. Wilkinson, F. G. A. Stone, E. W. Abel), Pergamon, Oxford, UK, **1982**, Section 31.2, pp. 331–376.

[12] A. Fürstner, H. Krause, C. W. Lehmann, *Angew. Chem.* **2006**, *118*, 454; *Angew. Chem. Int. Ed.* **2006**, *45*, 440; H. J. Spiegl, G. Groh, H. J. Berthold, *Z. Anorg. Allg. Chem.* **1973**, *398*, 225.

[13] C. Bolm, J. Legros, J. Le Paih, L. Zani, *Chem. Rev.* **2004**, *104*, 6217; J. K. Kochi, *J. Organomet. Chem.* **2002**, *653*, 11.

[14] G. Champetier, *Bull. Soc. Chim. Fr.* **1930**, *47*, 1131. For a detailed account of early results, see: F. A. Cotton, *Chem. Rev.* **1955**, *55*, 551.

[15] T. J. Kealy, P. L. Pauson, *Nature* **1951**, *168*, 1039.

[16] B. K. Bower, H. G. Tennent, *J. Am. Chem. Soc.* **1972**, *94*, 2512.

[17] P. J. Alonso, J. Forniés, M. A. García-Monforte, A. Martín, B. Menjón, C. Rillo, *Chem. Eur. J.* **2002**, *8*, 4056; P. J. Alonso, L. R. Falvello, J. Forniés, M. A. García-Monforte, A. Martín, B. Menjón, G. Rodríguez, *Chem. Commun.* **1998**, 1721.

[18] J. Cirera, P. Alemany, S. Alvarez, *Chem. Eur. J.* **2004**, *10*, 190.

[19] D. Jacoby, C. Floriani, A. Chiesi-Villa, C. Rizzoli, *J. Chem. Soc. Chem. Commun.* **1991**, 220.

[20] D. Bhattacharya, S. Dey, S. Maji, K. Pal, S. Sarkar, *Inorg. Chem.* **2005**, *44*, 7699.

[21] C. A. Reed, F. Guiset, *J. Am. Chem. Soc.* **1996**, *118*, 3281.

[22] Considering the different single-bond covalent radii of carbon (77 pm) and nitrogen (70 pm), the average Fe^{III}–C bond length in **1** (206 pm) is comparable to the average Fe^{III}–N distance (ca. 198 pm) in five-coordinate tetraphenylporphyrin (tpp) complexes of the type $[Fe^{III}(tpp)X]^-$, where X is a weakly coordinating ligand. Moreover, the small tetrahedral distortion discussed above for the anion $[Fe^{III}(C_6Cl_5)_4]^-$, as well as the helicoidal arrangement of the four aryl rings, can be related to the saddling (*sad*, B_{2u})- and propelling (*pro*, A_{1u})-type normal deformations of metalloporphyrins respectively: W. Jentzen, X.-Z. Song, J. A. Shelnutt, *J. Phys. Chem. B* **1997**, *101*, 1684.

[23] The Mössbauer spectra of **1** typically contain variable amounts of a minor species with the following spectral parameters: $\delta = 0.47(1)\ mm\,s^{-1}$ and $\Delta E_Q = 0.68(1)\ mm\,s^{-1}$. These parameters are attributable to a high-spin Fe^{III} by-product formed by thermal degradation and aging of **1** both in solution and in the solid state. The contribution of this by-product to the total signal in the spectrum in Figure 2a is less than 5%.

[24] H. Keutel, I. Käpplinger, E.-G. Jäger, M. Grodzicki, V. Schünemann, A. X. Trautwein, *Inorg. Chem.* **1999**, *38*, 2320.

[25] χ_{TI} was estimated from the temperature dependence of the χT product at high temperature. The contribution of the minor by-product detected by Mössbauer spectroscopy was also taken into account.[23]

[26] G. H. Loew in *Iron Porphyrins*, *Part I* (Eds.: A. B. P. Lever, H. B. Gray), Addison–Wesley, Reading, MA, **1983**, chap. 1, pp. 1–87; M. M. Maltempo, T. H. Moss, *Q. Rev. Biophys.* **1976**, *9*, 181; G. Harris, *Theor. Chim. Acta* **1968**, *10*, 155; G. Harris, *Theor. Chim. Acta* **1968**, *10*, 119.

[27] X.-Y. Kuang, I. Morgenstern-Badarau, *Phys. Status Solidi B* **1995**, *191*, 395.

[28] E. Bradford, W. Marshall, *Proc. Phys. Soc. London* **1966**, *87*, 731.

 © 2006 Wiley-VCH Verlag GmbH & Co. KGaA, Weinheim

Dipole–Dipole Interactions

DOI: 10.1002/anie.200602000

Dynamical Behavior and Dipole–Dipole Interactions of Tetrafluoromethane–Water**

Walther Caminati, Assimo Maris, Adele Dell'Erba, and Paolo G. Favero*

Water and tetrafluoromethane form a stable complex with dipole–dipole interaction as a leading factor in determining its configuration, according to the rotational spectra of several isotopologues of the complex observed in supersonic expansions. All of these spectra display the features of a symmetric top.

Nonbonding interactions play important roles in biology, supramolecular chemistry, and in solvation processes and have been the subject of numerous investigations.[1] Hydrogen bonding is the most important of such interactions; it involves many scientific areas and is invoked to explain the energetic and structural features of inorganic, organic, and biological systems.[2] Classical hydrogen bonds are O–H···O,[3] O–H···N,[4] O–H···S,[5] and N–H···O.[6] All of these are relatively

[*] Prof. W. Caminati, Dr. A. Maris, Dr. A. Dell'Erba,[+] Prof. P. G. Favero
Dipartimento di Chimica "G. Ciamician" dell'Università
Via Selmi 2, 40126 Bologna (Italy)
Fax: (+39) 051-209-9456
E-mail: walther.caminati@unibo.it

[+] Present address: Dipartimento di Ingegneria Civile ed Ambientale
2ª Facoltà di Ingegneria
Politecnico di Bari
Viale del Turismo 3, 74100 Taranto (Italy)

[**] We thank the Ministero dell'Istruzione, dell'Università e della Ricerca (MIUR, PRIN 2004) and the University of Bologna (ex 60% and funds for special topics) for financial support.

Supporting information for this article is available on the WWW under http://www.angewandte.org or from the author.

© 2006 Wiley-VCH Verlag GmbH & Co. KGaA, Weinheim

strong hydrogen bonds with energies in the range 15–25 kJ mol^{-1}.

The hydrogen bonding of water with halogens (O–H···X) is somewhat elusive. The O–H···F and O–H···Cl bonds have been characterized through analysis of the rotational spectra of the complexes of water with Freon-32 (difluoromethane)[7] and Freon-31 (chlorofluoromethane),[8] respectively. It has been shown that the O–H···Cl hydrogen bond is slightly preferred to the O–H···F one,[8] but their energies have been estimated to be rather small (4–5 kJ mol^{-1}).[8] These energy values are similar to those estimated for weak C–H···O,[9] C–H···F[10] or C–H···π[11] interactions, which are classified as weak[12] or blue-shifted hydrogen bonds.[1] The simplest molecules containing halogen atoms (F_2 and ClF) react with water. However, by using a fast-mixing nozzle, Legon and co-workers observed non-hydrogen-bonding adducts $H_2O\cdots F_2$ and $H_2O\cdots ClF$, which display an O···F or an O···Cl interaction.[13]

CF_4 is intermediate between CH_2F_2 and F_2 in that it has no permanent dipole moment, like F_2, but each of its C–F bonds is polar, like those in CH_2F_2. So, is the leading interaction in the complex $CF_4\cdots H_2O$ a hydrogen-bonding contact as in $CH_2F_2\cdots H_2O$, or an O···F contact as in $H_2O\cdots F_2$? Investigation of its rotational spectrum provides the answer.

$CF_4\cdots H_2O$ is an interesting quantum-mechanical system. It is a combination of a spherical top (CF_4) and of a planar top (H_2O). Classically it would be an asymmetric top, but its quantum mechanical behavior depends on the barriers hindering the internal motions of the water molecule, thus approaching the classical representation in the very high barrier limit. A detailed understanding of the system would require the use of permutation-inversion theory, which takes into account all feasible motions,[14] as is necessary in the case of methane–water.[15] However, we show that the higher mass of the CF_4 group allows the problem to be treated in a relatively simple way.

We assigned the spectra of the $CF_4\cdots H_2O$, $CF_4\cdots D_2O$, $CF_4\cdots HDO$, and $CF_4\cdots H_2{}^{18}O$ isotopologues by free-jet millimeter-wave absorption spectroscopy. All spectra consisted of evenly spaced bands. For each band, the band head at higher frequency showed the features of a symmetric-top spectrum. An example of such a symmetric-top spectrum is shown for $CF_4\cdots D_2O$ in Figure 1. The lower-frequency region of the bands is quite rich in lines, some of which are up to twice the intensity of those of the symmetric-top band head. Fitting these transitions was quite troublesome. To understand these features better, we performed some measurements at lower frequency with a supersonic expansion on a Fourier transform microwave spectrometer. The overall pattern was similar to that observed in the high-frequency region, but was simpler because of the smaller number of lines. All measured line frequencies are available in the Supporting Information. The spectroscopic constants obtained by fitting to the lines for a symmetric top are reported in Table 1 for all isotopologues.

The symmetric-top behavior can be explained by assuming water undergoes an almost free internal rotation. Ab initio computations at the MP2/6-311++G(d,p) level[16] converge to a global minimum that is in agreement with the experimental configuration (theoretical rotational constants

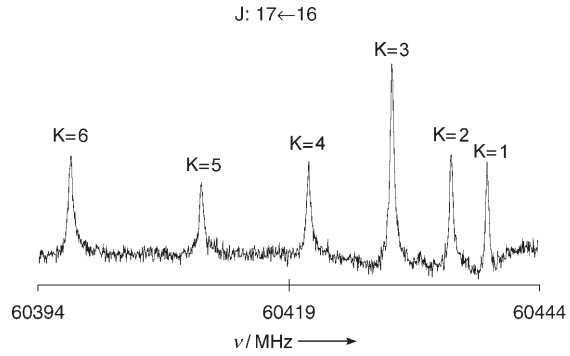

Figure 1. The rotational spectra of tetrafluoromethane–water isotopologues display symmetric-top behavior. The J = 17←16 transition of CF_4–D_2O is shown. The intensity differences are caused by the statistical weight resulting from the three equivalent F atoms of the CF_3 symmetric top with nuclear spin 1/2. The K = 0 component is missing because it is not Stark-modulated.

Table 1: Effective spectroscopic constants (A-state transitions) of the symmetric top $CF_4\cdots$water.

	$CF_4\cdots H_2O$	$CF_4\cdots H_2{}^{18}O$	$CF_4\cdots HDO$	$CF_4\cdots D_2O$
B/MHz	1918.0364(2)[a]	1814.684(5)	1845.5936(2)	1780.3609(2)
D_J/kHz^{-1}	5.391(4)	5.165(7)	5.078(5)	4.659(3)
D_{JK}/kHz	30.23(4)	28.0(3)	33.30(3)	34.47 (2)
H_{JJJ}/Hz	−0.081(7)		−0.10(1)	−0.079(5)
H_{JJK}/Hz	−1.36(8)	−1.0(3)	−0.59(7)	−0.67(5)
H_{JKK}/kHz	4.0(5)	3.5(15)	0.9(5)	−2.0(5)
N[b]	29	19	35	52
σ/σ_{exp}[c]	1.06	0.80	0.96	1.28

[a] Standard errors are given in parentheses in units of last digit. [b] Number of transitions in the fit. [c] Reduced deviation of the fit, relative to measurement errors of 3 and 50 kHz for the FTMW and conventional spectrometer, respectively.

are $A = 5603.4$, $B = 2052.2$, and $C = 2043.4$ MHz). The calculations also indicate that the barriers to the motions of the water molecule between CF_3 hollows are relatively high (Figure 2), whereas the barrier to the internal rotation of water is low ($V_3 \approx 24$ cm^{-1}; Figure 2). A calculation[17] with a simple flexible model indicates that in this case the ground-state torsional wavefunction describes a water molecule with

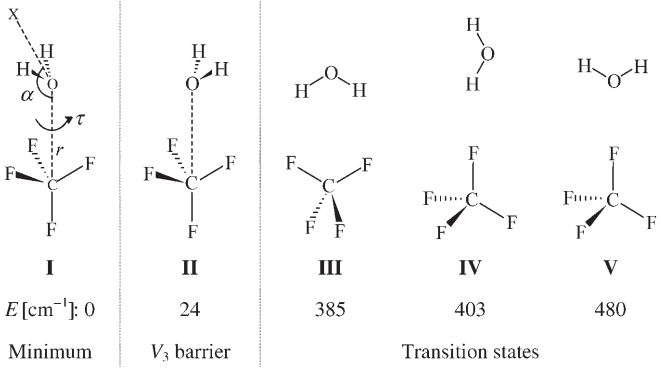

Figure 2. MP2/6-311++G** energy minimum of CF_4–H_2O and transition states for the motions of water between CF_3 hollows.

 © 2006 Wiley-VCH Verlag GmbH & Co. KGaA, Weinheim

the two hydrogen atoms completely delocalized with respect to the C_3 symmetry axis. As a consequence, the quantum-mechanical object is a symmetric top, and rotational constants B and C have the same value. The overall picture of the complex is shown in Figure 3.

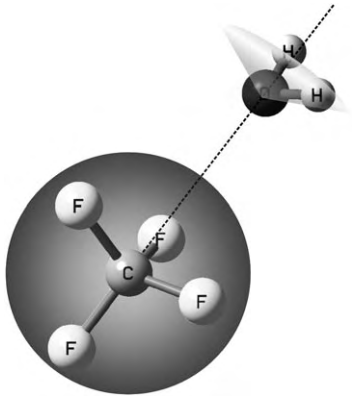

Figure 3. Cone of uncertainty of the orientation of the water moiety within a CF_3 hollow.

The parameters r (the distance between the C and O atoms; 3.371(3) Å) and α (125(2)°; see Figure 2) were estimated by assuming that the structures of water[18] and CF_4[19] are not altered upon formation of the complex. The shortest F···H, F···O, and C···O distances are 3.13, 2.75, and 3.30 Å, respectively, and the C–F bonds are nearly parallel with the axis of the cone of uncertainty defined by the delocalized H–O bonds.

The behavior of the "nonsymmetric-top" transitions (E-type) of $CF_4\cdots H_2O$ is very similar to that of benzene–water;[20] it cannot be interpreted with simple Hamiltonians,[21] but is described in Appendix 1 of the Supporting Information.

In view of the geometry and symmetry of the complex, it is likely that the stretching motion that leads to the dissociation of the complex is almost parallel to the a axis. This allows us to estimate the stretching force constant (k_s) by using the approximate Equation (1),[22] in which μ_{PD} is the pseudo-

$$k_s = 16\,\pi^4(\mu_{PD}R_{CM})^2[(B^2+C^2)^2+2(B^4+C^4)]/(h\,D_J) \quad (1)$$

diatomic reduced mass, R_{CM} is distance between the centers of mass, and D_J is the first-order centrifugal-distortion constant. A k_s value of 4.2 N m^{-1}, corresponding to a harmonic stretching frequency of 69 cm^{-1}, was obtained. The dissociation energy (E_D) was evaluated to be 5.0 kJ mol^{-1} by assuming a Lennard–Jones potential function and using the approximated Equation (2).[23] This energy is similar to that estimated

$$E_D = 1/72\,k_s{R_{CM}}^2 \quad (2)$$

for molecular complexes with three weak C–H···F–C or C–H···O hydrogen bonds. This seriously limits the consideration of weak hydrogen bonds as major factors in estimating the conformations of molecular complexes, as their energy is very similar to those of dispersion forces.

We believe that the configuration shown in Figure 3 results from favorable dipole–dipole interactions between the C–F and H–O bonds, whose electric dipole moments are almost antiparallel. Dipole–dipole interaction energy has been shown to be the leading factor also in determining the conformation of $CH_3F\cdots CF_3H$.[10b]

Experimental Section

Two experimental setups were used:

a) The 60–78-GHz Stark and pulse-modulated free-jet absorption millimeter-wave spectrometer used in this study is described elsewhere.[24] The best conditions to generate the adduct were obtained when flowing a mixture of approximately 30 mol% CF_4 (Linde) in helium at a pressure of 1.8 bar over water at room temperature and expanding it to about 5×10^{-3} mbar through a pulsed nozzle (repetition rate 5 Hz) with a diameter of 0.35 mm. An estimated "rotational" temperature of about 10–20 K was reached. All samples were obtained from commercial sources and used without further purification. The accuracy of the frequency measurements was estimated to be 0.05 MHz.

b) The COBRA-type[25] pulsed supersonic-jet Fourier transform microwave (FTMW) spectrometer[26] is described elsewhere.[27] It was recently updated with the FTMW++ set of programs.[28] A mixture of 2% in pressure CF_4 in He was flown over water at room temperature, and expanded to about 10^{-5} mbar. Each rotational transition is split by the Doppler effect and enhanced by the molecular-beam expansion in the direction of the coaxial supersonic-jet and resonator axes. The rest frequency was calculated as the arithmetic mean of the frequencies of the Doppler components. The estimated accuracy of frequency measurements is better than 3 kHz and lines separated by more than 7 kHz are resolvable.

Received: May 19, 2006
Revised: August 3, 2006
Published online: September 15, 2006

Keywords: hydrophobic interactions · molecular complexes · molecular dynamics · rotational spectroscopy · supersonic jets

[1] A full issue of Chemical Review has been dedicated to this topic: see for example the introduction: B. Brutschy, P. Hobza, *Chem. Rev.* **2000**, *100*, 3861, and the article: P. Hobza, Z. Havlas, *Chem. Rev.* **2000**, *100*, 4253–4264.

[2] See, for example, the two more recent books on the topic: a) A. Jeffrey, *An Introduction to Hydrogen Bonding*, Oxford University Press, New York, **1997**; b) S. Scheiner, *Hydrogen Bonding*, Oxford University Press, New York, **1997**.

[3] W. Caminati, A. Dell'Erba, S. Melandri, P. G. Favero, *J. Am. Chem. Soc.* **1998**, *120*, 5555; U. Spoerel, W. Stahl, W. Caminati, P. G. Favero, *Chem. Eur. J.* **1998**, *4*, 1974; W. Caminati, P. Moreschini, I. Rossi, P. G. Favero, *J. Am. Chem. Soc.* **1998**, *120*, 11144; P. Ottaviani, M. Giuliano, B. Velino, W. Caminati, *Chem.-Eur. J.* **2004**, *10*, 538; M. Becucci, G. Pietraperzia, M. Pasquini, G. Piani, A. Zoppi, R. Chelli, E. Castellucci, W. Demtroeder, *J. Chem. Phys.* **2004**, *120*, 5601; B. M. Giuliano, W. Caminati, *Angew. Chem.* **2005**, *117*, 609; *Angew. Chem. Int. Ed.* **2005**, *44*, 603.

[4] W. Caminati, A. Dell'Erba, G. Maccaferri, P. G. Favero, *J. Am. Chem. Soc.* **1998**, *120*, 2616; W. Caminati, L. B. Favero, P. G. Favero, A. Maris, S. Melandri, *Angew. Chem.* **1998**, *110*, 852; *Angew. Chem. Int. Ed.* **1998**, *37*, 792; W. Caminati, P. Moreschini, P. G. Favero, *J. Phys. Chem. A* **1998**, *102*, 8097; S. Melandri, M. E.

 © 2006 Wiley-VCH Verlag GmbH & Co. KGaA, Weinheim

Sanz, W. Caminati, P. G. Favero, Z. Kisiel, *J. Am. Chem. Soc.* **1998**, *120*, 11504.
[5] M. E. Sanz, J. C. Lopez, J. L. Alonso, A. Maris, P. G. Favero, W. Caminati, *J. Phys. Chem. A* **1999**, *103*, 5285.
[6] S. Blanco, J. C. Lopez, J. L. Alonso, P. Ottaviani, W. Caminati, *J. Chem. Phys.* **2003**, *119*, 880; T. M. Korter, D. W. Pratt, J. Küpper, *J. Phys. Chem. A* **1998**, *102*, 7211.
[7] W. Caminati, S. Melandri, I. Rossi, P. G. Favero, *J. Am. Chem. Soc.* **1999**, *121*, 10098.
[8] W. Caminati, S. Melandri, A. Maris, P. Ottaviani, *Angew. Chem.* **2006**, *118*, 2498; *Angew. Chem. Int. Ed.* **2006**, *45*, 2438.
[9] Y. Tatamitani, B. Liu, J. Shimada, T. Ogata, P. Ottaviani, A. Maris, W. Caminati, J. L. Alonso, *J. Am. Chem. Soc.* **2002**, *124*, 2739.
[10] W. Caminati, S. Melandri, P. Moreschini, P. G. Favero, *Angew. Chem. Int. Ed.* **1999**, *38*, 2924; W. Caminati, J. C. López, J. L. Alonso, J.-U. Grabow, *Angew. Chem.* **2005**, *117*, 3908; *Angew. Chem. Int. Ed.* **2005**, *44*, 3840.
[11] J. C. López, W. Caminati, J. L. Alonso, *Angew. Chem.* **2006**, *118*, 296; *Angew. Chem. Int. Ed.* **2006**, *45*, 290.
[12] G. R. Desiraju, T. Steiner, *The weak hydrogen bond*, Oxford University Press, Oxford, **1999**; P. Hobza, Z. Havlas, *Chem. Rev.* **2000**, *100*, 4253.
[13] S. A. Cooke, G. Cotti, C. M. Evans, J. H. Holloway, Z. Kisiel, A. C. Legon, J. M. A. Thumwood, *Chem. Eur. J.* **2001**, *7*, 2295.
[14] H. C. Longuet-Higgins, *Mol. Phys.* **1967**, *6*, 445.
[15] L. Dore, R. C. Cohen, C. A. Schmuttenmaer, K. L. Busarov, M. J. Elrod, J. G. Loeser, R. J. Saykally, *J. Chem. Phys.* **1994**, *100*, 862; R. D. Suenram, G. T. Fraser, F. J. Lovas, Y. Kawashima, *J. Chem. Phys.* **1994**, *101*, 7230.
[16] Gaussian 03 Revision B.04, M. J. Frisch et al., Gaussian, Inc., Pittsburgh PA, **2003**.
[17] R. Meyer, *J. Mol. Spectrosc.* **1979**, *76*, 266.
[18] F. C. de Lucia, P. Helminger, R. L. Cook, W. Gordy, *Phys. Rev. A* **1972**, *5*, 487.
[19] L. S. Bartell, J. G. Stanton, *J. Chem. Phys.* **1984**, *81*, 3792.
[20] S. Suzuki, P. G. Green, P. E. Bumgarner, S. Dasgupta, W. A. Goddard III, G. A. Blake, *Science*, **1992**, *257*, 942; H. S. Gutowsky, T. Emilsson, E. Arunan, *J. Chem. Phys.* **1993**, *99*, 4483; B. R. Prasad, M. S. Krishnan, E. Arunan, *J. Mol. Spectrosc.* **2005**, *232*, 308.
[21] D. R. Herschbach, *J. Chem. Phys.* **1959**, *31*, 91.
[22] a) D. Millen, *Can. J. Chem.* **1985**, *63*, 1477–1479; b) W. G. Read, E. J. Campbell, G. Henderson, *J. Chem. Phys.* **1983**, *78*, 3501–3508.
[23] R. P. A. Bettens, R. M. Spycher, A. Bauder, *Mol. Phys.* **1995**, *86*, 487–511.
[24] S. Melandri, W. Caminati, L. B. Favero, A. Millemaggi, P. G. Favero, *J. Mol. Struct.* **1995**, *352*, 253–258; S. Melandri, G. Maccaferri, A. Maris, A. Millemaggi, W. Caminati, P. G. Favero, *Chem. Phys. Lett.* **1996**, *261*, 267–271.
[25] J.-U. Grabow, W. Stahl, *Z. Naturforsch. A* **1990**, *45*, 1043; J.-U.Grabow, doctoral thesis, Christian-Albrechts-Universität zu Kiel, Kiel, **1992**; J.-U. Grabow, W. Stahl, H. Dreizler, *Rev. Sci. Instrum.* **1996**, *67*, 4072.
[26] T. J. Balle, W. H. Flygare, *Rev. Sci. Instrum.* **1981**, *52*, 33.
[27] W. Caminati, A. Millemaggi, J. L. Alonso, A. Lesarri, J. C. Lopez, S. Mata, *Chem. Phys. Lett.* **2004**, *392*, 1.
[28] J.-U. Grabow, Habilitationsschrift, Universität Hannover, Hannover, **2004**, http://www.pci.uni-hannover.de/~lgpca/spectroscopy/ftmw.

 © 2006 Wiley-VCH Verlag GmbH & Co. KGaA, Weinheim

Total Synthesis

DOI: 10.1002/anie.200602050

Stereocontrolled Total Synthesis of Bengazole A: A Marine Bisoxazole Natural Product Displaying Potent Antifungal Properties**

*James A. Bull, Emily P. Balskus, Richard A. J. Horan, Martin Langner, and Steven V. Ley**

Numerous oxazole-containing natural products have been isolated from marine sources in recent years[1] and have been the subject of extensive synthetic investigation.[2] A significant subsection of these natural products are bisoxazoles. In these cases, the two oxazole rings may be well separated, for example in phorboxazole[3] and the disorazoles,[4] or are directly linked as bisoxazole cores, such as in the hennoxazoles,[5] the diazonamides,[6] and in muscoride A.[7]

The bengazoles, on the other hand, are unique in that the two oxazole rings flank a single carbon atom. In bengazole A (**1**), this C10 position carries a myristate ester unit, which creates a sensitive isolated stereogenic center (Scheme 1). Moreover, the left hand oxazole ring is a biogenically unusual 5-monosubstituted ring while the central 2,4-disubstituted oxazole ring links to a stereochemically dense tetraol side chain.

Bengazole A was originally isolated in 1988 by Crews and co-workers from a sponge of the genus *Jaspis*,[8] and to date the bengazole family consists of 22 members.[9,10] The structure and absolute stereochemistry of this highly functionalized molecule was determined by a combination of NMR studies, analysis of degradation products, and circular dichroism.[8,10] The compound displays potent ergosterol-dependant antifungal activity comparable to that of amphotericin B, against *Candida albicans*,[11,12] and is active against fluconazole-resistant *Candida* strains.[13] Furthermore, bengazole A shows full anthelminthic activity against nematode *Nippostrongylus braziliensis* at just 50 $\mu g\,mL^{-1}$.[8]

There has been one reported previous synthesis of bengazole A (**1**), by Molinski and co-workers,[13] which used a regioselective metalation/addition strategy starting from 1,3-oxazole.[14,15] However, this gave a 1:1 mixture of the C10

[*] J. A. Bull, E. P. Balskus, Dr. R. A. J. Horan, Dr. M. Langner, Prof. Dr. S. V. Ley
Department of Chemistry
University of Cambridge
Lensfield Road, Cambridge CB21EW (UK)
Fax: (+44) 1223-336-442
E-mail: svl1000@cam.ac.uk
Homepage: http://leygroup.ch.cam.ac.uk

[**] We would like to thank Novartis for a Novartis Research Fellowship (S.V.L.), the EPSRC for a studentship (J.A.B.) and a postdoctoral fellowship (R.A.J.H.), the Winston Churchill Foundation of the USA for a scholarship (E.P.B.), and the DAAD for a postdoctoral fellowship (M.L.).

Supporting information for this article is available on the WWW under http://www.angewandte.org or from the author.

© 2006 Wiley-VCH Verlag GmbH & Co. KGaA, Weinheim

epimers, and once the resulting bisoxazole unit was in place, the C10 epimers could not be separated at any stage of the synthesis. Shioiri and co-workers achieved a synthesis of deacylbengazole[16] that was stereochemically enriched at the C10 position through an enantioselective reduction of a bisoxazole ketone which resulted in *ee* values up to 68%.[17]

Owing to the interesting biological profile and the challenging structural components, we devised a synthetic route to **1** that would provide both a single stereoisomer of the natural product and also allow for analogues to be prepared. We envisaged installing the C10 stereogenic center early in the synthesis, prior to construction of the bisoxazole unit. This somewhat risky strategy would require retention of stereochemical integrity at the C10 center during the formation of the central oxazole ring and on to the end of the synthesis. The desired bisoxazole unit would be derived from the diastereomerically pure serine amide **3** (Scheme 1), which in turn would be converted into a suitable precursor for a diastereoselective nitrile oxide 1,3-dipolar cycloaddition with alkene **4**, which contains a diol protected as a butane-2,3-diacetal (BDA). Cycloaddition product **2**, which contains the complete carbon backbone of **1**, would then be elaborated to reveal the tetraol side chain to complete the total synthesis.

BDA-protected diols have been used extensively by our research group as stable chiral building blocks.[18] The synthesis of amide fragment **3** relied upon stereocontrol derived from using our BDA-protected glyceraldehyde derivative **5**[18d] as a substrate for a Schöllkopf-type oxazole synthesis.[19] Treatment of aldehyde **5** with TosMIC and K_2CO_3 provided the desired 5-substituted oxazole **6** in excellent yield (Scheme 2). Oxazole **6** was isolated exclusively as the equatorially substituted diastereomer, hence efficiently establishing the desired stereochemistry at the C10 center for the natural product. Removal of the BDA group and manipulation of silyl protecting groups afforded the mono-TBDPS-protected diol **8**, with all reactions proceeding in excellent yields. Oxidation of the primary alcohol **8** proved to be difficult and was only achieved on using the Jones reagent, which provided carboxylic acid **9** in moderate yield. Subsequent amide coupling performed in DMSO gave the desired amide **3** as a single diastereomer, thus showing there was no loss of stereochemical integrity during the preceding steps.[20]

Having gained rapid access to amide **3** as a single diastereomer, the key challenge in this synthesis was the construction of the central 2,4-substituted oxazole ring under

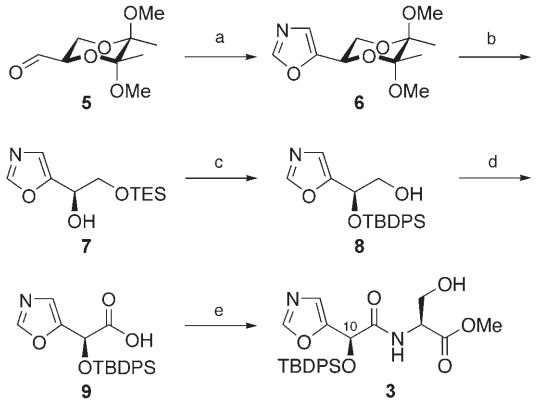

Scheme 2. Synthesis of amide fragment **3**. a) TosMIC, K_2CO_3, MeOH, reflux, 82%; b) 1. TFA, H_2O, RT; 2. TESCl, iPr_2NEt, CH_2Cl_2, −78 °C, 94% over 2 steps; c) 1. TBDPSCl, Et_3N, DMAP, CH_2Cl_2, RT; 2. PPTS MeOH, RT, 96% over two steps; d) Jones reagent, acetone, 0 °C, 49%; e) TBTU, H-(L)-Ser-OMe·HCl, iPr_2NEt, DMSO, RT, 64%. TosMIC = toluene-4-sulfonylmethylisocyanide, TFA = trifluoroacetic acid, TES = triethylsilyl, DMAP = 4-dimethylaminopyridine, PPTS = pyridinium*p*-toluenesulfonate, TBTU = 2-(1*H*-benzotriazole-1-yl)-1,1,3,3-tetramethyluronium tetrafluoroborate, DMSO = dimethylsulfoxide.

mild conditions in the presence of the sensitive C10 stereogenic center. Initial attempts to form this oxazole ring from serine amide **3** included: 1) oxazoline formation[21] followed by oxidation,[22] and 2) using conditions modified from those reported by Shin and co-workers[23] and involving dehydrative elimination followed by activation using *N*-bromosuccinimide, cyclization, and elimination. Although these approaches afforded the desired product, they proceeded in poor yields and caused significant racemization of the bisoxazole product.

We found that serine amide **3** could be converted into primary alcohol **10** in two steps (Scheme 3). Oxidation using buffered Dess–Martin periodinane[24] provided aldehyde **11**, which was subjected to Robinson–Gabriel-type oxazole formation under conditions reported by Panek and Beresis,[25] similar to those described previously by Wipf et al.[26] Treating the crude aldehyde **11** with PPh_3, 2,6-di-*tert*-butylpyridine, and dibromotetrachloroethane in CH_2Cl_2 to form the intermediate bromooxazoline, followed by the addition of 1,8-diazabicyclo[5.4.0]undec-7-ene (DBU) to eliminate HBr,

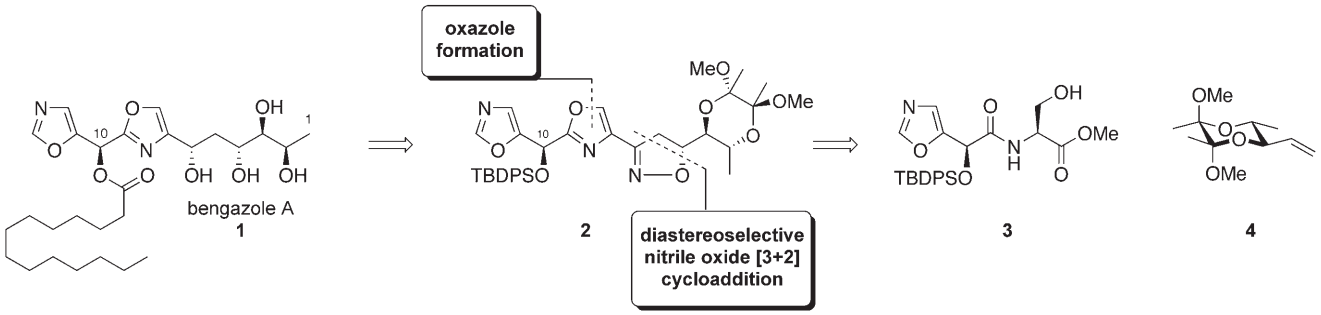

Scheme 1. Structure and retrosynthetic analysis of bengazole A (**1**). TBDPS = *tert*-butyldiphenylsilyl.

 © 2006 Wiley-VCH Verlag GmbH & Co. KGaA, Weinheim

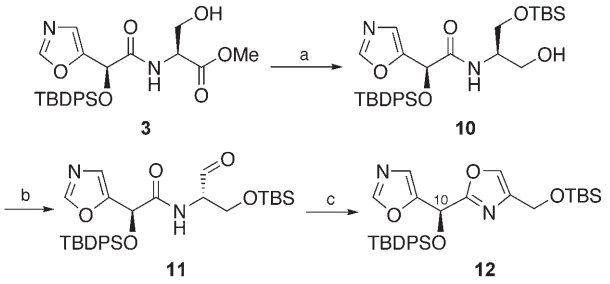

Scheme 3. Synthesis of bisoxazole **12**: a) 1. TBSCl, imidazole, DMAP, DMF, RT, 90%; 2. $NaBH_4$, LiCl, THF, MeOH, 0°C to RT, 80%; b) Dess–Martin periodinane, $NaHCO_3$, CH_2Cl_2, 0°C; c) PPh_3, $C_2Br_2Cl_4$, CH_2Cl_2, 2,6-di-*tert*-butylpyridine, 0°C, then Et_3N, MeCN, 0°C to RT, 89% over 2 steps. TBS = *tert*-butyldimethylsilyl.

provided the desired 2,4-disubstituted oxazole **12** in 72% yield over the two steps.

However, the product obtained from this process still displayed significant racemization (33–66% *ee*)[27] at the crucial C10 center. The cause of this was identified as the DBU, used to eliminate the proposed bromooxazoline intermediate.[26b] Replacing DBU with Et_3N completely prevented this racemization and also improved the yield over the two steps from alcohol **10** to an excellent 89%. Bisoxazole **12** was thus obtained with greater than 98% *ee* and the process was amenable to scale-up.[28,29] We believe this to be a potentially useful general modification for the formation of oxazole rings adjacent to highly epimerizable stereogenic centers.

With the enantiopure bisoxazole unit in hand, we turned our attention to the alkene fragment. Alkene **4** was readily synthesized in 71% yield over four steps from the commercially available acetonide **13** (Scheme 4). Transacetalization using CSA and 2,3-butanedione in methanol at reflux introduced the BDA protecting group as a 6:1 mixture of anomerically and non-anomerically stabilized products, which were then converted exclusively into the fully stabilized isomer **14** by using BF_3·THF. Reduction of ester **14** with DIBAL-H provided aldehyde **15** in 86% yield as a crystalline solid, and Wittig methylenation formed the required alkene **4** in quantitative yield. This synthesis was readily scalable through easily handled crystalline intermediates, which contrasts significantly with the synthesis of the simple acetonide-protected alkene derived from ester **13**; the known intermediate five-ring acetonide aldehyde[30] is prone to polymerization and the corresponding alkene is difficult to handle because of its volatility. Furthermore, we hoped the embedded chirality and rigidity of alkene **4** would provide enhanced side-chain diastereoselectivity in the planned dipolar cycloaddition.

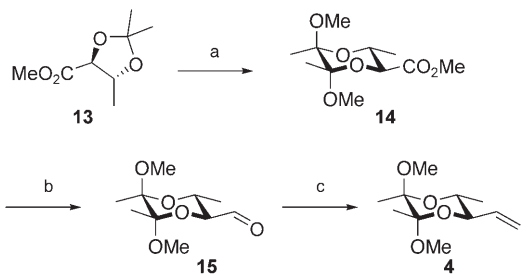

Scheme 4. Synthesis of alkene **4**: a) 1. 2,3-butanedione, CSA, trimethylorthoformate, MeOH, reflux; 2. BF_3·THF, CH_2Cl_2, RT, 83% over two steps; b) DIBAL-H, CH_2Cl_2, −78°C, 86%; c) Ph_3PCH_3Br, KHMDS, THF, −78°C to RT, quant. CSA = camphorsulfonic acid, DIBAL-H = diisobutylaluminum hydride, KHMDS = potassium hexamethyldisilazide.

Bisoxazole **12** was next converted into oxime **17** in readiness for the 1,3-dipolar cycloaddition (Scheme 5). This

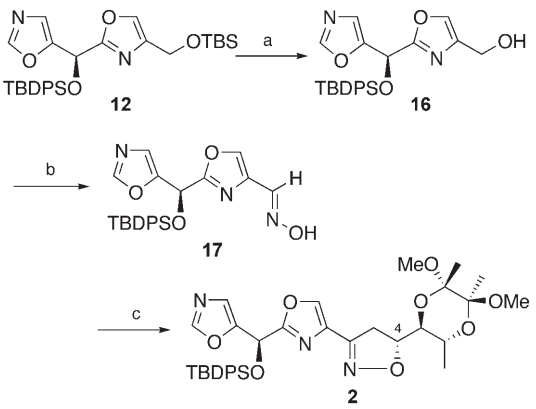

Scheme 5. Synthesis of isoxazoline **2**: a) PPTS, MeOH, RT, 93%; b) 1. Dess–Martin periodinane, $NaHCO_3$, CH_2Cl_2, 0°C; 2. NH_2OH·HCl, K_2CO_3, MeOH, H_2O, RT, 93% over two steps; c) 1. NCS, CH_2Cl_2, pyridine, RT, 2. alkene **4**, Cs_2CO_3, DME, RT; 77% over two steps, (d.r. 7:2). NCS = *N*-chlorosuccinimide, DME = 1,2-dimethoxyethane.

transformation proceeded in three steps, under mild conditions, with an average yield of 95%, and with complete retention of stereochemical integrity. The required nitrile oxide was generated from oxime **17** in two stages. Firstly, the oxime was chlorinated by treatment with NCS, and then Cs_2CO_3 was added to a solution of the chlorooxamic acid in DME in the presence of alkene **4**. The resulting 1,3-dipolar cycloaddition provided isoxazoline **2** in 60% yield of the major diastereomer.[31] The stereochemistry at C4 of the major cycloadduct is that found in the natural product and the result is consistent with that predicted by the "inside alkoxy" model reported by Houk et al.[32] The minor diastereomer (isolated in 17% yield) was easily removed by column chromatography and will be used in the studies towards analogues of **1**.

With the carbon skeleton complete, cycloadduct **2** was then elaborated to the natural product. Reductive cleavage of isoxazoline **2** using Raney nickel and boric acid in ethanol/water[33] gave β-hydroxy ketone **18** in 61% yield, which was subjected to a *syn*-selective reduction using diethylmethoxyborane and sodium borohydride (Scheme 6). Protection of the resulting diol (d.r. 14:1 by NMR spectroscopy) as acetonide **19** occurred in 89% yield over the two steps, with the minor C6 diastereomer being removed at this stage. Removal of the TBDPS group and installation of the myristoyl side chain proceeded in excellent yield to afford the acetal-protected bengazole A **20**. Acidic deprotection

 © 2006 Wiley-VCH Verlag GmbH & Co. KGaA, Weinheim

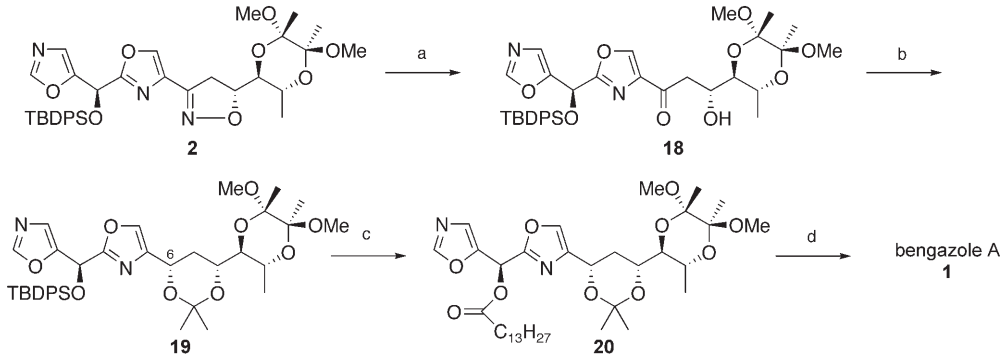

Scheme 6. Completion of the synthesis of bengazole A (**1**): a) Raney nickel, H_2, $B(OH)_3$, EtOH, H_2O, 61%; b) 1. Et_2BOMe, $NaBH_4$, THF, −78°C, (d.r. 14:1); 2. 2,2-dimethoxypropane, TsOH, 89% over 2 steps; c) 1. TBAF, THF, 0°C, quant.; 2. myristoyl chloride, NEt_3, CH_2Cl_2, 0°C, 85%; d) TFA, H_2O, RT, 95%. Ts = toluene-4-sulfonic acid, TBAF = tetrabutylammonium fluoride.

using TFA/water removed both the acetonide and the BDA groups from **20** in 95% yield to complete the total synthesis of bengazole A (**1**) in an overall yield of 3.4%. The data for our synthetic material were consistent with those reported for the natural product, and ^{1}HNMR spectroscopic analysis confirmed our product to be a single C10 epimer.[8,13,34–36]

In conclusion, we have completed a stereocontrolled total synthesis of bengazole A by using an oxazole synthesis under mild conditions and a diastereoselective 1,3-dipolar cycloaddition. Our route is the first to provide a single stereoisomer of the product and relies upon BDA building blocks to establish the stereogenic centers. Ongoing work in our laboratories is directed toward the synthesis of other members of the bengazole family and toward the synthesis of analogues for studies on structure–activity relationships.

Received: May 23, 2006
Revised: July 31, 2006
Published online: September 20, 2006

Keywords: antifungal agents · cycloaddition · heterocycles · natural products · total synthesis

[1] a) J. R. Lewis, *Nat. Prod. Rep.* **2002**, *19*, 223; b) Z. Jin, Z. Li, R. Huang, *Nat. Prod. Rep.* **2002**, *19*, 454, and references therein.
[2] a) V. S. C. Yeh, *Tetrahedron* **2004**, *60*, 11995; b) Y. Hamada, T. Shioiri, *Chem. Rev.* **2005**, *105*, 4441; c) P. Wipf, *Chem. Rev.* **1995**, *95*, 2115; d) P. Wipf, S. Venkatraman, *Synlett* **1997**, 1; e) L. O. Haustedt, I. V. Hartung, H. M. R. Hoffmann, *Angew. Chem.* **2003**, *115*, 2815; *Angew. Chem. Int. Ed.* **2003**, *42*, 2711; ; f) E. Riego, D. Hernández, F. Albericio, M. Álvarez, *Synthesis* **2005**, 1907, and references therein.
[3] P. A. Searle, T. F. Molinski, *J. Am. Chem. Soc.* **1995**, *117*, 8126.
[4] R. Jansen, H. Irschik, H. Reichenbach, V. Wray, G. Höfle, *Liebigs Ann. Chem.* **1994**, 759.
[5] T. Ichiba, W. Y. Yoshida, P. J. Scheuer, T. Higa, D. G. Gravalos, *J. Am. Chem. Soc.* **1991**, *113*, 3173.
[6] N. Lindquist, W. Fenical, G. D. Van Duyne, J. Clardy, *J. Am. Chem. Soc.* **1991**, *113*, 2303.
[7] A. Nagatsu, H. Kajitani, J. Sakakibara, *Tetrahedron Lett.* **1995**, *36*, 4097.
[8] M. Adamczeski, E. Quiñoà, P. Crews, *J. Am. Chem. Soc.* **1988**, *110*, 1598.
[9] a) J. Rodríguez, R. M. Nieto, P. Crews, *J. Nat. Prod.* **1993**, *56*, 2034; b) A. Rudi, Y. Kashman, Y. Benayahu, M. Schleyer, *J. Nat. Prod.* **1994**, *57*, 829; c) A. Groweiss, J. J. Newcomer, B. R. O'Keefe, A. Blackman, M. R. Boyd, *J. Nat. Prod.* **1999**, *62*, 1691; d) R. Fernández, M. Dherbomez, Y. Letourneux, M. Nabil, J. F. Verbist, J. F. Biard, *J. Nat. Prod.* **1999**, *62*, 678.
[10] P. A. Searle, R. K. Richter, T. F. Molinski, *J. Org. Chem.* **1996**, *61*, 4073.
[11] T. F. Molinski, *J. Nat. Prod.* **1993**, *56*, 1.
[12] J. Antonio, T. F. Molinski, *J. Nat. Prod.* **1993**, *56*, 54.
[13] a) R. J. Mulder, C. M. Shafer, T. F. Molinski, *J. Org. Chem.* **1999**, *64*, 4995; b) C. M. Shafer, T. F. Molinski, *Tetrahedron Lett.* **1998**, *39*, 2903.
[14] C. M. Shafer, T. F. Molinski, *Heterocycles* **2000**, *53*, 1167.
[15] a) J. C. Hodges, W. C. Patt, C. J. Connolly, *J. Org. Chem.* **1991**, *56*, 449; b) E. Vedejs, S. D. Monahan, *J. Org. Chem.* **1996**, *61*, 5192.
[16] P. Chittari, Y. Hamada, T. Shioiri, *Heterocycles* **2003**, *59*, 465.
[17] P. Chittari, Y. Hamada, T. Shioiri, *Synlett* **1998**, 1022.
[18] a) J. S. Barlow, D. J. Dixon, A. C. Foster, S. V. Ley, D. J. Reynolds, *J. Chem. Soc. Perkin Trans. 1* **1999**, 1627; b) D. J. Dixon, A. C. Foster, S. V. Ley, D. J. Reynolds, *J. Chem. Soc. Perkin Trans. 1* **1999**, 1631; c) S. V. Ley, D. K. Baeschlin, D. J. Dixon, A. C. Foster, S. J. Ince, H. W. M. Priepke, D. J. Reynolds, *Chem. Rev.* **2001**, *101*, 53; d) P. Michel, S. V. Ley, *Angew. Chem.* **2002**, *114*, 4054; *Angew. Chem. Int. Ed.* **2002**, *41*, 3898; .
[19] a) U. Schöllkopf, R. Schröder, *Angew. Chem.* **1971**, *83*, 358; *Angew. Chem. Int. Ed. Engl.* **1971**, *10*, 333; b) A. M. van Leusen, B. E. Hoogenboom, H. Siderius, *Tetrahedron Lett.* **1972**, 2369.
[20] The yield of the amide coupling to form amide **3** is highly dependent on the quality of carboxylic acid **9**, which is unstable and decomposes on storage. A more practical route on a large scale generates acid **9** through hydrolysis of the equivalent non-enantiopure methyl ester. The coupling with the enantiopure serine methyl ester resolves the acid into diastereomers, which are easily separated by column chromatography to provide amide **3** as a single stereoisomer.
[21] For oxazole-forming reactions using (diethylamino)sulfur trifluoride (DAST), see: a) W. J. Middleton, *J. Org. Chem.* **1975**, *40*, 574; b) P. Lafargue, P. Guenot, J.-P. Lellouche, *Heterocycles* **1995**, *41*, 947; c) A. J. Phillips, Y. Uto, P. Wipf, M. J. Reno, D. R. Williams, *Org. Lett.* **2000**, *2*, 1165; for reactions in which the Burgess reagent is used, see: d) G. M. Atkins, Jr., E. M. Burgess, *J. Am. Chem. Soc.* **1968**, *90*, 4744; e) P. Wipf, C. P. Miller, *Tetrahedron Lett.* **1992**, *33*, 907; for selected other methods, see: f) A. Sakakura, R. Kondo, K. Ishihara, *Org. Lett.* **2005**, *7*, 1971; g) P. Wipf, C. P. Miller, *Tetrahedron Lett.* **1992**, *33*, 6267.
[22] D. R. Williams, P. D. Lowder, Y.-G. Gu, D. A. Brooks, *Tetrahedron Lett.* **1997**, *38*, 331.
[23] N. Endoh, K. Tsuboi, R. Kim, Y. Yonezawa, C.-G. Shin, *Heterocycles* **2003**, *60*, 1567.
[24] D. B. Dess, J. C. Martin, *J. Am. Chem. Soc.* **1991**, *113*, 7277.
[25] J. S. Panek, R. T. Beresis, *J. Org. Chem.* **1996**, *61*, 6496.
[26] a) P. Wipf, C. P. Miller, *J. Org. Chem.* **1993**, *58*, 3604; b) P. Wipf, S. Lim, *J. Am. Chem. Soc.* **1995**, *117*, 558.

 © 2006 Wiley-VCH Verlag GmbH & Co. KGaA, Weinheim

[27] The *ee* value of bisoxazole **12** was determined using HPLC on a chiral stationary phase (Agilent 1100 series, Chiralcel AS, hexane/2-propanol 99:1, flow rate = 0.5 mL min^{-1}, 24 °C, λ = 215 nm, retention times: (*S*)-C10 isomer 10.35 min, (*R*)-C10 isomer 11.85 min).

[28] Using Et_3N in place of 2,6-di-*tert*-butylpyridine from the start of the reaction again provided bisoxazole **12** as a single enantiomer. However, these conditions gave a yield of only 47% and a reduced reaction time, thus suggesting a different reaction pathway.

[29] The *ee* value was determined by supercritical fluid chromatography on a chiral stationary phase following conversion into the primary alcohol **16** (Berger Minigram, Chiralcel AS column with 7% MeOH/CO_2, flow rate = 3 mL min^{-1} at 100 bar, 35 °C, λ = 210 nm, retention times: (*S*)-C10 isomer 8.66 min, (*R*)-C10 isomer 9.08 min).

[30] J. M. Gardiner, N. R. Panchal, W. T. Stimpson, J. M. Herbert, G. J. Ellames, *Synlett* **2005**, 2685.

[31] a) A. P. Kozikowski, A. K. Ghosh, *J. Am. Chem. Soc.* **1982**, *104*, 5788; b) A. P. Kozikowski, A. K. Ghosh, *J. Org. Chem.* **1984**, *49*, 2762; c) V. Jäger, R. Schohe, E. F. Paulus, *Tetrahedron Lett.* **1983**, *24*, 5501.

[32] a) K. N. Houk, S. R. Moses, Y.-D. Wu, N. G. Rondan, V. Jäger, R. Schohe, F. R. Fronczek, *J. Am. Chem. Soc.* **1984**, *106*, 3880; b) K. N. Houk, H.-Y. Duh, Y.-D. Wu, S. R. Moses, *J. Am. Chem. Soc.* **1986**, *108*, 2754.

[33] D. P. Curran, *J. Am. Chem. Soc.* **1983**, *105*, 5826.

[34] Molinski and co-workers report that the ^{1}H NMR spectra of the C10 epimers are very similar apart from the C15 (α-CH_2 on ester) and C1 proton signals (see reference [13]). These signals show no such splitting in the ^{1}H NMR spectra of our synthetic material.

[35] ^{1}H NMR (600 MHz, CD_3OD): δ = 0.89(3H, t, J = 7.4 Hz, H27), 1.15 (3H, d, J = 6.4 Hz, H1), 1.28 (20H, m, H17 to H26), 1.63 (2H, t, J = 7.0 Hz, H16), 1.90 (1H, ddd, J = 14.1, 9.2, 7.1 Hz, H5′), 2.23 (1H, ddd, J = 14.1, 6.9, 2.5 Hz, H5), 2.43 (2H, t, J = 7.3 Hz, H15), 3.18 (1H, dd, J = 6.8, 3.4 Hz, H3), 3.67 (1H, ddd, J = 9.2, 6.8, 2.5 Hz, H4), 3.92 (1H, dq, J = 6.4, 3.4 Hz, H2), 4.91 (1H, dd, J = 7.1, 6.9 Hz, H6), 7.11 (1H, s, H10), 7.31 (1H, s, H12), 7.85 (1H, s, H8), 8.25 ppm (1H, s, H13); ^{13}C NMR (150 MHz, CD_3OD): 14.4 (C27), 19.9 (C1), 23.7 (C26), 25.8 (C16), 30.8–30.0, 33.1 (C17 to C25), 34.5 (C15), 40.5 (C5), 62.9 (C10), 66.3 (C6), 67.8 (C2), 71.2 (C4), 78.8 (C3), 127.5 (C12), 138.0 (C8), 145.7 (C7), 147.7 (C11), 154.4 (C13), 159.7 (C9), δ = 173.4 ppm (C14); $[\alpha]_D^{25} = +6$ (c = 0.175, CH_3OH); HRMS (ESI) for $C_{27}H_{45}N_2O_8$: m/z calcd for $[M+H]^+$: 525.3176, found: 525.3163.

[36] We observed no racemization at the C10 atom on storage of synthetic bengazole A under argon at −20 °C over a period of one month.

 © 2006 Wiley-VCH Verlag GmbH & Co. KGaA, Weinheim

Transfer Hydrogenation

DOI: 10.1002/anie.200602122

On Water and in Air: Fast and Highly Chemoselective Transfer Hydrogenation of Aldehydes with Iridium Catalysts**

*Xiaofeng Wu, Jianke Liu, Xiaohong Li, Antonio Zanotti-Gerosa, Fred Hancock, Daniele Vinci, Jiwu Ruan, and Jianliang Xiao**

The use of water as a solvent for organic reactions has emerged as one of the most interesting fields for organic chemists, both in the laboratory and in industry, because of substantial economical and ecological gains.[1] Recently, Sharpless and co-workers demonstrated the benefits of performing C–C bond-formation reactions "on water".[2] We recently discovered that water is an excellent solvent for the asymmetric transfer hydrogenation of ketones.[3,4] Herein, we disclose that $[(Cp^*IrCl_2)_2]$ ($Cp^* = C_5Me_5$) in combination with monotosylated ethylenediamine is a good catalyst system for highly chemoselective transfer hydrogenation (TH) of aldehydes.[5] The reduction works in air and appears to occur on water.

TH reactions have been studied for more than one century. The reduction of ketones and aldehydes by the Meerwein–Ponndorf–Verley reaction was first described in 1925,[6] and since then a great deal of progress has been made in TH chemistry.[7–10] However, aldehydes are difficult to reduce by catalysts commonly used for TH, and controlling the chemoselectivity of the reaction presents a further challenge.[7b,11,12] To date, the most efficient TH catalyst appears to be the iridium complex of an N-heterocyclic carbene, which affords a turnover frequency (TOF) of up to 3000 h^{-1} in refluxing 2-propanol.[12a] With most other metal catalysts, the TOFs range from a few to several hundred per hour.[7–12] In fact, few catalysts have been reported that enable fast, selective, and productive TH of aldehydes with inexpensive, eco-friendly reductants, and that can tolerate the presence of synthetically useful functional groups.[7]

In continuing our investigation into aqueous TH reactions,[3] we examined the TH of benzaldehyde with HCOONa

[*] X. Wu, Dr. J. Liu, Dr. X. Li, Dr. D. Vinci, Dr. J. Ruan, Prof. J. Xiao
Liverpool Centre for Materials and Catalysis
Department of Chemistry
University of Liverpool
Liverpool L69 7ZD (UK)
Fax: (+44) 151-794-3589
E-mail: j.xiao@liv.ac.uk
Dr. A. Zanotti-Gerosa, Dr. F. Hancock
Johnson Matthey
Unit 28 Cambridge Science Park, Cambridge CB4 0FP (UK)

[**] We gratefully acknowledge the DTI MMI project and its industrial/academic partners (Prof. R. Cartlow, Royal Institution; Dr. A. Danopoulos, University of Southampton; Dr. A. Pettman, Pfizer; Dr. P. Hogan and Dr. M. Purdie, AstraZeneca; Dr. P. Ravenscroft, GlaxoSmithKline) for financial support and valuable suggestions.

WILEY InterScience DISCOVER SOMETHING GREAT
© 2006 Wiley-VCH Verlag GmbH & Co. KGaA, Weinheim

in water, initially using metal complexes with no additional ligands (Scheme 1). After the complexes had been stirred in water at 65 °C for 1 h, HCOONa and benzaldehyde (10.0 mmol) were introduced to start the reduction. As

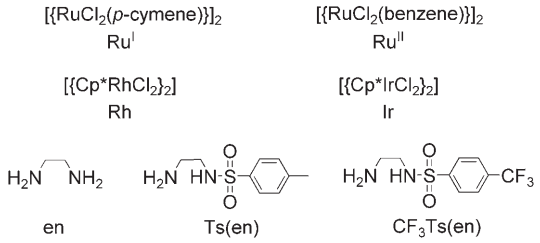

Scheme 1. Metal precursors and ligands screened in this study. Ts = toluene-4-sulfonyl.

shown in Table 1, the reaction was slow for all four complexes. However, the introduction of the readily available ethylenediamine (en) brought about a significant ligand-acceleration effect on the rates and, most remarkably, the monotosylated analogue Ts(en) led to around a 1000-fold increase in rate (Table 1, entries 3, 11, and 14).[13]

Table 1: Optimization of the TH reaction of benzaldehyde by HCOONa in water.[a]

Entry	Catalysts	*t* [h]	Conv. [%][b]	TOF[c] [mol mol^{-1} h^{-1}]
1	Ru^{I}	25	32	2
2	Rh	25	35	3
3	Ir	25	70	20
4	Ru^{II}	25	20	0.6
5	Ru^{I}–en	1	1.2	12[d]
6	Rh–en	1	74	900
7	Ir–en	1	99	1800
8	Ru^{II}–en	1	0.8	8[d]
9	Ru^{I}–Ts(en)	2	99	1000
10	Rh–Ts(en)	0.33	99	6000
11	Ir–Ts(en)	0.08	>99	12000
12	Ir–Ts(en), IPA[e]	1	2.6	26[d]
13	Ir–Ts(en), F/T[f]	1	1.5	15[d]
14	Ir–Ts(en)[g]	1.5	>99	20400
15	Ir–Ts(en)[h]	0.9	>99	28800
16	Ir–CF_3Ts(en)[h]	0.3	>99	42000
17	Ir–CF_3Ts(en)[i]	1	98	132000

[a] 65 °C, HCOONa (5 equiv) at S/C 1000:1 in water (10 mL). [b] Determined by GC. [c] Based on conversion after 5 min. [d] Based on conversion after 1 h. [e] 2-propanol (IPA) was used as hydrogen source and solvent, 3.2% conversion after 8 h. [f] HCOOH/Et_3N (F/T) azeotrope used, 9% conversion after 8 h. [g] S/C 1×10^4:1. [h] 80 °C, S/C 1×10^4:1. [i] 80 °C, S/C 5×10^4:1.

The precatalyst (M–ligand) was generated by simply reacting the precursor complex with the ligand in water at 65 °C for 1 h. It is apparent from Table 1 that the Ir^{III} catalysts with en and Ts(en) ligands proved to be the most active. For instance, benzaldehyde was reduced with almost complete conversion in 5 min using Ir–Ts(en) with a substrate/catalyst (S/C) ratio of 1000:1 at 65 °C (Table 1, entry 11). When the same reaction was carried out in 2-propanol or the azeotropic formic acid/triethylamine mixture, which are the two most commonly used solvents for TH reactions, the conversion was less than 3% (Table 1, entries 12 and 13). These results show the remarkable benefit of carrying out the reduction in the aqueous phase.

The effectiveness of using the Ir^{III} catalysts in synthesis was tested by carrying out the TH reaction at higher S/C ratios. At an S/C ratio of 1×10^4:1, Ir–Ts(en) led to a TOF of 28800 h^{-1} at 80 °C (Table 1, entry 15), and with the more electron-deficient Ir–CF_3Ts(en), a higher TOF of 42000 h^{-1} was achieved (Table 1, entry 16). Using Ir–CF_3Ts(en), the S/C ratio could be increased to 5×10^4:1 and a TOF as high as 1.3×10^5 h^{-1} was attained. Under these conditions, benzaldehyde (5.30 g) was reduced to give phenylmethanol in 98% yield (5.28 g after 1 h using 0.4 mg of [(Cp^*IrCl_2)$_2$]), demonstrating the superior activity,[7] robustness, and easy scalability of the aqueous Ir^{III} catalytic system. However, as seen with the TH of ketones using ruthenium catalysts,[1c,3b,14] the reduction is also pH dependent, with neutral conditions being most favorable (Figure 1).

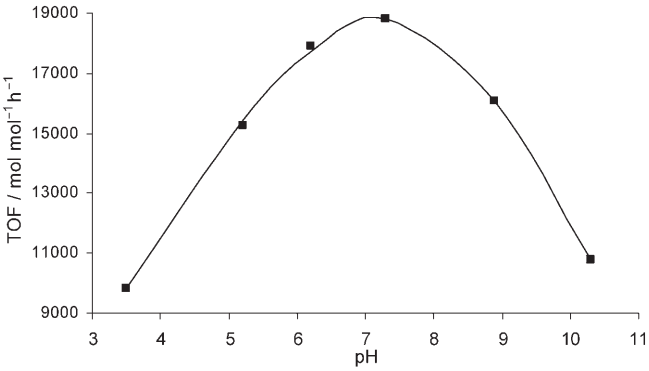

Figure 1. Plot showing the TOF against the initial solution pH values in the reduction of benzaldehyde (10 mmol), using Ir–Ts(en) and HCOONa (5 equiv) in water (10 mL) at 80 °C and S/C 5000:1. The initial pH value was determined by varying the HCOOH/NaOH molar ratios.

With these findings in hand, we were interested in extending this reduction system to a wider range of aldehydes. The results on the TH of aromatic aldehydes with Ir–Ts(en) at S/C 5000:1 and with Ir–CF_3Ts(en) at S/C 10000:1 are shown in Table 2. To our delight, most of the reactions were complete in a short time, and gave high yields. For example, the reductions of 4-halo- and 4-methoxybenzaldehyde with the Ir–Ts(en) catalyst both achieved over 99% conversion within 1 h (Table 2, entries 3, 4, 5, 7, and 10). With the more active Ir–CF_3Ts(en) catalyst, similar results were obtained at a higher S/C ratio (10000:1; Table 2, entries 6, 8, and 11). An exception to these results is the reduction of sulfur-containing substrates, probably because of coordination between sulfur and iridium. However, reduction of these substrates can be performed using a lower S/C ratio (1000:1; Table 2, entries 12, 25, and 26). The reduction also works well for sterically demanding substrates such as trisubstituted benzaldehydes (Table 2, entries 29 and 30) and significantly, the reduction

 © 2006 Wiley-VCH Verlag GmbH & Co. KGaA, Weinheim

Table 2: The TH reaction of aromatic aldehydes with HCOONa.[a]

Entry	Substr.	*t* [h]	Conv. [%][b]	Entry	Substr.	*t* [h]	Conv. [%][b]
1		0.6	>99 (98)	18		1.5	99
2		0.6[c]	>99	19		1.8[d]	99 (97)
3	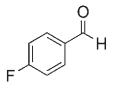	0.5	>99	20		7	99
4	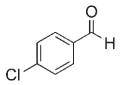	0.6	>99	21		1.5	>99
5	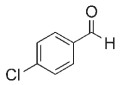	0.67[c]	>99 (98)	22		1.5	>99
6	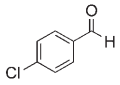	0.9[d]	>99	23	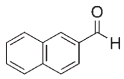	1.5	>99
7	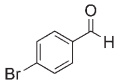	0.67	99	24		0.25	98
8	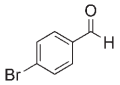	1.2[d]	99	25		0.5[f]	>99
9	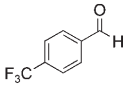	3	98	26	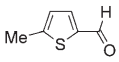	2[g]	99
10	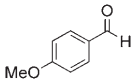	0.5	>99	27	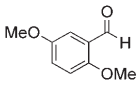	2	98 (97)
11	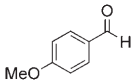	0.6[d]	>99	28	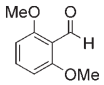	3	96 (94)
12	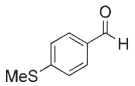	0.5[e]	>99	29	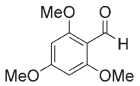	1.5[h]	99 (97)
13	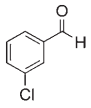	0.8	>99	30	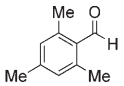	0.7[i]	99 (97)
14	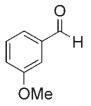	1	>99	31	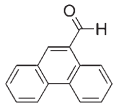	1.5	99 (98)
15	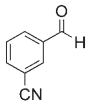	0.5	98	32	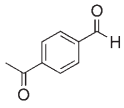	0.5	99 (95)
16	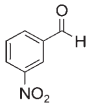	0.5	91	33	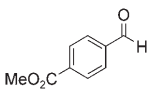	0.6	>99

tolerates a variety of functionalities. Of particular note is the reduction of 4-acetylbenzaldehyde, proceeding in 95% yield after 0.5 h, with no sign of ketone reduction (Table 2, entry 32). The results shown in Table 3 also prove that the aqueous Ir^{III} system is the most efficient, chemoselective catalyst for aldehyde reduction thus far reported. In addition, these TH reactions can be carried out in air without inert gas protection (Table 3, entries 2, 5, and 22).

Interestingly, under the same conditions, neither the water-soluble 4-carboxybenzaldehyde nor its sodium salt could be reduced. However, the ester analogue, methyl 4-formylbenzoate, was reduced with >99% conversion in 40 min (compare entries 33 and 34, Table 2). These results suggest that the catalysis takes place on water rather than in water in these biphasic reactions. This supposition is supported by the observation that the catalyst is more soluble in the organic phase and that the aqueous phase remains almost colorless during the reduction.

A further test of the chemoselectivity of the catalyst system is the TH of α,β-unsaturated aldehydes. Few catalysts are available that enable highly chemoselective TH of the carbonyl groups without reduction of the C=C bonds.[5,9] As shown in Table 3, various α,β-unsaturated aldehydes were selectively reduced on the formyl group. Notably, these include the acetylated cinnamaldehydes, in which both the alkenyl and acetyl groups remained intact during the reduction (Table 3, entries 7 and 8). To the best of our knowledge, no catalysts have been reported for the TH of these substrates.[15]

Surprisingly, when aliphatic aldehydes (for example, octanal) were subjected to TH under the conditions reported in Table 2, conversions were very low, even after prolonged reaction times. This reduction in the rate does not appear to result from product inhibition, as the TH of benzaldehyde was not affected by the presence of 1-octanol or 1-butanol as additives. Rather it is more likely related to the presence of α protons in these substrates. Thus, trimethylacetaldehyde was reduced in 3 h [Eq. (1)]. In sharp contrast, under the same conditions, the reduction of octanal proceeded in only 3%

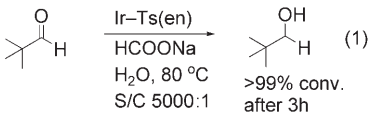

(1)

© 2006 Wiley-VCH Verlag GmbH & Co. KGaA, Weinheim

Table 2: (Continued)

Entry	Substr.	*t* [h]	Conv. [%][b]	Entry	Substr.	*t* [h]	Conv. [%][b]
17	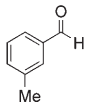	1.3	>99	34	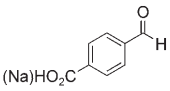	1	na[j]

[a] 80 °C, HCOONa (5 equiv) at S/C 5000:1 in water (15 mL). [b] Numbers in brackets refer to yields of isolated products. [c] The reaction was performed in air. [d] Ir–CF_3Ts(en), S/C 1×10^4:1. [e] S/C 1000:1; 48% conversion after 8 h at S/C 5000:1. [f] S/C 1000:1; 30% conversion after 5 h at S/C 5000:1. [g] S/C 1000:1; 32% conversion after 19 h at S/C 5000:1. [h] S/C 1000:1; 98% conversion after 12 h at S/C 5000:1. [i] S/C 1000:1; 99% conversion after 8 h at S/C 5000:1. [j] Not applicable (na); initial pH 6.8; no product was detected by NMR spectroscopy after 1 h.

Table 3: The TH reaction of α,β-unsaturated aldehydes with HCOONa.[a]

Entry	Aldehyde	Product	*t* [h]	Conv. [%][b]
1	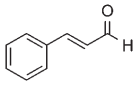	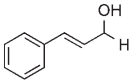	3	99 (97)
2			3[c]	>99
3			3[d]	98
4	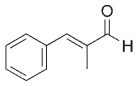	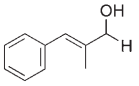	0.2	>99 (98)
5	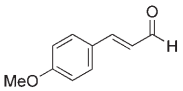	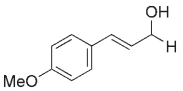	0.3	>99 (98)
6	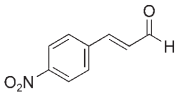	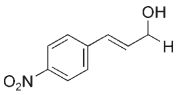	0.5	99 (98)
7	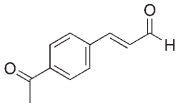	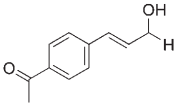	1.5	98 (96)
8	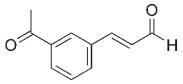	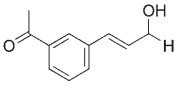	3	99 (97)
9	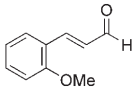	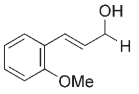	0.4	>99 (98)
10	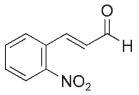	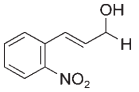	0.7	99 (98)
11	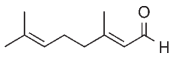	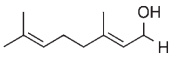	4	98 (97)
12	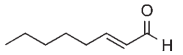	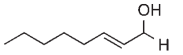	4.5	97
13	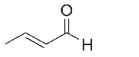	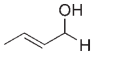	1	>99
14	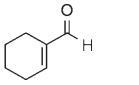	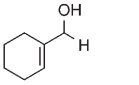	9	98

[a] 80 °C, HCOONa (5 equiv) at S/C 1000:1 in water (10 mL). [b] Numbers in brackets refer to yields of isolated products. [c] The reaction was performed in air. [d] Ir–CF_3Ts(en) used at S/C 5000:1.

yield after 18 h. One explanation is that under the reaction conditions, the α position in the aldehydes is deprotonated, leading to aldol products that might inhibit the iridium catalysis. The NMR and mass spectra of the reaction mixture arising from the reduction of octanal indeed show the presence of aldol and enol products.

If one assumes that the reduction is retarded by the aldol condensation,[1c,12a] lowering the concentration of substrates should disfavor the aldol reaction and enable TH of the aldehydes. Indeed, various aldehydes with α-hydrogen atoms could be reduced at S/C 2000:1 when the aldehyde was slowly added portionwise over the times shown in Table 4. Under such conditions, however, these aldehydes are still more difficult to reduce than aryl aldehydes. Thus, a competitive reduction of a mixture of benzaldehyde (30 mmol) and phenylacetaldehyde (6 mmol) with Ir–Ts(en) (0.01 mmol) gave a 98% conversion in 20 min for the former but required 5 h for the latter; as expected, when the concentration of phenylacetaldehyde was increased, the reduction rate decreased for both (equal molar mixture and total S/C 5000:1 gave 70% conversion for the former and 16% for the latter after 24 h).

Table 4: The TH reaction of aliphatic aldehydes using Ir–CF_3Ts(en) with HCOONa.[a]

Entry	Substrate	*t* [h]	Conv. [%]
1	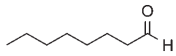	13[b]	95
2	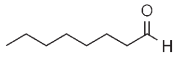	7	97
3	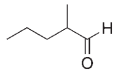	4	95
4		3.7	96
5		3.6	98
6	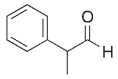	5[c]	90

[a] HCOONa (5 equiv) at 80 °C in water (10 mL). The aldehyde (20.0 mmol) was added dropwise in ten portions; 1-octanol (2.0 mmol) as a diluting agent was added initially; HCOOH was added to keep the pH neutral after the fifth addition. [b] Without diluting reagent. [c] S/C 1600:1.

In summary, we have demonstrated that Ir–Ts(en) and Ir–CF_3Ts(en) are highly active and chemoselective catalysts for the aqueous-phase TH of aldehydes. The catalytic reduction can be carried out with S/C ratios as high as 5×10^4:1, the initial TOFs near 1.3×10^5 h^{-1}, and an inert atmosphere is not required. Of significant practical importance is that the catalyst tolerates a wide variety of synthetically useful functional groups including nitro groups, halogens, ketones, esters, and olefins. To the best of our knowledge, this on-water Ir^{III}–diamine catalysis represents the most efficient, simple,

 © 2006 Wiley-VCH Verlag GmbH & Co. KGaA, Weinheim

and environmentally friendly catalytic system for the reduction of aldehydes to date.

Experimental Section

$[(Cp^*IrCl_2)_2]$ (1.6 mg, 0.002 mmol) and Ts(en) (1.2 mg, 0.0048 mmol) were suspended in degassed distilled water (15 mL). After the reaction mixture had been stirred at 80 °C for 1 h,[16] HCOONa (6.8 g, 0.1 mol) and benzaldehyde (2.1 g, 20 mmol) were added to the resulting solution. The reaction mixture was rapidly degassed three times through vacuum-nitrogen cycles and then heated at 80 °C for 0.6 h. The workup and analysis were conducted as previously reported.[3a]

Representative of a TH reaction (S/C ratio of 5×10^4:1): An aqueous solution of the catalyst Ir–CF_3Ts(en) (0.001 M, 1 mL) was added to degassed distilled water (30 mL), and the mixture was stirred at 80 °C for 10 min. HCOONa (17 g, 0.25 mol) and benzaldehyde (5.30 g, 50.0 mmol) were then introduced. A conversion of 98% was achieved after 1 h, and following workup, phenylmethanol was obtained as a colorless liquid (5.28 g, 98% yield).

Received: May 27, 2006
Published online: September 8, 2006

Keywords: aldehydes · chemoselectivity · iridium · transfer hydrogenation · water

[1] For recent reviews, see: a) K. H. Shaughnessy, *Eur. J. Org. Chem.* **2006**, 1827 – 1835; b) C. J. Li, L. Chen, *Chem. Soc. Rev.* **2006**, *35*, 68 – 82; c) F. Joó, *Acc. Chem. Res.* **2002**, *35*, 738 – 745.

[2] S. Narayan, J. Muldoon, M. G. Finn, V. V. Fokin, H. C. Kolb, K. B. Sharpless, *Angew. Chem.* **2005**, *117*, 3339 – 3343; *Angew. Chem. Int. Ed.* **2005**, *44*, 3275 – 3279.

[3] a) X. F. Wu, X. G. Li, W. Hems, F. King, J. Xiao, *Org. Biomol. Chem.* **2004**, *2*, 1818 – 8121; b) X. F. Wu, X. G. Li, F. King, J. Xiao, *Angew. Chem.* **2005**, *117*, 3473 – 3477; *Angew. Chem. Int. Ed.* **2005**, *44*, 3407 – 3411; c) X. F. Wu, D. Vinci, T. Ikariya, J. Xiao, *Chem. Commun.* **2005**, 4447 – 4449, and references therein.

[4] For recent examples of the aqueous-phase TH of ketones, see: a) C. Letondor, A. Pordea, N. Humbert, A. Ivanova, S. Mazurek, M. Novic, T. R. Wards, *J. Am. Chem. Soc.* **2006**, *128*, 8320 – 8328; b) Y. Xing, J. S. Chen, Z. R. Dong, Y. Y. Li, J. X. Gao, *Tetrahedron Lett.* **2006**, *47*, 4501 – 4503; c) J. S. Wu, F. Wang, Y. P. Ma, X. C. Cui, L. F. Cun, J. Zhu, J. G. Deng, B. L. Yu, *Chem. Commun.* **2006**, 1766 – 1768; d) J. Canivet, G. Labat, H. Stoeckli-Evans, G. Süss-Fink, *Eur. J. Inorg. Chem.* **2005**, 4493 – 4500; e) A. Schlatter, M. K. Kundu, W. D. Woggon, *Angew. Chem.* **2004**, *116*, 6899 – 6902; *Angew. Chem. Int. Ed.* **2004**, *43*, 6731 – 6734.

[5] For the aqueous-phase TH of aldehydes including α,β-unsaturated aldehydes, see reference [1c] and the references cited therein.

[6] For a recent review, see: K. Nishide, M. Node, *Chirality* **2002**, *14*, 759 – 767.

[7] For recent reviews, see: a) T. Ikariya, K. Murata, R. Noyori, *Org. Biomol. Chem.* **2006**, *4*, 393 – 406; b) S. Gladiali, E. Alberico, *Chem. Soc. Rev.* **2006**, *35*, 226 – 236; c) J. S. M. Samec, J.-E. Backvall, P. G. Andersson, P. Brandt, *Chem. Soc. Rev.* **2006**, *35*, 237 – 248; d) S. E. Clapham, A. Hadzovic, R. H. Morris, *Coord. Chem. Rev.* **2004**, *248*, 2201 – 2237; e) J. Blacker, J. Martin in *Asymmetric Catalysis on Industrial Scale: Challenges, Approaches and Solutions* (Eds.: H. U. Blaser, E. Schmidt), Wiley-VCH, Weinheim, **2004**, pp. 201 – 216.

[8] For recent examples of the TH of aldehydes, see: M. Kidwai, V. Bansal, A. Saxena, R. Shankar, S. Mozumdar, *Tetrahedron Lett.* **2006**, *47*, 4161 – 4165, and references therein.

[9] For examples of the TH of α,β-unsaturated aldehydes, see: a) P. Selvam, S. U. Sonavane, S. K. Mohapatra, R. V. Jayaram, *Adv. Synth. Catal.* **2004**, *346*, 542 – 544; b) T. Mizugaki, Y. Kanayama, K. Ebitani, K. Kaneda, *J. Org. Chem.* **1998**, *63*, 2378 – 2381, and references therein.

[10] For a recent review including hydrogenation of aldehydes (as well as α,β-unsaturated aldehydes), see: B. Chen, U. Dingerdissen, J. G. E. Krauter, H. G. J. Lansink Rotgerink, K. Möbus, D. J. Ostgard, P. Panster, T. H. Riermeier, S. Seebald, T. Tacke, H. Trauthwein, *Appl. Catal. A* **2005**, *280*, 17 – 46.

[11] For reviews, see: a) K. Nomura, *J. Mol. Catal. A* **1998**, *130*, 1 – 28; b) F. Joó, Á. Kathó, *J. Mol. Catal.* **1997**, *116*, 3 – 26.

[12] a) J. R. Miecznikowski, R. H. Crabtree, *Organometallics* **2004**, *23*, 629 – 631; b) J. W. Yang, M. T. Hechavarria Fonseca, N. Viganola, B. List, *Angew. Chem.* **2004**, *116*, 6829 – 6832; *Angew. Chem. Int. Ed.* **2004**, *43*, 6660 – 6662; c) A. N. Ajjou, J.-L. Pinet, *J. Mol. Catal. A* **2004**, *214*, 203 – 206; d) S. Naskar, M. Bhattacharjee, *J. Organomet. Chem.* **2005**, *690*, 5006 – 5010.

[13] R. Noyori, M. Yamakawa, S. Hashiguchi, *J. Org. Chem.* **2001**, *66*, 7931 – 7944.

[14] a) J. Carnivet, L. Karmazin-Brelot, G. Süss-Fink, *J. Organomet. Chem.* **2005**, *690*, 3209 – 3211; b) T. Abura, S. Ogo, Y. Watanabe, S. Fukuzumi, *J. Am. Chem. Soc.* **2003**, *125*, 4149 – 4154.

[15] We thank one referee for suggesting these substrates.

[16] The iridium compound isolated is consistent with [Cp*IrClL] (L = Ts(en) or CF_3Ts(en) without the amido hydrogen atom) with a structure probably similar to the related, structurally characterized Ir–Ts(dpen) compound (dpen = 1,2-diphenylethylenediamine).[17] Analytical data for the Ir–CF_3Ts(en) catalyst: ^{1}H NMR (400 MHz, $CDCl_3$/TMS): $\delta = 8.04$ ppm (d, $J = 8.1$ Hz, 2H) 7.63 (d, $J = 8.1$ Hz, 2H), 4.07 (br s, 2H), 2.74 (2H, m), 2.66 (m, 2H), 1.75 (s, 15H). HRMS (ES) for $C_{19}H_{26}ClF_3IrN_2O_2S$ ($[M+H]^+$): calcd: 631.0932 ($Ir^{191}Cl^{37}$) and 631.0985 ($Ir^{193}Cl^{35}$); found: 631.0950; for $C_{19}H_{25}F_3IrN_2O_2S$ ($[M-Cl]^+$): calcd: 595.1218 (Ir^{193}) and 593.1195 (Ir^{191}); found: 595.1190 and 593.1222. Elemental analysis: calcd for $C_{19}H_{25}ClF_3IrN_2O_2S$: C 36.21, H 4.00, N 4.45; found: C 36.40, H 4.12, N 4.31.

[17] K. Mashima, T. Abe, K. Tani, *Chem. Lett.* **1998**, 1199-1200.

 © 2006 Wiley-VCH Verlag GmbH & Co. KGaA, Weinheim

Analytical Methods

DOI: 10.1002/anie.200602144

Direct Identification of Tryptophan in a Mixture of Amino Acids by the Naked Eye**

*Zhijuan Bao, Shuna Sun, Jun Li, Xinqi Chen, Suying Dong, and Huimin Ma**

Tryptophan, an essential amino acid, plays a crucial part in biological processes such as protein biosynthesis, animal growth, and plant development.[1] Tryptophan is also one of the key factors that determines protein activity, hydrophobicity, and diversity.[2] The detection of tryptophan is thus of great importance for its biochemical study.[3,4] However, amino acids often coexist and have similar properties, and thus the detection of an individual one suffers from serious interference and usually has to be carried out through an efficient separation technique such as HPLC.[3] Over the past several decades, much effort has been devoted to seeking a simple and reliable method by which tryptophan could be identified in a mixture of amino acids directly by the naked eye.[3–5] Such a method is extremely desirable for amino acid production and the fast screening of tryptophan in proteolysates, but unfortunately it is still lacking.[2a,4]

It is known that a reversible formylation at the 1-position of tryptophan may occur upon treatment with anhydrous formic acid saturated with gaseous HCl.[6] In an effort to expand our research on developing site-specific labeling methods for proteins,[7] we were therefore interested in trying to introduce the formyl group at the N1 position of tryptophan. When we attempted to improve the formylation reaction by treating tryptophan in a mixed aqueous solution of formic acid and hydrochloric acid, a violet-blue color was surprisingly produced. More interestingly, this reaction exhibits a high selectivity toward tryptophan only, with no color observed with the other amino acids. We envision that this new color-generating reaction could be used as a specific identification method for tryptophan.

Figure 1 shows the absorption spectra of tryptophan in different media. It can be seen that water or formic acid has little effect on the absorption of tryptophan in the visible region, whereas hydrochloric acid causes a broad but rather weak absorption band, and the mixed aqueous solution of HCOOH and HCl leads to the emergence of two new bands at about 364 and 560 nm. It is noted that the addition of formic acid can induce the appearance of the violet-blue color only in HCl media, but not in other acids such as H_2SO_4 and H_3PO_4,[8] thus revealing the catalytic effect of HCl.[6a] Moreover, the violet-blue color becomes more intense with increasing temperature and time, and at a higher temperature (such as 70 °C) water-insoluble brown products can be partly formed, thus indicating a possible decomposition.

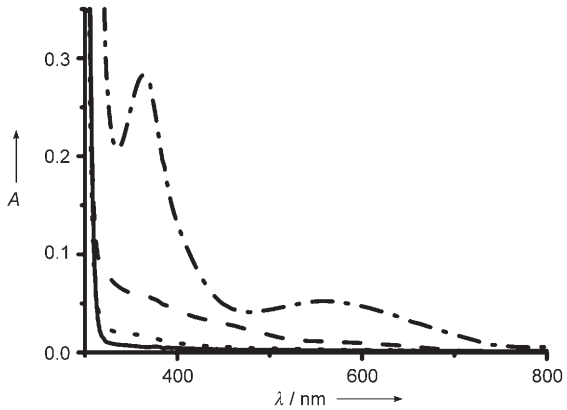

Figure 1. Absorption spectra of tryptophan (5 mM) in water (——), 18% (w/w) formic acid solution (••••), 6 M HCl (– – –), and the mixed solution of 18% formic acid and 6 M HCl (–•–•). See the Experimental Section for more details.

Several factors were examined in detail to enable the reaction conditions to be optimized. These studies showed that the violet-blue color is related to the acidity, the presence of oxygen, the reaction time, and the temperature, but independent of light. On the basis of this finding, a mixed solution of 6 M HCl and 18% formic acid with a heating time of 5 h at 50 °C were chosen for the present reaction, since under these conditions no apparent degradation of tryptophan was detected[8] and a distinct color change could be observed by the naked eye. The color reaction can also occur at room temperature, but takes a long time (usually completed within 4–7 days).

To assess the specificity of the reaction, 20 standard amino acids (alanine, arginine, asparagine, aspartic acid, cysteine, glutamic acid, glutamine, glycine, histidine, isoleucine, leucine, lysine, methionine, phenylalanine, proline, serine, threonine, tryptophan, tyrosine, and valine) were tested in parallel under the same conditions. The results showed that, with the exception of tryptophan, none of the other amino acids resulted in the generation of any color.[8] This unique property of tryptaphan enables it to be distinguished easily from the other amino acids directly by the naked eye. Figure 2 shows the results of such a preliminary study. As can be seen, tryptophan, whether present alone (C) or in mixed amino acids (D), exhibits the predicted violet-blue color, whereas the other amino acids do not produce any color (B). The method may also be applied to solving the question as to whether a peptide or protein contains tryptophan residues, as demonstrated in Figure 2 through the use of reduced glutathione (E) and egg white albumin (F) as examples. Moreover, by monitoring the absorbance at about 364 or 560 nm,[8] the

[*] Z. Bao, S. Sun, J. Li, X. Chen, S. Dong, Prof. H. Ma
Beijing National Laboratory for Molecular Sciences
Institute of Chemistry
Chinese Academy of Sciences
Beijing 100080 (China)
Fax: (+86) 10-6255-9373
E-mail: mahm@iccas.ac.cn
Homepage: http://mahm.iccas.ac.cn

[**] This work was supported by the National Science Fund for Distinguished Young Scholars (no. 20525517), the NSF of China (no. 20435030), and the Chinese Academy of Sciences.

Supporting information for this article is available on the WWW under http://www.angewandte.org or from the author.

 © 2006 Wiley-VCH Verlag GmbH & Co. KGaA, Weinheim

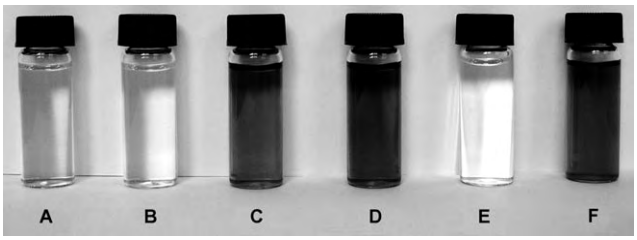

Figure 2. Photograph of solutions of HCOOH/HCl containing different compounds. A) Reagent blank (reaction solution of 18% formic acid and 6 M HCl); B) a mixture of 9 representative amino acids (L-alanine, L-arginine, L-glutamine, L-histidine, DL-methionine, L-phenylalanine, L-proline, DL-serine, and L-tyrosine) with various side-chain features; C) tryptophan; D) amino acid mixture (B) in the presence of tryptophan; E) reduced glutathione; F) egg-white albumin. The concentration of each of the amino acids as well as the reduced glutathione was 20 mM, while that of the egg-white albumin was 0.5 mM. The color reactions (A–D) were performed at 50 °C for 5 h and the reaction solutions were then allowed to stand at room temperature (25 °C) for 4 days, whereas those of E and F were conducted at room temperature for 7 days.

tryptophan content in samples could be estimated, although the sensitivity of the method is not high (detection limit: ca. 0.1 mM, signal/noise = 3:1).

To explore the reaction mechanism, the reactions of tryptophan and its reference compounds indole and indole-3-propanoic acid (IPA) were compared in the HCOOH/HCl system. It was found that all three compounds can react but give different colors: IPA, similar to tryptophan, produces a violet-blue color, while indole yields an orange-red color with an absorption peak at 484 nm.[8] Furthermore, the rate and intensity of the color reactions are increased in the following order: indole > IPA > tryptophan, clearly indicating that the indole skeleton is an essential moiety for the color reactions, and the steric hindrance of the substituent at the 3-position on the indole ring determines the reaction rate and intensity. It is known that carbolines can not be generated in HCOOH media,[9] and in this system the color interference from the corresponding carbolines could therefore be excluded. However, both indole and IPA, which do not have an α-amino group, produced color, which suggests that the α-amino group of tryptophan may not take part in the reaction process.

Isolation of the violet-blue pigment from the reaction solution was first attempted by column chromatography and extraction with organic solvents such as petroleum ether, chloroform, and ethyl acetate, but was unsuccessful. Subsequently, HPLC was used to isolate the pigment, and two chromatographic peaks appearing at 6.03 and 7.12 min[8] were characterized as tryptophan (m/z 205 $[M+H]^+$) and 1-formyltryptophan (m/z 233 $[M+H]^+$) by MS analysis.[8] However, the expected blue pigment that should have a large conjugated structure was not found, possibly because of its instability under the present test conditions. Therefore, the reaction solution was then subjected directly to electrospray ionization (ESI) MS analysis. Besides tryptophan and 1-formyltryptophan, two more products with higher molecular weights (m/z 463 and 491) were detected.[8] These high-molecular-weight ions, which have not been reported previously,[4,10] may contain at least two tryptophyl units, and be responsible for the violet-blue color.

The violet-blue color is quite stable in strong acid media (at least a week), but will disappear in neutral and basic media: the absorption maximum at about 560 nm gradually decreases and eventually vanishes as the pH value is increased. Conversely, acidification of the reaction solutions back to a strongly acidic pH results in the absorption spectra of the solutions being restored.[8] Moreover, the extent to which the absorption spectra is recovered depends on the time and pH value: the higher the pH value of the solutions, the slower and less complete is the recovery.

The peak indicative of 1-formyltryptophan in the HPLC chromatograms also changes with pH, and the trend of the change is consistent with that of the solution color: when the solution pH changes from a low to high value, the solution color fades away, and is concomitant with the gradual disappearance of the chromatographic peak corresponding to 1-formyltryptophan. Hence, 1-formyltryptophan may be a precursor of the colored derivative, and the reaction in which the violet-blue color is generated undoubtedly involves a quasireversible acid–base equilibrium. On the other hand, the recovery behaviors of the absorption spectra of indole and IPA resemble that of tryptophan (see the Supporting Information), but indole displays the fastest recovery, which can be attributed to the reduced steric hindrance at the 3-position of the indole ring.

Although the colored derivative has not been isolated, according to ESI-MS analysis it might be a rearranged compound (m/z 463 $[M+H]^+$ for compound **1**, or m/z 491 $[M+H]^+$ for compound **2**) of 1-formyltryptophan, whose mechanism of formation is shown in Scheme 1. Current

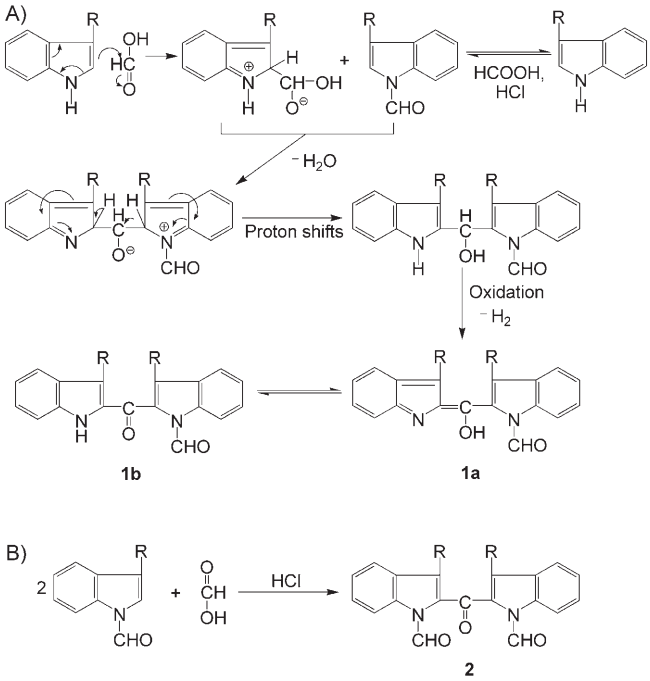

Scheme 1. Possible mechanism for the reaction of tryptophan in HCOOH/HCl media which generates the violet-blue color. R = $CH_2CH(NH_2)COOH$.

 © 2006 Wiley-VCH Verlag GmbH & Co. KGaA, Weinheim

evidence does not allow confirmation as to whether compound **1** (derived from 1 mol of tryptophan and 1 mol of 1-formyltryptophan) with a possible enolate tautomerization, compound **2** (derived from 2 mol of 1-formyltryptophan), or both result in the violet-blue color. It cannot be ruled out that a dimer formed directly by the coupling of 1-formyltryptophan through its 2-position makes a contribution to the violet-blue color, but this contribution, if it exists, would be a minor one, since such a dimer is difficult to form because of the large steric hindrance.

A comparative study of the current method was made with other known approaches,[5,11] in particular with the acid-ninhydrin method, in which both HCOOH and HCl are also involved.[11a] The reaction color in the acid-ninhydrin system is yellow, which may be attributed to the reaction of the α-amino group of tryptophan with ninhydrin to generate a yellow carboline product.[4b,12] In our system without ninhydrin, the resulting violet-blue color may be ascribed to the formation of compound **1** or/and compound **2**, as discussed above. The acid-ninhydrin method is fast and sensitive, but is inconvenient and unselective. In particular, cysteine and tyrosine interfere with the determination of tryptophan.[8] The reaction of tryptophan with *p*-dimethylaminobenzaldehyde and sodium nitrite in sulfuric acid has been widely used for the detection of tryptophan.[3,4a,11b] However, this method is also inconvenient because the reaction needs to be conducted in the dark because of the influence of light,[11b] and the accuracy is limited because of various interferences.[4a] A recently reported approach based on a diazo coupling reaction with *N*-(1-naphthyl)ethylenediamine is fast, but is subject to the interference of methionine and aromatic primary amines.[5] Thus, high selectivity and simplicity are the most noticeable advantages of the proposed method over the others discussed above.

In conclusion, the violet-blue color reaction of tryptophan in HCOOH/HCl has been characterized as a valuable method for identifying tryptophan in a mixture of amino acids, and for corroborating the existence of tryptophyl residues in peptides or proteins. The reaction investigated here may also provide a useful clue for a better understanding of the diseases blue diaper syndrome and purple urine bag syndrome which are caused by a metabolic disorder of tryptophan.[13]

Experimental Section

General procedure: In a typical experiment, tryptophan (25 mM, 1.0 mL) was added to a solution containing concentrated hydrochloric acid (37%, w/w, 2.5 mL) and formic acid (88%, w/w, 1.0 mL), and the final volume of the reaction solution was diluted to 5.0 mL with water. After the mixture was heated at 50 °C for 5 h in a water bath, and then cooled to room temperature, the absorption spectra were recorded in 1-cm quartz cells, with water used as the reference. When necessary, the pH value of the reaction solution was adjusted with NaOH or HCl. For comparison, indole and IPA were treated under the same conditions.

Received: May 30, 2006
Revised: August 7, 2006
Published online: September 19, 2006

Keywords: amino acids · analytical methods · tautomerism · tryptophan · UV/Vis spectroscopy

[1] a) J. E. Miller, C. Grădinaru, B. R. Crane, A. J. Di Bilo, W. A. Wehbi, S. Un, J. R. Winkler, H. B. Gray, *J. Am. Chem. Soc.* **2003**, *125*, 14220–14221; b) G. M. Mackay, C. M. Forrest, N. Stoy, J. Christofides, M. Egerton, T. W. Stone, L. G. Darlington, *Eur. J. Neurol.* **2006**, *13*, 30–42; c) S. Diem, J. Bergmann, M. Herderich, *J. Agric. Food Chem.* **2000**, *48*, 4913–4917; d) F. Von Nussbaum, *Angew. Chem.* **2003**, *115*, 3176–3179; *Angew. Chem. Int. Ed.* **2003**, *42*, 3068–3071.

[2] a) M. Friedman, J.-L. Cuq, *J. Agric. Food Chem.* **1988**, *36*, 1079–1093; b) N. Budisa, M. Rubini, J. H. Bae, E. Weyher, W. Wenger, R. Golbik, R. Huber, L. Moroder, *Angew. Chem.* **2002**, *114*, 4238–4242; *Angew. Chem. Int. Ed.* **2002**, *41*, 4066–4069.

[3] I. Molnár-Perl, *J. Chromatogr. A* **1997**, *763*, 1–10, and references therein.

[4] a) M. Friedman, J. W. Finley, *J. Agric. Food Chem.* **1971**, *19*, 626–631; b) M. Friedman, *J. Agric. Food Chem.* **2004**, *52*, 385–406, and references therein.

[5] W. T. Yu, H. M. Zhang, G. S. Chen, C. Y. Tu, P. K. Ouyang, *Microchim. Acta* **2004**, *146*, 285–290.

[6] a) A. Previero, M. A. Coletti-Previero, J.-C. Cavadore, *Biochim. Biophys. Acta* **1967**, *147*, 453–461; b) R. L. Lundblad, *Chemical Reagents for Protein Modification*, *2nd ed.*, CRC, Boca Raton, **1991**, pp. 225–226.

[7] a) S. Y. Dong, H. M. Ma, X. J. Duan, X. Q. Chen, J. Li, *J. Proteome Res.* **2005**, *4*, 161–166; b) X. J. Duan, Z. Zhao, J. P. Ye, H. M. Ma, A. D. Xia, G. Q. Yang, C. C. Wang, *Angew. Chem.* **2004**, *116*, 4312–4315; *Angew. Chem. Int. Ed.* **2004**, *43*, 4216–4219.

[8] See the Supporting Information.

[9] a) G. Cauzzo, G. Jori, *J. Org. Chem.* **1972**, *37*, 1429–1433; b) L. F. Tietze, Y. F. Zhou, *Angew. Chem.* **1999**, *111*, 2076–2078; *Angew. Chem. Int. Ed.* **1999**, *38*, 2045–2047.

[10] a) A. N. Mayeno, F. Lin, C. S. Foote, D. A. Loegering, M. M. Ames, C. W. Hedberg, G. J. Gleich, *Science* **1990**, *250*, 1707–1708; b) B. L. Williamson, L. M. Benson, A. J. Tomlinson, A. N. Mayeno, G. J. Gleich, S. Naylor, *Toxicol. Lett.* **1997**, *92*, 139–148; c) J. Adachi, Y. Mizoi, *J. Chromatogr.* **1991**, *538*, 331–339.

[11] a) M. K. Gaitonde, T. Dovey, *Biochem. J.* **1970**, *117*, 907–911; b) J. R. Spies, D. C. Chambers, *Anal. Chem.* **1949**, *21*, 1249–1266.

[12] A. Heesing, R. Muller-Matthesius, H. Rose, *Justus Liebigs Ann. Chem.* **1970**, *735*, 72–76.

[13] a) J. D. Sapira, S. Somani, A. P. Shapiro, E. T. Scheib, W. Reihl, *Metabolism* **1971**, *20*, 474–486; b) F. Vallejo-Manzur, E. Mireles-Cabodevila, J. Varon, *Am. J. Emerg. Med.* **2005**, *234*, 521–524.

 © 2006 Wiley-VCH Verlag GmbH & Co. KGaA, Weinheim

Synthetic Methods

DOI: 10.1002/anie.200602270

Diastereoselective Gold-Catalyzed Cycloisomerizations of Ene-Ynamides**

*Sylvain Couty, Christophe Meyer, and Janine Cossy**

Metal-catalyzed cycloisomerizations of ene-ynes lie among the most powerful methods for the elaboration of cyclic or polycyclic organic compounds.[1] In recent years, achievements in the field of platinum-[2–6] and gold-catalyzed[7–14] cycloisomerizations of ene-ynes have been particularly noteworthy. As a result of their high reactivity and mild reaction conditions, gold(I) salts or complexes are currently emerging as the most promising catalysts for these reactions.[15] Whereas the gold-catalyzed cycloisomerizations of ene-ynes accommodate the presence of oxygen or nitrogen atoms in the tether,[7a–c] and enol ethers as nucleophilic partners,[7a,9b] ene-ynamines[5d,e] and ene-ynol ethers[10b] have been seldom considered as substrates. Herein, we report the first examples of gold-catalyzed cycloisomerizations of 1,6-ene-ynamides that lead to substituted cyclobutanones or azabicyclic compounds, depending on the substitution pattern, and proceed with high levels of diastereoselectivity.

The platinum(II)-catalyzed cycloisomerization of ene-ynamides has already been investigated.[5d,e] Little difference, in terms of reactivity relative to the non-heterosubstituted series, was apparent for the most simple 1,6-ene-ynamide **1**, which was converted into the so-called "formal metathesis product" **2** (98%).[16] By contrast, the platinum(II)-catalyzed cycloisomerization of the homologous 1,7-ene-ynamide **3** led to the cyclobutene intermediate **4**, which was isolated in rather low yield (34%), and the latter was therefore best hydrolyzed directly to the corresponding cyclobutanone **5** (65%).[5d,e] Compounds **2** and **4** were assumed to originate from a cyclopropyl platinum carbene intermediate of type **A** ($M = PtCl_2$).[3,4,14] The latter underwent ring expansion to the cyclobutylcation **B**, stabilized by the nitrogen atom,[17] and demetalation afforded the cyclobutene intermediate of type **C**. For 1,6-ene-ynamides such as **1**, it was suggested that the double bond in the cyclobutene of type **C** ($n = 1$) remained in the more stable *exo* position but that this intermediate underwent electrocyclic ring opening to afford the 1,3-diene **2**. However, recent mechanistic investigations suggest that the formation of 1,3-dienes, such as **2**, may result from the skeletal rearrangements of the cyclopropyl metal carbenes of type **A** ($n = 1$) via intermediates of type **D** and/or **E**.[14] In the case of 1,7-ene-ynamides such as **3**, the migration of the double bond to the more stable *endo* position took place, thus resulting in lower ring strain, and led to the cyclobutene **4**. As a consequence of the platinum-catalyzed reaction pathways, any stereocenter generated in the initial stages of the cycloisomerization in the metal carbene of type **A** would be lost in subsequent steps (Scheme 1).

The use of milder reaction conditions should enable the rate of the skeletal rearrangements of the cyclopropyl metal carbene of type **A** to be decreased and/or avoid the electrocyclic ring opening of the intermediate cyclobutene of type **C**, both of which lead to the "formal metathesis product" **2**. To this end, we decided to investigate the gold-catalyzed cycloisomerizations of 1,6-ene-ynamides.

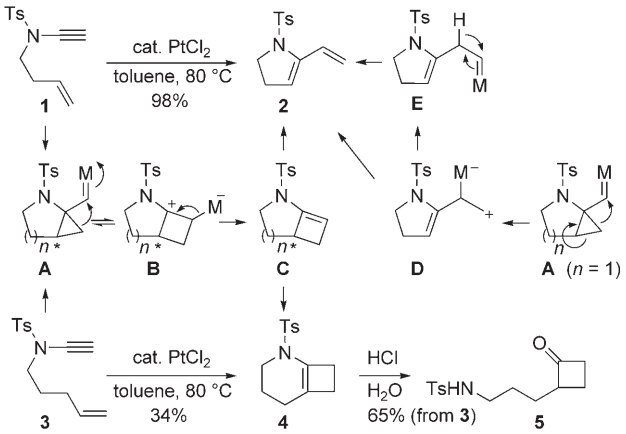

Scheme 1. Platinum(II)-catalyzed cycloisomerization of ene-ynamides. M = metal center, Ts = tosyl.

When the 1,6-ene-ynamide **1** was treated with AuCl (5 mol%) in CH_2Cl_2 at room temperature, a different reactivity profile was already apparent as the reaction led to the cyclobutanone **6** (40–50%), and the 1,3-diene **2** was only detected as a minor by-product (< 10%; Scheme 2).

Though the reaction was carried out under anhydrous conditions, subsequent exposure to atmospheric moisture during the workup seemed to be sufficient to promote the

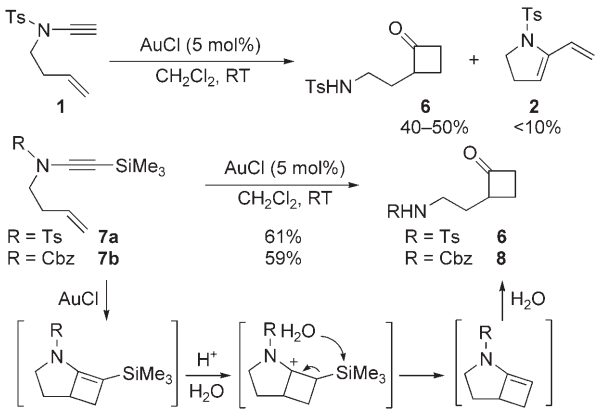

Scheme 2. Gold-catalyzed cycloisomerization of ene-ynamides. Cbz = carbobenzyloxy.

[*] S. Couty, Dr. C. Meyer, Prof. J. Cossy
Laboratoire de Chimie Organique, ESPCI
10 rue Vauquelin, 75231 Paris Cedex 05 (France)
Fax: (+33) 1-4079-4660
E-mail: janine.cossy@espci.fr

[**] Financial support from Johnson & Johnson (Focus Giving Award to J.C.) is gratefully acknowledged.

© 2006 Wiley-VCH Verlag GmbH & Co. KGaA, Weinheim

hydrolysis of the presumed cyclobutene intermediate of type **C** (M = AuCl) to the corresponding cyclobutanone **6**. Interestingly, the more stable ene-ynamides **7a** and **7b**, bearing either a tosyl or a benzyloxycarbonyl (Cbz) electron-withdrawing group on the nitrogen atom and a trimethylsilyl group as the alkyne substituent, also underwent gold-catalyzed cycloisomerizations to afford the cyclobutanones **6** (61%) and **8** (59%), respectively, without noticeable formation of the "formal metathesis" 1,3-diene by-products. As trimethylsilyl-ynamides do not undergo rapid protodesilylation in the presence of AuCl,[18] we propose that the loss of the trimethylsilyl group occurs during the hydrolysis process by protonation of the double bond of the initially formed trimethylsilyl-substituted cyclobutene intermediate with formation of trimethylsilanol (Scheme 2).

As a result of the milder reaction conditions, the cyclopropyl gold carbenes of type **A** (M = AuCl), generated by the gold-catalyzed cycloisomerizations of 1,6-ene-ynamides, do not seem to undergo skeletal rearrangements at a significant rate but instead undergo a preferential ring expansion to generate cyclobutenes of type **C** (Scheme 1; M = AuCl).[19] Although we have not been able, so far, to characterize the latter intermediates, presumably as a result of their sensitivity to moisture, they should retain any new stereogenic center created by the cycloisomerization process. Therefore, the previously unexplored opportunity of achieving diastereoselective cycloisomerizations of 1,6-ene-ynamides bearing stereogenic centers at the α or the β positions of the nitrogen atom could be investigated.

The 1,6-ene-ynamides **9**–**11** bearing a stereogenic center at the α position of the nitrogen atom[20] were subjected to a gold-catalyzed cycloisomerization (AuCl (5–20 mol%), CH_2Cl_2, room temperature). These reactions proceeded slowly (12–24 h) but efficiently and afforded the cyclobutanones **12** (76%), **13** (77%), and **14** (65%), respectively.[21] Examination of the ^{1}H NMR spectra of the crude materials indicated that the cycloisomerizations had proceeded with high levels of diastereoselection (d.r. > 95:5).[22,23] However, purification by flash chromatography on silica gel led to an erosion of the diastereoisomeric purity of the resulting cyclobutanones **12**–**14** (d.r. = 88:12–95:5). To avoid the purification of the latter sensitive cyclobutanones, their direct functionalization by a stereospecific transformation, such as a Baeyer–Villiger oxidation was envisaged.[24] Thus, treatment of cyclobutanone **13** (d.r. = 88:12) with peracetic acid (AcOOH, AcONa, AcOH, room temperature)[24b] provided the desired γ-lactone **15** (65%) without alteration of its diastereomeric purity owing to the well-known stereospecificity of the Baeyer–Villiger reaction (Scheme 3).[24,25]

When the gold-catalyzed cycloisomerization and the Baeyer–Villiger oxidation were carried out subsequently starting from ynamide **10**, without purification of the intermediate cyclobutanone **13**, the resulting γ-lactone **15** was isolated in a satisfactory overall yield (65%) and as a single diastereomer (d.r. > 95:5), thereby indicating the intrinsic high diastereoselectivity of the gold-catalyzed cycloisomerization. Similarly, the Baeyer–Villiger oxidation of cyclobutanone **14** afforded the functionalized γ-lactone **16** (67%; Scheme 3).[25]

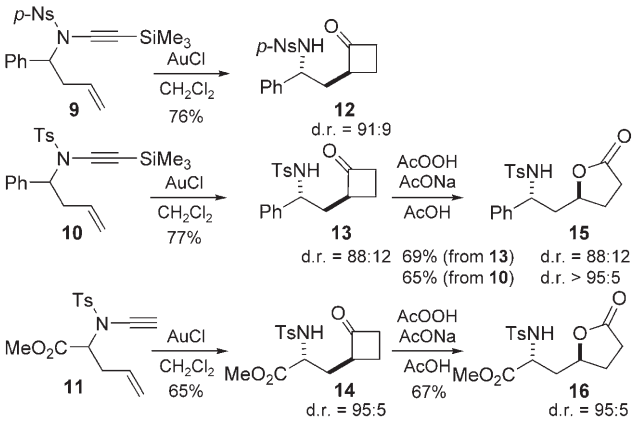

Scheme 3. Diastereoselective cycloisomerizations of ene-ynamides. *p*-Ns = $pNO_2(C_6H_4)SO_2$.

The cycloisomerization of the 1,6-ene-ynamide **17**, bearing a stereogenic center at the β position of the nitrogen atom, proceeded slowly (AuCl (5 mol%), CH_2Cl_2, room temperature), presumably as a result of the steric bulk around the nucleophilic alkene partner, and afforded the cyclobutanone **18** (d.r. = 90:10) in quite low yield (35%), which could be improved either by using a higher catalyst loading (20 mol%, 55% yield) or a more reactive cationic gold(I) complex (5 mol% $[Au(Ph_3P)(SbF_6)]$;[7a] 47% yield). When **17** was subjected to the cycloisomerization/Baeyer–Villiger rearrangement sequence, the γ-lactone **19** was obtained in satisfactory overall yield (56%, d.r. = 90:10; Scheme 4).

As the diastereoselectivity is set at the stage of the cyclopropyl gold carbene of type **A**, the possibility of retaining the interesting 2-azabicyclo[3.1.0]hexane substructure of the latter intermediate in the final cycloisomerization products was examined. Based on literature precedents disclosed in the non-heterosubstituted series,[8] the cycloisomerization of 1,6-ene-ynamides of type **F** bearing a propargylic alcohol moiety was investigated. For such substrates, the ring-expansion process should be diverted to an alternative event involving a 1,2-hydride shift followed by demetalation that leads to carbonyl derivatives of type **G** (Scheme 5).

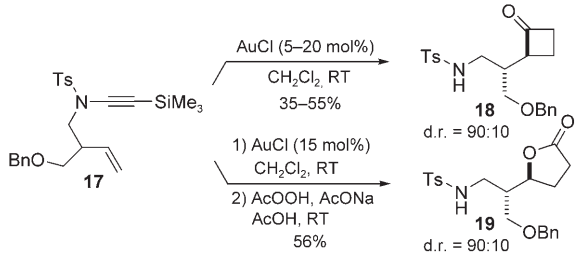

Scheme 4. Diastereoselective cycloisomerization of ene-ynamide **17**. Bn = benzyl.

The ynamides **20**–**23** bearing a propargylic alcohol moiety[26] were treated with AuCl (5 mol%) in CH_2Cl_2 at room temperature. Under these conditions, the primary alcohol **20a** was smoothly converted into the aldehyde **24a** (40%), whereas the secondary alcohols **20b** and **20c** led to the

 © 2006 Wiley-VCH Verlag GmbH & Co. KGaA, Weinheim

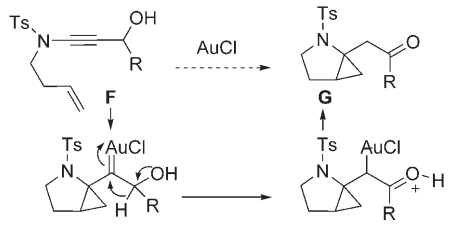

Scheme 5. Cycloisomerization of ene-ynamide bearing a propargylic alcohol moiety.

ketones **24b** (60%) and **24c** (42%), respectively. The ene-ynamides **21** and **22** bearing a stereocenter at the α position of the nitrogen atom were converted into the azabicylic aldehydes **25** (61%) and **26** (51%) with high diastereoselectivities (d.r. > 95:5). The cycloisomerization of the ene-ynamide **23** with a stereocenter at the β position of the nitrogen atom was also carried out, but the resulting aldehyde was directly reduced with $NaBH_4$ in MeOH to afford the alcohol **27** (60%, d.r. = 90:10; Table 1).[27]

We have reported the first examples of gold-catalyzed cycloisomerizations of 1,6-ene-ynamides, either unsubstituted or bearing a trimethylsilyl group at the acetylenic position, which led to cyclobutanones, or functionalized γ-lactones after a Baeyer–Villiger oxidation. High diastereoselectivities were observed for substrates bearing a stereocenter at the α or β positions of the nitrogen atom.[28] For 1,6-ene-ynamides bearing a propargylic alcohol moiety, the gold-catalyzed cycloisomerizations led to carbonyl compounds that incorporate a 2-azabicyclo[3.1.0]hexane framework. The gold-catalyzed cycloisomerization of other functionalized ynamides bearing different substitution patterns is currently under examination so that this methodology can be applied to natural and/or biologically active products.

Table 1: Cycloisomerization of ene-ynamides bearing a propargylic alcohol moiety.

Substrate		Product[a]		Yield [%][b]	d.r.
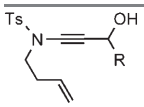	**20a** R = H **20b** R = Me **20c** R = *i*Pr	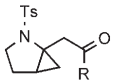	**24a** R = H **24b** R = Me **24c** R = *i*Pr	40 60 42	–
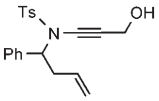	**21**	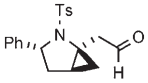	**25**	61	95:5
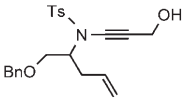	**22**	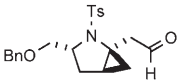	**26**	51	95:5
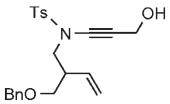	**23**		**27**	60[c]	90:10

[a] Treatment with AuCl (5 mol%) in CH_2Cl_2 at room temperature. [b] Yields of the isolated products as analytically pure materials. [c] Treatment with $NaBH_4$ in MeOH.

Experimental Section

4-Methyl-*N*-[(*R*)-2-{(2*S*)-2-oxocyclobutyl}-1-phenylethyl]benzenesulfonamide (**13**; representative procedure): AuCl (3.4 mg, 0.012 mmol, 0.05 equiv) was added to a solution of ynamide **10** (115 mg, 0.289 mmol) in CH_2Cl_2 (5 mL) at room temperature. The reaction mixture was filtered through a short plug of celite (CH_2Cl_2) after 24 h, and the filtrate was evaporated under reduced pressure. The crude material was purified by flash chromatography (petroleum ether/EtOAc = 80:20) to afford 77 mg (77%) of **13** as a colorless oil (88:12 mixture of diastereomers); IR $\tilde{\nu}_{max}$ = 3271, 1771, 1599, 1495, 1456, 1324, 1155, 1089, 813, 701, 666 cm^{-1}; ^1H NMR (400 MHz, $CDCl_3$): δ = 7.56 (br d, J = 8.1 Hz, 2H), 7.16–7.14 (m, 3H), 7.11 (d, J = 8.1 Hz, 2H), 7.05–7.01 (m, 2H), 6.04 (br d, J = 8.5 Hz, 1H), 4.53 (ddd, apparent dt, J = 8.5 and 6.0 Hz, 1H), 3.14–3.05 (m, 1H), 2.99 (dddd, J = 19.1, 11.0, 8.5 and 2.5 Hz, 1H), 2.85 (dddd, J = 18.0, 9.5, 4.5, and 2.5 Hz, 1H), 2.34 (s, 3H), 2.09 (m, 1H), 2.04–1.90 (m, 2H), 1.61 ppm (m, 1H); ^{13}C NMR (100 MHz, $CDCl_3$): δ = 212.0 (s), 142.9 (s), 139.8 (s), 137.9 (s), 129.3 (d, 2C), 128.5 (d, 2C), 127.4 (d), 127.0 (d, 2C), 126.3 (d, 2C), 56.2 (d), 55.9 (d), 44.1 (t), 36.8 (t), 21.4 (q), 14.2 ppm (t); MS (70 eV): *m/z* (%): 343 (1) [M^+], 315 (4) [M^+−CO], 261 (17), 260 (100), 188 (15), 155 (58), 130 (10), 106 (11), 104 (12), 91 (84), 77 (9), 65 (12), 55 (8).

(1*R*,3*R*,5*R*)-3-Phenyl-2-(4-methylbenzenesulfonyl)-2-azabicyclo-[3.1.0]hex-1-yl]ethanal (**25**): IR $\tilde{\nu}_{max}$ = 1726, 1597, 1493, 1450, 1340, 1160, 1085, 1029, 961, 812, 760, 729, 699, 657 cm^{-1}; ^1H NMR (400 MHz, $CDCl_3$): δ = 9.96 (t, J = 1.6 Hz, 1H), 7.45 (br d, J = 8.1 Hz, 2H), 7.18–7.10 (m, 5H), 7.12 (br d, J = 8.1 Hz, 2H), 4.12 (dd, apparent t, J = 8.8 Hz, 1H), 3.83 (dd, apparent br d, J = 17.4 Hz, 1H), 2.33 (dd, J = 17.4 and 1.6 Hz, 1H), 2.31 (s, 3H), 2.27 (dd, J = 13.1 and 8.8 Hz, 1H), 2.16 (ddd, J = 13.1, 8.8, and 5.5 Hz, 1H), 1.42 (ddd, apparent dt, J = 8.8 and 6.6 Hz, 1H), 0.61 (dd, J = 8.8 and 6.6 Hz, 1H), 0.47 ppm (dd, J = 6.6 and 5.5 Hz, 1H); ^{13}C NMR (100 MHz, $CDCl_3$): δ = 200.8 (d), 143.8 (s), 141.6 (s), 134.3 (s), 129.3 (d, 2C), 128.4 (d, 2C), 128.3 (d, 2C), 127.3 (d), 126.8 (d, 2C), 65.0 (d), 48.1 (t), 45.1 (s), 37.8 (t), 21.9 (d), 21.5 (q), 14.9 ppm (t); MS (70 eV): *m/z* (%): 355 (1) [M^+], 327 (2) [M^+−CO], 263 (32), 262 (20), 200 (51), 172 (26), 155 (15), 132 (16),131 (78), 129 (16), 117 (19), 116 (16), 105 (21), 104 (21), 103 (16), 91 (100), 77 (11), 65 (14).

Received: June 6, 2006
Published online: September 20, 2006

Keywords: cyclobutanones · cycloisomerization · cyclopropanes · gold · ynamides

[1] a) B. M. Trost, *Acc. Chem. Res.* **1990**, *23*, 34–42; b) B. M. Trost, V. K. Chang, *Synthesis* **1993**, 824–832; c) B. M. Trost, M. J. Krische, *Synlett* **1998**, 1–16; d) C. Aubert, O. Buisine, M. Malacria, *Chem. Rev.* **2002**, *102*, 813–834; e) G. C. Lloyd-Jones, *Org. Biomol. Chem.* **2003**, *1*, 215–236; f) I. J. S. Fairlamb, *Angew. Chem.* **2004**, *116*, 1066–1070; *Angew. Chem. Int. Ed.* **2004**, *43*, 1048–1052; g) S. T. Diver, A. J. Giessert, *Chem. Rev.* **2004**, *104*, 1317–1382; h) C. Bruneau, *Angew. Chem.* **2005**, *117*, 2380–2386; *Angew. Chem. Int. Ed.* **2005**, *44*, 2328–2334.

[2] For pioneering studies, see: a) N. Chatani, T. Morimoto, T. Muto, S. Murai, *J. Am. Chem. Soc.* **1994**, *116*, 6049–6050; b) J. Blum, H. Beer-Kraft, Y. Badrieh, *J. Org. Chem.* **1995**, *60*, 5567–5569; c) N. Chatani, N. Furukawa, H. Sakurai, S. Murai, *Organometallics* **1996**, *15*, 901–903; d) N. Chatani, K. Kataoka, S. Murai, N.

 © 2006 Wiley-VCH Verlag GmbH & Co. KGaA, Weinheim

Furukawa, Y. Seki, *J. Am. Chem. Soc.* **1998**, *120*, 9104 – 9105; for accounts, see: e) L. Añorbe, G. Domínguez, J. Pérez-Castells, *Chem. Eur. J.* **2004**, *10*, 4938 – 4943; f) A. M. Echavarren, C. Nevado, *Chem. Soc. Rev.* **2004**, *33*, 431 – 436.

[3] a) A. Fürstner, F. Stelzer, H. Szillat, *J. Am. Chem. Soc.* **2001**, *123*, 11863 – 11869; b) A. Fürstner, P. W. Davies, T. Gress, *J. Am. Chem. Soc.* **2005**, *127*, 8244 – 8245.

[4] a) M. Méndez, M. P. Muñoz, C. Nevado, D. J. Cárdenas, A. M. Echavarren, *J. Am. Chem. Soc.* **2001**, *123*, 10511 – 10520; b) C. Nevado, L. Charruault, V. Michelet, C. Nieto-Oberhuber, M. P. Muñoz, M. Méndez, M.-N. Rager, J.-P. Genêt, A. M. Echavarren, *Eur. J. Org. Chem.* **2003**, 706 – 713; c) C. Nevado, C. Ferrer, A. M. Echavarren, *Org. Lett.* **2004**, *6*, 3191 – 3194.

[5] a) E. Mainetti, V. Mouriès, L. Fensterbank, M. Malacria, J. Marco-Contelles, *Angew. Chem.* **2002**, *114*, 2236 – 2239; *Angew. Chem. Int. Ed.* **2002**, *41*, 2132 – 2135; b) C. Blaszykowski, Y. Harrak, M.-H. Gonçalves, J.-M. Cloarec, A.-L. Dhimane, L. Fensterbank, M. Malacria, *Org. Lett.* **2004**, *6*, 3771 – 3774; c) Y. Harrak, C. Blaszykowski, M. Bernard, K. Cariou, E. Mainetti, V. Mouriés, A.-L. Dhimane, L. Fensterbank, M. Malacria, *J. Am. Chem. Soc.* **2004**, *126*, 8656 – 8657; d) F. Marion, J. Coulomb, C. Courillon, L. Fensterbank, M. Malacria, *Org. Lett.* **2004**, *6*, 1509 – 1511; e) F. Marion, J. Coulomb, A. Servais, C. Courillon, L. Fensterbank, M. Malacria, *Tetrahedron* **2006**, *62*, 3856 – 3871.

[6] a) Y. Nishibayashi, M. Yoshikawa, Y. Inada, M. Hidai, S. Uemura, *J. Am. Chem. Soc.* **2004**, *126*, 16066 – 16072; b) G. B. Bajracharya, I. Nakamura, Y. Yamamoto, *J. Org. Chem.* **2005**, *70*, 892 – 897; c) T. J. Harrison, G. R. Dake, *Org. Lett.* **2004**, *6*, 5023 – 5026.

[7] a) C. Nieto-Oberhuber, M. P. Muñoz, E. Buñuel, C. Nevado, D. J. Cárdenas, A. M. Echavarren, *Angew. Chem.* **2004**, *116*, 2456 – 2460; *Angew. Chem. Int. Ed.* **2004**, *43*, 2402 – 2406; b) C. Nieto-Oberhuber, M. P. Muñoz, S. López, E. Jiménez-Núñez, C. Nevado, E. Herrero-Gómez, M. Raducan, A. M. Echavarren, *Chem. Eur. J.* **2006**, *12*, 1677 – 1693; c) C. Nieto-Oberhuber, S. López, M. P. Muñoz, E. Jiménez-Núñez, E. Buñuel, D. J. Cárdenas, A. M. Echavarren, *Chem. Eur. J.* **2006**, *12*, 1694 – 1702; d) C. Nieto-Oberhuber, S. López, A. M. Echavarren, *J. Am. Chem. Soc.* **2005**, *127*, 6178 – 6179.

[8] V. Mamane, T. Gress, H. Krause, A. Fürstner, *J. Am. Chem. Soc.* **2004**, *126*, 8654 – 8655.

[9] a) M. R. Luzung, J. P. Markham, F. D. Toste, *J. Am. Chem. Soc.* **2004**, *126*, 10858 – 10859; b) B. D. Sherry, F. D. Toste, *J. Am. Chem. Soc.* **2004**, *126*, 15978 – 15979.

[10] a) L. Zhang, S. A. Kozmin, *J. Am. Chem. Soc.* **2005**, *127*, 6962 – 6963; for the gold-catalyzed cycloisomerization of silyloxy enynes, see: b) L. Zhang, S. A. Kozmin, *J. Am. Chem. Soc.* **2004**, *126*, 11806 – 11807.

[11] a) F. Gagosz, *Org. Lett.* **2005**, *7*, 4129 – 4132; b) N. Mézailles, L. Ricard, F. Gagosz, *Org. Lett.* **2005**, *7*, 4133 – 4136.

[12] T. Shibata, Y. Ueno, K. Kanda, *Synlett* **2006**, 411 – 414.

[13] For some applications to natural product synthesis, see: a) A. Fürstner, P. Hannen, *Chem. Eur. J.* **2006**, *12*, 3006 – 3019; b) C. Fehr, J. Galindo, *Angew. Chem.* **2006**, *118*, 2967 – 2970; *Angew. Chem. Int. Ed.* **2006**, *45*, 2901 – 2904.

[14] For mechanistic studies, see: a) E. Soriano, P. Ballestros, J. Marco-Contelles, *Organometallics* **2005**, *24*, 3172 – 3181; b) C. Nieto-Oberhuber, S. López, M. P. Muñoz, E. Buñuel, C. Nevado, A. M. Echavarren, *Angew. Chem.* **2005**, *117*, 6302 – 6304; *Angew. Chem. Int. Ed.* **2005**, *44*, 6146 – 6148; c) C. Nevado, D. J. Cárdenas, A. M. Echavarren, *Chem. Eur. J.* **2003**, *9*, 2627 – 2635.

[15] a) G. Dyker, *Angew. Chem.* **2000**, *112*, 4407 – 4409; *Angew. Chem. Int. Ed.* **2000**, *39*, 4237 – 4239; b) A. S. K. Hashmi, *Gold Bull.* **2003**, *36*, 3 – 9; c) A. S. K. Hashmi, *Gold Bull.* **2004**, *37*, 51 – 65; d) A. Arcadi, S. Di Giuseppe, *Curr. Org. Chem.* **2004**, *8*, 795 – 812; e) A. Hoffmann-Röder, N. Krause, *Org. Biomol. Chem.* **2005**, *3*, 387 – 391; f) A. S. K. Hashmi, *Angew. Chem.* **2005**, *117*, 7150 – 7154; *Angew. Chem. Int. Ed.* **2005**, *44*, 6990 – 6993; for a recent account, see: g) S. Ma, S. Yu, Z. Gu, *Angew. Chem.* **2006**, *118*, 206 – 209; *Angew. Chem. Int. Ed.* **2006**, *45*, 200 – 203.

[16] M. Mori, H. Wakamatsu, N. Saito, Y. Sato, R. Narita, Y. Sato, R. Fujita, *Tetrahedron* **2006**, *62*, 3872 – 3881.

[17] For a review on additions to *N*-acyliminium ions, see: H. Hiemstra, W. N. Speckamp in *Comprehensive Organic Synthesis*, *Vol. 4* (Eds B. M. Trost, I. Fleming), Pergamon, Oxford, **1991**, pp. 1047 – 1082.

[18] Ynamide **28** was unaffected by treatment with AuCl.

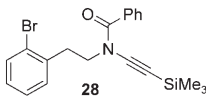

[19] The AuCl-catalyzed cycloisomerization of the 1,7-enyne **3** afforded the cyclobutanone **5** in only 26% yield; for the cycloisomerization of this class of substrate, $PtCl_2$ seems to be a more efficient catalyst relative to AuCl.

[20] a) B. Witulski, T. Stengel, *Angew. Chem.* **1998**, *110*, 495 – 498; *Angew. Chem. Int. Ed.* **1998**, *37*, 489 – 492; b) B. Witulski, M. Gößmann, *Chem. Commun.* **1999**, 1879 – 1880.

[21] Other gold(I) cationic catalysts such as $[Au(BF_4)(Ph_3P)]$[7a] and $[Au(NTf_2)(Ph_3P)]$[11] provided similar results.

[22] A 1:1 mixture of diastereomers was obtained by epimerization of the cyclobutanone **13** under alkaline conditions (K_2CO_3, MeOH, reflux).

[23] The Pt^{II}-catalyzed cycloisomerization of **10** ($PtCl_2$ (5 mol%), toluene, 80°C, 24 h) led to a mixture of compounds from which the cyclobutanone **13** was isolated in modest yield (39%) with low diastereoselectivity (d.r. = 55:45).

[24] a) G. R. Krow, *Org. React.* **1993**, *43*, 251 – 798; b) G. R. Krow, C. A. Johnson, J. P. Guare, D. Kubrak, K. J. Henz, D. A. Shaw, S. W. Szczepanski, J. T. Carey, *J. Org. Chem.* **1982**, *47*, 5239 – 5243.

[25] A chemical correlation from the 1,3-diol **29** (*syn*/*anti* = 70:30)[25a,b] was used to establish the relative configuration of compounds **15** and **13**; the relative configuration of the other cyclobutanones **12** and **14** was assumed to be similar.

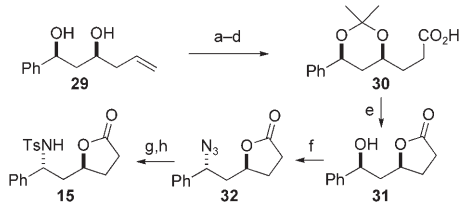

Reagents and conditions: a) $Me_2C(OMe)_2$, cat. camphorsulfonic acid (CSA), acetone; b) BH_3·THF, THF then NaOH, H_2O_2; c) 2-iodoxybenzoic acid (IBX), THF/dimethyl sulfoxide (DMSO); d) $NaClO_2$, NaH_2PO_4, 2-methylbut-2-ene, *t*BuOH; e) AcOH/H_2O, then toluene, cat. CSA, reflux (62% over 5 steps); f) $(PhO)_2P(=O)N_3$, 1,8-diazabicyclo[5.4.0]undec-7-ene (DBU), THF (64%);[25c] g) PPh_3, NaOH, THF/H_2O; h) *para*-toluenesulfonyl chloride (TsCl), pyridine (31% over 2 steps); a) X. Wang, Q. Meng, A. J. Nation, J. L. Leighton, *J. Am. Chem. Soc.* **2002**, *124*, 10672 – 10673; b) G. W. Kabalka, C. Narayana, N. K. Reddy, *Tetrahedron Lett.* **1996**, *37*, 2181 – 2184; c) A. S. Thompson, G. R. Humphrey, A. M. DeMarco, D. J. Mathre, E. J. J. Grabowski, *J. Org. Chem.* **1993**, *58*, 5886 – 5888.

[26] a) Y. Zhang, R. P. Hsung, M. R. Tracey, K. C. M. Kurtz, E. L. Vera, *Org. Lett.* **2004**, *6*, 1151 – 1154; b) D. Brückner, *Synlett* **2000**, 1402 – 1404.

[27] The following correlations observed in the NOESY spectra of **25** and **27** were used to assign their relative configurations. An *anti* relationship between H^1 and H^2 was also suggested by

 © 2006 Wiley-VCH Verlag GmbH & Co. KGaA, Weinheim

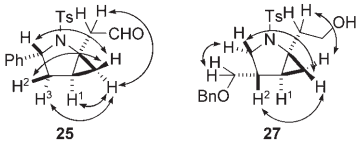

the absence of coupling ($J^3(H^1–H^2) \approx 0$ Hz), see: S. F. Martin, M. R. Spaller, S. Liras, B. Hartmann, *J. Am. Chem. Soc.* **1994**, *116*, 4493 – 4494.

[28] The initial coordination of AuCl by the alkyne should result in charge build up on the triple bond. The observed stereochemical outcome has been tentatively rationalized by assuming that interaction with the double bond may proceed through the formation of a π complex of chairlike conformation by analogy with cyclizations involving *N*-acyliminium ions;[17] whereas a substituent at Cβ should preferentially occupy a pseudoequatorial position, a pseudoaxial positioning of the substituent at Cα may be preferred in the cyclic transition state to avoid a gauche

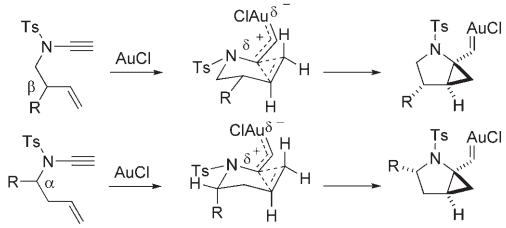

interaction with the *N*-tosyl substituent (similar to $A^{1,2}$ strain by assuming stabilization of the developing adjacent partial positive charge by the lone pair on the nitrogen atom).[17]

 © 2006 Wiley-VCH Verlag GmbH & Co. KGaA, Weinheim

Silicon Chemistry

DOI: 10.1002/anie.200602327

Low-Valent Silicon Cations with Two-Coordinate Silicon and Aromatic Character

Matthias Driess, Shenglai Yao, Markus Brym, and Christoph van Wüllen*

Dedicated to Professor Robert West

The parent silylium cation H_3Si^+[1] and the silyliumylidene cation HSi^+[2] are the simplest polyatomic silicon cations with low-coordinate silicon atoms. Because of their kinetic lability, they are very reactive species that can only be detected under mass spectrometric[1,3] and related astrophysical conditions.[2,4] However, because of their importance as basic building blocks in silicon chemistry, the quest for isolable derivatives of the free cations is one of the current challenges in contemporary silicon chemistry.

The isolation of free cations is particularly difficult in the case of silyliumylidene derivatives RSi^+ because of the redox lability of divalent versus tetravalent silicon in R_3Si^+. One successful method for the stabilization of low-coordinate silicon cations in the condensed phase is provided by using sterically encumbering substituents and/or π-donor ligands attached to the silicon in a noncoordinating environment. In line with that, the presence of a preferably weakly ("non"-) coordinating anion turned out to be crucial for the kinetic stability of highly Lewis acidic "free" cations in the solid state.[5] This has been impressively shown with the isolation of stable silylium salts that contain "free" R_3Si^+ cations,[6] including the remarkable synthesis of the first salt with a cyclotrisilylenium cation $[(RSi)_3]^+$.[7]

Recently, the concept of kinetic stabilization through the presence of appropriate bulky substituents has also paved the way to the isolation of the intriguing $[(\eta^5\text{-}C_5Me_5)Si]^+$ cation (**A**), the first and hitherto only known derivative of the elusive HSi^+ ion.[8] Apparently, the divalent (silylene-like) silicon atom in **A** benefits from the η^5-coordination mode of the C_5Me_5 ligand ("half-sandwich"), which leads to formally eight valence electrons and a lone electron pair at silicon (λ^5-Si^{II}). According to the Jemmis–Schleyer interstitial electron rule for half-sandwich (nido-cluster) species,[9] the cation **A** can be described as a 3D-aromatic compound. The existence of **A** prompted us to investigate whether HSi^+ derivatives **B** with two-coordinate Si^{II} atoms (λ^2-Si^{II}) are accessible by using

[*] Prof. Dr. M. Driess, Dr. S. Yao, Dr. M. Brym, Prof. Dr. C. van Wüllen
Institute of Chemistry: Metalorganics and Inorganic Materials
Technische Universität Berlin
Strasse des 17. Juni 135
Sekr. C2, 10623 Berlin (Germany)
Fax: (+49) 30-314-22168
E-mail: matthias.driess@tu-berlin.de

Supporting information for this article is available on the WWW under http://www.angewandte.org or from the author.

© 2006 Wiley-VCH Verlag GmbH & Co. KGaA, Weinheim

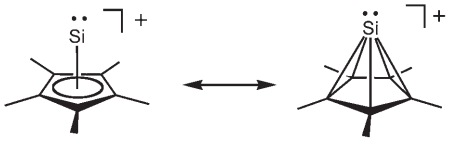

A: λ^5-Si^{II}, "half-sandwich"; nido-SiC_5^+ cluster, 3D aromatic

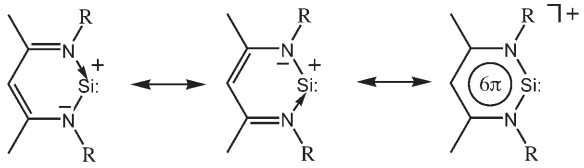

B: λ^2-Si^{II}, planar, 2D aromatic

sterically encumbered β-diketiminate ligands. The kinetic stabilization of the low-coordinate, divalent silicon center in **B** could be achieved by favorable N-coordination and a planar (Hückel-like) aromatic 6π-electron delocalization. Here we report the unexpected simple access and structural characterization of the novel silyliumylidene-like species **1** and **2**, starting from the potentially zwitterionic N-heterocyclic silylene **3** (Scheme 1).[10]

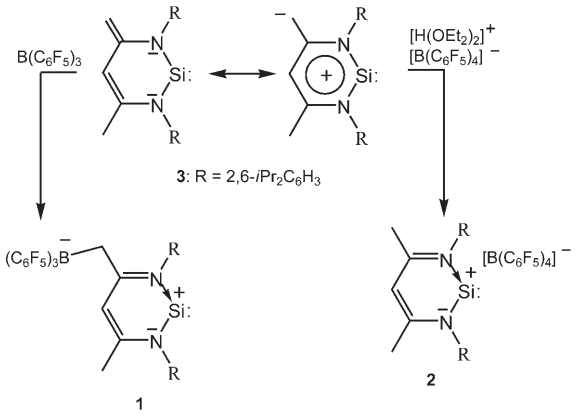

Scheme 1. Synthesis of the silyliumylidene compounds **1** and **2**.

Silylene **3** reacted gently with $B(C_6F_5)_3$ at ambient temperature to afford the zwitterionic adduct **1**, which was isolated as air- and moisture-sensitive colorless crystals in 69% yield. The structure of **1** was determined by a single-crystal X-ray diffraction analysis (Figure 1)[11] and NMR spectroscopy (see below). The zwitterion crystallizes in the triclinic space group $P\bar{1}$ and consists of a planar six-membered SiC_3N_2 ring with an exocyclic $B(C_6F_5)_3$ group attached to the C1 atom. The lengths of the C1–C2 (149.4(2) pm), C4–C5 (149.9(2) pm), and C1–B1 (165.6(2) pm) bonds indicate that they are single bonds, while those for C2–C3 (139.2(2) pm), C3–C4 (137.6(2) pm), N1–C2 (136.6(2) pm), and N2–C4 (136.4(2) pm) bonds are significantly shorter than those in **3**,[10] suggesting the presence of strongly conjugated π bonds. The Si–N bond lengths of 177.22(15) and 176.28(13) pm in **1** are approximately 3 pm longer than those in **3**. Additionally,

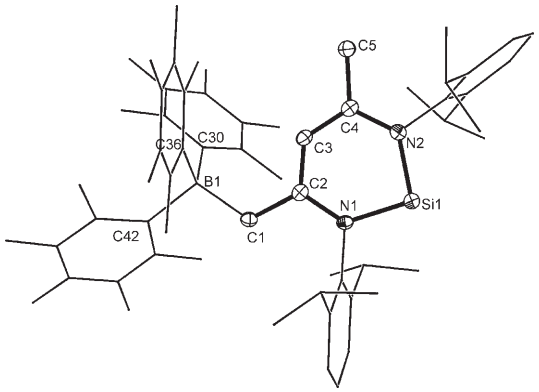

Figure 1. Molecular structure of **1**. Thermal ellipsoids (C1–C5, N1, N2, and Si1) are drawn at 50% probability level. Hydrogen and fluorine atoms are omitted for clarity. Selected distances [pm] and angles [°]: Si1–N1 177.22(15), Si1–N2 176.28(13), N1–C2 136.6(2), N2–C4 136.4(2), C1–C2 149.4(2), C2–C3 139.2(2), C3–C4 137.6(2), C4–C5 149.9(2), C1–B1 165.6(2), B1–C30 166.0(2), B1–C36 166.2(2), B1–C42 166.6(2); N1-Si1-N2 96.50(6), C2-N1-Si1 129.01(11), C4-N2-Si1 127.76(11, C2-C3-C4 127.16(14).

the endocyclic N1-Si1-N2 angle is only 3° smaller than that in **3**.

Crystals of **1** were insoluble in hydrocarbons but readily dissolved in ethereal solvents, whereas dissolution of **1** in CH_2Cl_2 led immediately to decomposition. Interestingly, dissolution of **1** in THF at room temperature led to an equilibrium mixture of **1** and silylene **3** in a molar ratio of 10:7 (^{1}H, ^{29}Si NMR spectroscopy), together with the $(F_5C_6)_3$B-THF adduct (^{1}H, ^{11}B NMR spectroscopy; see Supporting Information). However, the ^{1}H, ^{13}C, ^{11}B, ^{19}F, and ^{29}Si NMR signals of **1** could be unequivocally assigned and "extracted" from the difference spectra. Surprisingly, the ^{29}Si NMR spectrum of **1** revealed a resonance signal at $\delta = 40.5$ ppm, that is, the ^{29}Si nucleus is more shielded than that in **3** ($\delta =$ 88.4 ppm) by about 48 ppm,[10] in contrast to the expected higher Lewis acidity (electron-deficiency) of the low-valent Si atom in **1**. This can be explained by the presence of a stronger p_π–p_π donor–acceptor interaction between the π-electron system of the β-diketiminate ligand and the Si atom. In line with that, the ^{1}H NMR chemical shift of the γ-CH proton of the SiC_3N_2 ring at $\delta = 6.79$ ppm was significantly different from the respective value for **3** ($\delta = 5.44$ ppm) and thus indicative for the presence of an aromatic 6π-electron system.

This hypothesis was additionally corroborated by the synthesis of the separated ion pair $[\mathbf{2}\{B(C_6F_5)_4\}^-]$ through protonation of **3** with the convenient Brønsted acid $H(OEt_2)_2^+[B(C_6F_5)_4]^-$.[12] The desired product afforded colorless crystals, which were isolated in 61% yield. Its structure was elucidated by single-crystal X-ray diffraction analysis (Figure 2).[11] The salt $[\mathbf{2}\{B(C_6F_5)_4\}^-]$ crystallizes in the monoclinic space group $P2_1/n$ and consists of separated ion pairs (shortest Si–F distance 429.7 pm). As expected, the Si–N bond lengths and the N1-Si1-N2 angle (96.2(1)°) are almost identical with those observed in **1**. The same is true for the exocyclic C1–C2 and C4–C5, as well as the endocyclic C–C and C–N bond lengths, respectively. The geometrical parameters of the cation were very similar to those observed for

 © 2006 Wiley-VCH Verlag GmbH & Co. KGaA, Weinheim

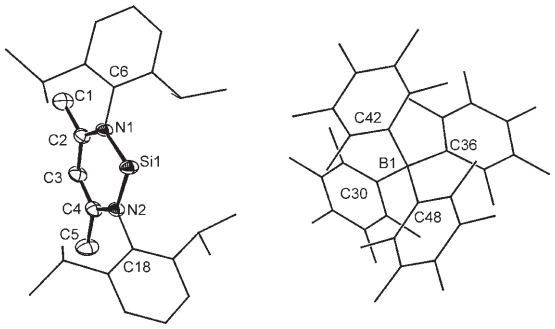

Figure 2. Molecular structure of the ion pair $[\mathbf{2}\{B(C_6F_5)_4\}^-]$. Thermal ellipsoids (C1–C5, N1, N2, and Si1) are drawn at 50% probability level. Hydrogen atoms of the cation **2** and the fluorine atoms in the $[B(C_6F_5)_4]^-$ anion are omitted for clarity. Selected distances [pm] and angles [°]: Si1–N1 177.0(3), Si1–N2 176.0(3), N1–C2 136.1(4), N2–C4 136.0(4), C1–C2 148.9(5), C2–C3 138.9(5), C3–C4 137.5(5), C4–C5 149.6(5), B1–C30 164.8(5), B1–C36 165.3(5), B1–C42 162.2(5), B1–C48 165.3(5); N1-Si1-N2 96.18(13), C2-N1-Si1 128.4(2), C4-N2-Si1 128.6(2), N1-C2-C3 119.8(3), C3-C2-C1 120.4(3), C4-C3-C2 126.6(3).

the germanium homologue.[13] Crystals of $[\mathbf{2}\{B(C_6F_5)_4\}^-]$ were slightly soluble in ethereal solvents, but readily dissolved in CH_2Cl_2 without decomposition. Its ^{29}Si NMR spectrum showed a singlet resonance signal at $\delta = 69.3$ ppm, indicating that the ^{29}Si nucleus in the cation **2** is less shielded than that in **1** by about 29 ppm.

It is also striking to compare the chemical shifts of the ^{29}Si nucleus in **1** and the cation **2** with that observed for the isovalent but λ^5-coordinate Si atom in the silyliumylidene cation $[(\eta^5\text{-}C_5Me_5)Si]^+$ (**A**). The latter shows a resonance signal at extremely high field ($\delta = -400.2$ ppm).[8] Apparently, the drastic shielding of the ^{29}Si nucleus in **A** is due to the higher coordination number and 3D-aromatic cluster stabilization. The similar ^1H NMR chemical shift of the γ-CH proton of the SiC_3N_2 ring in **2** ($\delta = 6.92$ ppm) and **1** ($\delta = 6.79$ ppm) suggests the presence of aromatic 6π-electron stabilization. This is supported by density functional theory (DFT) calculations of the model cation **2′**, in which the 2,6-diisopropylphenyl groups at nitrogen are replaced by 2,6-dimethylphenyl substituents (see Supporting Information).[14] The geometric parameters of the model cation **2′** were in good agreement with those for **2**. The calculation of the ^{29}Si NMR chemical shift of **2′** revealed a value of $\delta = 93.9$ ppm (IGLO B3LYP, TMS referenced), about 24.6 ppm lower than the experimental value of **2** as a result of typical overestimation of paramagnetic contributions to the chemical shielding in divalent silicon compounds.[15] The calculation of magnetic properties of **2′** clearly suggests the presence of some aromatic stabilization (i.e., a significant contribution of the resonance form **2B** with cyclic delocalization; Scheme 2), which is further supported by the negative nucleus-independent chemical shift (NICS) values calculated for **2′** (NICS(0) = −1.4 ppm, NICS(1) = −3.9 ppm).

The cyclic delocalization of the π electrons in **2** also becomes evident from the shortening of the endocyclic N–C bonds (by 5 pm), concomitant with an elongation of the Si–N bond length (by 3 pm) when going from **3** to **2**. While this can hardly be explained by the mesomeric form **2A** alone, it

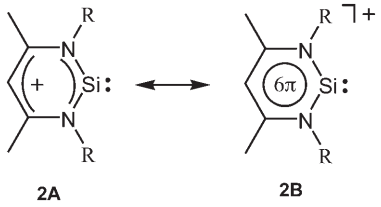

Scheme 2. Resonance structures **2A** and **2B**.

naturally follows from the changes in the π-bond orders when **2B** contributes. Additionally, the electronic situation of the cyclic cation **2** is similar to that for the known germanium homologue.[13a] In fact, this is clearly indicated by the similar negative NICS values (NICS(0) = −1.1 ppm, NICS(1) = −3.5 ppm; *zz* component of NICS(1) = −9.8 ppm) calculated for the germanium homologue of **2′** at the same theoretical level.[14] The highly electrophilic divalent silicon atom in the silyliumylidene cation in $[\mathbf{2}\{B(C_6F_5)_4\}^-]$ is expected to pave the way to new classes of divalent silicon compounds with terminal main-group and transition-metal substituents at the Si^{II} atom.

Received: June 9, 2006
Revised: August 7, 2006
Published online: September 20, 2006

Keywords: aromaticity · cations · N ligands · silicon · silylenes

[1] a) J. M. S. Henis, G. W. Stewart, M. K. Tripodi, P. P. Gaspar, *J. Chem. Phys.* **1972**, *57*, 389; b) T.-Y. Yu, T. M. H. Cheng, V. Kempter, F. W. Lampe, *J. Phys. Chem.* **1972**, *76*, 3321; see also Ref. [3] and references therein.
[2] E. Douglas, B. L. Lutz, *Can. J. Phys.* **1970**, *48*, 247.
[3] Reviews: a) "Gas-Phase Ion Chemistry of Silicon-Containing Molecules", N. Goldberg, H. Schwarz in *The Chemistry of Organic Silicon Compounds*, *Vol. 2*, Part 2 (Eds.: Z. Rappoport, Y. Apeloig), Wiley, Chichester, **1989**, pp. 1105–1142; b) "Ion-Molecule Reactions of Silicon Cations": S. Fornarini in *The Chemistry of Organic Silicon Compounds*, *Vol. 3* (Eds.: Z. Rappoport, Y. Apeloig), Wiley, Chichester, **2001**, pp. 1027–1057.
[4] a) N. Grevesse, A. Sauval, *Astron. Astrophys.* **1970**, *9*, 232; b) P. D. Singh, F. G. Vanlandingham, *Astron. Astrophys.* **1978**, *66*, 87; c) P. J. Bruna, S. D. Peyerimhoff, *Bull. Soc. Chim. Belg.* **1983**, *92*, 525.
[5] Reviews on recent results using noncoordinating counterions: a) C. Reed, *Acc. Chem. Res.* **1998**, *31* 133; b) S. H. Strauss, *Chem. Rev.* **1993**, *93*, 927; c) I. Krossing, I. Raabe, *Angew. Chem.* **2004**, *116*, 2116; *Angew. Chem. Int. Ed.* **2004**, *43*, 2066.
[6] "Free" silylium ions: a) K.-C. Kim, C. A. Reed, D. W. Elliott, L. J. Mueller, *Science* **2000**, *289*, 101; b) J. B. Lambert, L. Kania, S. Zhang, *Chem. Rev.* **1995**, 95, 1191; c) C. A. Reed, *Acc. Chem. Res.* **1998**, *31* 325.
[7] M. Ichinohe, M. Igarashi, K. Sanuki, A. Sekiguchi, *J. Am. Chem. Soc.* **2005**, *127*, 9978.
[8] P. Jutzi, A. Mix, B. Rummel, W. W. Schoeller, B. Neumann, H.-G. Stammler, *Science* **2004**, *305*, 849.
[9] a) E. D. Jemmis, P. v. R. Schleyer, *J. Am. Chem. Soc.* **1982**, *104*, 4781–4788; b) review: "Theory and Concepts in Main-Group Cluster Chemistry", R. B. King, P. v. R. Schleyer, in *Molecular*

 © 2006 Wiley-VCH Verlag GmbH & Co. KGaA, Weinheim

Clusters of the Main Group Elements (Eds.: M. Driess, H. Nöth), Wiley-VCH, Weinheim, **2004**, pp. 1–33.

[10] M. Driess, S. Yao, M. Brym, C. van Wüllen, D. Lentz, *J. Am. Chem. Soc.* **2006**, *128*, 9628–9629.

[11] Compound **1**: Triclinic, colorless rod, space group $P\bar{1}$, $a=12.099(3)$, $b=13.740(5)$, $c=15.0013(13)$ Å, $\alpha=109.756(18)$, $\beta=90.924(11)$, $\gamma=108.95(3)°$, $V=2197.4(10)$ Å^3, $Z=2$, $\rho_{calcd}=1.446$ Mg m^{-3}, $\mu(Mo_{K\alpha})=0.154$ mm^{-1}, 24382 collected reflections, 7710 crystallographically independent reflections [$R_{int}=0.0232$], 6120 reflections with $I>2\sigma(I)$, $\theta_{max}=25.00°$, $R(F_o)=0.0325$ ($I>2\sigma(I)$), $wR(F_o^2)=0.0496$ (all data), 604 refined parameters. Compound [**2**{B(C$_6$F$_5$)$_4$}$^-$]: Monoclinic, colorless rod, space group $P2(1)/n$, $a=12.5960(6)$, $b=24.2554(9)$, $c=17.8847(7)$ Å, $\beta=110.492(4)°$, $V=5118.4(4)$ Å^3, $Z=4$, $\rho_{calcd}=1.460$ Mg m^{-3}, $\mu(Mo_{K\alpha})=0.158$ mm^{-1}, 31527 collected reflections, 8885 crystallographically independent reflections [$R_{int}=0.0747$], 6318 reflections with $I>2\sigma(I)$, $\theta_{max}=25.00°$, $R(F_o)=0.0706$ ($I>2\sigma(I)$), $wR(F_o^2)=0.1166$ (all data), 704 refined parameters. Crystals were mounted on a glass capillary and measured in a cold N_2 flow. The data of **1** and [**2**{B(C$_6$F$_5$)$_4$}$^-$] were collected on a Oxford Diffraction Xcalibur S Sapphire at 88 K (**1**) and 150 K ([**2**{B(C$_6$F$_5$)$_4$}$^-$]), respectively ($Mo_{K\alpha}$ radiation, $\lambda=0.71073$ Å). The structures were solved by direct methods and refined on F^2 with the SHELX-97[16] software package. The positions of the H atoms were calculated and considered isotropically according to a riding model. Absorption corrections were performed by using the SCALE3 ABSPACK program.[17] CCDC 607460 (**1**) and 607461 ([**2**{B(C$_6$F$_5$)$_4$}$^-$]) contain the supplementary crystallographic data for this paper. These data can be obtained free of charge from The Cambridge Crystallographic Data Centre via www.ccdc.cam.ac.uk/data_request/cif.

[12] P. Jutzi, C. Müller, A. Stammler, H.-G. Stammler, *Organometallics* **2000**, *19*, 1442–1444.

[13] a) M. Stender, A. D. Phillips, P. P. Power, *Inorg. Chem.* **2001**, *40*, 5314; b) M. Driess, S. Yao, M. Brym, C. van Wüllen, *Angew. Chem.* **2006**, *118*, 4455–4458; *Angew. Chem. Int. Ed.* **2006**, *45*, 4349–4352.

[14] Geometry optimizations were performed with the TURBOMOLE program (see Supporting Information) at density functional level using the B3LYP hybrid exchange-correlation functional and polarized valence triple zeta (TZVP)basis sets. Nucleus-independent chemical shifts (NICS) were calculated by the (B3LYP) IGLO method with its integral direct implementation. NICS values were obtained at the ring centers (NICS(0) value) as well as at 100 pm above (NICS(1) value). See Supporting Informations for details..

[15] H.-G. Lee, R. West, T. Müller, *J. Am. Chem. Soc.* **2003**, *125*, 8114.

[16] G. M. Sheldrick, *SHELX-97 Program for Crystal Structure Determination*, Universität Göttingen (Germany) **1997**.

[17] CrysAlis RED, Oxford Diffraction, Ltd., Version 1.171.29.10.

 © 2006 Wiley-VCH Verlag GmbH & Co. KGaA, Weinheim

Homocyclic Phosphorus Compounds

DOI: 10.1002/anie.200602353

A Melt Approach to the Synthesis of *catena*-Phosphorus Dications To Access Derivatives of $[P_6Ph_4R_4]^{2+}$**

Jan J. Weigand, Neil Burford,* Michael D. Lumsden, and Andreas Decken*

Dedicated to Hartmut S. Huhn

catena-Phosphorus chemistry is underdeveloped in the context of the diagonal relationship between carbon and phosphorus.[1] Oligophosphines[2,3] such as hexaphenylcyclohexaphosphine $(PPh)_6$[4] provide analogies with cycloalkanes as the CR_2 methylene unit is isolobal with the phosphine (PR) unit. The familiar cationic phosphonium center is also isolobal to these units; however, while extensive series of *catena*-phosphide anions are well-known,[5,6] *catena*-phosphorus cations represent a newly developing family of compounds achieved through homoatomic coordination chemistry.[7–9] Examples of phosphinophosphonium dications are rare and are represented by the unique derivatives of **1**,[10–15] **2**,[16] **3**,[17] and **4**[18] (Scheme 1). Larger polyphosphorus frameworks such as **5** and **6**, which have not been reported so far, are expected to be more viable for the accommodation of multiple charges. We have now prepared the first cyclotetraphosphinodiphosphonium salts, **6a**-$[GaCl_4]_2$ and **6b**-$[GaCl_4]_2$, from molten mixtures of a cyclopolyphosphine, a chlorophosphine, and gallium chloride. This is a versatile potentially synthetic approach to a new direction in phosphorus chemistry using a melt medium.

Stirred mixtures of $^4/_5\,(PhP)_5$, $2\,Ph_2PCl$, and $2\,GaCl_3$ were gradually heated ($5\,°C\,min^{-1}$) over a period of 30 minutes and

[*] Dr. J. J. Weigand, Prof. N. Burford
Dalhousie University
Department of Chemistry
Halifax, NS B3H 4J3 (Canada)
Fax: (+1) 902-494-1310
E-mail: jan.weigand@dal.ca
neil.burford@dal.ca

Dr. M. D. Lumsden
Atlantic Region Magnetic Resonance Centre
Dalhousie University
Halifax, NS B3H 4J3 (Canada)

Dr. A. Decken
Department of Chemistry
University of New Brunswick
Fredericton, NB E3A 6E2 (Canada)

[**] We thank the Natural Sciences and Engineering Research Council of Canada, the Killam Foundation, the Canada Research Chairs Program, and the Alexander von Humboldt-Stiftung (Humboldt Fellowship for J.J.W.) for funding, and Dr. Ulrike Werner-Zwanziger for the ^{31}P MAS NMR data. We are grateful to Jared MacPherson for the cover illustration.

Supporting information for this article is available on the WWW under http://www.angewandte.org or from the author.

© 2006 Wiley-VCH Verlag GmbH & Co. KGaA, Weinheim

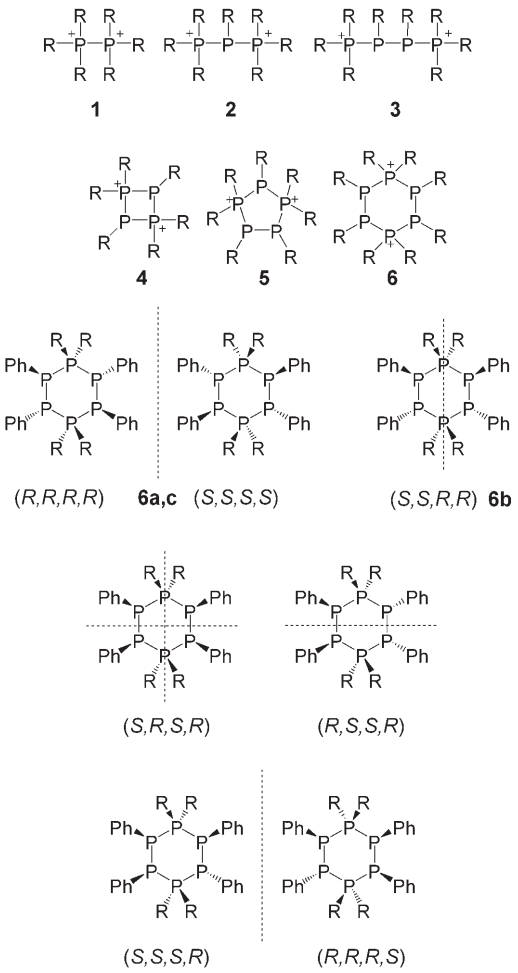

Scheme 1. Cyclic *catena*-phosphinodiphosphonium dications. Seven possible stereoisomers of **6** (**6a**: R = Ph; **6b**,**c**: R = Me) are shown. Dotted lines define mirror relationships or planes of symmetry.

gave a yellow melt between 70 and 125 °C, which became turbid and gradually solidified with increasing temperature up to about 165 °C.[19] The recrystallized solid, which has a decomposition point above 190 °C, was identified by X-ray crystallography as **6a**-$[GaCl_4]_2$,[19] which contains a P_6 homocycle composed of two phosphonium centers (1,4-positions) and four phosphine centers. The cation **6a** is conveniently named a 2,3,5,6-tetraphosphino-1,4-diphosphonium compound and represents the first example of a *catena*-hexaphosphorus dication. The racemic crystalline material contains only the *R*,*R*,*R*,*R* and *S*,*S*,*S*,*S* isomers of cation **6a**, which represent two of seven possible configurational isomers (two enantiomeric pairs and three *meso* forms) imposed by four phosphine stereocenters, as illustrated in Scheme 1. Consistently, the ^{31}P NMR spectrum of **6a**-$[GaCl_4]_2$ in CH_2Cl_2 at room temperature shows a rare and complex AA′A″A‴BB′ spin system.[20] At a field strength of 5.87 T, ^{31}P NMR spectra of **6a**-$[GaCl_4]_2$ show no evidence of dynamic behavior over the temperature range 190–300 K, suggesting preservation of the *R*,*R*,*R*,*R* and *S*,*S*,*S*,*S* configurations in solution within this temperature range based on molecular symmetry.[20]

In the solid state, (±)-**6a**-$[GaCl_4]_2$ (Figure 1)[19] adopts a twist-boat (TB) conformation (the P1–P4 vector represents the axis with P2, P3, P5, and P6 as the twisted plane) with the

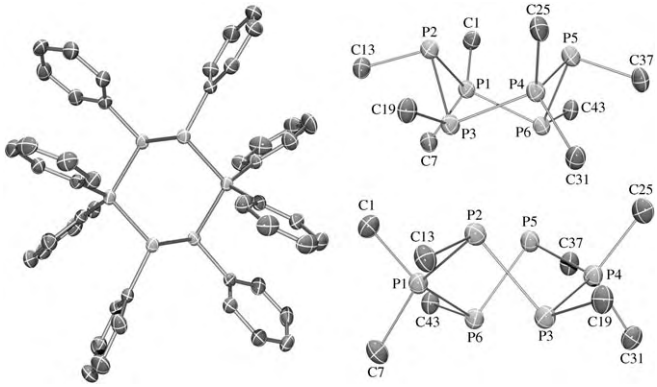

Figure 1. Left side: ORTEP plot of the solid-state structure of the cation in (±)-**6a**-$[GaCl_4]_2$ (H atoms are omitted). Right side: two different side views of the core structure showing the cyclohexane-like geometry in a twist-boat conformation (only the *ipso*-C atoms of the phenyl groups are shown). Thermal ellipsoids are set at 50% probability at 173(2) K. Selected bond lengths [Å] and angles [°]: P1-P2 2.242(2), P2-P3 2.231(2), P3-P4 2.217(2), P4-P5 2.233(2), P5-P6 2.227(1), P1-C1 1.792(3), P1-C7 1.801(3), P2-C13 1.835(3), P3-C19 1.826(3), P4-C25 1.801(3), P4-C31 1.788(3), P5-C37 1.835(3), P6-C43 1.827(3); P1-P2-P3 92.09(5), P2-P3-P4 95.64(6), P3-P4-P5 109.27(4), P4-P5-P6 93.16(6), P5-P6-P1 95.10(6), P6-P1-P2 109.93(4), C1-P1-C7 110.9(1), C1-P1-P2 106.6(1), C1-P1-P6 113.0(1), C7-P1-P2 110.3(1), C7-P1-P6 106.2(1), C25-P4-C31 110.3(1), C25-P4-P3 114.7(1), C25-P4-P5 106.2(1), C31-P4-P3 105.1(1), C31-P4-P5 111.4(1), P1-P6-C43 98.7(1), P4-P3-C19 101.39(9), P4-P5-C37 94.8(1), P1-P6-C43 987(1).

phenyl groups attached at the phosphino centers in an all-*trans* configuration, as defined by the Cremer and Pople puckering parameters ($Q = 1.7194(8)$ Å, $\theta = 89.84(3)°$ and $\varphi = 88.76(3)°$; ideal values: $\theta = 90°$ and $\varphi = 90°$).[21] The P–P and P–C bond lengths (P–P 2.231(2)–2.242(2) Å, P–C 1.792(3)–1.835(3) Å) are similar to those of phosphinophosphonium monocations[8] and are comparable with those of polyphosphines such as, for example, trigonal hexaphosphine $(PhP)_6$ (P–P 2.237(5) Å, P–C 1.843(7) Å).[4] The TB conformation of (±)-**6a**-$[GaCl_4]_2$ contrasts the chair conformation of $(PhP)_6$,[4] likely owing to the steric demand of the eight phenyl groups. Nevertheless, in comparison with cyclohexane analogues, the twisted-boat conformation of **6a** appears to be relatively strain-free because of the greater flexibility of the phosphorus ring and the larger bond lengths.

Interestingly, when the temperature of the reaction mixture did not exceed 100 °C and the melt was quenched to room temperature within seconds, ^{31}P NMR spectra of the resulting yellow oil in CH_2Cl_2 showed the presence of the cyclotetraphosphinophosphonium salt **7a**-$[GaCl_4]$,[8] the phosphinophosphonium salt **8a**-$[Ga_2Cl_7]$[7] (Scheme 2), and small amounts of **6a**-$[GaCl_4]_2$. Solutions of **6a**-$[GaCl_4]_2$ in CH_2Cl_2 at room temperature decompose ($t_{1/2} \approx 24$ h) to **7a**-$[GaCl_4]$, **8a**-$[Ga_2Cl_7]$, and $Ph_2(Cl)P{\cdot}GaCl_3$ (s, $\delta = 41$ ppm).[22]

A molten mixture of $^4/_5(PhP)_5$, $2\,Me_2PCl$, and $2\,GaCl_3$ at about 165 °C was cooled and extracted with CH_2Cl_2, thereby

 © 2006 Wiley-VCH Verlag GmbH & Co. KGaA, Weinheim

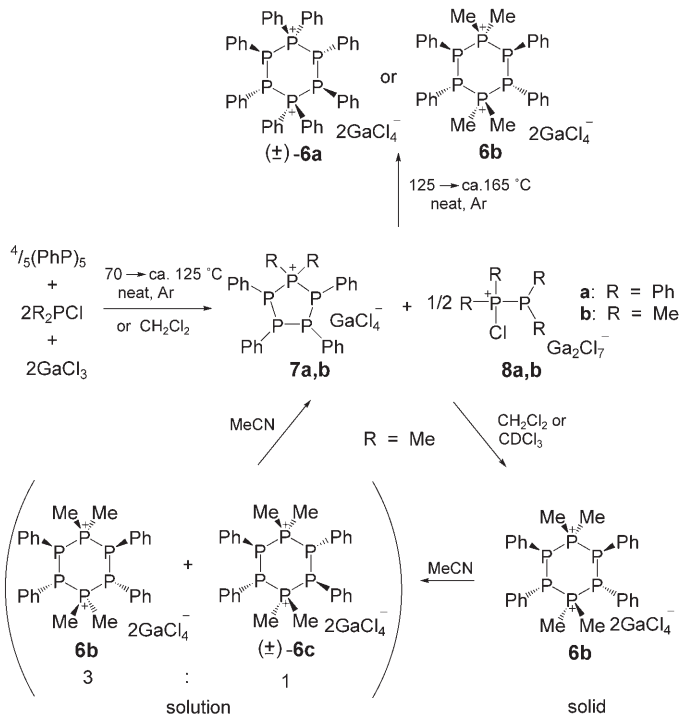

Scheme 2. Formation of (±)-**6a**-$[GaCl_4]_2$ and **6b**-$[GaCl_4]_2$, isomerization of **6b**-$[GaCl_4]_2$, and decomposition of **6b**-$[GaCl_4]_2$ and (±)-**6c**-$[GaCl_4]_2$ in MeCN solution. Only one enantiomer is depicted for (±)-**6a**-$[GaCl_4]_2$ and (±)-**6c**-$[GaCl_4]_2$.

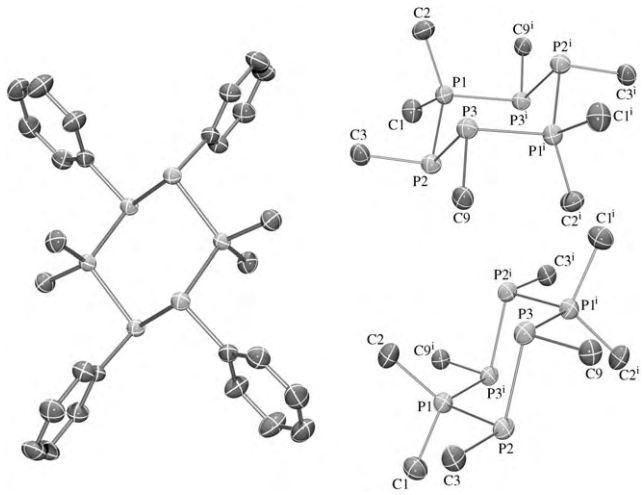

Figure 2. Left side: ORTEP plot of the solid-state structure of **6b**-$[GaCl_4]_2{\cdot}2\,CDCl_3$ (H atoms are omitted). Right side: two different side views of the core structure showing the cyclohexane-like chair conformation (only the *ipso*-C atoms of the phenyl groups are shown). Thermal ellipsoids are set at 50% probability at 173(2) K. Selected bond lengths [Å] and angles [°]: P1-P2 2.2014(9), P2-P3 2.2308(9), P3-P1^{i} 2.2081(9), P1-C1 1.802(3), P1-C2 1.795(2), P2-C3 1.839(2), P3-C9 1.837(2); P1-P2-P3 98.22(3), P2-P3-P1^{i} 97.31(3), P2-P1-P3^{i} 105.10(3), C1-P1-C2 108.9(1), C1-P1-P2 104.9(1), C1-P1-P3^{i} 104.4(1), C2-P1-P2 115.8(1), C2-P1-P3^{i} 116.7(1), P1-P2-C3 99.30(8), P2-P3-C9 97.65(8), P1^{i}-P3-C9 99.59(8).

leaving a colorless solid in low yield that was spectroscopically characterized as **6b**-$[GaCl_4]_2$. The same reaction mixture in CH_2Cl_2 solution slowly precipitated **6b**-$[GaCl_4]_2$ over about 48 hours (Scheme 2), and crystals grown from the mother liquor by slow removal of solvent at room temperature were identified crystallographically as **6b**-$[GaCl_4]_2{\cdot}3\,CH_2Cl_2$ with disorder in the solvent molecules. Recrystallization of **6b**-$[GaCl_4]_2$ from $CDCl_3$ yielded high-quality crystals of **6b**-$[GaCl_4]_2{\cdot}2\,CDCl_3$, and the solid-state structure of the dication **6b** is shown in Figure 2.[19] The observed P–P (2.231(2)–2.242(2) Å) and P–C bond lengths (1.792(3)–1.835(3) Å) are comparable to those of (±)-**6a**-$[GaCl_4]_2$. The side views of the structure show that the ring adopts a chair conformation similar to that of cyclohexane. While the internal C-C-C angle of cyclohexane is 111.4°,[23] the internal P-P-P angles at the phosphonium centers of **6b** (105.10(3)°) are smaller and comparable to those in S_6 (102.61°).[24] The internal P-P-P angles at the phosphine centers (98.22(3)°) are predictably smaller and are comparable to those in $(PhP)_6$. Owing to the longer bonds and flexibility of the P_6 ring, the chair form is indicated by the dihedral angle between the planes of the chair (101.55(5)° vs. 133° in cyclohexane).[25] This form is also reflected by the torsion angles $\tau_1 = -73.5(4)°$ and $\tau_2 = 79.4(1)°$,[26] which are larger than the ideal value in cyclohexane (55.9(2)°)[25] and are consistent with the observed puckering parameters ($Q = 1.2547(8)$ Å, $\theta = 0.37(1)°$ and $\varphi = 0°$),[21] which are very close to those of the chair conformation of cyclohexane (nearest ideal values: $\theta = 0°$ and $\varphi = 0°$).

The ^{31}P MAS NMR spectrum of **6b**-$[GaCl_4]_2$ as a microcrystalline precipitate confirmed the presence of only one symmetric isomer in the solid state with two broad multiplets at $\delta = 11.7$ and -50.1 ppm in the approximate ratio of 1:2.[20] Two complicated AA′A″A‴BB′ spin systems were observed in MeCN solution. Iterative analysis of the complex spectrum, performed at two external field strengths, revealed chemical shifts for one isomer at $\delta = 11.2$ and -53.5 ppm (Table 1), which are similar to those observed in the solid state for **6b**-$[GaCl_4]_2$, thus indicating retention of the solid-state configuration in solution. The other AA′A″A‴BB′ pattern with chemical shifts observed at $\delta = 12.4$ and -63.6 ppm is

Table 1: $^{31}P\{^1H\}$ NMR parameters[a] obtained from a simulated match of experimental spectra of (±)-**6a**-$[GaCl_4]_2$, **6b**-$[GaCl_4]_2$, and (±)-**6c**-$[GaCl_4]_2$ in $[D_3]$MeCN at two different external magnetic field strengths.

	4[b,c,d]	(±)-**6a**-$[GaCl_4]_2$	(±)-**6c**-$[GaCl_4]_2$	**6b**-$[GaCl_4]_2$
$\delta_A = \delta_{A'} = \delta_{A''} = \delta_{A'''}$	+2.2	−60.8	−63.6	−53.5
$\delta_B = \delta_{B'}$	+41.2	+29.8	+12.4	+11.2
$^1J_{AB} = {}^1J_{A'''B} = {}^1J_{A'B'} = {}^1J_{A''B'}$	−287.0	−310.5	−306.2	−295.2
$^1J_{AA'} = {}^1J_{A''A'''}$	–	−80.9	−85.8	−4.0
$^2J_{A'B} = {}^2J_{A''A} = {}^2J_{AB'} = {}^2J_{A''' B'}$	–	+89.4	+79.1	+54.9
$^2J_{AA'''} = {}^2J_{A'A''}$	–	−12.2	−11.1	−71.4
$^3J_{AA''} = {}^3J_{A'A'''}$	–	+98.5	+100.2	+92.5
$^3J_{BB'}$	–	+5.1	+10.2	+7.4

[a] The relative signs of the coupling constants result from the iterative fitting of the spectrum assuming negative values for the $^1J_{PP}$ constants.[27] [b] A_2B_2 spin system. [c] See reference [18]. [d] R = 2,6-dimethoxyphenyl.

 © 2006 Wiley-VCH Verlag GmbH & Co. KGaA, Weinheim

assigned to (±)-**6c**-$[GaCl_4]_2$ (see Table 1). Consistently, the $^1H\{^{31}P\}$ NMR spectrum shows three singlets corresponding to three different methyl groups for the two different stereoisomers **6b**-$[GaCl_4]_2$ and (±)-**6c**-$[GaCl_4]_2$. These compounds decompose in solution at room temperature ($t_{1/2} \approx 30$ min) to give **7b**-$[GaCl_4]$, **8b**-$[Ga_2Cl_7]$,[22] and traces of $Me_2(Cl)P{\cdot}GaCl_3$ (s, $\delta = 57$ ppm),[22] as shown in Figure 3.

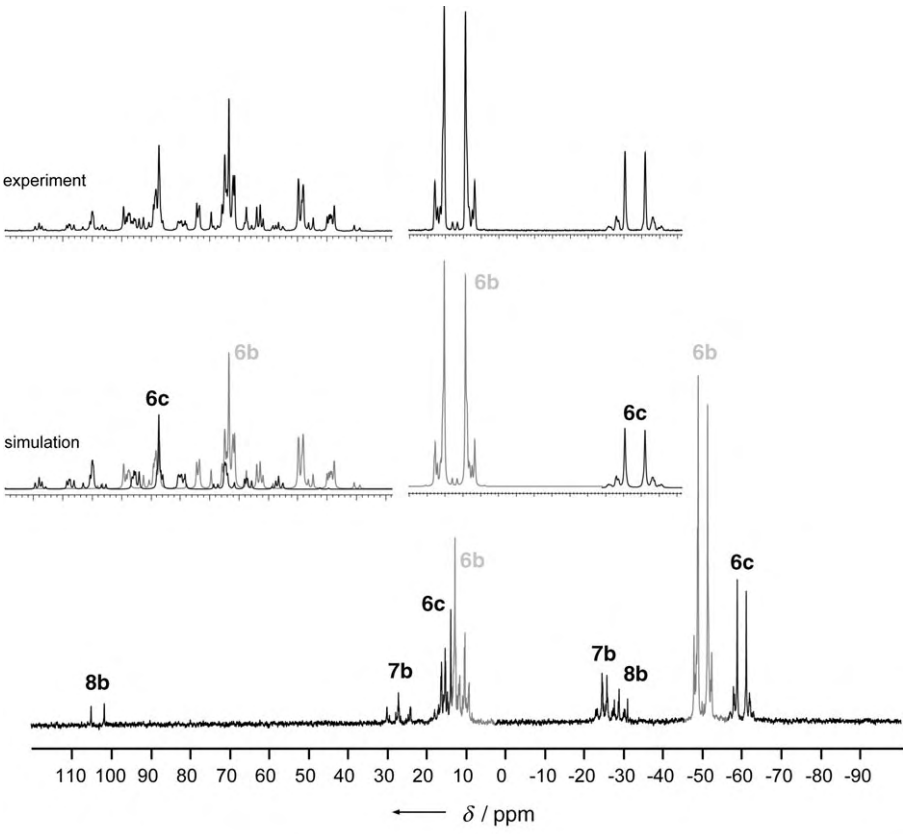

Figure 3. $^{31}P\{^1H\}$ NMR spectrum of **6b** at room temperature, 10 min after being dissolved in MeCN. Assignments: **6b** and (±)-**6c**, **7b** (complex multiplet, $\delta_A = 26$ ppm, $\delta_B = -29$ ppm);[8] **8b** (dd, $\delta(P_A) = +103$ ppm, $\delta(P_B) = -29$ ppm, $J_{PP} = 340$ Hz);[22] experimental (upper) and simulated (lower) for **6b** and (±)-**6c**.

Two peaks of equal integration at $\delta = 1.85$ and 2.25 ppm are tentatively assigned to the axial and equatorial methyl groups, indicating that **6b**-$[GaCl_4]_2$ (*meso*, *S*,*S*,*R*,*R*) exists as a chair conformer, and the sharp singlet at $\delta = 1.88$ ppm is assigned to (±)-**6c**-$[GaCl_4]_2$ (enantiomeric pair *R*,*R*,*R*,*R* and *S*,*S*,*S*,*S*) consistent with a twist-boat conformation.[20]

The $^{31}P\{^1H\}$ NMR data for (±)-**6a**-$[GaCl_4]_2$, **6b**-$[GaCl_4]_2$, and (±)-**6c**-$[GaCl_4]_2$ have been simulated and are summarized in Table 1. Chemical shifts at low field ($\delta = 30$ to 10 ppm) are assigned to the phosphonium centers, and the trivalent phosphorus centers have shifts at higher field ($\delta = -50$ to -60 ppm), in accordance with those for phosphinophosphonium monocations.[7,8]

In conclusion, molten mixtures of organophosphines and diorganochlorophosphines together with gallium trichloride provide a new synthetic approach to *catena*-phosphorus cations and represent a versatile method for the preparation of dications that do not form in solution (**6a**). The new hexaphosphorus dications highlight the potential to develop a diverse *catena*-phosphorus chemistry that parallels *catena*-carbon chemistry (organic chemistry).

Received: June 12, 2006
Published online: August 25, 2006

Keywords: catenation · cations · melt reactions · phosphorus · structure elucidation

[1] K. B. Dillon, F. Mathey, J. F. Nixon, *Phosphorus: The Carbon Copy*, Wiley, New York, **1998**.
[2] M. Baudler, K. Glinka, *Chem. Rev.* **1994**, *94*, 1273.
[3] A. Schisler, P. Lonnecke, T. Gelbrich, E. Hey-Hawkins, *Dalton Trans.* **2004**, 2895.
[4] a) J. J. Daly, *J. Chem. Soc.* **1965**, 4789; b) R. Schmutzler, L. Heuer, D. Schomburg, *Phosphorus Sulfur Silicon Relat. Elem.* **1993**, *83*, 149.
[5] M. Baudler, K. Glinka, *Chem. Rev.* **1993**, *93*, 1623–1667.
[6] J. Geier, J. Harmer, H. Grutzmacher, *Angew. Chem.* **2004**, *116*, 4093; *Angew. Chem. Int. Ed.* **2004**, *43*, 4093.
[7] N. Burford, P. J. Ragogna, R. McDonald, M. Ferguson, *J. Am. Chem. Soc.* **2003**, *125*, 14404.
[8] N. Burford, C. A. Dyker, A. Decken, *Angew. Chem.* **2005**, *117*, 2416; *Angew. Chem. Int. Ed.* **2005**, *44*, 2364.
[9] N. Burford, C. A. Dyker, M. D. Lumsden, A. Decken, *Angew. Chem.* **2005**, *117*, 6355; *Angew. Chem. Int. Ed.* **2005**, *44*, 6196.
[10] R. W. Alder, C. Ganter, C. J. Harris, A. G. Orpen, *J. Chem. Soc. Chem. Commun.* **1992**, 1170.
[11] R. W. Alder, C. Ganter, C. J. Harris, A. G. Orpen, *J. Chem. Soc. Chem. Commun.* **1992**, 1172.
[12] R. W. Alder, D. D. Ellis, R. Gleiter, C. J. Harris, H. Lange, A. G. Orpan, D. Read, P. N. Taylor, *J. Chem. Soc. Perkin Trans. 1* **1998**, 1657.
[13] D. Schomburg, G. Bettermann, L. Ernst, R. Schmutzler, *Angew. Chem.* **1985**, *97*, 971; *Angew .Chem. Int. Ed.* **1985**, *24*, 975.
[14] A. S. Romakhin et al., *Izv. Akad. Nauk. SSSR Ser. Khim.* **1990**, *3*, 664.
[15] E. V. Nikitin, A. S. Romakhin, V. A. Zagumennov, Yu. A. Babkin, *Electrochim. Acta* **1997**, *42*, 2217.
[16] A. Schmidpeter, S. Lochschmidt, K. Karaghiosoff, W. S. Sheldrick, *J. Chem. Soc. Chem. Commun.* **1985**, 1447.
[17] a) C. A. Dyker, N. Burford, M. D. Lumsden, A. Decken, *J. Amer. Chem. Soc.* **2006**, *128*, 9633; b) P. Kilian, A. M. Z. Slawin, J. D. Woollins, *Dalton Trans.* **2006**, 2175; c) S. Lochschmidt, G. Muller, B. Huber, A. Schmidpeter, *Z. Naturforsch. B* **1986**, *41*, 444.
[18] L. Heuer, L. Ernst, R. Schmutzler, D. Schomburg, *Angew. Chem.* **1989**, *101*, 1549; *Angew. Chem. Int. Ed. Engl.* **1989**, *28*, 1507.
[19] For experimental details, see the Supporting Information; Crystal data: X-ray quality crystals of (±)-**6a**-$[GaCl_4]_2$ were obtained by diffusion of Et_2O vapors into a colorless solution of the dication in fluorobenzene at room temperature over about 6 h. In the case of **6b**-$[GaCl_4]_2$ suitable crystals for the structure

 © 2006 Wiley-VCH Verlag GmbH & Co. KGaA, Weinheim

determination were obtained from the mother liquor after 5 days at room temperature in solvated form as **6b**-$[GaCl_4]_2 \cdot 3\,CH_2Cl_2$ or **6b**-$[GaCl_4]_2 \cdot 2\,CDCl_3$, depending on the solvent used during the preparation. Single crystals of (±)-**6a**-$[GaCl_4]_2$ and **6b**-$[GaCl_4]_2 \cdot 2\,CDCl_3$ were coated with Paratone N oil, mounted using a 20-micron cryoloop, and frozen in the cold nitrogen stream of the goniometer. A hemisphere of data was collected on a Bruker AXS P4/SMART 1000 diffractometer using ω and θ scans with a scan width of 0.3° and exposure times of 30 s for (±)-**6a**-$[GaCl_4]_2$ and 10 s for **6b**-$[GaCl_4]_2 \cdot 2\,CDCl_3$. The detector distance was 5 cm. The data were reduced using SAINT (SAINT 6.02, 1997–1999, Bruker AXS, Inc., Madison, Wisconsin, USA) and corrected for absorption with SADABS (SADABS, George Sheldrick, 1999, Bruker AXS, Inc., Madison, Wisconsin, USA). The structure was solved by direct methods and refined by full-matrix least squares on F^2 with SHELXTL (SHELXTL 6.14, 2000–2003, Bruker AXS, Inc., Madison, Wisconsin, USA). All non-hydrogen atoms were refined anisotropically. For (±)-**6a**-$[GaCl_4]_2$ hydrogen atoms were included in calculated positions and refined using a riding model. In the case of **6b**-$[GaCl_4]_2 \cdot 2\,CDCl_3$ hydrogen atoms were found in Fourier difference maps and refined isotropically. (±)-**6a**-$[GaCl_4]_2$: $C_{48}H_{40}Cl_8Ga_2P_6$, colorless, irregular, crystal size $0.45 \times 0.35 \times 0.10\ mm^3$, monoclinic, space group Cc, $a = 11.396(9)$, $b = 25.90(2)$, $c = 18.73(2)$ Å, $\beta = 104.57(1)°$, $V = 5349(8)$ Å^3, $Z = 4$, $\mu = 1.620\ mm^{-1}$; $\lambda(Mo_{K\alpha}) = 0.71073$ Å, $2\theta_{max} = 55.0°$, 18192 collected reflections (8670 independent), $R_{int} = 0.0314$, 577 refined parameters, $R_1 = 0.0291$, $wR_2 = 0.0561$ for all data, max/min residual electron density = 0.404/−0.265 e Å^{-3}. **6b**-$[GaCl_4]_2 \cdot 2\,CDCl_3$: $C_{15}H_{16}Cl_7DGaP_3$, colorless, irregular, crystal size $0.40 \times 0.30 \times 0.10\ mm^3$, monoclinic, space group $P2_1/n$, $a = 12.914(3)$, $b = 11.688(2)$, $c = 17.770(4)$ Å, $\beta = 111.189(4)°$, $V = 2500.8(9)$ Å^3, $Z = 4$, $\mu = 2.041\ mm^{-1}$; $\lambda(Mo_{K\alpha}) = 0.71073$ Å, $2\theta_{max} = 55.00°$, 16914 collected reflections (5629 independent), $R_{int} = 0.0294$, 303 refined parameters, $R_1 = 0.0462$, $wR_2 = 0.0830$ for all data, max/min residual electron density = 0.838/−0.611 e Å^{-3}. CCDC-607203 ((±)-**6a**-$[GaCl_4]_2$), -607204 ((±)-**6b**-$[GaCl_4]_2 \cdot 2\,CDCl_3$), and -607205 (**6b**-$[GaCl_4]_2 \cdot 3\,CH_2Cl_2$) contain the supplementary crystallographic data for this paper (excluding structure factors, which are included in the Supporting Information). These data can be obtained free of charge from The Cambridge Crystallographic Data Centre via www.ccdc.cam.ac.uk/data_request/cif.

[20] For NMR spectroscopic details, see the Supporting Information.

[21] a) D. Cremer, J. A. Pople, *J. Am. Chem. Soc.* **1975**, *97*, 1354; b) A. L. Spek, *J. Appl. Cryst.* **2003**, *36*, 7.

[22] N. Burford T. S. Cameron, D. LeBlanc, P. Losier, S. Sereda, G. Wu, *Organometallics* **1997**, *16*, 4712.

[23] H. J. Giese, H. R. Buys, F. C. Mijlhoff, *J. Mol. Struct.* **1971**, *9*, 447.

[24] J. Steidel, J. Pickardt, R. Steudel, *Z. Naturforsch. B* **1978**, *33*, 1554.

[25] D. A. Dixon, *J. Phys. Chem.* **1990**, *94*, 5630.

[26] The torsion angles τ_1 and τ_2 are defined by the Newman projection of **6b**-$[GaCl_4]_2$ down the P1–P2 and P2–P3 bonds (symmetry code: (i) $-x$, $-y$, $-2+z$), respectively (see the Supporting Information).

[27] M. Baudler, K. Glinka, *Chem. Rev.* **1993**, *93*, 1623.

 © 2006 Wiley-VCH Verlag GmbH & Co. KGaA, Weinheim

DOI: 10.1002/anie.200602683

Diels–Alder Approach to Polysubstituted Biaryls: Rapid Entry to Tri- and Tetra-*ortho*-substituted Phosphorus-Containing Biaryls**

*Bradley O. Ashburn and Rich G. Carter**

Biaryl compounds have garnered considerable synthetic interest as a result of their presence as a structural motif in natural products[1,2] and their utility as ligands in metal catalysis.[3] While synthetic methods have been reported for the construction of selected biaryls, innovative strategies are needed to broaden their accessibility. Effective methods for the synthesis of biaryl linkages have progressed dramatically in recent years, primarily as a result of the use of palladium-mediated strategies, such as the Kharasch, Negishi, Stille, and Suzuki reactions.[1a] Of equal recent importance are the considerable contributions in the area of iron-catalyzed couplings[4] and the use of other metals, such as manganese,[5] nickel,[6] and copper.[7] Although these approaches have yielded valuable routes to the target functionality, limitations in their effectiveness have been observed. For example, although successful cases do exist,[8] tetra-*ortho*-substituted biaryls often prove difficult to construct.[2b,9] One rational for this lack of general availability is due to the added degree of difficulty in coupling two bis-*ortho*-substituted aryl precursors.[10]

A conceptually different approach to the synthesis of biaryls is the use of a Diels–Alder cycloaddition. Diels–Alder reactions are well documented for their generality and broad applicability.[11] Despite this factor, no general approach to biaryl compounds using a cycloaddition strategy has been reported.[12] One added advantage to this Diels–Alder approach is the ability to incorporate functional-group combinations (e.g., halogenated biaryls) that would not be readily accessible by traditional metal-mediated aryl–aryl couplings. In addition, the proper choice of substituents on the diene and dienophile should allow for the combination of the atom-economic benefits of cycloadditions with the power of subsequent metal-mediated couplings on the Diels–Alder adducts. Herein, we disclose our application of this concept to

[*] B. O. Ashburn, Prof. R. G. Carter
Department of Chemistry
Oregon State University (OSU)
Corvallis, OR 97331 (USA)
Fax: (+1) 541-737-9496
E-mail: rich.carter@oregonstate.edu

[**] Financial support was provided by the National Science Foundation (CHE-0549884). The authors would also like to thank Professor Max Deinzer (OSU) and Dr. Jeff Morré (OSU) for mass-spectral data, Dr. Lev Zakharov (OSU) for the X-ray crystallographic analysis of **14**, and Dr. Roger Hanselmann (Rib-X Pharmaceuticals) for his helpful discussions.

Supporting information for this article is available on the WWW under http://www.angewandte.org or from the author.

 © 2006 Wiley-VCH Verlag GmbH & Co. KGaA, Weinheim InterScience

the rapid synthesis of a series of phosphorus-containing tri- and tetra-*ortho*-substituted biaryls.

The dienophile subunit can be constructed quickly from the commercially available toluene derivative **1** (Scheme 1). Treatment of **1** with the *N*,*N*-dimethylformamide (DMF)

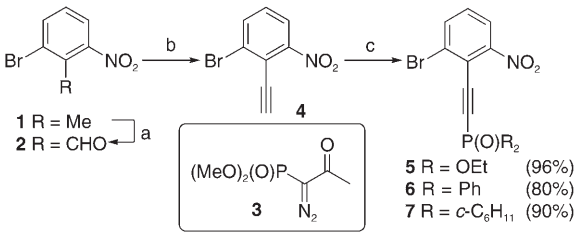

Scheme 1. Synthesis of phosphorus-containing dienophiles. Reagents and conditions: a) $(MeO)_2CH(NMe_2)$, DMF, 135 °C; then $NaIO_4$, DMF, H_2O, 0 °C (67%); b) **3**, K_2CO_3, MeOH (85%); c) LDA, $ClP(O)R_2$ (0.8 equiv).

dimethyl acetal at 135 °C followed by addition to a cooled (0 °C) solution of $NaIO_4$ in aqueous DMF yielded the aldehyde **2**.[13] This approach is based on a protocol developed by researchers at Pfizer;[14] however, use of their exact conditions led to formation of a significant amount of by-products. We found that cooling of the enamine solution to 0 °C and rapid addition to a vigorously stirred solution of $NaIO_4$ at 0 °C completely suppressed the formation of these impurities. Reaction of the aldehyde **2** with the Ohira–Bestmann reagent[15] **3** provided the desired alkyne **4**. Subsequent lithiation with lithium diisopropylamide (LDA; 1 equiv) followed by the addition of the requisite electrophiles (0.8 equiv) generated the dienophiles **5**–**7** in high yields (> 80%).

Diels–Alder cycloaddition of the dienophiles **5**–**7** with the known Brassard diene **8**[16] followed by aromatization in situ using Et_3N[17] yielded the target tetra-*ortho*-substituted biaryls (Scheme 2). We initially employed tetrabutylammonium

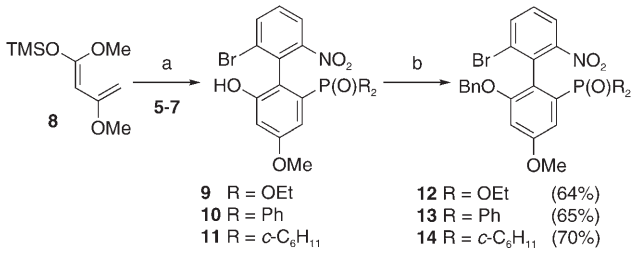

Scheme 2. Synthesis of biaryls by Diels–Alder cycloaddition. Reagents and conditions: a) PhMe, 80 °C, 16 h; then Et_3N, 0 °C; b) BnBr, NaH, DMF, THF, 0 °C→RT; yields reported over two steps (Bn = benzyl).

fluoride (TBAF) to induce silyl deprotection and aromatization; however, the yields were inconsistent and lower than with the work-up with Et_3N. This approach provides access to aryl- and alkyl-substituted phosphine oxides and phosphonates. As a result of the highly crystalline nature of the tetra-*ortho*-substituted phenolic biaryls, protection of the phenol as its benzyl ether was employed to improve solubility for subsequent transformations. X-ray crystallographic analysis of biaryl **14** shows the perpendicular orientation of the biaryl linkage (Figure 1).[18]

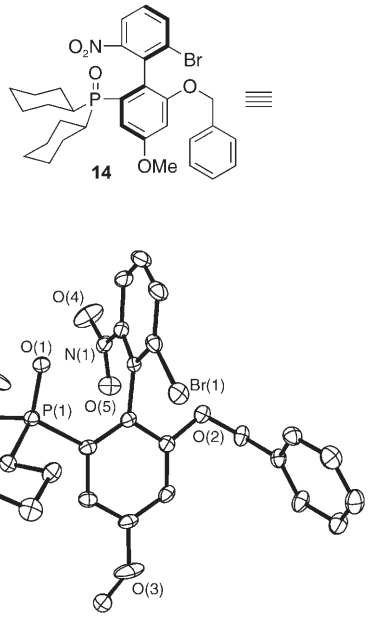

Figure 1. X-ray crystal structure of biaryl **14** as an ORTEP representation. Ellipsoids are shown at the 30% probability level.

Diels–Alder cycloadditions with acetylenic phosphonates are not limited to the Brassard diene (Scheme 3). Treatment of dienophiles **5**–**7** with the commercially available *tert*-butyldimethylsilyl (TBS) Danishefsky diene **15** followed by desilylation and aromatization in situ yielded the trisubstituted biaryls **16**–**18**. As demonstrated previously, benzylation of the resultant phenol was performed to improve solubility for subsequent transformations, and the yields were reported over the two steps (61–69%). We also found that oxygenated cyclohexadienes are active dienes for this process. The commercially available 1-methoxy derivative **22** gave the corresponding tetrasubstituted biaryls **23**–**25** in good yield (66–71%). Finally, use of the known 1,3-dialkoxy substrate **26**[19] efficiently provided the corresponding biaryls **30**–**32** in 67–88% yield after benzylation.

Metal-mediated couplings of the halide-containing biaryls could be accomplished in good yield (Scheme 4). As the pentasubstituted biaryls **12**–**14** possessed the highest degree of orthogonal functionalization, we decided to explore the coupling process with this series. After screening several of the commercially available catalyst systems developed for sterically challenging palladium couplings (including the Buchwald ligands,[20] $(P(c\text{-}C_6H_{11})_3/[Pd_2(dba)_3]$ (dba = dibenzylideneacetone),[21] $[Pd(dppf)Cl_2]$ (dppf = 1,1′-bis(diphenylphosphino)ferrocene), and $Pd(OAc)_2$/1,3-bis(diphenylphosphino)propane (dppp)[22]), we found that the Fu $[Pd(PtBu_3)_2]$ catalyst[23] proved the most effective in generating the coupled adducts **33**–**35**. For both the Suzuki[23a] and Stille couplings,[23b] high catalyst loading (20 mol%) and

 © 2006 Wiley-VCH Verlag GmbH & Co. KGaA, Weinheim

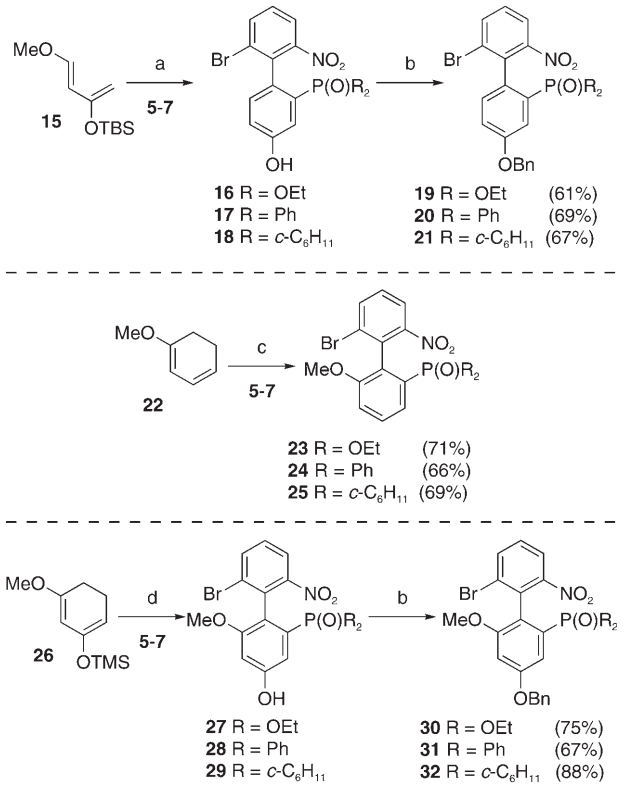

Scheme 3. Exploration of the diene scope in the Diels–Alder cycloaddition. Reagents and conditions: a) PhMe, 80 °C, 16 h; then TBAF, 0 °C; b) BnBr, NaH, DMF, THF, 0 °C→RT; yields reported over two steps; c) neat, 155 °C, 24 h; d) neat, 140 °C, 17 h.

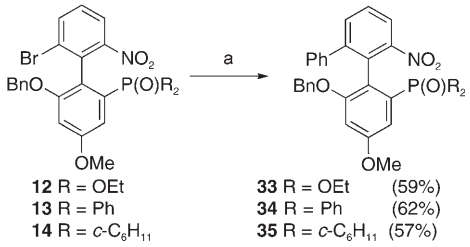

Scheme 4. Negishi coupling of biaryls. Reagents and conditions: a) [Pd(P*t*Bu$_3$)$_2$] (10 mol%), PhZnCl (1.5 equiv), NMP/THF, 80 °C, 16 h. NMP = *N*-methylpyrrolidone.

excess boronic acid or stannane (3 equiv) were required to drive the reaction to completion. In contrast, the Negishi-style organozinc couplings[23c] proceeded in good yield with a more reasonable catalyst loading (10 mol%) and lower amounts of the organozinc species (1.5 equiv). It should be noted that nickel-catalyzed couplings are not effective on substrates such as **12**–**14** because of the NO_2 functionality.[23c,24]

Given the efficiency of the Negishi couplings with tetra-*ortho*-substituted biaryls **12**–**14** and phenylzinc chloride, a range of organozinc species was explored to gauge the potential utility in the metal-mediated couplings (Scheme 5). As shown in Table 1, these palladium-couplings proved successful with a variety of substituents on the organozinc moiety. Both electron-donating and electron-

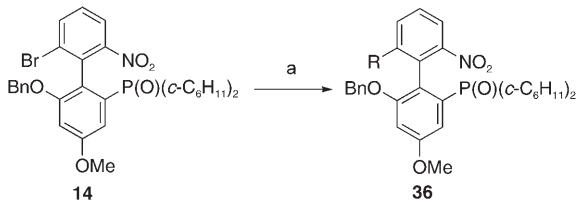

Scheme 5. Selected examples of Negishi couplings with biaryl **14**. Reagents and conditions: a) [Pd(P*t*Bu$_3$)$_2$] (10 mol%), RZnCl (1.5 equiv), NMP/THF, 80 °C, 16 h.

Table 1: Selected examples of Negishi couplings with biaryl **14**.

Entry	RZnCl[a]	Yield of **36** [%]
1	4-methoxyphenylzinc chloride	59
2	3-methoxyphenylzinc chloride	58
3	2-methoxyphenylzinc chloride	0
4	2-methylphenylzinc chloride	61
5	2,6-dimethylphenylzinc chloride[b]	66
6	pentafluorophenylzinc chloride	57

[a] The organozinc species was formed by addition of the in situ generated organomagnesium species to a solution of anhydrous zinc chloride in THF (1 M). [b] An extended reaction time (48 h) was employed for this coupling.

withdrawing groups are tolerated. One limitation can be found in our inability to achieve successful Negishi coupling with 2-methoxyphenylzinc chloride (Table 1, entry 3); however, *ortho*-substitution on the organozinc species is tolerated (entries 4 and 5). In fact, the more sterically hindered examples perform better in the coupling process. Finally, the pentafluorophenylzinc species could be cleanly coupled with bromide **14** to yield the pentafluorophenyl product **36 f** (Table 1, entry 6).

The reduction of selected biaryls was also studied (Scheme 6). The nitro arene **36 e** can be cleanly converted into the corresponding amine **37** by reduction with Zn/AcOH.

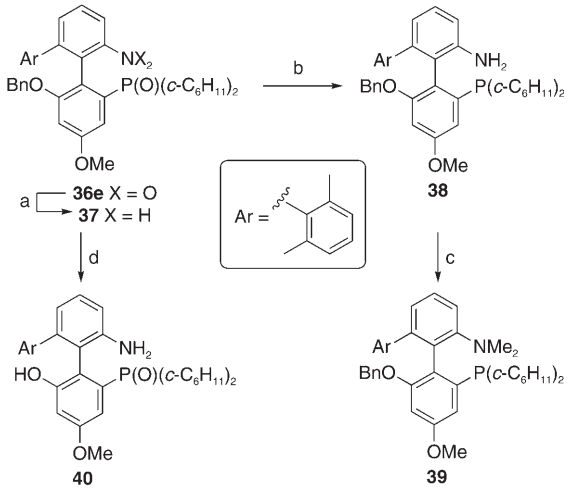

Scheme 6. Reduction of selected biaryls. Reagents and conditions: a) Zn, HOAc, 16 h (85%); b) [Ti(O*i*Pr)$_4$], PMHS, THF, 80 °C, 48 h (61%); c) $NaBH_3CN$, paraformaldehyde, MeCN, AcOH (80%); d) BCl_3, CH_2Cl_2, 0 °C, 3 h (70%).

 © 2006 Wiley-VCH Verlag GmbH & Co. KGaA, Weinheim

After screening a broad range of conditions for the conversion of the phosphine oxide **37** into its corresponding phosphine **38**, we found that this process could be accomplished in a reasonable yield using [Ti(O*i*Pr)$_4$]/poly(methylhydrosiloxane) (PMHS).[25] Reductive amination generated the dimethylaminophosphine **39**. Attempted removal of the benzyl moiety under hydrogenation conditions (Pd/C or PtO_2, H_2) gave problematic results. Fortunately, removal of the benzyl ether from **37** could be cleanly accomplished using BCl_3.

In order to show the utility of the synthesized materials, we chose to investigate palladium-mediated couplings using amino phosphine **39** as a ligand (Scheme 7). The structure of

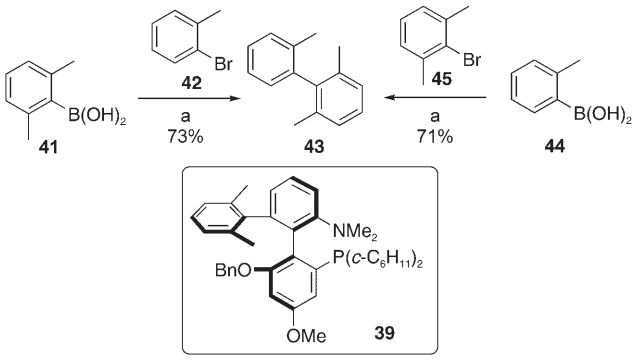

Scheme 7. Utility of the synthesized biaryl **39** in the Suzuki coupling. Reagents and conditions: a) $Pd(OAc)_2$ (5 mol%), **39** (10 mol%), K_3PO_4, PhMe, 100°C, 20 h.

this catalyst is based on the pioneering work of Buchwald and co-workers.[26] Preliminary screening of **39** appears to indicate that a highly active catalyst is generated for Suzuki couplings, as demonstrated in the synthesis of the sterically challenging tri-*ortho*-substituted biaryl **43**. It is important to note that the control experiment (in the absence of phosphine) with boronic acid **41** and bromide **42** ($Pd(OAc)_2$ (5 mol%), K_3PO_4, PhMe, 100°C, 20 h) gave only a minor amount (18%) of the desired coupled material **43**. Use of PPh_3 as the ligand also gave inferior results. Further exploration in the scope and utility of our Diels–Alder approach to biaryls for the synthesis of novel ligand systems will be reported in due course.

In summary, we have demonstrated a novel method for the construction of highly substituted, orthogonally functionalized biaryl compounds previously not accessible by traditional methods. Subsequent manipulation of the resultant biaryls through palladium-coupling and/or reduction provides access to a significant range of substitution patterns. Finally, the potential utility of aminophosphine **39** as a ligand in challenging cross-coupling reactions has been demonstrated.

Experimental Section

14: Compound **8** (4.14 g, 20.4 mmol) was added to a pressure vessel containing **7** (2.24 g, 5.11 mmol) and PhMe (10.2 mL) at room temperature. The reaction mixture was heated at 80°C. After 18 h, the reaction mixture was cooled to 0°C and Et_3N (2.59 g, 3.58 mL, 25.6 mmol) was slowly added. After the orange solution had been stirred for 6 h, the reaction mixture was quenched with saturated aqueous NH_4Cl (70 mL), diluted with EtOAc (70 mL), and washed with H_2O (70 mL) and saturated aqueous NaCl (70 mL). The dried extract ($MgSO_4$) was concentrated in vacuo. The crude product **12** was dissolved in DMF (25.6 mL) and cooled to 0°C. BnBr (17.5 g, 102 mmol, 11.8 mL) and NaH (1.02 g, 25.6 mmol, 60% in mineral oil) were added to this solution. After 8 h, the mixture was quenched with saturated aqueous NH_4Cl (100 mL), diluted with EtOAc (100 mL), and washed with H_2O (100 mL) and saturated aqueous NaCl (100 mL). The dried extract ($MgSO_4$) was concentrated in vacuo and purified by chromatography over silica gel eluting with EtOAc/hexanes (50:50) to give **14** (2.26 g, 3.62 mmol, 70%) as a bright-yellow crystalline solid. M.p.: 202–203°C; IR (neat): $\tilde{\nu}$ = 2930, 1597, 1524, 1302 cm^{-1}; ^{1}H NMR (400 MHz, $CDCl_3$): δ = 8.09 (dd, J = 8.2, 1.2 Hz, 1H), 7.87 (dd, J = 8.0, 1.2 Hz, 1H), 7.33 (t, J = 8.6 Hz, 1H), 7.25–7.31 (m, 3H), 7.18–7.19 (m, 2H), 6.75 (d, J = 2.1 Hz, 1H), 6.51 (dd, J = 11.5, 2.2 Hz, 1H), 5.10 (s, 2H), 3.87 (s, 3H), 1.20–1.96 ppm (m, 22H); ^{13}C NMR (100 MHz, $CDCl_3$): δ = 159.9 (d, $J_{C,P}$ = 16 Hz, 1C), 158.2 (d, $J_{C,P}$ = 14 Hz, 1C), 150.7, 136.7, 136.5, 134.1 (d, $J_{C,P}$ = 1.9 Hz, 1C), 130.6, 129.8, 128.6, 128.4, 127.7, 127.6, 126.4, 125.8, 123.2, 107.6 (d, $J_{C,P}$ = 12 Hz, 1C), 101.5 (d, $J_{C,P}$ = 1.7 Hz, 1C), 70.6, 55.5, 38.2, 37.6 (d, $J_{C,P}$ = 3.9 Hz, 1C), 36.9, 26.8 (d, $J_{C,P}$ = 8.5 Hz, 1C), 26.7 (d, $J_{C,P}$ = 8.9 Hz, 1C), 26.6 (d, $J_{C,P}$ = 2.0 Hz, 1C), 26.5 (d, $J_{C,P}$ = 3.3 Hz, 1C), 26.4 (d, $J_{C,P}$ = 3.3 Hz, 1C), 25.9 (d, $J_{C,P}$ = 1.4 Hz, 1C), 25.7 (d, $J_{C,P}$ = 2.1 Hz, 1C), 25.0 (d, $J_{C,P}$ = 3.3 Hz, 1C), 24.7 (d, $J_{C,P}$ = 3.6 Hz, 1C); HRMS (FAB+) calcd for $C_{32}H_{38}NO_5PBr$ [M+H]: 626.1671; found: 626.1653.

Received: April 4, 2005
Revised: July 5, 2006
Published online: September 15, 2006

Keywords: biaryls · Diels–Alder reaction · Negishi coupling · palladium · phosphanes

[1] a) G. Bringmann, A. J. P. Mortimer, P. A. Keller, M. J. Gresser, J. Garner, M. Breuning, *Angew. Chem.* **2005**, *117*, 5518–5563, *Angew. Chem. Int. Ed.* **2005**, *44*, 5384–5427; b) G. Bringmann, C. Gunther, M. Ochse, O. Schupp, S. Tasler in *Progress in the Chemistry of Organic Natural Products, Vol. 82* (Eds.: W. Herz, H. Falk, G. W. Kirby, R. E. Moore), Springer, New York **2001**, pp. 1–293; c) *Metal-Catalyzed Cross-Coupling Reactions* (Eds.: A. de Meijere, F. Diederich), Wiley, New York, **2004**.

[2] a) J. Hassan, M. Sévignon, C. Gozzi, E. Schulz, M. Lemaire, *Chem. Rev.* **2002**, *102*, 1359–1469; b) S. P. Stanforth, *Tetrahedron* **1998**, *54*, 262–303; c) M. Miura, *Angew. Chem.* **2004**, *116*, 2251–2253; *Angew. Chem. Int. Ed.* **2004**, *43*, 2201–2203; d) A. Zapf, M. Beller, *Chem. Commun.* **2005**, 431–440; e) see also: N. Miyaura, *Top. Curr. Chem.* **2002**, *219*, 1–241.

[3] M. McCarthy, P. J. Guiry, *Tetrahedron* **2001**, *57*, 3809–3844.

[4] A. Fürstner, A. Leitner, M. Mendez, H. Krause, *J. Am. Chem. Soc.* **2002**, *124*, 13856–13863.

[5] a) G. Cahiez, D. Luart, F. Lecomte, *Org. Lett.* **2004**, *6*, 4395–4398; b) A. S. Demir, Ö. Reis, E. Özgül-Karaaslan, *J. Chem. Soc. Perkin Trans. 1* **2001**, 3042–3045; c) W. E. Fristad, J. R. Peterson, A. B. Ernst, *J. Org. Chem.* **1985**, *50*, 3143–3148; d) J. B. Bush, H. Fikenbeiner, *J. Am. Chem. Soc.* **1968**, *90*, 5903–5905; e) E. I. Heiba, R. M. Dessau, W. J. Koehl, *J. Am. Chem. Soc.* **1968**, *90*, 5905–5906; f) B. B. Snider, *Chem. Rev.* **1996**, *96*, 339–364.

[6] R. Hong, R. Hoen, J. Zhang, G.-Q. Lin, *Synlett* **2001**, 1527–1530.

[7] M. F. Semmelhack, P. Helquist, L. D. Jones, L. Keller, L. Mendelson, L. S. Ryono, J. G. Smith, R. D. Stauffer, *J. Am. Chem. Soc.* **1981**, *103*, 6460–6471.

[8] a) Y. Liang, S. Gao, H. Wan, J. Wang, H. Chen, Z. Zheng, X. Hu, *Tetrahedron: Asymmetry* **2003**, *14*, 1267–1273; b) G.-Q. Lin, R.

 © 2006 Wiley-VCH Verlag GmbH & Co. KGaA, Weinheim

Hong, *J. Org. Chem.* **2001**, *66*, 2877 – 2880; c) J. T. Manka, F. Guo, J. Huang, H. Yin, J. M. Farrar, M. Sienkowska, V. Benin, P. Kaszynski, *J. Org. Chem.* **2003**, *68*, 9574 – 9588; d) J. E. Milne, S. L. Buchwald, *J. Am. Chem. Soc.* **2004**, *126*, 13028 – 13032; e) S. Narayan, W. R. Roush, *Org. Lett.* **2004**, *6*, 3789 – 3792.

[9] V. Snieckus, *Chem. Rev.* **1990**, *90*, 879 – 933.

[10] a) W. M. Seganish, P. DeShong, *J. Org. Chem.* **2004**, *69*, 6790 – 6795; b) A. N. Cammidge, K. V. L. Crepy, *J. Org. Chem.* **2003**, *68*, 6832 – 6835.

[11] A. Taticchi, *The Diels–Alder Reaction: Selected Practical Methods*, Wiley, New York, **2002**.

[12] a) J. A. Reed, C. L. Schilling, R. F. Tarvin, T. A. Rettig, J. K. Stille, *J. Org. Chem.* **1969**, *34*, 2188 – 2192; b) E. McDonald, A. Suksamrarn, R. D. Wylie, *J. Chem. Soc. Perkin Trans. 1* **1979**, 1893 – 1900; c) S. M. Weinreb, F. Z. Basha, S. Hibino, N. A. Khatri, D. Kim, W. E. Pye, T.-T. Wu, *J. Am. Chem. Soc.* **1982**, *104*, 536 – 544; d) D. L. Boger, J. S. Panek, S. R. Duff, *J. Am. Chem. Soc.* **1985**, *107*, 5745 – 5754; e) F. Effenberger, T. Ziegler, *Chem. Ber.* **1987**, *120*, 1339 – 1346; f) B. Sain, J. S. Sandhu, *J. Org. Chem.* **1990**, *55*, 2545 – 2546; g) D. M. Smith, B. J. L. Royles, *J. Chem. Soc. Perkin Trans. 1* **1994**, 355 – 358; h) M. D'Auria, *Tetrahedron Lett.* **1995**, *36*, 6567 – 6570; i) A. Avenoza, J. H. Busto, C. Cativiela, J. M. Peregrina, *Synthesis* **1995**, 671 – 674; j) L. Balázs, I. Kádas, L. Tõke, *Tetrahedron Lett.* **2000**, *41*, 7583 – 7587; k) M. D. Watson, A. Fechtenkotter, K. Mullen, *Chem. Rev.* **2001**, *101*, 1267 – 1300; l) W. D. Watson, A. Fechtenkotter, K. Mullen, *Chem. Rev.* **2001**, *101*, 1267 – 1300; m) S.-H. Min, Y.-W. Kim, S. Choi, K. B. Park, C.-G. Cho, *Bull. Korean Chem. Soc.* **2002**, *23*, 1021 – 1022; n) G. Hilt, K. I. Smolko, *Synthesis* **2002**, 686 – 692; o) J. E. Moore, M. York, J. P. A. Harrity, *Synlett* **2005**, 860 – 862; p) T. Yamato, M. Miyamoto, T. Hironaka, Y. Miura, *Org. Lett.* **2005**, *7*, 3 – 6.

[13] A three-step protocol for this aldehyde has been previously reported: J.-S. Li, Y.-H. Fan, Y. Zhang, L. A. Marky, B. Gold, *J. Am. Chem. Soc.* **2003**, *125*, 2084 – 2093.

[14] a) M. G. Vetlino, J. W. Coe, *Tetrahedron Lett.* **1994**, *35*, 219 – 222; b) S. Caron, E. Vazquez, R. W. Stevens, K. Nahao, H. Koike, Y. Murata, *J. Org. Chem.* **2003**, *68*, 4104 – 4107.

[15] a) S. Ohira, *Synth. Commun.* **1989**, *19*, 561 – 564; b) S. Müller, B. Liepold, G. J. Roth, J. Bestmann, *Synlett* **1996**, 521 – 522.

[16] J. Savard, P. Brassard, *Tetrahedron* **1984**, *40*, 3455 – 3464.

[17] R. B. Coleman, E. B. Grant, *J. Org. Chem.* **1991**, *56*, 1357 – 1359.

[18] CCDC-605862 (**14**) contains the supplementary crystallographic data for this paper. These data can be obtained free of charge from The Cambridge Crystallographic Data Centre via www.ccdc.cam.ac.uk/data_request/cif.

[19] J. N. Freskos, G. W. Morrow, J. S. Swenton, *J. Org. Chem.* **1985**, *50*, 805 – 810.

[20] a) T. E. Barder, S. D. Walker, J. R. Martinelli, S. L. Buchwald, *J. Am. Chem. Soc.* **2005**, *127*, 4685 – 4696; b) S. D. Walker, T. E. Barder, J. R. Martinelli, S. L. Buchwald, *Angew. Chem.* **2004**, *116*, 1907 – 1912; *Angew. Chem. Int. Ed.* **2004**, *43*, 1871 – 1876; c) J. E. Milne, S. L. Buchwald, *J. Am. Chem. Soc.* **2004**, *126*, 13028 – 13032.

[21] a) A. F. Littke, G. C. Fu, *Angew. Chem.* **2002**, *114*, 4350 – 4386; *Angew. Chem. Int. Ed.* **2002**, *41*, 4176 – 4211; b) F. Minutolo, M. Antonello, S. Bertini, S. Rapposelli, A. Rossello, S. Sheng, K. E. Carlson, J. A. Katzenellenbogen, M. Macchia, *Bioorg. Med. Chem.* **2003**, *11*, 1247 – 1257.

[22] W. Shen, *Tetrahedron Lett.* **1997**, *38*, 5575 – 5578.

[23] a) A. F. Littke, C. Dai, G. C. Fu, *J. Am. Chem. Soc.* **2000**, *122*, 4020 – 4028; b) A. F. Littke, L. Schwarz, G. C. Fu, *J. Am. Chem. Soc.* **2002**, *124*, 6343 – 6348; c) C. Dai, G. C. Fu, *J. Am. Chem. Soc.* **2001**, *123*, 2719 – 2724.

[24] E.-I. Negishi, A. O. King, N. Okukado, *J. Org. Chem.* **1977**, *42*, 1821 – 1823.

[25] T. Coumbe, N. J. Lawrence, F. Muhammad, *Tetrahedron Lett.* **1994**, *35*, 625 – 628.

[26] a) J. P. Wolfe, S. L. Buchwald, *Angew. Chem.* **1999**, *111*, 2570 – 2573; *Angew. Chem. Int. Ed.* **1999**, *38*, 2413 – 2416; b) J. P. Wolfe, R. A. Singer, B. H. Yang, S. L. Buchwald, *J. Am. Chem. Soc.* **1999**, *121*, 9550 – 9561.

 © 2006 Wiley-VCH Verlag GmbH & Co. KGaA, Weinheim

Homogeneous Chiral Catalysis

DOI: 10.1002/anie.200601084

A C_3-Symmetric Palladium Catalyst with a Phosphorus-Based Tripodal Ligand**

Marco Ciclosi, Julio Lloret, Francisco Estevan, Pascual Lahuerta, Mercedes Sanaú, and Julia Pérez-Prieto**

C_3 symmetry is intriguing in chemistry, therefore the synthesis of tripodal ligands and their applications in selective catalysts are receiving increasing interest.[1–4] Most of the C_3-symmetric metal complexes synthesized to date are based on nitrogen-based tripodal ligands,[2] although examples with ligands coordinating through oxygen and phosphorus have also been reported.[3,4] Most of these ligands are conformationally flexible, and the way they coordinate to the metal center is open to question in many cases. Gade et al. have noted the advantage of using ligands that can provide a relatively rigid and well-defined coordination geometry.[5] Along these lines, they have reported the synthesis of chiral and achiral 1,1,1-tris(oxazolinyl)alkane ligands with the capability to facially coordinate to transition metals (Cu^{I}/Cu^{II}, Rh^{I}, Zn^{II}, and Sc^{III}) as a tridentate ligand. To our knowledge, no analogous rigid phosphorus-based tripodal ligands that are able to coordinate

[*] J. Lloret, Prof. Dr. F. Estevan, Prof. Dr. P. Lahuerta, Prof. Dr. M. Sanaú
Departamento de Química Inorgánica
Universidad de Valencia
Doctor Moliner 50, 46100 Burjassot, Valencia (Spain)
Fax: (+34) 96-354-4322
E-mail: lahuerta@uv.es

M. Ciclosi, Prof. Dr. J. Pérez-Prieto
Departamento de Química Orgánica
Instituto de Ciencia Molecular
Universidad de Valencia
Polígono La Coma s/n, 46980 Paterna, Valencia (Spain)
Fax: (+34) 96-354-4939
E-mail: julia.perez@uv.es

Supporting Information for this article (general procedures, details of the syntheses of 2–4, standard catalytic reactions, poisoning experiments with Hg, and asymmetric cross-coupling reactions, as well as crystal data for **2**–**4**) is available on the WWW under http://www.angewandte.org or from the author.

© 2006 Wiley-VCH Verlag GmbH & Co. KGaA, Weinheim

a transition metal to form C_3-symmetric complexes have appeared in the literature.

Herein, we report the synthesis of the tripodal ligand **2** (Scheme 1), which is suitable for the formation of C_3-symmetric palladium complexes. The potential of the racemic complex as a catalyst is demonstrated in several Suzuki cross-coupling reactions. Interestingly, this complex is axially chiral, and both enantiomers were isolated by chiral HPLC and tested for asymmetric catalysis in a model reaction. Although the cross-coupling product was obtained with an *ee* value of only 7%, this complex could be an intriguing lead structure for an interesting new series of chiral catalysts.

The synthesis of ligand **2** was achieved in high yield (75%) by the treatment of **1**[6] with sodium hydride followed by the addition of chlorodiphenylphosphane (Scheme 1). In the

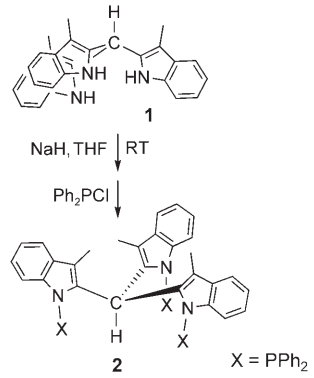

Scheme 1. Synthesis of tripodal ligand **2**.

^{1}H NMR of **2**, the methine hydrogen atom (H-C_{sp^3}) is highly deshielded ($\delta = 8.7$ ppm) and appears as a quadruplet, owing to coupling with three equivalent phosphorus atoms. X-ray analysis of a single crystal of this compound confirmed its structure and showed that the methine hydrogen atom (H(1)) is oriented towards the phosphanyl moieties (Figure 1).

To asses the binding capability of this new tripodal ligand, it was refluxed in a dry THF solution containing $PdCl_2$ (1.1 equiv) for 20 h. However, no C_3-symmetric complex was detected. Instead, compound **3**, with only two phosphorus atoms coordinated to the palladium center, was obtained with an 80% yield (Scheme 2). The structure of this complex was assigned by ^{1}H and ^{31}P NMR spectroscopy. X-ray analysis of a single crystal (grown in $CHCl_3/Et_2O$) confirmed this assignment and showed its square-planar geometry (Figure 2).

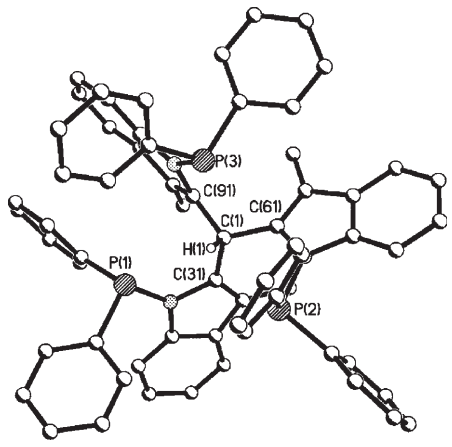

Figure 1. Molecular structure of tripodal ligand **2**, viewed along the virtual threefold molecular axis (hydrogen atoms, except H(1), are omitted for clarity). Selected bond angles [°]: C(91)–C(1)–C(31) 112.4(5), C(91)–C(1)–C(61) 116.0(4), C(31)–C(1)–C(61) 114.8(5).

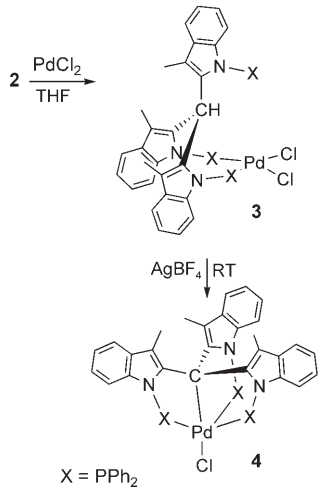

Scheme 2. Synthesis of palladium complexes **3** and **4**.

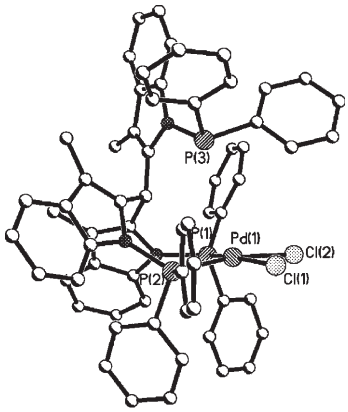

Figure 2. Molecular structure of palladium complex **3** (hydrogen atoms are omitted for clarity). Selected bond lengths [Å] and angles [°]: Pd(1)–P(1) 2.2783(19), Pd(1)–P(2) 2.3166(18), Pd(1)–Cl(1) 2.3263(19), Pd(1)–Cl(2) 2.3253(19); P(1)–Pd(1)–P(2) 104.01(6), P(1)–Pd(1)–Cl(2) 79.74(7), P(2)–Pd(1)–Cl(2) 170.51(7), P(2)–Pd(1)–Cl(1) 87.79(7).

In order to synthesize a C_3-symmetric structure, a dichloromethane solution of **3** was treated with silver tetrafluoroborate at room temperature for three hours (Scheme 2). Interestingly, the ^{31}P NMR spectrum of the resulting complex shows only one signal at $\delta = 49.4$ ppm, thereby indicating the formation of a threefold-symmetric complex. X-ray analysis of a single crystal (grown in $CHCl_3/Et_2O$) established the details of the molecular structure of compound **4**, which contains a pentacoordinate palladium atom bonded to the central carbon bridge of the tripod ligand (Figure 3). This result confirms the suitability of ligand **2** for facial coordination to metal atoms.

The ability of complex **4** to act as a catalyst in a model Ppalladium-based catalytic reaction was explored. Thus, it

 © 2006 Wiley-VCH Verlag GmbH & Co. KGaA, Weinheim

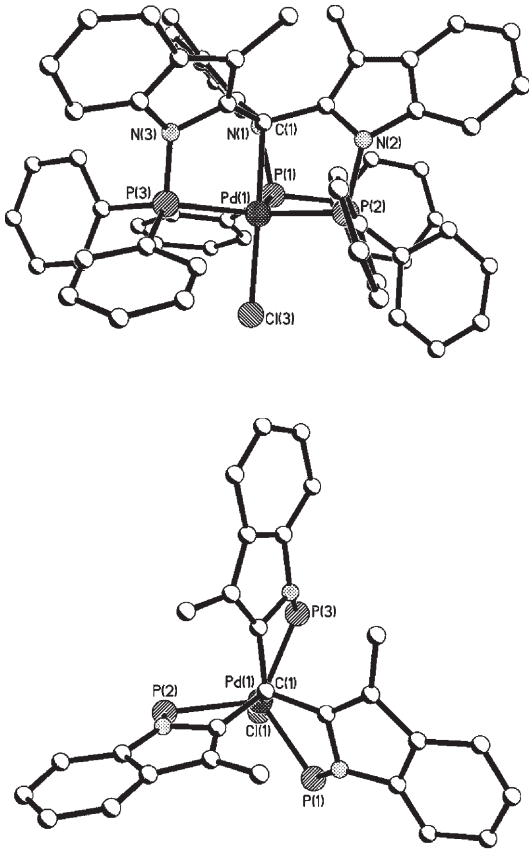

Figure 3. a) Molecular structure of palladium complex **4** (hydrogen atoms are omitted for clarity). Selected bond lengths [Å] and angles [°]: Pd(1)–C(1) 2.14(3), Pd(1)–P(1) 2.323(8), Pd(1)–P(3) 2.340(8), Pd(1)–P(2) 2.388(8), Pd(1)–Cl(1) 2.416(7); C(1)–Pd(1)–P(1) 83.7(9), C(1)–Pd(1)–P(3) 84.9(10), C(1)–Pd(1)–P(2) 83.7(9), C(1)–Pd(1)–Cl(1) 177.0(9). b) View along the virtual threefold axis of **4** (hydrogen atoms and the phenyl rings attached to the phosphorus atoms are omitted for clarity).

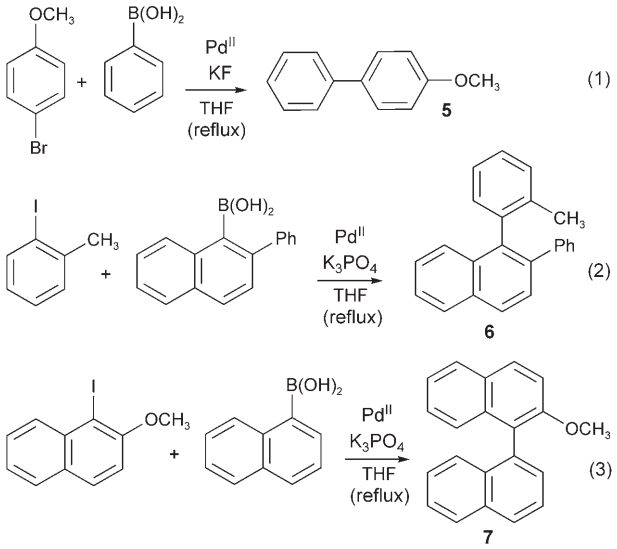

Scheme 3. Suzuki reactions catalyzed by **3** [Eq. (1)] or **4** [Eqs. (1)–(3)].

Table 1: Suzuki reactions with catalyst **3** or **4.**

	Reaction conditions[a]			Coupling yield[b] [%]		Biaryl
Run	Boronic acid [equiv]	Pd^{II} [%]	t [h]	Cat. **3**	Cat. **4**	
1	1.1	2	15	30	31	**5**
2	2	2	15	71	59	**5**
3	2	0.5	15	70	47	**5**
4	3	2	15	89	82	**5**
5	3	0.5	15	94	70	**5**
6	3	2	24	95	87	**5**
7	3	0.5	24	94	91	**5**
8	2	3	40	–	75	**6**
9	2	3	15	–	80	**7**

[a] Conditions: halogen compound (1 mmol), KF (3 mmol) or K_3PO_4 (2 mmol), palladium complex (0.5–2 mol%). Standard reaction: a solution of 4-bromoanisole (125 μL, 1 mmol), KF (174 mg, 3 mmol), $PhB(OH)_2$, and complex **3** or **4** was heated to reflux in THF (20 mL). The reaction mixture was then loaded onto a small plug of celite, washed with THF, and concentrated under vacuum. [b] Determined by ^1H NMR spectroscopy.

was used in various Suzuki reactions, which are well-known as being among the most versatile reactions for the selective construction of biaryl compounds.[7,8] Cross-coupling of *p*-bromoanisole and phenylboronic acid catalyzed by **4** was performed in refluxing dry THF in the presence of KF [Scheme 3, Eq. (1)]. As shown in Table 1 (runs 1–7), different reaction conditions were used. Comparison of the results with those obtained for complex **3** showed that a similar yield of *p*-methoxyphenylbenzene (**5**; higher than 90%) was obtained with both palladium complexes with three equivalents of phenylboronic acid and 0.5 mol% of catalyst. Catalyst **4** was also tested in the formation of rotationally more hindered biaryls, such as phenylnaphthyl [**6**; Scheme 3, Eq. (2); Table 1, run 8] and binaphthyl [**7**; Scheme 3, Eq. (3); Table 1, run 9]. This complex is also an efficient catalyst in the presence of iodo derivatives.

It is remarkable that in the case of complex **4**, the ^{31}P NMR spectrum of the crude reaction mixture after catalysis shows the presence of only one signal centered at $\delta = 47.4$ ppm (when using bromoanisole) or $\delta = 45.6$ ppm (when using the iodo derivatives), which is indicative of the formation of a new C_3-symmetric palladium complex. Fast-atom bombardment (FAB) GC/MS analysis was consistent with the exchange of the chloride ligand in complex **4** by bromide or iodide during the catalytic process.[9] In addition, the C_3-symmetric complex recovered after the catalytic process exhibited high stability in six subsequent reactions (reaction time: 15 h), affording similar yields in all cycles. Poisoning experiments were also carried out with metallic mercury to test for the presence of a palladium colloid. When 50 equivalents of Hg^0 (relative to the palladium complex) were added to the reaction mixture at the start, the catalytic activity was not suppressed.[10]

Control experiments showed low (<10%) ligand exchange when complex **4** was treated with either bromoanisole or a bromoanisole/KF mixture in refluxing THF. However, no change was observed when the complex was heated in the presence of phenylboronic acid.

When using complex **3**, ^{31}P NMR analysis of the crude reaction mixture after the catalytic process revealed a high degree of metal-complex decomposition. This fact confirms that a compound of type **3** is not involved in the catalytic

 © 2006 Wiley-VCH Verlag GmbH & Co. KGaA, Weinheim

reaction induced by **4**, where only one complex with C_3 symmetry is detected in the crude reaction mixture.

The view along the threefold molecular axis of the palladium complex reveals the C_3 chirality of the system in the solid state. In order to determine if the axial chirality of complex **4** remains in solution, attempts were made to exchange its chloride ligand for a chiral ligand, whereby the formation of diastereoisomers would lead to a doubling of the ^{31}P NMR signals and agree with the existence of **4** as a racemic mixture. As a first test of the feasibility of ligand exchange without loss of tripodal coordination, complex **4** was treated with $AgBF_4$ and then triphenylphosphane. The ^{31}P NMR spectrum of the complex shows a doublet at $\delta =$ 52.1 ppm for the phosphorus atoms of the tripodal ligand and a quadruplet at $\delta = 18.0$ ppm for the triphenylphosphane moiety, owing to P–P coupling (see Supporting Information). When using a chiral phosphane, such as (2*S*,5*S*)-2,5-dimethyl-1-phenylphospholane ((2*S*,5*S*)-**8**), the spectrum exhibits two doublets, at $\delta = 54.5$ and 53.3 ppm, and two quadruplets, at $\delta = 30.4$ and 28.2 ppm (see Supporting Information). Further confirmation of the formation of diastereoisomers was obtained by reaction of **4** with $AgBF_4$ followed by treatment with (*R*)-phenylethylamine: the ^{31}P NMR spectrum of the complex obtained shows two signals with the same intensity at $\delta = 52.9$ and 53.1 ppm (see Supporting Information). All these data indicate that the axial chirality of complex **4** is retained in solution.

Separation of the enantiomers was accomplished by chiral HPLC (Chirobiotic T, 1:3 hexane/ethyl acetate). Neither of them racemizes after heating under reflux in THF solution for 15 h, which is clear evidence that they are configurationally stable under the reaction conditions. The enantiomerically pure complex was tested for the asymmetric cross-coupling reaction between 1-iodo-2-methoxynaphthalene and 1-naphthylboronic acid, which led to compound **7** with only 7% *ee*. Despite the growing success of the Suzuki cross-coupling reaction for the construction of biaryls, its asymmetric variant still remains a challenge,[11–13] probably because of the inherent difficulty in coupling two sterically hindered arenes in a transition-metal-mediated process. Enantioselective couplings[13] have recently emerged as viable and more direct alternatives, thanks to the design of chiral ligands. However, no examples of an enantiomerically pure catalyst without chiral ligands has been used in a Suzuki reaction to date.

In summary, the rigid tripodal phosphorus-based ligand **2** has a facial-coordinating ability that allows it to form the C_3-symmetric palladium complex **4**. It has been successfully tested as a reusable catalyst in Suzuki cross-coupling. This complex, which has no chirality in either of the branches of the tripodal ligand but is intrinsically chiral, could be an intriguing lead structure for a new series of chiral catalysts.

Received: March 20, 2006
Revised: July 25, 2006
Published online: September 20, 2006

Keywords: biaryls · cross-coupling · P ligands · palladium · tripodal ligands

[1] C. Moberg, *Angew. Chem.* **1998**, *110*, 260; *Angew. Chem. Int. Ed.* **1998**, *37*, 248.
[2] a) H. Memmler, U. Kauper, L. H. Gade, D. Stalke, *Organometallics* **1996**, *15*, 3637; b) V. Christou, J. Arnold, *Angew. Chem.* **1993**, *105*, 1551; *Angew. Chem. Int. Ed. Engl.* **1993**, *32*, 1450; c) J. G. Verkade, *Acc. Chem. Res.* **1993**, *26*, 483.
[3] a) L. H. Gade, P. Renner, H. Memmler, F. Fecher, C. H. Galka, M. Laubender, S. Radojevic, M. McPartlin, J. W. Lauher, *Chem. Eur. J.* **2001**, *7*, 2563; b) C. Bianchini, A. Meli, M. Peruzzini, F. Vizza, F. Zanobini, *Coord. Chem. Rev.* **1992**, *120*, 193; c) M. J. Burk, R. L. Harlow, *Angew. Chem.* **1990**, *102*, 1511; *Angew. Chem. Int. Ed. Engl.* **1990**, *29*, 1462; d) C. A. Ghilardi, S. Midollini, L. Sacconi, *Inorg. Chem.* **1975**, *14*, 1790.
[4] a) T. Fang, D. M. Du, S. F. Lu, J. Xu, *Org. Lett.* **2005**, *7*, 2081; b) F. Di Furia, G. Licini, G. Modena, R. Motterle, W. A. Nugent, *J. Org. Chem.* **1996**, *61*, 5175; c) R. L. Harlow, *J. Am. Chem. Soc.* **1994**, *116*, 6142; d) W. A. Nugent, T. V. RajanBabu, M. J. Burk, *Science* **1993**, *259*, 479; e) M. J. Burk, R. L. Harlow, *Angew. Chem.* **1990**, *102*, 1511; *Angew. Chem. Int. Ed. Engl.* **1990**, *29*, 1462; f) T. R. Ward, L. M. Venanzi, A. Albinati, F. Lianza, T. Gerfin, V. Gramlich, T. Ramos, M. Gerardo, *Helv. Chim. Acta* **1991**, *74*, 983.
[5] a) B. D. Ward, S. Bellemin-Laponnaz, L. H. Gade, *Angew. Chem.* **2005**, *117*, 1696; *Angew. Chem. Int. Ed.* **2005**, *44*, 1668; b) C. Dro, S. Bellemin-Laponnaz, R. Welter, L. H. Gade, *Angew. Chem.* **2004**, *116*, 4579; *Angew. Chem. Int. Ed.* **2004**, *43*, 4479; c) S. Bellemin-Laponnaz, L. H. Gade, *Angew. Chem.* **2002**, *114*, 3623; *Angew. Chem. Int. Ed.* **2002**, *41*, 3473.
[6] U. Pindur, J. Müller, *Arch. Pharm.* **1984**, *317*, 555.
[7] A. Suzuki in *Handbook of Organopalladium Chemistry for Organic Synthesis* (Eds.: E. I. Negishi, A. de Meijere), Wiley, New York, **2002**, pp. 249.
[8] a) R. K. Arvela, N. E. Leadbeater, *Org. Lett.* **2005**, *7*, 2101; b) L. Botella, C. Nájera, *Angew. Chem.* **2002**, *114*, 187; *Angew. Chem. Int. Ed.* **2002**, *41*, 179; c) A. F. Littke, C. Dai, G. C. Fu, *J. Am. Chem. Soc.* **2000**, *122*, 4020; d) J. P. Wolfe, R. A. Singer, B. H. Yang, S. L. Buchwald, *J. Am. Chem. Soc.* **1999**, *121*, 9550.
[9] A trifluoroacetate for bromide substitution in a PCP pincer palladium complex involved in a Stille reaction has been reported previously: D. Olsson, P. Nilsson, M. Masnaouy, O. F. Wendt, *Dalton Trans.* **2005**, 1924.
[10] Poisoning experiments with mercury metal to test for the presence of a palladium colloid have proved very effective with homogeneous catalysts. Adding an excess (with respect to the metal complex) of metallic mercury to the reaction mixture leads to amalgamation on the surface of a heterogeneous metal particle, thus poisoning it, but does not suppress the catalytic activity of a homogeneous palladium complex: a) D. E. Bergbreiter, P. L. Osburn, J. D. Frels, *Adv. Synth. Catal.* **2005**, *347*, 172; b) M. R. Eberhard, *Org. Lett.* **2004**, *6*, 2125; c) D. R. Anton, R. H. Crabtree, *Organometallics* **1983**, *2*, 855; d) P. Foley, R. DiCosino, G. M. Whitesides, *J. Am. Chem. Soc.* **1980**, *102*, 6713.
[11] O. Baudoin, *Eur. J. Org. Chem.* **2005**, 4223.
[12] P.-E. Brouti, F. Colobert, *Eur. J. Org. Chem.* **2005**, 1113.
[13] a) K. Mikami, T. Miyamoto, M. Hatano, *Chem. Commun.* **2004**, 2082; b) J. Yin, S. L. Buchwald, *J. Am. Chem. Soc.* **2000**, *122*, 12051; c) A. N. Cammidge, K. V. L. Crépy, *Chem. Commun.* **2000**, 1723.

 © 2006 Wiley-VCH Verlag GmbH & Co. KGaA, Weinheim

Homoaromatics

DOI: 10.1002/anie.200602073

Strong Neutral Homoaromatics**

*Carsten Präsang, Peter Amseis, David Scheschkewitz, Gertraud Geiseler, Werner Massa, Matthias Hofmann, and Armin Berndt**

Dedicated to Professor Thomas Carell

While numerous charged homoaromatics have been described in the literature,[1] neutral species are rare.[2a] The latter exhibit only small homoaromatic stabilization energies and therefore have to be classified as "weak".[2–4] The hitherto "strongest" examples are bishomoaromatics: derivatives of bishomoborirene **Ia**,[2b] carbenanorbornene **IIa**,[2c] and metallacyclopentene **IIIa** [Eq. (3), Cp = cyclopentadienyl].[2d] Compounds **Ia** and **IIa** owe their high stabilization energies, computed to be 16.4[5] and 13.8 kcal mol^{-1},[2e] respectively, to their bicylic skeletons, which favor bishomoaromatic interactions for geometric reasons. Parent compounds **Ib**[1c] and **IIb**[2f] [Eq. (1),(2)] are higher in energy than monocyclic isomers **IV**[1c] and **V**[2f] without three-center, two-electron (3c2e) bonds. Derivatives of monocyclic 1-boracyclopent-3-ene **IV** are known experimentally.[6]

Particularly high homoaromatic stabilization energies arise in cases where the formal generation of classical reference molecules without cyclic delocalization involves charge separation.[1b] We computed an aromatic stabilization energy of 40.9 kcal mol^{-1} for bishomoaromatic **1a** [Eq. (4)], the parent compound of the nonclassical 1-sila-3,4-diboracyclopentanes.[1b] Herein, we present the synthesis and characterization of derivative **1b** [Eq. (5)], which is so far the strongest neutral homoaromatic compound to be reported.

Colorless crystals were obtained from the intensely yellow, concentrated thf solution of 1-sila-3,4-diboracyclopentane **2** (Dur = 2,3,5,6-tetramethylphenyl) after two days at room temperature.[1b] Solutions of **2**, which melts at 135 °C without decomposition, remain unchanged for weeks in $CDCl_3$, CD_2Cl_2, or toluene under exclusion of moisture. A single-crystal X-ray structure analysis[7] (Figure 1a) reveals that a thf adduct of nonclassical isomer **1b** was formed. The latter exhibits a B-H-B bridge, the H atom of which was previously bonded to the endocyclic silicon atom in **2**. The Si center in **1b** is coordinated by the oxygen atom of one thf molecule, and another molecule of thf is present in the lattice of $\{[\mathbf{1b}(thf)]\cdot thf\}_K$ (the index "K" indicates the complex in the crystal state). Figure 1b shows the solid-state structure of thf-free **1b**, which can be obtained from $\{[\mathbf{1b}(thf)]\cdot thf\}_K$ under suitable conditions as a toluene solvate.[8] Selected structural parameters of **1b**·$^1/_2$toluene and $\{[\mathbf{1b}(thf)]\cdot thf\}_K$ are compared with those computed for model compound **1c** [Eq. (9)] and its complex [**1c**(thf)] in Table 1.

The Si···B and B···B distances that were computed for **1c** differ by less than 1 pm from the experimental values of **1b**.

[*] Dr. C. Präsang, Dr. P. Amseis, Dr. D. Scheschkewitz, G. Geiseler, Prof. Dr. W. Massa, Prof. Dr. A. Berndt
Fachbereich Chemie der Universität Marburg
35032 Marburg (Germany)
Fax: (+49) 6421-282-8917
E-mail: berndt@chemie.uni-marburg.de
Dr. M. Hofmann
Anorganisch-Chemisches Institut
Ruprecht-Karls-Universität Heidelberg
Im Neuenheimer Feld 270, 69120 Heidelberg (Germany)

[**] This work was supported by the Deutsche Forschungs-gemeinschaft and Fonds der Chemischen Industrie. We are grateful for generous financial support for C.P. by Prof. T. Carell

Supporting information for this article is available on the WWW under http://www.angewandte.org or from the author.

 © 2006 Wiley-VCH Verlag GmbH & Co. KGaA, Weinheim

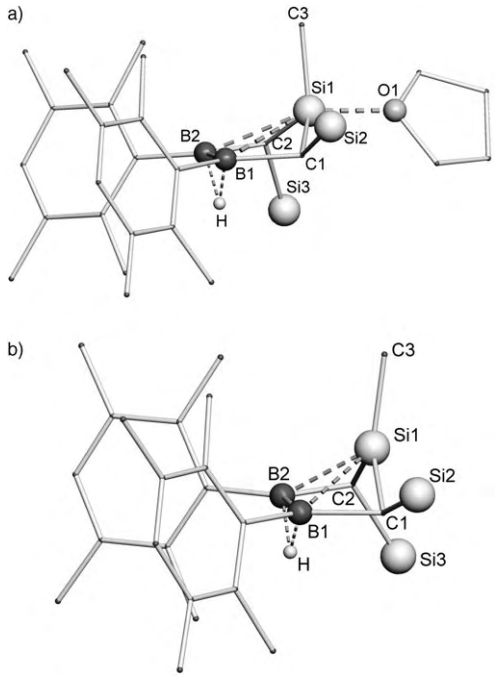

Figure 1. Crystal structures of $\{[\mathbf{1b}(thf)]\cdot thf\}_K$ (a) and $\mathbf{1b}\cdot{}^1/_2$ toluene (b). The methyl substituents at Si2 and Si3, most of the H atoms, and the solvate molecules have been omitted for clarity.

Table 1: Selected bond lengths [pm] and angles [°] of $\mathbf{1b}\cdot{}^1/_2$ toluene and $\{[\mathbf{1b}(thf)]\cdot thf\}_K$ (exptl) as well as of **1c**, [**1c**(thf)], and of [**1c**(thf)] in a reaction field: $\{[\mathbf{1c}(thf)]\}_R$ (calcd., B3LYP/6-311+G**).[9]

	$\mathbf{1b}\cdot{}^1/_2$ toluene	**1c**	$\{[\mathbf{1b}(thf)]\cdot thf\}_K$	[**1c**(thf)]	$\{[\mathbf{1c}(thf)]\}_R$
B1···Si1	211.6(2)	210.8	242.2(4)	214.8	236.6
B2···Si1	211.0(2)	210.8	244.0(4)	214.8	236.6
B1-B2	177.0(2)	176.3	166.5(5)	172.6	166.9
Si1···O	–	–	189.5(2)	266.7	198.9
B1,C1,C2,B2/C1,Si1,C2[a]	96.9(1)	94.6	128.9(2)	99.0	119.4

[a] Folding angle between planes.

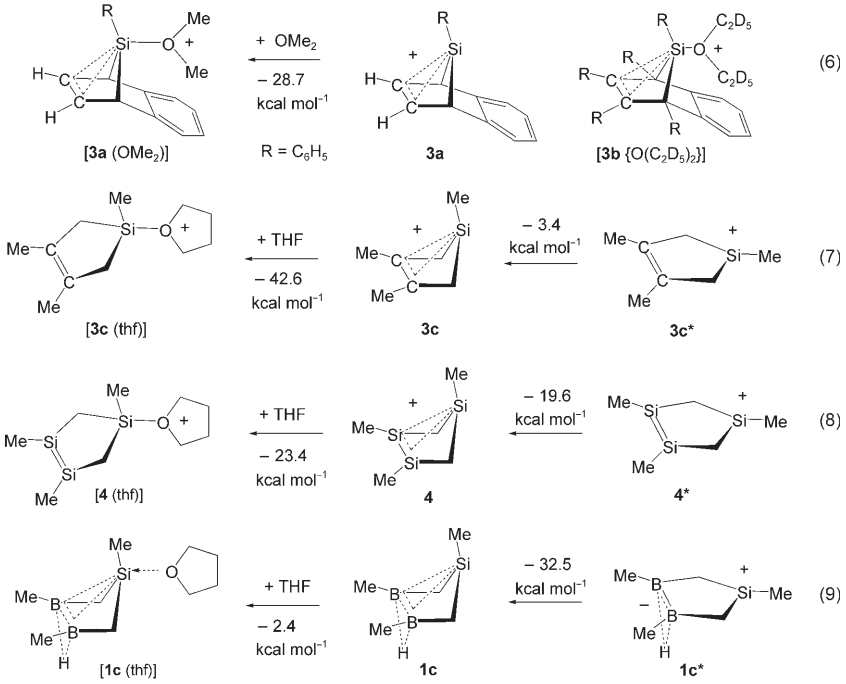

Apparently, **1c** is a reliable model for **1b** even though its substituents are smaller and the silyl groups have been omitted. In contrast, the adduct [**1c**(thf)] is a highly unsuitable model compound for complex $\{[\mathbf{1b}(thf)]\cdot thf\}_K$ in the solid state. The Si···O distance that was computed for [**1c**(thf)] is 77 pm longer than the experimental value of $\{[\mathbf{1b}(thf)]\cdot thf\}_K$, and the B···Si distance is shorter by 28 pm.

This discrepancy matches similar observations described for weak donor–acceptor complexes like $HCN\cdot BF_3$[10] and $H_2C{=}SiR_2\cdot O(CD_3)_2$[11] and can be largely overcome by employing a reaction field that models the polar environment in the crystal[12,11] (see data of $\{[\mathbf{1c}(thf)]\}_R$ in Table 1; the index "R" stands for "in a reaction field"). Thus, the strong influence of the crystal environment on the distance between the coordinating Si and O centers in $\{[\mathbf{1b}(thf)]\cdot thf\}_K$ is evidence that bishomoaromatic compound **1b** forms only a weak complex with thf. Computations for model compound [**1c**(thf)] resulted in a complexation energy of 2.4 kcal mol^{-1}. The weakness of their thf complexes, as will be demonstrated subsequently, is a consequence of the strength of homoaromaticity in compounds of type **1**; thus, this strength gains its first experimental support.

Weak bishomoaromatics of type **3** [Eq. (6)/(7)] form strong complexes with ether compounds, as has been demonstrated by Müller et al. for complexes of **3a** and **3b**.[1d] A complexation energy of 28.7 kcal mol^{-1} was computed for [**3a**(OMe_2)], and complex [**3b**$\{O(C_2D_5)_2\}$] was identified as a siloxonium ion by means of NMR spectroscopy. Our own computations for [**3c**(thf)], which is more suitable for comparisons with complexes of type [**1**(thf)], gave a complexation energy of 42.6 kcal mol^{-1} and a bishomoaromatic stabilization for **3c** of just 3.4 kcal mol^{-1}. The weak stabilization of **3c** relative to **1c** is primarily based on the absence of charge separation in **3c***, but also on the unequal electronegativities of those centers participating in cyclic delocalization. Isoelectronic **4** [Eq. (8)], which has centers of equal electronegativity, is stabilized by 19.6 kcal mol^{-1} relative to **4***.

We regard the kinetic stability of **1b** as another experimental indication of the strength of bishomoaromatic compounds of type **1**. Compound **1b** does not isomerize to its classical isomer **2** even after several hours at 135 °C, despite the fact that the latter is thermodynamically more stable.[13] The latter follows from the quantitative formation of **2** from **1b** at 25 °C within hours in the presence of a catalytic amount of thf. The strong bishomoaromaticity would have to be sacrificed during the uncatalyzed isomerization of **1b** to **2**, which can only take place intramolecularily because of the bulky substituents. Computations show that **1a*** and **1c*** are the transition states of the conversions of **1a** and **1c**, respectively, into their classical isomers of type **2**.

 © 2006 Wiley-VCH Verlag GmbH & Co. KGaA, Weinheim

Thus, charge separation in the reference molecule is an essential reason for the strength of the neutral homoaromatics described here. Molecules of type **5** are homoaromatics of even greater strength. At the level of theory employed in this work the parent compound **5a** is stabilized by 50.3 kcal mol^{-1} relative to **5a*** [Eq. (10)].

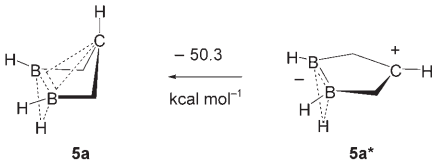

(10)

Received: May 24, 2006
Published online: September 22, 2006

Keywords: aromaticity · boron · density functional calculations · heterocycles · silicon

[1] a) R. V. Williams, *Chem. Rev.* **2001**, *101*, 1185, and references therein; b) D. Scheschkewitz, M. Hofmann, A. Ghaffari, P. Amseis, C. Präsang, W. Mesbah, G. Geiseler, W. Massa, A. Berndt, *J. Organomet. Chem.* **2002**, *646*, 262; c) Y. Sahin, A. Ziegler, T. Happel, H. Meyer, M. J. Bayer, H. Pritzkow, W. Massa, M. Hofmann, P. von R. Schleyer, W. Siebert, A. Berndt, *J. Organomet. Chem.* **2003**, *680*, 244; d) J. Schuppan, B. Herrschaft T. Müller, *Organometallics* **2001**, *20*, 4584, and references therein.

[2] a) P. K. Freeman, *J. Org. Chem.* **2005**, *70*, 1998, and references therein; D. A. Hrovat, E. C. Brown, R. V. Williams, H. Quast, W. T. Borden, *J. Org. Chem.* **2005**, *70*, 2627, and references therein; F. Stahl, P. von R. Schleyer, H. Jiao, H. F. Schaefer III, K. Chen, N. L. Allinger, *J. Org. Chem.* **2002**, *67*, 6599, and references therein; b) P. J. Fagan, E. G. Burns, J. C. Calabrese, *J. Am. Chem. Soc.* **1988**, *110*, 2979; P. J. Fagan, W. A. Nugent, J. C. Calabrese, *J. Am. Chem. Soc.* **1994**, *116*, 1880; C. Balzereit, H.-J. Winkler, W. Massa, A. Berndt, *Angew. Chem.* **1994**, *106*, 2394; *Angew. Chem. Int. Ed. Engl.* **1994**, *33*, 2306; c) P. K. Freeman, J. K. Pugh, *J. Org. Chem.* **2000**, *65*, 6107, and references therein; d) E. D. Jemmis, A. K. Phukan, H. Jiao, U. Rosenthal, *Organometallics* **2003**, *22*, 4958, and references therein; e) J. M. Schulman, R. L. Disch, P. von R. Schleyer, M. Bühl, M. Bremer, W. Koch, *J. Am. Chem. Soc.* **1992**, *114*, 7897; f) S. Olivella, N. Lopez, *Chem. Eur. J.* **2001**, *7*, 3951.

[3] Homoborirenes[4] were the first neutral homoaromatics to be characterized experimentally. The homoaromatic stabilization energy of their parent compound is computed to be 7.3 kcal mol^{-1} by using an isodesmic equation with boretane, cyclobutene, boracyclobutene, and cyclobutane.

[4] R. Wehrmann, H. Klusik, A. Berndt, *Angew. Chem.* **1984**, *96*, 369; *Angew. Chem. Int. Ed. Engl.* **1984**, *23*, 369; C. Pues, G. Baum, W. Massa, A. Berndt, *Z. Naturforsch. B* **1988**, *43*, 275.

[5] At the level of theory used for **IIa**; at the MP2/6-31G*//6-31G* level a value of 22.0 kcal mol^{-1} was computed.[2e]

[6] G. E. Herberich, H. W. Marx, T. Wagner, *Chem. Ber.* **1994**, *127*, 2135, and references therein.

[7] Crystal structure analysis: {[**1b**(thf)]·thf}$_K$: a colorless platelet ($0.40\times0.25\times0.05$ mm^3) was measured on an Stoe IPDS area detector system at −80 °C with Mo$_{K\alpha}$ radiation. $C_{37}H_{66}B_2O_2Si_3$, $M_r = 648.49$, triclinic, space group $P\bar{1}$, $Z = 2$, $a = 1068.6(1)$, $b = 1105.5(1)$, $c = 1808.8(2)$ pm, $\alpha = 81.81(1)$, $\beta = 85.58(1)$, $\gamma = 69.56(1)$°, $V = 1981.0(3)\times10^{-30}$ m^3, $\rho_{calcd} = 1.088$ g cm^{-3}, $\mu = 0.125$ mm^{-1}, total of 19640 reflections up to $\theta = 26.09$°, 7231 independent, $3425 > 4\sigma(F)$. The structure was solved with direct methods and refined against all F_o^2 with full matrix, non-H atoms with anisotropic displacement parameters. Hydrogen atoms on boron, C1, and C2 were freely refined, and the remaining ones were placed at calculated positions with displacement parameters set to 1.2 and 1.5 (CH_3) times U_{eq}(C); $wR_2 = 0.1298$, $R = 0.0539$. **1b**·$^1/_2$ toluene: a yellow block ($0.20\times0.15\times0.10$ mm^3) was measured with an Stoe IPDS-II area detector system at −80 °C with Mo$_{K\alpha}$ radiation. $C_{32.5}H_{54}B_2Si_3$, $M_r = 550.65$, triclinic, space group $P\bar{1}$, $Z = 2$, $a = 981.8(1)$, $b = 1076.1(1)$, $c = 1796.0(2)$ pm, $\alpha = 81.55(1)$, $\beta = 83.77(1)$, $\gamma = 66.81(1)$°, $V = 1722.6(3)\times10^{-30}$ m^3, $\rho_{calcd} = 1.062$ g cm^{-3}, $\mu = 0.157$ mm^{-1}. 29386 reflections up to $\theta = 26.24$°, 6907 independent, $5002 > 4\sigma(F)$. Structure solution and refinement analogous to {[**1b**(thf)]·thf}$_K$ with $wR_2 = 0.1044$, $R = 0.0394$. Per molecule **1b** half a molecule of toluene is found, which is disordered over a center of symmetry. CCDC-608193 ({[**1b**(thf)]·thf}$_K$) and CCDC-608194 (**1b**·$^1/_2$ toluene) contain the supplementary crystallographic data for this paper. These data can be obtained free of charge from The Cambridge Crystallographic Data Centre via www.ccdc.cam.ac.uk/data_request/cif.

[8] For this purpose {[**1b**(thf)]·thf}$_K$ is treated for about 30 minutes with diethyl ether at −100 °C, and the supernatant solution is removed with a cannula. The above procedure is repeated twice to give the product in about 60% yield, which contains only one equivalent of thf according to ^{1}H NMR spectroscopy. This procedure provides a route to obtain **1b** free of thf and impurities of **2** since the complex [**1b**(thf)] isomerizes considerably slower to **2** than [**1b**(thf)·thf]. All volatile components are removed in vacuo from a solution of [**1b**(thf)] in toluene within one hour, and the residue is crystallized from hot toluene. For selected physical data for **1b**, see the Supporting Information.

[9] All structures were optimized at the B3LYP/6-311 + G** level of theory. Relative energies were computed with Gaussian 03 at the B3LYP/6-311 + G**//B3LYP/6-311 + G** + ZPE(B3LYP/6-311 + G**) level (Gaussian 03 (Revision B.03): M. J. Frisch et al.; see the Supporting Information). Computations with a self-consistent reaction field are based on the polarizable continuum model (PCM) method with parameters for water and universal force field (UFF) atomic radii.

[10] W. A. Burns, K. R. Leopold, *J. Am. Chem. Soc.* **1993**, *115*, 11622; S. W. Reeve, W. A. Burns, F. J. Lovas, R. D. Suenram, K. R. Leopold, *J. Phys. Chem.* **1993**, *97*, 10630; related BF_3 complexes of haloacetonitriles: J. A. Phillips, J. A. Halfen, J. P. Wrass, C. C. Knutson, C. J. Cramer, *Inorg. Chem.* **2006**, *45*, 722.

[11] N. Auner, J. Grobe, T. Müller, H. W. Rathmann, *Organometallics* **2000**, *19*, 3476, and references therein.

[12] H. Jiao, P. von R. Schleyer, *J. Am. Chem. Soc.* **1994**, *116*, 7429; V. Jonas, G. Frenking, M. T. Reetz, *J. Am. Chem. Soc.* **1994**, *116*, 8741, and references therein.

[13] Compound **1c** is computed to be 6.6 kcal mol^{-1} higher in energy than its classical isomer at the level of theory employed in this work.[9]

 © 2006 Wiley-VCH Verlag GmbH & Co. KGaA, Weinheim

Antisense Agents

DOI: 10.1002/anie.200602346

An Anticoagulant with Light-Triggered Antidote Activity**

Alexander Heckel, Maximilian C. R. Buff, Marie-Sophie L. Raddatz, Jens Müller, Bernd Pötzsch, and Günter Mayer**

Drug-inhibiting antidotes are helpful tools for the prevention and treatment of unwanted side effects caused by overdosing. These are of particular importance in the case of anticoagulants, the overdosing of which may induce life-threatening bleeding. Among the available anticoagulants, unfractionated heparin is the only one that can be effectively neutralized by a specific antidote. The lack of a specific antidote is a serious disadvantage of all novel anticoagulants (e.g. synthetic heparin, factor Xa, and thrombin inhibitors) even though they are more effective antithrombotics and possess several other advantages over unfractionated heparin.[1] As a consequence unfractionated heparin remains the anticoagulant of choice for patients with a high risk of bleeding or in clinical situations in which rapid reversal of the anticoagulant activity is required, although its use is associated with potential drawbacks including immune reactions.

An alternative approach to the development of antidotes for anticoagulants was introduced recently by Sullenger and co-workers.[2] They used aptamers that target factor IXa of the blood-clotting cascade as effective anticoagulant. Aptamers are short, single-stranded nucleic acids that fold into well-defined three-dimensional shapes.[3] They bind with high affinity and specificity to their respective target molecules and can be used, for example, as potent inhibitors. For the development of an antidote, Sullenger took advantage of the inherent properties of nucleic acids and developed an antisense-based antidote molecule that is able to anneal to the aptamer and thus reverse its inhibitory function.

Another aptamer with anticoagulant activity is the 15mer single-stranded DNA molecule $\mathbf{A_W}$ (Scheme 1a) that binds to and inactivates thrombin, which is a key protein in the blood-clotting cascade.[4] The antithrombin aptamer folds under physiological conditions into a stable G-quadruplex structure and consists of six thymidine and nine guanosine nucleotides. In our studies on the development of methods to control biological processes spatiotemporally with light, we have shown that aptamer activity can be triggered by light after the active site has been temporarily blocked with a photolabile group[5] or the formation of the active conformation of the aptamer has been prevented by modification of a key residue.[6]

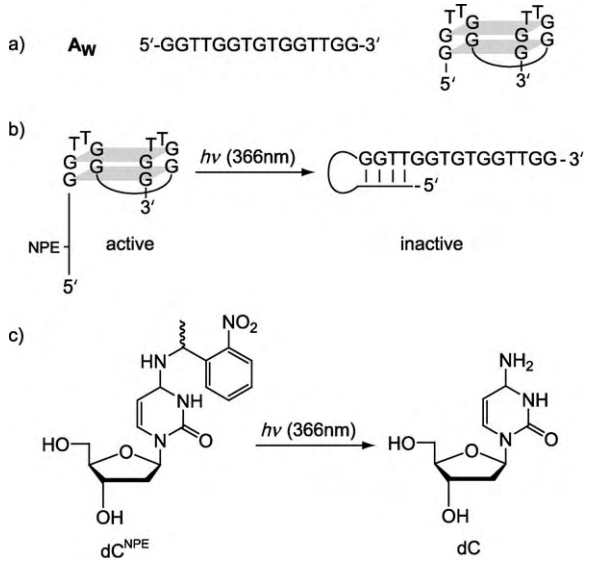

Scheme 1. a) The aptamer $\mathbf{A_W}$ binds thrombin selectively and can act as anticoagulant. b) Our concept of an aptamer that contains its own antidote (in an inactive form). The antidote activity is triggered by light irradiation. c) The "caged" nucleic acid residue dC^{NPE}, which acts as a temporary mismatch, synthesized for this purpose. NPE = 1-(2-nitrophenyl)ethyl.

Herein we describe the development of a single oligonucleotide that contains both an aptamer region and a temporarily inactivated "caged" antisense region in the one molecule and can hence act as both an anticoagulant and its own antidote, the latter function being triggered by light. We assumed that variants of the aptamer that bear an elongated 5′- or 3′-region that is complementary to the G-quadruplex sequence are inactive because they are locked in a hairpin conformation rather than folded into the active G-quadruplex (Scheme 1b). However, if the antisense region contains "temporary mismatches",[7] the hairpin is not formed until the molecule is irradiated and the photolabile group is removed.

To ascertain the ideal length of the antisense region we synthesized the aptamer variants $\mathbf{A_1}$–$\mathbf{A_3}$ (Figure 1a). The respective antisense regions are linked to the 5′-end of $\mathbf{A_W}$ by

[*] Dr. A. Heckel, Dipl.-Chem. M. C. R. Buff, Dipl.-Chem. M.-S. L. Raddatz, Dr. G. Mayer
Life and Medical Sciences (LIMES)
Program Unit Chemical Biology and Medicinal Chemistry
Kekulé Institute for Organic Chemistry and Biochemistry
University of Bonn
Gerhard-Domagk-Strasse 1, 53121 Bonn (Germany)
Fax: (+49) 228-73-4809
E-mail: heckel@uni-bonn.de
gmayer@uni-bonn.de
Dr. J. Müller, Prof. Dr. B. Pötzsch
Institute for Experimental Hematology and Transfusion Medicine
University Hospital Bonn
Sigmund-Freud-Strasse 25, 53105 Bonn (Germany)

[**] This work was made possible by grants of the Fonds der Chemischen Industrie (for A.H. and G.M.) and by an Emmy Noether Fellowship (DFG) for A.H. The authors thank Prof. M. Famulok for his continuing and encouraging support.

Supporting information for this article is available on the WWW under http://www.angewandte.org or from the author.

InterScience
© 2006 Wiley-VCH Verlag GmbH & Co. KGaA, Weinheim

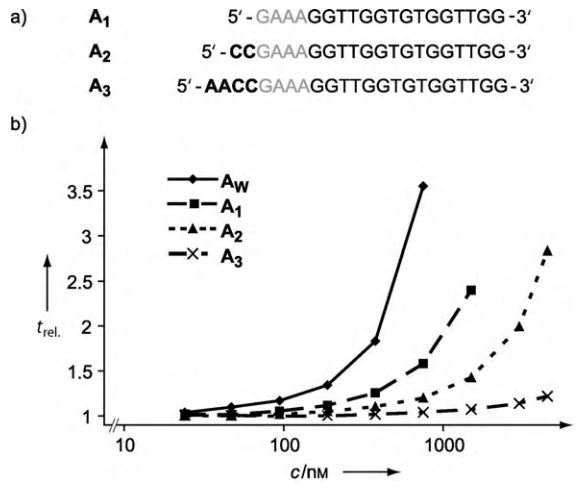

Figure 1. a) The sequence of the 5′-end-elongated aptamers $\mathbf{A_1}$–$\mathbf{A_3}$. b) Results of blood-clotting experiments with the aptamers $\mathbf{A_W}$ and $\mathbf{A_1}$–$\mathbf{A_3}$ (relative blood-clotting time versus aptamer concentration, see the Supporting Information for experimental details).

a GAAA sequence, which builds a stable GNRA tetraloop motif (N = any nucleotide, R = purine). We then performed filter-binding experiments with $\mathbf{A_1}$–$\mathbf{A_3}$ to determine which of the variants are still able to bind to thrombin (Table 1). The

Table 1: Dissociation constants (in nM) of aptamer variants determined by filter-binding experiments.

	Without irradiation	With irradiation[a]
$\mathbf{A_W}$	124 ± 16	n.d.
$\mathbf{A_1}$	155 ± 23	n.d.
$\mathbf{A_2}$	333 ± 44	n.d.
$\mathbf{A_3}$	> 5000	n.d.
$\mathbf{A_4}$	166 ± 12	> 5000
$\mathbf{A_5}$	297 ± 44	> 500

[a] n.d. = not determined.

elongation of the $\mathbf{A_W}$ aptamer with the tetraloop-forming stretch ($\mathbf{A_1}$) results in a slightly decreased affinity. The addition of two further dC nucleotides ($\mathbf{A_2}$) decreases the affinity of the aptamer even further, and almost no affinity was detected after addition of two more dA nucleotides ($\mathbf{A_3}$).[8] Thus, we conclude that already in the aptamer variant $\mathbf{A_3}$, the hairpin rather than the G-quadruplex conformation is predominant.

Furthermore, we analyzed which of the aptamer variants inhibits thrombin-mediated blood clotting in human plasma. As depicted in Figure 1b, aptamer $\mathbf{A_1}$ is still active. However, in comparison with $\mathbf{A_W}$, the same effect is obtained only at higher concentrations. This result has to be kept in mind because even with a completely inactive antisense region the resulting aptamer can only be as effective as $\mathbf{A_1}$. Aptamer $\mathbf{A_2}$ showed only very little remaining activity, and $\mathbf{A_3}$ was found to be inactive within error limits. Thus, the data obtained from the blood-clotting studies are in good accord with the results observed in the interaction studies.

On the basis of these data we decided to extend our toolbox of "caged" deoxynucleotides that can be activated by light to the residue dC^{NPE} (see Scheme 1c).[9] A protected phosphoramidite of dC^{NPE} was used to synthesize the caged aptamer–antidote chimeras $\mathbf{A_4}$ and $\mathbf{A_5}$ (Figure 2a; see the Supporting Information for synthetic details).

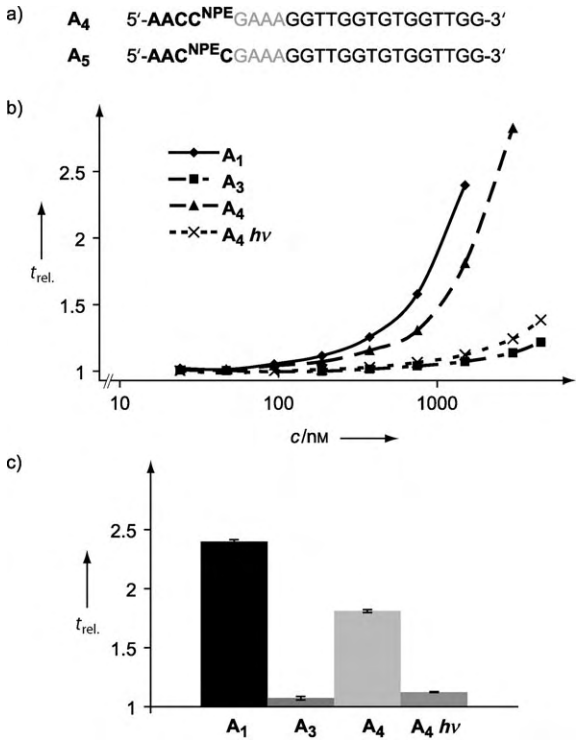

Figure 2. a) The sequence of the caged aptamer–antidote chimeras $\mathbf{A_4}$ and $\mathbf{A_5}$. b) Results of the blood-clotting experiments with the aptamers $\mathbf{A_1}$, $\mathbf{A_3}$, and $\mathbf{A_4}$ (before and after irradiation, relative blood-clotting time versus aptamer concentration, see the Supporting Information for experimental details). c) For a better comparison, the values $t_{rel.}$ in (b) are shown at an aptamer concentration of 1500 nM.

$\mathbf{A_4}$ and $\mathbf{A_5}$ were analyzed for their ability to bind to thrombin and to inhibit thrombin-dependent blood clotting. As demonstrated in Figure 2b and c, $\mathbf{A_4}$ is indeed able to prolong the blood-clotting time in a concentration-dependent manner and with only slightly less efficiency than $\mathbf{A_1}$. As anticipated, $\mathbf{A_4}$ becomes inactive upon irradiation—except at very high concentrations for which some remaining activity could be detected. $\mathbf{A_5}$, however, remained inactive before and after irradiation (data not shown). Circular dichroism (CD) spectra of the aptamers in this study can be found in the Supporting Information. From a photochemical standpoint, it was interesting for us to see how well the dC^{NPE} residue performed in the photodeprotection step. Generally, one might have anticipated from the literature that the removal of the NPE group would create problems because of the often-encountered difficulty to photocleave C–N bonds.[10] However, with our experimental setup (360 nm from three UV LEDs of ca. 100 mW each), 100 pmol of $\mathbf{A_4}$ could be deprotected in 7 s, and the deprotection step was remarkably clean.

 © 2006 Wiley-VCH Verlag GmbH & Co. KGaA, Weinheim

For the experiments discussed so far in the text, the irradiation of the caged aptamers was performed before the beginning of the experiment. Thus it was unclear whether a preformed complex of $\mathbf{A_4}$ and thrombin could also be destroyed by irradiation. Figure 3 shows the respective blood-clotting and filter-binding assays, which show that the photodeactivation also functions when $\mathbf{A_4}$ is already bound to thrombin—a fact that will be important for applications in vivo.

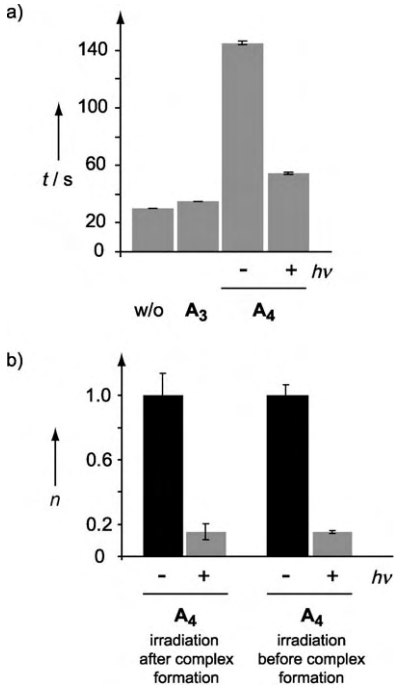

Figure 3. a) Results of blood-clotting assays in which the complex of thrombin and $\mathbf{A_4}$ was irradiated, as well as control experiments with $\mathbf{A_3}$ and without (w/o) aptamer (concentration of aptamer: 3 μM). b) Results of filter-binding assays in which the irradiation was performed before and after formation of the complex with thrombin (*y* axis: relative amount of $\mathbf{A_4}$ bound, concentration of thrombin 150 nM).

In conclusion, after having demonstrated that it is possible to activate an aptamer with light,[5,6] we have now demonstrated that deactivation with light is also possible by incorporating a caged antisense region. Before photodeactivation, the caged chimera showed only about half of the activity of the unmodified wild-type aptamer, but this activity can easily be compensated by increasing the concentration. It is more important that the aptamer becomes virtually inactive upon irradiation. As before,[6] the location of the caged residue (in this case the caged dC^{NPE}) is very important. The new aptamer described herein combines the advantages of a highly specific anticoagulant with rapid and effective control of its function. These characteristics are of potential benefit to patients who are at high risk of anticoagulant-associated bleeding and in clinical situations in which rapid reversal of the anticoagulant functions is required, such as in anticoagulation of extracorporeal circulation devices. Furthermore, this approach will be of general applicability to control the activity of nucleic acid based modulators of protein function in a spatiotemporal fashion.

Received: June 12, 2006
Published online: September 19, 2006

Keywords: antisense agents · aptamers · blood clotting · caged compounds · DNA

[1] a) J. Hirsh, M. O'Donnell, J. I. Weitz, *Blood* **2005**, *105*, 453–463; b) B. Poetzsch, J. Müller, J. M. Rox, *Transfus. Med. Hemother.* **2006**, *33*, 200–204.
[2] a) C. P. Rusconi, E. Scardino, J. Layzer, G. A. Pitoc, T. L. Ortel, D. Monroe, B. A. Sullenger, *Nature* **2002**, *419*, 90–94; b) C. P. Rusconi, J. D. Roberts, G. A. Pitoc, S. M. Nimjee, R. R. White, G. Quick, Jr., E. Scardino, W. P. Fay, B. A. Sullenger, *Nat. Biotechnol.* **2004**, *22*, 1423–1428.
[3] a) C. Tuerk, L. Gold, *Science* **1990**, *249*, 505–510; b) A. D. Ellington, J. W. Szostak, *Nature* **1990**, *346*, 816–820; c) M. Famulok, G. Mayer, *ChemBioChem* **2005**, *6*, 19–26.
[4] a) L. C. Bock, L. C. Griffin, J. A. Latham, E. H. Vermaas, J. J. Toole, *Nature* **1992**, *355*, 564–566; b) W. X. Li, A. V. Kaplan, G. W. Grant, J. J. Toole, L. L. K. Leung, *Blood* **1994**, *83*, 677–682.
[5] A. Heckel, G. Mayer, *J. Am. Chem. Soc.* **2005**, *127*, 822–823.
[6] G. Mayer, L. Kröck, V. Mikat, M. Engeser, A. Heckel, *ChemBioChem* **2005**, *6*, 1966–1970.
[7] L. Kröck, A. Heckel, *Angew. Chem.* **2005**, *117*, 475–477; *Angew. Chem. Int. Ed.* **2005**, *44*, 471–473.
[8] The same was true for aptamers with two or four more complementary nucleotides (data not shown).
[9] Literature on caged compounds in general and caged oligonucleotides in particular can be found in our recent review article: G. Mayer, A. Heckel, *Angew. Chem.* **2006**, *118*, 5020–5042; *Angew. Chem. Int. Ed.* **2006**, *45*, 4900–4921.
[10] R. O. Schoenleber, B. Giese, *Synlett* **2003**, 501–504.

 © 2006 Wiley-VCH Verlag GmbH & Co. KGaA, Weinheim

Brønsted Acid Catalysis

DOI: 10.1002/anie.200601832

Remarkably Low Catalyst Loading in Brønsted Acid Catalyzed Transfer Hydrogenations: Enantioselective Reduction of Benzoxazines, Benzothiazines, and Benzoxazinones**

Magnus Rueping, Andrey P. Antonchick, and Thomas Theissmann*

The asymmetric hydrogenation of imines represents an important topic in organic synthesis and catalysis, and many highly enantioselective processes based on chiral metal complexes have been described.[1] However, so far only few catalysts have been reported to catalyze the hydrogenation of cyclic imines, such as benzoxazine, benzothiazine, or benzoxazinone derivatives,[2,3] which is surprising since the corresponding dihydro-2*H*-benzoxazines, dihydro-2*H*-benzothiazines, and dihydro-2*H*-benzoxazinones represent the structural motif of various natural products with interesting biological activities. These heterocycles have also been employed as important chiral building blocks in the synthesis of many pharmaceuticals, such as promising antidepressants, calcium antagonists, as well as anti-inflammatory, antinociceptive, antibacterial, and antimicrobial agents.[4]

In view of the importance of this class of molecules, together with our recently developed biomimetic, enantioselective Brønsted acid catalyzed transfer hydrogenation of ketimines[5,6] and quinolines,[7] we believed it might be possible to extend our procedure for chiral ion-pair catalysis to the reduction of benzoxazines and benzothiazines. This would not only be the first example of an organocatalytic reduction of these substrates, but would, more importantly, give direct access to the valuable optically active dihydro-2*H*-benzoxazines or 2*H*-benzothiazines [Eq. (1)].

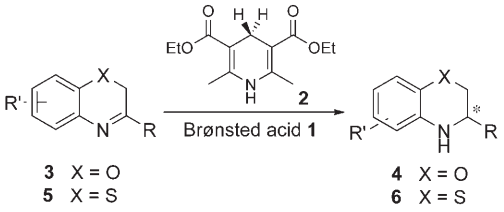

(1)

[*] Prof. M. Rueping, Dr. A. P. Antonchick, T. Theissmann
Degussa Endowed Professorship
Institute for Organic Chemistry und Chemical Biology
Johann Wolfgang Goethe-Universität Frankfurt am Main
Max-von-Laue Strasse 7, 60438 Frankfurt am Main (Germany)
Fax: (+49) 69-798-29248
E-mail: m.rueping@chemie.uni-frankfurt.de

[**] The authors acknowledge Degussa AG for generous support.

Supporting information for this article is available on the WWW under http://www.angewandte.org or from the author.

We reasoned that, similar to several biomimetic transfer hydrogenations, benzoxazines **3** and benzothiazines **5** would be activated by catalytic protonation through Brønsted acid **1** (Scheme 1). This activation would generate a chiral ion pair **A**, which would subsequently undergo a hydride transfer addition from Hantzsch dihydropyridine (HEH) **2** to give the desired dihydro-2*H*-benzoxazine **4** and dihydro-2*H*-benzothiazine **6** as well as the regenerated Brønsted acid **1**.

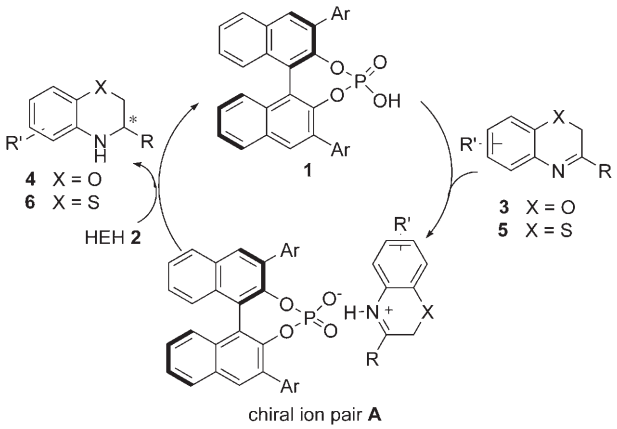

Scheme 1. Proposed catalytic cycle for the Brønsted acid catalyzed hydrogenation of benzoxazines and benzothiazines.

Hence, our initial investigations concentrated on finding the appropriate chiral Brønsted acid catalyst[5–10] **1** for the transformation of benzoxazine **3a** to the corresponding dihydro-2*H*-benzoxazine **4a** (Table 1). From this survey the best result with respect to reactivity, yield, and selectivity was obtained with the Brønsted acid catalyst **1f**, which provided the 3-phenyl-substitued product **4a** in 96% *ee* (Table 1, entry 6). Other Brønsted acid catalysts that were tested gave **4a** with lower enantioselectivity (Table 1, entries 1–5), which is in agreement with our recently developed Brønsted acid catalyzed ketimine[5] and quinoline reductions[7] and Strecker reactions.[10]

Table 1: Survey of chiral Brønsted acid catalysts for the transfer hydrogenation of benzoxazine **3a**.[a]

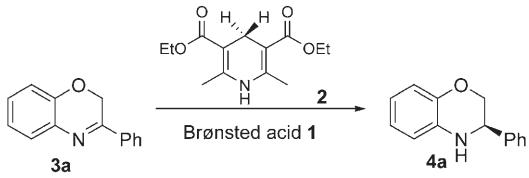

Entry		Ar	Yield [%][b]	*ee* [%][c]
1	**1a**	phenyl	94	6
2	**1b**	4-biphenyl	96	41
3	**1c**	1-naphthyl	95	74
4	**1d**	2-naphthyl	93	38
5	**1e**	3,5-(CF_3)-phenyl	94	61
6	**1f**	9-phenanthryl	**91**	**96**

[a] Reaction conditions: **3a**, **2** (1.25 equiv), and **1** (10 mol%) at 60°C in benzene. [b] Yield of isolated product after column chromatography. [c] Determined by HPLC analysis using a Chiralcel OD-H column.

 © 2006 Wiley-VCH Verlag GmbH & Co. KGaA, Weinheim

Having established a highly enantioselective transfer hydrogenation of benzoxazinone **3a**, we evaluated the catalyst loading (Table 2). Starting from 10 mol% of chiral

Table 2: Catalyst loading of the Brønsted acid catalyzed transfer hydrogenation.[a]

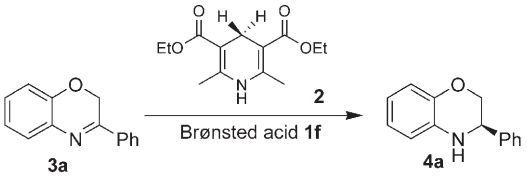

Entry	Loading of **1f** [%]	Yield [%][b]	*ee* [%][c]
1	10	91	96
2	5	95	96
3	2	93	96
4	1	94	96
5	0.1	95	96
6	0.01	90	93

[a] Reaction conditions: **3a**, **2** (1.25 equiv), and **1f** at 60° in benzene. [b] Yield of isolated product after column chromatography. [c] Determined by HPLC analysis using a Chiralcel OD-H column.

Brønsted acid catalyst **1f** we were able to decrease the catalyst loading to 0.01 mol% (substrate/catalyst ratio 10000:1) without a considerable loss in reactivity and selectivity (Table 2, entries 1–6). Even with 0.01 mol% of Brønsted acid **1f** the corresponding 2*H*-dihydro-benzoxazine **4a** could be isolated in a remarkable yield of 90% with 93% *ee* (Table 2, entry 6). It should be noted that this is, to date, the lowest catalyst loading to be reported for an organocatalytic enantioselective transformation.[11] Furthermore, if compared to enantioselective metal-catalyzed reductions of heterocyclic systems, which employ 0.5–5 mol%,[2,3] our metal-free transformation requires much lower amounts of catalyst, thus demonstrating the high potential of binol phosphates and Brønsted acid catalysts in general.

Our further examination of this transformation focused on the solvent employed since our earlier experiments suggested that solvent effects can play a crucial role in obtaining both good reactivity and selectivity.[5,7,10] While hydrogenations could be performed in all the solvents tested (Table 3), the best selectivities were obtained in chlorinated solvents at room temperature (Table 3, entries 2 and 3), followed by toluene and benzene (Table 3, entries 4 and 5) and tetrahydrofuran (Table 3, entry 6).

With the optimized conditions in hand we explored the scope of the Brønsted acid catalyzed transfer hydrogenation of 3-aryl-substituted benzoxazines **3a–f** (Table 4). In general, differently substituted 3-aryl dihydro-2*H*-benzoxazines **4a–f** (bearing either electron-withdrawing or electron-donating groups) were obtained in good yields and with excellent enantioselectivities (> 98% *ee*; Table 4, entries 1–6).

Next, we examined the extension of the hydrogenation procedure to benzothiazines **5** [Eq. (1)]. Gratifyingly, the reduction proceeded with similar enantiocontrol and without a considerable loss of reactivity (Table 5). The corresponding

Table 3: Solvent survey of the Brønsted acid catalyzed transfer hydrogenation of benzoxazine **3a**.[a]

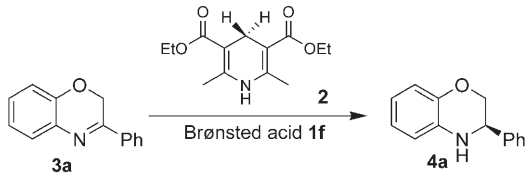

Entry	Solvent	Yield [%][c]	*ee* [%][d]
1	CCl_4	93	95
2	**$CHCl_3$**[b]	**95**	**98**
3	CH_2Cl_2[b]	95	97
4	PhH	91	96
5	PhMe	96	96
6	THF	88	96

[a] Reaction conditions: **3a**, **2** (1.25 equiv), and **1f** at 60°C. [b] At room temperature. [c] Yield of isolated product after column chromatography. [d] Determined by HPLC analysis using a Chiralcel OD-H column.

Table 4: Scope of the enantioselective Brønsted acid catalyzed hydrogenation of benzoxazines.[a]

Entry	Dihydrobenzoxazine **4**	Yield [%][b]	*ee* [%][c]
1	**4a** 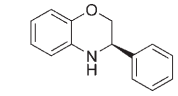	95	98
2	**4b** 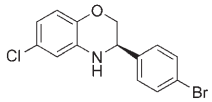	93	> 99
3	**4c** 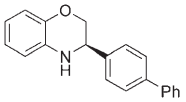	94	98
4	**4d** 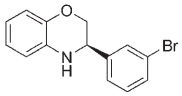	93	98
5	**4e** 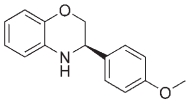	92	98
6	**4f** 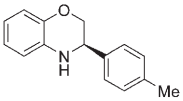	95	> 99

[a] Reaction conditions: **3**, **2** (1.25 equiv), and **1f** (0.1 mol%)[12] in $CHCl_3$ at ambient temperature. [b] Yield of isolated product after column chromatography. [c] Determined by HPLC analysis using a Chiralcel OD-H column.

3-aryl dihydro-2*H*-benzothiazines **6a–f** could be isolated with excellent enantioselectivities (93–99% *ee*; Table 5, entries 1–6). The developed procedure represents the first enantioselective hydrogenation of benzothiazines, and it demonstrates the advantage of this organocatalytic hydrogenation over the application of most metal catalysts, which are known to be poisoned by sulfur-containing substrates.

Having established a general and highly enantioselective transfer hydrogenation of 3-aryl-substituted benzoxazines **3** and benzothiazines **5**, we also decided to apply this efficient

 © 2006 Wiley-VCH Verlag GmbH & Co. KGaA, Weinheim

Table 5: Scope of the Brønsted acid catalyzed enantioselective hydrogenation of benzothiazines [see Eq. (1)].[a]

Entry	Dihydrobenzothiazine **6**	Yield [%][b]	*ee* [%][c]
1	**6a** 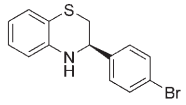	87	>99
2	**6b** 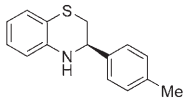	50	96
3	**6c** 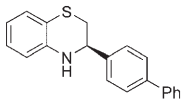	78	94
4	**6d** 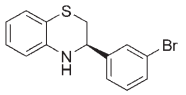	51	94
5	**6e** 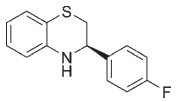	70	>99
6	**6f** 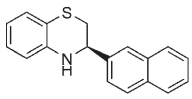	54	93

[a] Reaction conditions: **5**, **2** (1.25 equiv), and **1f** (1 mol%) in $CHCl_3$ at room temperature. [b] Yield of isolated product after column chromatography. [c] Determined by HPLC analysis using a Chiralcel OD-H column.

Table 6: Scope of the Brønsted acid catalyzed enantioselective hydrogenation of benzoxazinones.[a]

Entry	Dihydrobenzoxazinone **8**	Yield [%][b]	*ee* [%][c]
1	**8a** 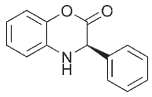	85	98
2	**8b** 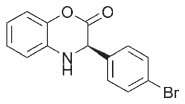	92	>99
3	**8c** 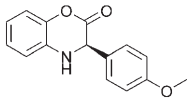	91	>99
4	**8d** 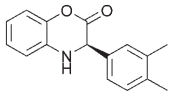	90[d]	>99
5	**8e** 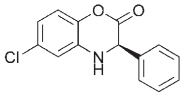	55[d]	96
6	**8f** 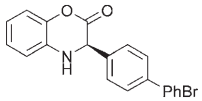	90	98
7	**8g** 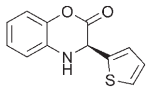	81	90

[a] Reaction conditions: **7**, **2** (1.25 equiv), and **1f** (1 mol%). [b] Yield of isolated product after column chromatography. [c] Determined by HPLC analysis using a Chiralcel OD-H column. [d] Yield of the open-chain amino acid amide after isolation.

methodology to the reduction of benzoxazinones **7** as this would lead to the valuable cyclic aryl-substituted amino acid derivatives **8** [Eq. (2)].

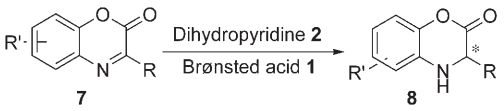

(2)

The synthesis of cyclic alkyl-substituted dihydrobenzoxazinone derivatives has been reported before and can be achieved either by reduction of the corresponding benzoxazinones or by starting from the readily available chiral amino acid precursors.[13] However, our interest lay in the development of an enantioselective hydrogenation of aryl-substituted benzoxazinones leading to aryl glycine derivatives which are both desirable and generally more difficult to prepare. Hence, we applied our organocatalytic enantioselective hydrogenation procedure to 3-aryl-substituted benzoxazinones **7a**–**7g** by using the same reaction conditions (Table 6). We were able to isolate the corresponding aryl glycine derivatives with electron-withdrawing and electron-donating substituents (**8a**–**f**; Table 6, entries 1–6) and heteroaryl glycine derivatives (**8g**; Table 6, entry 7) in good yields and with excellent enantioselectivities (90–99% *ee*).

To demonstrate that the cyclic aryl glycine derivatives can be opened to the corresponding linear amino acid amides without racemization, we tested various reaction conditions. After considerable effort we found that reaction of dihydrobenzoxazinones with pyridin-2-ol in the presence of primary amines results in the formation of amino acid amides without any loss of enantiomeric excess. For example, using these reaction conditions, we could simply convert the cyclic aryl glycine **8d** into amide **9** without observing any racemization (Scheme 2).

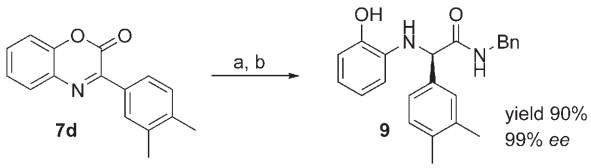

Scheme 2. Synthesis of the aryl glycine amide **9**. a) **7d**, **2** (1.25 equiv), **1f** (1 mol%), $CHCl_3$; b) Pyridin-2-ol (3 equiv), benzylamine (5 equiv), THF, 12 h, room temperature.

Concerning the mechanism, we assume that the first step in the enantioselective hydrogenation is the protonation of the cyclic imine through Brønsted acid **1f**, resulting in the formation of chiral ion pair **A** (Scheme 1), which in turn explains the observed stereochemical outcome.[14] A clarification of the activation is found in Figure 1, which shows a model derived from the X-ray crystal structure of catalyst **1f** and aryl glycine **8a**. Formation of the chiral ion pair[5,7,10] [$(\mathbf{1f})^-\cdot(\mathbf{8})^+$] favors the approach of the hydride from the less

 © 2006 Wiley-VCH Verlag GmbH & Co. KGaA, Weinheim

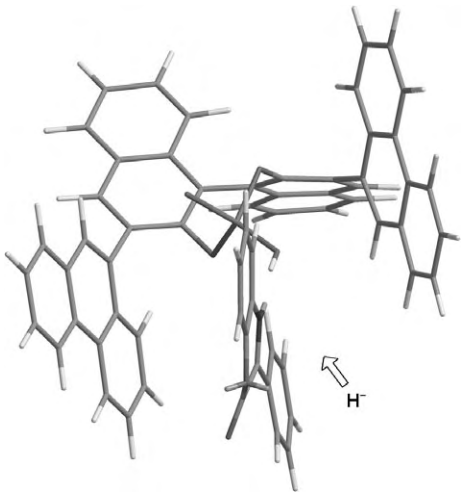

Figure 1. Model for the Brønsted acid catalyzed enantioselective hydride addition.

hindered *Si* face as the *Re* face is effectively shielded by the large phenanthryl group of Brønsted acid **1 f**.

In summary, we have successfully developed a highly efficient Brønsted acid catalyzed transfer hydrogenation of various aryl-substituted benzoxazines, benzothiazines, and benzoxazinones. This method represents the first metal-free reduction of benzoxazines and benzothiazines in general and provides the corresponding dihydro-2*H*-benzoxazine and dihydro-2*H*-benzothiazines in good yields and with excellent enantioselectivities (93–99 % *ee*). Furthermore, we were able to extend this valuable methodology to the enantioselective synthesis of cyclic and linear aryl and heteroaryl glycine derivatives. The presented enantioselective hydrogenations increase the diversity of possible Brønsted acid catalyzed transformations and render binol phosphates as widely applicable catalysts. Attractive features of our ion-pair-catalyzed hydrogenation process include the mild reaction conditions, operational simplicity and practicability, as well as a broad substrate scope which includes sulfur-containing substrates.

Furthermore, it should be highlighted that this organocatalytic procedure allows the lowering of catalyst loading to 0.01 mol % of **1 f** without considerable loss in reactivity and selectivity. This is not only the lowest catalyst amount to be used for an organocatalytic process to date, but more importantly, for the first time, it is a competitive procedure to enantioselective transition-metal-catalyzed hydrogenation processes. Further investigations will be directed toward the design of other efficient Brønsted acid catalysts and Brønsted acid catalyzed reactions.

Received: May 10, 2006
Revised: July 19, 2006
Published online: September 20, 2006

Keywords: binol phosphate · Brønsted acids · enantioselective hydrogenation · Hantzsch dihydropyridine · ion-pair catalysis

[1] For reviews: a) R. Noyori, *Angew. Chem.* **2002**, *114*, 2108; *Angew. Chem. Int. Ed.* **2002**, *41*, 2008; b) W. S. Knowles, *Angew. Chem.* **2002**, *114*, 2096; *Angew. Chem. Int. Ed.* **2002**, *41*, 1998; c) H. U. Blaser, C. Malan, B. Pugin, F. Spindler, H. Steiner, M. Studer, *Adv. Synth. Catal.* **2003**, *345*, 103; d) W. Tang, X. Zhang, *Chem. Rev.* **2003**, *103*, 3029; e) T. Ohkuma, M. Kitamura, R. Noyori in *Catalytic Asymmetric Synthesis*, 2nd ed. (Ed.: I. Ojima), Wiley-VCH, New York, **2000**, chap. 1; f) T. Ohkuma, R. Noyori in *Comprehensive Asymmetric Catalysis*, Suppl. 1 (Eds.: E. N. Jacobsen, A. Pfaltz, H. Yamamoto), Springer, New York, **2004**, S. 43; g) H. Nishiyama, K. Itoh in *Catalytic Asymmetric Synthesis*, 2nd ed. (Ed.: I. Ojima), Wiley-VCH, New York, **2000**, chap. 2; recent examples of highly enantioselective metal-catalyzed hydrogenations of imines: h) R. Kadyrov, T. H. Riermeier, *Angew. Chem.* **2003**, *115*, 5630; *Angew. Chem. Int. Ed.* **2003**, *42*, 5472; i) C. Moessner, C. Bolm, *Angew. Chem.* **2005**, *117*, 7736; *Angew. Chem. Int. Ed.* **2005**, *44*, 7564; j) Q. Yang, G. Shang, W. Gao, J. Deng, X. Zhang, *Angew. Chem.* **2006**, *118*, 3916; *Angew. Chem. Int. Ed.* **2006**, *45*, 3832; for efficient organocatalytic, enantioselective hydrosilylations of ketimines: k) A. V. Malkov, A. J. P. S. Liddon, P. Ramirez-Lopez, L. Bendova, D. Haigh, P. Kocovsky, *Angew. Chem.* **2006**, *118*, 1460; *Angew. Chem. Int. Ed.* **2006**, *45*, 1432; l) A. V. Malkov, A. Mariani, K. N. MacDougall, P. Kocovsky, *Org. Lett.* **2004**, *6*, 2253; m) F. Iwasaki, O. Omonura, K. Mishima, T. Kanematsu, T. Maki, Y. Matsumura, *Tetrahedron Lett.* **2001**, *42*, 2525.

[2] Metal-catalyzed reductions of benzoxazines: a) R. Noyori, *Acta Chem. Scand.* **1996**, *50*, 380; b) K. Satoh, M. Inenaga, K. Kanai, *Tetrahedron: Asymmetry* **1998**, *9*, 2657; c) Y.-G. Zhou, P.-Y. Yang, X.-W. Han, *J. Org. Chem.* **2005**, *70*, 1679.

[3] For a review on reductions of heteroaromatic compounds: a) F. Glorius, *Org. Biomol. Chem.* **2005**, *3*, 4171; metal-catalyzed enantioselective quinoline reductions: b) W.-B. Wang, S.-M. Lu, P.-Y. Yang, X.-W. Han, Y.-G. Zhou, *J. Am. Chem. Soc.* **2003**, *125*, 10536; c) S.-M. Lu, X. W. Han, Y.-G. Zhou, *Adv. Synth. Catal.* **2004**, *346*, 909; d) P.-Y. Yang, Y.-G. Zhou, *Tetrahedron: Asymmetry* **2004**, *15*, 1145; e) L. Xu, K. H. Lam, J. Ji, J. Wu, Q.-H. Fan, W.-H. Lo, A. S. C. Chan, *Chem. Commun.* **2005**, 1390; f) M. T. Reetz, X. Li, *Chem. Commun.* **2006**, 2159.

[4] a) K. S. Brown, C. Djerassi, *J. Am. Chem. Soc.* **1964**, *86*, 2451; b) A. Belattar, J. E. Saxton, *J. Chem. Soc. Perkin Trans. 1* **1992**, 679; c) *Antibiotics and Antiviral Compounds* (Eds.: K. Krohn, H. A. Kirst, H. Maag), VCH, Weinheim, **1993**; d) *Pharmaceutical Substances*, 4th ed. (Eds.: A. Kleemann, J. Engel, B. Kutscher, D. Reichert), Thieme, Stuttgart, New York, **2001**; e) B. Achari, S. B. Mandal, P. K. Dutta, C. Chowdhury, *Synlett* **2004**, 2449; f) J. Ilas, P. S. Anderluh, M. S. Dolenc, D. Kikelj, *Tetrahedron* **2005**, *61*, 7325.

[5] a) M. Rueping, C. Azap, E. Sugiono, T. Theissmann, *Synlett* **2005**, 2367; b) M. Rueping, E. Sugiono, C. Azap, T. Theissmann, M. Bolte, *Org. Lett.* **2005**, *7*, 3781.

[6] For a subsequent optimization of the hydrogenation procedure, see: a) S. Hofmann, A. M. Seayad, B. List, *Angew. Chem.* **2005**, *117*, 7590; *Angew. Chem. Int. Ed.* **2005**, *44*, 7424; b) R. I. Storer, D. E. Carrera, Y. Ni, D. W. C. MacMillan, *J. Am. Chem. Soc.* **2006**, *128*, 84.

[7] a) M. Rueping, A. P. Antonchick, T. Theissmann, *Synlett* **2006**, 1071; b) M. Rueping, A. P. Antonchick, T. Theissmann, *Angew. Chem.* **2006**, *118*, 3765; *Angew. Chem. Int. Ed.* **2006**, *45*, 3683.

[8] a) P. R. Schreiner, *Chem. Soc. Rev.* **2003**, *32*, 289; b) P. M. Pihko, *Angew. Chem.* **2004**, *116*, 2110; *Angew. Chem. Int. Ed.* **2004**, *43*, 2062; c) C. Bolm, T. Rantanen, I. Schiffers, L. Zani, *Angew. Chem.* **2005**, *117*, 1788; *Angew. Chem. Int. Ed.* **2005**, *44*, 1758.

[9] a) T. Akiyama, J. Itoh, K. Yokota, K. Fuchibe, *Angew. Chem.* **2004**, *116*, 1592; *Angew. Chem. Int. Ed.* **2004**, *43*, 1566; b) D.

 © 2006 Wiley-VCH Verlag GmbH & Co. KGaA, Weinheim

Uraguchi, M. Terada, *J. Am. Chem. Soc.* **2004**, *126*, 5356; c) D. Uraguchi, K. Sorimachi, M. Terada, *J. Am. Chem. Soc.* **2004**, *126*, 11804; d) T. Akiyama, H. Morita, J. Itoh, K. Fuchibe, *Org. Lett.* **2005**, *7*, 2583; e) T. Akiyama, Y. Saitoh, H. Morita, K. Fuchibe, *Adv. Synth. Catal.* **2005**, *347*, 1523; f) G. B. Rowland, H. Zhang, E. B. Rowland, S. Chennamadhavuni, Y. Wang, J. C. Antilla, *J. Am. Chem. Soc.* **2005**, *127*, 15696; g) M. Terada, K. Sorimachi, D. Uraguchi, *Synlett* **2006**, 13; h) T. Akiyama, Y. Tamura, J. Itoh, H. Morita, K. Fuchibe, *Synlett* **2006**, 141; i) J. Seayad, A. M. Seayad, B. List, *J. Am. Chem. Soc.* **2006**, *128*, 1087; j) M. Terada, K. Machioka, K. Sorimachi, *Angew. Chem.* **2006**, *118*, 2312; *Angew. Chem. Int. Ed.* **2006**, *45*, 2254.

[10] M. Rueping, E. Sugiono, C. Azap, *Angew. Chem.* **2006**, *118*, 2679; *Angew. Chem. Int. Ed.* **2006**, *45*, 2617.

[11] For organocatalytic transformations with catalyst loadings of less than 0.5 mol%, see: a) P. Vachal, E. N. Jacobsen, *J. Am. Chem. Soc.* **2002**, *124*, 10012; b) S. Saaby, M. Bella, A. K. Jørgensen, *J. Am. Chem. Soc.* **2004**, *126*, 8120; c) S. Shirakawa, K. Yamamoto, M. Kitamura, T. Ooi, K. Maruoka, *Angew. Chem.* **2005**, *117*, 631; *Angew. Chem. Int. Ed.* **2005**, *44*, 625; d) M. Kitamura, S. Shirakawa, K. Maruoka, *Angew. Chem.* **2005**, *117*, 1573; *Angew. Chem. Int. Ed.* **2005**, *44*, 1549, and reference [9j], which appeared during the preparation of this manuscript.

[12] The use of 0.01 mol% catalyst resulted in a loss of 3–6% *ee*. Hence, we decided to report the reactions carried out with 0.1 mol% of Brønsted acid catalyst **1f**. For comparison, metal-catalyzed reductions of heterocyclic compounds usually require 0.5–5 mol% of metal catalyst.[2,3]

[13] Recently, MacMillan and co-workers reported one methyl-substituted example, 3-methyl-2*H*-benzoxazinone, using 10 mol% of catalyst.[6b]

[14] The observed absolute configuration of the products was assigned by comparison of optical rotation and an X-ray crystal structure of compound **8g**.

 © 2006 Wiley-VCH Verlag GmbH & Co. KGaA, Weinheim

Oligosilanes

DOI: 10.1002/anie.200601598

Hydroxy-Substituted Oligosilane Dendrimers: Controlling the Electronic Properties through Hydrogen Bonding

*Ulrike Jäger-Fiedler, Martin Köckerling, Ralf Ludwig, Alexander Wulf, and Clemens Krempner**

Poly and oligosilanes have received considerable attention owing to their unique electronic properties arising from the extensive delocalization of σ-electrons along the silicon backbone.[1] Their intense electronic absorption in the near UV was found to be sensitive to the electronic nature of the substituents and the conformation of the silicon backbone, as reflected in the thermochromism,[2] solvatochromism,[3] and ionochromism[4] of some oligosilanes. Recent studies on linear derivatives with discrete conformations have shown that σ-conjugation is more effective in an *anti*-conformation (Si-Si-Si-Si dihedral angle $\omega = 180°$) than in conformations with small dihedral angles, such as *syn*, *cisoid*, or even *gauche* ($\omega =$ 0–60°).[5] We report herein the synthesis, structure, and remarkable thermochromism of the first hydroxy-substituted oligosilane dendrimers.[6] IR spectroscopic studies supported by density functional theory (DFT) calculations clearly show the electronic properties of these compounds to be determined by the conformation of the silicon backbone, which is controlled by hydrogen bonding.

The hydroxy-substituted dendrimer **3**, which has three identical stereogenic silicon centers has been prepared in two steps (Scheme 1). $MeSi(SiMeCl_2)_3$ (**1**) was treated with 3 equivalents of $KSi(SiMe_3)_2Me$ at −78 °C. The reaction proceeds regio- and diastereoselectively yielding the *l*,*l*-form of **2** as the main product.[7] Hydrolysis of **2** in the presence of $NH_4(NH_2COO)$ gave a racemic mixture of the two possible diastereomers *l*,*u*-**3** and *l*,*l*-**3** (see Supporting Information).

The molecular structures of *l*,*l*-**3** and *l*,*u*-**3** have been determined by X-ray crystallography (Figure 1 and 2).[8] Suitable crystals were grown from THF and *n*-heptane solutions, respectively. The results clearly reveal both compounds to be dimeric in the solid state.[9] In *l*,*l*-**3**, two molecules are connected to each other by six intermolecular hydrogen bonds, forming a cage structure that consists of eight-membered rings (Figure 1). The measured intermolecular O1···O1′ distance and O1-H···O1′ angle are found to be 279.9 pm and 135.3°, respectively. In *l*,*u*-**3**, the steric demand of the dendrimer wings ($-Si(SiMe_3)_2Me$) enforces an arrange-

[*] U. Jäger-Fiedler, Prof. Dr. M. Köckerling, Prof. Dr. R. Ludwig, A. Wulf, Dr. C. Krempner
Institut für Chemie der Universität Rostock
A.-Einstein-Strasse 3a, 18059 Rostock (Germany)
Fax: (+49) 381-498-6382
E-mail: clemens.krempner@uni-rostock.de

Supporting information for this article is available on the WWW under http://www.angewandte.org or from the author.

© 2006 Wiley-VCH Verlag GmbH & Co. KGaA, Weinheim

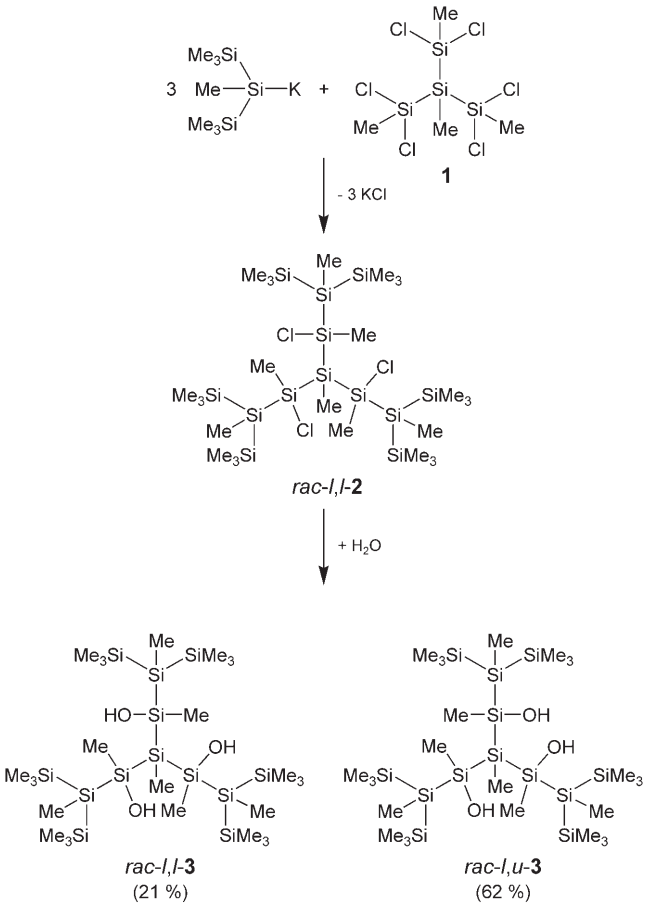

Scheme 1. Synthesis of *l*,*l*-**3** and *l*,*u*-**3**.

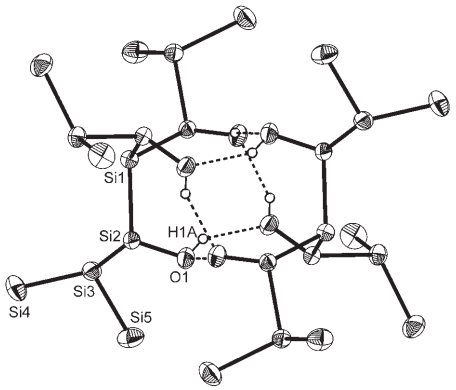

Figure 1. Molecular structure of the hydrogen-bonded dimer *l*,*l*-**3**. The thermal ellipsoids are set at 50% probability (methyl groups are omitted for clarity). Selected bond lengths [Å] and angles [°]: Si2–O1 1.6750(12); O1-Si2-Si1 109.68(5), Si2-Si1-Si2 108.94(2); Si2-Si1-Si2-Si3 83.11(3), Si2-Si1-Si2-Si3 157.43(3), Si1-Si2-Si3-Si4 92.36(3), Si1-Si2-Si3-Si5 147.51(3).

ment in which the non-equivalent hydroxy groups are linked differently to each other by hydrogen bonds. As a result, O1 and O2 are linked by intramolecular hydrogen bonds (O1···O2 280.0 pm), forming a six-membered ring structure. Intermolecular hydrogen bonding between O3′ and O2 or O3 (O2···O3′ 277.5 pm and O3···O3′ 285.2 pm), results in the formation of eight-membered ring motifs (Figure 2). Structural parameters indicate only slight strain in both molecules; the Si–Si distances with 233–238 pm, are in the normal range and the Si–O bond lengths (167–168 pm) are very similar to those found in other OH containing oligosilanes.[10]

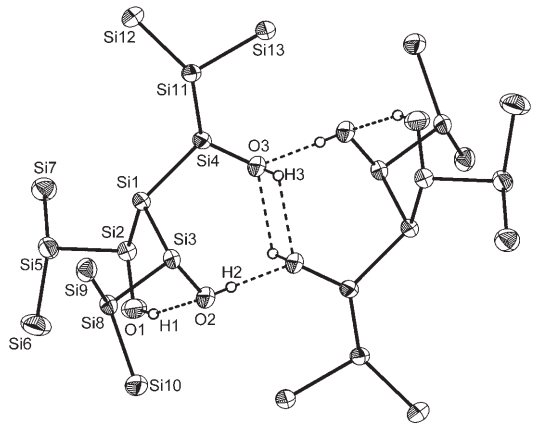

Figure 2. Molecular structure of the hydrogen-bonded dimer *l*,*u*-**3**. The thermal ellipsoids are set at 50% probability (methyl groups omitted for clarity). Selected bond lengths [Å] and angles [°]: Si2–O1 1.6757(15), Si3–O2 1.6782(14), Si4–O3 1.6715(14); O1-Si2-Si1 105.49(6), O2-Si3-Si1 104.82(5), O3-Si4-Si1 107.40(5), Si3-Si1-Si2 101.05(2), Si3-Si1-Si4 109.45(3), Si2-Si1-Si4 113.15(3); Si6-Si5-Si2-Si1 151.1, Si5-Si2-Si1-Si4 115.8, Si2-Si1-Si4-Si11 155.0, Si1-Si4-Si11-Si13 158.0.

Unexpectedly, both diastereomers exhibit different UV absorption behavior; the absorption curves of *l*,*u*-**3**, *l*,*l*-**3** and of the structural analogue $MeSi[SiMe_2Si(SiMe_3)_2Me]_3$ (**4**) are shown in Figure 3. For *l*,*u*-**3**, the intense peak at 282 nm ($\varepsilon = 3.7\times10^4$) with a shoulder near 260 nm is significantly shifted to longer wavelength compared to that of **4** ($\lambda_{max} = 269$ nm, $\varepsilon = 5.2\times10^4$).[11] This red-shift is attributable to reduction in the optical-band-gap resulting from effective interactions between silicon σ and oxygen lone pair nonbonding orbi-

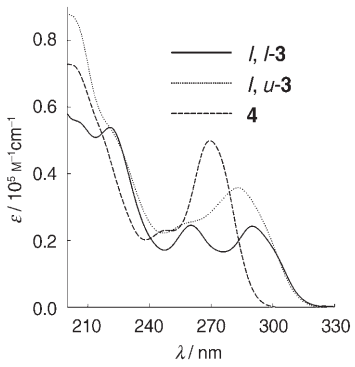

Figure 3. Room temperature UV spectra of *l*,*l*-**3**, *l*,*u*-**3**, and **4** in *n*-heptane ($c = 10^{-5}$ M).

 © 2006 Wiley-VCH Verlag GmbH & Co. KGaA, Weinheim

tals.[12] In striking contrast, *l*,*l*-**3** exhibits two distinct peaks at 260 nm and 290 nm with almost the same intensity ($\varepsilon = 2.5 \times 10^4$). The absorption maximum at 290 nm is not only significantly shifted to longer wavelengths relative to that of the stereoisomer *l*,*u*-**3**, it is also the longest observed to date for heptasilanes. To our knowledge, **3** is the first stereochemical active oligo or polysilane for which the UV spectroscopic behavior differs depending on the configuration.

It is well known that upon increasing the Si-Si-Si-Si dihedral angles, σ-conjugation becomes more effective, and hence the wavelength and intensity of the absorption maximum increase significantly. Consequently, the energy of the σ–σ* transition depends on both electronic and conformational factors. Therefore, the conformation of the heptasilane chains of *l*,*u*-**3** and *l*,*l*-**3**, which are defined by four dihedral angles, has been determined on the basis of the X-ray data (Supporting Information). Owing to the trigonal space group of *l*,*l*-**3**, there are only four different combinations of conformers; *D-D-O-D*, *D-D-O-O*, *D-O-D-O*, and *O-D-O-O* (*D* = deviant, $\omega \approx 150°$; *O* = *ortho*, $\omega \approx 90°$).[13] Note that the dihedral angles found in the heptasilane chains of *l*,*l*-**3** are similar to those of the nonfunctionalized dendrimer **4**[11] However, in *l*,*u*-**3**, the conformational arrangement is slightly different because a *D-D-E-D* conformer (*E* = eclipsed, $\omega \approx 120°$) was found which has the largest dihedral angles in the molecule. Clearly, this conformer arises from intramolecular hydrogen bonding between O1 and O2 that enforces a twisting of the Si5-Si2-Si1-Si4 dihedral angle to a value of 115.8°. However, none of the conformers found in *l*,*u*-**3** and *l*,*l*-**3** are close to an *all-anti* conformer (*A*, *anti*, $\omega \approx 180°$) that is believed to be optimal for σ-conjugation.[1]

The UV spectra of *l*,*l*-**3** in *n*-heptane, as a function of temperature, are shown in Figure 4. Remarkably, upon increasing the temperature, the intensity of the twin peaks slowly decreases. The peaks completely disappear at 343 K, and above 333 K, a new relatively broad signal appears at 280 nm. In contrast, the UV absorption curves of *l*,*u*-**3** and **4** remain unchanged at 343 K. Upon cooling *l*,*l*-**3** to room temperature, the twin peaks appear again at the original wavelengths, clearly indicating the process to be reversible; structural irreversible changes such as epimerization of the stereogenic silicon centers as well as skeletal rearrangements or condensation reactions to siloxanes did not occur according to NMR spectroscopic measurements. However, temperature dependent ^{1}H NMR spectroscopic investigations of *l*,*l*-**3** in [D$_8$]toluene ($c = 10^{-2}$ M) suggest the occurrence of intermolecular hydrogen exchange processes. The broadened OH signal ($\delta = 5.2$ ppm at 303 K) sharpens with increasing temperature and shifts upfield ($\delta = 1.6$ ppm at 353 K), whereas for *l*,*u*-**3** the chemical shifts of the three nonequivalent and sharp OH signals remain unchanged.

The IR spectra obtained for the O–H stretching region of *l*,*u*-**3** and *l*,*l*-**3** in CCl_4 ($c = 10^{-3}$ M), as a function of temperature, are shown in Figure 5 and Figure 6. To determine whether the observed stretching frequencies correspond to associated OH groups (intra- or intermolecular) or non-associated OH groups, ab initio calculations were performed at the density functional level (B3LYP) for the model compound $HSi(SiH_2OH)_3$; the structures corresponding to the energy minima are shown in Figure 5 and Figure 6. For *l*,*l*-**3**, the spectra provide clear evidence for an entropically driven dissociation process in solution. In fact, at room temperature a very broad absorption has been observed at 3329 cm^{-1} which is assigned to the stretching frequency of the intermolecularly hydrogen-bonded dimer. This is in good agreement with the IR spectrum in the solid state (Nujol) for which a broad signal at 3322 cm^{-1} has been found arising from the dimer. However, upon increasing the temperature, a shoulder assigned to the monomer with intramolecular hydrogen bonds appears at 3489 cm^{-1}. At 333 K, the spectrum is clearly dominated by the vibrational motion of the monomer, which results in a sharp absorption at 3664 cm^{-1} indicative of non-associated OH groups. In contrast, the IR spectra of *l*-*u*-**3** do not show significant temperature depend-

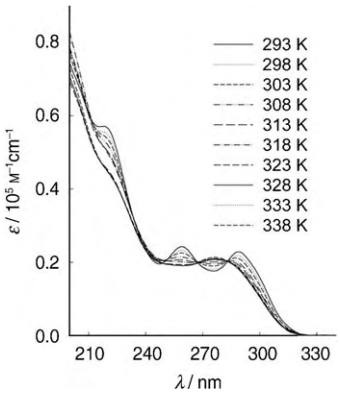

Figure 4. UV spectra of *l*,*l*-**3** in *n*-heptane as a function of temperature.

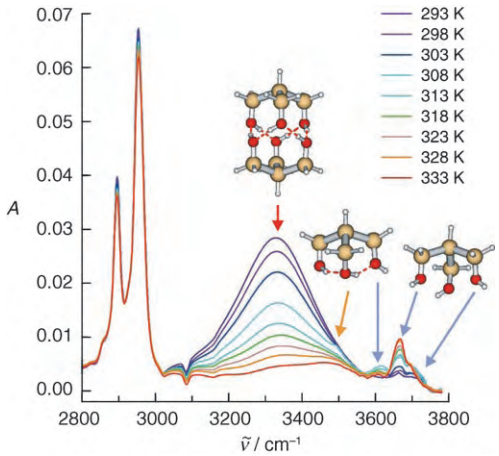

Figure 5. IR spectra of *l*,*l*-**3** in CCl_4 ($c = 10^{-3}$ M) as a function of temperature (O–H stretching vibrations region). Observed stretching frequencies for OH: 3329 (inter), 3489 (intra), 3612 (non-associated), 3664 (non-associated), and 3703 cm^{-1} (non-associated). At high temperatures the spectra are dominated by the vibrational motion of the monomer. Decreasing temperature results in the formation of monomers with intramolecular hydrogen bonds. At room temperature dimers with intermolecular hydrogen bonds exist as indicated by the red shift of the bands.

 © 2006 Wiley-VCH Verlag GmbH & Co. KGaA, Weinheim

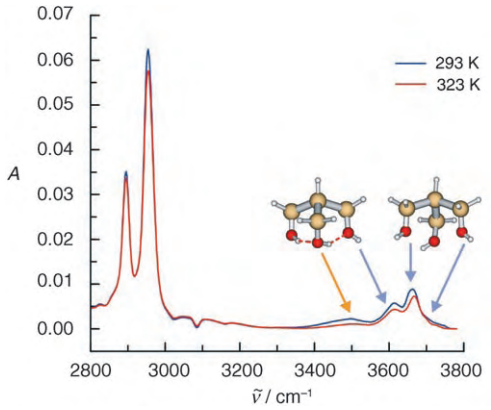

Figure 6. IR spectra of *l*,*u*-**3** in CCl_4 ($c = 10^{-3}$ M) at 293 and 323 K (O–H stretching vibrations region). Independent of the temperature, the spectra are dominated by the vibrational motion of the monomer. Observed stretching frequencies for OH: 3498 (intra), 3615 (non-associated), 3665 (non-associated), and 3705 cm^{-1} (non-associated).

ence, even at room temperature only stretching frequencies associated with the formation of monomers are found.

From these results and DFT calculations for *l*,*l*-**3** in the gas phase that clearly show the dimeric structure to be more stable than the monomeric one, it seems evident that *l*,*l*-**3** exists as a dimer at room temperature in solution.[14] Consequently, the remarkable red shift of the UV absorption maximum of *l*,*l*-**3** at room temperature arises from the dimer in which the conformation of the silicon backbone is controlled by steric repulsion of the three dendrimer wings (-Si(SiMe$_3$)$_2$Me) and, more importantly, through intermolecular hydrogen bonding. Assuming the conformational arrangement of *l*,*l*-**3** in the solid-state to be similar to that in solution, it can be concluded that the UV absorption maximum of *l*,*l*-**3** (290 nm at room temperature) most likely corresponds to conformers with large dihedral angles, such as *D-D-O-D* and *D-D-O-O*. The absorption at 260 nm may arise from the *O-D-O-O* or from the *D-O-D-O* conformer, in which both deviant segments are separated by *ortho* links, resulting in an interruption of σ-conjugation along the heptasilane chain. With increasing temperatures, a dissociation process occurs that leads to the formation of the monomer with non-associated OH groups. Clearly, this process is accompanied by an increased conformational flexibility of the oligosilane backbone because rotations around Si–Si bonds are not restricted through hydrogen bonding as in the dimer. As a consequence, a variety of different conformers exist, causing a broadened peak at 280 nm, which is blue-shifted with respect to the absorption maximum at room temperature. Such a situation is not evident for the stereoisomer *l*,*u*-**3** at room temperature, since the steric demand of the dendrimer wings enforces an arrangement that weakens the overall strength of intermolecular hydrogen bonding in the molecule tremendously. This weakening results in a rapid dissociation in solution to monomers with mainly non-associated OH groups.

In conclusion, we believe that the preliminary findings reported herein indicate that oxo-functionalized oligosilanes in general should have interesting and tunable electronic properties. The delocalized σ-electrons are strongly coupled with the oxygen lone pairs, which reduces the HOMO–LUMO band gap of these compounds significantly. We anticipate that the absorption can be moved into the visible region by increasing the number of oxo groups attached to silicon backbone and by controlling the conformation in larger dendritic oligosilanes. Further work in this area is in progress.

Received: April 24, 2006
Revised: June 22, 2006
Published online: September 15, 2006

Keywords: hydrogen bonds · IR spectroscopy · oligosilanes · silanols · UV spectroscopy

[1] a) J. Michl, R. D. Miller, *Chem. Rev.* **1989**, *89*, 1359; b) R. West in *The Chemistry of Organic Silicon Compounds* (Eds.: S. Patai, Z. Rappoport), Wiley, Chichester **1989**, p. 1207.
[2] S. S. Bukalov, L. A. Leites, R. West, *Macromolecules* **2001**, *34*, 6003, and references therein.
[3] K. Oka, N Fujiue, T. Dohmaru, C.-H. Yuan, R. West, *J. Am. Chem. Soc.* **1997**, *119*, 4074.
[4] C.-H. Yuan, R. West, *Chem. Commun.* **1997**, 1825.
[5] a) K. Tamao, H. Tsuji, M. Terada, M. Asahara, S. Yamaguchi, A. Toshimitsu, *Angew. Chem.* **2000**, *112*, 3425; *Angew. Chem. Int. Ed.* **2000**, *39*, 3287; b) H. Tsuji, M. Terada, A. Toshimitsu, K. Tamao, *J. Am. Chem. Soc.* **2003**, *125*, 7486.
[6] For permethylated oligosilane dendrimers see: a) J. B. Lambert, J. L. Pflug, C. L. Stern, *Angew. Chem.* **1995**, *107*, 106; *Angew. Chem. Int. Ed. Engl.* **1995**, *34*, 98; b) A. Sekiguchi, M. Nanjo, C. Kabuto, H. Sakurai, *J. Am. Chem. Soc.* **1995**, *117*, 4195; c) J. B. Lambert, J. L. Pflug, J. M. Denari, *Organometallics* **1996**, *15*, 615; d) J. B. Lambert, H. Wu, *Organometallics* **1998**, *17*, 4904; e) C. Krempner, H. Reinke, *J. Organomet. Chem.* **2003**, *685*, 134; f) C. Krempner, M. Köckerling, C. Mamat, *Chem. Commun.* **2006**, 720.
[7] For the Prelog–Seebach notation of *l* and *u*, see: D. Seebach, V. Prelog, *Angew. Chem.* **1982**, *94*, 696; *Angew. Chem. Int. Ed. Engl.* **1982**, *21*, 654.
[8] For details of X-ray structure analyses of *l*,*l*-**3** and *l*,*u*-**3**, see Supporting Information.
[9] For excellent reviews on solid-state structures of silanols see: a) P. D. Lickiss, *Adv. Inorg. Chem.* **1995**, *42*, 147; b) P. D. Lickiss in *The Chemistry of Organosilicon Compounds*, *Vol. 3*, Wiley, New York, **2001**, p. 695; c) R. Duchateau, *Chem. Rev.* **2002**, *102*, 3525.
[10] a) A. A. Korlyukov, D. Y. Larkin, N. A. Chernyavskaya, M. Y. Antipin, A. I. Chernyavskii, *Mendeleev Commun.* **2001**, *5*, 1; b) K. Jurkschat, *Coord. Chem. Rev.* **2001**, *215*, 267; c) C. Ackerhans, H. W. Roesky, T. Labahn, J. Magull, *Organometallics* **2002**, *21*, 3671; d) D. Hoffmann, H. Reinke, C. Krempner, *J. Organomet. Chem.* **2002**, *662*, 1; e) C. Krempner, J. Kopf, K. Mamat, H. Reinke, A. Spannenberg, *Angew. Chem.* **2004**, *116*, 5521; *Angew. Chem. Int. Ed.* **2004**, *43*, 5406.
[11] M. Nanjo, T. Sunaga, A. Sekiguchi, E. Horn, *Inorg. Chem. Commun.* **1999**, *2*, 203.
[12] a) C. G. Pitt, *J. Am. Chem. Soc.* **1969**, *91*, 6613; b) Z.-L. Hsiao, R. M. Waymouth, *J. Am. Chem. Soc.* **1994**, *116*, 9779; c) J. Koe, M. Motanaga, M. Fujiki, R. West, *Macromolecules* **2001**, *34*, 706; d) C. Krempner in *Organosilicon Chemistry*, *Vol. VI* (Eds.: N. Auner, J. Weis), VCH, Weinheim, **2005**, p. 337; e) H. Stueger, G.

 © 2006 Wiley-VCH Verlag GmbH & Co. KGaA, Weinheim

Fuerpass, K. Renger, J. Baumgartner, *Organometallics* **2005**, *24*, 6374.

[13] The conformations are roughly classified as *syn* (*S*, $\omega \approx 0°$), *gauche* (*G*, $\omega \approx 60°$), *ortho* (*O*, $\omega \approx 90°$), eclipsed (*E*, $\omega \approx 120°$), deviant (*D*, $\omega \approx 150°$) and *anti* (*A*, $\omega \approx 180°$); J. Michl, R. West, *Acc. Chem. Res.* **2000**, *33*, 821.

[14] The counterpoise-corrected binding energies are 103.45 and 107.31 kJ mol^{-1} depending in the monomer structure (two isomers shown in Figure 5). Gaussian 03 (Revision A.1), M. J. Frisch et al., see Supporting Information.

 © 2006 Wiley-VCH Verlag GmbH & Co. KGaA, Weinheim

Antimicrobial Coatings

DOI: 10.1002/anie.200602738

Contact-Active Antimicrobial Coatings Derived from Aqueous Suspensions**

*Andreas D. Fuchs and Joerg C. Tiller**

Antimicrobial surface modifications are currently being intensively investigated. Increasing hygiene standards and the threat of infectious disease demand materials with surfaces that inhibit the survival and proliferation of microbes. Most commercial materials of this type rely on impregnation with biocides, such as silver ions,[1] quaternary ammonium compounds,[2] triclosan,[3] chlorohexidine,[4] chlorine,[5] tributyltin,[6] and diverse antibiotics.[7] Although effective, the ongoing release of biocides contaminates the environment[8,9] and promotes the development of resistant microbial strains, which is one of the most important problems facing modern medicine.[10]

Since biofilms are the most problematic forms of biological contamination,[11] it is not necessary to kill all of the microbes in the surroundings, but only to prevent the proliferation of bacterial or fungal cells on surfaces. This goal can be achieved by microbe-repelling surfaces, which are mainly prepared through the grafting of protein-repelling polymers, such as poly(ethylene glycol) (PEG).[12] The combination of bacteria-repelling and biocide-releasing systems proved to be more effective than either approach alone.[13]

Surface modifications that effectively kill microbes on contact without releasing a biocide represent a modern approach towards permanently sterile materials. Contact-active surface modifications can be achieved through the chemical grafting of antimicrobial polymers, such as *N*-alkylated poly(4-vinylpyridine),[14] quarternized polyethylenimine,[15] and quaternary derivatives of acrylic acid,[16] to numerous common materials, such as glass,[14] cellulose,[16] and plastics.[17] In these systems, the polymers are not released and are effective against multiresistant bacteria.[18] Furthermore, the common bacterial strains *Escherichia coli* and *Staphylococcus aureus* do not develop noticeable resistance against these surfaces.[19] However, current methods for the preparation of contact-active antimicrobial surfaces are quite elaborate, and all require the use of organic solvents.[20] We, therefore, developed the broadly applicable coating method shown in Figure 1, which is based on emulsion polymerization using water-insoluble antimicrobial emulsifiers.

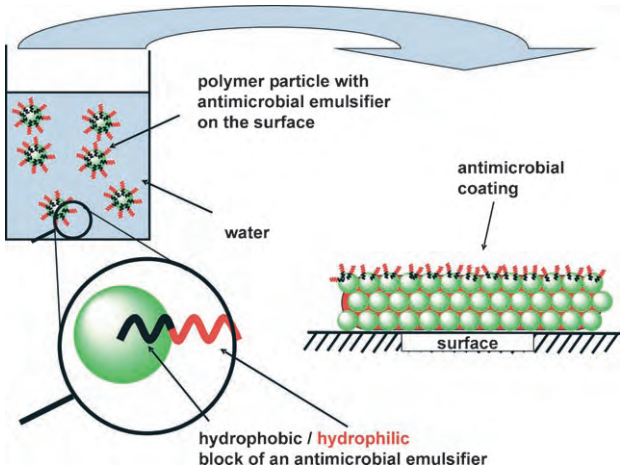

Figure 1. Preparation of a contact-active antimicrobial coating from an aqueous polymer suspension.

Suitable tailored polymeric emulsifiers consisting of a hydrophobic polystyrene (PS) block and a hydrophilic block of the established antimicrobial polymer poly(4-vinyl-*N*-methylpyridinium iodide) (P4VMP)[21] were synthesized by anionic polymerization[22] and subsequent methylation. The hydrophobic/hydrophilic balance was controlled by varying the molar ratio of PS/P4VMP between approximately 2:1 and 1:4 (Table 1). The resulting PS-*b*-P4VMP copolymers are soluble in dimethyl sulfoxide (DMSO), but not in water.

For the initial experiments, PS_{340}-*b*-$P4VMP_{710}$ was used as the emulsifier. After preswelling the block copolymer in water, 10 wt% styrene was added with stirring. Subsequently, a thermal radical polymerization was initiated with the neutral water-soluble azoinitiator 2,2′-azobis[2-methyl-*N*-(2-hydroxyethyl)propionamide], resulting in the formation of a stable suspension of polymer particles. Static light scattering

[*] A. D. Fuchs, Priv.-Doz. Dr. J. C. Tiller
University of Freiburg
Freiburg Materials Research Center (FMF) and
Institute for Macromolecular Chemistry
Stefan Meier Strasse 21, 79104 Freiburg (Germany)
Fax: (+49) 761-203-4709
E-mail: joerg.tiller@fmf.uni-freiburg.de

[**] This work was financially supported by the Deutsche Forschungsgemeinschaft (Emmy Noether-Programm) and by the Fonds der Chemischen Industrie. The azoinitiator was kindly provided by Wako (Germany). The authors are grateful to Matthias Thiel for experimental assistance, to Rainer Wissert for the ESEM images, to Dr. Ralf Thomann for the TEM images, and to Dr. Klaus Pelz for providing the *S. aureus* cells.

Supporting information for this article is available on the WWW under http://www.angewandte.org or from the author.

© 2006 Wiley-VCH Verlag GmbH & Co. KGaA, Weinheim

Table 1: PS-*b*-P4VMP diblock copolymers.

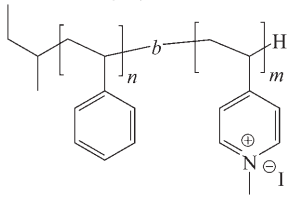

	Polymer			
	1	2	3	4
n	340	420	367	1330
m	710	450	183	325

revealed that the particles have a monomodal size distribution and an average diameter of approximately 150 nm. To obtain a stable dispersion, at least 2.5 wt% (with respect to the amount of styrene) of the polymeric emulsifier was required. Unfortunately, the coatings formed from this suspension are brittle. To obtain more elastic films, styrene was copolymerized with butyl acrylate (BA), which affords better film formation, owing to the lower glass transition temperature of the resulting PS-*co*-PBA copolymer.[23] With increasing BA content, the particle size increases from 150 nm for pure PS to 450 nm for PS-*co*-PBA with 50 wt% PBA. As expected, films derived from the polymer suspensions of PS-*co*-PBA with PS/PBA ratios (w:w) of 70:30 and 60:40 are transparent and more elastic. In contrast, films derived from a 50:50 PS-*co*-PBA suspension are highly elastic, but opaque, because the particles apparently aggregate in an early stage of the film formation.

The environmental scanning electron microscopy (ESEM) images shown in Figure 2 confirm the particle size and size distribution measured by light scattering. Furthermore, the film-forming ability of dispersions with different PS/PBA ratios is evident. Whereas the pure PS coating consists of isolated spheres (Figure 2a), a film prepared with 70:30 PS-*co*-PBA shows signs of sphere fusion (Figure 2b), which is a prerequisite for a closed polymer coating. The coalescence increases with increasing BA content, leading to a nearly completely closed coating of 60:40 PS-*co*-PBA (Figure 2c). A further increase in the BA content to 50 wt% produces a coating in which the individual particles are barely distinguishable (Figure 2d).

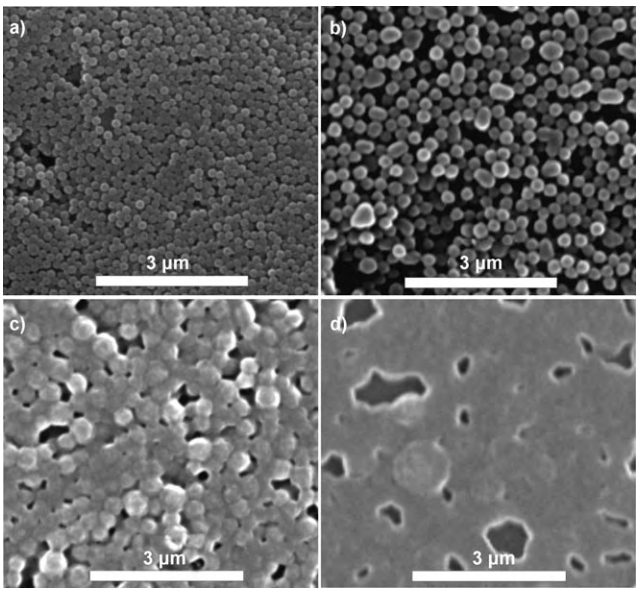

Figure 2. ESEM images of films derived from polymer suspensions of a) PS, b) 70:30 PS-*co*-PBA, c) 60:40 PS-*co*-PBA, and d) 50:50 PS-*co*-PBA. All suspensions contained 2.5 wt% PS_{340}-*b*-$P4VMP_{710}$.

All of the coatings are insoluble in solvents that dissolve the original PS-*co*-PBA copolymers, such as chloroform and acetone. This observation indicates that the PS-*co*-PBA particles are completely surrounded by the polymeric emulsifier. To determine whether the antimicrobial P4VMP blocks are located on the outer surfaces of the polymer particles, ultra thin sections of the films were treated with OsO_4 vapor, which selectively stains P4VMP. A transmission electron microscopy (TEM) image of a cross section of a 60:40 PS-*co*-PBA film with 2.5 wt% PS_{340}-*b*-$P4VMP_{710}$ is shown in Figure 3. The interfaces between the spheres have high contrast, indicating the presence of the stained P4VMP phase. The TEM image also confirms the size of the particles and their coalescence at the center of the film. Considering that most microbe cells are larger than 1 μm in diameter, the distribution of the antimicrobial polymer throughout the coating should also allow microbes to be eliminated in the film bulk.

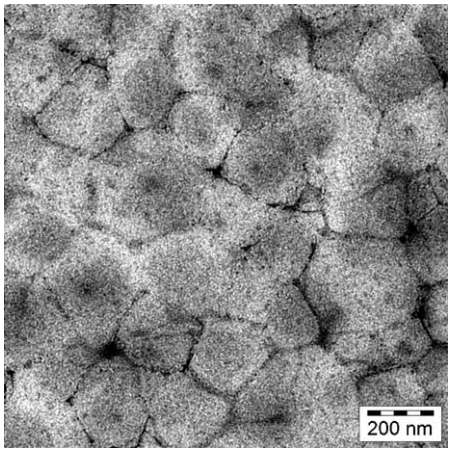

Figure 3. TEM image of a cross section of a film of 60:40 PS-*co*-PBA with 2.5 wt% PS_{340}-*b*-$P4VMP_{710}$, after staining with OsO_4.

The antimicrobial properties of the coatings were investigated for samples derived from suspensions of 60:40 PS-*co*-PBA particles with 2.5 wt% PS_{340}-*b*-$P4VMP_{710}$ or sodium dodecyl sulfate (SDS). The films were prepared by casting the suspensions onto glass slides. Upon drying in air, films of 30 μm in thickness with areas of $2.5 \times 2.5\ cm^2$ were formed. After thoroughly washing with water, the coated slides were sprayed with an aqueous suspension of cells of the ubiquitous and infectious Gram-positive bacterium *S. aureus*. During an incubation period of 24 h under growth agar, bacterial colonies grew from the individual cells. The colonies were then stained red with 2,3,5-triphenyl-tetrazolium chloride

 © 2006 Wiley-VCH Verlag GmbH & Co. KGaA, Weinheim

(TTC), a living-cell stain.[24] The number of *S. aureus* colonies grown on the uncoated areas of the slides was used as an internal control, because the density of bacterial cells sprayed onto the slides varied from 200–550 cells per cm^2 between experiments. As is apparent in Figure 4a, a 60:40 PS-*co*-PBA coating prepared with 2.5 wt% SDS as emulsifier allows the uninhibited growth of *S. aureus* cells sprayed onto its surface. In contrast, a coating of 60:40 PS-*co*-PBA with 2.5 wt% PS_{340}-*b*-$P4VMP_{710}$ completely prevents the growth of *S. aureus* cells (Figure 4b). Considering that the number of bacterial colonies on the control areas of the slides is at least 1300 (per 2.5 × 2.5 cm^2), the coated sample affords a reduction of more than 99.9% in the number of viable *S. aureus* cells on the surface. It is noteworthy that the bacterial cells in the uncoated areas grow even in close proximity to the coated areas (Figure 4b). If a biocide were released from the material, the bacteria would not grow within several millimeters of the coated area. The lack of such an inhibition zone indicates a contact-active antimicrobial effect.

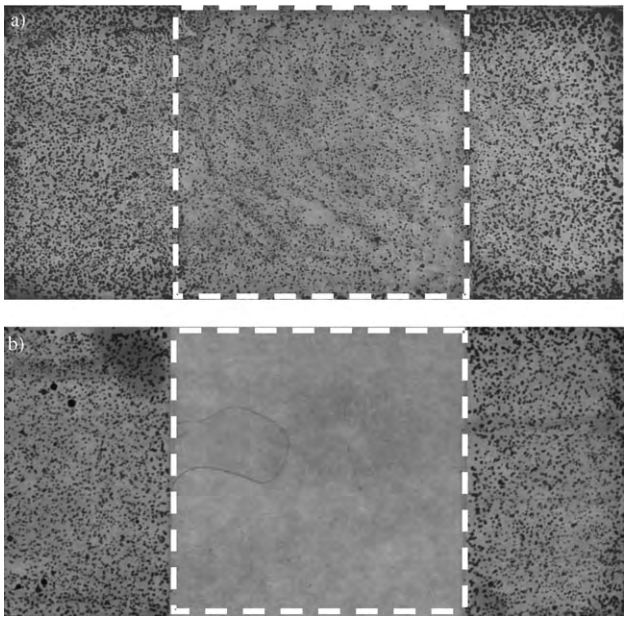

Figure 4. Photographs of *S. aureus* colonies grown on partially coated glass slides (5 × 2.5 cm^2). Films of 60:40 PS-*co*-PBA with a) 2.5 wt% SDS or b) 2.5 wt% PS_{340}-*b*-$P4VMP_{710}$ as emulsifier coat the framed areas (2.5 × 2.5 cm^2). Both slides were sprayed with *S. aureus* cells, incubated under growth agar at 37 °C for 24 h, and then stained with TTC.

The long-term activity of the polymer films was tested by continuous washing with water, whereby the washing solution was changed daily. Unfortunately, the coatings lost all of their microbial activity after one day of washing. Elemental analysis and IR spectroscopy did not reveal any detectable changes in the compositions of the coatings before and after washing. Thus, we presume that the top monolayers of the coatings were partially washed off. To obtain coatings with longer-term antimicrobial activity, PS-*b*-P4VMP emulsifiers with a higher PS content, that is, greater hydrophobicity, were used to prepare the suspensions. As expected, the antimicrobial effect strongly depends on the content of the emulsifier. The minimum amount of emulsifier necessary for the antimicrobial effect increases with higher PS content: 2.5 wt% PS_{420}-*b*-$P4VMP_{450}$, 5 wt% PS_{367}-*b*-$P4VMP_{183}$, or 10 wt% PS_{1330}-*b*-$P4VMP_{325}$. Surprisingly, the effective content of the antimicrobial polymer P4VMP in the coating was similar in each case, ranging from 1.3–1.7 wt% (with respect to the coating).

Washing tests of these coatings revealed that only the film prepared with 10 wt% PS_{1330}-*b*-$P4VMP_{325}$ was truly long-term biocidal. Even after 7 days of continuous washing, the antimicrobial effect of this film was not diminished. Preliminary results indicate that the coatings can also be successfully applied to other surfaces, for example, plastics and metals.

As observed in the TEM image in Figure 3, which is representative of all of the films prepared with the various biocidal emulsifiers, the antimicrobial polymer forms a continuous nanoscale network within the particle matrix. Thus, the films should be antimicrobially effective not only on the surface, but also in the bulk. To test this hypothesis, a disk with a thickness of 5 mm was prepared from a 60:40 PS-*co*-PBA dispersion with 10 wt% of the antimicrobial emulsifier PS_{1330}-*b*-$P4VMP_{325}$. The disk was then scratched on its surface or broken to produce a cross section. After washing the disk for one day, *S. aureus* cells were placed on the material and incubated overnight under growth agar. No bacterial growth was observed on the scratched areas of the surface, nor on the cross section of the disc. Thus, the films are also antimicrobial in the bulk. This bulk activity is a new quality for contact-active coatings, which usually consist of fragile monolayers that can be easily destroyed mechanically.

In closing, we have demonstrated that the water-insoluble diblock copolymer PS-*b*-P4VMP, which consists of a hydrophobic (PS) and an antimicrobial hydrophilic (P4VMP) block, can be used as an emulsifier in the aqueous emulsion polymerization of mixtures of styrene and BA. Coatings prepared from stable aqueous suspensions of these polymers act as contact-active antimicrobial surfaces. These coatings offer a promising alternative to biocide-releasing aqueous dispersions or to coatings prepared through elaborate chemical surface modifications with antimicrobial polymers. Experiments involving the variation of the hydrophobic blocks, for example, through the introduction of polymerizable groups, are presently underway. Furthermore, the emulsifiers will be tested in commercial paints, in the hope that they can replace the toxic water-soluble biocides that are currently used.

The Experimental Section (including polymer synthesis and analysis, antibacterial testing, and methods) is included in the Supporting Information.

Received: July 10, 2006
Published online: September 13, 2006

Keywords: antimicrobial emulsifiers · block copolymers · nanoparticle coatings · polymerization · surface chemistry

 © 2006 Wiley-VCH Verlag GmbH & Co. KGaA, Weinheim

[1] J. Chainer, *AISE Steel Technol.* **2001**, *78*, 59.
[2] J. C. Tiller, C. Sprich, L. Hartmann, *J. Controlled Release* **2005**, *103*, 355.
[3] B. D. Kalyon, U. Olgun, *Am. J. Infect. Control* **2001**, *29*, 124.
[4] A. A. Campbell, L. Song, X. S. Li, B. J. Nelson, C. Bottoni, D. E. Brooks, E. S. DeJong, *J. Biomed. Mater. Res.* **2000**, *53*, 400.
[5] M. W. Eknoian, S. D. Worley, J. Bickert, J. F. Williams, *Polymer* **1998**, *40*, 1367.
[6] E. Dyckman, J. A. Montemarano, E. C. Fischer, *Nav. Eng. J.* **1974**, *86*, 59.
[7] I. Raad, R. Darouiche, R. Hachem, M. Sacilowski, G. P. Bodey, *Antimicrob. Agents Chemother.* **1995**, *39*, 2397.
[8] D. W. Kolpin, E. T. Furlong, M. T. Meyer, E. M. Thurman, S. D. Zaugg, L. B. Barber, H. T. Buxton, *Environ. Sci. Technol.* **2002**, *36*, 1202.
[9] D. S. Page, C. C. Ozbal, M. E. Lanphear, *Environ. Pollut.* **1996**, *91*, 237.
[10] J. J. Bullen, H. J. Rogers, P. B. Spalding, C. G. Ward, *FEMS Immunol. Med. Microbiol.* **2005**, *43*, 325.
[11] K. Lewis, *Antimicrob. Agents Chemother.* **2001**, *45*, 999.
[12] D. Cunliffe, C. A. Smart, C. Alexander, E. N. Vulfson, *Appl. Environ. Microbiol.* **1999**, *65*, 4995.
[13] C. H. Ho, J. Tobis, C. Sprich, R. Thomann, J. C. Tiller, *Adv. Mater.* **2004**, *16*, 957.
[14] J. C. Tiller, C.-J. Liao, K. Lewis, A. M. Klibanov, *Proc. Natl. Acad. Sci. USA* **2001**, *98*, 5981.
[15] J. Lin, S. Qiu, K. Lewis, A. M. Klibanov, *Biotechnol. Prog.* **2002**, *18*, 1082.
[16] S. B. Lee, R. R. Koepsel, S. W. Morley, K. Matyjaszewski, Y. Sun, A. J. Russell, *Biomacromolecules* **2004**, *5*, 877.
[17] J. C. Tiller, S. B. Lee, K. Lewis, A. M. Klibanov, *Biotechnol. Bioeng.* **2002**, *79*, 465.
[18] J. Lin, J. C. Tiller, S. B. Lee, K. Lewis, A. M. Klibanov, *Biotechnol. Lett.* **2002**, *24*, 801.
[19] N. M. Milovic, J. Wang, K. Lewis, A. M. Klibanov, *Biotechnol. Bioeng.* **2005**, *90*, 715.
[20] D. Park, J. Wang, A. M. Klibanov, *Biotechnol. Prog.* **2006**, *22*, 584.
[21] N. Kawabata, M. Nishiguchi, *Appl. Environ. Microbiol.* **1988**, *54*, 2532.
[22] M. Antonietti, S. Heinz, M. Schmidt, C. Rosenauer, *Macromolecules* **1994**, *27*, 3276.
[23] S. Kirsch, J. Stubbs, J. Leuninger, A. Pfau, D. Sundberg, *J. Appl. Polym. Sci.* **2004**, *91*, 2610.
[24] T. Mosmann, *J. Immunol. Methods* **1983**, *65*, 55.

 © 2006 Wiley-VCH Verlag GmbH & Co. KGaA, Weinheim

Cover Picture

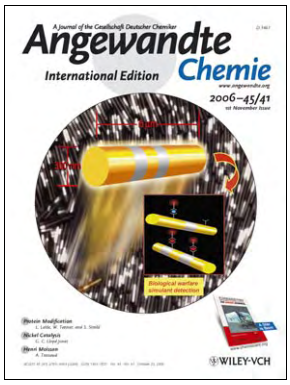

Jeffrey B.-H. Tok,* Frank Y. S. Chuang, Michael C. Kao, Klint A. Rose, Satinderpall S. Pannu, Michael Y. Sha, Gabriela Chakarova, Sharron G. Penn, and George M. Dougherty

Engineered nanowires offer an alternative substrate for performing single and multiplex sandwich immunoassays. In their Communication on page 6900 ff., J. B.-H. Tok et al. describe the use of antibody-conjugated Au/Ag-striped nanowires, as shown in the cover picture, in an immunoassay to analyze biological warfare agent simulants. Rapid identification of the stripe pattern and details on the degree of binding between the nanowires and the fluorophore-tagged antigen targets is possible by simultaneous analysis of reflectance and fluorescence images.

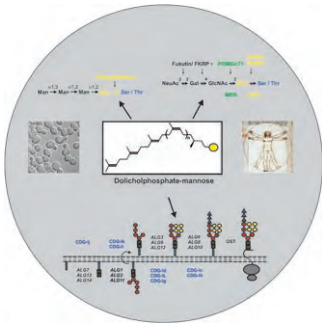

Protein Modification
Protein N-glycolsylation and protein O-mannosylation have been evolutionarily conserved from baker's yeast to man. This is vital in the explanation of the different genetic conditional diseases as is discussed in the Review by L. Lehle, W. Tanner, and S. Strahl on page 6802 ff.

Molecular Devices
In their Communication on page 6820 ff., N. R. Branda and co-workers describe the use of low-energy visible light to convert thermally stable cyclic dithienylethene derivatives into thermally unstable forms that fragment spontaneously.

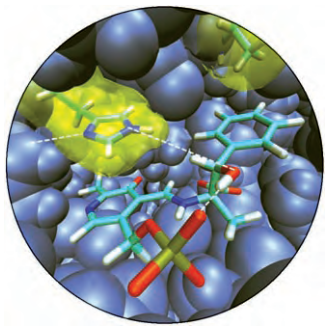

Enzyme Models
A single active-site mutation was used to convert a pyridoxal 5′-phosphate(PLP)-dependent alanine racemase into a retro-aldolase. D. Hilvert and co-workers describe this new catalyst in their Communication on page 6824 ff.

Contents

VIP *The following Communications have been judged by at least two referees to be "very important papers" and will be published online at www.angewandte.org soon:*

A. K. Sahoo, S. Mori, H. Shinokubo, A. Osuka**
Facile Peripheral Functionalization of Porphyrins through Pd-Catalyzed [3+2] Annulation with Alkynes

*M. Kanno, H. Kono, Y. Fujimura**
Control of π-Electron Rotation in Chiral Aromatic Molecules by Nonhelical Laser Pulses

M. Abe, E. Kubo, K. Nozaki, T. Matsuo, T. Hayashi*
An Extremely Long-Lived Singlet 4,4-Dimethoxy-3,5-diphenyl-pyrazolidine-3,5-diyl: A Notable Nitrogen Atom Effect on Intra- and Intermolecular Reactivity

E. E. Moushi, T. C. Stamatatos, W. Wernsdorfer, V. Nastopoulos, G. Christou, A. J. Tasiopoulos**
A New Family of 3D Coordination Polymers Composed of Mn_{19} Magnetic Units

W.-Y. Wong, C.-L. Ho, Z.-Q. Gao, B.-X. Mi, C.-H. Chen, K.-W. Cheah, Z. Lin*
Multifunctional Iridium Complexes Based on Carbazole Modules as Highly Efficient Electrophosphors

*C. M. Erben, R. P. Goodman, A. J. Turberfield**
Single-Molecule Protein Encapsulation in a Rigid DNA Cage

Obituary

Edgar Heilbronner (1921–2006) — *J. D. Dunitz* — **6784**

Books

Computational Chemistry of Solid State Materials — Richard Dronskowski — *reviewed by G. J. Miller* — **6785**

Flavonoids — Øyvind M. Andersen, Kenneth R. Markham — *reviewed by S. Quideau* — **6786**

Highlights

Nickel Catalysis

G. C. Lloyd-Jones* — **6788 – 6790**

The Remarkable Crossed Co-Isomerization Reaction of Cyclopropyl Ketones and Enones via Nickeladihydropyrans

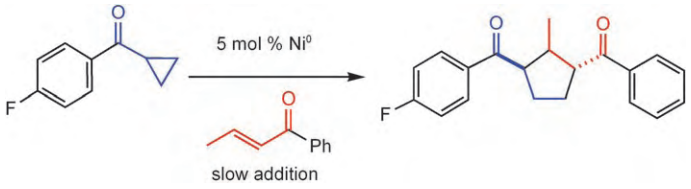

Nickel and Dimers: A Ni-catalyzed reaction between cyclopropylketones and enones to generate 1,3-diacyl 2-methylcyclopentanes has been recently reported (see scheme). The mechanism-inspired mode by which the process was designed suggests that nickeladihydropyrans, and nickel enolates in general, are catalytic reaction intermediates with considerable utility and potential.

WILEY InterScience DISCOVER SOMETHING GREAT
© 2006 Wiley-VCH Verlag GmbH & Co. KGaA, Weinheim

Essays

A Frenchman's revolution: The Nobel Prize for Chemistry in 1906 was awarded to Frenchman Henri Moissan, the first chemist to isolate fluorine and introduce the electrical furnace. A hundred years on, we remember these and other important breakthroughs that Moissan made during his career and discuss their impact on modern-day chemistry.

History of Science

A. Tressaud* _____ **6792 – 6796**

Henri Moissan: Winner of the Nobel Prize for Chemistry 1906

Positively electrifying: How did it come about that the brilliant mathematician, keen chemical theorist, but maladroit experimentalist, Joseph John Thomson, achieved such a major breakthrough as to discover the electron? This and allied topics are discussed in the Essay commemorating "J. J.", 100 years after he received the Nobel Prize for Physics.

History of Science

J. M. Thomas* _____ **6797 – 6800**

J. J. Thomson: Winner of the Nobel Prize for Physics 1906

Reviews

The rise of yeast: Protein N-glycosylation and O-Mannosylation are two protein modifications that, with very few exceptions, have been conserved throughout the process of evolution from yeast to man, and as a result, yeast has been studied in detail. With the help of yeast, many severe congenital glycosylation disorders in children have been explained.

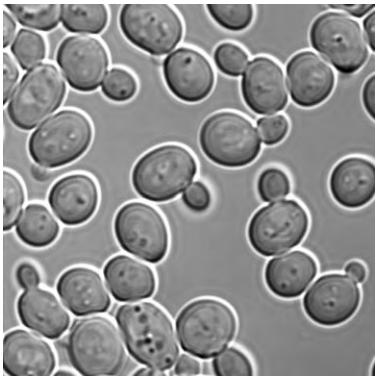

Protein Glycosylation

L. Lehle,* S. Strahl, W. Tanner* _____ **6802 – 6818**

Protein Glycosylation, Conserved from Yeast to Man: A Model Organism Helps Elucidate Congenital Human Diseases

For the USA and Canada:
ANGEWANDTE CHEMIE International Edition (ISSN 1433-7851) is published weekly by Wiley-VCH PO Box 191161, D 69451 Weinheim, Germany. Air freight and mailing in the USA by Publications Expediting Inc. 200 Meacham Ave., Elmont, NY 11003. Periodicals postage paid at Jamaica NY 11431. US POSTMASTER: send address changes to *Angewandte Chemie*, Wiley-VCH, 111 River Street, Hoboken, NJ 07030. Annual subscription price for institutions: US$ 5685/5168 (valid for print and electronic / print or electronic delivery); for individuals who are personal members of a national chemical society prices are available on request. Postage and handling charges included. All prices are subject to local VAT/sales tax.

© 2006 Wiley-VCH Verlag GmbH & Co. KGaA, Weinheim

The best in chemistry –

for more than a hundred years

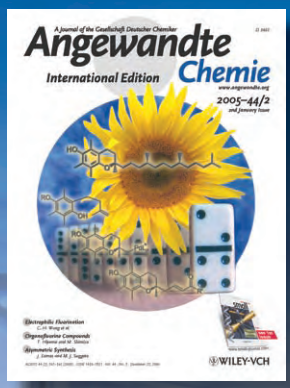

A Journal of the Gesellschaft Deutscher Chemiker

Angewandte
International Edition **Chemie**

www.angewandte.org

1888: ***The beginning of a success story***

Constant Innovations

1962: *First issue of the International Edition*
1976: *Graphical abstracts*
1979: *Cover pictures*
1988: *Centenary of Angewandte*
1989: *Routine use of color*
1991: *New section: Highlights*
1992: *Computerized editorial tracking system*
1995: *Internet service for readers*
1998: *Regular press service; full-text online*
2000: *New section: Essays; EarlyView: Communications available online ahead of the printed version*
2001: *New section: Minireviews*
2002: *Online submission of manuscripts*
2003: *Weekly publication; new section: News; new layout*
2004: *Backfiles (1962-1997); ManuscriptXpress: Online system for authors and referees*

Angewandte's advisors...

Martin Jansen
Max-Planck-Institut für Festkörperforschung, Stuttgart

»Professional presentation of the latest research in all fields of chemistry is the distinguishing characteristic that makes ***Angewandte Chemie*** *indispensable. This journal leads students to the cutting edge of chemical knowledge.«*

Angewandte Chemie International Edition *is a journal of the German Chemical Society (GDCh)*

GDCh

WILEY InterScience® DISCOVER SOMETHING GREAT

WILEY-VCH

1894504_gu

Communications

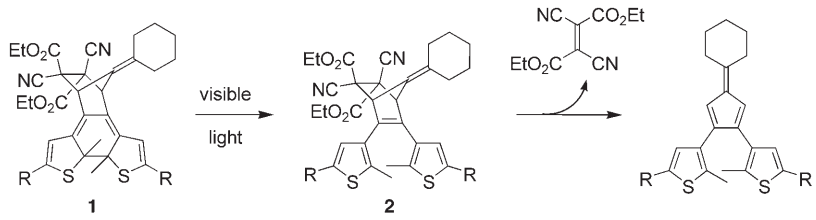

Effective release mechanism: Low-energy visible light is used to convert thermally stable cyclic dithienylethene derivatives **1** into thermally unstable forms **2** that undergo spontaneous fragmentation. The photoresponsive architecture is rationally designed so that one, the other, or both of two systems in a mixture can be selectively stimulated with different light sources to release their "loads".

Molecular Switches VIP

V. Lemieux, S. Gauthier, N. R. Branda* ——— **6820 – 6824**

Selective and Sequential Photorelease Using Molecular Switches

Optimizing the active site: A pyridoxal 5′-phosphate(PLP)-dependent alanine racemase was converted into a retro-aldolase by a single active-site mutation. This new catalyst reacts efficiently with quaternary β-hydroxy α-amino acids, a class of molecules that natural aldolases have not been evolved to handle. Computational docking experiments suggest a novel mechanism for this process and rationalize the stereochemical preferences of the enzyme.

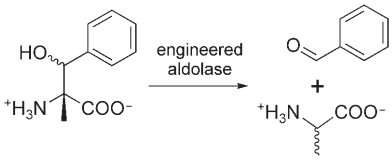

Engineered Aldolase VIP

F. P. Seebeck, A. Guainazzi, C. Amoreira, K. K. Baldridge, D. Hilvert* **6824 – 6826**

Stereoselectivity and Expanded Substrate Scope of an Engineered PLP-Dependent Aldolase

Out of bounds: The reversible immobilization of a fluorescent DNA–protein conjugate by strand displacement is achieved by specific DNA hybridization reactions (see picture). Binding and dissociation of the protein can be followed by observation of the protein's fluorescence, which is quenched upon binding to gold nanoparticles.

Nanobiotechnology

P. Hazarika, F. Kukolka, C. M. Niemeyer* ——— **6827 – 6830**

Reversible Binding of Fluorescent Proteins at DNA–Gold Nanoparticles

© 2006 Wiley-VCH Verlag GmbH & Co. KGaA, Weinheim

Contents

Molecular Recognition

A. P. Benfield, M. G. Teresk, H. R. Plake, J. E. DeLorbe, L. E. Millspaugh, S. F. Martin* _____ **6830 – 6835**

Ligand Preorganization May Be Accompanied by Entropic Penalties in Protein–Ligand Interactions

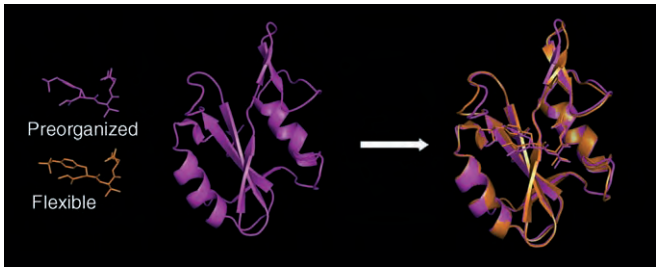

Fact or fiction? It is generally assumed that preorganization of a flexible ligand in the 3D shape it adopts when bound to a macromolecular receptor will provide a derivative with an increased binding affinity that benefits entropically (see picture). Contrary to this fundamental tenet of molecular recognition, it is shown that ligand preorganization in biological systems does not necessarily have a favorable entropic component.

High-Throughput Screening

X.-W. Zhao, Y. Cao, F. Ito, H.-H. Chen, K. Nagai, Y.-H. Zhao, Z.-Z. Gu* _____ **6835 – 6838**

Colloidal Crystal Beads as Supports for Biomolecular Screening

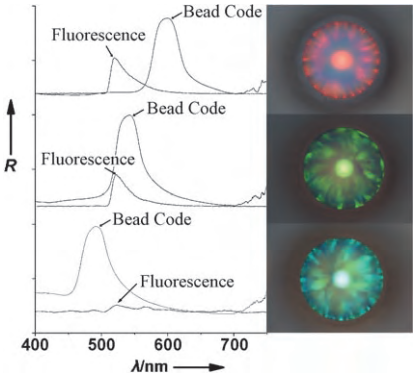

Crystal balls: Colloidal crystal microbeads with a three-dimensional photonic crystal structure can be fabricated with a droplet generator and their reflection spectra used as encoding elements. A multiplex bioassay demonstrates their reliability as encoded carriers (see picture: red, green, and blue beads are immobilized with human, mouse, and rabbit immunoglobulin, respectively).

Ferrocene Aggregates

K. Venkatasubbaiah, A. G. DiPasquale, M. Bolte, A. L. Rheingold, F. Jäkle* _____ **6838 – 6841**

Mono- and Dimetalated Ferrocenylcopper Complexes by Tin–Copper Exchange

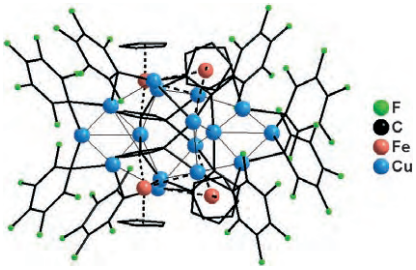

Fe binds simultaneously: Reaction of 1,2-fc(SnMe$_3$)$_2$ (fc = (C$_5$H$_5$)Fe(C$_5$H$_3$)) with [C$_6$F$_5$Cu]$_4$ selectively leads to the multimetallic aggregate [(1,2-fcCu$_2$)$_4$(C$_6$F$_5$Cu)$_8$] (see picture), which offers rare insight into the structural complexity of highly aggregated arylenedicopper species and provides the first evidence that the central iron atom in ferrocene can interact simultaneously with multiple Lewis acidic transition-metal centers.

Polycycles

T. Hamura, T. Arisawa, T. Matsumoto, K. Suzuki* _____ **6842 – 6844**

Two-Directional Annelation: Dual Benzyne Cycloadditions Starting from Bis(sulfonyloxy)diiodobenzene

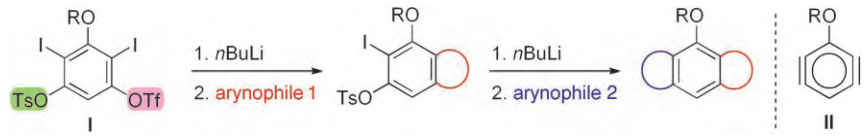

Double up: Dual cycloadditions of benzynes are demonstrated from bis(sulfonyloxy)diiodobenzene **I**, which can be viewed as a synthetic equivalent of 3-alkoxy-1,4-benzdiyne **II**. Importantly, selective halogen–lithium exchange of **I** enables the tandem generation of benzynes and dual cycloadditions with arynophiles 1 and 2, thus allowing the rapid construction of various highly functionalized bis-cycloadducts.

© 2006 Wiley-VCH Verlag GmbH & Co. KGaA, Weinheim

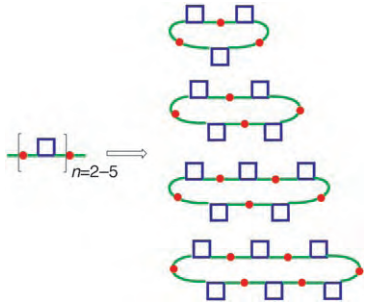

Hydrogen-bonding interactions drive oligosquaramides of different lengths to fold into hairpin-like structures both in nonprotic and protic solvents. These compounds are useful preorganized precursors in macrocyclization reactions.

Macrocycles

C. Rotger,* M. N. Piña, M. Vega, P. Ballester, P. M. Deyà, A. Costa* ——— 6844 – 6848

Efficient Macrocyclization of Preorganized Palindromic Oligosquaramides

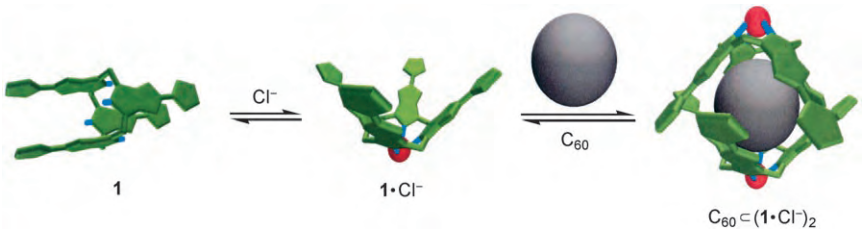

Seeing is believing: Treatment of a tetrathiafulvalene-functionalized calix[4]pyrrole **1** with chloride anions in CH_2Cl_2 produces bowl-like receptor **1**·Cl^-, which is able to encapsulate C_{60} in a 2:1 barrel-like manner. The color of $C_{60}\subset(\mathbf{1}\cdot Cl^-)_2$ (green in CH_2Cl_2) differs dramatically from its constituents (yellow and magenta for **1** and C_{60}, respectively), thus allowing its formation to be monitored visually.

Host–Guest Systems

K. A. Nielsen, W.-S. Cho, G. H. Sarova, B. M. Petersen, A. D. Bond, J. Becher, F. Jensen, D. M. Guldi, J. L. Sessler,* J. O. Jeppesen* ——— 6848 – 6853

Supramolecular Receptor Design: Anion-Triggered Binding of C_{60}

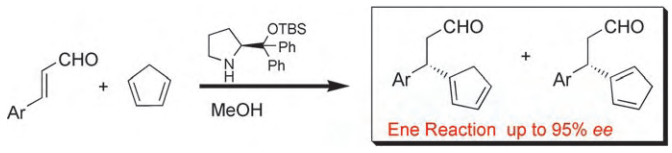

The opposite result: A diphenylprolinol silyl ether promotes an intermolecular enantioselective ene reaction of α,β-enals with cyclopentadiene. This is the first example of cyclopentadiene acting as the ene component, and not the diene, with α,β-enals.

Organocatalysis

H. Gotoh, R. Masui, H. Ogino, M. Shoji, Y. Hayashi* ——— 6853 – 6856

Enantioselective Ene Reaction of Cyclopentadiene and α,β-Enals Catalyzed by a Diphenylprolinol Silyl Ether

Modeling enzyme catalysis: High-level ab initio QM/MM calculations yield activation enthalpies and free energies for chorismate mutase and *para*-hydroxybenzoate hydroxylase that are in excellent agreement with experimental results. Enzyme reactivity is described quantitatively by transition-state theory.

Computational Enzymology

F. Claeyssens, J. N. Harvey, F. R. Manby, R. A. Mata, A. J. Mulholland,* K. E. Ranaghan, M. Schütz, S. Thiel, W. Thiel,* H.-J. Werner* ——— 6856 – 6859

High-Accuracy Computation of Reaction Barriers in Enzymes

© 2006 Wiley-VCH Verlag GmbH & Co. KGaA, Weinheim

Contents

DNA Damage

P. Simon, J.-L. Décout,*
M. Fontecave* ——— **6859 – 6861**

Sequence-Specific Nucleic Acid Damage Induced by Peptide Nucleic Acid Conjugates That Can Be Enzyme-Activated

Recruitment drive: A 12 mer peptide nucleic acid(PNA)–flavin conjugate is prepared. When the PNA moiety is hybridized to its complementary sequence in a 25 mer oligo-2′-deoxyribonucleotide, the flavin moiety can recruit an NADPH:flavin oxidoreductase. This complex allows the activation of molecular oxygen in the presence of NADH and the selective oxidation of the oligonucleotide target (see scheme).

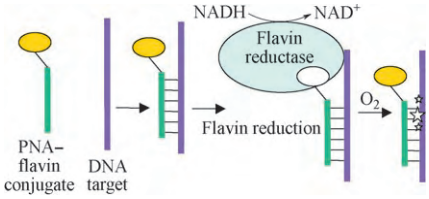

Interfaces

P. Jing, M. Zhang, H. Hu, X. Xu, Z. Liang, B. Li, L. Shen, S. Xie, C. M. Pereira,* Y. Shao* ——— **6861 – 6864**

Ion-Transfer Reactions at the Nanoscopic Water/*n*-Octanol Interface

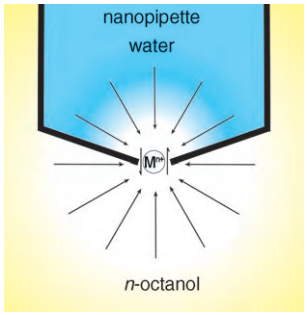

Sharp practice: A water/*n*-octanol interface can be formed at the tip of a very short and sharp nanopipette, and can be polarized externally (see picture). This interface has been used to investigate various ion-transfer processes and evaluate partition coefficients for ionizable species.

Heterogeneous Catalysis

Z.-P. Liu,* C.-M. Wang, K.-N. Fan ——— **6865 – 6868**

Single Gold Atoms in Heterogeneous Catalysis: Selective 1,3-Butadiene Hydrogenation over Au/ZrO_2

The origin of the species: The first principles method reveals the origin and activity of a heterogeneous Au monomer in the catalysis of a selective 1,3-butadiene hydrogenation. The active Au species is an Au^{I} complex, produced from Au^{III} in situ by reduction, stabilized by ZrO_2 defects. The high catalytic activity and selectivity comes from the stable, but flexible, structure of the Au^{I} catalytic center, which dissociates H_2 heterolytically.

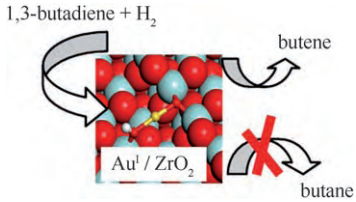

Coordination Chemistry

N. A. Eckert, S. Vaddadi, S. Stoian, R. J. Lachicotte, T. R. Cundari,* P. L. Holland* ——— **6868 – 6871**

Coordination-Number Dependence of Reactivity in an Imidoiron(III) Complex

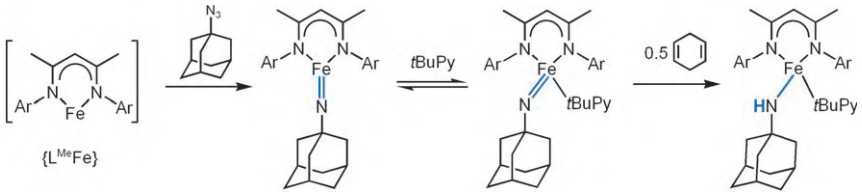

Reaction of the $\{L^{Me}Fe\}$ fragment with adamantyl azide (AdN_3) in the presence of 4-*tert*-butylpyridine (*t*BuPy) gives an $S = 3/2$ species that has been examined by ^1H NMR, IR, EPR, and Mössbauer spectroscopies. DFT calculations point toward an identification as $[L^{Me}FeNAd]$. This species abstracts hydrogen atoms from the ligand or external reagents only through its pyridine adduct (see scheme; $Ar = 2,6\text{-}iPr_2C_6H_3$).

© 2006 Wiley-VCH Verlag GmbH & Co. KGaA, Weinheim

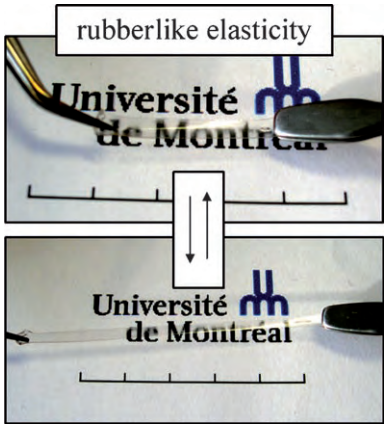

Stretching exercises: A family of degradable thermoplastic elastomers has been synthesized by entropy-driven ring-opening metathesis polymerization of macrocycles based on bile acids. These polyesters display elongation moduli closely matching those of elastin and other soft tissues, such as skin, elastic cartilage, and aorta, which make them good candidates for biomedical engineering applications where mechanical properties are of importance.

Degradable Elastomers

J. E. Gautrot, X. X. Zhu* ___ **6872 – 6874**

Main-Chain Bile Acid Based Degradable Elastomers Synthesized by Entropy-Driven Ring-Opening Metathesis Polymerization

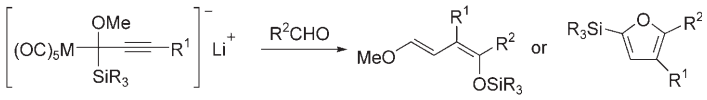

The unique reactivity of silylated propargyltungsten and -molybdenum species with electrophiles provides a route to synthetically useful compounds. In the reaction with aldehydes, 1,4-dioxy-1,3-dienes or, when conducted in the presence of Et_3Al, silylated furans were generated in good yield. In reactions with enones or CO_2, allenyl silane derivatives and silylated butenolides were obtained in good yield.

Carbene Complexes

T. Asakura, T. Kojima, T. Miura, N. Iwasawa* _____ **6874 – 6877**

Useful Reactions of Silylated Propargyltungsten or Propargylmolybdenum Species

Metal in microfluidic channels: The fabrication of electromagnets (solder) with micron-scale dimensions in poly(dimethylsiloxane) in close proximity (ca. 10-μm separation) to microfluidic channels is described (see pictures, top view and cross section). The method only has four steps and can be completed in 10 min. By passing an electric current through the magnets, magnetic field gradients are generated inside the microfluidic channels, which can be used to capture and release superparamagnetic beads in the microfluidic channel.

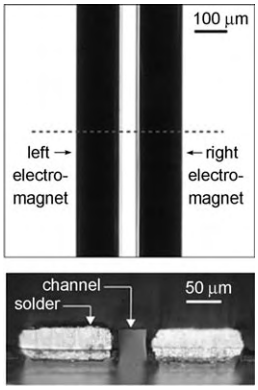

Microdevices

A. C. Siegel, S. S. Shevkoplyas, D. B. Weibel, D. A. Bruzewicz, A. W. Martinez, G. M. Whitesides* _____ **6877 – 6882**

Cofabrication of Electromagnets and Microfluidic Systems in Poly(dimethylsiloxane)

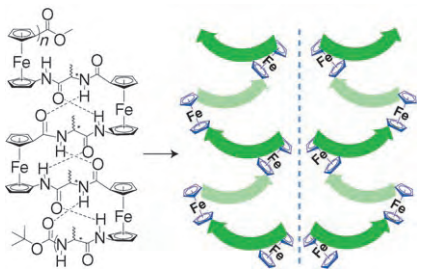

Twists and turns: A series of alanine conjugates of ferrocene amino acid (Fca) were prepared based on the idea that an alternating sequence of a natural α-amino acid and a turn-inducing molecule may result in the formation of a robust model foldamer for β-helical peptides. Right- and left-handed pseudo-β-helical Fca–alanine foldamers were obtained, and their structures were studied in solution and the solid state.

Peptides

S. Chowdhury, G. Schatte, H.-B. Kraatz* _____ **6882 – 6884**

Rational Design of Bioorganometallic Foldamers: A Potential Model for Parallel β-Helical Peptides

© 2006 Wiley-VCH Verlag GmbH & Co. KGaA, Weinheim

Contents

Homogeneous Catalysis

Y.-T. Hong, A. Barchuk, M. J. Krische* ——— **6885 – 6888**

Branch-Selective Intermolecular Hydroacylation: Hydrogen-Mediated Coupling of Anhydrides to Styrenes and Activated Olefins

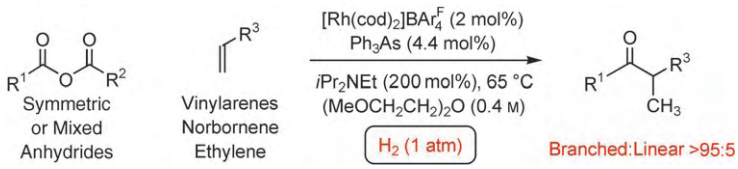

Branching out with hydrogen: Hydrogenation of symmetric or mixed carboxylic anhydrides in the presence of styrenes or activated olefins generates intermolecular hydroacylation products. The use of cationic rhodium catalysts ligated by triphenylarsine (Ph_3As) results in the formation of branched coupling products as single regioisomers in high yields (see scheme; cod = cycloocta-1,5-diene, Ar^F = 3,5-$(CF_3)_2C_6H_3$).

Molecular Switches

Y. L. Yang, Q. L. Chan, X. J. Ma, K. Deng, Y. T. Shen, X. Z. Feng,* C. Wang* ——— **6889 – 6893**

Electrical Conformational Bistability of Dimesogen Molecules with a Molecular Chord Structure

Touching a chord: A field-dependent conformational change occurs in dimesogen molecules with flexible linking chains, which illustrates a molecular chord structure that is switchable by an electric field (see picture; HOPG = highly oriented pyrolytic graphite). No discernible changes are observed for dimesogen molecules with rigid linkers.

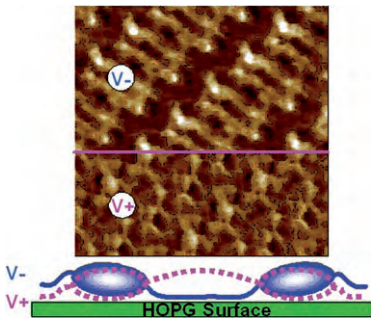

Palladium Catalysis

J. Barluenga,* C. Valdés, G. Beltrán, M. Escribano, F. Aznar ——— **6893 – 6896**

Developments in Pd Catalysis: Synthesis of 1*H*-1,2,3-Triazoles from Sodium Azide and Alkenyl Bromides

Another star for the Palladium: The discovery of reactions promoted by the ubiquitous Pd^0 catalysts is still possible. 1*H*-1,2,3-Triazoles are directly obtained by reaction of alkenyl bromides and sodium azide in the presence of a Pd^0–xantphos catalyst (see scheme, xantphos = 9,9-dimethyl-4,5-bis(diphenylphosphino)xanthene, dba = *trans*,*trans*-dibenzylideneacetone).

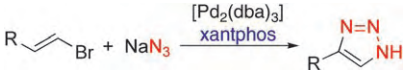

Hybrid Composites

S.-H. Ng, J. Wang, D. Wexler, K. Konstantinov, Z.-P. Guo, H.-K. Liu* ——— **6896 – 6899**

Highly Reversible Lithium Storage in Spheroidal Carbon-Coated Silicon Nanocomposites as Anodes for Lithium-Ion Batteries

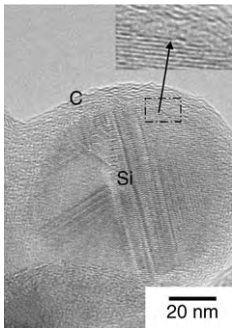

High-performance cycling: Spray pyrolysis has been used to generate a new type of spheroidal nanosized carbon-coated silicon composite (see TEM image). This nanocomposite shows superior electrochemical cycling properties as an anode material for use in lithium-ion batteries, delivering a reversible capacity of 1489 mA h g^{-1} after 20 cycles.

© 2006 Wiley-VCH Verlag GmbH & Co. KGaA, Weinheim

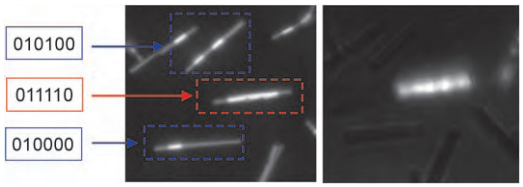

The white stripes in the reflectance image (left; Au = 0, Ag = 1) correspond to Ag in Au/Ag-striped nanowires employed in a suspended format to enable the rapid and sensitive single and multiplex immunoassays for biowarfare agent simulants. Simultaneous analysis of both the reflectance and the fluorescence images (right) of a mixture of nanowires enables easy identification of the antigen present.

Nanotechnology

J. B.-H. Tok,* F. Y. S. Chuang, M. C. Kao, K. A. Rose, S. S. Pannu, M. Y. Sha, G. Chakarova, S. G. Penn, G. M. Dougherty _____ **6900 – 6904**

Metallic Striped Nanowires as Multiplexed Immunoassay Platforms for Pathogen Detection

---

Smell of success: The stereoselective synthesis of Superambrox in 27% overall yield is based on two original highly selective reactions: the type III intramolecular ene reaction and the OH-assisted Ru- (or Ir-) catalyzed C–C double-bond isomerization.

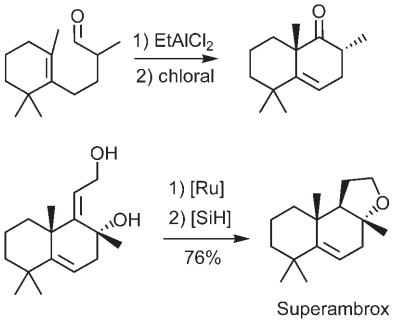

Asymmetric Synthesis

C. Fehr,* I. Farris _____ **6904 – 6907**

Stereoselective Synthesis of Superambrox: Stereoselective Type III Intramolecular Ene Reaction and OH-Assisted Ru-Catalyzed Isomerization

---

Confused, but not dazed: Totally in contrast to Sn^{IV} complexes of normal porphyrins, Sn^{IV} complexes of N-confused oxoporphyrins can strongly bind halides at the axial position with pronounced fluorescence enhancement (see scheme; Ar = Ph, *p*-$CF_3C_6H_4$, *p*-$CH_3C_6H_4$) and can thus be regarded as a novel prototype of fluorescence halide sensors.

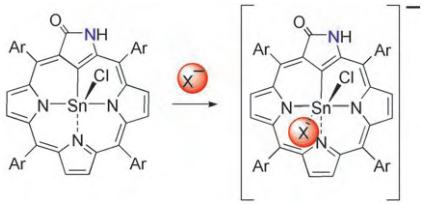

Anion Sensors

Y. Xie, T. Morimoto, H. Furuta* _____ **6907 – 6910**

Sn^{IV} Complexes of N-Confused Porphyrins and Oxoporphyrins—Unique Fluorescence "Switch-On" Halide Receptors

---

Stepwise down: Reaction of [Cu(Me$_2$-tpa)]$^+$ (tpa = bis(6-methyl-2-pyridylmethyl)(2-pyridylmethyl)amine) with H_2O_2 results in regioselective oxidation of a methyl group of the Me$_2$-tpa ligand to produce an alkylperoxocopper(II) complex [Cu(Me-tpa-CH_2OO)]$^+$ as a reaction intermediate, which undergoes further decomposition to give aldehyde and alcohol copper(I) complexes as well as alkoxo- and carboxylatocopper(II) complexes (see scheme; blue N, green Cu, red O).

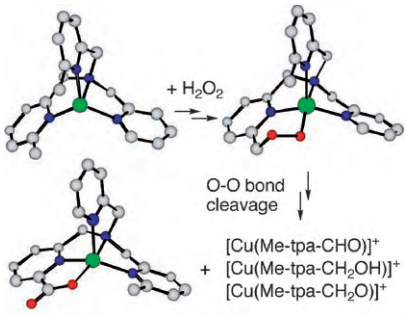

Alkylperoxocopper Complexes

M. Mizuno, K. Honda, J. Cho, H. Furutachi, T. Tosha, T. Matsumoto, S. Fujinami, T. Kitagawa, M. Suzuki* _____ **6911 – 6914**

A Mononuclear Alkylperoxocopper(II) Complex as a Reaction Intermediate in the Oxidation of the Methyl Group of the Supporting Ligand

© 2006 Wiley-VCH Verlag GmbH & Co. KGaA, Weinheim

Contents

Homogenous Catalysis

J. Piera, K. Närhi,
J.-E. Bäckvall* ——— 6914 – 6917

Pd^{II}-Catalyzed Aerobic Allylic Oxidative Carbocyclization of Allene-Substituted Olefins: Immobilization of an Oxygen-Activating Catalyst

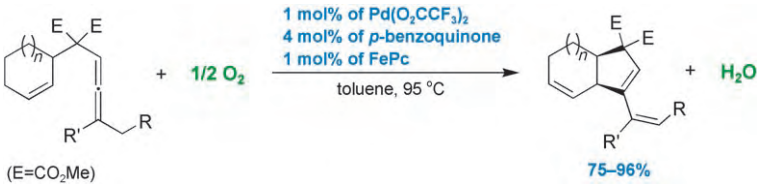

A good couple: Highly selective aerobic allylic oxidation with C–C bond formation is achieved by the use of coupled palladium and iron catalysis (see scheme; FePc = iron phthalocyanine). The use of an oxygen-activating catalyst is necessary for an efficient electron transfer from Pd^0 to O_2. The utility of this method is enhanced by the immobilization of the iron catalyst onto a resin.

Porous Materials

E. Brunet,* H. M. H. Alhendawi, C. Cerro, M. J. de la Mata, O. Juanes, J. C. Rodríguez-Ubis ——— 6918 – 6920

Hydrogen Storage in a Highly Porous Solid Derived from γ-Zirconium Phosphate

Having a gas: Topotactic exchange (65 %) of γ-zirconium phosphate with terphenyldiphosphonic acid yielded a pillared material with a specific area of 90 $m^2 g^{-1}$. Subsequent treatment with hypophosphorous acid afforded a material of α type, with no incorporated hypophosphite and a specific area of 400 $m^2 g^{-1}$, which took up 74 $cm^3 g^{-1}$ of H_2 at 650 Torr and 77 K.

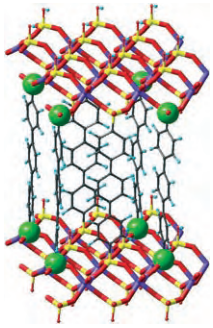

Anion Receptors

V. Amendola, M. Boiocchi, B. Colasson, L. Fabbrizzi,* M.-J. Rodriguez Douton, F. Ugozzoli ——— 6920 – 6924

A Metal-Based Trisimidazolium Cage That Provides Six C–H Hydrogen-Bond-Donor Fragments and Includes Anions

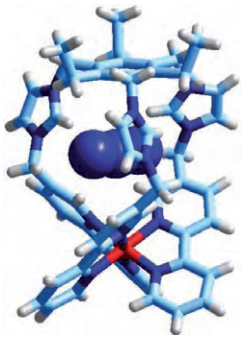

Sheltering under the roof: A trisimidazolium cage is capped with a {Fe^{II}(bpy)$_3$}$^{2+}$ subunit to produce a receptor that can bind small anions (bpy = 2,2′-bipyridine). Rodlike "pseudohalide" (N_3^-, NCO^-, and NCS^-) and spherical halide (Cl^-, Br^-, and I^-) anions accept hydrogen bonds from C–H fragments in the receptor cavity. The N_3^- ion forms the most stable inclusion compound (see structure; Fe red, C light blue, H white, N dark blue).

Organocatalysis

B. Rodríguez, T. Rantanen, C. Bolm* ——— 6924 – 6926

Solvent-Free Asymmetric Organocatalysis in a Ball Mill

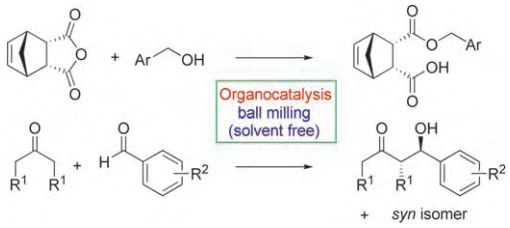

Milling around: Aldol and enantioselective anhydride opening reactions were effected in a ball mill under solvent-free conditions to afford products in high yields and with high enantioselectivities after short reaction times (see scheme).

The issues for October 2006 appeared online on the following dates
Issue 37: September 11. · Issue 38: September 19. · Issue 39: September 29. · Issue 40: October 10

© 2006 Wiley-VCH Verlag GmbH & Co. KGaA, Weinheim

Sources

Product and Company Directory

You can start the entry for your company in "Sources" in any issue of *Angewandte Chemie*.

If you would like more information, please do not hesitate to contact us.

Wiley-VCH Verlag – Advertising Department
Tel.: 0 62 01 - 60 65 65
Fax: 0 62 01 - 60 65 50
E-Mail: MSchulz@wiley-vch.de

Service

Keywords ____ 6930

Authors ____ 6931

Angewandte's Sister Journals ____ 6928 – 6929

Vacancies ____ 6783

Preview ____ 6933

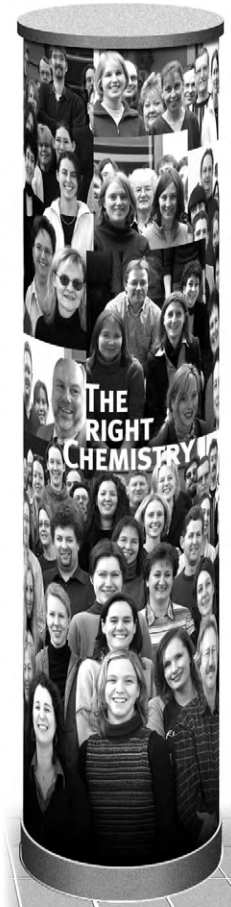

WILEY-VCH, a subsidiary of the distinguished publishers John Wiley & Sons Inc. New Jersey, is an international science publisher based in Germany with 80 years experience of producing high-quality professional magazines, scientific journals, books, and electronic media in Chemistry, Physics, and Life Sciences.

As part of the expansion of the editorial department of our book programme in physics at Wiley-VCH and John Wiley & Sons we are offering the position of a

Senior Commissioning Editor Physics

Applicants should be innovative, self-motivated, and have the desire to contribute with their publishing experience to the further development of one of the world's top scientific book publishers in physics and electrical engineering. You will be responsible for ensuring effective management and expansion of our international book programme in physics and electrical engineering, including the acquisition and development of books, book series, and reference works. In addition you will be responsible for the development and implementation of the strategic publishing plan to contribute to our goal to become the leading book publisher in physics on a mid-term perspective. The successful applicant will also attend international meetings and conferences, visit laboratories and further expand his/her excellent contacts with the international community in physics. Therefore affinity, flexibility, and ability for travelling on a global scale are highly required.

Candidates must be experienced in commissioning scientific book projects with at least five years experience. You should already have had responsibility for the development of a scientific book programme in physics or in a subject area closely related to physics at an international level. A broad interest in science and technology, excellent organizational and communication skills (written and verbal), diplomacy, and flexibility are needed. You have strong negotiation skills to deal with authors and you are highly motivated as well as results-oriented. You have excellent analytical skills and judgement to identify opportunities and projects with high potential for success. You possess a broad education in physics (PhD required) and have the ability to work independently as well as closely with our head of the international physics book programme, our motivated team of acquisition editors, marketing and production colleagues.

Your native tongue should be either English whilst having very good knowledge in German as well or German with excellent knowledge in English (both written and verbal).

The Editorial Office for John Wiley & Sons' international book and journal programme in physics is based at WILEY-VCH in Berlin, Germany. Applicants should send their full CV with a covering letter describing their suitability for the post to:

WILEY-VCH Verlag GmbH & Co. KGaA
Human Resources
Christiane Rabe
Boschstrasse 12 • 69469 Weinheim • Germany
E-Mail: CRabe@wiley-vch.de
For further information on the post please contact our Editorial Director Dr. Alexander Grossmann by E-Mail: AGrossmann@wiley-vch.de.

WILEY-VCH

The place to be

http://www.wiley-vch.de

© 2006 Wiley-VCH Verlag GmbH & Co. KGaA, Weinheim

Nickel Catalysis

DOI: 10.1002/anie.200602629

The Remarkable Crossed Co-Isomerization Reaction of Cyclopropyl Ketones and Enones via Nickeladihydropyrans

*Guy C. Lloyd-Jones**

Keywords:
cyclopropanes · enolates · enones · homogeneous catalysis · nickel

Nickel complexes have long been viewed as the poor cousin of the more forgiving, user-friendly, palladium-based systems in the discovery and development of transition-metal-catalyzed organic transformations. However, nickel can prove advantageous in terms of cost and reactivity, and recently there has been a significant resurgence of interest in the field.[1] Despite their vertical relationship in the transition series, the organometallic chemistry of nickel and palladium are rather different to each other, albeit with significant overlap in the general class of transformations that they catalyze. The distinct reactivity of organonickel species is exquisitely represented in recent publications from Ogoshi, Nagata, and Kurosawa,[2] and Liu and Montgomery[3] on the "dimerization" reaction of **1** to generate 1,3-diacyl 2-methylcyclopentanes **2** (Scheme 1).

Because of their atypical C–C bonding and the associated ring-strain, cyclopropanes provide a wealth of organic reactivity.[4] However, the "unassisted" oxidative insertion of transition metals into the cyclopropane C–C bond is problematic owing to only weak precoordination to the metal center. By analogy to vinylcyclopropanes, which undergo a variety of transition-metal-catalyzed reactions,[5] cyclopropylketones **1** might be expected to facilitate

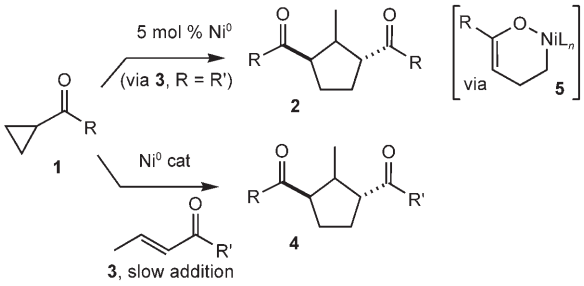

Scheme 1. Ni-catalyzed "dimerization" of cyclopropyl ketones **1** to generate 1,3-diacyl 2-methylcyclopentanes **2**, and the "crossed" reaction with enones **3** developed on the basis of dual isomerization and capture (→**4**) of nickeladihydropyran intermediates **5**.

precoordination via an η^1 or η^2 mode.[6] On this basis, two groups of researchers[2,3] have explored the reaction of compounds of type **1** with electron-rich "[L_nNi^0]" complexes generated in situ from [Ni(cod)$_2$] (cod = 1,5-cyclooctadiene) and L, where L = R_3P (R = Bu or Cy),[2] or an N-heterocyclic carbene (NHC).[3] Both papers ultimately report on the Ni-mediated reaction of cyclopropylketones **1** with enones **3** to give the crossed cyclopentane products **4**. This process is strongly suggestive that there is significant potential for the discovery and development of a broad range of nickel-catalyzed cycloaddition reactions. Liu and Montgomery focus on the exploration and development of the catalytic reaction,[3] using clues from a side reaction in **1**→**2**, to design reaction conditions for **1** + **3**→**4** (Scheme 1). In contrast, the work conducted by Ogoshi, Nagata, and Kurosawa[2] predominantly involves a stoichiometric investigation of the reaction mechanism for **1**→**2**, primarily by ^{1}H, ^{13}C, and ^{31}P NMR spectroscopy whereby the $^nJ_{P,X}$ scalar couplings provide key diagnostic structural information.

Liu and Montgomery began by investigating the process **1**→**2** where R is an aryl group. This was found to proceed efficiently at 90 °C in toluene (5 mol % [L_nNi]),[7] giving **2** in 83–90 % yield with high selectivity for the *anti* diastereoisomer (90–99 % d.r.). The reaction was proposed to proceed via a nickeladihydropyran-type enolate[8] (**5**), which was generated by what might be considered as a "conjugate addition" of [L_nNi^0] to the cyclopropylketone **1**.

A key observation was that the more hindered methyl-bearing cyclopropylketone **6** (Scheme 2) underwent rather inefficient dimerization to give **7** in 24 % yield as a *single* regioisomer, together with the 3-methyl enone $\mathbf{8_A}$ (66 %). An insightful analysis of the regiochemistry of **7** (see dashed line passing through **7** in Scheme 2) and the potential nickeladihydropyran intermediates ($\mathbf{9_A}$/$\mathbf{9_B}$) demonstrated that generation of **7** requires parallel insertion into the less hindered cyclopropane bond (A) of one molecule of **6** and into the more hindered cyclopropane bond (B) of a second molecule of **6**. Moreover, the material balance of the reac-

[*] Prof. Dr. G. C. Lloyd-Jones
School of Chemistry
University of Bristol
Cantock's Close, Bristol BS8 1TS (UK)
Fax: (+44) 117-929-8611
E-mail: guy.lloyd-jones@bris.ac.uk

InterScience
© 2006 Wiley-VCH Verlag GmbH & Co. KGaA, Weinheim

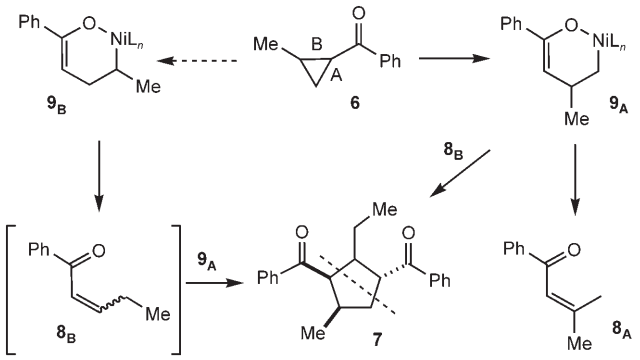

Scheme 2. Ni-catalyzed reaction of methylcyclopropyl ketone **6** and corresponding nickeladihydropyran intermediates **9** generated by insertion into the more (B) or less (A) hindered cyclopropane bonds.

tion suggests that the insertion into the less hindered cyclopropane bond (A) is favored, thus diverting more than 50% of **6** to 3-methyl enone $\mathbf{8_A}$ (resulting in a low yield of **7**) and implicating the *unobserved* 4-methyl enone $\mathbf{8_B}$ as a reactive intermediate.

The stage then appeared set for the informed design of a novel Ni-catalyzed coupling of enones with cyclopropanes (**1**+**3**→**4**); however, the simple stoichiometric reaction failed to proceed at all. It transpired that keeping the concentration of the enone much lower than that of the cyclopropane is crucial for success. The process becomes reasonably efficient (41–77% yields) with a diverse range of cyclopropylketones and enones when the enone component is added slowly (syringe pump, 2 h).

The origin of the inhibiting effect of the enone clearly emerges from the work of Ogoshi, Nagata, and Kurosawa,[2] who found that the rather stable bridged *dimeric* enone complex $(\mathbf{10})_2$ was generated in 72–100% yield on reaction of **1** (R = Ph or Me) with $[L_nNi^0]$ ($L = Cy_3P$) in toluene (100 °C, 1.5 h; Scheme 3). When the reaction was conducted in benzene at 40 °C with two equivalents of **1** (R = Ph), two precursor complexes were observed. An η^2-keto complex (**11**) was initially generated, which then underwent C–C insertion to generate the nickeladihydropyran intermediate **5** (R = Ph; proposed to be an O-bridged dimer $(\mathbf{5})_2$).[9] This key intermediate could then be observed by NMR spectroscopy to undergo a slow partitioning between isomerization to the enone complex $(\mathbf{10})_2$ (60%), versus reaction with residual **1** to generate the cyclopentane dimer **2** (R = Ph; 40%).

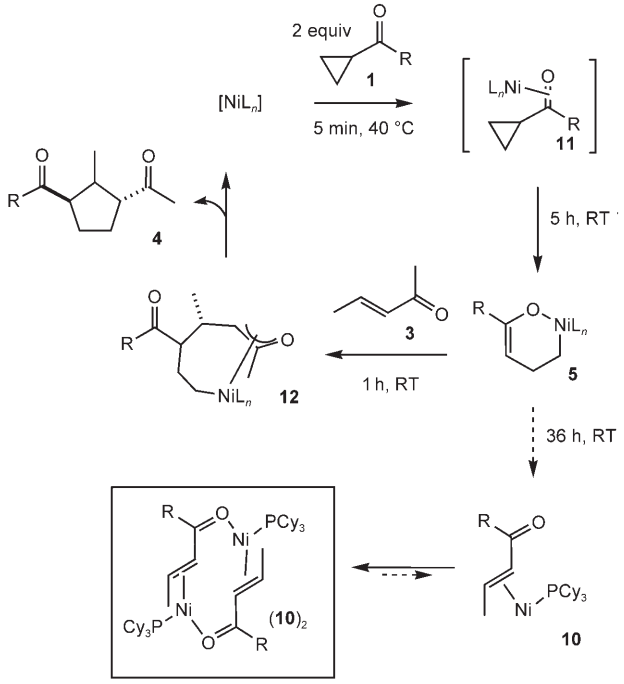

Scheme 3. Stepwise stoichiometric exploration of the Ni-catalyzed reaction of cyclopropyl ketones **1** with enones **3**. Note that in **4**, there is some ambiguity with regard to the relative configuration of the CH(Me) center between the acyl groups (see reference [12]).

When pure nickeladihydropyran intermediate **5**[9] was dissolved in benzene, it underwent slow but quantitative isomerization (formally via a β-H elimination sequence) over a period of 36 hours at room temperature to generate solely $(\mathbf{10})_2$.[10] However, in the presence of enone **3** (R = Me) nickeladihydropyran intermediate **5** undergoes a much faster, and again quantitative, reaction (1 h, room temperature) to generate alkyl π-oxoallyl nickel complex **12**, in which one of the two C–C bonds requisite for generation of **4** (or analogously **1**) have been generated. To complete their stoichiometric journey around the cycle, Ogoshi, Nagata, and Kurosawa[2] demonstrated that **12** can be persuaded to undergo reductive elimination (5 atm CO)[11] to set up the final C–C connectivity, thus liberating the crossed dimer **4** (R = Ph, R′ = Me).[12]

In conclusion, a rather unique reaction has emerged from two pioneering investigations into low-valent nickel chemistry. What is remarkable about these chronologically coincident but independent reports[2,3] is the truly complementary nature of the two pieces of research. When taken as a whole, they present a very detailed account of the scope and mechanism of the "dimerization" reaction of **1** with enones **3** to generate mixed 1,3-diacyl 2-methylcyclopentanes **4**. It is intriguing that the nickeladihydropyran intermediate **5** reacts with enones as an enolate rather than as an alkyl nickel complex, thus suggestive of a rich vein of organometallic nickel enolate chemistry for the imaginative and creative synthetic chemist to explore.

Published online: September 22, 2006

 © 2006 Wiley-VCH Verlag GmbH & Co. KGaA, Weinheim

[1] For selected recent examples, see: a) C. Böing, G. Franciò, W. Leitner, *Adv. Synth. Catal.* **2005**, *347*, 1537 – 1541; b) M. Kimura, M. Mori, N. Mukai, K. Kojima, Y. Tamaru, *Chem. Commun.* **2006**, 2813 – 2815; c) V. E. Albrow, A. J. Blake, R. Fryatt, C. Wilson, S. Woodward, *Eur. J. Org. Chem.* **2006**, 2549 – 2557; d) T. Hirashita, K. Akutagawa, T. Kamei, S. Araki, *Chem. Commun.* **2006**, 2599 – 2600.

[2] S. Ogoshi, M. Nagata, H Kurosawa, *J. Am. Chem. Soc.* **2006**, *128*, 5350 – 5351.

[3] L. Liu, J. Montgomery, *J. Am. Chem. Soc.* **2006**, *128*, 5348 – 5349.

[4] a) H. N. C. Wong, M. Y. Hon, C. W. Tse, Y. C. Yip, J. Tanko, T. Hudlicky, *Chem. Rev.* **1989**, *89*, 165 – 198, and references therein; b) H. Lebel, J. F. Marcoux, C. Molarino, A. B. Charette, *Chem. Rev.* **2003**, *103*, 977 – 1050, and references therein.

[5] G. Zuo, J. Louie, *J. Am. Chem. Soc.* **2005**, *127*, 5798 – 5799, and references therein.

[6] S. Ogoshi, M. Oka, H Kurosawa, *J. Am. Chem. Soc.* **2005**, *127*, 12810 – 12811, and references therein.

[7] Curiously, the schemes in reference [3] are suggestive of processes that are stoichiometric in nickel; however, experimental procedures given in the supporting information clearly indicate that 5 or 10 mol % Ni complex is employed.

[8] a) H. P. Hratchian, S. K. Chowdury, V. M. Gutiérrez-García, K. K. D. Amarasinghe, M. J. Heeg, H. B. Schlegel, J. Montgomery, *Organometallics* **2004**, *23*, 4636 – 4646, and references therein; for a discussion of O-bound versus C-bound Ni (and Pd) enolates, see: b) J. Cámpora, C. M. Maya, P. Palma, E. Carmona, E. Gutiérrez, C. Ruiz, C. Graiff, A. Tiripicchio, *Chem. Eur. J.* **2005**, *11*, 6889 – 6904.

[9] Reaction in THF allows **5** (R = Ph) to be isolated in 25 % yield as an analytically pure, fully characterized, orange solid.

[10] The bridged dimeric enone complex $(\mathbf{10})_2$ was proven to be active as a precatalyst (10 mol %) for dimerization of **1** (R = Ph), but is one order of magnitude less efficient than Cy_3P + [$Ni(cod)_2$], thus demonstrating that $(\mathbf{10})_2$ is an "off-cycle" species in slow and disfavored equilibrium with monomeric **10** or with free enone **3** and η^2-keto complex **11**. Whilst not directly translatable to the conditions developed by Montgomery (reference [3]), this result explains why slow addition of enone is crucial for success under catalytic conditions.

[11] The coproduct is catalytically inert [$Ni(Cy_3P)(CO)_3$]. No mention of thermally triggered reductive elimination, for example, in the presence of **1**, is made.

[12] Note that there is in interesting conflict of assignment of relative configuration in **4** (R = Ph, R′ = Me) between references [2] and [3]. No explicit mention is made in either publication, or the supporting information, on how the relative configuration of **4** (and related crossed co-isomerization products) was assigned. It is noted in reference [3] that the products are kinetically controlled (thus, there is no epimerization). Reference [2] gives NMR data for two diastereomers of **4** (R = Ph, R′ = Me). Comparison of NMR data for both isomers with that for the only isomer reported in reference [3] suggests that (whilst the data is nonidentical) the same diastereoisomer is isolated as the major one under both sets of conditions (L = Cy_3P or NHC).

 © 2006 Wiley-VCH Verlag GmbH & Co. KGaA, Weinheim

History of Science

DOI: 10.1002/anie.200601600

Henri Moissan: Winner of the Nobel Prize for Chemistry 1906

*Alain Tressaud**

Keywords:
electrochemistry · fluorine · high-temperature chemistry · history of science

On December 10, 1906, Henri Moissan (1852–1907) became the first French chemist to be awarded the Nobel Prize. At the award ceremony in Stockholm, the President of the Royal Swedish Academy of Sciences, P. Klason, described the two essential aspects of this great scientist's work in the following terms, saying the prize had been awarded to Moissan, "*for having isolated and investigated the chemical element fluorine and for having introduced the electric furnace into the service of science—exploits whereby he has opened up new fields for scientific research and industrial activity*".[1] Indeed, Moissan had isolated fluorine twenty years earlier during a historic experiment; he also paved the way for high-temperature synthesis.

Figure 1. Henri Moissan (1852–1907).

The Early Years

Henri Moissan was born in Paris in 1852 but spent much of his teenage years and his early professional life in Meaux, where he was an apprentice clockmaker (Figure 1). In 1870 war against Prussia obliged his family to return to Paris, and he joined the army for a year before enrolling at the Ecole Supérieure de Pharmacie de Paris. Henri Moissan was divided for many years between his two loves, pharmacy and experimental chemistry, and enrolled first in 1872 at the Ecole de Chimie Expérimentale, headed by Edmond Frémy at the Muséum, before joining P. P. Dehérain's research group, also at the Muséum, where he carried out research into vegetable physiology, the absorption of oxygen, and the emission of carbon dioxide in plants kept in obscurity. He was appointed a senior chemist in 1879. An account of his research during this period into the chemistry of pyrophoric iron and metal oxides of the iron family can be found in the doctoral thesis he wrote in 1880. At the same time, he climbed the hierarchical ladder at the Ecole Supérieure de Pharmacie de Paris. In 1880 he was appointed Maître de Conférences and Chef de Travaux Pratiques, before becoming Professeur Agrégé in 1882 with a thesis entitled "*Série du Cyanogène*" (The Cyanogen Series).[2,3]

It was only in 1884 that Moissan began to concentrate solely on isolating fluorine, a halogen discovered in the early years of the 19th century thanks to the work of A. M. Ampère in France and H. Davy in England (see inset).[4–7] Yet the gas had never been isolated because of its violent reactivity.

1886: A Great Year for Fluorine

Several generations of chemists had tried in vain to isolate fluorine, notably by electrolyzing phosphorus and arsenic fluorides, but Moissan was determined to find a way. His genius lay in the idea of turning the bath into a conductor by adding a molten potassium fluoride salt, KHF_2. (Pure hydrogen fluoride, HF, could not suffice as its capacity as an electric conductor was too weak.) Moissan devised a platinum electrolyzer and lowered the reaction temperature of the electrolytic solution of HF + KHF_2 to limit corrosion. The platinum electrolyzer was U-shaped and stopped with fluorite (CaF_2) stoppers (Figure 2). The cathode and the anode were made of irridated platinum to provide better resistance to the fluorine. The traces of hydrogen fluoride were condensed at the end of the apparatus in a low-temperature trap and also by sodium fluoride. On June 28, 1886, a gaseous product was identified at the anode of the electrolyzer: Fluorine (F_2) had been successfully isolated, thus resolving one of the most difficult challenges in the realm of inorganic chemistry (Figure 3).[8] The yellow-green gas obtained was highly toxic and proved to be a

[*] Dr. A. Tressaud
Institut de Chimie de la Matière Condensée de Bordeaux (ICMCB-CNRS)
Université Bordeaux 1
87 Avenue Dr. A. Schweitzer
33608 Pessac Cedex (France)
Fax: (+33) 5-4000-2761
E-mail: tressaud@icmcb-bordeaux.cnrs.fr

InterScience
© 2006 Wiley-VCH Verlag GmbH & Co. KGaA, Weinheim

Figure 2. Moissan's Nobel Prize diploma and the electrolytic cell used for producing fluorine (courtesy of the Moissan Museum, Faculté de Pharmacie, Université Paris 5—René Descartes; photograph taken by A. Tressaud).

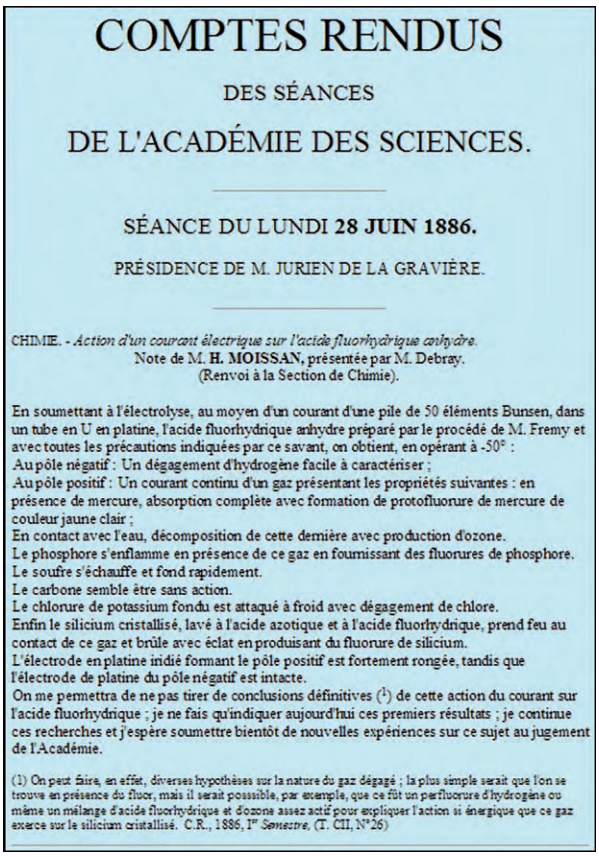

COMPTES RENDUS

DES SÉANCES

DE L'ACADÉMIE DES SCIENCES.

SÉANCE DU LUNDI **28 JUIN 1886.**

PRÉSIDENCE DE M. JURIEN DE LA GRAVIÈRE.

CHIMIE. - *Action d'un courant électrique sur l'acide fluorhydrique anhydre.* Note de M. **H. MOISSAN**, présentée par M. Debray. (Renvoi à la Section de Chimie).

En soumettant à l'électrolyse, au moyen d'un courant d'une pile de 50 éléments Bunsen, dans un tube en U en platine, l'acide fluorhydrique anhydre préparé par le procédé de M. Fremy et avec toutes les précautions indiquées par ce savant, on obtient, en opérant à -50° :
Au pôle négatif : Un dégagement d'hydrogène facile à caractériser ;
Au pôle positif : Un courant continu d'un gaz présentant les propriétés suivantes : en présence de mercure, absorption complète avec formation de protofluorure de mercure de couleur jaune clair ;
En contact avec l'eau, décomposition de cette dernière avec production d'ozone.
Le phosphore s'enflamme en présence de ce gaz en fournissant des fluorures de phosphore.
Le soufre s'échauffe et fond rapidement.
Le carbone semble être sans action.
Le chlorure de potassium fondu est attaqué à froid avec dégagement de chlore.
Enfin le silicium cristallisé, lavé à l'acide azotique et à l'acide fluorhydrique, prend feu au contact de ce gaz et brûle avec éclat en produisant du fluorure de silicium.
L'électrode en platine iridié formant le pôle positif est fortement rongée, tandis que l'électrode de platine du pôle négatif est intacte.
On me permettra de ne pas tirer de conclusions définitives (1) de cette action du courant sur l'acide fluorhydrique ; je ne fais qu'indiquer aujourd'hui ces premiers résultats ; je continue ces recherches et j'espère soumettre bientôt de nouvelles expériences sur ce sujet au jugement de l'Académie.

(1) On peut faire, en effet, diverses hypothèses sur la nature du gaz dégagé ; la plus simple serait que l'on se trouve en présence du fluor, mais il serait possible, par exemple, que ce fût un perfluorure d'hydrogène ou même un mélange d'acide fluorhydrique et d'ozone assez actif pour expliquer l'action si énergique que ce gaz exerce sur le silicium cristallisé. C.R., 1886, I^er^ *Semestre*, (T. CII, N°26)

Figure 3. Moissan's very first note on the isolation of fluorine.[8a]

powerful oxidizing agent, causing organic materials to burst into flames on entering into contact with it and combining directly, and often violently, with almost all other elements.[9–11]

Henri Moissan: The Great Scientist

Several months after having isolated fluorine, Moissan was appointed Professor of Toxicology at the Ecole Supérieure de Pharmacie. Although this discipline was not his specialty, he taught toxicology for 13 years. During this period, he drew up a highly detailed list of rules to be respected for drafting expert reports in, for instance, the study of epidemics. He also carried out studies into hygiene in the professional environment, the analysis of air in factories, urban sanitation, diet and food, and so on. His rethinking of the teaching of toxicology was rewarded with a seat on the prestigious Académie de Médecine in 1888. Yet Moissan's work as Professor of Toxicology did not stifle his passion for inorganic chemistry, and his research in this field quickly brought him to the forefront of chemistry in France along with wide international acclaim. In 1891 he was appointed to the Académie des Sciences, and in July 1900 he became Professor of Inorganic Chemistry at the Faculté des Sciences, Université de Paris. Until 1890, his research was devoted entirely to fluorine and the properties of its derivatives, in collaboration with his students, Lebeau, Meslans, and Poulenc,[12–14] or eminent colleagues such as Becquerel or Berthelot. Moissan was a first-class teacher and published a multitude of books dealing with the main aspects of the inorganic chemistry of his era.[15]

In the latter part of his career, Moissan had great success in the field of inorganic synthesis. He obtained a pure state of boron together with a good number of borides. From 1890 on, he worked on an even more challenging task than that of isolating fluorine—that of artificially creating diamonds.[16a] In order to achieve the extremely high temperatures required to transform carbon into diamond, he designed an electric furnace based on the principle of an electric arc between two blocks of limestone (Figure 4). He described this furnace in a report dating from 1892,[16b] and explained how the furnace could reach temperatures between 3000–3500 °C, quite exceptional at that time. He heated a compound of iron and sugar carbon to a temperature of 3000 °C, and then immersed the carbon crucible into cold water. High pressure was thus created inside the solid. Moissan found microscopic crystals of different types of diamond in the residues, although in quantities of only a few milligrams.

 © 2006 Wiley-VCH Verlag GmbH & Co. KGaA, Weinheim

The Search for the Missing Halogen through the 19th Century: From A.-M. Ampère and H. Davy to E. Frémy

In 1809, when the discovery of sodium and potassium by English chemist Humphrey Davy (1778–1829) was announced in France, André-Marie Ampère (1775–1836) grasped the idea that chlorine and fluorine were both chemical elements but did not publish his hypotheses. He was astonished by the analogies between muriatic acid (chlorhydric acid) and fluoric acid (fluorhydric acid) and concluded that an element first called *oxy-fluoric* and later *fluorine* (in French) must exist, once he had understood that fluorhydric acid did not contain any oxygen. Among the letters that he exchanged with Davy during the war raging between their two nations, he even suggested on November 1, 1810, the possibility of isolating the element fluorine through the electrolysis of anhydrous fluorhydric acid.[4] "*What remains to be discovered is whether the electricity will not decompose the hydrofluoric acid into its liquid form, when we have removed the water to the greatest extent, by bringing the hydrogen to one side and the oxy-fluoric to the other.*" In his reply in February 1811, Davy does not concede that a single body be present as Ampère asserts, but rather, considers that this body also contains oxygen. At that time, Davy could not state categorically that fluorine was an element: "*In the views that I have ventured to develop, neither oxygen, chlorine or fluorine are asserted to be elements*". However, Ampère allowed Davy, who was now convinced that the French scientist's views were correct after 3 years of corresponding with him, to reap the glory of announcing in 1813 that a new element had been discovered.[5] An autobiographical note by Ampère, in which he refers to himself in the third person, does however establish the anteriority of his own discovery, which is also fully recognized by Davy: "*During the period I was engaged in these investigations, I received two letters from M. Ampère of Paris, containing many ingenious and original arguments in favour of the analogy between the muriatic and fluoric compounds. M. Ampère communicated his views to me in the most liberal manner; they were formed in consequence of my ideas on chlorine and supported by reasonings drawn from the experiments of [...] Gay-Lussac and Thénard*".

The isolation of this new element continued to occupy many researchers for most of the nineteenth century. A first step was the preparation of pure water-free hydrofluoric acid by L. J. Thénard (1777–1857) and L. J. Gay-Lussac (1778–1850). Their product fumed strongly in air, rapidly dissolved glass, and caused extraordinary burns if it entered into contact with the skin—a phenomenon the authors described in great detail. Later on, J. J. Berzelius (1779–1848) characterized ammonium fluoride. Other researchers paid a high price to the even more toxic effects of this element, without for so much succeeding in isolating the element: G. and T. Knox were severely intoxicated, and the Belgian chemist P. Louyet lost his life. Meanwhile, J. C. Marignac (1817–1894) described in minute detail around 1860, the preparation and crystal morphology of a good number of anhydrous or hydrated fluorosalts, such as fluorotitanates or fluorozirconates, and most of his accurate conclusions are still valid today.[6] Many new inorganic fluorides were also characterized by scientists such as H. Sainte-Claire Deville (1818–1881) or E. Frémy (1814–1894). Nevertheless, it seemed almost impossible to synthesize fluorine, despite numerous attempts carried out during the latter part of the century.

An important step was made by Frémy, Moissan's first mentor, when he succeeded in preparing pure anhydrous HF as well as KHF_2, the so-called Frémy's salt expressed as "KFl·HFl" using the notations of that time.[7] Frémy had come very close to solving the puzzle by electrolyzing anhydrous HF, molten calcium fluoride, or potassium fluoride, but he seemed not to have had the idea of replacing these compounds by KHF_2, perhaps because of the high melting point of the compound (m.p. 293 °C), which would have led to insurmountable technical difficulties.

Although Moissan was never able to totally fulfill his dream in this field and his research was contested by Le Chatelier and Parsons, his ideas were nonetheless visionary and paved the way for high-pressure experiments that led to the industrial synthesis of an artificial diamond by General Electric fifty years later. Today, the annual global production of synthetic diamonds is estimated at around 450–500 million carats.[17]

With the technological breakthrough brought by the electrical furnace, Moissan turned over a new page in the history of chemistry, that of high-temperature chemistry. The list of his discoveries is impressively long and includes:

- crystallization of a large number of oxides that were reputedly infusible,
- obtaining refractory metals by reducing their oxides in the presence of carbon,
- discovering a large number of metallic carbides such as calcium carbide, which then made way for the discovery of acetylene, but also new borides, nitrides, and silicides,
- development of a method for preparing calcium in a pure state by reducing calcium iodide with excess sodium, and developing metallic hydrides, etc.

We may also conclude that, along with Collongues, Moissan is the forebear of high-temperature chemistry.[18]

The Nobel Prize crowned the career of this great scientist. However, Moissan also received an impressive number of other titles and distinctions, including entry into the scientific academies of France and various foreign countries, honorary doctorates, and other prestigious distinctions. The dedication of Moissan to his work did not mean that he neglected the other sides of intellectual life. Although he cared little for music and the theatre, he showed great admiration for the work of Jean-Baptiste Corot and had several magnificent canvasses by the painter that he would sit and contemplate to rest his mind. He was also a passionate collector of works by contemporary artists and antique engravings. He also had a very fine collection of autographs relating to the French Revolution.[19]

© 2006 Wiley-VCH Verlag GmbH & Co. KGaA, Weinheim

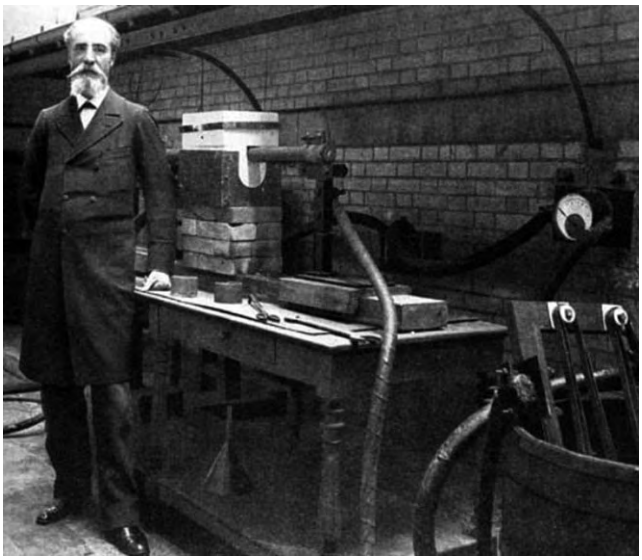

Figure 4. Moissan and his electric furnace at the Faculté des Sciences, Université de Paris.

Moissan died on February 20, 1907, at the age of 54 from acute appendicitis, just two months after receiving his Nobel Prize. Fluorine and its highly toxic gaseous derivatives, together with the carbon monoxide that was emitted from his electric furnace, had no doubt weakened his health and may well have been responsible for his low resistance to the infection.

Our Inheritance from Henri Moissan

Moissan is still considered to be a pioneer in most of the fields in which he carried out his research, and a long list of new technological methods and important scientific discoveries are the direct result of his innovative work. In 1986, the Moissan Prize was created in recognition of stimulating research in the field of fluorine chemistry.[20]

The electric furnace paved the way for breakthroughs in the fields of electrometallurgy, in aluminothermics, and the acetylene and calcium cyanamide industries. The production of crystalline oxides, the industrial production of ceramics, and refractory techniques also owe a great deal to his innovative work. The importance of carbides, as Moissan foresaw, is illustrated by the important role played by composites in a wide range of strategic fields.[21]

Today, fluorine is still synthesized electrochemically using the principle elaborated by Moissan.[22,23] One of the main uses of this process today is the transformation of uranium tetrafluoride into its hexafluoride, an essential stage in the production of nuclear energy.[24] There are over 600000 compounds that contain at least one atom of fluorine, and the chemistry of fluorine and fluorine-based products has allowed huge breakthroughs to be made in a wide variety of fields, including organic chemistry,[25] materials science,[26] polymers,[27] drugs, and medical applications.[28] Some of the great discoveries that emerged in the 20th century as a result include:

- the use of organic and/or inorganic fluorine in a number of energy-conversion processes (e.g. in Li ion batteries, fuel cells, and nuclear energy);[24,29]
- the use of fluoride polymers such as Teflon, which resist corrosion so remarkably, in packaging highly reactive products, nonstick kitchen utensils, materials for cardiovascular implants, and membranes for fuel cells;[27]
- the use of fluorine and fluoride gases in microelectronics within the production process of silicon components, which means that all impurities can be eliminated from the surface of a semiconductor, thus allowing our computers to function efficiently;
- the use of fluoro-surfactants to protect fabrics, carpets, and leather, and as a fire-retardant material;
- the surface coating of materials with fluorinated compounds to make them graffiti-proof or UV-absorbent, or to protect our cultural heritage by injecting fluoride polymers into lithic objects and coating metallic structures (as an example, coating the metallic framework of the Louvre Pyramid or the metallic parts supporting the structure of the Grande Arche at La Défense in Paris);
- the use of fluorinated molecules in cancer-repressant drugs, anti-inflammatories, antibiotics, neuroleptics, or antihypertensive drugs as a result of their associated therapeutic properties, and there are possibilities for using perfluorocarbons in vitreoretinal surgery and as substitutes for blood in emergency transfusions;[28]
- the use of molecules containing one or several atoms of fluorine as efficient herbicides, fungicides, or insecticides;
- the use of ^{18}F positron emission tomography or ^{19}F NMR for medical imaging to detect the early presence of tumors and for diagnosing some diseases of the brain, such as Alzheimer's Disease.

It is clear that some problems caused to our environment by fluorinated products should not be underestimated.[30] A great challenge for the groups dealing with fluorine and fluoride products is to find solutions to overcome these problems, such as supervising the use of fluoride molecules in agrochemicals, developing a definitive substitute for chlorofluorocarbons (CFCs), which are partly to blame for destroying the ozone layer, and the defluoridation of drinking water in many areas of the world where there is a risk of people contracting fluorosis.[31] Although the isolation of fluorine by Henri Moissan dates back over a century, the fabulous destiny of this element seems to be only in its early years today, as the breakthroughs and new vistas brought by it to so many fields of science brim with potential.[32]

Published online: September 7, 2006

 © 2006 Wiley-VCH Verlag GmbH & Co. KGaA, Weinheim

[1] *Nobel Lectures, Chemistry 1901–1921*, Elsevier, Amsterdam, **1966**.

[2] "Vie et Œuvre de H. Moissan": C. Viel, J. Flahaut, *J. Fluorine Chem.* **1986**, *33*, 27 – 44, a lecture given during the *International Symposium on the Centenary of the Discovery of Fluorine*, Paris, **1986**.

[3] "Aspects historiques de l'isolement du fluor. Travaux d'Henri Moissan et de ses collaborateurs directs jusqu'au début du XX^{e} siècle", C. Viel in the special issue of *Actualité Chimique*, Société Française de Chimie, **2006**.

[4] "*Reste à savoir si l'électricité ne décomposerait pas l'acide hydro-fluorique sous sa forme liquide, lorsqu'on en aurait écarté l'eau le plus possible, en portant l'hydrogène d'un côté et l'oxy-fluorique de l'autre.*" Taken from "*Correspondance du Grand Ampère*", Gauthiers-Villars, Paris, **1936**, including correspondence between the two scientists from 1810 to 1825.

[5] H. Davy, *Philos. Trans. R. Soc. London* **1812**, *102*, 352; H. Davy, *Philos. Trans. R. Soc. London* **1813**, *103*, 263; H. Davy, *Philos. Trans. R. Soc. London* **1814**, *104*, 62.

[6] J.-C. Galissard de Marignac, *Œuvres Complètes",* Tomes 1 & 2 (**1840**–**1887***)*, Société de Physique de Genève, Masson, Paris, **1890**; A. De Cian, J. Fisher, *Acta Crystallogr.* **1967**, *22*, 338; J. Fisher, G. Keib, R. Weiss, *Acta Crystallogr.* **1967**, *22*, 340; W. Massa, *Z. Anorg. Allgem. Chem.* **1977**, *436*, 29.

[7] E. Frémy, *Ann. Chim. Phys.* **1856**, *47*, 5 – 50.

[8] a) H. Moissan, *C. R. Hebd. Seances Acad. Sci.* **1886**, *102*, 1543 – 1544; b) H. Moissan, *C. R. Hebd. Seances Acad. Sci.* **1886**, *103*, 202 – 205; c) H. Moissan, *C. R. Hebd. Seances Acad. Sci.* **1886**, *103*, 256 – 258.

[9] E. Banks, *J. Fluorine Chem.* **1986**, *33*, 3 – 26 and *Fluorine Chemistry at the Millennium: Fascinated by Fluorine* (Ed.: R. E. Banks), Elsevier, Dordrecht, **2000** (partly in *J. Fluorine Chem.* **1999,** *100*).

[10] H. Moissan, *Das Fluor und seine Verbindungen*, Krayn, Berlin, **1900**.

[11] P. Lebeau, *Bull. Soc. Chim. Fr.* **1908**, *4*, 3 – 4; the same text appeared in "Hommage à Henri Moissan": *Chimie et Industrie*, Paris, **1932**.

[12] For some representative reports on fluorine and fluoride compounds, see: "Recherches sur l'isolement du fluor", H. Moissan, *Ann. Chim. Phys.* **1887**, *12*, 472; "Nouvelles recherches sur le fluor", H. Moissan, *Ann. Chim. Phys.* **1891**, *24*, 224; "Fluorure double de chrome et potassium", H. Moissan, *Ann. Chim. Phys.* **1894**, *2*, 66; "Le bifluorure de platine anhydre", H. Moissan, *C. R. Hebd. Seances Acad. Sci.* **1889**, *109*, 807.

[13] C. Poulenc, *Ann. Chim. Phys.* **1894**, *2*, 5.

[14] H. Becquerel, H. Moissan, *C. R. Hebd. Seances Acad. Sci.* **1890**, *111*, 669 – 672.

[15] H. Moissan, *Le Fluor et ses Composés*, Steinhel, Paris, **1900**; *Le four électrique*, Steinhel, Paris, **1897**; *Traité de Chimie Minérale*, Masson, Paris, **1904**–**1906**.

[16] a) O. Krätz, *Angew. Chem.* **2001**, *113*, 4739 – 4745; *Angew. Chem. Int. Ed.* **2001**, *40*, 4604 – 4610; b) H. Moissan, *C. R. Hebd. Seances Acad. Sci.* **1892**, *115*, 1031 – 1033.

[17] The Canadian Encyclopedia, **2006**, http://www.thecanadianencyclopedia.com; search "diamonds".

[18] R. Collongues, F. Galtier, *Pour la Science* **1996**, *230*, 46 – 52.

[19] At the auction of his collection of autographs at Drouot on October 14, 1921, more than 6000 items and manuscripts were sold off.

[20] Following an international symposium in 1986 commemorating the isolation of fluorine, the Moissan Prize was established by co-chairmen, P. Hagenmüller and P. Plurien, in recognition of achievements in the various fields of fluorine chemistry. Since then, the prize has been awarded at every International Symposium on Fluorine Chemistry: 1988: G. Cady (Seattle, USA) and N. Bartlett (Berkeley, USA); 1991: H. J. Emeléus (Cambridge, UK); 1994: R. N. Haszeldine (UMIST-Manchester, UK); 1997: P. Hagenmüller (Bordeaux, France); 2000: K. O. Christe (USC-Los Angeles, USA); 2003: R. Chambers (Durham, UK); 2006: D. D. DesMarteau (Clemson, SC, USA). Besides this prize, Moissan grants are regularly proposed to students by the Fluorine Division of the American Chemical Society.

[21] W. Krenkel, R. Naslain, H. Schneider, *High Temperature Ceramic Matrix Composites*, Wiley, New York, **2001**.

[22] M. Jaccaud, F. Nicolas, *Techniques de l'Ingénieur* **1990**, J6020–J1453.

[23] D. Pletcher, *Industrial Electrochemistry*, Chapman and Hall, London, **1982**, chap. 5.

[24] "Synthèse électrochimique du fluor de 1886 à 2006: le fluor, élément clef pour l'énergie nucléaire", H. Groult, F. Lantelme, C. Belhomme, B. Morel, F. Nicolas, J. P. Caire in the special issue of *Actualité Chimique*, Société Française de Chimie, **2006**.

[25] K. Uneyama, *Organofluorine Chemistry*, Blackwell, Malden, USA, **2006**; R. Chambers, *Fluorine in Organic Chemistry*, Blackwell, Malden, USA, **2004**; *Handbook of Fluorous Chemistry* (Eds.: J. A. Gladysz, D. P. Curran, I. T. Horvath), Wiley, New York, **2004**; P. Kirsch, *Modern Organofluorine Chemistry—Synthesis & Applications*, Wiley-VCH, Weinheim, **2004**; R. E. Banks, B. E. Smart, J. C. Tatlow, *Organofluorine Chemistry: Principles & Commercial Applications*, Kluwer/Plenum, New York, **1994**; G. A. Olah, G. K. S. Prakash, R. D. Chambers, *Synthetic Fluorine Chemistry*, Wiley, New York, **1992**.

[26] *Advanced Inorganic Fluorides: Synthesis, Characterization and Applications* (Eds.: T. Nakajima, B. Zemva, A. Tressaud), Elsevier, Dordrecht, **2000**; N. Watanabe, T. Nakajima, H. Touhara, *Graphite Fluorides*, Elsevier, Dordrecht, **1988**; *Inorganic Solid Fluorides: Chemistry and Physics* (Ed.: P. Hagenmüller), Academic Press, New York, **1985**.

[27] B. Ameduri, B. Boutevin, *Well-Architectured Fluoropolymers*, Elsevier, Dordrecht, **2004**.

[28] J. P. Bégué, D. Bonnet-Delpon, *Chimie Bioorganique et Médicinale du Fluor*, EDP-Sciences, Paris, **2005**; I. Ojima, J. R. McCarthy, J. T. Welch, *Biomedical Frontiers in Fluorine Chemistry*, American Chemical Society, Washington DC, **1996**; J. T. Welch, S. Eswarakrishnan, *Fluorine in Bioorganic Chemistry*, Wiley, New York, **1991**.

[29] *Fluorinated Materials for Energy Storage* (Eds.: T. Nakajima, H. Groult), Elsevier, Dordrecht, **2005**.

[30] L. H. Weinstein, A. Davison, *Fluorides in the Environment: Effect on Plants and Animals*, CABI Publishing, Cambridge, MA, **2004**.

[31] Volumes dedicated to "*Fluorine and the Environment*" in the book series *Advances in Fluorine Science* (Ed.: A. Tressaud), Elsevier, Dordrecht, **2006**.

[32] Celebrations in 2006 for the centenary of Henri Moissan's Nobel Prize include a session at the 18th International Symposium on Fluorine Chemistry, Bremen, August 3, 2006; special issues of "*Actualité Chimique*" (Société Française de Chimie) and *J. Fluorine Chem*; the International Colloquium at Maison de la Chimie, Paris (November 10, 2006); and celebrations in the city of Meaux, France.

 © 2006 Wiley-VCH Verlag GmbH & Co. KGaA, Weinheim

History of Science

DOI: 10.1002/anie.200602651

J. J. Thomson: Winner of the Nobel Prize for Physics 1906**

*John Meurig Thomas**

Keywords:
cathode rays · electric discharge · history of science · magnetism

In 1881, during the course of his Faraday Lecture at the Royal Institution of Great Britain, London, the German physiologist-turned-physicist Hermann von Helmholtz, having earlier ruminated deeply on the significance of Faraday's laws of electrolysis, asserted that electricity must have a unitary structure, the maximum value of the unit being that which is sufficient to react with one univalent atom. Lecturing in the same theatre 16 years later on the topic of cathode rays,[1] Joseph John Thomson, Cavendish Professor of Experimental Physics, University of Cambridge, announced his discovery of electrons, which at the time he designated "corpuscles". In 1906, J. J. Thomson became the second British physicist (Rayleigh was the first) to win the Nobel Prize "*for his theoretical and experimental investigations on the conduction of electricity by gases*" (Figure 1).

How did it come about that this brilliant mathematician, keen chemical theorist, but maladroit experimentalist—a man who, when he was appointed Master of Trinity College, Cambridge, in 1918 was described by the British Prime Minister at the time, David Lloyd George, as a physicist of "super-eminence"—achieved such a major breakthrough as to discover the first subatomic particle? And how was it that Ernest Rutherford (later his immediate successor as Cavendish Professor and universally regarded as the "prince of experimentalists") became his research student? These and allied topics constitute the subject matter of this Essay, which also touches upon cultural aspects of science that are relevant to the pursuit of knowledge in all disciplines. In this summarized account[2] of "J. J."—as he was widely known in Cambridge and beyond—we shall be reminded of the role that enthusiasm, discipline, and

Figure 1. J. J. Thomson (1856–1940). Source: Trinity College, Cambridge.

[*] Prof. Sir J. M. Thomas
Department of Materials Science and Metallurgy
University of Cambridge
Pembroke Street
Cambridge, CB2 3QZ (UK)
Fax: (+44) 1223-334-567
E-mail: jmt2@cam.ac.uk
and
Davy–Faraday Research Laboratory
Royal Institution of Great Britain
21 Albemarle Street
London, W1S 4BS (UK)

[**] I am grateful to Professor E. A. Davis for constructive comments and Rebecca Pritchard for help in preparing the manuscript.

© 2006 Wiley-VCH Verlag GmbH & Co. KGaA, Weinheim

unpredictable consequences of what the Dutch physicist Casimir called "haphazard reality" play in the progress and evolution of science.

The Formative Years

J. J. Thomson was born on December 18, 1856, in a suburb of Manchester, the son of an antiquarian bookseller. As part of his early education (at small private schools) he learnt the rules of Latin grammar, passages of English literature, and the propositions of Euclid, all by heart. At the age of 14 he went to Owen's College (now the University of Manchester), where he was much impressed by the brilliant, if somewhat eccentric, teaching of Osborne Reynolds[3] and John H. Poynting,[4] among others. He soon won an open scholarship in mathematics at Trinity College, Cambridge, and he began his studies there in 1876 (he spent most of every term there until his death in 1940).

At Cambridge, Thomson became absorbed into the world of the so-called Mathematical Tripos, and particularly of those aspiring to a high place in it. In the late 19th century, the Mathematical Tripos was a major focus of intellectual challenge, and enormous kudos was attached to achieving a high result. The examination itself, taken after three years, consisted of 15–20 three-hour exams, sat over a period of three weeks. When the results were later declared, students were divided into Wranglers (first class), Senior Optimes (second class), and Junior Optimes (third class). The Senior Wrangler (top man) was feted throughout Cambridge, by his school, and in his hometown. *"Aspiring Wranglers took their training extremely seriously, working intensively for eight hours each day, taking two hours exercise, generally in the form of long fast walks in pairs, relaxing after dinner, and keeping themselves celibate*".[5]

It was the famous coach Edward J. Routh (a Fellow of Peterhouse and himself a Senior Wrangler at the time when James Clerk Maxwell was Second Wrangler) who guided Thomson through the Mathematical Tripos. In the second half of the 19th century, Routh taught all the brightest young stars in the Cambridge mathematical firmament, including Joseph Larmor (of Larmor frequency renown). Writing about Routh in his autobiography,[6] J. J. Thomson said that "*Perhaps no other man has ever exerted so much influence on the teaching of mathematics; for about half a century the vast majority of Professors of Mathematics in English, Scottish, Welsh and Colonial universities had been pupils of his*". During 1855–1888, Routh had 27 Senior Wranglers. Interestingly, J. J. Thomson was Second Wrangler in the year that his Irish friend Joseph Larmor was Senior Wrangler.

Fellow and Lecturer in Mathematics, Trinity College

After taking his degree, Thomson began at once to carry out research; he had even published one or two short papers on purely mathematical subjects before graduating. For the first four years thereafter, his work was dominated by his commitment to analytical dynamics and to Maxwell's electrodynamics. Aiming high, as was his style throughout his career, he tried for a Fellowship at Trinity—and to the surprise of many he was awarded it. He settled down to carry out research work in mathematical and experimental physics. His experimental work included a determination of the ratio of the electromagnetic to the electrostatic unit, which he carried out under the direction of Lord Rayleigh, the then Cavendish Professor.[7]

On Lord Rayleigh's retirement from the chair at the end of 1884, Thomson became a candidate, to the surprise of many. Even more remarkably, he was appointed Rayleigh's successor—at the tender age of 27 and with the reputation already of being a clumsy experimentalist (in marked contrast to Rayleigh). However, any doubts that may have been entertained were soon dispelled by his success in the leadership of the experimental school at Cambridge.

Cavendish Professor of Experimental Physics

At the time of his appointment to this prestigious post (the first occupant was Clerk Maxwell), Thomson was not, and he never became, a skilful manipulator. Nevertheless, his great intrinsic abilities and his innate inventiveness largely negated these difficulties, and he commanded the willing help of others whose qualities were complementary to his own. Moreover, he could instill enthusiasm and pertinacity into those who worked alongside him.

For two years or so from 1885 onwards, he was preoccupied with attempts to explain atomic valency and the periodic properties of the elements. His vortex atom model—shades of the latent influence of Osborne Reynolds perhaps—seemed to do this; indeed, one of his papers was entitled "*The Vortex Ring Theory of Gases: On the Law of Distribution of Energy among the Molecules*".[8]

However, soon he devoted his main attention to the discharge of electricity through gases, the subject on which his great achievements in the future were to come. As the fourth Baron Rayleigh—the son of Thomson's immediate predecessor in the Cavendish Chair—said in his perceptive obituary notice of Thomson, "*His earlier investigations on the discharge of electricity through gases were largely exploratory. He was, as it were, searching for a clue by which he might thread his way through the mazes of this subject, so rich in experimental detail but with so few clues for theoretical guidance*".

Thomson also spent much time in investigating the electrolysis of steam[9] and in determining the apparent velocity with which luminosity was propagated along a long vacuum tube. Yet, the real turning point in his work on electric discharge began with Wilhelm Conrad Röntgen's momentous discovery of X-rays in 1896.

However, there were other, almost adventitious developments at that time which led to dramatic advances in Cambridge science. It so happened that, in 1893, Thomson appended a supplement (entitled "*Recent Researches in Electricity and Magnetism*") to J. Clerk Maxwell's monumental "*Treatise on Elec-*

 © 2006 Wiley-VCH Verlag GmbH & Co. KGaA, Weinheim

tricity and Magnetism" that had been published in 1873. The enlarged version of this classic monograph, carrying the exciting addition by Thomson, was avidly read by natural philosophers the world over. Many exceptionally able young scientists elsewhere in the British Isles and in foreign lands were anxious to take the opportunity of studying with him. Fortunately, in the early 1890s the University of Cambridge decreed that postgraduate students from other universities were allowed to "come into residence"—a quaint term that is still used—and to obtain a degree either by advanced study or by research in the course of two years. At the same time, a change in the regulations of the 1851 Exhibition Commission allowed that influential body to fund science research scholarships for overseas students. A group of men of quite exceptional capacity thus came together. Among these were Ernest Rutherford from Canterbury College, Christchurch, New Zealand; P. Langevin from Paris; J. S. E. Townsend from Trinity College, Dublin; and J. C. McLennon from Toronto. (Rutherford, for example, in due course became the first holder of an 1851 Exhibition to go on to win the Nobel Prize).

Following Röntgen's discovery, Thomson soon discovered that gases exposed to the influence of X-rays became conductors of electricity under small electromotive forces. Thomson invited Rutherford to assist him, and an important joint paper[10] was published in which it was shown that the function of the X-rays was to liberate charged ions in the gas. Shortly thereafter, Thomson redoubled his efforts to pin down the nature of cathode rays. He was convinced that the views of Sir William Crookes,[11] that these rays consisted of negatively electrified particles fired out from the cathode, rang true; in opposition to the view that they were waves taken by such notable physicists as Heinrich Hertz and Philipp Lenard. His main reason for adopting Crookes' proposition was the fact that the rays were deflected by a magnetic force transverse to their direction. On measuring the amount of the magnetic deflection he began seriously to question the view that the electrified particles were atoms or molecules. Soon, by working with the highest attainable vacuum and by combining the electrostatic and magnetic deviation, he was able to obtain the necessary data for calculating the velocity of the rays and the value of the ratio of charge to mass (e/m). This value was of quite a different order of magnitude from that which is found for hydrogen atoms in electrolysis. It was over 1000 times as large as the ratio for ionized hydrogen. Immediately, he concluded that this was due to the smallness of the mass and that particles with this small mass were universal constituents of matter, as they were the same whatever the chemical nature of the gas carrying the discharge and the electrodes through which it entered and left.

Positively Charged Particles and the Origins of Mass Spectrometry

The second great period of Thomson's activity as an experimentalist (from about 1906 to 1914) was occupied with his development of the subject of positive rays. Originally discovered by the German physicist Eugen Goldstein, the positive rays (originally called "canal rays") are found in low-pressure discharge tubes which have a hole in the cathode: they proceed into the force-free space behind the cathode. Although Wien[12] had already shown that these rays were corpuscular and of atomic dimensions, noone had succeeded in obtaining a clear separation of the different kinds of atoms which might be present in them. By measuring their e/m ratio, Thomson showed that they all have masses of atomic magnitude and that there were very many different kinds of them. This was the clue to the development of mass spectrometry—then called spectrography because the signals were recorded on photographic plates. In conjunction with F. W. Aston,[13] Thomson found strong evidence that the noble gas neon comprised atoms of at least two different masses. Aston later showed that neon had three isotopes.

Thomson's Public and Private Persona

During his tenure of the Cavendish Professorship, Thomson succeeded in creating a school of research which, up until that time, had seldom, if ever, been equaled. As many as 40 research students were working under his guidance. (This is no longer exceptional in other departments in Cambridge, but it had never been achieved before Thomson's era.) The huge successes of his research school depended very largely on his personality, his fertility in suggestion, his kindly interest in his pupils, and his genuine enthusiasm when they achieved any success. There were, however, some tensions. For example, J. S. E. Townsend (later Sir John), the Irish physicist who joined the Cavendish at the same time as Rutherford in the mid-1890s, left the laboratory to take up the first Wykeham Professorship of Experimental Physics in Oxford in 1900, partly because he felt that Thomson had given less credit than was his due for some of his researches.[14]

Much later, after Rutherford returned in 1919 to succeed Thomson as Cavendish Professor, when the latter had become Master of Trinity College, it seemed that Rutherford felt aggrieved about Thomson's treatment (as Master) of Rutherford's protégées who tried but failed to get Fellowships at that College.

As Master of Trinity, a post that he held from the age of 62 until he passed away aged 84, Thomson was a great success. As Chairman of the College Council—its governing body—he was, in the words of Rayleigh junior,[15] "*never seen to lose his equanimity even if those [Fellows] who took a view different from his own were betrayed into temporary lack of courtesy of speech*".[16] He took the view that such lapses were best ignored[15] so that they would be most easily forgotten.

Not only could Thomson feel gratified that he had done much to create atmosphere where men—there were very few women in those days—of genius could flourish and fulfil their potential, but also his son, George Paget Thomson (later Sir George), became a physicist of the highest order, winning the Nobel Prize jointly with C. J. Davidson in 1937 for their experimental discovery of the diffraction of electrons by

 © 2006 Wiley-VCH Verlag GmbH & Co. KGaA, Weinheim

crystals. G. P. Thomson's work almost appeared to contradict his father's. In the obituary notice of J. J. Thomson composed by Max Born,[17] the following perceptive passage appears: "*It is a fascinating fact that father and son have given the most striking evidence for the apparently contradictory properties of the electron: the father proving its character as a particle, the son its character as a wave*".

We see, therefore, both in a consanguineous and a scientific sense that his progeny were a great success.

[1] The term cathode rays originated in Germany (Kathodenstrahlen). They were the subject of investigations by Plucker, von Helmholtz, Heinrich Hertz, Wiedemann, Goldstein, Lenard, Kaufmann, and Wiechert. They were also studied by Perrin in France.

[2] Many admirable books have been written on J. J. Thomson from which the author strongly recommends: E. A. Davis, I. J. Falconer, *J. J. Thomson and the Discovery of the Electron*, Taylor and Francis, London, **1997**.

[3] Osborne Reynolds (1842–1912) is remembered for pioneering studies of turbulent motion and many theoretical contributions to engineering. In 1877, in his paper on hydrodynamics, he proved the production of vortices by the motion of flat plates or solid bodies through water. He had earlier introduced the dimensionless Reynolds Number depending on the viscosity, density, and the linear dimensions of the flow, a ratio that has played a central role in all subsequent work on viscous fluids.

[4] John Henry Poynting (1852–1914) is renowned for his work on the transmission of energy in the electromagnetic field and for his determination of the gravitational constant.

[5] E. A. Davis, I. J. Falconer, *J. J. Thomson and the Discovery of the Electron*, Taylor and Francis, London, **1997**, p. 8.

[6] J. J. Thomson, *Recollections and Reflections*, G. Bell, London, **1936**, p. 35.

[7] "Argon and the Non-Inert Pair: Rayleigh and Ramsay": J. M. Thomas, *Angew. Chem.* **2004**, *116*, 6578; *Angew. Chem. Int. Ed.* **2004**, *43*, 6418.

[8] J. J. Thomson, *Proc. R. Soc. London* **1885**, *39*, 23.

[9] J. J. Thomson, *Proc. R. Soc. London* **1893**, *53*, 90.

[10] "On the Passage of Electricity through Gases Exposed to Röntgen-rays": E. Rutherford, J. J. Thomson, *Philos. Mag.* **1896**, *42*, 392.

[11] Sir William Crookes (1832–1919) was the inventor of the radiometer and the evacuated tubes named after him, as well as discoverer of the element thallium. At various times he was the President of the Chemical Society, the Institution of Electrical Engineers, the Society of the Chemical Industry, the British Association, and the Royal Society.

[12] Wilhelm Carl Werner Otto Fritz Franz Wien (1864–1928) was the German physicist who was highly competent both as a theorist and experimentalist. Renowned for his work on blackbody radiation that inspired Max Planck, Wien was awarded the Nobel Prize for Physics in 1911 for his discoveries regarding the laws governing the radiation of heat.

[13] Francis William Aston (1877–1945) is the acknowledged inventor of the mass spectrograph around 1919. His first spectrograph could cope only with gases, but by 1927 he had found a way of dealing with solids. His precise measurement of atomic mass, and its frequent departure from whole numbers, led him to the notion of the "packing fraction", a measure of the stability of the atom.

[14] A. L. Hodgkin, Nobel Prize winner for Physiology or Medicine, was a student, Fellow, and Master of Trinity College. He describes how J. S. E. Townsend became disenchanted with J. J. Thomson in his autobiography: A. L. Hodgkin, *Chance and Design*, Cambridge University Press, **1992**, p. 73.

[15] Lord Rayleigh, *Obituary Notice of Fellows of the Royal Society*, **1941**, *3*, 586.

[16] The temptation to excoriate Fellows of a Cambridge college is one that the Master, who often has to hear interminable and frequently self-inculpatory outbursts by rather ineffective individuals, must learn to resist.

[17] M. Born in *Obituary Notice of Fellows of the Royal Society* (see Ref. [15]).

 © 2006 Wiley-VCH Verlag GmbH & Co. KGaA, Weinheim

DOI: 10.1002/anie.200601645

Protein Glycosylation

Protein Glycosylation, Conserved from Yeast to Man: A Model Organism Helps Elucidate Congenital Human Diseases

Ludwig Lehle, Sabine Strahl, and Widmar Tanner**

Keywords:
congenital disorders of glycosylation · dolichol · glycosylation · protein modification · transferases

Dedicated to Professor Kandler on the occasion of his 85th birthday

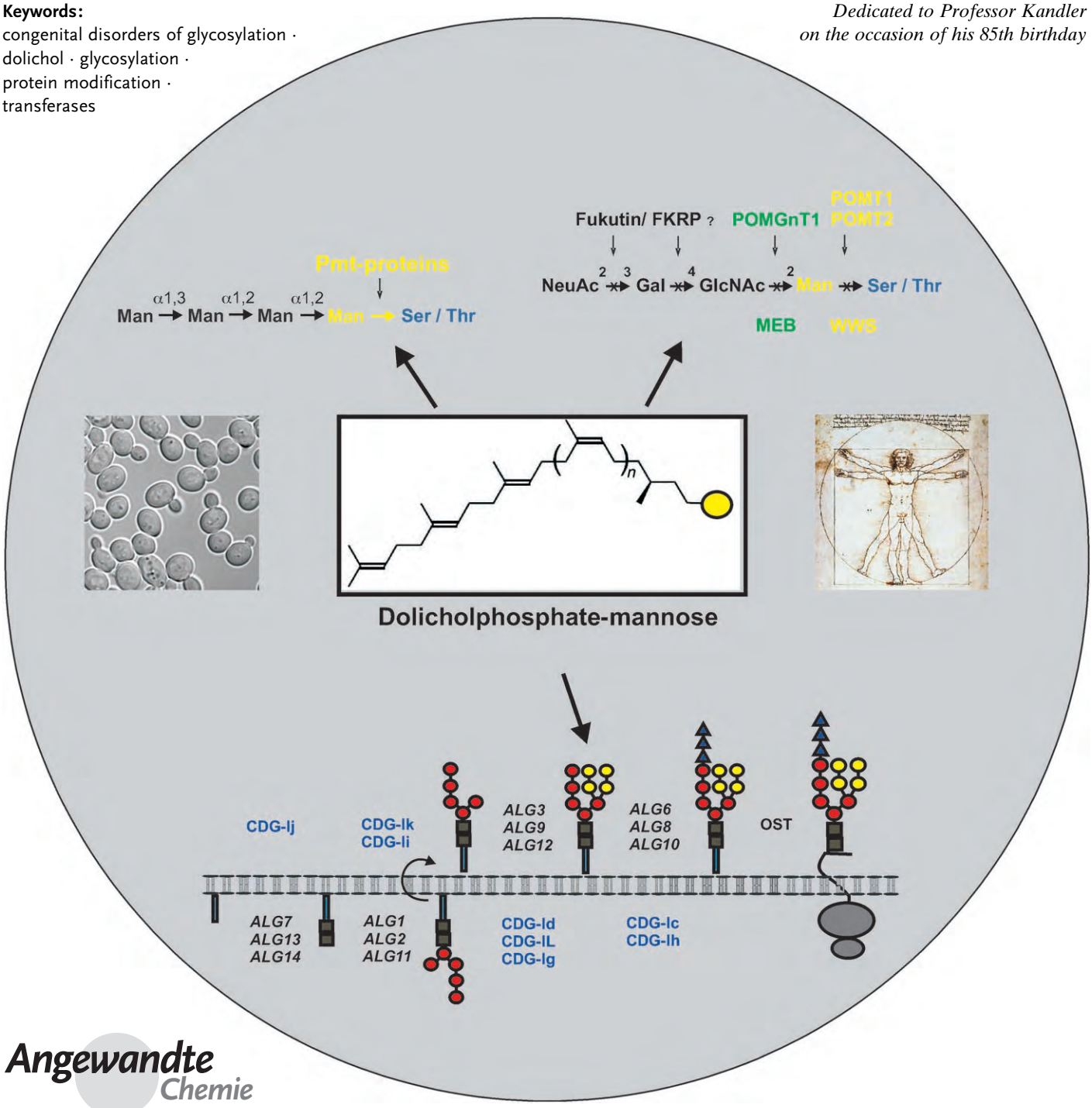

© 2006 Wiley-VCH Verlag GmbH & Co. KGaA, Weinheim

Proteins can be modified by a large variety of covalently linked saccharides. The present review concentrates on two types, protein N-glycosylation and protein O-mannosylation, which, with only a few exceptions, are evolutionary conserved from yeast to man. They are also distinguished by some special features: The corresponding glycosylation processes start in the endoplasmatic reticulum, are continued in the Golgi apparatus, and require dolichol-activated precursors for the initial biosynthetic steps. With respect to the molecular biology of both types of protein glycosylation, the pathways and the genetic background of the reactions have most successfully been studied with the genetically easy-to-handle baker's yeast, Saccharomyces cerevisae. Many of the severe developmental disturbances in children are related to protein glycosylation, for example, the CDG syndrome (congenital disorders of glycosylation) as well as congenital muscular dystrophies with neuronal-cell-migration defects have been elucidated with the help of yeast.

From the Contents

1. Introduction	6803
2. Biosynthesis of Glycoproteins	6804
3. Functional Aspects of Protein Glycosylation	6809
4. The Role of Yeast in Elucidating CDG	6813
5. Outlook	6814

1. Introduction

Proteins of all living organisms are generally modified in many different ways. A functionally important posttranslational modification is the phosphorylation of proteins. The presence or absence of a phosphate group at specific hydroxy amino acids regulates the activity, stability, localization, and oligomerization of proteins and in this way influences the flow through metabolic pathways, the transduction of external and internal signals, as well as the timing of developmental steps.[1] The most complex and at the same time energetically most-costly protein modification is, however, the glycosylation of proteins. Already, the many different sugars, which are either N- or O-glycosidically linked to the amino acid asparagine or to the hydroxy amino acids threonine, serine, hydroxyproline, hydroxylysine, and tyrosine (Figure 1), reflect the complexity of protein glycosylation.[2] In addition, there is a large variety of more or less highly branched oligo- and polysaccharides of varying composition that are linked to the proximal sugar of the protein. The functional importance of protein glycosylation, however, remained poorly understood for a long time, apart from the role of saccharides as blood-group antigens.[3] Only within the last few years has it become increasingly evident that the lack of individual glycosyl transferases contributing to the synthesis of sugar "trees" of specific proteins can cause most severe congenital diseases in children. Although the molecular details leading to these diseases are only vaguely understood, it seems clear that sugar components of proteins play a major role in embryonic and postembryonic development of humans as well as of all higher eukaryotes.

Baker's yeast, *Saccharomyces cerevisiae*, a frequently used eukaryotic model organism, only possesses two kinds of protein glycosylation, N-glycosylation of asparagine residues and O-mannosylation of threonine and serine residues. For the formation of the glycan chains, more than 100 gene products are required. N-glycosylation and O-mannosylation

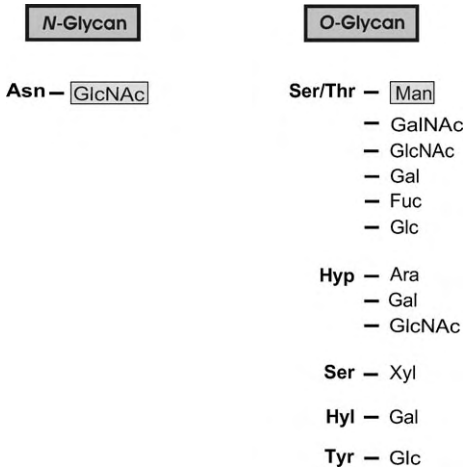

Figure 1. Types of sugar-peptide bonds in eucaryotes. Asn = asparagine, Ser = serine, Thr = threonine, Hyl = hydroxylysine, Hyp = hydroxyproline, Tyr = tyrosine, GlcNAc = *N*-acetylglucosamine, GalNAc = *N*-acetylgalactosamine, Glc = glucose, Gal = galactose, Rha = rhamnose, Xyl = xylose, Ara = arabinose, Man = mannose, Fuc = fucose. For the corresponding anomeric configurations, see reference [2].

are highly conserved from yeast to man; they are distinguishable, however, from all the other types of protein glycosylation shown in Figure 1 by two important details. Firstly, both

[*] Prof. Dr. L. Lehle, Prof. Dr. W. Tanner
Lehrstuhl für Zellbiologie und Pflanzenphysiologie
Universität Regensburg
Universitätstrasse 31, 93053 Regensburg (Germany)
Fax: (+49) 941-943-3352
E-mail: luwig.lehle@biologie.uni-regensburg.de
widmar.tanner@biologie.uni-regensburg.de
Prof. Dr. S. Strahl
Heidelberger Institut für Pflanzenwissenschaften
Abteilung V, Zellchemie
Universität Heidelberg
Im Neuenheimer Feld 360, 69120 Heidelberg (Germany)

 © 2006 Wiley-VCH Verlag GmbH & Co. KGaA, Weinheim

types are initiated at the endoplasmatic reticulum (ER) and secondly, lipid-activated sugars and non-sugar nucleotides serve as immediate precursors forming the linkage to the protein.[4,5]

Moreover, most of the above-mentioned congenital diseases in humans are related to defects in exactly these two pathways of protein glycosylation. This review, therefore, concentrates on the modifications conserved from yeast to man. They will be discussed with respect to their specialties and their functional importance. Furthermore, it will be shown to what extent baker's yeast has been very useful to elucidate biochemical features of more complex systems. Other types and aspects of protein glycosylation will only briefly be touched upon as they have been dealt with in numerous excellent reviews.[2,6–10,11]

Ludwig Lehle studied Biology and Chemistry and received his doctoral degree from the Ludwig-Maximilians-Universität München in 1972 (Profs. O. Kandler and W. Tanner). He was a research fellow at the University of California at Berkeley with Prof. C.E. Ballou from 1978–79 and habilitated in 1980 at the University of Regensburg. Since 1990 he has been professor of Cell Biology and Plant Physiology at the University of Regensburg. His research interests focus on biochemistry and molecular biology of protein glycosylation and the investigation of molecular defects of congenital disorders of glycosylation in humans. In 2004, he received the Körber European Science Award.

Sabine Strahl studied Biology at the University of Regensburg and received her PhD with Prof. W. Tanner in 1991. After postdoctoral study with Prof. M. Grunstein at the University of California Los Angeles, she became group leader at the University of Regensburg and completed her habilitation in the fields of botany and cell biology in 2000. For her achievements in the field of protein O-mannosylation, she received the Alfred Sommerfeld award of the Bavarian Academy of Sciences in 2003. In 2004 she was appointed professor at the Heidelberg Institute of Plant Sciences of the University of Heidelberg.

Widmar Tanner studied Biology, Chemistry, and Geography at the LMU Munich. He carried out his PhD work with Prof. Harry Beevers at Purdue University, Indiana, and obtained his degree from the LMU in 1964. As scientific assistant, he worked with Prof Otto Kandler in the areas of oligosaccharide biosynthesis (discovery of a cofactor role of myo-inositol) and of photophosphorylation. In 1969, he obtained his habilitation in Botany and was appointed Professor of Cell Biology and Plant Physiology at the University of Regensburg in 1970. His main research fields are now protein glycosylation and membrane transport.

2. Biosynthesis of Glycoproteins

Glycoproteins are proteins containing covalently linked oligosaccharides that consist of different monomers and are mostly branched.[12] The carbohydrate moiety amounts to about 20% of the molecular weight, but can be as much as 90% in some cases. In animal cells, glycoproteins are distinguished from proteoglycans, extracellular proteins with mostly long, unbranched polysaccharides, consisting of serially repeating units.[12] The so-called N-glycosylated proteins contain oligosaccharides that are N-glycosidically linked to the γ-amido group of asparagines. This type of glycoprotein has been most intensively studied with respect to their structure, biosynthesis, and function; they occur in all eukaryotes and in many archaea but only exceptionally in bacteria.[13] Commonly, N-glycosylated proteins are secretory proteins, that is, they are transferred through the secretory pathway to the cell surface where they either get exported or anchored to the plasma membrane, to the extracellular matrix, or to the cell wall. The carbohydrate moiety of these glycoproteins faces the outside of the cell and forms part of the glycocalyx.

Among the O-glycosylated proteins, the mucine type has been intensively investigated. Mucins contain long-chain, hardly branched saccharides linked through GalNAc to serine and threonine. On the other hand, *N*-acetylglucosamine (GlcNAc)-type O-glycosylated proteins possess only a single amino sugar, likewise bound to serine or threonine. They represent an exception among the glycoproteins as they occur intracellularly. Finally, there is an *O*-mannose type of glycosylated proteins, which was originally discovered in yeast, but has recently also been described in mammals. Lately, they have attracted considerable attention owing to their great functional importance. Their carbohydrate chain starts with a serine/threonine-linked mannose, which, in the case of yeast, is extended to an oligomannose chain, whereas in higher eukaryotes a linear heterosaccharide is attached consisting of GlcNAc, galactose (Gal), and neuraminic acid.

2.1. N-Glycosylated Proteins

2.1.1. Early Experiments

In all eukaryotes, the sugar attached to the γ-amido group of asparagine is a GlcNAc, which was already identified in the sixties.[14] Studies of the biosynthesis of glycosylated proteins was hampered by the fact that sugar nucleotides, the activated sugars discovered in the fifties,[15] did not serve as immediate precursors for certain glycosyl transferases. A breakthrough was achieved when a new principle for the formation of glycosidic linkages was discovered: the use of polyprenol-phosphate-activated saccharides, the so-called lipid intermediates, as was described for the biosynthesis of bacterial polysaccharides and peptidoglycans (murein).[16] The eucaryoatic polyprenols have a saturated α-position isoprene moiety and are called dolichols. The main components of the yeast dolichols consist of 14–18 isoprene units, whereas in mammals, the chain is three isoprene units longer. Dolichol-phosphate monosaccharides (Dol-P-Man, Dol-P-Glc)[17] and

 © 2006 Wiley-VCH Verlag GmbH & Co. KGaA, Weinheim

Dol-PP-oligosaccharides (P = monophosphate, PP = diphosphate)[18] were isolated and characterized from *S. cerevisiae* and mammalian cells. The structure of the oligosaccharide was elucidated by painstaking analyses in Kornfeld's laboratory (Figure 2). In addition, it was shown that the formation of the highly variable *N*-linked oligosaccharides, from many different proteins, starts in each case with the transfer of the $GlcNAc_2Man_9Glc_3$ unit, called the core oligosaccharide, from the Dol-PP-activated state to the protein. Subsequently the protein-bound oligosaccharide is modified in a protein- and tissue-specific manner by splitting off definite sugar residues and by adding others.[4,19]

In the following sections, the biosynthesis of the lipid-bound precursor and its transfer to proteins will be discussed in detail. This is based on data from *S. cerevisiae* and from mammals as the most complete information has been obtained from these organisms. As far as it is known, the corresponding reactions proceed almost identically in other eukaryotes, for example, in plants.[20]

2.1.2. *Biosynthesis of the Dolichol-PP-oligosaccharide: The Dolichol Cycle*

In Figure 2, the sequence of the reactions are shown, leading to the formation of the core oligosaccharide Dol-PP-$GlcNAc_2Man_9Glc_3$. The saccharide moiety is subsequently transferred as a whole to the nascent polypeptide chain. The protein is synthesized by ER-associated ribosomes and is translocated through a transmembrane channel, the Sec61 complex, into the lumen of the ER. The active centre of the oligosaccharyl transferase (OST), responsible for the transfer of the oligosaccharide to the protein, is located at the luminal side of the ER. It is a membrane complex consisting of several subunits.

Synthesis of the core oligosaccharide starts with the transfer of an α-linked *N*-acetylglucosaminephosphate from uridinediphosphate (UDP)-GlcNAc to dolicholphosphate giving rise to GlcNAc-PP-Dol. This reaction is very specifically inhibited by tunicamycin,[21] which was originally developed as an antiviral substance.[22] Following the transfer of a second GlcNAc residue and five mannose groups to the cytosolic side of the ER, whereby the sugar nucleotides, UDP-GlcNAc or guanosinediphosphate (GDP)-Man, function as sugar donors. Subsequently, the $Man_5GlcNAc_2$-PP-Dol was transferred to the luminal side.[23] There, the residual four mannoses and three glucoses were added according to a defined reaction sequence determined by the specificity of the individual glycosyl transferases. The transmembrane translocation of the dolicholpyrophosphate-bound heptasaccharide is biochemically not well understood; in yeast, the product of the *RFT1* gene is required.[24] In the ER lumen, the lipid-activated sugars Dol-P-Man and Dol-P-Glc serve as sugar donors. With an artificial vesicle system, it was shown that following the synthesis of Dol-P-Man on the vesicle outer side, a translocation of the mannose residue occurs to the vesicle lumen.[25] It remains uncertain, however, whether Dol-

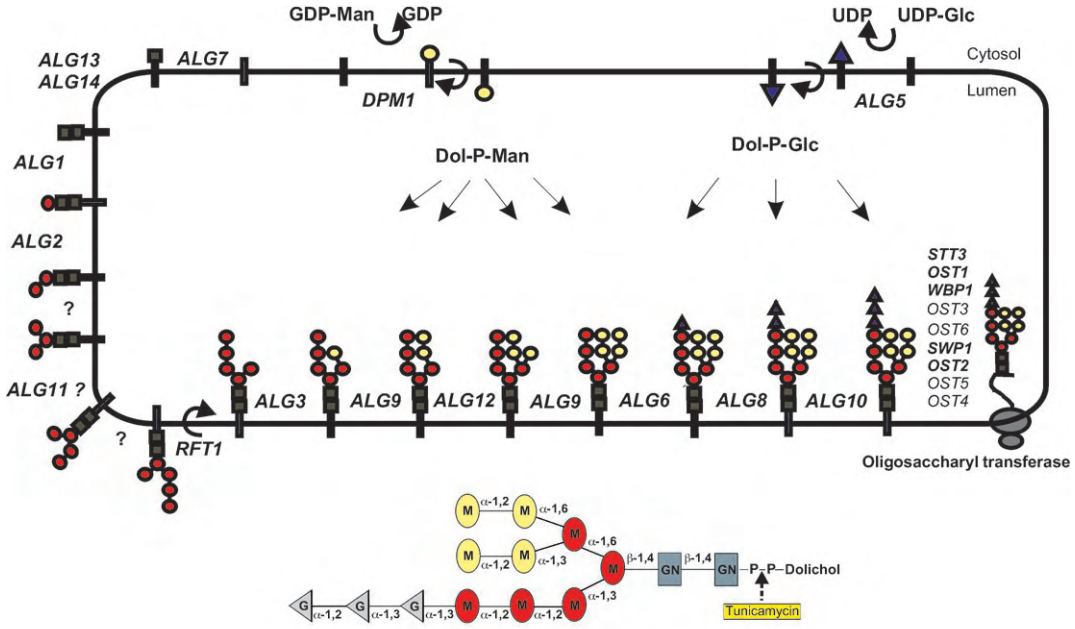

Figure 2. Biosynthesis of the lipid-bound oligosaccharide and transfer of the nascent polypeptide in the endoplasmic reticulum in *Saccharomyces cerevisiae*. The identified *ALG* genes for the respective glycosylation reactions are indicated (for the corresponding human genes, see Table 1). Synthesis starts at the cytoplasmic face with UDP-GlcNAc and GDP-Man as glycosyl donors (UDP = uridinediphosphate, GDP = guanosinediphosphate). The $Man_5GlcNAc_2$-PP-Dol heptasaccharide is then transferred to the luminal side with the help of *Rft1* and elongated to the full-length lipid-linked oligosaccharide $Glc_3Man_9GlcNAc_2$-PP-Dol by using Dol-P-Man and Dol-P-Glc. The oligosaccharide is subsequently transferred to the amido group of the asparagine residues within the consensus sequence Asn-X-Ser/Thr of nascent secretory proteins. This reaction is catalyzed by the oligosaccharyl transferase OST (essential genes of the nine subunits are in bold). Tunicamycin inhibits specifically the first step of lipid-linked oligosaccharide assembly, the transfer of GlcNAc-phosphate from UDP-GlcNAc to Dol-P. The mannose units in red are donated from GDP-Man, whereas mannose groups shown in yellow are derived from Dol-P-Man; Glc-residues (△) are from Dol-P-Glc. GN = *N*-acetylglucosamine, M = mannnose, G = glucose, Dolichol-P or Dolichol-PP.

© 2006 Wiley-VCH Verlag GmbH & Co. KGaA, Weinheim

P-Man synthase, with the active site oriented to the cytosol, also catalyzes the transmembrane step or whether additional, not yet identified proteins, participate.

In yeast, the genes and gene products responsible for the synthesis of the Dol-PP-oligosacchride are largely known. In 1982, Huffacker and Robbins selected more than one dozen different mutants that had a defect in the carbohydrate moiety.[26] They applied a [^{3}H] mannose suicide method as selection procedure. It is based on the principle that the desired mutants contain a reduced amount of [^{3}H] mannose and thus are exposed to a lower dose of lethal radioactivity. The mutants were designated as *alg* mutants, the corresponding genes as *ALG* genes (*a*sparagine-*l*inked *g*lycosylation). In Figure 2, they are assigned to the respective reaction. With the help of the yeast-genome project completed in 1996, for most reaction steps of the dolichol cycle, the genes have been identified through complementation of the corresponding *alg* mutants. They are listed in Table 1 and are compared with the known orthologous genes of mammals. Even more laborious was the identification of the oligosaccharyl transferase consisting of nine subunits, the genes of which did not emerge in the suicide screen.

2.1.3. The Oligosaccharyl Transferase

Two proteins contained in dog-pancreas extract, ribophorin I and II, to which name and function had already been erroneously assigned (ribosome carrier, believed to be responsible for fixing ribosomes to the rough ER), were recognized as components of a protein complex with oligosaccharyl transferase activity.[27] Similarly, a protein thought to be part of the nuclear pore complex of yeast cells, Wbp1 (*w*heat germ agglutinin *b*inding *p*rotein), turned out to be, by chance, an essential component of the OST.[28] Biochemical and genetic investigations have led to the discovery of nine protein subunits in yeast, five of which are essential for growth.[29] In mammals, seven proteins have meanwhile been identified as components of the OST; they are listed in Table 1 in comparison with those from yeast. The specific role of the individual subunits is not well understood. Cross-linking Stt3 with the nascent polypeptide chain[30,31] and the observation that an Stt3 homologue in the prokaryote *Campylobacter* catalyzes protein N-glycosylation,[32] strongly support the idea that Stt3 is the catalytic subunit of OST. Subunits Ost3 and Ost6 are alternatively present in the yeast OST complex; they modify the transfer specificity towards proteins to be glycosylated and they specify the interaction with different translocation complexes.[33] In mammals, two OST complexes exist that contain either one of two isoforms of Stt3, which show tissue-specific expression.[34]

The consensus sequence or sequon, asparagine-X-serine/threonine (N-X-S/T; whereby X can be any amino acid except proline) within the proteins to be glycosylated are recognized by OST.[35,36] As only 66% of the sequons are glycosylated,[37] further structural requirements have to be fulfilled for N-glycosylation to occur. Thus, the amino acids within and around the sequon, the position of the sequon in the peptide chain, the rate of protein folding and the availability of the dolichol precursor saccharide, all influence the efficiency of glycosylation.[38] The preferred glycosyl donor is the full-length saccharide $Glc_3Man_9GlcNAc_2$-PP-Dol, although shorter dolichol-bound saccharides can be transferred.[39]

Table 1: Homologies of genes of N-glycosylation between yeast and human.[a]

Yeast	Human	
	Annotation	Gene
genes for enzymes of LLO synthesis		
ALG1	AA67521	*MAT-1**
ALG2	AAH31095	h*ALG2**
ALG3	AAH02839	*NOT56**
ALG5	AAH12531	h*ALG5**
ALG6	Q9Y672	h*ALG6**
ALG7	AAH00325	*DPAGT1*
ALG8	NP_076984	h*ALG8**
ALG9	AF395532	h*ALG9**/*DIBD1*
ALG10	AAH0347	h*ALG10**
ALG11	CAI12890	
ALG12	Q9BV10	h*ALG12**
ALG13	NP_060936	h*ALG13**
ALG14	NP_659425	h*ALG14**
genes for subunits of OST		
STT3	NP_689926	*STT3A**
	NP_849193	*STT3-B**
OST1	NP_002941	*RPN1* (Ribophorin I)
WBP1	P39656	*OST48/DDOST*
SWP1	P04844	*RPN2* (Ribophorin II)
OST2	NP_001335	*DAD1**
OST3 und *OST6*	NP_006756	*N33* (Isoform a)*
	NP_839952	*N33* (Isoform b)*
	NP_115497	*IAP**
OST4	XP_376043	
OST5		

[a] Human sequences marked by asterisks were identified or their specific function has been elucidated on the basis of known yeast sequences. LLO = lipid-linked oligosaccharide, ALG = asparagine-linked glycosylation; STT = staurosporine temperature sensitive; OST = oligosaccharyl transferase; WBP = wheat-germ binding protein; SWP = suppressor of WBP; MAT = mannosyl transferase; NOT = Not56-like protein; DPAGT = dolicholphosphate *N*-acetyl glucosaminephosphate transferase; DIBD = disrupted in bipolar disorder; DAD = defender against apoptotic death; N33 = tumor suppressor candidate 3; IAP = implantation associated protein.

The reaction mechanism of OST has been intensively discussed. Bause and Legler suggested that a hydrogen bond between a carboxamide proton of asparagine and the hydroxy oxygen of the hydroxy amino acid is formed, thereby increasing the nucleophilicity of the carboxamide nitrogen (Figure 3)[36]. The reaction mechanism proposed by Imperiali and Hendrickson is based on experiments with defined peptide acceptors and suggests an Asx turn as the recognition motif for OST. [40] Hydrogen bonds are postulated between the asparagine β-carbonyl group and the α-NH peptide group on one hand and the β-OH group of serine/threonine on the other, both of which act as hydrogen donors (Figure 3). The enzyme-catalyzed deprotonation of the nitrogen induces a tautomerization of the carboxamide to imidol allowing a nucleophilic attack at the electrophilic lipid-linked oligosaccharide. The active centre of OST is oriented to the luminal

 © 2006 Wiley-VCH Verlag GmbH & Co. KGaA, Weinheim

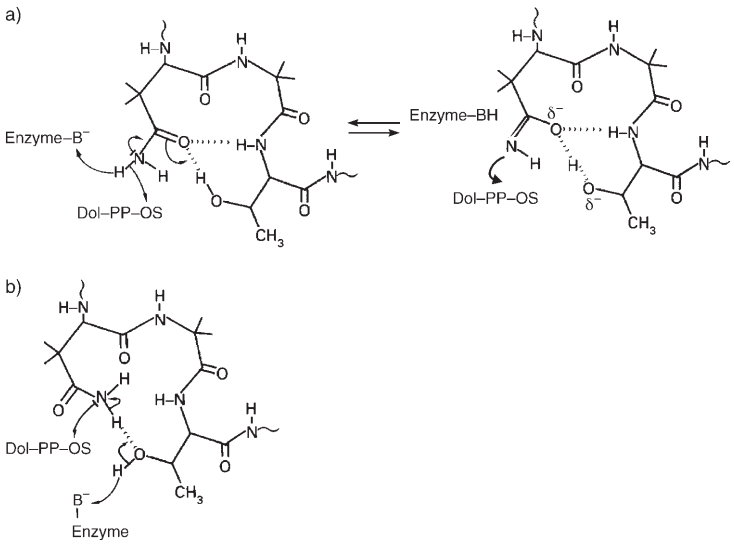

Figure 3. Proposed reaction mechanism for oligosaccharyl transferase. a) The model by Imperiali and Hendrickson[40] favors hydrogen bonding between the carbonyl group of the asparagine with the backbone amide and the hydroxy group of threonine and serine. The enzyme mediated deprotonation of the asparagine nitrogen by a basic residue in the active site induces tautomerization of the carboxamide to imidol. The generated nucleophile reacts with the electrophilic lipid-linked oligosaccharide. The model is based on studies with acceptor peptides adopting an Asx-turn conformation. b) Bause and Legler[36] assumed the existence of a β turn or other loop structures that are stabilized by hydrogen bonds between the β-amide nitrogen and the hydroxy group of the hydroxy amino acid, yielding deprotonation of the amide.

side of the ER. The potential glycosylation site has been determined to be approximately 65 amino acids away from the ribosomal peptidyl–tRNA binding site and thus interacts with the polypeptide chain shortly after it has entered the ER lumen.[31,41] As the hydroxy group of serine or threonine within the sequon is essential for the reaction, N-glycosylation can be regulated by modifying this group. Thus, it has been demonstrated that the O-mannosylation of an N-glycosylation sequon within the yeast cell-wall protein Ccw5p is the reason that the corresponding N-glycosylation site is not used.[42]

2.1.4. *Variations in the Saccharide Moiety in the Golgi Apparatus*

Although the reactions of N-glycosylation in the ER hardly differ between yeast and animals, subsequent reactions, taking place in the Golgi cisternae, differ considerably. This is due to the fact that a series of different sugars and their transferases exist in mammalian cells that do not exist in yeast. As shown in Figure 4, the protein-bound oligosaccharide is first reduced in size by splitting off all three glucoses and one mannose, while the protein is still in the ER. Subsequently, in mammalian cells, a complicated sequence of hydrolytic reactions takes place in the Golgi apparatus, called processing or trimming reactions, and may remove five mannose groups before a

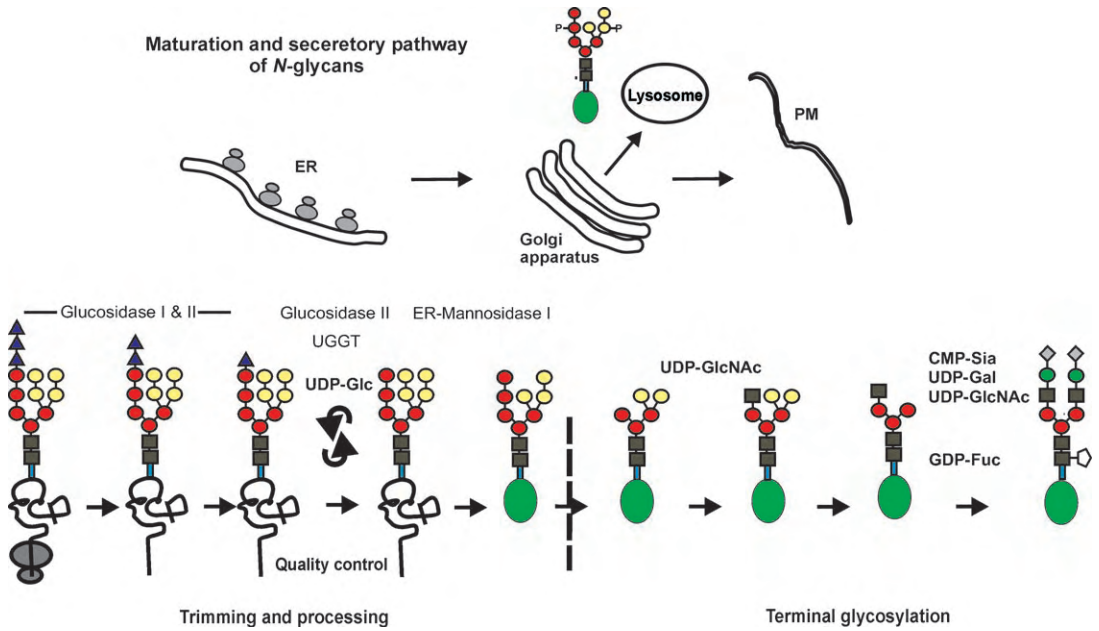

Figure 4. Processing and maturation of *N*-glycan chains. After the first trimming steps in the ER, the exit of the correctly folded glycoprotein (symbolized by a green ellipse) occurs from the ER to the Golgi apparatus where, in a strictly defined reaction sequence, a further demannosylation takes place, followed by transfer of a GlcNAc residue, and finally removal of two further mannose residues. In terminal glycosylation reactions, the mature glycan structure is built up in a protein-dependent, tissue- and organism-specific manner. The generated glycans are classified as high-mannose-type, complex-type, and hybrid-type glycan structures. In the Figure, only one possible terminal pathway is depicted leading to a biantennary-complex-type glycan chain; the number of antennae may vary up to six. In the case of soluble, lysosomal glycoproteins, a mannose-6-phosphate determinant is generated that functions as the signal for targeting the protein to the lysosome (see Section 3.2). PM = plasma membrane.

 © 2006 Wiley-VCH Verlag GmbH & Co. KGaA, Weinheim

varying number of GlcNAc, Gal, sialic acid, and fucose residues are added (also xylose in plants). In this way, the enormous diversity of glycan structures of the so-called "complex type" arises. These reactions follow a strict order determined by the specificity of the corresponding glycosyl transferases.[7] If the number of mannoses is not reduced, the glycan chain is defined as an "oligomannose type", which only exists in yeast, but, dependent on the protein, it may be further extended in the Golgi apparatus with more than 100 mannose units forming the so-called outer chain.[43]

2.2. O-Glycosylated Proteins

2.2.1. Protein O-Mannosylation

Mannosylated threonine and serine residues in proteins were considered for a long time as fungal-specific protein modifications. In 1969, this protein modification was first described in *S. cerevisiae* (baker's yeast) by Sentandreu and Northcote[44] and 30 years later, it was also discovered in mammals. A dominant protein, α-dystroglycan, which contains an O-glycosidically attached tetrasaccharide of the type NeuAc2→3Gal→4GlcNAc→2Man was isolated from muscle and nerve cells.[45,46] The yeast-type mannosylation most likely occurs in all animals, with the exception of nematodes (for example, *Caenorhabditis elegans*); it also could not be detected in plants (*Arabidopsis thaliana*, *Oryza sativa*). However, O-mannosylation has also been discovered in one bacterial species (*Mycobacterium tuberculosis*).[47]

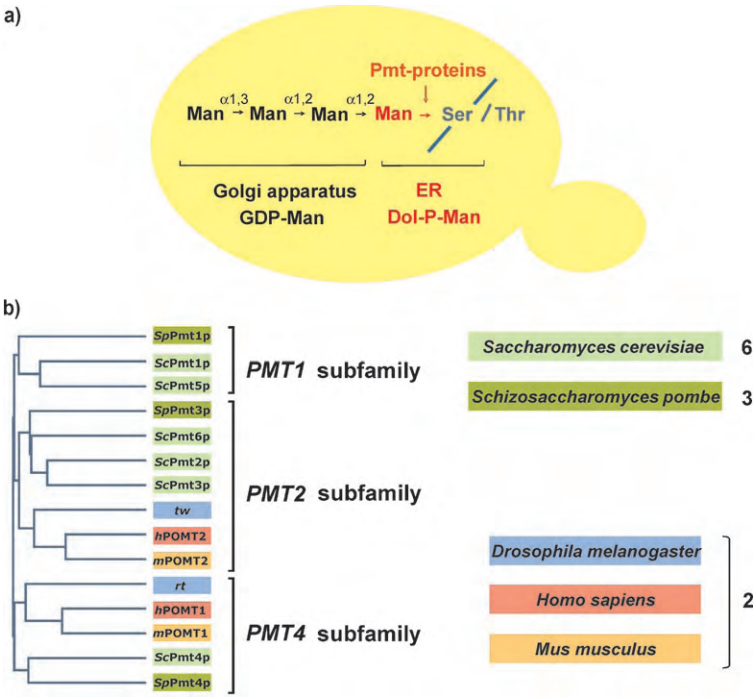

Figure 5. a) Protein O-mannosylation in baker's yeast *Saccharomyces cerevisiae*. The first mannose (red) is transferred from Dol-P-Man to the nascent secretory protein (blue) in the lumen of the ER. The reaction is catalyzed by the protein *O*-mannosyl transferases, product of the *PMT* genes. Further extension of the saccharide proceeds in the Golgi apparatus through GDP-Man. In (b), the evolutionary relationship of the protein *O*-mannosyl transferases is depicted. Yeast possess three *PMT* subfamilies; in all higher eucaryotes only two subfamilies exist, whereby in each case one member belongs to subfamily 2 and one to subfamily 4. The *PMT* genes of higher eucaryotes are called *POMT*. The numbers indicate how many different transferases are present in the corresponding genome altogether. In *S. cerevisiae*, there is also a seventh, significantly shorter homologue that exists (not shown here).

The biosynthesis of sugar chains bound through *O*-mannoside has been uncovered in *S. cerevisiae*. Unexpectedly, and contrary to the synthesis of the various other types of protein *O*-glycans (Figure 1), the transfer of the first mannose residue takes place in the ER lumen during the transmembrane translocation of the peptide chain. The activated sugar is supplied by Dol-P-Man and not by a sugar nucleotide.[48] The additional mannoses are transferred in the Golgi apparatus with GDP-Man as the mannosyl donor (Figure 5). The biosynthesis of sugar chains linked through *O*-mannoside proceeds in mammals in the same way as in yeast, as was recently shown.[49,50]

A family of *PMT* genes (*p*rotein *O*-*m*annosyl *t*ransferases) was discovered in baker's yeast. The purification of the first protein mannosyl transferase was hindered by the extremely small amount and the great lability of the enzyme. With the help of an antibody, which inhibited the in vitro reaction, sufficient immunopositive, although enzymatic inactive, material was obtained for protein sequencing, and the *PMT1* gene was cloned.[51] The disruption of this gene disclosed the existence of further mannosyl transferases with the same activity. The gene family, eventually unravelled, consists of seven members that show a high similarity in the hydropathy plot even though the homology in the amino acid sequence is rather low. The *PMT* genes of *S. cerevisiae,* and those identified from other fungi, can be grouped into three subfamilies (Figure 5).[5,52] In contrast with *Saccharomyces cerevisiae* and the closely related *Candida albicans*, *Schizosaccharomyces pombe* as well as filamentous fungi (for example, *Neurospora crassa*) possess only one representative of each subfamily. In higher eukaryotes and in *Drosophila*, only two genes are present, one of which belongs to the *PMT2* subfamily and the other to the *PMT4* subfamily (Figure 5).[49,53,54]

The question of why *PMT* genes always occur with several copies can only partly be answered. Thus, in yeast, the active enzyme consists of a Pmt1 and Pmt2 heterodimer. In the meantime, heteromeric and homomeric combinations have been detected in yeast and also in mammals, and it has been shown that the enzyme is active only as a heterodimer.[50,55,56] In addition, it has been shown that the various Pmt complexes of yeast have different substrate specificities. They all use Dol-P-Man as the mannosyl donor, but the target proteins differ.[57] Even within one protein, different domains are mannosylated by different Pmt proteins.[42]

The topology of Pmt1 in the ER membrane has been solved: The protein has seven transmembrane-spanning domains. The N terminus is oriented to the cytosol, whereas

 © 2006 Wiley-VCH Verlag GmbH & Co. KGaA, Weinheim

the C-terminal end faces the ER lumen (Figure 6). The two main protein loops, loop 1 and loop 5, are located in the lumen of the ER.[58] Loop 1 binds the peptide substrate and, therefore, most likely participates in the formation of the active site. Transmembrane spanning interactions are required for formation of the Pmt–Pmt complex.[55]

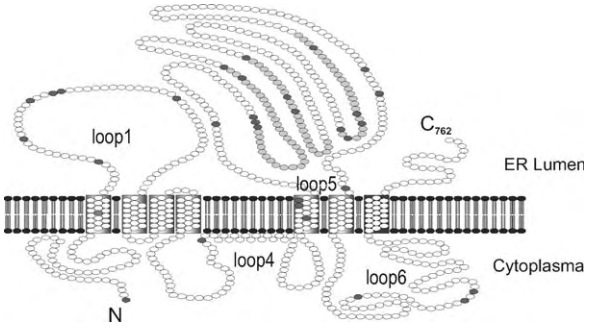

Figure 6. Membrane topology of the protein *O*-mannosyl transferase 1 of *S. cerevisiae*. Each circle represents one amino acid; the black circles correspond to amino acids, which are identical in all members of the *PMT* family, and the gray circles correspond to highly conserved residues. The experimental evidence as well as the methods applied can be found in reference [58].

In yeast, the stepwise extension of sugar chains linked by *O*-mannoside takes place in the Golgi apparatus and is catalyzed by α-1,2-mannosyl transferases of the *KTR* (*k*iller *t*oxin *r*esistant) family and by α-1,3-mannosyl transferases of the *MNN1* (mannan) family.[59] Different from Pmts, these enzymes are type-II membrane proteins containing only one transmembrane spanning region, a short cytoplasmic N terminus, and a large luminal, catalytic C-terminal domain. In mammals, the enzyme POMGnT1 (Protein *O*-mannose–β-1,2-*N*-acetylglucosaminyl transferase) transfers, in the Golgi apparatus, a GlcNAc residue from UDP-GlcNAc to form an α-1,2-bond with the protein-bound mannose.[60,61] The galactosyl and sialyl transferases required for further extensions have not yet been identified. Possible candidates are fukutin and FKRP (fukutin-related protein).

2.2.2. *Further Protein O-Glycosylation Reactions*

In animals, additional *O*-linked saccharides are known as protein modifications. The most intensively studied saccharides are *O*-glycans that are attached through GalNAc to the protein. They were originally discovered in extracellular mucines, which led to the designation of mucine-type glycoproteins. More than eight have been characterized and indications for more exist in literature. GalNAc transferases that perform the initial sugar transfer are known in mammals. They specifically transfer GalNAc from UDP-GalNAc to distinct mucine proteins in the *cis*-Golgi apparatus.[8] For the transfer of GalNAc, no recognition sequence has been identified. A typical sugar sequence of GalNAc-linked glycans is the sialyl-Lewis^X tetrasaccharide NeuNAc-α-2,3-Gal-β-1,4-(Fuc-α-1,3)-GlcNAc-β-1,3-Gal, which occurs in differently modified versions and for which important functions are known (see Section 3.3). Biosynthesis, molecular biology, and function of mucine-type glycoproteins have frequently been reviewed;[6,7,8,62] therefore, additional detailed discussion was not undertaken in the this review.

A further type of protein O-glycosylation, which has intensively been studied and which occurs in all higher eukaryotes including plants and filamentous fungi (not however in *S. cerevisiae*), is the posttranslational addition of a single, β-*O*-linked GlcNAc residue to serine and threonine.[63] Cytosolic and nuclear proteins are affected, for example, transcription factors, nuclear pore proteins, and nuclear oncoproteins. This GlcNAc transfer represents a reversible reaction and as such differs from other types of permanent extracellular protein glycosylations. A specific nucleocytoplasmic β-*N*-acetylglucosaminidase, active at neutral pH, can again remove the amino sugar from the protein. This dynamic process of synthesis and degradation is involved in a number of cellular functions, such as transcription or proteasomal protein degradation, and competes in some cases (e.g. SV40-T antigen and c-Myc oncogene) with protein phosphorylation/dephosphorylation at identical hydroxy residues.[9] For this type of protein modification, a considerable number of reviews are also available.[10,63]

3. Functional Aspects of Protein Glycosylation

3.1. General Considerations

A protein modification that has been evolutionarily conserved from unicellular yeast to man in structure and biosynthetic pathway, must be of great functional importance. For this reason, it was irritating that there was, for decades, no generally valid role ascribed to this most elaborate modification.[64] Hakomori called it an enigma.[65] If one wonders in what respect oligo- and polyaccharides differ from other biological polymers, the most obvious difference is the number of possible isomers that can be formed from only a few monomers.[66] Thus, from two glucose units, 11 different disaccharides can be formed (by considering exclusively the pyranose forms), whereas from two glycines, only one dipeptide arises. Three different monosaccharides could result in 1056 isomeric trisaccharides, compared to only six peptides that can be built from three different amino acids. As each isomer corresponds to a unit of information, carbohydrates can be considered as molecules with the highest potential information density. Even if only a small part of this potential is used in reality, this capacity of carbohydrates is expected to be related to their function.

By using the technique of gene disruption, it has become increasingly clear that the lack of a large number of individual glycosylation reactions is lethal for lower eukaryotes as well as for animals and plants.[26,67] But what do we definitely know today about the functions, for example, of the saccharide chains of N-glycosylated proteins? Principally, we have to distinguish between two kinds of functions: First, functions that are as important for simple unicellular organisms as for mammals have been conserved during evolution for this very reason. Second, functions related to the complex-type oligosaccharides (do not exist in yeast) and the existence of which

 © 2006 Wiley-VCH Verlag GmbH & Co. KGaA, Weinheim

correlates with their occurrence in higher multicellular organisms. In the first case, important functions must be restricted mainly to intracellular events, whereas the second type of function is extracellular, for example, cell–cell interactions, which may give rise to signalling in development. Thus, for example, in yeast, the only cell–cell interaction of importance is the mating reaction between a- and α-cells. Although two highly glycosylated cell-surface proteins, the agglutinins, significantly increase mating efficiency, the effect in this case is based on protein–protein rather than on carbohydrate–protein interactions.[68]

3.2. Intracellular Functions

At the moment, convincing evidence exists for two intracellular phenomena in which *N*-linked saccharides play a decisive role as signalling compounds: 1) sorting of lysosomal proteins and 2) a quality control for the folding of secretory proteins, which ensures that only correctly folded proteins are delivered to the secretory path from the ER lumen to the cell surface. When correct folding is not achieved, an ER-specific, saccharide-dependent pathway of protein degradation (ERAD, *ER-a*ssociated *d*egradation) takes care of the misfolded proteins.

Since the 1970s, it has been known that lysosomal proteins possess mannose-6-phosphate residues on their mannose-rich oligosaccharides, which constitute the sorting signal for the transport of these proteins into the lysosome, the digestive organelle of mammalian cells.[69] Although the corresponding type of protein modification has also been observed in a vacuolar yeast protein (functionally, the vacuole corresponds to the lysosome), mannose-6-phosphate in yeast is not responsible for the correct cellular localization and thus is not a universal signal.[70]

The final reactions in the biosynthesis of the Dol-PP-oligosaccharide are the additions of three glucose units (see Section 2.1.2). Immediately after transfer of the complete oligosaccharide to the protein, these glucose units are removed again by two specific glucosidases (see Figure 4 and Figure 7). The presence of glucose units at the lipid-bound oligosaccharide was not at all understood for a long time as no carbohydrate moiety of the known glycoproteins contained glucose as a constituent. The role of glucose became even more mysterious when Parodi and Trombetta discovered an enzyme that reglucosylated the glycoprotein directly after the glucose had just been removed.[71]

Today we know that glucosylation is both a signal for the efficient transfer of the dolichol-bound saccharide to the protein[39] and that it is involved in the correct folding of secretory glycoproteins.[72] As long as glucose residues are present at the newly synthesized protein, it will not be translocated to the Golgi apparatus compartment. The protein remains attached to components of the ER, the membrane-bound calnexin, and/or to its soluble homologue calreticulin (Figure 7). If the protein is still not correctly folded once the three glucose residues are removed, it is then recognized by the UDP-Glc–glycoprotein glucosyl transfer-

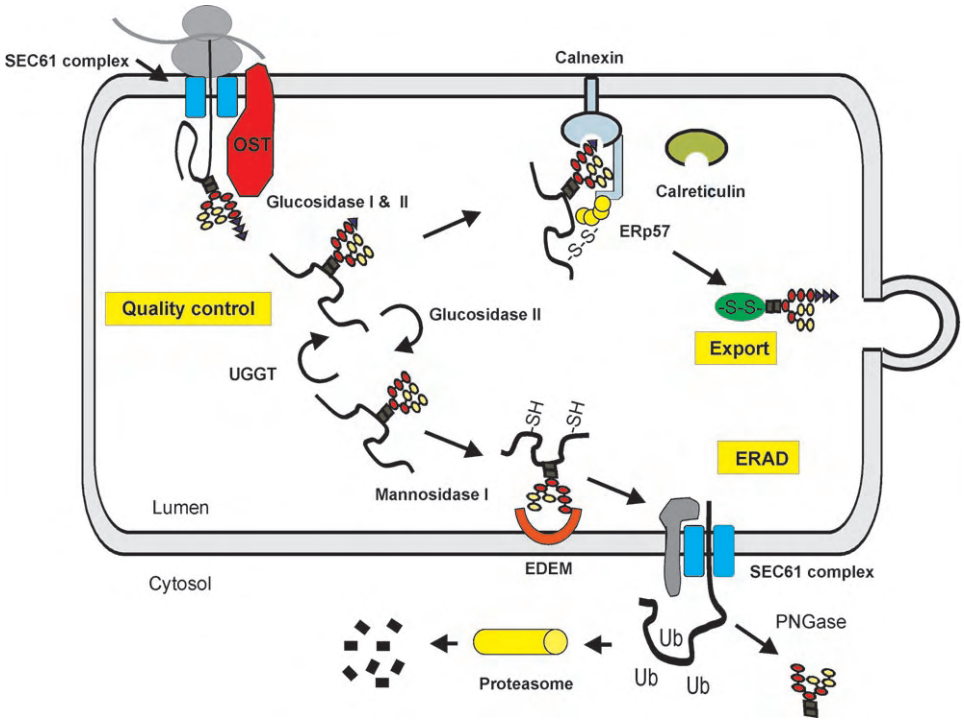

Figure 7. Control of protein folding in the ER by the calnexin/calreticulin cycle. During translocation of the newly synthesized protein through the Sec61 complex (translocon), the sequence Asn-X-Ser/Thr is recognized by the oligosaccharyltransferse (OST) and glycosylated with the preassembled $Glc_3Man_9GlcNAc_2$ oligosaccharide precursor. The two terminal glucose residues are then removed by glucosidase I and II, respectively, and the generated $Glc_1Man_9GlcNAc_2$ oligosaccharide is recognized by membrane-bound calnexin and/or soluble calreticulin, two homologous ER lectins for monoglycosylated oligosaccharides. Thereby, the protein is exposed to ERp57, a thioldisulfid oxidoreductase, which assists in the formation of disulfide bonds and interacts with both calnexin and calreticulin. If the third remaining glucose residue is removed by glycosidase II, the complex dissociates. The glycoprotein is then subject to one of three possibilities: If it has reached its native conformation, the protein leaves the ER and enters the secretory pathway. In the event of incomplete folding, UGGT re-glucosylates the $GlcNAc_2Man_9$ oligosaccharide and the protein re-associates with the calnexin/calreticulin. The third possibility, if the protein remains in the unfolded state for too long, is ER-associated degradation (ERAD). The misfolded protein is retranslocated to the cytosol and subsequent to splitting off the glycan chain by a membrane-associated PNGase, it is ubiquitinated (Ub) and degraded by the proteasome. In this case, a $Man_8GlcNAc_2$ structure, generated by ER mannosidase I, is recognized by the ER-resident lectin EDEM/Htm1p, which binds to mannose residues and assists in the retranslocation.

© 2006 Wiley-VCH Verlag GmbH & Co. KGaA, Weinheim

ase ("Parodi" enzyme). It acts as a folding sensor by recognizing the hydrophobic subdomains and reglucosylates the $Man_9GlcNAc_2$ oligosaccharide by one glucose unit. In this way, the protein receives another chance to reach its native 3D structure. Protein molecules that do not gain their native structure in the lumen of the ER must be removed and degraded. Surprisingly, this is the fate of a large amount of some secretory proteins. For example, the CFTR (*c*ystic *f*ibrosis *t*ransmembrane conductance *r*egulator) protein, a chloride channel that causes cystic fibrosis, is degraded to more than 50% and thus turns over very rapidly in healthy individuals. In patients suffering from cystic fibrosis, the protein is metabolized even faster and this is the reason that too little of the channel protein reaches the plasma membrane where it should carry out its essential function.[73] Irreversibly misfolded proteins eventually get degraded in the proteasome. For this to be achieved, the proteins have to leave the ER through the Sec61 complex (Figure 7). Thus, the same protein-translocation channel is used as that which allows nascent protein chains to enter the ER during their biosynthesis.[74] In the cytosol, the protein destined to be decomposed is polyubiquitinated. In the case of glycoproteins, the whole process of degradation is most likely initiated by a modified carbohydrate structure of the protein.[75]

With the help of *pmt* mutants, it was shown in baker's yeast, and later also in fission yeast, that protein O-mannosylation is an essential protein modification in fungal cells. In *S. cerevisiae*, the simultaneous disruption of at least one member of each *PMT* subfamily causes cell death, whereas in *S. pombe* the deletion of the gene homologous to the *S. cerevisiae PMT2* is already lethal.[76,77] The characterization of the nonlethal *pmt* mutants showed O-mannosylation to play a critical role in a number of important physiological processes, such as in polar cell growth and in the formation of an intact cell wall.[77,78] For the human pathogen *Candida albicans*, an interrelation between virulence and O-mannosylation was demonstrated.[79]

Some of the molecular mechanisms that cause these phenomena are known. Thus, it was shown that many cell-surface proteins with key functions, for example, receptors of the plasma membrane, are highly O-mannosylated and that this modification is of importance for their stability, secretion, localization, and/or their immediate function.[80] Furthermore, the role of O-mannosylation in processing incorrect folded proteins in the ER[81] and in regulating N-glycosylation is currently in discussion.[42] If O-mannosylation in fungi comes to a halt, various cellular processes proceed incorrectly and as a result cell death occurs.

Knocking out O-mannosylation in mice causes death in the early embryo,[82] whereas in humans, a recessive congenital disease arises, the Walker–Warburg syndrome, which is discussed in detail in Section 3.4.

3.3. Extracellular Functions

Although indications and speculations for a role of carbohydrate components in cell–cell recognition and interaction have been around for a long time, well-founded evidence was only obtained in the 1980s. It was shown that leucocytes interact through specific carbohydrate-binding cell-adhesion molecules, the selectins, with endothelial cells. The selectins constitute a family of membrane proteins that are present at the cell surface of leucocytes as well as on endothelial cells. The interaction of glycan structures of certain cell-surface glycoproteins with selectins eventually causes leucocytes, which are transported in the blood stream at high velocity, to slow down. Once rolling with reduced velocity along the endothelium, stronger interactions are established through integrins activated at the leucocyte surface. These are the prerequisites required for the leucocyte to exit the endothelium and for arriving at the loci of inflammation and infection. The selectin-mediated process can be inhibited by a number of added oligosaccharides; the saccharides of the $Lewis^X$ type (see Section 2.2.2) are especially potent inhibitors. Owing to the important medical implications of these phenomena, above all in relation the potential relief of chronic inflammation, a large number of detailed reviews on the function of these protein-bound saccharides and selectins are available.[62]

Deficiencies in the glycosylation of proteins have been discovered lately in the context of analyzing patients with multisystemic congenital diseases. These deficiencies will be covered in the following section. In the case of deficiencies, as far as is known, the saccharide side chains of the proteins carry out their functions extracellularly.

3.4. Congenital Defects of Glycosylation in Humans

The known cases of congenital underglycosylation of proteins cause very severe health problems in children and typically result in multisystemic presentation involving interference with normal development of the brain and functions of the nerve-, liver-, stomach-, and intestinal systems. As far as protein N-glycosylation is involved, the disease is called CDG-syndrome (*c*ongenital *d*isorders of *g*lycosylation) and the whole phenomenon demonstrates most convincingly the enormous biological importance of protein glycosylation.

The history of the discovery of CDG began with two patients of the Belgian paediatrician Jaak Jaeken in the beginning of the 1980s (Figure 8). Jaeken observed a series of severe motor anomalies as well as seriously retarded mental development in a set of twins.[83] The obvious genetic base of the disease was accompanied by changes in a number of functionally quite different enzymes, which was contrary to the accepted theory that one gene defect corresponds to one protein defect. Jaekens discovered that the affected proteins were glycoproteins. In the case of a genetic defect in one of the many enzymes responsible for protein glycosylation (see Section 2), many different glycoproteins must be influenced, which could then result in smaller amounts of glycoproteins or less active or stable glycoproteins. Jaeken et al. developed a simple test to rapidly detect underglycosylated proteins in the serum samples of patients.[84] Figure 8 shows how the serum glycoprotein transferrin, an iron-transport protein, changes its electrophoretic running behavior with alteration in its glycosylation. This protein possesses two N-glycosylation sites,

 © 2006 Wiley-VCH Verlag GmbH & Co. KGaA, Weinheim

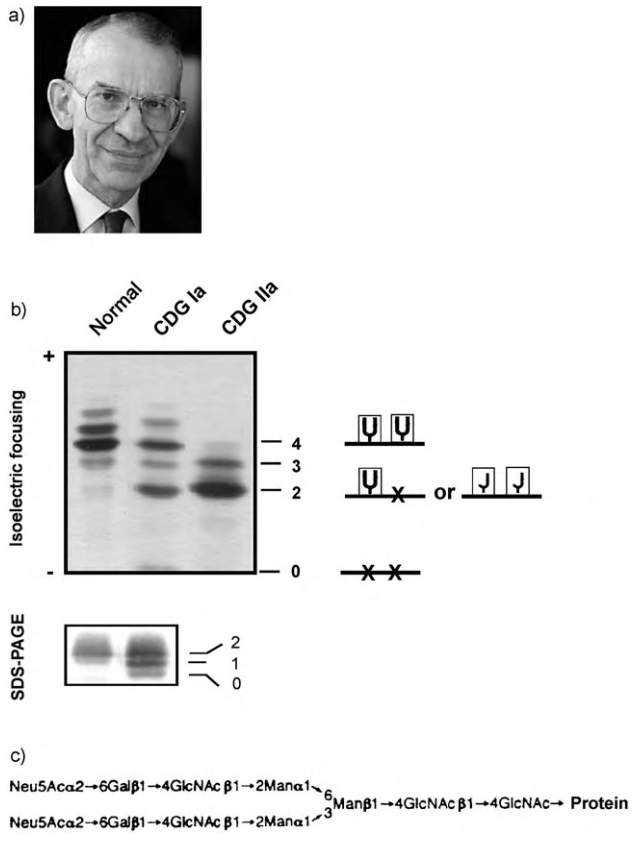

Figure 8. Serum transferrin, a diagnostic marker for CDG. a) Jaak Jaeken discovered and described the first CDG case. Transferrin contains two glycan chains of the biantennary complex type (c); occasionally it can be branched to a triantennary structure (not shown). In isoelectric focusing (IEF) (b), therefore, the dominant form of a healthy person is tetrasialo-transferrin. In CDG-I patients, additional bands are visible, representing disialo- and asialo-transferrin (as an example, CDG-Ia is depicted). Possible structural alterations are schematically depicted. Moreover, with the help of SDS-PAGE, the complete or partial loss of glycan chains can be made visible.

which, in a healthy person, are occupied by two biantennary (partly triantennary) saccharides of the complex type. Owing to terminal sialic acids, the molecule carries at least four negative charges, which determine its mobility during isoelectric focussing. The transferrin of CDG patients shows a clearly different pattern that is caused by underglycosylation or even a complete lack of oligosaccharides. In addition, SDS-PAGE distinguishes between a complete or partial loss of glycan chains.

With these simple analyses, approximately 1000 patients with congenital N-glycosylation defects have been so far identified. The individual step in the complicated biosynthetic reaction sequence that is affected by a mutation, either a glycosyl transferase of the dolichol cycle (Figure 2), an enzyme involved in subsequent processing reactions, or an enzyme for the delivery of the starting substrates, has to be analyzed for each individual patient by more intricate methods (see the next section). So far, nineteen subtypes of CDG are known; in each a different reaction or rather the responsible gene is defective. A detailed analysis of the mutations has shown that in patients of the different CDG types, there is still some residual enzyme activity. A complete loss of oligosaccharide biosynthesis results in embryonic lethality.[85] How glycosylation defects in specific proteins or groups of proteins cause the different, extraordinarily variable disease symptoms is largely not understood in molecular terms, not to mention the lack of knowledge of the causal relationship between the affected gene product and the biological phenomena.

For the last four years, it has been known that similar serious developmental disorders in humans can arise by underglycosylations related to protein O-mannosylation. The corresponding diseases are congenital neuromuscular disorders associated with neuronal cell migration defects, described as the Walker–Warburg syndrome (WWS) or the so-called MEB disease (*m*uscle-*e*ye-*b*rain disease).[52,86,87] Protein underglycosylations of this type should actually be classified as a special subclass of the CDG syndrome as it is, without doubt, a "congenital disorder of glycosylation". CDG nomenclature so far, however, is restricted to disorders of protein N-glycosylation.

The history of the discovery of congenital diseases caused by protein O-mannosylation began when specific *Drosophila* mutants were analyzed. One mutant from the classical mutant collection from the 1920s and 1930s has a twisted abdomen. Martin–Blanco and García–Ballida found that the mutant, which was classified as "rt" for "rotated abdomen", had a defect in a gene homologous to *PMT4* of yeast.[53] The microscopic phenotype of the mutated fly showed a disturbed embryonic muscle development with an anomaly in the fixation of muscle fibers. A connection between protein O-mannosylation and specific congenital muscle dystrophies was postulated. Shortly afterwards, a protein was identified in mammals, the α/β-dystroglycan, which is an anchor molecule and links the intracellular cytoskeleton of the muscle cell to the extracellular matrix (Figure 9).[87,88] Finally, Endo and coworkers[46] demonstrated that the extracellularly exposed dystroglycan domain, the α subunit, carries *O*-mannosyl glycans (see Section 2.2.1), which are responsible for this interconnection. In the meantime, seven WWS patients were identified with a defect in *POMT1* and four patients with a mutated *POMT2*.[89,90] The patients frequently do not reach the age of three and besides dramatic motoric deficiencies, they show defects in brain development. The latter is certainly related to the observation that in the brain, 30% of all O-glycosylated proteins carry the yeast-type *O*-mannose linkage.[45] The brains from the corresponding patients are generally heavily malstructured,[91] suggesting a role of α-dystroglycan and its sugar components in the migration of neuronal cells during the early developmental period. In the mouse, knock-out of *POMT1* is embryonal lethal, caused by aberrant processing of α-dystroglycan and by faulty formation of the so-called Reicherts membrane, a basal membrane typical for rodents.[82]

In the meantime, it has become clear that the tetrasaccharides that are bound to α-dystroglycan are of eminent importance and that not only the total lack of saccharides, but also their shortening, for example, owing to the lack of POMGnT1 transferase,[60] leads to the severe MEB disease

 © 2006 Wiley-VCH Verlag GmbH & Co. KGaA, Weinheim

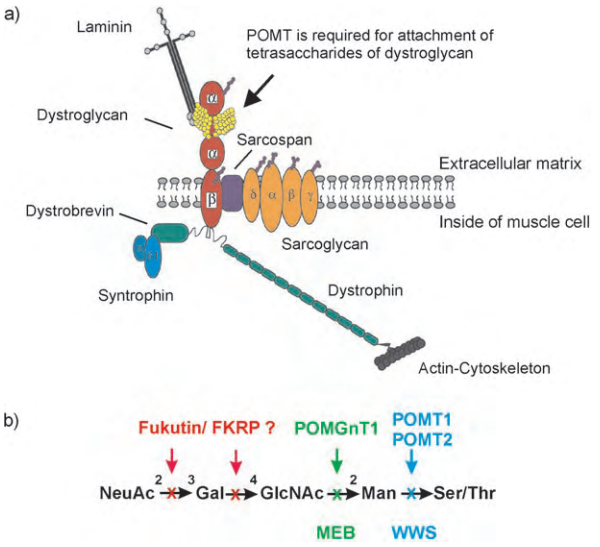

Figure 9. a) The dystrophin-glycoprotein complex. It contains a number of transmembrane proteins, one of which, the dystroglycan consists of two subunits and connects the intracellular cytoskeleton with the extracellular laminin. The dumb-bell-shaped extracellular α-dystroglycan is highly O-mannosylated in its central domain. The respective tetrasaccharides are essential for the interaction with laminin. b) The O-mannosyl glycan chain and the underlying congenital muscle dystrophy and neuronal migration defects are depicted. MEB, *m*uscle-*e*ye-*b*rain disease; WWS, Walker–Warburg syndrome.

(Figure 9). In contrast to the multisystemic CDG diseases caused by defects in N-glycosylation, the molecular details of faulty protein O-mannosylation are understood, at least in part. Astonishingly, so far only one defined protein is known in mammals with this glyco modification.

4. The Role of Yeast in Elucidating CDG

It is evident that the molecular understanding of those neuromuscular diseases, which are caused by hypoglycosylation of α-dystroglycan, has profited considerably from the yeast work. Baker's yeast *Saccharomyces cerevisiae* was also of great help for the characterization of the various subtypes of CDG. The principal procedure used hereby will be explained for two examples. The various CDG types known so far correspond to defects in one of the many genes required for the complex biosynthetic pathway of protein N-glycosylation. The present knowledge of CDG types identified by biochemical and/or genetic means are summarized in Table 2.

How were the corresponding genes identified, especially in those cases where the human gene was not yet known? In *S. cerevisiae*, almost all of the genes involved in *N*-glycosylation have been identified. In addition, knock-out mutants for each individual nonessential gene are available. As long as these mutants possess a phenotype, in some cases only after an additional mutation has been introduced, one can check whether it can be cured with the potential analogous human DNA. When the corresponding patient DNA is subsequently used and no complementation of the yeast mutant is achieved, it can be concluded that the patient has a mutation in exactly this very gene. In this way, for example, the CDG-Ii type was identified as a mutation in a gene corresponding to the yeast *ALG2* (Figure 10).[92] The *alg2* yeast mutant grows very poorly under specific conditions. Upon transformation with

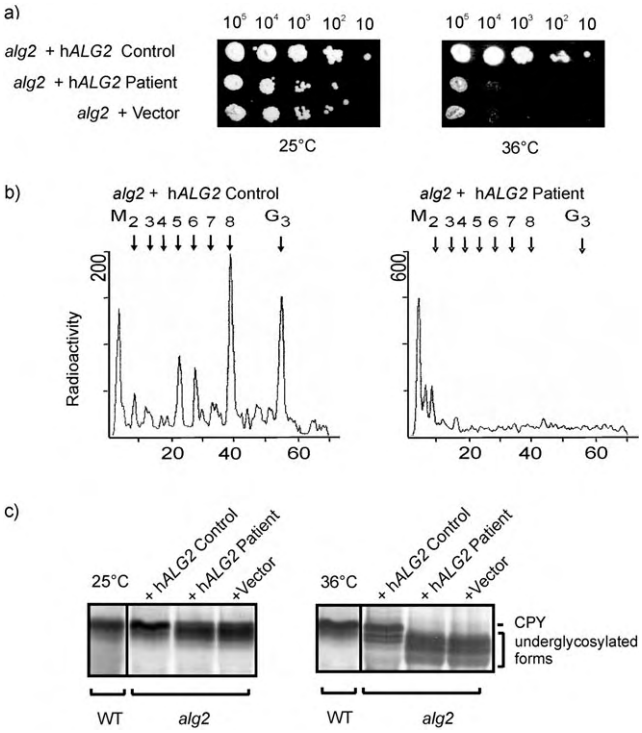

Figure 10. Yeast, a model for the identification of CDG subtypes. Complementation of the growth defect (a), a defect in lipid-linked oligosaccharide biosynthesis (b), and CPY underglycosylation (c) by human *ALG2*. The *alg2* yeast mutant has a temperature growth defect at 36 °C. This can be suppressed by h*ALG12* of a control person, but not of a CDG-Ii patient with Δ1040G mutation (a). Serial 1:10 dilutions of *alg2* cells and growth at permissive temperature (25 °C) or at the restrictive temperature of 36 °C. In (b), yeast cells were metabolically labeled with [2-^{3}H] mannose and the lipid-linked oligosaccharides analyzed by HPLC upon mild acid hydrolysis to cleave off the oligosaccharide from the lipid. The *alg2* mutant, transformed with h*ALG2* from the patient accumulates $Man_2GlcNAc_2$, whereas h*ALG2* from a healthy person restores synthesis of the full-length $Glc_3Man_9GlcNAc_2$ precursor. In (c), the glycosylation status of yeast carboxypeptidase CPY is shown. CPY of wild-type yeast exhibits four *N*-glycan chains and migrates in SDS-PAGE as one distinct band. In *alg2* mutant cells at the restrictive temperature of 36 °C, the shortened chains are less efficiently transferred to the protein resulting in hypoglycosylation owing to the fact that they are nonoptimal substrate for OST. The defect is restored by an intact h*ALG2*.

the yeast wild-type gene, or also with the analogous human DNA (not with patient DNA), a wild-type growth rate is re-established. Of importance was also the information obtained beforehand that, in cultivated skin fibroblasts of the patient, the biosynthetic intermediate Dol-PP-$GlcNAc_2Man_1$ accumulates like in the *alg2* yeast mutant, whereas in control fibroblasts the full-length intermediate Dol-PP-$GlcNAc_2Man_9Glc_3$ is the main product.

The expression of the human *ALG2* in yeast also complements the underglycosylation of the model protein carboxy-

 © 2006 Wiley-VCH Verlag GmbH & Co. KGaA, Weinheim

Table 2: CDG-type and congenital disturbances of O-glycosylation.[a]

Type	Gene	Activity	References
CDG I			
CDG-Ia	*PMM2*	Phosphomannomutase	[98]
CDG-Ib	*MPI*	Phosphomannose isomerase	[99]
CDG-Ic	*ALG6*	Dol-P-Glc: $Man_9GlcNAc_2$-PP-Dol glucosyl transferase	[100]
CDG-Id	*ALG3*	Dol-P-Man: $Man_5GlcNAc_2$-PP-Dol mannosyl transferase	[101]
CDG-Ie	*DPM1*	Dol-P-Man synthase I GDP-Man: Dol-P-mannosyl transferase	[102]
CDG-If	*MPDU1*	Mannose-P-dolichol utilization defect MPDU1/Lec35	[103]
CDG-Ig	*ALG12*	Dol-P-Man: $Man_7GlcNAc_2$-PP-Dol Mannosyl transferase	[93,94]
CDG-Ih	*ALG8*	Dol-P-Glc: $Glc_1Man_9GlcNAc_2$-PP-Dol glucosyl transferase	[104]
CDG-Ii	*ALG2*	GDP-Man: $Man_1GlcNAc_2$-PP-Dol mannosyl transferase	[92]
CDG-Ij	*DPAGT1*	UDP-GlcNAc: dolichol phosphate *N*-acetylglucosamin-1-phosphate transferase	[105]
CDG-Ik	*ALG1*	GDP-Man: $GlcNAc_2$-PP-Dol mannosyl transferase	[106]
CDG-I*L*	*ALG9*	Dol-P-Man: Man_6 und $Man_8GlcNAc_2$-PP-Dol mannosyl transferase	[107]
CDG II			
CDG-IIa	*MGAT2*	GlcNAc transferase II	[108]
CDG-IIb	*GLS1*	Glucosidase I	[109]
CDG-IIc	*SLC35C1*	GDP-fucose transporter (LAD II)	[110]
CDG-IId	*B4GALT1*	β1,4-galactosyl transferase	[111]
CDG-IIf	*SLC35A1*	CMP-sialic acid transporter	[112]
CDG-IIx	*COG7*	COG complex, subunit 7	[113]
CDG-IIx	*COG1*	COG complex, subunit 1	[114]

Name	Gene	Activity	References
defects in *O*-mannosylglycan synthesis			
Walker–Warburg syndrome	POMT1/ POMT2	*O*-mannosyl transferase	[89]
muscle-eye-brain disease	POMGnT1	*O*-mannosyl-β1,2-N-acetylglucosaminyl transferase 1	[60]
defects in *O*-xylosylglycan synthesis			
Ehlers–Danlos syndrome (progeroid form)	β4GALT7	β1,4-galactosyl transferase 7	[115]
multiple exostoses syndrome	EXT1/EXT2	Glucuronyl transferase/*N*-acetylhexosaminyl transferase	[116]

[a] Defects in the assembly of the lipid-linked oligosaccharide precursor including OST are named CDG I, whereas defects in the processing of the *N*-glycan chain are named CDG II. Transferrin of group I patients lack sialic acid residues because of nonoccupied glycosylation sequons that are normally glycosylated (i.e. complete glycan chains are absent). Disturbances in LLO synthase (not the optimal substrate for the OST) or in the transfer cause under glycosylation. The glycan chains are normal or only slightly altered. In contrast, the two glycosylation sites of transferrin of group II patients are glycosylated, but the structure of the oligosaccharides is altered.

peptidase Y. Similarily restored are the defects of the biosynthesis of dolichol-linked oligosaccharide in vivo as well as the mannosyl transferase activity in vitro (Figure 10).[92] It is indeed astonishing how precisely the gene products of yeast and man correspond to each other. When the mutations of another CDG subtype, CDG-Ig, were identified as L158P[93] and T61M[94] exchange, and the corresponding mutations were introduced into the yeast *ALG12* gene, the mutated yeast gene was not able to complement the *alg12* mutation in yeast cells; it thus behaved identical to human mutations.

As demonstrated, yeast cells have been extremely helpful in identifying the biosynthetic machinery of protein N-glycosylation in mammalian cells. The knowledge of the great majority of the mammalian genes involved in this pathway is built on information previously obtained in yeast (Table 1). The same holds true for the investigation and elucidation of CDG. Certainly, it will be supportive in the biochemical and molecular identification of CDG in the future. It does not have to be especially emphasized that the role of this model organism is not restricted to protein glycosylation.

5. Outlook

During the exciting time of molecular biology within the past 50 years, proteins and nucleic acids dominated the field. Carbohydrates (besides their role in energy metabolism) remained very much in the shade. There exists an increasing awareness, however, that carbohydrates as information molecules par excellence, play increasingly important roles especially in the regulation the development of higher organisms. The better we understand the different roles of oligo- and polysaccharides as modifications of proteins and lipids, the more pronounced their contribution will be to

 © 2006 Wiley-VCH Verlag GmbH & Co. KGaA, Weinheim

successfully tackle medical and pharmaceutical challenges in the future.[95] The enormous advances in the last years in the field of organic synthesis of glycans and complex glycopeptides up to distinct glycoprotein variants are remarkable.[96] A similar progress occurs in the analysis of complex carbohydrate mixtures with new forms of mass spectrometry, NMR spectroscopy, and high-resolution separation methodologies.[97] The occupation with the chemistry and biology of carbohydrates promises fascinating science, the solution of fundamental biological questions, and eventually the successful transfer of the knowledge to applied fields.

The experimental work from the laboratories of the authors has been supported by the Deutsche Forschungsgemeinschaft (DFG), by the Fonds der Chemischen Industrie, and by the Körber-Stiftung. Owing to space limitations, we have had to frequently refer to reviews and we apologize for not having been able to refer to all the relevant original literature.

Received: April 26, 2006
Published online: October 6, 2006

[1] B. Alberts, A. Johnson, J. Lewis, M. Raft, K. Roberts, P. Walter, *The Molecular Biology of the Cell*, 4th ed., Garland Science, New York **2002**; S. K. Hanks, T. Hunter, *FASEB J.* **1995**, *9*, 576–596.
[2] R. G. Spiro, *Glycobiology* **2002**, *12*, 43R–56R; H. Lis, N. Sharon, *Eur. J. Biochem.* **1993**, *218*, 1–27.
[3] K. Landsteiner, *Wien. Klin. Wochenschr.* **1901**, *14*, 1132–1134; W. M. Watkins, *Pure Appl. Chem.* **1991**, *63*, 561–568.
[4] R. Kornfeld, S. Kornfeld, *Annu. Rev. Biochem.* **1985**, *54*, 631–664; L. Lehle, W. Tanner in *Glycoproteins, New Comprehensive Biochemistry, Vol. 29a* (Eds.: J. Montreuil, J. F. G. Vliegenthart, H. Schachter), Elsevier, Amsterdam, **1995**, pp. 475–509.
[5] S. Strahl-Bolsinger, M. Gentzsch, W. Tanner, *Biochim. Biophys. Acta* **1999**, *1426*, 297–307.
[6] I. Brockhausen, *Biochim. Biophys. Acta* **1999**, *1473*, 67–95; F. G. Hanisch, *Biol. Chem.* **2001**, *382*, 143–149; K. G. Ten Hagen, T. A. Fritz, L. A. Tabak, *Glycobiology* **2003**, *13*, 1R-16R.
[7] H. Schachter, *Glycobiology* **1991**, *1*, 453–461.
[8] M. Amado, R. Almeida, T. Schwientek, H. Clausen, *Biochim. Biophys. Acta* **1999**, *1473*, 35–53; J. Marth, in *Essentials of Glycobiology* (Eds.: A. Varki, R. D. Cummings, J. D. Esko, H. H. Freeze, G. W. Hart, J. Marth), Cold Spring Harbor Laboratory Press, New York, **1999**, pp. 101–113.
[9] X. Cheng, G. W. Hart, *J. Biol. Chem.* **2001**, *276*, 10570–10575; K. Kamemura, B. K. Hayes, F. I. Comer, G. W. Hart, *J. Biol. Chem.* **2002**, *277*, 19229–19235.
[10] G. W. Hart in *Essentials of Glycobiology* (Eds.: A. Varki, R. D. Cummings, J. D. Esko, H. H. Freeze, G. W. Hart, J. Marth), Cold Spring Harbor Laboratory Press, New York, **1999**, pp. 171–194.
[11] R. Schauer, *Glycoconjugate J.* **2000**, *17*, 485–499; O. T. Keppler, R. Horstkorte, M. Pawlita, C. Schmidt, W. Reutter, *Glycobiology* **2001**, *11*, 11R–18R.
[12] A. Gottschalk, in *Glycoproteins, their composition, structure and function, Vol. 5* (Ed.: A. Gottschalk), B.B.A. Library, **1972**, pp. 24–30.
[13] J. Lechner, F. Wieland, *Annu. Rev. Biochem.* **1989**, *58*, 173–194; P. Messner, *Glycoconjugate J.* **1997**, *14*, 3–11; P. Messner, *J. Bacteriol.* **2004**, *186*, 2517–2519.
[14] P. G. Johansen, R. D. Marshall, A. Neuberger, *Biochem. J.* **1961**, *78*, 518–527; R. H. Nuenke, L. W. Cunningham, *J. Biol. Chem.* **1961**, *236*, 2452–2460.
[15] L. F. Leloir, *Science* **1971**, *172*, 1299–1303.
[16] Y. Higashi, J. L. Strominger, C. C. Sweeley, *Proc. Natl. Acad. Sci. USA* **1967**, *57*, 1878–1884; M. Scher, W. J. Lennarz, C. C. Sweeley, *Proc. Natl. Acad. Sci. USA* **1968**, *59*, 1313–1320; A. Wright, M. Dankert, P. Fennessey, P. W. Robbins, *Proc. Natl. Acad. Sci. USA* **1967**, *57*, 1798–1803.
[17] N. H. Behrens, L. F. Leloir, *Proc. Natl. Acad. Sci. USA* **1970**, *66*, 153–159; P. Jung, W. Tanner, *Eur. J. Biochem.* **1973**, *37*, 1–6; W. Tanner, *Biochem. Biophys. Res. Commun.* **1969**, *35*, 144–150.
[18] N. H. Behrens, A. J. Parodi, L. F. Leloir, *Proc. Natl. Acad. Sci. USA* **1971**, *68*, 2857–2860; L. Lehle, *Eur. J. Biochem.* **1980**, *109*, 589–601; L. Lehle, W. Tanner, *Biochim. Biophys. Acta* **1975**, *399*, 364–374.
[19] P. W. Robbins, S. C. Hubbard, S. J. Turco, D. F. Wirth, *Cell* **1977**, *12*, 893–900; E. Li, I. Tabas, S. Kornfeld, *J. Biol. Chem.* **1978**, *253*, 7762–7770; S. Kornfeld, E. Li, I. Tabas, *J. Biol. Chem.* **1978**, *253*, 7771–7778.
[20] G. P. Kaushal, A. D. Elbein, *Methods Enzymol.* **1989**, *179*, 452–475; L. Lehle, W. Tanner, *Biochem. Soc. Trans.* **1983**, *11*, 568–574; L. Faye, A. Boulaflous, M. Benchabane, V. Gomord, D. Michaud, *Vaccine* **2005**, *23*, 1770–1778; I. B. Wilson, *Curr. Opin. Struct. Biol.* **2002**, *12*, 569–577.
[21] A. Takatsuki, K. Arima, G. Tamura, *J. Antibiot.* **1971**, *24*, 215–223.
[22] L. Lehle, W. Tanner, *FEBS Lett.* **1976**, *71*, 167–170; J. S. Tkacz, O. Lampen, *Biochem. Biophys. Res. Commun.* **1975**, *65*, 248–257.
[23] M. D. Snider, L. A. Sultzman, P. W. Robbins, *Cell* **1980**, *21*, 385–392.
[24] J. Helenius, D. T. Ng, C. L. Marolda, P. Walter, M. A. Valvano, M. Aebi, *Nature* **2002**, *415*, 447–450.
[25] A. Haselbeck, W. Tanner, *Proc. Natl. Acad. Sci. USA* **1982**, *79*, 1520–1524; A. Haselbeck, W. Tanner, *FEMS Microbiol. Lett.* **1984**, *21*, 305–308.
[26] T. C. Huffaker, P. W. Robbins, *J. Biol. Chem.* **1982**, *257*, 3203–3210; T. C. Huffaker, P. W. Robbins, *Proc. Natl. Acad. Sci. USA* **1983**, *80*, 7466–7470.
[27] D. J. Kelleher, G. Kreibich, R. Gilmore, *Cell* **1992**, *69*, 55–65.
[28] R. Knauer, L. Lehle, *FEBS Lett.* **1994**, *344*, 83–86; S. te Heesen, B. Janetzky, L. Lehle, M. Aebi, *EMBO J.* **1992**, *11*, 2071–2075.
[29] R. Knauer, L. Lehle, *Biochim. Biophys. Acta* **1999**, *1426*, 259–273; S. Silberstein, R. Gilmore, *FASEB J.* **1996**, *10*, 849–858; A. Yan, W. J. Lennarz, *J. Biol. Chem.* **2005**, *280*, 3121–3124.
[30] I. Nilsson, D. J. Kelleher, Y. Miao, Y. Shao, G. Kreibich, R. Gilmore, G. von Heijne, A. E. Johnson, *J. Cell Biol.* **2003**, *161*, 715–725.
[31] A. L. Karamyshev, D. J. Kelleher, R. Gilmore, A. E. Johnson, G. von Heijne, I. Nilsson, *J. Biol. Chem.* **2005**, *280*, 40489–40493.
[32] M. Wacker, D. Linton, P. G. Hitchen, M. Nita-Lazar, S. M. Haslam, S. J. North, M. Panico, H. R. Morris, A. Dell, B. W. Wren, M. Aebi, *Science* **2002**, *298*, 1790–1793; D. Linton, N. Dorrell, P. G. Hitchen, S. Amber, A. V. Karlyshev, H. R. Morris, A. Dell, M. A. Valvano, M. Aebi, B. W. Wren, *Mol. Microbiol.* **2005**, *55*, 1695–1703.
[33] M. Schwarz, R. Knauer, L. Lehle, *FEBS Lett.* **2005**, *579*, 6564–6568; A. Yan, W. J. Lennarz, *Glycobiology* **2005**, *15*, 1407–1415; U. Spirig, D. Bodmer, M. Wacker, P. Burda, M. Aebi, *Glycobiology* **2005**, *15*, 1396–1406.
[34] D. J. Kelleher, D. Karaoglu, E. C. Mandon, R. Gilmore, *Mol. Cell* **2003**, *12*, 101–111.
[35] C. Ronin, S. Bouchilloux, C. Granier, J. van Rietschoten, *FEBS Lett.* **1978**, *96*, 179–182; E. Bause, L. Lehle, *Eur. J. Biochem.*

 © 2006 Wiley-VCH Verlag GmbH & Co. KGaA, Weinheim

1979, *101*, 531 – 540; G. W. Hart, K. Brew, G. A. Grant, R. A. Bradshaw, W. J. Lennarz, *J. Biol. Chem.* **1979**, *254*, 9747 – 9753.
[36] E. Bause, *Biochem. J.* **1983**, *209*, 331 – 336; E. Bause, G. Legler, *Biochem. J.* **1981**, *195*, 639–644.
[37] R. Apweiler, H. Hermjakob, N. Sharon, *Biochim. Biophys. Acta* **1999**, *1473*, 4 – 8; A. J. Petrescu, A. L. Milac, S. M. Petrescu, R. A. Dwek, M. R. Wormald, *Glycobiology* **2004**, *14*, 103 – 114.
[38] L. Kasturi, H. Chen, S. H. Shakin-Eshleman, *Biochem. J.* **1997**, *323*, 415 – 419; J. L. Mellquist, L. Kasturi, S. L. Spitalnik, S. H. Shakin-Eshleman, *Biochemistry* **1998**, *37*, 6833 – 6837; R. S. Senger, M. N. Karim, *Biotechnol. Prog.* **2005**, *21*, 1653 – 1662; T. Roitsch, L. Lehle, *Eur. J. Biochem.* **1989**, *181*, 525 – 529.
[39] C. B. Sharma, L. Lehle, W. Tanner, *Eur. J. Biochem.* **1981**, *116*, 101 – 108; D. Karaoglu, D. J. Kelleher, R. Gilmore, *Biochemistry* **2001**, *40*, 12193 – 12206.
[40] B. Imperiali, T. L. Hendrickson, *Bioorg. Med. Chem.* **1995**, *3*, 1565 – 1578; E. Bause, G. Legler, *Biochem. J.* **1981**, *195*, 639 – 644.
[41] P. Whitley, I. M. Nilsson, G. von Heijne, *J. Biol. Chem.* **1996**, *271*, 6241 – 6244.
[42] M. Ecker, V. Mrsa, I. Hagen, R. Deutzmann, S. Strahl, W. Tanner, *EMBO Rep.* **2003**, *4*, 628 – 632.
[43] C. E. Ballou, *Methods Enzymol.* **1990**, *185*, 440 – 470.
[44] R. Sentandreu, D. H. Northcote, *Carbohydr. Res.* **1969**, *10*, 584 – 585.
[45] W. Chai, C. T. Yuen, H. Kogelberg, R. A. Carruthers, R. U. Margolis, T. Feizi, A. M. Lawson, *Eur. J. Biochem.* **1999**, *263*, 879 – 888; C. T. Yuen, W. Chai, R. W. Loveless, A. M. Lawson, R. U. Margolis, T. Feizi, *J. Biol. Chem.* **1997**, *272*, 8924 – 8931.
[46] A. Chiba, K. Matsumura, H. Yamada, T. Inazu, T. Shimizu, S. Kusunoki, I. Kanazawa, A. Kobata, T. Endo, *J. Biol. Chem.* **1997**, *272*, 2156 – 2162.
[47] B. C. VanderVen, J. D. Harder, D. C. Crick, J. T. Belisle, *Science* **2005**, *309*, 941 – 943.
[48] P. Babczinski, W. Tanner, *Biochem. Biophys. Res. Commun.* **1973**, *54*, 1119 – 1124; G. Larriba, M. V. Elorza, J. R. Villanueva, R. Sentandreu, *FEBS Lett.* **1976**, *71*, 316 – 320; A. Haselbeck, W. Tanner, *FEBS Lett.* **1983**, *158*, 335 – 338.
[49] T. Willer, W. Amselgruber, R. Deutzmann, S. Strahl, *Glycobiology* **2002**, *12*, 771 – 783.
[50] H. Manya, A. Chiba, A. Yoshida, X. Wang, Y. Chiba, Y. Jigami, R. U. Margolis, T. Endo, *Proc. Natl. Acad. Sci. USA* **2004**, *101*, 500 – 505.
[51] S. Strahl-Bolsinger, T. Immervoll, R. Deutzmann, W. Tanner, *Proc. Natl. Acad. Sci. USA* **1993**, *90*, 8164 – 8168; S. Strahl-Bolsinger, W. Tanner, *Eur. J. Biochem.* **1991**, *196*, 185 – 190.
[52] T. Willer, M. C. Valero, W. Tanner, J. Cruces, S. Strahl, *Curr. Opin. Struct. Biol.* **2003**, *13*, 621 – 630.
[53] E. Martin-Blanco, A. Garcia-Bellido, *Proc. Natl. Acad. Sci. USA* **1996**, *93*, 6048 – 6052; L. A. Jurado, A. Coloma, J. Cruces, *Genomics* **1999**, *58*, 171 – 180.
[54] D. Lyalin, K. Koles, S. D. Roosendaal, E. Repnikova, L. Van Wechel, V. M. Panin, *Genetics* **2006**, *172*, 343 – 353.
[55] V. Girrbach, S. Strahl, *J. Biol. Chem.* **2003**, *278*, 12554 – 12562; V. Girrbach, T. Zeller, M. Priesmeier, S. Strahl-Bolsinger, *J. Biol. Chem.* **2000**, *275*, 19288 – 19296.
[56] M. Gentzsch, T. Immervoll, W. Tanner, *FEBS Lett.* **1995**, *377*, 128 – 130.
[57] M. Gentzsch, W. Tanner, *Glycobiology* **1997**, *7*, 481 – 486.
[58] S. Strahl-Bolsinger, A. Scheinost, *J. Biol. Chem.* **1999**, *274*, 9068 – 9075.
[59] M. Lussier, A. M. Sdicu, H. Bussey, *Biochim. Biophys. Acta* **1999**, *1426*, 323 – 334.
[60] A. Yoshida, K. Kobayashi, H. Manya, K. Taniguchi, H. Kano, M. Mizuno, T. Inazu, H. Mitsuhashi, S. Takahashi, M. Takeuchi, R. Herrmann, V. Straub, B. Talim, T. Voit, H. Topaloglu, T. Toda, T. Endo, *Dev. Cell* **2001**, *1*, 717 – 724.
[61] W. Zhang, D. Betel, H. Schachter, *Biochem. J.* **2002**, *361*, 153 – 162.
[62] K. Ebnet, D. Vestweber, *Histochem. Cell Biol.* **1999**, *112*, 1 – 23; M. Fukuda, N. Hiraoka, J. C. Yeh, *J. Cell Biol.* **1999**, *147*, 467 – 470; R. P. McEver, *Curr. Opin. Cell Biol.* **2002**, *14*, 581 – 586; D. Vestweber, J. E. Blanks, *Physiol. Rev.* **1999**, *79*, 181 – 213; R. D. Cummings, D. F. Smith, *BioEssays* **1992**, *14*, 849 – 856.
[63] G. W. Hart, R. S. Haltiwanger, G. D. Holt, W. G. Kelly, *Annu. Rev. Biochem.* **1989**, *58*, 841 – 874; G. W. Hart, *Annu. Rev. Biochem.* **1997**, *66*, 315 – 335; F. I. Comer, G. W. Hart, *J. Biol. Chem.* **2000**, *275*, 29179 – 29182; C. Slawson, M. P. Housley, G. W. Hart, *J. Cell. Biochem.* **2006**, *97*, 71 – 83.
[64] A. Varki, *Glycobiology* **1993**, *3*, 97 – 130.
[65] S. Hakomori in *Science and scientists* (Eds.: M. Kageyoma, K. Nakamura, T. Oshima, T. Uchida), Japan Scientific Societies and D. Reidel Publ. Co., Tokyo and Dordrecht, **1981**, pp. 199 – 205.
[66] R. A. Laine, *Glycobiology* **1994**, *4*, 759 – 767.
[67] E. Ioffe, P. Stanley, *Proc. Natl. Acad. Sci. USA* **1994**, *91*, 728 – 732; M. Metzler, A. Gertz, M. Sarkar, H. Schachter, J. W. Schrader, J. D. Marth, *EMBO J.* **1994**, *13*, 2056 – 2065; H. Koiwa, F. Li, M. G. McCully, I. Mendoza, N. Koizumi, Y. Manabe, Y. Nakagawa, J. Zhu, A. Rus, J. M. Pardo, R. A. Bressan, P. M. Hasegawa, *Plant Cell* **2003**, *15*, 2273 – 2284; O. Lerouxel, G. Mouille, C. Andeme-Onzighi, M. P. Bruyant, M. Seveno, C. Loutelier-Bourhis, A. Driouich, H. Hofte, P. Lerouge, *Plant J.* **2005**, *42*, 455 – 468.
[68] C. Cappellaro, C. Baldermann, R. Rachel, W. Tanner, *EMBO J.* **1994**, *13*, 4737 – 4744; C. Cappellaro, K. Hauser, V. Mrsa, M. Watzele, G. Watzele, C. Gruber, W. Tanner, *EMBO J.* **1991**, *10*, 4081 – 4088.
[69] S. Hickman, L. J. Shapiro, E. F. Neufeld, *Biochem. Biophys. Res. Commun.* **1974**, *57*, 55 – 61; K. von Figura, A. Hasilik, *Annu. Rev. Biochem.* **1986**, *55*, 167 – 193; S. Kornfeld, *FASEB J.* **1987**, *1*, 462 – 468; W. S. Sly, *J. Clin. Invest.* **2000**, *105*, 563 – 564.
[70] C. Hashimoto, R. E. Cohen, W. J. Zhang, C. E. Ballou, *Proc. Natl. Acad. Sci. USA* **1981**, *78*, 2244 – 2248; H. Schwaiger, A. Hasilik, K. von Figura, A. Wiemken, W. Tanner, *Biochem. Biophys. Res. Commun.* **1982**, *104*, 950 – 956.
[71] A. J. Parodi, *Annu. Rev. Biochem.* **2000**, *69*, 69 – 93; E. S. Trombetta, A. J. Parodi, *Methods* **2005**, *35*, 328 – 337.
[72] S. Dejgaard, J. Nicolay, M. Taheri, D. Y. Thomas, J. J. Bergeron, *Curr. Issues Mol. Biol.* **2004**, *6*, 29 – 42; L. Ellgaard, A. Helenius, *Nat. Rev. Mol. Cell Biol.* **2003**, *4*, 181 – 191; R. G. Spiro, *Cell. Mol. Life Sci.* **2004**, *61*, 1025 – 1041; D. B. Williams, *J. Cell Sci.* **2006**, *119*, 615 – 623.
[73] C. L. Ward, R. R. Kopito, *J. Biol. Chem.* **1994**, *269*, 25710 – 25718; J. R. Riordan, *Annu. Rev. Physiol.* **2005**, *67*, 701 – 718.
[74] B. Tsai, Y. Ye, T. A. Rapoport, *Nat. Rev. Mol. Cell Biol.* **2002**, *3*, 246 – 255.
[75] C. A. Jakob, D. Bodmer, U. Spirig, P. Battig, A. Marcil, D. Dignard, J. J. Bergeron, D. Y. Thomas, M. Aebi, *EMBO Rep.* **2001**, *2*, 423 – 430; N. Hosokawa, I. Wada, K. Hasegawa, T. Yorihuzi, L. O. Tremblay, A. Herscovics, K. Nagata, *EMBO Rep.* **2001**, *2*, 415 – 422; K. Nakatsukasa, S. Nishikawa, N. Hosokawa, K. Nagata, T. Endo, *J. Biol. Chem.* **2001**, *276*, 8635 – 8638.
[76] M. Gentzsch, W. Tanner, *EMBO J.* **1996**, *15*, 5752 – 5759.
[77] T. Willer, M. Brandl, M. Sipiczki, S. Strahl, *Mol. Microbiol.* **2005**, *57*, 156 – 170.
[78] B. D. Shaw, M. Momany, *Fungal Genet. Biol.* **2002**, *37*, 263 – 270.
[79] M. Rouabhia, M. Schaller, C. Corbucci, A. Vecchiarelli, S. K. Prill, L. Giasson, J. F. Ernst, *Infect. Immun.* **2005**, *73*, 4571 – 4580.
[80] C. M. Coughlan, J. L. Walker, J. C. Cochran, K. D. Wittrup, J. L. Brodsky, *J. Biol. Chem.* **2004**, *279*, 15289 – 15297; M. Lommel, M. Bagnat, S. Strahl, *Mol. Cell. Biol.* **2004**, *24*, 46 – 57; T. J.

 © 2006 Wiley-VCH Verlag GmbH & Co. KGaA, Weinheim

Proszynski, K. Simons, M. Bagnat, *Mol. Biol. Cell* **2004**, *15*, 1533 – 1543.

[81] C. Harty, S. Strahl, K. Romisch, *Mol. Biol. Cell* **2001**, *12*, 1093 – 1101; K. Nakatsukasa, S. Okada, K. Umebayashi, R. Fukuda, S. Nishikawa, T. Endo, *J. Biol. Chem.* **2004**, *279*, 49762 – 49772.

[82] T. Willer, B. Prados, J. M. Falcon-Perez, I. Renner-Muller, G. K. Przemeck, M. Lommel, A. Coloma, M. C. Valero, M. H. de Angelis, W. Tanner, E. Wolf, S. Strahl, J. Cruces, *Proc. Natl. Acad. Sci. USA* **2004**, *101*, 14126 – 14131.

[83] J. Jaeken, M. Vanderschueren-Lodeweyckx, P. Casaer, L. Snoeck, L. Corbeel, E. Eggermont, R. Eeckels, *Pediatr. Res.* **1980**, *14*, 179.

[84] J. Jaeken, H. G. van Eijk, C. van der Heul, L. Corbeel, R. Eeckels, E. Eggermont, *Clin. Chim. Acta* **1984**, *144*, 245 – 247.

[85] K. W. Marek, I. K. Vijay, J. D. Marth, *Glycobiology* **1999**, *9*, 1263 – 1271.

[86] T. Endo, T. Toda, *Biol. Pharm. Bull.* **2003**, *26*, 1641 – 1647; F. Muntoni, M. Brockington, S. Torelli, S. C. Brown, *Curr. Opin. Neurol.* **2004**, *17*, 205 – 209; H. Schachter, J. Vajsar, W. Zhang, *Glycoconjugate J.* **2004**, *21*, 291 – 300.

[87] D. E. Michele, K. P. Campbell, *J. Biol. Chem.* **2003**, *278*, 15457 – 15460.

[88] R. Barresi, K. P. Campbell, *J. Cell Sci.* **2006**, *119*, 199 – 207; M. Durbeej, K. P. Campbell, *Curr. Opin. Genet. Dev.* **2002**, *12*, 349 – 361.

[89] D. Beltran-Valero de Bernabe, S. Currier, A. Steinbrecher, J. Celli, E. van Beusekom, B. van der Zwaag, H. Kayserili, L. Merlini, D. Chitayat, W. B. Dobyns, B. Cormand, A. E. Lehesjoki, J. Cruces, T. Voit, C. A. Walsh, H. van Bokhoven, H. G. Brunner, *Am. J. Hum. Genet.* **2002**, *71*, 1033 – 1043.

[90] J. van Reeuwijk, M. Janssen, C. van den Elzen, D. Beltran-Valero de Bernabe, P. Sabatelli, L. Merlini, M. Boon, H. Scheffer, M. Brockington, F. Muntoni, M. A. Huynen, A. Verrips, C. A. Walsh, P. G. Barth, H. G. Brunner, H. van Bokhoven, *J. Med. Genet.* **2005**, *42*, 907 – 912.

[91] J. G. Gleeson, C. A. Walsh, *Trends Neurosci.* **2000**, *23*, 352 – 359; M. Haltia, I. Leivo, H. Somer, H. Pihko, A. Paetau, T. Kivela, A. Tarkkanen, F. Tome, E. Engvall, P. Santavuori, *Ann. Neurol.* **1997**, *41*, 173 – 180; C. Longman, E. Mercuri, F. Cowan, J. Allsop, M. Brockington, C. Jimenez-Mallebrera, S. Kumar, M. Rutherford, T. Toda, F. Muntoni, *Arch. Neurol.* **2004**, *61*, 1301 – 1306; E. Mercuri, H. Topaloglu, M. Brockington, A. Berardinelli, A. Pichiecchio, F. Santorelli, M. Rutherford, B. Talim, E. Ricci, T. Voit, F. Muntoni, *Arch. Neurol.* **2006**, *63*, 251 – 257.

[92] C. Thiel, M. Schwarz, J. Peng, M. Grzmil, M. Hasilik, T. Braulke, A. Kohlschutter, K. von Figura, L. Lehle, C. Korner, *J. Biol. Chem.* **2003**, *278*, 22498 – 22505.

[93] C. Thiel, M. Schwarz, M. Hasilik, U. Grieben, F. Hanefeld, L. Lehle, K. von Figura, C. Koerner, *Biochem. J.* **2002**, *367*, 195 – 201.

[94] C. E. Grubenmann, C. G. Frank, S. Kjaergaard, E. G. Berger, M. Aebi, T. Hennet, *Hum. Mol. Genet.* **2002**, *11*, 2331 – 2339.

[95] P. H. Seeberger, D. B. Werz, *Nat. Rev. Drug Discovery* **2005**, *4*, 751 – 763.

[96] C. Brocke, H. Kunz, *Bioorg. Med. Chem.* **2002**, *10*, 3085 – 3112; S. Mezzato, M. Schaffrath, C. Unverzagt, *Angew. Chem.* **2005**, *117*, 1677 – 1681; *Angew. Chem. Int. Ed.* **2005**, *44*, 1650 – 1654; H. Weiss, C. Unverzagt, *Angew. Chem.* **2003**, *115*, 4389 – 4392; *Angew. Chem. Int. Ed.* **2003**, *42*, 4261 – 4263; S. Hanashima, S. Manabe, Y. Ito, *Angew. Chem.* **2005**, *117*, 4290 – 4296; *Angew. Chem. Int. Ed.* **2005**, *44*, 4218 – 4224; M. V. Chiesa, R. R. Schmidt, *Eur. J. Org. Chem.* **2000**, 3541 – 3554.

[97] Y. Mechref, M. V. Novotny, *Chem. Rev.* **2002**, *102*, 321 – 369.

[98] E. Van Schaftingen, J. Jaeken, *FEBS Lett.* **1995**, *377*, 318 – 320.

[99] R. Niehues, M. Hasilik, G. Alton, C. Koerner, M. Schiebe-Sukumar, H. G. Koch, K. P. Zimmer, R. Wu, E. Harms, K. Reiter, K. von Figura, H. H. Freeze, H. K. Harms, T. Marquardt, *J. Clin. Invest.* **1998**, *101*, 1414 – 1420.

[100] C. Koerner, R. Knauer, U. Holzbach, F. Hanefeld, L. Lehle, K. von Figura, *Proc. Natl. Acad. Sci. USA* **1998**, *95*, 13200 – 13205; T. Imbach, P. Burda, P. Kuhnert, R. A. Wevers, M. Aebi, E. G. Berger, T. Hennet, *Proc. Natl. Acad. Sci. USA* **1999**, *96*, 6982 – 6987.

[101] C. Koerner, R. Knauer, U. Stephani, T. Marquardt, L. Lehle, K. von Figura, *EMBO J.* **1999**, *18*, 6816 – 6822.

[102] T. Imbach, B. Schenk, E. Schollen, P. Burda, A. Stutz, S. Grunewald, N. M. Bailie, M. D. King, J. Jaeken, G. Matthijs, E. G. Berger, M. Aebi, T. Hennet, *J. Clin. Invest.* **2000**, *105*, 233 – 239; S. Kim, V. Westphal, G. Srikrishna, D. P. Mehta, S. Peterson, J. Filiano, P. S. Karnes, M. C. Patterson, H. H. Freeze, *J. Clin. Invest.* **2000**, *105*, 191 – 198.

[103] C. Kranz, J. Denecke, M. A. Lehrman, S. Ray, P. Kienz, G. Kreissel, D. Sagi, J. Peter-Katalinic, H. H. Freeze, T. Schmid, S. Jackowski-Dohrmann, E. Harms, T. Marquardt, *J. Clin. Invest.* **2001**, *108*, 1613 – 1619; B. Schenk, T. Imbach, C. G. Frank, C. E. Grubenmann, G. V. Raymond, H. Hurvitz, I. Korn-Lubetzki, S. Revel-Vik, A. Raas-Rotschild, A. S. Luder, J. Jaeken, E. G. Berger, G. Matthijs, T. Hennet, M. Aebi, *J. Clin. Invest.* **2001**, *108*, 1687 – 1695.

[104] I. Chantret, J. Dancourt, T. Dupre, C. Delenda, S. Bucher, S. Vuillaumier-Barrot, H. Ogier de Baulny, C. Peletan, O. Danos, N. Seta, G. Durand, R. Oriol, P. Codogno, S. E. Moore, *J. Biol. Chem.* **2003**, *278*, 9962 – 9971.

[105] X. Wu, J. S. Rush, D. Karaoglu, D. Krasnewich, M. S. Lubinsky, C. J. Waechter, R. Gilmore, H. H. Freeze, *Hum. Mutat.* **2003**, *22*, 144 – 150.

[106] M. Schwarz, C. Thiel, J. Lubbehusen, B. Dorland, T. de Koning, K. von Figura, L. Lehle, C. Korner, *Am. J. Hum. Genet.* **2004**, *74*, 472 – 481; C. Kranz, J. Denecke, L. Lehle, K. Sohlbach, S. Jeske, F. Meinhardt, R. Rossi, S. Gudowius, T. Marquardt, *Am. J. Hum. Genet.* **2004**, *74*, 545 – 551; C. E. Grubenmann, C. G. Frank, A. J. Hulsmeier, E. Schollen, G. Matthijs, E. Mayatepek, E. G. Berger, M. Aebi, T. Hennet, *Hum. Mol. Genet.* **2004**, *13*, 535 – 542.

[107] C. G. Frank, C. E. Grubenmann, W. Eyaid, E. G. Berger, M. Aebi, T. Hennet, *Am. J. Hum. Genet.* **2004**, *75*, 146 – 150.

[108] J. Jaeken, H. Schachter, H. Carchon, P. De Cock, B. Coddeville, G. Spik, *Arch. Dis. Child.* **1994**, *71*, 123 – 127; J. Tan, J. Dunn, J. Jaeken, H. Schachter, *Am. J. Hum. Genet.* **1996**, *59*, 810 – 817.

[109] C. M. De Praeter, G. J. Gerwig, E. Bause, L. K. Nuytinck, J. F. Vliegenthart, W. Breuer, J. P. Kamerling, M. F. Espeel, J. J. Martin, A. M. De Paepe, N. W. Chan, G. A. Dacremont, R. N. Van Coster, *Am. J. Hum. Genet.* **2000**, *66*, 1744 – 1756.

[110] T. Luebke, T. Marquardt, K. von Figura, C. Koerner, *J. Biol. Chem.* **1999**, *274*, 25986 – 25989; T. Luebke, T. Marquardt, A. Etzioni, E. Hartmann, K. von Figura, C. Koerner, *Nat. Genet.* **2001**, *28*, 73 – 76; K. Luhn, M. K. Wild, M. Eckhardt, R. Gerardy-Schahn, D. Vestweber, *Nat. Genet.* **2001**, *28*, 69 – 72.

[111] B. Hansske, C. Thiel, T. Lubke, M. Hasilik, S. Honing, V. Peters, P. H. Heidemann, G. F. Hoffmann, E. G. Berger, K. von Figura, C. Korner, *J. Clin. Invest.* **2002**, *109*, 725 – 733.

[112] I. Martinez-Duncker, T. Dupre, V. Piller, F. Piller, J. J. Candelier, C. Trichet, G. Tchernia, R. Oriol, R. Mollicone, *Blood* **2005**, *105*, 2671 – 2676.

[113] X. Wu, R. A. Steet, O. Bohorov, J. Bakker, J. Newell, M. Krieger, L. Spaapen, S. Kornfeld, H. H. Freeze, *Nat. Med.* **2004**, *10*, 518 – 523.

[114] F. Foulquier, E. Vasile, E. Schollen, N. Callewaert, T. Raemaekers, D. Quelhas, J. Jaeken, P. Mills, B. Winchester, M. Krieger, W. Annaert, G. Matthijs, *Proc. Natl. Acad. Sci. USA* **2006**, *103*, 3764 – 3769.

 © 2006 Wiley-VCH Verlag GmbH & Co. KGaA, Weinheim

[115] E. Quentin, A. Gladen, L. Roden, H. Kresse, *Proc. Natl. Acad. Sci. USA* **1990**, *87*, 1342 – 1346; T. Okajima, S. Fukumoto, K. Furukawa, T. Urano, *J. Biol. Chem.* **1999**, *274*, 28841 – 28844.
[116] W. Wuyts, S. Ramlakhan, W. Van Hul, J. T. Hecht, A. M. van den Ouweland, W. H. Raskind, F. C. Hofstede, E. Reyniers, D. E. Wells, B. de Vries, E. U. Conrad, A. Hill, D. Zalatayev, J. Weissenbach, M. J. Wagner, E. Bakker, D. J. J. Halley, P. J. Willems, *Am. J. Hum. Genet.* **1995**, *57*, 382 – 387; W. Wuyts, W. Van Hul, J. Wauters, M. Nemtsova, E. Reyniers, E. V. Van Hul, K. De Boulle, B. B. de Vries, J. Hendrickx, I. Herrygers, P. Bossuyt, W. Balemans, E. Fransen, L. Vits, P. Coucke, N. J. Nowak, T. B. Shows, L. Mallet, A. M. van den Ouweland, J. McGaughran, D. J. Halley, P. J. Willems, *Hum. Mol. Genet.* **1996**, *5*, 1547 – 1557.

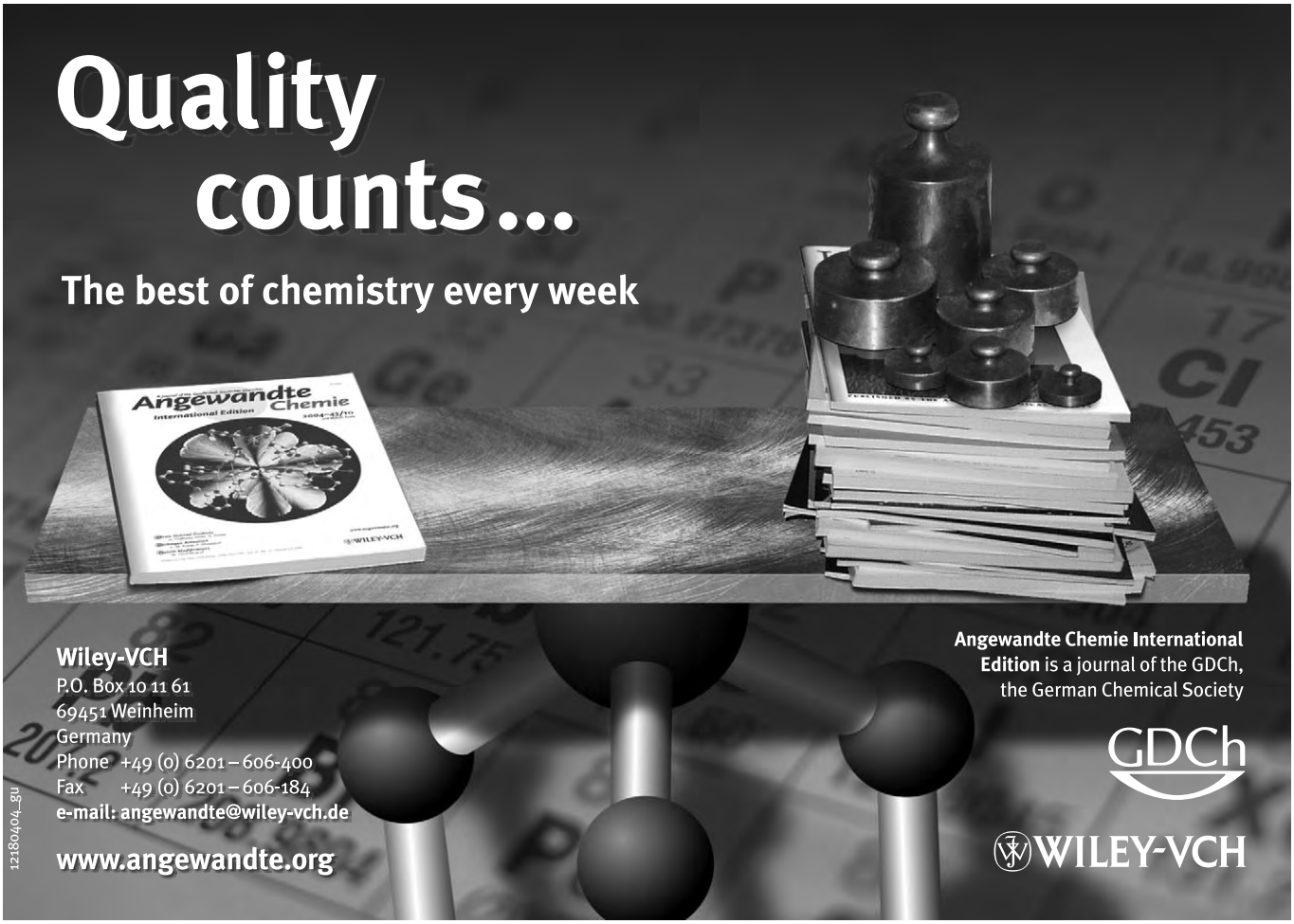

 © 2006 Wiley-VCH Verlag GmbH & Co. KGaA, Weinheim

VIP Molecular Switches

DOI: 10.1002/anie.200601584

Selective and Sequential Photorelease Using Molecular Switches**

*Vincent Lemieux, Simon Gauthier, and Neil R. Branda**

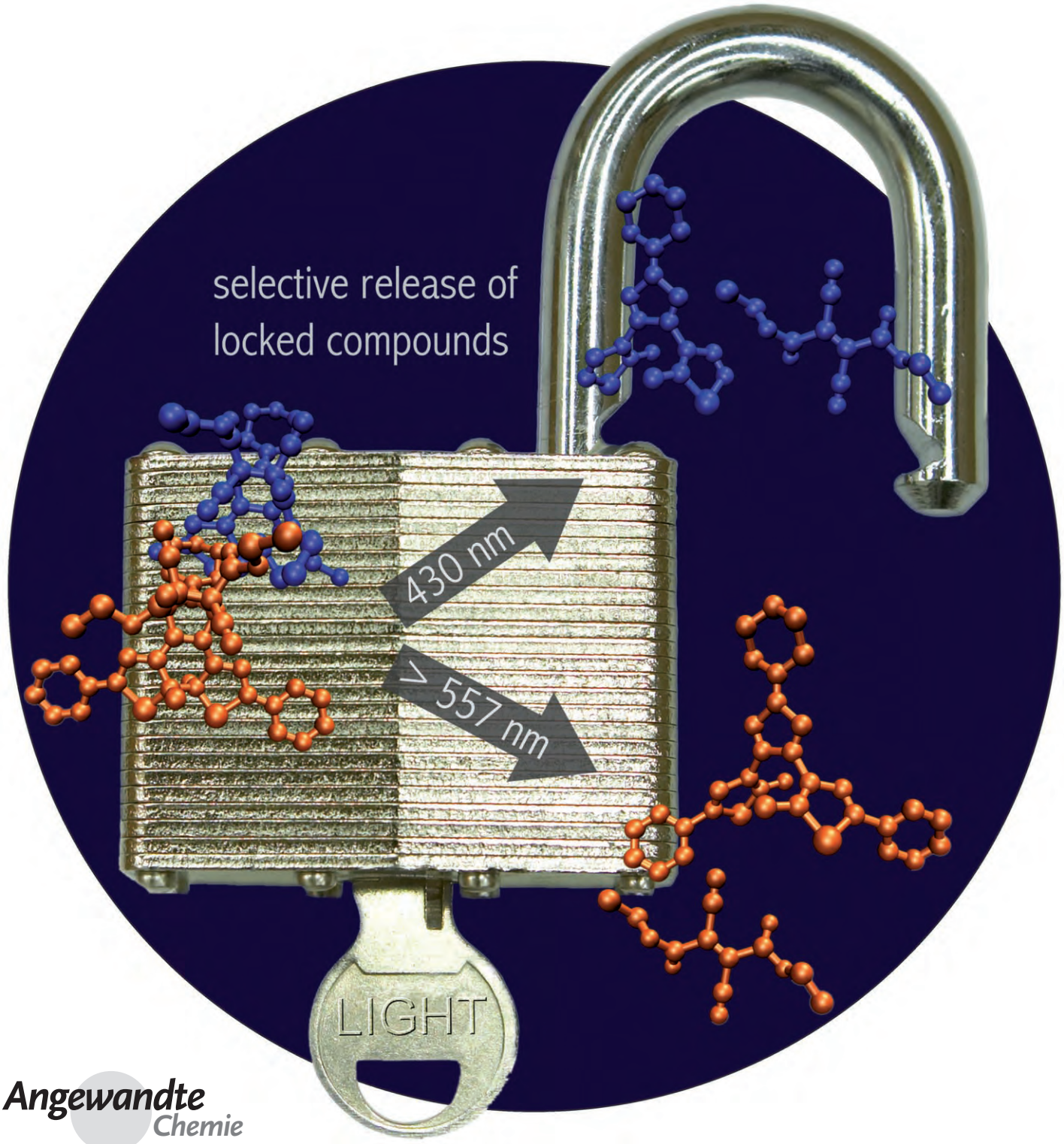

WILEY InterScience DISCOVER SOMETHING GREAT

© 2006 Wiley-VCH Verlag GmbH & Co. KGaA, Weinheim

Light is an effective trigger for the release of active chemical and biological species from masked, innocuous forms.[1] It offers the precise temporal and spatial control needed to deliver therapeutics,[2] agents to initiate biological phenomena,[3] and designer reagents for chemical transformations,[4] as well as for photolithography.[4]

The number of classes of molecular structures that can be photochemically cleaved to free a species of interest is relatively small. Most existing systems are based on the photochemical redox reactions of the 2-nitrobenzyl group, with others based on 7-nitroindoline, coumarin, hydroxyphenacyl, and benzoin chromophores.[1,5] Widespread use of these systems in practical applications is limited by a number of factors such as the generation of reactive side products, the need for high-energy radiation sources (200–400 nm), which may lead to undesirable side reactions, and most significantly, the inability to selectively stimulate photocleavable groups in the presence of others due to their absorbing light in the same general spectral range.[1,3,5]

Our goal is to develop a universal photorelease system by using a common photoresponsive molecular scaffold that 1) can be easily tailored to fine-tune its electronic properties without adversely affecting its performance, 2) strongly absorbs long-wavelength light to minimize cellular damage, 3) generates photoreleased products which absorb at wavelengths that are shifted out of the spectral region that triggers the photorelease to minimize side reactions, and 4) is modified using synthetic methods tolerant to a wide range of chemistries.[6] A system that fits this description will offer a means to sequentially release different species by using light of different wavelengths. Here, we report our success in developing a versatile approach to the selective and sequential light-initiated release of an easily functionalized chemical species by using two different thermally bistable dithienylethene (DTE) photoswitches and low-energy visible light of two different wavelengths.

Dithienylethenes are molecular switches, which contain hexatriene architectures, that undergo reversible ring-closing and ring-opening reactions (**1a**⇌**1b** in Scheme 1) when irradiated with UV and visible light, respectively.[7] Scheme 1 also illustrates how the optical properties of the ring-closed forms (**1b**) can be fine-tuned by rationally decorating the two heterocycles on the DTE backbone; an attribute that is central in reports that describe the selective photoreactions of multicolored, multifrequency systems.[8] The same feature makes compounds based on the DTE architecture appealing for use in photodelivery applications.

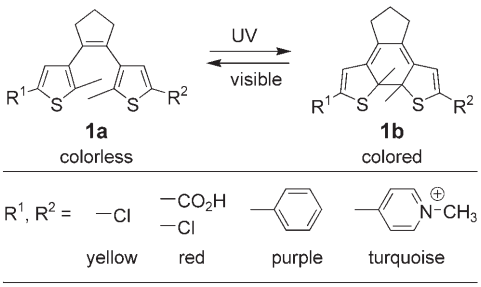

Scheme 1. Photochemical reactions of the dithienylethene (DTE) architecture. The absorption properties attainable in the ring-closed forms **1b** can be fine-tuned by modifying the groups R^1 and R^2 at the ends of the π-conjugated backbone.

Our use of the DTE architecture as a photocleavable group combines two approaches to integrate chemical reactivity with light (reactivity-gated photoswitching and photogated reactivity) and is based on the Diels–Alder reaction between photostable dienes and a small dienophile to generate photoswitchable DTE derivatives (Scheme 2).[9] In reactivity-gated photoswitching, light does not induce a molecular transformation unless it is preceded by a chemical reaction between two or more species.[9] For example, dithienylfulvenes **2** and **3** are not photoswitchable as they lack the required hexatriene functionality. However, the butadiene portions of the compounds (highlighted in bold) spontaneously undergo thermal Diels–Alder cycloadditions with an electron-deficient alkene **4** to result in the formation of racemic **5a** and **6a**.[10] The rearrangement of the π bonds creates the DTE architecture and renders **5a** and **6a** photoactive. UV light can now be used to convert both DTE derivatives into their thermally stable ring-closed forms, **5b** and **6b**. Thus, the thermal reaction has gated the photochemistry.

In photogated reactivity, light triggers a structural change in the molecule and imparts chemical reactivity unique to each form of the compound. This approach is also illustrated in Scheme 2, where the reverse Diels–Alder reactions can proceed only from the ring-open forms of the compounds because **5b** and **6b** lack the cyclohexene structures required for the fragmentation reactions. UV light has effectively locked the systems in their "armed" states which removes all molecules from the initially established Diels–Alder equilibria. The ring-closed forms can be considered to act as phototriggers as visible light regenerates the cyclohexenes in **5a** and **6a** and allows the thermal Diels–Alder equilibria to be reestablished, spontaneously releasing the dienophile. Thus, the photochemistry has gated the thermal reaction.

Because the release mechanism is thermally driven and independent of the photochemistry, the photochemical triggers can be tailored to harness a wide range of wavelengths to release the small auxiliary agent, thus offering a relatively universal approach to photorelease technology. Also, the light absorbed by the ring-open isomers, the fulvenes, and the dienophile is significantly higher in energy and lies far outside

[*] V. Lemieux, S. Gauthier, Prof. N. R. Branda
4D LABS
Department of Chemistry
Simon Fraser University
8888 University Drive, Burnaby, BC V5A 1S6 (Canada)
Fax: (+1) 604-291-3765
E-mail: nbranda@sfu.ca

[**] This work was supported by the Natural Sciences and Engineering Research Council of Canada (PGS-A and PGS-D to V.L.), the Canada Research Chair Program, and Simon Fraser University. We thank Philippe Reutenauer for helpful guidance about the use of the fumarate dienophiles.

Supporting information for this article is available on the WWW under http://www.angewandte.org or from the author.

 © 2006 Wiley-VCH Verlag GmbH & Co. KGaA, Weinheim

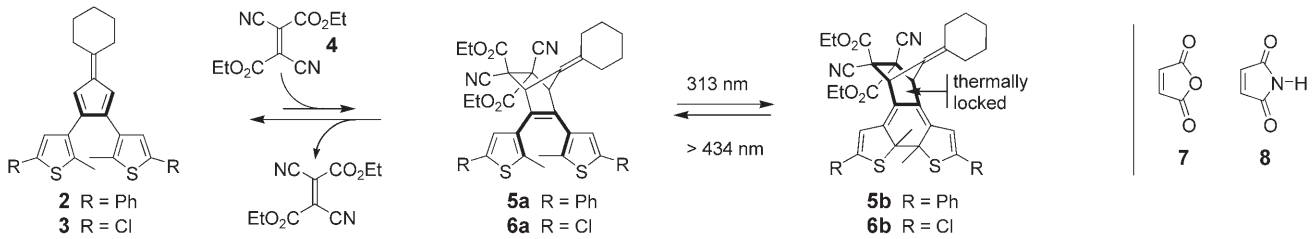

Scheme 2. Reversible Diels–Alder reactions of fulvenes **2** and **3** with dienophile **4** to generate racemic DTEs **5a** and **6a**, which undergo cyclization when irradiated with UV light. The thermally stable "armed" states, **5b** and **6b**, are unlocked with visible light to induce ring-opening, regenerating the cyclohexene necessary for fragmentation. Note that the stereochemistry of **5a**, **6a**, **5b**, and **6b** is arbitrary and does not imply the formation of specific stereoisomers.

the region used to trigger the photochemistry, thus minimizing photochemical side reactions. Another appealing feature is that the two photoisomers of DTE derivatives display a wide range of properties unique to their structure, offering a means to "release and report",[11] that is, to quantify the extent and location of discharge by monitoring a readout signal (color, refractive index, luminescence, or redox chemistry).[12]

We chose the fulvene structure as the Diels–Alder diene component because it undergoes both forward and reverse cycloaddition reactions[13] under milder conditions than those required for other dienes.[14] Dithienylfulvenes **2** and **3** can be prepared from two known DTE derivatives ($R^1, R^2 = Ph$;[15] $R^1, R^2 = Cl$[16] in Scheme 1).[17] As anticipated, compounds **2** and **3** show good photostability and their irradiation with UV or visible light results in minimal degradation.

Dithienylfulvenes **2** and **3** readily undergo Diels–Alder reactions when treated with electron-deficient dienophiles such as maleic anhydride (**7**) and maleimide (**8**; Scheme 2) to afford the bicyclic products in nearly quantitative yields as observed by ^{1}H NMR spectroscopy. The products of these reactions show excellent photoresponsive activity, and irradiating them at $\lambda = 313$ nm[17] leads to an immediate decrease in the intensities of the high-energy absorptions with simultaneous appearance of absorptions in the visible region as is typical for DTE derivatives. These changes are a result of the ring-closing reactions of the compounds, and the solutions are transformed from colorless to pink (when **2** is used) and yellow (when **3** is used). Irradiation of the colored solutions with visible light ($\lambda > 434$ nm) results in ring-opening, regeneration of the original absorption spectra, and bleaching of the solutions.

Although the Diels–Alder products formed using **7** or **8** show excellent photoactivity and are ideal models to characterize the photochemistry of the cycloaddition products, they are not suitable for photorelease applications as their cycloaddition reactions are not significantly reversible at room temperature. The esters of dicyanofumarate are more suitable and establish equilibrating mixtures of starting materials and products under much milder conditions.[18] When solutions of fulvenes **2** and **3** in CD_2Cl_2 are treated with diethyl dicyanofumarate (**4**), reversible reactions are immediately observed and the equilibria between the fulvenes and the racemic, bicyclic products **5a** and **6a** stabilize within 20 minutes (Figure 1a and b) and contain 40–45% of the ring-open products.[19] Equilibrium constants at 22 °C were

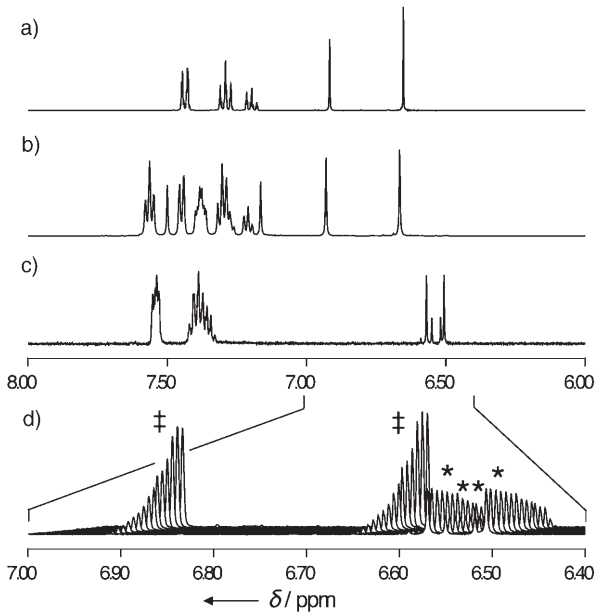

Figure 1. Partial ^{1}H NMR spectra (500 MHz, CD_2Cl_2) showing the peaks corresponding to the aromatic protons in a) fulvene **2**, b) a 1:1 mixture of **2** and diethyl dicyanofumarate (**4**) measured when the equilibrium with racemic **5a** has been reached, c) the isolated mixture of the ring-closed stereoisomers of **5b**, and d) a solution of **5b** periodically irradiated with visible light ($\lambda > 490$ nm) showing the disappearance of the ring-closed compound **5b** (*) and the appearance of fulvene **2** (‡).

determined to be $16\,M^{-1}$ for **2** + **4** ⇌ **5a** and $13\,M^{-1}$ for **3** + **4** ⇌ **6a** from the ^{1}H NMR spectra.

The reverse cycloaddition reactions to generate compounds **2**, **3**, and **4** can be prevented by locking the structures in their ring-closed, "armed" forms **5b** and **6b**. Irradiation of solutions containing the fulvenes and fumarate **4** with 313-nm light produces compounds that are thermally stable and can be isolated by column chromatography (Figure 1c). As long as they are kept in the dark, both **5b** and **6b** can be stored with no observable degradation in solution and in the solid state at room temperature. Irradiation of the solutions with light of the appropriate wavelength in the visible range ($\lambda > 557$ nm for **5b** and $\lambda > 434$ nm for **6b**) triggers the ring-opening reactions and subsequent release of dienophile **4** (Figure 1d). In the case of **5b**, only the two starting materials (**2** and **4**)

 © 2006 Wiley-VCH Verlag GmbH & Co. KGaA, Weinheim

could be observed by ^{1}H NMR spectroscopy by the time a spectrum could be acquired.[20] Under the conditions used to monitor the release reactions by ^{1}H NMR spectroscopy (3×10^{-3} M) and UV/Vis absorption spectroscopy (3×10^{-5} M), there is quantitative release of the fumarate dienophile within the first 3 minutes of irradiation. When the release experiment using compound **5b** is repeated at lower temperatures (−10 to 0 °C), the ring-open isomer **5a** can be briefly observed before it undergoes the rapid thermal fragmentation reaction, illustrating that the photorelease mechanism proceeds through the ring-open isomer **5a** and not by a direct photochemical reaction.

Because **5b** and **6b** absorb different types of visible light, selective and sequential release can be achieved by tuning the light source to trigger the ring-opening reaction of only one of the ring-closed compounds. Figure 2 demonstrates the success of the selective ring-opening using UV/Vis absorption spectroscopy (Figure 2a–d) and the selective release using ^{1}H NMR spectroscopy (Figure 2e–h).[22] An equimolar mixture of compounds **5b** and **6b** could be irradiated at $\lambda=$ 430 nm to selectively ring-open only derivative **6b** (Figure 2b), as it absorbs more significantly in this spectral region. Derivative **5b** is more effective at absorbing lower energy light and is virtually unaffected during this irradiation. Fulvene **3** and fumarate **4** are the only new products observed by ^{1}H NMR spectroscopy when the 1:1 mixture in CD_2Cl_2 is irradiated at $\lambda=430$ nm (Figure 2f). Repeating the irradiation with lower energy light ($\lambda>557$ nm) selectively ring-opens **5b** (Figure 2c) and releases the fumarate **4** from **5a** (Figure 2g) without affecting **6b**. Both compounds can be triggered to release the dienophile when irradiated at $\lambda>$ 434 nm (Figure 2d and h).

In summary, we have presented a new approach to deliver chemical species based on combining reactivity-gated photochemistry and photogated reactivity. The light used to trigger the release reaction is in the visible range, leading to the dual advantages of limiting biological damage and increasing the penetration depth. In addition, the DTE substructure will facilitate the monitoring of the release events by using a wide range of physical properties, such as the absorbance or emission of light, or electrochemical properties which are unique to the "armed" and "released" systems. The economical size and chemistry of the fumarate auxiliary implies that it can be modified with various chemical species without significantly interfering with the role of the component of interest, thus offering a great potential for practical applications.

Received: April 21, 2006
Published online: July 20, 2006

Keywords: cycloaddition · molecular devices · photochromism · retro reactions · UV/Vis spectroscopy

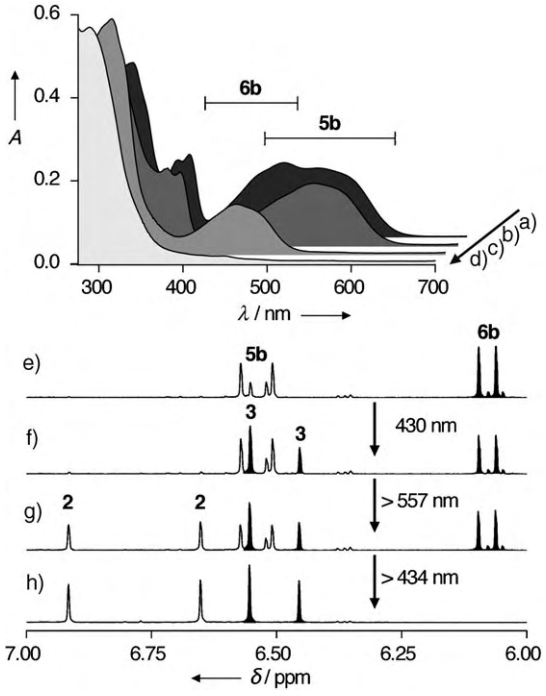

Figure 2. a–d) UV/Vis absorption spectra of a 1:1 mixture (in CH_2Cl_2) of the ring-closed compounds **5b** and **6b** (a), after irradiating the solution at $\lambda=430$ nm (b), after irradiating a similar 1:1 sample at $\lambda>557$ nm (c), and after irradiating either sample at $\lambda>434$ nm (d). e–h) Partial ^{1}H NMR spectra (500 MHz, CD_2Cl_2) of a 1:1 mixture of **5b** and **6b**[20] (e), after irradiating the solution at $\lambda=430$ nm to partially ring-open compound **6b** (f), after irradiating the same sample at $\lambda>557$ nm to partially ring-open compound **5b** (g), and after irradiating the same sample at $\lambda>434$ nm to fully ring-open both compounds (h).

[1] M. Goeldner, R. Givens, *Dynamic Studies in Biology: Phototriggers, Photoswitches and Caged Biomolecules*, Wiley-VCH, Weinheim, **2005**.
[2] H. J. Montgomery, B. Perdicakis, D. Fishlock, G. A. Lajoie, E. Jervis, J. G. Guillemette, *Bioorg. Med. Chem.* **2002**, *10*, 1919–1927; Y. Zhang, F. Erdmann, R. Baumgrass, M. Schutkowski, G. Fisher, *J. Biol. Chem.* **2005**, *280*, 4842–4850.
[3] A. P. Pelliccioli, J. Wirz, *Photochem. Photobiol. Sci.* **2002**, *1*, 411–458.
[4] S. P. A. Fodor, J. L. Read, M. C. Pirrung, L. Stryer, A. T. Lu, D. Solas, *Science* **1991**, *251*, 767–773.
[5] C. G. Bochet, *J. Chem. Soc. Perkin Trans. 1* **2002**, 125–142.
[6] C. Sundararajan, D. E. Falvey, *J. Am. Chem. Soc.* **2005**, *127*, 8000–8001; A. Banerjee, C. Grewer, L. Ramakrishnan, J. Jager, A. Garneiro, H.-G. A. Breitinger, K. R. Gee, B. K. Carpenter, G. P. Hess, *J. Org. Chem.* **2003**, *68*, 8361–8367.
[7] M. Irie in *Organic Photochromic and Thermochromic Compounds, Vol. 1* (Eds.: J. C. Crano, R. J. Guglielmetti), Plenum, New York, **1999**, pp. 207–222; M. Irie in *Molecular Switches* (Ed.: B. L. Feringa), Wiley-VCH, Weinheim, **2001**, pp. 37–62; Special issue on photochromism: M. Irie, *Chem. Rev.* **2000**, *100*, 1685–1716.
[8] T. J. Wigglesworth, N. R. Branda, *Chem. Mater.* **2005**, *17*, 5473–5480; K. Higashiguchi, K. Matsuda, N. Tanifuji, M. Irie, *J. Am. Chem. Soc.* **2005**, *127*, 8922–8923; M. Morimoto, S. Kobatake, M. Irie, *J. Am. Chem. Soc.* **2003**, *125*, 11080–11087; A. Fernandez-Acebes, J.-M. Lehn, *Adv. Mater.* **1999**, *11*, 910–913.
[9] V. Lemieux, N. R. Branda, *Org. Lett.* **2005**, *7*, 2969–2972.
[10] The stereochemistry of **5a**, **6a**, **5b**, and **6b** is arbitrarily drawn in Scheme 2. Compounds **5a** and **6a** are produced as racemates, while **5b** and **6b** are produced as a mixture of enantiomers and diastereomers. See Supporting Information for details.
[11] For a recent account of "release and report" using fluorescence, see: J. R. R. Majjigapu, A. N. Kurchan, R. Kottani, T. P. Gustafson, A. G. Kutateladze, *J. Am. Chem. Soc.* **2005**, *127*, 12458–12459.

 © 2006 Wiley-VCH Verlag GmbH & Co. KGaA, Weinheim

[12] H. Tian, S. Yang, *Chem. Soc. Rev.* **2004**, *33*, 85 – 97.
[13] E. P. Kohler, J. Kable, *J. Am. Chem. Soc.* **1935**, *57*, 917 – 918.
[14] F. Fringuelli, A. Taticchi, *The Diels-Alder Reaction: Selected Practical Methods*, Wiley, New York, **2002**; A. Wassermann, *Diels-Alder Reactions: Organic Background and Physico-Chemical Aspects*, Elsevier, Amsterdam, **1965**.
[15] J. J. D. de Jong, L. N. Lucas, R. Hania, A. Pugzlys, R. M. Kellogg, B. L. Feringa, K. Duppen, J. H. van Esch, *Eur. J. Org. Chem.* **2003**, 1887 – 1893.
[16] L. N. Lucas, J. van Esch, R. M. Kellogg, B. L. Feringa, *Chem. Commun.* **1998**, 2313 – 2314.
[17] See Supporting Information for details.
[18] P. J. Boul, P. Reutenauer, J.-M. Lehn, *Org. Lett.* **2005**, *7*, 15 – 18.
[19] To obtain measurable equilibria at the concentrations used for the experiment ($1–7 \times 10^{-2}$ M), 4 equivalents of **4** were added to the solutions of the fulvenes. The same results were obtained when dimethyl dicyanofumarate was used.
[20] The thermal release of **3** and **4** was significantly slower, and appreciable amounts of the ring-open isomer **6a** could be observed by ^{1}H NMR spectroscopy.
[21] Derivative **5b** was purified as a mixture of stereoisomers by column chromatography. Derivative **6b** was further purified by recrystallization (hexanes), which resulted in the enrichment of specific stereoisomers.
[22] Selective ring-opening was pushed almost to completion using different samples (Figure 3a–d) to demonstrate the high level of selectivity. In the case of the release experiments (Figure 3e–h), the same NMR sample was used to show sequential release. Irradiation of each compound was stopped after partial release for easy comparison of the spectra.

 © 2006 Wiley-VCH Verlag GmbH & Co. KGaA, Weinheim

Engineered Aldolase

DOI: 10.1002/anie.200602529

Stereoselectivity and Expanded Substrate Scope of an Engineered PLP-Dependent Aldolase**

*Florian P. Seebeck, Angelo Guainazzi, Celine Amoreira, Kim K. Baldridge, and Donald Hilvert**

Biocatalysis has become an invaluable tool for industrial scale chemical synthesis.[1] Aldolases are particularly interesting for practical applications owing to their proficiency at enantioselective C–C bond making and breaking. Indeed, natural aldolases have been used to catalyze a wide range of aldol reactions on synthetically useful scales.[2] Furthermore, enzyme-engineering methods have been applied to generate catalysts with higher activities or altered substrate specificities to match a growing demand for molecular diversity in the chemical and pharmaceutical industries.[3]

In a previous report, we showed that aldolase activity can also be recruited from unexpected origins: a single active-site mutation (Y265A) in a pyridoxal 5′-phosphate (PLP)-dependent alanine racemase from *Geobacillus stearothermophillus* (alr) was found to increase retro-aldolase activity against phenylserine **1** (Scheme 1) by five orders of magnitude.[4] The

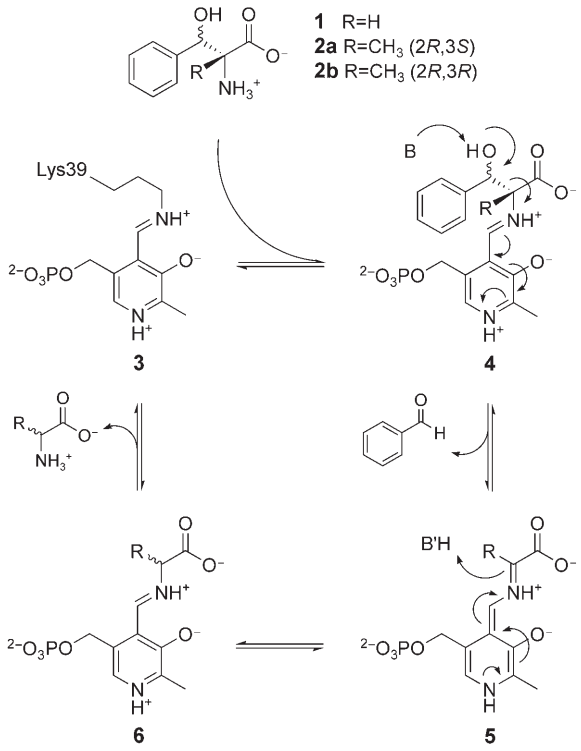

Scheme 1. Mechanism of the alrY265A-catalyzed retroaldol reaction of the β-phenylserine derivatives **1** and **2**. The substrate initially reacts with the enzyme-bound PLP **3** to form the external aldimine adduct **4**. Cleavage of the Cα–Cβ bond affords benzaldehyde and quinonoid intermediate **5**. Subsequent protonation to give **6**, followed by hydrolysis, liberates glycine or alanine and regenerates the catalyst. The cofactor phosphate is the likely base (B) for the retroaldol reaction (see text), and either Lys39 or water may protonate **5** (B′H).

conversion of the racemase into an aldolase profited from the similarity of the central PLP-quinonoid intermediates formed in the course of both reactions. Interestingly, natural evolution appears to have exploited this chemical relationship as well. Genetic analyses have demonstrated that alanine racemases and natural D-threonine aldolases share a common evolutionary origin.[5] However, alanine racemase evolved to accommodate an alanyl-PLP quinonoid intermediate (**5**, R = CH_3), whereas D-threonine aldolases stabilize a glycyl-PLP quinonoid species (**5**, R = H). In the case of our alrY265A variant, one could imagine that the residual binding pocket

[*] Dr. F. P. Seebeck, A. Guainazzi, Prof. Dr. D. Hilvert
Laboratorium für Organische Chemie
ETH Zürich
Hönggerberg HCI F339, 8093 Zürich (Switzerland)
Fax: (+41) 44-632-1486
E-mail: hilvert@org.chem.ethz.ch
C. Amoreira, Prof. Dr. K. K. Baldridge
Organisch-Chemisches Institut
Universität Zürich
Winterthurstrasse 190, 8057 Zürich (Switzerland)

[**] We thank the ETH Zürich, the University of Zürich, and the Schweizerischer Nationalfonds for financial support. PLP = pyridoxal 5′-phosphate.

Supporting information for this article is available on the WWW under http://www.angewandte.org or from the author.

© 2006 Wiley-VCH Verlag GmbH & Co. KGaA, Weinheim

for the alanine methyl group might be exploited together with the new aldolase activity to catalyze the cleavage (or, in the synthetic direction, formation) of quaternary α-amino acids like **2** (Scheme 1). Such activity has not been reported for natural aldolases but would have considerable synthetic utility.[6]

To examine the ability of alrY265A to process β-hydroxy amino acids bearing an additional α substituent, we synthesized (2*R*,3*S*)- and (2*R*,3*R*)-α-methyl-β-phenylserines (**2a** and **2b**, respectively) following published procedures,[7] and measured the kinetic parameters associated with their alrY265A-catalyzed conversion into alanine and benzaldehyde. As shown in Table 1, the two diastereomers are consumed with an even higher catalytic efficiency ($k_{cat}/K_m > 10^3\,M^{-1}min^{-1}$) than the previously examined (2*R*,3*S*)-β-phenylserine (**1**; $670\,M^{-1}min^{-1}$). Although the individual steady-state parameters k_{cat} and K_m are likely to be complex amalgams of different microscopic rate and binding constants, the fact that the K_m values observed for **2a** and **2b** are lower than that for **1** can be attributed to favorable interactions of the extra α-methyl group with the binding pocket. Furthermore, while its k_{cat} parameter is only twofold lower than that of **1**, substrate **2a** shows a k_{cat}/k_{uncat} ratio that is twofold higher (Table 1).

Table 1: Steady-state parameters for the conversion of β-phenyl-serines into benzaldehyde and glycine/alanine.[a]

Substrate	k_{cat} [min^{-1}]	K_m [mM]	k_{cat}/K_m [$M^{-1}min^{-1}$]	k_{uncat}[c] [min^{-1}]
(2*R*,3*S*)-β-phenyl-serine (**1**)[b]	5.7	8.5	670	0.0015
(2*R*,3*S*)-α-methyl-β-phenylserine (**2a**)	2.8	2.8	1000	0.00033
(2*R*,3*R*)-α-methyl-β-phenylserine (**2b**)	0.16	0.14	1100	–

[a] The enzymatic reactions were performed with alrY265A at 30 °C in 100 mM HEPES buffer (pH 8). [b] See Ref. [4]. [c] The rate constant for the pyridoxal-dependent retroaldol reaction of β-phenylserines in the absence of enzyme was determined following procedures described in Refs.[4, 13]; the standard error on all kinetic parameters is ≤20%.

Natural D-threonine aldolases exhibit stringent stereoselectivity at Cα in the cleavage of β-hydroxy amino acids but relaxed selectivity at Cβ.[8] alrY265A is similarly selective with respect to Cα, accepting only D-configured amino acids.[4] However, the fact that **2a** and **2b** afford similar k_{cat}/K_m values (Table 1) indicates poor stereochemical control at the β carbon. Nor does the enzyme exhibit strict stereochemical fidelity in the final stages of the reaction. In principle, the quinonoid intermediate **5** (R = CH_3) could be protonated either from the *si* face of the imine to give D-alanine, or from its *re* face to give L-alanine.[9] The partitioning of **5** (R = CH_3) was quantified by measuring the amount of D-alanine formed in the alrY265A-catalyzed cleavage of **2b** relative to benzaldehyde. D-Alanine-dependent oxidation of NADH, using D-amino acid oxidase and lactate dehydrogenase as coupling enzymes, showed that 80% (±10%) of the alanine product has the D configuration. Preferential formation of D- over L-alanine is consistent with the participation of Lys39, the active-site residue that protonates the quinonoid intermediate from the *si* face in native alr, and the absence of Tyr265, which normally protonates **5** from the opposite face. The small amount of L-alanine that is formed presumably arises by direct protonation of the intermediate by water from the same face as the departing benzaldehyde.

To rationalize the stereochemical preferences of alrY265A, we performed hybrid docking and ab initio investigations[10] with the aldimines of all four α-methyl-β-phenylserine diastereomers (**2a** and **2b**, and the corresponding L-amino acids) bound at the enzyme active site.[11] In accord with our experimental findings, the modified binding pocket readily accommodates both 2*R* diastereomers, whereas neither of the 2*S* isomers fits without clashes with active-site residues. Moreover, energy minimization of the models reveals that the 2*R* aldimines exploit very similar interactions with the binding pocket and the cofactor (Figure 1). As expected, the carboxylate and α-methyl groups lock these substrates in an orientation that places the benzyl side chain perpendicular to the plane of the PLP cofactor, with the aryl ring inserted into the cavity created by the Y265A substitution. The preferred conformations of the two diastereomers differ by a 30° rotation around the Cα–β bond, so that the aryl ring of the 2*R*,3*R* isomer (**2b**) is a little closer to the side chain of His166. As a consequence of this difference in dihedral angle, the β-hydroxy group of both isomers points toward the cofactor phosphate. The resulting O···O distance is 2.70 and 3.05 Å for **2a** and **2b**, respectively, which corresponds to a favorable hydrogen bond.

Although His166 was originally proposed as a possible candidate for the base that initiates proton abstraction from the substrate hydroxy group (Scheme 1, **4**→**5**),[4] the modeling results indicate that its imidazole ring adopts the wrong tautomeric form and is too far from the alcohol to assume this role. Instead, as shown in Figure 1, the PLP phosphate group is well positioned to serve as the catalytic base for both diastereomers. The postulated recruitment of the cofactor phosphate for catalysis has some precedent in the reaction catalyzed by serine dehydratase.[12] If this mechanistic hypothesis can be confirmed, it may be possible to exploit subtle steric changes within the active site to disrupt the crucial hydrogen bond for one but not the other substrate epimer, thereby enhancing the Cβ stereoselectivity of the enzyme.

In conclusion, we have shown that an engineered alr catalyzes a biologically unprecedented retroaldol reaction of α-substituted β-phenylserines with high stereoselectivity at the α carbon but low stereochemical control at the β carbon. Not only is this reaction catalyzed some 10^4-fold more efficiently than by the cofactor in solution, but our computational model provides a basis for further optimization of the alrY265A active site by means of site-directed mutagenesis or directed evolution. Such improvement may yield practical catalysts for the enantioselective synthesis of novel amino acids and their derivatives.

Received: June 23, 2006
Published online: September 26, 2006

 © 2006 Wiley-VCH Verlag GmbH & Co. KGaA, Weinheim

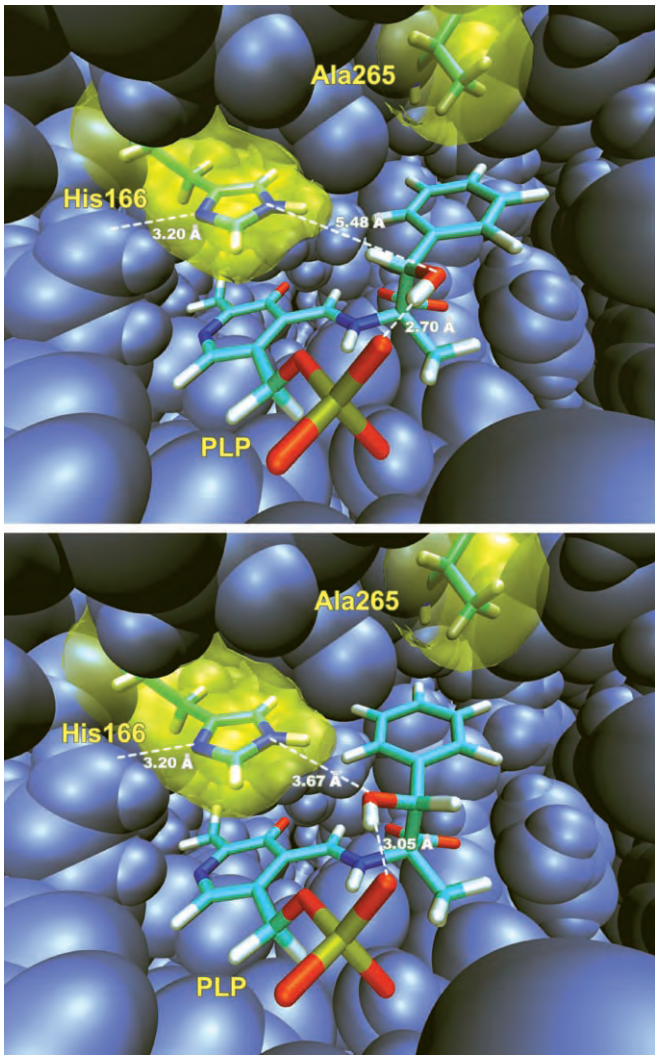

Figure 1. Energy-minimized structures of (2*R*,3*S*)-α-methyl-β-phenylserine (top) and (2*R*,3*R*)-α-methyl-β-phenylserine (bottom) bound to the active site of alrY265A as external aldimines with PLP. The β-hydroxy group of both substrates is within hydrogen-bonding distance of the phosphate group of PLP. A hydrogen bond between Arg219 and His166 (dotted line to the protein), which is also present in the parent enzyme,[20] dictates the tautomeric form of the imidazole.

Keywords: β-hydroxy amino acids · aldolases · enzyme models · stereoselectivity

[1] A. Schmid, J. S. Dordick, B. Hauer, A. Kiener, M. Wubbolts, B. Witholt, *Nature* **2001**, *409*, 258; H. E. Schoemaker, D. Mink, M. G. Wubbolts, *Science* **2003**, *299*, 1694.

[2] T. Kimura, V. P. Vassilev, G.-J. Shen, C.-H. Wong, *J. Am. Chem. Soc.* **1997**, *119*, 11734; T. D. Machajewski, C.-H. Wong, *Angew. Chem.* **2000**, *112*, 1406; *Angew. Chem. Int. Ed.* **2000**, *39*, 1352; J.-Q. Liu, T. Dairi, N. Itoh, M. Kataoka, S. Shimizu, H. Yamada, *J. Mol. Catal. B* **2000**, *10*, 107; W. D. Fessner, V. Helaine, *Curr. Opin. Biotechnol.* **2001**, *12*, 574; W. A. Greenberg, A. Varvak, S. R. Hanson, K. Wong, H. J. Huang, P. Chen, M. J. Burk, *Proc. Natl. Acad. Sci. USA* **2004**, *101*, 5788; H. J. Lamble, M. J. Danson, D. W. Hough, S. D. Bull, *Chem. Commun.* **2005**, 124.

[3] S. Fong, T. D. Machajewski, C. C. Mak, C.-H. Wong, *Chem. Biol.* **2000**, *7*, 873; N. Wymer, L. V. Buchanan, D. Henderson, N. Mehta, C. H. Botting, L. Pocivavsek, C. A. Fierke, E. J. Toone, J. H. Naismith, *Structure* **2001**, *9*, 1; G. DeSantis, J. J. Liu, D. P. Clark, A. Heine, I. A. Wilson, C.-H. Wong, *Bioorg. Med. Chem.* **2003**, *11*, 43; J. S. Griffiths, M. Cheriyan, J. B. Corbell, L. Pocivavsek, C. A. Fierke, E. J. Toone, *Bioorg. Med. Chem.* **2004**, *12*, 4067; G. J. Williams, S. Domann, A. Nelson, A. Berry, *Proc. Natl. Acad. Sci. USA* **2003**, *100*, 3143; D. Franke, C.-C. Hsu, C.-H. Wong, *Methods Enzymol.* **2004**, *388*, 224.

[4] F. P. Seebeck, D. Hilvert, *J. Am. Chem. Soc.* **2003**, *125*, 10158.

[5] A. Paiardini, R. Contestabile, S. D'Aguanno, S. Pascarella, F. Bossa, *Biochim. Biophys. Acta* **2003**, *1647*, 214.

[6] C. Cativiela, M. D. Diaz-de-Villegas, *Tetrahedron: Asymmetry* **1998**, *9*, 3517.

[7] U. Schöllkopf, *Tetrahedron* **1983**, *39*, 2085; U. Schöllkopf, U. Groth, W. Hartwig, *Liebigs Ann. Chem.* **1981**, 2407; U. Schöllkopf, U. Groth, K.-O. Westphalen, C.-Z. Deng, *Synthesis* **1981**, 969.

[8] M. Kataoka, M. Ikemi, T. Morikawa, T. Miyoshi, K. Nishi, M. Wada, H. Yamada, S. Shimizu, *Eur. J. Biochem.* **1997**, *248*, 385; J. Q. Liu, M. Odani, T. Yasuoka, T. Dairi, N. Itoh, M. Kataoka, S. Shimizu, H. Yamada, *Appl. Microbiol. Biotechnol.* **2000**, *54*, 44.

[9] M. A. Spies, J. J. Woodward, M. R. Watnik, M. D. Toney, *J. Am. Chem. Soc.* **2004**, *126*, 7464.

[10] Computational methods: Binding of the four diastereomeric aldimine adducts of α-methyl-β-phenylserine at the alrY265A active site was investigated using ab initio and docking methods. Ab initio calculations were performed using GAMESS[14] at the B3LYP/DZV + (2d,p) level of theory ($\varepsilon = 4$),[15] with CHELPG charges[16] and standard radii. Initial docking was performed with QMView,[17] and energy maps were generated by varying the torsional angles corresponding to rotation around the Cα–Cβ and Cβ–Cγ bonds of the intermediates in 30° increments. Electrostatic binding energies were calculated with APBS.[18] Following molecular dynamics simulations with AMBER,[19] the most favorable conformers were optimized with ab initio methods. See the Supporting Information for details.

[11] A. Watanabe, T. Yoshimura, B. Mikami, H. Hayashi, H. Kagamiyama, N. Esaki, *J. Biol. Chem.* **2002**, *277*, 19166.

[12] T. Yamada, J. Komoto, Y. Takata, H. Ogawa, H. C. Pitot, F. Takusagawa, *Biochemistry* **2003**, *42*, 12854.

[13] K. Tatsumoto, A. E. Martell, *J. Am. Chem. Soc.* **1978**, *100*, 5549.

[14] M. W. Schmidt, K. K. Baldridge, J. A. Boatz, S. T. Elbert, M. S. Gordon, J. H. Jensen, S. Koseki, N. Matsunaga, K. A. Nguyen, S. J. Su, T. L. Windus, M. Dupuis, J. A. Montgomery, Jr., *J. Comput. Chem.* **1993**, *14*, 1347.

[15] C. T. Lee, W. T. Yang, R. G. Parr, *Phys. Rev. B* **1988**, *37*, 785.

[16] C. M. Breneman, K. B. Wiberg, *J. Comput. Chem.* **1990**, *11*, 361.

[17] K. K. Baldridge, J. P. Greenberg, *J. Mol. Graphics* **1995**, *13*, 63.

[18] N. A. Baker, D. Sept, M. J. Holst, J. A. McCammon, *IBM J. Res. Dev.* **2001**, *45*, 427.

[19] J. M. Wang, P. Cieplak, P. A. Kollman, *J. Comput. Chem.* **2000**, *21*, 1049.

[20] J. P. Shaw, G. A. Petsko, D. Ringe, *Biochemistry* **1997**, *36*, 1329.

 © 2006 Wiley-VCH Verlag GmbH & Co. KGaA, Weinheim

Nanobiotechnology

DOI: 10.1002/anie.200602049

Reversible Binding of Fluorescent Proteins at DNA–Gold Nanoparticles**

*Pompi Hazarika, Florian Kukolka, and Christof M. Niemeyer**

Protein-functionalized gold nanoparticles (AuNPs) are currently attracting increasing interest as a result of their applications in the detection of antigens, which are specific biomarkers in disease diagnostics.[1,2] Protein–AuNPs have long been known as versatile probes in immunohistochemistry and related techniques,[3] while mixed hybrid particles containing both nucleic acid fragments and proteins have recently been established,[4–7] because they offer additional functionality on account of the presence of both classes of biomolecular recognition elements. For instance, DNA–AuNPs containing a low number of antibody molecules have been successfully employed in the highly sensitive detection of a soluble pathogenic biomarker for Alzheimer's disease.[6]

The synthesis of DNA–protein hybrid particles has been achieved by either chemisorption of the sulfhydryl groups of proteins to AuNPs followed by saturation of the particles with thiolated DNA oligonucleotides,[5,6] or specific DNA hybridization using DNA–AuNPs and appropriate protein conjugates bearing the complementary DNA oligomer moiety.[4,7] Herein, we report the extension of the latter approach to render the binding of DNA–protein conjugates to DNA–AuNPs reversible. To this end, we employed the concept of DNA oligonucleotide strand displacement, which has frequently been used in the development of nanomechanical DNA devices,[8–14] and we have recently used this approach to reversibly switch the aggregation of DNA–AuNPs.[15] The realization of the DNA-directed immobilization and detachment of proteins to gold nanoparticles, which is depicted schematically in Figure 3a, would be advantageous over conventional chemisorption, because both immobilization and dissociation of the protein can be achieved under physiological conditions, thereby maintaining the full biological activity of the proteins.[4] Moreover, this approach should also open up ways to restore functional proteins from nanoparticle probes subsequent to their use in bioanalytical assays.

To experimentally investigate our hypothesis, we chose DNA conjugates of enhanced yellow fluorescent protein (EYFP), a mutant derivative of the naturally occurring green fluorescent protein from the North Pacific jellyfish *Aequorea victoria*, as a model system. This choice was made because the DNA–EYFP conjugate is considered to be a promising building block for the construction of biomimetic antennae and light-harvesting devices.[16,17] We also expected it to be a convenient reporter because the fluorescence of the EYFP should be quenched upon binding to the gold nanoparticles, as previously reported for organic fluorescent dyes.[18–24]

Initial experiments were carried out to investigate the binding of the covalent DNA–EYFP conjugate (**1** in Figure 1, EYFP-5′-AGC GGA TAA CAA TTT CAC ACA GGA-3′) with DNA-coated 25-nm AuNPs **2**–**4**, which contain either complementary (**2**: AuNP-5′-TCC TGT GTG AAA TTG TTA TCC GCT-3′, **3**: AuNP-3′-TCG CCT ATT GTT AAA GTG TGT CCT-5′) or, as a control, noncomplementary DNA oligomers (**4**: AuNP-5′-TTT TTT TTT TTT GAT CCA GTA GAT A-3′) as specific binding sites. Gel electrophoretic analysis was used to confirm the specific binding (Figure 1). In the case of DNA–AuNPs bearing complementary oligomers, which lead to conjugates **1**·**2** and **1**·**3**, a clear decrease in the electrophoretic mobility of the nanoparticles indicated the binding of the DNA–EYFP conjugate. In contrast, incubation of particles **4** with **1** only led to very small shifts of the respective bands (Figure 1d, lanes J–L), thus confirming that the binding of **1** with **2** and **3** occurs primarily as a result of specific Watson–Crick base pairing of the oligonucleotides.[25]

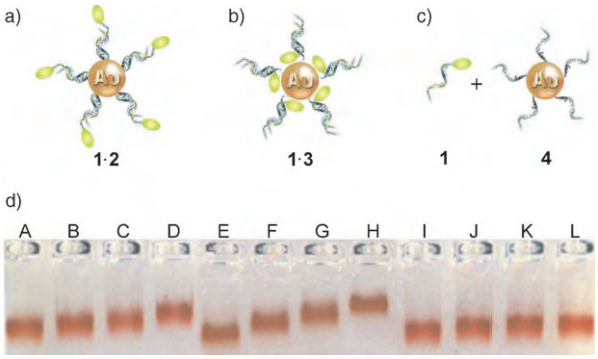

Figure 1. DNA–AuNPs **2** and **3** functionalized with EYFP conjugate **1** to form hybrid conjugates a) **1**·**2** and b) **1**·**3**, along with c) free conjugate **1** and noncomplementary DNA–AuNP **4.** d) Electrophoretic analysis of functionalization of gold nanoparticles with EYFP on a 1.5% agarose gel. The bands indicate the mobility of **2** (lane A), **2** coupled with 16, 32, and 64 molar equivalents of **1** (lanes B–D, respectively), **3** (lane E), **3** coupled with 16, 32, and 64 molar equivalents of **1** (lanes F–H, respectively), **4** (lane I), and **4** mixed with 16, 32, and 64 molar equivalents of **1** (lanes J–L, respectively).

We then investigated whether the binding of **1** to the gold nanoparticle does indeed lead to quenching of the EYFP fluorescence (Figure 2). Fluorescence measurements were carried out with a solution of **1** (1.2 pmol in TETBS (Tris-HCl

[*] Dr. P. Hazarika, Dipl. Chem. F. Kukolka, Prof. Dr. C. M. Niemeyer
Biologisch–Chemische Mikrostrukturtechnik
Fachbereich Chemie
Universität Dortmund
Otto-Hahn Strasse 6, 44227 Dortmund (Germany)
Fax: (+49) 231-755-7082
E-mail: christof.niemeyer@uni-dortmund.de

[**] This work was supported in part by Deutsche Forschungsgemeinschaft (DFG, grants Ni-399/6-1/6-2) and by the Zentrum für Angewandte Chemische Genomik, a joint research initiative founded by the European Union and the Ministry of Innovation and Research of the state of North Rhine-Westfalia.

Supporting information for this article is available on the WWW under http://www.angewandte.org or from the author.

© 2006 Wiley-VCH Verlag GmbH & Co. KGaA, Weinheim

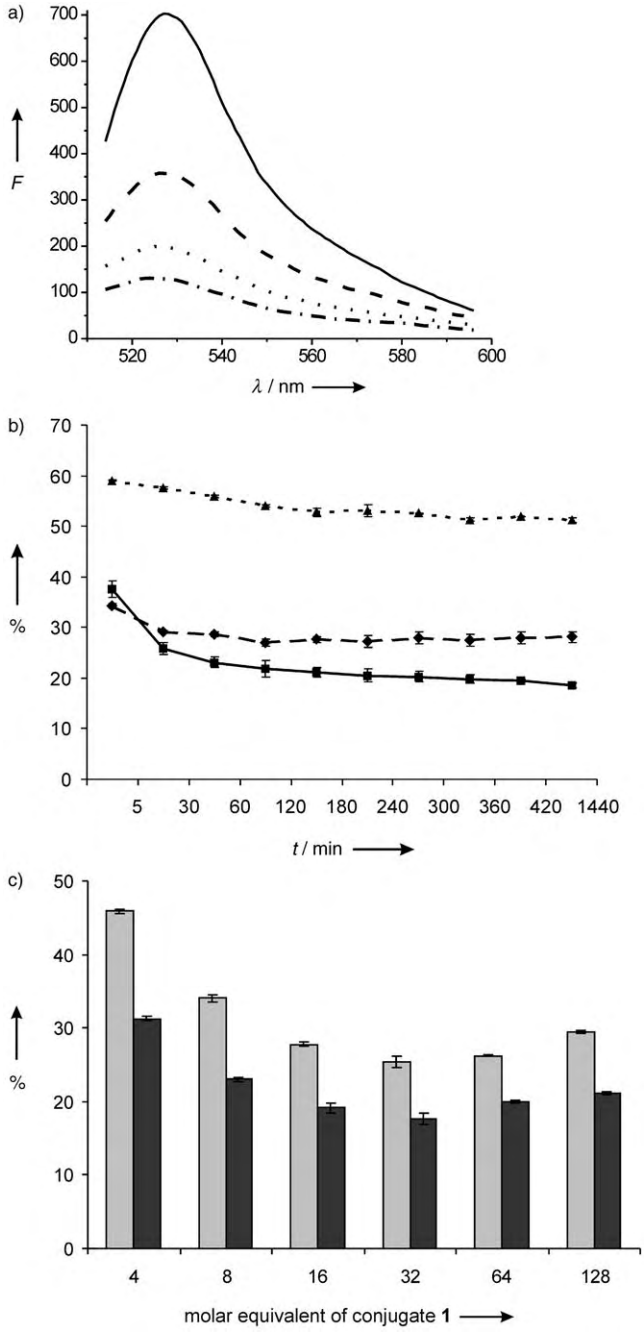

Figure 2. a) Fluorescence emission spectra of **1** (——), **1** mixed with **4** (-----), **1** coupled with **2** (•••••), and **1** coupled with **3** (–•–•). b) Relative fluorescence of **1**·**2** (-----), **1**·**3** (——), and **1**·**4** (•••••) with respect to the fluorescence of **1** (100%) at 528 nm versus different incubation times. c) Relative fluorescence at 528 nm against various molar equivalents of **1** used for hybridization with DNA–AuNPs **2** (gray bars) and **3** (black bars). Note that the results obtained from end-point measurements are shown.

(20 mM), NaCl (150 mM), EDTA (5 mM), Tween (0.05%); pH 7.3; Tris = tris(hydroxymethyl)aminomethane) to which a solution of **2**, **3**, or **4** (36 fmol in TETBS buffer, corresponding to 32 molar equivalents of **1** to **2**, **3**, and **4**) was added. After incubation for 6 h, fluorescence spectra were recorded using the excitation wavelength $\lambda_{exc} = 490$ nm. As shown in Figure 2a, the addition of noncomplementary AuNPs **4** led to a decrease in fluorescence emission by about 50% as a result of strong absorption and scattering caused by the AuNPs. Addition of the complementary AuNPs, however, led to a significantly higher quenching of the EYFP fluorescence, and this effect was markedly different for particles **2** and **3**. In the case of **1**·**2**, where Watson–Crick hybridization should lead to the formation of a 24-base-pair double-stranded DNA (dsDNA) spacer approximately 8.5 nm in length between the protein and the gold surface, quenching was less efficient (approximately 44% of the fluorescence intensity of the respective control **1**·**4**) than in the case of conjugate **1**·**3** (approximately 64% of the fluorescence intensity of the control **1**·**4**), where hybridization should localize the protein in direct proximity to the particle's surface. The relatively small difference in quenching efficiency of only 20% observed for the two different configurations realized in **1**·**2** and **1**·**3** suggests that complex mechanisms form the basis of the quenching process.[26]

The two different configurations in **1**·**2** and **1**·**3** (Figure 1) also affected the kinetics of protein immobilization (Figure 2b). Time-dependent fluorescence measurements showed that **1** rapidly hybridized with **2** and the reaction was completed within about 60 minutes. In contrast, the binding of **1** to **3** was significantly slower and led to a gradual decrease in relative fluorescence.[27] The quenching reached a maximum after about 24 hours (data not shown), and consequently all the following experiments were carried out with incubation overnight. The slower binding of **3** is in agreement with the proposed configuration (see Figure 1b) because in the conjugate **1**·**3** the bulky EYFP needs to penetrate, at least partially, the dense layer of DNA oligomers attached to the surface of the particle.[26]

We also studied the influence of surface coverage of AuNPs with EYFP on the amount of quenching (Figure 2c) by measuring the fluorescence emission intensities of **1**, and **2** and **3** coupled with various molar equivalents of **1**.[27] The fluorescence decreased for the binding of up to about 32 molar equivalents of **1**, whereas a further increase of **1** led to an increase in fluorescence as a result of the increasing amount of free **1** in the solution. Hence, the data of Figure 2c indicate that about 32 molar equivalents of **1** can hybridize to 25-nm AuNPs, which correlates with an approximately 18% hybridization efficiency of the about 175 oligonucleotide molecules[27] bound at the AuNP. This quantitative result is in very good agreement with earlier studies.[28,29]

We also investigated whether the immobilized proteins can be restored from the gold nanoparticles. To this end, we synthesized DNA–AuNPs **5** and **6** (Figure 3a), which contain a four-nucleotide single-stranded overhang appended to the coding sequence (**5**: AuNP-5′-TCC TGT GTG AAA TTG TTA TCC GCT TACG-3′, **6**: AuNP-3′-TCG CCT ATT GTT AAA GTG TGT CCT TACG-5′; the bases forming the dangling end are underlined). Hybridization of DNA–AuNPs **4**, **5**, and **6** with 32 molar equivalents of **1** led to quenching of the EYFP fluorescence in the case of **5** and **6**, similar to the case described above (light gray bars in Figure 3b). Then 1000 molar equivalents of the displacement oligomers **7** (corresponding to **1**·**5**; 5′-CGT AAG CGG ATA ACA ATT

 © 2006 Wiley-VCH Verlag GmbH & Co. KGaA, Weinheim

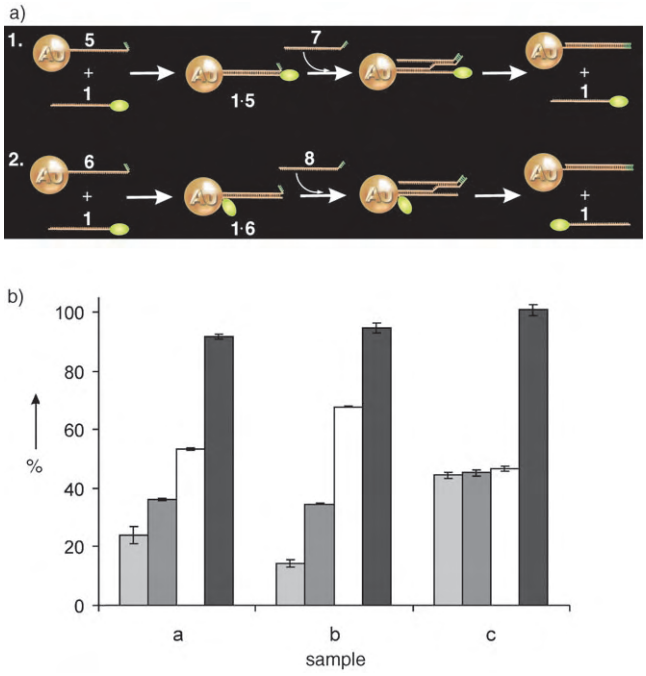

Figure 3. a) DNA-directed binding and detachment of DNA–AuNPs with/from DNA–EYFP conjugate **1**. DNA–AuNPs **5** or **6** were functionalized with EYFP conjugate **1** through specific nucleic acid hybridization, and subsequently strand-displacement oligonucleotides **7** and **8** were added to the conjugates **1·5** and **1·6**, respectively, which led to the formation of dsDNA-functionalized nanoparticles and regeneration of **1**. b) Quenching and regeneration of the EYFP fluorescence. The relative fluorescence values at 528 nm are shown. The light-gray bars represent the fluorescence of **1** in the presence of **5** (sample a), **6** (sample b), or **4** (sample c). The dark-gray bars represent the increased fluorescence of conjugate **1** upon addition of strand-displacement oligomer **7** (samples a and c) or **8** (sample b). The white bars represent the further increase in fluorescence upon increase of the NaCl concentration to 0.5 M within samples a–c. The black bars represent the fluorescence obtained after treatment of **1·5** (sample a), **1·6** (sample b), and unhybridized **4** (sample c) with mercaptoethanol. Note that 100% represents the fluorescence of the original solution containing **1**.

TCA CAC AGG A-3′) or **8** (corresponding to **1·6**; 5′-AGC GGA TAA CAA TTT CAC ACA GGA ATG C-3′), complementary to DNA–AuNPs **5** and **6**, respectively, were added and the mixture was incubated overnight. As shown in Figure 3b (dark gray bars), the restoration of the fluorescence was clearly observable in the case of particles **5** and **6**, and this led to almost identical fluorescence intensities compared with that of the control reaction containing the noncomplementary particles **4**. Further variations of the amount of **7** or **8** indicated that 500 molar equivalents led to restoration of about 75% of the control value, while 250 equivalents led to restoration of about 70% (data not shown). Taking into account the surface coverage of the AuNPs (about 175 oligonucleotides/particle), these data suggest that an approximately sixfold excess of the displacement oligomer with respect to the AuNP-bound DNA is necessary to effectively drive the equilibrium toward complete dissociation of the DNA–EYFP conjugate.

To verify that the decrease in fluorescence observed upon mere addition of AuNPs is a result of bulk effects, we studied whether the dsDNA–AuNPs formed upon strand displacement might be precipitated by an increase in salt concentration. This phenomenon was recently observed and elaborated by Maeda and co-workers.[30–32] Indeed, increasing the salt concentration of the reaction samples, prepared as described above, to 0.5 M NaCl led to immediate precipitation of the AuNPs within about 15 minutes in the case of **5** and **6**, as could be clearly observed by naked-eye inspection of the samples. Fluorescence measurements of these samples confirmed that the fluorescence after particle precipitation was higher (white bars in Figure 3b) than in the presence of the dispersed particles (dark gray bars in Figure 3b); however, complete restoration of the original EYFP fluorescence was not observed in any of the samples.

As an alternative to the liberation of the EYFP by DNA strand displacement, we also tested whether it is possible to restore the protein by complete stripping of the particle-attached DNA by treatment with mercaptoethanol.[28] Naked-eye observation indicated that here precipitation occurred significantly slower than in the experiments described above (about 4 h). As shown in Figure 3b (black bars), the addition of mercaptoethanol (12 mM final concentration) led to almost complete restoration of the initial EYFP fluorescence. Thus, fluorescence almost equal to that of the original EYFP solution (that is, 100%) was observed, which indicates that quenching was not persistent in the AuNP-containing samples after precipitation. Although the liberated DNA–protein conjugate now contains dsDNA, this approach might be well-suited for applications in which the DNA–AuNP-bound protein, for instance, comprises antibody or receptor moieties to specifically capture a target molecule from a complex biological matrix.

In conclusion, we have shown that proteins can be reversibly bound to DNA–gold nanoparticles without compromising their biological activity. The use of fluorescent proteins also demonstrates for the first time that these biological fluorophores can be incorporated into nanoparticle-based devices, thus leading to optically coupled hybrid architectures. The utilization of this system would also allow a systematic study of distance-dependent fluorescence quenching to be carried out by simply varying the lengths of the oligonucleotides attached to protein and the AuNPs. Further optimization of these approaches with respect to experimental parameters, such as temperature, salt concentration, and pH, by using oligofunctional DNA–nanoparticles[29] and, in particular, by design of appropriate oligomer sequences[14] and recombinant fluorescent protein mutants, should pave the way toward nanostructured materials with programmable functionalities for a broad range of applications in nanobiotechnology.

Received: May 23, 2006
Revised: June 29, 2006
Published online: September 26, 2006

Keywords: DNA · fluorescence · nanostructures · proteins · supramolecular chemistry

 © 2006 Wiley-VCH Verlag GmbH & Co. KGaA, Weinheim

[1] N. L. Rosi, C. A. Mirkin, *Chem. Rev.* **2005**, *105*, 1547 – 1562.
[2] E. Katz, I. Willner, *Angew. Chem.* **2004**, *116*, 6166 – 6235; *Angew. Chem. Int. Ed.* **2004**, *43*, 6042 – 6108.
[3] C. M. Niemeyer, *Angew. Chem.* **2001**, *113*, 4254 – 4287; *Angew. Chem. Int. Ed.* **2001**, *40*, 4128 – 4158.
[4] C. M. Niemeyer, B. Ceyhan, *Angew. Chem.* **2001**, *113*, 3798 – 3801; *Angew. Chem. Int. Ed.* **2001**, *40*, 3685 – 3688.
[5] J. M. Nam, C. S. Thaxton, C. A. Mirkin, *Science* **2003**, *301*, 1884 – 1886.
[6] D. G. Georganopoulou, L. Chang, J. M. Nam, C. S. Thaxton, E. J. Mufson, W. L. Klein, C. A. Mirkin, *Proc. Natl. Acad. Sci. USA* **2005**, *102*, 2273 – 2276.
[7] P. Hazarika, B. Ceyhan, C. M. Niemeyer, *Small* **2005**, *1*, 844 – 848.
[8] B. Yurke, A. J. Turberfield, A. P. Mills, Jr., F. C. Simmel, J. L. Neumann, *Nature* **2000**, *406*, 605 – 608.
[9] J. J. Li, W. Tan, *Nano Lett.* **2002**, *2*, 315 – 318.
[10] H. Yan, X. Zhang, Z. Shen, N. C. Seeman, *Nature* **2002**, *415*, 62 – 65.
[11] W. U. Dittmer, E. Reuter, F. C. Simmel, *Angew. Chem.* **2004**, *116*, 3634 – 3637; *Angew. Chem. Int. Ed.* **2004**, *43*, 3554 – 3557.
[12] Y. Chen, M. Wang, C. Mao, *Angew. Chem.* **2004**, *116*, 3638 – 3641; *Angew. Chem. Int. Ed.* **2004**, *43*, 3550 – 3553.
[13] F. C. Simmel, W. U. Dittmer, *Small* **2005**, *1*, 284 – 299.
[14] U. Feldkamp, C. M. Niemeyer, *Angew. Chem.* **2006**, *118*, 1888 – 1910; *Angew. Chem. Int. Ed.* **2006**, *45*, 1856 – 1876.
[15] P. Hazarika, B. Ceyhan, C. M. Niemeyer, *Angew. Chem.* **2004**, *116*, 6631 – 6633; *Angew. Chem. Int. Ed.* **2004**, *43*, 6469 – 6471.
[16] F. Kukolka, C. M. Niemeyer, *Org. Biomol. Chem.* **2004**, *2*, 2203 – 2206.
[17] F. Kukolka, B. K. Mueller, S. Paternoster, A. Arndt, C. M. Niemeyer, C. Braeuchle, D. C. Lamb, *Small* **2006**, *2*, 1083 – 1089.
[18] B. Dubertret, M. Calame, A. J. Libchaber, *Nat. Biotechnol.* **2001**, *19*, 365 – 370.
[19] E. Dulkeith, A. C. Morteani, T. Niedereichholz, T. A. Klar, J. Feldmann, S. A. Levi, F. C. van Veggel, D. N. Reinhoudt, M. Moller, D. I. Gittins, *Phys. Rev. Lett.* **2002**, *89*, 203002.
[20] Z. Gueroui, A. Libchaber, *Phys. Rev. Lett.* **2004**, *93*, 166108.
[21] C. S. Yun, A. Javier, T. Jennings, M. Fisher, S. Hira, S. Peterson, B. Hopkins, N. O. Reich, G. F. Strouse, *J. Am. Chem. Soc.* **2005**, *127*, 3115 – 3119.
[22] E. Dulkeith, M. Ringler, T. A. Klar, J. Feldmann, A. Munoz Javier, W. J. Parak, *Nano Lett.* **2005**, *5*, 585 – 589.
[23] P. C. Ray, A. Fortner, J. Griffin, C. K. Kim, J. P. Singh, H. Yu, *Chem. Phys. Lett.* **2005**, *414*, 259 – 264.
[24] J. R. Lakowicz, *Anal. Biochem.* **2005**, *337*, 171 – 194.
[25] EYFP has an isoelectric point of about 6.2, and thus its slightly negative net charge at pH 7.3 should prevent the nonspecific binding of **1** to the negatively charged DNA–AuNPs. The small degree of binding observed in gel electrophoresis might be a result of Van der Waals interaction, which was previously observed in EYFP bioconjugation.[16]
[26] The fundamentals of the quenching processes occurring in organic fluorophores attached to the surface of metal particles are still under investigation.[19–24] AuNPs have been shown to quench organic fluorophores by decreasing their radiative rate and increasing their nonradiative rate,[19] and the energy transfer has been shown to follow a distance dependence that is proportional to $1/r^4$ [21] rather than the Förster-type $1/r^6$ proportional transfer efficiency dependence observed for fluorescent quantum dots on the surface of AuNPs.[20] In contrast, the enhancement in fluorescence has also been reported for organic fluorophores in the vicinity of AuNP surfaces.[24] A crucial aspect in all these studies concerns the correct determination of the distance between the chromophore and the metal surface. In the case reported here, the NP-bound DNA should be able to adopt a number of different conformations, such as being fully stretched and pointing perpendicularly from the surface, adopting a random coil shape, or perhaps being tilted and interacting with the surface of the AuNP (W. J. Parak, T. Pellegrino, C. M. Micheel, D. Gerion, S. C. Williams, A. P. Alivisatos, *Nano Lett.* **2003**, *3*, 33 – 36). Hence, the nominal difference in distance of about 8.5 nm for assemblies **1**·**2** and **1**·**3** is likely to be affected by the presence of various conformational states, and therefore this might contribute to the explanation of the similarity in fluorescence quenching observed. Moreover, slight changes in protein loading should also induce different distances and/or different dynamics, and thus might also affect the quenching efficiency.
[27] A detailed description of the experimental protocols, the original fluorescence data, and the determination of the surface coverages of AuNPs with the thiolated oligonucleotides are available in the Supporting Information.
[28] L. M. Demers, C. A. Mirkin, R. C. Mucic, R. A. Reynolds, R. L. Letsinger, R. Elghanian, G. Viswanadham, *Anal. Chem.* **2000**, *72*, 5535 – 5541.
[29] C. M. Niemeyer, B. Ceyhan, P. Hazarika, *Angew. Chem.* **2003**, *115*, 5944 – 5948; *Angew. Chem. Int. Ed.* **2003**, *42*, 5766 – 5770.
[30] K. Sato, K. Hosokawa, M. Maeda, *J. Am. Chem. Soc.* **2003**, *125*, 8102 – 8103.
[31] K. Sato, K. Hosokawa, M. Maeda, *Nucleic Acids Res.* **2005**, *33*, e4.
[32] K. Sato, M. Onoguchi, Y. Sato, K. Hosokawa, M. Maeda, *Anal. Biochem.*, **2006**, *350*, 162 – 164.

 © 2006 Wiley-VCH Verlag GmbH & Co. KGaA, Weinheim

Molecular Recognition

DOI: 10.1002/anie.200600844

Ligand Preorganization May Be Accompanied by Entropic Penalties in Protein–Ligand Interactions**

*Aaron P. Benfield, Martin G. Teresk, Hilary R. Plake, John E. DeLorbe, Laura E. Millspaugh, and Stephen F. Martin**

A prevailing hypothesis in the field of molecular recognition in chemistry and biology is that the preorganization of flexible hosts and their guests in a manner corresponding to the three-

[*] A. P. Benfield, M. G. Teresk, Dr. H. R. Plake, J. E. DeLorbe, L. E. Millspaugh, Prof. S. F. Martin
Department of Chemistry and Biochemistry
and The Institute of Cellular and Molecular Biology
University of Texas at Austin
1 University Station–A5300, Austin, TX 78712-1167 (USA)
Fax: (+1) 512-471-4180
E-mail: sfmartin@mail.utexas.edu
Homepage: http://research.cm.utexas.edu/smartin/

[**] Acknowledgment is made to the National Institutes of Health, The Robert A. Welch Foundation (F-652), the Texas Advanced Research Program, Pfizer, Inc., and Merck Research Laboratories for their generous support of this research. We are also grateful to Professor Gabriel Waksman (University College London, Birkbeck College), Andrew Prongay (Schering-Plough Research Institute), and Dr. John H. Clements (The University of Texas) for helpful discussions.

Supporting information for this article is available on the WWW under http://www.angewandte.org or from the author.

WILEY InterScience DISCOVER SOMETHING GREAT
© 2006 Wiley-VCH Verlag GmbH & Co. KGaA, Weinheim

dimensional structures they adopt upon complex formation will lead to higher association constants. In simple host–guest complexes, changes in free energy ΔG that result from introducing such constraints can be highly favorable, an observation that led Cram to characterize preorganization as "a central determinant of binding power".[1,2] Ligand preorganization has also emerged as a strategy for structure-based drug design, and restricting the flexibility of peptides and other small molecules has indeed led to the discovery of selective and bioavailable drug leads that may exhibit increased potencies.[3–5]

Although the energetic consequences of ligand preorganization on protein binding affinities are necessarily both enthalpic and entropic, preorganization seems universally regarded as having a favorable entropic component. Enhanced affinities arising from preorganization are thus typically, albeit simplistically, regarded as being primarily entropic in origin, provided that the constrained and flexible molecules make the same pairwise interactions with the protein and solvent. Fully restricting each independent rotor in a flexible ligand should accordingly be accompanied by an entropic advantage of about 0.7–1.6 kcal mol^{-1}.[6,7] However, increases in potency accompanying ligand preorganization are commonly much less than those predicted based upon reducing the entropic binding penalties that are associated with conformational flexibility.

Identification of the specific origin of differences in the protein binding affinities of preorganized ligands relative to their flexible analogues is problematic for several reasons. Firstly, there are few cases where association constants are determined for a pair of constrained and flexible ligands having the same number and type of heavy atoms, the same functional groups, and the same number of hydrogen-bond donors and acceptors. Appropriate controls are thus generally absent, although there are reports where the ligands either meet the above criteria[8–10] or differ only slightly in elemental composition and functionality.[7,11–15] Secondly, structural information for complexes of the constrained and flexible ligands with the biological target is typically lacking, so whether both ligands interact similarly with the biomacromolecule is unknown. Ligands also frequently bind to proteins in conformations that are higher in energy than their global minima in solution,[16] and the analysis of how differential conformational strain energies affect affinities of similar compounds is a complex matter. Finally, the specific contributions to ΔS and ΔH of binding are rarely determined, so the extent to which entropic and enthalpic factors play a role in the relative potencies of constrained and flexible ligand pairs cannot be assessed.[15] There is thus little compelling scientific evidence supporting the widely asserted hypothesis that ligand preorganization will lead to more favorable binding entropies in protein–ligand interactions.

Toward explicitly elucidating the energetic and structural consequences of ligand preorganization in protein–ligand interactions, we have prepared pseudopeptides in which cyclopropane rings serve as rigid replacements for the Cα and Cβ carbon atoms and the NH groups of an amino acid residue, thereby constraining the backbone and orienting the side chain.[17] In one study, constrained and flexible derivatives of the tetrapeptide Ac-pTyr-Glu-Glu-Ile-OH, the consensus sequence in Src SH2 domain binding ligands,[18,19] were prepared that contained substituted cyclopropane and succinyl replacements for the phosphotyrosine residue.[20,21] The thermodynamic parameters for complex formation of these ligands with the Src SH2 domain were determined by isothermal titration calorimetry (ITC). Although the constrained ligands bound with more favorable entropies of binding than their flexible counterparts, this expected entropic advantage was always offset by a corresponding enthalpic penalty that resulted in comparable binding affinities of the various ligand pairs. There was thus no net energetic advantage associated with ligand preorganization because of balancing enthalpy–entropy compensation,[22,23] a ubiquitous phenomenon in host–guest and protein–ligand systems. Comparison of the X-ray crystal structures of the Src SH2 domain complexed with the cyclopropane-derived ligand and an 11-mer peptide containing the pTyr-Glu-Glu-Ile sequence revealed that both bound similarly, and all interatomic distances between the domain and the ligand in each of the two structures were in close agreement. Hence, the origin of the observed enthalpic disadvantage attending ligand preorganization was enigmatic, and investigations of other protein–ligand complexes would be required to gain further insights.

Phosphotyrosine peptides with the consensus sequence of Ac-pTyr-Xaa-Asn-NH_2, wherein Xaa is typically a hydrophobic residue, bind to the SH2 domain of the growth receptor binding protein 2 (Grb2).[18,19] The pseudopeptides **2** and **3** (see Table 1) were thus prepared as constrained and

Table 1: Thermodynamic parameters for complex formation between the Grb2 SH2 domain and pseudopeptides **2**–**7**.[a]

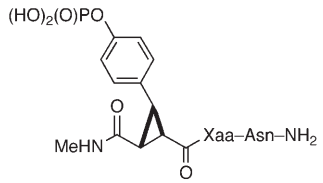

2: Xaa = Val
4: Xaa = Ile
6: Xaa = Leu

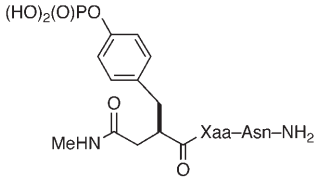

3: Xaa = Val
5: Xaa = Ile
7: Xaa = Leu

Cmpd.	K_a [M^{-1}]	ΔG [kcal mol^{-1}]	ΔH [kcal mol^{-1}]	ΔS [cal mol^{-1} K]
2	$(1.0\pm0.1)\times10^6$	-8.2 ± 0.1	-7.0 ± 0.1	4.2 ± 0.1
3	$(4.4\pm0.4)\times10^5$	-7.7 ± 0.1	-5.3 ± 0.1	8.2 ± 0.2
4	$(1.6\pm0.1)\times10^6$	-8.5 ± 0.1	-6.7 ± 0.1	6.0 ± 0.1
5	$(3.7\pm0.1)\times10^5$	-7.6 ± 0.1	-4.9 ± 0.1	9.1 ± 0.2
6	$(2.3\pm0.1)\times10^5$	-7.3 ± 0.1	-5.6 ± 0.1	5.9 ± 0.1
7	$(1.7\pm0.1)\times10^5$	-7.1 ± 0.1	-4.6 ± 0.1	8.6 ± 0.2

[a] ITC experiments were conducted at 25 °C in duplicate with the same batch of ligand and Grb2 SH2 domain in 2-[4-(2-hydroxyethyl)piperazin-1-yl]ethanesulfonic acid (HEPES, 50 mM) with NaCl (150 mM) at pH 7.5. Uncertainties in K_a, ΔG, ΔH, and ΔS values represent deviations from the average. Similar experiments conducted with **4** and **5** in Tris buffer gave comparable results.

© 2006 Wiley-VCH Verlag GmbH & Co. KGaA, Weinheim

flexible analogues of Ac-pTyr-Val-Asn-NH_2 (**1**).[24] As in our previous studies of Src SH2 binding ligands, the cyclopropane ring in **2** serves as a rigid mimic of the pTyr residue in **1**, whereas a benzyl succinyl moiety is a flexible pTyr replacement in the control **3**. The thermodynamic parameters (ΔG, ΔH, ΔS) for binding of **2** and **3** to the Grb2 SH2 domain were determined by ITC (Table 1), and the constrained ligand **2** was observed to bind approximately twofold better than its flexible counterpart **3**. However, in an unprecedented finding that is inconsistent with the conventional wisdom regarding the putative effects of preorganization, the entropy of binding for **2** was significantly less favorable than for **3**.

In an extension of these studies, the amino acid at the pY + 1 position of **2** and **3** was changed from Val to Ile and Leu, thus giving the corresponding ligand pairs **4**–**7** to assess the influence that variations of this hydrophobic residue might have on the energetics of binding. The thermodynamic parameters for binding of **4**–**7** to the Grb2 SH2 domain were determined (Table 1), and the constrained pseudopeptides **4** and **6** were observed to bind with slightly higher affinities than their corresponding flexible controls **5** and **7**. However, the increased affinities for the preorganized ligands **4** and **6** were again the consequence of more favorable binding enthalpies, and the binding entropies for **4** and **6** were unfavorable relative to those of their flexible counterparts **5** and **7**. The ΔC_p values for **4** and **5** were determined to be −88 and −94 cal mol^{-1} K, respectively, so differences in binding free energies do not appear to arise from solvation/desolvation or hydrophobic effects.[25] Based upon these unprecedented findings, it is now apparent that ligand preorganization may be accompanied by unfavorable binding entropies, yet more favorable binding free energies.

To explore whether structural factors might be responsible for the differential binding enthalpies of the constrained and flexible ligands, complexes of the monomeric Grb2 SH2 domain with **2** and **3** were co-crystallized for X-ray analysis. Data for the complexes of **2** and **3** with the Grb2 SH2 domain were collected to 1.9 and 1.7 Å resolution, respectively, and the structures were solved by molecular replacement using a known structure.[26,27] Similar to other Grb2 SH2 binding ligands,[26,28,29] **2** and **3** bind to the domain in a β-turn-like conformation. There are two Grb2 SH2–**2** complexes in the asymmetric unit, and the backbone atoms of the domain in these align with a root-mean-square deviation (rmsd) of 0.3 Å; atoms of **2** in the two complexes align with an rmsd of 0.2 Å. An overlay of the two Grb2 SH2–**2** complexes with that of the Grb2 SH2-**3** complex is shown in Figure 1a. The backbone atoms of the Grb2 SH2 domain in the complexes of **2** align with those in the complex of **3** with rms deviations of 0.5 and 0.6 Å. The variations occur primarily in the flexible loops, but the most notable difference, which is revealed by the close-up superimposition in Figure 1b, is the position of the BC loop that forms part of the phosphate binding pocket. In particular, the Cα and nitrogen backbone atoms of Ser90 and Glu89 in the BC loop in each of the complexes of **2** are displaced toward the ligand so they are about 2.0 Å *closer* to the phosphate group of **2** than they are in the corresponding complex with **3**. The atoms of the Val and Asn residues in the complexes of **2** and **3** superimpose with an rmsd of 0.1 Å, and the direct interactions between the domain and the Val-Asn dipeptide subunits of **2** and **3** are virtually identical. However, there are significant variations in the positions of the atoms in the constrained and flexible phosphotyrosine replacements of **2** and **3**, as these align with an rmsd of 0.6 Å. Dissimilarities in the positioning of the N-terminal methyl amide moieties of **2** and **3** appear inconsequential, whereas variations in the orientations of the phosphate groups lead to significant differences in the interactions of the phosphate oxygen atoms of **2** and **3** with the SH2 domain.

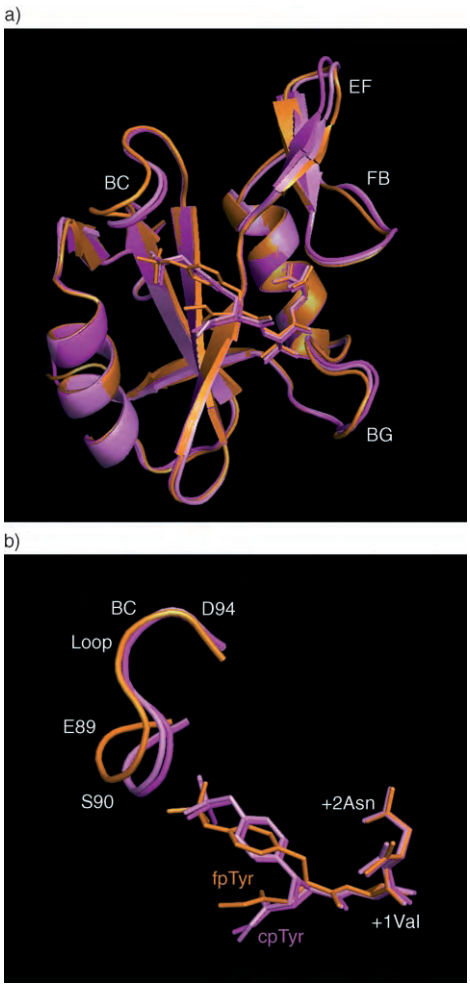

Figure 1. Superimposition of the structures of the complexes of **2** and **3** with the monomeric Grb2 SH2 domain. The protein is shown as a ribbon representation, whereas the ligands are shown as stick representations. The complex between **2** and the Grb2 SH2 domain crystallized with two molecules in the asymmetric unit, and the structure was refined to a R_{cryst} of 19.4% and a R_{free} of 22.5%. The complex between the Grb2 SH2 domain and **3** crystallized with one molecule in the asymmetric unit, and the structure was refined to a R_{cryst} of 20.7% and a R_{free} of 23.4%. a) Alignment of the two complexes in the asymmetric unit of **2** (magenta and violet) with the complex of **3** (orange). b) Close-up overlay of the structures of the two molecules of **2** from the two complexes in the asymmetric unit (magenta and violet) with the structure of **3** (orange) showing their relationship with residues Ser88-Asp94 in the BC loop. The constrained and flexible phosphotyrosine replacements are labeled cpTyr and fpTyr, respectively.

 © 2006 Wiley-VCH Verlag GmbH & Co. KGaA, Weinheim

The detailed interactions between the Grb2 SH2 domain, ordered water molecules, and the phosphotyrosine replacements in **2** and **3** are presented in Figure 2a and b. An analysis of these interactions reveals that the aforementioned displacement of the BC loop and the different orientations of the phosphate group in the phosphotyrosine replacements in **2** and **3** result in a number of closer contacts between the ligand and the Grb2 SH2 domain in the complex with **2**. For example, the backbone amide N-H of Glu89 is directly hydrogen-bonded to a nonbridging oxygen atom of the phosphate group in the Grb2 SH2–**2** complex, whereas a water molecule mediates this interaction in the complex with **3**. The amide N-H of Ser90 in the Grb2 SH2–**2** complex forms a direct hydrogen bond with a nonbridging oxygen atom of the phosphate group, but there are no comparable direct interactions in the complex with **3**. The side chain of Glu89 in the complex of **2** is oriented toward the ligand, so the carboxy group interacts via a water molecule with a nonbridging oxygen atom of the phosphate group. There is no interaction between the carboxy group of Glu89 and the phosphate group in the complex of **3**.

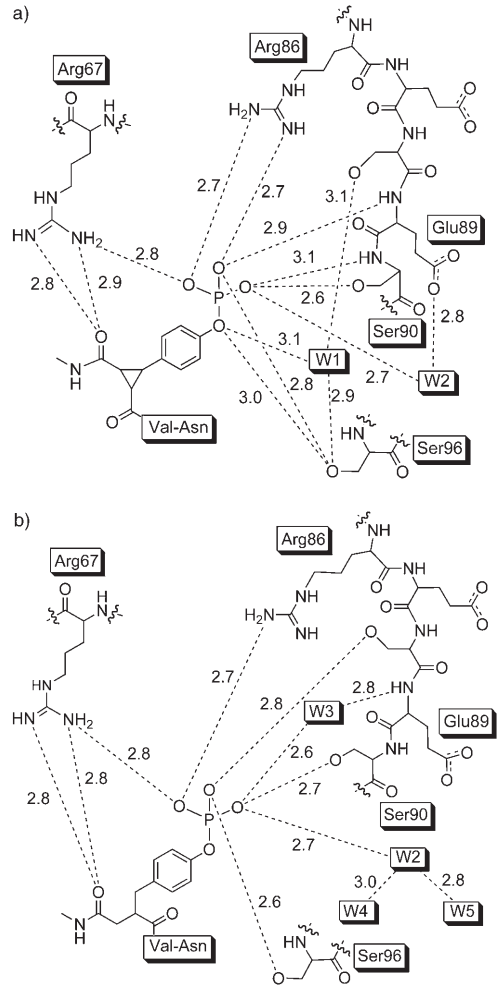

Figure 2. Hydrogen-bonding and polar interactions in the phosphotyrosine binding site of complexes of **2** and **3** with the Grb2 SH2 domain showing those water molecules, W, involved in binding networks. Polar contact distances between heavy atoms of ≤ 3.1 Å are indicated, but some hydrogen atoms involved in these interactions are omitted for clarity. a) One complex in an asymmetric unit of **2**; the corresponding pairwise distances in the other complex of **2** in the asymmetric unit are ± 0.1 Å. b) Complex of **3**.

The spatial dispositions of the atoms in the constrained and flexible phosphotyrosine replacements in **2** and **3** are different, so we queried whether these replacements might be uniquely responsible for the observed differences in the pairwise interactions with the Grb2 SH2 domain and the conformational perturbation of the BC loop. These complexes were thus compared with the structures of **8**, in which a 22-membered macrocycle constrains the pTyr-Val-Asn sequence in its biologically active conformation,[9] and the linear nonapeptide Ala-Pro-Ser-pTyr-Val-Asn-Val-Gln-Asn (**9**) bound to the Grb2 SH2 domain (Figure 3a, b).[26] The backbone atoms of the domain in the two complexes of **2** and the complex of **8** align with an rmsd of 0.3–0.4 Å; the corresponding atoms in **2** and **8** align with an rmsd fit of about 0.6 Å (Figure 3b). The polar interactions and their respective contact distances between the domain and the phosphate groups of **2** and **8** in these complexes are comparable. Hence, two different tactics for introducing a conformational constraint into a pYVN-derived ligand result in similar displacement of the BC loop toward the ligand. When the complexes of the Grb2 SH2 domain with **3** and the nonapeptide **9** are superimposed, the backbone atoms of the domain in the two complexes align with an rmsd of 0.5 Å; the corresponding atoms in **3** and **9** align with an rmsd of 0.3 Å (Figure 3c). There are slight variations in the pairwise polar interactions and contact distances between the ligands and the SH2 domain in these two complexes, but the differences are similar to those observed when comparing the structures of other phosphotyrosine ligands bound to the Grb2 SH2 domain.[9,26,28,29] These comparisons suggest that the cyclopropane ring in **2** is a good mimic of the phosphotyrosine residue in the macrocycle **8**, and that the succinyl moiety in **3** serves as a reasonable replacement of the phosphotyrosine in the linear peptide **9**. Hence, the specific phosphotyrosine replacements in **2** and **3** do not themselves appear to induce any unusual structural changes in the Grb2 SH2 domain upon binding.

The greater number and closer contact distances associated with the pairwise interactions in the Grb2 SH2–**2** complex relative to those in the Grb2 SH2–**3** complex are consistent with the more favorable enthalpy of binding observed for **2**. However, identification of the specific origins of this enthalpic advantage is problematic because of the complexity of these interactions, some of which involve bridging water molecules. Further complicating the analysis is the flexible nature of proteins and the energetic consequences thereof. Namely, the formation of a protein–ligand complex can result in an overall decrease or increase in protein flexibility that is accompanied by corresponding changes in nonbonded interactions and order throughout the complex.[23,30] The effect these changes have upon the relative magnitudes of the compensating enthalpies and entropies of

 © 2006 Wiley-VCH Verlag GmbH & Co. KGaA, Weinheim

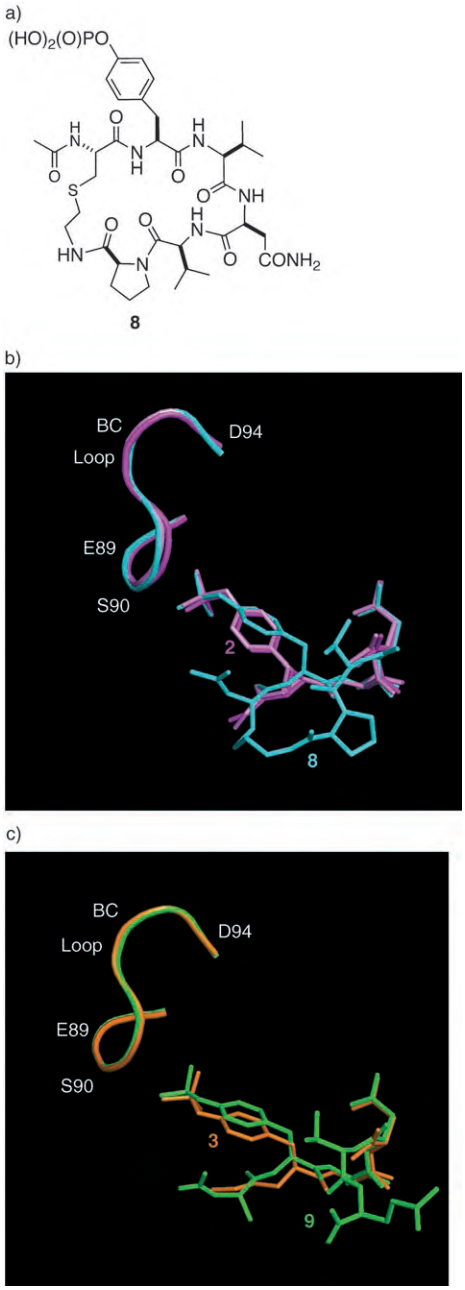

Figure 3. Complexes of different ligands with the Grb2 SH2 domain, with the protein shown in ribbon representation and the ligands shown in stick representation. a) Chemical structure of **8**. b) Alignment of the two complexes in the asymmetric unit of **2** (magenta and violet) with the published structure (2.1 Å resolution) of the complex of macrocycle **8** (cyan) in reference [9] (1BM2), which shows their relationship with residues Ser88-Asp94 in the BC loop of the respective Grb2 SH2 domains. c) Overlay of structures of **3** (orange) with the published structure (1.55 Å resolution) of the linear nonapeptide **9** (green) in reference [26] (1JYR), which has been truncated for clarity and shows their relationship with residues Ser88-Asp94 in the BC loop.

binding cannot be evaluated, because crystallographic data do not provide a reliable measure of protein flexibility in solution. Nevertheless, it is interesting in this context that a comparison of B-factors in the complexes of the Grb2 SH2 domain with **2** and **3** suggests there is *more* thermal motion in the BC loop of the Grb2 SH2–**2** complex. This observation is opposite to that which might be expected from the tighter interactions that are evident between this loop and the phosphate moiety of **2** relative to those in the Grb2 SH2–**3** complex. It is also inconsistent with the relative binding entropies of **2** and **3**.

Although preorganized ligands may bind to proteins with higher affinities than those of their flexible counterparts, we are not aware of any convincing evidence that the process must be entropically favored, as is widely assumed. Indeed, we have shown that the entropies of binding of preorganized ligands may be disfavored relative to their less potent, flexible controls. Increased affinities arising from ligand preorganization may thus result solely from more favorable enthalpies of binding. This study suggests that the enhanced enthalpy of binding can arise from an unexpected increase in the number and proximity of polar contacts between the protein and ligand; however, changes in individual nonbonded interactions throughout the complex will also contribute. These results clearly indicate that the prevailing view of the energetic consequences associated with ligand preorganization, which focuses largely if not exclusively on the ligand itself, in protein–ligand interactions must be modified. Future models must include explicit consideration of the enthalpic and entropic contributions arising from changes in nonbonded interactions and order that occur in the protein upon complex formation, and how these changes vary as a function of ligand structure and flexibility. Interactions with water molecules must also be taken into account.

Received: March 4, 2006
Revised: August 3, 2006
Published online: September 26, 2006

Keywords: ligand effects · molecular recognition · peptides · proteins · thermodynamics

[1] D. J. Cram, *Angew. Chem.* **1986**, *98*, 1041 – 1060; *Angew. Chem. Int. Ed. Engl.* **1986**, *25*, 1039 – 1057.
[2] K. N. Houk, A. G. Leach, S. P. Kim, X. Zhang, *Angew. Chem.* **2003**, *115*, 5020 – 5046; *Angew. Chem. Int. Ed.* **2003**, *42*, 4872 – 4897.
[3] H. Nakanishi, M. Kahn in *The Practice of Medicinal Chemistry*, 2nd ed. (Ed.: C. G. Wermuth), Academic Press, London, **2003**, pp. 477 – 500.
[4] D. F. Veber, S. R. Johnson, H. Y. Cheng, B. R. Smith, K. W. Ward, K. D. Kopple, *J. Med. Chem.* **2002**, *45*, 2615 – 2623.
[5] A. Mann in *The Practice of Medicinal Chemistry*, 2nd ed. (Ed.: C. G. Wermuth), Academic Press, London, **2003**, pp. 233 – 250.
[6] U. Gerhard, M. S. Searle, D. H. Williams, *Bioorg. Med. Chem. Lett.* **1993**, *3*, 803 – 808.
[7] A. R. Khan, J. C. Parrish, M. E. Fraser, W. W. Smith, P. A. Bartlett, M. N. G. James, *Biochemistry* **1998**, *37*, 16839 – 16845.
[8] B. P. Morgan, D. R. Holland, B. W. Matthews, P. A. Bartlett, *J. Am. Chem. Soc.* **1994**, *116*, 3251 – 3260.
[9] P. Ettmayer et al., *J. Med. Chem.* **1999**, *42*, 971 – 980; see Supporting Information.
[10] Y. S. Tsantrizos et al., *Angew. Chem.* **2003**, *115*, 1394 – 1398; *Angew. Chem. Int. Ed.* **2003**, *42*, 1356 – 1360; see Supporting Information.

 © 2006 Wiley-VCH Verlag GmbH & Co. KGaA, Weinheim

[11] R. W. Marquis et al., *J. Med. Chem.* **2001**, *44*, 1380 – 1395; see Supporting Information.
[12] S. K. Sia, P. A. Carr, A. G. Cochran, V. N. Malashkevich, P. S. Kim, *Proc. Natl. Acad. Sci. USA* **2002**, *99*, 14664 – 14669.
[13] F. J. Dekker, N. J. de Mol, M. J. E. Fischer, J. Kemmink, R. M. J. Liskamp, *Org. Biomol. Chem.* **2003**, *1*, 3297 – 3303.
[14] A. K. Ghosh, L. M. Swanson, H. Cho, S. Leshchenko, K. A. Hussain, S. Kay, D. E. Walters, Y. Koh, H. Mitsuya, *J. Med. Chem.* **2005**, *48*, 3576 – 3585.
[15] T. Li, D. Saro, M. R. Spaller, *Bioorg. Med. Chem. Lett.* **2004**, *14*, 1385 – 1388.
[16] E. Perola, P. S. Charifson, *J. Med. Chem.* **2004**, *47*, 2499 – 2510.
[17] A. Reichelt, S. F. Martin, *Acc. Chem. Res.* **2006**, *39*, 433 – 442.
[18] J. M. Bradshaw, G. Waksman, *Adv. Protein Chem.* **2002**, *61*, 161 – 210.
[19] K. Machida, B. J. Mayer, *Biochim. Biophys. Acta* **2005**, *1747*, 1 – 25.
[20] J. P. Davidson, O. Lubman, T. Rose, G. Waksman, S. F. Martin, *J. Am. Chem. Soc.* **2002**, *124*, 205 – 215.
[21] J. P. Davidson, PhD thesis, The University of Texas, **2001**.
[22] J. D. Dunitz, *Chem. Biol.* **1995**, *2*, 709 – 712.
[23] D. H. Williams, E. Stephens, D. P. O'Brien, M. Zhou, *Angew. Chem.* **2004**, *116*, 6760 – 6782; *Angew. Chem. Int. Ed.* **2004**, *43*, 6596 – 6616.
[24] H. R. Plake, T. B. Sundberg, A. R. Woodward, S. F. Martin, *Tetrahedron Lett.* **2003**, *44*, 1571 – 1574.
[25] J. M. Sturtevant, *Proc. Natl. Acad. Sci. USA* **1977**, *74*, 2236 – 2240.
[26] P. Nioche, W.-Q. Liu, I. Brouitin, F. Charbonnier, M.-T. Latreille, M. Vidal, B. Roques, C. Garbay, A. Ducruix, *J. Mol. Biol.* **2002**, *315*, 1167 – 1177.
[27] X-ray crystallographic data are deposited in the Protein Data Bank under the accession codes 2HUW and 2HUY.
[28] J. Rahuel et al., *Nat. Struct. Biol.* **1996**, *3*, 586 – 589; see Supporting Information.
[29] J. Rahuel, C. Garcia-Echeverria, P. Furet, A. Strauss, G. Caravatti, H. Fretz, J. Schoepfer, B. Gay, *J. Mol. Biol.* **1998**, *279*, 1013 – 1022.
[30] C.-Y. Yang, R. Wang, S. Wang, *J. Med. Chem.* **2005**, *48*, 5648 – 5650.

 © 2006 Wiley-VCH Verlag GmbH & Co. KGaA, Weinheim

High-Throughput Screening

DOI: 10.1002/anie.200601302

Colloidal Crystal Beads as Supports for Biomolecular Screening**

*Xiangwei Zhao, Yun Cao, Fuyumi Ito, Hai-Hua Chen, Keiji Nagai, Yu-Hua Zhao, and Zhong-Ze Gu**

In high-throughput screening and multiplex analysis, a number of individual assays need to be carried out simultaneously within the same sample.[1] One approach is based on encoded carriers, on which probe biomolecules such as DNA strands or proteins are immobilized to bind the target molecules. When the carriers are encoded, they can be mixed and subjected to an assay simultaneously and then many binding events can be distinguished by their codes. The carriers may be spots on a microarray chip that are encoded by their coordinates. The advantage of this method is that the well-developed microfabrication technique can be utilized for chip fabrication. However, the probing speed needs to be improved because the molecular interaction on the chip is diffusion-limited.[2,3] The key is to immobilize biomolecules on encoded particles such as rods or beads, which can undergo free rotation and movement. These particles, known as fluidic carriers, have been drawing more and more attention.

Spectrum encoding is a well-used method of encoding because of its simplicity in detection and operation. Fluorescent dyes and quantum dots are the main spectrum-encoding elements.[4–7] These carriers, which are usually employed by the encoded fiber optics or Luminex system, are widely applied to genotyping, proteomics, and diagnostics.[7–10] However, the encoding elements tend to be quenched or bleached and their degree of multiplexing is limited because the optical spectra overlap. Recently, the reflection spectrum of a one-dimensional photonic crystal was proposed as a new encoding element.[11,12] The spectra come from the physical structure of the carriers, and therefore these codes are extremely stable compared with the organic or fluorescent

[*] X.-W. Zhao, Y. Cao, H.-H. Chen, Prof. Dr. Z.-Z. Gu
State Key Laboratory of Bioelectronics
Southeast University
Nanjing 210096 (China)
Fax: (+86) 25-8379-5635
E-mail: gu@seu.edu.cn
X.-W. Zhao, Prof. Y.-H. Zhao
College of Life Science
Zhejiang University
Hangzhou 310029 (China)
Dr. F. Ito, Dr. K. Nagai
Institute of Laser Engineering (ILE)
Osaka University
Osaka 565-0871 (Japan)

[**] This work was supported by the National Natural Science Foundation (grants 20573018 and 60121101).

Supporting information for this article is available on the WWW under http://www.angewandte.org or from the author.

© 2006 Wiley-VCH Verlag GmbH & Co. KGaA, Weinheim

dyes. However, it is inconvenient that 1D photonic crystal microcarriers have to be properly dispersed and correctly orientated to avoid stacking or standing of the flakes during the decoding process.[11] Recently, we found that these problems might be solved by microbeads with a three-dimensional photonic crystal structure.

One simple way to fabricate 3D photonic crystals is the assembly of monodisperse colloidal nanoparticles, which are also known as colloidal crystals.[13–19] Up to now, the main contribution was devoted to the fabrication of film, and there are only a few reports on the formation of spherical colloidal crystals.[15,17,20,21] Herein, we show an apparatus with which colloidal crystal beads of well-controlled size can be continuously fabricated. Figure 1 depicts the apparatus which was

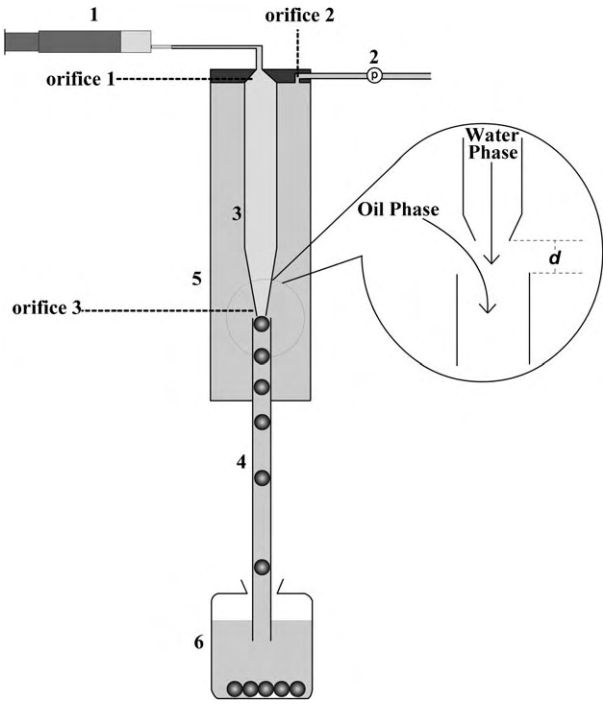

Figure 1. Diagram of the fabrication apparatus. 1) Syringe pump for aqueous suspension; 2) magnetic pump equipped with a flow meter for oil; 3) tapered glass tube; 4) glass tube; 5) cylinder; 6) collector. The magnified area in the circle shows the integration of orifice 3 and the glass tube 4.

originally developed for the fabrication of oil emulsions in water.[22,23] An aqueous-phase solution containing cross-linked monodisperse poly(methyl methacrylate) (PMMA) colloidal nanoparticles and an oil-phase solution are injected continuously into the droplet generator. Droplets of the aqueous solution are then generated on the tip of the tapered glass tube and flow into the collector. When the water in the droplets evaporates slowly, the monodisperse nanoparticles self-assemble into ordered lattices. The droplets are dried, and colloidal crystal beads are produced in which van der Waals forces hold the nanoparticles together.

The size of the colloidal crystal beads depends on both the concentration of nanoparticles and the size of the droplet. The beads enlarge when the concentration of particles in the droplet increases. Generally, the size of the droplets increases when the diameter of the tapered orifice, the extrusion rate of the water phase, or the distance *d* (see Figure 1) increases, and decreases when the velocity of the oil phase increases. Therefore, the size of the colloidal crystal beads can be well-controlled by manipulation of the above factors. Up to now, we have prepared colloidal crystal beads from tens of micrometers to several millimeters in diameter.

Figure 2 shows the reflection spectra of six kinds of colloidal crystal beads composed of monodisperse nanoparticles of different sizes. The reflection of the bead comes

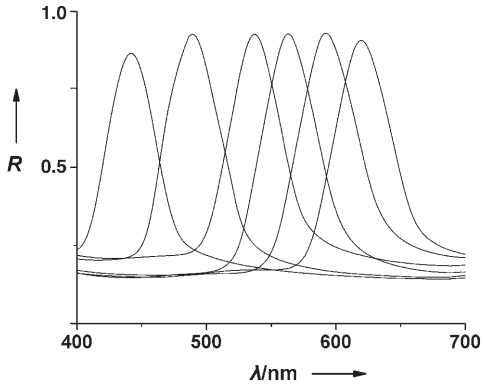

Figure 2. Reflection spectra of six colloidal crystal beads composed of PMMA nanoparticles with different sizes. From left to right, the sizes of the nanoparticles are 195, 208, 220, 230, 248, and 268 nm.

from the diffraction of light from the ordered structure (see Figure 3), which shifts to a long wavelength as the diameter of the nanoparticles increases. The reflection peak of one single bead is almost orientation-invariant, because the shift of the reflection peak at different positions is less than 5 nm. Hence, the orientation of the beads does not need to be considered during the decoding process.

Figure 3 shows scanning electron microscopy (SEM) images of a colloidal crystal bead. It can be observed that

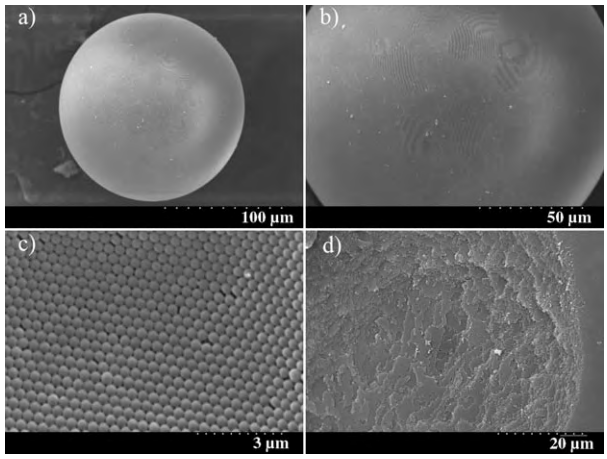

Figure 3. SEM images of the colloidal crystal beads. a) Low-magnification image of the colloidal crystal bead showing the smooth bead surface. b) Domains can be observed on the bead surface but no apparent cracks are visible. c) High-magnification image of the bead surface showing the hexagonal alignment of nanoparticles. d) Image of a split bead showing the inner structure.

 © 2006 Wiley-VCH Verlag GmbH & Co. KGaA, Weinheim

the surface of the bead is smooth over a large area. Unlike the colloidal crystal film in which there are cracks every 10 to 50 μm, cracks are hardly observed in the colloidal crystal bead. The high-magnification image of the bead surface shows that the nanoparticles mainly form a hexagonal symmetry, which is the same in the colloidal crystal films. The cross section of a split bead shows that the nanoparticles also form an ordered structure inside the bead. All the beads fabricated by this method exhibit brilliant colors and sharp reflection peaks, which can be used as codes for carriers in high-throughput screening or multiplex bioassays. The codes of the beads can also be customized by varying the size of the nanoparticles according to Bragg's law. The reflection spectra of the beads, unlike those of fluorescent dyes, are very stable to light irradiation and long-term storage. No apparent spectral change was detected after several months of storage at room temperature.

To demonstrate the reliability of the colloidal crystal beads as encoded carriers in a multiplex bioassay, we prepared three kinds of beads composed of 250-, 220-, and 210-nm cross-linked PMMA nanoparticles, which were red, green, and blue, respectively (Figure 4). Human, mouse, and rabbit immunoglobulin G (IgG) were physically absorbed onto the red, green, and blue colloidal crystal beads, respectively, by overnight incubation at 4 °C. The sites on the bead surfaces that did not absorb protein were blocked with a solution of bovine serum albumin (BSA). The three kinds of beads were mixed and exposed to a solution containing fluorescein isothiocyanate (FITC)-conjugated goat anti-human and anti-rabbit IgG. After incubation and rinsing, the fluorescence and reflection spectra were measured using a microscope equipped with a fiber optics spectrometer (Figure 4). Fluorescence was detected on the red and green beads at 520 nm, while no fluorescence signal was detected on the blue beads. The result indicated that human and mouse IgG on red and green beads bond specifically with goat anti-human and anti-mouse IgG tagged with FITC. This finding is consistent with the content of the sample to which the beads were exposed.

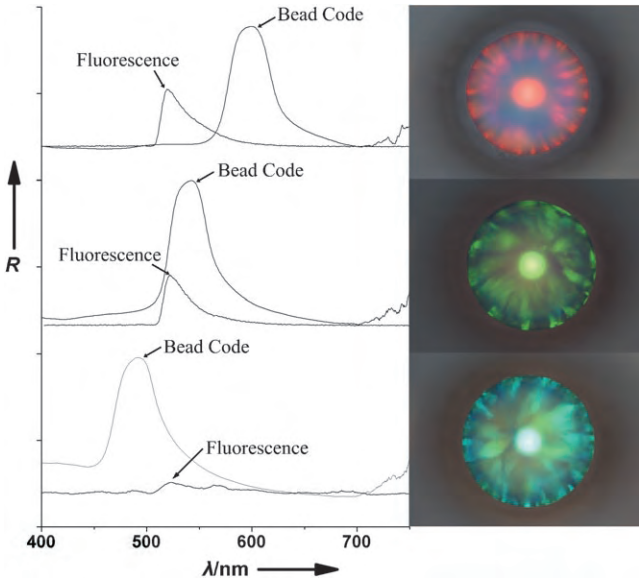

Figure 4. Fluorescence and optical reflection spectra (left) and bright-field microscopic images (right) of three colloidal crystal beads with a diameter of 400 μm. The red, green, and blue beads were immobilized with human, mouse, and rabbit IgG, respectively. They were exposed to a sample containing FITC-tagged goat anti-human IgG and goat anti-rabbit IgG. Both the fluorescence and reflection measurements were performed on an Olympus fluorescence microscope with a 10× objective coupled to an Ocean Optics spectrofluorometer (USB2000-FLG). Spectra are offset along the *R* axis for clarity.

In summary, we have developed an approach for fabricating colloidal crystal beads of controllable size and demonstrated their use in multiplex bioassays. This approach has the following advantages over the reported methods. 1) The beads are fabricated continuously. Both the apparatus and fabrication process are suitable for mass production. 2) The reflection peak of the colloidal crystal bead is both sharp and orientation-invariant. No orientation is needed for the optical decoding. In addition, the fabrication method can be extended to core–shell beads, in which core and shell are composed of nanoparticles of different sizes. In this case, the colloidal crystal beads are encoded by two or more reflection peaks, which can greatly increase the encoding capacity. 3) As the colloidal crystal beads are assemblies of nanoparticles, the surface functional groups such as NH_2 and COOH or surface wettability can be customized by selecting appropriate nanoparticles. 4) As they are composed of hexagonal close-packed nanoparticles, the bead surfaces are coarse in the submicrometer scale, which increases the surface-to-volume ratio and thus the detection sensitivity. 5) Compared with the optical absorption encoded carriers, the code generated by photonic crystals is very stable to light irradiation and long-term storage. In addition to the reflective features of photonic crystals, the fluorescence absorption from the surface fluorescent dyes can be reduced and as a result the fluorescence intensity and the sensitivity are enhanced.[24] Therefore, wide applications of colloidal crystal beads are anticipated in genomic or proteomic studies, drug screening, clinical diagnostics, and combinatorial chemistry.

Received: April 3, 2006
Revised: August 5, 2006
Published online: September 26, 2006

Keywords: colloids · high-throughput screening · immunoassays · nanoparticles · self-assembly

[1] K. Braeckmans, S. De Smedt, M. Leblans, R. Pauwels, J. Demeester, *Nat. Rev. Drug Discovery* **2002**, *1*, 447.
[2] S. R. Nicewarner-Pena, R. G. Freeman, B. D. Reiss, L. He, D. J. Pena, I. D. Walton, R. Cromer, C. D. Keating, M. J. Natan, *Science* **2001**, *294*, 137.
[3] M. R. Henry, P. W. Stevens, J. Sun, D. M. Kelso, *Anal. Biochem.* **1999**, *276*, 204.
[4] M. Trau, B. J. Battersby, *Adv. Mater.* **2001**, *13*, 975.
[5] R. J. Fulton, R. L. McDade, P. L. Smith, L. J. Kienker, J. John, R. Kettman, *Clin. Chem.* **1997**, *43*, 1749.
[6] M. Han, X. Gao, J. Su, S. Nie, *Nat. Biotechnol.* **2001**, *19*, 631.
[7] F. Steemers, J. Ferguson, D. Walt, *Nat. Biotechnol.* **2000**, *18*, 91.
[8] F. Szurdoki, K. L. Michael, D. R. Walt, *Anal. Biochem.* **2001**, *291*, 219.

 © 2006 Wiley-VCH Verlag GmbH & Co. KGaA, Weinheim

[9] J. Ferguson, F. Steemers, D. Walt, *Anal. Chem.* **2000**, *72*, 5618.
[10] www.luminexcorp.com.
[11] F. Cunin, T. Schmedake, J. Link, Y. Li, J. Koh, S. Bhatia, M. Sailor, *Nat. Mater.* **2002**, *1*, 39.
[12] J. Y. Kim, F. E. Osterloh, *J. Am. Chem. Soc.* **2006**, *128*, 3868.
[13] O. D. Velev, K. Nagayama, *Langmuir* **1997**, *13*, 1856.
[14] A. Imhof, D. J. Pine, *Nature* **1997**, *389*, 948.
[15] G. R. Yi, J. H. Moon, S. M. Yang, *Adv. Mater.* **2001**, *13*, 1185.
[16] G. R. Yi, V. N. Manoharan, S. Klein, K. R. Brzezinska, D. J. Pine, F. F. Lange, S. M. Yang, *Adv. Mater.* **2002**, *14*, 1137.
[17] J. H. Moon, G. R. Yi, S. M. Yang, D. J. Pine, S. Bin Park, *Adv. Mater.* **2004**, *16*, 605.
[18] Z. Z. Gu, Y. H. Yu, H. Zhang, H. Chen, Z. Lu, A. Fujishima, O. Sato, *Appl. Phys. A* **2005**, *81*, 47.
[19] G. R. Yi, J. H. Moon, V. N. Manoharan, D. J. Pine, S. M. Yang, *J. Am. Chem. Soc.* **2002**, *124*, 13354.
[20] Z. Z. Gu, A. Fujishima, O. Sato, *Chem. Mater.* **2002**, *14*, 760.
[21] P. Jiang, J. F. Bertone, K. S. Hwang, V. L. Colvin, *Chem. Mater.* **1999**, *11*, 2132.
[22] H. Yang, K. Nagai, X. Zhao, H. Chen, Z.-Z. Gu, *J. Nanosci. Nanotechnol.* **2005**, *5*, 1821.
[23] K. Nagai, M. Nakajima, T. Norimatsu, Y. Izawa, T. Yamanaka, *J. Polym. Sci. Part A* **2000**, *38*, 3412.
[24] P. Vukusic, I. Hooper, *Science* **2005**, *310*, 1151.

 © 2006 Wiley-VCH Verlag GmbH & Co. KGaA, Weinheim

Ferrocene Aggregates

DOI: 10.1002/anie.200601820

Mono- and Dimetalated Ferrocenylcopper Complexes by Tin–Copper Exchange**

*Krishnan Venkatasubbaiah, Antonio G. DiPasquale, Michael Bolte, Arnold L. Rheingold, and Frieder Jäkle**

Metalated ferrocenes have received tremendous interest owing to their importance as reagents in the preparation of other ferrocene derivatives and their often intriguing structural features.[1] For instance, lithioferrocene and 1,1′-dilithioferrocene are key intermediates for a variety of ferrocene derivatives, including ferrocene-based ligands for catalysis and ferrocene-containing polymers.[1] The pentamethyldiethylenetriamine (pmdeta) complex of 1,1′-dilithioferrocene[2] has been confirmed to be a dimer with the lithium atoms bridging the two cyclopentadienyl (Cp) rings of one ferrocene and another Cp ring of a neighboring ferrocene. Complexation with tetramethylethylenediamine (tmeda) leads to a trimeric structure in which the Cp rings of one of the ferrocene moieties are doubly bridged by lithium.[3] Similarly unusual multiply deprotonated species with sodium and magnesium have been reported recently.[4] Although organocopper compounds play an increasingly important role as reagents in organic and organometallic synthesis,[5] the respective ferrocenylcopper derivatives have received comparatively less attention and little is known about their structural features. The only crystallographically characterized derivative of ferrocenylcopper to date is the tetrameric *ortho*-substituted derivative $[2\text{-}FcCH_2NMe_2Cu]_4$ ($Fc = (\eta^5\text{-}C_5H_5)Fe(\eta^5\text{-}C_5H_3)$).[6] Polymeric structures are presumably formed in the absence of the dimethylaminomethyl groups,[5c] and these break up in the presence of donor solvents and can only be solubilized in the form of the adducts.[7]

Herein we describe a new approach taking advantage of the facile and highly selective formation of heteroleptic copper complexes in a novel reaction between aryltin species and pentafluorophenylcopper.[8] The resulting soluble aggregates provide a rare insight into the structural complexity of highly aggregated arylenedicopper species. We also discuss possible interactions between the iron atom of ferrocene and the pendant Lewis acidic organocopper substituents. The ability of the central metal to form dative bonds to other Lewis acidic metals is an intriguing feature of metallocenes that has direct implications for the mechanism of electrophilic aromatic substitution with metallocenes.[9] In the case of ferrocene, bonding metal–metal interactions were first discovered for adducts with mercury salts[10,11] and have since been confirmed for [3]ferrocenophanes, such as $[Fe(C_5H_4S)_2M(PR_3)]$ (M = Ni, Pd, Pt)[12] and $[\{Fe(C_5H_4NSiMe_3)_2TiCl\}_2]^{2+}$[13] and are broadly debated for other ferrocene species.[2,3,14,15] We report on the discovery of an intriguing ferrocene complex in which the iron atom appears to interact simultaneously with two Lewis acidic metal centers.

A solution of $[FcSnMe_3]$ (**1**) in hexanes was treated with half an equivalent of $[C_6F_5Cu]_4$[16,17] in toluene at ambient temperature (Scheme 1).[18] The color of the mixture gradually changed from yellow to orange. Crystallization at −35 °C yielded the arylcopper complex **2** as an orange crystalline solid in 83 % yield. In contrast to the reported insolubility of $[FcCu]_n$,[5c] complex **2** was found to be very soluble in noncoordinating solvents. The incorporation of both ferrocenyl and pentafluorophenyl groups in the product was evident from the ^1H and ^{19}F NMR spectra. The typical signal pattern for a monosubstituted ferrocene was observed in the ^1H NMR spectrum, with two pseudo-triplets corre-

[*] Dr. K. Venkatasubbaiah, Prof. F. Jäkle
Department of Chemistry
Rutgers University Newark
73 Warren Street, Newark, NJ 07102 (USA)
Fax: (+1) 973-353-1264
E-mail: fjaekle@rutgers.edu
Homepage: http://www.andromeda.rutgers.edu/~fjaekle/
Dr. A. G. DiPasquale, Prof. A. L. Rheingold
Department of Chemistry and Biochemistry
University of California, San Diego
9500 Gilman Drive, La Jolla, CA 92093-0358 (USA)
Dr. M. Bolte
Institut für Anorganische Chemie
Johann Wolfgang Goethe-Universität Frankfurt
Max-von-Laue Strasse 7, 60438 Frankfurt am Main (Germany)

[**] Acknowledgment is made to the National Science Foundation (Career award CHE-0346828 to F.J.), to the Petroleum Research Fund, administered by the American Chemical Society, and to the Rutgers University Research Council for support of this research. F.J. is an Alfred P. Sloan Research Fellow.

Supporting Information for this article is available on the WWW under http://www.angewandte.org or from the author.

InterScience
© 2006 Wiley-VCH Verlag GmbH & Co. KGaA, Weinheim

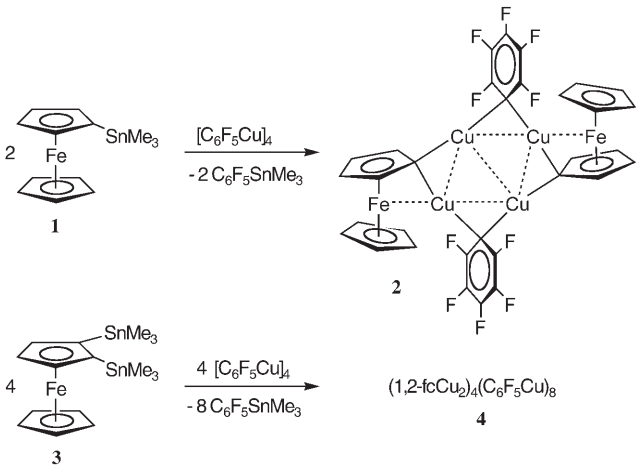

Scheme 1. Synthesis of **2** and **4** by tin–copper exchange. fc = $(\eta^5\text{-}C_5H_5)Fe(\eta^5\text{-}C_5H_3)$.

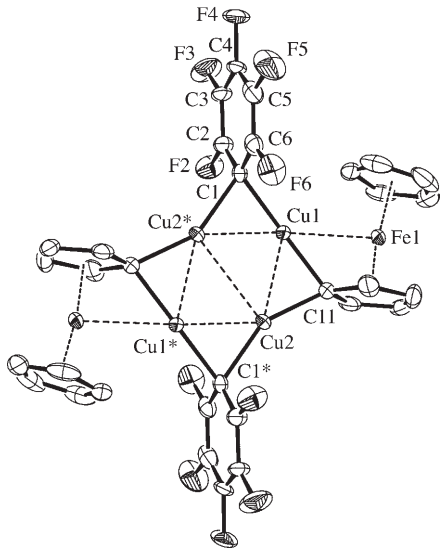

Figure 1. Molecular structure of **2**; hydrogen atoms and cocrystallized toluene molecules have been omitted for clarity. Selected interatomic distances [Å] and angles [°]: Cu1–Cu2 2.4865(8), Cu1–Cu2* 2.4331(8), Cu2–Cu2* 2.9631(12), Cu1–C1 2.018(5), Cu1–C11 1.971(5), Cu2–C11 1.969(5), Cu2–C1* 2.031(5), Cu1–Fe1 2.7011(9); C1–Cu1–C11 170.5(2), C11–Cu2–C1* 150.7(2), Cu1–Cu2–Cu1* 105.94(3), Cu2–Cu1–Cu2* 74.06(3), Cu1–Cu2–Cu2* 52.14(2), Cu1*–Cu2–Cu2* 53.79(2), Cu2–Cu1–Fe1 101.69(3), Cu2*–Cu1–Fe1 174.99(3). Symmetry operator for generating equivalent atoms (*): $1-x$, $1-y$, $1-z$.

sponding to the α- and β-protons ($\delta = 4.13$ and 4.82 ppm, respectively) and a singlet for the free Cp ring ($\delta = 3.99$ ppm). The chemical shift difference between the α- and β-protons ($\Delta\delta = 0.69$ ppm) is remarkable and reminiscent of that typically found for ring-tilted ferrocenophanes and/or metallocenes in which the metal is acting as a donor to other Lewis acidic metal centers.[11–13,15] The ^{19}F NMR spectrum of **2** shows a set of three slightly broadened resonances at $\delta = -106.9$, -148.9, and -160.2 ppm, which are in a similar range to those of $[C_6F_5Cu]_4$ (in $CDCl_3$: $\delta = -104.1$, -141.5, and -158.1 ppm),[17] thereby confirming the incorporation of "C_6F_5Cu" units into the product. However, the chemical shift difference ($\Delta\delta_{m,p} = 11.3$ ppm) between the *meta*- and *para*-fluorine substituents is considerably smaller than that observed for $[C_6F_5Cu]_4$ ($\Delta\delta_{m,p} = 16.6$ ppm).[17] This result indicates an increase in electron density at the copper sites owing to the presence of the ferrocenyl moieties. We have observed similar effects upon coordination of aromatic solvents, such as toluene or mesitylene, to $[C_6F_5Cu]_4$.[17]

A single-crystal X-ray analysis of **2** confirmed the formation of a rare example of a heteroleptic arylcopper complex with two ferrocene and two pentafluorophenyl units (Figure 1).[18] The ferrocene moieties are *trans* to each other and the central Cu_4 core in **2** shows a parallelogram geometry with one small and one large diagonal Cu···Cu distance (2.9631(12) and 3.9275(13) Å, respectively). These features are typical of tetrameric structures of arylcopper species in which two of the copper centers are coordinated by an additional donor ligand.[7,17] In contrast, the noncoordinated complexes $[2\text{-}FcCH_2NMe_2Cu]_4$[6] and $[C_6F_5Cu]_4$[16,17] adopt a square-planar geometry. The ferrocene moieties appear to act as additional coordinating groups, with Fe–Cu distances of 2.7011(9) Å that are close to the sum of the covalent radii of Cu and Fe (2.53 Å[19]) and considerably shorter than the Fe–Cu distances of 2.945(5) Å in $[2\text{-}FcCH_2NMe_2Cu]_4$.[6] The Cp rings are no longer parallel in **2**, presumably a result of the short Fe–Cu contacts, and show a tilt angle of 10.7° (for $[2\text{-}FcCH_2NMe_2Cu]_4$: 6.5°). Bending of metallocenes is known to lead to distinct changes in the frontier orbitals[20] and enhancement of the basicity of the central metal, which favors complex formation.[11] A comparison with a recent study by Enders et al. is noteworthy. They used quinolyl substituents in the 1,1′-positions of ferrocene and ruthenocene to support the binding of Cu and Zn salts to the metal center.[21] A short Ru···Cu contact of 2.633(1) Å was observed for the ruthenocene complex $[1,1'\text{-}Rc(quin)_2Cu]BF_4$ (Rc = ruthenocene, quin = 8-quinolyl) and the tilt angle between the Cp planes was found to be 7.6°.[22]

To investigate the possibility of multiple interactions[23] of Lewis acidic copper centers with the iron atom of ferrocene we treated the distannylated species $[1,2\text{-}fc(SnMe_3)_2]$ (**3**)[24] with $[C_6F_5Cu]_4$ (Scheme 1).[18] Treatment of a solution of **3** in hexanes with one equivalent of $[C_6F_5Cu]_4$ in toluene at ambient temperature led to a gradual change of the color of the mixture from light orange to wine red. Crystallization of the mixture at −35 °C yielded the arylcopper complex **4** as a dark-red crystalline solid in 77% yield. The thermal stability of **4** ($T_{decomp.} = 153$ °C) is similar to that of $[C_6F_5Cu]_4$, but **4** is comparatively less sensitive to air and moisture according to ^1H NMR studies.

The ^1H NMR spectrum of **4** shows one resonance for the free Cp rings at $\delta = 4.60$ ppm and three strongly downfield shifted signals of equal intensity for the substituted Cp rings at $\delta = 6.05$ (d), 5.77 (t), and 4.64 ppm (d), which suggests that the two α-hydrogen aroms are in different environments. Four doublets for the *ortho*-F, two triplets for the *para*-F, and four overlapping multiplets for the *meta*-F are observed in the ^{19}F NMR spectrum. This pattern is consistent with the presence of two different types of C_6F_5 groups in the product, where hindered rotation of the C_6F_5 groups leads to nonequivalent *ortho*- and *meta*-F atoms. This result suggests the

 © 2006 Wiley-VCH Verlag GmbH & Co. KGaA, Weinheim

presence of a highly rigid molecular framework, in contrast to the commonly observed fluxionality of copper aggregates in solution.[7]

Dark-red single crystals of [**4**(toluene)$_x$] (x is approximately 4 according to integration of the ^{1}H NMR spectrum) were obtained by recrystallization from toluene at low temperature. While the toluene molecules are highly disordered and were therefore removed using the "Squeeze" routine, the copper aggregate **4** itself showed no disorder and refined well (Figure 2a).[18] The crystal-structure analysis reveals that **4** is one of the most highly aggregated copper complexes to date, consisting of four 1,2-fcCu$_2$ and eight CuC$_6$F$_5$ groups for a total of 16 copper and four iron atoms.

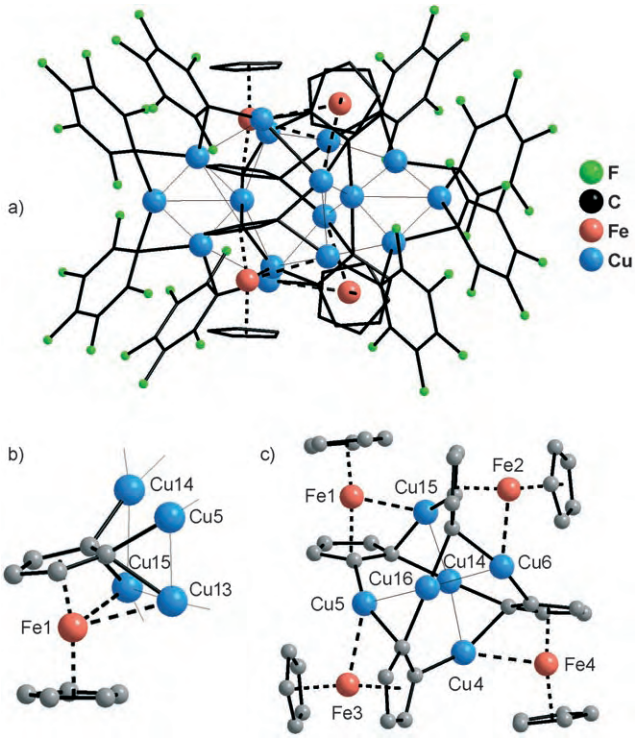

Figure 2. a) Molecular structure of **4**; hydrogen atoms have been omitted for clarity. Selected geometric parameters are provided in the Supporting Information. b) View of one ferrocene moiety with all Cu substituents; c) view of the $[fc_4Cu_6]^{2-}$ core.

Each ferrocene moiety is bound to four bridging copper centers, two of which are located above the Cp plane with the other two bound from the *endo* side (Figure 2b). However, in contrast to the arrangement in **2**, the ferrocene moieties are directly linked by copper atoms ("fc-Cu-fc" fragments in Figure 2c). Among the four copper atoms attached to each ferrocene moiety, three are involved in bridging interactions with other ferrocene units, which leads to a core of four ferrocene units and six copper centers. The fourth copper atom only bridges C$_6$F$_5$ groups. This arrangement results in the formation of two interlocked crown-like substructures, each of which consists of four CuC$_6$F$_5$ moieties (Figure 2a).

The Fe–Cu contacts in **4** range from 2.5702(9) to 2.6963(10) Å, and are thus even shorter than those in **2**. Interestingly, one shorter (2.5702(9)–2.5757(9) Å) and one longer Fe–Cu contact (2.6365(10)–2.6963(10) Å) are observed for each ferrocene moiety. Most closely related are the trianionic clusters (Bu$_4$N)$_3$[Cu$_5$(Fe(CO)$_4$)$_n$] (n = 3,5),[25] in which n Fe(CO)$_4$ fragments are covalently bound to a Cu$_n$ fragment, and the neutral clusters [Fe$_2$(CO)$_8$(μ-CuPR$_3$)$_2$] (R = *t*Bu, cyclohexyl).[26] The Fe–Cu contacts in **4** are close to or within the range of bonding Fe–Cu distances in these clusters (2.394–2.638 Å). Additional support for bonding interactions in **4** is provided by the strong bending of the *endo* Cu atoms toward Fe, which is reflected in small Cp$_{centroid}$–C–Cu angles that range from 132.28(2) to 124.78(2)° (*exo* Cu atoms: 150.61(2)–161.02(2)°). Moreover, the Cp rings in **4** are highly tilted, with interplanar angles of 15.4°, 15.5°, 16.7°, and 16.8° for the four ferrocene units (Figure 2b). A considerable deviation from linear geometry is observed for the Cu atoms that are close to Fe (C···Cu···C 153.8(2)–161.5(2)°), thus suggesting coordination by the Fe atoms, while Cu14 and Cu16 show a nearly linear arrangement (C···Cu···C 176.7(2)° and 179.5(2)°) (Figure 2c). Finally, it is noteworthy that the two Cu atoms in the *endo* positions are in close proximity to one another, with Cu···Cu distances (2.7180(9)–2.8255(9) Å) that are considerably smaller than those of the Cu pairs in the *exo* position (3.403–3.433 Å) and close to those in reported "FeCu$_2$" cluster fragments (2.582–2.691 Å).[25] The Cu–Fe–Cu angles of 62.06(3)–65.59(3)° compare favorably with the H–Mo–H angle of 75.5° in the related complex [Cp$_2$Mo(H)$_2$], which displays a similar bent geometry and has been shown to involve a set of suitable metallocene orbitals of 4a$_1$, 2b$_1$, and 3a$_1$ symmetry in bonding to the hydrogen atoms.[20,27]

The NMR spectroscopic data and geometric parameters of **2** and **4** suggest the possibility for (multiple) Fe–Cu interactions, which should also be reflected in the UV/Vis spectra. For instance, unusually strong absorption bands at 380 nm for the [2]ferrocenophane adduct [(C$_5$H$_4$CH$_2$)$_2$Fe]Hg(ClO$_4$)$_2$[11] and at 330 nm (ε = 35000 M^{-1} cm^{-1}) for the ruthenocene (Rc) complex [Rc-Hg-Rc](ClO$_4$)$_2$[28] have been reported. The UV/Vis spectra of orange **2** and dark-red **4** in CH$_2$Cl$_2$ are shown in comparison to those of ferrocene and [C$_6$F$_5$Cu]$_4$ in Figure 3. A strong enhancement and red-shift of the ferrocene absorption band at 438 nm (ε = 77) to 465 nm (ε = 450) for **2** and 457 nm (ε = 15750) for **4** is evident, and the intense red color of **4** can be attributed to tailing of the band

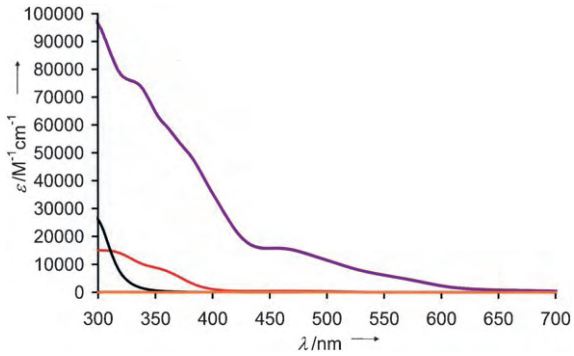

Figure 3. The UV/Vis spectra of **4** (purple), **2** (red), [C$_6$F$_5$Cu]$_4$ (black), and ferrocene (orange).

© 2006 Wiley-VCH Verlag GmbH & Co. KGaA, Weinheim

to about 650 nm. In addition, a very strong high-energy absorption band is found at 332 nm ($\varepsilon = 75\,500$) for **4**.

In conclusion, we have reported a new synthetic route to organocopper species by reaction of arylstannanes with pentafluorophenylcopper. The reaction offers an exceptionally mild route to heteroleptic complexes of organocopper species that are otherwise not easily accessible. Complex **4** provides a first insight into the structural complexity of multimetallic arylcopper species $ArCu_n$, which typically form polymeric aggregates and hence have evaded detailed structural characterization. Finally, the first structural and spectroscopic evidence that the iron atom in ferrocene may interact simultaneously with multiple transition-metal sites is presented. Further studies on the binding of multiple Lewis acid centers to ferrocene and other metallocenes are currently in progress.

Received: May 9, 2006
Published online: September 20, 2006

Keywords: clusters · copper · Lewis acids · sandwich complexes · tin

[1] *Ferrocenes* (Eds.: A. Togni, T. Hayashi), VCH, Weinheim, **1995**.
[2] M. Walczak, K. Walczak, R. Mink, M. D. Rausch, G. Stucky, *J. Am. Chem. Soc.* **1978**, *100*, 6382.
[3] I. R. Butler, W. R. Cullen, J. Ni, S. J. Rettig, *Organometallics* **1985**, *4*, 2196.
[4] a) K. W. Henderson, A. R. Kennedy, R. E. Mulvey, C. T. O'Hara, R. B. Rowlings, *Chem. Commun.* **2001**, 1678; b) W. Clegg, K. W. Henderson, A. R. Kennedy, R. E. Mulvey, C. T. O'Hara, R. B. Rowlings, D. M. Tooke, *Angew. Chem.* **2001**, *113*, 4020; *Angew. Chem. Int. Ed.* **2001**, *40*, 3902; c) P. C. Andrikopoulos, D. R. Armstrong, W. Clegg, C. J. Gilfillan, E. Hevia, A. R. Kennedy, R. E. Mulvey, C. T. O'Hara, J. A. Parkinson, D. M. Tooke, *J. Am. Chem. Soc.* **2004**, *126*, 11612; d) see also: H. R. L. Barley, W. Clegg, S. H. Dale, E. Hevia, G. W. Honeyman, A. R. Kennedy, R. E. Mulvey, *Angew. Chem.* **2005**, *117*, 6172; *Angew. Chem. Int. Ed.* **2005**, *44*, 6018.
[5] a) N. Krause, *Modern Organocopper Chemistry*, Wiley-VCH, Weinheim, **2002**; b) A. Sundararaman, F. Jäkle, *J. Organomet. Chem.* **2003**, *681*, 134; c) Y. Qin, G. Cheng, A. Sundararaman, F. Jäkle, *J. Am. Chem. Soc.* **2002**, *124*, 12672. For the use of $(FcCu)_n$ and $(1,1'\text{-}fcCu_2)_n$ as intermediates in organic synthesis see, for example: d) A. N. Nesmeyanov, N. N. Sedova, V. A. Sazonova, S. K. Moiseev, *J. Organomet. Chem.* **1980**, *185*, C6; e) H. Schottenberger, M. Buchmeiser, J. Polin, K.-E. Schwarzhans, *Z. Naturforsch. Teil B* **1993**, *48*, 1524.
[6] A. N. Nesmeyanov, Y. T. Struchkov, N. N. Sedova, V. G. Andrianov, Y. V. Volgin, V. A. Sazonova, *J. Organomet. Chem.* **1977**, *137*, 217.
[7] G. van Koten, S. L. James, J. T. B. H. Jastrzebski in *Comprehensive Organometallic Chemistry*, *Vol. 3* (Eds.: E. W. Abel, F. G. A. Stone, G. Wilkinson), Pergamon, Oxford, **1995**, chap. 2.
[8] The Sn/Cu exchange with $[C_6F_5Cu]_4$ is a general reaction that is applicable to a wide variety of $ArSnMe_3$ substrates.
[9] A. F. Cunningham, *Organometallics* **1997**, *16*, 1114.
[10] a) W. H. Morrison, Jr., D. N. Hendrickson, *Inorg. Chem.* **1972**, *11*, 2912; b) M. Watanabe, A. Nagasawa, M. Sato, I. Motoyama, T. Takayama, *Bull. Chem. Soc. Jpn.* **1998**, *71*, 1071.
[11] M. Watanabe, H. Ichikawa, I. Motoyama, H. Sano, *Bull. Chem. Soc. Jpn.* **1983**, *56*, 3291.
[12] a) D. Seyferth, B. W. Hames, T. G. Rucker, M. Cowie, R. S. Dickson, *Organometallics* **1983**, *2*, 472; b) M. Cowie, R. S. Dickson, *J. Organomet. Chem.* **1987**, *326*, 269; c) S. Akabori, T. Kumagai, T. Shirahige, S. Sato, K. Kawazoe, C. Tamura, M. Sato, *Organometallics* **1987**, *6*, 526; d) S. Takemoto, S. Kuwata, Y. Nishibayashi, M. Hidai, *Inorg. Chem.* **1998**, *37*, 6428.
[13] A. Shafir, J. Arnold, *J. Am. Chem. Soc.* **2001**, *123*, 9212.
[14] a) A. N. Nesmeyanov, E. G. Perevalova, K. I. Grandberg, D. A. Lemenovskii, T. V. Baukova, O. B. Afanasova, *J. Organomet. Chem.* **1974**, *65*, 131; b) R. Broussier, A. Da Rold, B. Gautheron, Y. Dromzee, Y. Jeannin, *Inorg. Chem.* **1990**, *29*, 1817; c) W. R. Cullen, S. J. Rettig, T. C. Zheng, *Organometallics* **1992**, *11*, 3434; d) A. Bucaille, T. Le Borgne, M. Ephritikhine, J.-C. Daran, *Organometallics* **2000**, *19*, 4912; e) A. Althoff, P. Jutzi, N. Lenze, B. Neumann, A. Stammler, H.-G. Stammler, *Organometallics* **2002**, *21*, 3018; f) M. Scheibitz, R. F. Winter, M. Bolte, H.-W. Lerner, M. Wagner, *Angew. Chem.* **2003**, *115*, 954; *Angew. Chem. Int. Ed.* **2003**, *42*, 924; g) H. Braunschweig, C. Burschka, G. K. B. Clentsmith, T. Kupfer, K. Radacki, *Inorg. Chem.* **2005**, *44*, 4906; h) I. Sänger, J. B. Heilmann, M. Bolte, H.-W. Lerner, M. Wagner, *Chem. Commun.* **2006**, 2027.
[15] A. Berenbaum, H. Braunschweig, R. Dirk, U. Englert, J. C. Green, F. Jäkle, A. J. Lough, I. Manners, *J. Am. Chem. Soc.* **2000**, *122*, 5765.
[16] A. Cairncross, W. A. Sheppard, E. Wonchoba, W. J. Guildford, C. B. House, R. M. Coates, *Org. Synth.* **1980**, *59*, 122.
[17] A. Sundararaman, R. A. Lalancette, L. N. Zakharov, A. L. Rheingold, F. Jäkle, *Organometallics* **2003**, *22*, 3526.
[18] Experimental details are provided in the Supporting Information. CCDC-606886 (**2**) and CCDC-606885 (**4**) contain the supplementary crystallographic data for this paper. These data can be obtained free of charge from The Cambridge Crystallographic Data Centre via www.ccdc.cam.ac.uk/data_request/cif.
[19] J. E. Huheey, E. A. Keiter, R. L. Keiter, *Inorganic Chemistry: Principles of Structure and Reactivity*, 4th ed., Harper Collins, New York, **1993**.
[20] J. C. Green, *Coord. Chem. Rev.* **1998**, *27*, 263.
[21] M. Enders, G. Kohl, H. Pritzkow, *Organometallics* **2002**, *21*, 1111.
[22] A relatively large Fe–Cu distance of 3.23 Å has been observed for a related complex with 2-pyridyl groups as ligands: B. Neumann, U. Siemeling, H.-G. Stammler, U. Vorfeld, J. G. P. Delis, P. W. N. M. van Leeuwen, K. Vrieze, J. Fraanje, K. Goubitz, F. Fabrizi di Biani, P. Zanello, *J. Chem. Soc. Dalton Trans.* **1997**, 4705.
[23] Multiply borylated ferrocenes have been reported, but recent studies indicate that a delocalized interaction through the Cp ligands rather than direct Fe–B bonding is operative in these systems: a) M. Scheibitz, M. Bolte, J. W. Bats, H.-W. Lerner, I. Nowik, R. H. Herber, A. Krapp, M. Lein, M. Holthausen, M. Wagner, *Chem. Eur. J.* **2005**, *11*, 584. See also: b) W. Ruf, T. Renk, W. Siebert, *Z. Naturforsch. Teil B* **1976**, *31*, 1028; c) B. Wrackmeyer, U. Dörfler, M. Herberhold, *Z. Naturforsch. Teil B* **1993**, *48*, 121; d) A. Appel, H. Nöth, M. Schmidt, *Chem. Ber.* **1995**, *128*, 621; e) K. Venkatasubbaiah, L. N. Zakharov, W. S. Kassel, A. L. Rheingold, F. Jäkle, *Angew. Chem.* **2005**, *117*, 5564; *Angew. Chem. Int. Ed.* **2005**, *44*, 5428.
[24] K. Venkatasubbaiah, J. W. Bats, A. L. Rheingold, F. Jäkle, *Organometallics* **2005**, *24*, 6043.
[25] G. Doyle, K. A. Eriksen, D. V. Engen, *J. Am. Chem. Soc.* **1986**, *108*, 445.
[26] H. Deng, D. W. Knoeppel, S. G. Shore, *Organometallics* **1992**, *11*, 3472.
[27] A. J. Schultz, K. L. Stearley, J. M. Williams, R. Mink, G. D. Stucky, *Inorg. Chem.* **1977**, *16*, 3303.
[28] D. N. Hendrickson, Y. S. Sohn, W. H. Morrison, Jr., H. B. Gray, *Inorg. Chem.* **1972**, *11*, 808.

 © 2006 Wiley-VCH Verlag GmbH & Co. KGaA, Weinheim

Polycycles

DOI: 10.1002/anie.200602539

Two-Directional Annelation: Dual Benzyne Cycloadditions Starting from Bis(sulfonyloxy)diiodobenzene**

*Toshiyuki Hamura, Tetsu Arisawa, Takashi Matsumoto, and Keisuke Suzuki**

The construction of polycyclic structures with diverse functionalities is one of the subjects often encountered in the synthesis of natural and non-natural products. In this context, we became interested in two-directional annelations, that is, dual annelation of two rings onto a given core ring [Eq. (1)],

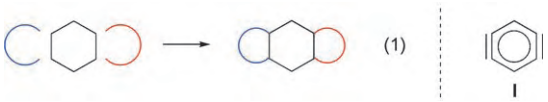

which would allow for the expeditious assembly of polycycles.[1] In particular, we were intrigued by the use of a formal equivalent to 1,4-benzdiyne (**I**), as it could serve as a reactive platform for linearly fused polycyclic compounds.[2,3]

We previously reported an efficient protocol for the generation of benzyne species from a 2-iodoaryl triflate by the rapid halogen–lithium exchange with *n*BuLi at low temperature,[4] and its regioselective trapping by furans,[4] nitrones,[5] and ketene silyl acetals (KSAs).[6] Herein, we disclose dual cycloadditions of benzynes successively generated in one pot from bis(sulfonyloxy)diiodobenzene (**III**), which can be viewed as a synthetic equivalent of 3-alkoxy-1,4-benzdiyne **II** (Scheme 1).[7] Importantly, selective halogen–lithium exchange of **III** enables the tandem generation of benzynes and dual cycloadditions with two identical or different arynophiles (steps 1 and 2). The presence of an alkoxy group on the central benzene ring is key to this strategy, as it directs the regioselectivity of both cycloaddition steps, thus allowing access to selectively functionalized polycyclic compounds.

Scheme 2 shows the model reactions for the stepwise generation of two benzyne species from bis-sulfonate **1**,[8] which was trapped by KSA **2** as an arynophile. Upon treatment of **1** with *n*BuLi (0.53 M in hexane; 1.05 equiv) in

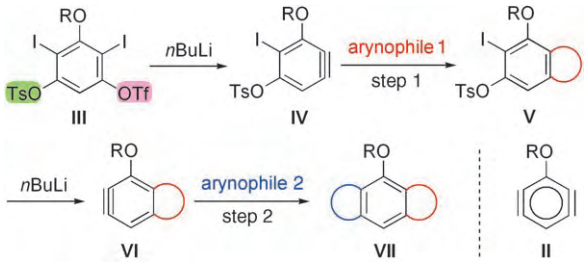

Scheme 1. Stepwise generation of benzynes and iterative cycloadditions. Ts = *p*-toluenesulfonyl; Tf = trifluoromethanesulfonyl.

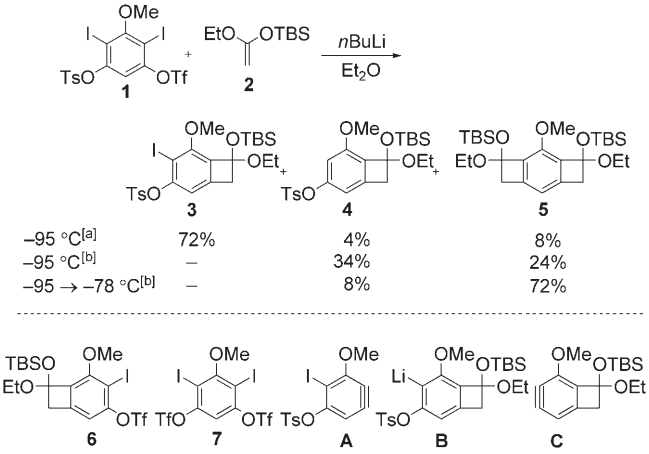

Scheme 2. Stepwise generation of benzynes from bis-sulfonate **1**. [a] 1.05 equiv *n*BuLi. [b] 2.3 equiv *n*BuLi. TBS = *tert*-butyldimethylsilyl.

the presence of KSA **2** (Et_2O, −95 °C, 5 min), the [2+2] cycloaddition proceeded cleanly to give mono-cycloadduct **3** in 72 % yield. Small amounts of mono-cycloadduct **4** without an iodine atom (4 %) and bis-adduct **5** (8 %) were also obtained.[9–11]

Importantly, note that no trace was identified of the alternative cycloadduct **6**, which arises from the benzyne generation at the iodo-tosylate side of **1**. In sharp contrast, a similar reaction of bis-triflate **7** (Et_2O, −95 °C, 5 min) did not stop at the mono-cycloaddition stage, thus giving a low yield of mono-cycloadduct **6** (14 %) and bis-cycloadduct **5** (13 %).

Careful choice of the stoichiometry and the reaction temperature proved decisive for the controlled generation of the second benzyne species. When the reaction of bis-sulfonate **1** was performed with 2.3 equivalents of *n*BuLi at −95 °C, bis-cycloadduct **5** was obtained (24 %) along with a considerable amount of mono-cycloadduct **4** which lacks the iodine atom (34 %). This result implies that aryllithium species **B** generated by the I–Li exchange of the initial product **3** has a finite lifetime at −95 °C.

On the other hand, if the same reaction was performed initially at −95 °C followed by warming to −78 °C, bis-cycloadduct **5** was obtained as almost the exclusive product in high yield and as a single regioisomer. Lithiated species **B** undergoes 1,2-elimination of lithium *p*-toluenesulfonate (LiOTs) at −78 °C to generate the second benzyne species **C**. These behaviors provided us with the handle to control bis-annelations in one pot with different arynophiles (see below).

[*] Dr. T. Hamura, T. Arisawa, Dr. T. Matsumoto, Prof. Dr. K. Suzuki
Department of Chemistry
Tokyo Institute of Technology
and SORST Japan Science and Technology Agency (JST)
2-12-1 O-okayama, Meguro-ku, Tokyo 152-8551 (Japan)
Fax: (+81) 3-5734-2788
E-mail: ksuzuki@chem.titech.ac.jp

[**] Partial financial support provided by the 21st Century COE program is gratefully acknowledged.

Supporting information for this article is available on the WWW under http://www.angewandte.org or from the author.

InterScience
© 2006 Wiley-VCH Verlag GmbH & Co. KGaA, Weinheim

The selective formation of cycloadduct **5** is notable for two points: 1) this cycloadduct is a highly strained benzene unit that comprises two four-membered rings,[12] and 2) it is a sterically encumbered regioisomer, in which the two silyl acetals are located near the methoxy group. As reported previously, a methoxy group located *ortho* to the benzyne species exerts a significant directing effect to encourage head-to-head cycloaddition,[6] which in the present case worked twice in two successive cycloadditions of benzynes **A** and **C** (Scheme 3).

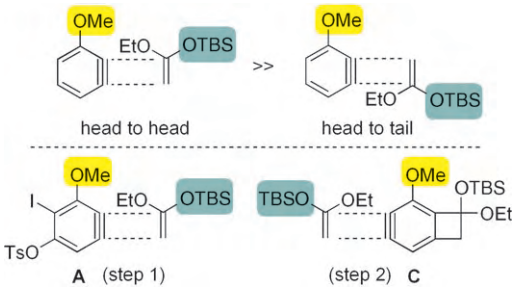

Scheme 3. Head-to-head mode in two iterative [2+2] cycloadditions.

Table 1 shows the results of this one-pot bis-cycloaddition with various arynophiles. A typical experimental procedure is represented by double furan cycloadditions (Table 1, entry 1): *n*BuLi (2.4 equiv in hexane) was slowly added at −78 °C to a mixture of bis-sulfonate **1** and furan (**8**, 3.0 equiv) in THF. The reaction was stopped after 5 minutes by adding water. Extractive workup followed by purification by column chromatography on silica gel gave bis-cycloadduct **11** in 81 % yield.[13] Similarly, isobenzofuran **9** proved to be applicable for dual [2+4] cycloadditions, thus affording heptacycle **12** in 69 % yield (Table 1, entry 2). The corresponding reaction with nitrone **10** (Table 1, entry 3) proceeded regioselectively to give the single regioisomeric bis-[2+3] cycloadduct **13**, in which the oxygen atom of the nitrone is located away from the methoxy group, in 41 % yield.

Moreover, two different rings could be fused to the central benzene unit in one pot by using two different arynophiles at different temperatures (Table 2). Upon treatment of bis-sulfonate **1** with *n*BuLi (1.1 equiv) in hexane in the presence of KSA **2** (1.2 equiv) in Et_2O at −95 °C, the starting material was quickly consumed and the formation of the mono-cycloadduct **3** was observed by TLC. The second arynophile, nitrone **10** (3.0 equiv), in THF[14] was added to the reaction mixture at −95 °C, and the temperature was raised to −78 °C. *n*BuLi (1.1 equiv) was slowly added to the reaction mixture to give the unsymmetrical bis-cycloadduct **14** in 68 % yield as a single regioisomer (Table 2, entry 1). In a similar manner, the successive [2+4] and [2+2] cycloadditions with furan (**8**) and KSA **2** gave the corresponding cycloadduct **15** in 68 % yield with perfect regioselectivity

Table 1: Symmetrical dual cycloaddition of the 1,4-benzdiyne equivalent **1** with various arynophiles.

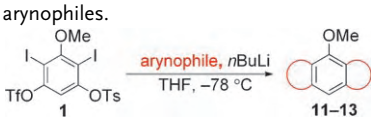

Entry	Arynophile		Bis-cycloadduct		Yield [%][a]
1		**8**	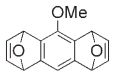	**11**	81
2		**9**	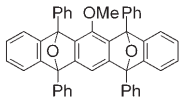	**12**	69
3		**10**	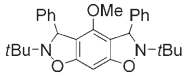	**13**	41

[a] *Syn*/*anti* mixture (see Ref. [8]).

(Table 2, entry 2). The dual reactions with **8** (arynophile 1) and nitrone **10** (arynophile 2) also gave cycloadduct **16** exclusively (Table 2, entry 3). In these reactions, each cycloaddition should be performed with consideration of the relative reactivity of the arynophiles, because the remaining highly reactive arynophile after the first cycloaddition can compete with the second arynophile with lower reactivity in the second cycloaddition to give a significant amount of the symmetrical bis-cycloadduct.[15] The successive processes also proved to be applicable to KSA **2** and 2-methoxyfuran (**18**), thus giving the highly oxygenated tricycle **17**, which could serve as a synthetic intermediate for further elaboration to polyaromatic systems (Table 2, entry 4).

In summary, dual cycloadditions of 1,4-benzdiyne equivalents with various arynophiles allowed the rapid construction of various highly functionalized bis-cycloadducts, which are amenable to selective transformation en route to polycyclic compounds. Synthetic applications are under active investigation.

Table 2: Unsymmetrical dual cycloaddition of the 1,4-benzdiyne equivalent with various arynophiles.

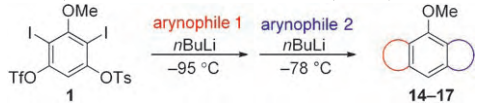

Entry	Arynophile 1		Arynophile 2		Bis-cycloadduct		Yield [%]
1[a]		**2**		**10**	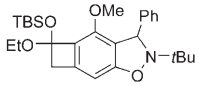	**14**	68[b]
2[c]		**8**	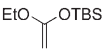	**2**	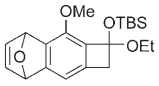	**15**	68[b]
3[a]		**8**		**10**	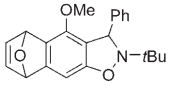	**16**	61[b]
4[c]		**2**		**18**	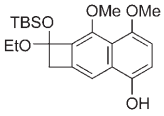	**17**	58

[a] Et_2O was used as the solvent for the first cycloaddition; the second arynophile was added as a solution in THF. [b] *Syn*/*anti* mixture (see Ref. [8]). [c] In Et_2O.

© 2006 Wiley-VCH Verlag GmbH & Co. KGaA, Weinheim

Experimental Section

Synthesis of bis-adduct **14**: *n*BuLi (0.53 M in hexane, 0.50 mL, 0.27 mmol) was added to a mixture of bis-sulfonate **1** (170 mg, 0.25 mmol) and KSA **2** (58.4 mg, 0.29 mmol) in Et_2O (2.5 mL) at −95 °C. After 5 min, nitrone **10** (135 mg, 0.76 mmol) in THF (1.0 mL) was added to the reaction mixture at −95 °C, to which *n*BuLi (0.53 M in hexane, 0.50 mL, 0.27 mmol) was then slowly added at −78 °C. After 5 min, the reaction was quenched by adding water. The products were extracted with EtOAc (3 × 10 mL), and the combined organic extracts were washed with brine, dried (Na_2SO_4), and concentrated in vacuo. The residue was purified by flash column chromatography on silica gel (98:2 hexane/EtOAc) to afford the less polar adduct **14** (39.9 mg, 32.9 %) and more polar adduct **14** (42.5 mg, 35.0 %).

Received: June 24, 2006
Revised: July 29, 2006
Published online: September 22, 2006

Keywords: arynes · chemoselectivity · cycloaddition · polycycles · regioselectivity

[1] K. P. C. Vollhardt, *Angew. Chem.* **1984**, *96*, 525 – 541; *Angew. Chem. Int. Ed. Engl.* **1984**, *23*, 539 – 556.
[2] For reviews on arynes, see: a) R. W. Hoffmann, *Dehydrobenzene and Cycloalkynes*, Academic, New York, **1967**; b) S. V. Kessar in *Comprehensive Organic Synthesis*, *Vol. 4* (Ed.: B. M. Trost), Pergamon, Oxford, UK, **1991**, pp. 483 – 515; c) H. Pellissier, M. Santelli, *Tetrahedron* **2003**, *59*, 701 – 730; d) H. H. Wenk, M. Winkler, W. Sander, *Angew. Chem.* **2003**, *115*, 518 – 546; *Angew. Chem. Int. Ed.* **2003**, *42*, 502 – 528.
[3] Use of this reactive species, even as its synthetic equivalents, has been quite limited; for pioneering studies on the generation and trapping of 1,4-benzdiyne equivalents, see: a) H. Hart, D. Ok, *J. Org. Chem.* **1986**, *51*, 979 – 986; b) H. Hart, C.-Y. Lai, G. Nwokogu, S. Shamouilian, A. Teuerstein, C. Zlotogorski, *J. Am. Chem. Soc.* **1980**, *102*, 6649 – 6651; for other recent examples, see: c) Y.-L. Chen, J.-Q. Sun, X. Wei, W.-W. Wong, A. W. M. Lee, *J. Org. Chem.* **2004**, *69*, 7190 – 7197; d) G. E. Morton, A. G. M. Barrett, *J. Org. Chem.* **2005**, *70*, 3525 – 3529; e) I. I. Schuster, L. Cracium, D. M. Ho, R. A. Pascal, Jr., *Tetrahedron* **2002**, *58*, 8875 – 8882; f) H. M. Duong, M. Bendikov, D. Steiger, Q. Zhang, G. Sonmez, J. Yamada, F. Wudl, *Org. Lett.* **2003**, *5*, 4433 – 4436.
[4] a) T. Matsumoto, T. Hosoya, M. Katsuki, K. Suzuki, *Tetrahedron Lett.* **1991**, *32*, 6735 – 6736; b) T. Hosoya, E. Takashiro, T. Matsumoto, K. Suzuki, *J. Am. Chem. Soc.* **1994**, *116*, 1004 – 1015.
[5] T. Matsumoto, T. Sohma, S. Hatazaki, K. Suzuki, *Synlett* **1993**, 843 – 846.
[6] a) T. Hosoya, T. Hasegawa, Y. Kuriyama, T. Matsumoto, K. Suzuki, *Synlett* **1995**, 177 – 179; b) T. Hosoya, T. Hamura, Y. Kuriyama, K. Suzuki, *Synlett* **2000**, 520 – 522; c) T. Hamura, T. Hosoya, H. Yamaguchi, Y. Kuriyama, M. Tanabe, M. Miyamoto, Y. Yasui, T. Matsumoto, K. Suzuki, *Helv. Chim. Acta* **2002**, *85*, 3589 – 3604.
[7] We recently reported a viable route to functionalized tricyclobutabenzenes by exploiting benzyne–KSA [2+2] cycloaddition chemistry; see: a) T. Hamura, Y. Ibusuki, H. Uekusa, T. Matsumoto, K. Suzuki, *J. Am. Chem. Soc.* **2006**, *128*, 3534 – 3535; b) T. Hamura, Y. Ibusuki, H. Uekusa, T. Matsumoto, J. S. Siegel, K. K. Baldridge, K. Suzuki, *J. Am. Chem. Soc.* **2006**, *128*, 10032 – 10033.
[8] See the Supporting Information for details.
[9] Recently, the related chemoselective generation of polyfunctionalized arynes by I–Mg exchange of 2-iodophenyl sulfonates was developed; see: a) I. Sapountzis, W. Lin, M. Fisher, P. Knochel, *Angew. Chem.* **2004**, *116*, 4464 – 4466; *Angew. Chem. Int. Ed.* **2004**, *43*, 4364 – 4366; b) W. Lin, I. Sapountzis, P. Knochel, *Angew. Chem.* **2005**, *117*, 4330 – 4333; *Angew. Chem. Int. Ed.* **2005**, *44*, 4258 – 4261.
[10] For related regioselective halogen–lithium exchange of dihalobenzenes, see: M. Dabrowski, J. Kubicka, S. Lulinski, J. Serwatowski, *Tetrahedron* **2005**, *61*, 6590 – 6595.
[11] When the same reaction was performed in THF, mono-cycloadduct **3** and bis-cycloadduct **5** were obtained (52 and 10 %, respectively).
[12] R. Gray, L. G. Harruff, J. Krymowski, J. Peterson, V. Boekelheides, *J. Am. Chem. Soc.* **1978**, *100*, 2892 – 2893.
[13] The use of Et_2O as solvent led to a lower yield of **11** (71 %), presumably as a result of the low solubility of the initially formed mono-cycloadduct.
[14] The second arynophile, nitrone **10** was added in solution with THF because of its insolubility in Et_2O.
[15] The following order of reactivity was assessed by a competition experiment: nitrone **10** > KSA **2** > furan (**8**). The reaction of alkoxybenzyne with the same amount of **2**, **10**, and **8** gave the [2+3] cycloadduct (56 %), the [2+2] cycloadduct (30 %), and the [2+4] cycloadduct (13 %), respectively (see the Supporting Information).

 © 2006 Wiley-VCH Verlag GmbH & Co. KGaA, Weinheim

Macrocycles

DOI: 10.1002/anie.200602790

Efficient Macrocyclization of Preorganized Palindromic Oligosquaramides**

Carmen Rotger, M. Neus Piña, Manuel Vega, Pablo Ballester, Pere M. Deyà, and Antoni Costa**

Nature has evolved polymers with highly specific functions. In the last decade, a new generation of natural circular proteins has been found in bacteria, plants, and mammals.[1] These large cycles show exceptional stability and a wide range of

[*] Dr. C. Rotger, Dr. M. N. Piña, M. Vega, Prof. P. M. Deyà, Prof. A. Costa
Departament de Química
Universitat de les Illes Balears
Ctra. Valldemossa km 7.5
07122 Palma de Mallorca (Spain)
Fax: (+34) 971-173-426
E-mail: carmen.rotger@uib.es
antoni.costa@uib.es

Dr. P. Ballester
ICREA and Institute of Chemical Research of Catalonia (ICIQ)
Avgda. Països Catalans
s/n, 43007, Tarragona (Spain)

[**] We thank the DGI of Spain for support of this study (CTQ2005-08989) and Dr. Gabriel Martorell (SCT) for technical assistance. C.R. thanks the MEC and the DGR+D+I (Govern Balear) for cofunding within the Ramón y Cajal program, and M.N.P. thanks the DGR+D+I (Govern Balear) for a predoctoral fellowship.

Supporting information for this article is available on the WWW under http://www.angewandte.org or from the author.

WILEY InterScience DISCOVER SOMETHING GREAT
© 2006 Wiley-VCH Verlag GmbH & Co. KGaA, Weinheim

biomedical activities, from insecticidal and antimicrobial to anti-HIV properties. Furthermore, they are ideal templates for engineering similar macromolecules of non-natural oligomers for potential biomedical applications.[2]

The incorporation of turn segments in the linear precursor is frequently the strategy of choice for cyclization reactions.[3] However, to our knowledge, examples of successful macrocyclization that occur with non-natural hydrogen-bonded self-templated precursors in polar solvents are rare.[4] Herein, we report on the application of preorganized oligosquaramides of different sizes, for the synthesis of tailor-made macrocycles in methanol.

The most studied families of non-natural oligomers with well-defined conformations in solution are aliphatic,[5] but several aromatic oligomers based on amide,[6] urea,[7] and hydrazide[8] linkages have also been shown to adopt stable conformations in solution. Such molecules, termed foldamers,[9,5b] represent a significant step forward to achieving fully synthetic protein analogues. Among those, squaramides, which can be considered as vinylogous amides, are versatile molecules with considerable hydrogen-bonding capabilities and favorable dynamic properties that allow them to adopt secondary structures. Previously, we have shown the ability of some secondary disquaramides, stabilized by an intramolecular hydrogen bond, to fold into a U-turn module in polar and nonpolar solvents.[10]

The new family of oligomer reported herein is based on squaramide modules and aliphatic linkages, as represented by the general structure shown in Figure 1. These oligomers are palindromically constituted with a flexible backbone and have a related structure to the foldable module.

The modular synthesis of the novel oligosquaramides **1**–**5** was achieved through standard condensation reactions of the squaramide building blocks in good-to-moderate yields (55–95%).[11]

The resulting structural symmetry of **1**–**5** is readily apparent in the 1D ^{1}H NMR spectra recorded in $CDCl_3$ (Figure 1). The peaks are relatively sharp, and the resonance for the squaramide hydrogen atoms are concentration-independent (0.5–20 mM) and shifted downfield relative to the corresponding chemical shift found for squaramide hydrogen atoms ($\delta = 6.2$–5.4 ppm), which lack hydrogen-bonding potential.[10] Compounds **2**–**5** show two different peaks assignable to the squaramide hydrogen atoms at $\delta = 7.5$ and 8.2 ppm, respectively, thus suggesting that they reside in different chemical environments. The downfield area of the squaramide hydrogen peaks varies depending on the number of squaramide modules in the oligomer skeleton, and the integrated area of the upfield peak remains equal to two in all the oligomers.

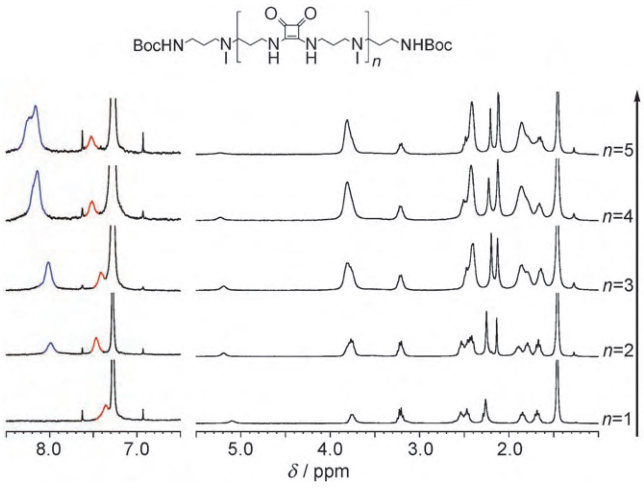

Figure 1. Top: General structure of the oligosquaramides ($n = 1$–5 for **1**–**5**, respectively; Boc = *tert*-butyloxycarbonyl). Bottom: Partial ^{1}H NMR (300 MHz) spectra of **1**–**5** in $CDCl_3$.

Stabilization of a well-defined and stable folded conformation with common structural features to all the oligomers was studied by ^{1}H NMR and UV/Vis spectroscopy. A diffusion NMR experiment (DOSY) of **1**–**5** in $CDCl_3$ completely discards any aggregation at the oligomer level, and a good correlation was found for the logarithms of molecular weight and the diffusion coefficients (Figure 2).

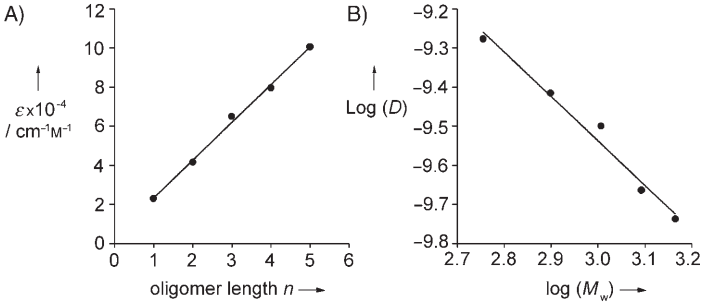

Figure 2. A) The molar extinction coefficients (ε at 292 nm) in $CHCl_3$ versus oligomer length (n). B) Logarithmic plot of the diffusion coefficient (D) versus the molecular weight (M_w) of the oligomer.

Furthermore, variable-temperature (VT) ^{1}H NMR experiments from 243 to 298 K performed in $CDCl_3$ of samples of **1**–**5** (2 mM) revealed a small upfield shift for all the squaramide protons signals. The observed coefficients for the rate of change of the NH squaramide protons with temperature are less than or equal to -6.56 ppb K^{-1}, as expected for intramolecularly hydrogen-bonded protons.[12] It is also observed that the values of these coefficients decrease when the number of squaramide units in the oligomer skeleton increase. The NH squaramide peak at $\delta = 8.2$ ppm in **3**–**5** splits at 283 K, thus suggesting the existence of a dynamic process involving the hydrogen-bonded protons.

The UV/Vis spectra of **1**–**5** were also recorded in $CDCl_3$. The molar extinction coefficient (ε) was determined for each oligomer over the range of concentrations 10^{-4}–10^{-5} M. The Lambert–Beer law was observed for each compound, as expected for monomeric systems. The calculated ε values at 292 nm ($\varepsilon = 23088$, 41585, 64921, 79544, and 100559 M^{-1} cm^{-1} for **1**–**5**, respectively) exhibit linear relationships with the number of squaramide residues in the strand, thus implying an absence of stacking for the squaramide chromophore as a result of the secondary structure (Figure 2).

From these data, we obtained preliminary results that support the hypothesis that the oligosquaramides prefer a folded structure in solution, driven by intramolecular hydrogen-bonding interactions that increase with oligomer length.

 © 2006 Wiley-VCH Verlag GmbH & Co. KGaA, Weinheim

To further characterize the U-turn module for the folded oligosquaramides, **6** was synthesized and an NMR ROESY spectroscopic experiment was conducted in $CDCl_3$ (Figure 3). Cross-peaks were observed between the *tert*-butyl protons (f) and the NH (a) and α-methylene (c) protons of the *n*-butyl side chain. The α′-methylene protons (d) give also a cross-peak with the methylene protons (e) of the Boc-protected alkylamino chain. From this data, we propose a folded structure for **6** in which the squaramide proton (b) is hydrogen-bonded to the *N*-methyl donor atom, thus forming a six-membered ring as observed in related systems.[10] Moreover, an additional hydrogen-bond interaction occurs between the carbamate carbonyl group and the squaramide proton (a), which stabilizes the folded structure.

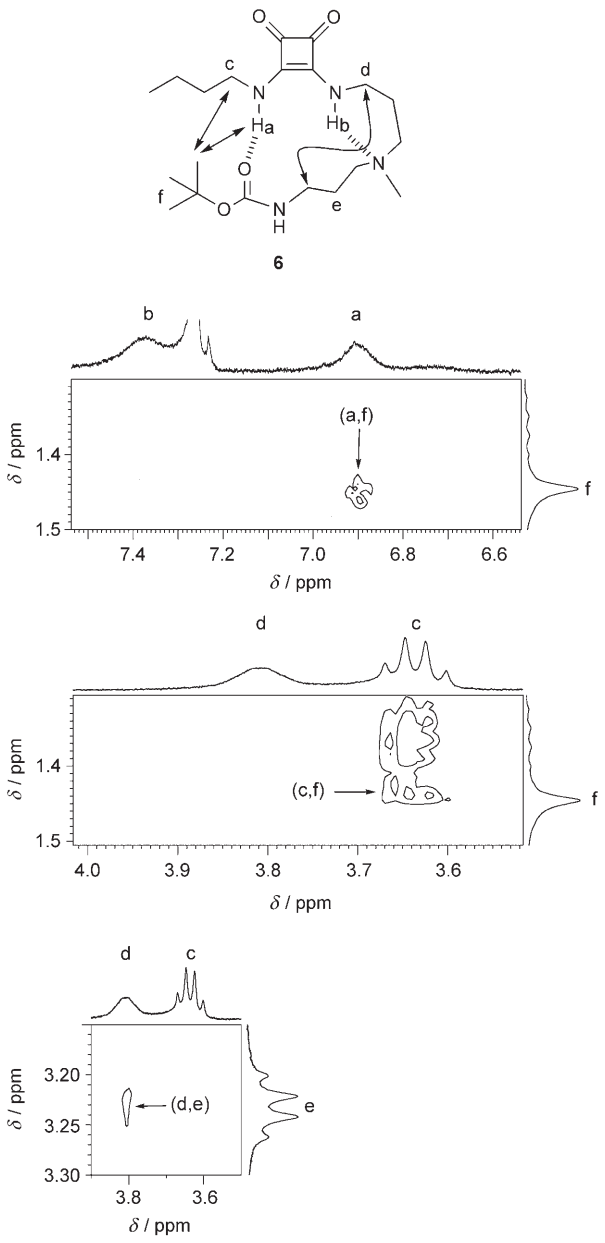

Figure 3. Top: Folded conformation of **6** showing H atom labels and the corresponding NOE interactions. Bottom: NOE interactions as revealed by the NOESY spectrum of **6** in $CDCl_3$.

NOE correlations were more difficult to identify for longer oligomers because of the C_2 symmetry of the strand. Under the assumption that all the oligomers have the characterized U-turn in common and all the NH protons are intramolecularly hydrogen-bonded and distributed in two different chemical environments, related folded structures can be anticipated to occur in longer oligosquaramide skeletons in a hairpin-like structure. In these cases, more interactions between the two strands occur and contribute to the stabilization of the folded conformation (Figure 4). As a result of the palindromic nature of these molecules, a dynamic process will occur in which the hydrogen-bonding pattern slips from one end to other, thus yielding conformational and energetically equivalent structures in solution.

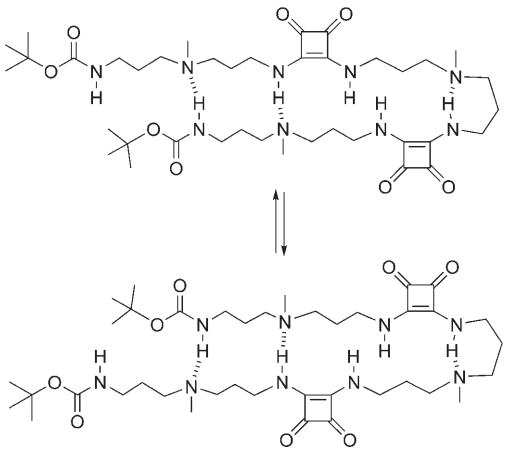

Figure 4. Proposed folded structure for **2** and the slipping equilibrium end-to-end of the hydrogen-bonding pattern.

Typically, the folded structures driven essentially by hydrogen-bonding interactions have been detected in non-protic solvents.[5] The proposed folded state for the oligosquaramides resists competition from externally added protic solvents, such as MeOH.[13] The ^{1}H NMR spectra of **2** and **4** at 285 K (3 mM) in $CDCl_3$/MeOH mixtures containing up to 40% MeOH display little perturbation and persistent deshielded squaramide NH signals, as expected for intramolecular hydrogen bonds; however, the NH carbamate signals move upfield, thus showing solvent exposure.

Differential scanning calorimetry (DSC) experiments were run on the oligosquaramides **2**–**5** to fully characterize the folded structures in protic solvents, ($EtOH/CHCl_3$ (95:5, v/v)) by increasing the temperature from 10 to 80 °C at a rate of 10 °C h^{-1} (Figure 5). All the tested oligomers undergo a sharp and reversible structural transition as a function of temperature, thus indicating the existence of a well-defined secondary structure. The excess heat capacity peak is complete within a 15–20 °C range, evident of a cooperative nature of the oligomer unfolding.[14] The ΔH values obtained for the unfolding processes (0.16, 0.32, 0.48, and 0.61 kcal mol^{-1} for **2**–**5**, respectively) show a clear dependence on the chain length of the oligomers, which is consistent with other observed data.

The melting temperature ($T_m = 63 \pm 2$ °C) was found to be similar for all the tested oligomers and comparable to those

 © 2006 Wiley-VCH Verlag GmbH & Co. KGaA, Weinheim

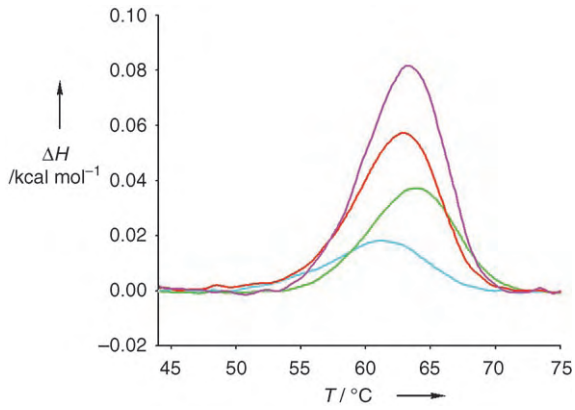

Figure 5. DSC melting curves of **2** (blue), **3** (green), **4** (red), and **5** (purple).

determined for unfolding of the hairpin peptide structure in water.[15] The ΔH value per residue (≈ 0.1 kcal mol^{-1}) reflects, mainly, the hydrogen-bond component because the solvophobic effect, as a result of the alkyl chains of the oligoamide skeleton, is assumed to have a minimum contribution on the overall folding–unfolding process.

As we have shown, the proposed folded structures for the oligosquaramides constitute a series of self-organized precursors applicable to one-step macrocyclization reactions in protic solvents without standard high-dilution conditions. Squaramides are particularly well suited to take advantage of the template effect in alcoholic solvents, given that the condensation of amines with squaramide esters is routinely carried out in ethanol or methanol. Cleavage of the Boc groups leaves two reactive amino groups in each oligomer that are close enough to react with a molecule of diethylsquarate in a one-step cyclization reaction to obtain the corresponding macrocycles. Therefore, the corresponding diamines of oligosquaramides **2**–**5** were condensed in methanol at millimolar concentrations with one equivalent of diethylsquarate. In all the cases, the macrocyclization of the oligosquaramides gave very high and comparable yields (80%) of the corresponding macrocycles **7**–**10** (Figure 6).[11] Further oligomerization was not detected by ESI MS studies of the crude product. These results support the dominance of the folded structure for the oligosquaramides under the macrocyclization reaction conditions. The generality of the oligosquaramides macrocyclization is also manifest. In some examples of highly efficient one-step macrocyclizations

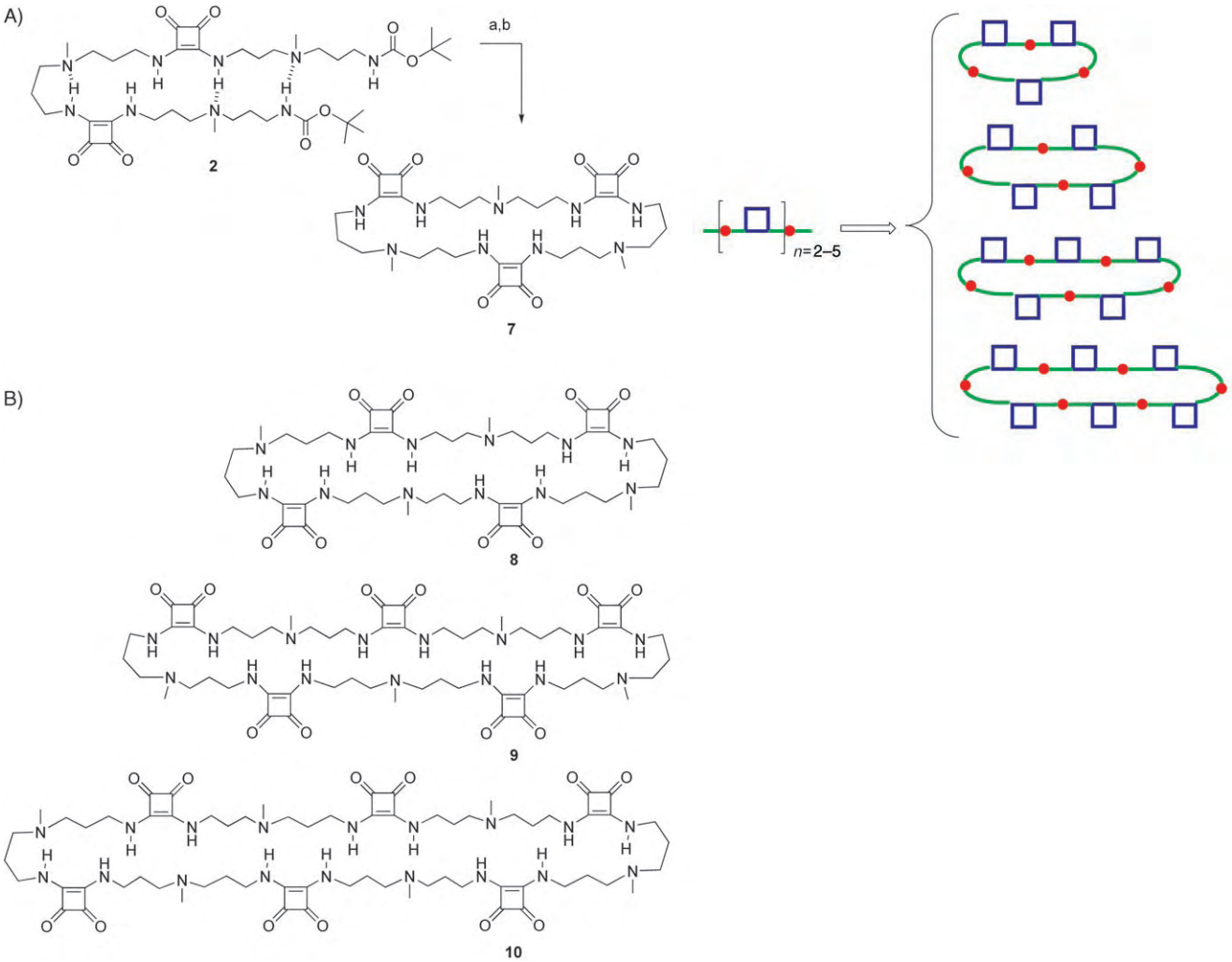

Figure 6. A) Synthesis of macrocycle **7**: a) HCl, 50 °C, 3 h; b) diethyl squarate, MeOH, room temperature, 12 h. B) Structures of macrocycles **8**–**10**.

 © 2006 Wiley-VCH Verlag GmbH & Co. KGaA, Weinheim

assisted by folding of precursor oligomers, the macrocycle sizes are limited to a determined length because of the rigidity of their backbones.[16] The nature of the folded structure adopted by the squaramides permits no size restrictions on the macrocycle synthesis. Therefore, a versatile synthetic strategy to obtain tailor-made macrocycle cavities with squaramide groups, which maintain their considerable hydrogen-bonding capability, has been demonstrated.

In summary, we have demonstrated that oligosquaramides of different length that contain a donor atom (N) in the δ position of the alkyl linker chains, fold to form stable monomeric structures that possess a hairpin-like pattern driven by intramolecular hydrogen-bonding interactions.[17] The stability of the folded structure increases with oligomer length, but the shortest oligomers also display a well-defined and stable conformation. The characterized folded structures are stable in polar solvents, as indicated by denaturation studies and DSC experiments. Thus, the preorganization shown by the oligosquaramide skeleton make them useful precursors in macrocyclization reactions. The study presented herein is the first example of how unnatural oligomers with designed folded structures driven by hydrogen-bonding interactions can be used to efficiently yield large macrocyclic structures.

Received: July 13, 2006
Published online: September 26, 2006

Keywords: foldamers · hydrogen bonds · macrocyclization · squaramides

[1] D. J. Craik, *Science* **2006**, *311*, 1563 – 1564.
[2] R. J. Clark, H. Fischer, L. Dempster, N. L. Daly, K. J. Rosengren, S. T. Nevin, F. A. Meunier, D. J. Adams, D. J. Craik, *Proc. Natl. Acad. Sci. USA* **2005**, *102*, 13767 – 13772.
[3] J. Blankenstein, J. Zhu, *Eur. J. Org. Chem.* **2005**, 1949 – 1964.
[4] a) J. C. Wu, N. Tang, W. S. Liu, M. Y. Tan, A. S. C. Chan, *Chin. Chem. Lett.* **2001**, *12*, 757 – 760; b) M. Bru, I. Alfonso, M. I. Burguete, S. V. Luis, *Tetrahedron Lett.* **2005**, *46*, 7781 – 7785.
[5] a) R. P. Cheng, S. H. Gellman, W. F. DeGrado, *Chem. Rev.* **2001**, *101*, 3219 – 3232; b) J. D. Hill, M. J. Mio, R. B. Prince, T. S. Hughes, J. S. Moore, *Chem. Rev.* **2001**, *101*, 3893 – 4011.
[6] L. Yuan, A. R. Sanford, W. Feng, A. Zhang, J. Zhu, H. Zeng, K. Yamato. M. Li, J. S. Ferguson, B. Gong, *J. Org. Chem.* **2005**, *70*, 10660 – 10669.
[7] a) P. S. Corbin, S. C. Zimmerman, *J. Am. Chem. Soc.* **2000**, *122*, 3779 – 3780; b) P. S. Corbin, S. C. Zimmerman, P. A. Thiessen, N. A. Hawryluk, T. J. Murray, *J. Am. Chem. Soc.* **2001**, *123*, 10475 – 10488.
[8] J. Garric, J.-M. Léger, A. Grelard, M. Ohkita, I. Huc, *Tetrahedron Lett.* **2003**, *44*, 1421 – 1424.
[9] H. S. Gellman, *Acc. Chem. Res.* **1998**, *31*, 173 – 180.
[10] M. C. Rotger, M. N. Piña, A. Frontera, G. Martorell, P. Ballester, P. M. Deyà, A. Costa, *J. Org. Chem.* **2004**, *69*, 2302 – 2308.
[11] Experimental details regarding the synthesis and characterization of the squaramide compounds are available in the Supporting Information.
[12] N. H. Andersen, J. W. Neidigh, S. M. Harris, G. M. Lee, Z. Liu, T. Tong, *J. Am. Chem. Soc.* **1997**, *119*, 8547 – 8561.
[13] E. R. Gillies, C. Dolain, J.-M. Lèger, I. Huc, *J. Org. Chem.* **2006**, in press.
[14] K. Kirshenbaum, A. E. Barrow, R. A. Goldsmith, P. Armand, E. K. Bradley, K. T. V. Truong, K. A. Dill, F. E. Cohen, R. N. Zuckermann, *Proc. Natl. Acad. Sci. USA* **1998**, *95*, 4303 – 4308.
[15] R. M. Fesinmeyer, F. M. Hudson, N. H. Andersen, *J. Am. Chem. Soc.* **2004**, *126*, 7238 – 7243.
[16] L. Yuan, W. Feng, K. Yamato, A. R. Sanford, D. Xu, H. Guo, B. Gong, *J. Am. Chem. Soc.* **2004**, *126*, 11120 – 11121.
[17] The macrocyclation reaction fails when the donor atom in the δ position on the alkyl chain is absent;[10] moreover, unpublished results show that a different atom sequence in the linker chain gives insoluble squaramide compounds in $CHCl_3$ and protic solvents.

 © 2006 Wiley-VCH Verlag GmbH & Co. KGaA, Weinheim

Host–Guest Systems

DOI: 10.1002/anie.200602724

Supramolecular Receptor Design: Anion-Triggered Binding of C_{60}**

Kent A. Nielsen, Won-Seob Cho, Ginka H. Sarova, Bo M. Petersen, Andrew D. Bond, Jan Becher, Frank Jensen, Dirk M. Guldi, Jonathan L. Sessler, and Jan O. Jeppesen**

Self-assembled structures are widespread in nature and are a key feature of many biological small-molecule recognition motifs. Not surprisingly, therefore, considerable effort has been devoted to developing synthetic self-assembled receptor systems, multicomponent molecular hosts that are able to

[*] Dr. W.-S. Cho, Prof. J. L. Sessler
Department of Chemistry and Biochemistry
University of Texas at Austin
1 University Station, A5300
Austin, TX 78712-0165 (USA)
Fax: (+1) 512-471-7550
E-mail: sessler@mail.utexas.edu

Dr. K. A. Nielsen, B. M. Petersen, Dr. A. D. Bond, Prof. J. Becher, Prof. F. Jensen, Prof. J. O. Jeppesen
Department of Chemistry
University of Southern Denmark (Odense University)
Campusvej 55, 5230, Odense M (Denmark)
Fax: (+45) 6615-8780
E-mail: joj@chem.sdu.dk

Dr. G. H. Sarova, Prof. D. M. Guldi
Institute for Physical and Theoretical Chemistry
Universität Erlangen-Nürnberg
Egerlandstrasse 3, 91058 Erlangen (Germany)

[**] This work was supported by Lundbeckfonden, the Strategic Research Council in Denmark through the Young Researchers Program (project no. 2117-05-0115); the Danish Natural Science Research Council (SNF, project nos 21-03-0317 and 21-03-0164); the Danish Natural Science Research Council (SNF, project no. 21-03-0268) through the SONS Program of the European Science Foundation, which is also funded by the European Commission, Sixth Framework Program; the Danish Center for Scientific Computing; the US National Institutes of Health (grant no. GM 69492 to J.L.S.); the Deutsche Forschungsgemeinschaft (SFB 583); FCI; and the Office of Basic Energy Sciences of the US Department of Energy.

Supporting information for this article is available on the WWW under http://www.angewandte.org or from the author.

WILEY InterScience DISCOVER SOMETHING GREAT
© 2006 Wiley-VCH Verlag GmbH & Co. KGaA, Weinheim

interact with, and bind to, specifically targeted substrates.[1,2] To date, systems based on metal coordination[3–8] and hydrogen-bond recognition[3,9–11] have received the greatest attention. Singularly lacking from the lexicon of known self-assembled receptor systems are those in which anion recognition plays a key structural or controlling role. Anion binding has, however, been used to template the formation of various large structures,[12–19] regulate the formation of a pseudorotaxane,[20] induce the translocation of a macrocycle in a molecular shuttle,[21] and stabilize the formation of several supramolecular host–guest complexes.[22,23]

Herein, we show how treatment of a solution of a tetrathiafulvalene-functionalized calixpyrrole with chloride anions in dichloromethane produces a bowl-like receptor that is able to encapsulate C_{60} in a 2:1 barrel-like manner. The use of a two-step molecular-recognition approach, which first involves an anion-triggered conformational change followed by binding of C_{60}, allows for the controlled assembly of five individual components (two chloride anions, two tetrathiafulvalene-functionalized calixpyrroles, and one C_{60} unit) and the production of a complex host–guest ensemble of well-defined structure and stoichiometry. The color of this ensemble (green in dichloromethane) differs dramatically from that of its constituents (yellow and magenta in the case of the tetrathiafulvalene-functionalized calixpyrrole and C_{60}, respectively), thus allowing its formation to be monitored visually. The present strategy differs fundamentally from previous approaches to assembled receptor design in that anion binding provides the key element of structural control. It thus defines a new approach to the generation of complex supramolecular assemblies.

The unique nature of C_{60} and other fullerenes[24,25] have made these species important targets for molecular receptor design. However, the need to match the shape of the receptor to the convex surfaces of fullerenes and to overcome the inherently weak associations that C_{60} and related species display in host–guest complexes has made this a particular challenge. To date, a number of "molecular containers", including cyclodextrins,[26] (benzotri(benzonorbornadienes),[27] calixarenes,[28–31] calixnaphthalenes,[32] and cyclotriveratrylene,[33] have been used to achieve fullerene recognition. Porphyrins and metalloporphyrins,[34,35] which benefit from favorable van der Waals interactions with the π surface of fullerenes, have also been used to achieve C_{60} recognition, as have individual tetrathiafulvalene[36,37] (TTF) subunits in the solid state.[38] However, in all cases the receptor is a discrete entity (that is, the product of fermentation or synthesis), rather than a scaffold built up through self-assembly. The use of a self-assembled approach potentially confers a number of advantages, including savings in synthetic investment and the ability to effect control through the regulation of more than one supramolecular chemical event (e.g., the formation of the self-assembled receptor and, separately, fullerene recognition). As described below, the use of a tetrathiafulvalene-functionalized calix[4]pyrrole, TTF-calix[4]pyrrole **1** (Figure 1 A), allows this strategy to be implemented.

The synthesis of **1** (Figure 1 A) was carried out as described previously.[39,40] As is true for most other calix[4]-pyrroles, **1** exists (Figure 1 B) predominantly in the 1,3-alternate conformation in the absence of anions. However, in halogenated solvents **1** binds chloride anions very tightly—a binding constant (K_a) of $2.5 \times 10^6\ M^{-1}$ has been reported[39,40] for the complexation of **1** with chloride ions in 1,2-dichloroethane (DCE) at 298 K, thus leading it to adopt (Figure 1 C) a bowl-like conformation. In the case of **1**, the resulting bowl-shaped receptor system possesses TTF-derived electron-rich "walls" and was thus expected to act as a receptor for electron-deficient spherical guests such as fullerene, for example.

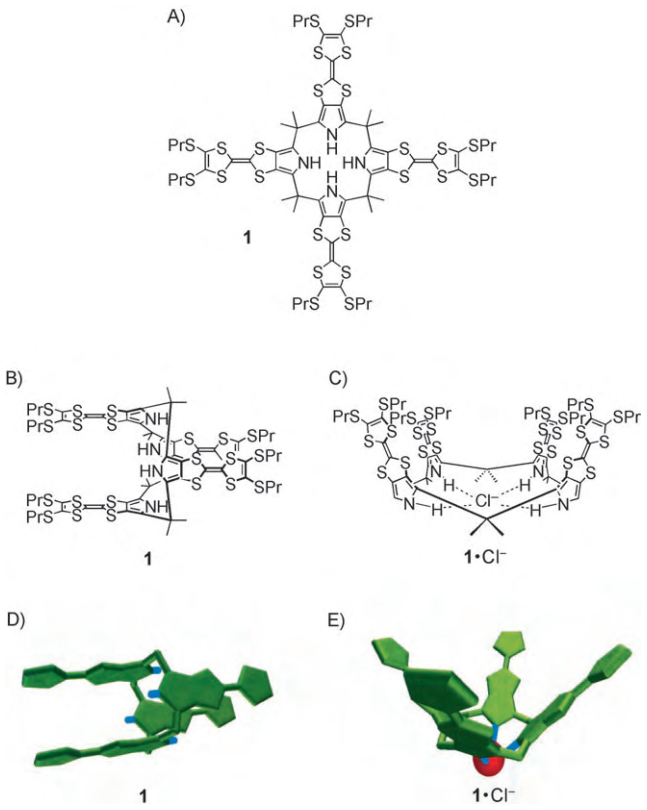

Figure 1. A) A 2D representation of **1**. B) A 3D representation of **1** in its 1,3-alternate conformation. C) A 3D representation of the chloride-bound receptor **1**·Cl^- in its cone conformation. D) A cartoon representation of **1** in its 1,3-alternate conformation. E) A cartoon representation of **1**·Cl^- in its cone conformation.

Support for the notion that the electron-rich TTF-derived walls of **1** would stabilize interactions with the electron-deficient guest C_{60} came from an X-ray crystal structural study carried out on crystals[41] obtained from a mixture of tetrabutylammonium chloride, receptor **1**, and C_{60} in toluene. This structure revealed[42] an extraordinary cubic ensemble $[(\mathbf{1}\cdot Cl)_6(C_{60})_8(toluene)_5]^{6-}$ (Figure 2), in which eight C_{60} molecules define the corners of a cube and **1**·Cl^- units lie within each cube face locked in the bowl-shaped conformation. The chloride anions lie to the inside of the cube, which also encapsulates five toluene solvent molecules. All four TTF-derived subunits on each **1**·Cl^- unit interact with C_{60} molecules, and each C_{60} moiety lies within a threefold symmetric cavity defined by the electron-rich TTF subunits. In the solid state, the internal cavities of the bowl-shaped

 © 2006 Wiley-VCH Verlag GmbH & Co. KGaA, Weinheim

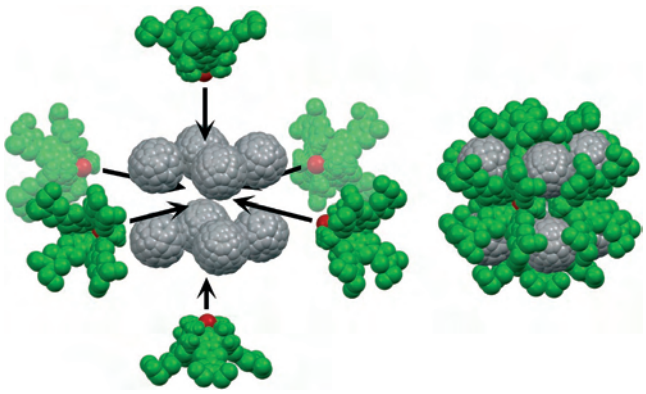

Figure 2. Enlarged view (right) of the $[(\mathbf{1}\cdot Cl)_6(C_{60})_8(toluene)_5]^{6-}$ ion, as determined by X-ray crystallography. As shown on the left, the C_{60} molecules (gray) define the corners of a cube and $\mathbf{1}\cdot Cl^-$ units (green/red) lie within each cube face, locked in the bowl-shaped conformation. The chloride anions (red) lie to the inside of the cube, which also encapsulates five toluene solvent molecules (not shown).

$\mathbf{1}\cdot Cl^-$ receptors are occupied by tetrabutylammonium cations. Characterization of this complex established the viability of the interactions between $\mathbf{1}\cdot Cl^-$ and C_{60}, although it seemed unlikely that the complex cubic ensemble would persist in solution. It was expected that more limited $\mathbf{1}\cdot Cl^-$ to C_{60} stoichiometries would be seen in solution, as concentrations are inherently lower and better controlled and long-range interensemble interactions are minimized.

For reasons of solubility, solution-state binding studies involving **1**, chloride anions (studied as the tetrabutylammonium salt), and C_{60} were carried out in dichloromethane. Both absorption and emission spectroscopy were used to monitor the putative binding events.

The absorption spectrum recorded in dichloromethane of **1** in its 1,3-alternate conformation (Figure 3A) did not reveal (Figure 3B, curve a) any visible absorption bands at $\lambda \geq 550$ nm. Likewise, no significant absorption features were seen at $\lambda \geq 650$ nm in the absorption spectrum (Figure 3B, curve b) of C_{60} in dichloromethane. These solutions, thus, appear yellow and magenta (Figure 3C), respectively. The addition of five equivalents of tetrabutylammonium chloride to a solution of **1** in dichloromethane serves to shift the 1,3-alternate conformation to the cone conformation, thus producing the bowl-shaped receptor $\mathbf{1}\cdot Cl^-$ almost exclusively (Figure 3A). Although this chloride-mediated conformational change is readily visualized by ^{1}H NMR spectroscopy,[39] it does not give rise to any appreciable change in the color of the solution; thus, solutions of the cone complex $\mathbf{1}\cdot Cl^-$ appear yellow (Figure 3D), as do those of the neutral **1** in its 1,3-alternate conformation. However, when 0.5 equivalents of C_{60} (in dichloromethane) are added to the yellow solution of $\mathbf{1}\cdot Cl^-$, the solution turns green (Figure 3E) essentially instantaneously. The absorption spectrum (Figure 3B, curve c) of this solution showed a strong charge-transfer (CT) band centered around $\lambda_{max} = 725$ nm ($\varepsilon = 1900\,M^{-1}cm^{-1}$). This diagnostic spectroscopic feature is most readily accounted for by the formation (Figure 3A) of the well-ordered, multicomponent supramolecular ensemble $C_{60}\subset(\mathbf{1}\cdot Cl^-)_2$, wherein one C_{60} molecule is encapsulated by two bowl-shaped receptors (that

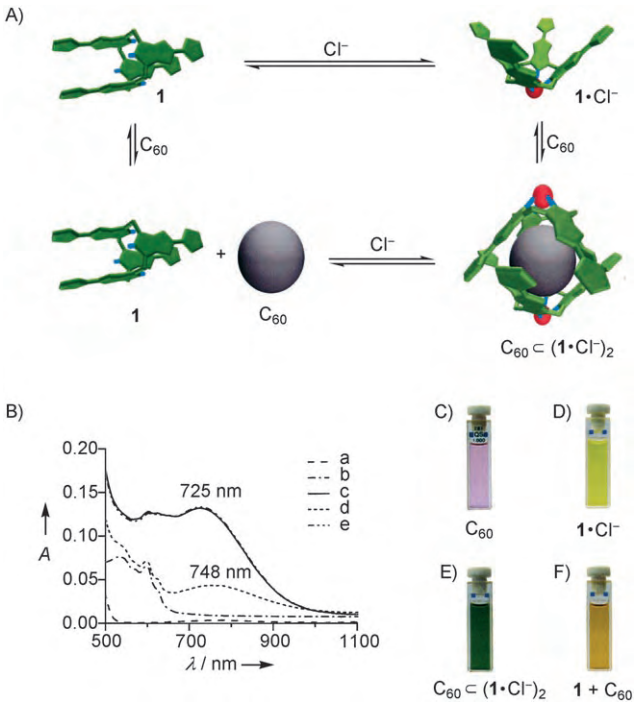

Figure 3. A) Mechanistic scheme for the proposed complex formation between **1** and C_{60} in the presence of chloride ions. B) Absorption spectra recorded in dichloromethane at 298 K of a) **1** (0.135 mM), b) C_{60} (0.0687 mM), c) $\mathbf{1}\cdot Cl^- + C_{60}$ (0.5 equiv), d) **1** + C_{60} (0.5 equiv), and e) **1** + C_{60} (0.5 equiv) and then nBu$_4$NCl (excess). C–F) Solutions in dichloromethane of C) C_{60}, D) $\mathbf{1}\cdot Cl^-$, E) $\mathbf{1}\cdot Cl^- + C_{60}$ (0.5 equiv), and F) **1** + C_{60} (0.5 equiv).

is, $\mathbf{1}\cdot Cl^-$) produced by the binding of the chloride anion to calix[4]pyrrole **1**. Presumably, the formation of this ensemble reflects an appropriate size and shape matching, as well as favorable CT interactions between the electron-rich TTF donor units and the electron-accepting C_{60} moiety. Analysis of the spectral features allows this CT interaction to be quantified in terms of a fairly pronounced electronic coupling element (V) of 2687/340 Å cm^{-1}.

A Job plot carried out[41] in dichloromethane between $\mathbf{1}\cdot Cl^-$ and C_{60} exhibits a maximum around 0.35, a finding that is consistent with the formation of the proposed 2:1 complex between $\mathbf{1}\cdot Cl^-$ and C_{60}. Addition of two equivalents of the yellow receptor **1** in its 1,3-alternate conformation (that is, in the absence of chloride anions) to a solution (magenta) of C_{60} in dichloromethane produced (Figure 3A) a brown solution (Figure 3F). This solution was characterized by the presence of a weak, broad absorption band centered around $\lambda_{max} = 748$ nm ($\varepsilon = 500\,M^{-1}cm^{-1}$) in the visible spectral region (Figure 3B, curve d), a finding that is consistent with the presence of only a minimal intermolecular interaction[43] between C_{60} and **1** in its 1,3-alternate conformation. However, the addition of five equivalents of tetrabutylammonium chloride to this 2:1 mixture of **1** and C_{60} resulted in an immediate color change from brown to green and the appearance (Figure 3B, curve e) of a strong CT absorption band centered at $\lambda_{max} = 725$ nm ($\varepsilon = 1900\,M^{-1}cm^{-1}$). Such a finding provides support for the proposal that C_{60} is only encapsulated after **1** undergoes a change (Figure 3A) from

 © 2006 Wiley-VCH Verlag GmbH & Co. KGaA, Weinheim

the 1,3-alternate conformation to the corresponding chloride-bound cone conformation (that is, **1**·Cl^-).

Force-field modeling of the proposed 2:1 complex (that is, $C_{60}\subset(\mathbf{1}\cdot Cl^-)_2$) that formed as the result of these two very different binding events (chloride binding and C_{60} encapsulation) was undertaken. For these calculations, the thiopropyl groups were replaced by thiomethyl groups for simplicity. Carried out in this way, a complexation energy of 7.4 kcal mol^{-1} was derived using the Merck molecular force field (MMFF) and the generalized Born/surface area (GB/SA) solvent model[44] for chloroform. This value is in good agreement with the experimental result of 5.6 kcal mol^{-1} (see below). The geometry was reoptimized[41] at the B3LYP/3-21G level,[45] and single-point calculations were performed with the larger 6-31G(d) basis set. As the B3LYP method underestimates the dispersion energy, it is not possible to obtain realistic complexation energies at this level. A natural bond orbital (NBO) population analysis indicated a charge transfer of 0.03 electrons to C_{60} from the TTF units. Although these calculations refer to the gas phase, they provide important support for the proposed interaction between the C_{60} guest and the electron-rich TTF "walls" of the calix[4]pyrrole "bowl".

A UV/Vis titration experiment (Figure 4B) was carried out to determine the binding constants (K_1 and K_2) that lead to the formation of the putative 2:1 complex between **1**·Cl^- and C_{60} (Figure 4A). In particular, the change in the intensity of the CT band ($\lambda_{max} = 725$ nm) was monitored as increasing quantities of **1**·Cl^- were added to a solution of C_{60} in dichloromethane at 298 K. A saturation point was reached after the addition of two equivalents of **1**·Cl^- to this latter solution of C_{60} (Figure 4B, curve d), with no perceptible changes being observed as additional equivalents of **1**·Cl^- were added (Figure 4B, curve e). The binding profile obtained in this way (Figure 4C) was subject to a standard nonlinear (2:1 host/guest) curve fitting analysis,[46] from which

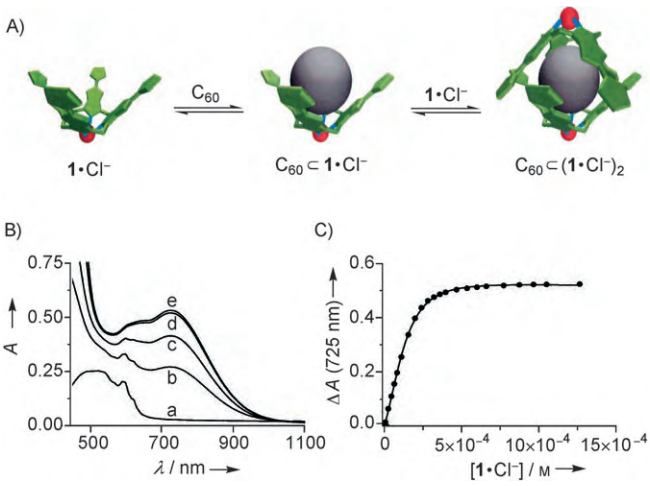

Figure 4. A) Equilibriums that lead to the formation of $C_{60}\subset$**1**·Cl^- and $C_{60}\subset(\mathbf{1}\cdot Cl^-)_2$. B) Absorption spectra recorded in dichloromethane at 298 K of a) C_{60} (0.2 mM), b) C_{60} + **1**·Cl^- (0.5 equiv), c) C_{60} + **1**·Cl^- (1.0 equiv), d) C_{60} + **1**·Cl^- (2.0 equiv), and e) C_{60} + **1**·Cl^- (6.0 equiv). C) Changes in the CT band at 725 nm in the titration of C_{60} (0.2 mM) with **1**·Cl^- in dichloromethane at 298 K.

binding constants[47] $K_1 = 2.3\times10^3\,M^{-1}$ and $K_2 = 1.3\times10^4\,M^{-1}$—reflecting the formation of $C_{60}\subset$**1**·Cl^- and $C_{60}\subset(\mathbf{1}\cdot Cl^-)_2$, respectively—were obtained. These values correspond to ΔG_1 and ΔG_2 values of −4.6 and −5.6 kcal mol^{-1}, respectively, at 298 K in dichloromethane.

Electrochemical measurements with C_{60}, **1**·Cl^-, and $C_{60}\subset(\mathbf{1}\cdot Cl^-)_2$ in dichloromethane provided further support for the proposed binding events. In particular, the half-wave potential associated with the first reduction of the fullerene in $C_{60}\subset(\mathbf{1}\cdot Cl^-)_2$ was found to be shifted to a more negative potential (by −74 mV) relative to the first reduction of C_{60}. Such a finding is completely consistent with a partial shift of electron density from the electron-donating TTF subunits to the bound C_{60} guest. The unusually high shift seen for the C_{60} half-wave potential also serves to corroborate the strong electronic coupling within the $C_{60}\subset(\mathbf{1}\cdot Cl^-)_2$ self-assembled host–guest complex.

A gradual decrease in the C_{60} steady-state fluorescence spectral intensity ($\Phi = 2.0\times10^{-4}$) was also seen (Figure 5A)

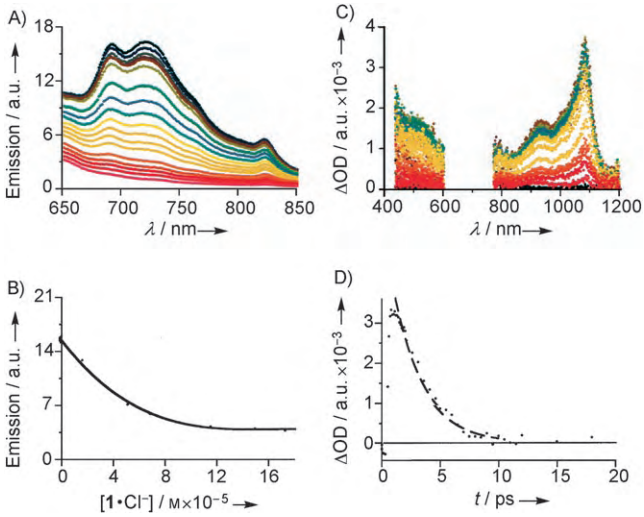

Figure 5. A) Steady-state fluorescence of a 5.38×10^{-5} M solution of C_{60} in dichloromethane upon adding variable concentrations of **1**·Cl^- (1.72×10^{-5} M to 2.87×10^{-4} M). B) Fluorescence intensity at 690 nm of $C_{60}\subset$**1**·Cl^-/$C_{60}\subset(\mathbf{1}\cdot Cl^-)_2$ in dichloromethane—the concentrations of **1**·Cl^- vary from 1.72×10^{-5} M to 2.87×10^{-4} M, whereas the concentration of C_{60} is constant at 5.38×10^{-5} M. C) Differential absorption spectra (visible) obtained upon femtosecond flash photolysis (740 nm) of $C_{60}\subset(\mathbf{1}\cdot Cl^-)_2$ in nitrogen-saturated dichloromethane with several time delays between 0 and 10 ps at room temperature; arrows indicate the evolution of differential changes. D) Time versus absorption profiles of the spectra shown above as recorded at 1080 nm.

when increasing quantities of **1**·Cl^- were added to solutions of C_{60} in dichloromethane. This decrease is attributed to an electron-transfer process that evolved from the singlet excited state of C_{60}. As in the case of the absorption-based studies, the change in intensity could be used to determine the binding constants for the formation of the successive $C_{60}\subset$**1**·Cl^- and $C_{60}\subset(\mathbf{1}\cdot Cl^-)_2$ complexes. Data taken at 690 nm were plotted (Figure 5B) versus the concentration of **1**·Cl^-.[48] Most importantly, the values obtained—$K_1 = 2.4\times10^3\,M^{-1}$ (that is, for $C_{60}\subset$**1**·Cl^-) and $K_2 = 2.8\times10^4\,M^{-1}$ (that is, for $C_{60}\subset$

 © 2006 Wiley-VCH Verlag GmbH & Co. KGaA, Weinheim

($\mathbf{1}\cdot Cl^-)_2$)—are in good agreement with those values determined using the UV/Vis titrations described above.

In addition, the fluorescence spectra recorded at the end of the titrations, that is, at the plateau value of each assay, were evaluated to assess the dynamics of the excited-state deactivation. A quenching factor of 17 ($\Phi = 1.1 \times 10^{-5}$) relative to bare C_{60} in the tightly organized $C_{60}\subset(\mathbf{1}\cdot Cl^-)_2$ complex leads to an appreciably fast electron-transfer rate of $1.4 \times 10^{10}\ s^{-1}$ relative to the intrinsic decay of the singlet excited-state decay of C_{60} (that is, an intersystem-crossing rate of $8 \times 10^8\ s^{-1}$).

Transient absorption spectroscopy provided support for this proposed electron-transfer mechanism. In particular, femtosecond excitation into the CT absorption bands revealed features that correspond to the one-electron-reduced fullerene radical anion at 1080 nm[49] and the one-electron-oxidized TTF radical cation, a species that is known to absorb at 400 nm. Although the latter lies near the detection limit[41] of our femtosecond transient apparatus, it is clearly discernable (Figure 5C). Mapping the radical-ion-pair formation rate to a first-order kinetic model, we determined a rather fast electron-transfer rate on the order of $10^{12}\ s^{-1}$, a value that is in good agreement with that obtained from an extrapolation of the steady-state fluorescence-quenching studies discussed above. Consistent with the proposed strong electron–donor interactions in $C_{60}\subset(\mathbf{1}\cdot Cl^-)_2$, the resulting radical ion pair is short-lived with a lifetime of only 3.1 ps (Figure 5D).[50]

In summary, we have demonstrated a step-by-step assembly of a complex calix[4]pyrrole-derived host–guest ensemble that contains two electron-rich TTF-functionalized calix[4]-pyrroles, an anion (that is, chloride), and an electron-deficient substrate (fullerene). In contrast to other self-assembled receptor systems, initial anion binding in the present ensemble serves as a "trigger" for the crucial reorganization of the calix[4]pyrrole receptor needed to produce a "cone" conformation, wherein multiple TTF units are appropriately arranged to allow for fullerene binding. The dramatic color change that accompanies the C_{60} binding event allows the recognition process to be followed readily, and thus the presence of this fullerene to be readily "sensed". As the size of the calixpyrrole receptor, may be varied (by the use of, for example, calix[5]pyrrole or calix[6]pyrrole) and the nature of the TTF substituents readily fine-tuned, this approach to elaborated receptor design could prove to be quite general, as may be the use of anion recognition as a triggering mechanism to generate complex supramolecular ensembles.

Received: July 9, 2006
Published online: September 26, 2006

Keywords: calix[4]pyrroles · fullerenes · self-assembly · sensors · tetrathiafulvalenes

[1] J.-M. Lehn, *Science* **2002**, *295*, 2400 – 2403.
[2] D. Philp, J. F. Stoddart, *Angew. Chem.* **1996**, *108*, 1242 – 1286; *Angew. Chem. Int. Ed. Engl.* **1996**, *35*, 1154 – 1196.
[3] B. Linton, A. D. Hamilton, *Chem. Rev.* **1997**, *97*, 1669 – 1680.
[4] N. Takeda, K. Umemoto, K. Yamaguchi, M. Fujita, *Nature* **1999**. *398*, 794 – 796.
[5] B. Olenyuk, J. A. Whiteford, A. Fechtenkötter, P. J. Stang, *Nature* **1999**, *398*, 796 – 799.
[6] D. Fiedler, D. H. Leung, R. G. Bergman, K. N. Raymond, *Acc. Chem. Res.* **2005**, *38*, 349 – 358.
[7] T. S. Koblenz, H. L. Dekker, C. G. de Koster, P. W. N. M. van Leeuwen, J. N. H. Reek, *Chem. Commun.* **2006**, 1700 – 1702.
[8] M. W. Hosseini, *Acc. Chem. Res.* **2005**, *38*, 313 – 323.
[9] T. Heinz, D. M. Rudkevich, J. Rebek, Jr., *Nature* **1998**, *394*, 764 – 766.
[10] A. D. Far, A. Shivanyuk, J. Rebek, Jr., *J. Am. Chem. Soc.* **2002**, *124*, 2854 – 2855.
[11] J. Rebek, Jr., *Angew. Chem.* **2005**, *117*, 2104 – 2115; *Angew. Chem. Int. Ed.* **2005**, *44*, 2068 – 2078.
[12] G. F. Swiegers, T. J. Malefetse, *Chem. Rev.* **2000**, *100*, 3483 – 3537.
[13] M. C. T. Fyfe, J. F. Stoddart, *Acc. Chem. Res.* **1997**, *30*, 393 – 401.
[14] B. Hasenknopf, J.-M. Lehn, N. Boumediene, A. Dupont-Gervais, A. Van Dorsselaer, B. Kneisel, D. Fenske, *J. Am. Chem. Soc.* **1997**, *119*, 10956 – 10962.
[15] M. C. T. Fyfe, P. T. Glink, S. Menzer, J. F. Stoddart, A. J. P. White, D. J. Williams, *Angew. Chem.* **1997**, *109*, 2158 – 2160; *Angew. Chem. Int. Ed. Engl.* **1997**, *36*, 2068 – 2070.
[16] X. Yang, C. B. Knobler, M. F. Hawthorne, *J. Am. Chem. Soc.* **1992**, *114*, 380 – 382.
[17] D. Seidel, V. Lynch, J. L. Sessler, *Angew. Chem.* **2002**, *114*, 1480 – 1483; *Angew. Chem. Int. Ed.* **2002**, *41*, 1422 – 1425.
[18] T. Köhler, D. Seidel, V. Lynch, F. O. Arp, Z. Ou, K. M. Kadish, J. L. Sessler, *J. Am. Chem. Soc.* **2003**, *125*, 6872 – 6873.
[19] R. Vilar, *Angew. Chem.* **2003**, *115*, 1498 – 1516; *Angew. Chem. Int. Ed.* **2003**, *42*, 1460 – 1477.
[20] M. Montalti, L. Prodi, *Chem. Commun.* **1998**,1461 – 1462.
[21] C. M. Keaveney, D. A. Leigh, *Angew. Chem.* **2004**, *116*, 1242 – 1244; *Angew. Chem. Int. Ed.* **2004**, *43*, 1222 – 1224.
[22] J. W. Jones, L. N. Zakharov, A. L. Rheingold, H. W. Gibson, *J. Am. Chem. Soc.* **2002**, *124*, 13378 – 13379.
[23] A. Arduini, G. Giorgi, A. Pochini, A. Secchi, F. Ugozzzoli, *J. Org. Chem.* **2001**, *66*, 8302 – 8308.
[24] L. Sánchez, N. Martín, D. M. Guldi, *Angew. Chem.* **2005**, *117*, 5508 – 5516; *Angew. Chem. Int. Ed.* **2005**, *44*, 5374 – 5382.
[25] D. M. Guldi, F. Zerbetto, V. Georgakilas, M. Prato, *Acc. Chem. Res.* **2005**, *38*, 38 – 43.
[26] K. Komatsu, *Top. Curr. Chem.* **2005**, *254*, 185 – 206.
[27] C. Zonta, S. Cossu, O. De Lucchi, *Eur. J. Org. Chem.* **2000**, 1965 – 1971.
[28] J. L. Atwood, G. A. Koutsantonis, C. L. Raston, *Nature* **1994**, *368*, 229 – 231.
[29] M. Takeuchi, M. Ikeda, A. Sugasaki, S. Shinkai, *Acc. Chem. Res.* **2001**, *34*, 865 – 873.
[30] T. Haino, M. Yanase, Y. Fukazawa, *Angew. Chem.* **1997**, *109*, 288 – 290; *Angew. Chem. Int. Ed. Engl.* **1997**, *36*, 259 – 260.
[31] F. C. Tucci, D. M. Rudkevich, J. Rebek, *J. Org. Chem.* **1999**, *64*, 4555 – 4559.
[32] S. Mizyed, M. Ashram, D. O. Miller, P. E. Georghiou, *J. Chem. Soc. Perkin Trans. 2* **2001**, 1916 – 1919.
[33] J. W. Steed, P. C. Junk, J. L. Atwood, M. J. Barnes, C. L. Raston, R. S. Burkhalter, *J. Am. Chem. Soc.* **1994**, *116*, 10346 – 10347.
[34] D. M. Guldi, *Chem. Soc. Rev.* **2002**, *31*, 22 – 36.
[35] P. D. W. Boyd, C. A. Reed, *Acc. Chem. Res.* **2005**, *38*, 235 – 242.
[36] J. L. Segura, N. Martín, *Angew. Chem.* **2001**, *113*, 1416 – 1455; *Angew. Chem. Int. Ed.* **2001**, *40*, 1372 – 1409.
[37] J. O. Jeppesen, M. B. Nielsen, J. Becher, *Chem. Rev.* **2004**, *104*, 5115 – 5132.
[38] A. Izuoka, T. Tachikawa, T. Sugawara, Y. Suzuki, M. Konno, Y. Saito, H. Shinohara, *J. Chem. Soc. Chem. Commun.* **1992**, 1472 – 1473.

 © 2006 Wiley-VCH Verlag GmbH & Co. KGaA, Weinheim

[39] K. A. Nielsen, W.-S. Cho, J. O. Jeppesen, V. M. Lynch, J. Becher, J. L. Sessler, *J. Am. Chem. Soc.* **2004**, *126*, 16296 – 16297.
[40] K. A. Nielsen, W.-S. Cho, J. Lyskawa, E. Levillain, V. M. Lynch, J. L. Sessler, J. O. Jeppesen, *J. Am. Chem. Soc.* **2006**, *128*, 2444 – 2451.
[41] Details are available in the Supporting Information.
[42] The cubic cluster motif $[(\mathbf{1}\cdot Br)_6(C_{60})_8]^{6-}$ is found also in crystals obtained from a mixture of **1** and C_{60} with tetrabutylammonium bromide. Although the bulk crystal structures of the Cl^- and Br^- derivatives are quite different, the cubic cluster is apparently robust in the solid state.
[43] The nature of the interaction between **1** in its 1,3-alternate conformation and C_{60} is most likely such that C_{60} is complexed alongside one or more of the TTF units present in **1**.
[44] W. C. Still, A. Tempczyrk, R. C. Hawley, T. Hendrickson, *J. Am. Chem. Soc.* **1990**, *112*, 6127 – 6129.
[45] F. Jensen, *Introduction to Computational Chemistry*, Wiley, Chichester, **1999**.
[46] K. A. Conners, *Binding Constants: The Measurement of Molecular Complex Stability*, Wiley, New York, **1987**.
[47] Estimated errors $< 15\,\%$.
[48] B. Valeur, *Molecular Fluorescence: Principles and Applications*, Wiley-VCH, Weinheim, **2002**.
[49] D. M. Guldi, M. Prato, *Acc. Chem. Res.* **2000**, *33*, 695 – 703.
[50] Although such a short lifetime is a good reflection of the strong electronic coupling, it is, notwithstanding, in sharp contrast to values reported on supramolecular (M. Segura, L. Sánchez, J. de Mendoza, N. Martín, D. M. Guldi, *J. Am. Chem. Soc.* **2003**, *125*, 15093 – 15100) and supermolecular (J. L. Segura, E. M Priego, N. Martín, C. Luo, D. M. Guldi, *Org. Lett.* **2000**, *2*, 4021 – 4024) hybrid structures.

 © 2006 Wiley-VCH Verlag GmbH & Co. KGaA, Weinheim

Organocatalysis

DOI: 10.1002/anie.200602925

Enantioselective Ene Reaction of Cyclopentadiene and α,β-Enals Catalyzed by a Diphenylprolinol Silyl Ether**

*Hiroaki Gotoh, Ryouhei Masui, Hiroshi Ogino, Mitsuru Shoji, and Yujiro Hayashi**

The ene reaction is a useful carbon–carbon bond-forming reaction.[1] Although several excellent asymmetric carbonyl ene reactions have been reported,[2] no highly enantioselective intermolecular ene reactions with an alkene as the enophile have been described yet, with only two reports on the intramolecular reaction by Narasaka et al. (including one of the present authors)[3] and Desimoni et al.[4]

On the other hand, the scope of organocatalysis-mediated reactions is expanding very rapidly, and many new chiral organocatalysts have been developed in recent years.[5] Jørgensen and co-workers[6] and our group[7] both independently developed a diarylprolinol silyl ether as an effective organocatalyst.[8] During our application of this catalyst to the asymmetric Diels–Alder reaction, which is known to be mediated by organocatalysis,[9] we found that the reaction of cyclopentadiene and α,β-enals afforded not the Diels–Alder product, but rather the ene product with high enantioselectivity, as described herein. This behavior appears to be highly unusual. Since the discovery of the mechanistically related Diels–Alder reaction in 1928,[10] cyclopentadiene has often been employed as one of the most versatile dienes.[11] However, as far as we are aware there have been no reports of it acting as the ene component in an ene reaction, though the reaction of cyclopentadiene with benzalacetone or benzalacetophenone to give 1,2-dihydropentalenes, in which a Michael-type adduct is postulated as an intermediate, has been reported.[12]

The reaction of cyclopentadiene and cinnamaldehyde was selected as a model and various organocatalysts were examined (Table 1).[13] When diphenylprolinol (**1**) was employed, no reaction proceeded. On the other hand, its trimethylsilyl (TMS) ether **2** is an effective catalyst and ene products **7a** and **8a** were generated in good yield. As there is isomerization between **7a** and **8a**, the ratio of **7a** and **8a** changed according to the reaction conditions and time. The optical purity of the products was determined for the mixture of **7a** and **8a** by chiral HPLC analysis, after reduction with $NaBH_4$ and hydrogenation, and showed that high enantioselectivity (83% *ee*) had been achieved. Modification of the

Table 1: Effect of catalyst on the ene reaction of cyclopentadiene.[a]

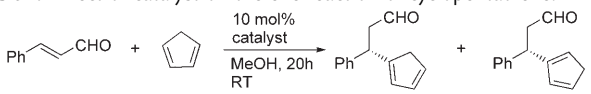

Entry	Catalyst	Yield [%][b]	**7a**/**8a**[c]	*ee* [%][d]
1	**1**	0	–	–
2	**2**	83	56:44	83
3	**3**	67	59:41	85
4	**4**	68	54:46	91
5	**5**	63	65:35	85
6	**6**	0	–	–
7[e]	**4**	0	–	–
8[f]	**4**	84	70:30	92

[a] Unless otherwise shown, the reaction was conducted with 0.07 mmol of catalyst, 0.7 mmol of cinnamaldehyde, and 2.1 mmol of cyclopentadiene at room temperature. [b] Yield of the isolated products **7a** and **8a**. [c] Determined by ^{1}H NMR spectroscopic analysis. [d] The *ee* value of a mixture of **7a** and **8a** (see the text and Supporting Information). [e] CF_3CO_2H (20 mol%) was used as an additive. [f] *p*-Nitrophenol (20 mol%) was used as an additive.

[*] H. Gotoh, R. Masui, H. Ogino, Dr. M. Shoji, Prof. Dr. Y. Hayashi
Department of Industrial Chemistry
Faculty of Engineering, Tokyo University of Science
Kagurazaka, Shinjuku-ku, Tokyo 162-8601 (Japan)
Fax: (+81) 3-5261-4631
E-mail: hayashi@ci.kagu.tus.ac.jp
Homepage: http://www.ci.kagu.tus.ac.jp/lab/org-chem1/

[**] This work was partially supported by the Toray Science Foundation and a Grand-in-Aid for Scientific Research on Priority Areas 16073219 from MEXT.

Supporting information for this article is available on the WWW under http://www.angewandte.org or from the author.

 © 2006 Wiley-VCH Verlag GmbH & Co. KGaA, Weinheim

catalyst was investigated to improve this result further. The silyl moiety affected the enantioselectivity, and the presence of the bulkier *tert*-butyldimethylsilyl (TBS) ether in catalyst **4** led to higher enantioselectivity with a decrease in reactivity. Changing the phenyl group to the 3,5-dimethylphenyl group in catalyst **5** had little effect, but the 3,5-bis(trifluoromethyl)-phenyl-containing catalyst **6** was completely inactive in the

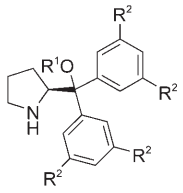

Catalyst	R^1	R^2
1	H	H
2	TMS	H
3	TES	H
4	TBS	H
5	TMS	Me
6	TMS	CF_3

present reaction, which is in marked contrast to the asymmetric reactions reported by Jørgensen and co-workers.[6] The additive is also important: The strong acid (CF_3CO_2H) does not promote the reaction and only affords the dimethyl acetal of cinnamaldehyde instead. When 20 mol% of *p*-nitrophenol was employed in combination with the TBS ether **4**, the reaction rate increased and a good yield (84%) was obtained without compromising the enantioselectivity (92% *ee*). When the MacMillan catalyst[9a] was employed with *p*-nitrophenol under our optimal reaction conditions, no reaction was observed. The reaction scarcely proceeded when our catalyst **4** was employed as its HCl salt under the MacMillan Diels–Alder reaction conditions ($MeOH/H_2O$),[9a] thus affording the Diels–Alder adduct in 12% yield after 20 h without formation of the ene product. The ene reaction also proceeded with the same efficiency on a larger scale (4.0 mmol).

The generality of the reaction was next examined (Table 2). Not only the phenyl group but also a naphthyl substituent can be successfully employed as a β-substituent of

Table 2: Asymmetric ene reaction of cyclopentadiene catalyzed by **4**.[a]

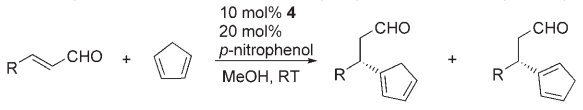

Entry	R	*t* [h]	Yield [%][b]	**7**/**8**[c]	*ee* [%][d]
1	phenyl	20	84	70:30	92
2[e]	2-naphthyl	3	70	57:43	93
3[e]	*p*-nitrophenyl	3	60[f]	43:57	90
4[e]	*p*-bromophenyl	6	79	67:33	95
5	*p*-methoxyphenyl	8	82	57:43	93
6	3,4-methylenedioxyphenyl	5	78	60:40	93
7[e]	2-furyl	2	80	63:37	91
8	2-thienyl	3	82	40:60	77
9[e]	*o*-methoxyphenyl	3	80	82:18	95

[a] The reaction was conducted with 0.07 mmol of catalyst **4**, 0.14 mmol of *p*-nitrophenol, 0.7 mmol of aldehyde, and 2.1 mmol of cyclopentadiene in MeOH (1.4 mL) at room temperature. [b] Yield of the isolated products **7a** and **8a**. [c] Determined by ^{1}H NMR spectroscopic analysis. [d] Determined by chiral HPLC analysis after reduction and hydrogenation. [e] 20 mol% of catalyst was employed. [f] Diels–Alder products were obtained in 11% yield.

the acrylaldehyde, thus affording the ene adduct with excellent enantioselectivity. The reaction rate is slow for electron-deficient substituents, such as *p*-nitro- and *p*-bromophenyl groups, for which 20 mol% of the catalyst was employed to provide good yield with excellent enantioselectivity. In the former reaction, a small amount of the Diels–Alder products was obtained. For electron-rich rings, such as *p*-methoxy- or 3,4-methylenedioxyphenyl, the reaction rate is increased with excellent enantioselectivity. A heteroaromatic substituent at the β-position of the acrylaldehyde is also suitable, and although enantioselectivity was 77% in the case of thienyl, 91% *ee* was obtained when furyl was employed. When the β-substituent is an alkyl group, as in 3-cyclohexylpropenal and hept-2-enal, a complex mixture was obtained.

The absolute configuration was determined as follows: The mixture of **7a** and **8a** was treated with $NaBH_4$ to afford an alcohol, which was converted into its TBS ether **9** (see Scheme 1). Ozonolysis followed by reduction with $NaBH_4$

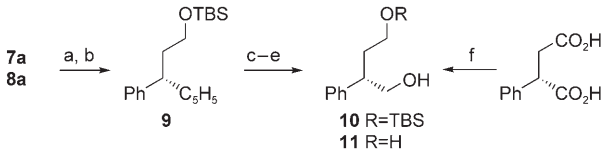

Scheme 1. Determination of the absolute configuration. Reagents: a) $NaBH_4$; b) TBSCl, imidazole (79%, 2 steps); c) 1. O_3; 2. $NaBH_4$; d) 1. $NaIO_4$; 2. $NaBH_4$; 3. separation of alcohol (11%) and diol (16%; for 4 steps); e) TBAF (quant.); f) $LiAlH_4$, 75%. TBAF = tetrabutylammonium fluoride.

afforded an alcohol, which on oxidation with $NaIO_4$ and reduction with $NaBH_4$ gave **10** in 11% over four steps. Removal of the TBS group provided diol **11**, which is in good agreement, as determined by chiral HPLC analysis, with an authentic sample prepared by the reduction of (*S*)-phenylsuccinic acid.

The reaction would proceed as follows: Catalyst **4** and α,β-enal combine to give an iminium ion, which reacts with cyclopentadiene, as described in Scheme 2, to avoid the steric repulsion caused by the bulky diphenyl silyl ether group. The 5-substituted 1,3-cyclopentadiene unit would be formed by this mechanism and then readily isomerize to the more stable 1- and 2-substituted isomers.[14,15]

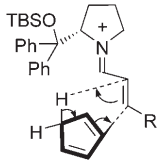

Scheme 2. Transition-state model.

An intramolecular Diels–Alder reaction was investigated as a synthetic application of these ene products.[16] Cyclopentadiene derivatives **7a** and **8a** were treated with a Wittig reagent to afford *trans* α,β-unsaturated esters **12** and **13**, respectively, in good yield. Although the 1- and 2-substituted cyclopenta-1,3-dienes **12** and **13** were formed and isolated, the 5-substituted isomer **14** was not detected,[14] but the Diels–Alder reaction proceeded via the latter in toluene at 120°C to afford tricyclic compound **15** stereoselectively in 68% yield (Scheme 3). As the Diels–Alder reaction proceeded from the most reactive

 © 2006 Wiley-VCH Verlag GmbH & Co. KGaA, Weinheim

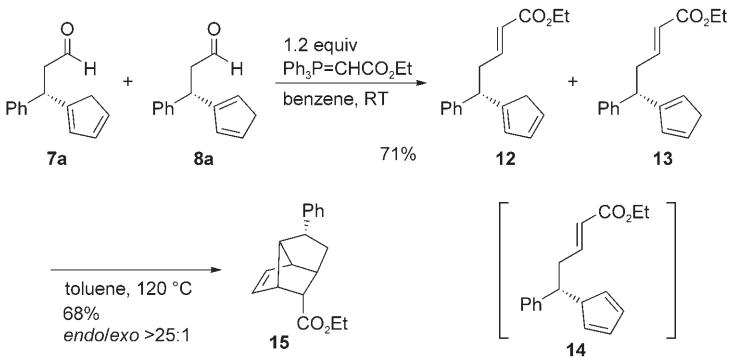

Scheme 3. Synthesis of a chiral tricyclic compound.

isomer **14**, separation of the regioisomers is not necessary for obtaining the Diels–Alder adduct.

In summary, we have discovered the first enantioselective intermolecular ene reaction that uses α,β-enals as the enophile, is catalyzed by diphenylprolinol silyl ether, and affords chiral cyclopentadienes as versatile synthetic intermediates. This reaction is also the first in which cyclopentadiene acts as the ene component in an ene reaction with α,β-enals despite the numerous reports of it acting as a diene in the Diels–Alder reaction.

Experimental Section

(*E*)-Cinnamaldehyde (500 μL, 4.0 mmol) was added to a solution of catalyst **4** (146.3 mg, 0.40 mmol) and *p*-nitrophenol (110.7 mg, 0.80 mmol) in MeOH (8.0 mL) at room temperature. The solution was stirred for 1 min and then cyclopentadiene (0.98 mL, 12 mmol) was added. The reaction mixture was stirred for 20 h at room temperature, and then excess cyclopentadiene was azeotropically removed with benzene. The residue was purified by column chromatography on silica gel (AcOEt/hexane, 1:20) to afford ene products **7a** and **8a** (667.2 mg, 84%). The ratio of **7a** and **8a** was determined by ^{1}H NMR (400 MHz) spectroscopic analysis. As the isomers **7a** and **8a** were separated by HPLC with an OJ-H column (254 nm, 2-propanol/hexane (1:200), 1.0 mL min^{-1}; **7a** $t_R = 15.7$ min, **8a** $t_R = 18.0$ min), a small amount of **7a** and **8a** was isolated and analyzed.

$NaBH_4$ (7.3 mg, 0.194 mmol) was added to a solution of **7a** and **8a** (12.8 mg, 0.065 mmol) in MeOH (0.65 mL) at 0 °C. The reaction mixture was stirred for 20 min at this temperature, then the reaction was quenched with phosphate buffer solution (pH 7.0). The organic materials were extracted with AcOEt, were dried over anhydrous Na_2SO_4, concentrated under reduced pressure, and the residue was used in the next reaction without further purification.

Pd/C (10 mol%, 3.2 mg) was added to a solution of this crude mixture in AcOEt (0.65 mL) at room temperature, and the reaction mixture was stirred overnight under a H_2 atmosphere. The reaction mixture was filtered through a pad of celite and concentrated in vacuo. The residue was purified by preparative TLC (AcOEt/hexane, 1:3) to afford (*R*)-3-cyclopentyl-3-phenylpropan-1-ol (13.2 mg, quant.). The enantiomeric excess was determined by HPLC using an AS-H column at 254 nm (2-propanol/hexane (1:200), 1.0 mL min^{-1}; major enantiomer $t_R = 13.4$ min, minor enantiomer $t_R = 11.5$ min).

Received: July 21, 2006
Published online: September 26, 2006

Keywords: asymmetric synthesis · cyclopentadiene · Diels–Alder reaction · ene reaction · organocatalysis

[1] a) H. M. R. Hoffmann, *Angew. Chem.* **1969**, *81*, 597; *Angew. Chem. Int. Ed. Engl.* **1969**, *8*, 556; b) W. Oppolzer, V. Snieckus, *Angew. Chem.* **1978**, *90*, 506; *Angew. Chem. Int. Ed. Engl.* **1978**, *17*, 476; c) B. B. Snider, *Acc. Chem. Res.* **1980**, *13*, 426; asymmetric ene reaction, see: d) K. Mikami, K. Terada in *Comprehensive Asymmetric Catalysis III*, *Vol. III* (Ed.: E. N. Jacobsen, A. Pfaltz, H. Yamamoto), Springer, Berlin, **1999**, pp. 1143–1174.

[2] Reviews, see: a) K. Mikami, M. Shimizu, *Chem. Rev.* **1992**, *92*, 1021; b) D. J. Berrisford, C. Bolm, *Angew. Chem.* **1995**, *107*, 1862; *Angew. Chem. Int. Ed. Engl.* **1995**, *34*, 1717; c) L. C. Dias, *Curr. Org. Chem.* **2000**, *4*, 305.

[3] a) K. Narasaka, Y. Hayashi, S. Shimada, *Chem. Lett.* **1988**, 1609; b) K. Narasaka, Y. Hayashi, S. Shimada, J. Yamada, *Isr. J. Chem.* **1991**, *31*, 261.

[4] G. Desimoni, G. Faita, P. P. Righetti, N. Sardone, *Tetrahedron* **1996**, *52*, 12019.

[5] a) A. Berkssel, H. Groger, *Asymmetric Organocatalysis*, Wiley-VCH, Weinheim, **2005**; b) P. I. Dalko, L. Moisan, *Angew. Chem.* **2004**, *116*, 5248; *Angew. Chem. Int. Ed.* **2004**, *43*, 5138; c) Y. Hayashi, *J. Syn. Org. Chem. Jpn.* **2005**, *63*, 464.

[6] a) M. Marigo, T. C. Wabnitz, D. Fielenbach, K. A. Jørgensen, *Angew. Chem.* **2005**, *117*, 804; *Angew. Chem. Int. Ed.* **2005**, *44*, 794; b) M. Marigo, D. Fielenbach, A. Braunton, A. Kjarsgaard, K. A. Jørgensen, *Angew. Chem.* **2005**, *117*, 3769; *Angew. Chem. Int. Ed.* **2005**, *44*, 3703; c) M. Marigo, J. Franzen, T. B. Poulsen, W. Zhuang, K. A. Jørgensen, *J. Am. Chem. Soc.* **2005**, *127*, 6964; d) M. Marigo, T. Schulte, J. Franzen, K. A. Jørgensen, *J. Am. Chem. Soc.* **2005**, *127*, 15710; e) W. Zhuang, M. Marigo, K. A. Jørgensen, *Org. Biomol. Chem.* **2005**, *3*, 3883; f) J. Franzen, M. Marigo, D. Fielenbach, T. C. Wabnitz, A. Kjarsgaard, K. A. Jørgensen, *J. Am. Chem. Soc.* **2005**, *127*, 18296; g) M. Marigo, S. Bertelsen, A. Landa, K. A. Jørgensen, *J. Am. Chem. Soc.* **2006**, *128*, 5475; h) S. Brandau, A. Landa, J. Franzen, M. Marigo, K. A. Jørgensen, *Angew. Chem.* **2006**, *118*, 4411; *Angew. Chem. Int. Ed.* **2006**, *45*, 4305.

[7] Y. Hayashi, H. Gotoh, T. Hayashi, M. Shoji, *Angew. Chem.* **2005**, *117*, 4284; *Angew. Chem. Int. Ed.* **2005**, *44*, 4212.

[8] For another application of diphenylprolinol silyl ether, see: a) Y. Chi, S. H. Gellman, *Org. Lett.* **2005**, *7*, 4253; b) H. Sunden, I. Ibrahem, A. Cordova, *Tetrahedron Lett.* **2006**, *47*, 99; c) I. Ibrahem, A. Cordova, *Chem. Commun.* **2006**, 1760; d) Y. Chi, S. H. Gellman, *J. Am. Chem. Soc.* **2006**, *128*, 6804; e) D. Enders, M. R. M. Huttl, C. Grondal, G. Raabe, *Nature* **2006**, *441*, 861.

[9] a) K. A. Ahrendt, C. J. Borths, D. W. C. MacMillan, *J. Am. Chem. Soc.* **2000**, *122*, 4243; b) A. B. Northrup, D. W. C. MacMillan, *J. Am. Chem. Soc.* **2002**, *124*, 2458; c) R. M. Wilson, W. S. Jen, D. W. C. MacMillan, *J. Am. Chem. Soc.* **2005**, *127*, 11616; d) K. Ishihara, K. Nakano, *J. Am. Chem. Soc.* **2005**, *127*, 10504; e) A. Sakakura, K. Suzuki, K. Nakano, K. Ishihara, *Org. Lett.* **2006**, *8*, 2229.

[10] O. Diels, K. Alder, *Justus Liebigs Ann. Chem.* **1928**, *460*, 98.

[11] *Encyclopedia of Reagents for Organic Synthesis*, *Vol. 2* (Ed.: L. O. Paquette), Wiley, Chichester, **1995**, pp. 1449–1451.

[12] A. G. Griesbeck, *J. Org. Chem.* **1989**, *54*, 4981.

[13] During the preparation of this Communication, Diels–Alder adducts were obtained when the same reaction was catalyzed by *N*-methylaniline derivatives: T. Kano, Y. Tanaka, K. Maruoka, *Org. Lett.* **2006**, 8, 2687.

[14] V. A. Korenevsky, N. M. Sergeev, *J. Am. Chem. Soc.* **1972**, *94*, 8586.

 © 2006 Wiley-VCH Verlag GmbH & Co. KGaA, Weinheim

[15] A two-step mechanism involving allylic cation by a Friedel–Craft-type reaction might be a possible reaction path.
[16] a) O. Wallquist, M. Rey, A. S. Dreiding, *Helv. Chim. Acta* **1983**, *66*, 1891; b) R. L. Snowden, *Tetrahedron* **1986**, *42*, 3277; c) A. G. Stern, A. Nickon, *J. Org. Chem.* **1992**, *57*, 5342; d) B. Lei, A. G. Fallis, *J. Org. Chem.* **1993**, *58*, 2186.

 © 2006 Wiley-VCH Verlag GmbH & Co. KGaA, Weinheim

Computational Enzymology

DOI: 10.1002/anie.200602711

High-Accuracy Computation of Reaction Barriers in Enzymes**

Frederik Claeyssens, Jeremy N. Harvey, Frederick R. Manby, Ricardo A. Mata, Adrian J. Mulholland, Kara E. Ranaghan, Martin Schütz, Stephan Thiel, Walter Thiel,* and Hans-Joachim Werner**

The accurate prediction of enzyme kinetics from first principles is one of the central goals of theoretical biochemistry. Currently there is considerable debate[1–3] about the applicability of transition state theory (TST) to compute rate constants of enzyme-catalyzed reactions. Classical TST is known to be insufficient in some cases, but corrections for dynamical recrossing and quantum mechanical tunneling can be included.[1,2,4] Many effects that go beyond the framework of TST have been proposed, particularly focusing on the possible role of protein dynamics and conformational effects on the enzyme activity. Unfortunately, the overall importance of these effects for the effective reaction rate is difficult (if not impossible) to determine experimentally. However, if one could compute the quasi-thermodynamical free energy of activation with chemical accuracy (i.e. 1 kcal mol^{-1}), comparison with the effective measured free energy of activation would directly show the importance of other effects.

Combined quantum mechanical/molecular mechanical (QM/MM) methods have become an important tool for computational modeling of enzyme-catalyzed reactions. Only the substrate(s) and relevant residues in the active site are treated quantum mechanically, the rest of the protein is described at the empirical MM level. This lowers the computational expense, making it possible to treat large enzyme systems and the surrounding solvent, and to sample phase space. Nevertheless, the number of QM atoms is still relatively large, and until now only low levels of QM theory, such as semiempirical methods or density functional theory (DFT), have been feasible. Semiempirical methods, though applicable to large systems, are generally not accurate enough because computed free energies of activation may have an error of ten or more kcal mol^{-1}. DFT (especially with the B3LYP functional[5]) offers improved accuracy but still lacks key physical interactions (e.g., dispersion). Often, DFT underestimates barrier heights by several kcal mol^{-1}, which cannot be systematically improved. Thus, when theoretical barriers do not agree with those from experiment, it is not clear whether the discrepancy arises from deficiencies in the electronic structure theory and the sampling, in the experimental observations, or in the underlying theoretical framework of QM/MM and TST.

Consequently, there is a need for high-level electronic structure calculations for reliable predictions of enzyme reactivity. The ab initio electron correlation methods MP2 (Møller–Plesset second-order perturbation theory), CCSD (coupled-cluster theory with single and double excitations), and CCSD(T) (CCSD with a perturbative treatment of triple excitations) provide a well-established hierarchy that converge reliably to give high accuracy, and rate constants of gas-phase reactions involving only a few atoms can be predicted with error bars comparable to those found experimentally.[6,7] However, the computational expense of these methods increases very rapidly with the number of atoms (doubling the system size increases the cost of CCSD(T) by two orders of magnitude), and this has restricted the applications of such methods to small molecules.

The steep increase in the computational cost is mainly a consequence of the delocalized character of the molecular orbitals from the Hartree–Fock (HF) theory. However, in covalent molecules, dynamic electron correlation is a short-ranged phenomenon, and by localizing the molecular orbitals it is possible to introduce a hierarchy of approximations[8,9] that lead to linear scaling of all computational resources with system size. Recent developments[10–14] have made it possible to treat systems that are one order of magnitude larger with a

[*] Dr. F. Claeyssens, Dr. J. N. Harvey, Dr. F. R. Manby, Dr. A. J. Mulholland, K. E. Ranaghan
School of Chemistry
University of Bristol
Cantocks Close, Bristol, BS8 1TS (UK)
Fax: (+44) 117-925-1295
E-mail: adrian.mulholland@bristol.ac.uk
Dr. S. Thiel, Prof. W. Thiel
Max-Planck-Institut für Kohlenforschung
Kaiser-Wilhelm-Platz 1, 45470 Mülheim an der Ruhr (Germany)
Fax: (+49) 208-306-2996
E-mail: thiel@mpi-muelheim.mpg.de
R. A. Mata, Prof. H.-J. Werner
Institut für Theoretische Chemie
Universität Stuttgart
Pfaffenwaldring 55, 70569 Stuttgart (Germany)
Fax: (+49) 711-685-64442
E-mail: werner@theochem.uni-stuttgart.de
Prof. M. Schütz
Institut für Physikalische und Theoretische Chemie
Universität Regensburg
Universitätsstrasse 31, 93040 Regensburg (Germany)

[**] The authors are grateful for financial support from the Royal Society (F.R.M.), EPSRC (F.R.M., A.J.M., J.N.H., K.E.R.), BBSRC (A.J.M.), IBM (A.J.M., F.C.), Deutsche Forschungsgemeinschaft (Leibniz program and SFB 706, H.J.W.), Fonds der Chemischen Industrie (W.T., H.J.W.), Volkswagenstiftung (W.T.), and Fundação para a Ciência e Tecnologia (R.A.M.).

Supporting information for this article is available on the WWW under http://www.angewandte.org or from the author.

 InterScience © 2006 Wiley-VCH Verlag GmbH & Co. KGaA, Weinheim

comparable level of accuracy. In the present study, we use these new high-level local correlation methods in QM/MM calculations on two biochemically well-characterized enzymes, chorismate mutase (CM) and *para*-hydroxybenzoate hydroxylase (PHBH). Combining the ab initio results with thorough sampling, we predict activation enthalpies that approach chemical accuracy.

The CM enzyme catalyzes the Claisen rearrangement of chorismate to prephenate, a key conversion in the shikimic acid pathway that produces aromatic amino acids (Scheme 1).

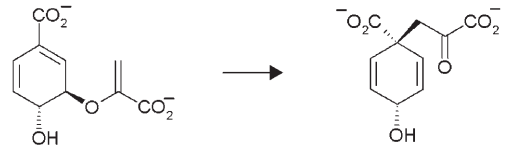

Scheme 1. Claisen rearrangement in CM.

This enzyme has been the object of extensive experimental[15,16] and computational[17–19] research, which have conclusively shown that catalysis proceeds without covalent binding of the substrate to the enzyme. The chemical step is believed to be largely rate-limiting in *Bacillus subtilis* CM, and the uncatalyzed reaction in water proceeds by the same mechanism. This makes CM a particularly convenient target for QM/MM studies,[17–19] which have focused on aspects such as the structure of the enzyme–substrate complex, reaction pathways, and the role of active-site residues in transition-state stabilization. Calculations demonstrate that the key catalytic interactions are primarily electrostatic and are well described in the QM/MM model.[17,18] However, almost all of this previous reaction modeling has been carried out by using semiempirical or DFT methods, which do not predict barrier heights with chemical accuracy.

PHBH is a flavoprotein monooxygenase that catalyzes the hydroxylation of the substrate *p*-hydroxybenzoate (Scheme 2). It plays a crucial role in the oxidative degradation

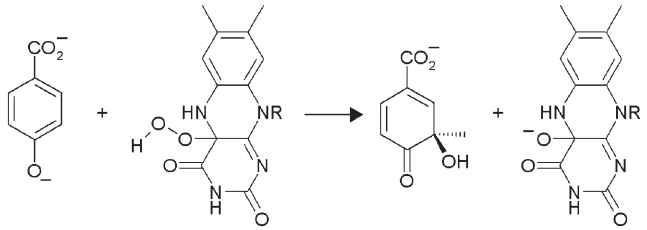

Scheme 2. Hydroxylation reaction in PHBH.

of aromatic compounds, such as lignin, by soil bacteria. The active hydroxylation agent is a flavin hydroperoxide (FAD-HOOH) that hydroxylates *p*-hydroxybenzoate in the *meta* position.

The extensive experimental work on PHBH has been reviewed,[20] and the mechanistically relevant results for the hydroxylation step have been summarized recently.[21] There is a consensus that the hydroxylation involves an electrophilic aromatic substitution on the dianionic substrate, and at around pH 8 (pH at which the enzyme is most active) the hydroxylation is considered to be the rate-determining step.[22,23] An activation enthalpy of 12 kcal mol^{-1} has been obtained at pH 8 from temperature-dependent measurements of the overall rate between 277 and 298 K.[24] The measured rates of hydroxylation at pH 6.5[23,25] and the reported turnover rates at pH 8[22,23] indicate free energies of activation of 14 and 15 kcal mol^{-1},[21] respectively. On the theoretical side, the hydroxylation mechanism in PHBH has been the subject of several QM/MM studies[21,26,27] in which the QM region has been described by the semiempirical AM1 method (in one case also at the HF level[26]). As with CM, tests showed that the key interactions are well captured in the QM/MM model.[21,26]

In the current work, MP2, LMP2, and LCCSD(T0) calculations on CM and PHBH have been carried out (the L in the acronyms indicates that local approximations were used, and T0 is an approximate triples correction[10,11]). These are certainly by far the largest coupled-cluster calculations ever performed (for PHBH correlating 284 electrons by using 1294 basis functions). To account for the effects of conformational fluctuations, the results were averaged over multiple pathways (16 for CM and 10 for PHBH). Initial structures were sampled from semiempirical QM/MM dynamics, and reaction pathways were optimized by using B3LYP/MM. To establish the reliability with respect to all other approximations, extensive convergence studies were performed. The use of an extended QM region for CM (including Arg 7, Arg 63, Glu 78, and Arg 90 side chains and three water molecules in addition to the substrate) changes the B3LYP barrier by only around 0.7 kcal mol^{-1}. Calculations at the MP2 level with very large basis sets (up to quintuple zeta) alter the MP2 barrier heights by less than 0.5 kcal mol^{-1}. This excellent convergence with respect to basis has been confirmed by calculations that use the recently developed explicitly correlated method MP2-F12(loc),[14] which essentially delivers the MP2 basis-set limit. Further extensive tests, as fully described in the Supporting Information, have shown that the effect of local approximations is smaller than 0.5 kcal mol^{-1}. These studies indicate that the computed LCCSD(T0) barrier heights are likely to agree with the full CCSD(T) values at the basis-set limit to within 1 kcal mol^{-1}. This accuracy is unprecedented and was previously difficult to achieve even for small molecules.

An underlying assumption in these calculations is that the CCSD(T) method in the basis-set limit would predict barrier heights accurately. Small-molecule calculations show that the error is unlikely to exceed 1 kcal mol^{-1}. Furthermore, it is assumed that the B3LYP geometries are reliable. This is justified by the fact that the B3LYP and LCCSD(T) transition states appear at almost the same reaction-coordinate value along the B3LYP pathways. The averaged activation enthalpies are summarized in Table 1, and the energy profiles along one typical pathway in CM are shown in Figure 1.

Through comparison of the HF and LCCSD(T0) results, it can be seen that electron correlation effects lower the activation enthalpies by about a factor of 3. This is due to the fact that near the transition state more electrons are spatially close, leading to a significant increase in the

 © 2006 Wiley-VCH Verlag GmbH & Co. KGaA, Weinheim

Table 1: Computed[a] activation enthalpies $\Delta H^{\neq}$ (300 K) for CM and PHBH in kcal mol^{-1}.[b]

Method	CM	PHBH
HF	28.3 (2.1)	36.7 (2.6)
B3LYP	10.2 (1.8)	8.4 (1.4)
LMP2	9.5 (1.0)	10.7 (1.2)
LCCSD(T0)[c]	13.1 (1.1)	13.3 (1.5)
experimental	12.7[d]	12.0[e]

[a] Activation enthalpies were derived from averages of energy differences from single-point QM/MM calculations for the reactant complex and the TS on different adiabatic pathways. The aug-cc-pVTZ basis was used on oxygen and cc-pVTZ on all other atoms, and a point-charge representation of the MM environment was included in the QM calculations. Starting points for adiabatic pathways were derived from snapshots from molecular-dynamics sampling described elsewhere.[21,28] The geometries along the adiabatic pathways were obtained from separate QM/MM optimizations by using B3LYP for the QM part. Zero-point energy and 300 K thermal corrections were derived from QM-only calculations on cluster models. For CM, the cluster included chorismate and surrounding residues and was treated with B3LYP; for PHBH, the QM region was used and treated with AM1. Full details can be found in the Supporting Information. [b] In parentheses: root-mean-square deviations for 16 (CM) and 10 (PHBH) snapshots. [c] LCCSD(T0) denotes local coupled cluster with an approximate treatment of the (T) triples correction in which certain couplings are neglected.[10,11] [d] Reference [15]. [e] Reference [24].

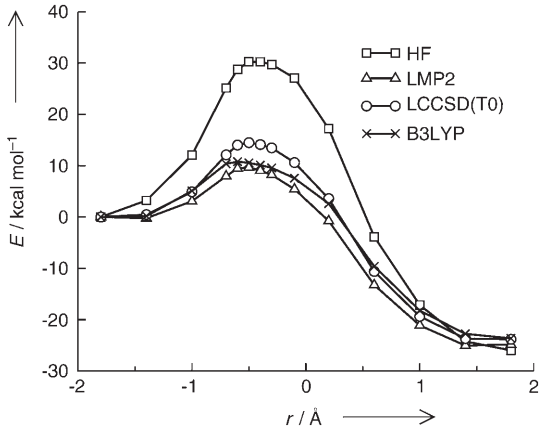

Figure 1. QM/MM potential-energy curves (without thermal corrections) for a single representative reaction pathway in CM. The reaction coordinate *r* is defined as the difference between the length of the breaking C–O bond and the forming C–C bonds. See Table 1 for details of methods used.

correlation energy relative to the reactants. LMP2 and B3LYP overestimate the correlation effect and predict barriers that are too low by 3–5 kcal mol^{-1}. Only the LCCSD(T0) results are in close agreement with experimental results. These results indicate that a high-level electron correlation treatment, such as LCCSD(T0), is necessary to make quantitative predictions of barrier heights or other energetic properties in enzymes. It is likely that the limiting factor for the overall accuracy is now the QM/MM approximation and not the QM treatment as in previous semi-empirical or DFT studies. It should be noted in this context that the barrier height has been found to be insensitive to the size of the chosen QM region.[18,19]

Reaction rates depend on activation free energies rather than on the enthalpies shown in Table 1. The difference between these two quantities can be estimated with the use of low-level QM/MM methods by comparing mean activation enthalpies with activation free energies. The free energies are computed by umbrella sampling (CM)[29] or thermodynamic integration (PHBH).[21] For CM, the entropic contribution at 300 K is computed to be 2.5 kcal mol^{-1}, in good agreement with the experimental value of 2.7 kcal mol^{-1}.[15] For PHBH, the computed entropic contribution is 0.4 kcal mol^{-1}, which, together with the best activation enthalpy computed herein, gives $\Delta G^{\neq}(300\ \mathrm{K}) = 13.7$ kcal mol^{-1}. This is in good agreement with the experimental values of 14–15 kcal mol^{-1}.[22,23,25]

Our high-level QM/MM calculations provide near-quantitative results for the activation enthalpies and free energies of the reactions catalyzed by CM and PHBH. The agreement with experimental results indicates that transition-state theory provides a good general framework for understanding the rates of such enzyme-catalyzed reactions. Our results show that it is now possible to perform electronic structure calculations on large systems approaching chemical accuracy, thus allowing quantitative studies of reaction mechanisms in enzymes. This development opens new horizons for theoretical biochemistry and many other areas of computational chemistry.

Received: July 7, 2006
Published online: September 22, 2006

Keywords: ab initio calculations · enzyme catalysis · QM/MM calculations · reaction mechanisms · transition-state theory

[1] A. Warshel, *Annu. Rev. Biophys. Biomol. Struct.* **2003**, *32*, 425–443.
[2] M. Garcia-Viloca, J. Gao, M. Karplus, D. G. Truhlar, *Science* **2004**, *303*, 186–195.
[3] W. Min, B. P. English, G. Luo, B. J. Cherayil, S. C. Kov, X. S. Xie, *Acc. Chem. Res.* **2005**, *38*, 923–931.
[4] L. Masgrau, A. Roujeinikova, L. O. Johannissen, P. Hothi, J. Basran, K. E. Ranaghan, A. J. Mulholland, M. J. Sutcliffe, N. S. Scrutton, D. Leys, *Science* **2006**, *312*, 237–241.
[5] A. D. Becke, *J. Chem. Phys.* **1993**, *98*, 5648–5652.
[6] D. G. Truhlar, B. C. Garrett, S. J. Klippenstein, *J. Phys. Chem.* **1996**, *100*, 12771–12800.
[7] T. Wu, H.-J. Werner, U. Manthe, *Science* **2004**, *306*, 2227–2229.
[8] P. Pulay, *Chem. Phys. Lett.* **1983**, *100*, 151–154.
[9] C. Hampel, H.-J. Werner, *J. Chem. Phys.* **1996**, *104*, 6286–6297.
[10] M. Schütz, H.-J. Werner, *Chem. Phys. Lett.* **2000**, *318*, 370–378.
[11] M. Schütz, *J. Chem. Phys.* **2000**, *113*, 9986–10001.
[12] M. Schütz, H.-J. Werner, *J. Chem. Phys.* **2001**, *114*, 661–681.
[13] H.-J. Werner, F. R. Manby, P. Knowles, *J. Chem. Phys.* **2003**, *118*, 8149–8160.
[14] F. R. Manby, H.-J. Werner, T. B. Adler, A. J. May, *J. Chem. Phys.* **2006**, *124*, 094103 (6 pages).
[15] P. Kast, M. Asif-Ullah, D. Hilvert, *Tetrahedron Lett.* **1996**, *37*, 2691–2694.
[16] S. K. Wright, M. S. DeClue, A. Mandal, L. Lee, O. Wiest, W. W. Clieland, D. Hilvert, *J. Am. Chem. Soc.* **2005**, *127*, 12957–12964.
[17] B. Szefczyk, A. J. Mulholland, K. E. Ranaghan, W. A. Sokalski, *J. Am. Chem. Soc.* **2004**, *126*, 16148–16159.
[18] F. Claeyssens, K. E. Ranaghan, F. R. Manby, J. N. Harvey, A. J. Mulholland, *Chem. Commun.* **2005**, 5068–5070.

 © 2006 Wiley-VCH Verlag GmbH & Co. KGaA, Weinheim

[19] A. Crespo, M. A. Marti, D. A. Estrin, A. E. Roitberg, *J. Am. Chem. Soc.* **2005**, *127*, 6940 – 6941.
[20] B. Entsch, W. J. H. van Berkel, *FASEB J.* **1995**, *9*, 476 – 483.
[21] H. M. Senn, S. Thiel, W. Thiel, *J. Chem. Theory Comput.* **2005**, *1*, 494 – 505.
[22] M. Husain, B. Entsch, D. P. Ballou, V. Massey, P. J. Chapman, *J. Biol. Chem.* **1980**, *255*, 4189 – 4197.
[23] B. Entsch, B. A. Palfey, D. P. Ballou, V. Massey, *J. Biol. Chem.* **1991**, *266*, 17341 – 17349.
[24] W. J. H. van Berkel, F. Müller, *Eur. J. Biochem.* **1989**, *179*, 307 – 314.
[25] M. Ortiz-Maldonado, L. J. Cole, S. M. Dumas, B. Entsch, D. P. Ballou, *Biochemistry* **2004**, *43*, 1569 – 1579.
[26] L. Ridder, J. N. Harvey, I. M. C. M. Rietjens, J. Vervoort, A. J. Mulholland, *J. Phys. Chem. B* **2003**, *107*, 2118 – 2126.
[27] S. R. Billeter, C. F. W. Hanser, T. Z. Mordasini, M. Scholten, W. F. Van Gunsteren, *Phys. Chem. Chem. Phys.* **2001**, *3*, 688 – 695.
[28] K. E. Ranaghan, B. Szefczyk, W. A. Sokalski, J. C. Hermann, A. J. Mulholland, *Org. Biomol. Chem.* **2004**, *2*, 968 – 980.
[29] L. Ridder, I. M. C. M. Rietjens, J. Vervoort, A. J. Mulholland, *J. Am. Chem. Soc.* **2002**, *124*, 9926 – 9936.

 © 2006 Wiley-VCH Verlag GmbH & Co. KGaA, Weinheim

DNA Damage

DOI: 10.1002/anie.200601681

Sequence-Specific Nucleic Acid Damage Induced by Peptide Nucleic Acid Conjugates That Can Be Enzyme-Activated**

Philippe Simon, Jean-Luc Décout, and Marc Fontecave**

Sequence-specific targeting and cleavage of nucleic acids (in DNA or RNA) can be achieved using oligo-2′-deoxyribonucleotides (ODN) or peptide nucleic acids (PNA) covalently attached to a reactive chemical.[1] These conjugates combine the ability to recognize (through the ODN or the PNA) and react (through the chemical) with a selected sequence, which thus can be either redox cleaved or hydrolyzed. However, the great majority of the chemical reactants used in this context to date are non-natural compounds (such as, transition-metal complexes, polyamines, photosensitizers) and, as a consequence, such systems in general require an activating mechanism (e.g., light, strong reductants) unavailable within the cell. An attractive solution to this problem might be provided by ODN conjugates carrying a chemical moiety serving to recruit a cellular enzyme and directing the action of that enzyme towards selective nucleic acid cleavage. Such a chemical can be a substrate or an inhibitor of the enzyme. To our knowledge, there is only one example of such a conjugate that can be "enzyme activated" illustrating this strategy.[2] It is provided by studies of ODN-camptothecin (or rebeccamycin) conjugates in which the chemical moieties are selective inhibitors of Topoisomerase I.[2] In that case the chemical group has two roles: 1) by recruiting Topoisomerase I, it directs its action to the selected sequence; 2) by blocking the religation step, it ensures the persistence of DNA breaks. There is no reported example of a PNA conjugate used in this application. Herein we report a PNA–flavin conjugate **1** (Figure 1) in which the flavin moiety can recruit an NAD(P)H:flavin oxidoreductase (flavin reductase) allowing the flavin–enzyme combination to activate molecular oxygen in the presence of NADH and to selectively damage a complementary ODN in vitro.

PNAs, which are non-ionic ODN analogues with a non-natural polyamide backbone, have many advantages over ODN: 1) they are resistant to nucleases and proteases; 2) they display a very high affinity for complementary DNA and RNA and can bind to single- and double-stranded DNA targets.[3] Flavin reductases are ubiquitous enzymes, present in all living organisms, which catalyze the reduction of free

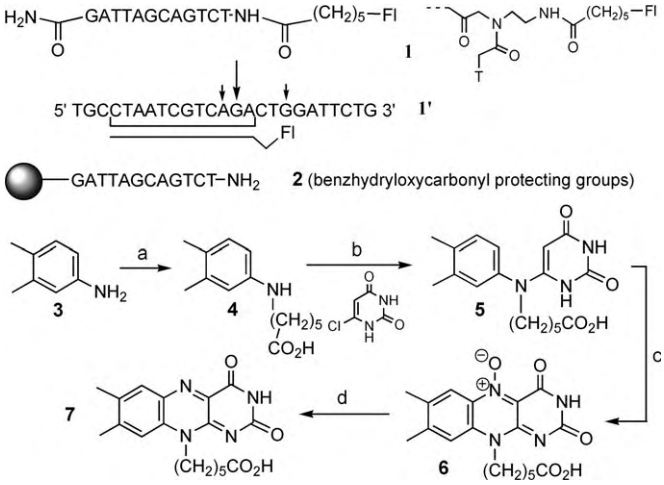

Figure 1. Structures of the compounds reported herein. Flavin **7** was prepared in 4 steps: a) 6-chlorohexanoic acid, TEA, EtOH, reflux (53%); b) dioxane/H_2O (1:1), pH 7.5, reflux (71%); c) $NaNO_2$, acetic acid (81%); d) DTT, dioxane/EtOH (1:1), reflux (90%). The arrows on top of **1′** indicate the sites of oxidation. The bridge marks the sequence in **1′** that is complementary to the PNA sequence in **1**. The orientation of **1** when hybridized to **1′** is also indicated. Fl indicates the isoalloxazine ring system of the flavin. The carboxylic acid side chain on N^{10} in **7** is a highly modified version of the normal flavin ribityl chain. TEA = triethylamine, DDT = 4,4′-dichlorodiphenyl-1,1,1-trichloroethane.

[*] Dr. P. Simon, Prof. J.-L. Décout, Prof. M. Fontecave
Département de Pharmacochimie Moléculaire
UMR 5063 CNRS/Université Joseph Fourier-Grenoble I
ICMG-FR CNRS 2607
5 Avenue de Verdun, 38240 Meylan (France)
Fax: (+33) 4-7604-1007
E-mail: jean-luc.decout@ujf-grenoble.fr
mfontecave@cea.fr
Dr. P. Simon
Laboratoire de Chimie et Biochimie des Centres Rédox Biologiques
UMR 5047 CEA/CNRS/Université Joseph Fourier-Grenoble I
CEA-Grenoble
17 Rue des Martyrs, 38054 Grenoble Cedex 9 (France)
Fax: (+33) 4-3878-9124

[**] The authors thank Christine Saint-Pierre and Didier Gasparutto (CEA Grenoble) for expert assistance.

Supporting information for this article is available on the WWW under http://www.angewandte.org or from the author.

 © 2006 Wiley-VCH Verlag GmbH & Co. KGaA, Weinheim

flavins (riboflavin, flavin mononucleotide (FMN), or flavin adenine dinucleotide (FAD)) by reduced pyridine nucleotides (NAD(P)H). Reduced flavins react with oxygen efficiently thus generating radical and oxidizing species (hydroxyl radicals and H_2O_2) potentially reactive towards DNA.[4] They also efficiently transfer electrons to ferric ions.[5] In a recent study, flavin reductase was shown to promote oxidative DNA damage in *E. coli* cells through reduction of intracellular free iron by enzymatically reduced flavins.[6] This observation is the basis for studying the PNA–flavin/flavin reductase combination for selectively destroying a DNA target.

There is only one reported synthesis of flavin-tethered PNA.[7,8] In that case the synthetic procedure allows a given nucleic base to be replaced at various positions along the PNA chain by the isoalloxazine ring system of the flavin which attaches through nitrogen atoms, either N^3 or N^{10}.[8] The novel compounds reported herein, with N^{10} of the isoalloxazine ring system linked to the N terminal of the PNA through a highly modified version of the ribityl chain of riboflavin, are shown in Figure 1.

The PNA–flavin conjugate **1** was synthesized (see Supporting Information) by coupling the carboxylic acid function of **7** to the N terminal end of the protected 12-mer PNA **2** attached to the solid support of synthesis using *O*-(7-azabenzotriazol-1-yl)-1,1,3,3-tetramethyluronium hexafluorophosphate (HATU) as coupling agent (Figure 1). After release and deprotection using trifluoroacetic acid (TFA)/*m*-cresol, the resulting conjugate **1** was purified by HPLC on C_{18} reversed phase and characterized by mass spectrometry and UV/Vis spectroscopy.

Strong binding of compound **1** to the 25-mer ODN **1′** containing a complementary sequence (Figure 1) and **1**:**1′** duplex formation were confirmed by melting assays (4 μM, 0.1M NaCl, $T_m = 61\,°C$).

Flavin reductase activity is generally assayed from the oxidation of NAD(P)H and spectrophotometrically monitored at 340 nm during aerobic incubation with the enzyme and a flavin substrate. The enzyme used herein as a model is the flavin reductase from *E. coli* named Fre. We have previously shown that Fre has very broad substrate specificity since it accepts riboflavin, FMN, or FAD as a substrate.[9] This indicates that the ribityl chain of a flavin plays almost no role in its recognition by Fre. The crystal structure of the Fre–riboflavin complex has been determined and indeed shows that the protein/substrate interaction almost exclusively involves the isoalloxazine ring system and not the ribityl chain located at the surface.[10] Riboflavin analogues with modified lateral chains at N^{10} are excellent substrates.[9] The flexibility is such that ODN–flavin conjugates, with the isoalloxazine ring system attached to the 5′-end of the ODN are also substrates.[11] Using increasing concentrations of **1** as the unique flavin component in the assay mixture and 200 μM NADH at pH 7.8 and 25 °C, we observed a saturation behavior for the enzyme activity. The data could be fitted with a V_m value of 18000 nmol oxidized NADH/min mg^{-1} protein and a K_m value for **1** of 3 μM (data not shown), which are in the same order-of-magnitude range as the values obtained with FAD ($V_m = 26000$, $K_m = 1$ μM) and riboflavin ($V_m = 70000$, $K_m = 1.5$ μM), thus showing that **1** is well recognized as a substrate by Fre.

The most remarkable result is that flavin reductase retains as much as approximately 25% activity when **1** (10 μM) is hybridized to **1′** (1 equiv) at 25 °C (below the T_m value). This activity remained unchanged upon further addition of **1′**. The **1**:**1′** complex is thus a substrate of Fre and this is in marked contrast with comparable ODN–flavin conjugates which were shown to be unable to promote NADH oxidation in the presence of small excesses of a complementary ODN.[11] Further studies are required to understand the molecular basis for such a drastic difference.

The above result thus made PNA–flavin conjugates good candidates as DNA (or RNA) damaging agents that can be enzyme activated. This potential was evaluated in an in vitro system in which **1** was incubated with a 2-fold excess of **1′** (to ensure full complexation) in the presence of NADH (5 mM), various concentrations of $FeSO_4$ and Fre (1 μM) in 50 mM Tris buffer (tris(hydroxmethyl)aminomethane) pH 7.8. The reaction was carried out in the dark to avoid photoreactions of the flavin moiety and the reaction mixture was analyzed by gel electrophoresis after 30 min incubation and piperidine treatment (see Supporting Information). The results are shown in Figure 2. They demonstrate an interesting selectivity of the

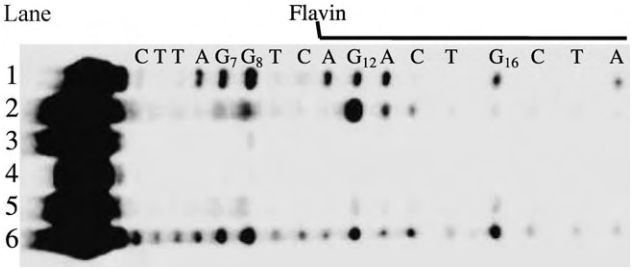

Figure 2. Phosphoimager picture of a 15% polyacrylamide/7 M urea gel showing the cleavage products of the 25 base-pair target **1′** ^{32}P-labeled at the 5′-end. Lane 1: Sequencing products (G + A) from **1′** in formic acid; lane 2: **1**:**1′** duplex (4 μM with **1′** in 2-fold excess) incubated in the dark at 37 °C, pH 7.8 (50 mM Tris buffer) for 30 min in the presence of NADH (5 mM), flavin reductase (Fre; 1 μM), $FeSO_4$ (40 μM); lane 3: as in lane 2 but without NADH and Fre; lane 4: as in lane 2 but without any iron; lane 5: as in lane 2 with the addition of SOD (4 μM) and catalase (0.5 μM); lane 6: as in lane 2 but with **1′** (8 μM) and riboflavin (4 μM) instead of the **1**:**1′** duplex; see text for details. The orientation of the complementary chain of the PNA–flavin **1** is also shown.

reaction promoted by the Fre/**1** combination. Indeed, cleavage occurred mainly at the duplex junction where the flavin is located. The major product resulted from the oxidation of the closest guanine residue (G12) within the PNA binding site and a minor one was observed at the closest guanine (G8) of the GG sequence adjacent to the duplex-simplex junction (lane 2). This result is consistent with a flavin-dependent production of reactive species and a short diffusion of the latter. The cleavage was both enzyme- and iron-dependent (lanes 3 and 4, respectively) and was inhibited by addition of superoxide dismutase (SOD) and catalase (lane 5) or by exclusion of oxygen. This result suggests that the reaction proceeds by: 1) reduction of the isoalloxazine ring system of

 © 2006 Wiley-VCH Verlag GmbH & Co. KGaA, Weinheim

the **1**:**1**′ complex by NADH, catalyzed by Fre; 2) reduction of O_2 by the reduced flavin, generating H_2O_2 in close proximity of the target, 3) oxidation of adjacent reactive bases by OH· radicals (Fenton reaction). The cleavage yield was iron-concentration dependent but cleavage could be observed with no addition of iron as a result of the presence of iron impurities in the buffer. Accordingly, no cleavage could be observed after treating the buffer with chelating resins (Chelex) to remove these impurities (lane 4). When riboflavin was used in place of **1**, the selectivity was lost and almost all bases of the target were oxidized, with guanines (in particular GG doublets) being, as expected, the most reactive sites (lane 6). Furthermore, the efficiency of the reaction was significant with a 20% yield based on the target obtained after only 30 min reaction.

In conclusion, we report herein the first PNA-based artificial agent that can be enzyme activated for nucleic acid oxidation. The PNA–flavin **1** displays two interesting properties: 1) in complex with a complementary strand, it is recognized as a substrate by a flavin reductase; 2) under enzyme-activity conditions, specific and efficient oxidation of the complementary strand at reactive guanines adjacent to the flavin moiety occurs. Thus **1** combines DNA damaging activity, arising from its flavin moiety, and selectivity, arising from its PNA moiety.

Future experiments will aim at finding whether such PNA–flavin compounds might function in vivo by recruiting cellular flavin reductases to direct their action against a target sequence. Flavin reductases are ubiquitous enzymes found in all living organisms and have been shown to promote intracellular Fenton reactions and DNA damaging in vivo.[6] Thus the flavin- and iron-dependent DNA damage reaction studied herein occurs in vivo and the question is whether we can make it sequence-selective with PNA-flavins as shown herein in vitro. A limitation might be the very poor cellular uptake of PNAs in general and thus specific transfection strategies might be required.[12] On the other hand, since riboflavin conjugation has been shown to facilitate protein entry into human cells in culture[13] and PNA conjugation to lipophilic groups results in improved cell uptake,[12] conjugates such as **1** could have better cell-penetrating properties than the corresponding flavin-free PNA. This is under investigation.

Received: April 28, 2006
Revised: June 30, 2006
Published online: September 26, 2006

Keywords: DNA damage · enzymes · flavins · oligonucleotides · oxidoreductases

[1] P. B. Arimondo, A. S. Boutorine, J.-C. François, *Recent Res. Dev. Bioconjugate Chem.* **2002**, *1*, 29–53; A. S. Boutorine, P. B. Arimondo, *Nucleic Acids Mol. Biol.* **2004**, *18*, 243–268.
[2] M. Matteucci, K.-Y. Lin, T. Huang, R. Wagner, D. Sternbach, M. Mehrotra, J. M. Besterman, *J. Am. Chem. Soc.* **1997**, *119*, 6939–6940; P. B. Arimondo, G. S. Laco, C. J. Thomas, L. Halby, D. Pez, P. Schmitt, A. Boutorine, T. Garestier, Y. Pommier, S. M. Hecht, J.-S. Sun, C. Bailly, *Biochemistry* **2005**, *44*, 4171–4180.
[3] P. Wittung, S. K. Kim, O. Buchardt, P. Nielsen, B. Nordèn, *Nucleic Acids Res.* **1994**, *22*, 5371–5377.
[4] P. Gaudu, D. Touati, V. Nivière, M. Fontecave, *J. Biol. Chem.* **1994**, *269*, 8182–8188.
[5] M. Fontecave, J. Covès, J.-L. Pierre, *Biometals* **1994**, *7*, 3–8.
[6] A. N. Woodmansee, J. A. Imlay, *J. Biol. Chem.* **2002**, *277*, 34055–34066.
[7] H. Ikeda, K. Yoshida, M. Ozeki, I. Saito, *Tetrahedron Lett.* **2001**, *42*, 2529–2531.
[8] M. K. Cichon, C. H. Haas, F. Grolle, A. Mees, T. Carell, *J. Am. Chem. Soc.* **2002**, *124*, 13984–13985.
[9] F. Fieschi, V. Nivière, C. Frier, J.-L. Décout, M. Fontecave, *J. Biol. Chem.* **1995**, *270*, 30392–30400.
[10] M. Ingelman, S. Ramaswamy, V. Nivière, M. Fontecave, H. Eklund, *Biochemistry* **1999**, *38*, 7040–7049.
[11] P. Simon, C. Dueymes, M. Fontecave, J.-L. Décout, *Angew. Chem.* **2005**, *117*, 2824–2827; *Angew. Chem. Int. Ed.* **2005**, *44*, 2764–2767.
[12] U. Koppelhus, P. E. Nielsen, *Adv. Drug Delivery Rev.* **2003**, *55*, 267–280.
[13] S. R. Holladay, Z.-F. Yang, M. D. Kennedy, C. P. Leamon, R. J. Lee, M. Jayamani, T. Mason, P. S. Low, *Biochim. Biophys. Acta* **1999**, *1426*, 195–204.

 © 2006 Wiley-VCH Verlag GmbH & Co. KGaA, Weinheim

Interfaces

DOI: 10.1002/anie.200601826

Ion-Transfer Reactions at the Nanoscopic Water/*n*-Octanol Interface**

Ping Jing, Meiqin Zhang, Hu Hu, Xiaodong Xu, Zhongwei Liang, Bo Li, Li Shen, Shubao Xie, Carlos M. Pereira, and Yuanhua Shao**

Lipophilicity is recognized as one of the most important properties for understanding the role of drugs in living systems. The common method of assessing the lipophilicity of

[*] P. Jing, M. Zhang, H. Hu, X. Xu, Z. Liang, B. Li, L. Shen, S. Xie, Prof. Dr. Y. Shao
Beijing National Laboratory for Molecular Sciences
College of Chemistry and Molecular Engineering
Peking University
Beijing 100871 (China)
Fax: (+86) 10-6275-1708
E-mail: yhshao@pku.edu.cn
Prof. Dr. C. M. Pereira
Departamento de Química CIQ-L4
Faculdade de Ciências da Universidade do Porto
R. do Campo Alegre 687, Porto 4169-007 (Portugal)
Fax: (+351) 226-082-959
E-mail: cmpereir@fc.up.pt
Homepage: http://www.chem.pku.edu.cn/shaoyh/eindex.htm

[**] This work was supported by NSFC (20235010, 20475003, and 20420130137), the special 985 project of Peking University, and FCT (BSAB/502/2005).

Supporting information for this article is available on the WWW under http://www.angewandte.org or from the author.

© 2006 Wiley-VCH Verlag GmbH & Co. KGaA, Weinheim
InterScience

a compound is to determine its partition coefficient in a two-solvent system. *n*-Octanol has similarities with lecithins, which are the main constituent of biological membranes, and that attribute makes the water/*n*-octanol (W/OC) interface a suitable system to mimic the charge-transfer processes through biomembranes. The partition coefficients ($\log P$) measured in the W/OC system are standard data in chemistry and pharmacy.[1] Experimentally, there are several methods that can be employed to determine the $\log P$ values of neutral compounds, such as HPLC, but the $\log P$ of ionic species in this system is seldom reported. Several works have shown that ion partition diagrams can be satisfactorily used for evaluation of the lipophilicity of ionizable compounds at a water/1,2-dichloroethane (W/DCE) interface.[2,3] The standard potentials, the Gibbs energies of transfer, and the $\log P$ can be evaluated from these ion partition diagrams, and these parameters have well-defined relationships that are summarized in Equation (1), where z and F are the number of ions transferred and the Faraday constant, respectively.[3,4]

$$z F \Delta_{O}^{W}\phi_{t}^{0} = \Delta G_{tr,i}^{0,w\rightarrow o} = -2.303 R T \log P_{i}^{0} \quad (1)$$

Scholz et al.[4,5] studied ion transfer (IT) at the W/OC interface by the three-phase junction method for a series of anions. Using an electrochemical technique, they were able to measure the standard potential of tetraphenylborate (TPB^-) IT at the W/OC interface ($\Delta_{OC}^{W}\phi_{TPB^-}^{0} = 160$ mV). According to Born theory the Gibbs energy of an IT has a linear relationship with $1/r$. The radius r of the TPB^- anion is almost same as that of a tetraphenylarsonium ($TPAs^+$) cation, so their values of the Gibbs energy of transfer are assumed to be equal. This constitutes the principle known as the TATB assumption (TATB = tetraphenylphosphonium tetraphenylborate),[6] which has been widely used in electrochemistry at liquid/liquid interfaces.

The use of a W/OC interface for performing electrochemical measurements is usually difficult, mainly because there are very few base electrolytes that can dissolve reasonably in the *n*-octanol phase. Kihara et al.[7] reported that tetrapentylammonium tetrakis[3,5-bis(trifluoromethyl)-phenyl]borate ($TPenA^+TFPB^-$) can dissolve in *n*-octanol, but they did not provide any direct transfer wave at a micro-W/OC interface. In addition, the presence of hydrogen bonds between water and *n*-octanol at the interface introduces dramatic changes in the interfacial structure of such a system. Molecular dynamic studies present a value for the width of the W/OC interface of 5.5 Å,[8,9] which is similar to that of the W/DCE interface of 6 Å.[10] However, at the W/DCE interface an interfacial mixed-solvent region, which is not thicker than two to three molecule diameters,[11] is observed at both sides of the interface, whereas in the case of the W/OC interface there are drastic effects from the structure of the solvents. Particularly, a depletion layer (alkane-like region) is observed on the organic side of the interface with a minimum at about 6 Å from the Gibbs surface but which exerts its effect up to 20 Å from the Gibbs surface.[12] Compared to a W/DCE interface, a W/OC interface is broader and rougher.

A liquid/liquid interface supported at the tip of a nanopipette was first introduced in 1997,[13] and the main advantages of such a technique are the possibility of reducing the iR drop completely, increasing significantly the mass transport, and performing measurements with or without supporting electrolyte.[14] These valuable features make it a viable method to polarize the W/OC interface supported on a nanopipette.

Herein, we report that the W/OC interface supported at the tip of a nanopipette can be polarized. The transfer waves of anionic form of lauric acid (LA^-), $TPAs^+$, and tetrabutylammonium (TBA^+) were obtained and their thermodynamic data were evaluated. The kinetic behavior of LA^- was analyzed and compared with that at the W/DCE system. Among familiar supporting electrolytes in the organic phase, bis(triphenylphosphoranylidene)ammonium tetrakis(4-chlorophenyl)borate (BTPPATPBCl) can dissolve in small amounts in *n*-octanol and be used as the supporting electrolyte.

Electrochemical studies of the transfer processes of these species at the W/OC interface were carried out using a two-electrode setup, and cells I and II:

Cell I: Ag | AgTPBCl | BTPPATBCl (0.12 mM) (*n*-octanol or DCE) || Li_2SO_4 (10 mM) + TBACl or TPAsCl (x mM) || Ag_2SO_4 | Ag

Cell II: Ag | AgTPBCl | BTPPATPBCl (0.12 mM) (*n*-octanol or DCE) || Li_2SO_4 (10 mM) + Lauric acid (y mM) (+ LiOH or HNO_3 to desired pH) || Ag_2SO_4 | Ag

Figure 1 shows that the cyclic voltammograms of these IT reactions can be observed within the potential window, and they have reasonably good steady-state waves after background subtraction. For micro- and nanopipettes, an asymmetric cyclic voltammogram should normally be obtained because of the hemispherical diffusion of ions from the outside to the inside of the pipette; the peak-shaped wave is a result of the linear diffusion of ions from the inside to the outside of the pipette.[15] However, for the cases of very short and sharp nanopipettes, nearly steady-state voltammograms have already been reported.[16] This is probably a consequence of the special shape of the nanopipettes, which have a

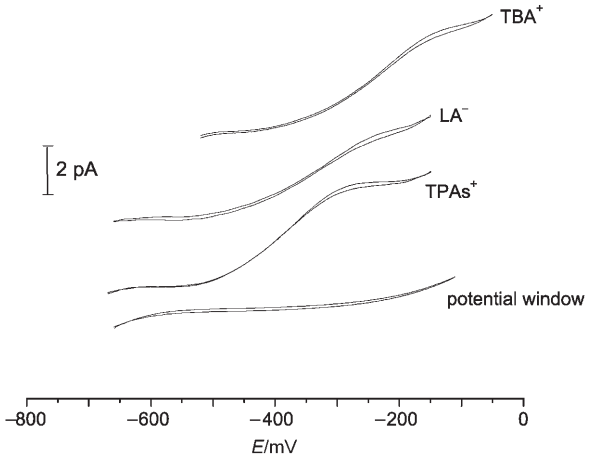

Figure 1. Potential window and background-subtracted cyclic voltammograms of IT at the W/OC interface. The systems are shown in Cells I and II: $x = 1$ mM, $y = 1$ mM. The sweep rate is 50 mV s^{-1}. The radii of the nanopipettes are 45, 60, 56, and 42 nm for $TPAs^+$, LA^-, TBA^+, and the potential window, respectively.

 © 2006 Wiley-VCH Verlag GmbH & Co. KGaA, Weinheim

hemispherical diffusion field at both sides (see Figure 2). As a result of the shape of the cyclic voltammograms and the evident difficulties in analyzing the experimental data, differential pulse voltammetry (DPV) was applied in further

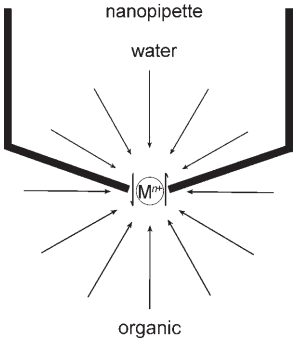

Figure 2. The possible diffusion field at a very short and sharp nanopipette.

studies. Using the TATB assumption and published data for the standard potential of TPB^- transfer at the W/OC interface, the value for the standard potential of $TPAs^+$ transfer at the W/OC interface can be evaluated as $\Delta^{W}_{OC}\phi^{0}_{TPAs^+} = -160$ mV. To evaluate the formal transfer potential of TBA^+ across the W/OC interface, TPAsCl and TBACl were mixed together to experimentally assess the potential separation between the peaks of their transfers. From Equation (2) and Figure 3, the formal potential of TBA^+ transfer

$$\Delta^{W}_{OC}\phi^{0\prime}_{m} - \Delta^{W}_{OC}\phi^{0\prime}_{n} = \Delta^{W}_{OC}\phi^{p}_{m} - \Delta^{W}_{OC}\phi^{p}_{n} \quad (2)$$

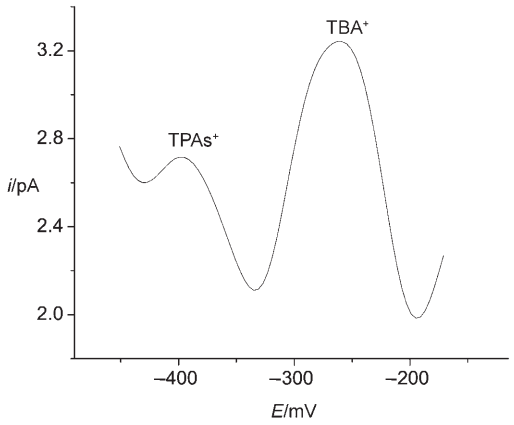

Figure 3. Differential pulse voltammograms of TBA^+ and $TPAs^+$ at the W/OC interface with Cell I. The concentrations of TBA^+ and $TPAs^+$ are both 0.5 mM.

across the W/OC interface can be calculated as −20 mV, where $\Delta^{W}_{OC}\phi^{0\prime}_{i}$ is the formal Galvani potential of transfer for an ion and $\Delta^{W}_{OC}\phi^{p}_{i}$ is the experimental peak potential of this ion.

Based on Figure 1 and the Supporting Information, it is possible to obtain the formal potential of LA^- transfer at the W/OC interface, which is equal to −134 mV. The peak potential of LA^- transfer at the W/OC interface remains almost unchanged between pH 8 and 12. It is not possible to access experimentally the transfer of LA^- when the pH values are lower than 7.5, which is similar to the case of a W/DCE system.[3] As expected, the peak potential of LA^- transfer at a liquid/liquid interface is not affected by pH when it is higher than the pK_a of lauric acid ($pK_a = 4.98$).[3]

Clearly, it is easier to analyze experimental data by DPV. The diffusion coefficients of TBA^+, $TPAs^+$, and LA^- can be calculated (see the Supporting Information) and the values are listed in Table 1.

Table 1: Thermodynamic data for LA^-, $TPAs^+$, and TBA^+ obtained at W/DCE and W/OC interfaces.

	W/OC		
	Diffusion coefficient D [$\times 10^{-6}$ cm^2 s^{-1}]	Formal potential $\Delta^{W}_{O}\phi^{0\prime}_{m}$ [mV]	log P
LA^-	2.89 ± 0.04	−134	−2.29
TBA^+	2.53 ± 0.03	−20	0.34
$TPAs^+$	0.85 ± 0.01	−160	2.73
	W/DCE		
	Diffusion coefficient D [$\times 10^{-6}$ cm^2 s^{-1}]	Formal potential $\Delta^{W}_{O}\phi^{0\prime}_{m}$ [mV]	log P
LA^-	3.49 ± 0.02	−179[3]	−3.03
TBA^+	2.95 ± 0.02	−230[19]	3.93
$TPAs^+$	1.03 ± 0.01	−364[19]	6.22

Cell II was employed to compare the results with IT at the W/DCE interface. In this system a nearly steady-state cyclic voltammogram for IT at the W/DCE interface was also obtained (see Figure 4). The tetraethylammonium ion (TEA^+) was used as the internal reference in the DCE phase ($\Delta^{W}_{DCE}\phi^{0\prime}_{TEA^+} = 48$ mV).[11] The diffusion coefficient can also be calculated from Equation (3),[15,17] where i_{ss} is the

$$i_{ss} = 3.35\, n\, \pi F\, D\, c\, r \quad (3)$$

steady-state current, r is the inner pipette radius, and the other parameters have the usual meanings. The thermody-

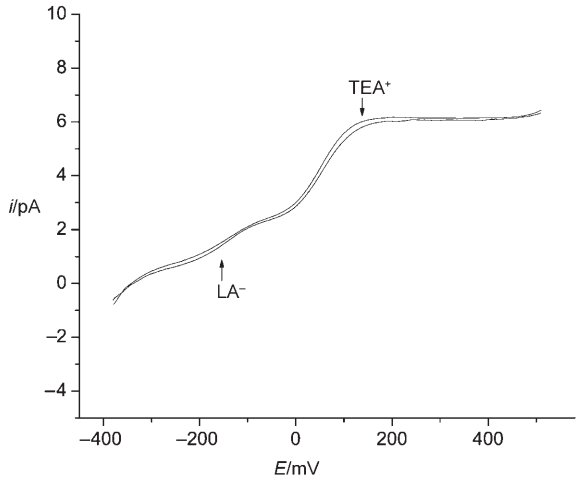

Figure 4. Cyclic voltammograms of LA^- and TEA^+ transfer at the W/DCE interface with Cell II. The radius of the nanopipette is 39 nm; $\gamma = 1$ mM, pH 10.47.

 © 2006 Wiley-VCH Verlag GmbH & Co. KGaA, Weinheim

namic parameters of the two systems including $\log P$ are summarized in Table 1.

At these soft nano-liquid/liquid interfaces, both W/OC and W/DCE systems show a nearly (or pseudo) steady-state quasi-reversible voltammogram. Bard and Mirkin[18] developed a three-point method for extracting the heterogeneous electron-transfer kinetic parameters from the steady-state voltammogram of a quasi-reversible reaction, and Shao and Mirkin[13] introduced this method into charge transfer at liquid/liquid interfaces. Table 2 shows the kinetic parameters

Table 2: Kinetic parameters for LA^- transfer at the W/OC and W/DCE interfaces.

	Radius [nm]	$\Delta E_{1/4}$ [mV]	$\Delta E_{3/4}$ [mV]	α	k^0 [cm s^{-1}]
W/OC	71	36.0	39.0	0.73	0.265
	60	35.0	37.0	0.78	0.211
	48	33.0	34.5	0.86	0.198
	42	49.0	55.0	0.47	0.295
W/DCE	55	37.0	34.0	0.65	1.07
	45	33.0	34.0	0.68	2.02
	39	32.0	35.0	0.74	1.30
	28	31.5	32.5	0.88	1.01

calculated according to this method for transfer of LA^- at both interfaces. The mean values of the standard rate constants (k^0) obtained are (0.24 ± 0.05) and (1.35 ± 0.65) cm s^{-1} at the W/OC and W/DCE systems, respectively. These results are further evidence that the W/OC interface is broader and rougher than the W/DCE interface. The mean values of the transfer coefficient (α) are 0.71 ± 0.24 for the W/OC system and 0.74 ± 0.10 for the W/DCE system.

In conclusion, we have shown that the W/OC interface can be polarized, and that a potential window of about 400 mV can be obtained and some IT processes observed by using the nano-W/OC interface supported on the tip of a nanopipette. This actually opens up a new and more straightforward way of obtaining the $\log P$ values of ionizable drugs. The diffusion coefficients of IT at the W/OC interface are slightly smaller than those at the W/DCE interface. The formal potentials of these ions at the W/OC interface are shifted to less negative values compared with those of the transfer processes at the W/DCE interface. As the effective width of a W/OC interface is wider than that of the W/DCE interface, the kinetic rate constant of LA^- is about six times less than that at the W/DCE interface. However, the potential window remains rather small for carrying out studies of drug lipophilicity and establishing partition diagrams of ionizable drugs. Work with the goal of extending the potential window is being undertaken.

Experimental Section

Chemicals: 1,2-Dichloroethane (DCE), lithium sulfate, lithium hydroxide, nitric acid, and lauric acid (LAH) were obtained from Beijing Chemical Co. and were all A.R. grade. Tetrabutylammonium chloride (TBACl, $\geq 97\%$), tetraphenylarsonium chloride (TPAsCl, $\geq 97\%$), bis(triphenylphosphoranylidene)ammonium chloride (BTPPACl, $\geq 98\%$), potassium tetrakis(4-chlorophenyl)borate (KTPBCl, $\geq 98\%$), and *n*-octanol ($\geq 99.5\%$) were purchased from Fluka. Bis(triphenylphosphoranylidene)ammonium tetrakis(4-chlorophenyl)borate (BTPPATPBCl) was synthesized according to published procedures[14a] and used as the supporting electrolyte in the organic phase. Millipore water was employed for the preparation of aqueous solutions.

Fabrication of nanopipettes: A Model P-2000 laser puller (Sutter Instruments) was used to fabricate the nanopipette with an orifice radius in the range of 20–100 nm from quartz capillaries (1 mm outer diameter, 0.7 mm inner diameter). The aqueous solution was filled from the back of the nanopipette using a 10-μL syringe. The nanopipette was checked with an optical microscope (BX-51, Olympus) prior to each measurement to ensure there was no bubble trapped inside.

Electrochemical measurements: Cyclic and differential pulse voltammetry were performed by a BAS 100B electrochemical workstation (Bioanalytical Systems). Silver wire (0.125 mm in diameter) coated with Ag_2SO_4 was inserted into the nanopipette as the reference electrode. A Ag | AgTPBCl electrode was the reference electrode in the organic phase. All the experiments were carried out at room temperature (22 ± 2 °C).

Received: May 10, 2006
Revised: July 19, 2006
Published online: September 26, 2006

Keywords: electrochemistry · interfaces · ion transfer · lipophilicity · nanotechnology

[1] A. Leo, C. Hansch, D. Elkins, *Chem. Rev.* **1971**, *71*, 525–616.
[2] F. Reymond, G. Steyaert, P.-A. Carrupt, B. Testa, H. Girault, *J. Am. Chem. Soc.* **1996**, *118*, 11951–11957.
[3] F. Reymond, V. Chopineaux-Courtois, G. Steyaert, G. Bouchard, P.-A. Carrupt, B. Testa, H. Girault, *J. Electroanal. Chem.* **1999**, *462*, 235–250.
[4] R. Gulaboski, A. Galland, G. Bouchard, K. Caban, A. Kretschmer, P.-A. Carrupt, Z. Stojek, H. H. Girault, F. Scholz, *J. Phys. Chem. B* **2004**, *108*, 4565–4572.
[5] R. Gulaboski, V. Mirčeski, F. Scholz, *Electrochem. Commun.* **2002**, *4*, 277–283.
[6] E. Grunwald, G. Baughman, G. Kohnstam, *J. Am. Chem. Soc.* **1960**, *82*, 5801–5811.
[7] H. Ohde, A. Uehara, Y. Yoshida, K. Maeda, S. Kihara, *J. Electroanal. Chem.* **2001**, *496*, 110–117.
[8] R. L. Napoleon, P. B. Moore, *J. Phys. Chem. B* **2006**, *110*, 3666–3673.
[9] W. H. Steel, R. A. Walker, *Nature* **2003**, *424*, 296–299.
[10] I. Benjamin, *J. Chem. Phys.* **1992**, *97*, 1432–1445.
[11] H. H. Girault, D. J. Schiffin in *Electroanalytical Chemistry, Vol. 15* (Ed.: A. J. Bard), Marcel Dekker, New York, **1989**, pp. 1–141.
[12] I. Benjamin, *Chem. Phys. Lett.* **2004**, *393*, 453–456.
[13] Y. Shao, M. V. Mirkin, *J. Am. Chem. Soc.* **1997**, *119*, 8103–8104.
[14] a) F. Li, Y. Chen, M. Zhang, P. Jing, Z. Gao, Y. Shao, *J. Electroanal. Chem.* **2005**, *579*, 89–102; b) P. Sun, F. O. Laforge, M. V. Mirkin, *J. Am. Chem. Soc.* **2005**, *127*, 8596–8597.
[15] A. A. Stewart, Y. Shao, C. M. Pereira, H. Girault, *J. Electroanal. Chem.* **1991**, *305*, 135–139.
[16] a) Y. Tong, Y. Shao, E. Wang, *Anal. Chem.* **2001**, *11*, 1241–1245 (in Chinese); b) C. Cai, Y. Tong, M. V. Mirkin, *J. Phys. Chem. B* **2004**, *108*, 17872–17878.
[17] P. D. Beattie, A. Delay, H. Girault, *J. Electroanal. Chem.* **1995**, *380*, 167–175.
[18] M. V. Mirkin, A. J. Bard, *Anal. Chem.* **1992**, *64*, 2293–2302.
[19] T. Kakiuchi in *Liquid/Liquid Interface: Theory and Methods* (Eds.: A. G. Volkov, D. W. Deamer), CRC, Boca Raton, FL, **1996**, pp. 1–17.

 © 2006 Wiley-VCH Verlag GmbH & Co. KGaA, Weinheim

Heterogeneous Catalysis

DOI: 10.1002/anie.200601853

Single Gold Atoms in Heterogeneous Catalysis: Selective 1,3-Butadiene Hydrogenation over Au/ZrO_2**

Zhi-Pan Liu, Chuan-Ming Wang, and Kang-Nian Fan*

Oxide-supported metal systems are perhaps the most common heterogeneous catalysts, in which metal particles are long believed to be responsible for the catalytic activity.[1] This general concept is, however, challenged by recent studies, particularly on Au-based catalysts.[2–6] It was reported that single Au atoms/cations supported on certain oxides can catalyze reactions such as CO oxidation,[3] the water gas shift reaction ($CO + H_2O$),[4] and hydrogenation.[5,6] These findings imply the cost of noble-metal catalysts may be decreased dramatically and homogeneous catalysis may be mimicked in a heterogeneous environment if metal cations are highly dispersed on oxides. Such a linkage between heterogeneous and homogeneous catalysis, if established, is of huge incentive.[2] Although homogeneous catalysis by cationic gold has been well documented,[7,8] their heterogeneous analogues are newly identified and many fundamental issues are illusive, such as the active-site structure, the oxidation state of Au, and the microscopic reaction mechanism. Our aim is to provide deeper insight into the single Au heterogeneous catalysis; therefore, the selective hydrogenation of 1,3-butadiene ($H_2C{=}HC\text{-}HC{=}CH_2$) on Au/ZrO_2 is studied herein as a model reaction using density functional theory (DFT) slab calculations.

The activity of Au complexes deposited on various oxides, such as La_2O_3,[3a] MgO,[5a] zeolite NaY,[3b] ceria,[4] and zirconia,[6] has been tested over recent years in investigations into the possibility of performing homogeneous catalytic reactions under heterogeneous conditions. In particular, Zhang et al.[6] reported that the Au/ZrO_2 catalyst remains highly active at very low loadings of Au for the hydrogenation of 1,3-butadiene and that butene is selectively produced without any butane by-product. The Au species in the catalyst was found to be Au^{III} by using X-ray photoelectron spectroscopy (XPS) and H_2 titration. The high selectivity is rather surprising as 1,3-butadiene hydrogenation is conventionally catalyzed by precious transition metals (Pd, Pt), in which the deep hydrogenation to butane is a known problem. It is therefore highly desirable to understand the origin of this single Au heterogeneous catalysis by comparing it with traditional heterogeneous catalysis on metal particles and also with Au-based homogeneous catalysis.

Knowledge of how Au monomers bind to ZrO_2 is the first step towards a systematic understanding of the selective butadiene hydrogenation. We considered four possible Au monomers on zirconia, namely, Au atom (Au^0), AuOH (Au^I), AuOOH, and $Au(OH)_3$ (Au^{III}) for this purpose. Tetragonal ZrO_2 (t-ZrO_2) was chosen as the support because it is one of the common phases in the prepared ZrO_2.[9] Both flat and stepped t-ZrO_2 surfaces were then used to anchor the four Au monomers (ZrO_2 can hardly be reduced,[10] and thus surface O vacancies were not considered). The modeled flat t-ZrO_2 surface is the most stable surface (that is, the flat t-ZrO_2{101} as shown in Figure 1a,b). In addition, two types of stepped surfaces, {001}- and {100}-type, which can be naturally cleaved from the t-ZrO_2{101} surface are modeled, as represented by the low Miller index surfaces, {203} and {201}, respectively (Figure 1c,d). The {001}- and {100}-type steps are expected to be the most common structural defects in t-ZrO_2 because the {001} and {100} surfaces of t-ZrO_2 are more stable than any other surface planes, except for the most stable {101} surface.[10b] All DFT slab calculations were performed using

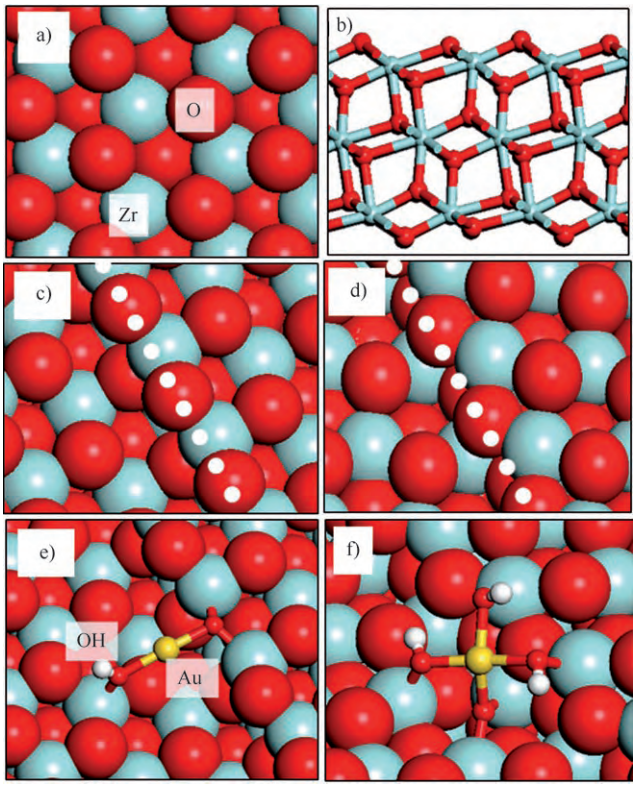

Figure 1. The modeled surface structures and the structures of the cationic Au monomer adsorption at the steps (O red, Zr blue, Au yellow, H gray). a,b) Top and side views, respectively, of t-ZrO_2{101}; c) t-ZrO_2{203} with {001}-type steps; d) t-ZrO_2{201} with {100}-type steps; e) AuOH/t-ZrO_2{203}; and f) $Au(OH)_3$/t-ZrO_2{201}. The dotted lines in (c) and (d) are drawn along the step edges to guide the eye.

[*] Prof. Z.-P. Liu, C.-M. Wang, Prof. K.-N. Fan
Shanghai Key Laboratory of Molecular Catalysis and Innovative Materials
Department of Chemistry, Fudan University
Shanghai 200433 (China)
Fax: (+86) 21-6564-2400
E-mail: zpliu@fudan.edu.cn

[**] This work was supported by the NSF of China (20573023, 20433020), Pujiang Plan, and NSF of Shanghai Sci. Tech. Committee (06PJ14011, 02JD14023, and 05DZ22313). The authors thank the Shanghai Supercomputing Center for computing time.

Supporting information for this article is available on the WWW under http://www.angewandte.org or from the author.

© 2006 Wiley-VCH Verlag GmbH & Co. KGaA, Weinheim

the SIESTA package with a GGA-PBE functional (see Supporting Information for calculation details).[11,12]

The adsorption of the four Au monomers on the t-ZrO_2 surfaces were investigated first. The structures were checked with Nose thermostat molecular dynamics at 300 K to avoid trapping in local minima. We measured the thermodynamic stability of the Au monomers by using the reaction shown as Equation (1), in which Au(X) represents the four Au monomers (see Table 1) and y and z are coefficients to balance the reaction.

$$Au(OH)_3 + ZrO_2 \rightarrow [Au(X)]/ZrO_2 + y\,H_2O + z\,O_2 \quad (1)$$

The reaction describes the formation of the Au/ZrO_2 catalyst starting from the Au^{III}-containing solution ($HAuCl_4$ in alkaline solutions), which then undergoes calcination at 473 K in the experimental investigation.[6] The calculated reaction energies ΔE_f of the most stable Au(X) monomer are listed in Table 1 (the calculated Au–O bond lengths are listed in the Supporting Information). The ΔE_f values were obtained directly from the DFT total energy (E is, strictly speaking, the Helmohotz free energy at 0 K with zero-point vibrations being neglected). For solid states, such as ZrO_2 and Au(X)/ZrO_2 in Equation (1), this is a good approximation to the Gibbs free energy (G) as the temperature T and pressure p contributions are small. The E values for gas-phase molecules can be quite different from the G values, mainly as a result of the large entropy term at elevated temperatures.[13,14] Herein, we utilize standard thermodynamic data to estimate the temperature contribution to the free energy of gas-phase H_2O and O_2 following the procedure as described previously.[14] Our calculations showed that for 1 mol O_2 at (500 K, 1 atm), $G(O_2)$ is lower than $E(O_2)$ (with zero-point energy included) by 0.93 eV, whereas it is 0.89 eV for H_2O. Then, the ΔG_f values at 500 K/1 atm for the formation of the Au monomers could be estimated (Table 1).

Table 1: The reaction energies (ΔE_f) and reaction free energies (ΔG_f; 500 K, 1 atm) of Au monomers (Au(X)) deposited on the flat {101}, stepped {203}, and {201} t-ZrO_2 surfaces.

Au(X)	{101}		{203}		{201}	
	ΔE_f [eV]	ΔG_f [eV]	ΔE_f [eV]	ΔG_f [eV]	ΔE_f [eV]	ΔG_f [eV]
$Au(OH)_3$	−2.64	−2.64	−3.23	−3.23	−3.66	−3.66
AuO_2H	−1.35	−2.25	−1.61	−2.51	−1.53	−2.43
AuOH	−1.76	−3.12	−2.33	−3.69	−1.94	−3.30
Au	0.03	−2.00	0.53	−1.51	0.45	−1.59

It can be seen from Table 1 that the $Au(OH)_3$ moieties (Au^{III}) at the oxide defects are the most stable of the four different Au monomers at low temperatures, whereas the neutral Au^0 atoms adsorb most weakly on all ZrO_2 surfaces. This result agrees with the experimental evidence for the presence of Au^{III}.[3,6] Another stable Au species is Au^I, whose stability quickly "catches up" as the temperature increases. Au^I on the flat {101} and stepped {203} surfaces at 500 K are already more stable than Au^{III}. By further considering the formation of Au metal starting from $Au(OH)_3$, that is, $Au(OH)_3 \rightarrow Au^0$ atom $\rightarrow$ Au bulk, we can deduce that the ΔE_f value for the formation of bulk Au is approximately −3 eV (Au cohesive energy is −3.2 eV from our DFT studies). As metallic Au is also less stable than $Au(OH)_3$ on ZrO_2, we can conclude that Au^{III} on ZrO_2 is the most stable Au species at low temperatures (e.g., below 500 K). The entropy terms of the decomposition products, H_2O and O_2, will shift the equilibrium towards the reduced form of Au at high temperatures and finally lead to bulk Au.

Table 1 also shows that relative to the flat {101} surface, generally stepped sites can stabilize ionic Au monomers (Au^I and Au^{III}) better. But, why? On metal surfaces, it is well known that defects bond to many adsorbates more strongly as a result of the metal atom being less coordinated with more reactive d states.[12b,14] However, we found that the physical origin of the enhanced bonding for ionic Au at oxide defects is quite different. We have illustrated the structure of the two most stable ionic Au species, that is, AuOH/t-ZrO_2{203} and $Au(OH)_3$/t-ZrO_2{201} in Figure 1e,f. Similar to the structure of cationic Au in solution,[7,8] our results show that the most stable Au^I center has a two-coordinate linear structure (Figure 1e) and Au^{III} has a four-coordinate planar structure (Figure 1f). Such saturated Au monomers are generally more stable than unsaturated ones. Clearly, to achieve the particular structure for Au, a suitable local geometry is required for lattice O atoms (O_{latt}) that surround the Au cation, and the OH groups attached to the Au center should be stabilized by Zr cations. This behavior leads to the formation of Au-O-Zr linkages. At defected sites of the oxide, it is more convenient to achieve the linear or planar structure for ionic Au. By contrast, the flat {101} surface has to undergo significant relaxation to achieve the Au linear or planar structure. Thus, the Au cations there are generally less stable.

As the hydrogenation of 1,3-butadiene is performed under reductive conditions at 400 K, one may argue that the oxidized form Au^{III} may not be stable for this reaction. We analyzed the possibility of Au^I formation from Au^{III} from thermodynamic data by using the chemical formula shown in Equation (2).

$$Au(OH)_3/ZrO_2 + H_2 \rightarrow AuOH/ZrO_2 + 2\,H_2O \quad (2)$$

On the basis of the data in Table 1, we calculated that the ΔE_f values of the reaction [Eq. (2)] are −1.58, −1.55, and −0.74 eV for the flat and stepped surfaces, respectively. As all the values are negative, it is indicated that the $Au^{III} \rightarrow Au^I$ reduction is thermodynamically favored. In addition, we further checked the kinetic possibility of H_2 dissociation on Au^{III} at the reaction temperature (400 K). As a representative, we examined the transition state for H_2 dissociations on $Au(OH)_3$ at the stepped {201} surface, in which the ΔE_f value of $Au^{III} \rightarrow Au^I$ is the highest. The reaction barrier is calculated to be only 0.16 eV. Therefore, both the thermodynamic and kinetic data indicate that the $Au^{III} \rightarrow Au^I$ conversion under these reaction conditions is allowed. By considering that Au^I may already be produced at the calcination stage on the {101} and {001} steps, it is expected that Au^I is the dominant Au species under the reaction conditions instead of Au^{III}.

To shed light on the Au^I-catalyzed hydrogenation of 1,3-butadiene, we studied the reaction on the AuOH/t-ZrO_2{203}

 © 2006 Wiley-VCH Verlag GmbH & Co. KGaA, Weinheim

surface, in which AuOH is the most stable Au^I species (Table 1). AuOH attaches to the {001} step through an Au–O_{latt} bond and HO–Zr bond, in which the O_{latt} atom is a step-edge lattice O atom and the Zr atom is located on the {101} terrace (Figure 1e). The reaction pathways and the reaction barriers were determined, as shown in the reaction profile in Figure 2.

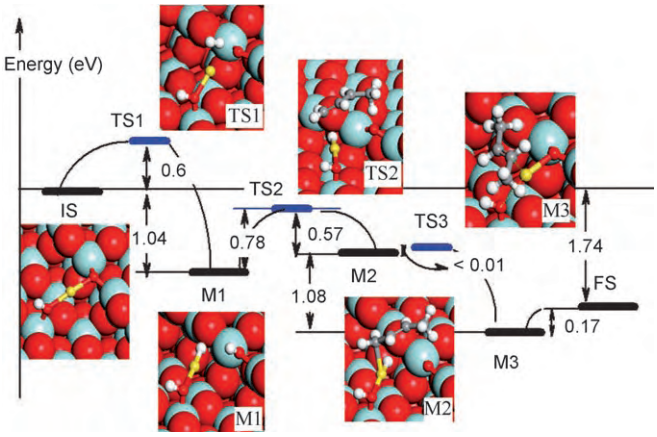

Figure 2. The overall energy profile and reaction snapshots for 1,3-butadiene hydrogenation (formation of butene) on the AuOH/t-ZrO_2-{203} surface. IS = initial state, FS = final state, M = intermediate state, and TS = transition state.

This lowest energy reaction pathway is described as follows. 1) Heterolytic H_2 dissociation: As H_2 approaches AuOH, the Au–O_{latt} bond must break to dissociate H_2 (TS1 in Figure 2), thus leading to H–AuOH and HO_{latt} species (M1 in Figure 2). Mulliken charge analysis of the dissociated product showed that the two dissociated H species are quite different in nature: the one at the O_{latt} atom is protonlike (charge: +0.34), whereas the H species at the Au center is negatively charged (−0.01) and hydridelike. This behavior indicates that H_2 dissociation at Au^I belongs to heterolytic dissociation. It was also noticed that after H_2 dissociation, the charge on the Au center is reduced remarkably from +0.42 to +0.01.

2) Hydrogenation of 1,3-butadiene: 1,3-Butadiene (C_4H_6) could react with either the H–AuOH or HO_{latt} species. As 1,3-butadiene only weakly adsorbs on the surface (below 0.2 eV), the initial state of butadiene is considered to be a gas-phase molecule. Among the two possibilities of H addition, we found that butadiene cannot react with the hydride, but can react with the proton of HO_{latt}. In searching for the hydride reaction pathway, we found that the structural optimization of the hydrogenated intermediate (C_4H_7) is not stable and can spontaneously transform back to the initial state, H-Au-OH, and 1,3-butadiene. This finding may not be surprising as butadiene is a nucleophilic molecule that does not tend to react with a negative hydride species. On the other hand, for butadiene to react with the proton at the O_{latt} atom, a transition state (Figure 2, TS2) can be located when the distance between H and O_{latt} is 1.40 Å and that between C and H is 1.31 Å. The calculated reaction barrier of this step is 0.78 eV. After the TS, the newly formed C_4H_7 adsorbs at the Au center to form a metastable state M2, H-Au-(C_4H_7)OH (Figure 2). This metastable state can readily undergo intermolecular rearrangement by passing the hydride to the adsorbed C_4H_7 species to finally yield adsorbed butene (Figure 2, M3). The final desorption of butene requires 0.17 eV.

It is of interest to ask whether the deep-hydrogenation process, that is, the conversion of butene into butane (C_4H_{10}), can occur. Clearly, the deep hydrogenation (if having taken place) is a secondary process: the newly formed butene at one Au site can only be hydrogenated at a second Au site. Following this process, we identified a pathway for butene → butane conversion, which is very similar to that for butadiene → butene (see Supporting Information for details). The highest barrier (0.82 eV) occurs also at the first hydrogenation step (butene reacts with HO_{latt}). On the basis of these findings, we suggest that the lack of a deep-hydrogenation product in the experimental investigation[6] cannot be justified by energetics. Instead, we may understand it by the following: First, the secondary process is intrinsically slow and the resulting butene needs to compete with butadiene for hydrogenation reaction sites. Second, the butene when produced will desorb as a "hot" molecule, as a result of the large exothermicity of the hydrogenation (Figure 1). Because of the high kinetic energy of butene, the deep hydrogenation that requires the gas-phase butene to react directly with the HO_{latt} species of an Au site (Eley–Rideal mechanism) becomes kinetically unlikely, as our calculations show that the correct geometry for butene in the approach to HO_{latt} is crucial. Consistent with our suggestions, we noticed that ethene → ethane has been observed on cationic Au supported on MgO.[5]

We are now in the position to compare the single Au heterogeneous catalysts with their homogeneous analogues. As mentioned, the oxide enables AuOH to achieve a two-coordinate linear structure, and the Au–O_{latt} bond must break to form free two sites to accommodate two H species (Figure 2, M1).[15] During the hydrogenation process, the linear structure of Au^I is conserved (see Figure 2). This mechanism is rather striking, as the Au^I on the oxide shows the similar ligand attacking/leaving chemistry as those that usually occur in homogeneous catalysis. It should also be emphasized that although ZrO_2 does play an important role in the stabilization of cationic Au, it is not merely a support. As the lattice O atom of ZrO_2 attracts the proton from H_2, it acts as a base to provide additional reaction sites. This behavior implies that oxides with strong acid–base pairs may enhance the catalyst activity.

In summary, our structures of Au cationic monomers on ZrO_2 show a clear resemblance to those in solution. We found that Au^I on ZrO_2 is the catalytically active species that is produced from Au^{III} in situ by reduction. The catalytic roles of the oxide defects and the dynamic ligand effect in reactions have been highlighted. It is shown that in single Au heterogeneous catalysis, the oxide not only stabilizes Au monomers as the solution does in homogeneous catalysis but can also act as a catalyst by providing additional reaction sites.

Received: May 11, 2006
Revised: July 1, 2006
Published online: September 25, 2006

 © 2006 Wiley-VCH Verlag GmbH & Co. KGaA, Weinheim

Keywords: density functional calculations · gold · heterogeneous catalysis · hydrogenation

[1] a) M. Haruta, *Catal. Today* **1997**, *36*, 153; b) G. C. Bond, D. T. Thompson, *Catal. Rev. Sci. Eng.* **1999**, *41*, 319.
[2] a) J. M. Thomas, R. Raja, D. W. Lewis, *Angew. Chem.* **2005**, *117*, 6614; *Angew. Chem. Int. Ed.* **2005**, *44*, 6456; b) D. K. Böhme, H. Schwarz, *Angew. Chem.* **2005**, *117*, 2388; *Angew. Chem. Int. Ed.* **2005**, *44*, 2336.
[3] a) J. C. Fierro-Gonzalez, V. A. Bhirud, B. C. Gates, *Chem. Commun.* **2005**, 5275; b) J. C. Fierro-Gonzalez, B. C. Gates, *J. Phys. Chem. B* **2004**, *108*, 16999.
[4] a) Q. Fu, H. Saltsburg, M. Flytzani-Stephanopoulos, *Science* **2003**, *301*, 935; b) Z. P. Liu, S. J. Jenkins, D. A. King, *Phys. Rev. Lett.* **2005**, *94*, 196102.
[5] a) J. Guzman, B. C. Gates, *Angew. Chem.* **2003**, *115*, 714; *Angew. Chem. Int. Ed.* **2003**, *42*, 690; b) A. Comas-Vives, C. Gonzalez-Arellano, A. Corma, M. Iglesias, F. Sanchez, G. Ujaque, *J. Am. Chem. Soc.* **2006**, *128*, 4756.
[6] X. Zhang, H. Shi, B. Q. Xu, *Angew. Chem.* **2005**, *117*, 7294; *Angew. Chem. Int. Ed.* **2005**, *44*, 7132.
[7] a) A. Hoffmann-Röder, N. Krause, *Org. Biomol. Chem.* **2005**, *3*, 387; b) P. Pyykkö, *Angew. Chem.* **2004**, *116*, 4512; *Angew. Chem. Int. Ed.* **2004**, *43*, 4412, and references therein.
[8] a) D. E. De Vos, B. Sels, *Angew. Chem.* **2005**, *117*, 30; *Angew. Chem. Int. Ed.* **2005**, *44*, 30; b) C. J. Jones, D. Taube, V. R. Ziatdinov, R. A. Periana, R. J. Nielsen, J. Oxgaard, W. A. Goddard III, *Angew. Chem.* **2004**, *116*, 4726; *Angew. Chem. Int. Ed.* **2004**, *43*, 4626.
[9] Z. Liu, M. D. Amiridis, Y. Chen, *J. Phys. Chem. B* **2005**, *109*, 1251.
[10] a) A. Eichler, *Phys. Rev. B* **2005**, *71*, 125418; b) A. Christensen, E. A. Carter, *Phys. Rev. B* **1998**, *58*, 8050.
[11] a) J. M. Soler, E. Artacho, J. D. Gale, A. Garcia, J. Junquera, P. Ordejon, S. Portal, *J. Phys. Condens. Matter* **2002**, *14*, 2745; b) N. Troullier, J. L. Martins, *Phys. Rev. B* **1991**, *43*, 1993; c) J. P. Perdew, K. Burke, M. Ernzerhof, *Phys. Rev. Lett.* **1996**, *77*, 3865.
[12] a) Z. P. Liu, X. Q. Gong, J. Kohanoff, C. Sanchez, P. Hu, *Phys. Rev. Lett.* **2003**, *91*, 266102; b) Z. P. Liu, P. Hu. A. Alavi, *J. Am. Chem. Soc.* **2002**, *124*, 14770.
[13] K. Reuter, M. Scheffler, *Phys. Rev. B* **2001**, *65*, 035406.
[14] Z. P. Liu, S. J. Jenkins, D. A. King, *J. Am. Chem. Soc.* **2004**, *126*, 10746.
[15] Breaking of the Au–O_{latt} bond was reported experimentally in CO oxidation on cationic Au/zeolite: J. C. Fierro-Gonzalez, B. C. Gates, *Langmuir* **2005**, *21*, 5693.

 © 2006 Wiley-VCH Verlag GmbH & Co. KGaA, Weinheim

Coordination Chemistry

DOI: 10.1002/anie.200601927

Coordination-Number Dependence of Reactivity in an Imidoiron(III) Complex**

Nathan A. Eckert, Sridhar Vaddadi, Sebastian Stoian, Rene J. Lachicotte, Thomas R. Cundari, and Patrick L. Holland**

Mononuclear oxoiron species are postulated as intermediates in enzymatic oxidations, and have been characterized in heme systems and in the nonheme monoiron enzyme TauD.[1] Many of the differences in reactivity between the enzymatic intermediates are attributed to the spectator ligands.[2] Recently, the observation and isolation of synthetic iron oxo (L_nFeO)[3] and iron imido (L_nFeNR)[4] complexes has permitted the systematic variation of the ligand environment in species with Fe–O and Fe–N multiple bonds. The six-coordinate $[(tmc)(L)Fe(O)]^{2+}$ system (tmc = 1,4,8,11-tetramethyl-1,4,8,11-tetraazacyclotetradecane) in particular has been amenable to variation of the ligand L.[3,5] In this context, it is important to understand how the number and identity of the spectator ligands modulate the reactivity of compounds with iron–ligand multiple bonds. As a part of this effort, this communication describes data that suggest the formation of a metastable three-coordinate iron(III) imido complex. Unexpectedly, coordination of a fourth ligand induces hydrogen-atom abstraction reactivity. These results contrast with the

[*] S. Vaddadi, Prof. T. R. Cundari
Department of Chemistry
University of North Texas
Denton, TX 76203 (USA)
Fax: (+1) 940-565-4318
E-mail: tomc@unt.edu
Homepage: http://www.chem.unt.edu/faculty/cundari.htm
Dr. N. A. Eckert, Dr. R. J. Lachicotte, Prof. P. L. Holland
Department of Chemistry
University of Rochester
Rochester, NY 14627 (USA)
Fax: (+1) 585-276-0205
E-mail: holland@chem.rochester.edu
Homepage: http://hollandimac.chem.rochester.edu
Dr. S. Stoian
Department of Chemistry
Carnegie Mellon University
Pittsburgh, PA 15213 (USA)

[**] The authors acknowledge funding from the National Science Foundation (CHE-0134658 to P.L.H. and MCB-0424494 to Eckard Münck), the A. P. Sloan Foundation (P.L.H.), the University of Rochester (Weissberger Fellowship; N.A.E.), and the U.S. Departments of Education and Energy (DEFG02-03ER15387; T.R.C.). Calculations were performed on the UNT computational chemistry resource, for which S.V. and T.R.C. acknowledge the NSF for support through grant CHE-0342824. We thank Eckard Münck for support in recording and interpreting the EPR and Mössbauer spectra, and for valuable discussions.

Supporting information for this article is available on the WWW under http://www.angewandte.org or from the author.

WILEY InterScience DISCOVER SOMETHING GREAT
© 2006 Wiley-VCH Verlag GmbH & Co. KGaA, Weinheim

typical situation in which more unsaturated metals give higher reactivity. We also report electronic structure calculations that indicate possible reasons for this interesting phenomenon.

Addition of organic azides to low-valent metal precursors is a well-precedented tactic for introducing the imido ligand into late transition metal complexes.[4,6] We recently demonstrated that the diketiminate-supported dinitrogen complex [L^{Me}FeNNFeL^{Me}] is a source of the iron(I) fragment {L^{Me}Fe} (L^{Me} = 2,4-bis(2,6-diisopropylphenylimino)pent-3-yl).[7] Addition of adamantyl azide (AdN_3) to a blue solution of [L^{Me}FeNNFeL^{Me}] and 4-*tert*-butylpyridine (*t*BuPy, 2 equiv) gave effervescence and immediate formation of an orange-red solution.[8] The ^{1}H NMR and X-band EPR spectra of samples generated in this way are shown in Figure 1.

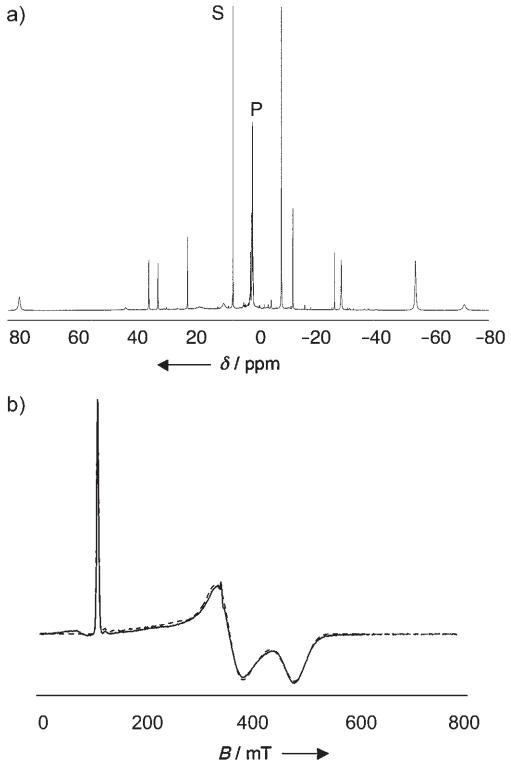

Figure 1. a) ^{1}H NMR spectrum of **A** in C_6D_6, generated from mixing [L^{Me}FeNNFeL^{Me}], 2 equiv AdN_3, and 2 equiv *t*BuPy. The solvent signal is indicated with S, and the *t*BuPy signal with P. b) Solid line: X-band EPR spectrum of **A** diluted to toluene/C_6D_6 (9:1). Conditions: 9.65 GHz, 0.75 mT modulation amplitude, 0.2 mW microwave power, T = 7.5 K. The dotted line shows the simulation that gave the values in the text.

The ^{1}H NMR spectra of the solution display resonances for a paramagnetic complex containing only L^{Me}, an adamantyl group, and perhaps *t*BuPy (Figure 1a). The NMR-active species is formed in about 70% yield. The X-band EPR spectrum (Figure 1b) corresponds to an isolated Kramers doublet with g_{eff} = 6.12, 1.94, and 1.42. The EPR spectrum is reminiscent of a spin quartet and can be simulated as an S = 3/2 species with E/D = 0.33, g_x = 1.94, g_y = 2.20, and g_z = 1.94. The temperature dependence of the signal shows that the ground Kramers doublet is well separated from the excited doublet ($|D| > 30\ cm^{-1}$). Quantitation (by simulation or by double integration) of the observed signal yields a spin concentration of up to 73% of the expected Fe concentration. Mössbauer spectra of samples at 150 K showed two quadrupole doublets in a 3:1 ratio with ΔE_Q = 0.98(4) mm s^{-1} and δ = 0.47(2) mm s^{-1} for the majority species (see Supporting Information). Thus, one major product is formed in roughly 70% yield, and we label this majority species **A**.

We consider three assignments for **A** that are consistent with these combined data: the four-coordinate iron(I) azide complex [L^{Me}Fe(N_3Ad)(*t*BuPy)] (**1**), the three-coordinate iron(III) imido complex [L^{Me}FeNAd] (**2**), and the four-coordinate iron(III) imido complex [L^{Me}Fe(NAd)(*t*BuPy)] (**3**). A dinuclear structure is disfavored for steric reasons, and is difficult to reconcile with an S = 3/2 spin state. Known transition-metal azide complexes present an intense band around 2100 cm^{-1}, but solution FT-IR spectra of **A** showed no bands between 1600 and 3000 cm^{-1}.[9] As shown below, kinetic evidence is also inconsistent with this assignment. Therefore possibility **1** is unlikely. We infer that **A** is an iron(III) imido complex in an unusual intermediate-spin electronic configuration.

To help distinguish between assignments **2** and **3**, hybrid QM/MM computations were carried out on full models with density-functional treatment of the metal core and molecular mechanics treatment of the aryl and adamantyl (excepting the carbon bonded to the imido nitrogen) groups.[10] In model **2**, the S = 3/2 electronic state is lowest in energy by 10 kcal mol^{-1}. Model **3** has a calculated S = 5/2 ground state with a low-lying S = 3/2 excited state 4 kcal mol^{-1} higher in energy. The experimental observation of a single ground spin state up to 40 K by EPR, and no sign of an S = 5/2 signal, implicate [L^{Me}FeNAd] (**2**) as the most reasonable assignment for **A**. Consistent with this idea, the experimental Mössbauer isomer shift (δ = 0.47(4) mm s^{-1}) is closer to that calculated for quartet **2** (δ = 0.40 mm s^{-1}) than that calculated for quartet **3** (δ = 0.62 mm s^{-1}).[10]

In the S = 3/2 ground state of computational model **2**, the Fe=N–C unit is nearly linear, with an Fe–N distance of 1.68 Å and Fe-N-C angle of 174.1°. The ordering of the d orbitals is similar to that for other three-coordinate iron-diketiminate complexes (Figure 2).[11] In the plane of the diketiminate, the d_{yz} orbital is high in energy from σ antibonding interactions with the diketiminate nitrogen atoms and π antibonding interactions with the imido group. The inability to occupy this orbital explains the stability of the quartet spin state. There is near degeneracy of the doubly occupied d_{xy} orbital and the singly occupied $d_{x^2-y^2}$ orbital,[11] and spin–orbit coupling between these orbitals rationalizes the large zero-field splitting.

We have not been able to isolate **A** because it converts to a purple high-spin iron(III) complex (**B**) over a few hours at room temperature. X-ray crystallography identifies **B** as a neutral, high-spin iron(III) adamantylamido complex with coordinated *t*BuPy (Figure 3a). There is a C–C bond between the erstwhile isopropyl group of the diketiminate and a carbon atom of the diketiminate backbone, rendering it a dianionic ligand. The Fe–N distances of 1.905(3) Å and 1.925(3) Å in the new ligand are similar to the Fe–N(ada-

 © 2006 Wiley-VCH Verlag GmbH & Co. KGaA, Weinheim

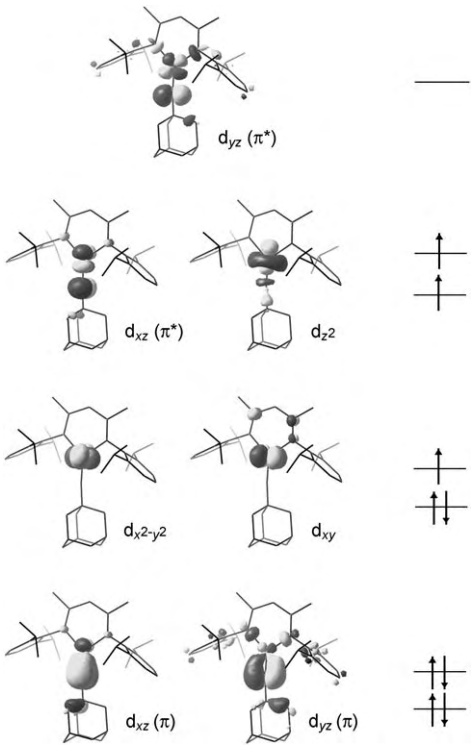

Figure 2. Qualitative ligand-field orbital-splitting diagram for [L^{Me}FeNAd] (**2**) obtained from density functional calculations.

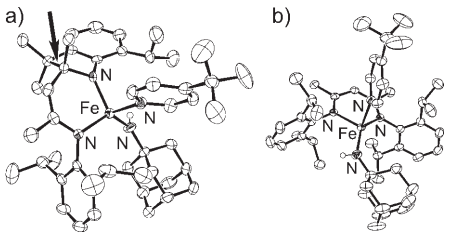

Figure 3. Plots of the X-ray crystal structures of a) **B** and b) [L^{Me}Fe(NHAd)(*t*BuPy)] showing 50% probability ellipsoids. In **B**, the new C–C bond is indicated with an arrow. Hydrogen atoms are omitted for clarity.

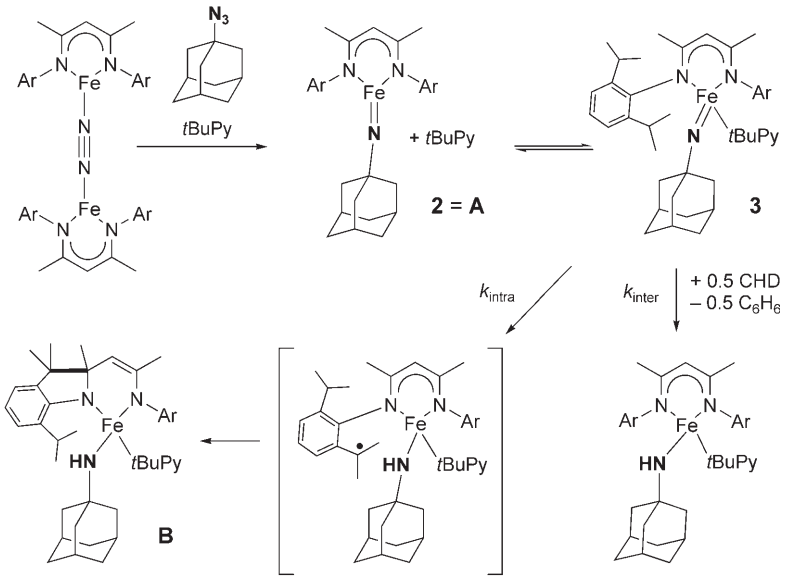

Scheme 1. Proposed assignments for the discussed compounds. *t*BuPy = 4-*tert*-butylpyridine.

mantylamido) distance of 1.882(3) Å, and to the Fe–N(arylamido) distance of 1.880(2) Å in [L^{Me}Fe(NHdipp)(OTf)] (dipp = 2,6-diisopropylphenyl, Tf = trifluoromethanesulfonyl).[12] Hydrogen-atom abstraction (HAA) by an iron-imido intermediate accounts for the formation of **B** (Scheme 1). The key hydrogen-atom abstraction step of this reaction is similar to those attributed to inferred iron(IV) imido species, and isolated nickel(III) and cobalt(III) imido complexes.[6,13]

The HAA reaction was examined through kinetic studies in which disappearance of **A** was monitored by ^{1}H NMR spectroscopy at 31(1) °C.[14] The observed rate constants show a first-order dependence on [*t*BuPy] with an intercept near zero, suggesting that a pyridine adduct of **A** is the only species undergoing intramolecular HAA. Addition of 10 equiv (based on [L^{Me}FeNNFeL^{Me}]) of 1,4-cyclohexadiene (CHD) to **A** in C_6D_6 leads to rapid formation of [L^{Me}Fe(NHAd)(*t*BuPy)], isolated in 91% yield (Figure 3b). This intermolecular HAA reaction is much faster than the intramolecular HAA reaction to form **B**. The observed pseudo-first-order rate constant has a first-order dependence on [CHD] at −51(1) °C in [D_8]toluene, showing that the *t*BuPy adduct of **A** reacts directly with CHD. This observation is inconsistent with identifying **A** as the potential azide complex **1** or another compound that irreversibly forms the imido complex. The combined spectroscopic and kinetic results are most readily explained using the reaction manifold depicted in Scheme 1.

In the presence of *t*BuPy, **A** also reacts rapidly with indene at low temperature, but does not react with 9,10-dihydroanthracene (DHA) even at room temperature before intramolecular conversion to **B**. We attribute this large difference to a steric effect, because the three substrates have similar C–H bond energies (CHD 76(1) kcal mol^{-1}, indene 79(1) kcal mol^{-1}, DHA 78(1) kcal mol^{-1}).[15] The lack of reactivity with DHA argues against HAA by free radicals.

The QM/MM calculations indicate some differences between three-coordinate (**2**) and four-coordinate (**3**) iron(III) imido complexes that might explain the higher reactivity of the latter. In **3**, the geometry at iron is pseudotetrahedral, which results in a smaller splitting of the ligand-field orbitals (despite the increased coordination number) and hence an $S = 5/2$ ground state. (Because no such species is evident in EPR spectra, we suspect that the active species is present in extremely low concentration and is not observed.) As a result of populating the second π* orbital in the high-spin state of four-coordinate **3**, the Fe–N bond is lengthened to 1.74 Å (compared to 1.68 Å for the quartet state of three-coordinate **2**). Binding of pyridine also causes substantial bending of the imido ligand (Fe-N-C 155.1°). Finally, the nitrogen atom has much more spin density in four-coordinate **3** (0.82 e$^-$) than in three-coordinate **2** (0.23 e$^-$).

In conclusion, we have presented spectroscopic studies on an observable species **A** with an $S = 3/2$ ground state. Considering that **A** is the majority species, that its ground state is consistent with that calculated for [L^{Me}FeNAd], that it

 © 2006 Wiley-VCH Verlag GmbH & Co. KGaA, Weinheim

reacts directly with hydrogen-atom donors when pyridine is added, and can undergo an intramolecular reaction with the ligand isopropyl groups in the presence of pyridine, it is most reasonable to assign **A** as a three-coordinate iron(III) imido complex with an intermediate-spin electronic configuration. While other formulations of **A** that can rapidly interconvert with an imido complex are also compatible with the data, they are unnecessarily complicated.

Given this interpretation, it appears that the three-coordinate imido complex becomes active for HAA only upon addition of a fourth ligand. Calculations suggest that the ligand-induced change in reactivity is accompanied by 1) a weaker ligand field at iron, which has been observed to increase hydrogen-atom abstraction reactivity in octahedral iron(IV) oxo complexes;[5] 2) a weaker Fe–N bond and a more bent Fe-N-C angle, which decreases the reorganization energy for proton-coupled electron transfer;[16] and 3) a possible spin-state change that leads to enhanced radical reactivity at the imido nitrogen atom, which echoes the two-state reactivity proposed for cytochrome P450 enzymes.[17] The ability to modulate the reactivity of the imido complex through addition of a fourth ligand suggests that this diketiminate system will be useful for elucidating the effects of ligand field strength and geometry on the reactions of metal–nitrogen multiple bonds.

Received: May 16, 2006
Revised: July 12, 2006
Published online: September 22, 2006

Keywords: coordination number · hydrogen-atom abstraction · imido ligands · iron

[1] a) M. Costas, M. P. Mehn, M. P. Jensen, L. Que, *Chem. Rev.* **2004**, *104*, 939; b) M. M. Abu-Omar, A. Loaiza, N. Hontzeas, *Chem. Rev.* **2005**, *105*, 2227; c) D. A. Proshlyakov, T. F. Henshaw, G. R. Monterosso, M. J. Ryle, R. P. Hausinger, *J. Am. Chem. Soc.* **2004**, *126*, 1022; d) P. J. Riggs-Gelasco, J. C. Price, R. B. Guyer, J. H. Brehm, E. W. Barr, J. M. Bollinger, Jr., C. Krebs, *J. Am. Chem. Soc.* **2004**, *126*, 8108.

[2] M. Sono, M. P. Roach, E. D. Coulter, J. H. Dawson, *Chem. Rev.* **1996**, *96*, 2841.

[3] Terminal oxo-iron complexes: a) C. E. MacBeth, A. P. Golombek, V. G. Young, Jr., C. Yang, K. Kuczera, M. P. Hendrich, A. S. Borovik, *Science* **2000**, *289*, 938; b) C. A. Grapperhaus, B. Mienert, E. Bill, T. Weyhermüller, K. Wieghardt, *Inorg. Chem.* **2000**, *39*, 5306; c) J. U. Rohde, J. H. In, M. H. Lim, W. W. Brennessel, M. R. Bukowski, A. Stubna, E. Münck, W. Nam, L. Que, *Science* **2003**, *299*, 1037; d) M. H. Lim, J.-U. Rohde, A. Stubna, M. R. Bukowski, M. Costas, R. Y. N. Ho, E. Münck, W. Nam, L. Que, *Proc. Natl. Acad. Sci. USA* **2003**, *100*, 3665; e) J. Kaizer, E. J. Klinker, N. Y. Oh, J.-U. Rohde, W. J. Song, A. Stubna, J. Kim, E. Münck, W. Nam, L. Que, *J. Am. Chem. Soc.* **2004**, *126*, 472; f) V. Balland, M.-F. Charlot, F. Banse, J.-J. Girerd, T. A. Mattioli, E. Bill, J.-F. Bartoli, P. Battioni, D. Mansuy, *Eur. J. Inorg. Chem.* **2004**, 301; g) M. Martinho, F. Banse, J.-F. Bartoli, T. A. Mattioli, P. Battioni, O. Horner, S. Bourcier, J.-J. Girerd, *Inorg. Chem.* **2005**, *44*, 9592.

[4] Terminal imido-iron complexes: a) A. K. Verma, T. N. Nazif, C. Achim, S. C. Lee, *J. Am. Chem. Soc.* **2000**, *122*, 11013; b) S. D. Brown, T. A. Betley, J. C. Peters, *J. Am. Chem. Soc.* **2003**, *125*, 322; c) T. A. Betley, J. C. Peters, *J. Am. Chem. Soc.* **2003**, *125*, 10782; d) S. D. Brown, J. C. Peters, *J. Am. Chem. Soc.* **2004**, *126*, 4538; e) T. A. Betley, J. C. Peters, *J. Am. Chem. Soc.* **2004**, *126*, 6252; f) S. D. Brown, J. C. Peters, *J. Am. Chem. Soc.* **2005**, *127*, 1913; g) S. C. Bart, E. Lobkovsky, E. Bill, P. J. Chirik, *J. Am. Chem. Soc.* **2006**, *128*, 5302; h) C. M. Thomas, N. P. Mankad, J. C. Peters, *J. Am. Chem. Soc.* **2006**, *128*, 4956.

[5] a) M. R. Bukowski, K. D. Koehntop, A. Stubna, E. L. Bominaar, J. A. Halfen, E. Münck, W. Nam, L. Que, *Science* **2005**, *310*, 1000; b) O. Pestovsky, S. Stoian, E. L. Bominaar, X. Shan, E. Münck, L. Que, A. Bakac, *Angew. Chem.* **2005**, *117*, 7031; *Angew. Chem. Int. Ed.* **2005**, *44*, 6871; ; c) J.-U. Rohde, L. Que, *Angew. Chem.* **2005**, *117*, 2295; *Angew. Chem. Int. Ed.* **2005**, *44*, 2255; ; d) C. V. Sastri, M. J. Park, T. Ohta, T. A. Jackson, A. Stubna, M. S. Seo, J. Lee, J. Kim, T. Kitagawa, E. Münck, L. Que, W. Nam, *J. Am. Chem. Soc.* **2005**, *127*, 12494.

[6] a) D. T. Shay, G. P. A. Yap, L. N. Zakharov, A. L. Rheingold, K. H. Theopold, *Angew. Chem.* **2005**, *117*, 1532; *Angew. Chem. Int. Ed.* **2005**, *44*, 1508; ; b) E. Kogut, H. L. Wiencko, L. Zhang, D. E. Cordeau, T. H. Warren, *J. Am. Chem. Soc.* **2005**, *127*, 11248.

[7] J. M. Smith, A. R. Sadique, T. R. Cundari, K. R. Rodgers, G. Lukat-Rodgers, R. J. Lachicotte, C. J. Flaschenriem, J. Vela, P. L. Holland, *J. Am. Chem. Soc.* **2006**, *128*, 756.

[8] If no pyridine donor is present, one obtains a different product without an imido group. This reaction will be reported separately.

[9] H. V. R. Dias, S. A. Polach, S.-K. Goh, E. F. Archibong, D. S. Marynick, *Inorg. Chem.* **2000**, *39*, 3894.

[10] The Gaussian 98 package was used.[10a] Hybrid quantum mechanics/molecular mechanics (QM/MM) calculations employed the Universal Force Field[10b] to describe the methyl and 2,6-diisopropylphenyl groups of the β-diketiminate, the *t*Bu group of *t*BuPy (if present), and the entire adamantyl group except the alpha carbon. The remaining atoms were modeled at the B3LYP/6-31G(d) level of theory.[10c] Hybrid QM/MM calculations were performed with the ONIOM[10d] formalism. Mössbauer isomer shift calculations used the Scheme in reference [10e]. a) M. J. Frisch, J. A. Pople et al., Gaussian 98 (Revision A.1), Gaussian Inc., Pittsburgh PA, **2001**; b) A. K. Rappé, C. J. Casewit, K. S. Colwell, W. A. Goddard III, W. M. Skiff, *J. Am. Chem. Soc.* **1992**, *114*, 10024; c) A. D. Becke, *Phys. Rev. A* **1998**, *38*, 3098; C. Lee, W. Yang, R. G. Parr, *Phys. Rev. B* **1998**, *37*, 785; d) F. Maseras, K. Morokuma, *J. Comput. Chem.* **1995**, *16*, 1170; e) I. Mao, Y. Zhang, E. Oldfield, *J. Am. Chem. Soc.* **2002**, *124*, 7829.

[11] a) H. Andres, E. Bominaar, J. M. Smith, N. A. Eckert, P. L. Holland, E. Münck, *J. Am. Chem. Soc.* **2002**, *124*, 3012; b) S. A. Stoian, Y. Yu, J. M. Smith, P. L. Holland, E. L. Bominaar, E. Münck, *Inorg. Chem.* **2005**, *44*, 4915. Note that the choice of axes used in these papers is different than the one used here.

[12] N. A. Eckert, J. M. Smith, R. J. Lachicotte, P. L. Holland, *Inorg. Chem.* **2004**, *43*, 3306.

[13] a) M. P. Jensen, M. P. Mehn, L. Que, *Angew. Chem.* **2003**, *115*, 4493; *Angew. Chem. Int. Ed.* **2003**, *42*, 4357; b) R. L. Lucas, D. R. Powell, A. S. Borovik, *J. Am. Chem. Soc.* **2005**, *127*, 11596.

[14] Details from the kinetics studies may be found in the Supporting Information.

[15] a) F. G. Bordwell, J. Cheng, J. A. Harrelson, *J. Am. Chem. Soc.* **1988**, *110*, 1229; b) F. G. Bordwell, J. Cheng, G. Ji, A. V. Satish, X. Zhang, *J. Am. Chem. Soc.* **1991**, *113*, 9790; c) V. D. Parker, *J. Am. Chem. Soc.* **1992**, *114*, 7458; d) I. W. C. E. Arends, P. Mulder, K. B. Clark, D. D. M. Wayner, *J. Phys. Chem.* **1995**, *99*, 8182.

[16] J. M. Mayer, *Annu. Rev. Phys. Chem.* **2004**, *55*, 363.

[17] a) S. Shaik, M. Filatov, D. Schröder, H. Schwarz, *Chem. Eur. J.* **1998**, *4*, 193; b) S. Shaik, S. P. de Visser, F. Ogliaro, H. Schwarz, D. Schröder, *Curr. Opin. Chem. Biol.* **2002**, *6*, 556; c) S. Shaik, S. P. de Visser, D. Kumar, *J. Biol. Inorg. Chem.* **2004**, *9*, 661.

 © 2006 Wiley-VCH Verlag GmbH & Co. KGaA, Weinheim

Degradable Elastomers

DOI: 10.1002/anie.200602096

Main-Chain Bile Acid Based Degradable Elastomers Synthesized by Entropy-Driven Ring-Opening Metathesis Polymerization**

*Julien E. Gautrot and X. X. Zhu**

Despite the tremendous progress made in the field of biomedical engineering, many challenges still remain to be addressed—especially in the design of new materials. The biodegradable synthetic polymers currently used for biomedical applications are almost exclusively based on short aliphatic moieties, such as lactides, glycolides, ε-caprolactone, and sebacic acid, which all display relatively "hard" mechanical properties that adjust poorly to those of tissues, and therefore cause considerable stress mismatches at the interface responsible for necrosis or abnormal regeneration.[1]

Materials based on bile acids show great promise for drug delivery[2] and controlled release[3] applications, and their rigid steroidal backbone and amphiphilicity appear to make them candidates of choice for fine-tuning the mechanical and interfacial properties of synthetic degradable polymers. However, reports on main-chain bile acid based polyesters, polyamides, and polyurethanes are still scarce in the literature, and their synthesis constitutes a real challenge, especially when higher molecular weights are required. Most techniques used to date rely on the use of toxic coupling agents.

Ring-opening polymerization (ROP) is a very versatile technique that has been applied to the synthesis of polyesters with a controlled molecular weight. In virtually all cases, small strained cycles (3–8-membered rings) are used and enthalpy drives the polymerization. However, macrocycles, including those based on esters and alkenes, could be polymerized, and afforded appreciably high molecular weights, depending on the conditions.[4] In these cases, polymerization is driven by entropy, as described by the Jacobson–Stockmayer theory for ring-chain equilibria.[5]

Entropy-driven ring-opening polymerization (ED-ROP) therefore appears to be a method of choice for the synthesis of high-molecular-weight polyesters based on bile acids. Furthermore, the use of this technique means that the use of large amounts of coupling agents often required in polycondensations can be avoided, thus considerably lowering the toxicity of the material. Furthermore, metathesis chemistry has proved to be a powerful tool for both the preparation of macrocycles[6] and the polymerization of alkenes.[3a,7] We describe here the synthesis of novel macrocycles by the simple ring-closure metathesis (RCM) of two flexible chains attached to a bile acid core through ester bonds, and their entropy-driven ring-opening metathesis polymerization (ED-ROMP) using ruthenium-based Grubbs catalysts. The polymers obtained show typical rubberlike elasticity, with elongation moduli that favorably compare to those of soft tissues and elastin[1c,8] (Figure 1) and constitute, to the best of our knowledge, the first example of degradable thermoplastic amorphous elastomers.

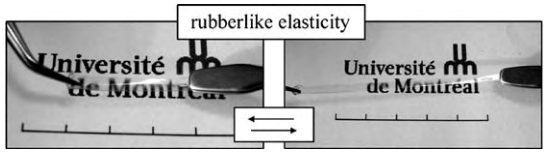

Figure 1. Elongation of a film of polymer **3** (0.1 mm thick) displaying rubberlike elasticity.

Cyclic bile acids **1** (38-membered ring) and **2** (35-membered ring) were synthesized (Scheme 1) in relatively high yields (73 and 59%, respectively) from their corresponding dienes, at high dilution.[9] Cyclic oligomers were also formed during the reaction (which is in agreement with the Jacobson–Stockmayer theory[5a]) as evidenced by MALDI-TOF mass spectrometric analysis.[9] Such high yields in cyclic monomers from an equilibrium reaction are clear indication of the flexibility introduced through the aliphatic chains and the extremely low strain of the macrocycles formed.

ED-ROMP of **1** and **2** at high concentrations using the highly efficient and stable second generation Grubbs catalyst afforded high-molecular-weight polymers in high yields after precipitation from methanol/hexane mixtures (Table 1). In comparison, the acyclic diene metathesis (ADMET) polymerization of the diene precursor of **1** only afforded low-molecular-weight materials with a typical M_n value of 22300.[10] It is thus clear that ED-ROMP, in which only end groups arising from the reaction with the catalyst are present, affords much higher molecular weights than ADMET polycondensation, in which "end groups" must be eliminated from the reaction mixture under vacuum.

The fact that ED-ROMP is a ring-chain equilibrium is perfectly depicted by the increase in the degree of conversion and cyclic oligomer-to-polymer ratio with an increase in the initial concentration of the monomer (Table 1). Higher conversions and lower total amounts of cyclic oligomers are observed at higher concentrations, which are again consistent with the predictions from Jacobson–Stockmayer theory.

Polymers **3** and **4** both display a glass transition temperature T_g below room temperature ($T_g = 2.3 \pm 0.2$ and 14.6 ± 1.0 °C for **3** and **4**, respectively) without any evidence of

[*] Dr. J. E. Gautrot, Prof. Dr. X. X. Zhu
Department of Chemistry
Université de Montéal
C.P. 6128 Succursale Centre-ville
Montréal, Québec, H3C 3J7 (Canada)
Fax: (+1) 514-340-5290
E-mail: julien.gautrot@umontreal.ca
julian.zhu@umontreal.ca

[**] The financial support from the NSERC of Canada, FQRNT of Quebec, and the Canada Research Chair program is gratefully acknowledged. The authors also thank Marc Gauthier for his help and comments on dynamic mechanical analysis measurements.

Supporting information for this article is available on the WWW under http://www.angewandte.org or from the author.

InterScience
© 2006 Wiley-VCH Verlag GmbH & Co. KGaA, Weinheim

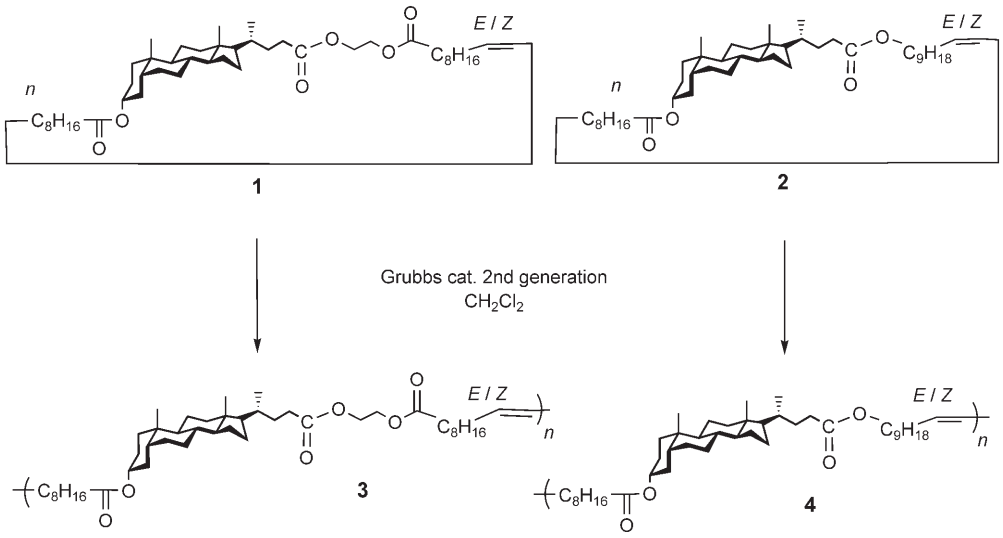

Scheme 1. ED-ROMP of macrocycles **1** and **2** based on bile acids.

Table 1: ED-ROMP of macrocycles **1** and **2** based on bile acids with the 2nd generation Grubbs catalyst (1 mol%) at room temperature.

Monomer	[Monomer] [M]	Conv. [%]	Cycl. olig./ poly.[a]	M_n ($\times 10^3$)[b]	M_w ($\times 10^3$)[b]
1	1.07	98.2	2.4/97.6	151.5	266.5
1	0.23	95.9	5.8/94.2	73.1	121.7
1	0.12	94.3	8.5/91.5	63.8	112.0
2	0.77	98.6	1.4/98.6	146.0	273.5
2	0.13	95.2	9.1/90.9	58.7	106.7

[a] Total cyclic oligomers/polymer ratio determined by GPC.[9] [b] Molecular weights determined by GPC.[10]

melting before decomposition starts to occur, as evidenced by differential scanning calorimetry (DSC). This fact, together with the transparency of films made from these polymers, suggests that these materials are amorphous. The glass transition of the polymer films was also measured by dynamic mechanical analysis (DMA) in the multifrequency mode ($T_g = 12.4 \pm 0.4$ and 19.9 ± 0.6 °C for **3** and **4**, respectively) (Figure 2). Below these temperatures, the materials are relatively hard and brittle ($E = 531 \pm 107$ and 672 ± 150 MPa for **3** and **4**, respectively, at -10 °C), whereas above these temperatures, they display typical rubberlike elasticity ($E = 1.23 \pm 0.06$ and 2.09 ± 0.32 MPa for **3** and **4**, respectively, at 37 °C), with maximum elongations higher than 400% (geometrical limit of the equipment). It is important to stress that **3** and **4** are thermoplastics and that their elasticity behavior is solely due to chain entanglement and weak physical cross-links, as demonstrated by stress-relaxation experiments, which clearly show that stress relaxes to zero over several hours.[9] This property constitutes an important advantage over other thermoplastic degradable materials, since crystalline and amorphous domains are known to degrade at very different rates.[11]

In conclusion, ED-ROMP of macrocycles based on bile acids affords high-molecular-weight polyesters in high yields. The polymers obtained showed typical rubberlike elasticity

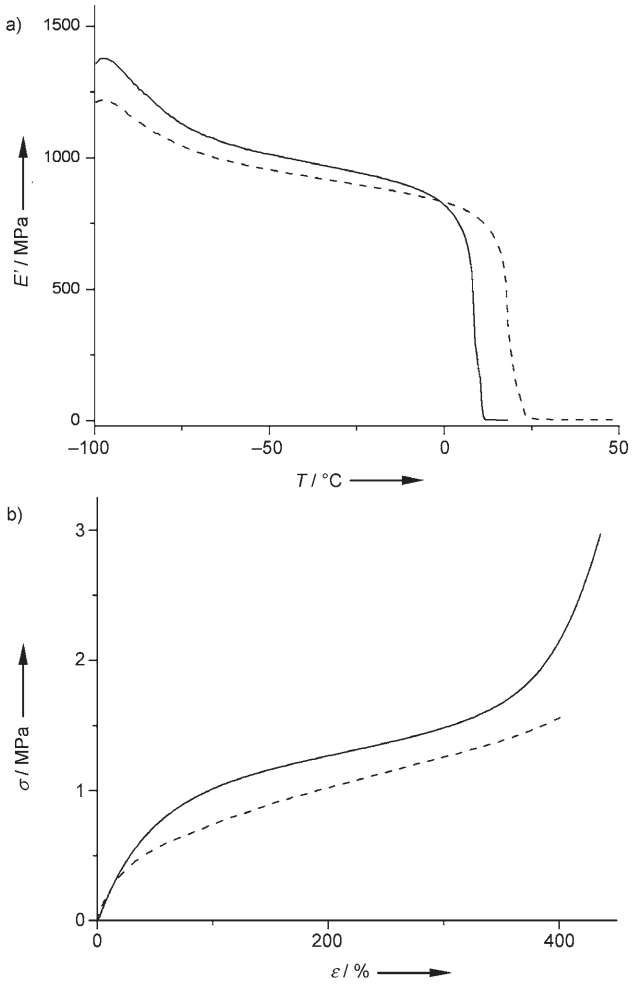

Figure 2. DMA results obtained for films of polymers **3** (solid line) and **4** (dashed line) prepared by evaporation of a CH_2Cl_2 solution (100 mg mL^{-1}) in a mold and subsequent drying in vacuo. a) Multifrequency experiments at 1 Hz; b) stress–strain curves obtained at 37 °C (maximal elongations correspond to travel limits of the equipment geometry rather than elongations at break).

 © 2006 Wiley-VCH Verlag GmbH & Co. KGaA, Weinheim

and constitute the first family of degradable amorphous thermoplastics, with elongation moduli closely matching those of many soft tissues, such as elastic cartilage, aortic heart valves, and aorta.[1c] Moreover, the use of bile acids as rigid moieties should provide low systemic toxicity. The high pK_a value[12] of the ultimate degradation products released after complete hydrolysis of the two polymers synthesized, together with their high molar mass, also ensures low inflammation response arising from a local decrease in the pH value, in contrast to the case observed for smaller acids such as lactic acid.[13] Preliminary results show that polymers **3** and **4** degrade slowly over a period of several months at 37 °C in phosphate-buffered saline solutions, as evidenced by weight loss and a decrease in the molecular weight.

More generally, ED-ROP could prove extremely useful for the synthesis of polyesters, polyamides, or polyurethanes bearing large moieties within the polymer backbone, while avoiding the use of large quantities of toxic coupling agents incompatible with biomedical applications. From an industrial point of view, ED-ROP offers the advantage of releasing no heat, unlike enthalpy-driven polymerizations,[4b] and no volatiles, which allows in situ polymerizations to be carried out in biosystems with, for example, transesterification enzymes. Furthermore, the lower viscosity typical of macrocycles, relative to high-molecular-weight polymers, makes ED-ROP a promising technique for micromolding, a topic of importance for the design of a new generation of biomedical devices.

Received: May 25, 2006
Published online: September 26, 2006

Keywords: bile acids · elastomers · metathesis · polyesters · ring-opening polymerization

[1] a) Y. Wang, G. A. Ameer, B. J. Sheppard, R. Langer, *Nat. Biotechnol.* **2002**, *20*, 602 – 606; b) A. Lendlein, R. Langer, *Science* **2002**, *296*, 1673 – 1676; c) J. B. Park, R. S. Lakes, *Biomaterials: An Introduction*, 2nd ed., Plenum, New York, **1992**.

[2] a) V. Janout, S. L. Regen, *J. Am. Chem. Soc.* **2005**, *127*, 22 – 23; b) V. Janout, C. Di Giorgio, S. L. Regen, *J. Am. Chem. Soc.* **2000**, *122*, 2671 – 2672; c) E. Virtanen, E. Kolehmainen, *Eur. J. Org. Chem.* **2004**, 3385 – 3399.

[3] a) S. Gouin, S. Lehnert, X. X. Zhu, *Macromolecules* **2000**, *33*, 5379 – 5383; b) J. H. Park, S. Kwon, J. O. Nam, R. W. Park, H. Chung, S. B. Seo, I. S. Kim, I. C. Kwon, S. Y. Jeong, *J. Controlled Release* **2004**, *95*, 579 – 588.

[4] a) P. Hodge, S. D. Kamau, *Angew. Chem.* **2003**, *115*, 2514 – 2516; *Angew. Chem. Int. Ed.* **2003**, *42*, 2412 – 2414; b) P. Hodge, H. M. Colquhoun, *Polym. Adv. Technol.* **2005**, *16*, 84 – 94; c) A. R. Tripathy, W. J. MacKnight, S. N. Kukureka, *Macromolecules* **2004**, *37*, 6793 – 6800; d) S. D. Kamau, P. Hodge, M. Helliwell, *Polym. Adv. Technol.* **2003**, *14*, 492 – 501; e) R. Nomura, A. Ueno, T. Endo, *Macromolecules* **1994**, *27*, 620 – 621.

[5] a) H. Jacobson, W. H. Stockmayer, *J. Chem. Phys.* **1950**, *18*, 1600 – 1606; b) J. A. Semlyen, *Adv. Polym. Sci.* **1976**, *21*, 41 – 75; c) Z.-R. Chen, J. P. Claverie, R. H. Grubbs, J. A. Kornfield, *Macromolecules* **1995**, *28*, 2147 – 2154.

[6] a) A. Fürstner, K. Langermann, *J. Org. Chem.* **1996**, *61*, 3942 – 3943; b) B. Mohr, M. Weck, J.-P. Sauvage, R. H. Grubbs, *Angew. Chem.* **1997**, *109*, 1365 – 1367; *Angew. Chem. Int. Ed. Engl.* **1997**, *36*, 1308 – 1310.

[7] a) R. Singh, C. Czekelius, R. R. Schrock, *Macromolecules* **2006**, *39*, 1316 – 1317; b) A. Hejl, O. A. Scherman, R. H. Grubbs, *Macromolecules* **2005**, *38*, 7214 – 7218; c) C. W. Bielawski, R. H. Grubbs, *Angew. Chem.* **2000**, *112*, 3025 – 3028; *Angew. Chem. Int. Ed.* **2000**, *39*, 2903 – 2906.

[8] J. Gosline, M. Lillie, E. Carrington, P. Guerette, C. Ortlepp, K. Savage, *Philos. Trans. R. Soc. London* **2002**, *357*, 121 – 132.

[9] See Supporting Information for experimental procedures, MALDI-TOF, GPC, stress-relaxation data, and ^1H and ^{13}C NMR spectra of polymer **4**.

[10] Molecular weights were obtained by GPC, with polystyrene standards used and a correction factor of 0.55, as determined by intrinsic molecular-weight analysis of a series of oligomers.

[11] a) D. Cohn, A. H. Salomon, *Biomaterials* **2005**, *26*, 2297 – 2305; b) H. M. Younes, E. Bravo-Grimaldo, B. G. Amsden, *Biomaterials* **2004**, *25*, 5261 – 5269; c) B. G. Amsden, G. Misra, F. Gu, H. M. Younes, *Biomacromolecules* **2004**, *5*, 2479 – 2486.

[12] A. F. Hofmann, A. Roda, *J. Lipid Res.* **1984**, *25*, 1477 – 1489.

[13] K. Fu, D. W. Pack, A. M. Klibanov, R. Langer, *Pharm. Res.* **2000**, *17*, 100 – 106.

 © 2006 Wiley-VCH Verlag GmbH & Co. KGaA, Weinheim

Carbene Complexes

DOI: 10.1002/anie.200602188

Useful Reactions of Silylated Propargyltungsten or Propargylmolybdenum Species**

*Toshimichi Asakura, Takuto Kojima, Tomoya Miura, and Nobuharu Iwasawa**

The generation of silylated organometallic species is of high importance because of their unique reactivity, caused by the synergistic effects of the silyl group.[1] During studies into the addition reaction of Fischer-type carbene complexes of Group 6 metals,[2] we thought of generating silylated propargyltungsten or -molybdenum species[3] from the addition of an alkynyl lithium to a carbene complex in which the carbene carbon atom was substituted with a silyl group.[4]

[*] T. Asakura, T. Kojima, Dr. T. Miura,[+] Prof. Dr. N. Iwasawa
Department of Chemistry
Tokyo Institute of Technology
2-12-1 E1-2, O-okayama, Meguro-ku, Tokyo 152-8551 (Japan)
Fax: (+81) 3-5734-2931
E-mail: niwasawa@chem.titech.ac.jp

[+] Present Address:
Department of Synthetic Chemistry and Biological Chemistry
Kyoto University
Katsura, Kyoto 615-8510 (Japan)

[**] This research was partly supported by a Grant-in-Aid for Scientific Research from the Ministry of Education, Culture, Sports, Science, and Technology of Japan. The Japan Society for the Promotion of Science for Young Scientists granted T.M. a Research Fellowship.

Supporting information for this article is available on the WWW under http://www.angewandte.org or from the author.

WILEY InterScience DISCOVER SOMETHING GREAT
© 2006 Wiley-VCH Verlag GmbH & Co. KGaA, Weinheim

Herein, we describe the unique behavior of these silylated propargyl metal species in their reaction with electrophiles which enabled the preparation of a variety of synthetically useful compounds.

The dimethylphenylsilyl-substituted tungsten carbene complex **1** was treated with octynyllithium in THF at −78 °C (Scheme 1). The addition reaction occurred smoothly to give

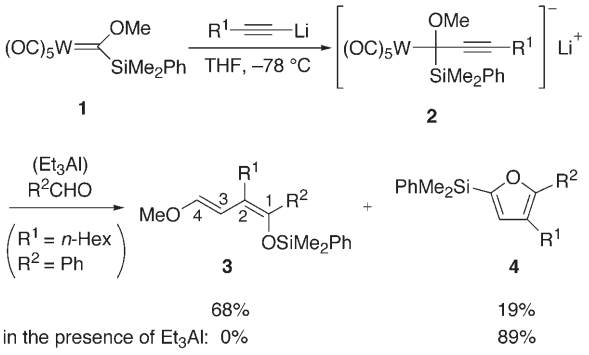

Scheme 1. Reaction of silylated propargyltungsten species.

the silylated propargyltungsten species **2**. Further reaction with PhCHO afforded (*Z*,*E*)-1,4-dioxy-1,3-diene **3** ($R^1 = n$-Hex, $R^2 = Ph$), a useful electron-rich diene, in 68% yield, along with a small amount (19%) of another useful synthetic intermediate **4**. Alternatively, silylated furan derivative **4**, could be selectively obtained by carrying out the reaction in the presence of Et_3Al (Scheme 1).[5] Thus, the two types of addition product are available by selecting the reaction conditions.

The scope of the reaction for the selective preparation of 1,4-dioxy-1,3-diene and furan derivatives is summarized in Table 1. The reaction was carried out without Et_3Al but using various combinations of aldehydes and alkyl- or aryl-substituted alkynyl lithium reagents to give the corresponding 1,4-dioxy-1,3-dienes **3** in reasonable yields (conditions A, Table 1). In particular, alkyl-substituted alkynyl lithium reagents generally gave the products in higher yields. In all cases, the geometrical isomer **3** was obtained with high selectivity (99:1 to 96:4). In contrast, the reaction in the presence of Et_3Al selectively gave the corresponding silylated furan products **4** in high yield (conditions B, Table 1).

Table 1: Scope of the reaction between **1**, alkynyl lithium reagents, and aldehydes.

Entry	R^1	R^2	Cond. A:[a] Yield **3**[c] (**4**) [%]	Cond. B:[b] Yield **4** [%]
1	*n*-Hex	Ph	68 (19)	89
2	*n*-Hex	*i*Pr	68 (16)	84
3	*n*-Hex	*c*-Hex	84 (5)	90
4	Ph	Ph	43 (45)	92
5	Ph	*i*Pr	49 (43)	85
6	$-(CH_2)_2OTBS$	*i*Pr	70 (17)	75

[a] Without Et_3Al. [b] In the presence of Et_3Al. [c] Obtained as a single geometrical isomer (>95:5). *c*-Hex = cyclohexyl, TBS = *tert*-butyldimethylsilyl.

We propose the reaction pathway shown in Scheme 2 to explain the formation of the 1,4-dioxy-1,3-dienes **3**. Reaction of the silylated propargyltungsten species **2** with aldehydes would proceed with 1,2-migration of $W(CO)_5$ to give zwitterionic addition intermediates **5**.[6] Rather than undergoing nucleophilic attack of the oxyanion on the oxonium moiety to give dihydrofuran derivatives,[2d] intermediates **5** would instead undergo an intramolecular 1,4-hydride shift[7] to give γ-silyl-α,β-unsaturated ketones **6**. These ketones would then undergo a 1,5-silyl migration[8] to give the dienyltungsten intermediates **7**.[9,10] Finally protonation of these intermediates on workup gives the 1,4-dioxy-1,3-dienes **3**. The fact that the reaction in the presence of Et_3Al gave the corresponding furans can be explained by considering the coordination of the oxyanion to Et_3Al, which prevents the 1,4-hydride shift.

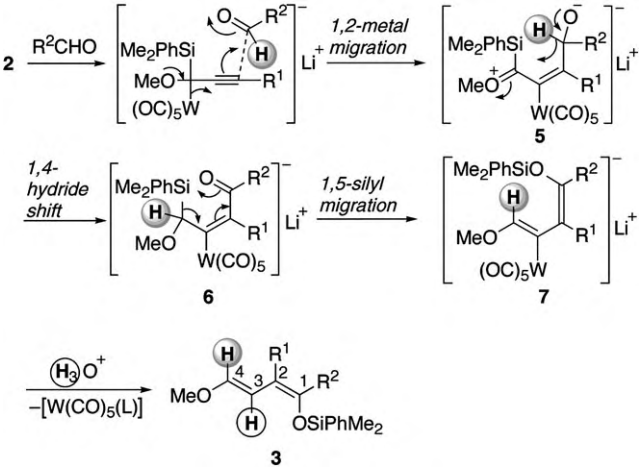

Scheme 2. Proposed mechanism for the addition reaction.

A series of deuteration experiments were carried out to confirm these suppositions. Thus, on quenching the reaction with D_2O, around 60% of the hydrogen atoms on C3 (see Scheme 2, compound **3**) were exchanged with deuterium atoms. Furthermore, when the reaction was carried out using deuterated benzaldehyde (PhCDO), the product **3** was obtained in which nearly all the hydrogen atoms on C4 had been exchanged with deuterium atoms. Therefore, the hydrogen atom on C3 arises from protonation of the carbon–tungsten bond and the hydrogen atom on C4 is derived from the aldehyde through a 1,4-hydride shift.

The enhanced reactivity of the silylated propargyl metal species is demonstrated by the following reaction with α,β-unsaturated carbonyl compounds. We found that neither propargyltungsten nor -molybdenum species derived from alkyl or aryl carbene complexes reacted well with α,β-unsaturated carbonyl compounds. However, the silylated propargylmolybdenum species reacted smoothly to give the corresponding [3+2] cycloaddition products **9** or 1,4-addition products **10** in good yields (Scheme 3).[11,12]

Furthermore, we investigated the reaction between the silylated propargyl metal species and CO_2. Again, the molybdenum complex **8** gave better results than the non-silylated derivatives, and after a mild acidic workup led to the

 © 2006 Wiley-VCH Verlag GmbH & Co. KGaA, Weinheim

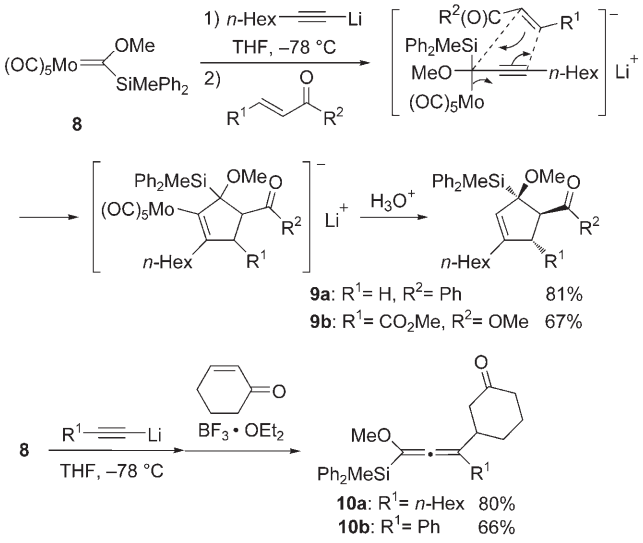

Scheme 3. Reaction with α,β-unsaturated carbonyl compounds.

silylated methoxybutenolide products **11** in good yield (Scheme 4).

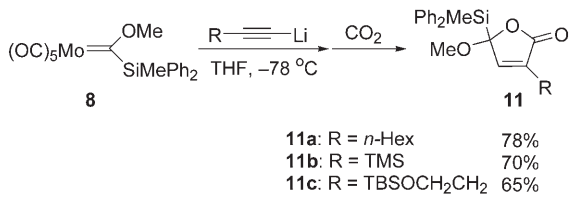

Scheme 4. Reaction with carbon dioxide. TMS = trimethylsilyl.

Finally, regioselective synthesis of succinic acid mono ester **13** was achieved by treatment of the silyl-substituted butenolide **11a** with $BF_3{\cdot}Et_2O$ in acetic acid at room temperature. Protonation of the allylsilane moiety of **11a** by acetic acid proceeded to give lactone **12**, which was then hydrolyzed to give **13** in 91% yield (Scheme 5). This method provides a concise preparation of succinic acid mono esters, which are not necessarily simple to synthesize.[13]

In conclusion, propargyltungsten or -molybdenum species with a synergic effect of a silyl substituent show enhanced and unique reactivity on reaction with electrophiles. A range of synthetically useful compounds were prepared by using these reactions.

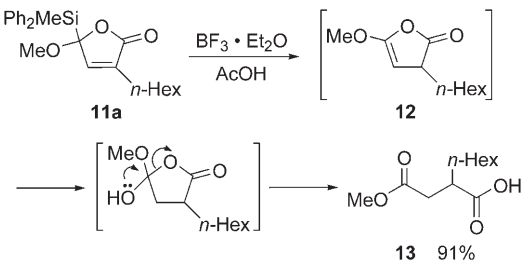

Scheme 5. Synthesis of succinic acid mono ester.

Experimental Section

A typical procedure for the preparation of **3**: A solution of *n*-butyllithium (1.54 M, 0.24 mL, 0.37 mmol) in hexane was added dropwise to a solution of 1-octyne (62 mg, 0.55 mmol) in THF (0.5 mL) at −78 °C. After 30 minutes, a solution of the silyl carbene complex **1** (90 mg, 0.18 mmol) in THF (5 mL) was added. The red color of the carbene complex **1** changed to yellow within a few minutes. After 30 minutes, benzaldehyde (47 μL, 0.46 mmol) was added and the reaction mixture was stirred for a further 4 h at this temperature. Then pH 7 phosphate buffer (15 mL) was added and the mixture was extracted three times with EtOAc. The combined organic layers were dried over anhydrous magnesium sulfate and the solvent was removed under reduced pressure. The residue was purified by column chromatography on silica gel (hexane/EtOAc = 100:1) under argon to give 1-(dimethylphenylsiloxy)-2-hexyl-4-methoxy-1-phenylbuta-1,3-diene **3a** (48 mg, 0.12 mmol) in 68% yield as a bright yellow oil.

Received: June 1, 2006
Published online: September 26, 2006

Keywords: carbene complexes · molybdenum · silicon · transition metals · tungsten

[1] *The Chemistry of Organic Silicon Compounds*, *Vol. 2* (Eds.: Z. Rappoport, K. Apelog), Wiley, New York, **1998**, chap. 7.
[2] a) N. Iwasawa, K. Maeyama, M. Saitou, *J. Am. Chem. Soc.* **1997**, *119*, 1486; b) N. Iwasawa, K. Maeyama, *J. Org. Chem.* **1997**, *62*, 1918; c) N. Iwasawa, T. Ochiai, K. Maeyama, *Organometallics* **1997**, *16*, 5137; d) N. Iwasawa, T. Ochiai, K. Maeyama, *J. Org. Chem.* **1998**, *63*, 3164.
[3] For reviews on transition-metal propargyl species, see: a) M. E. Welker, *Chem. Rev.* **1992**, *92*, 97; b) H.-W. Fruhauf, *Chem. Rev.* **1997**, *97*, 523; c) C.-L. Li, R.-S. Liu, *Chem. Rev.* **2000**, *100*, 3127; d) A. Wojcicki, *Inorg. Chem. Commun.* **2002**, *5*, 82.
[4] a) N. Iwasawa, M. Saitou, *Chem. Lett.* **1994**, 231; b) N. Iwasawa, M. Saitou, H. Kusama, *J. Organomet. Chem.* **2001**, *617*–618, 741; c) U. Schubert, *J. Organomet. Chem.* **1988**, *358*, 215.
[5] In previous reactions in which alkyl carbene complexes were employed, $BF_3{\cdot}OEt_2$ was required to promote the addition reaction with aldehydes. However, the corresponding reaction of the silylated propargyltungsten **2** proceeded smoothly without needing a Lewis acid, thus demonstrating its enhanced reactivity.
[6] J. Barluenga, J. Alonso, F. J. Fañanás, *Chem. Eur. J.* **2005**, *11*, 4995, and references therein.
[7] a) D. T. H. Chou, X. Huang, R. J. Batchelor, F. W. B. Einstein, A. J. Bennet, *J. Org. Chem.* **1998**, *63*, 575; b) J. E. Hofferberth, H. Y. Lo, L. A. Paquette, *Org. Lett.* **2001**, *3*, 1777.
[8] a) C. P. Casey, C. R. Jones, H. Tukada, *J. Org. Chem.* **1981**, *46*, 2089; b) M. Saito, A. Saito, Y. Ishikawa, M. Yoshioka, *Org. Lett.* **2005**, *7*, 3139.
[9] A variable-temperature NMR study was carried out into the reaction of diphenylmethylsilyl-substituted propargyl metal species derived from tungsten complex **1′** and phenylacetylene labeled with ^{13}C at the terminal carbon atom. After addition of

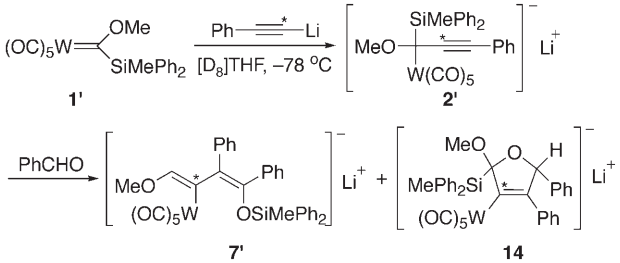

 © 2006 Wiley-VCH Verlag GmbH & Co. KGaA, Weinheim

PhCHO, formation of a dienyltungsten intermediate **7′** and a dihydrofuranyltungsten intermediate **14** were observed at −78 °C. Further details will be reported in due course.

[10] It is possible that an anionic pentacoordinate silicate intermediate is generated for species **5**, in which the formation of dihydrofuran intermediate may be suppressed (Scheme 2). We would like to thank one of the referees for suggesting this possibility.

[11] In general, propargylmolybdenum species are more reactive than propargyltungsten species. However, the tungsten silyl carbene complex is more stable than the corresponding molybdenum complex. Thus, we employed the tungsten complex in most of our studies, but for the reaction with CO_2 and electrophiles with lower activity, such as α,β-unsaturated carbonyl compounds, the use of the molybdenum complex gave better results.

[12] **9a**,**b** were obtained as single stereoisomers as shown, while **10a**,**b** were obtained as mixtures of isomers.

[13] R. Ballini, G. Bosica, A. Palmieri, M. Petrini, C. Pierantozzi, *Tetrahedron* **2003**, *59*, 7283, and references therein.

 © 2006 Wiley-VCH Verlag GmbH & Co. KGaA, Weinheim

Microdevices

DOI: 10.1002/anie.200602273

Cofabrication of Electromagnets and Microfluidic Systems in Poly(dimethylsiloxane)**

*Adam C. Siegel, Sergey S. Shevkoplyas, Douglas B. Weibel, Derek A. Bruzewicz, Andres W. Martinez, and George M. Whitesides**

Herein we describe a simple method for fabricating electromagnets with micron-scale dimensions in poly(dimethylsiloxane) (PDMS) in close proximity (ca. 10-μm separation) to microfluidic channels. The method has four steps: 1) fabrication of microchannels, which subsequently form both the microfluidic channels and the templates that become the wires for the electromagnets; 2) silanization of the microchannels destined to become wires with 3-mercaptopropyltrimethoxysilane, to make their surfaces wettable by metals; 3) injection of molten solder into the channels; and 4) cooling the channels to form solid metallic wires. These solder wires can be formed into nonplanar structures (if desired), by remelting, shaping the PDMS template, and recooling the solder. By passing electrical current through the wires, we generated magnetic fields up to 2.8 mT, and magnetic field gradients up to 40 $T m^{-1}$, inside adjacent microfluidic channels. To demonstrate the application of the electromagnets in microfluidic systems, we: 1) modeled the magnetic field and Joule heating of an electromagnet; 2) characterized the capture and release of superparamagnetic beads in a microfluidic channel by turning the electromagnets on and off; and 3) sorted superparamagnetic beads into one of two microfluidic channels by applying an electrical signal to a pair of electromagnets (one on each side of a channel).

Magnetic components have the potential to be useful in lab-on-a-chip systems: they form the basis of microfluidic pumps,[1] mixers,[2] and valves,[3] have been integrated into microfluidic systems to trap and move paramagnetic particles,[4,5] and have been used to guide the self-assembly of particles into structures.[6] There are many biochemical applications of magnetic fields: in immunoassays,[7] they have been used to accelerate the hybridization of DNA and RNA,[8] and for the filtration of biomolecules;[9–11] in cell biology, magnets have been used to isolate cells from blood,[12] extract DNA from cells,[13] move magnetotactic bacteria,[14] and to measure the mechanical properties of cells.[15] The use of magnetics in microfluidic systems has been reviewed recently.[16]

Electromagnets have two advantages over permanent magnets in lab-on-a-chip systems: 1) they can be switched on/off rapidly using electrical signals, and 2) the strength of their magnetic field can be adjusted. They have the disadvantage that they usually produce weaker magnetic fields than do permanent magnets. Several groups have fabricated electromagnets in microfluidic systems to manipulate superparamagnetic beads magnetically. Ahn et al. fabricated 3D electromagnets surrounding a microfluidic chamber by electroplating copper wires around a nickel–iron core.[17] Wirix-Speetjens et al. and Smistrup et al. made electromagnets that produced magnetic fields in channels etched in Si/SiO_2.[18,19] Choi et al. fabricated Cu/Ti electrodes in microfluidic channels comprising polyimide, silicon, and glass.[20] Deng and coworkers patterned gold wires with a width of 50–100 μm and thickness of 10–20 μm, and used the wires to produce magnetic fields in PDMS channels.[4] They demonstrated that their wires carried electrical currents as large as 10 A for hours without failure; when the wires were positioned adjacent to a permanent magnet, the wires produced a peak magnetic fields of tens of mT. Lee et al. used lift-off techniques to fabricate gold wires with a width of 1–10 μm and a thickness of approximately 100 nm; an electrical current applied to the wires at a current density $< 5 \times 10^7$ $A cm^{-2}$ produced a magnetic field < 100 mT.[5] Redesigning the wires in a crossbar-array pattern made it possible to trap yeast cells attached to magnetic beads.[21] Suzuki et al.

[*] A. C. Siegel, Dr. S. S. Shevkoplyas, Dr. D. B. Weibel, D. A. Bruzewicz, A. W. Martinez, Prof. G. M. Whitesides
Department of Chemistry and Chemical Biology
Harvard University
12 Oxford Street, Cambridge, MA 02138 (USA)
Fax: (+1) 617-495-9857
E-mail: gwhitesides@gmwgroup.harvard.edu

[**] This research was supported by grants from the National Institutes of Health (NIH) (GM065364), DARPA and the Office of Naval Research. We used the Materials Research Science and Engineering Centers (MRSEC) shared facilities supported by the National Science Foundation under award no. DMR-0213805. This work was also supported by predoctoral fellowships from the Howard Hughes Medical Institute (A.C.S) and the NSF (A.W.M.), and a postdoctoral fellowship from the National Institutes of Health (D.B.W., GM067445).

Supporting information for this article is available on the WWW under http://www.angewandte.org or from the author.

 © 2006 Wiley-VCH Verlag GmbH & Co. KGaA, Weinheim

micromachined copper wires in silicon to move superparamagnetic beads in a microchannel; applying a current of 1 A produced forces on the beads < 0.3 pN.[22]

While these methods for fabricating electromagnets are useful in some applications, many of them are limited for general use because they require: 1) a bulky off-chip permanent magnet which must be aligned to features on the microchip, or 2) costly and time-consuming deposition of thick (> 1 μm) layers of metal (e.g. Au) to minimize Joule heating in the wires. These techniques require at least two steps of lithography that must be repeated in the fabrication of each device, and also require precise alignment of electrodes to the microfluidic channels.

Herein we describe a method of fabricating electromagnets that does not require an external permanent magnet, or fabrication by evaporation, electrodeposition, or sputtering of metal. It also avoids alignment steps, because the microstructures (e.g. microchannels) that form the wires (that is, the electromagnets) are fabricated in the same plane and at the same time as the microfluidic channels. This cofabrication is essential for practical, low-cost devices, and is part of a strategy we are developing that will allow cofabrication of a range of functions (microfluidic channels, optical waveguides,[23] light sources,[24,25] electrical systems such as wires, electrodes, and heaters[26] and electromagnets) in a single step of molding.

Fabrication procedure: We fabricated electromagnets in microchannels embossed in PDMS, but the general strategy for cofabrication is applicable to many microchannel systems. The PDMS channels were made using soft lithography and rapid prototyping.[27] The interior surfaces of the channels (which had been oxidized by exposure to a plasma prior to contact sealing)[28,29] were made wettable to metal by silanization with a solution of 3-mercaptopropyltrimethoxysilane; liquid solder did not wet untreated channels. We injected molten solder (for example, 52% indium, 48% tin, m.p. 117 °C, or 100% indium, m.p. 158 °C)[30] into the channels by heating them on a hotplate and applying pressure to a heated syringe that was prefilled with the molten solder (Figure 1a); on cooling, the solder solidified into electrically conductive wires. The channels for electromagnets were fabricated in close proximity (ca. 10-μm separation), and in the same plane as the channels used to transport fluid (Figure 1b). By relying on cofabrication, it is straightforward to achieve small separations and excellent registration of microfluidic and electric/magnetic structures. A detailed description of the fabrication procedure is in the Supporting Information.

This method of fabricating electromagnets near microfluidic channels is rapid, simple, reproducible, and requires minimal equipment; silanizing the plasma-oxidized channels, heating, injecting the molten solder into the channels, connecting the copper wires, and cooling is complete in under 10 min. Channels for fluids and electromagnets were cofabricated in the same plane and in a single step; this approach makes it possible to fabricate multiple electromagnets in a microfluidic system using one mask for lithography (no alignment is necessary). Compared to lift-off fabrication using Au, Al, or Cu (metals with slightly higher conductivity and substantially higher melting points than solder), injection of solder makes it possible to fabricate wires with large cross-sectional area rapidly and economically. To generate a given magnetic field, these "thick" wires are

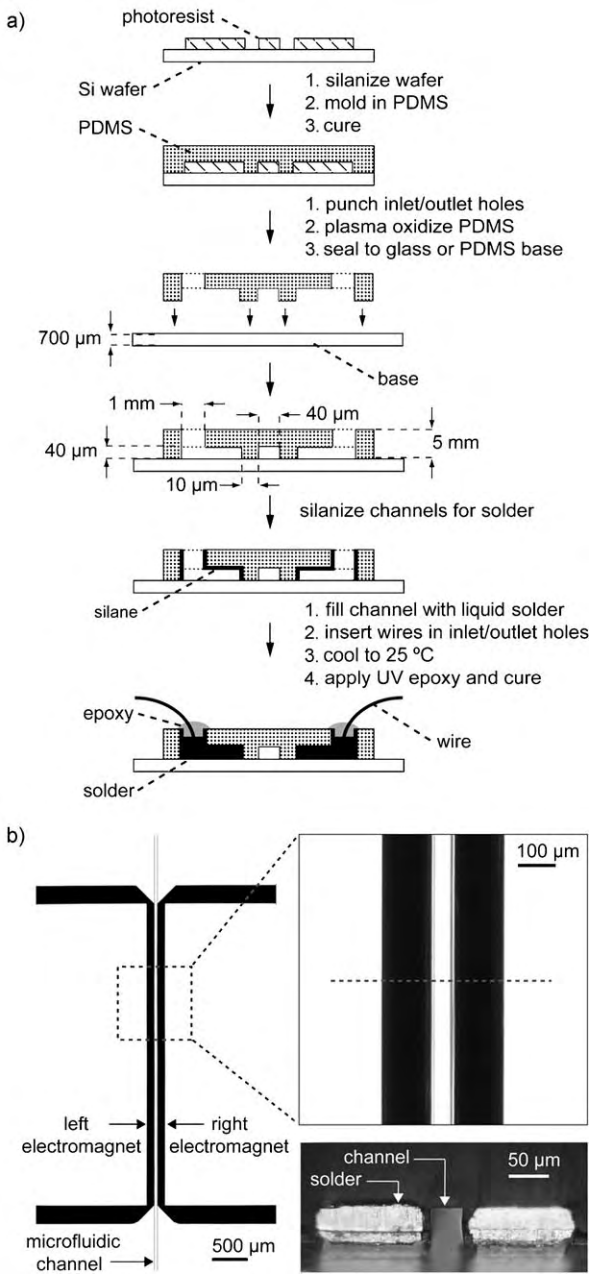

Figure 1. a) A schematic diagram depicting the fabrication of electromagnets in PDMS. The completed device has three microfluidic channels: two outer channels filled with solder (length = 1.5 cm, width = 120 μm, height = 40 μm), and a central channel for fluids (length = 1.5 cm, width = 40 μm, height = 40 μm). b) Photographs of the three channels as viewed from above at low magnification (left), high magnification (upper right) and the cross-section of the three channels (lower right). The photograph of the cross-section was obtained by sectioning the channels with a razor blade (shown as the dashed line in the upper right image); the dark line in the left electromagnet is the result of imperfect sectioning; the light areas at the bottom of the image are reflections of the metal. In the photograph at low magnification, lines were drawn to outline the location of the microfluidic channel.

 © 2006 Wiley-VCH Verlag GmbH & Co. KGaA, Weinheim

subjected to lower current density and less heating than smaller wires that generate equivalent fields. We have also been interested in producing complex metallic microstructures in three dimensions;[31,32] in separate work, we have applied this technique to produce flexible 3D structures by bending/twisting/coiling the devices after injecting the solder, or by filling multilayer channels with molten solder and cooling.[26]

We verified that the electromagnets are electrically insulated from the adjacent microfluidic channel. We filled the microfluidic channel shown in Figure 1b with a solution of 0.1M NaCl in Millipore water; the resistance between the adjacent electromagnet and a silver electrode immersed in the solution was 35.5 GΩ. For comparison, the resistance measured between two electrodes immersed in opposite ends of the microfluidic channel filled with the electrolytic solution was 7.6 MΩ, corresponding to a resistivity of 83.4 Ω cm; the resistivity of a solution of 0.1M NaCl in water calculated from the literature is 93.7 Ω cm.[33]

We passed an electrical current through the wires to generate magnetic fields and field gradients in adjacent microfluidic channels; the orientation of these fields and gradients in relation to the direction of the electrical current in the wires is shown in Figure 2. We adjusted the strength of the magnetic field and field gradient by controlling the magnitude of the electrical current through the wires.

Model of the magnetic field: An electrical current passed through a wire generates a magnetic field $\boldsymbol{B}$ (T) around the wire in the direction determined by the right-hand-rule.[34] Equation (1) describes the intensity of this field as a function

$$|\boldsymbol{B}| = \mu_0 \frac{I_{\text{wire}}}{2\pi x} \quad (1)$$

of the distance from the axial center of a cylindrical wire of unlimited length, where I_{wire} (A) is the current through the wire, x (m) is the distance from the center of the wire, and μ_0 ($4\pi \times 10^{-7}$ T m A^{-1}) is the permeability of free space.[35]

Figure 2b shows a plot of the magnitude of the magnetic field produced by passing a constant current through a wire with a rectangular cross section; we approximate this magnetic field using Equation (1). The electromagnets described herein have a cross-sectional area of approximately 4800 μm^2 and can withstand electrical currents >1 A and current densities >22 kA cm^{-2} before Joule heating causes excessive heating of the adjacent fluid; these characteristics make it possible to produce magnetic fields <2.8 mT and field gradients <40 T m^{-1} in microfluidic channels adjacent to the electromagnets (10-μm separation). By comparison, a typical refrigerator magnet produces a magnetic field of approximately 2.5 mT; the strongest permanent rare-earth magnets produce fields up to 1.5 T.[36]

A magnetic field gradient produces a force $\boldsymbol{F}$ (N) on a superparamagnetic bead in the direction of the increase in the magnitude of the field. Lee et al. derived a formula [Eq. (2)]

$$\boldsymbol{F} = \frac{V\chi}{\mu_0} \nabla(\boldsymbol{B}^2) \quad (2)$$

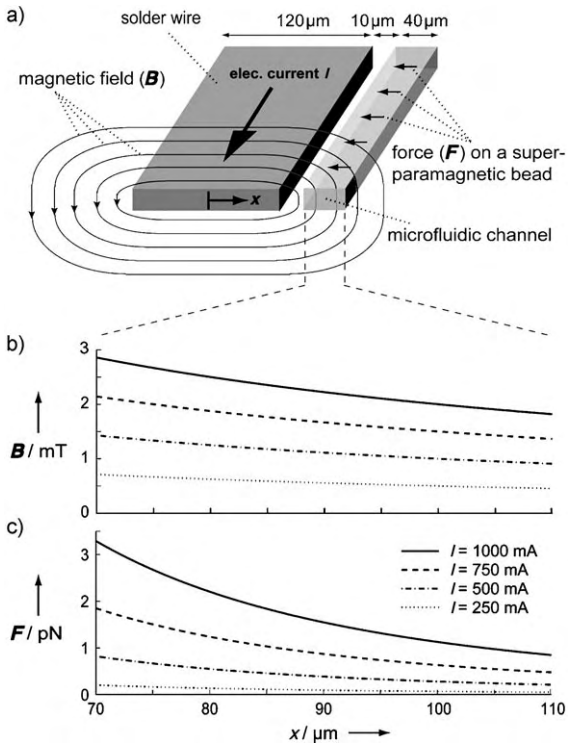

Figure 2. a) A graphical model with corresponding plots of b) the magnetic field (symbols as in (c)), and c) the force exerted on a superparamagnetic bead by an electrical current applied through an electromagnet positioned 10 μm from a microfluidic channel. In the model, the magnetic field is described by field lines orthogonal to the orientation of the solder wire of the electromagnet; horizontal lines in the microfluidic channel describe the force field; x describes the distance from the center of the wire. The microfluidic channel is located between 70 and 110 μm from the center of the wire; the plots are drawn across this range of x. We assume a solder wire of infinite length and uniform current density. In (c), we assume perfectly spherical beads with a susceptibility of 0.170 and a diameter of 5.9 μm. For currents of 250, 500, 700, and 1000 mA, we observed peak magnetic-field intensities (and peak forces) of 0.714 (0.206), 1.43 (0.823), 2.14 (1.85), and 2.86 mT (3.29 pN), respectively.

for calculating this force as function of: 1) the gradient of the square of the magnetic field, $\nabla(\boldsymbol{B}^2)$ (T^2 m^{-1}); 2) the volume of the bead, V (m^3); and 3) the magnetic susceptibility of the bead, χ (dimensionless).[21,37]

Combining Equations (1) and (2) produces an expression for the force exerted on a superparamagnetic bead in the x direction when a direct current (DC) is flowing through a wire [Eq. (3)]. Figure 2c shows a plot of the force as a

$$\boldsymbol{F}_x = -V\chi\mu_0 \frac{I_{\text{wire}}^{\,2}}{2\pi^2 x^3} \quad (3)$$

function of x.

Herein, we calculate a maximum force of approximately 3.3 pN on a superparamagnetic bead (5.9-μm diameter, $\chi = 0.170$).[38] By comparison, typical forces for moving similar superparamagnetic beads range from 0.1–40 pN.[16] Equation (3) suggests that the most effective strategy for making magnetic interactions strong in these systems is to reduce the

 © 2006 Wiley-VCH Verlag GmbH & Co. KGaA, Weinheim

distance between the center of the wire and the superparamagnetic bead. We used this strategy to determine the optimal width of the wires used for the electromagnets (see Supporting Information).

Capture and release of superparamagnetic beads: To demonstrate the capture of superparamagnetic beads in microfluidic systems, we fabricated electromagnets in PDMS channels bonded to glass slides using the procedure described in Figure 1a. In these devices, two outer channels were filled with solder to form the electromagnets and the central channel was used for fluids (Figure 1b). We used an electronic circuit to control the electrical current applied to the two electromagnets (see Supporting Information). By turning the electromagnets on either side of the central microfluidic channel on and off, we captured and released superparamagnetic beads[38] from either side of the microfluidic channel at a frequency of 0.3 Hz for over 5000 cycles (one cycle = across the channel and back) (Figure 3a–c). In each cycle, we applied a current of 1 A at a 4 V bias through each electromagnet for 1.6 s. While the electromagnets supported frequencies over 100 kHz, the maximum frequency at which we could observe movement/oscillation of the beads was 50 Hz; this limitation is probably because viscous drag on the magnetic beads prevents them from accelerating quickly in the aqueous media (we give an analysis in the Supporting Information). The maximum frequency at which we could continuously cycle beads across the channel and back was 1 Hz.

We measured the time required to capture a population of superparamagnetic beads[38] in buffer in a microfluidic channel (Figure 3d). We flowed a suspension of beads into a channel, stopped the flow, and imaged a section of the channel that contained 20 beads. We passed a current through an adjacent electromagnet, and recorded the time to "capture" 90% of the beads—that is, to move beads from inside the microfluidic channel into contact with the wall. The "time of capture" was measured at various currents applied to the wire between 130 mA and 1090 mA. The average time to capture the beads was 29 s at 130 mA and 0.75 s at 1090 mA.

The time, t_{cap} (s), required to move a superparamagnetic bead from one sidewall of the microchannel to the opposite wall is approximated by Equation (4); η (10^{-3} kg(m s)$^{-1}$) is

$$t_{cap} = \frac{9}{4}\frac{\pi^2 \eta}{\chi \mu_0 R^2}\frac{(b^4 - a^4)}{{I_{wire}}^2} \quad (4)$$

the dynamic viscosity of the medium, R (m) is the radius of the bead, a (m) is the distance from the center of the electromagnet to the center of a bead resting against the sidewall of the channel, and b (m) is the distance from the center of the electromagnet to the initial position of the bead. A derivation of Equation (4) is in the Supporting Information.

The results of the model are shown as a dashed line in Figure 3d; in the range of 190 mA to 1090 mA, the predicted value of the capture time falls within the range of the measured data. For a current of 130 mA, the predicted value of the capture time is larger than the largest measured value. According to specifications provided by the manufacturer, the beads are weakly magnetized, even in the absence of an applied magnetic field. This factor may explain why the

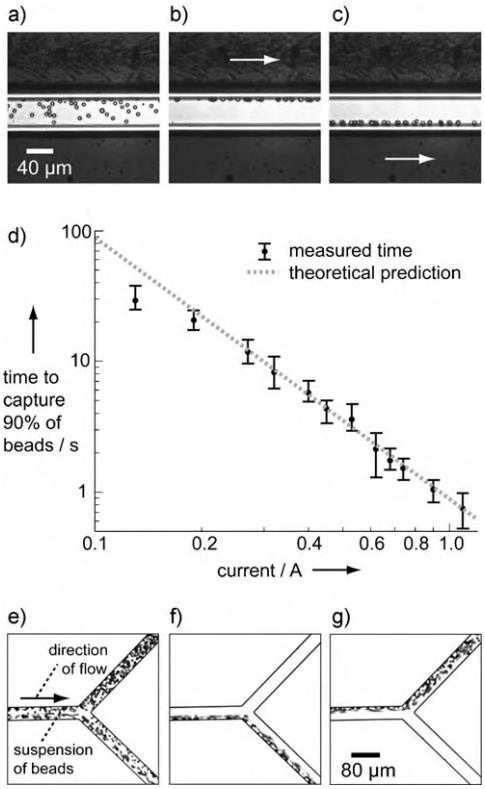

Figure 3. a–c) The capture and release of superparamagnetic beads[38] in a microfluidic channel in proximity to two electromagnets (black). The series of images was taken over 3.2 s. a) The microfluidic channel with no current applied to the electromagnets. b) The microfluidic channel after a current (1 A, in the direction of the arrow) was applied for 1.6 s to the left electromagnet (shown above the channel in the image); the current generated a magnetic field oriented into the plane of the page, with greatest magnitude at the top surface of the microfluidic channel. The gradient in the magnetic field exerted a force on the beads; turning the current on/off made it possible to capture and release beads from the surface of the microfluidic channel. c) The microfluidic channel after the current in the left electromagnet was turned off, and a current of 1 A was applied to the right electromagnet (shown below the channel in the image) for 1.6 s. The process was repeated over 5000 times with similar results. d) Model and measurements of the response time of beads after activation of the electromagnet. Data are the average time to capture (i.e. place in contact with the wall) 90% of a population of superparamagnetic beads measured over 5 experiments; the error bars represent the range of the measured values. The time to capture the beads follows an inverse power relationship with the current [Eq. (4)]. e–g) Sorting superparamagnetic beads in microfluidic channels. Two electromagnets were fabricated on either side of a microfluidic channel 1 cm upstream of a junction; we flowed a suspension of beads through the channel at a rate of approximately 10 μL h^{-1}. e) An image of the junction when both electromagnets were turned off; f) the junction after the right electromagnet was activated for 1 s (and the left electromagnet was turned off); g) the junction after the left electromagnet was activated for 1 s (and the right electromagnet was turned off). For all experiments, the beads were suspended in a buffer at a concentration of 5×10^8 beads mL^{-1} prior to injecting them into the microfluidic channel; the height and width of the channel was 40 μm; the distance between each electromagnet and the channel was 10 μm.

 © 2006 Wiley-VCH Verlag GmbH & Co. KGaA, Weinheim

model—which assumes no initial magnetization of the beads—predicts a longer capture time of the beads for small currents, where the relative contribution of the initial magnetization is the strongest.[38]

Sorting superparamagnetic beads: We used the electromagnets to build a switch to sort a stream of superparamagnetic beads[38] flowing in a microfluidic channel into one of two downstream microfluidic channels (Figure 3e–g). When both electromagnets were off, a suspension of beads flowed into both the left and right microfluidic channels at the junction. When the right electromagnet was activated (the left electromagnet was off), the beads were pulled to the right wall of the channel, and were directed into the right microfluidic channel. When the left electromagnet was activated (the right electromagnet was off), the beads were pulled to the left wall of the channel and were directed into the left microfluidic channel. Using an electronic circuit, we alternated the movement of the beads into the left and right channels with a frequency of 0.5 Hz.

In conclusion, the method described herein makes it possible to fabricate metal wires with micron-scale dimensions close to, and in the same plane as, microfluidic channels, while maintaining an insulating barrier between the wires and the channels. The procedure is based on the cofabrication of channels for wires and channels for fluids; this cofabrication dramatically simplifies the process required for fabrication of microdevices. Although the focus is on using 2D wires to make electromagnets, and on their application in manipulating superparamagnetic beads, these structures will also make it possible to produce electrical fields (with strength approaching $10^8\,V\,m^{-1}$) across microfluidic channels by applying an electrical potential between two wires separated by a channel, and to heat fluid in microfluidic channels by running high currents through wires adjacent to the channels. Multiple electromagnets can be constructed in a microfluidic device to produce distinct and independently variable magnetic fields at specific locations in the device (e.g. at distinct locations along the length of a microfluidic channel). Each electromagnet can be activated discretely using independent electrical signals; this capability may be useful for automated capture and release of superparamagnetic beads at specific "stations" in a lab-on-a-chip device.

We believe that this method for cofabricating electromagnets and microfluidic systems will be useful to chemists and biochemists (for manipulating beads functionalized with biomolecules or cells), microsystem engineers (as a new component for microfluidics and integrated function), and applied physicists (as a means of generating electrically controlled magnetic fields in microsystems).

Received: June 7, 2006
Published online: September 26, 2006

Keywords: analytical chemistry · electromagnets · magnetochemistry · metal–polymer materials · microfluidic systems

[1] J. Atencia, D. Beebe, *Lab Chip* **2004**, *4*, 598–602.
[2] L. Lu, K. Ryu, C. Liu, *J. Microelectromech. Syst.* **2002**, *11*, 462–469.
[3] W. C. Jackson, H. D. Tran, M. J. O'Brien, E. Rabinovich, G. P. Lopez, *J. Vac. Sci. Technol. B* **2001**, *19*, 596–599.
[4] T. Deng, G. M. Whitesides, M. Radhakrishnan, G. Zabow, M. Prentiss, *Appl. Phys. Lett.* **2001**, *78*, 1775–1777.
[5] C. S. Lee, H. Lee, R. M. Westervelt, *Appl. Phys. Lett.* **2001**, *79*, 3308–3310.
[6] M. A. Hayes, N. A. Polson, A. A. Garcia, *Langmuir* **2001**, *17*, 2866–2871.
[7] J. Choi, K. W. Oh, J. H. Thomas, W. R. Heineman, H. B. Halsall, J. H. Nevin, A. J. Helmicki, H. T. Henderson, C. H. Ahn, *Lab Chip* **2002**, *2*, 27–30.
[8] H. A. Ferreira, N. Feliciano, D. L. Graham, L. A. Clarke, M. D. Amaral, P. P. Freitas, *Appl. Phys. Lett.* **2005**, *87*, 013901/1–013901/3.
[9] B. L. Hirschbein, D. W. Brown, G. M. Whitesides, *CHEMTECH* **1982**, *12*, 172–179.
[10] S. Ostergaard, G. Blankenstein, H. Dirac, O. Leistiko, *J. Magn. Magn. Mater.* **1999**, *194*, 156–162.
[11] T. Deng, M. Prentiss, G. M. Whitesides, *Appl. Phys. Lett.* **2002**, *80*, 461–463.
[12] I. Safarik, M. Safarikova, *J. Chromatogr. B* **1999**, *722*, 33–53.
[13] S. W. Yeung, I. M. Hsing, *Biosens. Bioelectron.* **2006**, *21*, 989–997.
[14] H. Lee, A. M. Purdon, V. Chu, R. M. Westervelt, *Nano Lett.* **2004**, *4*, 995–998.
[15] N. Wang, D. E. Ingber, *Biochem. Cell Biol.* **1995**, *73*, 327–335.
[16] N. Pamme, *Lab Chip* **2006**, *6*, 24–38.
[17] C. H. Ahn, M. G. Allen, W. Trimmer, Y. Jun, S. Erramilli, *J. Microelectromech. Syst.* **1996**, *5*, 151–158.
[18] R. Wirix-Speetjens, W. Fyen, K. Xu, J. De Boeck, G. Borghs, *IEEE Trans. Magn.* **2005**, *41*, 4128–4133.
[19] K. Smistrup, O. Hansen, H. Bruus, M. F. Hansen, *J. Magn. Magn. Mater.* **2005**, *293*, 597–604.
[20] J. Choi, C. Ahn, S. Bhansali, H. T. Henderson, *Sens. Actuators B* **2000**, *68*, 34–39.
[21] H. Lee, A. M. Purdon, R. M. Westervelt, *Appl. Phys. Lett.* **2004**, *85*, 1063–1065.
[22] H. Suzuki, C. Ho, N. Kasagi, *J. Microelectromech. Syst.* **2004**, *13*, 779–790.
[23] O. J. A. Schueller, X. Zhao, G. M. Whitesides, S. P. Smith, M. Prentiss, *Adv. Mater.* **1999**, *11*, 37–41.
[24] D. V. Vezenov, B. T. Mayers, D. B. Wolfe, G. M. Whitesides, *Appl. Phys. Lett.* **2005**, *86*, 041104/1–041104/3.
[25] B. T. Mayers, D. V. Vezenov, V. I. Vullev, G. M. Whitesides, *Anal. Chem.* **2005**, *77*, 1310–1316.
[26] A. C. Siegel, D. A. Bruzewicz, D. B. Weibel, G. M. Whitesides, submitted..
[27] Y. Xia, G. M. Whitesides, *Angew. Chem.* **1998**, *110*, 568–594; *Angew. Chem. Int. Ed.* **1998**, *37*, 550–575.
[28] D. C. Duffy, J. C. McDonald, O. J. A. Schueller, G. M. Whitesides, *Anal. Chem.* **1998**, *70*, 4974–4984.
[29] A. Y. N. Hui, G. Wang, B. Lin, W. Chan, *Lab Chip* **2005**, *5*, 1173–1177.
[30] Many compositions of solders can be injected into the microfluidic channels to form electromagnets, including: 100% In, m.p. 157°C; 80% In, 15% Pb, 5% Ag, m.p. 148°C; 97% In, 3% Ag, m.p. 146°C; 52% In, 48% Sn, m.p. 118°C. The highest m.p. solder we have used had m.p. 157°C.
[31] S. T. Brittain, O. J. A. Schueller, H. Wu, S. Whitesides, G. M. Whitesides, *J. Phys. Chem. B* **2000**, *104*, 347–350.
[32] H. Wu, S. T. Brittain, J. R. Anderson, B. Grzybowski, S. Whitesides, G. M. Whitesides, *J. Am. Chem. Soc.* **2001**, *123*, 12691–12699.
[33] *CRC Handbook of Chemistry and Physics*, Internet Version (Ed.: D. R. Lide), Taylor and Francis, Boca Raton, **2006**.

 © 2006 Wiley-VCH Verlag GmbH & Co. KGaA, Weinheim

[34] M. N. O. Sadiku, *Elements of Electromagnetics*, Saunders, New York, **1989**.
[35] We define the magnetic field in tesla (T), where $1\,T = 1\,N\,(A\,m)^{-1}$.
[36] "About Neodymium Iron Boron" can be found under http://www.mceproducts.com/knowledge-base/article/article-dtl.asp?id=2, **2006**.
[37] Refs. [16], [21], and [22] report slightly different formulas for calculating the force upon a superparamagnetic bead as a function of the gradient of the magnetic field. Our model is based on the formula reported in Ref. [21]; in this model, we neglect any initial magnetization of the superparamagnetic beads and do not consider the inertia of the beads, the contribution of the channel walls to the drag on the beads, or the magnetic susceptibility of the suspending medium.
[38] We purchased COMPEL superparamagnetic beads (5.9-μm diameter) from Bangs Laboratories, Inc. We calculated the magnetic susceptibility of the beads χ using the magnetization curves provided by the manufacturer. The susceptibility ranges from $\chi = 0.174$ at low magnetic fields (0.0–0.5 mT) to $\chi = 0.167$ at high magnetic fields (1.0–3.0 mT); the value of susceptibility that we use ($\chi = 0.170$), is the average value calculated over the general range of applied magnetic fields 0.0–3.0 mT used in our experiments.

 © 2006 Wiley-VCH Verlag GmbH & Co. KGaA, Weinheim

Peptides

DOI: 10.1002/anie.200602248

Rational Design of Bioorganometallic Foldamers: A Potential Model for Parallel β-Helical Peptides**

*Somenath Chowdhury, Gabriele Schatte, and Heinz-Bernhard Kraatz**

The design of structurally well-defined peptide motifs has been an active area of research aimed at gaining a deeper understanding of biochemical processes[1] to generate molecules with potential biological applications[2] or to develop novel biomaterials.[3] Synthetic foldamers that resemble the structure of helical[4] and sheet conformations,[5] two of the major secondary structural motifs in proteins, can now be designed de novo by using non-proteinogenic amino acids or a molecular scaffold. In some cases, as for gramicidin A, alternating D- and L-amino acid sequences can adopt a β-helical conformation.[6] In 1993, a new kind of β-helix, in which only L-amino acids are present, was discovered in bacterial *Pectate Lyase C*.[7] and was recognized to play various important roles in biological systems.[8] In this structural motif, a series of β strands are linked by a turn region, thus resulting in a virtually perpendicular arrangement of the individual β strands with respect to the axis of the helix. Little effort has been dedicated to designing the model for this important secondary structural domain. In 2001, Nolte and co-workers reported the synthetic analogue, in which peptide strands are attached to a central polyisocyanide backbone and adopt a β sheet conformation, which runs the length of the central helical core.[9] Disubstituted ferrocene compounds, and ferrocene amino acid (Fca) in particular, are known to induce β turns in peptide conjugates and have the appropriate structural rigidity as a result of efficient hydrogen-bonding interactions between the peptide chains attached to the two cyclopentadienyl (Cp) rings.[10] Thus, we hypothesized that it should be possible to design a helical foldamer that exploits the turn-inducing properties of Fca and links them to α-amino acids. It was thought that the hydrogen-bonding interactions between the peptide substituents on opposite Cp rings would favor the formation of a helical foldamer that displays the main features of the natural β-helical motif. Herein, we present the results of a synthetic and structural study of a series of helical foldamers formed from L- and D-alanine and Fca. Our results unequivocally show the utility of our design approach for the formation of a series of unprecedented helical foldamers that display right- and left-handedness.

Starting from the fully protected Fca derivative **1**,[11] the desired "monomers" Fca–L-alanine (**2**) and Fca–D-alanine (**3**), their corresponding oligomers **6**–**11**, and poly(Fca–L-alanine) (**12**) were synthesized in solution by peptide-coupling strategies (Scheme 1) and were characterized spectroscopically (see Supporting Information). The ^{1}H NMR spectra of **2** and **3** in $CDCl_3$ show the presence of an amide NH signal at $\delta = 7.61$ (NH of Fca) and 6.50 ppm (NH of Ala). As the length of the peptide increases, the amide resonances gradually shift downfield, thus indicating an increasingly hydrogen-bonded system. In the case of the polymeric **12**, the two amide NH resonances are observed at $\delta = 10.87$ (for NH attached to Cp) and 9.07 ppm (for NH of Ala), as is expected for strongly hydrogen-bonded systems. ROESY NMR spectroscopic studies of the Fca foldamers **6**, **8**, and **10** in solution show the cross-correlations between Fc–NH_i and β-H of Ala_{i+1}, Ala-NH_{i+1} and α-H of Ala_i, and β-H of Ala_{i+1} and α-H of Ala_i (see Supporting Information), which correspond to the β-helical conformations. Circular dichroism (CD) spectroscopy is a reliable tool to evaluate the conformation of chiral Fc conjugates that display a band (+ or −) at about 450 nm.[12] CD studies of solutions of our foldamers in acetonitrile (Figure 1) show that the oligomers **6**, **8**, and **10**, derived from L-Ala, exhibit a weak positive Cotton effect (*P* helicity) in the ferrocene region at $\lambda = 450$ nm, whereas the D-Ala derivatives

[*] S. Chowdhury, Prof. H.-B. Kraatz
Department of Chemistry
University of Saskatchewan
110 Science Place, Saskatoon, SK S7N 5C9 (Canada)
Fax: (+1) 306-966-4730
E-mail: kraatz@skyway.usask.ca
Dr. G. Schatte
Saskatchewan Structural Science Centre
University of Saskatchewan
110 Science Place, Saskatoon, SK S7N 5C9 (Canada)

[**] We acknowledge support from the NSERC in the form of an operating grant. H.-B.K. holds the Canada Research Chair in Biomaterials.

Supporting information for this article is available on the WWW under http://www.angewandte.org or from the author.

InterScience
© 2006 Wiley-VCH Verlag GmbH & Co. KGaA, Weinheim

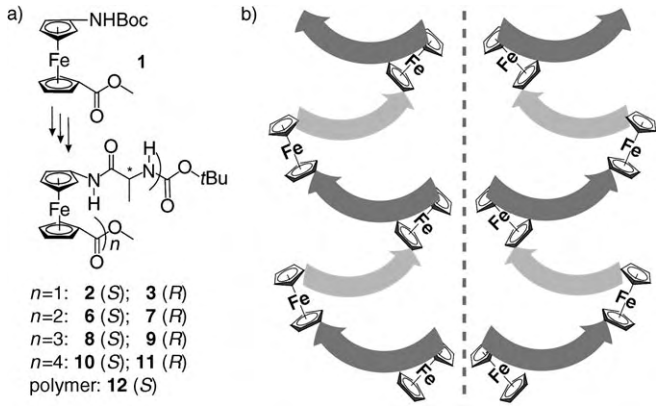

Scheme 1. a) Preparation of *P*- and *M*-helical foldamers from the conjugates of Fca with L- and D-alanine, respectively (see Supporting Information for a detailed description of the synthesis and characterization). b) Schematic representation of the formation of right- and left-handed β-helical structures from the alternating conjugates of Fca and L- and D-amino acids, respectively, which are mirror images of each other.

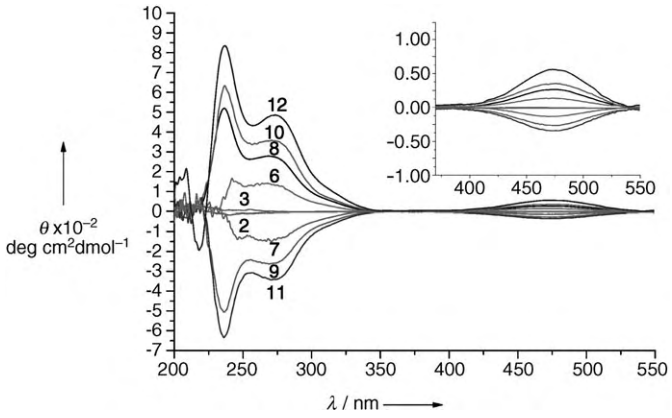

Figure 1. CD spectra of the Fca–Ala "monomers" **2** and **3** and the right- and left-handed parallel β-helical Fca–Ala oligomers (**6**–**11**) and polymer (**12**) in acetonitrile at 25 °C. The intensity is normalized for one repeating unit.

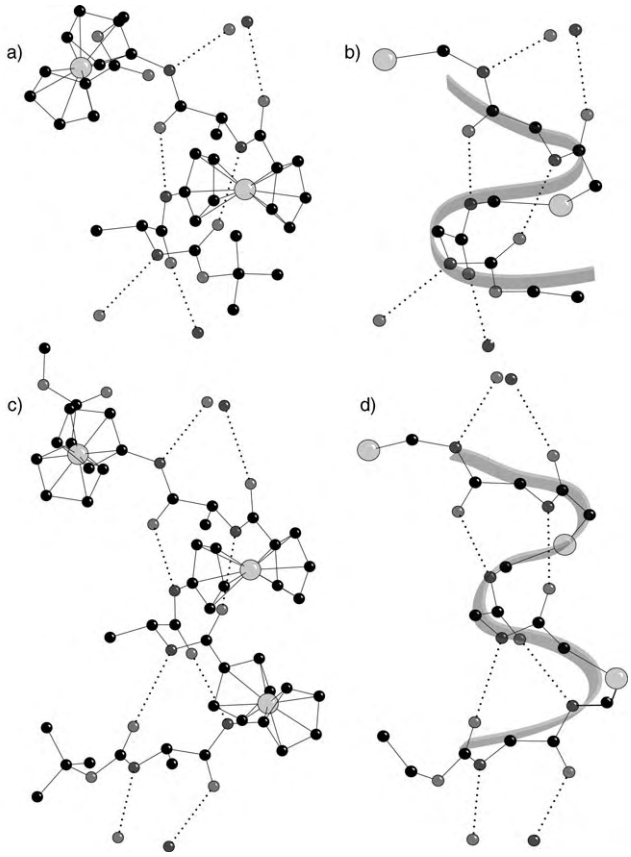

Figure 2. a) Crystal structure of **6**, b) the helical backbone of **6**, c) crystal structure of **8**, and d) the helical backbone of **8**. C black; N dark gray; O mid-gray; Fe pale gray (large spheres). Hydrogen atoms are omitted for clarity, and the dashed lines represent hydrogen bonds. The intramolecular and intermolecular hydrogen-bonding patterns are identical (12-membered rings including the hydrogen atoms, parallel β-sheet-like). The crystal structure of **7** is the mirror image of **6**, and that of **9** is the mirror image of **8** (see Supporting Information).

7, **9**, and **11** exhibit a negative Cotton effect (*M* helicity). The Fca–Ala "monomers" **2** and **3** do not exhibit any Fca-based band but display a weak signal in the peptide region, which are mirror images of each other. The absence of the band in the Fca region is not surprising, as the intramolecular hydrogen-bonding required to establish a stable secondary structure is not possible in these "monomers". For the dimers **6** and **7**, in which two Fca–Ala units are connected by hed-to-tail strong intramolecular hydrogen bonding (see Figure 2 and below) exists between the two Ala groups. The resulting effect on the CD spectrum normalized to a single Fca–Ala unit is significant enhancement of the bands.

Additional Fca–Ala units increase the signal intensity of the normalized CD spectrum in both the Fca and peptide regions. Peptides of equal length have CD signals of equal magnitude but of opposite sign, thus indicating that the helicity pattern is identical but of opposite handedness. Upon elongation, the conjugates are able to establish stronger intramolecular hydrogen bonding between adjacent Ala units, thus resulting in a more rigid helical arrangement. Importantly, the polymer displays a characteristic band at 215 nm indicative of β-sheet peptides, which is absent in the smaller oligomers. The helices are stable at elevated temperatures and do not show a distinct melting behavior at temperatures up to 70 °C (see Supporting Information).

The dimers (**6** and **7** in $P2_12_12_1$ space group) and trimers (**8** in $P4_12_12$ and **9** in $P4_32_12$ space group) were readily crystallized either by slow diffusion of nonsolvent into the sample solution or by slow evaporation of solvent from the solution (see Supporting Information). The single-crystal structural analyses of those show the expected axial chirality for each of the Fca residues. All systems derived from L-Ala adopt a *P*-helical conformation, whereas D-Ala gives rise to *M* helicity, thus corroborating the CD results. The amino acid residues are involved in intramolecular hydrogen bonding, thereby forming a parallel β-sheet-like structure with 12-membered hydrogen-bonded rings. As the length of the helix increases, the number of 12-membered hydrogen-bonded rings increases. The intramolecular hydrogen-bonding distances (N···O) are 2.95–2.92 Å between the NH of Fca and C=O of

 © 2006 Wiley-VCH Verlag GmbH & Co. KGaA, Weinheim

Ala, and 2.99–2.97 Å between the NH of Ala and C=O of Fca. The dihedral angles of all peptide segments for **6** and **8** are $-79 > \varphi > -67$ and $155 < \psi < 138°$, respectively.[13] The dihedral angles for the foldamers **7** and **9** derived from D-Ala are similar in magnitude but opposite in sign. Importantly, on the supramolecular level, the same hydrogen-bonding pattern as intramolecular (a 12-membered parallel β-sheet-like ring formation and similar N–O distances) is propagated and forms a continuous helical structure. The individual supramolecular helices arrange parallel to each other to generate solvent-filled hydrophobic pockets (CH_2Cl_2 for **6** and **7**, hexane for **8**, $CHCl_3$ for **9**). FTIR spectroscopy of the foldamers in KBr show the amide A absorption in the range 3266–3272 cm^{-1}, which clearly indicates the involvement of the amide NH group in the hydrogen bonding. The amide I and II regions of the conjugates are complex and show a series of bands (1627–1639 and 1680–1690 cm^{-1}) that may be attributed to a β-sheet conformation.[14]

In conclusion, we presented the results of a study into the preparation and structural properties of organometallic peptide conjugate foldamers that adopt a structure that shows some structural similarities to the β-helical motif found in naturally occurring proteins, thus exploiting the turn-inducing ability of Fca. This novel redox-active β-helical system may have potential for the electrochemical screening of "β-breakers". We are now exploring the electronic and electrochemical properties of these and related systems in solution and on a surface using surface-supported helical foldamers.[15]

Received: June 6, 2006
Published online: September 25, 2006

Keywords: bioorganometallic compounds · ferrocene · foldamers · helical structures · peptides

[1] a) M. A. Shogren-Knaak, P. J. Alaimo, K. M. Shokat, *Annu. Rev. Cell Dev. Biol.* **2001**, *17*, 405–433; b) J. D. Sadowsky, M. A. Schmitt, H. S. Lee, N. Umezawa, S. M. Wang, Y. Tomita, S. H. Gellman, *J. Am. Chem. Soc.* **2005**, *127*, 11966—11968.

[2] a) M. Zasloff, *Nature* **2002**, *415*, 389–395; b) M. A. Schmitt, B. Weisblum, S. H. Gellman, *J. Am. Chem. Soc.* **2004**, *126*, 6848–6849; c) S. Fernandez-Lopez, H. S. Kim, E. C. Choi, M. Delgado, J. R. Granja, A. Khasanov, K. Kraehenbuehl, G. Long, D. A. Weinberger, K. M. Wilcoxen, M. R. Ghadiri, *Nature* **2001**, *412*, 452–455.

[3] a) S. G. Zhang, *Nat. Biotechnol.* **2003**, *21*, 1171–1178; b) S. Hecht, *Mater. Today* **2005**, 48–55.

[4] a) D. Seebach, M. Overhand, F. N. M. Kuhnle, B. Martinoni, L. Oberer, U. Hommel, H. Widmer, *Helv. Chim. Acta* **1996**, *79*, 913–941; b) S. H. Gellman, *Acc. Chem. Res.* **1998**, *31*, 173–180; c) J. S. Nowick, *Acc. Chem. Res.* **1999**, *32*, 287–296; d) D. H. Appella, L. A. Christianson, I. L. Karle, D. R. Powell, S. H. Gellman, *J. Am. Chem. Soc.* **1999**, *121*, 6206–6212; e) R. P. Cheng, S. H. Gellman, W. F. DeGrado, *Chem. Rev.* **2001**, *101*, 3219–3232; f) D. J. Hill, M. J. Mio, R. B. Prince, T. S. Hughes, J. S. Moore, *Chem. Rev.* **2001**, *101*, 3893–4011; g) J. Venkatraman, S. C. Shankaramma, P. Balaram, *Chem. Rev.* **2001**, *101*, 3131–3152; h) J.-M. L. J. Garric, I. Huc, *Angew. Chem.* **2005**, *117*, 1990–1994; *Angew. Chem. Int. Ed.* **2005**, *44*, 1954–1958; i) W. S. Horne, M. K. Yadav, C. D. Stout, M. R. Ghadiri, *J. Am. Chem. Soc.* **2004**, *126*, 15366–15367; j) G. V. M. Sharma, P. Nagendar, P. Jayaprakash, P. R. Krishna, K. V. S. Ramakrishna, A. C. Kunwar, *Angew. Chem.* **2005**, *117*, 6028–6032; *Angew. Chem. Int. Ed.* **2005**, *44*, 5878–5882; k) M. A. Schmitt, S. H. Choi, I. A. Guzei, S. H. Gellman, *J. Am. Chem. Soc.* **2005**, *127*, 13130–13131; l) C. Baldauf, R. Gunther, H. J. Hofmann, *Angew. Chem.* **2004**, *116*, 1621–1624; *Angew. Chem. Int. Ed.* **2004**, *43*, 1594–1597, ; m) G. V. M. Sharma, K. R. Reddy, P. R. Krishna, A. R. Sankar, P. Jayaprakash, B. Jagannadh, A. C. Kunwar, *Angew. Chem.* **2004**, *116*, 4051–4055; *Angew. Chem. Int. Ed.* **2004**, *43*, 3961–3965; n) A. Hayen, M. A. Schmitt, F. N. Ngassa, K. A. Thomasson, S. H. Gellman, *Angew. Chem.* **2004**, *116*, 511–516; *Angew. Chem. Int. Ed.* **2004**, *43*, 505–510; o) S. De Pol, C. Zorn, C. D. Klein, O. Zerbe, O. Reiser, *Angew. Chem.* **2004**, *116*, 517–520; *Angew. Chem. Int. Ed.* **2004**, *43*, 511–514, ; p) C. Baldauf, R. Gunther, H.-J. Hofmann, *J. Org. Chem.* **2006**, *71*, 1200–1208.

[5] a) J. P. Schneider, J. W. Kelly, *Chem. Rev.* **1995**, *95*, 2169–2187; b) T. A. Martinek, G. K. Toth, E. Vass, M. Hollosi, F. Fulop, *Angew. Chem.* **2002**, *114*, 1794–1797; *Angew. Chem. Int. Ed.* **2002**, *41*, 1718–1721, ; c) W. A. Loughlin, J. D. A. Tyndall, M. P. Glenn, D. P. Fairlie, *Chem. Rev.* **2004**, *104*, 6085–6117.

[6] a) P. De Santis, S. Morosetti, R. Rizzo, *Macromolecules* **1974**, *7*, 52–58; B. A. Wallace, *Biophys. J.* **1986**, 49, 295–306; b) G. N. Ramachandran, R. Chandrasekaran, *Indian J. Biochem. Biophys.* **1972**, *9*, 1–11; c) E. Navarro, E. Fenude, B. Celda, *Biopolymers* **2002**, *64*, 198; d) C. Baldauf, R. Gunther, H. J. Hofmann, *Biopolymers* **2005**, *80*, 675.

[7] M. D. Yoder, N. T. Keen, F. Jurnak, *Science* **1993**, *260*, 1503.

[8] a) Y. C. Liou, A. Tocilj, P. L. Davies, Z. C. Jia, *Nature* **2000**, *406*, 322; b) J. Jenkins, R. Pickersgill, *Prog. Biophys. Mol. Biol.* **2001**, *77*, 111.

[9] J. Cornelissen, J. Donners, R. de Gelder, W. S. Graswinckel, G. A. Metselaar, A. E. Rowan, N. Sommerdijk, R. J. M. Nolte, *Science* **2001**, *293*, 676.

[10] a) T. Moriuchi, A. Nomoto, K. Yoshida, A. Ogawa, T. Hirao, *J. Am. Chem. Soc.* **2001**, *123*, 68–75; b) D. R. van Staveren, N. Metzler-Nolte, *Chem. Rev.* **2004**, *104*, 5931–5985; c) T. Moriuchi, T. Hirao, *Chem. Soc. Rev.* **2004**, *33*, 294; d) L. Barisic, M. Dropucic, V. Rapic, H. Pritzkow, S. I. Kirin, N. Metzler-Nolte, *Chem. Commun.* **2004**, 2004–2005; e) S. Chowdhury, K. A. Mahmoud, G. Schatte, H. B. Kraatz, *Org. Biomol. Chem.* **2005**, *3*, 3018–3023.

[11] L. Barisic, W. Rapic, V. Kovac, *Croat. Chem. Acta* **2002**, *75*, 199–210.

[12] S. I. Kirin, H. B. Kraatz, N. Metzler-Nolte, *Chem. Soc. Rev.* **2006**, *35*, 348–354.

[13] These dihedral angles fall within the regions of the Ramachandran plot ($-180° < \varphi < -45°$ and $45° < \psi < 225°$) assigned to β-sheet conformations; G. N. Ramachandran, V. Sasisekharan, *Adv. Protein Chem.* **1968**, 23, 283–437.

[14] a) S. Krimm, J. Bandekar, *Adv. Protein Chem.* **1986**, 38, 181–364; b) A. Barth, C. Zscherp, *Q. Rev. Biophys.* **2002**, *35*, 369–430; c) M. R. Ghadiri, J. R. Granja, R. A. Milligan, D. E. McRee, N. Khazanovich, *Nature* **1993**, *366*, 324–327.

[15] The Supporting Information includes experimental and spectroscopic details; IR spectra for all compounds; variable-temperature (VT) CD spectra and NMR stack plots for the L-series; ROESY spectra of **6**, **8**, and **10**; and single-crystal data and intermolecular arrangements of **6**–**9**.

 © 2006 Wiley-VCH Verlag GmbH & Co. KGaA, Weinheim

Homogeneous Catalysis

DOI: 10.1002/anie.200602377

Branch-Selective Intermolecular Hydroacylation: Hydrogen-Mediated Coupling of Anhydrides to Styrenes and Activated Olefins**

*Young-Taek Hong, Andriy Barchuk, and Michael J. Krische**

Alkene hydroformylation is the largest volume application of homogeneous metal catalysis and the prototypical example of hydrogen-mediated C–C bond formation.[1] Remarkably, while hydroformylation is practiced on a vast scale, systematic efforts toward the development of hydrogenative C–C coupling reactions that extend beyond carbon monoxide insertion have only recently been described.[2,3] Ideally, it would be desirable to couple two or more organic molecules simply through their exposure to gaseous hydrogen in the presence of a metal catalyst. This goal represents the primary focus of research in our laboratory.[2]

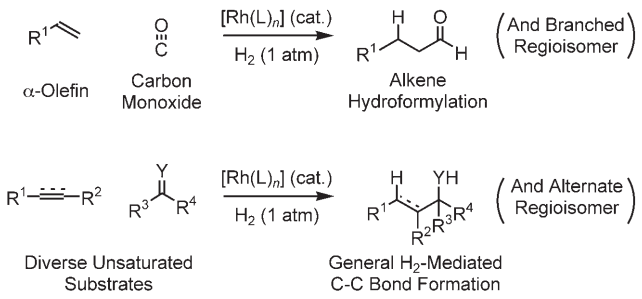

In connection with ongoing efforts toward the development of hydrogen-mediated C–C coupling reactions, we herewith disclose studies on the hydrogen-mediated reductive coupling of carboxylic anhydrides, including mixed anhydrides, to styrenes and activated olefins, and thus generate a protocol for intermolecular alkene hydroacylation.[3b,4–7] Notably, we find that cationic rhodium catalysts ligated by triphenylarsine (Ph_3As)[8] enable formation of branched hydroacylation products with exceptionally high levels of regiocontrol [Eq. (1)]. The significance of these findings is twofold. First, while catalytic systems for intramolecular

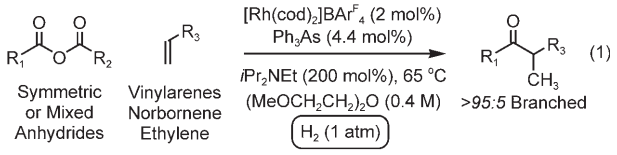

hydroacylation involving aldehydes as acyl donors are well developed,[4] corresponding intermolecular hydroacylations[5–7] are far more limited in scope because of competitive decarbonylation of aldehydes.[9] Secondly, prior to the results reported herein, the catalytic reductive coupling of alkenes to carbonyl compounds has only been achieved intramolecularly by cyclization of olefinic aldehydes.[10]

Our initial studies focused on the reductive coupling of styrene and benzoic anhydride. Such hydroacylations find precedent in the reaction of acid chlorides and ethylene mediated by stoichiometric quantities of $[RhH(PPh_3)_3(CO)]$,[11a] the reductive coupling of dienes and acid chlorides catalyzed by palladium and mediated by silane,[11b] and, most importantly, a single report by Miura and co-workers of the hydrogen-mediated coupling of benzoic anhydride to styrene catalyzed by $[RhCl(cod)]_2$ (cod = cycloocta-1,5-diene) with $(PhO)_3P$ as the ligand. Under these conditions, a 3:1 mixture of branched and linear products is obtained in 30% yield.[3b] However, it was found that increased catalyst loading did little to improve the yield of the coupling product (Table 1, entries 1 and 2). A survey of

Table 1: Optimization of hydrogen-mediated intermolecular hydroacylation.[a]

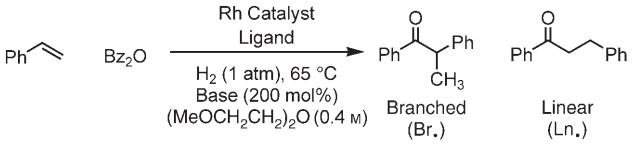

Entry	Catalyst (mol%)	L (mol%)	Base	Yield [%]	Br./Ln.
1	$[\{RhCl(cod)\}_2]$ (0.5)	PhO_3P (2)	iPr_2NEt	30	3:1
2	$[\{RhCl(cod)\}_2]$ (5)	PhO_3P (20)	iPr_2NEt	45	3:1
3	$[\{RhCl(cod)\}_2]$ (5)	Ph_3P (20)	iPr_2NEt	15	6:1
4	$[\{RhCl(cod)\}_2]$ (5)	Fur_3P (20)	iPr_2NEt	22	>95:5
5	$[\{RhCl(cod)\}_2]$ (5)	Ph_3As (20)	iPr_2NEt	57	>95:5
6	$[\{RhCl(cod)\}_2]$ (5)	Ph_3Bi (20)	iPr_2NEt	trace	
7	$[\{RhOMe(cod)\}_2]$ (5)	Ph_3As (20)	iPr_2NEt	67	>95:5
8	$[Rh(cod)_2]OTf$ (5)	Ph_3As (12)	iPr_2NEt	79	>95:5
9	$[Rh(cod)_2]OTf$ (5)	Ph_3As (12)	Li_2CO_3	63	>95:5
10	$[Rh(cod)_2]BF_4$ (5)	Ph_3As (12)	iPr_2NEt	82	>95:5
11	$[Rh(cod)_2]PF_6$ (5)	Ph_3As (12)	iPr_2NEt	85	>95:5
12	$[Rh(cod)_2]SbF_6$ (5)	Ph_3As (12)	iPr_2NEt	84	>95:5
13	$[Rh(cod)_2]BAr^F_4$ (5)	Ph_3As (12)	iPr_2NEt	93	>95:5
14	$[Rh(cod)_2]BAr^F_4$ (2)	Ph_3As (4.4)	iPr_2NEt	93	>95:5

[a] Cited yields are of isolated material. For the experiments above, 400 mol% of styrene and 100 mol% of Bz_2O were used. However, under the conditions cited in entry 13, but using 100 mol% of styrene and 200 mol% of Bz_2O, an 87% yield of the branched reductive coupling product was obtained. See the Supporting Information for detailed experimental procedures.

[*] Y.-T. Hong, A. Barchuk, Prof. M. J. Krische
University of Texas at Austin
Department of Chemistry and Biochemistry
1 University Station – A5300
Austin, TX 78712-1167 (USA)
Fax: (+1) 512-471-8696
E-mail: mkrische@mail.utexas.edu

[**] Acknowledgment is made to the Research Corporation Cottrell Scholar Award (CS0927), the Alfred P. Sloan Foundation, the Dreyfus Foundation, Eli Lilly, Johnson & Johnson, the NIH-NIGMS (RO1-GM69445), and the Robert A. Welch Foundation for partial support of this research.

Supporting information for this article is available on the WWW under http://www.angewandte.org or from the author.

© 2006 Wiley-VCH Verlag GmbH & Co. KGaA, Weinheim

monodentate ligands proved more fruitful. Whereas Rh catalysts ligated by PPh_3 gave only a 15% yield of the coupling product, more electron-deficient ligands $(2\text{-Fur})_3P$ (Fur = furanyl) and Ph_3As provided the branched coupling product as a single regioisomer and, for the latter case, in substantially improved yield (Table 1, entries 3–5). Given these results, the ligand Ph_3As was screened against a series of Rh^I sources (Table 1, entries 7–13). It was found that cationic Rh^I complexes were especially effective precatalysts. Indeed, upon use of $[Rh(cod)_2]BAr^F{}_4$ as precatalyst ($Ar^F = 3,5\text{-}(CF_3)_2C_6H_3$), the coupling product is obtained in 93% yield as a single regioisomer (Table 1, entry 13). Enhanced reactivity conferred through the use of noncoordinating counterions, and in particular $BAr^F{}_4^-$, has been noted for cationic Rh^I- and Ir^I-based hydrogenation catalysts.[12] Catalyst loading could be reduced to 2 mol% without any decline in the yield (Table 1, entry 14). Notably, the present second-generation catalytic system (Table 1, entries 13 and 14) provides better yields and better regioselectivities at less than half the catalyst loading than the original catalytic system described in the pioneering study by Miura and co-workers (Table 1, entries 1 and 2).

Various substrate combinations were explored under these optimized conditions. It was found that substituted styrenes and related vinylarenes reductively couple to benzoic anhydride in good to excellent yield with complete regiocontrol favoring the branched product (Table 2, top). As demonstrated by the formation of product **7**, arenes containing nitro groups are not subject to reduction under the conditions of hydrogen-mediated coupling. Simple aliphatic alkenes gave diminished yields of the reductive coupling product and exhibit incomplete levels of regioselection.[13] To further assess the scope of the reaction, different carboxylic anhydrides were hydrogenated in the presence of styrene. Aromatic, heteroaromatic, and α,β-unsaturated anhydrides couple in good to excellent yield and with complete branch-selective regiocontrol (Table 2, bottom). Notably, α,β-unsaturated coupling products **14**–**17**, are not subject to over-reduction under the conditions of hydrogen-mediated coupling. Aliphatic anhydrides, such as acetic anhydride, provide diminished yields of the coupling product.[13] As demonstrated by the formation of **19**–**24** (Table 3), norbornene also

Table 2: Hydrogen-mediated coupling of Bz_2O to different vinylarenes (top) and hydrogen-mediated coupling of different anhydrides to styrene (bottom).[a]

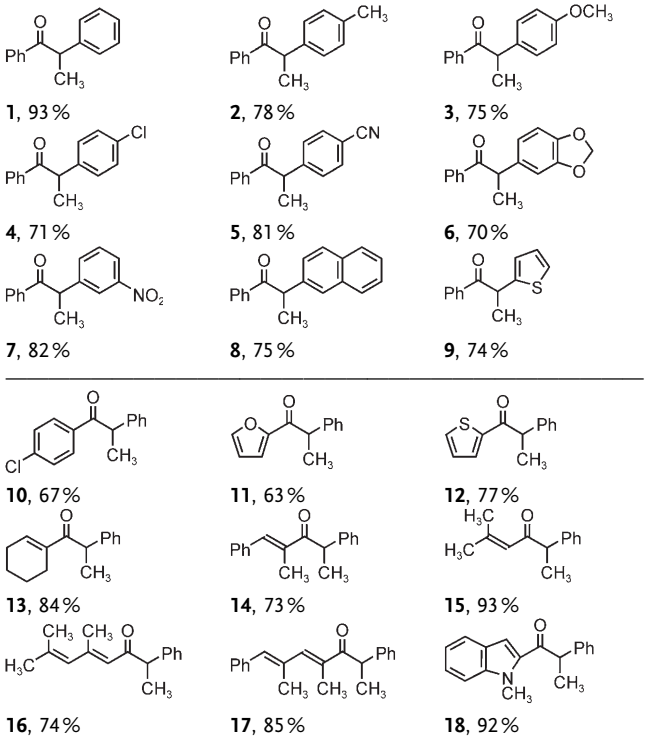

[a] Cited yields are of isolated material. In all cases, >95:5 regioselection is observed. See the Supporting Information for detailed experimental procedures.

Table 3: Hydrogen-mediated coupling of assorted carboxylic anhydrides to norbornene.[a]

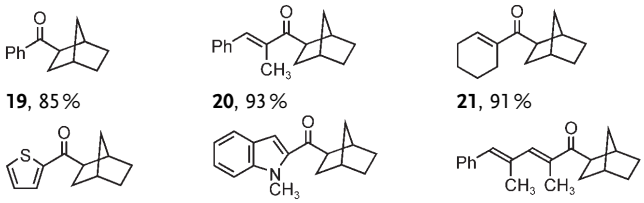

[a] Cited yields are of isolated material. See the Supporting Information for detailed experimental procedures.

couples readily to heteroaromatic and α,β-unsaturated carboxylic anhydrides. Of greater interest, gaseous ethylene participates in the coupling. For example, the 2-carboxyindole anhydride shown in Equation (2) (chosen because of the low

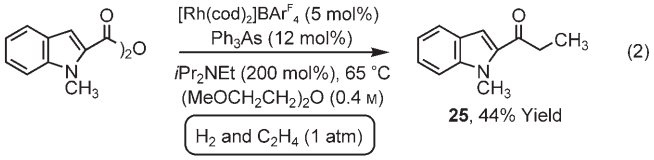

(2)

volatility of the product) is converted into the corresponding ethyl ketone in an unoptimized 44% yield simply by using a balloon containing roughly equal volumes of hydrogen and ethylene gas.

Coupling to mixed anhydrides would be desirable for more highly functionalized carboxylic acid precursors. Accordingly, mixed anhydrides derived from trimethylacetic acid (pivalic acid) and various α,β-unsaturated acids were prepared and subjected to the optimized conditions for coupling to styrene and norbornene. Gratifyingly, transfer of the α,β-unsaturated acyl moiety was observed exclusively. Complete levels of branch regioselectivity were also observed in coupling reactions to styrene (Table 4).

To gain insight into the catalytic mechanism, the coupling of benzoic anhydride and styrene was conducted in a deuterium atmosphere. Deuterium is incorporated primarily at the β position, but the extent of incorporation is base-

 © 2006 Wiley-VCH Verlag GmbH & Co. KGaA, Weinheim

Table 4: Hydrogen-mediated coupling of mixed anhydrides to styrene and norbornene.[a]

Entry	Mixed anhydride	Product	Yield [%]
1	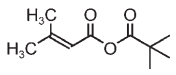	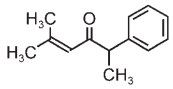	71
2	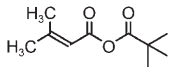	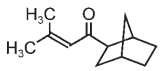	62
3	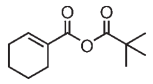	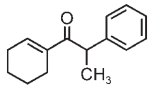	70
4	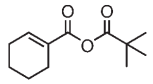	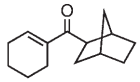	86
5	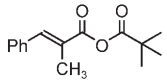	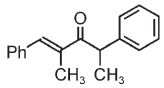	80
6	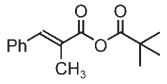	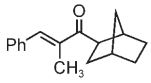	84
7	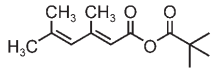	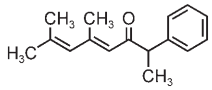	73

[a] Cited yields are of isolated material. In all cases involving styrene, >95:5 regioselection is observed. See the Supporting Information for detailed experimental procedures.

dependant. When iPr$_2$NEt or Li$_2$CO$_3$ are used as the base, 0.4 and 0.8 deuterium atoms are incorporated, respectively. These data are consistent with the catalytic mechanism **A** (Scheme 1) initially proposed by Miura and co-workers[3b] which involves heterolytic activation of hydrogen by way of the dihydride. Incomplete incorporation of deuterium may result from reversible coordination and hydrometalation of styrene. Furthermore, dehydrogenation of iPr$_2$NEt may compete with hydrogen activation, thus contributing further to the incomplete incorporation of deuterium. Dissociation of the weakly coordinating ligand Ph$_3$As prior to hydrometalation may direct the formation of the branched alkyl rhodium intermediate, as this would allow the resulting coordinatively unsaturated Rh center to interact with the adjacent arene. However, the regio-determining hydrometalation of mechanism **A**, which occurs prior to any interaction with the anhydride, is inconsistent with the fact that different acyl donors, such as the *O*-2-pyridyl ester, exhibit different levels of regioselection. It is known that low-valent rhodium complexes undergo oxidative addition to carboxylic anhydrides under mild conditions to afford acyl metal carboxylates.[14] Hence, catalytic mechanism **B**, which involves oxidative addition of an anhydride followed by insertion of styrene and hydrogenolytic cleavage of the rhodium–carbon bond is herewith proposed to account for the changes in the regiochemistry arising from the use of different acyl derivatives.

In summary, we have reported a regioselective intermolecular hydroacylation of vinylarenes in which symmetric and mixed carboxylic anhydrides are used as acyl donors. High levels of branch selectivity are promoted through the use of cationic rhodium catalysts ligated by triphenylarsine. Future studies will focus on the hydrogen-mediated coupling of simple α-olefins to aliphatic carboxylic anhydrides and acid chlorides, as well the development of enantioselective variants involving chirally modified triphenylarsine ligands.

Received: June 13, 2006
Revised: August 8, 2006
Published online: September 22, 2006

Keywords: alkenes · homogeneous catalysis · hydroacylation · hydrogenation · rhodium

[1] For selected reviews on hydroformylation, see: a) P. Eilbracht, L. Barfacker, C. Buss, C. Hollmann, B. E. Kitsos-Rzychon, C. L. Kranemann, T. Rische, R. Roggenbuck, A. Schmidt, *Chem. Rev.* **1999**, *99*, 3329–3365; b) K. Nozaki in *Comprehensive Asymmetric Catalysis*, *Vol. 1* (Eds.: E. N. Jacobsen, A. Pfaltz, H. Yamamoto), Springer, Berlin, **1999**, pp. 381–413; c) C. D.

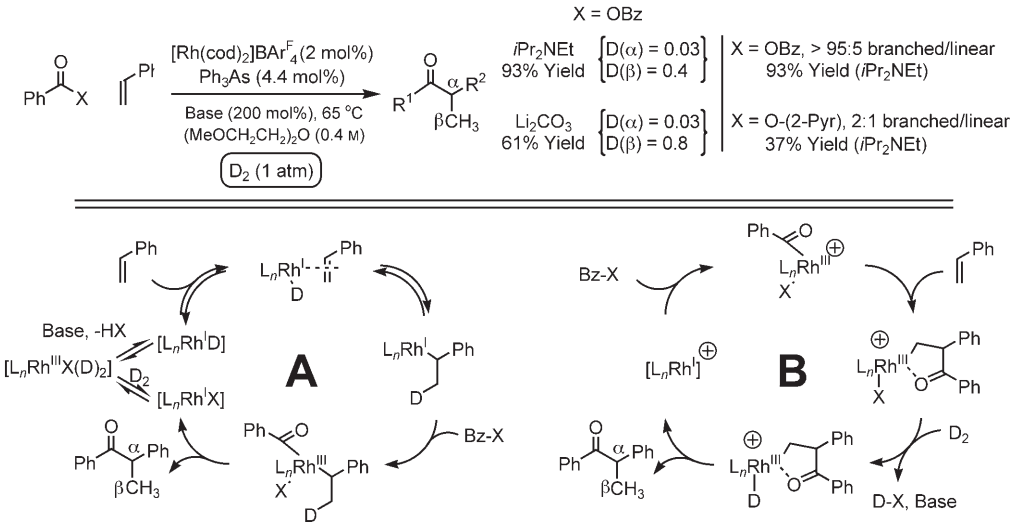

Scheme 1. Plausible catalytic mechanism as supported by deuterium labeling studies. Bz = benzyl.

 © 2006 Wiley-VCH Verlag GmbH & Co. KGaA, Weinheim

Frohning, C. W. Kohlpainter, H. W. Bohnen in *Applied Homogeneous Catalysis with Organometallic Compounds*, *Vol. 1* (Eds.: B. Cornils, W. A. Herrmann), Wiley-VCH, Weinheim, **2002**, pp. 31 – 103; d) B. Breit, *Acc. Chem. Res.* **2003**, *36*, 264 – 275.

[2] For hydrogen-mediated C–C bond formations developed in our laboratory, see: a) H.-Y. Jang, R. R. Huddleston, M. J. Krische, *J. Am. Chem. Soc.* **2002**, *124*, 15156 – 15157; b) R. R. Huddleston, M. J. Krische, *Org. Lett.* **2003**, *5*, 1143 – 1146; c) H.-Y. Jang, R. R. Huddleston, M. J. Krische, *Angew. Chem.* **2003**, *115*, 4208 – 4211; *Angew. Chem. Int. Ed.* **2003**, *42*, 4074 – 4077; d) R. R. Huddleston, H.-Y. Jang, M. J. Krische, *J. Am. Chem. Soc.* **2003**, *125*, 11488 – 11489; e) P. K. Koech, M. J. Krische, *Org. Lett.* **2004**, *6*, 691 – 694; f) G. A. Marriner, S. A. Garner, H.-Y. Jang, M. J. Krische, *J. Org. Chem.* **2004**, *69*, 1380 – 1382; g) H.-Y. Jang, R. R. Huddleston, M. J. Krische, *J. Am. Chem. Soc.* **2004**, *126*, 4664 – 4668; h) H.-Y. Jang, M. J. Krische, *J. Am. Chem. Soc.* **2004**, *126*, 7875 – 7880; i) H.-Y. Jang, F. W. Hughes, H. Gong, J. Zhang, J. S. Brodbelt, M. Krische, *J. Am. Chem. Soc.* **2005**, *127*, 6174 – 6175; j) J.-R. Kong, C.-W. Cho, M. J. Krische, *J. Am. Chem. Soc.* **2005**, *127*, 11269 – 11276; k) C.-K. Jung, S. A. Garner, M. J. Krische, *Org. Lett.* **2006**, *8*, 519 – 522; l) J.-R. Kong, M.-Y. Ngai, M. J. Krische, *J. Am. Chem. Soc.* **2006**, *128*, 718 – 719; m) C.-W. Cho, M. J. Krische, *Org. Lett.* **2006**, *8*, 891 – 894.

[3] Prior to our work, only two hydrogen-mediated C–C bond formations under CO-free conditions were reported: a) G. A. Molander, J. O. Hoberg, *J. Am. Chem. Soc.* **1992**, *114*, 3123 – 3125; b) K. Kokubo, M. Miura, M. Nomura, *Organometallics* **1995**, *14*, 4521 – 4524. In the latter study, yields of the styrene–Bz_2O coupling product were not obtained, and under the optimum reported conditions, a 66% conversion was determined by GC analysis. In our hands, under their optimum reported conditions, a 30% yield of the styrene–Bz_2O coupling product was reproducibility obtained as a 3:1 ratio of branched and linear isomers.

[4] For reviews encompassing rhodium-catalyzed hydroacylation involving aldehyde donors, see: a) B. Bosnich, *Acc. Chem. Res.* **1998**, *31*, 667 – 674; b) M. Tanaka, K. Sakai, H. Suemune, *Curr. Org. Chem.* **2003**, *7*, 353 – 367; c) G. C. Fu in *Modern Rhodium-Catalyzed Organic Reactions* (Ed.: P. A. Evans), Wiley-VCH, Weinheim, **2005**, chap. 7, pp. 79 – 91.

[5] To suppress decarbonylation in the intermolecular rhodium-catalyzed hydroacylation, aldehyde donors that possess an adjacent site of coordination are required (for example, salicyladehydes and β-sulfido aldehydes). Alternatively, conventional aldehyde donors may be converted into the corresponding (*N*-2-pyridyl)aldimines, which are then used as aldehyde equivalents: a) K. P. Vora, C. F. Lochow, R. G. Miller, *J. Organomet. Chem.* **1980**, *192*, 257 – 264; b) E. Rode, M. E. Davis, B. E. Hanson, *J. Chem. Soc. Chem. Commun.* **1985**, 716 – 717; c) T. B. Marder, D. C. Roe, D. Milstein, *Organometallics* **1988**, *7*, 1451 – 1453; d) C.-H. Jun, H. Lee, J.-B. Hong, *J. Org. Chem.* **1997**, *62*, 1200 – 1201; e) C.-H. Jun, D.-Y. Lee, H. Lee, J.-B. Hong, *Angew. Chem.* **2000**, *112*, 3214 – 3216; *Angew. Chem. Int. Ed.* **2000**, *39*, 3070 – 3072; f) C.-H. Jun, J.-W. Chung, D.-Y. Lee, A. Loupy, S. Chatti, *Tetrahedron Lett.* **2001**, *42*, 4803 – 4805; g) M. C. Willis, S. Sapmaz, *Chem. Commun.* **2001**, 2558 – 2559; h) M. Tanaka, M. Imai, Y. Yamamoto, K. Tanaka, M. Shimowatari, S. Nagumo, N. Kawahara, H. Suemune, *Org. Lett.* **2003**, *5*, 1365 – 1367; i) M. Imai, M. Tanaka, K. Tanaka, Y. Yamamoto, N. Imai-Ogata, M. Shimowatari, S. Nagumo, N. Kawahara, H. Suemune, *J. Org. Chem.* **2004**, *69*, 1144 – 1150; j) M. C. Willis, S. J. McNally, P. J. Beswick, *Angew. Chem.* **2004**, *116*, 344 – 347; *Angew. Chem. Int. Ed.* **2004**, *43*, 340 – 343; k) K. Tanaka, M. Tanaka, H. Suemune, *Tetrahedron Lett.* **2005**, *46*, 6053; l) M. C. Willis, H. E. Randell-Sly, R. L. Woodward, G. S. Currie, *Org. Lett.* **2005**, *7*, 2249 – 2251.

[6] Intermolecular ruthenium-catalyzed hydroacylation has been described, but generally requires exceptionally high reaction temperatures and provides mixtures of linear and branched coupling products: a) P. Isnard, B. Denise, R. P. A. Sneeden, J. M. Cognion, P. Durual, *J. Organomet. Chem.* **1982**, *240*, 285 – 288; b) P. Isnard, B. Denise, R. P. A. Sneeden, J. M. Cognion, P. Durual, *J. Organomet. Chem.* **1983**, *256*, 135 – 139; c) T. Kondo, Y. Tsuji, Y. Watanabe, *Tetrahedron Lett.* **1987**, *28*, 6229 – 6230; d) T. Kondo, M. Akazome, Y. Tsuji, Y. Watanabe, *J. Org. Chem.* **1990**, *55*, 1286 – 1291; e) T. Kondo, N. Hiraishi, Y. Morisaki, K. Wada, Y. Watanabe, T.-A. Mitsudo, *Organometallics* **1998**, *17*, 2131.

[7] Intermolecular cobalt-catalyzed hydroacylation has been described, but is restricted to the use of vinyl silanes as coupling partners: a) C. P. Lenges, M. Brookhart, *J. Am. Chem. Soc.* **1997**, *119*, 3165 – 3166; b) C. P. Lenges, P. S. White, M. Brookhart, *J. Am. Chem. Soc.* **1998**, *120*, 6965 – 6979.

[8] An advantageous effect of triphenylarsine (Ph_3As) has been noted in Stille coupling reactions: a) V. Farina, B. Krishnan, *J. Am. Chem. Soc.* **1991**, *113*, 9585 – 9895; b) V. Farina, *Pure Appl. Chem.* **1996**, *68*, 73 – 78.

[9] For rhodium-catalyzed decarbonylation of aldehydes, see: a) J. M. O'Conner, J. Ma, *J. Org. Chem.* **1992**, *57*, 5075 – 5077; b) C. M. Beck, S. E. Rathmill, Y. J. Park, J. Chen, R. H. Crabtree, *Organometallics* **1999**, *18*, 5311 – 5317.

[10] For catalytic reductive cyclization of olefinic carbonyl compounds, see a) N. M. Kablaoui, S. L. Buchwald, *J. Am. Chem. Soc.* **1995**, *117*, 6785 – 6786; b) W. E. Crowe, M. J. Rachita, *J. Am. Chem. Soc.* **1995**, *117*, 6787 – 6788; c) N. M. Kablaoui, S. L. Buchwald, *J. Am. Chem. Soc.* **1996**, *118*, 3182 – 3191.

[11] a) J. Schwartz, J. B. Cannon, *J. Am. Chem. Soc.* **1974**, *96*, 4721 – 4723; b) Y. Obora, Y. Tsuji, T. Kawamura, *J. Am. Chem. Soc.* **1993**, *115*, 10414 – 10415.

[12] X. Cui, K. Burgess, *Chem. Rev.* **2005**, *105*, 3272 – 3296, and references therein.

[13] Under the optimum conditions described in Table 1, 4-phenyl-1-butene couples to benzoic acid in 34% yield with a 1:2.5 ratio of the branched to linear regioisomers, respectively, and acetic anhydride couples to styrene in 27% yield with a 9:1 ratio of branched to linear regioisomers, respectively.

[14] J. A. Miller, J. A. Nelson, *Organometallics* **1991**, *10*, 2958 – 2961, and references therein.

 © 2006 Wiley-VCH Verlag GmbH & Co. KGaA, Weinheim

Molecular Switches

DOI: 10.1002/anie.200600925

Electrical Conformational Bistability of Dimesogen Molecules with a Molecular Chord Structure**

Yan-Lian Yang, Qi-Lin Chan, Xiao-Jing Ma, Ke Deng, Yong-Tao Shen, Xi-Zeng Feng, and Chen Wang**

The design of molecular structures that can respond effectively to external conditions such as an electric field is a topic of continued interest. Electrically induced conformational changes at the single-molecule level were demonstrated by Qiu et al.[1] They observed reversible transitions between the planar and nonplanar conformational states of the porphyrin macrocycle as a result of structural flexibility. It has also been reported that controlled conformational changes can be achieved in the case of self-assembled monolayers (SAMs) with low-density functional groups.[2] Yet, it has been challenging to obtain conformational switching in densely packed SAMs by using an electric field because of strong intermolecular interactions. Herein, we demonstrate that conformational changes induced by an electric field can be achieved in densely packed SAMs consisting of dimesogen molecules with a soft linker unit, which gives rise to new alternatives in designing field-responsive molecular interfaces.

The category of dimesogen molecules contains molecular structures with two mesogenic units connected by a linker unit.[3] A number of studies have revealed that the rigidity of the linker unit could significantly affect the properties of symmetric cholesteric liquid crystals (ChLCs). As an example, dicholesteryl esters containing a diacetylene unit as a rigid linker in the flexible chain showed slower crystallization and formed a cholesteric solid by cooling from the cholesteric temperature to 0 °C.[4] These studies suggested that the rigidity of the linker and the intermolecular interactions are very important for the thermal and optical properties of dimesogen ChLCs, which are widely applied in molecular photonics or information technology, such as e-paper, commercial billboards, and power-saving liquid crystal displays.[3,5,6]

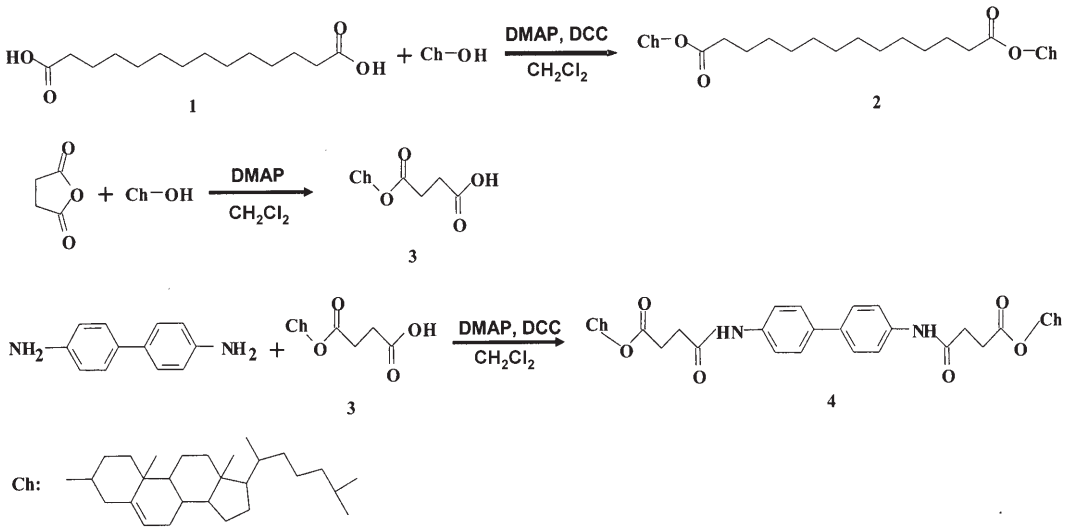

Scheme 1. Synthesis of cholesteryl esters Ch-14 (**2**) and CBC (**4**). DMAP = 4-dimethylaminopyridine, DCC = dicyclohexylcarbodiimide.

The submolecular resolution capability of scanning tunneling microscopy (STM) makes it possible to investigate the molecular arrangements in the self-assembled structures. Furthermore, the capability of STM measurement at different bias polarities allows in situ investigation of the electric field effects on the molecular assemblies. In this work, we designed and synthesized two kinds of low-molecular-weight compounds of cholesterol mesogens to explore the effects of the rigidity of the linker unit on the response to an electric field by using STM. As illustrated in Scheme 1, dicholesteryl tetradecanedioate (Ch-14, **2**; the linking unit is referred to as C_{14}) and 4,4′-([1,1′-biphenyl]-4,4′-diyldiimido)dibutanoic acid, bis(4-oxo-dicholesteryl ester) (CBC, **4**) were both synthesized

[*] Dr. Y. L. Yang, X. J. Ma, Dr. K. Deng, Prof. Dr. C. Wang
National Center for Nanoscience and Technology
Beijing 100080 (P.R. China)
Fax: (+86) 10-6256-2871
E-mail: wangch@nanoctr.cn
Q. L. Chan, Y. T. Shen, Prof. Dr. X. Z. Feng
College of Life Science
Nankai University
Tianjin 300071 (P.R. China)
Fax: (+86) 10-2350-7022
E-mail: xzfeng@nankai.edu.cn

[**] This work was supported by the National Natural Science Foundation of China (grant nos. 20473097, 90403140, 90406019, and 90406024) and the Tianjin Science Technology Research Funds of China (no. TJ043801111). Y.L.Y. acknowledges support from the State Key Laboratories of Transducer Technology.

Supporting information for this article is available on the WWW under http://www.angewandte.org or from the author.

 © 2006 Wiley-VCH Verlag GmbH & Co. KGaA, Weinheim

through condensation reactions using DCC as the condensation reagent (see Supporting Information for detailed characterizations of the two compounds). The Ch-14 molecules contain two cholesterol mesogens linked by a flexible alkyl chain. The other specimen of CBC contains two mesogens connected by a rigid linker, biphenylene.

The molecular assembly structures of Ch-14 and CBC were studied by STM. Stripe-patterned images with a head-to-head configuration were observed for both types of molecules with slightly different assembly arrangements. More interestingly, when the bias polarity was switched during imaging, drastic changes in the molecular image were observed for Ch-14, while no discernible changes could be observed for CBC molecules. This phenomenon illustrates the impact of linker rigidity on the field-dependent conformational change of dimesogen ChLCs.

The dependence on bias polarity of the STM imaging of a Ch-14 monolayer physisorbed on a highly oriented pyrolytic graphite (HOPG) surface is illustrated in Figure 1. Distinctively different stripe-patterned images can be observed for Ch-14 assemblies under negative and positive bias conditions (Figure 1a and c). The two-row brighter bands composed of Ch groups with alternately brighter and slightly dimmer structures are ascribed to the stereoscopic structure of the five- and six-membered rings in the Ch groups, and the darker bands in the image correspond to the flexible alkane chains linking the two cholesteric moieties. The medium-contrast image in the middle of the bright bands corresponds to the aligned isohexyl groups at both ends of the Ch-14 molecules. The proposed packing model for Ch-14 assembly indicates apparent dimer structures.

As a result of the stereoscopic structure of the Ch groups, these groups and the alkyl chains cannot be clearly resolved simultaneously in the same STM image because of their different height positions. By reducing the bias to a lower value, the orientation of the alkyl chain can be identified with a loss of Ch resolution (Figure 1b). The Ch-14 molecules are adsorbed with their alkyl chains oriented at a $(30 \pm 1)°$ angle to the axis of the bright band. The distances between the neighboring alkane chains (1.1 nm) are restricted by the width of the head groups. Note that the van der Waals interaction between the alkane chains in such an arrangement should be much weaker than that for the close-packed chains in assemblies of alkanes or alkane derivatives ((4.28 ± 0.02) Å for alkanes and (4.56 ± 0.05) Å for alkanols[7]). Therefore, the driving interactions for the assembly are considered to originate from the interaction between the cholesteric head groups. A schematic model of two Ch-14 molecules superimposed on the image of Figure 1b shows that the tilt angle of the two adjacent mesogen groups to the alkane chain is different, which would result in an asymmetric conformation with one Ch group higher than another, as demonstrated by the alternating contrast of Ch groups in Figure 1a.

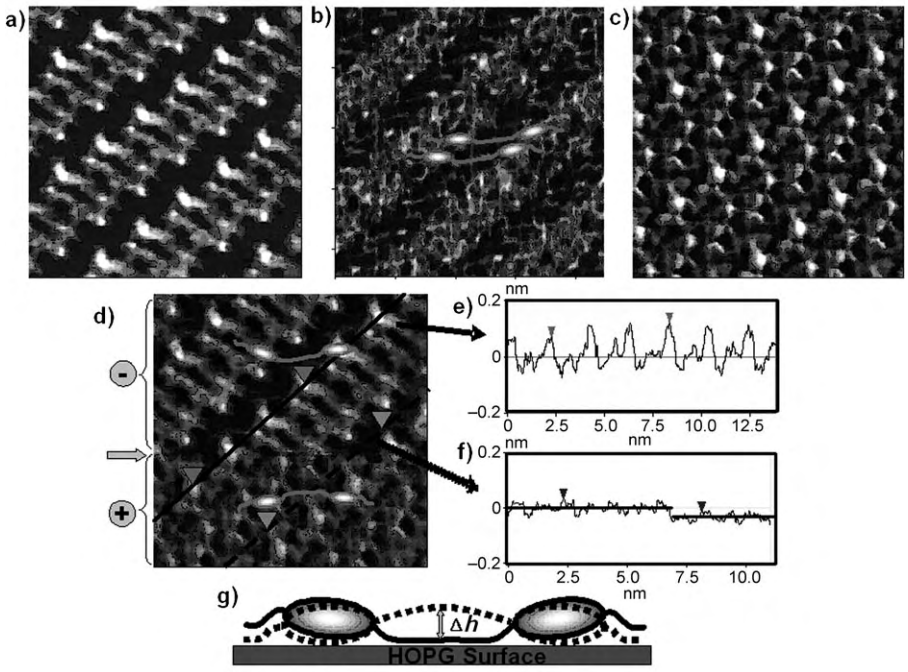

Figure 1. a) HR STM image of a SAM of Ch-14 molecules at negative bias (imaging conditions: 250 pA and −891 mV). b) The alkyl chain is resolved at low bias voltage (imaging conditions: 270 pA and −589 mV). A schematic model of two Ch-14 molecules is superimposed on the image. c) HR STM image of a SAM of Ch-14 molecules at positive bias (imaging conditions: 232 pA and 891 mV). d) HR STM image of Ch-14 molecular assembly structure at alternate bias polarities. The line where the bias change took place is marked by a gray arrow. For each section, the tunneling conditions are $|V_{bias}| = 890$ mV, $I_{set\ point} = 232$ pA; the choice of bias polarity is indicated by − or +. The image sizes for (a)–(d) are 11.2×11.2 nm^2. e, f) Cross-sectional profiles corresponding to the white solid line and the white dashed line in (d), respectively. The marked lines in (f) represent sections corresponding to positive (left) and negative (right) bias regions. g) Proposed model for the conformation change of the molecular chord. The solid line represents the side-view molecular structure at negative bias, and the dashed line represents the molecular structure at positive polarity. The height difference of alkane chains in the two conformations is shown as Δh.

When a positive sample bias was applied, the apparent contrast distribution of the stripe structure was transformed as indicated in the high-resolution (HR) STM image of the Ch-14 assembly (Figure 1c). This reversible image change is clearly shown in Figure 1d, in which the bias polarity was opposite for the upper (negative bias) and lower (positive bias) regions. The switching of bias voltage during scans generated only negligible disturbance to the STM image, mostly identified as a barely noticeable jump of scan line in the original STM image that can assist with the recognition of the position of bias switching. The difference between the two opposite bias voltages is about or less than 2 V, which is below the typical value of voltage pulses that can generate appreciable damage to the graphite surface,[8] and the feedback is kept active during such switching. Such instant contrast variation of Ch-14 that is changed by reversing the electric field direction can also be seen in the accompanying cross-sectional profiles in Figure 1e and f, which correspond to the white solid and dashed lines in Figure 1d, respectively. The

 © 2006 Wiley-VCH Verlag GmbH & Co. KGaA, Weinheim

measured height of the alkane chains at negative bias is (0.05 ± 0.02) nm lower than that at the positive bias, while the measured height of the head groups at negative bias is nearly identical to that at the positive bias. Such bias-polarity-dependent contrast variation associated with alkane linking units in Ch-14 was reproducible in repeated experiments under different imaging conditions (see Supporting Information), and has never been reported for simple alkanes and alkane derivatives.

The same bias-dependent conformational changes can be observed at different imaging conditions, with higher contrast at positive bias and lower contrast at negative bias for alkane linking chains (see Supporting Information). The consistency in the contrast variation of the linking units is supportive of the results presented in Figure 1. Note that systematic variations can be identified in association with the cholesteric groups, as revealed by the sectional profiles at different tunneling conditions (see Figure 1e and the Supporting Information). Therefore, the contrast variations from the localized swaying of the mesogen parts schematically illustrated in Figure 1g could be considered insignificant. In addition, variations of mesogen parts among independent images could be attributed to different image conditions and different STM tips.

In the case of alkane derivatives, the vertical contrast in the STM image of the methylene regions is dominated by the hydrogen atom positions predicted by perturbation theory and extended Hückel calculations, and is therefore dominated by topography effects and does not have any discernible dependence on the magnitude and polarity of the bias voltage.[9–11] The variation in vertical contrast of the functional groups of various alkane derivatives relative to the methylene units was affected by both topographic and electronic factors, with ionization potential (IP) accounting for the observed contrast. A lower IP leads to higher contrast in the STM images. This correlation could originate from the contribution of the HOMO to the tunneling current in STM. A lower IP corresponds to closer energy levels between the HOMO and the Fermi level of the tip, and more diffuse molecular orbital structures. Both effects are beneficial to the enhancement of the coupling between the adsorbate and the tip.

It has been concluded that no dependence on bias polarity can be observed for either methylene units or terminal functional groups.[9–11] These studies are complementary to our observations, which show little observable dependence on bias polarity of the mesogen unit in both specimens examined, while the contrast variation is solely associated with the methylene portion. It is therefore reasonable to conclude that the contrast of the mesogen unit does not contribute to the observed contrast reversal of the methylene units.

A control STM experiment was conducted with alkanes and Ch-14 molecules in the same image (see Supporting Information). An apparent contrast variation for the C_{14} linking chains in Ch-14 molecules can be observed, while no observable contrast changes can be found for the alkane molecules. Therefore, the observed contrast variation of alkane linking units at alternate bias polarities can only be attributed to the positional variation, rather than the electronic structures of the HOMO and LUMO of the alkanes.

According to the above results and analysis, it is plausible to attribute the image contrast variations to the field-dependent bistable conformational change of the dimesogen ChLCs with flexible chains. The proposed conformational change induced by an electric field is illustrated in Figure 1g with a side view of the molecular structure. The long connecting lines stand for the C_{14} flexible linking chains and the spindle-shaped structures for the stereoscopic structure of Ch groups. The short tails attached to the spindles represent the isohexyl tails on the Ch groups. This scheme is a simplified description that ignores the asymmetric conformation observed in STM images.

It has been reported that large dipole moments exist in cholesteric molecules.[4] We calculated the charge populations of the Ch-14 molecules (see Supporting Information) and found that the linker alkane chains are almost neutrally charged, while the dipole moments are mainly contributed by the mesogen part (the dipole moment vectors of the mesogen part are presented in the Supporting Information). It is clear that the dominant dipole moment vector is along the y and z axes, that is, approximately perpendicular to the direction of the linking unit. As demonstrated in Figure 1g, when a negative bias is applied the alkyl chains tend to position themselves close to the graphite surface (illustrated as a solid-line structure). When the bias polarity was abruptly switched to positive, the dipoles of the Ch head group tend to rotate accordingly, which results in upward swinging of the flexible linking chains (illustrated as a dashed-line structure). The height difference of the alkane chains (Δh) is determined from the measured cross-sectional profile. The value of Δh measured from different images is (0.05 ± 0.02) nm (see Figure 1d and the Supporting Information). This molecular chord structure of the Ch-14 molecule can be switched between two bistable states using an electric field.

In a parallel study, large-scale assembly structures of CBC molecules containing a rigid linker unit can be observed on a HOPG surface. The assembly structure of CBC is also in the form of a stripe pattern, with bright bands composed of stereoscopic cholesteric moieties and relatively low-contrast bands corresponding to the rigid linking chains of biphenylene groups (Figure 2a). The contrast of the biphenyl groups is reduced in comparison with that of the Ch groups because of their lower topographical position. Identical structures and contrast of the CBC monolayer can be observed independent of bias polarities and bias values (Figure 2b), which is indicated in the sectional profiles in Figure 2c and d. No clear alternative arrangement of Ch groups was observed because of the flat conformation of biphenylene groups parallel to the HOPG surface. Different images for CBC assemblies at different locations using different tips were obtained for verification (see Supporting Information).

According to the packing model of CBC illustrated in Figure 2e, the isohexyl groups are aligned nearly perpendicular to the molecular axis. The two isohexyl groups show higher contrast as brighter dots located at both sides of Ch head groups. This observation is illustrative of the appreciable effects of linker units on the details of the assembling characteristics as a result of varied intermolecular interactions.

 © 2006 Wiley-VCH Verlag GmbH & Co. KGaA, Weinheim

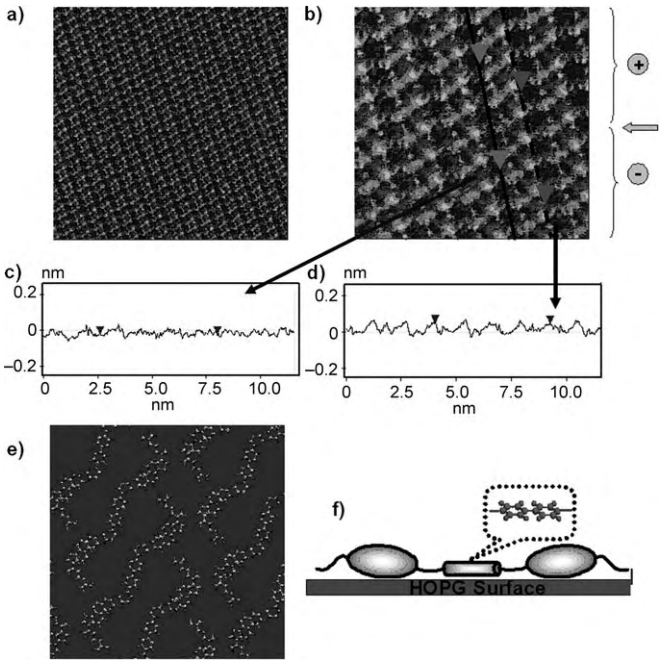

Figure 2. a) STM image (35.5×35.5 nm^2) of a CBC molecular assembly (imaging conditions: 300 pA and 700 mV). b) HR STM image (11.3×11.3 nm^2) of a CBC molecular assembly at both negative and positive bias polarities. The scan line where bias changes took place is marked by gray arrow. The tunneling conditions are 300 pA and 700 mV for the upper region and 300 pA and −950 mV for the lower region. The choice of bias polarity is indicated by − or +. c, d) Cross-sectional profiles corresponding to the white solid line and the white dashed line in (b), respectively. e) Proposed packing model of CBC molecules. f) Proposed side view of the molecular conformation of the CBC molecule. The rodlike feature in the middle represents the biphenylene group.

The proposed side view of the molecular conformation of the CBC molecule is shown in Figure 2 f. The spindle-shaped features and the short tails represent the Ch groups and the isohexyl tails, respectively. The rod in the middle represents the biphenylene group, which is illustrated as a flat configuration parallel to the graphite surface. As a result of the rigid biphenylene linker in CBC molecules, the electrically induced dipole rotation of the Ch groups is restricted with no observable conformational changes as shown for Ch-14 with flexible linking chains. Additionally, the π–π interaction between the graphite substrate and the biphenylene groups in CBC molecules may contribute partially to this restriction on conformational change.

In summary, two kinds of low-molecular-weight cholesterol dimesogens have been synthesized with a flexible alkyl chain (Ch-14) and a rigid biphenylene linker (CBC). The molecular assembly structures of Ch-14 and CBC were studied by STM. Conformational bistability was observed for Ch-14 molecules when the bias polarity was switched abruptly during imaging, while no discernible conformational changes were observed for the CBC molecules containing a rigid linking unit. This drastic difference in the conformational response of Ch-14 and CBC can be ascribed to the structural flexibility of Ch-14 with a flexible linker, while the response is restricted by the rigid biphenylene linker in CBC molecules. This in situ investigation of the field-dependent conformational bistability of ChLCs with a soft linker unit may lead to new design strategies for ChLC molecules, as well as functional molecular surfaces.

Experimental Section

Synthesis of Ch-14 (**2**): Ch-14 was synthesized by esterification of the commercially available tetradecanedioic acid (**1**) and cholesterol (Ch-OH) with DCC and 4-dimethylaminopyridine (DMAP) as described in the literature.[12,13] Ch-OH (15.47 g, 40 mmol), DCC (8.41 g, 40 mmol), and DMAP (0.49 g, 4 mmol) were dissolved in CH_2Cl_2 (70 mL), then **1** (5.16 g, 20 mmol) was added with stirring over 30 min. The mixture was stirred at room temperature for an additional 12 h. After removal of the precipitate by filtration, the solution was concentrated by rotary evaporation. The crude product was purified by column chromatography (silica gel) with hexane/ethyl acetate/acetic acid (10:1:1) as eluent to obtain pure Ch-14 as a white powder.

Synthesis of CBC (**4**): Ch-OH (3.867 g, 10 mmol), succinic anhydride (1.001 g, 10 mmol), and DMAP (0.122 g, 1 mmol) were dissolved in CH_2Cl_2 (100 mL), and the mixture was heated at reflux for 24 h. The solvent was removed by rotary evaporation, and the residual solid was recrystallized twice in glacial acetic acid to give cholesteryl hydrogen succinate (**3**) as a white powder. Compound **3** (0.973 g, 2 mmol), benzidine (0.184 g, 1 mmol), DMAP (0.0122 g, 0.1 mmol), and DCC (0.412 g, 2 mmol) were dissolved in CH_2Cl_2 (100 mL). The mixture was heated at reflux for 24 h and then cooled to room temperature. The solvent was removed by rotary evaporation, and the residual solid was washed three times with water. The crude product was further purified by column chromatography (silica gel) with CH_2Cl_2/petroleum ether (3:1) as eluent.

STM investigations: For preparation of the STM samples, the compounds were dissolved in toluene (HPLC grade) at a concentration of less than 1 mmol L^{-1}. The surface assembly of ChLC molecules was performed by depositing a droplet of the toluene solution directly onto a freshly cleaved graphite surface. The STM experiments were carried out with a Nanoscope IIIa system (Veeco Metrology Group, USA) at room temperature. Mechanically formed Pt/Ir (80:20) tips were used in the STM experiments. All images were recorded in the constant-current mode, and the specific tunneling conditions are given in the figure captions.

Computational details: Theoretical calculations were performed using density functional theory (DFT) provided by the DMol3 code.[14] The Perdew and Wang parameterization[15] of the local exchange-correlation energy was applied in the local spin density approximation (LSDA) to describe exchange and correlation. We expanded the all-electron spin-unrestricted Kohn–Sham wave functions in a local atomic orbital basis. In the double-numerical basis set, the valence s and p orbitals were represented by two basis functions each, and the d-type wave function on each atom was used to describe polarization. An angular momentum number one greater than the maximum angular momentum number in the atomic orbital basis was applied to specify the multipolar fitting that describes the analytical forms of the charge density and the Coulombic potential.[16] All calculations were all-electron and performed with the Extra-Fine mesh. The self-consistent field procedure was carried out with a convergence criterion of 10^{-5} a.u. on the energy and electron density.

Received: March 9, 2006
Revised: August 10, 2006
Published online: September 26, 2006

Keywords: dimesogens · liquid crystals · monolayers · scanning tunneling microscopy · single-molecule studies

 © 2006 Wiley-VCH Verlag GmbH & Co. KGaA, Weinheim

[1] X. H. Qiu, G. V. Nazin, W. Ho, *Phys. Rev. Lett.* **2004**, *93*, 196806.
[2] J. Lahann, S. Mitragotri, T.-N. Tran, H. Kaido, J. Sundaram, I. S. Choi, S. Hoffer, G. A. Somorjai, R. Langer, *Science* **2003**, *299*, 371.
[3] V. A. Mallia, N. Tamaoki, *Chem. Soc. Rev.* **2004**, *33*, 76.
[4] N. Tamaoki, G. Kruk, H. Matsuda, *J. Mater. Chem.* **1999**, *9*, 2381.
[5] T. Ikeda, *J. Mater. Chem.* **2003**, *13*, 2037.
[6] N. Tamaoki, *Adv. Mater.* **2001**, *13*, 1135.
[7] K. Morishige, Y. Takami, Y. Yokota, *Phys. Rev. B* **1993**, *48*, 8277.
[8] T. R. Albrecht, M. M. Dovek, M. D. Kirk, C. A. Lang, C. F. Quate, D. P. E. Smith, *Appl. Phys. Lett.* **1989**, *55*, 1727.
[9] C. L. Claypool, F. Faglioni, A. J. Matzger, W. A. Goddard III, N. S. Lewis, *J. Phys. Chem. B* **1999**, *103*, 9690.
[10] C. L. Claypool, F. Faglioni, W. A. Goddard III, H. B. Gray, N. S. Lewis, R. A. Marcus, *J. Phys. Chem. B* **1997**, *101*, 5978.
[11] L. Giancarlo, D. Cyr, K. Muyskens, G. W. Flynn, *Langmuir* **1998**, *14*, 1465.
[12] G. Höfle, W. Steglich, H. Vorbrüggen, *Angew. Chem.* **1978**, *90*, 602; *Angew. Chem. Int. Ed. Engl.* **1978**, *17*, 569.
[13] A. Theis, H. Ritter, *Macromolecules* **2003**, *36*, 7552.
[14] A. Becke, *J. Chem. Phys.* **1988**, *88*, 2547.
[15] J. P. Perdew, Y. Wang, *Phys. Rev. B* **1992**, *45*, 13244.
[16] E. J. Baerends, D. E. Ellis, P. Ros, *Chem. Phys.* **1973**, *2*, 41.

 © 2006 Wiley-VCH Verlag GmbH & Co. KGaA, Weinheim

Palladium Catalysis

DOI: 10.1002/anie.200601045

Developments in Pd Catalysis: Synthesis of 1*H*-1,2,3-Triazoles from Sodium Azide and Alkenyl Bromides**

José Barluenga, Carlos Valdés, Gustavo Beltrán, María Escribano, and Fernando Aznar*

1,2,3-Triazoles are an important class of heterocycles which display an ample spectrum of biological activities and are widely employed as pharmaceuticals and agrochemicals. Moreover, compounds containing 1,2,3-triazoles have found industrial applications as dyes, corrosion inhibitors, and photostabilizers.[1] The conventional route to triazoles is the Huisgen dipolar cycloaddition of alkynes with organic azides. The development of the copper(I)-catalyzed reaction between organic azides and terminal alkynes to give 1,4-disubstituted 1,2,3-triazoles[2] has represented a definitive advance in triazole chemistry, and has become a paradigm of a "click chemistry" reaction.[3] The reaction is effective in the preparation of a wide variety of triazole-containing molecules.[4] However, the reaction has a limitation in that inorganic azides are not good substrates. Consequently 1*H*-1,2,3-triazoles, which also have a wide range of uses,[5] cannot be prepared directly by using the click chemistry strategy, but instead require sequences involving deprotection steps and the employment of more elaborated azides.[6] Other routes to 1*H*-1,2,3-triazoles include dipolar cycloadditions between sodium azide and alkynes with an electron-withdrawing substituent,[7] the reaction of sodium azide with nitroalkenes,[8] and the rearrangement of propargyl azides.[9]

Over the last few years, we have been interested in Pd-catalyzed reactions between alkenyl halides and nitrogenated species for the formation of C–N bonds.[10] During our search for new coupling partners for such processes, we decided to explore the potential ability of the azide anion to participate in a Pd-catalyzed cross-coupling reaction.[11] We expected that the coupling of an azide with alkenyl halides would lead to vinyl azides. However, vinyl azides were never detected and instead 1*H*-1,2,3-triazoles were obtained under the standard reaction conditions. This unexpected result represents a novel method for the preparation of 1*H*-1,2,3-triazoles and a new

Table 1: Influence of the ligand in the reaction of β-bromostyrene with sodium azide.[a]

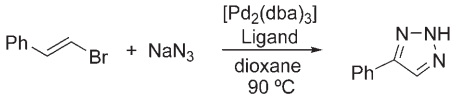

1a **2a**

Entry	Ligand	Pd [%]	Conv. [%]
1	PPh_3	2	15
2	davephos	2	0
3	johnphos	2	0
4	xphos	2	0
5	binap	2	0
6	dpephos	2	100
7	xantphos	2	100
8	no ligand	2	0
9	no ligand	0	0

[a] Reaction conditions: Alkenyl bromide **1** (1 mmol), sodium azide (3 mmol), 2:1 ligand/Pd, solvent (3 mL), 90 °C, 12 h. dba = *trans*,*trans*-dibenzylideneacetone, Cy = cyclohexyl.

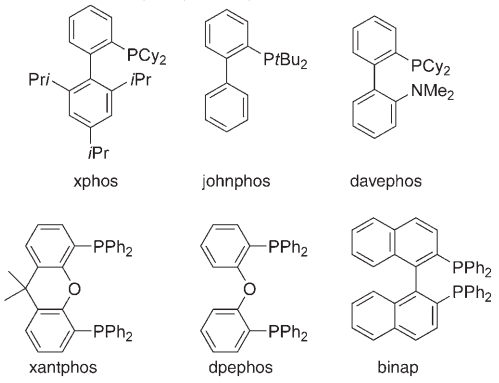

[*] Prof. J. Barluenga, Dr. C. Valdés, G. Beltrán, M. Escribano, Prof. F. Aznar
Instituto Universitario de Química Organometálica "Enrique Moles"
Unidad Asociada al CSIC
Universidad de Oviedo
Julián Clavería 8, 33006 Oviedo (Spain)
Fax: (+34) 98-510-3450
E-mail: barluenga@uniovi.es

[**] We acknowledge financial support from the Fundación Ramón Areces and the DGICYT.

Supporting information for this article is available on the WWW under http://www.angewandte.org or from the author.

 © 2006 Wiley-VCH Verlag GmbH & Co. KGaA, Weinheim

reactivity for Pd^0 catalysts. Herein, we report our findings regarding this new and intriguing reaction.

In a preliminary set of experiments we studied the reaction of β-bromostyrene (**1a**) with sodium azide in dioxane in the presence of $[Pd_2(dba)_3]$ and a range of supporting ligands. In most cases, **1a** was recovered with no trace of any reaction product (Table 1). However, when the bidentate ligand xantphos was employed, no **1a** was recovered and instead the 1*H*-1,2,3-triazole **2a** was obtained in near quantitative yield.

The ligand specificity of the reaction is remarkable indeed. Only the chelating diphosphines xantphos and dpephos, in which the bite angle is large, promoted the reaction to a considerable extent.[12] Very low conversion was achieved with triphenylphosphine and no conversion at all was observed for binap, a bidentate phosphine with a smaller bite angle, nor for the bulky electron-rich monophosphines, johnphos, davephos, and xphos, which are usually very active. Moreover, no conversion at all was observed for control experiments in the absence of ligand (Table 1, entry 8) and in the absence of metal and ligand (Table 1, entry 9), thereby indicating the important role of the catalytic system.

The scope of the reaction was examined using the optimized experimental conditions (Table 2). The formation of triazoles **2** occurred in very high yields for substituted β-bromostyrenes. The substitution on the aromatic ring had no influence on the outcome of the reaction, as systems substituted with neutral (Table 2, entry 1), electron-withdrawing (entries 3 and 4), or electron-releasing groups (entries 2 and 9) provided similar results. The reaction tolerates sensitive functional groups such as methyl esters or nitriles, *ortho* substitution in the aromatic ring (Table 2, entries 5–7), and heteroaromatic rings such as the 2-furan group (entry 8). The chemoselectivity of the reaction is noteworthy, as the presence of a halide (bromide or chloride) on the aromatic ring furnishes the triazole **2** as the sole reaction product.

Formation of the triazoles derived from alkyl-substituted bromoethylenes required a different set of reaction conditions. Thus, when the reaction of 1-bromodecene was carried out under the same conditions as previously used, we observed no conversion. By changing the solvent to DMSO, which enhances the solubility of the inorganic azide, we observed formation of the triazole with 55% conversion after 24 h. After some experimentation, we determined that the optimal conditions for this transformation required an increase in the catalyst loading and reaction temperature (to 110°C) (Table 2, entries 10 and 11). Finally, reaction of 1-bromo-4-phenyl-1,3-butadiene, as a representative bromodiene, proceeded in a very short time under the standard reaction conditions (dioxane, 90°C). However, the alkenyl-substituted triazole suffered partial dimerization,[13] which reduced the overall yield of the triazole (Table 2, entry 13). Nevertheless, when the reaction was conducted in DMSO, the dimerization was inhibited, and gave rise to the corresponding triazole as the sole reaction product (Table 2, entry 12).

This novel transformation represents an unprecedented Pd-catalyzed reaction, which adds to the already enormous repertoire of processes promoted by this transition metal.[14] It is also worth noting the differential behavior of Pd and Cu catalysts in their reactions with sodium azide and alkenyl halides. While the Cu-catalyzed reaction furnishes alkenyl azides,[11] these compounds are not even detected in the reaction with Pd, which provides only 1*H*-1,2,3-triazoles.

A tentative reaction pathway (Scheme 1) might involve oxidative addition of the bromoalkene to the Pd^0 complex **I** to form alkenylpalladium complex **II**, followed by substitution of the bromine by the azide to provide complex **III**. Reductive elimination would furnish the alkenyl azide **IV** and release the Pd^0 catalyst.[15] Finally, a Pd-promoted 1,5-electrocyclization followed by tautomerization would furnish the 1*H*-1,2,3-triazole **V**.

Table 2: Triazoles prepared by the Pd-catalyzed reaction of alkenyl bromides and sodium azide.[a]

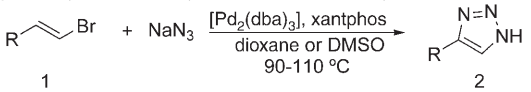

1 2

Entry	Triazole		Pd [%]	Method[b]	t[c] [h]	Yield[d] [%]
1	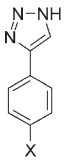	X = H **2a**	2	A	14	93
2		X = OMe **2b**	2	A	14	92
3		X = CN **2c**	2	A	14	89
4		X = CO_2Me **2d**	2	A	14	74
5	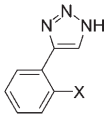	X = Cl **2e**	2	A	14	72
6		X = Br **2f**	2	A	14	70
7		X = Me **2g**	2	A	14	73
8	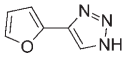	**2h**	2	A	14	94
9	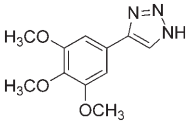	**2i**	2	A	14	76
10		R = n-C_8H_{17} **2j**	8	B	24	62
11		R = CH_2OBn **2k**	10	B	20	80
12	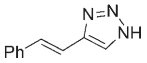		4	B	20	84
13		**2l**	2	A	10	45[e]

[a] Reaction conditions: Alkenyl bromide 1 (1 mmol), sodium azide (3 mmol), $[Pd_2(dba)_3]$ (see Table), xantphos (2:1, xantphos/Pd), solvent (3 mL). [b] Method A: Dioxane, 90°C; Method B: DMSO, 110°C. [c] Reaction times are not optimized. [d] Yields after column chromatography. [e] Complete conversion of the starting material.

© 2006 Wiley-VCH Verlag GmbH & Co. KGaA, Weinheim

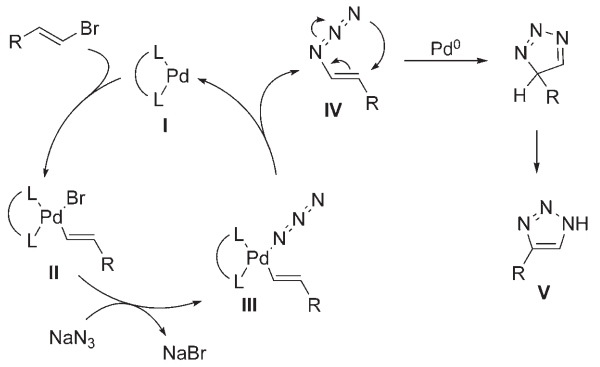

Scheme 1. Tentative mechanism for the Pd-catalyzed formation of triazoles from alkenyl bromides and sodium azide.

It must be noted that vinyl azides do not undergo cyclization to 1,2,3-triazoles upon heating; instead 2*H*-azirines and nitriles are formed with evolution of nitrogen.[16] For this reason, if this mechanistic manifold were operative, the Pd catalyst should play a role in promoting the electrocyclization of the intermediate vinyl azide. In an attempt to validate this mechanistic hypothesis we carried out several experimental and computational studies.

First of all, we have found evidence that the oxidative addition step is indeed occurring. The alkenylpalladium bromide complex **II** ligated with xantphos was generated following a procedure reported by Buchwald and co-workers for the analogous aryl bromides,[12d,e] in which a mixture of $[Pd_2(dba)_3]$, xantphos, and β-bromostyrene were stirred in benzene at room temperature for 22 h. Treatment of the resulting solid crude material with sodium azide in dioxane at 90 °C led to the formation of the triazole (Scheme 2). This observation clearly indicates that **II** is an intermediate in the catalytic process and therefore that the oxidative addition step takes place.

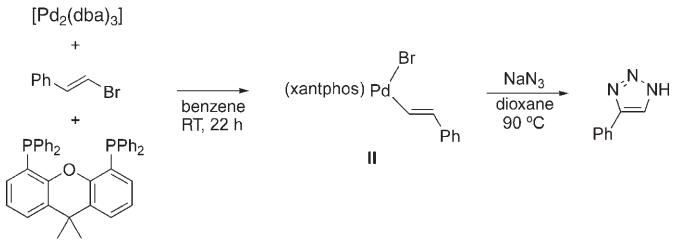

Scheme 2. Evidence for the oxidative addition step.

However, we have not found any experimental support for the reductive elimination/electrocyclization sequence (Scheme 3).[17] We attempted to transform the preformed styryl azide (**3**)[16a,b,18] into triazole **2a** by treatment with the Pd–xantphos catalytic system. Despite extensive experimentation involving different temperatures and reaction conditions, we never detected formation of the triazole, only decomposition of the vinyl azide.

On the other hand, when 3-bromoanisole (**4**), a typical aryl bromide, was subjected to the array of reaction conditions described during the optimization of the synthesis of

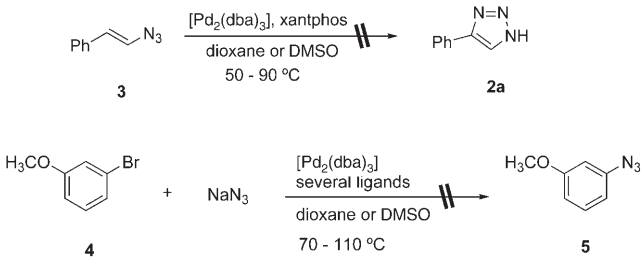

Scheme 3. Reactions that are not consistent with the mechanism depicted in Scheme 1.

the triazoles, no reaction ever occurred and the aryl bromide was always recovered unaltered. From these observations, we conclude that formation of the vinyl azide through a reductive elimination process might not be occurring and therefore discount the mechanism proposed in Scheme 1.

After excluding a reaction pathway involving a reductive elimination step and taking into account that the vinylpalladium complex **II** is in fact an intermediate of the reaction, the formation of the triazole can be only explained by a [3+2] cycloaddition (either concerted or stepwise) of the azide anion with a vinylpalladium complex (Scheme 4). The dihydrotriazolylpalladium complex **VI** would then undergo

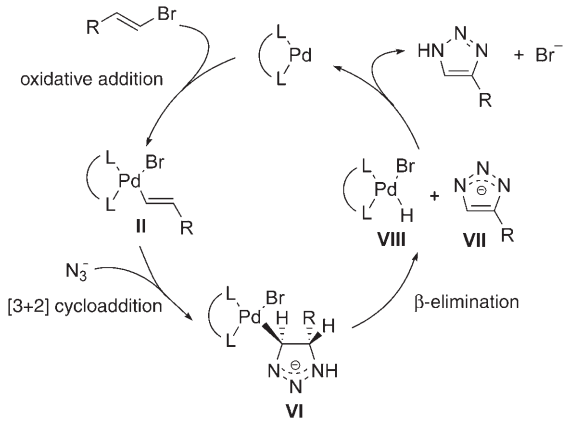

Scheme 4. Proposed mechanism for the Pd-catalyzed formation of triazoles from alkenyl bromides and sodium azide.

β elimination to release the triazolide **VII** and the hydridopalladium complex **VIII**. Finally, reductive elimination releases HBr which protonates the triazolyl anion and regenerates the Pd^0 complex.

In summary, we have reported a new methodology for the Pd-catalyzed synthesis of 1*H*-triazoles from alkenyl halides and sodium azide. Importantly, the process represents a completely new reactivity pattern in the context of Pd chemistry. Detailed investigations to clarify the mechanism of this intriguing reaction and further synthetic applications are underway.

Received: March 16, 2006
Revised: August 16, 2006
Published online: September 26, 2006

 © 2006 Wiley-VCH Verlag GmbH & Co. KGaA, Weinheim

Keywords: amination · azides · heterocycles · palladium catalysis · triazoles

[1] For general reviews on the chemistry and applications of 1,2,3-triazoles: W.-Q. Fan, A. R. Katritzky in *Comprehensive Heterocyclic Chemistry II*, *Vol. 4* (Eds.: A. R. Katritzky, C. W. Rees, E. F. V. Scriven), Elsevier Science, Oxford, **1996**, pp. 1–126.

[2] V. V. Rostovtsev, L. G. Green, V. V. Fokin, K. B. Sharpless, *Angew. Chem.* **2002**, *114*, 2708; *Angew. Chem. Int. Ed.* **2002**, *41*, 2596; .

[3] H. C. Kolb, M. G. Finn, K. B. Sharpless, *Angew. Chem.* **2001**, *113*, 2056; *Angew. Chem. Int. Ed.* **2001**, *40*, 2004.

[4] For a very recent review: V. D. Bock, H. Hiemstra, J. H. van Maarseveen, *Eur. J. Org. Chem.* **2006**, 51.

[5] a) L. S. Kallander, Q. Lu, W. Chen, T. Tomaszek, G. Yang, D. Tew, T. D. Meek, G. A. Hofmann, C. K. Schulz-Pritchard, W. W. Smith, C. C. Janson, M. D. Ryan, G.-F. Zhang, K. O. Johanson, R. B. Kirkpatrick, T. F. Ho, P. W. Fisher, M. R. Mattern, R. K. Johnson, M. J. Hansbury, J. D. Winkler, K. W. Ward, D. F. Veber, S. K. Thompson, *J. Med. Chem.* **2005**, *48*, 5644; b) D. Amantini, F. Fringuelli, O. Piermatti, F. Pizzo, E. Zunino, L. Vaccaro, *J. Org. Chem.* **2005**, *70*, 6526, and references therein.

[6] a) T. Jin, S. Kamijo, Y. Yamamoto, *Eur. J. Org. Chem.* **2004**, 3789; b) S. Kamijo, Z. Huo, T. Jin, C. Kanazawa, Y. Yamamoto, *J. Org. Chem.* **2005**, *70*, 6389; c) J. C. Loren, A. Krasiñski, V. V. Fokin, K. B. Sharpless, *Synlett* **2005**, 2847.

[7] a) M. Journet, D. Cai, J. J. Kowal, R. D. Larsen, *Tetrahedron Lett.* **2001**, *42*, 9117; b) A. R. Katritzky, Y. Zhang, S. Singh, *Heterocycles* **2003**, *60*, 1225.

[8] a) N. S. Zefirov, N. K. Chapovskaya, V. V. Kolesnikov, *J. Chem. Soc. D* **1971**, 1001; b) B. Quiclet-Sire, S. Z. Zard, *Synthesis* **2005**, 3319.

[9] a) K. Banert, *Chem. Ber.* **1989**, *122*, 911; b) K. Banert, *Chem. Ber.* **1989**, *122*, 1175; c) K. Banert, *Chem. Ber.* **1989**, *122*, 1963; d) K. Banert, M. Hagedorn, *Angew. Chem.* **1989**, *101*, 1710; *Angew. Chem. Int. Ed. Engl.* **1989**, *28*, 1675; e) J. C. Loren, K. B. Sharpless, *Synthesis* **2005**, 1514.

[10] a) J. Barluenga, M. A. Fernández, F. Aznar, C. Valdés, *Chem. Commun.* **2002**, 2362; b) J. Barluenga, M. A. Fernández, F. Aznar, C. Valdés, *Chem. Eur. J.* **2004**, *10*, 494; c) J. Barluenga, F. Aznar, C. Valdés, *Angew. Chem.* **2004**, *116*, 347; *Angew. Chem. Int. Ed.* **2004**, *43*, 343; ; d) J. Barluenga, C. Valdés, *Chem. Commun.* **2005**, 4891.

[11] Aryl and vinyl azides have been recently prepared by Cu^{I}-catalyzed cross-couplings of sodium azide with the corresponding iodides and bromides: a) W. Zhu, D. Ma, *Chem. Commun.* **2004**, 888; b) J. Andersen, U. Madsen, F. Björkling, X. Liang, *Synlett* **2005**, 2209.

[12] Xantphos and other biphosphine ligands with large bite angles have been reported to feature unique properties as ligands in several Pd-catalyzed processes which have been related to their ability to behave as *trans*-chelating ligands: a) Y. Guari, G. P. F. van Strijdonck, M. D. K. Boele, J. N. H. Reek, P. C. J. Kamer, P. W. N. M. van Leeuwen, *Chem. Eur. J.* **2001**, *7*, 475; b) P. C. J. Kamer, P. W. N. M. van Leeuwen, J. N. H. Reek, *Acc. Chem. Res.* **2001**, *34*, 895; c) J. Yin, S. L. Buchwald, *J. Am. Chem. Soc.* **2002**, *124*, 6043; d) L. M. Klingensmith, E. R. Strieter, T. E. Barder, S. L. Buchwald, *Organometallics*, **2006**, *25*, 82; e) K. Fujita, M. Yamashita, F. Puschmann, M. Martinez Alvarez-Falcon, C. D. Incarvito, J. F. Hartwig, *J. Am. Chem. Soc.* **2006**, *128*, 9044.

[13] The dimer derives from the addition of the N–H group of one triazole to the double bond of another alkenyl triazole molecule.

[14] For some general references on the application of Pd catalysts in organic synthesis: a) *Handbook of Organopalladium Chemistry for Organic Synthesis* (Ed.: E. Negishi), Wiley-Interscience, New York, **2002**; b) *Metal-Catalyzed Cross Coupling Reactions* (Eds.: A. de Meijere, F. Diederich) Wiley-VCH, Weinheim, **2004**.

[15] To the best of our knowledge, the participation of the azide anion in a Pd-catalyzed coupling might be an unprecedented reaction.

[16] a) G. Smolinsky, *J. Org. Chem.* **1962**, *27*, 3557; b) J. H. Boyer, W. E. Krueger, G. J. Mikol, *J. Am. Chem. Soc.* **1967**, *89*, 5504; c) G. L'abbe, G. Mathys, *J. Org. Chem.* **1974**, *39*, 1778; d) L. A. Burke, G. Leroy, M. T. Nguyen, M. Sana, *J. Am. Chem. Soc.* **1978**, *100*, 3668; e) R. Huisgen, *Angew. Chem.* **1980**, *92*, 979; *Angew. Chem. Int. Ed. Engl.* **1980**, *19*, 947; f) H. Bock, R. Dammel, S. Aygen, *J. Am. Chem. Soc.* **1983**, *105*, 7681; g) A. S. Timén, E. Risberg, P. Somfai, *Tetrahedron Lett.* **2003**, *44*, 5339, and references therein.

[17] DFT calculations (employing the B3LYP functional with the 6-31G* basis set for C, H, N, O, and P and the LANL2DZ pseudopotential for Pd) showed that complexation of $[PdL_2]$ with the terminal N=N bond of the vinyl azide breaks the linearity of the azide moiety and thus lowers the activation energy of the electrocyclization by nearly 7 kcal mol^{-1}. However, these theoretical results have found no experimental support (see text).

[18] V. Nair, T. G. George, *Tetrahedron Lett.* **2000**, *41*, 3199.

 © 2006 Wiley-VCH Verlag GmbH & Co. KGaA, Weinheim

Hybrid Composites

DOI: 10.1002/anie.200601676

Highly Reversible Lithium Storage in Spheroidal Carbon-Coated Silicon Nanocomposites as Anodes for Lithium-Ion Batteries**

*See-How Ng, Jiazhao Wang, David Wexler, Konstantin Konstantinov, Zai-Ping Guo, and Hua-Kun Liu**

Rechargeable lithium-ion batteries are key devices for today's information-based mobile society. One of the major challenges for designing electrode materials is to combine

[*] S.-H. Ng, Dr. J. Wang, Dr. K. Konstantinov, Dr. Z.-P. Guo, Prof. H.-K. Liu
Institute for Superconducting & Electronic Materials
and ARC Centre of Excellence for Electromaterials Science
University of Wollongong
Wollongong, NSW 2522 (Australia)
Fax: (+61) 2-4221-5731
E-mail: hua_liu@uow.edu.au
Homepage: http://www.uow.edu.au/eng/research/isem/staff/hkliu.html

Dr. D. Wexler
Faculty of Engineering
University of Wollongong
Wollongong, NSW 2522 (Australia)

[**] Financial support provided by the Australian Research Council (ARC) through the ARC Centre of Excellence funding (CE0561616) is gratefully acknowledged. Moreover, the authors are grateful to Sau-Yen Chew at the University of Wollongong for experimental assistance. Finally, we also thank Dr. Tania Silver at the University of Wollongong for critical reading of the manuscript.

Supporting information for this article is available on the WWW under http://www.angewandte.org or from the author.

WILEY InterScience DISCOVER SOMETHING GREAT
© 2006 Wiley-VCH Verlag GmbH & Co. KGaA, Weinheim

both high Li storage capacity and coulombic efficiency (that is, a high ratio of extractable Li to inserted Li).[1] Graphite and $LiCoO_2$, both commonly used in Li-ion batteries, have high coulombic efficiencies (> 95 %) but rather low capacities (372 and 145 $mA\,h\,g^{-1}$, respectively).[2,3] Many new materials, especially those that form alloys with lithium (for example, Sn, Sb, Si, and Ge),[4–7] have shown high capacity values, but generally suffer from low coulombic efficiencies (< 60 %) on the first few cycles. The low coulombic efficiencies can be attributed to a variety of shortcomings: for example, irreversible trapping of inserted Li ions by host materials, formation of the solid/electrolyte interface (SEI) layer, or the loss of electrical contact between the electrode material and the current collector. This low coulombic efficiency reduces the energy density of the Li-ion batteries significantly and poses a serious trade-off in battery technology.

Silicon-based negative electrodes for lithium-ion batteries have attracted great interest because of their high theoretical specific capacity of 4212 $mA\,h\,g^{-1}$.[6] Of particular note are studies on nanostructured Si-based anodes, where it has been shown that a nanoparticle-based system improves the cycle lifetime.[8–10] Although nanocrystalline Si shows a high capacity for the first charge (ca. 2000 $mA\,h\,g^{-1}$, depending on the compositions studied), it exhibits poor retention of capacity as a result of material degradation, which makes it unsuitable for practical commercial applications. This serious drawback, also known as the pulverization of silicon, is caused by the large change in volume during lithium-ion insertion/extraction. It is necessary to relieve such morphological changes to improve the cycling characteristics of this material. One possible solution to overcome this problem is by using composite materials, in which an electrochemically active phase is homogeneously dispersed within an electrochemically inactive matrix.[11,12] The inactive phase would accommodate the mechanical stresses/strains experienced by the active phase and maintain the structural integrity of the composite electrode during the alloying/de-alloying processes.

Recently, Holzapfel et al. obtained promising results for nanosized silicon/graphite composites prepared by a reductive decomposition of a silicon precursor. This composite shows a stable capacity of 1000 $mA\,h\,g^{-1}$, with a Si content of 20 wt %.[13] However, the specific capacity has been limited by the small amount of Si in the composite material. Herein we report on carbon-coated Si nanocomposites produced by a spray-pyrolysis technique, which can reversibly store lithium with both a high capacity of 1489 $mA\,h\,g^{-1}$ and a high coulombic efficiency above 99.5 %, even after 20 cycles. The spray-pyrolysis method used in this study is instantaneous, versatile, inexpensive, industrially oriented, and can be operated over a large temperature range (150–1400 °C).[14]

Thermogravimetric analysis (TGA) of the carbon-coated Si nanocomposites carried out in air showed that the carbon content was 56 wt %, with the remaining 44 wt % estimated to be silicon. The TGA curves also show that Si will only be oxidized rapidly in air above 500 °C. Therefore, any spray-pyrolysis process conducted in air under 500 °C will not give rise to the presence of impurities such as SiO_2. The X-ray-diffraction (XRD) pattern of the carbon-coated Si nanocomposites also shows only the Si peaks, thus confirming that there no bulk SiO_2 crystalline phase was formed during the spray-pyrolysis process at 400 °C in air. Moreover, no diffraction lines from crystalline carbon (graphite) were observed in the XRD pattern, thereby indicating the amorphous nature of the carbon in the nanocomposites.

Figure 1 shows TEM images of the carbon-coated Si nanocomposites. The size of the individual composite particles ranged from below 10 nm to approximately 100 nm

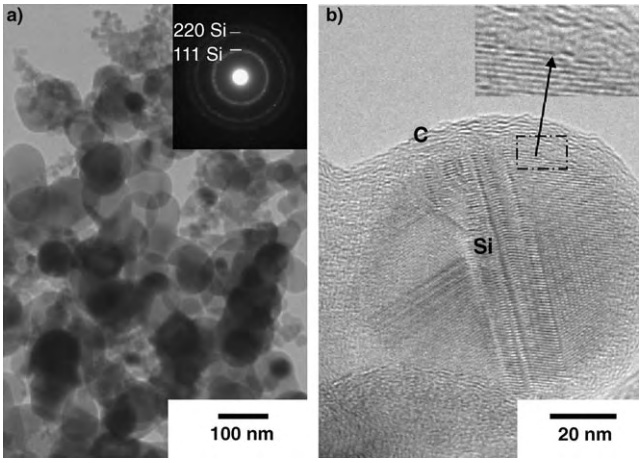

Figure 1. TEM images of spheroidal carbon-coated Si nanocomposites produced by spray pyrolysis in air: a) low-magnification image of a sample produced at 400 °C, with the indexed diffraction pattern (inset) confirming the presence of Si nanoparticles; b) high-resolution image showing the carbon-coated Si nanocomposite, with the inset showing the interface between a crystalline Si particle and the pyrolyzed carbon coating layer (ca. 10 nm thickness).

(Figure 1 a). The fine dotted rings of the associated selected-area electron-diffraction pattern (inset in Figure 1 a) correspond to nanocrystalline Si, although additional diffuse contrast within the diffraction rings may also indicate the presence of minor amounts of amorphous Si. Figure 1 b clearly demonstrates the coexistence of two phases. The nanocrystalline Si particles were generally spheroidal, although some of the larger ones were facetted. The spheroidal Si particle in Figure 1 b also contains microtwins and stacking faults. It is surrounded by an amorphous or semiamorphous carbon layer (C; ca. 10 nm in thickness). Contrast from carbon under high-magnification (see inset, Figure 1 b) also indicated that the pyrolyzed carbon was predominately amorphous carbon although further high-resolution imaging experiments are required to confirm that no graphitic carbon is also present.

The electrochemical performance of the nanocrystalline Si precursor powder and the carbon-coated Si nanocomposite electrodes was systematically investigated. Figure 2 summarizes the discharge (lithiation) and charge (delithiation) capacity data for nanocrystalline Si and carbon-coated Si nanocomposite electrodes. The calculated capacities were solely based on the active material, either Si or carbon-coated Si-composite particles in the electrode. Even though the first discharge and charge capacities of the Si electrode (Fig-

 © 2006 Wiley-VCH Verlag GmbH & Co. KGaA, Weinheim

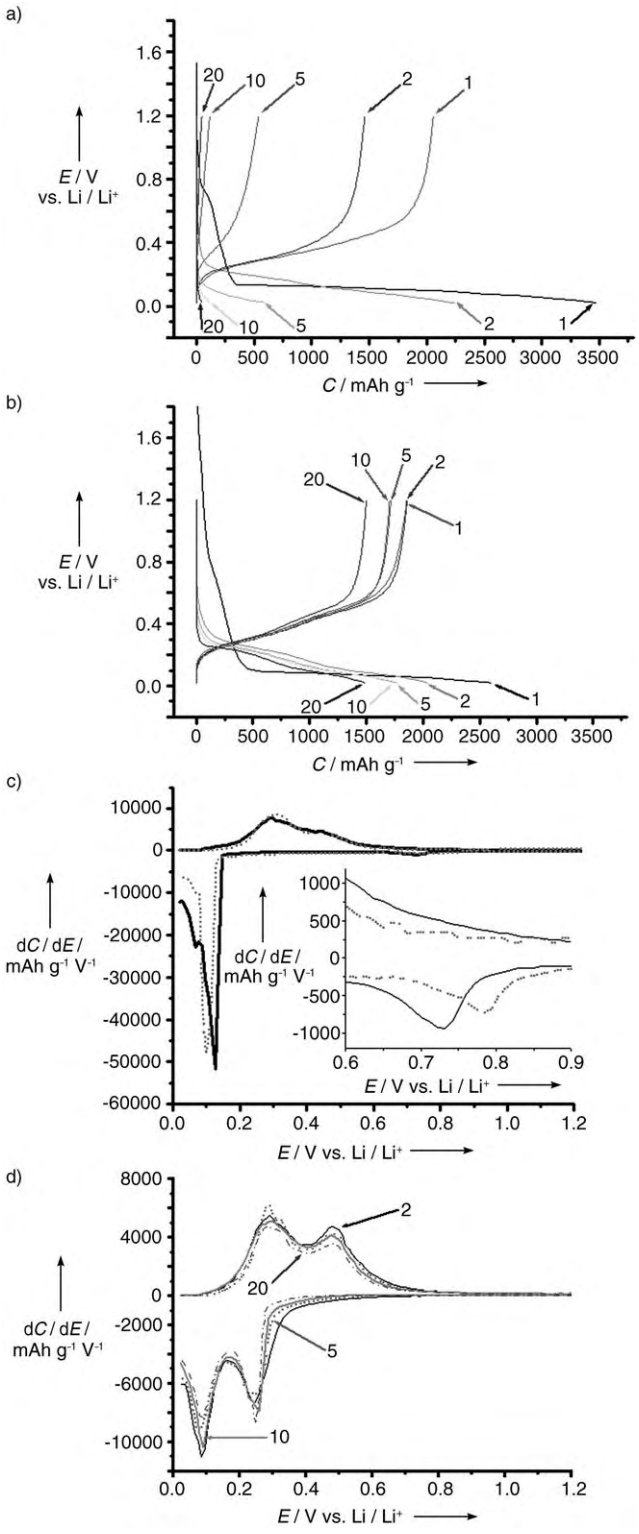

Figure 2. Charge–discharge plots of: a) a nanocrystalline Si electrode and b) a carbon-coated Si nanocomposite electrode with 44 wt% Si content (the numbers indicate the cycle number). c) First-cycle differential capacity plots of nanocrystalline Si (solid line) and carbon-coated Si nanocomposite (dotted line) electrodes (inset: enlarged plot of (c)). d) Differential capacity plots for the carbon-coated Si nanocomposite electrode (the numbers indicate the cycle number). Cycling took place between 0.02 V and 1.20 V versus Li/Li^+ at a cycling rate of 100 $mA\,g^{-1}$. C = capacity, E = cell potential, dC/dE = differential capacity.

ure 2a) were 3474 $mA\,h\,g^{-1}$ and 2058 $mA\,h\,g^{-1}$, respectively, further cycling led to a rapid decay of the capacity to 47 $mA\,h\,g^{-1}$ after 20 cycles. Note that the initial ratio of the irreversible capacity was 41%. This result is consistent with those reported by Yang et al. for a nanocrystalline Si (< 100 nm) electrode.[15] This result indicates that a reduction in the particle size cannot prevent aggregation of Si on the micrometer scale. In contrast, the first discharge and charge capacities of the amorphous carbon-coated Si nanocomposite electrode (Figure 2b) were 2600 $mA\,h\,g^{-1}$ and 1857 $mA\,h\,g^{-1}$, respectively. The initial ratio of the irreversible capacity was 29%, which is 12% lower than that of the Si particles only. In addition, the amorphous carbon-coated Si nanocomposite electrodes exhibited an excellent cycling properties, retaining a specific capacity of approximately 1489 $mA\,h\,g^{-1}$ after 20 cycles.

The differential capacity curves of the carbon-coated Si nanocomposite electrode exhibited essentially the same peak features as the Si electrode below 0.3 V (Figure 2c). However, the first cathodic peak was shifted from 0.12 V (Si) to 0.09 V (Si-C). This effect arises because the solid/electrolyte interface is different for both cases (namely, Si/electrolyte and carbon/electrolyte, respectively). Therefore, the surface kinetics will be different, thus resulting in the shifted peaks that are seen in the differential capacity curves.[16] Furthermore, a clear irreversible reaction corresponding to formation of the Si/electrolyte interface near 0.73 V was not found for the carbon-coated Si nanocomposite electrode, but instead formation of a carbon/electrolyte interface layer was observed near 0.78 V for the carbon-coated Si nanocomposite electrode. This phenomenon could be attributed to the masking effects from the spray-pyrolyzed carbon layer.[17] It was also clearly demonstrated (Figure 2d) that the carbon-coated Si nanocomposite electrode maintained high activity and reversibility, even after 20 cycles. The improved performance could be attributed to the amorphous carbon coating with high electronic conductivity, which not only buffered the large changes in the volume during the cycling process but also avoided possible agglomeration of the uniformly distributed silicon particles.[15–17]

Figure 3 shows the cycling behavior of the carbon-coated Si nanocomposite electrode. An initial lithiation capacity of

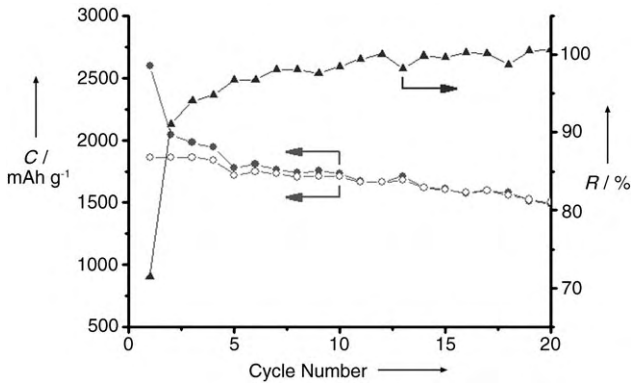

Figure 3. Cycling behavior of the carbon-coated Si nanocomposite electrode with 44 wt% Si content, cycled between 0.02 V and 1.20 V at a cycling rate of 100 $mA\,g^{-1}$. ● = Li^+ insertion, ○ = Li^+ extraction, ▲ = coulombic efficiency; C = capacity, R = coulombic efficiency.

 © 2006 Wiley-VCH Verlag GmbH & Co. KGaA, Weinheim

2600 mA h g^{-1} and a delithiation capacity of 1857 mA h g^{-1} for the active materials (44 % Si + 56 % C) was obtained by using a nonrestricted cycling procedure. This low initial coulombic efficiency (71.4 %) of the carbon-coated Si nanocomposites is mainly a consequence of the large insertion capacity (ca. 700 mA h g^{-1}) contributed by the amorphous carbon content. Subsequently, the carbon-coated Si nanocomposite electrode retained a specific capacity of about 1489 mA h g^{-1} after 20 cycles. By subtracting the capacity of the spray-pyrolyzed carbon from that of citric acid (ca. 100 mA h g^{-1} after 20 cycles), which was measured separately, the discharge capacity delivered by the Si component (44 wt %) was estimated to be approximately 1433 mA h. Therefore, the specific capacity of Si in the composite electrode was calculated to be 3257 mA h g^{-1}, which amounts to an impressive 77 % of the theoretical value (4212 mA h g^{-1}). This result shows the beneficial effect of the carbon coating on the enhanced dimensional stability of the Si particles during the Li alloying/de-alloying process, which makes possible further significant improvement to the electric conductivity of the composites.[15–17]

In conclusion, spheroidal carbon-coated Si nanocomposite, prepared by a spray-pyrolysis method in air, is a promising candidate for use as an anode material in lithium-ion batteries, as it has excellent retention of specific capacity, high coulombic efficiency, and low cost (because of the abundance of both Si and carbon sources).

Experimental Section

Citric acid ($C_6H_8O_7$, Sigma Aldrich) was dissolved in absolute ethanol (200 mL, 99.99 wt %, Merck) with continuous stirring. Nanocrystalline Si powder (< 100 nm, Nanostructured and Amorphous Materials Inc.,) was then mixed into the initial citric acid/ethanol solution (1:10 Si:citric acid w/w) by ultrasonication for 90 mins. The nanocomposite material was obtained in situ by spray-pyrolyzing the Si/citric acid/ethanol suspensions at 400 °C with a flow rate of 4 mL min^{-1} into a vertical-type spray-pyrolysis reactor. The spray-pyrolysis reaction of Si in citric acid/ethanol solution can be expressed as Equation (1).

$$Si + C_6H_8O_7/C_2H_6O \rightarrow Si/C + CO_2\uparrow + H_2O\uparrow + \text{energy}\uparrow \quad (1)$$

Accurate carbon contents in the spray-pyrolyzed composites were determined by TGA and differential thermal analyses on Setaram 92 equipment. The sprayed powders were characterized by XRD using a Philips PW1730 diffractometer with $Cu_{K\alpha}$ radiation and a graphite monochrometer. TEM investigations were performed using a JEOL 2011 200 KeV analytical electron microscope. TEM samples were prepared by deposition of ground particles onto lacey carbon support films.

The anode was prepared by mixing nanocrystalline Si, spray-pyrolyzed carbon-coated Si nanocomposites, or spray-pyrolyzed carbon from citric acid as active materials with 10 wt % carbon black (Super P, MMM, Belgium) and 10 wt % polyvinylidene fluoride binder in *N*-methyl-2-pyrrolidinone solvent to form a homogeneous slurry, which was then spread onto a copper foil. The coated electrodes (average thickness of ca. 50 μm) were dried in a vacuum oven at 110 °C for 24 h and then pressed. Electrochemical measurements were carried out using coin-type cells. CR 2032 coin-type cells were assembled in an argon-filled glove box (Mbraun, Unilab, Germany) by stacking a porous polypropylene separator containing liquid electrolyte between the composite electrodes and a lithium-foil counter electrode. The electrolyte used was 1 M $LiPF_6$ in a 50:50 (v/v) mixture of ethylene carbonate and dimethyl carbonate obtained from MERCK KgaA, Germany. The cells were galvanostatically charged and discharged in the range of 0.02–1.20 V at a constant current density of 100 mA g^{-1}.

Received: April 28, 2006
Revised: July 31, 2006
Published online: September 26, 2006

Keywords: batteries · carbon · electrochemistry · lithium · silicon

[1] J.-M. Tarascon, M. Armand, *Nature* **2001**, *414*, 359.
[2] J. R. Dahn, T. Zheng, Y. Liu, J. S. Xue, *Science* **1995**, *270*, 590.
[3] M. Winter, J. O. Besenhard, M. E. Spahr, P. Novak, *Adv. Mater.* **1998**, *10*, 725.
[4] Y. Idota, T. Kubota, A. Matsufuji, Y. Maekawa, T. Miyasaka, *Science* **1997**, *276*, 1395.
[5] H. Li, L. Shi, W. Lu, X. Huang, L. Chen, *J. Electrochem. Soc.* **2001**, *148*, A915.
[6] B. A. Boukamp, G. C. Lesh, R. A. Huggins, *J. Electrochem. Soc.* **1981**, *128*, 725.
[7] N. Pereira, M. Balasubramanian, L. Dupont, J. McBreen, L. C. Klein, G. G. Amatucci, *J. Electrochem. Soc.* **2003**, *150*, A1118.
[8] J. Yang, B. F. Wang, K. Wang, Y. Liu, J. Y. Xie, Z. S. Wen, *Electrochem. Solid-State Lett.* **2003**, *6*, A154.
[9] C. S. Wang, G. T. Wu, X. B. Zhang, Z. F. Qi, W. Z. Li, *J. Electrochem. Soc.* **1998**, *145*, 2751.
[10] A. M. Wilson, J. R. Dahn, *J. Electrochem. Soc.* **1995**, *142*, 326.
[11] O. Mao, R. L. Turner, I. A. Courtney, B. D. Fredericksen, M. I. Buckett, L. J. Krause, J. R. Dahn, *Electrochem. Solid-State Lett.* **1999**, *2*, 3.
[12] I. S. Kim, P. N. Kumta, G. E. Blomgren, *Electrochem. Solid-State Lett.* **2000**, *3*, 493.
[13] M. Holzapfel, H. Buqa, W. Scheifele, P. Novak, F.-M. Petrat, *Chem. Commun.* **2005**, *12*, 1566.
[14] S. H. Ng, J. Wang, K. Konstantinov, D. Wexler, J. Chen, H. K. Liu, *J. Electrochem. Soc.* **2006**, *153*, A787.
[15] X. Yang, Z. Wen, X. Zhu, S. Huang, *Electrochem. Solid-State Lett.* **2005**, *8*, A481.
[16] N. Dimov, S. Kugino, M. Yoshio, *Electrochim. Acta* **2003**, *48*, 1579.
[17] Y. Liu, T. Matsumura, N. Imanishi, A. Hirano, T. Ichikawa, Y. Takeda, *Electrochem. Solid-State Lett.* **2005**, *8*, A599.

 © 2006 Wiley-VCH Verlag GmbH & Co. KGaA, Weinheim

Nanotechnology

DOI: 10.1002/anie.200601104

Metallic Striped Nanowires as Multiplexed Immunoassay Platforms for Pathogen Detection**

Jeffrey B.-H. Tok, Frank Y. S. Chuang, Michael C. Kao, Klint A. Rose, Satinderpall S. Pannu, Michael Y. Sha, Gabriela Chakarova, Sharron G. Penn, and George M. Dougherty*

The rapid growth and development in biodetection technology has largely been driven by the emergence of new and deadly infectious diseases and the realization of biological warfare as new means of terrorism.[1,2] To address the need for portable, multiplex biodetection systems, we report here a novel biosensing platform using engineered nanowires as an alternative substrate for sandwich immunoassays (Figure 1 A). The nanowires are built through submicrometer layering of different metals by electrodeposition within a porous alumina template.[3,4] A variety of metals can be deposited: in this study, we employed stripes of gold, silver, and nickel. Owing to the permutations in which the metals can be deposited, a large number of unique yet easily identifiable encoded nanowires can be included in a multiplex array format.

Image processing of an optical reflectance image can enable the stripe pattern to be identified rapidly, while fluorescence images report information on the degree of binding between the antibody-conjugated nanowires and a fluorophore-tagged antigen target. Such nanowires have been utilized to efficiently detect and report both DNA hybridization and immunoassay processes.[5,6] Herein, we demonstrate the feasibility of using multistriped metallic nanowires (Figure 1 A) in a suspended format to enable rapid and sensitive single and multiplex immunoassays for biowarfare agent simulants.

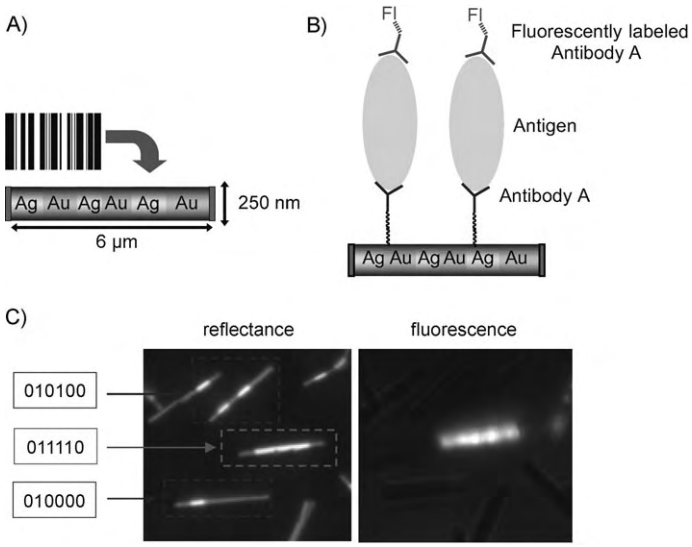

Figure 1. A) Analogy between a conventional barcode and a metallic stripe-encoded nanowire (diameter ≈ 250 nm; length ≈ 6 μm). Ni segments (50 nm) are deposited at both ends on the magnetic nanowire (not drawn to scale). B) Schematic of the sandwich immunoassay performed on a nanowire. C) Post-assay reflectance and fluorescence readout of the nanowires. The identity of the antigen present can be easily identified from the stripe pattern of the nanowires; for example, the fluorescently lit nanowire to which anti-Bg spore Ab was attached has a stripe pattern of 011110 (0 = Au, 1 = Ag). This indicates that Bg spores are present in the test sample mixture. Nanowires with the stripe patterns 010000 (functionalized with anti-Ova Ab) or 010100 (functionalized with BSA; negative control) are not fluorescently lit, thus indicating that the test sample does not contain Ova proteins.

Both the hybridization and kinetics of the capture of the target analyte in solution favor the nanowires over conventional fixed array-based formats. The incorporation of an appropriate ferromagnetic metallic component, for example, Ni, enables the nanoparticles to be manipulated by using magnetic fields.[7–10] To demonstrate the capability of directly detecting potential biological warfare agents in both clinical and environmental samples, a reagent set of three antigens generally accepted for use in simulating actual biothreat agents was chosen. The three nonpathogenic simulants include 1) *Bacillus globigii* (Bg) spores to simulate *Bacillus anthracis* and other bacterial species, 2) RNA MS2 bacteriophage to simulate *Variola* (virus for smallpox) and other pathogenic viruses, and 3) ovalbumin (Ova) protein to simulate protein toxins such as ricin or botulinum toxin. Besides the relative handling safety of these simulants, they were also chosen to reflect the variation in target sizes, ranging from large bacterial spores (≈ 2 μm) to small protein molecules (≈ 2 nm).

[*] Dr. J. B.-H. Tok, Dr. F. Y. S. Chuang, M. C. Kao, Dr. K. A. Rose, Dr. S. S. Pannu, Dr. G. M. Dougherty
Lawrence Livermore National Laboratory
Livermore, CA 94551 (USA)
Fax: (+1) 925-422-3570
E-mail: tok2@llnl.gov
Dr. K. A. Rose
Stanford University
Stanford, CA 94305 (USA)
Dr. M. Y. Sha, Dr. G. Chakarova, Dr. S. G. Penn
Nanoplex Technologies Inc.
Mountain View, CA 94043 (USA)
Dr. F. Y. S. Chuang
NSF Center for Biophotonics Science and Technology
University of California at Davis
Sacramento, CA 95817 (USA)

[**] This work was performed under the auspices of the US Department of Energy by the University of California, Lawrence Livermore National Laboratory, under contract no. W-7405-Eng-48. The authors thank Ian Walton and Scott Norton of Nanoplex Technologies for their assistance in imaging and analysis of the nanowires, and Frances Wong of Nanoplex Technologies for supplying the nanowires. J.B.T. acknowledges the partial support of NIH grant AI065359. Nanoplex Technologies Inc. acknowledges funding from the National Institute of Standards and Technology, Advanced Technology Program Grant (no. 70NANB1H3028).

Supporting information for this article is available on the WWW under http://www.angewandte.org or from the author.

WILEY InterScience DISCOVER SOMETHING GREAT
© 2006 Wiley-VCH Verlag GmbH & Co. KGaA, Weinheim

We first analyzed antibody-coated nonmagnetic nanowires containing only Au and Ag segments, using the sandwich immunoassay (Figure 1B). Both single- and multiplex assays were carried out using the panel of biodetection simulants, and the results obtained demonstrated specific, concentration-dependent fluorescence proportional to the amount of target antigen present in solution. Simultaneous analysis of both the reflectance and the fluorescence images of a mixture of three different nonmagnetic nanowires enabled easy identification of the antigen present (Figure 1C). The identity of the antibodies (Abs) was known through analysis of the corresponding stripe pattern of the nanowire to which they were attached. For example, the indicated fluorescent nanowire has a stripe pattern of 011110 (0 = Au and 1 = Ag). Given that anti-Bg spore Ab was attached to this type of nanowire, it is concluded that Bg spore antigens are present in the test sample mixture. At the same time, nanowires with the stripe pattern 010000 which are conjugated with anti-Ova protein Ab are nonfluorescent, thus indicating that the test sample does not contain Ova proteins (stripe pattern 010100, conjugated with BSA, was used as a negative control).

Multiplex titration graphs for Bg spores, Ova protein, and MS2 bacteriophage were obtained upon performing a detailed concentration-dependent titration experiment for each simulant antigen (Figure 2A–C, respectively; data for single assays are not shown). We observed an increase in the fluorescence signal with an increasing concentration of the simulant antigens. There was nonetheless a small corresponding gradual increase in cross-reactivity with other simulants. Employing such steps as increasing the number of washes prior to particle imaging and restricting the number of nanowires loaded in each well (96-well plate utilized) for analysis can reduce the level of cross-reactivity. The number of nanowires loaded in each well should not exceed approximately 1×10^5 in quantity to prevent aggregation of the nanowires during the imaging process. Over the course of approximately 5–10 assays, a signal-to-noise ratio of about 8–12 was consistently observed for the panel of three simulants studied. This observation suggests that the reproducibility of this assay is high.

During the incubation steps, the nanowires have a tendency to settle out of solution, thus the solution was placed on a mixer or vortexed intermittently to maintain active mixing in a suspended format. From the obtained titration curves (Figure 2A–C), the sensitivity, or limit-of-detection (LoD), for the Bg spores, MS2 bacteriophage, and Ova protein was estimated to be 1×10^5 cfu mL^{-1}, 1×10^5 pfu mL^{-1} and 5 ng mL^{-1}, respectively (cfu = colony-forming units; pfu = plaque-forming units). The LoDs estimated for the antigens studied are comparable with other previously reported platforms such as luminex beads and microarrays.[11–13] To directly compare the sensitivity of this nanowire-based immunoassay against ELISA (enzyme-labeled immunosorbant assay), cytokines could be detected in both approaches at concentrations as low as 10 pg mL^{-1} (unpublished data). Interestingly, the sensitivity or LoD of this assay is also directly proportional to the amount of antibody-coated nanowires employed. We observed that when about 1×10^6 nanowires were employed for the detection of cytokine FGF4, the LoD obtained was around 1000 pg mL^{-1}. Upon decreasing the number of nanowires to 1×10^4, there was a corresponding decrease in the LoD to about 10 pg mL^{-1}, which reflects a 100-fold increase (unpublished data). However, the handling of such a small number of nanowires presents a significant challenge during the numerous washing steps. Through a series of optimizing steps to enable an easy-to-implement protocol, we employed approximately 10^8 nanowires in this immunoassay to ensure an optimal LoD and ease in manipulation.

Another approach to enhance the LoD is to ensure that all the capture antibodies are optimally positioned to maximize

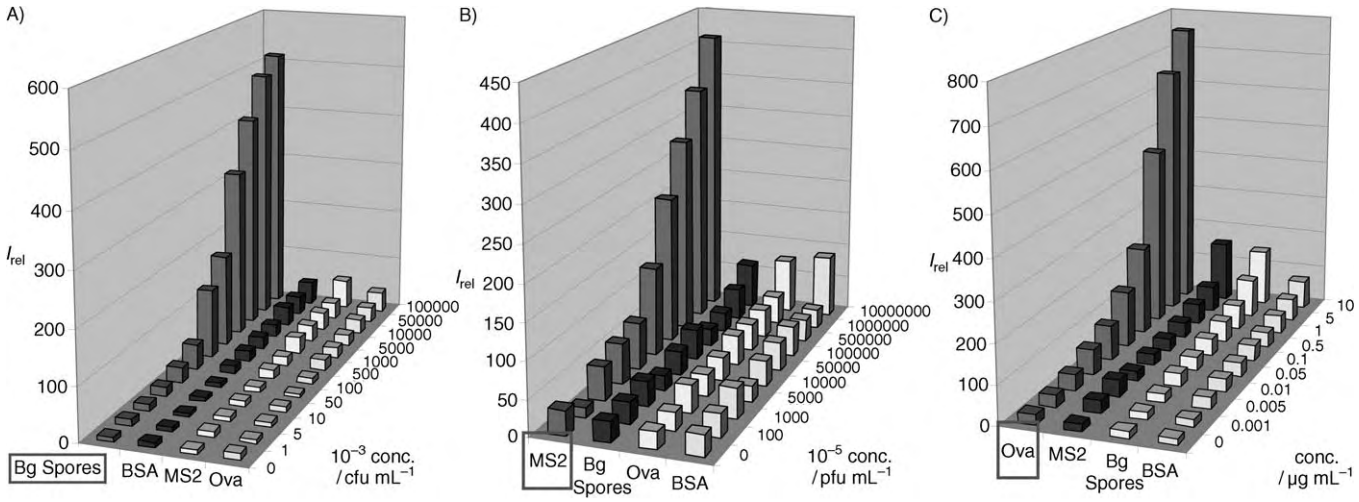

Figure 2. Titration charts of a tetraplex assay consisting of anti-Bg Ab, anti-Ova Ab, anti-MS2 Ab, and BSA-conjugated nanowires versus increasing concentrations of the following simulants: A) Bg spore antigen (from 0 to 1×10^8 cfu mL^{-1}, with 1×10^3 cfu mL^{-1} being the next lowest tested concentration), B) MS2 antigen (from 0 to 1×10^9 pfu mL^{-1}, with 1×10^4 pfu mL^{-1} being the next lowest tested concentration), and C) ovalbumin antigen (from 0 to 1×10 µg mL^{-1}, with 1×10^{-2} µg mL^{-1} being the next lowest tested concentration).

 © 2006 Wiley-VCH Verlag GmbH & Co. KGaA, Weinheim

the detection of the antigen. However, owing to the availability of several free amino groups in the capture antibodies, the antibodies may be randomly oriented on the nanowires surface. It was therefore assumed that only a fraction of the conjugated antibodies participate in the antigen-binding event, thus resulting in the observation of a lower LoD value. Additionally, the affinities of the antibodies employed in this study to their respective antigen could also be a factor. Note that both the anti-MS2 and anti-Ova antibodies are polyclonal and may contribute to the high LoD values observed. This indicates that the affinity of the antibody to its antigen is also an important factor to enhance their assay sensitivity.

Second, we investigated if magnetic nanowires are amendable to the above-described immunoassay against the simulated pathogens. As mentioned above, short segments of Ni can confer magnetic properties to nanowire particles. To this end, varying length of Ni segments (25–150 nm) were integrated at both ends of the nanowires and the resulting magnetic properties were investigated. The magnetic easy axis for these disk-shaped segments is perpendicular to the nanowire axis.[14] The particles therefore align perpendicular to the applied magnetic field. It was observed that longer Ni segments result in stronger magnetophoresis but also increased aggregation between the magnetic nanowires after exposure to the magnets during 30 minutes (Figure 3 A and Figure 4), which hinders subsequent imaging. Interestingly, the mobility of the nanowires tipped with 25-nm Ni was an order of magnitude greater than reported values for magnetite-infused polystyrene beads with a diameter of 1 μm used in similar assays.[15,16] Nickel segments with lengths greater than the corresponding diameter exhibit an easy axis parallel to the nanowire axis, causing the particle to align parallel to the magnetic field.[14] This alignment reduces hydrodynamic drag and should further increase particle mobility. Thus, to ensure ease of magnetic manipulation by a magnetic field and minimization of clumping as a result of magnetism, nanowires tipped with 50-nm Ni were chosen for our subsequent immunoassay. The introduction of Ni at the ends helps to ensure both the structural robustness and the decoding process of the nanowires.

Custom electromagnets and several commercially available microfuge tube magnetic separators were investigated for their ability to recover the magnetic nanowires. With a suspended mixture of nanowires tipped with 50 nm Ni, it was observed that all the nanoparticles are able to fully migrate towards the Dynal Biotechnology microfuge tube magnetic separator (Brown Deer, WI) within 4 minutes (Figure 3 B).

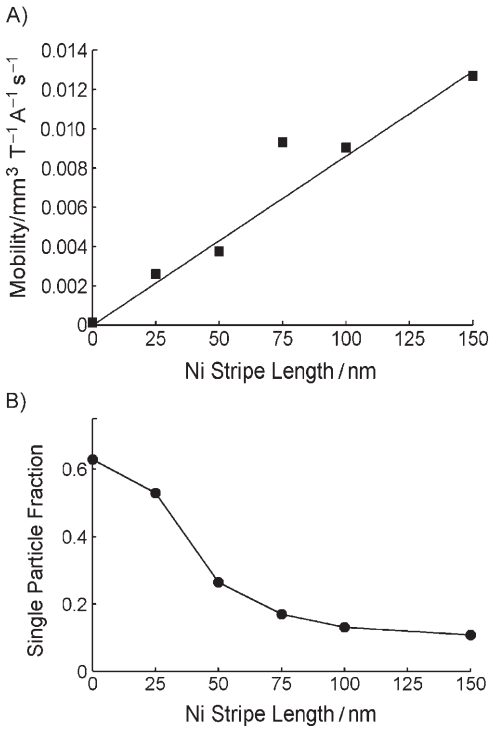

Figure 4. Comparison of characteristics of pure Au nanowires (stripe pattern: 30000003; 0 = Au, 3 = Ni) for various lengths of Ni segments deposited at both ends (total Ni amount is twice the stripe length). A) Magnetophoretic mobility of the nanowires in deionized water, assuming an orientation perpendicular to the direction of motion. Each data point is extracted from measurements of particle velocities for five magnetic energy density values. The solid line shows the approximate linearity of the mobility with the length of the Ni segment. B) The fraction of single (non-overlapping) nanowires versus the number of nanowires in clumps is calculated for each Ni stripe length. Each data point represents cumulative data from 10 to 30 images, with approximately 50 nanowires per image.

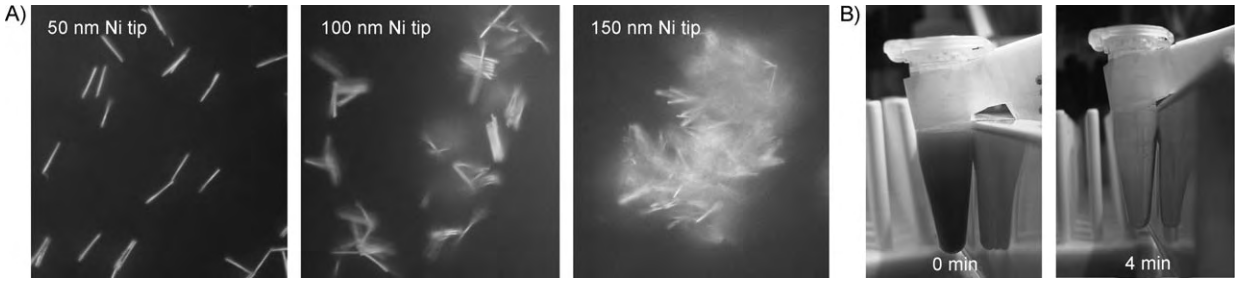

Figure 3. A) Images of the "residual magnetic clumping" effect on various Ni segments deposited at both ends of pure Au nanowires (stripe pattern 30000003; 0 = Au, 3 = Ni). The images were taken after the Ni nanowires were exposed to a Dynal Biotech magnetic strip for 30 min. Nanowires with Ni segments greater than 100 nm (total Ni amount is twice the stripe length) led to a marked increase in the residual clumping upon exposure to magnetic fields. B) Pictures of a suspended mixture of nanowires tipped with 50-nm Ni migrating towards a commercial Dynal magnetic strip after 4 min.

 © 2006 Wiley-VCH Verlag GmbH & Co. KGaA, Weinheim

We also observed that electromagnets are equally efficient in the recovery process of the nanowires (data not shown), which is an important factor in our current efforts to fabricate a portable device to miniaturize the magnetic nanowire-based immunoassay on a fluidic card. While the present work focuses on demonstrating the nanowire-based immunoassay on a microfuge tube, our eventual goal is to use the magnetic properties of the nanowires to carry out an automated version of the assay within a fluidic card. Therefore, we performed tests to verify the ability to capture and isolate the nanowires by using reasonable magnetic fields. However, as a relatively high quantity of nanowires was utilized for the immunoassay in the present study (in a microfuge tube based assay rather than in a microscale system), they were recovered by the centrifugation process.

To ensure that the Ni segments at both ends of the nanowires do not affect the performance of Au- and Ag-striped nanowires in the immunoassay, a concentration-dependent titration experiment was repeated using the Ni-tipped nanowires against Bg spores and Ova proteins. The results obtained for the assays (data not shown) indicate that the LoD values observed for the two antigens studied are the same as those obtained when using the nonmagnetic nanowires. Hence, it was concluded that the presence of the flanking Ni tips does not affect the overall biosensing capabilities of the nanowires.

The development of biological nanosensors has been of interest lately as a result of their potential application in fundamental biology research and genetic screenings. In particular, both nanowires and nanorods have been recently reported to function as sensors, vehicles for gene delivery, and as nanotools for separating His-tagged proteins from underivatized proteins.[17–19] Here, we have demonstrated that metallic nanowires (both magnetic and nonmagnetic) can be employed as novel platforms for multiplex immunoassays. The described suspended array system takes advantage of the unique properties of these nanowires for efficient analysis (and potentially recovery) and holds much promise for novel diagnostic immunoassay platforms. The entire assay can be performed within 3–4 h, thus making it feasible to be employed on a rapid diagnostic platform. Ongoing work is focused on incorporating the assay onto a microfluidic device to allow for a portable biosensing system for biological warfare agents. The platform will ultimately enable an affordable and portable multiplex biodetection system for both first responders and clinicians such that the identity of the infectious agents can be accurately detected and confirmed, thus facilitating point-of-care applications.

Experimental Section

Surface Biofunctionalization: The nanowires were coated with a self-assembled monolayer of mercaptoundecanoic acid (MUA), which increased their dispersity and resulted in a functionalized surface of carboxylate groups that allowed the use of carbodiimide chemistry to attach primary amine groups of the capture antibody to the carboxylate groups on the nanowires. The nanowires were readily extracted from aqueous solution by quick centrifugation (5000 rpm × 1 min) and resuspended by sonicating and vortexing prior to use. The self-assembled MUA monolayers surrounding the nanowires were observed to be intact and functional for at least 1 year when the particles were stored in MUA-containing phosphate buffered saline (PBS; 10 mM, pH 7.4) at room temperature in a nitrogen storage box. Carboxylate-coated nanowires were conjugated to the capture antibody using 1-ethyl-3-(3-dimethylaminopropyl)carbodiimide (EDC; Pierce; Rockford, IL). Briefly, 100 μL of the stock suspension of the nanowires ($\approx 10^8$ particles) were washed twice with 100 μL of 2-morpholinoethanesulfonic acid (MES) buffer (50 mM, pH 4.5; Sigma, St. Louis, MO) and then resuspended in 145 μL of MES buffer (50 mM, pH 4.5) and 18 μL of the appropriate capture antibody ($\approx 1\ mg\,mL^{-1}$ stock concentration). The reaction vessel was placed on ice, and then 15 μL of EDC (20% w/v in 50 mM MES, pH 7.0) was added to the reaction mixture. The mixture was allowed to incubate at 4 °C with agitation for 1 h. Another 15 μL of EDC solution was subsequently added with an additional hour of incubation at room temperature. The antibody-derivatized nanowires were then washed once in 500 μL of PBS (10 mM, pH 7.4) containing 0.1% bovine serum albumin (BSA) and twice in 500 μL of PBS (10 mM, pH 7.4). The antibody-coated nanowires can be stored in 10 mM PBS (pH 7.4) at 4 °C for up to 2 months.

Multiplex Bioassay: 5 μL of each of the stock solutions of the selected Ab-conjugated nanowires ($\approx 10^5$ particles) was added to 100 μL of the antigen sample. The concentration ranges of the antigens tested are as follows: Bg spores at 1×10^8, 5×10^7, 1×10^7, 5×10^6, 1×10^6, 5×10^5, 1×10^5, 5×10^4, 1×10^4, 5×10^3, 1×10^3, and 0 $cfu\,mL^{-1}$; MS2 bacteriophage at 1×10^9, 5×10^8, 1×10^8, 5×10^7, 1×10^7, 5×10^6, 1×10^6, 5×10^5, 1×10^5, 5×10^4, 1×10^4, and 0 $pfu\,mL^{-1}$; and Ova protein at 10, 5, 1, 0.5, 0.1, 0.05, 0.01, and 0 $mg\,mL^{-1}$. The mixture was placed on a shaker and incubated for 30 min at room temperature. The particles were subsequently extracted by centrifugation (5000 rpm × 1 min), washed once in 100 μL of 10 mM PBS–0.1% BSA, and resuspended in 100 μL of a secondary reporter biotin-labeled antibody solution (5 $\mu g\,mL^{-1}$ in 50 mM PBS) for 30 min. After two additional washes with 100 μL of PBS-BSA buffer, the nanowires were incubated with 15 μL of streptavidin–AlexaFluor647 fluorescent reporter conjugate solution (Molecular Probes, 5 $mg\,mL^{-1}$ stock solutions) for 3 min. The particles were then extracted by centrifugation, washed twice with 10 mM PBS–0.1% BSA (pH 7.4), washed twice with 10 mM PBS containing Tween20 (0.05% v/v, pH 7.4), and resuspended in 100 μL of 5 mM PBS solution for imaging analysis.

Imaging and Data Analysis: Approximately 10^5 of the nanoparticles were placed in wells of a clear glass-bottomed 96-well microplate (MMI, Molecular Machines & Industries Gmbh; Eching, Germany) and imaged with a Zeiss Axiovert S100 inverted microscope equipped with a brightfield reflectance filter set (Chroma, 460/50X excitation, Q660LP dichroic, and 0.3ND) and AlexaFluor647 fluorescence filter set (HQ620/60X excitation, Q660LP dichroic, HQ700/75M emission) using a 63X oil immersion lens (NA = 1.4). The light source was a Lambda LS 300-W Xe arc lamp (LBLS/30 Sutter Instruments Inc., Novato, CA). Image acquisition consisted of collecting multiple image pairs (brightfield/fluorescence) over each well of the microplate. The reflectance image was used to delineate the stripe pattern (due to differential reflectivity) of the hexastriped Au/Ag nanoparticles, as each nanoparticle stripe pattern is matched with a particular ligand. The fluorescence images acquired over the same regions as the brightfield images were used to quantify the bound AlexaFluor647 fluorescent-labeled analyte of interest. Usually 25 reflectance and fluorescence image pairs (5 × 5) were acquired in a single well, taking less than 1 min to accomplish.

Received: March 21, 2006
Published online: August 4, 2006

Keywords: biological warfare · immunoassays · magnetic properties · nanotechnology · transition metals

 © 2006 Wiley-VCH Verlag GmbH & Co. KGaA, Weinheim

[1] H. C. Lane, J. L. Montagne, A. S. Fauci, *Nat. Med.* **2001**, *7*, 1271.
[2] B. Durodie, *Curr. Opin. Biotechnol.* **2004**, *15*, 264.
[3] S. R. Nicewarner-Pena, R. G. Freeman, B. D. Reiss, L. He, D. J. Pena, I. D. Walton, R. Cromer, C. D. Keating, M. J. Natan, *Science* **2001**, *294*, 137.
[4] C. D. Keating, M. J. Natan, *Adv. Mater.* **2003**, *15*, 451.
[5] I. D. Walton, S. M. Norton, A. Balasingham, L. He, D. F. Oviso, Jr., D. Gupta, P. A. Raju, M. J. Natan, R. G. Freeman, *Anal. Chem.* **2002**, *74*, 2240.
[6] H. F. Finkel, X. Lou, C. Wang, L. He, *Anal. Chem.* **2004**, *76*, 353A.
[7] P. Gambardella, A. Dallmeyer, K. Maiti, M. C. Malagoli, W. Eberhardt, K. Kern, C. Carbone, *Nature* **2002**, *416*, 301.
[8] G. Iacob, O. Rotariu, N. J. C. Strachan, U. O. Hafeli, *Biorheology* **2004**, *41*, 599.
[9] A. Hultgren, M. Tanase, E. J. Felton, K. Bhadriraju, A. K. Salem, C. S. Chen, D. H. Reich, *Biotechnol. Prog.* **2005**, *21*, 509.
[10] M. Tanase, L. A. Bauer, A. Hultgren, D. M. Silevitch, L. Sun, D. H. Reich, P. C. Searson, G. J. Meyer, *Nano Lett.* **2001**, *1*, 155.
[11] M. T. McBride, D. Masquelier, B. J. Hindson, A. J. Makarewicz, S. Brown, K. Burris, T. Metz, R. G. Langlois, K. W. Tsang, R. Bryan, D. A. Anderson, K. S. Venkateswaran, F. P. Milanovich, B. W. Colston, Jr., *Anal. Chem.* **2003**, *75*, 5293.
[12] M. T. McBride, S. Gammon, M. Pitesky, T. W. O'Brien, T. Smith, J. Aldrich, R. G. Langlois, B. Colston, K. S. Venkateswaran, *Anal. Chem.* **2003**, *75*, 1924.
[13] R. S. Rao, M. T. McBride, J. S. Albala, D. L. Matthews, M. A. Coleman, *J. Proteome Res.* **2004**, *3*, 736.
[14] M. Chen, L. Siun, J. E. Bonevich, D. H. Reich, C. L. Chien, P. C. Searson, *Appl. Phys. Lett.* **2003**, *82*, 3310–3312.
[15] L. D. Garcia, L. C. Cheung, J. C. Mikkelsen Jr., J. G. Santiago, A. F. Bernhardt, V. Malba, *Proc. ASME Meeting* **2001**, 559.
[16] L. B. Bangs, *Pure Appl. Chem.* **1996**, *68*, 1973.
[17] S. G. Penn, L. He, M. J. Natan, *Curr. Opin. Chem. Biol.* **2003**, *7*, 609.
[18] A. K. Salem, P. C. Searson, K. W. Leong, *Nat. Mater.* **2003**, *2*, 668.
[19] K. B. Lee, S. Park, C. A. Mirkin, *Angew. Chem.* **2004**, *116*, 3110; *Angew. Chem. Int. Ed.* **2004**, *43*, 3048.

 © 2006 Wiley-VCH Verlag GmbH & Co. KGaA, Weinheim

Asymmetric Synthesis

DOI: 10.1002/anie.200602879

Stereoselective Synthesis of Superambrox: Stereoselective Type III Intramolecular Ene Reaction and OH-Assisted Ru-Catalyzed Isomerization**

Charles Fehr and Iris Farris*

Dedicated to Professor Georg Fráter on the occasion of his 65th birthday

In the 1990s, chemists from Firmenich[1a] reported the isolation of (−)-**1** by chemical degradation of the labdane diterpene (+)-larixol.[1b] This unsaturated analogue of Ambrox[2] was named "Superambrox" as a result of its excellent odor qualities (Scheme 1).

Scheme 1. (−)-Superambrox and (−)-Ambrox (Laevo–Cetalox).

To our knowledge, the only synthetic approaches towards Superambrox are based on acid-mediated polyene cyclizations,[3] which afford the racemate with low stereoselectivity in only moderate yields. We now report a concise, highly selective synthesis of racemic Superambrox (±)-**1**. The creation of the C–C double bond in a highly substituted environment presents a special challenge, as this subunit is known to be prone to isomerization or skeletal rearrangement. A second difficulty lies in the stereoselective elaboration of the heterocycle.

Our synthetic plan consists of the development of a new tandem type III intramolecular ene reaction/Oppenauer oxidation of dihydro-β-C14-aldehyde (**2**), a high-tonnage raw material, thus allowing a direct approach to the decalone **3**, which has the properly positioned double bond. Acetoxylation from the less-hindered α face followed by intra-

[*] Dr. C. Fehr, I. Farris
Firmenich SA
Corporate R&D Division
P.O. Box 239, 1211 Geneva 8 (Switzerland)
Fax: (+41) 22-780-33-34
E-mail: charles.fehr@firmenich.com

[**] We thank Dr. Horst Sommer (Firmenich SA, Geneva, Switzerland) for the extensive measurement and interpretation of the NMR spectra (COSY, NOE interactions) and Dr. Lionel Saudan (Firmenich SA, Geneva, Switzerland) for stimulating discussions and assistance with the isomerization reaction.

 WILEY InterScience DISCOVER SOMETHING GREAT © 2006 Wiley-VCH Verlag GmbH & Co. KGaA, Weinheim

molecular aldolization of the formed acetoxy ketone should afford, after dehydration, butenolide **4**. Chemo- and diastereoselective 1,4-reduction of **4** was expected to correctly install the third stereogenic center and give access, after reduction, to Superambrox (Scheme 2).

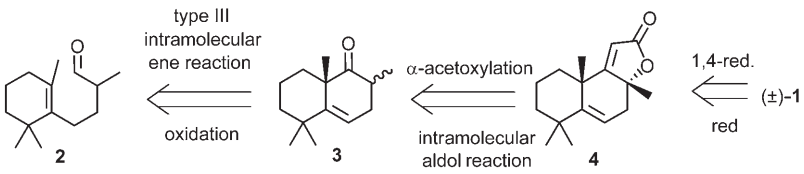

Scheme 2. Retrosynthetic analysis of (±)-Superambrox.

Earlier work[4] showed that **2** undergoes a cyclization/1,2-methyl shift under Brønsted acidic conditions to afford decalin **5** exclusively in approximately 40% yield (Scheme 3). To avoid the formation of rearrangement products, we therefore tested several Lewis acids and found that the use of $EtAlCl_2$ resulted in a clean and selective type III intramolecular ene reaction to afford the desired, nonrearranged decalin **6** in 72% yield. This unusual and probably concerted reaction[5] is thought to proceed through the participation of the ethyl group on the Al center via an eight-membered-ring transition state. When the primarily formed cyclized Al alkoxide was treated with two equivalents of chloral, an Oppenauer oxidation ensued to yield **3** in one pot and high yield (Scheme 3).[6] This hitherto unknown ketone is interesting both as a fragrance component (powdery, ionone, Myrrhone, patchouli, woody) and as a building block for higher terpenoids.[7]

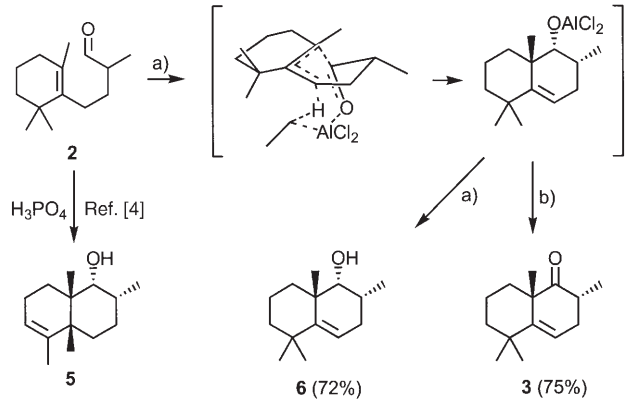

Scheme 3. Preparation of decalone **3** by a type III carbonyl ene reaction/Oppenauer oxidation of **2**. a) $EtAlCl_2$ (1.0 equiv), CH_2Cl_2, 0°C, 30 min; b) Cl_3CCHO (2.0 equiv), 0°C, 90 min.

For the stereocontrolled synthesis of acetoxy ketone **9**, we surmised that site-selective epoxidation of silyl enol ether **7**, readily derived from **3**, would occur from the face opposite the neighboring axial methyl group. Indeed, application of the procedure developed by Rubottom and Juve[8] afforded the silyloxy ketone **8** in excellent yield and with perfect stereocontrol.[9] Treatment of **8** with Ac_2O under acidic conditions afforded the acetoxy ketone **9** directly (Scheme 4).

Subsequent deprotonation of acetate **9** using lithium diisopropyl amide (LDA) at −70°C, resulted in a smooth intramolecular aldol reaction,[10] thus affording hydroxy lactone **10** (94% yield). The dehydration of **10** was effected with thionyl chloride in pyridine to afford **4** in 87% yield (Scheme 5).

The planned 1,4-reduction of the lactone C–C double bond in the presence of the decalin C–C double bond of **4** was expected to proceed chemo- and diastereoselectively from the face opposite the two pseudoaxial methyl groups to afford **11**. However, by using excess $NaBH_4$ and 18 mol% of $NiCl_2$ in methanol,[11] the sole product isolated was the undesired diastereomer **12**.[12] It can be seen from molecular modeling studies that the bicyclic subunit represented by the middle ring and the lactone is bent, thus allowing ready nucleophilic attack from the convex face of **4**.

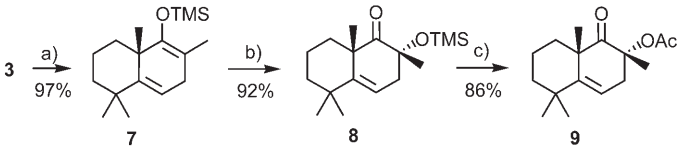

Scheme 4. Stereoselective introduction of the acetoxy function by epoxidation of **7**. a) LDA (1.25 equiv), THF, −5°C, 30 min; then TMSCl (2.4 equiv), −30→−10°C, 10 min; b) *m*CPBA (1.1 equiv), CH_2Cl_2, 0°C, 90 min; c) Ac_2O/H_2O (10:1), $TsOH{\cdot}H_2O$ (5% by weight), 20–30°C, 1 h. *m*CPBA = *meta*-chloroperoxybenzoic acid, TMS = trimethylsilyl, Ts = *para*-toluenesulfonyl.

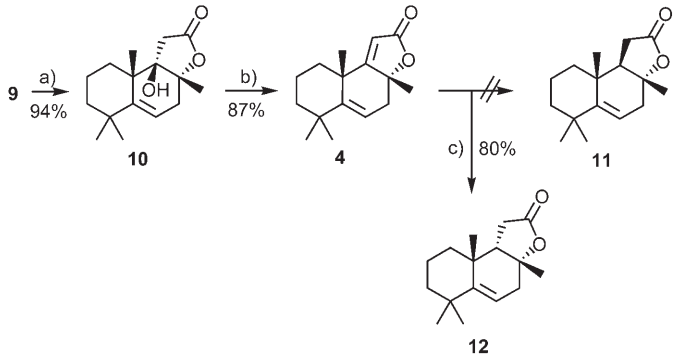

Scheme 5. Synthesis and 1,4-reduction of **4**. a) LDA (1.25 equiv), THF, −70°C, 20 min; b) $SOCl_2$ (5.0 equiv), pyridine, −30°C, 15 min; c) $NaBH_4$, (3.9 equiv), $NiCl_2$ (0.18 equiv), MeOH, −10°C, 1 h.

We therefore reduced lactone **4** to diol **13** in the hope that OH-assisted hydrogenation with the Crabtree catalyst $[Ir(cod)(py)(PCy_3)][PF_6]$ (cod = 1,5-cyclooctadiene, py = pyridine, Cy = cyclohexyl) would occur exclusively at the proximal C–C double bond and from the bottom face, occupied by the tertiary alcohol, to afford **14** (Scheme 6).

To our surprise, no hydrogenation took place, but a diastereoselective, OH-directed isomerization that led to

 © 2006 Wiley-VCH Verlag GmbH & Co. KGaA, Weinheim

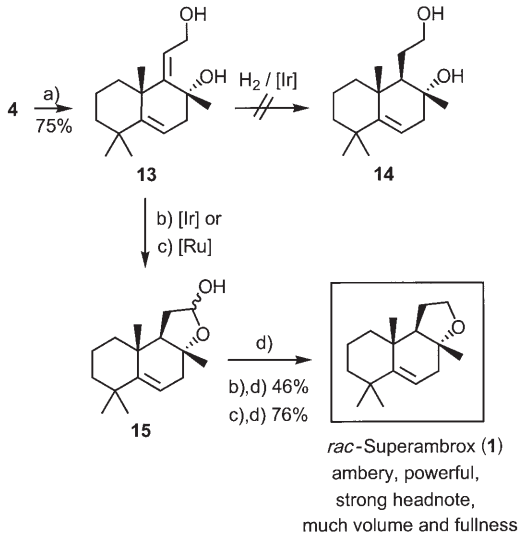

Scheme 6. OH-directed isomerization of **13**. a) $LiAlH_4$ (1.00 equiv), Et_2O, room temperature, 1 h; b) $[Ir(cod)(py)(PCy_3)][PF_6]$ (2 mol%; Crabtree catalyst), H_2, CH_2Cl_2, room temperature, 30 min; c) $[RuH(\eta^5\text{-}C_8H_{11})_2][BF_4]$ (0.5 mol%; Chaudret catalyst), CH_2Cl_2, room temperature, 90 min; d) Et_3SiH (2.0 equiv), Amberlyst 15, room temperature, 1 h; e) TsCl (1.2 equiv), pyridine, 0°C→RT, 1 h.

lactol **15** occurred instead! Subsequent reduction of **15** using Et_3SiH under acidic conditions[13] afforded isomerically pure Superambrox (**1**), which exhibited the expected strong, rich ambery odor, as the only volatile material in 46% yield.[14] Alternatively, the same isomerization took place readily at room temperature with only 0.5 mol% of the Chaudret Ru catalyst $[RuH(\eta^5\text{-}C_8H_{11})_2][BF_4]$.[15] After reduction of lactol **15**, **1** was isolated in 76% yield from **13**. We are currently studying the mechanism of this new OH-assisted isomerization[16] and expanding its scope to the synthesis of other *trans*-fused tetrahydrofurans.

In conclusion, we have achieved the first stereoselective synthesis of Superambrox (**1**) in 27% overall yield, based on two original highly selective reactions: the type III intramolecular ene reaction and the OH-assisted Ru- (or Ir-) catalyzed C–C double-bond isomerization. As the key precursor **3** can be prepared in enantiomerically pure form by resolution of aldehyde **2**,[7] this approach will also allow the synthesis of enantiomerically pure Superambrox.

Experimental Section

(±)-**3**: A solution of $EtAlCl_2$ in hexane (1M, 192 mL, 192 mmol; depending on the quality of $EtAlCl_2$, it may be beneficial to use a 5–10 mol% excess of reagent) was added under N_2 over 12 min to a cooled ($-10 < T < -5$°C), stirred solution of (±)-**2** (40.0 g, 192 mmol) in CH_2Cl_2 (500 mL). The orange reaction mixture was stirred for 30 min at 0°C and treated over 7 min with chloral (37.5 mL, 56.6 g, 384 mmol). The reaction mixture was stirred for 90 min at 0°C and poured with stirring into an Erlenmeyer flask containing 5% HCl, ice, and Et_2O. After stirring for 5 min, the phases were separated, and the organic phase was washed successively (H_2O, saturated aqueous $NaHCO_3$, and saturated aqueous NaCl), dried (Na_2SO_4), and concentrated (62.9 g). Bulb-to-bulb distillations in three portions (oven temp.: 125°C/0.02 mbar) afforded 42.6 g of distillate (79% yield by GC analysis) and 5.14 g of residue. Purification of the distillate (containing chloral-derived by-products) by flash chromatography on SiO_2 (400 g) twice with cyclohexane/EtOAc (98:2) as eluent afforded 29.6 g of **3** (75%). ^{1}H NMR (400 MHz, $CDCl_3$): $\delta = 5.54$ (m, 1H), 2.99 (m, 1H; NOE interactions with angular Me), 2.61 (m, 1H), 2.02 (m, 1H), 1.68–1.82 (m, 2H), 1.59 (m, 1H), 1.41–1.52 (m, 2H), 1.37 (s, 3H), 1.21 (m, 1H), 1.18 (s, 3H), 1.08 (s, 3H), 1.05 ppm (d, $J = 6$ Hz, 3H); ^{13}C NMR (100 MHz, $CDCl_3$): $\delta = 216.6$ (s), 149.1 (s), 117.7 (d), 47.8 (s), 41.0 (t), 37.2 (d), 36.5 (s), 35.8 (t), 33.4 (t), 32.3 (q), 29.6 (q), 27.6 (q), 18.0 (t), 14.4 ppm (q); MS: *m/z* (%): 206 [M^+] (46), 163 (18), 150 (47), 135 (100), 107 (19), 93 (16), 91 (13).

(±)-**1**: In a first flask, a solution of **13** (2.00 g, 8.00 mmol) in dry CH_2Cl_2 (20 mL; dried over 4-Å molecular sieves) was degassed (freezing in liquid N_2, then vacuum, the purging with N_2—the process was repeated twice). A Schlenk tube was charged (in the glove box) with the Chaudret Ru catalyst (16.0 mg, 0.04 mmol, 0.5 mol%). The content of the first flask was added to the catalyst under N_2, and the reaction mixture was stirred at room temperature. A yellow precipitate formed after 5 min. As shown by TLC analysis, all the starting material **13** was consumed after 90 min. The formed lactol **15** was treated with Et_3SiH (1.86 g, 2.54 mL, 16.0 mmol) and Amberlyst 15 (4.00 g). The reaction mixture was stirred open to the air[13b] for 1 h at room temperature, filtered, and concentrated to afford 2.57 g (contains $(Et_3Si)_2O$) of product.

The experiment was repeated on the same scale and afforded 2.83 g of crude product. Purification of the combined products (5.40 g) by flash chromatography on SiO_2 (180 g) with cyclohexane/EtOAc (96:4) as the eluent afforded 2.14 g of $(Et_3Si)_2O$ and 2.85 g of **1** (76%). The analytical data are identical with those given in references [1a] and [1b], but as both references contain minor errors in the ^{1}H NMR spectra, we report here the correct spectral data: ^{1}H NMR (400 MHz, $CDCl_3$): $\delta = 5.44$ (dd, $J = 4$, 4 Hz, 1H), 3.97 (ddd, $J = 9$, 8, 3 Hz, 1H; NOE interactions with Me group on the THF ring ($\delta = 1.05$ ppm)), 3.85 (ddd, $J = 8$, 8, 8 Hz, 1H), 2.23 (m, 2H), 1.76–1.93 (m, 3H), 1.63–1.74 (m, 2H), 1.40–1.52 (m, 2H), 1.10–1.30 (m, 2H), 1.13 (s, 3H), 1.12 (s, 3H), 1.09 (s, 3H), 1.05 ppm (s, 3H; NOE interactions with one H of CH_2O ($\delta = 3.97$ ppm)); ^{13}C NMR (100 MHz, $CDCl_3$): $\delta = 18.3$ (t), 19.5 (q), 21.8 (q), 23.4 (t), 29.0 (q), 33.2 (q), 36.2 (s), 38.3 (s), 41.5 (t), 42.0 (t), 42.3 (t), 57.3 (d), 65.4 (t), 78.3 (s), 117.6 (d), 149.8 ppm (s); MS: *m/z* (%): 234 [M^+] (8), 219 (24), 175 (8), 150 (72), 135 (100), 84 (57), 43 (23).

Received: July 19, 2006
Revised: August 10, 2006
Published online: September 25, 2006

Keywords: iridium · isomerization · odoriferous compounds · ruthenium · tetrahydrofurans

[1] a) R. L. Snowden, S. Escher (Firmenich), EP 558928, **1993** [*Chem. Abstr.* **1994**, *120*, 107408]; b) for another isolation of **1**, see: M. G. Bolster, B. J. M. Jansen, A. de Groot, *Tetrahedron* **2001**, *57*, 5663.
[2] G. Fráter, J. A. Bajgrowicz, P. Kraft, *Tetrahedron* **1998**, *54*, 7633.
[3] a) R. L. Snowden, S. Linder, unpublished results; b) for other unsaturated Ambrox analogues, see: R. L. Snowden, J.-C. Eichenberger, S. Linder, P. Sonnay, *Helv. Chim. Acta* **2004**, *87*, 1711.
[4] G. Saucy, R. E. Ireland, J. Bordner, R. E. Dickerson, *J. Org. Chem.* **1971**, *36*, 1195.
[5] In type III intramolecular ene reactions, the allylic proton on the linker between the two reacting groups is involved: W. Oppolzer, V. Snieckus, *Angew. Chem.* **1978**, *90*, 506; *Angew. Chem. Int. Ed. Engl.* **1978**, *17*, 476; ; B. B. Snider, *Compr. Org. Synth.* **1991**, *2*, 527; K. Mikami, M. Shimizu, *Chem. Rev.* **1992**, *92*, 1021; M.

 © 2006 Wiley-VCH Verlag GmbH & Co. KGaA, Weinheim

Santelli, J.-M. Pons in *Lewis Acids and Selectivity in Organic Synthesis*, CRC, Boca Raton, FL, **1995**; for an example of a type III Prins cyclization which affords (via a carbocationic intermediate) a mixture of two isomers, see: D. C. Braddock, K. K. Hii, J. M. Brown, *Angew. Chem.* **1998**, *110*, 1798; *Angew. Chem. Int. Ed.* **1998**, *37*, 1720; ; see also: N. H. Andersen, F. A. Golec, Jr., *Tetrahedron Lett.* **1977**, *18*, 3783; A. Barbero, P. Castreno, G. Fernandez, F. J. Pulido, *J. Org. Chem.* **2005**, *70*, 10747, and reference therein.

[6] For Oppenauer oxidations with aluminum catalysts, see: T. Ooi, H. Otsuka, T. Miura, H. Ichikawa, K. Maruoka, *Org. Lett.* **2002**, *4*, 2669, and reference therein; for a single report of ene reactions with an Oppenauer oxidation in situ, see: B. B. Snider, B. E. Goldman, *Tetrahedron* **1986**, *42*, 2951.

[7] C. Fehr, I. Farris (Firmenich SA), patent submitted **2005**.

[8] G. M. Rubottom, H. D. Juve, Jr., *J. Org. Chem.* **1983**, *48*, 422.

[9] C. Fehr, I. Farris, H. Sommer, *Org. Lett.* **2006**, *8*, 1839.

[10] J. R. Bull, A. Tuinman, *J. Chem. Soc. Perkin Trans. 1* **1976**, 212; B. Goyau, F. Rouessac, *Bull. Soc. Chim. Fr.* **1978**, 590 and reference [8].

[11] J. Schröer, P. Welzel, *Tetrahedron* **1994**, *50*, 6839.

[12] For a recently reported precedent, see Ref. [3b].

[13] a) G. A. Kraus, K. A. Frazier, B. D. Roth, M. J. Taschner, K. Neuenschwander, *J. Org. Chem.* **1981**, *46*, 2417; b) M. C. Hansen, X. Verdaguer, S. L. Buchwald, *J. Org. Chem.* **1998**, *63*, 2360.

[14] For an isomerization of a C=C double bond using the Crabtree catalyst, see: M. Krel, J.-Y. Lallemand, C. Gouillou, *Synlett* **2005**, 2043.

[15] F. Bouachir, B. Chaudret, F. Dahan, F. Agbossou, I. Tkachenko, *Organometallics* **1991**, *10*, 455; C. Chapuis, G. H. Büchi, H. Wüest, *Helv. Chim. Acta* **2005**, *88*, 3069; D. Jacoby, B. Neffah, C. Chapuis (Firmenich), WO 2005/061426, **2003** [*Chem. Abstr.* **2005**, *143*, 115303].

[16] H. Suzuki, T. Takao in *Ruthenium in Organic Synthesis*, Wiley-VCH, Weinheim, **2004**, pp. 309–315; R. Uma, C. Crévisy, R Grée, *Chem. Rev.* **2003**, *103*, 27; B. Martin-Matute, K. Bogar, M. Edin, F. B. Kaynak, J.-E. Bäckvall, *Chem. Eur. J.* **2005**, *11*, 5832; B. M. Trost, R. J. Kulawiec, *J. Am. Chem. Soc.* **1993**, *115*, 2027; D. V. McGrath, R. H. Grubbs, *Organometallics* **1994**, *13*, 224.

 © 2006 Wiley-VCH Verlag GmbH & Co. KGaA, Weinheim

Anion Sensors

DOI: 10.1002/anie.200602481

Sn^{IV} Complexes of N-Confused Porphyrins and Oxoporphyrins—Unique Fluorescence "Switch-On" Halide Receptors**

*Yongshu Xie, Tatsuki Morimoto, and Hiroyuki Furuta**

In recent years, novel porphyrin isomers and expanded porphyrins have attracted intensive interest, which is related to their novel structures and properties that cannot be realized in normal porphyrin systems.[1] One of the most interesting classes of porphyrin isomers is the N-confused porphyrin (ncp) which contains an α,β′ linkage of one pyrrole ring in the framework. Since the synthesis of such a porphyrin in 1994 by us and Latos-Grażyński's group,[2] research on its metal complexes has been expanding rapidly owing to its rich structural diversity and interesting properties, such as the stabilization of unusual metal oxidation states, outer coordination, and anion binding at the outer NH site.[3] The central metal ions have been extended from transition metals to main-group metals and lanthanides.[4] However, the corresponding complexes of tetravalent metals have still remained unknown, despite the fact that Sn^{IV} complexes of normal porphyrins (for example, **1**) are very well known.[5]

Herein, we report the synthesis of Sn^{IV} complexes of N-confused tetraphenylporphyrin [Sn(nctpp)Cl_2] (**2**) and N-confused oxoporphyrins [Sn(ncop)Cl] (**3a–c**). Complex **2** can bind halides at the outer NH site, and more interestingly, **3** can bind halides at the axial position of the Sn^{IV} center. This binding mode has not been observed until now for either Sn^{IV} complexes of normal porphyrins or other metal complexes of ncp ligands.

Anion binding by synthetic receptors has been investigated extensively in recent years owing to the importance of various anions in biological systems and the possibility of binding toxic anions in environmental science.[6] Fluorescence is one of the most important methods for sensing anions, as a result of its simplicity and high sensitivity. Most of the fluorescent anion-binding systems are based on fluorescence quenching mechanisms,[7] which has some inherent drawbacks.[8] Therefore, anion sensors based on fluorescence

[*] Dr. Y. Xie, T. Morimoto, Prof. Dr. H. Furuta
Department of Chemistry and Biochemistry
Graduate School of Engineering
Kyushu University
Fukuoka 819-0395 (Japan)
Fax: (+81) 92-802-2865
E-mail: hfuruta@cstf.kyushu-u.ac.jp
Prof. Dr. H. Furuta
PRESTO, Japan Science and Technology Agency (JST)
Kawaguchi, Saitama 332-0012 (Japan)

[**] Thanks to Dr. Kenji Yoza at Bruker AXS and Jia Ni at Shantou University for the help with crystallograhic data analysis.

Supporting information for this article is available on the WWW under http://www.angewandte.org or from the author.

© 2006 Wiley-VCH Verlag GmbH & Co. KGaA, Weinheim

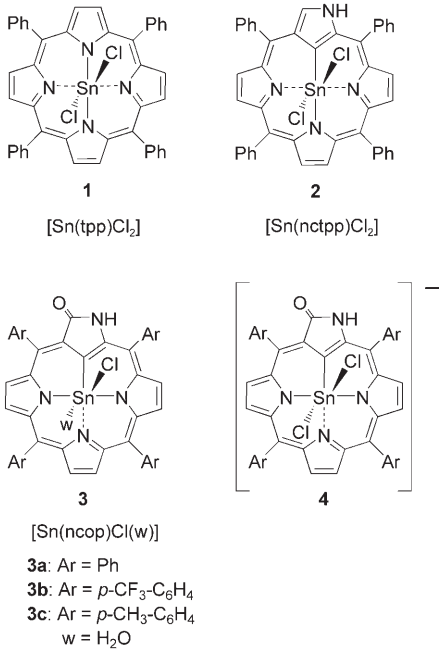

enhancement are highly desirable, but rather challenging to synthesize.[9] Herein, the fluorescence of the Sn^{IV} complexes of ncop is unexpectedly enhanced upon the unique axial binding to various halides, including F^-, Cl^-, Br^-, and even I^-. These complexes provide a novel prototype of fluorescence "switch-on" sensors for halides.

The complexes were synthesized in high yields by the reaction of nctpp with excess $SnCl_2$ in pyridine under aerobic conditions. In contrast to the trianionic form of nctpp in the corresponding Ag^{III} and Sb^V complexes,[10] **2** contains a dianionic nctpp ligand with an outer NH site, which gives a signal at $\delta = 10.67$ ppm in the ^1H NMR spectrum. In contrast, in **3a** the nctpp species has been converted to an N-confused tetraphenyloxoporphyrin (ncop),[11] which coordinates as a trianionic ligand as indicated by the crystal structure (Figure 1).[12] The axial positions of the Sn^{IV} center are occupied by a chloride and water ligand.

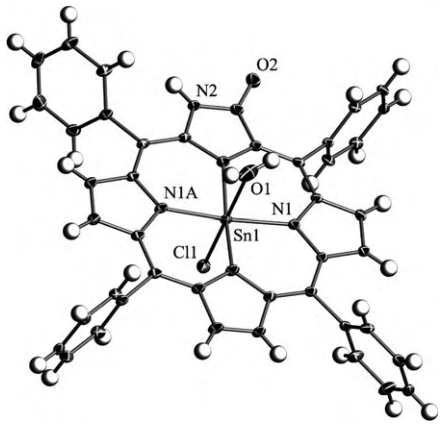

Figure 1. Perspective view of the X-ray crystal structure of **3a**. Selected bond length (Å): Sn1—Cl1 2.405(2). The thermal ellipsoids are scaled to the 30% probability level.

The binding of halides with the Sn^{IV} complexes was checked by changes in the electronic spectra (Supporting Information). Interestingly, the binding constants and UV/Vis changes for complex **3a** are much larger than those for complex **2**. This observation can be explained by the different binding modes of **2** and **3a** (Scheme 1). For complex **2**,

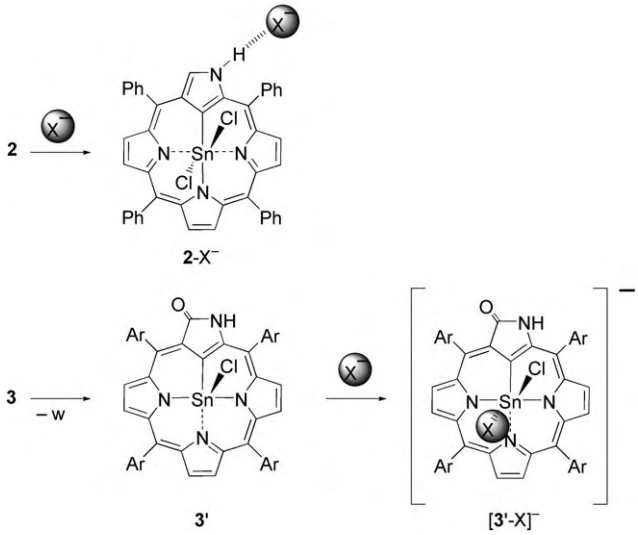

Scheme 1.

chloride binds at the peripheral NH site, and the signal of the outer NH proton in the ^1H NMR spectrum was shifted significantly to lower field from $\delta = 10.67$ to 12.22 ppm upon adding one equivalent of Bu_4NCl (Supporting Information). Compared with NH, other proton signals were only slightly shifted. In contrast, **3a** is dissociated in $CDCl_3$ to give a pentacoordinate species, with the absence of signals for coordinated H_2O in the ^1H NMR spectrum. Then the vacant axial position of the Sn^{IV} center can bind a halide to afford an octahedral complex anion, resulting in a significant change in the electronic state of Sn^{IV}, and consequently, a significant change in its UV/Vis spectra. Meanwhile, all the ^1H NMR signals are shifted similarly to higher field. For the NH proton, the signal is shifted from $\delta = 8.80$ to 8.62 ppm upon adding one equivalent of Bu_4NCl.

The axial binding of Cl^- with complex **3a** was also clearly evidenced by the crystal structure of complex **4** (Figure 2),[13] which was obtained from the recrystallization of **3a** in the presence of Me_4NCl. The axial Sn^{IV}—Cl bond length in **4** (2.498(1) Å) is longer than that in **3a** (2.405(2) Å), thus indicating the weakening of the Sn^{IV}—Cl bond by the additional coordination of Cl^-. For different halides, the binding constants decrease in the sequence $F^- > Cl^- > Br^- > I^-$, and the values for F^- are too large to be precisely measured (Table 1).

Upon binding of Cl^- with **3a**, the intensity of fluorescence was enhanced significantly (Figure 3). This observation can be ascribed mainly to the better rigidity and planarity of the anion-bound octahedral complex anion compared with the neutral complex, as can be evidenced from the crystal structure data. In the neutral complex **3a**, the Sn^{IV} center is

 © 2006 Wiley-VCH Verlag GmbH & Co. KGaA, Weinheim

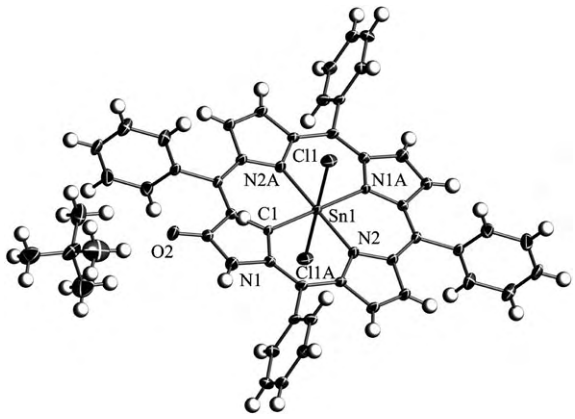

Figure 2. Perspective view of the X-ray crystal structure of **4**. Selected bond length (Å): Sn1–Cl1 2.498(1). The thermal ellipsoids are scaled to the 30% probability level.

Table 1: Anion binding constants (M^{-1}) of the Sn^{IV} ncp complexes.

	Cl	Br	I
2	$4.2(2)\times10^3$	$1.09(8)\times10^3$	40(5)
3a (Ar = C_6H_5)	$1.15(7)\times10^5$	$2.1(1)\times10^4$	$6.1(3)\times10^2$
3b (Ar = *p*-CF_3-C_6H_4)	$2.2(3)\times10^6$	$1.2(1)\times10^5$	$1.1(1)\times10^4$
3c (Ar = *p*-CH_3-C_6H_4)	$1.4(2)\times10^4$	$2.7(3)\times10^3$	$3.8(4)\times10^2$

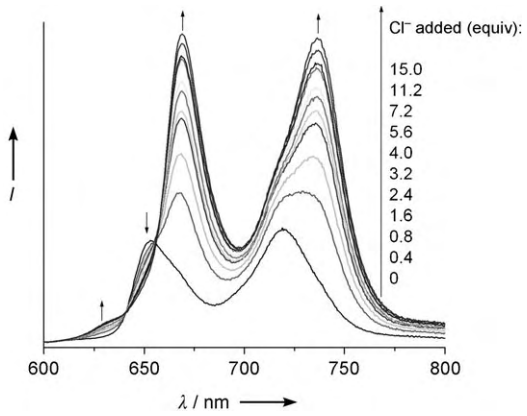

Figure 3. Fluorescence changes during the titration of **3a** with Bu_4NCl in CH_2Cl_2. Excitation wavelength was fixed at 465 nm (one of the isosbestic points) during titration. [**3a**] = 6.63×10^{-6} M.

displaced 0.170 Å towards the Cl^- ion from the least-squares plane defined by the coordinated C and N atoms of the porphyrin ring, which can be ascribed to the stronger coordination of Cl^- compared with that of water at the other axial site (Sn–O 2.364(5) Å). It can be inferred that this displacement becomes more pronounced in solution when the coordination bond of Sn–OH_2 is disrupted.[14] In contrast, in the crystal structure of the anionic complex **4**, the bonding of Sn–Cl is weakened upon Cl^- binding, and owing to the symmetrical axial ligation, the Sn^{IV} center is located exactly within the porphyrin plane. Consequently, the fluorescence quenching is also weakened. Finally, the quenching through collision between the complex anion and the free halide anions in solution may also be negligible, owing to their electrostatic repulsion, as supported by the observation that when even a large excess of Br^- or I^- is added, the fluorescence intensity is not decreased (Supporting Information).

For derivatives of complex **3a**, when the electron-withdrawing group CF_3 is introduced (**3b**), the Sn^{IV} center has more positive charge; thus, larger binding constants are observed. In contrast, the constants become smaller when the electron-donating group CH_3 is introduced (**3c**; Table 1).

As shown above, in solution the neutral ncop complex has a vacant coordination site and the Sn center has a high valency of +4. Thus, it has a strong tendency to bind an additional anion to form an octahedral complex anion. The carbonyl group in the ncop ligand also creates a favorable situation for axial anion binding owing to the electron-withdrawing effect. Such a unique axial binding mode has not yet been observed for N-confused porphyrin complexes of other metals. For the divalent[15] and trivalent[10a] metal complexes of N-confused porphyrins, the tendency for the central ion to bind an additional anionic ligand is weaker compared to Sn^{IV} owing to the lower valence. In contrast, for the complexes of higher valence metals, such as Sb^V, no additional axial position is available because both the coordination sites are already occupied by the anionic ligands.[4a,10b] In the case of normal porphyrin Sn^{IV} complexes, such as [Sn(tpp)Cl_2], the tpp ligand binds in a dianionic form, and thus, the axial positions of the Sn^{IV} center are occupied by the two chloride ligands. Therefore, further binding of the halide at the axial position is only possible by anion exchange or substitution.[16] On the other hand, transition-metal complexes of normal porphyrins have been well-known to serve as anion receptors in polymeric membrane electrodes.[17,18] However, no fluorescent anion receptors based on these metalloporphyrins have been reported, which may be partly a result of the strong fluorescence quenching by the transition metals.

In conclusion, Sn^{IV} complexes of nctpp and ncop ligands were synthesized in high yields. The nctpp and ncop species coordinate in the dianionic and trianionic forms, respectively. The nctpp complex binds halides at the outer NH site, whereas the ncop complexes bind halides at the axial position with larger binding constants and more pronounced fluorescence enhancement. These complexes can thus be regarded as a novel prototype of fluorescence "switch-on" halide sensors. Such a feature results from a vacant site for the axial coordination of external anions, which seems to originate from the combination of a tetravalent (nontransition) metal and the trianionic nature of the ligand. Similar types of porphyrin-based fluorescent anion receptors could be expected from the porphyrin analogues including corroles.[19]

Experimental Section

2: A mixture of nctpp (61 mg, 0.1 mmol) and $SnCl_2$ (3.8 g, 20 mmol) was heated at reflux in pyridine (15 mL) for 5 min, poured into hexane (50 mL), and filtered, and the solid was washed with CH_2Cl_2. The resulting CH_2Cl_2 solution was rotary evaporated to dryness, and the residue was purified by a silica gel column using CH_2Cl_2/MeOH (4% MeOH) as the eluent to afford a dark purple crystalline solid of **2**

 © 2006 Wiley-VCH Verlag GmbH & Co. KGaA, Weinheim

(55 mg, 69%). ^{1}H NMR ($CDCl_3$, 300 MHz, 298 K): $\delta = 10.69$ (br, 1H, outer NH), 8.90 (s, 1H, α-H), 8.48 (d, $J = 5.1$ Hz, 1H, β-H), 8.44 (d, $J = 4.2$ Hz, 1H, β-H), 8.24 (s, 2H, β-H), 8.12 (t, $J = 4.8$ Hz, 2H, β-H), 8.01 (s, 8H, *o*-Ph), 7.67–7.74 (m, 12H, *m*-Ph, *p*-Ph); MALDI-MS: *m*/*z*: 767 $[M-Cl]^+$; UV/Vis (CH_2Cl_2): λ_{max} (ε) = 353 (22600), 460 (132000), 571 (4600), 662 (3700), 716 (6100), 788 nm (11800 $mol^{-1}\,dm^3\,cm^{-1}$).

3a: The reaction and work-up procedure are the same as those for **2**, except that the reaction mixture was stirred at room temperature for 3 days instead of heating, and the eluent for the column contained 2% MeOH. A dark purple shiny solid of **3a** (63 mg, 79%) was collected. ^{1}H NMR ($CDCl_3$, 300 MHz, 298 K): $\delta = 9.02$ (d, $J = 3.9$ Hz, 1H, β-H), 8.99 (d, $J = 3.3$ Hz, 1H, β-H), 8.87–8.91 (m, 4H, β-H), 8.80 (d, $J = 4.8$ Hz, 1H, outer NH), 8.20–8.30 (m, 3H *o*-Ph), 8.05–8.15 (m, 3H, *o*-Ph), 7.72–7.89 (m, 14H, Ph); MALDI-MS: *m*/*z*: 782 $[M-H_2O]^+$; UV/Vis (CH_2Cl_2): λ_{max} (ε) = 388 (15100), 446 (172000), 458 (146000), 560 (11600), 597 (10600), 647 nm (4100 $mol^{-1}\,dm^3\,cm^{-1}$).

Compounds **3b**,**c** were synthesized by a procedure similar to that of **3a** in yields of 96% and 72%, respectively. **4** was obtained from the recrystallization of **3a** with one equivalent of Me_4NCl in $CHCl_3$/hexane by the vapor-diffusion method. **3b**: ^{1}H NMR ($CDCl_3$, 300 MHz, 298 K): $\delta = 8.91$ (d, $J = 4.8$ Hz, 1H, β-H), 8.80–8.87 (m, 4H, β-H), 8.75 (d, $J = 4.8$ Hz, β-H), 8.68 (s, 1H, outer NH), 7.95–8.40 (m, 16H, *o*-, *m*-Ph); MALDI-MS: *m*/*z*: 1054 $[M-H_2O]^+$; UV/Vis (CH_2Cl_2): λ_{max} (ε) = 387 (16500), 445 (195000), 457 (161000), 559 (12700), 597 (11200), 647 nm (5600 $mol^{-1}\,dm^3\,cm^{-1}$). **3c**: ^{1}H NMR ($CDCl_3$, 300 MHz, 298 K): $\delta = 8.99$ (d, $J = 4.8$ Hz, 1H, β-H), 8.96 (d, $J = 5.1$ Hz, 1H, β-H), 8.85–8.91 (m, 4H, β-H), 8.80 (d, $J = 4.5$ Hz, 1H, outer NH), 8.09–8.12. (m, 3H, *o*-Ph), 7.92–8.00 (m, 3H, *o*-Ph), 7.72–7.79 (m, 2H, *o*-Ph), 7.50–7.65 (m, 8H, *m*-Ph), 2.65–2.70 (m, 12H, *p*-CH_3); MALDI-MS: *m*/*z*: 838 $[M-H_2O]^+$; UV/Vis (CH_2Cl_2): λ_{max} (ε) = 390 (16900), 448 (185000), 458 (160000), 561 (12900), 597 (12200), 647 nm (4100 $mol^{-1}dm^3\,cm^{-1}$).

Received: June 20, 2006
Published online: September 26, 2006

Keywords: anion binding · coordination modes · fluorescence · porphyrinoids · tin

[1] a) J. L. Sessler, D. Seidel, *Angew. Chem.* **2003**, *115*, 5292; *Angew. Chem. Int. Ed.* **2003**, *42*, 5134; b) J. L. Sessler, S. Camiolo, P. A. Gale, *Coord. Chem. Rev.* **2003**, *240*, 17; c) M. Stępień, L. Latos-Grażyński, *Acc. Chem. Res.* **2005**, *38*, 88.

[2] a) H. Furuta, T. Asano, T. Ogawa, *J. Am. Chem. Soc.* **1994**, *116*, 767; b) P. J. Chmielewski, L. Latos-Grażyński, K. Rachlewicz, T. Głowiak, *Angew. Chem.* **1994**, *106*, 805; *Angew. Chem. Int. Ed. Engl.* **1994**, *33*, 779.

[3] a) J. D. Harvey, C. J. Ziegler, *Coord. Chem. Rev.* **2003**, *247*, 1; b) P. J. Chmielewski, L. Latos-Grażyński, *Coord. Chem. Rev.* **2005**, *249*, 2510; c) A. Srinivasan, H. Furuta, *Acc. Chem. Res.* **2005**, *38*, 10; d) J. D. Harvey, C. J. Ziegler, *J. Inorg. Biochem.* **2006**, *100*, 869.

[4] a) T. Ogawa, H. Furuta, M. Takahashi, A. Morino, H. Uno, *J. Organomet. Chem.* **2000**, *61*, 551; b) C. H. Hung, W. C. Chen, G. H. Lee, S. M. Peng, *Chem. Commun.* **2002**, 1516; c) J. D. Harvey, C. J. Ziegler, *Chem. Commun.* **2004**, 1666; d) X. J. Zhu, W. K. Wong, W. K. Lo, W. Y. Wong, *Chem. Commun.* **2005**, 1022; e) M. Toganoh, H. Furuta, *Chem. Lett.* **2005**, *34*, 1034; f) M. Toganoh, J. Konagawa, H. Furuta, *Inorg. Chem.* **2006**, *45*, 3852.

[5] D. P. Arnold, J. Blok, *Coord. Chem. Rev.* **2004**, *248*, 299.

[6] a) P. D. Beer, P. A. Gale, *Angew. Chem.* **2001**, *113*, 502; *Angew. Chem. Int. Ed.* **2001**, *40*, 487; b) R. Martinez-Manez, F. Sancenon, *Chem. Rev.* **2003**, *103*, 4419; c) C. Suksai, T. Tuntulani, *Chem. Soc. Rev.* **2003**, *32*,192; d) K. Kavallieratos, Jay M. Rosenberg, W. Z. Chen, T. Ren, *J. Am. Chem. Soc.* **2005**, *127*, 6514.

[7] a) J. Kang, J. Kim, *Tetrahedron Lett.* **2005**, *46*, 1759; b) T. Gunnlaugsson, A. P. Davis, J. E. O'Brien, M. Glynn, *Tetrahedron Lett.* **2005**, *46*, 48.

[8] J. R. Lakowicz, *Principles of Fluorescence Spectroscopy*, 2nd ed., Kluwer Academic/Plenum Publishers, New York, **1999**, p. 238.

[9] a) M. Shionoya, H. Furuta, V. Lynch, A. Harriman, J. L. Sessler, *J. Am. Chem. Soc.* **1992**, *114*, 5714; b) G. X. Xu, M. A. Tarr, *Chem. Commun.* **2004**, 1050; c) Y. Kubo, A. Kobayashi, T. Ishida, Y. Misawa, T. D. James, *Chem. Commun.* **2005**, 2846; d) Y. M. Chung, B. Raman, D. S. Kim, K. H. Ahn, *Chem. Commun.* **2006**, 186.

[10] a) H. Furuta, T. Ogawa, Y. Uwatoko, K. Araki, *Inorg. Chem.* **1999**, *38*, 2676; b) J. C. Liu, T. Ishizuka, A. Osuka, H. Furuta, *Chem. Commun.* **2003**, 1908.

[11] I. Schmidt, P. J. Chmielewski, *Tetrahedron Lett.* **2001**, *42*, 6389.

[12] Crystallographic data for **3a**: $C_{44}H_{29}ClO_2N_4Sn$, $M_r = 799.85$, monoclinic, space group *C*2/*c*, $a = 13.546(1)$, $b = 19.522(2)$, $c = 13.239(1)$ Å, $\beta = 91.119(2)°$, $V = 3500.2(5)$ Å^3, $Z = 4$, $\rho_{calcd} = 1.518\,g\,cm^{-3}$, $T = -150\,°C$, 12858 measured reflections, 4222 unique reflections ($R_{int} = 0.0543$), 3249 with $I \geq 2\sigma(I)$ used in refinement, $R = 0.0541$, $R_w = 0.1141$, GOF = 1.052.

[13] Crystallographic data for **4**: $C_{48}H_{39}Cl_2N_5OSn$, $M_r = 891.43$, monoclinic, space group *C*2/*c*, $a = 18.752(1)$, $b = 13.409(1)$, $c = 19.757(1)$ Å, $\beta = 116.607(1)°$, $V = 4441.9(6)$ Å^3, $Z = 4$, $\rho_{calcd} = 1.333\,g\,cm^{-3}$, $T = -150\,°C$, 15962 measured reflections, 5295 unique reflections ($R_{int} = 0.0329$), 4421 with $I \geq 2\sigma(I)$ used in refinement, $R = 0.0440$, $R_w = 0.0992$, GOF = 1.084. CCDC-271378 (**3a**) and 271380 (**4**) contain the supplementary crystallographic data for this paper. These data can be obtained free of charge from The Cambridge Crystallographic Data Centre via www.ccdc.cam.ac.uk/data_request/cif.

[14] When the axial H_2O ligand of **3** was replaced with an EtOH molecule, ^{1}H NMR signals of unbound EtOH were detected in the solution.

[15] H. Maeda, H. Furuta, A. Osuka, *J. Inclusion Phenom. Macrocyclic Chem.* **2004**, *49*, 33.

[16] D. M. Collims, W. R. Scheidt, J. L. Hoard, *J. Am. Chem. Soc.* **1972**, *94*, 6689.

[17] a) N. A. Chaniotakis, A. M. Chasser, M. E. Meyerhoff, J. T. Groves, *Anal. Chem.* **1988**, *60*, 185; b) X. Z. Li, D. J. Harrison, *Anal. Chem.* **1991**, *63*, 2168.

[18] In the study of ion-selective membrane electrodes, a working mechanism of anion coordination by metalloporphyrins is classified as either *neutral carrier* or *charged carrier* based on the charged state of the host molecules. The former, though the examples are rare, contains Co^{III} porphyrin complexes which accept anions similarly to **3**; see: L. Groski, E. Malinowska, P. Parzuchowski, W. Zhang, M. E. Meyerhoff, *Electroanalysis* **2003**, *15*, 1229.

[19] L. Simkhovich, A. Mahammed, I. Goldberg, Z. Gross, *Chem. Eur. J.* **2001**, *7*, 1041.

 © 2006 Wiley-VCH Verlag GmbH & Co. KGaA, Weinheim

Alkylperoxocopper Complexes

DOI: 10.1002/anie.200602477

A Mononuclear Alkylperoxocopper(II) Complex as a Reaction Intermediate in the Oxidation of the Methyl Group of the Supporting Ligand**

*Masayasu Mizuno, Kaoru Honda, Jaeheung Cho, Hideki Furutachi, Takehiko Tosha, Takahiro Matsumoto, Shuhei Fujinami, Teizo Kitagawa, and Masatatsu Suzuki**

Functionalization of aliphatic C–H bonds by using active oxygen species mediated by copper complexes is of great interest because of its biological significance and industrial applicability. Various types of Cu_n–O_n complexes have been developed and extensively investigated to elucidate possible reaction intermediates that play an essential role in the functionalization of aliphatic C–H bonds.[1] Previously, we have found that the reaction of a copper(I) complex bearing the tetradentate tripodal ligand Me_2-tpa (bis(6-methyl-2-pyridylmethyl)(2-pyridylmethyl)amine), namely $[Cu(Me_2\text{-tpa})]^+$ (**1**), with O_2 generates the bis(μ-oxo)dicopper(III) complex $[Cu_2(Me_2\text{-tpa})_2(O)_2]^{2+}$ (**2**), which undergoes regioselective N-dealkylation of the Me_2-tpa ligand by H-atom abstraction from a methylene group upon decomposition (Scheme 1).[2] We also found that reaction of the bis(μ-hydroxo)dinickel(II) complex $[Ni_2(Me_2\text{-tpa})_2(OH)_2]^{2+}$ with H_2O_2 produces a bis(μ-oxo)dinickel(III) complex. Unlike **2**, under O_2 this bis(μ-oxo)dinickel(III) complex oxidizes one of the 6-methyl groups of the Me_2-tpa ligand to generate the bis(μ-alkylperoxo)dinickel(II) complex $[Ni_2(Me\text{-tpa-}CH_2OO)_2]^{2+}$ (**5**) together with N-dealkylation of the Me_2-tpa ligand.[3,4] A similar bis(μ-alkylperoxo)dicopper(II) complex (**6**) has been reported by Tolman and co-workers in the reaction of the (μ-η^2:η^2-peroxo)dicopper(II) complex $[Cu_2(L^{iPr_3})_2(O_2)]^{2+}$ (L^{iPr_3} = 1,4,7-triisopropyl-1,4,7-triazacyclononane) with 2,4-*tert*-butylphenol in the presence of O_2.[5] Herein we report the formation of the novel mononuclear alkylperoxocopper(II) complex $[Cu(Me\text{-tpa-}CH_2OO)]^+$ (**4**) by the regioselective oxidation of a methyl group of Me_2-tpa in the reaction of $[Cu(Me_2\text{-tpa})]^+$ (**1**) or $[Cu_2(Me_2\text{-tpa})_2(OH)_2]^{2+}$ (**3**) with H_2O_2, its structural and spectroscopic characterization, and its reactivity. Complex **4** is the first example of a structurally characterized alkylperoxocopper(II) complex that is a reactive intermediate and provides a fundamental basis for the functionalization of aliphatic C–H bonds by Cu_n–O_n species.

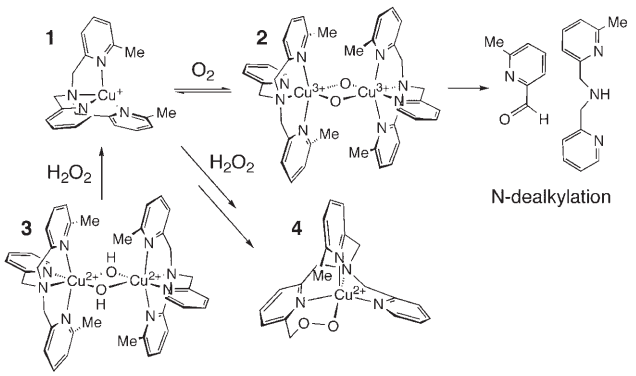

Scheme 1. Reactions of the copper species, see text for details.

Addition of 10 equivalents of 1 M H_2O_2, prepared by dilution of 30% H_2O_2 with acetonitrile, to an acetonitrile solution of **3**[2,6] at −40 °C resulted in a rapid color change from pale blue to green. The ESI-TOF mass spectrum of the green solution shows a prominent signal at *m*/*z* 412.1, which can be assigned to the mononuclear complex **4** (see Supporting Information). Stepwise addition of H_2O_2 to an acetonitrile solution of **3** at −40 °C under N_2 revealed that **3** is reduced to the copper(I) complex $[Cu(Me_2\text{-tpa})]^+$ (**1**),[2] as confirmed by the ESI-TOF mass spectrum. Compound **1** then reacts with further H_2O_2 to give the selective formation of **4** (Supporting Information). This result clearly shows that the oxidation of the methyl group of Me_2-tpa starts with the reaction of **1** with H_2O_2. For the maximum yield of **4** from the reaction of **1** with H_2O_2 under N_2, no more than about three equivalents of H_2O_2 is needed (Figure S2 in Supporting Information).

We succeeded in isolating single crystals of **4** from the reaction of an acetonitrile solution of **1** with five equivalents of H_2O_2 at −40 °C under N_2. The crystal structure clearly shows that one of the 6-methyl groups of Me_2-tpa has been oxidized to a ligand alkylperoxide group (Figure 1). The structure is best described as an intermediate between a square pyramid and a trigonal bipyramid, with an N_4O donor set. The O–O bond length is 1.477(5) Å, which is comparable to those in $[Cu\{HB(3,5\text{-}iPr_2pz)_3\}(OOCMe_2Ph)]^+$ (1.460(6) and 1.454(6) Å)[7] and the closely related dinuclear alkylperoxodinickel(II) complex **5** (1.458(4) Å).[3] Thus, the alkylperoxocopper(II) complex can be produced as well as the corresponding nickel complex **5**, although the formation process is quite different.

The electronic spectrum of **4** in acetonitrile at −40 °C shows two absorption bands at about 379 (ε = 2000) and 636 nm ($\varepsilon = 190\,M^{-1}cm^{-1}$), as shown in Figure 2, which can be assigned to the π_σ*(OOR)-to-Cu^{II} ligand-to-metal charge transfer (LMCT) and d–d transitions, respectively, by analogy with the features of **6** (λ_{max} = 380 nm ($\varepsilon = 2800\,M^{-1}cm^{-1}$))[5]

[*] M. Mizuno, K. Honda, Dr. J. Cho, Dr. H. Furutachi, T. Matsumoto, Prof. S. Fujinami, Prof. M. Suzuki
Division of Material Sciences
Graduate School of Natural Science and Technology
Kanazawa University
Kakuma-machi, Kanazawa 920-1192 (Japan)
Fax: (+81) 76-264-5742
E-mail: suzuki@cacheibm.s.kanazawa-u.ac.jp
Dr. T. Tosha, Prof. T. Kitagawa
Center for Integrative Bioscience
Okazaki National Research Institutes
Myodaiji, Okazaki, 444-8585 (Japan)

[**] Financial support by Grants-in-Aid for Scientific Research from the Ministry of Education, Culture, Sports, Science and Technology, Japan to H.F., T.K., and M.S. is acknowledged.

Supporting Information for this article is available on the WWW under http://www.angewandte.org or from the author.

 © 2006 Wiley-VCH Verlag GmbH & Co. KGaA, Weinheim

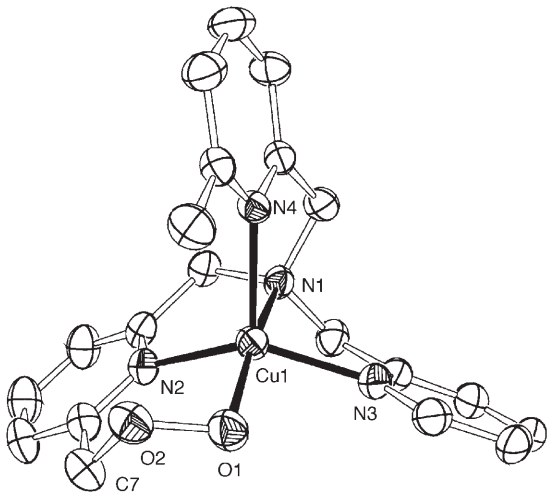

Figure 1. ORTEP drawing (thermal ellipsoids set at 50% probability) of $[Cu(Me\text{-}tpa\text{-}CH_2OO)]^+$ (**4**). Hydrogen atoms have been omitted for clarity. Selected bond lengths [Å] and angles [°]: Cu1–O1 1.887(4), Cu1–N1 2.031(4), Cu1–N2 2.026(3), Cu1–N3 2.022(4), Cu1–N4 2.197(3), O1–O2 1.477(5); O1–Cu1–N1 165.9(2), O1–Cu1–N2 92.3(1), O1–Cu1–N3 93.0(2), N1–Cu1–N2 82.9(1), N1–Cu1–N3 81.4(2), N2–Cu1–N3 135.1(1), Cu1–O1–O2 107.4(2), O1–O2–C7 107.1(3).

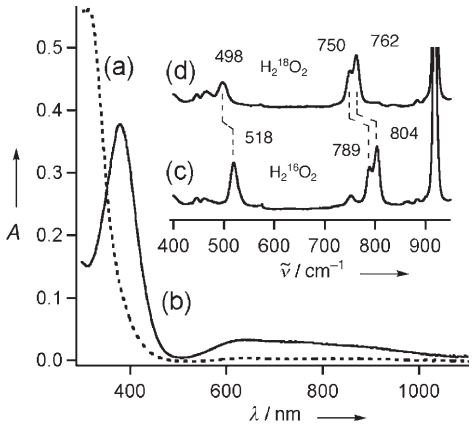

Figure 2. Electronic spectra of a) $[Cu(Me_2\text{-}tpa)]^+$ (**1**) and b) $[Cu(Me\text{-}tpa\text{-}CH_2OO)]^+$ (**4**) in acetonitrile at −40 °C (optical path length = 0.427 cm, [Cu] = 0.38 mM). The inset shows the resonance Raman spectra of c) **4** and d) **4**-^{18}O-^{18}O prepared from $H_2{}^{18}O_2$ in acetonitrile at −40 °C (laser excitation at 406.7 nm).

and hydroperoxocopper(II) complexes.[8] The LMCT energy of **4** is in the range of those of the mononuclear square-pyramidal and trigonal-bipyramidal hydroperoxocopper(II) complexes and significantly higher than the tetrahedral complex $[Cu\{HB(3\text{-}t\text{Bu-}5\text{-}i\text{Prpz})_3\}(OOR)]^+$ (570–610 nm)[9] owing to the lower Lewis acidity of the five-coordinate copper(II) center of **4**. The resonance Raman spectrum of **4** given in Figure 2 shows the isotope-sensitive bands at 804, 789, and 518 cm^{-1} for a $^{16}O_2$ sample (762, 750, and 498 cm^{-1} for an $^{18}O_2$ sample). The bands at 804 and 789 cm^{-1} can be assigned to the ν(O–O) vibrations on the basis of their $^{16}\Delta-{}^{18}\Delta$ values of 42 and 39 cm^{-1}, respectively, and the band at 518 cm^{-1} to the ν(Cu–O) vibration on the basis of its $^{16}\Delta-{}^{18}\Delta$ value of 20 cm^{-1}. Such large isotope shifts and similar band shapes of the ν(O–O) vibrations upon ^{18}O substitution in **4** suggest that mixing of the ν(O–O) and ν(O–C and C–C) stretching vibrations of the alkylperoxo ligand is not significant, in contrast to those observed for $[Cu\{HB(3\text{-}t\text{Bu-}5\text{-}i\text{Prpz})_3\}(OOR)]^+$.[9] Although the origin of the two ν(O–O) bands around 800 cm^{-1} is not known at present, because there is no significant change in the relative intensities of those two bands upon $^{18}O_2$ substitution suggests that they are not due to a Fermi doublet; there is a possibility that they are due to the presence of two geometrical and/or conformational isomers, as proposed for $[Cu\{HB(3,5\text{-}i\text{Pr}_2\text{pz})_3\}(OOCMe_2Ph)]^+$.[9]

As mentioned already, the selective oxidation of the methyl group of Me_2-tpa starts with the reaction of **1** with H_2O_2. To clarify the formation pathway of **4**, we investigated the source of the oxygen in Me-tpa-CH_2OO^-. The ESI-TOF mass spectrum of **4** produced in the presence of a mixture of H_2O_2 and $H_2{}^{18}O_2$ (1:1) under N_2 shows the formation of a mixture of **4** and $[Cu(Me\text{-}tpa\text{-}CH_2{}^{18}O{}^{18}O)]^+$ (**4**-^{18}O-^{18}O) in a 1:1 ratio. No isotope scrambled species (**4**-^{16}O-^{18}O) was detected (Supporting Information). These findings indicate that the oxygen atoms of Me-tpa-CH_2OO^- come from the same molecule of hydrogen peroxide. We also found that the reaction of an acetonitrile solution (10 mL in a 20-mL vial) of **1** (0.02 mmol) with five equivalents of $H_2{}^{16}O_2$ (0.1 mmol) in the presence of $^{18}O_2$ (ca. 6.4 mL, 0.27 mmol) at −40 °C produces a mixture of **4**-^{16}O-^{16}O (67%) and **4**-^{18}O-^{18}O (33%), as shown in Figure 3.[10] This result indicates that

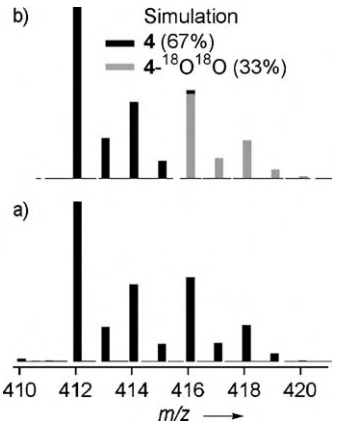

Figure 3. a) ESI-TOF mass spectrum of **4** generated from $H_2{}^{16}O_2$ in the presence of $^{18}O_2$ as described in the text; b) a simulated spectrum consisting of **4** (67%) and **4**-^{18}O-^{18}O (33%).

exogenous O_2 can be incorporated into the alkylperoxo ligand. However, the amount of **4**-^{18}O-^{18}O formed (33%) seems to be too low for these experimental conditions as the amount of $^{18}O_2$ present is significantly larger than that of $^{16}O_2$ (if present, at most 0.04 mmol), which can only be generated from H_2O_2 by reactions such as disproportionation. A combination of the above two experimental results suggests that both exogenous O_2 and some modified species derived from H_2O_2, such as $^{\bullet}$OOH generated by radical chain reactions, act as oxygen sources of the Me-tpa-CH_2OO^- and that some unidentified reactions proceed simultaneously. This

 © 2006 Wiley-VCH Verlag GmbH & Co. KGaA, Weinheim

situation is in marked contrast to the formation of **5** and **6**, where exogenous O_2 is the sole oxygen source.[3–5]

A possible reactive species derived from the Me_2-tpa ligand and some modified species derived from H_2O_2 and O_2 is the ligand radical Me-tpa-$CH_2^{\bullet}$, which has also been proposed for the formation of **5** and **6**.[3–5] This ligand radical may be generated as follows: **1** reacts with H_2O_2 to produce an active oxygen species by either O–O bond homolysis or heterolysis (Cu^{II}-OH + $^{\bullet}$OH or Cu^{III}=O + H_2O) that is capable of performing the selective H-atom abstraction from the methyl group to generate the ligand radical Me-tpa-$CH_2^{\bullet}$. This situation is in marked contrast with the reactivity of complex **2**, which selectively oxidizes the methylene group of Me_2-tpa.[2] Although the reaction of Me-tpa-$CH_2^{\bullet}$ with a reactive species derived from H_2O_2 remains unclear, a possible reactive species is $^{\bullet}$OOH, which can be generated by a radical-chain reaction and which produces the alkylperoxide directly. In the case of the reaction with O_2, Me-tpa-$CH_2^{\bullet}$ produces the ligand peroxyl radical Me-tpa-$CH_2OO^{\bullet}$, as in the case of the formation of **5** and **6**.[3–5] The conversion pathway from Me-tpa-$CH_2OO^{\bullet}$ into Me-tpa-CH_2OO^{-} is not known at present.

The alkylperoxo ligand in **4** in acetonitrile at 20 °C under N_2 undergoes O–O bond cleavage by either homolysis or heterolysis to generate a ligand aldehyde, as proposed for **5**.[3,4] The ESI-TOF mass spectra of the resulting solution reveal the formation of the alkoxo- and carboxylatocopper(II) complexes $[Cu(Me\text{-}tpa\text{-}CH_2O)]^+$ (**7**) and $[Cu(Me\text{-}tpa\text{-}COO)]^+$ (**8**) together with the aldehyde and alcohol copper(I) complexes $[Cu(Me\text{-}tpa\text{-}CHO)]^+$ and $[Cu(Me\text{-}tpa\text{-}CH_2OH)]^+$,[11] although the relative amounts of these complexes are not known at present. Thus, unlike the decomposition of **5**, decomposition of **4** proceeds by some rather complicated reactions. Complex **8** was characterized by comparison of an authentic sample prepared separately and X-ray crystallography (Figure 4). Further study of the decomposition pathways and products is under investigation.

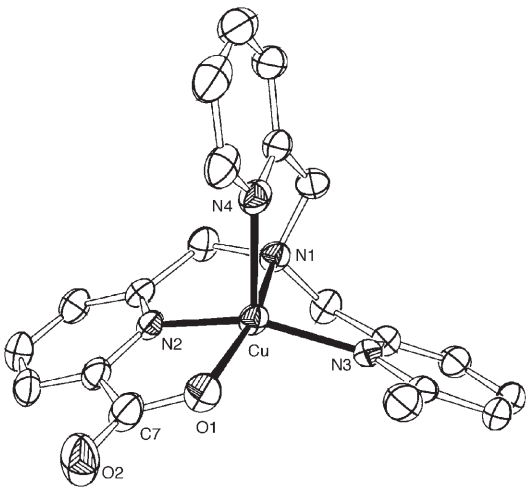

Figure 4. ORTEP drawing (thermal ellipsoids set at 50% probability) of $[Cu(Me\text{-}tpa\text{-}COO)]^+$ (**8**). Hydrogen atoms have been omitted for clarity.

In conclusion, we have succeeded in the selective formation of the mononuclear alkylperoxocopper(II) complex **4** derived from the reaction of the copper(I) complex **1** with H_2O_2 via the ligand radical Me-tpa-$CH_2^{\bullet}$. The reactivity of an active intermediate generated in the present reaction is quite different from that of the bis(μ-oxo)dicopper(III) species **2**. Decomposition of **4** gives alkoxo and carboxylato complexes together with aldehyde and alcohol complexes by O–O bond cleavage and subsequent reactions.

Experimental Section

4·PF_6·0.5 H_2O was prepared under N_2 using Schlenk techniques. 5 equivalents of 1M H_2O_2, prepared by dilution of 30% H_2O_2 (4.3 mmol) with acetonitrile, was added to an acetonitrile solution (5 mL) of **1**·PF_6[2] (450 mg, 0.85 mmol) at −40 °C to produce a green solution, which was stirred for 3 h at the same temperature. Diethyl ether (ca. 50 mL) was added to the resulting solution to yield a green powder, which was collected by filtration, washed with diethyl ether, and dried in vacuum at −40 °C. Single crystals suitable for X-ray crystallography were obtained by vapor diffusion of diethyl ether into an acetonitrile solution of the complex at −40 °C. UV/Vis (acetonitrile): λ_{max} (ε) = 379 (2000), 636 nm (190 $M^{-1}cm^{-1}$); elemental analysis (%) calcd for $C_{20}H_{22}CuF_6N_4O_{2.5}P$: C 42.37, H 3.91, N 9.88; found: C 42.81, H 4.15, N 9.63; ESI-TOF/MS (acetonitrile): *m*/*z* 412.1 $[M]^+$. Although the elemental analysis was satisfactory, the ESI-TOF mass spectra of the samples always showed additional unidentified signals at *m*/*z* 411.1 and 428.1 (relative intensities of 5–10% based on that of **4**). Repeated purification by addition of diethyl ether to an acetonitrile solution of **4** did not remove the impurity.

X-ray crystallographic data for **4** and **8** are given in the Supporting Information. CCDC-603442 (**4**) and CCDC-603443 (**8**) contain the supplementary crystallographic data for this paper. These data can be obtained free of charge from The Cambridge Crystallographic Data Centre via www.ccdc.cam.ac.uk/data_request/cif.

Received: June 20, 2006
Published online: September 26, 2006

Keywords: C–H activation · copper · oxidation · peroxo ligands

[1] a) K. D. Karlin, A. D. Zuberbühler in *Bioinorganic Catalysis*, 2nd ed. (Eds.: J. Reedijk, E. Bouwman), Marcel Dekker, New York, **1999**, pp. 469–534; b) E. I. Solomon, P. Chen, M. Metz, S.-K. Lee, A. E. Palmer, *Angew. Chem.* **2001**, *113*, 4702; *Angew. Chem. Int. Ed.* **2001**, *40*, 4570; c) E. A. Lewis, W. B. Tolman, *Chem. Rev.* **2004**, *104*, 1047; d) L. M. Mirica, X. Ottenwaelder, T. D. Stack, *Chem. Rev.* **2004**, *104*, 1013; e) L. Q. Hatcher, K. D. Karlin, *J. Biol. Inorg. Chem.* **2004**, *9*, 669.

[2] H. Hayashi, S. Fujinami, S. Nagatomo, S. Ogo, M. Suzuki, A. Uehara, Y. Watanabe, T. Kitagawa, *J. Am. Chem. Soc.* **2000**, *122*, 2124.

[3] J. Cho, H. Furutachi, S. Fujinami, M. Suzuki, *Angew. Chem.* **2004**, *116*, 3362; *Angew. Chem. Int. Ed.* **2004**, *43*, 3300.

[4] J. Cho, H. Furutachi, S. Fujinami, H. Ohtsu, T. Tosha, O. Ikeda, A. Suzuki, M. Nomura, T. Uruga, H. Tanida, T. Kawai, K. Tanaka, T. Kitagawa, M. Suzuki, *Inorg. Chem.* **2006**, *45*, 2873.

[5] J. A. Halfen, V. G. Young, Jr., W. B. Tolman, *Inorg. Chem.* **1998**, *37*, 2102.

[6] Unlike the solid sample, the ESI-TOF mass spectrum of an acetonitrile solution of **3** shows that the complex is monomeric under the ESI-TOF conditions.

[7] N. Kitajima, T. Katayama, K. Fujisawa, Y. Iwata, Y. Moro-oka, *J. Am. Chem. Soc.* **1993**, *115*, 7872.

 © 2006 Wiley-VCH Verlag GmbH & Co. KGaA, Weinheim

[8] a) A. Wada, M. Harata, K. Hasegawa, K. Jitsukawa, H. Masuda, M. Mukai, T. Kitagawa, H. Einaga, *Angew. Chem.* **1998**, *110*, 874; *Angew. Chem. Int. Ed.* **1998**, *37*, 798; b) T. Fujii, A. Naito, S. Yamaguchi, A. Wada, Y. Funahashi, K. Jitsukawa, S. Nagatomo, T. Kitagawa, H. Masuda, *Chem. Commun.* **2003**, 2700; c) K. Ito, H. Hayashi, H. Furutachi, T. Matsumoto, S. Nagatomo, T. Tosha, S. Terada, S. Fujinami, M. Suzuki, T. Kitagawa, *J. Am. Chem. Soc.* **2005**, *127*, 5212.

[9] P. Chen, K. Fujisawa, E. I. Solomon, *J. Am. Chem. Soc.* **2000**, *122*, 10177.

[10] Although addition of $^{18}O_2$ caused a slight color change from colorless to pale brown as a result of the formation of a small amount of **2**, its presence has no significant influence on the formation of **4**.

[11] The ESI-TOF mass spectra of the solution after decomposition for 2 days revealed the formation of the copper(I) aldehyde and alcohol complexes $[Cu(Me\text{-}tpa\text{-}CHO)]^+$ and $[Cu(Me\text{-}tpa\text{-}CH_2OH)]^+$ (Supporting Information). Formation of copper(I) complexes was confirmed as follows: addition of 2,9-dimethyl-1,10-phenanthroline to the decomposed acetonitrile solution under N_2 generated $[Cu(Me_2phen)_2]^+$. The total amount of copper(I) species was 20–25% (Supporting Information). We also found that these copper(I) complexes disappear upon addition of O_2.

 © 2006 Wiley-VCH Verlag GmbH & Co. KGaA, Weinheim

Homogenous Catalysis

DOI: 10.1002/anie.200602421

Pd^{II}-Catalyzed Aerobic Allylic Oxidative Carbocyclization of Allene-Substituted Olefins: Immobilization of an Oxygen-Activating Catalyst**

*Julio Piera, Katja Närhi, and Jan-E. Bäckvall**

Oxidation reactions are of fundamental importance in nature, and they are key transformations in organic synthesis.[1] Traditional oxidation methods include the use of stoichiometric amounts of high-oxidation-state metal reagents. These methods are still used in the production of a large number of organic compounds.[2] Recently, there has been an increasing demand for environmentally friendly and sustainable chemical processes ("green chemistry").[3] As a consequence, considerable efforts are being made to replace stoichiometric methods by catalytic processes, and importantly, it is highly desirable in oxidation reactions that the oxidant is either molecular oxygen or hydrogen peroxide.[1a,4] These oxidants are environmentally friendly and give no effluents (at most, water). At present there is a lack of efficient oxidative C–C bond-forming reactions with molecular oxygen as the oxidant, as these reactions are associated with the formation of radicals, thus leading to by-products from auto-oxidation. Herein, we report a novel aerobic oxidative carbocyclization reaction through a multistep electron-transfer process. The oxygen-activating catalyst FePc (Pc = phthalocyanine) was immobilized on a resin, and it was demonstrated that the immobilized catalyst can be recycled five times without any detectable loss of activity.

In a catalytic oxidation reaction, the substrate-selective catalyst, which may be a transition metal, oxidizes the substrate to the desired product (Scheme 1). The reduced form of the catalyst is subsequently reoxidized by the oxidant, which in a "green process" should be O_2 or H_2O_2.

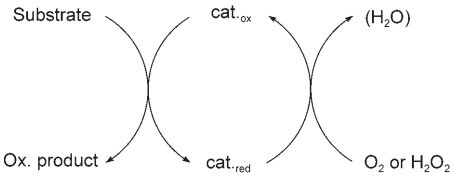

Scheme 1. "Green" catalytic oxidation (cat. = substrate-selective catalyst; for example, a transition metal).

However, one problem to overcome is the often high energy barrier for the reoxidation of the reduced form of the catalyst. This problem can be avoided by mimicking biological oxidation processes, in which large jumps in oxidation potentials are avoided by the use of several coupled redox catalysts as electron-transfer mediators (ETMs).[1a,5–10] We have designed and developed coupled catalytic systems for the 1,4-oxidation of dienes,[5] allylic oxidation,[5a,6] oxidation of alcohols,[7] dihydroxylation of olefins,[8] and oxidation of amines.[9] In the area of aerobic palladium-catalyzed oxidations, there are examples in which palladium is directly reoxidized by O_2 without ETMs. These examples involve the oxidation of alcohols to ketones, alkenes to carbonyl compounds, and intramolecular heterocyclizations of alkenes,[11,12] whereas oxidation with the formation of C–C bonds are less common.[11,13–16] In most of these aerobic oxidation reactions with C–C bond formation, catalytic loadings of 5–10 mol% of Pd are required, except in a few cases.[11a,15] For example, Jacobs and co-workers reported a highly efficient palladium-catalyzed oxidative Heck coupling between anisole and ethyl *trans*-cinnamate under O_2.[15] The use of 1 mol% of $Pd(OAc)_2$ gave the product in 98% yield, but 8 atm (0.8 MPa) of O_2 pressure was required. Our group recently described a palladium-catalyzed allylic oxidation of allene-substituted olefins by *para*-benzoquinone.[17] Stoichiometric amounts of *para*-benzoquinone as the oxidant leads to a large waste of hydroquinone, and it is desirable to replace the oxidant with, for example, molecular oxygen. The aerobic oxidation of enallenes **1** to carbocyclization products **2** carried out in the

[*] Dr. J. Piera, Dr. K. Närhi, Prof. Dr. J.-E. Bäckvall
Department of Organic Chemistry
Arrhenius Laboratory, Stockholm University
106 91 Stockholm (Sweden)
Fax: (+46) 8-154-908
E-mail: jeb@organ.su.se

[**] We are grateful for financial support from the Swedish Research Council, the Swedish Foundation for Strategic Research, and the Ministerio de Educación y Ciencia of Spain.

Supporting information for this article is available on the WWW under http://www.angewandte.org or from the author.

© 2006 Wiley-VCH Verlag GmbH & Co. KGaA, Weinheim

present work is shown in Scheme 2. The reaction involves highly efficient carbon–carbon bond formation with low catalytic loading under aerobic conditions.

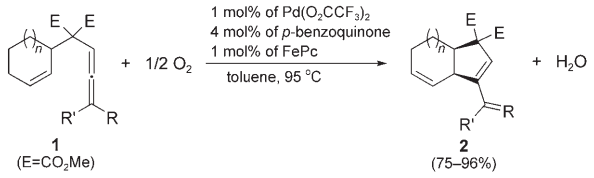

Scheme 2. Oxidative cyclization of allene-substituted olefins.

The new process developed is an aerobic oxidation through a multistep electron-transfer process involving three redox systems: Pd^{II}/Pd^{0}–*para*-benzoquinone/hydroquinone–ML^{m}_{ox}/ML^{m}_{red}, where ML^{m} is FePc, an oxygen-activating macrocyclic metal complex (Scheme 3). The only stoichiometric waste product is water.

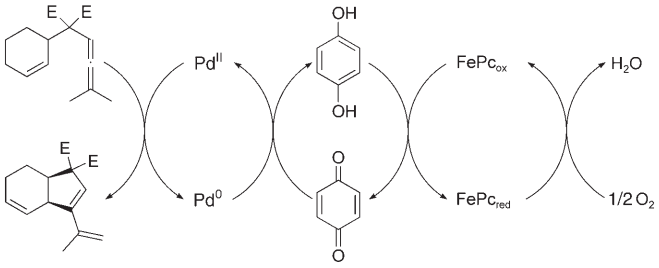

Scheme 3. Triple-coupled catalytic system for aerobic allylic oxidation.

The requisite starting materials **1a–g** were prepared as described previously (see Supporting Information).[17–19] Initial attempts to oxidize **1a** with molecular oxygen at room temperature in the presence of catalytic amounts of $Pd(O_2CCF_3)_2$ (5 mol%), *para*-benzoquinone (20 mol%), and FePc (5 mol%) in THF in an O_2 atmosphere were unsuccessful, thereby resulting in poor yields and long reaction times. A few solvents (THF, dichloromethane, acetonitrile, and toluene) were investigated, but no significant solvent effect was observed for the reaction. An increased reaction temperature led to efficient aerobic oxidation, and **2a** was obtained in 99% yield after 3 h when the reaction was performed in toluene at 95°C in an O_2 atmosphere. A decrease in the catalytic loading to 1 mol% of $Pd(O_2CCF_3)_2$, 4 mol% of *para*-benzoquinone, and 1 mol% of FePc together with a slow addition of **1a** gave **2a** in 96% yield after 8 h.

Contrary to previous quinone-mediated palladium-catalyzed aerobic oxidations for C–O bond formation[5,6] which required protic solvents, the present aerobic oxidation works efficiently in toluene. The mechanism of this reaction was discussed and investigated in an earlier report on the anaerobic reaction.[17]

As mentioned above, there are other systems in which Pd^{0} is reoxidized to Pd^{II} directly by O_2.[11–15] The background reactions of the triple catalytic system were investigated to show that this system is necessary for an efficient aerobic oxidation. We therefore carried out the reaction 1) without *para*-benzoquinone and 2) without $Fe^{II}Pc$. The reaction was nonselective in both experiments, and the desired oxidation product was obtained only in moderate yield together with substantial amounts of by-products (Scheme 4). One of the

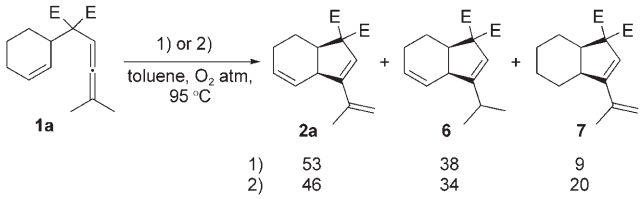

Scheme 4. Aerobic allylic oxidation of allene-substituted olefin **1a**. 1) $Pd(O_2CCF_3)_2$ (5 mol%) and FePc (5 mol%); 2) $Pd(O_2CCF_3)_2$ (5 mol%) and *para*-benzoquinone (20 mol%).

by-products **6** was formed through a palladium(0)-catalyzed cycloisomerization reaction of the enallene[18] and another **7** was formed through a thermal ene reaction.[20] When both *para*-benzoquinone and $Fe^{II}Pc$ were omitted, the yield of **2a** was very low.[21] Clearly, the triple catalytic system is necessary for this reaction to proceed in a selective manner.

To study the scope of the reaction, a variety of substrates were tested under the reaction conditions described above for the aerobic oxidation of **1a**. Cyclohexene substrates **1a–d** reacted to furnish **2a–d** in high yields (Table 1, entries 1–4). Note that **2c** was obtained as a mixture of *E*/*Z* isomers in a ratio of 1:2, in contrast to the anaerobic version, in which the *E*/*Z* isomer ratio was 4:1.[17] This result is probably due to the higher temperature of the aerobic reaction, thus leading to the more thermodynamically stable product.

The effect of the ring size was studied (Table 1, entries 5 and 6). The five-membered ring derivative **1e** gave a mixture of isomers **2e** and **2e′** (3:1) in the aerobic oxidation. The formation of **2e′** can be explained by a Pd^{II}-catalyzed isomerization of **2e**.[22] In contrast to the six- and five-membered ring derivatives, which led to *cis*-fused ring systems, the seven-membered ring derivative afforded a *trans*-fused product **2f**. The two acyclic substrates **1g** and **1h** reacted to give the expected products **2g** and **2h**, respectively, in high yields (Table 1, entries 7 and 8).

To increase the synthetic utility of the reaction, FePc was attached to a polystyrene resin (Figure 1).[23] In this way, the macrocyclic complex **8** can be recovered and reused. When employing **8** in the oxidation of **2**, a slightly slower reoxidation occurred than with free FePc, and under these conditions we observed the formation of small amounts of cycloisomerization product **6** (10%) and the ene reaction product **7** (8%). An increase in the amount used of **8** led to a decrease in the amounts of by-products **6** and **7**, and use of 20 and 40 mol% of **8a** gave **2a** in 89 and 93% yield, respectively.

Different quinones were tested to elucidate the effect on the overall rate and selectivity. Electron-deficient quinones gave a less selective reaction than *para*-benzoquinone with lower yields of **2a** and higher amounts of **6** and **7** (see Supporting Information). In contrast, the use of the electron-rich quinone 2-methoxybenzoquinone gave an efficient and

 © 2006 Wiley-VCH Verlag GmbH & Co. KGaA, Weinheim

Table 1: Palladium(II)-catalyzed aerobic allylic oxidation of **1**.[a]

Entry	Substrate	Product	Yield [%]
1	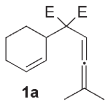	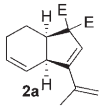	96
2	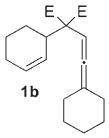	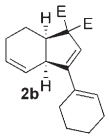	86[b] 96[c]
3	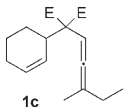	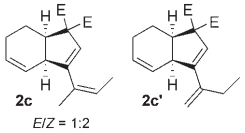 *E*/*Z* = 1:2	81 **2c**/**2c′** 1:1
4	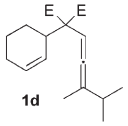	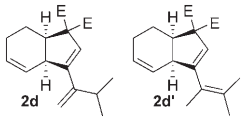	83 **2d**/**2d′** 1:1
5	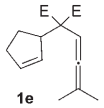	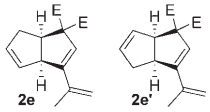	75[b] **2e**/**2e′** 3:1
6	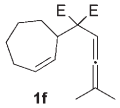	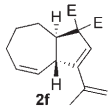	90
7	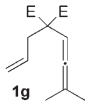	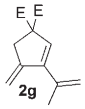	90[c]
8	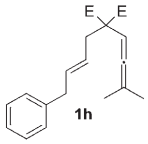	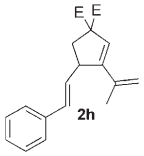	93[c]

[a] Unless otherwise noted, the reactions were carried out on a 1-mmol scale with $Pd(O_2CCF_3)_2$ (1 mol%), *p*-benzoquinone (4 mol%), and FePc (1 mol%) in toluene (2 mL) at 95°C for 8 h under O_2 (1 atm.) with slow addition of **1**. [b] Reaction time of 14 h for full conversion. [c] 0.2-mmol scale, with $Pd(O_2CCF_3)_2$ (5 mol%), *p*-benzoquinone (20 mol%), and FePc (5 mol%) in toluene (2 mL) at 95°C for 3 h.

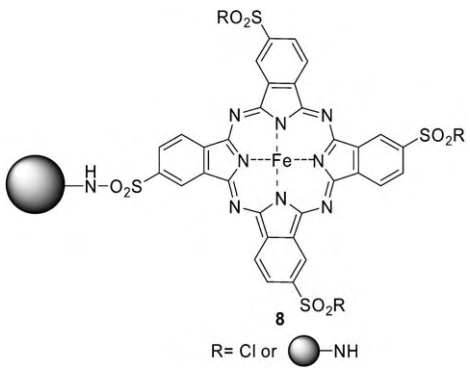

Figure 1. Complex **8**: FePc linked to a resin.

more selective reaction with no formation of **6.** With this quinone, it was possible to obtain a 100% selectivity for **2a** in essentially quantitative yield with a slow addition of the starting material **1a** for 12 h.[24] The mechanism for palladium reoxidation by the quinone appears to be different to that operating in acetic acid.[25] The previous mechanism involved a Pd^0–quinone complex that requires acid to rearrange to Pd^{II} and hydroquinone. In the present mechanism, a Pd–H species may react with the *para*-benzoquinone to give hydroquinone.

After the reaction of **1a** with **8**, the latter was recovered and used again (Table 2). We performed the reaction with either *para*-benzoquinone or 2-methoxy-*para*-benzoquinone. The FePc–resin catalyst **8** was recovered, and it was demonstrated that the reaction can be run five times with the same resin catalyst **8** without any detectable loss of activity.

Table 2: Aerobic allylic oxidation of **1a** using different quinones after recycling **8**.[a,b]

Run	*p*-benzoquinone Yield[c] [%]			2-methoxy-*p*-benzoquinone Yield[c] [%]		
	2a	**6**	**7**	**2a**	**6**	**7**
1	89	5	6	94	0	6
2	83	3	11	92	0	8
3	86	9	5	96	0	4
4	88	6	5	92	0	8
5	90	5	5	95	0	5

[a] The reactions were carried out on a 0.2-mmol scale with $Pd(O_2CCF_3)_2$ (5 mol%), quinone (20 mol%), and **8** (20 mol%) in toluene (2 mL) at 95°C overnight with gentle stirring. [b] Conversion was 100% in all cases. [c] Determined by ^1H NMR spectroscopic analysis.

Although palladium-catalyzed oxidation reactions with direct reoxidation of Pd^0 by molecular oxygen are highly efficient in many cases, this approach fails in other cases as a result of unfavored electron transfer between Pd^0 and O_2. Thus, the use of cocatalysts (ETMs) for many Pd-catalyzed aerobic oxidation reactions are required to obtain high selectivity and high efficiency of the reaction. The oxidation reported herein is a good example of such a coupled catalytic system in which a palladium-catalyzed aerobic allylic oxidation that leads to C–C bond formation was developed. We believe that the use of coupled catalytic systems (such as that in Scheme 3) will be an important complement to the simple systems with direct reoxidation of Pd^0 by O_2 and significantly extend the use of aerobic palladium-catalyzed reactions to cases in which the latter approach fails. The immobilization of the oxygen-activating catalyst onto a resin provides a practical catalyst that can be reused many times without any detectable loss of activity and should further increase the utility of the present aerobic allylic oxidation.

Experimental Section

General procedure for the aerobic allylic oxidation of compounds **1a**–**h**: Oxidation of **1a** to **2a**: $Pd(CF_3CO_2)_2$ (3.3 mg, 0.01 mmol), *para*-benzoquinone (4.3 mg, 0.04 mmol), and iron phthalocyanine (5.7 mg, 0.01 mmol) were mixed and stirred in toluene (2 mL). Compound **1a**

 © 2006 Wiley-VCH Verlag GmbH & Co. KGaA, Weinheim

(278 mg, 1 mmol) was added to the resulting slurry (slow addition during 6 h) with stirring at 95 °C in an oxygen atmosphere. The reaction mixture was cooled down to room temperature after a further 2 h, and 2 M NaOH (10 mL) was added. The resulting mixture was extracted with Et_2O (3 × 5 mL), the combined organic phases were dried (Na_2SO_4), and the solvent was removed under vacuum to yield 265 mg (96 %) of pure product **2a**. Purification of **2**, when needed, was carried out by using Biotage SP1 flash chromatography with eluent system pentane/ethyl acetate (10:1).

Received: June 15, 2006
Revised: August 9, 2005
Published online: September 26, 2006

Keywords: aerobic oxidation · allenes · allylic oxidation · homogeneous catalysis · palladium

[1] a) J.-E. Bäckvall, *Modern Oxidation Methods* (Ed.: J.-E. Bäckvall), Wiley-VCH, Weinheim, **2004**; b) M. Hudlicky, *Oxidations in Organic Chemistry*, American Chemical Society, Washington, DC, **1990** (ACS Monograph Ser. 186); c) B. M. Trost, I. A. Fleming, *Comprehensive Organic Synthesis*, Pergamon, Oxford, **1991**.

[2] a) J. Muzart, *Chem. Rev.* **1992**, *92*, 113; b) R. A. Sheldon, J. K. Kochi, *Metal-Catalyzed Oxidations of Organic Compounds*, Academic Press, New York, **1981**.

[3] R. A. Sheldon, I. W. C. E. Arends, G. J. ten Brink, A. Dijksman, *Acc. Chem. Res.* **2002**, *35*, 774.

[4] a) P. T. Anastas, J. C. Warner, *Green Chemistry, Theory and Practice*, Oxford University Press, Oxford, **1998**; b) R. Noyori, M. Aoki, K. Sato, *Chem. Commun.* **2003**, 1977; c) P. T. Anastas, T. C. Williamson, *Green Chemistry, Frontiers in Benign Chemical Syntheses and Processes*, Oxford University Press, Oxford, **1998**.

[5] a) J.-E. Bäckvall, R. B. Hopkins, H. Grennberg, M. Mader, A. K. Awasthi, *J. Am. Chem. Soc.* **1990**, *112*, 5160; b) J. Wöltinger, J.-E. Bäckvall, A. Zsigmond, *Chem. Eur. J.* **1999**, *5*, 1460.

[6] a) H. Grennberg, K. Bergstad, J.-E. Bäckvall, *J. Mol. Catal. A* **1996**, *113*, 355; b) T. Yokota, S. Fujibayashi, Y. Nishiyama, S. Sakaguchi, Y. Ishii, *J. Mol. Catal. A* **1996**, *114*, 113.

[7] a) J.-E. Bäckvall, R. L. Chowdhury, U. Karlsson, *J. Chem. Soc. Chem. Commun.* **1991**, 473; b) G.-Z. Wang, U. Andreasson, J.-E. Bäckvall, *J. Chem. Soc. Chem. Commun.* **1994**, 1037; c) G. Csjernyik, A. H. Éll, L. Fadini, B. Pugin, J.-E. Bäckvall, *J. Org. Chem.* **2002**, *67*, 1657.

[8] a) K. Bergstad, S. Y. Jonsson, J.-E. Bäckvall, *J. Am. Chem. Soc.* **1999**, *121*, 10424; b) S. Y. Jonsson, K. Färnegårdh, J.-E. Bäckvall, *J. Am. Chem. Soc.* **2001**, *123*, 1365; c) S. Y. Jonsson, H. Adolfsson, J.-E. Bäckvall, *Chem. Eur. J.* **2003**, *9*, 2783; d) A. Closson, M. Johansson, J.-E. Bäckvall, *Chem. Commun.* **2004**, 1494.

[9] J. S. M. Samec, H. E. Alida, J.-E. Bäckvall, *Chem. Eur. J.* **2005**, *11*, 2327.

[10] D. V. Deubel, *J. Am. Chem. Soc.* **2004**, *126*, 996, and references therein.

[11] S. S. Stahl, *Angew. Chem.* **2004**, *116*, 3480; *Angew. Chem. Int. Ed.* **2004**, *43*, 3400, and references therein.

[12] See, for example: a) R. M. Trend, Y. K. Ramtohul, B. M. Stoltz, *J. Am. Chem. Soc.* **2005**, *127*, 17778; b) M. J. Schultz, M. S. Sigman, *J. Am. Chem. Soc.* **2006**, *128*, 1460; c) M. M. Rogers, J. E. Wendlandt, I. A. Guzei, S. S. Stahl, *Org. Lett.* **2006**, *8*, 2257; d) C. C. Scarborough, S. S. Stahl, *Org. Lett.* **2006**, *8*, 3251.

[13] a) M. Rönn, P. G. Andersson, J.-E. Bäckvall, *Tetrahedron Lett.* **1997**, *38*, 3603; b) E. M. Ferreira, B. M. Stoltz, *J. Am. Chem. Soc.* **2003**, *125*, 9578; c) K. T. Yip, J.-H. Li, O.-Y. Lee, D. Yang, *Org. Lett.* **2005**, *7*, 5717; d) E. M. Beck, N. P. Grimster, R. Hatley, M. J. Gaunt, *J. Am. Chem. Soc.* **2006**, *128*, 2528.

[14] C. Adamo, C. Amatore, I. Ciofini, A. Jutand, H. Lakmini, *J. Am. Chem. Soc.* **2006**, *128*, 6829, and references therein.

[15] M. Dams, D. E. De Vos, S. Selen, P. A. Jacobs, *Angew. Chem.* **2003**, *115*, 3636; *Angew. Chem. Int. Ed.* **2003**, *42*, 3512.

[16] For a recent interesting anaerobic oxidation with C–C bond formation through an outer-sphere nucleophilic attack of indole on an (olefin)palladium complex, see: C. Liu, R. A. Widenhoefer, *Chem. Eur. J.* **2006**, *12*, 2371.

[17] J. Franzén, J.-E. Bäckvall, *J. Am. Chem. Soc.* **2003**, *125*, 6056.

[18] K. Närhi, J. Franzén, J.-E. Bäckvall, *Chem. Eur. J.* **2005**, *11*, 6937.

[19] The acyclic starting materials **1g–h** were obtained in the same way as the cyclic starting materials **1a–e** from the corresponding acyclic allylic acetates.

[20] For more information on the thermal ene reaction, see: K. Närhi, J. Franzén, J.-E. Bäckvall, *J. Org. Chem.* **2006**, *71*, 2914.

[21] With **1a** and $Pd(O_2CCF_3)_2$ (5 mol %) in toluene at 95 °C in an O_2 atmosphere, a mixture of **2a**, **6**, **7**, and additional unidentified byproducts were formed; unfortunately the ratio between **2a**, **6**, and **7** could not be determined.

[22] A similar isomerization occurs in the palladium(0)-catalyzed cycloisomerization reaction of enallenes. See Ref. [18].

[23] The FePc was attached to a polystyrene resin (aminomethylated polystyrene (50–100 mesh)) through a sulfonamide group; for reviews on solid-phase reactions, see: a) B. A. Lorsbach, M. Kurth, *Chem. Rev.* **1999**, *99*, 1549; b) R. E. Sammelson, M. Kurth, *Chem. Rev.* **2001**, *101*, 137.

[24] These results are consistent with the rate-determining step being the reoxidation of the hydroquinone to its corresponding quinone.

[25] Further studies on the mechanism of the reoxidation of palladium by the quinone species are in development and will be presented in a future paper; for information about the previously described mechanism, see, for example: a) H. Grennberg, A. Gogoll, J.-E. Bäckvall, *Organometallics* **1993**, *12*, 1790; b) J.-E. Bäckvall, A. Gogoll, *Tetrahedron Lett.* **1988**, *29*, 2243.

 © 2006 Wiley-VCH Verlag GmbH & Co. KGaA, Weinheim

Porous Materials

DOI: 10.1002/anie.200602445

Hydrogen Storage in a Highly Porous Solid Derived from γ-Zirconium Phosphate**

Ernesto Brunet, Hussein M. H. Alhendawi, Carlos Cerro, María José de la Mata, Olga Juanes, and Juan Carlos Rodríguez-Ubis*

The clean production of hydrogen by renewable power sources will make this element the energy vector of the future.[1] However, the handling of this tiny molecule poses extraordinary problems, especially in vehicles, because of the enormous volume occupied by this gas under normal conditions (ca. 12 $L\,g^{-1}$). Efficient hydrogen storage is thus paramount for the safe application of this technology. One approach to accomplish this goal involves its physisorption in porous solid materials, where the packing of hydrogen molecules must be as dense as possible so as to achieve the maximum volumetric density with the lowest feasible amount of additional material. The number of reports on this topic is vast[2] but, to the best of our knowledge, organic–inorganic layered structures have never been tried for this purpose.

The layered salts of zirconium phosphate (ZrP) readily yield pillared scaffolds.[3] We have shown in previous studies that the surface phosphate groups in γ-ZrP layers are amenable to sequential replacement by phosphonates and hypophosphite which leads to drastic changes in the porosity.[4]

We describe herein the incorporation of rigid 4,4″-terphenyldiphosphonate into γ-ZrP and an attempt to further exchange the residual surface phosphate groups with hypophosphite, in the hope that the resultant nonpolar material would be highly porous and able to store reasonable levels of hydrogen gas.

The exchange reaction with 4,4″-terphenyldiphosphonic acid led to material **I**, the solid-state MAS (10 kHz) ^{31}P NMR spectrum of which is shown in Figure 1 (relaxation delay 20 s; internal phosphates: $\delta = -27.4$ ppm, remaining surface ones: $\delta = -13.5$ ppm, phosphonate groups: $\delta = 4.4$ and 17.3 ppm).

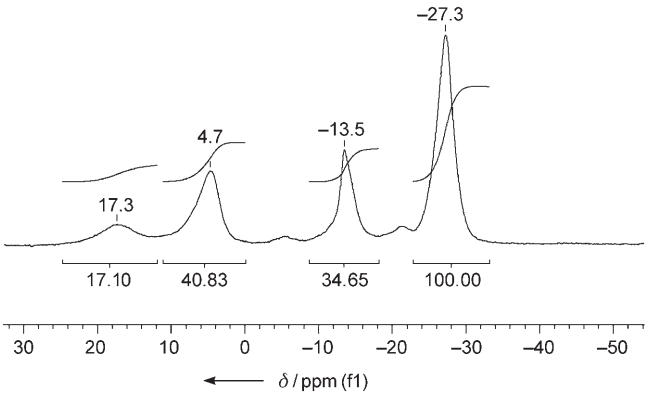

Figure 1. Solid-state MAS (10 kHz) ^{31}P NMR spectrum of material **I**.

The presence of two resonances for the phosphonate groups may indicate that some of the diphosphonates do not form pillars but are bonded only by one end to the inorganic layers.[5] The relative integrals (100:35:41:17) and thermogravimetric analysis (TGA) allowed for the calculation of the molecular formula as $Zr(PO_4)(H_2PO_4)_{0.35}[HO_3P\text{-}(C_{18}H_{14}P_2O_6)PO_3H]_{0.20}[HO_3P(C_{18}H_{14}P_2O_6)PO_3H_2]_{0.17}\cdot 1.4\,H_2O$, which is in very good accordance with the elemental analysis (calcd: C 20.6, H 2.3; found: C 20.0, H 2.6). Therefore, 65% of the surface phosphate groups were replaced by phosphonates, which is in reasonable agreement with the estimated maximum possible exchange considering the available area surrounding each phosphate group (0.36 nm^2) and the cross-section of the phenyl groups (0.44 nm^2). Powder X-ray diffraction studies showed an interlayer distance of 2.43 nm (Figure 2), which corresponds to an inclination of the 4,4″-terphenyl pillars of about 14° with respect to the axis perpendicular to the layers.

BET analysis of material **I** showed a moderate specific area (90 $m^2\,g^{-1}$). Treatment of material **I** with hypophosphorous acid gave material **II**. This material had a similar carbon (20.7%) and hydrogen content (2.6%) as material **I**, thus showing that the reaction with hypophosphite did not involve loss of terphenyldiphosphonate. However, the interlayer distance, as well as the crystallinity, of the sample was

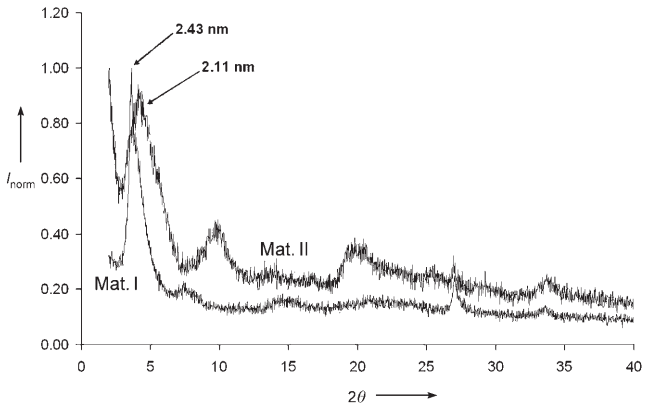

Figure 2. Powder XRD spectra of materials **I** and **II**.

[*] Prof. Dr. E. Brunet, Dr. H. M. H. Alhendawi, Ldo. C. Cerro, Prof. Dr. O. Juanes, Prof. Dr. J. C. Rodríguez-Ubis
Departamento de Química Orgánica
Universidad Autónoma de Madrid
28049 Madrid (Spain)
Fax: (+34) 91-497-3966
E-mail: ernesto.brunet@uam.es
Dr. M. J. de la Mata
Servicio Interdepartamental de Investigación (SIdI)
Facultad de Ciencias C-I
Universidad Autónoma de Madrid (Spain)

[**] Financial support from the Ministry of Science and Education of Spain is gratefully recognized (grants MAT2002-03243 and MAT2006-00570). We are also indebted to FYSE-ERCROS S.A. (Aranjuez, Spain) for generous indirect funding. C.C. and H.M.H.A. are grateful to the Ministries of Science and Education and Foreign Affairs of Spain, respectively, for research fellowships.

InterScience
© 2006 Wiley-VCH Verlag GmbH & Co. KGaA, Weinheim

reduced (2.11 nm, see Figure 2). More importantly, the solid-state MAS ^{31}P NMR spectrum obtained for **II** was unexpected (Figure 3).

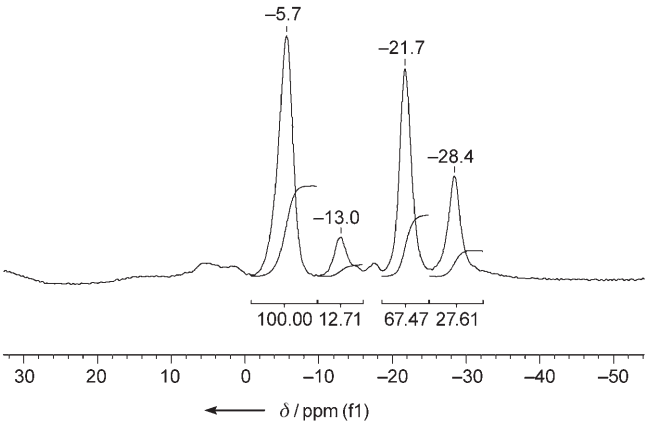

Figure 3. Solid-state MAS (10 kHz) ^{31}P NMR spectrum of material **II**.

In previous cases, the reaction of hypophosphite with pillared γ-ZrP containing nonrigid polyethylenoxadiphosphonates led to the complete elimination of the signal corresponding to the surface phosphate groups (ca. $\delta = -14$ ppm) and the appearance of a new one at about $\delta = 14$ ppm, which corresponds to hypophosphite. However, the latter signal was not observed in material **II**, thus suggesting that hypophosphite was not incorporated into the matrix. In contrast, two new signals were evident at $\delta = -21.7$ and -5.7 ppm, which were assigned to phosphate and phosphonate groups, respectively. The chemical shifts of these signals were compatible with the groups bonding to Zr through three oxygen atoms, that is, corresponding to α-ZrP-type phosphorus instead to the starting γ-ZrP type. However, the signals of lower intensity at $\delta = -28.4$ and -13.0 ppm (Figure 3) are characteristic of the latter phase. It should also be noted that the true α-ZrP phase derived from 4,4′′-terphenyldiphosphonic acid bears an interlayer distance of 1.77 nm,[6] which is much shorter than that measured for material **II** (2.11 nm). Therefore, the reaction with hypophosphite was not topotactic, as occurred in the case of pillared γ-ZrP with polyethylenoxadiphosphonates. In turn, a mixed phase was obtained.[7] Interestingly, BET analysis of material **II** gave a specific area of approximately 400 $m^2 g^{-1}$. It is thus evident that the hypophosphite treatment produced a much more porous solid, which was worth testing for its capacity to store hydrogen. Figure 4 shows the hydrogen-sorption isotherm of material **II** at 77 K.

It may be seen that hydrogen uptake amounts to 74 cm^3 per gram of material at 650 Torr, which is among the highest reported in the literature for related systems, namely metal–organic frameworks (MOFs).[8] We should also point out that the present work concerning the development of new sorbents for hydrogen and other combustible gases by means of ZrP-derived solid matrices is the first one reported in the literature. Therefore, our successful preliminary findings should constitute an excellent starting point to promote

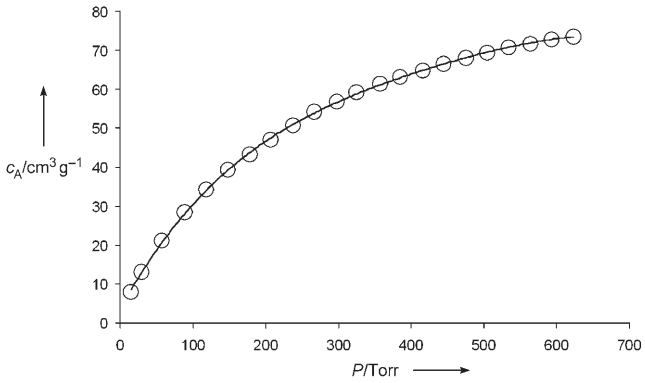

Figure 4. Hydrogen-sorption isotherm at 77 K of material **II**. c_A = concentration absorbed.

research in the application of layered organic–inorganic salts to this important area. Furthermore, the modular rationale followed in the assembly of these layered materials from discrete, preformed building units provide a set of porous solids with finely tuned structures to elucidate the still unknown properties that nanoporous materials must convey for enhancement of hydrogen storage.

Experimental Section

γ-ZrP (0.3 g, 0.94 mmol) was suspended in water/acetone (130 mL, 2:8) and the mixture stirred vigorously and refluxed for 1 h. 4,4′′-Terphenyldiphosphonic acid (183 mg, 0.47 mmol) was then dissolved in water/acetone (300 mL, 2:8) and the mixture slowly added at a constant rate of 0.65 mL min^{-1}. The reflux was continued for four days. After a standard work up, a solid was obtained (0.38 g; material **I**). This material was suspended in a 1M solution of hypophosphorous acid (25 mL) containing a small amount of of 4,4′′-terphenyldiphosphonic acid (15 mg), to compensate for possible losses of diphosphonate during the reaction, and the mixture was maintained overnight at 80 °C. After a standard work up, a solid was obtained (material **II**).

Received: June 17, 2006
Published online: September 26, 2006

Keywords: hydrogen storage · organic–inorganic hybrid composites · porous materials · zirconium

[1] D. Kennedy, *Science* **2004**, *305*, 917, editorial and the following articles.
[2] See, for example: Y. Tamou, R. Omori, *Materia* **2005**, *44*, 188; F. Schueth, B. Bogdanovic, M. Felderhoff, *Chem. Commun.* **2004**, 2249; X. Zhao, B. Xiao, A. J. Fletcher, K. M. Thomas, D. Bradshaw, M. J. Rosseinsky, *Science* **2004**, *306*, 1012.
[3] E. Brunet, M. J. Mata, H. M. H. Alhendawi, C. Cerro, M. Alonso, O. Juanes, J. C. Rodriguez-Ubis, *Chem. Mater.* **2005**, *17*, 1424.
[4] E. Brunet, M. J. Mata, O. Juanes, J. C. Rodriguez-Ubis, *Angew. Chem.* **2004**, *116*, 629; *Angew. Chem. Int. Ed.* **2004**, *43*, 619.
[5] A. Clearfield, Z. Wang, *J. Chem. Soc. Dalton Trans.* **2002**, 2937.
[6] Z. Wang, J. M. Heising, A. Clearfield, *J. Am. Chem. Soc.* **2003**, *125*, 10375.
[7] The mechanism of the transformation induced by the reaction with hypophosphorous acid will be discussed elsewhere. Suggested clues to it by one of the referees can be found in: B. Zhang,

 © 2006 Wiley-VCH Verlag GmbH & Co. KGaA, Weinheim

D. M. Poojary, A. Clearfield, A. G. Peng, *Chem. Mater.* **1996**, *8*, 1333; B. Zhang, A. Clearfield, *J. Am. Chem. Soc.* **1997**, *119*, 2751.
[8] B. L. Chen, M. Eddaoudi, S. T. Hyde, M. Okeeffe, O. M. Yaghi, *Science* **2001**, *291*, 1021; P. M. Forster, J. Eckert, J. S. Chang, S. E. Park, G. Férey, A. K. Cheetham, *J. Am. Chem. Soc.* **2003**, *125*, 1309.

 © 2006 Wiley-VCH Verlag GmbH & Co. KGaA, Weinheim

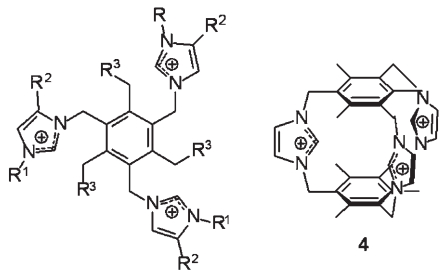

4

1 R^1 = *n*-Bu R^2 = H R^3 = H
2 R^1 = Me R^2 = NO_2 R^3 = H
3 R^1 = CH_2–(2,2′-bipyridine) R^2 = H R^3 = CH_3

Anion Receptors

DOI: 10.1002/anie.200602598

A Metal-Based Trisimidazolium Cage That Provides Six C–H Hydrogen-Bond-Donor Fragments and Includes Anions**

Valeria Amendola, Massimo Boiocchi, Benoît Colasson, Luigi Fabbrizzi, Maria-Jesús Rodriguez Douton, and Franco Ugozzoli*

Dedicated to Professor Vincenzo Balzani on the occasion of his 70th birthday

There is increasing interest in the design of anion receptors, because of the relevance of anions in physiology, environmental disciplines, and food science. In most cases, anion receptors, either neutral or positively charged, contain N–H fragments (from amides, ureas, pyrroles, ammonium cations, or guanidinium cations), which behave as hydrogen-bond donors toward the anion.[1] However, the C–H fragment, when polarized by a proximate positive charge, can also act as a hydrogen-bond donor toward anions. A recent, intriguing case involves a receptor containing the imidazolium subunit.[2] In the first example, **1**, three imidazolium fragments are appended to a 1,3,5-trialkylbenzene platform.[3]

The formation of stable 1:1 complexes of **1** with halides in MeCN was ascertained through ^{1}H NMR spectroscopic titration experiments. Of the various tripodal receptors that have since been reported, the highest anion affinity was observed for **2**, in which the hydrogen-bond-donating abilities of the C–H fragments are enhanced by the proximate NO_2 substituent on each imidazolium ring.[4] The 1,3,5-trialkylbenzene platform is known to favor the formation of a cavity suitable for the inclusion of anions.[5] However, the flexible nature of the pendant arms is expected to depress the stability of the hydrogen-bonded complex, owing to a loss in the conformational entropy of the receptor, and to provide only moderate binding selectivity, in view of the tendency of the tripodand to adapt its cavity to the steric requirements of the anion. Both disadvantages could be eliminated, or substantially reduced, by moving from an open to a closed cavity, that is, from a tripod to a cage. Indeed, a trisimidazolium cage equipped with two 1,3,5-trialkylbenzene caps, **4**, has been synthesized, but no evidence of the inclusion of an anion into the cavity has been reported. Moreover, in all of the crystal structures of tribromide salts of **4**, the cavity is empty and the anions are far from the cage.[6] The cavity opening is probably too small to include an anion.

Thus, we decided to prepare a trisimidazolium cage by following a different approach. First, we appended a 2,2′-bipyridine (bpy) subunit to each imidazolium fragment of the tripod to give **3**-$(PF_6)_3$. Then, the **3**-$(PF_6)_3$ salt was treated with $Fe^{II}(CF_3SO_3)_2$ to give a red-violet complex, which was precipitated as $[Fe^{II}(\mathbf{3})](PF_6)_5$. The Fe^{II} ion is known to form a very stable 1:3 complex of octahedral geometry with bpy. Moreover, the low-spin d^6 electronic configuration of the metal center affords substitutional inertness to the complex. Molecular modeling suggested that the spherical trisimidazolium cavity in the $[Fe^{II}(\mathbf{3})]^{5+}$ complex could be suitable for anion inclusion.

Titration experiments in a variety of media indicated a definite tendency of the $[Fe^{II}(\mathbf{3})]^{5+}$ receptor to include halide ions (see Supporting Information). Figure 1 displays the ^{1}H NMR spectra of a solution of $[Fe^{II}(\mathbf{3})](PF_6)_5$ in CD_3CN/D_2O (4:1 v/v) in the absence and presence of 4.4 equiv of $[Bu_4N]Br$. Upon anion addition, a distinct downfield shift in the signal of the H_g hydrogen atoms was observed, indicating a direct interaction with the anion. Note that the signal of the H_c hydrogen atoms was not observed, probably owing to fast

[*] Dr. V. Amendola, Dr. B. Colasson, Prof. L. Fabbrizzi, Dr. M.-J. Rodriguez Douton
Dipartimento di Chimica Generale
Università di Pavia
via Taramelli 12, 27100 Pavia (Italy)
Fax: (+39) 0382-528-544
E-mail: luigi.fabbrizzi@unipv.it
Dr. M. Boiocchi
Centro Grandi Strumenti
Università di Pavia
via Bassi, 27100 Pavia (Italy)
Prof. F. Ugozzoli
Dipartimento di Chimica Generale ed Inorganica
Università di Parma
Parco Area delle Scienze 17/A, 43100 Parma (Italy)

[**] The financial support of the Italian Ministry of University and Research (PRIN Dispositivi Supramolecolari; FIRB Project RBNE019H9K) is gratefully acknowledged.

Supporting information for this article is available on the WWW under http://www.angewandte.org or from the author.

InterScience DISCOVER SOMETHING GREAT
© 2006 Wiley-VCH Verlag GmbH & Co. KGaA, Weinheim

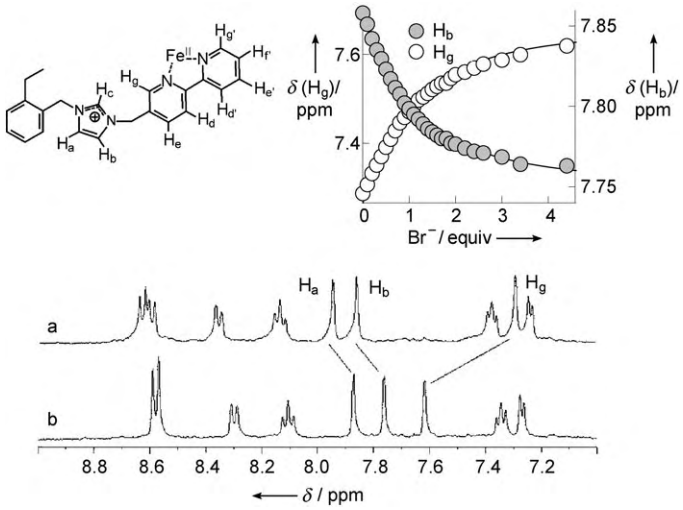

Figure 1. Titration of a 1.00×10^{-3} M solution of $[Fe^{II}(\mathbf{3})](PF_6)_5$ in CD_3CN/D_2O (4:1 v/v) with $[Bu_4N]Br$, monitored by ^1H NMR spectroscopy: labeling scheme (top left); titration profiles for the H_b and H_g signals (top right); aromatic regions of the spectra recorded prior to the addition of $[Bu_4N]Br$ (a) and after the addition of 4.4 equiv of $[Bu_4N]Br$ (b).

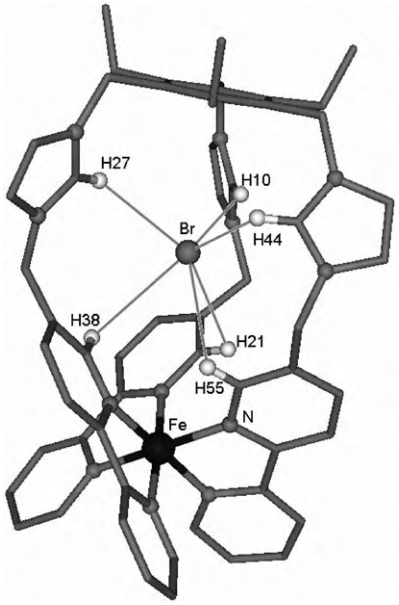

Figure 2. Molecular structure of the $[Fe^{II}(\mathbf{3})\cdots Br]^{4+}$ complex. Only hydrogen atoms involved in hydrogen bonds (thin lines) with the anion are shown. Selected interatomic contacts [Å]: Br···H10 2.640(10), Br···H27 2.716(10), Br···H44 2.786(11), Br···H21 3.026(8), Br···H38 3.106(9), Br···H55 3.059(9).

exchange with D_2O. However, the involvement of the C–H_c fragments in anion binding was indirectly suggested by the moderate, yet well distinguishable upfield shift in the signals of the H_a and H_b hydrogen atoms of the imidazolium ring. Nonlinear least-squares treatment of the titration data, using dedicated software,[7] indicated the formation of an $[Fe^{II}(\mathbf{3})\cdots Br]^{4+}$ complex with an association constant of $\log K = 3.26 \pm 0.02$. Moreover, unambiguous information on the nature of the receptor–anion complex came from X-ray diffraction studies on a single crystal of the red-violet $[Fe^{II}(\mathbf{3})\cdots Br](PF_6)_4\cdot 2H_2O\cdot MeCN$ salt.

Figure 2 shows a view of the $[Fe^{II}(\mathbf{3})\cdots Br]^{4+}$ complex: the Br^- ion is included within the trisimidazolium cavity and participates in three hydrogen bonds with the C–H_c fragments from each of the imidazolium subunits (H_c = H10, H27, H44; average $H_c\cdots Br$ 2.714(10) Å) and three hydrogen bonds with the C–H_g fragments of the nearest pyridine rings (H_g = H21, H38, H55; average $H_g\cdots Br$ 3.063(10) Å). Thus, the coordination of the anion by the C–H_g fragments, which was preliminarily inferred from the ^1H NMR spectroscopic titration, has been demonstrated by X-ray diffraction. The hydrogen-bond-donating tendencies of the C–H_g fragments from the neutral heterocyclic rings have been activated by the coordination of adjacent nitrogen atoms to the Fe^{II} center. The metal-induced polarization of a C–H fragment of an isoquinoline unit has been observed in a Pt^{II}-based receptor containing isoquinoline and urea subunits.[8] The $[Fe^{II}(\mathbf{3})\cdots Br]^{4+}$ complex represents the first example of anion coordination by six C–H fragments. Noticeably, the Br^- ion sits near the line that connects the centroid of the 1,3,5-triethylbenzene platform and the Fe^{II} ion. In particular, the displacement of the Br^- ion from the line is only 0.06(5) Å, the Br···centroid(C_6) distance is 3.81(1) Å, and the Br···Fe distance is 4.76(1) Å. The three C–H_c and the three C–H_g fragments do not point directly towards the Br^- ion, probably because of steric constraints imposed by the coordination of the bpy subunits to the metal center. The six coordinated hydrogen atoms occupy the corners of a slightly distorted trigonal prism (twist angle = 12.4°). Pseudo-octahedral coordination by amide N–H fragments has been previously observed for an F^- ion included within a bistren (tren = tris(2-aminoethyl)amine) amine–amide cryptand.[9]

An ^1H NMR spectrum similar to that observed with $[Bu_4N]Br$ was obtained upon titration of a solution of $[Fe^{II}(\mathbf{3})](PF_6)_5$ in CD_3CN/D_2O (4:1 v/v) with $[Bu_3BnN]Cl$, and an association constant of $\log K = 3.80 \pm 0.03$ was determined. Moreover, inclusion of the Cl^- ion could also be followed in UV/Vis spectra. In particular, the intensity of the band centered at 300 nm and ascribed to a π–π* transition in the bpy framework decreases upon addition of $[Bu_3BnN]Cl$. A multiwavelength least-squares treatment of the spectrophotometric titration data gave an association constant of $\log K = 3.9 \pm 0.1$, in good agreement with that obtained from the ^1H NMR spectroscopic titration experiment. Similar titration experiments were carried out with the I^- ion, but little change was observed in the UV/Vis spectra, indicating that no complex with an association constant of $\log K > 2$ forms in this case.

To evaluate solvation effects on complex formation, titration experiments were carried out in pure MeCN. With Cl^- and Br^- ions, the spectrophotometric titration profiles obtained were very steep, indicating an association constant of $\log K > 7$ in each case. In contrast, upon titration of $[Fe^{II}(\mathbf{3})](PF_6)_5$ with $[Bu_4N]I$, a smooth profile was obtained, from which an association constant of $\log K = 4.40 \pm 0.03$ was determined (Figure 3). No spectral modifications were observed upon titration with $[Bu_4N]H_2PO_4$ or $[Bu_4N]HSO_4$, even after the addition of a large excess of the titrant.

 © 2006 Wiley-VCH Verlag GmbH & Co. KGaA, Weinheim

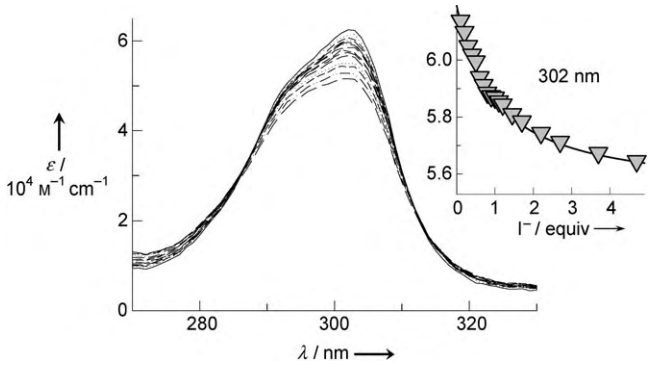

Figure 3. Titration of a 1.00×10^{-4} M solution of $[Fe^{II}(\mathbf{3})](PF_6)_5$ in MeCN with $[Bu_4N]I$, monitored by UV/Vis spectrophotometry: spectra recorded over the course of the titration; titration profile at $\lambda = 302$ nm (inset).

These results disclose an interesting selectivity pattern: $[Fe^{II}(\mathbf{3})]^{5+}$ is able to include the spherical, monoatomic halide anions with the affinity sequence $Cl^- > Br^- > I^-$. This sequence may reflect a decrease in the hydrogen-bond-accepting ability of the anion, or a decrease in its ability to fit into the cavity with increasing size. On the other hand, the "spherical" $H_2PO_4^-$ and HSO_4^- ions seem to be too large to be accommodated in the $[Fe^{II}(\mathbf{3})]^{5+}$ receptor. The geometrical selectivity for a spherical shape was verified by investigating other anions. No spectral modifications were observed upon addition of an excess of the triangular NO_3^- ion to a solution of $[Fe^{II}(\mathbf{3})]^{5+}$ in MeCN/H_2O (4:1 v/v).

Nevertheless, a well-defined interaction pattern was observed upon titration of $[Fe^{II}(\mathbf{3})]^{5+}$ with the rodlike anions N_3^-, NCO^-, and NCS^-. Figure 4 shows ^1H NMR spectra taken over the course of the titration of a solution of $[Fe^{II}(\mathbf{3})](PF_6)_5$ in CD_3CN with a solution of NaN_3 in CD_3OD: a distinct downfield shift of the H_g signal was observed. In particular, the titration profile indicated the formation of a 1:1 complex, but the absence of curvature prevented the determination of the association constant. A value of $\log K = 5.7 \pm 0.1$ was calculated from a spectrophotometric titration experiment carried out on a solution 1.00×10^{-4} M solution of $[Fe^{II}(\mathbf{3})]^{5+}$ in MeCN/H_2O (4:1 v/v), in which the decrease in the intensity of the π–π^* band at 300 nm was monitored.

Most significantly, red crystals of the complex salt $[Fe^{II}(\mathbf{3})\cdots N_3](PF_6)_4\cdot1.5\,H_2O\cdot3\,MeCN$ that were suitable for X-ray diffraction studies formed from the slow diffusion of diethyl ether into a MeCN/MeOH solution containing equimolar amounts of $[Fe^{II}(\mathbf{3})](PF_6)_5$ and NaN_3. In the crystal structure, the N_3^- ion is statistically distributed over two different orientations within the host cavity (see Supporting Information). Therefore, the mutual attraction between the two charged species occurs in two different ways. In one case, the N_3^- ion accepts seven hydrogen bonds from the receptor (Figure 5). In particular, the terminal N13A atom participates in three hydrogen bonds: two with the two H_c hydrogen atoms H10 and H27 and one with the H_g hydrogen atom H38. The terminal N15A atom is stabilized by two hydrogen bonds, one with the H_c hydrogen atom H44 and one with the H_g hydrogen atom H55. This hydrogen-bonding arrangement is consistent with the Lewis structural formula of the N_3^- ion (**5**), in which a formal negative charge is located at each terminal nitrogen atom.

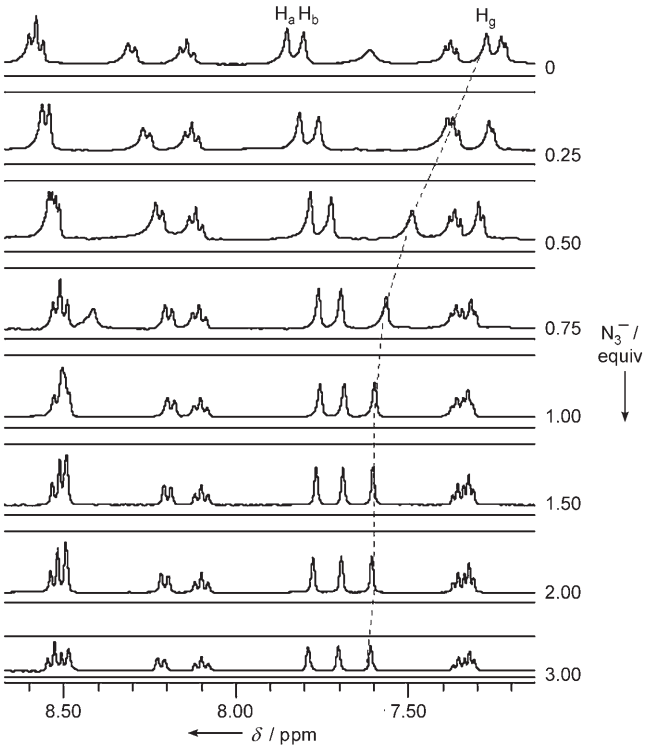

Figure 4. Titration of a 1.00×10^{-3} M solution of $[Fe^{II}(\mathbf{3})](PF_6)_5$ in CD_3CN with NaN_3 in CD_3OD, monitored by ^1H NMR spectroscopy: aromatic regions of spectra recorded over the course of the titration.

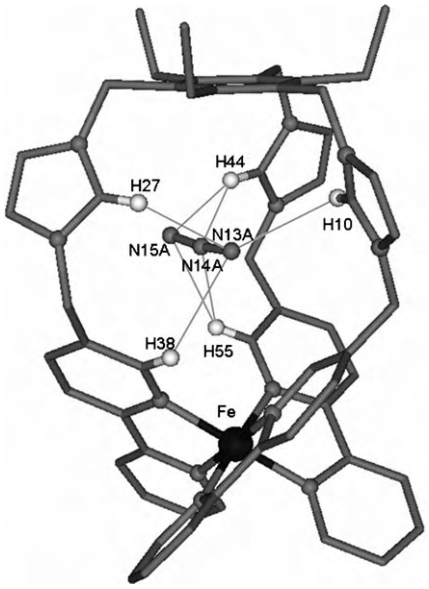

Figure 5. Molecular structure of the $[Fe^{II}(\mathbf{3})\cdots N_3]^{4+}$ complex with the N_3^- ion in one of the two disordered orientations. Only hydrogen atoms involved in hydrogen bonds (thin lines) with the anion are shown. Selected interatomic contacts [Å]: N13A···H10 2.707(5), N13A···H38 2.733(5), N13A···H27 2.598(5), N14A···H44 2.571(6), N14A···H55 2.711(5), N15A···H44 2.155(5), N15A···H55 2.579.

 © 2006 Wiley-VCH Verlag GmbH & Co. KGaA, Weinheim

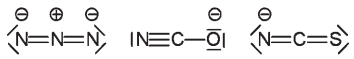

5 6 7

However, the central nitrogen atom of the N_3^- ion is also involved in the hydrogen-bond network: N14A interacts with H44 and H55 (which produce bifurcate hydrogen bonds). Interestingly, a plot of the molecular electrostatic potential (MEP) onto the molecular isodensity surface (at 0.002 e Å^{-3}) of the N_3^- ion, obtained from an ab initio calculation (at the HF/6-311G* level), demonstrates that a negative electrostatic potential is distributed over the whole surface of the ion, even if the central nitrogen atom is distinctly less negative (see Supporting Information). It is anticipated that the form illustrated in Figure 5 should correspond to the inclusion complex present in solution.

In the other form of the $[Fe^{II}(\mathbf{3})\cdots N_3]^{4+}$ complex, the molecular axis of the N_3^- ion is still normal to the line connecting the centroid of the 1,3,5-triethylbenzene platform and the Fe^{II} center, but the molecule is displaced toward the outside of the cavity (see Supporting Information). The N_3^- ion is bound to the receptor through only three hydrogen bonds, but one terminal nitrogen atom protrudes outside the cavity just enough to form a hydrogen bond with a water molecule. This water molecule plays a pivotal role in the solid state; it bridges two N_3^- ions belonging to different complexes through hydrogen bonds and, thus, directs the self-assembly of the complexes into dimers. It is assumed that this dimeric species is formed only in the solid state, whereas the structure illustrated in Figure 5 better reflects the binding arrangement of the inclusion complex in solution. The stability of the monomeric form is ascribed to the multipoint hydrogen bonds established by all of the nitrogen atoms of the anion with C–H fragments of the receptor.

In spectrophotometric titrations of solutions of $[Fe^{II}(\mathbf{3})]^{5+}$ in MeCN/H_2O (4:1 v/v) with the rodlike anions NCO^- (**6**) and NCS^- (**7**), the formation of 1:1 inclusion complexes with association constants $\log K = 4.2 \pm 0.1$ and 4.09 ± 0.02, respectively, was ascertained. The lower affinity of the NCO^- and NCS^- ions toward the $[Fe^{II}(\mathbf{3})]^{5+}$ receptor, compared to the N_3^- ion, in absence of definite structural details, can be tentatively ascribed to the fact that the formal negative charge in these two anions is not symmetrically distributed over the two terminal atoms, as it is in the N_3^- ion. Indeed, an asymmetric distribution of the electrostatic potential of both anions was indicated by ab initio calculations (see Supporting Information). Such an asymmetric arrangement of the electrical charge could decrease anion tendencies to take full benefit of the coordinating properties of the receptor.

The symmetric encapsulation of an N_3^- ion by a bistren hexammonium receptor, with the formation of six N–H···N hydrogen bonds (three for each terminal nitrogen atom), was observed by Lehn and co-workers in the early days of anion coordination chemistry.[10] Positively charged cages capable of establishing hydrogen bonds with both N–H and C–H fragments have also been described.[11] On the other hand, an imidazolium-functionalized acyclic $[Ru^{II}(bpy)_3]^{2+}$ receptor has recently been investigated for anion sensing in aqueous MeCN.[12] Moreover, a triple-helicate complex containing terminal $\{Fe^{II}(bpy)_3\}^{2+}$ subunits and benzamide spacers has been shown to incorporate one Cl^- ion in solution by ^{1}H NMR spectroscopic titration experiments.[13]

This work has demonstrated that the C–H_c fragment of the imidazolium subunit is a powerful hydrogen-bond donor toward anions, even in aqueous media. It has also shown that the combination of a 1,3,5-trialkylbenzene platform and an $\{Fe^{II}(bpy)_3\}^{2+}$ subunit generates a versatile cavity for anion encapsulation. In particular, the coordination of the bpy nitrogen atoms to the d^6 metal center activates the proximate C–H_g fragments, which contribute to the unprecedented coordination of an anion by six C–H groups. The rodlike N_3^- ion profits to the largest extent from inclusion within the "spherical" cavity of the $[Fe^{II}(\mathbf{3})]^{5+}$ receptor (giving an inclusion constant 80 times larger than that observed for the spherical Cl^- ion), because of its inherent tendency to establish multipoint hydrogen bonds.

From another point of view, the high stability of the investigated complexes could be ascribed to the occurrence of strong electrostatic interactions between the charged $[Fe^{II}(\mathbf{3})]^{5+}$ receptor and the X^- anion: short H···X^- distances, as well as significant shifts in the signals of the H_a,H_b, and H_g hydrogen atoms in the ^{1}H NMR spectra, would result from the close proximity to the anion imposed by the strictly delimited space. However, even if purely electrostatic interactions, enhanced by space restrictions, contribute to the high solution stabilities of the investigated complexes, it seems that hydrogen bonding also plays a major role. In fact, the crystal structures reveal that the included anions lie at a relatively large distance from the metal center (Fe···Br^- 4.76 Å, Fe···centroid(N_3^-) 4.57 Å), compared to distances of 2.6–2.7 Å from the C–H hydrogen atoms. Moreover, the fact that the N_3^- ion forms a distinctly more stable complex than the NCO^- and NCS^- ions suggests that the charge distribution on the anion plays a significant role in complex formation, which points to a directional interaction, that is, hydrogen bonding.

Finally, it should be noted that systems such as $[Fe^{II}(\mathbf{3})]^{5+}$ offer the unique possibility of controlling the reactivity of a d^6 metal center with a close (and caged) anion. This possibility would be especially interesting if a photoactive $\{Ru^{II}(bpy)_3\}^{2+}$ capping subunit were combined with a caged anion with a tendency to undergo oxidation or reduction. We are currently studying this prospect.

Experimental Section

The experimental details can be found in the Supporting Information, this includes details of the syntheses of **3**-$(PF_6)_3$ and $[Fe^{II}(\mathbf{3})](PF_6)_5$, crystallographic data for $[Fe^{II}(\mathbf{3})\cdots Br](PF_6)_4\cdot 2\,H_2O\cdot MeCN$ and $[Fe^{II}(\mathbf{3})\cdots N_3](PF_6)_4\cdot 1.5\,H_2O\cdot 3\,MeCN$, and ab initio calculations on the N_3^-, NCO^-, and NCS^- ions.

Received: June 29, 2006
Revised: July 14, 2006
Published online: September 20, 2006

Keywords: anion binding · hydrogen bonds · iron · N ligands · receptors

 © 2006 Wiley-VCH Verlag GmbH & Co. KGaA, Weinheim

[1] a) V. Amendola, D. Esteban-Gómez, L. Fabbrizzi, M. Licchelli, *Acc. Chem. Res.* **2006**, *39*, 343 – 353; b) K. Bowman-James, *Acc. Chem. Res.* **2005**, *38*, 671 – 678; c) R. Martínez-Máñez, F. Sancenón, *Chem. Rev.* **2003**, *103*, 4419 – 4476.
[2] J. Yoon, S. K. Kim, N. J. Singh, K. S. Kim, *Chem. Soc. Rev.* **2006**, *35*, 355 – 360.
[3] K. Sato, S. Arai, T. Yamagishi, *Tetrahedron Lett.* **1999**, *40*, 5219 – 5222.
[4] H. Ihm, S. Yun, H. G. Kim, J. K. Kim, K. S. Kim, *Org. Lett.* **2002**, *4*, 2897 – 2900.
[5] J. W. Steed, *Chem. Commun.* **2006**, 2637 – 2649.
[6] a) M. V. Baker, M. J. Bosnich, C. C. Williams, B. W. Skelton, A. H. White, *Aust. J. Chem.* **1999**, *52*, 823 – 825; Y. Yuan, H. Zhou, Z. Jiang, J. Yan, R. Xie, *Acta Crystallogr. Sect. C* **2000**, *56*, e34 – e35.
[7] C. Frassineti, S. Ghelli, P. Gans, A. Sabatini, M. S. Moruzzi, A. Vacca, *Anal. Biochem.* **1995**, *231*, 374 – 382.
[8] C. R. Bondy, P. A. Gale, S. J. Loeb, *J. Am. Chem. Soc.* **2004**, *126*, 5030 – 5031.
[9] S. O. Kang, D. Powell, K. Bowman-James, *J. Am. Chem. Soc.* **2003**, *125*, 10152 – 10153.
[10] B. Dietrich, J. Guilhem, J.-M. Lehn, C. Pascard, E. Sonveaux, *Helv. Chim. Acta* **1984**, *67*, 91 – 104.
[11] C. A. Ilioudis, D. A. Tocher, J. W. Steed, *J. Am. Chem. Soc.* **2004**, *126*, 12395 – 12402.
[12] M. S. Vickers, K. S. Martindale, P. D. Beer, *J. Mater. Chem.* **2005**, *15*, 2784 – 2790.
[13] S. Goetz, P. E. Kruger, *Dalton Trans.* **2006**, 1277 – 1284.

 © 2006 Wiley-VCH Verlag GmbH & Co. KGaA, Weinheim

synthetic organic chemistry is relatively scarce, and the few reported examples include the functionalization of fullerenes,[2a] the reductive benzylation of malonitrile,[2b] the preparation of phosphorus ylides,[3] the protection of amines,[4] and Heck-type cross-coupling reactions.[5] The latter transformation caught our attention as it represents a scalable metal catalysis under solvent-free reaction conditions.[6] Utilizing otherwise cheap and simple starting materials, it allows a significant decrease in the amount of harmful organic reagents, thus leading to an improved and benign chemical synthesis.

As impressive advances have recently been achieved in asymmetric organocatalysis[7] and with the vision that such metal-free reactions could benefit from the inherent solvent-free conditions of the ball-milling technology, we initiated a program that studies a combination of both approaches.

The alkaloid-mediated asymmetric opening of a cyclic *meso* anhydride was studied as the initial organocatalytic test reaction in the ball mill (Scheme 1).[8] Usually this reaction is

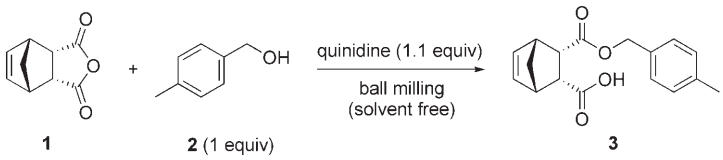

Scheme 1. Alkaloid-mediated asymmetric opening of a cyclic *meso* anhydride.

performed at low temperatures (e.g., −60 °C) in an organic solvent, such as toluene or toluene/carbon tetrachloride mixtures, with methanol or benzyl alcohol as the nucleophile; products with high enantiomeric excess (up to 99 % *ee*) are formed after 24–48 hours in almost quantitative yields. The solvent-free variant was performed in a commercially available planetary micromill with two 45-mL grinding bowls containing 5-mm diameter balls, both composed of chemically inert and nonabrasive zirconium oxide. To allow comparison with previous results obtained in solution, structurally related, yet solid, starting materials (anhydride **1** and *p*-methylbenzyl alcohol (**2**) in combination with quinidine) were chosen. To prevent "overheating" of the reaction mixture, a milling cycle with a rotational speed of 250 rpm for 25 min followed by a 5-min cooling pause (to be repeated for 24–36 h until full consumption of the educts) was selected.[9] Under those conditions, the following observations were made: 1) The solvent-free asymmetric anhydride opening proceeded well and afforded hemiester **3** in high yield (91 %). 2) An enantioselective excess of 61 % *ee* was achieved, which compares well with reactions performed in solution at comparable temperatures (ambient and higher). 3) Whereas the reaction in solution generally requires three equivalents of the nucleophile to achieve high conversion after a reasonable reaction time, the ball-milling conditions allow the amount of this starting material to be lowered to one equivalent without significantly affecting the yield. As a consequence, a tedious extractive workup can be avoided and a simple acid wash to remove the alkaloid yields the hemiester in high purity.[10]

Organocatalysis

DOI: 10.1002/anie.200602820

Solvent-Free Asymmetric Organocatalysis in a Ball Mill**

*Belén Rodríguez, Toni Rantanen, and Carsten Bolm**

Ball milling is a mechanochemical technique, which is widely applied to the grinding of minerals into fine particles and the preparation and modification of inorganic solids.[1] Its use in

[*] Dr. B. Rodríguez, M.Sc. T. Rantanen, Prof. Dr. C. Bolm
Institut für Organische Chemie
Rheinisch-Westfälische Technische Hochschule Aachen
Landoltweg 1, 52056 Aachen (Germany)
Fax: (+49) 241-809-2391
E-mail: carsten.bolm@oc.rwth-aachen.de

[**] We are grateful to the Fonds der Chemischen Industrie and Deutsche Forschungsgemeinschaft (DFG) within the SPP 1179 ("Organocatalysis") for financial support. We also thank Dr. I. Schiffers for continuous support and Prof. Dr. H. Wotruba (Department of Mineral Processing, RWTH Aachen University) for stimulating discussions and the permission to use his ball-mill equipment in the initial phase of this study.

Supporting information for this article is available on the WWW under http://www.angewandte.org or from the author.

InterScience
© 2006 Wiley-VCH Verlag GmbH & Co. KGaA, Weinheim

Whereas these initial results served as proof of concept for the applicability of the ball-milling technology in metal-free asymmetrically mediated reactions, its potential in organocatalytic enantioselective processes (with substoichiometric amounts of an organocatalyst) still needed to be demonstrated. The proline-catalyzed intermolecular aldol reaction is a well-studied and efficient C–C bond-forming reaction, which proceeds via enamine intermediates generated in situ, thus affording products with high chemo- and stereoselectivity under very mild conditions.[11] Generally, it is conducted in highly polar solvents, such as dimethyl sulfoxide (DMSO).[12]

For the experiments in the ball mill, a 1.1:1 ratio of ketones **4** and aldehydes **5** in combination with 10 mol% of (*S*)-proline was used. All the reactants were ball milled, with a rotation speed of 250–400 rpm until the reaction was complete. The results are summarized in Table 1.

As shown in Table 1, the (solvent-free) ball-milling conditions allow a highly efficient catalysis to occur, and the use of simple (unmodified) (*S*)-proline leads to the formation of *anti*-aldol products with excellent stereoselectivities (up to >99% *ee*). A comparative study using conventional magnetic stirring revealed the beneficial effect of the ball milling. Although under those (solvent-free) conditions the aldol products were stereoselectively obtained in high yields as well, those reactions proceeded much more slowly, which indicates the advantage of the ball-milling technology.[13–15]

The generality of the organocatalytic aldol reaction in a ball mill was examined by varying the substrate combinations (Table 1). In reactions with cyclohexanone, aldehydes with electron-withdrawing substituents afforded products with high stereoselectivities in short reaction times (Table 1, entries 1–3). More electron-rich groups lowered both the reactivity and stereoselectivity (Table 1, entries 4 and 5). Cyclopentanone and acetone could also be used as keto components (Table 1, entries 6–8). In the former case, poor diastereoselectivities were observed, whereas the enantioselectivities were high (Table 1, >90–95% *ee*). In contrast, acetone afforded a product with only 56% *ee* (Table 1, entry 8). Note that the above-mentioned trends of the electronic effects and the dependence of the stereoselectivity on the substrate structure are analogous to those observed in aldol reactions under alternative reaction conditions (e.g., in organic or aqueous solvents and solvent-free conditions).[11,12]

In summary, ball milling has been used in solvent-free asymmetric organocatalysis for the first time. The mechanically induced desymmetrization of *meso* anhydrides mediated by quinidine leads to optically active hemiesters in high yields and with moderate enantioselectivities. Under the same conditions, a proline-catalyzed asymmetric aldol reaction proceed efficiently and *anti*-aldol products are formed with excellent diastereo- and enantioselectivities.

Table 1: Solvent-free enantioselective aldol reaction catalyzed by (*S*)-proline under ball-milling conditions.[a]

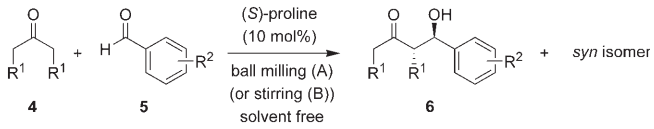

4 **5** **6**

Entry	Product	Method[b]	*t* [h]	Yield [%][c]	*anti*/*syn*[d]	*ee* [%][e]
1	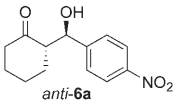 *anti*-**6a**	A	5.5	99	89:11	94
		B	96	98	87:13	94
2	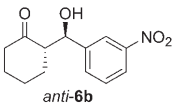 *anti*-**6b**	A	7	94	88:12	>99
		B	16	89 (10)	82:18	98
3	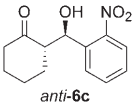 *anti*-**6c**	A	7	97	93:7	97
		B	36	89	91:9	97
4	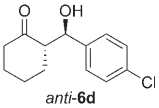 *anti*-**6d**	A	20	87 (10)	74:26	75
		B	72	85 (9)	78:22	67
5	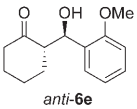 *anti*-**6e**	A	36	65 (25)	66:34	63
		B	96	64 (26)	71:29	67
6	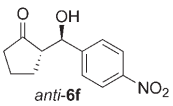 *anti*-**6f**	A	5	53	57:43	95
		B	24	90	52:48	87
7	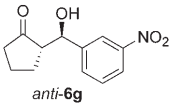 *anti*-**6g**	A	5	93	50:50	90
		B	36	93	46:54	75
8	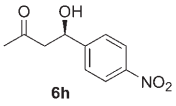 **6h**	A[f]	19	73	–	56
		B	36	69	–	54

[a] Reaction conditions: ketone **4** (2.2 mmol), aldehyde **5** (2.0 mmol), and (*S*)-proline (0.2 mmol). [b] Method A: the grinding bowl containing the reaction mixture was rotated in the ball mill at a rotation speed of 250–400 rpm (see Experimental Section for details). Method B: the reaction mixture was stirred at room temperature using conventional magnetic stirring. [c] Combined yield of the isolated diastereomers. The data in parentheses indicate the amounts of recovered aldehyde. [d] Determined by ^{1}H NMR spectroscopic analysis of the crude product. [e] Determined by chiral-phase HPLC analysis of the *anti* isomer. [f] Acetone (4.0 mmol, 2.0 equiv) was employed.

Experimental Section

General procedure for the anhydride opening in the ball mill (Fritsch Planetary Micro Mill model "Pulverisette 7"): A ball-mill vessel was charged with 60 zirconium oxide balls, the anhy-

 © 2006 Wiley-VCH Verlag GmbH & Co. KGaA, Weinheim

dride (1 mmol), the alkaloid (1.1 equiv of quinine or quinidine; 0.1 equiv of hydroquinone anthraquinone-1,4-diyl diether ($(DHQ)_2AQN$), and the alcohol (1.0 equiv). The vessel was closed, and the milling was started (milling time: 24–36 h at 250 rpm; sequential intervals of 25-min milling followed by a 5-min pause).[9] After completion of the reaction, the mixture was carefully washed with 2 N HCl and transferred into a separation funnel using EtOAc. The mixture was extracted three times with EtOAc, and the organic fractions were combined and dried ($MgSO_4$). The solvent was evaporated and if required, the product was purified by flash chromatography.

General procedure for the proline-catalyzed solvent-free aldol reaction: A reaction vessel was charged with aldehyde **5** (2.0 mmol, 1.0 equiv), ketone **4** (2.2 mmol, 1.1 equiv), and (*S*)-proline (23 mg, 0.2 mmol, 0.1 equiv). Stirring was either started in a grinding bowl using the ball mill with a rotation speed of 250–400 rpm (Table 1, method A), or in a round-bottomed flask using a conventional magnetic stirring bar (method B). After an appropriate reaction time, the crude product was washed off the reaction vessel with Et_2O (4 × 40 mL), and the combined organic fractions were filtered and concentrated in vacuo. The diastereoselectivity of the reaction was determined by ^1H NMR spectroscopic analysis of the crude product. Purification by flash chromatography on silica gel (pentane/EtOAc, 100:0→80:20) afforded the pure aldol product **6a–h** in the yields and enantioselectivities reported in Table 1. The identity and purity of the products were confirmed by ^1H and ^{13}C NMR spectroscopic analysis (see Supporting Information for full details).

Received: July 14, 2006
Published online: September 26, 2006

Keywords: aldol reaction · anhydrides · ball mill · organocatalysis · solvent-free reactions

[1] a) G. Kaupp, M. R. Naimi-Jamal, H. Ren, H. Zoz in *Advanced Technologies Based on Self-Propogating and Mechanochemical Reactions for Environmental Protection* (Eds.: G. Cao, F. Delogu, R. Orrù), Research Signpost, Kerala, **2003**, pp. 83–100; b) S. Kipp, V. Sepelák, K. D. Becker, *Chem Unsere Zeit* **2005**, *39*, 384–392.

[2] a) K. Komatsu, *Top. Curr. Chem.* **2005**, *254*, 185–206; b) Z. Zhang, J. Gao, J.-J. Xia, G.-W. Wang, *Org. Biomol. Chem.* **2005**, *3*, 1617–1619.

[3] a) V. P. Balema, J. W. Wiench, M. Pruski, V. K. Pecharsky, *J. Am. Chem. Soc.* **2002**, *124*, 6244–6245.

[4] G. Kaupp, M. R. Naimi-Jamal, V. Stepanenko, *Chem. Eur. J.* **2003**, *9*, 4156–4160.

[5] a) E. Tullberg, D. Peters, T. Frejd, *J. Organomet. Chem.* **2004**, *689*, 3778–3781; b) E. Tullberg, F. Schacher, D. Peters, T. Frejd, *Synthesis* **2006**, 1183–1189.

[6] For an overview on solvent-free organic reactions, see: a) G. W. Cave, C. L. Raston, J. L. Scott, *Chem. Commun.* **2001**, 2159–2169; b) K. Tanaka, *Solvent-Free Organic Synthesis*, Wiley-VCH, Weinheim, **2003**; for organic solid-state reactions, see: c) G. Kaupp, J. Schmeyers, J. Boy, *J. Prakt. Chem.* **2000**, *342*, 269–280; d) G. Kaupp, *Top. Curr. Chem.* **2005**, *254*, 95–183.

[7] For some recent reviews on enantioselective organocatalysis, see: a) A. Berkessel, H. Gröger, *Asymmetric Organocatalysis*, Wiley-VCH, Weinheim, **2005**; b) J. Seayad, B. List, *Org. Biomol. Chem.* **2005**, *3*, 719–724; c) P. M. Pihko, *Angew. Chem.* **2006**, *118*, 558–561; *Angew. Chem. Int. Ed.* **2006**, *45*, 544–547; d) B. List, *Chem. Commun.* **2006**, 819–824.

[8] a) C. Bolm, A. Gerlach, C. L. Dinter, *Synlett* **1999**, 195–196; b) C. Bolm, I. Schiffers, C. L. Dinter, A. Gerlach, *J. Org. Chem.* **2000**, *65*, 6984–6991; c) C. Bolm, I. Atodiresei, I. Schiffers, *Org. Synth.* **2005**, *82*, 120–125; d) see also: Y. Chen, P. McDaid, L. Deng, *Chem. Rev.* **2003**, *103*, 2965–2984.

[9] Decreasing the rotational speed or trying to perform the reaction in a round-bottom flask led to lower substrate conversions as a result of inefficient mixing. Ball milling without pause resulted in a product with a lower *ee* value, presumably as a result of the observed temperature increase. Use of more than one equivalent of quinidine had no positive effect on the enantioselectivity. Low substrate conversions were observed when the alkaloid amount was reduced to 10 mol% or $(DHQ)_2AQN$ was applied as the catalyst (compare protocols reported by Deng and co-workers in Ref. [8d]).

[10] Reactions between other *meso* anhydrides and alcohols led to analogous results; details of this study will be reported in due course.

[11] For some selected examples, see: a) B. List, R. A. Lerner, C. F. Barbas III, *J. Am. Chem. Soc.* **2000**, *122*, 2395–2396; b) P. M. Pihko, K. M. Laurikainen, A. Usano, A. I. Nyberg, J. A. Kaavi, *Tetrahedron* **2006**, *62*, 317–328; c) review: B. List, *Acc. Chem. Res.* **2004**, *37*, 548–557.

[12] For organocatalytic aldol reactions in water, see: a) Y. Hayashi, T. Sumiya, J. Takahashi, H. Gotoh, T. Urushima, M. Shoji, *Angew. Chem.* **2006**, *118*, 972–975; *Angew. Chem. Int. Ed.* **2006**, *45*, 958–961; b) N. Mase, Y. Nakai, N. Ohara, H. Yoda, K. Takabe, F. Tanaka, C. F. Barbas III, *J. Am. Chem. Soc.* **2006**, *128*, 734–735; c) for a general concept article, see: M. C. Pirrung, *Chem. Eur. J.* **2006**, *12*, 1312–1317, and references therein.

[13] Isolated examples of solvent-free organocatalytic aldol reactions can be found in references [11] and [12]. However, to the best of our knowledge, such approach has never been the focus of an intense study. It should also be noted that in these cases an excess of liquid ketone (≥ 5 equiv) appears essential for achieving both high yields and stereoselectivities.

[14] For interesting phenomena in this organocatalysis based on the solid–liquid phase behavior of proline, see: a) M. Klussmann, H. Iwamura, S. P. Mathew, D. H. Wells, Jr., U. Pandya, A. Armstrong, D. G. Blackmond, *Nature* **2006**, *441*, 621–623; b) Y. Hayashi, M. Matsuzawa, J. Yamaguchi, S. Yonehara, Y. Matsumoto, M. Shoji, D. Hashizume, H. Koshino, *Angew. Chem.* **2006**, *118*, 4709–4713; *Angew. Chem. Int. Ed.* **2006**, *45*, 4593–4597.

[15] This rate enhancement might also be due to the elevated temperature in the ball-mill experiment; for proline-catalyzed Mannich reactions, the significant temperature tolerance has recently been established: B. Rodríguez, C. Bolm, *J. Org. Chem.* **2006**, *71*, 2888–2891.

 © 2006 Wiley-VCH Verlag GmbH & Co. KGaA, Weinheim

Cover Picture

Thomas J. Taylor, Vladimir I. Bakhmutov, and François P. Gabbaï*

Alkane storage is generally problematic. Therefore, gases such as ethane, propane, and butane are often burned off in the flares of oil wells and petrochemical plants (cover picture background). A new solid consisting of a hexagonal array of columns and channels (cover picture foreground) reversibly adsorbs short-chain alkanes in its alkylated micropores. In their Communication on page 7030 ff., F. P. Gabbaï and co-workers report its preparation from $(HgC_6F_4)_3$ and 1,3,5-$(Me_3SiC{\equiv}C)_3C_6H_3$, and describe its sorption properties.

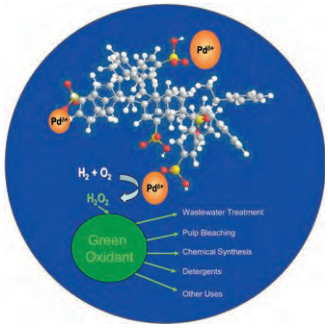

Hydrogen Peroxide Synthesis
The industrially established anthraquinone method for the synthesis of hydrogen peroxide suffers from high energy requirements and waste accumulation. The state of the art of alternative methods (e.g. direct synthesis) is discussed by J. L. G. Fierro and co-workers in their Review on page 6962 ff.

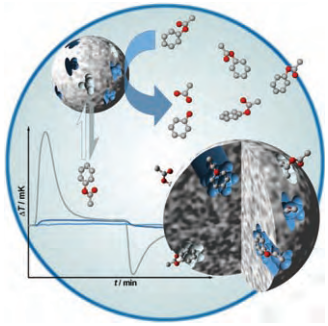

Molecular Recognition
In their Communication on page 6986 ff., F. W. Scheller et al. report that, on a bifunctional molecularly imprinted polymer, enzyme-like catalysis and antibody-analogue binding occur simultaneously and yet can be distinguished.

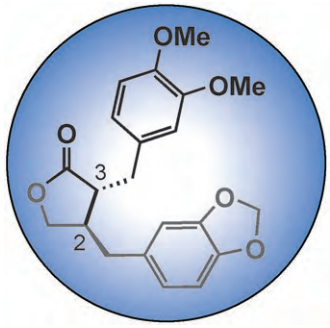

C–C Coupling
An intermolecular oxidative heterocoupling of imides and oxindoles to esters, ketones, and lactones which does not require a prefunctionalization step is described by P. S. Baran and M. P. DeMartino in their Communication on page 7083 ff.

Contents

The following Communications have been judged by at least two referees to be "very important papers" and will be published online at www.angewandte.org soon:

*N. Borho, Y. Xu**
Lock-and-Key Principle on a Microscopic Scale: The Case of the Propylene Oxide·Ethanol Complex

A. K. Sahoo, S. Mori, H. Shinokubo, A. Osuka**
Facile Peripheral Functionalization of Porphyrins through Pd-Catalyzed [3+2] Annulation with Alkynes

*M. Kanno, H. Kono, Y. Fujimura**
Control of π-Electron Rotation in Chiral Aromatic Molecules by Nonhelical Laser Pulses

M. Abe, E. Kubo, K. Nozaki, T. Matsuo, T. Hayashi*
An Extremely Long-Lived Singlet 4,4-Dimethoxy-3,5-diphenylpyrazolidine-3,5-diyl: A Notable Nitrogen Atom Effect on Intra- and Intermolecular Reactivity

E. E. Moushi, T. C. Stamatatos, W. Wernsdorfer, V. Nastopoulos, G. Christou, A. J. Tasiopoulos**
A New Family of 3D Coordination Polymers Composed of Mn_{19} Magnetic Units

W.-Y. Wong, C.-L. Ho, Z.-Q. Gao, B.-X. Mi, C.-H. Chen, K.-W. Cheah, Z. Lin*
Multifunctional Iridium Complexes Based on Carbazole Modules as Highly Efficient Electrophosphors

News

Nobel Prizes 2006: Life, the Universe, and Everything ——— **6948**

Books

Controlled Synthesis of Nanoparticles in Microheterogeneous Systems — Vincenzo Turco Liveri — *reviewed by G. B. Sukhorukov* ——— **6949**

Highlights

Asymmetric Synthesis

M. Braun,* T. Meier ——— **6952 – 6955**

Tsuji–Trost Allylic Alkylation with Ketone Enolates

The traditional restriction of the palladium-catalyzed allylation to stabilized carbanions has been overcome. Recent studies reveal that preformed "hard" enolates can serve as nucleophiles, and routes to novel stereoselective variants of the Tsuji–Trost method have thus been opened.

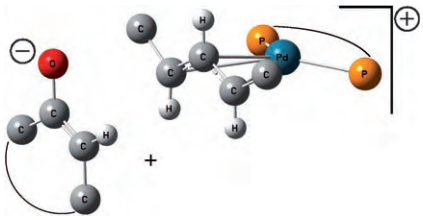

High Oxidation States

P. J. Chirik* ——— **6956 – 6959**

An Fe^{VI} Nitride: There Is Plenty of Room at the Top!

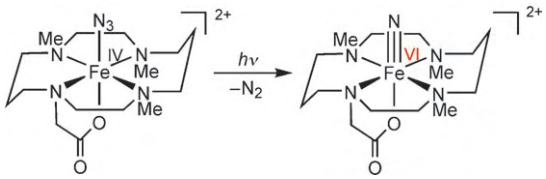

Movin' on up: Recent developments in the coordination chemistry of high-oxidation-state iron nitrido compounds are highlighted. Special attention is devoted to a newly synthesized Fe^{VI} compound (see scheme), only the second known example of a hexavalent iron complex.

InterScience

© 2006 Wiley-VCH Verlag GmbH & Co. KGaA, Weinheim

Reviews

The industrial synthesis of hydrogen peroxide by the anthraquinone process requires multiple unit operations and bears several disadvantages, such as the generation of by-products and significant energy requirements. Thus, the direct synthesis of hydrogen peroxide from H_2 and O_2 (for example, with the aid of a Pd catalyst, see scheme) is a chemically and technologically significant alternative.

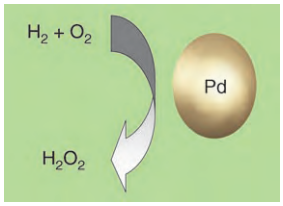

Green Chemistry

J. M. Campos-Martin, G. Blanco-Brieva, J. L. G. Fierro* _____ **6962 – 6984**

Hydrogen Peroxide Synthesis: An Outlook beyond the Anthraquinone Process

Communications

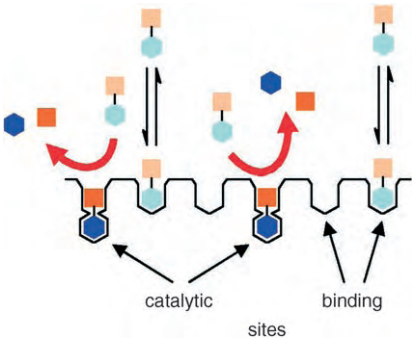

Binding or catalysis? Both can be distinguished with a molecularly imprinted polymer (MIP) by the different patterns of heat generation. The catalytically active sites, like in the corresponding enzyme, generate a steady-state temperature increase. Thus, enzyme-like catalysis and antibody-analogue binding are analyzed simultaneously in a bifunctional MIP for the first time (see scheme).

Molecular Recognition

K. Lettau, A. Warsinke, M. Katterle, B. Danielsson, F. W. Scheller* _____ **6984 – 6990**

A Bifunctional Molecularly Imprinted Polymer (MIP): Analysis of Binding and Catalysis by a Thermistor

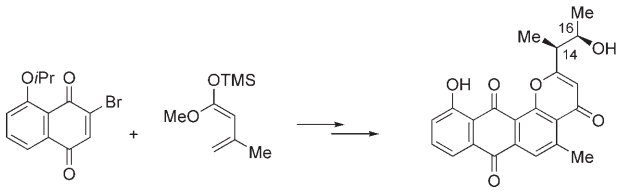

The antiherpetic anthrapyran antibiotic (14*S*,16*R*)-AH-1763 IIa (see right-hand structure) and its (14*R*,16*R*) diastereomer have been prepared in enantioselective total syntheses. The relative and absolute stereochemistry of the natural product was established as (14*R*,16*S*), and a general high-yielding, selective approach to anthrapyran antibiotics was developed.

Anthrapyran Natural Products

L. F. Tietze,* K. M. Gericke, R. R. Singidi _____ **6990 – 6993**

Enantioselective Total Synthesis and Structure Determination of the Antiherpetic Anthrapyran Antibiotic AH-1763 IIa

For the USA and Canada:
ANGEWANDTE CHEMIE International Edition (ISSN 1433-7851) is published weekly by Wiley-VCH PO Box 191161, D 69451 Weinheim, Germany. Air freight and mailing in the USA by Publications Expediting Inc. 200 Meacham Ave., Elmont, NY 11003. Periodicals postage paid at Jamaica NY 11431. US POSTMASTER: send address changes to *Angewandte Chemie*, Wiley-VCH, 111 River Street, Hoboken, NJ 07030. Annual subscription price for institutions: US$ 5685/5168 (valid for print and electronic / print or electronic delivery); for individuals who are personal members of a national chemical society prices are available on request. Postage and handling charges included. All prices are subject to local VAT/sales tax.

© 2006 Wiley-VCH Verlag GmbH & Co. KGaA, Weinheim

Contents

Tailored Nanorods

A. Ghicov, S. Aldabergenova, H. Tsuchyia, P. Schmuki* _____ **6993 – 6996**

TiO_2–Nb_2O_5 Nanotubes with Electrochemically Tunable Morphologies

Made to measure: TiO_2–Nb_2O_5 nanotubes are grown on a Ti–Nb alloy (Ti45Nb) by anodization in a fluoride-containing electrolyte (see micrograph), and their lengths and diameters can be controlled by adjusting the potential. The low rate of chemical dissolution of Nb_2O_5 in the electrolyte allows the formation of long nanotubes with regular morphology.

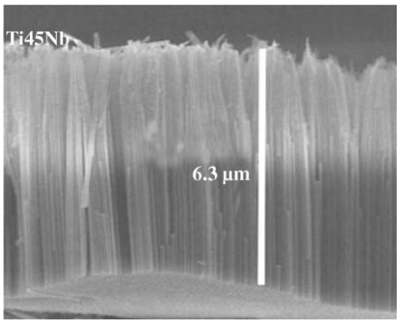

Silver Alkoxides and Silyl Oxides

A. Reisinger, D. Himmel, I. Krossing* _____ **6997 – 7000**

$AgOC(CF_3)_3$ and $AgOSiiPr_3$—Synthesis and Characterization of a Donor-Free Silver(I) Alkoxide and Silyl Oxide

Over 30 years after the first successful syntheses of Cu^I alkoxides and silyl oxides, the first homologous Ag^I compounds were synthesized and characterized (see scheme). $AgOC(CF_3)_3$ was furthermore found to be a promising precursor for chemical vapor deposition processes and the deposition of AgF.

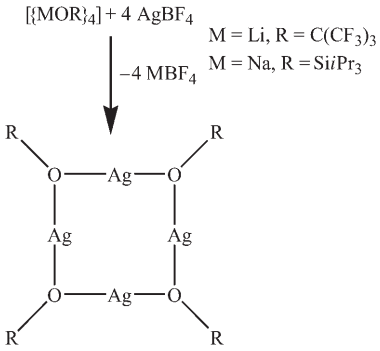

Microreactors

O. Flögel, J. D. C. Codée, D. Seebach, P. H. Seeberger* _____ **7000 – 7003**

Microreactor Synthesis of β-Peptides

Taming the insoluble: The reaction parameters of a β-peptide synthesis were optimized using only small amounts of reagents in a silicon microreactor (see picture). The use of unusually high temperatures (up to 120 °C) reduces the reaction times. The insertion of a fluorous benzyl protecting group enhances the efficiency of the synthesis.

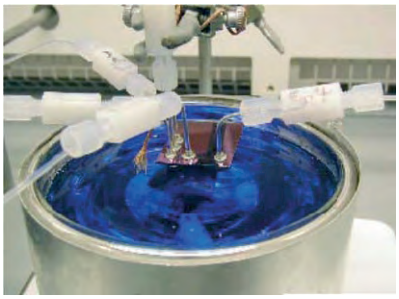

Enantioselective Reactions

A. Kirschner, U. T. Bornscheuer* _____ **7004 – 7006**

Kinetic Resolution of 4-Hydroxy-2-ketones Catalyzed by a Baeyer–Villiger Monooxygenase

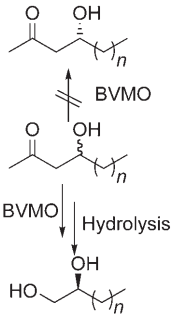

Two with one stroke: The kinetic resolution of racemic 4-hydroxy-2-ketones catalyzed by Baeyer–Villiger monooxygenase (BVMO) afforded not only the unreacted enantiomer in good optical purity but also allows access to optically active 1,2-diols (see scheme). Thus, this enzymatic approach provides a range of products in a single reaction accessible otherwise only from reactions with ketoreductases *and* hydrolases.

© 2006 Wiley-VCH Verlag GmbH & Co. KGaA, Weinheim

The smell of money and chemical weapons: The perplexing metallic odor from touching iron tools or coins (see picture) is a type of human body odor linked to the decomposition of skin peroxides. Fe^{2+} ion containing rust, drinking water, and blood all cause a similar metallic odor. Another "garlic" metallic odor, that of phosphorus-alloyed iron under acid attack, is caused by organophosphines, including C–P compounds which are monitored under the Chemical Weapons Convention.

Iron

D. Glindemann,* A. Dietrich, H.-J. Staerk, P. Kuschk ——— **7006 – 7009**

The Two Odors of Iron when Touched or Pickled: (Skin) Carbonyl Compounds and Organophosphines

Secondary structures of biopolymers have a significant influence on their molecular interactions with surfaces. With the aid of machine learning through support vector regression, the retention of oligonucleotides was modeled in ion-pair reversed-phase chromatography with high prediction accuracy (see diagram).

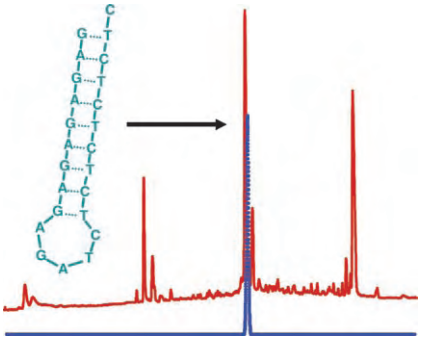

Bioinformatics

O. Kohlbacher, S. Quinten, M. Sturm, B. M. Mayr, C. G. Huber* — **7009 – 7012**

Structure–Activity Relationships in Chromatography: Retention Prediction of Oligonucleotides with Support Vector Regression

NMR dipolar couplings are a sensitive spectroscopic probe of the structure and dynamics of biomolecules. It is demonstrated that molecular alignment of intrinsically disordered proteins depends critically on electrostatic interactions, is scaled with the ionic strength of the solution, and can be predicted by using a simplified electrostatic model.

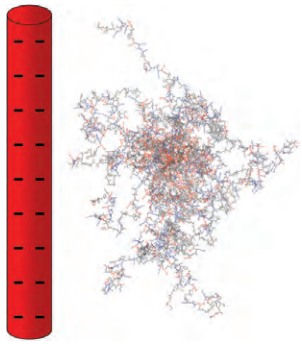

NMR Methods

L. Skora, M.-K. Cho, H.-Y. Kim, S. Becker, C. O. Fernandez, M. Blackledge, M. Zweckstetter* ——— **7012 – 7015**

Charge-Induced Molecular Alignment of Intrinsically Disordered Proteins

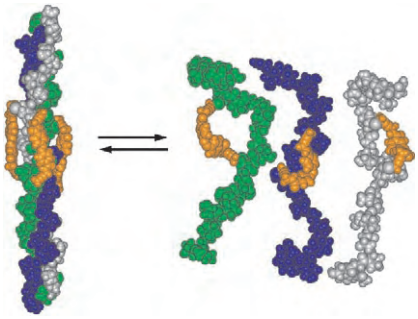

At the flick of a switch: Two side chains of a collagen peptide containing (2*S*,4*S*)-mercaptoproline at two defined positions are linked with a diiodo azobenzene derivative. With the *trans* isomer of the azobenzene clamp (orange), the peptide folds into the collagen triple helix (green, blue, gray), which unfolds upon irradiation at 330 nm. The light-controlled folding/unfolding processes are fully reversible, making this system well-suited for ultrafast spectroscopic analysis.

Collagen

U. Kusebauch, S. A. Cadamuro, H.-J. Musiol, M. O. Lenz, J. Wachtveitl, L. Moroder,* C. Renner ——— **7015 – 7018**

Photocontrolled Folding and Unfolding of a Collagen Triple Helix

© 2006 Wiley-VCH Verlag GmbH & Co. KGaA, Weinheim

Contents

Supramolecular Chemistry

S. J. Dalgarno, D. B. Bassil, S. A. Tucker,* J. L. Atwood* ——— **7019 – 7022**

Cocrystallization and Encapsulation of a Fluorophore with Hexameric Pyrogallol[4]arene Nanocapsules: Structural and Fluorescence Studies

Throwing light on encapsulation: The fluorescent probe molecule 4-[3-(9-anthryl)propyl]-*N*,*N*-dimethylaniline (C gray, N blue) crystallizes either *exo* or *endo* to the cavity of pyrogallol[4]arene hexamers (O red) and displays markedly different fluorescence emission behavior as a result. In the *exo* array, the guest alters the packing of the hexamer by forming channels through the extended structure in the solid state (see picture).

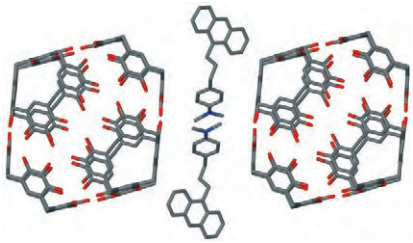

Metal Phosphate Clusters

R. Murugavel,* S. Kuppuswamy ——— **7022 – 7026**

Octameric and Decameric Aluminophosphates

Big Al: The title compounds are not only among the largest molecular aluminophosphates synthesized thus far, but are also rare polyhedral cages that contain AlO_4, AlO_5, and AlO_6 coordination geometries (see structure; red O, blue Al, pink P). The cores of these aluminophosphates represent new structural building units (SBUs) in zeolite chemistry.

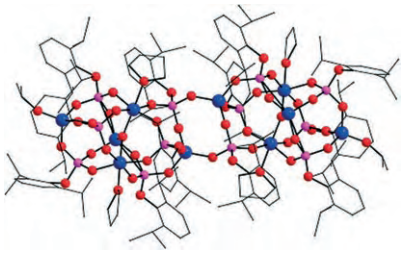

Supramolecular Chemistry

U. Rösch, S. Yao, R. Wortmann,* F. Würthner* ——— **7026 – 7030**

Fluorescent H-Aggregates of Merocyanine Dyes

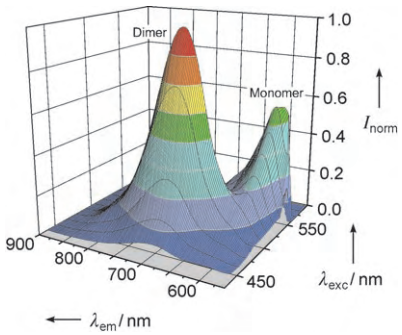

Unexpected lighting up: A slight rotational twist and rigidification of merocyanine dyes in a face-to-face π-π-stacked dimer aggregate resulted in an unexpected increase in the fluorescence intensity and lifetime (see graph). This result contrasts the common perception that the fluorescence of H-aggregates is strongly quenched, but can be rationalized within the concept of exciton theory.

Microporous Materials

T. J. Taylor, V. I. Bakhmutov, F. P. Gabbaï* ——— **7030 – 7033**

Hydrocarbon Uptake in the Alkylated Micropores of a Columnar Supramolecular Solid

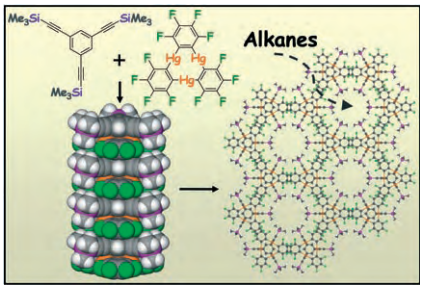

Neither Doric, Ionic, nor Corinthian! $(HgC_6F_4)_3$ interacts with 1,3,5-$(Me_3SiC{\equiv}C)_3C_6H_3$ to form columns with peripheral trimethylsilyl groups. These columns self-aggregate into a hexagonal solid containing pores lined by nonpolar methyl groups (see picture; Hg orange, Si purple, C gray, F green, H white), which can adsorb alkanes reversibly.

© 2006 Wiley-VCH Verlag GmbH & Co. KGaA, Weinheim

Packing a punch: The 2′-hydroxy group has a strong effect on the structural and dynamic properties of RNA and DNA, and governs the hydration of the RNA minor groove. The conformation of this group was previously investigated using NOEs and ^2J(C2′,OH2) and ^3J(C1′/C3′/H2′,OH2) couplings at low temperature in water. In the present study, ab initio calculations were used to derive appropriate Karplus-like equations for the couplings (see picture).

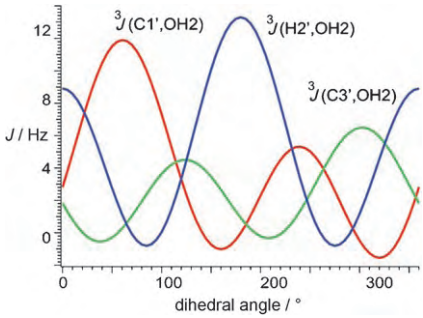

RNA Structures

J. Fohrer, U. Reinscheid, M. Hennig, T. Carlomagno* ——— **7033 – 7036**

Calculation of the Dependence of Homo- and Heteronuclear ^3J and ^2J Scalar Couplings for the Determination of the 2′-Hydroxy Conformation in RNA

One-electron reduction of a diphosphafulvenium dication gives the first stable diphosphafulvenium monoradical cation (see scheme). An X-ray crystal structure analysis, EPR measurements, and DFT calculations clearly show that reduction takes place at the exocyclic double bond and that the excess of electron density is stabilized by the two electron-withdrawing phosphonium groups (see SOMO; P orange, C dark gray, H light gray).

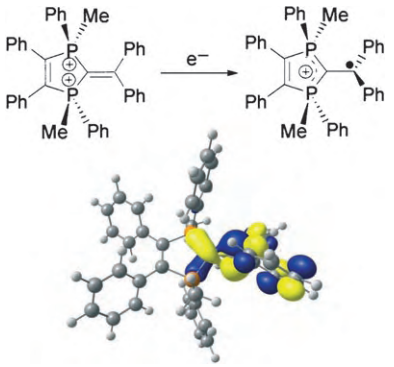

Persistent Radical Cations

F. Biaso, T. Cantat, N. Mézailles, L. Ricard, P. Le Floch,* M. Geoffroy* – **7036 – 7039**

Formation and Structure of a Stable Monoradical Cation by Reduction of a Diphosphafulvenium Salt

Two into one does go: A high-yield preparation of carbon nanotube (CNT)-encapsulated Sn–Sb nanorods that exhibit excellent lithium storage properties is described. The perceived growth process involves a) antimony tin oxide nanoparticles, b) growth of carbon nanotubes induced by molten Sn–Sb alloy, and c) capillary encapsulation of molten Sn–Sb into carbon-nanotube interior (see scheme).

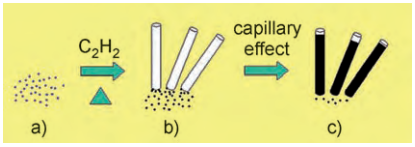

Lithium-Ion Batteries

Y. Wang, J. Y. Lee* ——— **7039 – 7042**

One-Step, Confined Growth of Bimetallic Tin–Antimony Nanorods in Carbon Nanotubes Grown In Situ for Reversible Li^+ Ion Storage

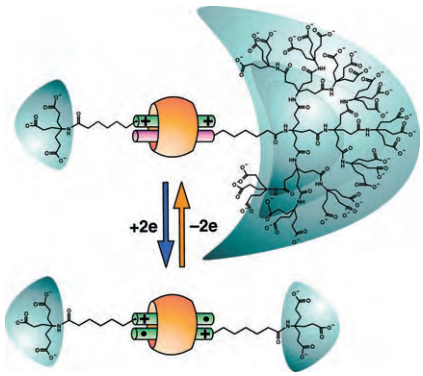

A host of possibilities: Cucurbit[8]uril acts as a host to mediate in a highly effective way the formation of charge-transfer complexes between dendrimers containing accessible π-donor and π-acceptor units (see scheme). Redox switching of the self-assembly affords control over the size of the predominant dendrimer assemblies.

Supramolecular Chemistry

W. Wang, A. E. Kaifer* ——— **7042 – 7046**

Electrochemical Switching and Size Selection in Cucurbit[8]uril-Mediated Dendrimer Self-Assembly

© 2006 Wiley-VCH Verlag GmbH & Co. KGaA, Weinheim

Contents

Diffusion

A. U. Nilekar, J. Greeley, M. Mavrikakis* ——— **7046 – 7049**

A Simple Rule of Thumb for Diffusion on Transition-Metal Surfaces

On the surface: Diffusion on transition-metal surfaces plays a key role in the transport of atomic and molecular species on catalytic surfaces. Density functional calculations show that there is a simple linear relation that allows the prediction of the diffusion barrier from the binding energy of the diffusing species on the respective metal surface.

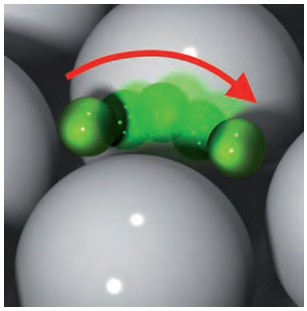

Catalyst Reactivation

C. Temple, A. Jabri, P. Crewdson, S. Gambarotta,* I. Korobkov, R. Duchateau* ——— **7050 – 7053**

The Question of the Cr Oxidation State in the {Cr(SNS)} Catalyst for Selective Ethylene Trimerization: An Unanticipated Re-Oxidation Pathway

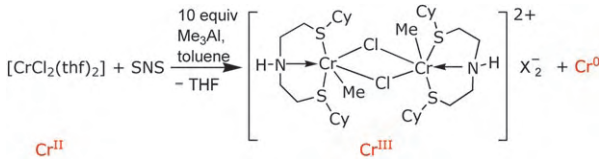

An unprecedented oxidation of chromium(II) by trimethylaluminum which, despite the reducing environment, forms a cationic organochromium(III) complex (see picture; SNS = $RSCH_2CH_2N(H)$-CH_2CH_2SR, Cy = cyclohexyl, X = $[Me_6Al_2Cl]$), provides a possible catalyst re-activation pathway.

Gas Separation

H. Guo, G. Zhu,* H. Li, X. Zou, X. Yin, W. Yang, S. Qiu,* R. Xu ——— **7053 – 7056**

Hierarchical Growth of Large-Scale Ordered Zeolite Silicalite-1 Membranes with High Permeability and Selectivity for Recycling CO_2

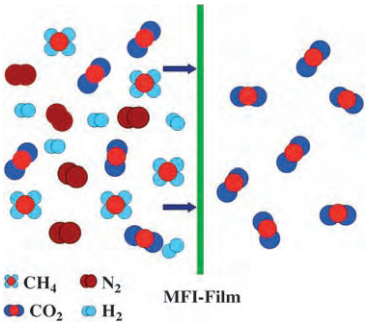

Another fine mesh you've got me into: A stainless-steel-net-imbedded silicalite-1 membrane (MFI film) is synthesized by a hydrothermal method. A hierarchical growth mechanism of the membrane formation is deduced. The MFI film has high thermal and mechanical stability, large-scale order, and exhibits high permeation flux and excellent permeation selectivity for CO_2 (see scheme).

Dinuclear Complexes

G. Feng, D. Natale, R. Prabaharan, J. C. Mareque-Rivas,* N. H. Williams* ——— **7056 – 7059**

Efficient Phosphodiester Binding and Cleavage by a Zn^{II} Complex Combining Hydrogen-Bonding Interactions and Double Lewis Acid Activation

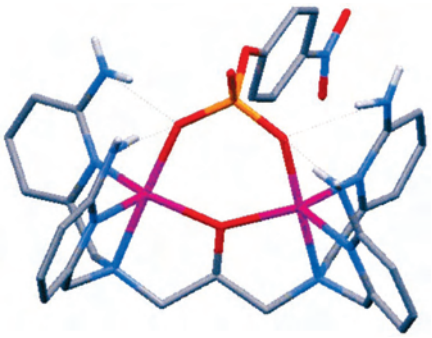

A combined attack: Hydrogen-bonding interactions with double Lewis acid activation generate a dinuclear Zn^{II} complex that is exceptionally effective for binding monoanionic phosphate diesters in water and for catalyzing phosphodiester transesterifications. The complex catalyzes the hydrolytic cleavage of RNA-like activated, artificial substrates and nonactivated, natural substrates with similar efficiencies.

© 2006 Wiley-VCH Verlag GmbH & Co. KGaA, Weinheim

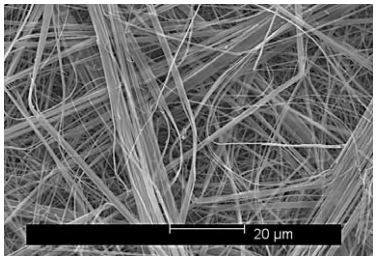

Super skinny: TaS_2 nanowires with a high aspect ratio (50000:1; see micrograph) are synthesized from the elements in a one-step reaction. The single-crystalline 2H-TaS_2 nanowires are superconducting, with a transition temperature ($T_c = 3.4$ K) that is enhanced compared to that of the bulk material ($T_c = 0.8$ K).

Superconductors

C. W. Dunnill, H. K. Edwards, P. D. Brown, D. H. Gregory* ——— **7060 – 7063**

Single-Step Synthesis and Surface-Assisted Growth of Superconducting TaS_2 Nanowires

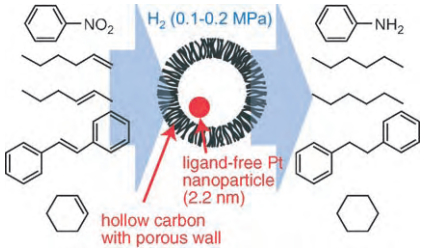

Wrapped up but still active: A platinum nanoparticle that is 2.2 nm in diameter and not coated by any stabilizing agent can be encapsulated in a hollow carbon shell 30–40 nm in diameter with a micro- to nanoporous wall structure (see picture). This encapsulated nanoparticle acts as an efficient and recyclable heterogeneous catalyst for various liquid-phase hydrogenation reactions.

Encapsulated Catalysts

S. Ikeda,* S. Ishino, T. Harada, N. Okamoto, T. Sakata, H. Mori, S. Kuwabata, T. Torimoto, M. Matsumura ——— **7063 – 7066**

Ligand-Free Platinum Nanoparticles Encapsulated in a Hollow Porous Carbon Shell as a Highly Active Heterogeneous Hydrogenation Catalyst

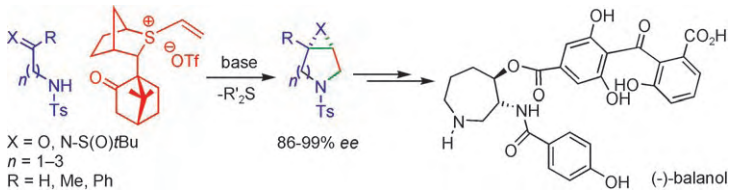

Lift your ylides: An asymmetric, epoxy-annulation reaction mediated by a vinyl sulfonium salt converts aminoaldehydes and -ketones into fused heterocyclic epoxides. The methodology was extended to an aziridine-annulation reaction, which was used to complete the shortest known formal synthesis of balanol (see scheme, Ts = toluene-*p*-sulfonyl, Tf = trifluoromethanesulfonyl).

Annulation

M. G. Unthank, N. Hussain, V. K. Aggarwal* ——— **7066 – 7069**

The Use of Vinyl Sulfonium Salts in the Stereocontrolled Asymmetric Synthesis of Epoxide- and Aziridine-Fused Heterocycles: Application to the Synthesis of (−)-Balanol

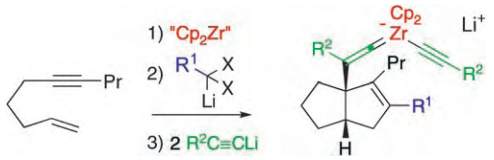

Sequential insertion of 1-lithio-1,1-dihaloalkanes and lithium acetylides into zirconacyclopentenes and -pentanes affords complex bicyclo[3.3.0]octenes and bicyclo[3.3.0]octanes through a novel rearrangement of a zirconium–alkynyl to a zirconate—alkenylidene species (see scheme; Cp = cyclopentadienyl).

Multicomponent Reactions

E. Thomas, S. Dixon, R. J. Whitby* ——— **7070 – 7072**

A Rearrangement to a Zirconium–Alkenylidene in the Insertion of Dihalocarbenoids and Acetylides into Zirconacycles

© 2006 Wiley-VCH Verlag GmbH & Co. KGaA, Weinheim

Contents

Natural Products

W. H. Kim, S. K. Hong, S. M. Lim, M.-A. Ju, S. K. Jung, Y. W. Kim, J. H. Jung, M. S. Kwon, E. Lee* ——— **7072 – 7075**

Total Synthesis of IKD-8344

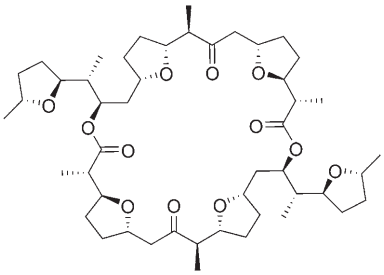

Complete construction: The total synthesis of IKD-8344, a novel 28-membered ring macrodiolide antibiotic (see structure), was accomplished by employing Williamson ether synthesis, β-alkoxymethacrylate radical cyclization, and Yamaguchi lactonization reactions. This synthesis is another example of the application of β-alkoxymethacrylate radical cyclization reactions for the stereoselective construction of complex oxacyclic natural products.

Surface Chemistry

X. Deng, T. A. Baker, C. M. Friend* ——— **7075 – 7078**

A Pathway for NH Addition to Styrene Promoted by Gold

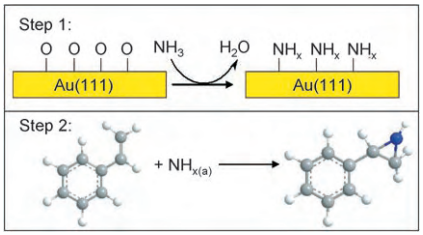

Going for gold! The synthesis of aziridines using heterogeneous gold catalysts has an unanticipated potential. Chemisorbed atomic oxygen is used to activate ammonia, producing NH bound to the gold surface (see scheme). Addition of NH across the double bond of styrene gave 2-phenylaziridine on a single-crystal Au(111) surface.

Heterogeneous Catalysis

R. Martín, M. Rodríguez Rivero, S. L. Buchwald* ——— **7079 – 7082**

Domino Cu-Catalyzed C–N Coupling/Hydroamidation: A Highly Efficient Synthesis of Nitrogen Heterocycles

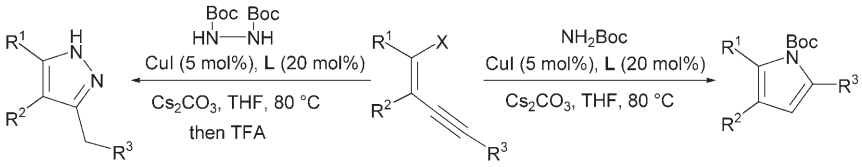

Working in tandem: Highly functionalized pyrroles and pyrazoles can be synthesized from a domino Cu-catalyzed C–N coupling/hydroamidation sequence. The scope and the generality of the method is noteworthy as a wide variety of substituents, either in the alkene or alkyne counterparts, are well tolerated.

Oxidative C–C Coupling

P. S. Baran,* M. P. DeMartino ——— **7083 – 7086**

Intermolecular Oxidative Enolate Heterocoupling

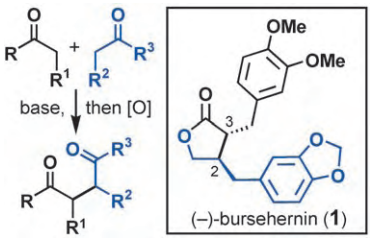

No priming necessary: The intermolecular oxidative heterocoupling of imides and oxindoles to esters, ketones, and lactones is shown for the first time to be synthetically viable. Strategic use of the initial oxidation state of the reactants allows for the excision of prefunctionalization steps (halogenation, enol-silane formation) and allows for the concise synthesis of unsymmetrical lignans, such as (–)-bursehernin (**1**).

© 2006 Wiley-VCH Verlag GmbH & Co. KGaA, Weinheim

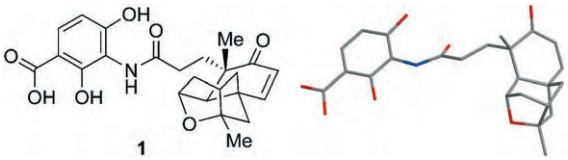

Beat the superbugs: The newly discovered antibiotic platensimycin (**1**) promises to combat current drug-resistant infections. The natural product shows potent activity against Gram-positive bacteria and contains a novel molecular architecture. The total synthesis of this intriguing natural product that opens the way to a variety of otherwise inaccessible analogues has now been achieved (calculated structure shown on the right).

Antibiotics

K. C. Nicolaou,* A. Li, D. J. Edmonds ——— **7086 – 7090**

Total Synthesis of Platensimycin

Supporting information on the www (see article for access details).

A video clip is available as Supporting Information on the www (see article for access details).

Sources

Product and Company Directory

You can start the entry for your company in "Sources" in any issue of ***Angewandte Chemie***.

If you would like more information, please do not hesitate to contact us.

Wiley-VCH Verlag – Advertising Department
Tel.: 0 62 01 - 60 65 65
Fax: 0 62 01 - 60 65 50
E-Mail: MSchulz@wiley-vch.de

Service

Keywords ——— ***7094***

Authors ——— ***7095***

Angewandte's Sister Journals ——— ***7092 – 7093***

Vacancies ——— ***7096***

Preview ——— ***7097***

RSS Feed

Journal content prior to print publication can be found online on our Early View page at www.angewandte.org. Stay updated on the latest journal content by registering for our free e-mail alerts at http://interscience.wiley.com/alerts.

Keep up with the latest research with our RSS feed, which provides the titles, authors, and the Digital Object Identifiers (DOIs) of Early View articles, including links to the full texts. RSS is an XML-based format for sharing and distributing web content. To receive the RSS feed, just click on the orange feed icon at www.angewandte.org, or visit http://interscience.wiley.com/rss for more information.

© 2006 Wiley-VCH Verlag GmbH & Co. KGaA, Weinheim

Awarded...

The announcement of the Nobel Prizes creates more excitement than any other occasion in the natural sciences. The prize money of 10 million Swedish kronor (US$ 1.4 million) for each discipline is certainly not the only reason for this…

Chemistry: R. D. Kornberg

The Royal Swedish Academy of Sciences has awarded this year's Nobel Prize in Chemistry to Roger D. Kornberg (Stanford School of Medicine, CA, USA; born 1947). Kornberg's work on the molecular basis of eukaryotic transcription is a key contribution to our understanding of how living cells synthesize proteins with the help of DNA and RNA. If transcription stops, an organism will soon die. Disruption of transcription leads to illnesses such as cancer, heart disease, and infections. Kornberg was able to use X-ray crystallography to elucidate the structure of RNA polymerase, the transcription enzyme responsible for ensuring that an exactly matching, complementary strand of RNA is produced from DNA. After a nucleotide is produced, a small helical section takes care of the further transport of the DNA strand to the next nucleotide. Kornberg and co-workers succeeded in capturing a snapshot of this process by leaving out a nucleotide from the surrounding solution. The reaction stopped because of a lack of supply, and they were able to crystallize the complex of polymerase, DNA, and half-finished RNA and determine its structure.

R. D. Kornberg

If the name Kornberg sounds familiar, that's because Roger's father Arthur Kornberg (also at Stanford University) received the 1959 Nobel Prize in Physiology or Medicine together with Severo Ochoa (New York University) for their works on the mechanisms of the synthesis of DNA and RNA.[1] The young Roger accompanied his father to Stockholm for the award ceremony. He later studied at Harvard University and completed his PhD in 1972 at Stanford. His undertook postdoctoral work in the group of Francis Crick (1962 Nobel Prize for the structure of DNA) at the Medical Research Council (MRC) in Cambridge (UK). In 1976, he became assistant professor at Harvard University and since 1978 has been the professor for structural biology at Stanford School of Medicine. The last unshared Nobel Prize in Chemistry was awarded to A. Zewail in 1999.

Medicine: A. Z. Fire and C. C. Mello

The Nobel Assembly at Karolinska Institutet (Stockholm, Sweden) awarded the 2006 Nobel Prize in Physiology or Medicine jointly to Andrew Z. Fire (Stanford University, USA; born 1959) and Craig C. Mello (University of Massachusetts, Worcester, USA; born 1960) for their discovery of RNA interference. RNA interference is of great importance for the regulation of gene expression and is a part of the defense against viral infection. Double-stranded RNA activates the process by which a gene with an identical genetic code to that of the double-stranded RNA is degraded.[2] The work of Fire and Mello was celebrated by the journal Science as breakthrough of the year 2002, and they also received the Wiley Prize in Biomedical Sciences 2003 together with T. Tuschl and D. Baulcombe.

A. Z. Fire

Fire studied mathematics at the University of California in Berkeley and received his PhD in biology in 1983 from the Massachusetts Institute of Technology. He undertook postdoctoral stays at MRC Cambridge with Nobel Prize laureate Sydney Brenner (Physiology or Medicine, 2002) and at the Carnegie Institution of Washington in Baltimore, MD (USA). In 1989 he became a professor at the Johns Hopkins University (also in Baltimore) before moving to the Stanford School of Medicine in 2003. Mello received a degree in biochemistry and a PhD in biology from Harvard University. He then worked at the Fred Hutchinson Cancer Research Center in Seattle, WA. Since 1994 he has been at the University of Massachusetts, where he held the chair for molecular medicine since 2003.

C. C. Mello

Physics: J. C. Mather and G. F. Smoot

The Nobel Prize in Physics this year has been awarded to the NASA researcher John C. Mather (born 1946) and the Berkeley professor George F. Smoot (born 1945) for their work on cosmic background radiation, which provided support for the Big Bang theory. The work was made possible by the COBE satellite, which was launched in 1989. The measurements showed that the background radiation in the microwave region has the form of blackbody radiation, and that it displays anisotropy in the range of a hundred-thousandth of a degree. These variations in temperature explain the aggregation of matter following the big bang.

Photos: Stanford University and Robert Carlin

[1] a) A. Kornberg, *Angew. Chem.* **1960**, *72*, 231–236, b) S. Ochoa , *Angew. Chem.* **1960**, *72*, 225–231.
[2] a) T. Tuschl, *ChemBioChem* **2001**, *2*, 239, b) U. Schepers, *RNA Interference in Practice*, Wiley-VCH, Weinheim, **2005**.

DOI: 10.1002/anie.200604075

WILEY InterScience DISCOVER SOMETHING GREAT
© 2006 Wiley-VCH Verlag GmbH & Co. KGaA, Weinheim

Asymmetric Synthesis

DOI: 10.1002/anie.200602169

Tsuji–Trost Allylic Alkylation with Ketone Enolates

Manfred Braun and Thorsten Meier*

Keywords:
chirality · homogeneous catalysis · palladium · stereoselectivity · substitutions

The palladium-catalyzed allylic substitution with carbon nucleophiles, first discovered by Tsuji and thoroughly developed by the research group of Trost, turns out to be a very fruitful and versatile method for carbon–carbon bond formations. In general, the reaction starts with an allylic substrate **1** (usually an acetate or carbonate) that, upon treatment with a suitable palladium(0) compound, forms a π-allyl complex **2** (Scheme 1). Thereby, the transition metal adopts the +2 oxidation state, and the allyl moiety becomes a strong carbon electrophile. In the subsequent reaction with the carbon nucleophile, the allylation products **3** are obtained under concomitant liberation of the noble metal in the oxidation state 0, thus closing the catalytic cycle.[1]

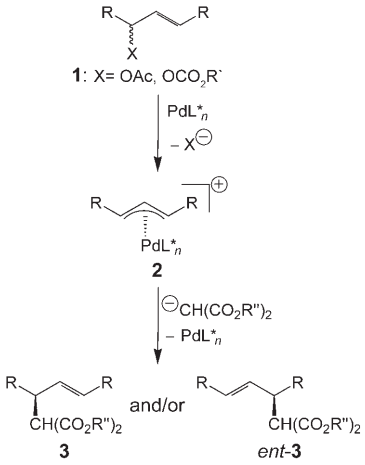

Scheme 1. "Standard" enantioselective version of the Tsuji–Trost allylation.

Various chiral ligands L* have been developed which direct the attack of the nucleophile to one of the diastereotopic termini in the π-allyl complex **2**, so that the alkenes **3** and *ent*-**3** can be obtained from racemic starting material **1** in an enantioselective manner. Moreover, solutions to the problem of regioisomer formation arising from substrates **1** with nonidentical residues R have been reported more recently.[2]

Despite the impressive progress this reaction has made since the 1970s, it has continued to suffer from a significant drawback: the limitation in the type of carbon nucleophile. Thus, "soft" carbanions derived from carbon acids with pK_a values lower than 20 were used almost exclusively, and the combination of malonates with diphenylallyl acetate **1** (R = Ph) became a kind of standard procedure in palladium-catalyzed allylations, particularly for evaluating the performance of chiral ligands L*. It is obvious that, in this combination, just one stereogenic center is formed in the allylic position. If, however, the formation of stereogenic centers in the homoallylic position ($R^2 \neq R^3$, $R^4 = H$) or in both the allylic and the homoallylic position ($R^2 \neq R^3$, $R^4 \neq H$) is the target, as outlined in the retrosynthetic synthesis for alkenyl ketones **4** (Scheme 2), the nucleophilic reagents of choice are preformed "hard" metal enolates **5**.

The chemistry of preformed enolates on the one hand and the Tsuji-Trost reaction on the other hand emerged and evolved at the same time, since the 1970s.[3] Surprisingly, however, only very few attempts were made to combine both concepts. It seems that,

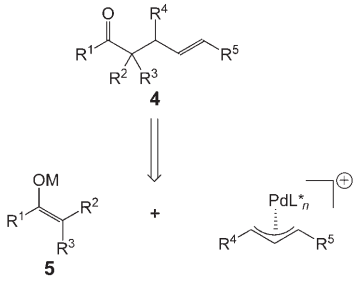

Scheme 2. Retrosynthesis of alkenyl ketones **4** based on preformed enolates **5** and allylpalladium complexes. R^1 = alkyl, aryl; R^2–R^5 = H, alkyl, aryl.

owing to early disappointing results, organic chemists avoided attempts to carry out palladium-catalyzed allylation reactions with preformed "hard" enolates. The few approaches did not have much success[4a] or remained unnoticed.[4b,c] Stereoselective variants of this transformation, in particular, had not been developed until the beginning of this decade.[5]

In 1999, the first enantioselective allylic alkylation of a nonstabilized ketone enolate was reported by Trost and Schroeder.[6a] Thus, the tin enolate **7b**, generated from 2-methyl tetralone (**6**), was submitted to a palladium-catalyzed allylation that was mediated by the C_2-symmetric ligand **8** (Scheme 3). Thereby, ketone (*R*)-**9** was obtained in 88% *ee* and 99% yield when the ligand (*S*,*S*)-**8**, which causes the allylpalladium intermediate to attack the enolate from its *Si* face, was used.

This stereochemical outcome is plausibly explained by the simplified "mnemonic" illustration of the C_2-symmetric ligand (*S*,*S*)-**8** in the lower portion of Scheme 3. It is quite clear that the disfavored topicity involves substantial steric hindrance. The protocol has been applied to different allylic sub-

[*] Prof. Dr. M. Braun, Dr. T. Meier
Institut für Organische Chemie und Makromolekulare Chemie I
Universität Düsseldorf
Universitätsstrasse 1
40225 Düsseldorf (Germany)
Fax: (+49) 211-81-15079
E-mail: braunm@uni-duesseldorf.de

InterScience
© 2006 Wiley-VCH Verlag GmbH & Co. KGaA, Weinheim

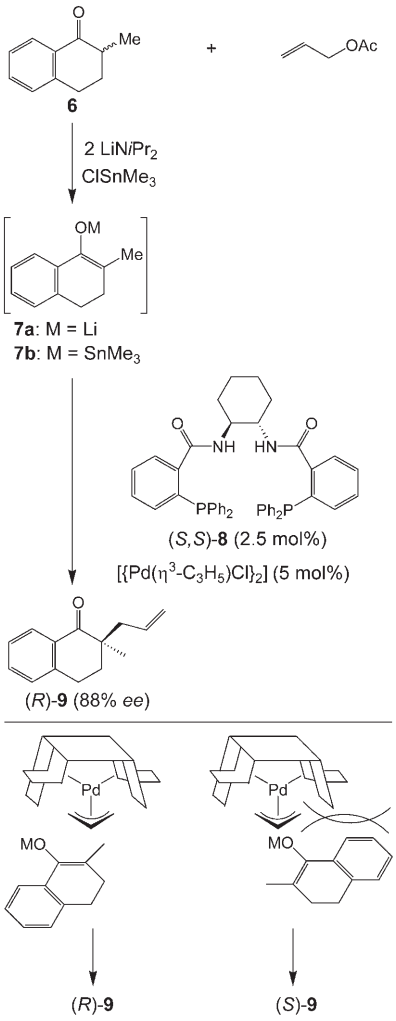

Scheme 3. Enantioselective allylation of 2-methyl tetralone (**6**) mediated by the C_2-symmetric ligand **8**.

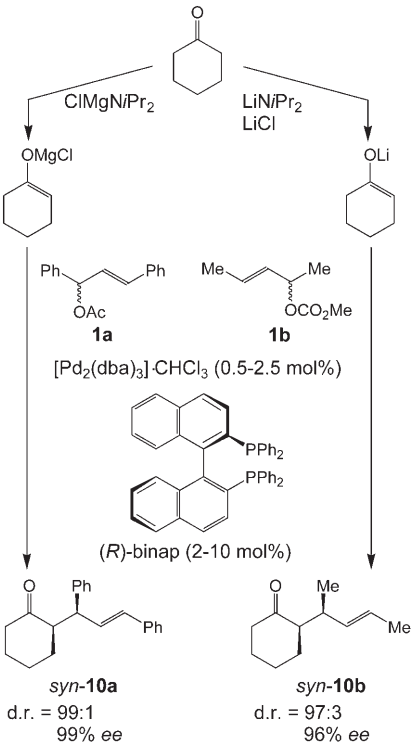

Scheme 4. Diastereo- and enantioselective allylation of cyclohexanone enolates.

strates as well as various six- and five-membered ketone rings.[6] In all cases, the carbonyl compounds featured an α-methyl substituent, thus avoiding a later racemization that would inevitably occur as a result of the excess of base (lithium diisopropylamide). Moreover, the ketones that were used did not contain hydrogen substituents in the α′ position so that double allylation was excluded. The research groups of Trost[6] as well as Hou and Dai[7a] were able to demonstrate that the enantioselective allylation of methyl tetralone **6** is also feasible through the lithium enolate **7a** by using different chiral ligands at the palladium center.

The first diastereoselective and enantioselective allylic alkylation of cyclohexanone was reported by us in 2000.[8] It turned out that the magnesium enolate gave the optimum results when the reaction with diphenylallyl acetate **1a** was mediated by the binap–palladium complex, as shown in Scheme 4. The *syn* diastereomer **10a** formed predominantly, and an enantiomeric excess of 99% *ee* resulted.

The reaction could be extended to the dimethyl-substituted analogue **1b**. In this case, a more reactive enolate was necessary because of the more sluggish electrophile. Thus, the combination of the lithium enolate and lithium chloride turned out to be the suitable reagent, thus leading to the formation of the allylation product **10b** in a *syn*/*anti* diastereomeric ratio of 97:3, whereby the predominant diastereomer formed in 96% *ee*.[9a] Lithium enolates of acyclic ketones have been found to be suitable nucleophiles for palladium-catalyzed allylic substitution reactions as well.[8] To obtain high stereoselectivity in the allylation process, control of the enolate geometry is necessary, and addition of silver salts is advantageous.[7b]

The research group of Hartwig recently presented a solution to the problem of regio- and enantioselective allylation of nonstabilized ketone enolates.[10] If the formation of the branched product **14** instead of the thermodynamically more stable linear product **15** is the target in nucleophilic substitutions on nonsymmetrically substituted allylic substrates like **12**, iridium rather than palladium complexes are preferential. Thus, enolsilanes **11** derived from aryl methylketones were allowed to react with carbonates **12** in the presence of catalysts that were generated from [{Ir(cod)Cl}$_2$] and several phosphoramidites, of which the C_2-symmetric ligand **13** gave optimum results. The reactive enolate was generated from the enolsilanes **11** by treatment with a mixture of cesium fluoride and zinc fluoride (Scheme 5). The branched products **14** were obtained predominantly, and their enantiomeric excesses ranged from 91 to 96% *ee* (ratio of regioisomers **14**/**15** between 85:15 and 99:1). Concerning the reactive nucleophile, it remains uncertain whether a cesium, zinc, or hypervalent silicon enolate plays that role.

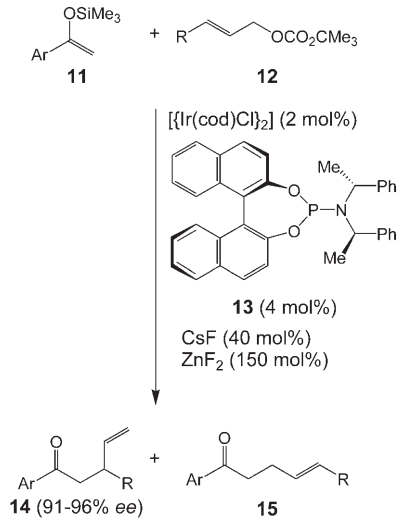

Scheme 5. Regio- and enantioselective iridium-catalyzed allylation of fluoride-activated enolsilanes **11**.

An elegant solution to the problem of the enantioselective allylic alkylation of nonstabilized enolates relies on their in situ generation. Thus, the research groups of Stoltz[11] and Trost[12] have independently shown that allyl enol carbonates can serve as suitable enolate precursors. The method, which has been

© 2006 Wiley-VCH Verlag GmbH & Co. KGaA, Weinheim

applied to various cyclic[11,12a,b] and acyclic[12c] ketones, is illustrated for the enantioselective allylation of 2-methylcyclohexanone in Scheme 6. Thus, treatment of the enol carbonate **16** with a chiral catalyst, generated from $[Pd_2(dba)_3]\cdot CHCl_3$ and phosphanes such as **8**, **20**, or **21**, leads to the formation of the allylated ketone **18** (up to 88% *ee*). Obviously, the allylpalladium complex is formed initially under liberation of the enol carbonate anion, which spontaneously undergoes decarboxylation. Through the advantage of CO_2 formation as a driving force of the reaction, the ion pair **17** is formed. The combination of the enolate anion and allylpalladium complex in **17** leads to the allylation product **18**. Crossover experiments have shown the intramolecular course of the reaction, so that only minor leakage from the caged contact ion pair occurs.[12a] On the other hand, a scrambling of the deuterium label was observed when selectively deuterated allyl enol carbonates were submitted to the palladium-mediated reaction, a result that led the authors to postulate a "discrete ketone enolate".[11b]

Another kind of precursor for the in situ generation of enolates are allyl β-keto esters, whereby the formation of carbon dioxide again serves as the driving force.[12b,13] As a representative of recently developed enantioselective variants,[11b,12b,13] the allylation of allyl β-ketoester **19**[12b] is outlined in Scheme 6.

A remarkable insight into the nature of the enolate species comes from the stereochemical outcome of the different allylation protocols. As shown in Scheme 3, the tin (and also the lithium) enolates **7** are attacked predominantly from the *Si* face when the reaction is mediated by the ligand (*S*,*S*)-**8**. This *lk* topicity is, however, reversed when the corresponding enol carbonate is used as a substrate. In this case, the allylpalladium species approaches the enolate in a *ul* manner from the *Si* face, provided that the *R*,*R*-configured ligands **8** or **20** are used. The opposite stereochemical outcome implies that different mechanisms are operating: on the one hand, a lithium or tin enolate reacts with an allylpalladium complex or, on the other hand, an enolate anion and allylpalladium cation combine in a caged pair **17**. For the allylation through β-ketoesters, a reductive elimination of the palladium center bound to the allyl moiety and the enolate oxygen atom has been proposed as the carbon–carbon bond-forming step.[12b]

At a glance, the enantioselective allylation of simple ketones[14] such as cyclohexanone appears to be rather facile. As there is no restriction, however, that prevents double allylation and particularly subsequent racemization of the product, the simplicity of the cyclohexanone substrate makes it the most challenging. Nevertheless, the allylation through the enol carbonate **22** yields allylcyclohexanone (*R*)-**23** in 78% *ee* when mediated by the ligand (*R*,*R*)-**20**. Moreover, we have recently been able to show that the simple lithium enolate of cyclohexanone can be allylated to give the ketone (*S*)-**23** in up to 98% *ee* (Scheme 7).[9b] A prerequisite to this reaction, which is mediated by the ligand (*S*)-**24**, is the presence of lithium chloride.[9a]

These results clearly demonstrate that the combination of allylpalladium and preformed enolate chemistry provides a new tool for synthetic chemists. The elaboration of this concept will be followed by applications in the syntheses of drugs and natural products. Thus, students in advanced chemistry courses should no longer be taught that the

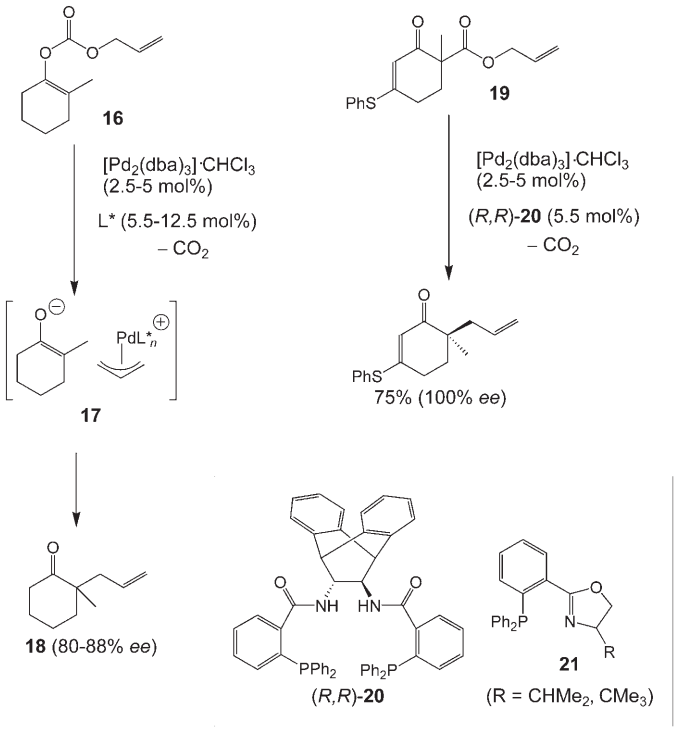

Scheme 6. Enantioselective allylation through in situ generation of enolates from enol carbonates and allyl β-keto esters. L* = (*R*,*R*)-**8**, (*R*,*R*)-**20**, (*R*)-**21**, or (*S*)-**21**.

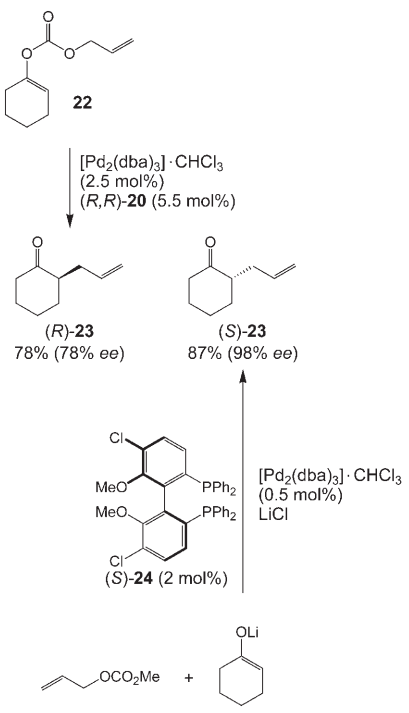

Scheme 7. Enantioselective allylations of cyclohexanone through enol carbonate and lithium enolate.

 © 2006 Wiley-VCH Verlag GmbH & Co. KGaA, Weinheim

Tsuji–Trost method is limited to stabilized carbanions.

Published online: October 9, 2006

[1] a) B. M. Trost, *Pure Appl. Chem.* **1981**, *53*, 2357; b) J. Tsuji, *Pure Appl. Chem.* **1982**, *54*, 197; c) B. M. Trost, T. R. Verhoeven in *Comprehensive Organometallic Chemistry, Vol. 8* (Eds.: G. Wilkinson, F. G. A. Stone, E. W. Abel), Pergamon, Oxford, **1982**, p. 799; d) J. A. Davies in *Comprehensive Organometallic Chemistry II, Vol. 9* (Eds.: E. W. Abel, F. G. A. Stone, G. Wilkinson), Pergamon, Oxford, **1995**, p. 323.

[2] Reviews: a) O. Reiser, *Angew. Chem.* **1993**, *105*, 576; *Angew. Chem. Int. Ed. Engl.* **1993**, *32*, 547; b) J. M. J. Williams, *Synlett* **1996**, 705; c) B. M. Trost, D. L. Van Vranken, *Chem. Rev.* **1996**, *96*, 395; d) G. Helmchen, *J. Organomet. Chem.* **1999**, *576*, 203; e) G. Helmchen, A. Pfaltz, *Acc. Chem. Res.* **2000**, *33*, 336; f) B. M. Trost, M. L. Crawley, *Chem. Rev.* **2003**, *103*, 2921; g) U. Kazmaier, *Curr. Org. Chem.* **2003**, *7*, 317.

[3] C. H. Heathcock in *Modern Synthetic Methods* (Ed.: R. Scheffold), VHCA/VCH, Basel, Weinheim, **1992**, p. 1, and references therein.

[4] a) B. M. Trost, E. Keinan, *Tetrahedron Lett.* **1980**, *21*, 2591; b) J.-C. Fiaud, J.-L. Malleron, *J. Chem. Soc. Chem. Commun.* **1981**, 1159; c) B. Åkermark, A. Jutand, *J. Organomet. Chem.* **1981**, *217*, C41.

[5] M. Braun, T. Meier, *Synlett* **2006**, 661.

[6] a) B. M. Trost, G. M. Schroeder, *J. Am. Chem. Soc.* **1999**, *121*, 6759; b) B. M. Trost, G. M. Schroeder, *Chem. Eur. J.* **2005**, *11*, 174.

[7] a) S.-L. You, X.-L. Hou, L.-X. Dai, X.-Z. Zhu, *Org. Lett.* **2001**, *3*, 149; b) X.-X. Yan, C.-G. Liang, Y. Zhang, W. Hong, B.-X. Cao, L.-X. Dai, X.-L. Hou, *Angew. Chem.* **2005**, *117*, 6702; *Angew. Chem. Int. Ed.* **2005**, *44*, 6544.

[8] M. Braun, F. Laicher, T. Meier, *Angew. Chem.* **2000**, *112*, 3637; *Angew. Chem. Int. Ed.* **2000**, *39*, 3494.

[9] a) M. Braun, T. Meier, *Synlett* **2005**, 2968; b) M. Braun, P. Meletis, M. Fidan, unpublished results.

[10] T. Graening, J. F. Hartwig, *J. Am. Chem. Soc.* **2005**, *127*, 17192.

[11] a) D. C. Behenna, B. M. Stoltz, *J. Am. Chem. Soc.* **2004**, *126*, 15044; b) J. T. Mohr, D. C. Behenna, A. M. Harned, B. M. Stoltz, *Angew. Chem.* **2005**, *117*, 7084; *Angew. Chem. Int. Ed.* **2005**, *44*, 6924.

[12] a) B. M. Trost, J. Xu, *J. Am. Chem. Soc.* **2005**, *127*, 2846; b) B. M. Trost, R. N. Bream, J. Xu, *Angew. Chem.* **2006**, *118*, 3181; Angew. *Chem. Int. Ed.* **2006**, *45*, 3109; c) B. M. Trost, J. Xu, *J. Am. Chem. Soc.* **2005**, *127*, 17180.

[13] a) E. C. Burger, J. A. Tunge, *Org. Lett.* **2004**, *6*, 4113; b) J. A. Tunge, E. C. Burger, *Eur. J. Org. Chem.* **2005**, 1715.

[14] Promising, however not enantioselective, allylations of aldehyde enolates have been reported recently: M. Kimura, Y. Horino, R. Mukai, S. Tanaka, Y. Tamaru, *J. Am. Chem. Soc.* **2001**, *123*, 10401; I. Ibrahem, A. Córdova, *Angew. Chem.* **2006**, *118*, 1986; *Angew. Chem. Int. Ed.* **2006**, *45*, 1952.

© 2006 Wiley-VCH Verlag GmbH & Co. KGaA, Weinheim

High Oxidation States

DOI: 10.1002/anie.200603056

An Fe^{VI} Nitride: There Is Plenty of Room at the Top!**

*Paul J. Chirik**

Keywords:
coordination compounds · iron · Moessbauer spectroscopy · nitrides · nitrogen fixation

When it comes to iron coordination chemistry, Fe^{VI} is considered to be "top" with respect to valency—the +6 oxidation state is thought to be the highest available.[1] Until early in 2006,[2] the ferrate ion $[Fe^{VI}O_4]^{2-}$ (with a variety of different countercations) stood alone atop the oxidation-state scale as the only known Fe^{VI} species.[3] However, the synthesis and characterization of an iron(VI) nitride by Wieghardt and co-workers demonstrates that hexavalent iron can be prepared in the laboratory and in fact there is plenty of room at the top.

Interest in high-oxidation-state iron chemistry derives from the potential intermediacy of such compounds during the function of many metalloenzymes and in other catalytic reactions.[4,5] Low-molecular-weight model compounds have been synthetic targets for quite some time in an attempt to gain insight into both the spectroscopic features and reactivity patterns of these otherwise transient, yet important, species.

Given the role of iron in oxidation chemistry, considerable attention has been devoted to the preparation of Fe^{IV}=O coordination compounds and many successes have recently appeared.[6] Somewhat surprisingly, the chemistry of related high-valent, terminal iron nitrido compounds remains relatively underdeveloped. The paucity of known molecular iron nitrides should not be interpreted as a lack of utility but should rather provide an appreciation for the challenges associated with their synthesis. These compounds are of considerable interest given their likely role in both industrial[4] and biological[7] nitrogen fixation schemes and their potential to serve as efficient N-atom transfer agents.

The traditional synthetic approach to molecular iron nitrides has focused on the photooxidation of iron azido compounds (Scheme 1). Both the expulsion of the stable dinitrogen molecule and the ease with which the Fe–N_3 linkage can be assembled make this route attractive. It is often the case, however, that photochemical conversion of the azido compound to the desired nitrido species is accompanied by competing photoreduction, a process that initially generates the azine radical, which then quickly decomposes to dinitrogen.

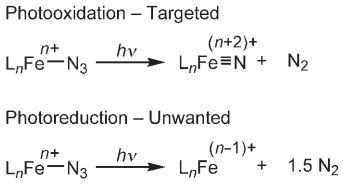

Scheme 1. Photooxidation versus photoreduction of iron azido compounds.

The first successful application of the photooxidation method to prepare iron nitrides was reported by Wagner and Nakamoto.[8] Observation of substituted porphyrin (Por) iron nitrido compounds was achieved at 30 K by using resonance Raman spectroscopy. Raising the temperature yielded relatively common μ-nitrido diiron compounds. While at first glance [(Por)FeN] species appear to be examples of Fe^{V} compounds, these molecules are probably better described as Fe^{IV} ions that are ligated by porphyrin radical cations.[9]

To avoid complications from redox- and spectroscopically active ligands, Wieghardt and co-workers introduced saturated cyclam (1,4,8,11-tetraazacyclotetradecane) tetradentate chelates into iron nitride chemistry. Photolysis of low-spin *trans*-$[(cyclam)Fe(N_3)_2]^+$ in a frozen CH_3CN matrix at 4.2 K yielded 29% of an iron(II) species generated by photoreduction and 54% of the desired iron nitride *trans*-$[(cyclam)Fe(N)(N_3)]^+$, as determined by Mössbauer and EPR spectroscopy (Scheme 2).[10]

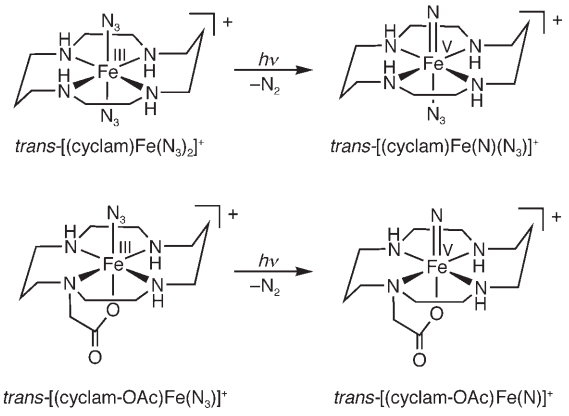

Scheme 2. Synthesis of iron(V) nitrides by photolysis of ferric azides.

[*] Dr. P. J. Chirik
Department of Chemistry and Chemical Biology
Cornell University
Ithaca, NY 14853 (USA)
Fax: (+1) 607-255-4137
E-mail: pc92@cornell.edu

[**] In reference to Richard Feynman's famous lecture on meso- and nanoscale science. For a transcript of the lecture, see: http://www.zyvex.com/nanotech/feynman.html.

WILEY InterScience DISCOVER SOMETHING GREAT
© 2006 Wiley-VCH Verlag GmbH & Co. KGaA, Weinheim

Conditions for generating the terminal iron(V) nitride are exquisitely sensitive. Performing the photolysis at higher temperatures yields a localized μ-nitrido diiron compound, $[(cyclam)(N_3)Fe^{IV}\text{-}N\text{-}Fe^{III}(N_3)(cyclam)]^{2+}$, a result of the combination of photooxidation and photoreduction products. Remarkably, isomeric, high-spin *cis*-$[(cyclam)Fe(N_3)_2]^+$ does not undergo photooxidation to yield the terminal iron nitride. Irradiation again yields a μ-nitrido diiron complex arising from combination of both photooxidation and photoreduction products.[10]

Since these initial studies, a "second-generation" version of the cyclam ligand has been introduced where an acetate group is appended to one of the nitrogen donors.[11] Photolysis of the low-spin ferric azide at $\lambda > 420$ nm resulted in over 80% conversion to the desired iron(V) nitride (Scheme 2). Magnetic studies and Mössbauer spectroscopy in combination with DFT calculations established an $S = 1/2$ ground state, thus indicating a low-spin Fe^V d^3 ion. XAS and EXAFS data established the Fe=N bond length to be approximately 1.60 Å.[12]

At this point it is useful to discuss the indispensable role Mössbauer spectroscopy has played in cyclam-substituted iron nitride chemistry. The synthesis of a family of $[(cyclam)FeL_x]^{n+}$ compounds where the oxidation states range between +2 and +5 has allowed systematic evaluation of the experimental zero-field isomer shifts (δ) as a function of oxidation level. Because covalent variations in this series of compounds are minimal, δ varies linearly with charge density and is described by the relationship $\delta = -\alpha\{|\Psi(0)|^2 - C\}$, where α accounts for the general electronic and nuclear properties and C is a scaling constant for the reference scale. As the oxidation state increases, charge density increases (a result of the lower d count and less penetration) and because of the negative sign, lower values of δ result.[13] Thus, compounds of relatively low oxidation states such as *trans*-$[(cyclam)Fe^{II}(N_3)_2]$ have relatively high isomer shifts ($\delta = 0.55$ mm s^{-1}) while high-valent compounds such as *trans*-$[(cyclam)Fe^{V}(N)(N_3)]$ have low isomer shifts ($\delta = -0.04$ mm s^{-1}). As we will see, it is this near-linear relationship that allows *prediction* of the Mössbauer isomer shift for a rare oxidation state such as iron(VI) (Figure 1). A similar correlation was also noted in the X-ray absorption data where the energies of the pre-edge peaks and the edge energies vary consistently by approximately 1 eV per unit change in the oxidation state.[2]

Cyclam complexes are not the only examples of iron nitrides. Recently, Betley and Peters have reported the synthesis and characterization of a four-coordinate iron(IV) nitride, $[\{PhB(P^{iPr})_3\}Fe^{IV}N]$ $(PhB(P^{iPr})_3 = PhB(CH_2P{i}Pr_2)_3^-)$.[14] In this case, the supporting tridentate phosphine ligand is monoanionic by virtue of the apical borate, a feature known to have a profound impact on the electronic structure of the resulting metal complex. Notably, the synthesis of $[\{PhB(P^{iPr})_3\}Fe^{IV}N]$ was achieved under thermal rather than photochemical conditions by salt metathesis of $[\{PhB(P^{iPr})_3\}Fe^{II}Cl]$ with the N-atom transfer agent Li(dbabh).[15] As was pioneered by Mindiola and Cummins for the synthesis of chromium nitrides,[16] loss of anthracene from the intermediate iron amide yielded the desired nitride product (Scheme 3). DFT calculations on $[\{PhB(P^{iPr})_3\}Fe^{IV}N]$ established a $(xy)^2(x^2-y^2)^2(z^2)^0$ d-electron configuration with a large HOMO–LUMO gap (ca. 4 eV), consistent with the diamagnetic ($S = 0$) ground state observed experimentally. In an argon atmosphere or when concentrated under vacuum, $[\{PhB(P^{iPr})_3\}Fe^{IV}N]$ couples to form the iron(I) dinitrogen complex $[\{\{PhB(P^{iPr})_3\}Fe^{I}\}_2(\mu_2\text{-}N_2)]$, which represents a unique example of a six-electron redox process mediated by two iron centers. It is also noteworthy that $[\{PhB(P^{iPr})_3\}Fe^{IV}N]$ can be treated with proton/electron equivalents to yield NH_3.

In recent studies, the Wieghardt laboratory has reported a subsequent variation of the acetato-substituted cyclam ligand.[17] Replacing the amine

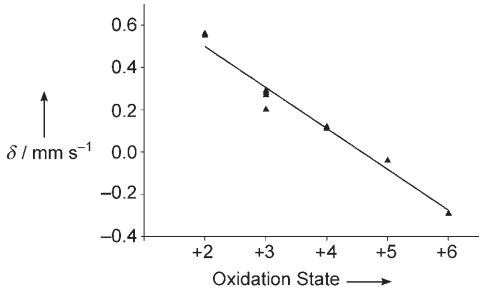

Figure 1. Correlation of Mössbauer isomer shifts (δ) with oxidation state for a family of cyclam iron coordination compounds.

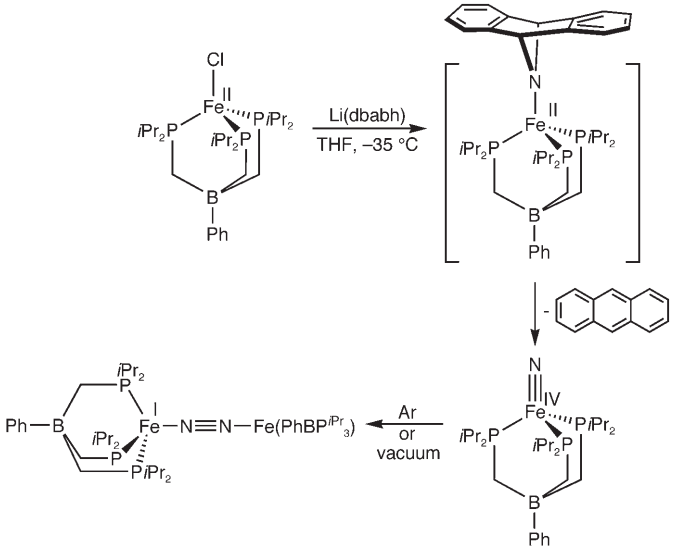

Scheme 3. Thermal synthesis of the iron(IV) nitrido complex, $[\{PhB(P^{iPr})_3\}Fe^{IV}N]$.

© 2006 Wiley-VCH Verlag GmbH & Co. KGaA, Weinheim

hydrogen atoms with methyl groups yielded a high-spin, instead of a low-spin, ferric azido compound, $[(Me_3\text{-cyclam-OAc})Fe^{III}(N_3)]^+$.[18] Importantly, this substitution also produces a molecule that undergoes reversible one-electron oxidation to furnish a stable iron(IV) azido compound, $[(Me_3\text{-cyclam-OAc})Fe^{IV}(N_3)]^{2+}$ (Scheme 4).

The stability of the electrochemically generated iron(IV) azide allows photooxidation at 77 K with light of wavelength 650 nm to furnish a new major product with a zero-field Mössbauer isomer shift of $\delta = -0.29\ mm\,s^{-1}$.[2] The low value of δ is as predicted for the +6 oxidation state according to Figure 1, thus supporting assignment as the iron(VI) nitride $[(Me_3\text{-cyclam-OAc})Fe^{VI}(N)]^{2+}$. This compound joins $[FeO_4]^{2-}$ as the only known hexavalent iron compounds and is the first to be synthesized in a laboratory!

As was observed with the parent cyclam complex, the photooxidation procedure is sensitive to the nature of the precursor. Irradiation of the high-spin ferric azide $[(Me_3\text{-cyclam-OAc})Fe^{III}(N_3)]^+$ did not yield an iron(V) nitride, but rather only photoreduction to iron(II) resulted. To date, only low-spin compounds have resulted in mononuclear iron nitride photooxidation products.

Additional evidence for the formation of $[(Me_3\text{-cyclam-OAc})Fe^{VI}(N)]^{2+}$ was provided by XAS and EXAFS. In the X-ray absorption spectrum, an intense pre-edge peak was observed, which is consistent with a covalent iron–ligand multiple bond. Likewise, the EXAFS data yielded an Fe≡N bond length of 1.57 Å, slightly contracted from the values measured for related iron(V) nitrides.

Much like Mössbauer spectroscopy, DFT calculations have proven invaluable in the development of iron nitride coordination chemistry. For $[(Me_3\text{-cyclam-OAc})Fe^{VI}(N)]^{2+}$, the DFT-optimized structure predicts an octahedral geometry with an Fe≡N bond length of 1.53 Å, in agreement with the experimental value. The calculations also reproduced the experimental infrared stretch of the carbonyl group in the acetate ligand as well as the zero-field Mössbauer isomer shift.[2]

With a firm computational model in hand, the nature of the Fe≡N bond can be understood and its bond order and spectroscopic properties rationalized in the context of the other iron(IV) and (V) molecular nitrides. The Fe–N bond in $[(Me_3\text{-cyclam-OAc})Fe^{VI}(N)]^{2+}$ is best described as a triple bond (bond order = 2.8 from DFT),[2] where two π bonds are formed from the linear combination of nitrogen p_x and p_y orbitals with two cloverleaf iron d orbitals. As a consequence, the frontier d_{xz} and d_{yz} orbitals (LUMO) are significantly destabilized by the antibonding character of the π* interaction with the nitrogen p orbitals.

The $(d_{xy})^2$ electronic configuration of $[(Me_3\text{-cyclam-OAc})Fe^{VI}(N)]^{2+}$ produces a short iron–nitrogen bond length and a high-frequency Fe≡N vibration at 1064 cm^{-1}. This value is comparable to the Fe≡N stretch of 1034 cm^{-1} reported for $[\{PhB(P^{iPr})_3\}Fe^{IV}N]$, where population of nonbonding d orbitals (for example, $(xy)^2(x^2-y^2)^2$) does not reduce the iron–nitrogen bond order.[14] These complexes stand in contrast to the cyclam-ligated iron(V) nitrides in which the ^2E ground state results in population of a degenerate antibonding d orbital (xz, yz), thus reducing both the Fe=N bond order (d(Fe=N) = 1.60 Å) and the vibrational frequency (850–950 cm^{-1}).

Taken together, the results from the Wieghardt and Peters laboratories clearly demonstrate how careful design and manipulation of the architecture surrounding the metal coordination sphere can result in completely new compounds in the mature field of iron coordination chemistry. These fundamental studies into the synthesis and nature of the Fe–N linkage are merely the beginning—much more remains to be uncovered. For example, harnessing the reactivity of these molecules is just one new frontier awaiting exploration. Is it also possible that Fe^{VIII} compounds, much like RuO_4 and OsO_4 but with a combination of oxido and nitrido ligands, are awaiting discovery? Only time will tell but no matter the outcome, one fact is true—another entry into the rarefied air of the Fe^{VI} oxidation state demonstrates that there is plenty of room at the top!

Published online: October 9, 2006

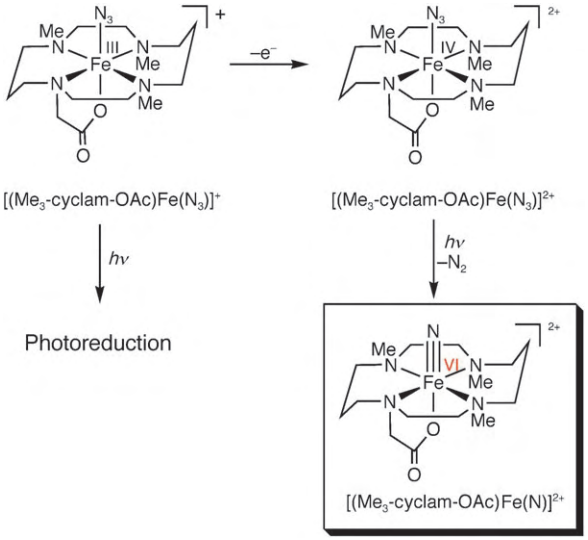

Scheme 4. Photolysis of an iron(IV) azide to yield an iron(VI) nitride.

[1] F. A. Cotton, G. Wilkinson, *Advanced Inorganic Chemistry*, *5th ed.*, Wiley, New York, **1988**, pp. 711–723.
[2] J. F. Berry, E. Bill, E. Bothe, S. D. George, B. Mienert, F. Neese, K Wieghardt, *Science* **2006**, *312*, 1937–1941.
[3] R. J. Audette, J. W. Quail, *Inorg. Chem.* **1972**, *11*, 1904–1908.
[4] G. Ertl, *Chem. Rec.* **2001**, *1*, 33–45.
[5] M. Costas, M. P. Mehn, M. P. Jensen, L. Que, Jr., *Chem. Rev.* **2004**, *104*, 939–986.
[6] X. P. Shan, L. Que, *J. Inorg. Biochem.* **2006**, *100*, 421–433.
[7] J. B. Howard, D. C. Rees, *Chem. Rev.* **1996**, *96*, 2965–2982.
[8] a) W. D. Wagner, K. Nakamoto, *J. Am. Chem. Soc.* **1988**, *110*, 4044–4045; b) W. D. Wagner, K. Nakamoto, *J. Am. Chem. Soc.* **1989**, *111*, 1590–1598.

 © 2006 Wiley-VCH Verlag GmbH & Co. KGaA, Weinheim

[9] J. E. Falk, *Porphyrins and Metalloporphyrins* (Ed.: K. M. Smith), Elsevier, Amsterdam, **1975**.
[10] K. Meyer, E. Bill, B. Mienert, T. Weyhermüller, K. Wieghardt, *J. Am. Chem. Soc.* **1999**, *121*, 4859 – 4876.
[11] C. A. Grapperhaus, B. Mienert, E. Bill, T. Weyhermüller, K. Wieghardt, *Inorg. Chem.* **2000**, *39*, 5306 – 5317.
[12] N. Aliaga-Alcalde, S. DeBeer George, B. Mienert, E. Bill, K. Wieghardt, F. Neese, *Angew. Chem.* **2005**, *117*, 2968; *Angew. Chem. Int. Ed.* **2005**, *44*, 2908 – 2912.
[13] a) P. Gütlich, R. Link, A. Trautwein, *Mössbauer Spectroscopy and Transition Metal Chemistry*, Springer, Berlin, **1978**; b) this relationship is true for low-spin compounds because electrons are systematically removed for the t_{2g} set of molecular orbitals.
[14] T. A. Betley, J. C. Peters, *J. Am. Chem. Soc.* **2004**, *126*, 6252 – 6254.
[15] dbabh = 2,3:5,6-dibenzo-7-azabicyclo-[2.2.1]hepta-2,5-diene.
[16] D. J. Mindiola, C. C. Cummins, *Angew. Chem.* **1998**, *110*, 983; *Angew. Chem. Int. Ed.* **1998**, *37*, 945.
[17] J. F. Berry, E. Bill, E. Bothe, T. Weyhermüller, K. Wieghardt, *J. Am. Chem. Soc.* **2005**, *127*, 11550.
[18] J. F. Berry, E. Bill, R. Garcia-Serres, F. Neese, T. Weyhermüller, K. Wieghardt, *Inorg. Chem.* **2006**, *45*, 2027 – 2037.

© 2006 Wiley-VCH Verlag GmbH & Co. KGaA, Weinheim

Green Chemistry

DOI: 10.1002/anie.200503779

Hydrogen Peroxide Synthesis: An Outlook beyond the Anthraquinone Process

*Jose M. Campos-Martin, Gema Blanco-Brieva, and Jose L. G. Fierro**

Keywords:
direct synthesis · green chemistry · hydrogen peroxide · liquid-phase reactions · oxidation

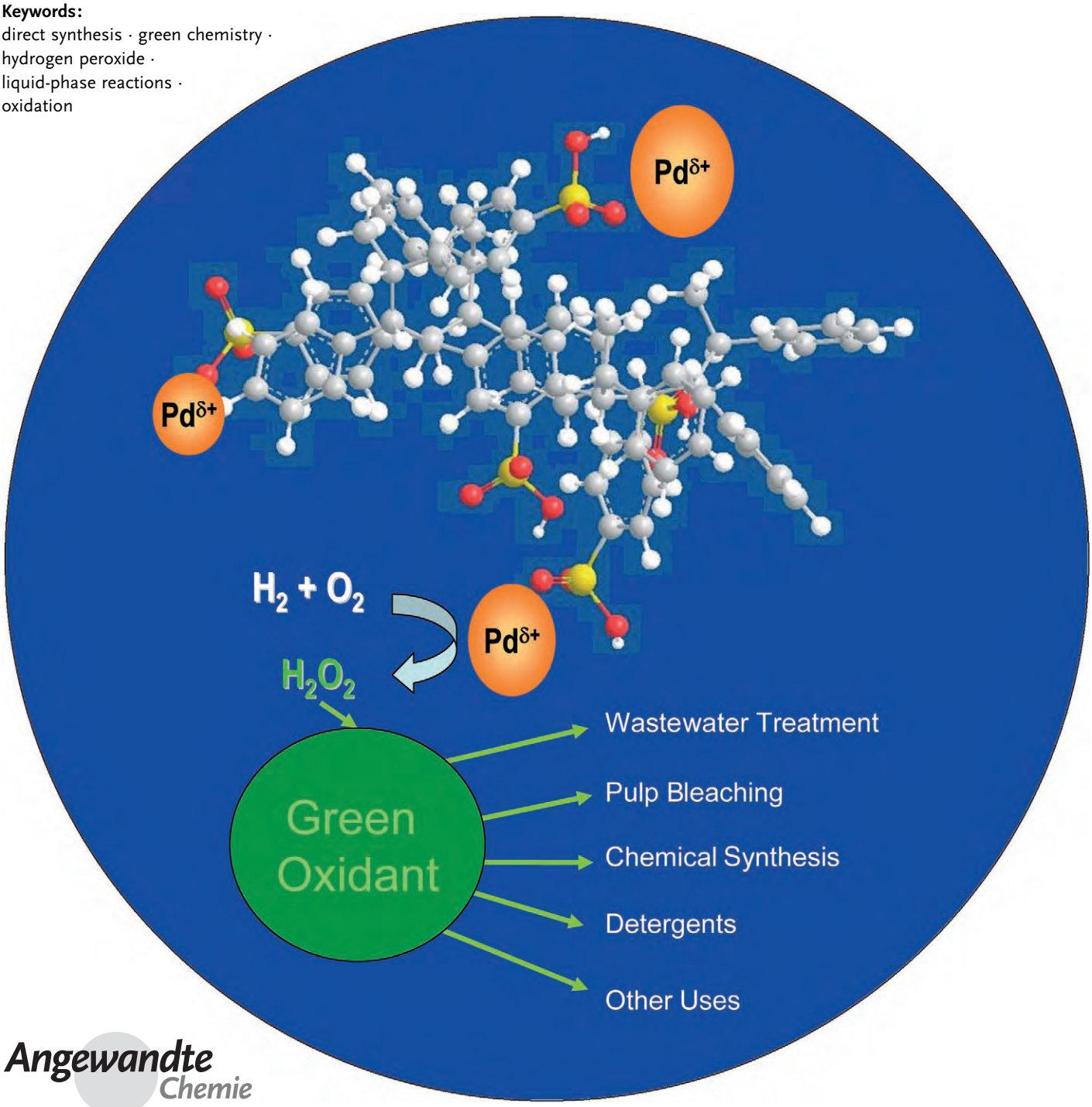

© 2006 Wiley-VCH Verlag GmbH & Co. KGaA, Weinheim

Hydrogen peroxide (H_2O_2) is widely used in almost all industrial areas, particularly in the chemical industry and environmental protection. The only degradation product of its use is water, and thus it has played a large role in environmentally friendly methods in the chemical industry. Hydrogen peroxide is produced on an industrial scale by the anthraquinone oxidation (AO) process. However, this process can hardly be considered a green method. It involves the sequential hydrogenation and oxidation of an alkylanthraquinone precursor dissolved in a mixture of organic solvents followed by liquid–liquid extraction to recover H_2O_2. The AO process is a multistep method that requires significant energy input and generates waste, which has a negative effect on its sustainability and production costs. The transport, storage, and handling of bulk H_2O_2 involve hazards and escalating expenses. Thus, novel, cleaner methods for the production of H_2O_2 are being explored. The direct synthesis of H_2O_2 from O_2 and H_2 using a variety of catalysts, and the factors influencing the formation and decomposition of H_2O_2 are examined in detail in this Review.

From the Contents

1. General Aspects of the Chemistry of Hydrogen Peroxide 6963
2. Requirements in an Expanding Market 6963
3. Large-Scale Production 6965
4. Emerging Alternatives 6970
5. Other Methodologies 6977
6. Summary and Outlook 6979

1. General Aspects of the Chemistry of Hydrogen Peroxide

Hydrogen peroxide (H_2O_2) was first recognized by Thenard in 1818 as the product of the reaction of barium peroxide with nitric acid. Hydrogen peroxide is a versatile oxidant that is effective over the whole pH range with high oxidation potential ($E_o = 1.763$ V at pH 0, $E_o = 0.878$ V at pH 14) and water as the only coproduct. Equations (1)–(5) summarize the reactions that hydrogen peroxide may undergo, depending on the type of substrate: decomposition, oxidation, molecular addition, reduction, and substitution.

$$\text{Decomposition}: \quad 2\,H_2O_2 \rightarrow 2\,H_2O + O_2 \tag{1}$$

$$\text{Oxidation}: \quad H_2O_2 + M \rightarrow MO + H_2O \tag{2}$$

$$\text{Addition}: \quad H_2O_2 + A \rightarrow AH_2O_2 \tag{3}$$

$$\text{Reduction}: \quad H_2O_2 + R \rightarrow RH_2 + O_2 \tag{4}$$

$$\text{Substitution}: \quad H_2O_2 + RX \rightarrow ROOH + HX \tag{5}$$

The decomposition of hydrogen peroxide [Eq. (1)] must be controlled because the reaction produces gaseous oxygen and heat (100.4 kJ mol^{-1}). The rate of decomposition depends on the temperature and concentration of the peroxide, as well as on the presence of impurities and stabilizers. Peroxide decomposes in the presence of many substances, for example most of the transition metals and their compounds, as well as certain organic compounds, which catalyze the decomposition. The decomposition reaction is also catalyzed by the enzyme catalase, whose main function in the body is to remove the toxic by-products of metabolism and to reduce oxidative stress. The rate of decomposition of a solution of H_2O_2 can be minimized by the removal of impurities and addition of stabilizers. Sodium pyrophosphate is often employed as a chelating agent for catalytic impurities. Another option is the use of sodium stannate, which forms a protective colloid.

Hydrogen peroxide is a strong oxidant [Eq. (2)], which can oxidize a broad variety of inorganic and organic substrates in liquid-phase reactions under very mild reaction conditions. In the liquid phase, hydrogen peroxide binds molecularly to metal peroxides (M_2O_2, M = alkali metal; or $M'O_2$, M′ = alkaline-earth metal), oxoacid salts, zirconyl acetate, percarbonates, urea (to form urea–hydrogen peroxide adduct, UHP), and nitrogen compounds [Eq. (3)] to form crystalline peroxyhydrates. As a strong reducing agent, hydrogen peroxide reduces other stronger oxidizing compounds, such as $KMnO_4$, $Ce(SO_4)_2$, NaClO, and Cl_2 [Eq. (4)]; $KMnO_4$ and $Ce(SO_4)_2$ are used as standards for the volumetric determination of hydrogen peroxide. Substitution reactions of hydrogen peroxide with organic reagents produce a variety of peroxido compounds [Eq. (5)] that are widely used in organic synthesis and a number of applications.

2. Requirements in an Expanding Market

Hydrogen peroxide is currently produced almost exclusively with the anthraquinone oxidation (AO) process,[1,2] in which hydrogen, atmospheric oxygen, and an anthraquinone derivative (typically 2-ethylantraquinone) are employed in the reaction cycle, the latter acting as a "reaction carrier". The crude hydrogen peroxide obtained is then purified and concentrated and is usually marketed with an added stabilizer as aqueous solutions at concentrations of 35, 50, and 70% by

[*] Dr. J. M. Campos-Martin, G. Blanco-Brieva, Prof. Dr. J. L. G. Fierro
Instituto de Catálisis y Petroleoquímica, CSIC
Marie Curie 2, Cantoblanco, 28049 Madrid (Spain)
Fax: (+34) 91-585-4800
E-mail: jlgfierro@icp.csic.es
Homepage: http://www.icp.csic.es/eac/index.htm

 © 2006 Wiley-VCH Verlag GmbH & Co. KGaA, Weinheim

weight. For certain applications, such as in detergents, it is commonly delivered as a stable solid precursor such as sodium perborate or sodium percarbonate, which produce hydrogen peroxide in solution. Owing to its low molecular weight, hydrogen peroxide is a more efficient oxidizing agent than other oxidants, such as nitric acid and sodium hypochlorite (Table 1). It is a stable and safe chemical when handled correctly and offers the advantage of being soluble in water and many organic solvents or in the substrate itself. H_2O_2 has an environmentally benign profile since it decomposes to give only water and oxygen as the only reaction products, which makes it one of the cleanest, most versatile chemical oxidants available (Figure 1). These characteristics render hydrogen peroxide an environmentally safe oxidizing agent for many large-scale applications, such as pulp and paper bleaching, textile applications, detergent applications, wastewater treatment, and chemical oxidation processes.

Table 1: Common industrially oxidants available.

Oxidant	Active oxygen (% w/w)	By-product
H_2O_2	47.1	H_2O
*t*BuOOH	17.8	*t*BuOH
HNO_3	25.0	NO_x, N_2O, N_2
N_2O	36.4	N_2
NaClO	21.6	NaCl
$NaClO_2$	35.6	NaCl
NaBrO	13.4	NaBr
"$KHSO_5$"[a]	10.5	$KHSO_4$
$NaIO_4$	29.9[b]	NaI
PhIO	7.3	PhI

[a] Stabilized and marketed as the "triple salt" $2\,KHSO_5 \cdot KHSO_4 \cdot K_2SO_4$ (oxone). [b] Assuming that all four oxygen atoms are used.

One of the most important applications of hydrogen peroxide is currently its use in pulp and paper bleaching.[3–6] Its use for this process replaces chlorine-based bleaches and avoids halogenated products in waste streams. Its use as a bleach relies on the hydrogenperoxide(1−) anion in alkaline media, which eliminates various chromophores in the lignin structures. In a similar manner to that described for the bleaching of tea stains, the carbonyl structures are prone to react with nucleophilic HO_2^-. As well as for colored lignin residues in chemical and mechanical pulp, hydrogen peroxide is also used in the bleaching of recycled paper. For this process, a combination of H_2O_2 and reductive bleaching steps with sodium dithionite are employed to remove the printing dyes.

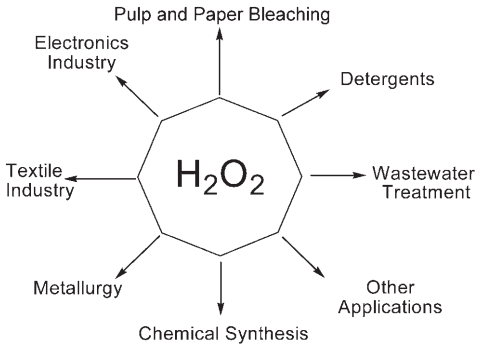

Figure 1. Principal uses of hydrogen peroxide.

Hydrogen peroxide is widely used as a bleaching agent in the textile industry. It has advantages over other alternatives such as sodium hypochlorite and sodium hydrosulfite in that it is suitable for continuous processing, has no severe toxicity or effluent problems, and is noncorrosive.

Color-safe laundry bleaches containing hydrogen peroxide have increasingly replaced bleaches containing hypochlorite. In this case, the hydrogen peroxide is used with stable precursors such as sodium percarbonate and sodium perborate, which release hydrogen peroxide when dissolved in water. Sodium percarbonate is being increasingly used in preference to sodium perborate in detergent formulations because of its lower dissolution temperature in water. Detergent or bleach compositions formulated with sodium percarbonate/perborate have strong stain-removal capabilities, are color safe, brighten colors, and do not lead to yellowing or darkening of the fabric, which is a problem with bleaches containing hypochlorite. Sodium percarbonate/perborate is effective as a disinfectant against bacteria and viruses.

Hydrogen peroxide is used in municipal wastewater treatment for the removal of hydrogen sulfide (H_2S), which forms in sewer pipes. The most significant environmental application of hydrogen peroxide is the treatment of a broad variety of industrial wastes. Cyanide, thiocyanate, nitrite, chloride, hypochlorite, and organic matter can be efficiently

Jose M. Campos-Martin, born in 1968 in Valencia, studied chemical engineering at the University of Valencia (B.S. 1991) and attained his PhD from the Instituto de Catálisis y Petroleoquímica (Madrid) with Prof. J. L. G. Fierro and Dr. A. Guerrero-Ruíz on the conversion of syngas to high alcohols and hydrocarbons over copper-modified catalysts. Many postdoctoral fellowships and stipendiums followed, including one at Repsol-YPF. His current research interests are directed to the development and optimization of catalytic processes, especially in the area of petrochemistry.

Gema Blanco Brieva, born in 1974 in Madrid, studied chemistry at the Autonomous University of Madrid (B.S. 1997) and then worked on a joint project between the Instituto de Catálisis y Petroleoquímica in Madrid and the company Repsol-YPF (M.S. 2002). She is currently at the Instituto de Catálisis y Petroleoquímica in Madrid conducting research towards her PhD on the direct synthesis of hydrogen peroxide.

 © 2006 Wiley-VCH Verlag GmbH & Co. KGaA, Weinheim

removed by H_2O_2 treatment.[7] Hydrogen peroxide is also used as a source of hydroxyl radicals in more complex advanced oxidation processes.[8] Hydroxyl radicals are, after fluorine, the second most powerful oxidant available. After absorption in an aqueous scrubbing liquor, oxides of nitrogen and sulfur, mercaptans, and several other toxic odorous components of waste gases can be removed by oxidation with hydrogen peroxide. Examples include the removal of NO_x during pickling processes, the deodorization of gaseous effluents from animal carcasses, and the oxidation of sulfur dioxide. Hydrogen peroxide can be used as a source of oxygen, in the biological treatment of bulking sludges, and for the prevention of denitrification in settling tanks. The in situ bioremediation of contaminated soils has recently been developed. This process consists of the injection into the ground of microorganisms and nutrients together with hydrogen peroxide as a source of oxygen.

Hydrogen peroxide currently finds many applications in the chemical industry. It is employed, either directly or following transformation into a peroxocarboxylic acid, in the manufacture of many organic and inorganic chemicals, for example, hydrazine, cyanogen, cyanogen chloride, bromine, iodic acid, high-purity ferric sulfate, perborates, and percarbonates. Typical applications of hydrogen peroxide in organic syntheses include oxidation,[9–26] epoxidation, hydroxylation,[27–29] and oxohalogenation reactions (flame retardants),[30] as well as for the initiation of emulsion polymerization reactions (benzyl peroxide, lauryl peroxide).[31]

A number of applications in mining and metal processing involve the hydrogen peroxide.[32] Typical applications in this field include the extraction and purification of uranium, gold recovery, the extraction and separation of chromium, copper, cobalt, tungsten, molybdenum, and other metals, and metal finishing (etching, stainless steel pickling, non-ferrous metal finishing). High-purity hydrogen peroxide is used in the electronics industry for cleaning of germanium and silicon semiconductor wafers and etching printed circuit boards. For various electronic and semiconductor applications, high-purity hydrogen peroxide is available with total cationic impurity levels below 10 ppb (parts per billion), 1 ppb, 0.1 ppb, and 0.01 ppb. Hydrogen sulfide, S-containing hydrocarbons, nitrogen oxides, and sulfur dioxide can be removed by hydrogen peroxide from exhaust gases generated in chemical and pharmaceutical syntheses, the production of graphite, titanium dioxide, and sulfuric acid, as well as in the combustion of sulfur-containing fuels.

The annual world production of hydrogen peroxide is approximately 2.2 million metric tons.[6] About 50% is used for pulp and paper bleaching and 10% for textile bleaching. However, its use depends on the market region. The two major areas of demand in Europe are chemical synthesis, mainly in detergent applications (43%), and pulp and paper bleaching (41%; Figure 2). The demand for hydrogen peroxide in pulp bleaching is expected to grow slowly in the near future, but the commercialization of the integrated HPPO (hydrogen peroxide–propylene oxide) process, in which the hydrogen peroxide required for the epoxidation of propylene is produced on site, should lead to a large growth in the proportion of hydrogen peroxide used in chemical syntheses. BASF and Dow Chemical announced a new HPPO plant expected to begin production in 2008 with a yearly capacity of about 2×10^5 metric tons.[33] Most segments of the Japanese hydrogen peroxide market are mature, and, as in Europe, the major areas of demand are pulp and paper production and chemical synthesis. Growth in the demand for chemical synthesis in Japan stems from the commercialization of Sumitomo's route to caprolactam. The circumstances in the USA are slightly different. The demand for hydrogen peroxide is dominated by the pulp and paper bleaching markets (about 59%), whereas both organic and inorganic synthesis together represent only 13% and electronics etching accounts for approximately 5%.

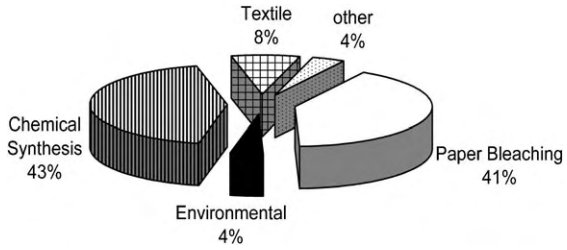

Figure 2. Distribution of hydrogen peroxide consumption in Europe.

3. Large-Scale Production

3.1. Anthraquinone Autoxidation

The first commercial anthraquinone autoxidation process (1 metric ton H_2O_2 per day) was introduced by IG Farbenindustrie in Germany in the 1940s. All subsequent anthraquinone-based production plants built worldwide in the following five decades maintained the original concept. However, important improvements were made in each of the four major steps: hydrogenation, oxidation, hydrogen peroxide extraction, and treatment of the working solution. A simplified flow diagram of the process steps is given in Figure 3. The main reactions involved the Riedl–Pfleiderer process,[34] which currently accounts for the largest part of hydrogen peroxide production, are shown in Scheme 1. A 2-alkylanthraquinone

Jose Luis G. Fierro studied chemistry at the University of Oviedo (1973) and received his PhD at the Complutense University of Madrid (1976). In 1978 he took up tenure in the Institute of Catalysis and Petrochemistry in Madrid, where he was promoted to a Research Scientist in 1985 and to Professor in 1988. Over many postdoctoral stays he worked on NMR studies of micro- and mesoporous systems, oxygen isotopic exchange on metal oxide semiconductors, and the development of heterogeneous catalysts for oil refining. His current research focuses on heterogeneous catalysis, chemical technology, environmental catalysis, and the chemistry of materials.

© 2006 Wiley-VCH Verlag GmbH & Co. KGaA, Weinheim

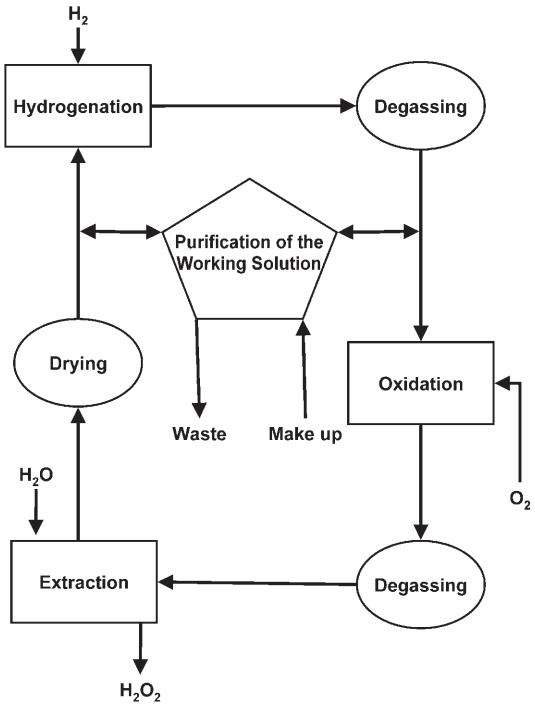

Figure 3. Block diagram of the steps involved in the anthraquinone method for the synthesis of hydrogen peroxide.

(AQ; usually 2-ethylantraquinone) in an appropriate solvent or mixture of solvents is hydrogenated catalytically to the corresponding anthraquinol or anthrahydroquinone (AHQ; Scheme 1a). However, a side reaction is the hydrogenation of the unsubstituted aromatic ring to yield 5,6,7,8-tetrahydroanthrahydroquinone (Scheme 1b). The solution containing the AHQ is separated from the hydrogenation catalyst and then oxidized with air to re-form the original anthraquinone (Scheme 1c,d) and simultaneously produce equimolecular amounts of hydrogen peroxide.[1,2] The hydrogen peroxide is stripped from the organic working solution by demineralized water in a countercurrent column to produce a solution that is usually 30% by weight H_2O_2. The aqueous H_2O_2 is then distilled to remove impurities and increase the concentration to as high as 70%, and the solvent/anthraquinone mixture is recycled. The reactions a–d in Scheme 1 represent only an oversimplification of the reactions involved in this process. A series of side reactions can occur in this process, which leads to a net consumption of anthraquinone.

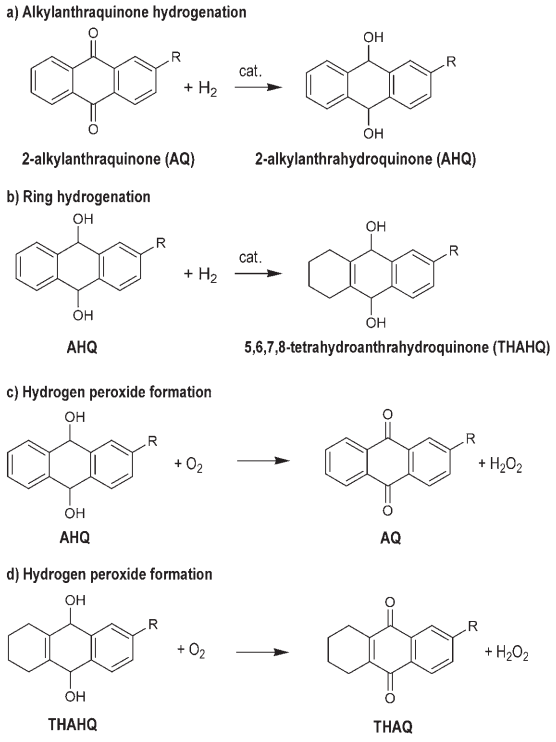

Scheme 1. Anthraquinone autoxidation reactions.

The advantage of the AO process is the very high yield of hydrogen peroxide per cycle. However, its major disadvantages come not only from the side reactions, which require regeneration of the solution and the hydrogenation catalyst, but also from the separation steps involved in the removal of organic impurities from the hydrogen peroxide product. Despite the high yield of hydrogen peroxide per cycle, improvements have been proposed in the literature for each process step.

3.1.1. *Hydrogenation*

The working solution is hydrogenated over a catalyst at temperatures of 40–50 °C under a hydrogen partial pressure up to 4 bar. The extent of hydrogenation (conversion of AQ to AHQ) is carefully controlled and kept under 60% to minimize secondary hydrogenation reactions. Nickel and supported Pd catalysts have been used in the hydrogenation step.[35,36]

Raney nickel catalysts were used in the original process for the reduction of AQ, but this process has two serious drawbacks: excessive hydrogenation and rapid deactivation. The second generation of catalysts, based on palladium, is more selective, but hydrogenation by-products can not be completely avoided (extra consumption of hydrogen and anthraquinone). Thus, a highly selective catalyst that hydrogenates only the carbonyl group and leaves the aromatic ring intact would be highly desirable. These requirements are fulfilled by a new generation of catalysts based on chemically reduced nanosized amorphous Ni/B[37,38] and Ni/Cr/B[39] alloys.

Amorphous Ni/B alloys show good performance in AQ hydrogenation.[37] The hydrogenation activity of the amorphous Ni/B alloy increases upon La incorporation up to an atomic ratio of La/Ni = 0.034; the more efficient hydrogenation step leads to an improvement in the overall process. The better performance of these Ni/B catalysts can essentially be attributed to their amorphous structure, which was shown to be favorable for the hydrogenation reactions.[40,41] The increase in activity can be ascribed to the better dispersion of Ni in the presence of La, which leads to a greater number of active hydrogenation centers.

The incorporation of chromium increases the stability of Ni/B catalysts, as is shown by the relatively constant gradients of AQ and THAHQ concentrations in Figure 4. A stable

 © 2006 Wiley-VCH Verlag GmbH & Co. KGaA, Weinheim

reaction system minimizes the formation of side products and leads to increased yields of H_2O_2.[36] The yield of H_2O_2 increases sharply up to 100% over a reaction time of 60 min and then drops very slowly. The Cr^{III} species acts as a Lewis

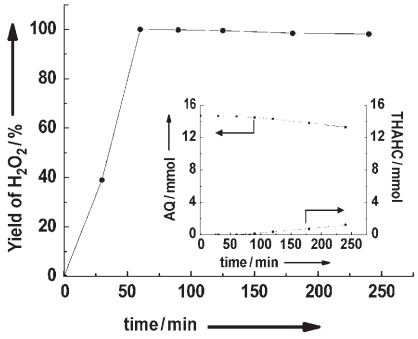

Figure 4. Yield of H_2O_2 and amounts of AQ and THAHQ in the working solution after oxidation as a function of time.[43]

acid to activate the carbonyl group by accepting the lone electron pair on the oxygen atom.[41] This activation favors the nucleophilic attack of the carbon atom by hydrogen dissociatively adsorbed on the nickel, thus leading to enhanced hydrogenation activity of the carbonyl group and hence greater selectivity in the hydrogenation of AQ to AHQ.

The most common catalysts for the hydrogenation stage of the anthraquinone process are based on palladium supported on Al_2O_3, SiO_2, and SiO_2/Al_2O_3.[36] The selectivity of supported Pd catalysts can be improved by adding promoters or by changing the nature of the support. A new generation of hydrogenation catalysts for both slurry and fixed-bed operation are based on palladium catalysts supported on functionalized resins.[42,43] In the patent literature,[44] a Pd^{2+}-polyethyleneimine system is described that has recently been applied with success. Substrates such as poly(4-vinylpyridine) (PVP) and polyaniline (PANI) (Scheme 2) containing 1–10% Pd were shown to be efficient for AQ hydrogenation.[45,46] Very small Pd^0 particles produced by reduction of palladium hydroxide (or oxide) precipitated on polymer grains show the highest activity and also the lowest tendency towards AHQ degradation.

Another substantial improvement of the hydrogenation step is based on the concept of the foam regime developed by Solvay.[47] The hydrogenation reaction is conducted at moderate temperature (50–70°C) with a surface velocity of the hydrogenating gas in the range from 3 to 10 $cm\,s^{-1}$ and a liquid surface velocity in the range of 0.5 to 1.0 $cm\,s^{-1}$, while the liquid/gas ratio is kept at below 0.15. Under these conditions, no degradation of the working solution by overhydrogenation is observed despite the high hydrogenation rates achieved. The hydrogenation reaction can also be enhanced by microwave radiation. An example is the approach of Kemira,[48] which uses a 5% Pd/C catalyst and a working solution containing AQ/THAHQ in a mixture containing 70% aromatic hydrocarbon solvent as well as trioctylphosphate and tetrabutyl urea.

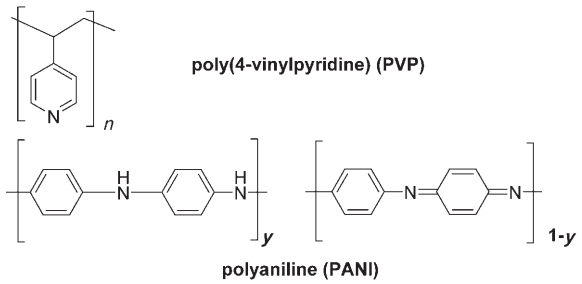

Scheme 2. Polymeric support for hydrogenation catalysts.

3.1.2. *Oxidation*

The hydroquinone is oxidized—usually by air—to produce hydrogen peroxide and to regenerate the quinone. The oxidation is carried out noncatalytically by bubbling air through the solution at 30–60°C and near atmospheric pressure. This reaction occurs by means of a well-documented free-radical chain mechanism (Scheme 3).[49] In the first step, a tertiary hydrogen atom of AHQ is abstracted by an initiator, which can be an impurity in the hydrogen peroxide. The radical produced reacts with oxygen to form a hydroperoxyl radical, which reacts with a second AHQ molecule to give an instable alcohol hydroperoxide and an AHQ radical. The former product decomposes to a ketone and hydrogen peroxide, and the latter starts another propagation cycle. An improved method proposed by Degussa involves a secondary amine as catalyst for the oxidation of the a THAHQ-containing working solution.[50] The oxidation reaction can be accelerated by addition of 0.1% w/w of a slightly water-soluble secondary amine such as di-*n*-octylamine to the

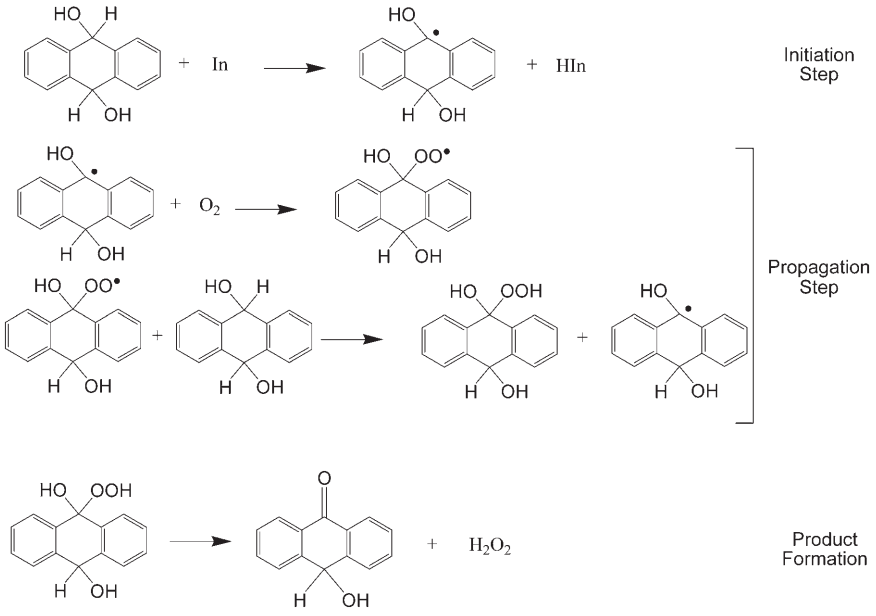

Scheme 3. H_2O_2 synthesis by the anthrahydroquinone oxidation reaction.

 © 2006 Wiley-VCH Verlag GmbH & Co. KGaA, Weinheim

working solution. The hydrogen peroxide is extracted with water, and the yield is about 95% of the theoretical amount of hydrogen peroxide.

The oxidation of THAHQ is another key reaction in the industrial production of hydrogen peroxide. This reaction occurs with molecular oxygen at the gas–liquid interface, and its rate is strongly affected by the mass transfer of oxygen across the liquid film.[51,52] Therefore, both the interfacial area and the liquid containment volume in industrial reactors should be maximized. A second-order kinetic equation satisfactorily describes the reaction rates. It is possible that oxygen might form a complex with the hydroquinone, followed by the formation of two radicals that rapidly react to yield the corresponding hydroperoxide, as depicted in Scheme 3. The formation of radicals would be the rate-determining step, and consequently the reaction rates can be expressed by Equation (6), in which K_e is the equilibrium constant for the formation of the complex, k is the true kinetic constant, and $[C_R]$ is the concentration of the THAHQ radical.

$$r = k\,[\text{complex}] = k\,K_e\,[C_R]\,[O_2] \qquad (6)$$

An activation energy of 62.7 kJ mol^{-1} was calculated from experiments performed under batch conditions[54] at different temperatures. This result confirms that the radical mechanism [Eq. (6)] is more reliable than the classic autoxidation mechanism.

3.1.3. Extraction

Hydrogen peroxide can be separated from the working solution by different methods, but those most generally used involve extraction with water. The hydrogen peroxide in the working solution has a concentration between 0.8 and 1.9% w/w and efficient extractors can recover more than 95%. The concentration of hydrogen peroxide in this crude product is between 25 and 45%, and further steps are required to meet commercial grades for purity and concentration.

An extremely useful concept for combining the oxidation of AHQ and the separation of hydrogen peroxide in a single step is the recently developed reactive separation process.[54–59] This approach improves the yield of H_2O_2, because immediate separation of by-products avoids their participation in the reaction equilibrium. Reactive separation technology thus leads to substantial savings in capital and operation costs. When the oxidation of AHQ with oxygen and the extraction of hydrogen peroxide from the anthraquinone working solution are carried out in a sieve plate column, both the conversion of AHQ and the extraction efficiency increase with the superficial velocity of the gaseous phase.[60] This increase may be caused by an increase in the contact time of oxygen (reactive gas) and the dispersed phase (reactive liquid phase) owing to their oscillatory motion and/or an increase in the containment volumes of dispersed and gaseous phases.[61] Alternatively, the mass-transfer coefficient at the gas–liquid interface increases with increasing flow rate of the reactive gas,[62,63] and thus the rate of oxidation increases and the conversion of AHQ is improved.

3.2. Oxidation of Alcohols

3.2.1. 2-Propanol

Another alternative for producing hydrogen peroxide is the partial oxidation of primary or secondary alcohols, which produces an aldehyde or ketone as a coproduct.[64,65] This liquid-phase process is based on the autoxidation of 2-propanol (Scheme 4). In this process, which was used by

Scheme 4. H_2O_2 synthesis by the oxidation of a secondary alcohol.

Shell Chemical from 1957 to 1980, the 2-propanol/water azeotrope containing hydrogen peroxide is oxidized by an oxygen-enriched gas stream (80–90% O_2) at moderate temperatures (90–140 °C) under pressure (10–20 bar). To reduce the formation of acetic acid and other by-products, the isopropyl conversion per cycle is kept below 15%, and the oxidation reaction is conducted in several consecutive steps at decreasing temperatures. The reaction vessel must be constructed with enamel-lined steel or passivated steel to avoid the decomposition of hydrogen peroxide formed. The product mixture containing unconverted 2-propanol, acetone, and hydrogen peroxide is separated by evaporation. Water and organic compounds are then further distilled to recover acetone and 2-propanol. The hydrogen peroxide, which concentrates at the base of evaporator, is diluted with water to maintain its concentration below 50% and further purified in a countercurrent solvent-extraction column. The quality of the hydrogen peroxide produced by alcohol oxidation is worse than that from the AO process owing to the solubility of the alcohol in peroxide phase, which makes it difficult to obtain a high purity of H_2O_2.

3.2.2. Methylbenzylalcohol

Lyondell Chemical (formerly Arco Chemical) and Repsol Química developed in parallel a process for the production of hydrogen peroxide based on the oxidation of a methylbenzyl-alcohol (MBA; Scheme 5). MBA is a coproduct of their propylene/oxide/styrene process.

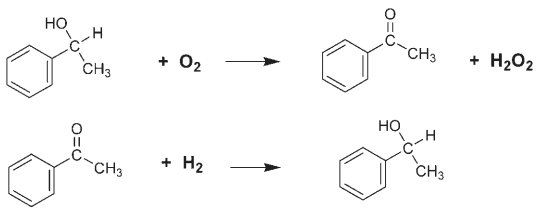

Scheme 5. H_2O_2 synthesis by oxidation of MBA.

 © 2006 Wiley-VCH Verlag GmbH & Co. KGaA, Weinheim

The oxidation of MBA in the liquid phase is usually conducted in the absence of catalyst at temperatures from 120 to 180 °C and pressures between 3 and 10 bar.[66] The patent claims a conversion of MBA of 32 % and a selectivity for H_2O_2 of 97 %.[66] The hydrogen peroxide content attained in the liquid phase of about 7.5 % is much higher than that achieved with the conventional anthraquinone-based process. The liquid hydrogen peroxide stream is fed to the extraction and distillation units to recover the hydrogen peroxide product at the desired concentration. The distillate is hydrogenated to recycle acetophenone back into methylbenzylalcohol.

Although in the original concept involves noncatalytic oxidation of the methylbenzylalcohol[53] to give hydrogen peroxide and acetophenone, the oxidation can also be performed in the presence of a catalyst. Several nickel(II) β-diketone complex were employed as homogenous catalysts, as these complexes do not catalyze the decomposition of hydrogen peroxide.[67] As a general rule, the addition of nickel increases the alcohol conversion, but the yield of hydrogen peroxide depends on the nature of the ligand employed. Cyclic β-diketones, such as 2-acetylcyclopentanoate or 2-acetylcyclohexanoate, increase the yield and selectivity for H_2O_2, but nickel complexes with basic ligands inhibit the oxidation reaction.

A recent patent[68] claims that the oxidation of primary and secondary alcohols with molecular oxygen can efficiently yield hydrogen peroxide in the presence of an *N*-hydroxyimide (Scheme 6). The *N*-hydroxyimide in this process favors the formation of radicals from the secondary alcohol.[69] A promoter can also be used in combination with the imide catalyst to enhance both the reaction rate and selectivity. Many compounds have been found to promote the target reaction, including carbonyl-containing organic compounds, transition-metal salts, and organic salts of Group 15 and 16 elements. A significant improvement of this process was achieved by adding a reactive solvent that allows cooxidation of the MBA.[67,70,71] The cooxidation of hydrocarbons has been known for a long time,[72–75] but this methodology has not been applied to the oxidation of secondary alcohols. This method affords high concentrations of H_2O_2 and very high selectivity for H_2O_2 with respect to consumed MBA (> 99 %).[70,71]

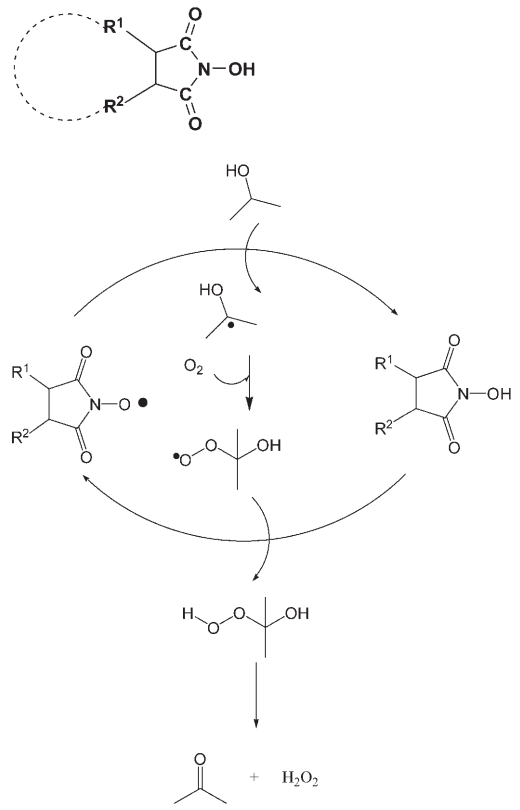

Scheme 6. Activation of *N*-hydroxyimide and proposed catalytic cycle for oxidation of secondary alcohols.

3.3. Electrochemical Synthesis

Hydrogen peroxide can be synthesized by electrolysis of a dilute solution of NaOH in an electrochemical cell (Dow process). The anodic and cathodic reactions are given in Equations (7)–(9).

$$\text{Anode}: \ 2\,OH^- \rightarrow H_2O + {}^1/_2O_2 + 2\,e^- \quad (7)$$

$$\text{Cathode}: \ H_2O + O_2 + 2\,e^- \rightarrow HO_2^- + OH^- \quad (8)$$

$$\text{Overall reaction}: \ NaOH + {}^1/_2O_2 \rightarrow HO_2Na \quad (9)$$

The alkaline peroxide is synthesized at an H_2O_2/NaOH weight ratio of 1:1.7 by cathodic reduction of oxygen on a trickle-bed cathode. This cathode consists of graphite chips coated with carbon black and a fluorocarbon binder to facilitate O_2 transfer at atmospheric pressure.[76,77] A cell operating at 2.3 V and 62 mA cm^{-2} yields an NaOH/HO_2^- weight ratio of 1.6–1.8:1 at a current efficiency of 90 %. Combining the trickle-bed cathode with an ion-exchange membrane affords a 2.1 % w/w HO_2^- solution in 5.0 % w/w NaOH with 95 % current efficiency.[78] The anolyte, which consists of a solution of NaOH in demineralized water, is fed into the anode compartment of the cell. A solution of Na_4edta (edta = ethylenediamine-*N*,*N*,*N*′,*N*′-tetraacetate) is added to the anolyte as a trace-metal scavenger at a rate sufficient to maintain a solution concentration above 0.002 % in the electrolyte. This alkali peroxide technology is best suited to applications for which it is not necessary to separate the peroxide from the caustic soda in the product, for example, pulp bleaching. An integrated electrochemical synthetic process for pulp bleaching has been patented.[79]

A new membrane-type electrochemical cell with a sulfuric acid solution as electrolyte has also been reported.[80] The addition of poly(4-vinylpyridinium-*p*-toluensulfonate (PVPPTS) enhances the cell performance, and higher current density, lower cell voltage, and higher peroxide concentrations are obtained.

 © 2006 Wiley-VCH Verlag GmbH & Co. KGaA, Weinheim

3.4. Comparison of Large-Scale Production Methods

The AO process has supplanted all its competitors (primary and secondary alcohol oxidation, electrochemical) and accounts for more than 95 % of the world's production of H_2O_2. One reason for this is that H_2O_2 is produced continuously at mild temperatures and direct contact of O_2 and H_2 is avoided. However, the AO process suffers from inefficiencies caused by mass-transport limitations in the hydrogenation and oxidation reactors, as well as organic contamination of H_2O_2 during its recovery by liquid–liquid extraction. As a consequence, heavier equipment and higher temperatures than those for kinetically controlled reactions are required. The difficulty in controlling the H_2/AQ ratio and the AQ residence time during the hydrogenation step leads to the formation of by-products (overhydrogenated AQ and solvent), which must be continually removed. A further problem is cross-contamination of the phases as a result of contact between the working solution and water within the stripping column. Furthermore, the partition coefficient of H_2O_2 between water and the organic phase is not optimal, and thus distillation of both the concentrated and purified H_2O_2 is required, which is associated with considerable consumption of energy.[1,2]

4. Emerging Alternatives

To take advantage of the full potential of hydrogen peroxide, a simple production process that can be implemented at the point of use is needed. This is the goal of recent approaches based on a clean technology that generates hydrogen peroxide directly from H_2 and O_2.

4.1. Direct Synthesis

One alternative route to H_2O_2 that avoids the use of AQ is the direct synthesis from hydrogen and oxygen in the presence of a catalyst. A real breakthrough in H_2O_2 chemistry would be a one-pot process involving the direct synthesis of H_2O_2 from its elements[81] and its direct application in an oxidation reaction.[28,82] The reaction $H_2 + O_2 \rightarrow H_2O_2$ is in principle the simplest method to form hydrogen peroxide and should lead to a reduction in the capital investment and operating costs. Notwithstanding, the reaction scheme is more complex because of the occurrence of simultaneous or consecutive reactions, all of which are thermodynamically favored and highly exothermic (Scheme 7). Among these unwanted reactions are: a) the formation of water (reaction 2), b) the decomposition of hydrogen peroxide (reaction 3), and c) the reduction of H_2O_2 (reaction 4). Each of these reactions can be favored depending on the catalyst used, the promoters or additives in the reaction medium, and the reaction conditions. Although the catalytic liquid-phase oxidation of hydrogen for the production of hydrogen peroxide has been known since 1914[83] and several patents have been issued since,[84–118] this process has not yet been put into practice.

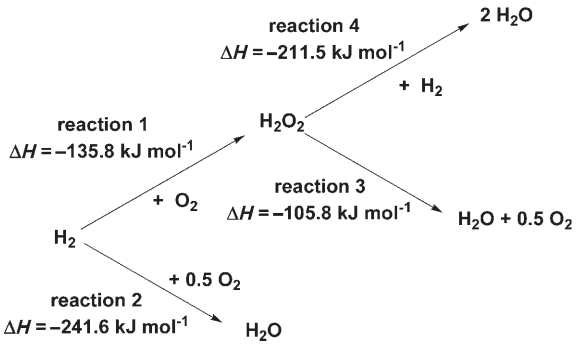

Scheme 7. Reactions involved in the direct production of H_2O_2.

There are two major drawbacks to the direct synthesis of hydrogen peroxide. First, hydrogen/oxygen mixtures are explosive over a wide range of concentrations,[88] so either the ratio of hydrogen to oxygen needs to be carefully controlled or a diluent such as nitrogen, carbon dioxide, or argon must be added. As the stoichiometry that corresponds to the best selectivity for H_2O_2 lies the explosive regime for O_2/H_2 mixtures (5:1 to 20:1), large quantities of nitrogen must be added for safety reasons, which naturally greatly reduces productivity.[84] A strategy to avoid direct contact between O_2 and H_2 reagents is the use of catalytic membrane reactors, in which pure gases can be used. The other major problem in obtaining good selectivity for hydrogen peroxide over water is that catalysts for the production of hydrogen peroxide are also active for the combustion of hydrogen to water and the decomposition of hydrogen peroxide.[119–122] As pure hydrogen peroxide is highly unstable and decomposes into water and oxygen, the reaction between H_2 and O_2 to yield hydrogen peroxide must be conducted in the presence of an appropriate solvent. Thus, three phases, namely gases (H_2 and O_2), a liquid (solvent), and a solid (catalyst) are required, which makes the process exceedingly complicated. Therefore, in many works attempts were made to minimize the mass-transport barrier between the gas phase and the solvent. For example, one innovative idea to deal with the inherent transport limitations of the process is the proposal to employ microbubbles of H_2 and O_2.[109]

These drawbacks, however, appear to be controllable, as Degussa-Headwaters have announced the construction in 2007 of a new production plant for the direct synthesis of hydrogen peroxide coupled with propylene oxide production.[123] The patents of these companies reveal that an industrial method is possible involving an active catalyst based on palladium nanoparticles deposited on carbon and an appropriate solvent (in general an alcohol), as well as the use of concentrations of hydrogen outside the flammability limits.

4.1.1. Catalysts

The catalysts described in the literature are based on noble metals or combinations thereof supported on a great variety of substrates such as alumina, silica, and carbon.[96,119–124] Palladium is the most suitable active metal in most catalyst formulations. Acids are often incorporated into the reaction medium in addition to the heterogeneous

 © 2006 Wiley-VCH Verlag GmbH & Co. KGaA, Weinheim

catalyst to delay or prevent the decomposition of hydrogen peroxide, which occurs in the presence of base.[119] Another approach involves the addition of catalyst poisons (i.e., halides) to delay the water production and increase the hydrogen peroxide selectivity.[126] Although halides show good selectivity for H_2O_2 formation, they also delay the hydrogen conversion.[119,121] This suggests that the halide ions are adsorbed on the metal centers that participate in the surface reaction between hydrogen and oxygen.[125] Chlorides[101] and bromides[111] are the most commonly employed halides.[125] An obvious choice as promoters are the hydrogen halides, as these combine the function of the acidic proton with the effect of the anion on the catalyst centers.[90,91,125] Phosphoric acid is also often used as stabilizer of hydrogen peroxide because it has not only a stabilization effect but also the function of an acid.[114] Special equipment is required for operation with highly concentrated acid solutions to avoid corrosion. The presence of acid solutions and halogen ions also favors the dissolution of the active metal,[127,128] which results in deactivation of the catalyst. Colloidal Pd is believed to be involved in the catalytic cycle of palladium catalysts, which may, in part, be homogeneous. Although such a system is very interesting at a fundamental level, the management of a colloid would be difficult in a commercial process, because its recovery is not viable at the very low concentration of dissolved metal involved.

For these reasons, acidic supports are often used to reduce the required concentration of inorganic acid and hence minimize its impact on corrosion. Among the solid acids, regularly cited examples include a superacid consisting of tungsten oxide on a zirconia substrate,[99] acidic supports such as molybdenum oxide on zirconia, vanadium oxide on zirconia, supported sulfuric acid catalysts,[97,118,129] and fluorinated alumina.[119] However, only very low yields of hydrogen peroxide are obtained with this methods. In contrast, excellent yields have been reported recently with neutral solutions and heterogeneous catalysts consisting of functionalized carbons with sulfonic acid groups,[123] or sulfonic acid functionalized polystyrene resins (PS-SO_3H).[130–133] These PS-SO_3H resins exhibit moderate specific surface areas of approximately 40 $m^2 g^{-1}$ and a high degree of cross-linking. Neither property seems to be detrimental to the liquid-phase reaction because the resins swell in the presence of solvent, and access of the reagents (H_2 and O_2) to the active sites is thus facilitated.[134]

Catalysts prepared by anchoring Pd^{II} ions onto PS-SO_3H ion-exchange resins (1.34–1.49 % w/w Pd) are highly effective for the direct synthesis of hydrogen peroxide with methanol as solvent at 40 °C. The consumption of hydrogen is in all cases fairly high (> 90 %), and the H_2O_2 concentration profiles depend linearly on reaction time, which indicates that the reaction proceeds at a constant rate (Figure 5). The hydrogen peroxide production rates are very high (close to 1100 mmol $H_2O_2 h^{-1} g(Pd)^{-1}$) and are almost two orders of magnitude higher than the value for methods with acid-free solvents.[135] The high performance of these catalytic systems results from the ability of the sulfonic acid groups of the resin to interact with and stabilize the Pd^{II} ions without further reduction to metallic palladium, as revealed by photoelectron spectroscopy. The Pd $3d_{5/2}$ peak shows a component at 336.5 eV, which is assigned to PdO clusters, and a second component at 338.2 eV associated with Pd^{II} ions interacting with the SO_3H groups of the resins (Figure 6). The ratio of these species depends on the type of resin employed in the

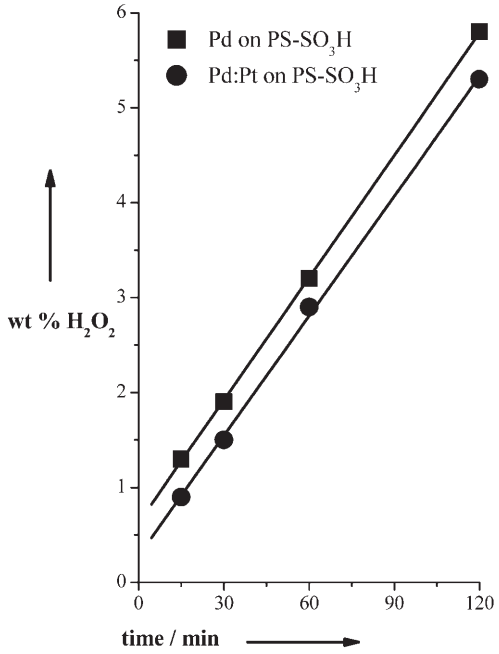

Figure 5. Hydrogen peroxide concentration profile versus time for the direct reaction of hydrogen and oxygen at 313 K.[132]

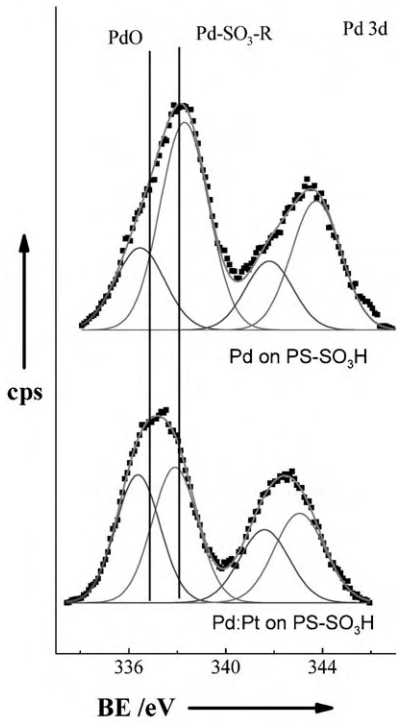

Figure 6. Photoelectron spectra of the Pd 3d region of catalysts supported on PS-SO_3H exchange resins.[132] cps = counts per second, BE = binding energy.

 © 2006 Wiley-VCH Verlag GmbH & Co. KGaA, Weinheim

preparation; resins with high surface densities of sulfonic acid groups lead to higher amounts of Pd^{II} ions interacting with the SO_3H groups. Thus, photoelectron spectroscopy provides direct evidence of the interaction between small palladium particles and the sulfonic acid groups of the resin.[132] This interaction creates a positive charge on the Pd particles which enhances the selectivity for hydrogen peroxide.

Appropriate modification of the support substrate also appears to be of great importance for the optimization of catalyst performance. For example, hydrophobic substrates are especially well suited for this purpose as mass transport is facilitated after the formation of hydrogen peroxide. Thus, the extent of secondary reactions of hydrogen peroxide, such as hydrogenation or decomposition into water, is minimized. Supports modified with this objective include carbon treated with fluorine,[101] inorganic supports such as alumina, silica/alumina, zeolites, etc. coated with a thin layer of hydrophobic polymer,[137] as well as sulfonic acid functionalized carbon.[138]

Most catalysts employed in the direct synthesis of H_2O_2 are based on palladium. These catalysts are activated by mild, carefully controlled reduction to form small metallic Pd clusters on the support surface. Recent studies propose that palladium nanoparticles with a high number of Pd atoms with a low degree of coordination are active and selective catalysts for hydrogen peroxide (Figure 7).[118,139] Owing to their

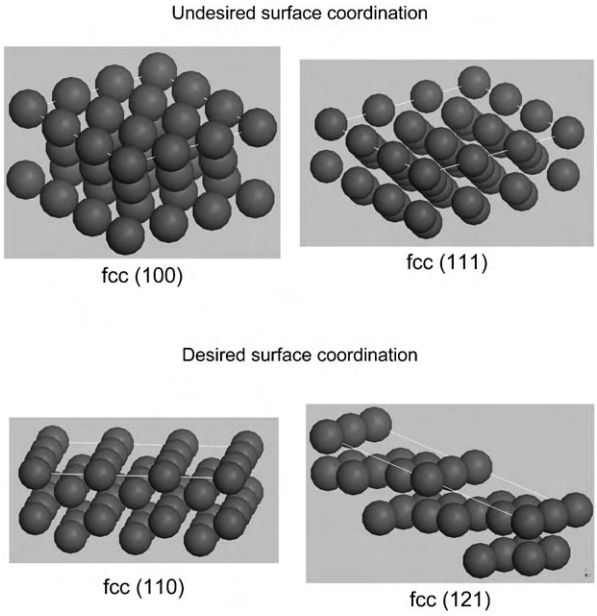

Figure 7. Desired and undesired surface coordinations of metal particles for the synthesis of H_2O_2 from H_2 and O_2.

electrodeficiency, these locations appear particularly well suited for interacting with promoters present in the reaction medium. This particular structure of Pd particles may be related to the promoter effect observed upon adding small amounts of a second metal to palladium.[91,118,140] It can also be inferred that the improvement in performance is not associated with alloy formation between Pd and the second metal, as the proportion of promoter is very low.

It has recently been demonstrated that high selectivity for H_2O_2 can be achieved in the presence of cationic palladium species. No prior reduction of the catalyst is required in this case,[123–132] and the selectivity for H_2O_2 is improved upon oxidation of the catalyst by oxygen[136] or treatment with acid following impregnation.[117,138] This observation may be understood by assuming that the reduced Pd species readily form H_2O_2 but are also able to oxidize the formed H_2O_2 to give H_2O at a high rate, whereas a mild oxidation treatment of the catalyst to some extent inhibits the metallic character of the metal particles, which results in a net higher rate of H_2O_2 production.[142]

The in situ production of H_2O_2 from O_2/H_2 mixtures over supported Au catalysts was investigated with a view to a possible combination with the oxidation of propene to propene oxide.[143,144] The presumed oxidant in this reaction is a surface hydroperoxide species formed on the metal surface. Studies of the energetics of the elementary reactions involved in the synthesis of hydrogen peroxide over noble-metal catalysts (Pd, Pt, Ag, and Au) by the bond order conservation Morse potential (BOC-MP) approach showed that the formation of hydrogen peroxide is most selective on gold catalysts.[145] This observation supports the notion that gold is an active metal for the direct synthesis of hydrogen peroxide. Such an early prediction was then confirmed experimentally by using alumina,[146] silica,[147] titania,[148] and iron oxide[135] as substrates for gold particles. The catalytic behavior was also studied by theoretical calculations, which revealed that small gold clusters can act as viable sites for the direct synthesis of hydrogen peroxide.[149–153] It was found that the rate of H_2O_2 formation decreased with an increase in the mean diameter of the Au nanoparticles.[147] This tendency was also corroborated with an Au/SiO_2 catalyst, prepared by impregnation methodology and with a mean diameter of the Au particles of about 30 nm. Only H_2O but in no H_2O_2 was produced.[147]

Substantial improvements in the yield of H_2O_2 can be obtained with Au catalysts containing a second metal. The best suited combination is gold and palladium,[135,146,148,154,155] for which the rate of H_2O_2 production is higher than the sum of the rates provided by the individual monometallic systems.[133,135,146,148,154,155] A atomic ratio of the two metals of 1:1 gives the best results.[135,146,154] This effect in Pd/Au alloys was recently attributed to the isolation of Pd atoms within the gold matrix, whereby these isolated atoms are the most active catalytic centers.[156] However, it should be emphasized that both the selectivity and production rate of H_2O_2 are far below the levels required for industrial application.

4.1.2. ***Solvents***

Water is the most suitable solvent because it offers the greatest safety of the process, is nontoxic, nonflammable, and highly miscible with hydrogen peroxide. A major drawback is the very low solubility of reagent gases (both H_2 and O_2) in water, which strongly limits the rate of hydrogen peroxide production. Solvents other than water have been used with a view to overcoming this limitation, for example, a biphasic mixture of water and a fluorinated solvent, which leads to a

 © 2006 Wiley-VCH Verlag GmbH & Co. KGaA, Weinheim

high solubility of oxygen and hydrogen.[157,158] Mitsubishi has also reported a process for the direct generation of H_2O_2 in an organic solvent.[159] However, contamination of the aqueous phase by the organic solvent is still an unsolved problem.

CO_2 is a more suitable as a solvent under both liquid and supercritical operating conditions. H_2 and O_2 are miscible with CO_2 in all proportions, and, even under subcritical conditions, the solubility of H_2 and O_2 in CO_2 is much higher than in organic solvents or water. However, supercritical conditions are preferred to avoid mass transport limitations between the gas and liquid phase.[160] Furthermore, CO_2/H_2 mixtures do not react to form CO over a Pd catalyst at temperatures below 100 °C.[161–162] Also, the solubility of hydrogen peroxide in CO_2 is low, which means that H_2O_2 is expelled from the solvent once formed and a biphasic system is formed. The direct synthesis of H_2O_2 has been achieved following these principles with either CO_2-soluble Pd^{II} or Pd^0 catalysts.[163–165]

Mixtures of hydrogen peroxide and organic solvents are of practical importance, as they can be used in oxidation reactions in which H_2O_2 is the source of oxygen.[9–32] Organic solvents, especially alcohols, are potentially better suited than water for the synthesis because of the greater solubility of H_2 and O_2.[166–168] The performance of a palladium-supported catalyst on a hafnium phosphate/viologen phosphonate material was studied in several different organic solvents (methanol, ethanol, 2-propanol, dioxane, and acetone), as well as in water, as the liquid phase.[169] Even though the system appears to be limited by mass transfer at the liquid–gas interface, differences in the rate of H_2O_2 formation are observed among the organic solvents. Methanol gave the highest rate of reaction. The results obtained with water depend greatly on the acid added to the reaction medium (an acid is always required for the direct formation of H_2O_2). The rate of H_2O_2 formation in water with HCl, at least initially, was comparable to that observed in organic solvents. However, solvents such as methanol,[170] acetone,[114] and acetonitrile[171] enhance both H_2 conversion and H_2O_2 selectivity. Solvents such as toluene and hexane increase the solubility of hydrogen and oxygen in the liquid phase,[119] and hence enhance the reaction rate, although they impair the selectivity for H_2O_2. These results underscore the fact that the solubility of the reagent gases O_2 and H_2 in the solvent is indeed an important condition for the production of hydrogen peroxide,[172] but the catalytically active phase within the reaction medium also plays a deciding role. Thus, if the concentration of H_2 gas in the liquid phase is too high, the palladium component is reduced to Pd^0 metal, which in turn favors the decomposition/hydrogenation of hydrogen peroxide.[142] A low concentration of dissolved hydrogen would result in a low reaction rate.

The principal role of the solvent is to increase the solubility of hydrogen in the liquid phase, although it can also act in different ways. Solvents such as ethanol (or oxidized species derived from it) and acetonitrile are prone to coordinate palladium and hence may act as an inhibitors of the water-forming reaction.[173,174] Another interesting observation is the almost complete suppression of Pd colloids in the bulk liquid when organic solvents are used.[173,174] This observation confirms that the supported Pd is the primary form of the active catalyst, and explains why catalysts become more stable in industrial reactors when through the use of solvents.

4.1.3. Membranes

A recent, elegant approach to direct hydrogen peroxide synthesis involves the use of membrane catalysts to keep the two reactants separate and thus avoid the major safety concerns of hydrogen/oxygen mixtures.[136,137,141,175–179] In particular, dense palladium membranes display good performance for the liquid-phase synthesis of hydrogen peroxide from H_2 and O_2.[136] Another important role of these membranes is to supply atomic hydrogen to a catalyst deposited on the pores of the surface, which is in contact with an oxygen-containing liquid phase.

A significant increase in the selectivity for H_2O_2 was observed in a Pd membrane consisting of a thin film of Pd metal deposited on the stable surface of a Pd/Ag alloy on α- or γ-Al_2O_3.[136] The marked increase results from the bulk oxidation of the Pd film. The selectivity can be increased slightly further by covering the oxidized Pd film with a hydrophobic polymer membrane. This membrane is only permeable to H atoms, but inhibits the transport of molecular H_2 to the other side of the membrane, where O_2 gas is bubbled in the liquid phase (0.02 M H_2SO_4).[136] As H atoms are more reactive than molecular H_2, the permeated H atoms react with molecular oxygen to yield H_2O_2 at the catalyst surface. The H_2O_2 produced remains in the aqueous phase. The hydrophobic nature of the polymeric layer prevents further contact of the produced H_2O_2 with the catalyst surface. This design leads to complete consumption of H_2, which indicates that the transport of H_2 through the membrane is rate-limiting. This situation allows the production of H_2O_2 to be modulated by controlling, for example, the pressure of H_2. Besides conversion and selectivity, the H_2O_2 concentration attained in the liquid phase is essential for potential applications. Although the use of membranes avoids the formation of explosive mixtures, the reaction rate of H_2O_2 formation, which is essentially controlled by mass transport, is too low for industrial applications.

4.2. Photocatalysis

Photocatalytic reactions over semiconductor oxides have been investigated in some detail in recent years.[175] Reactive O-containing species, namely $OH^{\bullet}$, O_2^-, and H_2O_2, are usually formed at the surface of semiconductor oxides under UV irradiation.[180–184] Illumination of an aqueous suspension of TiO_2 particles at an energy above 3.23 eV ($\lambda > 385$ nm for anatase) excites an electron from the valence band (VB) to the conduction band (CB) of the semiconductor, while a positively charged hole is formed in the VB. The positive hole (h^+) oxidizes H_2O to form an $OH^{\bullet}$ radical, and the electron reduces O_2 to O_2^-. Thus, the edges of the VB and CB represent the oxidation and reduction sites, respectively, on a TiO_2 particle. Hydrogen peroxide is produced through

© 2006 Wiley-VCH Verlag GmbH & Co. KGaA, Weinheim

dismutation of superoxide of a radical and also by recombination of hydroxyl radicals at the liquid interface or in the bulk solution.[185,186] Both anatase and rutile crystalline forms of TiO_2 are photoactive but their reactivities are different. As the anatase phase is produced at lower temperatures than the rutile one, a higher density of surface defects is expected in the anatase phase. This may be the reason for the high catalytic activity observed for the production of hydrogen peroxide on anatase powder.

The concentrations of H_2O_2 formed on these UV-irradiated TiO_2 surfaces are in the micromolar range. The production of H_2O_2 can be increased by up to 20 times by the addition of small amounts of Cu^{II} solution to the suspension of TiO_2 particles. The concentration of H_2O_2 increases progressively with 0–50 μM added Cu^{II} and then levels off. Cu^{2+} ions are released from the surface of the Cu/TiO_2 particles upon illumination of an O_2-purged suspension and are redeposited on the surface upon purging with nitrogen.[187] It is assumed that dissolved oxygen reacts with the photogenerated electron to form O_2^- species.

Two alternative mechanisms have been proposed for the formation of H_2O_2.[188,189] The first involves oxidation of H_2O by the photogenerated hole according to Equation (10). The second considers the reduction of dissolved O_2 by the photogenerated electron as shown in Equation (11), in which h_{VB}^+ and e_{CB}^- are the photogenerated hole in the VB and the electron in the CV, respectively.

$$2\,H_2O + 2\,h_{VB}^+ \rightarrow H_2O_2 + 2\,H^+ \quad (10)$$

$$O_2 + 2\,H^+ + 2\,e_{CB}^- \rightarrow H_2O_2 \quad (11)$$

Comparison of the amount of hydrogen peroxide produced in the presence and absence of O_2 over Cu^{II} ions allows the mechanism involved to be resolved. H_2O_2 is only formed when O_2 is bubbled through the TiO_2–Cu^{2+} suspension but not under O_2-free conditions.[183] These results are conclusive that the mechanism of H_2O_2 formation involves the reduction of O_2 by the photogenerated e_{CB}^- (Figure 8).

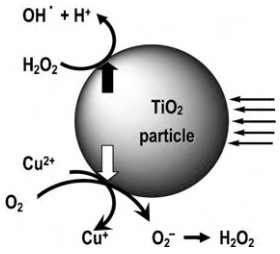

Figure 8. Photocatalytic formation of H_2O_2 and OH• in the presence of copper(II) ions.

The principal species involved in photocatalytic reactions on TiO_2 surfaces are OH•, H_2O_2, and O_2^-. The OH• radical is the most reactive of these species, and is also formed from H_2O_2 in the Fenton reaction in the presence of Fe^{2+} [Eq. (12)].[190]

$$Fe^{2+} + H_2O_2 \rightarrow Fe^{3+} + OH^{\cdot} + OH^- \quad (12)$$

The tandem reactions of H_2O_2 production by the TiO_2–Cu^{2+} system and the decomposition of H_2O_2 into OH• radicals through the Fenton reaction can be exploited for the oxidation of organic substrates in the liquid phase. Similarly, the quantum yield of the photocatalytic oxidation of aromatic compounds by TiO_2 increases by about 16-fold in the presence of Cu^{II}.[190] However, addition of H_2O_2 to the reaction system inhibits the photoxidation ability of TiO_2 owing to the formation of a peroxido complex on the TiO_2 surface.

As stated above, the most plausible mechanism of H_2O_2 formation involves O_2 reduction by an electron in the CB.[182,183] However, little is known about the influence of the presence of anions or the nature and concentration of the hole scavenger. If H_2O_2 were formed mainly through dismutation of superoxide radicals then the rate of formation would be pH-dependent. F^- ions adsorbed on the surface of TiO_2 particles have a strong influence on the photocatalytic oxidation mechanism of organic substrates.[191,192] The photodegradation of phenol in the TiO_2/F system proceeds almost entirely through oxidation mediated by free OH radicals, whereas on pure TiO_2 about 10% if the reaction results from direct hole oxidation and 90% from adsorbed OH. It was reported recently that UV irradiation of fluorinated TiO_2 suspensions in water in the presence of oxygen and a hole scavenger leads to the production of H_2O_2 with a steady-state concentration of up to 1.3 mM when the TiO_2 surface is completely covered by fluoride ions.[193] A possible role of the inert ligand is the inhibition of the formation of surface peroxido/superoxido species.

4.3. Fuel Cells

Large-scale production of hydrogen peroxide by electrolysis can be traced back to 1895.[194] The Consortium für Elektrochemische Industrie investigated the electrolysis of sulfuric acid and successfully obtained peroxomono- and peroxodisulfuric acid, further hydrolysis of which yielded hydrogen peroxide. This proved to be an economically viable process for the production of highly concentrated solutions of hydrogen peroxide of high purity and stability. Electrogenerated hydrogen peroxide is currently employed as a bleach in the pulp and paper industry. The production of H_2O_2 relies on the electrolysis of O_2 in alkaline solutions in an electrochemical cell containing a carbon cathode.[76,77] On-site electrochemical production of H_2O_2 for industrial applications requires a production method with high reaction rates, high efficiency, and low costs.

Hydrogen peroxide can be electrosynthesized through two-electron reduction of O_2 in acidic and alkaline media by using a large variety of three-dimensional electrodes (e.g., carbon-particle bed, reticulated vitreous carbon (RVC), and gas-diffusion electrodes. As described in Equations (7) and (8) in Section 3.3, the hydroperoxide ion HO_2^- (the conjugate base of hydrogen peroxide) is produced in alkaline media through anodic oxidation of OH^- as well as cathodic reduction of O_2. The overall four-electron reaction for this electrolytic process is depicted in Equation (13).

$$O_2 + 2\,OH^- \rightarrow 2\,HO_2^- \quad (13)$$

 © 2006 Wiley-VCH Verlag GmbH & Co. KGaA, Weinheim

The electrochemical production of HO_2^- according to Equation (13) on an industrial scale in alkaline solution has been developed.[34,35,195] The yield for a small cell with a carbon-felt cathode at a cell voltage of 1.6 V and 100 mA cm^{-2} at 60 °C was 2% w/w HO_2^- with a current efficiency of 75%.[195]

A promising alternative is the production of hydrogen peroxide with inexpensive fuel cells, which, unlike electrolytic devices, do not require electrical energy. Several methods have been proposed for the direct and continuous production of hydrogen peroxide in fuel cells. The simplest design consists of a fuel cell divided by an electrolyte membrane (nafion 117). The anodic face of this membrane (where H_2 is oxidized) is deposited with Pt, and the cathode face (where O_2 is reduced to hydrogen peroxide) is covered with graphite or an Au mesh.[196] A current density of 10–30 mA cm^{-2} was obtained for a 0.1 M HCl solution in contact with the cathode. The current efficiency sharply dropped from 100 to 70% during 3 h of operation. Another design of divided fuel cells comprises a membrane of polyfluorosulfonic acid monomer sandwiched between an H_2-diffusion anode and an O_2-diffusion cathode with different catalysts, and a water flow with O_2 is directly injected into the cathode. This system yields current efficiencies below 70%.[197]

The limiting factor in these designs is the O_2 concentration in the cathode compartment. This problem has been solved recently in a new fuel-cell setup for the synthesis of H_2O_2.[198] The underlying concept of this fuel cell is the application of a three-phase boundary (solid cathode/aqueous electrolyte/gaseous O_2) for the formation of hydrogen peroxide. The use of a porous membrane electrode prepared from carbon powder (vapor-grown carbon fiber, VGCF) allows an O_2 pressure as high as 1 bar at the active site at the three-phase boundary.[199] In this way, the reduction of O_2 to H_2O_2 is enhanced and the consecutive degradation of H_2O_2 into H_2O is minimized. By feeding pure O_2 (1 bar) into the cathode, a concentration of H_2O_2 as high as 6% w/w can be reached after 2 h at a high current efficiency of about 90%. Both the formation rate of H_2O_2 and current density are slightly decreased when air is used instead pure O_2, but the performance of the cell is not altered. For the industrial production of H_2O_2 by this method, the replacement of O_2 with air has a considerable cost advantage.

Another design for on-site production of HO_2^- is an undivided alkaline fuel cell (AFC) containing an H_2-diffusion anode and a commercial O_2-diffusion electrode.[200] H_2 gas is oxidized to water in a two-electron reaction at the anode [Eq. (14)], and O_2 gas is reduced to HO_2^- at the cathode. The overall two-electron process of the AFC is given in Equation (15).

$$H_2 + 2\,OH^- \rightarrow 2\,H_2O + 2\,e^- \quad (14)$$

$$H_2 + O_2 + OH^- \rightarrow H_2O + HO_2^- \quad (15)$$

As for an electrolytic system, 1 mol of OH^- is also consumed per mol of HO_2^- generated. Quasi-steady-state behavior is observed when a fresh KOH solution is continuously injected into the cell at rates of 20 mL min^{-1}, and current densities of about 100 mA cm^{-2} and current efficiencies close to 100% are obtained for 1.0 M KOH at 20 °C.[201] However, lower electrolyte flow rates lead to diminished electrogeneration of HO_2^-. A drop in the liquid flow rate from 20 to 2.1 mL min^{-1} diminishes the average current density by 11% and the current efficiency by 27%. This loss of cell performance may be related to the adsorption of HO_2^- on the anode surface, followed by its decomposition to O_2 catalyzed by the Pt anode.

Another important parameter for the production of HO_2^- is the external resistance between the electrodes, as this regulates the cell voltage and current density supplied by the flow AFC. For external resistances above 100 Ω, the experimental conditions exert only a slight influence on the voltage–current density curves. Cell voltages over 0.650 V always lead to current densities lower than 10 mA cm^{-2}, which suggests that the cell process is limited mainly by the charge-transfer reactions.[201] When the external resistance decreases from 100 to 0.10 Ω, the activation can also be influenced by mass transfer and ohmic losses.

Another innovative approach for the production of hydrogen peroxide from H_2 and air with the simultaneous generation of electricity in a fuel cell relies on the chemical attachment of quinones to a carbon electrode.[202] In the classical anthraquinone process (Section 3.1), the quinone is hydrogenated catalytically in an appropriate solvent to give the corresponding hydroanthraquinone (AHQ), which is then oxidized with air to re-form the original anthraquinone and simultaneously produce hydrogen peroxide (see Scheme 1). In this new approach, the quinone moiety is attached on the surface of a glassy-carbon electrode (Figure 9). Anthraquinone, and especially phenanthrenequinone (PQ), reduce oxygen in alkaline media to the superoxide radical. This reaction is mediated by the semiquinone anion of AQ or PQ ($AQ^{\bullet -}$, $PQ^{\bullet -}$), formed by the electrochemical reduction of the quinone. It has been proposed that these semiquinones provide the adsorption sites for oxygen; thus, the first step

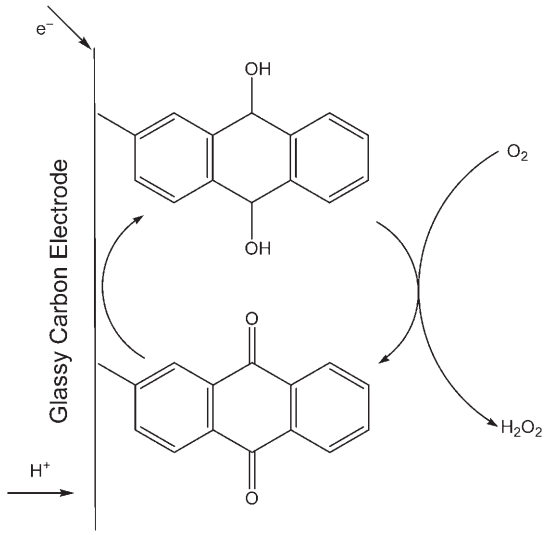

Figure 9. Attachment of a quinone on the surface of a glassy-carbon electrode for the electrochemical synthesis of H_2O_2.

© 2006 Wiley-VCH Verlag GmbH & Co. KGaA, Weinheim

in the reduction of O_2 in alkaline solutions is the formation of superoxide. The adsorbed superoxide is then further reduced to peroxide.[203] The reaction mechanism most probably involves partially reduced C=O surface groups, and it has been speculated that the very active native surface groups on glassy carbon interact with the *o*-quinone functionalities.[204]

H_2O_2 generated in situ from O_2 and H_2 in a polymer electrolyte membrane fuel cell can be used for the direct hydroxylation of benzene to phenol with the simultaneous generation of electricity in both the liquid[205] and gas phase.[206] The essence of this process is the electrochemical production of hydrogen peroxide at the cathode through reduction of O_2 and subsequent chemical reaction with an organic substrate.[207] Figure 10 illustrates the experimental setup of the membrane–electrode assembly. The electrochemical reduction of O_2 proceeds through two pathways, which are mainly determined by the electrocatalyst and electrode potential: direct four-electron reduction of O_2 into H_2O [Eq. (16)] and two-electron reduction of O_2 into H_2O_2 [Eq. (17)].[208]

$$O_2 + 4\,H^+ + 4\,e^- \rightarrow 2\,H_2O \quad (16)$$

$$O_2 + 2\,H_2O + 2\,e^- \rightarrow H_2O_2 + 2\,OH^- \quad (17)$$

The rate of phenol formation depends on the current and increases to a maximum value of 0.17 mmol min^{-1} at 600 mA and 60 °C (or 0.25 μmol min^{-1} at 900 mA and 80 °C) and then decreases at higher currents (Figure 10, bottom).[209] From an electrochemical point of view, the current—as a kinetic parameter—accounts for the reaction rate of the electrochemical reaction, whereas the voltage—as a thermodynamic parameter—determines which reaction occurs. The observed dependence of phenol formation is assumed to be closely related to the in situ formation of H_2O_2. At higher voltages, O_2 reduction may occur through the peroxide pathway. The amount of in situ generated H_2O_2 increases with the current, which leads to an increased rate of phenol formation.

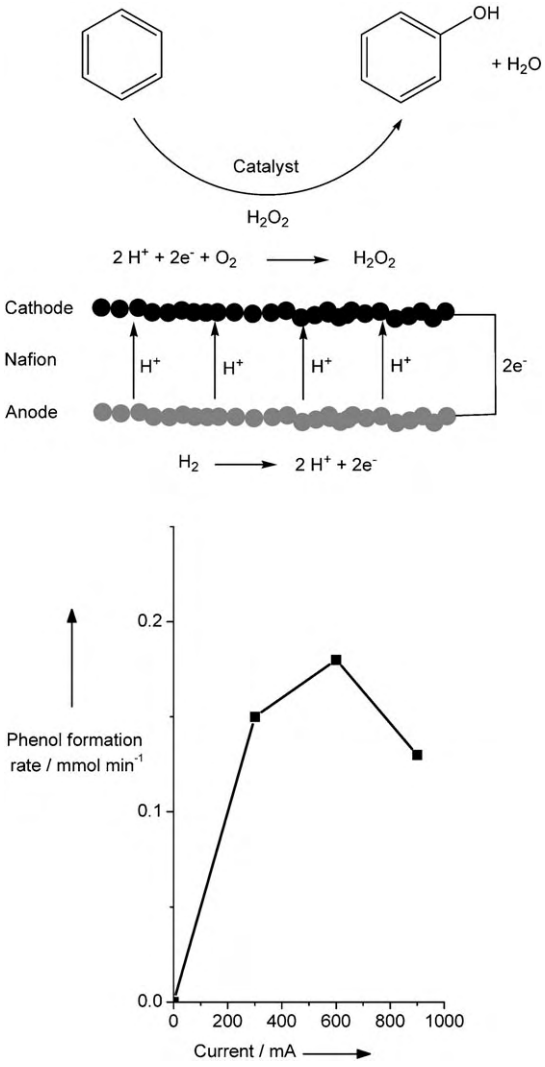

Figure 10. Top: Reaction scheme for phenol synthesis with in situ generated H_2O_2 in a proton-exchange membrane fuel cell (PEMFC). Bottom: Influence of current on the rate of formation of phenol at 60 °C. Cathode: Pd black; anode: Pt black.[209]

4.4. Synthesis from $CO/O_2/H_2O$ Mixtures

The production of H_2O_2 is possible not only by direct synthesis from H_2/O_2 mixtures, but also from mixtures of CO, O_2, and H_2O [Eq. (18)], as first demonstrated in the presence of metal complexes.[210]

$$CO + O_2 + H_2O \rightarrow CO_2 + H_2O_2 \quad (18)$$

The reaction is thermodynamically favorable, as the standard free energy is highly negative ($\Delta G^\circ = -134.2$ kJ mol^{-1}). The feasibility of the concept was first demonstrated by using homogeneous palladium triphenylphosphate complexes. The turnover (TON) values (moles of H_2O_2 produced per mol of Pd), however, were no higher than 5, thus the catalyst seem to be unsuitable for technical application. Furthermore, the system is rapidly deactivated as a result of oxidation of phosphate ligands and subsequent formation of colloidal palladium nanoparticles within the liquid phase. The efficiency of this reaction can be significantly improved (TON = 87) by using the more-stable ligand triphenylarsane,[211] although not sufficient for practical application.

Ligand oxidation can be minimized by carrying out the reaction in a biphasic medium in the presence of palladium complexes with bidentate phenanthroline ligands.[212–214] The formation of H_2O_2 depends strongly on the type of the substituent at the 2,9-positions of the phenathroline ligand. Ligands bearing bulky substituents such as 2,9-di-*n*-butyl-1,10-phenanthroline or 2,9-diphenyl-1,10-phenanthroline do not form binuclear species as a result of steric hindrance close to the N donor atom, but instead give soluble Pd^0 complexes that dissociate rapidly to form colloidal Pd nanoparticles. In contrast, the highest rate of H_2O_2 production is obtained with the ligands 2,9-dimethyl-1,10-phenanthroline and 2,9-dimethyl-4,7-diphenyl-1,10-phenanthroline. The electron-

 © 2006 Wiley-VCH Verlag GmbH & Co. KGaA, Weinheim

withdrawing Cl substituents in 2,9-dichloro-1,10-phenanthroline lead to lower reaction rates.

The palladium phenanthroline complexes are most stable when halogen-free solvents are used and HCl is added to the reaction mixture (Cl/Pd equimolar) to prevent the formation of colloidal Pd^0 particles. Under these reaction conditions, H_2O_2 concentrations in the aqueous phase as high as 8% w/w can be achieved.[212] Moreover, the catalyst can easily be recovered from the organic phase and used in consecutive reaction cycles with no significant loss in activity. However, only a little is known about the reaction mechanism. It is assumed that the Pd^{II} complex is reduced by CO to form a Pd^0 complex (Scheme 8) via a palladium–hydride intermediate.[215] The subsequent oxidation of the Pd^0 species to afford a Pd^{II} peroxido species and finally, in acidic media, hydrogen peroxide is already known.[216] Although similar complexes, stabilized by phosphane ligands, have long been known,[216] analogous nitrogen-donor complexes have not yet been reported.[216,217] Carbon monoxide[218] and carbon dioxide[219] are inserted in the O–O bond of the $[(PPh_3)_2Pd(\eta^2\text{-}O_2)]$ complex, each yielding $[(PPh_3)_2Pd(\eta^2\text{-}CO_3)]$. CO_2 likely first forms the percarbonate complex $[(PPh_3)_2Pd(\eta^2\text{-}CO_4)]$, which undergoes further transformation into $[(PPh_3)_2Pd(\eta^2\text{-}CO_3)]$ through oxidation of a PPh_3 ligand. Although both insertion reactions are feasible, the corresponding N,N-chelate complexes of palladium did not produce any H_2O_2, but only consumed CO and O_2 ($2\,CO + O_2 \rightarrow 2\,CO_2$).[217] Key issues for the development of this approach to the synthesis of H_2O_2 are a detailed knowledge of this mechanism as well as optimization of the ligands.

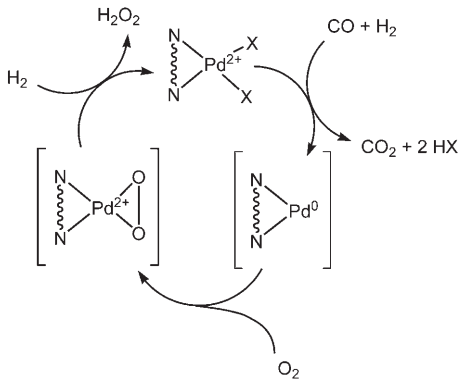

Scheme 8. Reaction mechanism for hydrogen peroxide synthesis from $CO/O_2/H_2O$ mixtures with palladium N,N catalysts (NN is a bidentate N ligand).

Comparatively little effort has been directed towards the development of heterogeneous catalysts for the production of H_2O_2 from $CO/O_2/H_2O$ mixtures. Palladium supported on calcite and ruthenium on graphite display reasonable activity in this reaction, but selectivity for H_2O_2 is still far from satisfactory.[220] Non-noble metal catalysts, such as rare-earth-modified alumina-supported nickel[221] and alumina-supported copper[222] systems also exhibit good performance, although only the performance of the latter surpasses that of noble-metal-based catalysts. The rate of H_2O_2 formation with a $Ni/La/B/Al_2O_3$ catalyst with La/Ni atomic ratio of 1:15[221] is comparable (0.07 mmol g^{-1} h) to the value (0.100 mmol g^{-1} h) achieved with the $Pd/CaCO_3$ catalyst. However, the catalyst becomes deactivated after a few hours under reaction conditions through poisoning by water and loss of surface-active nickel species, the active NiO species reacts with H_2O in the medium to form the catalytically inactive $Ni(OH)_2$ species. This species undergoes further reaction by phosphoric acid, added as a stabilizing agent for H_2O_2, to yield nickel phosphate, which is slowly solubilized. In contrast, the Cu/Al_2O_3 catalyst catalyzes the formation of H_2O_2 more than three times faster (0.326 mmol g^{-1} h) than the $Pd/CaCO_3$ catalyst (0.100 mmol g^{-1} h). Although supported noble metals such as Pd and Au are the best candidates for the direct synthesis of H_2O_2 from H_2/O_2 mixtures,[223] this is not the case for $CO/O_2/H_2O$ mixtures. In the limited known studies, the superior performance of these Cu/Al_2O_3 systems for the production of H_2O_2 from $CO/O_2/H_2O$ mixtures is associated with a two-step reaction mechanism. This mechanism involves the water-gas-shift reaction (WGS) [Eq. (19)], followed by the reaction between O_2 and the H_2 produced by the WGS reaction.

$$CO + H_2O \rightarrow CO_2 + H_2 \qquad (19)$$

Thus, it is plausible why the copper catalyst widely used in industrial-scale WGS reactions exhibits better performance than other supported metals for the synthesis of H_2O_2.[224]

The catalytic activity of the Cu/Al_2O_3 system for the target reaction depends, among other reasons, on the type of solvent employed. Acetone appears to be the most appropriate solvent in that it affords a high H_2O_2 production rate (0.326 mmol g^{-1} h), although this solvent may result in safety concerns because of the possibility of the formation of explosive peroxides. It has been shown for the related Pd/Al_2O_3 system that the reaction rate for H_2O_2 synthesis from H_2/O_2 mixtures is affected by the reaction medium. The transport of the reagent from the gas to the liquid phase appears to be the rate-limiting process.[225] Furthermore, the particle size of the copper crystallites also influences catalyst performance. The highest reaction rate is observed for copper particles with an average diameter of 12 nm. These are generated by wet reduction of the Cu^{2+} precursor with an aqueous solution of KBH_4 in presence of KOH.[222]

5. Other Methodologies

5.1. Bioinspired Approach

Hydrogen peroxide is formed in living organisms either through one-electron reduction of dioxygen or as a by-product of autoxidation reactions. The synthesis is enzymatic, and organic substrates are often oxidized by dioxygen. The reduction step of oxygen is often overshadowed by two major parasitic reactions which result in the loss of product. H_2O_2 is oxidized above pH 7 to O_2, but reduced to OH^- below pH 7. H_2O_2 can also be lost by dismutation into OH^- and O_2. The enzyme galactose oxidase is a versatile biocatalyst that not

© 2006 Wiley-VCH Verlag GmbH & Co. KGaA, Weinheim

only oxidizes the primary OH groups of galactose to form the corresponding aldehyde but also allows the conversion of simple primary alcohols.[226,227] The enzymatic oxidation of organic substrates is a conceptually simple and safe approach to the production of hydrogen peroxide under very mild conditions [Eq. (20)]. This is illustrated by the flavoenzyme glucose oxidase, which catalyzes the oxidation of β-D-glucose by molecular oxygen to δ-D-gluconolactone with simultaneous production of equimolecular amounts of hydrogen peroxide.

$$C_6H_{12}O_6 + O_2 \rightarrow H_2O_2 + C_6H_{10}O_6 \quad (20)$$

Few of the many oxidoreductase enzymes are able to yield significant concentrations ($\geq 1\,\%$) of H_2O_2.[228] H_2O_2 is often generated in living organisms through dioxygen reduction by oxygenases, but catalase enzymes are invariably produced as well and these destroy H_2O_2 at a high rate without release of other active oxidants. Peroxidase enzymes catalyze many organic oxidations, among which the removal of phenolic pollutants[229,230] and the recovery of industrially important azo dyes[231–233] from aqueous solutions are prominent. However, peroxidases work naturally with small concentrations of peroxide and are not very stable to oxidation (immobilized enzymes have a strictly limited lifetime). Interestingly, Novo Nordisk has developed peroxidases that can survive high concentrations of H_2O_2 (ARP enzymes). These make it possible to use peroxidases under conditions more suitable to practical applications. The instability of peroxidases is alleviated in part by co-immobilization of glucose oxidase and peroxidases.[234] The immobilization of glucose oxidase on inorganic substrates is an attractive option for the reaction and the possible recovery and recycling of the enzyme. The methods for immobilization of glucose oxidase explored to date include sol–gel[235,236] and chemical bonding to a silica surface.[237] In the sol–gel approach, the enzyme is physically dispersed in the matrix, which allows good accessibility of the substrate to the enzyme locations in the aqueous phase. This method affords a very high rate of epoxidation for 4-styrenesulfonic acid (Figure 11). However, recycling the sol–gel leads to loss of enzyme activity. A much more effective methodology is the covalent attachment of enzymes to a silica substrate.[238] In other cases, as with ligninases, self-destruction is a normal part of the mode of action. It is conceivable that this drawback could be overcome by using cells rather than isolated enzymes. This practice is not widespread in the chemical industry at present. Furthermore, the low concentration limit and high molecular weight of the enzyme mean that the space yield is low and recovery/recycling of the enzyme is difficult. Therefore, peroxidases as such are not particularly attractive as catalysts in industrial oxidation. This conclusion applies particularly to heme-based systems. Vanadium and molybdenum enzymes are more robust, but also less active towards substrates of industrial interest.

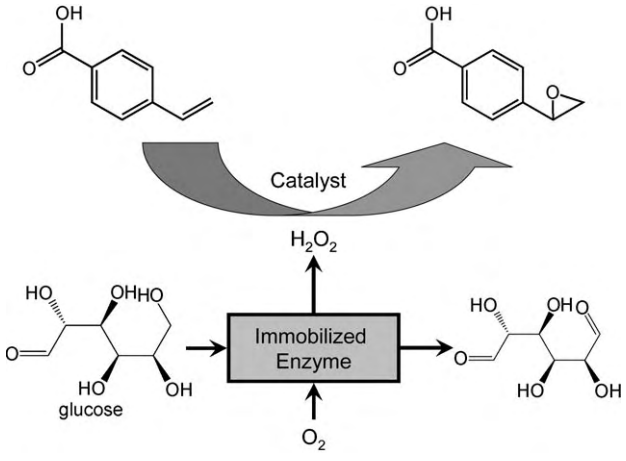

Figure 11. Reactions with immobilized glucose oxidase.

5.2. Plasma

H_2O_2 can be synthesized from hydrogen and oxygen mixtures by plasma and other physical methods. The activation of H_2 and O_2 molecules in a nonequilibrium plasma by silent electric discharge yields H_2O_2 and H_2O at atmospheric pressure.[239,240] This method has some advantages in that it does not involve any reagents other than H_2 and O_2 and the stoichiometry of the H_2/O_2 mixtures for optimum selectivity for H_2O_2 is far from the explosive regime of H_2/O_2 mixtures.[239] The plasma method also avoids the mass-transfer limitations associated with heterogeneously catalyzed three-phase reactions.

Dielectric barrier discharge (DBD) at atmospheric pressure allows quite high yields of H_2O_2 to be obtained from the gas reaction of H_2/O_2 plasma, although this is depends strongly on the reactor configuration.[241] With a suitable reactor configuration, H_2O_2 can be obtained in the product solution from an H_2/O_2 mixture containing $3.6\,\%$ O_2 (the lower explosive limit for mixture is $6\,\%$) fed at a rate of $10\,L\,h^{-1}$. The concentration of H_2O_2 increases almost linearly with time, with concentrations of 1.5, 4.1, and 14.3 % w/w obtained for discharge times of 1, 3, and 11 h, respectively.

5.3. Oxygen Reduction

Transition-metal complexes with cathecol and semiquinone ligands display facile electron transfer between the metal and chelate ligand and are thus redox-active.[242] It has long been known that these redox characteristics play a role in several enzyme-catalyzed reactions, for example, in ribonucleotide reductase[243] and galactose oxidase.[244] The redox nature of the cathecolate complex arises from the relative ease with which cathecol ligands can be oxidized to semiquinones and *o*-quinones (Scheme 9).

High-valent manganese complexes have been studied in detail because they play a key role in the formation of photosynthetic oxygen.[245] Valence tautomerism has been observed between Mn^{IV}-cathecolate and Mn^{II}-semiquinone structures, and interconversion may occur with only small changes in temperature. The synthesis of these Mn-cathecol complexes is complicated because cathecols are prone to

 © 2006 Wiley-VCH Verlag GmbH & Co. KGaA, Weinheim

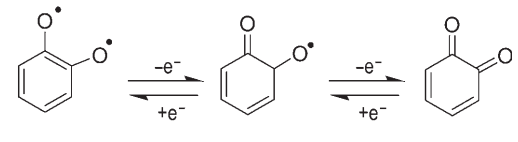

Scheme 9. Cathecol oxidation to semiquinone and *o*-quinone.

polymerization and oxidation by air, and only a few examples are known.[246,247]

The complexes $(Bu_4N)_2[Mn(Cl_4Cat)_3]$ (**1**) and $(Bu_4N)[Mn(Cl_4Cat)_2(H_2O)(EtOH)$ (**2**) facilitate the production of hydrogen peroxide from the substrates dioxygen and hydroxylamine in acetonitrile/water mixtures under ambient conditions. The rate of H_2O_2 production increases with increasing amounts of complex, but a rapid decomposition of H_2O_2 occurs at concentrations of the complexes above 10 μM, which suggests a slower manganese-catalyzed decomposition of H_2O_2. The similarity of the rates of H_2O_2 production with **1** and **2** suggests that neither the oxidation state of the manganese nor the labile coordination sites around the Mn metal are important for catalysis. The turnover numbers of approximately 10000 h^{-1} (mol H_2O_2 per mol Mn) compare very favorably with those for the commercial AO process.

The complexes **1** and **2** contain Mn^{III} and Mn^{IV} ions, which are reduced in the presence of hydroxylamine. The corresponding Mn^{II} complexes act as the active catalysts.[248] There is evidence that hydroxylamine is highly effective at reducing the $Mn^{III/IV}$ centers in Mn-containing catalase enzymes to Mn^{II}_2 centers.[249] This may explain the equal rates of H_2O_2 production for Mn^{III} or Mn^{IV} complexes. Further insights into the reaction mechanism come from the observation that labile ligands around the central Mn ion have little influence on the reactivity. It appears that H_2O_2 formation takes place through an outer-sphere mechanism in which O_2 and NH_2OH are not coordinated to the central Mn^{II} ion.[250] A reaction mechanism has been proposed for the production of hydrogen peroxide through reduction of bound O_2 by coordinated cathecol in which NH_2OH acts as a sacrificial reducing agent to regenerate the catalyst from the oxidized quinone.[242] This mechanism can be reconciled with the kinetic results for **1** and **2** if it is assumed that the reduction of O_2 by hydroxylamine proceeds via a key hydrogen-bonded intermediate.

The possible two-electron oxidation of cathecolate ligands to semiquinone and quinone species, the electronic properties of substituents on the cathecolate ring, and the nature of the manganese center with stable oxidation states Mn^{II}, Mn^{III}, and Mn^{IV} provide these complexes with enzymelike character. These properties allow the complexes to activate O_2 molecules for reduction to hydrogen peroxide by low-molecular-weight amines such as hydroxylamine and hydrazine.

6. Summary and Outlook

Hydrogen peroxide is often considered a key reagent of green chemistry, as water is the only reaction by-product in oxidation reactions. The AO process for the production of H_2O_2 is commercially successful because it produces H_2O_2 continuously at moderate temperatures while avoiding direct contact between O_2 and H_2. In comparison with its competitors (oxidation of primary and secondary alcohols, electrochemical methods), the AO method has many advantages, but also disadvantages. For example, the hydrogenation and oxidation steps are subject to mass-transport limitations, the H_2O_2 recovered by liquid–liquid extraction is contaminated by organic compounds, which requires substantial investment in purification equipment in industrial plants. The newer methods for H_2O_2 production outlined herein avoid these drawbacks.

A promising new method it the synthesis of H_2O_2 from $CO/O_2/H_2O$ mixtures ($CO + O_2 + H_2O \rightarrow CO_2 + H_2O_2$). This process is an interesting option for cases in which a source of carbon monoxide is available. However, it can not considered a green process, as carbon dioxide is produced along with the hydrogen peroxide. Critical issues for technological development of liquid-phase reactions in the presence of palladium complexes are ligand optimization and in-depth mechanistic investigations of the reaction. Comparatively little attention has been paid to the development of heterogeneous catalysts for $CO/O_2/H_2O$ mixtures. The systems employed for this purpose are reasonably active, but their selectivity for H_2O_2 is still far from satisfactory. A major problem to be overcome is deactivation of the catalysts by water. A substantial improvement in performance, specifically for copper catalysts, is obtained with a modification of the liquid-phase. The two-step reaction mechanism involves first the water-gas-shift reaction ($CO + H_2O \rightarrow CO_2 + H_2$) and then further reaction of the generated H_2 with solubilized O_2. Mass-transfer limitations are unavoidable,[225] but a suitable choice of solvent helps to increase the transfer rate of oxygen to the catalytic site.

An undoubtedly greater challenge in the long term is the production of H_2O_2 over semiconductor surfaces in the presence of water under irradiation with UV or visible light. As H_2O_2 formation involves reduction of O_2 by a photogenerated electron in the conduction band, precise design of the semiconductor is a key issue for further improvements in efficiency. A high concentration of charge carriers must be attained at the conduction band and the recombination of electron–hole pairs within the solid must be largely avoided. This can be realized with new semiconductors or through appropriate doping of conventional materials.

The bioinspired production of hydrogen peroxide under very mild conditions is a conceptually simple and safe approach. However, immobilized peroxidases have limited lifetimes at high concentrations of hydrogen peroxide, which limits the practical application of enzymes. Nevertheless, Novo Nordisk has developed peroxidases that can survive high concentrations of H_2O_2 (ARP enzymes). The broad range of substrates susceptible to oxidation by certain enzymes allows the conversion of OH groups of monosaccharide or primary alcohols into the corresponding aldehydes with release of equimolecular amounts of H_2O_2 and selectivity close to 100%. However, as these reactions are stoichiometric, a tremendous amount of waste is produced, and thus this

© 2006 Wiley-VCH Verlag GmbH & Co. KGaA, Weinheim

method would only be justifiable if this waste could be completely recycled. An important advantage of biomimetic reactions is their selectivity, which may lead to some industrial applications, such as coupling of the in situ generation of H_2O_2 with reactions of certain substrates (e.g., epoxidation of olefins). Precise design and optimization of ligands could lead to improved stability. Notwithstanding, the use of oxidoreductase enzymes is difficult because they seldom yield significant concentrations ($\geq 1\%$) of H_2O_2. H_2O_2 is often generated through dioxygen reduction by oxygenases, but a catalase enzyme is invariably also produced which quickly destroys H_2O_2 without producing other active oxidants. Peroxidase enzymes catalyze many organic oxidations with H_2O_2. However, they likewise involve small peroxide concentrations and are not very stable against oxidation and hence have severely limited lifetimes.

The direct reaction of $H_2 + O_2 \rightarrow H_2O_2$ is conceptually the most straightforward method for producing hydrogen peroxide and is the method of choice in the medium term. As extraction of H_2O_2 is not required and the purification steps are simplified, the capital investment and operating costs are expected to be lower than for the AO process. This alternative appears of great relevance to the basic chemical industry, as shown by the integrated HPPO process. The direct synthesis of H_2O_2 on site allows the costs and hazards associated with the transport and handling of concentrated hydrogen peroxide to be significantly minimized. Several chemical companies have investigated the direct synthetic route over the past 25 years, and the number of patents in this field continues to grow. However, none of the processes available has been able to deliver both productivity and safety. A possible solution to the safety problem is the use of catalytic membranes. Following this approach, pure O_2 and H_2 can be used without a diluting agent since contact between the two streams is avoided. However, owing to the low permeation rates, the product yields are too low to be competitive with those attained in flow systems.

Most catalyst formulations employ palladium as the active metal. As well as the heterogeneous catalyst, acids are often incorporated into the reaction medium to delay or prevent the decomposition of hydrogen peroxide. Under these conditions, palladium is partly dissolved and forms a colloidal suspension that deactivates the catalyst. Although such a system is very interesting fundamentally, a colloid would be difficult to manage in a commercial process and its recovery would not be viable at the very low concentrations of dissolved metal employed. Notwithstanding, excellent yields of hydrogen peroxide have been recently reported with neutral solutions and heterogeneous catalysts consisting of functionalized carbons with sulfonic acid groups,[123] or polystyrene resins functionalized with sulfonic acid.[130–132] It has been demonstrated for a system with palladium loaded on a sulfonic acid modified divinylbenzene-cross-linked polystyrene resin that interactions occur between small palladium particles and the sulfonic acid groups of the resin.[132] This interaction creates a positive charge on the Pd particles which enhances the selectivity for hydrogen peroxide.

Industry is expected to increase its focus the development of inorganic catalysts for hydrogen peroxide synthesis, particularly for the production of fine chemicals. Complexes and enzymes will have little large-scale impact, even though these should improve further in robustness. The future will show whether the predicted developments actually occur.

We are grateful to our colleagues Dr. J. A. Delgado-Oyagüe and Dr. M. P. de Frutos for their stimulating contributions to our endeavors as well as to our research sponsors Repsol-YPF and CICyT (Spain) (Project: ENE2004-07345-c03-01/ALT). J.M.C.M. acknowledges financial support from the Ministerio de Educación y Ciencia (Spain) through the Ramon y Cajal Program.

Received: October 25, 2005
Revised: May 26, 2006

[1] G. Goor, W. Kunkel, O. Weiberg in *Ullmann's Encyclopedia of Industrial Chemistry*, *Vol. A13* (Eds.: B. Elvers, S. Hawkins, M. Ravenscroft, G. Schulz), VCH, Weinheim, **1989**, pp. 443–466.
[2] J. R. Kirchner in *Kirk-Othmer Encyclopedia of Chemical Technology*, *Vol. 13* (Eds.: M. Grayson, D. Eckroth), 3rd ed., Wiley, New York, **1979**, pp. 12–38.
[3] W. H. Hart, S. J. Hsieh, *Am. Inst. Chem. Eng. Symp.* **1998**, *319*, 73–76.
[4] S. Ljunggren, *J. Pulp Pap. Sci.* **1986**, *12*, J54–J55.
[5] C. W. Walker, J. T. McDonough, J. R. Dinus, K. E. Eriksson, *Am. Inst. Chem. Eng. Symp.* **1998**, *94*, 57–60.
[6] R. Hage, A. Lienke, *Angew. Chem.* **2006**, *118*, 212–229; *Angew. Chem. Int. Ed.* **2006**, *45*, 206–222.
[7] K. Kosaka, H. Yamada, K. Shishida, S. Echigo, R. A. Minear, H. Tsuno, S. Matsui, *Water Res.* **2001**, *35*, 3587–3594.
[8] C. B. Chidambara Raj, H. L. Quen, *Chem. Eng. Sci.* **2005**, *60*, 5305–5311.
[9] M. Taramaso, G. Perego, B. Notari (Enichem), US4410501, **1983** [*Chem. Abstr.* **1983**, *95*, 206272]. (As a consequence of the large industrial interest in the production of hydrogen peroxide, this Review contains many references to the patent literature. A useful "free" access to this literature can be found, among other places, at: http://www.espacenet.com/.)
[10] M. A. Camblor, A. Corma, A. Martínez, J. Perez-Pariente, *J. Chem. Soc. Chem. Commun.* **1991**, 589–590.
[11] M. G. Clerici, P. Ingallina, *J. Catal.* **1993**, *140*, 71–83.
[12] P. T. Tanev, M. Chibwe, T. J. Pinnavaia, *Nature* **1994**, *368*, 321–323.
[13] R. Hutter, D. C. M. Dutroit, T. Mallat, M. Schneider, A. Baiker, *J. Chem. Soc. Chem. Commun.* **1995**, 163–164.
[14] T. Maschmeyer, F. Rey, G. Sankar, J. M. Thomas, *Nature* **1995**, *378*, 159–162.
[15] R. van Grieken, J. L. Sotelo, C. Martos, J. L. G. Fierro, M. López-Granados, R. Mariscal, *Catal. Today* **2000**, *61*, 49–54.
[16] M. C. Capel-Sanchez, J. M. Campos-Martin, J. L. G. Fierro, M. P. de Frutos, A. P. Polo, *Chem. Commun.* **2000**, 855–856.
[17] M. C. Capel-Sanchez, J. M. Campos-Martin, J. L. G. Fierro, *Appl. Catal. A* **2003**, *246*, 69–77.
[18] M. C. Capel-Sanchez, J. M. Campos-Martin, J. L. G. Fierro, *J. Catal.* **2003**, *217*, 195–202.
[19] J.-M. Brégeault, *Dalton Trans.* **2003**, 3289–3302.
[20] R. Noyori, M. Aoki, K. Sato, *Chem. Commun.* **2003**, 1977–1986.
[21] D. E. De Vos, B. F. Sels, P. A. Jacobs, *Adv. Synth. Catal.* **2003**, *345*, 457–473.
[22] B. S. Lane, K. Burgess, *Chem. Rev.* **2003**, *103*, 2457–2473.
[23] J. M. Campos-Martin, M. C. Capel-Sanchez, J. L. G. Fierro, *Green Chem.* **2004**, *6*, 557–562.

 © 2006 Wiley-VCH Verlag GmbH & Co. KGaA, Weinheim

[24] A. Campanella, M. A. Baltanas, M. C. Capel-Sanchez, J. M. Campos-Martin, J. L. G. Fierro, *Green Chem.* **2004**, *6*, 330 – 334.
[25] P. Ratnasamy, D. Srinivas, H. Knözinger, *Adv. Catal.* **2004**, *48*, 1 – 169.
[26] M. C. Capel-Sanchez, J. M. Campos-Martin, J. L. G. Fierro, *J. Catal.* **2005**, *234*, 488 – 495.
[27] D. H. Bremner, A. E. Burgess, L. Feng-Bin, *Appl. Catal. A* **2000**, *203*, 111.
[28] S. Niwa, M. Eswaramoorthy, J. Nair, A. Raj, N. Itoh, H. Shoji, T. Namba, F. Mizukami, *Science* **2002**, *295*, 105 – 107.
[29] P. Jiajian, S. Feng, G. Yanlong, D. Youquan, *Green Chem.* **2003**, *5*, 224 – 226.
[30] A. G. J. Ligtenbarg, R. Hage, B. L. Feringa, *Coord. Chem. Rev.* **2003**, *237*, 89 – 101.
[31] C. D. Immanuel, F. J. Doyle III, C. F. Cordeiro, S. S. Sundaram, *AIChE J.* **2003**, *49*, 1392 – 1404.
[32] S. R. Jennings, D. J. Dollhopf, W. P. Inskeep, *Appl. Geochem.* **2000**, *15*, 35 – 243.
[33] *Hydrocarbon Process.* **2006**, *85(1)*, 29.
[34] H.-J. Riedl, G. Pfleiderer (I. G. Farbenindustrie AG.), US 2158525, **1939** [*Chem. Abstr.* **1939**, *33*, 49 337].
[35] R. Edvinsson Albers, M. Nyström, M. Sivertström, A. Sellin, A. C. Dellve, U. Andersson, W. Herrmann, T. Berglin, *Catal. Today* **2001**, *69*, 247 – 252.
[36] Y. Hou, Y. Wang, F. He, S. Han, Z. Mi, W. Wu, E. Min, *Matt. Lett.* **2004**, *58*, 1267 – 1272.
[37] B. Liu, M. Qiao, J. Wang, K. Fan, *Chem. Commun.* **2002**, 1236 – 1237.
[38] X. Chen, H. Hu, B. Liu, M. Qiao, K. Fan, H. He, *J. Catal.* **2003**, *220*, 254 – 257.
[39] M. Kralik, A. Biffis, *J. Mol. Catal. A* **2001**, *177*, 113 – 257.
[40] A. Molnar, G. V. Smith, M. Bartok, *Adv. Catal.* **1989**, *36*, 329 – 383.
[41] P. Gallezot, P. J. Cerino, B. Blanc, G. Flèche, P. Fuertes, *J. Catal.* **1994**, *146*, 93 – 102.
[42] A. Biffis, R. Ricoveri, S. Campestrini, M. Kralik, K. Jereqabek, B. Corain, *Chem. Eur. J.* **2002**, *8*, 2962 – 2967.
[43] M. Shibata, T. Masumoto. *Prep. Catal.* **1987**, *4*, 353 – 359.
[44] S. Dietolf (Peroxid Chemie GMBH), DE 3538816, **1987** [*Chem. Abstr.* **1987**, *107*, 61501].
[45] A. Drelinkiewicz, M. Hasik, *J. Mol. Catal. A* **2001**, *177*, 149 – 164.
[46] A. Drelinkiewicz, M. Hasik, M. Kloc, *Catal. Lett.* **2000**, *64*, 41 – 47.
[47] D. Vandenberg, J.-P. Ganhy, N. Vanlautem (Solvay), WO 9940024, **1999** [*Chem. Abstr.* **1999**, *131*, 131938].
[48] A. Reijo, P. Juhani (Kemira Chemicals Oy), EP 1245534, **2002** [*Chem. Abstr.* **2002**, *137*, 281446].
[49] R. A. Sheldon, J. K. Kochi in *Metal-Catalyzed Oxidations of Organic Compounds*, Academic Press, New York, **1981**.
[50] T. Haas, J. Glenneberg, R. Wagner, R. Van Heertum (Degussa AG.), WO 02076886, **2002** [*Chem. Abstr.* **2002**, *137*, 265163].
[51] E. Santacesaria, R. Ferro, S. Ricci, S. Carra, *Ind. Eng. Chem. Res.* **1987**, *26*, 155 – 159.
[52] E. Santacesaria, M. Di Serio, A. Ruso, U. Leone, R. Velotti, *Chem. Eng. Sci.* **1999**, *54*, 2799 – 2806.
[53] T. H. James, A. Weissberger, *J. Am. Chem. Soc.* **1938**, *60*, 98 – 104.
[54] K. D. Samant, K. M. Ng, *AIChE J.* **1998**, *44*, 1363 – 1381.
[55] K. D. Samant, K. M. Ng, *AIChE J.* **1998**, *44*, 2212 – 2228.
[56] K. D. Samant, K. M. Ng, *Chem. Eng. Technol.* **1999**, *22*, 877 – 890.
[57] J. Sheikh, L. S. Kershenbaum, E. Alpay, *Chem. Eng. Sci.* **1998**, *53*, 2933 – 2939.
[58] R. Krishna, *Chem. Eng. Sci.* **2002**, *57*, 1491 – 1504.
[59] S. Lü, Z. Mi, L. Wang, Y. Wand, Z. Zhu, S. Fu, *Chem. Eng. Sci.* **2005**, *60*, 6298 – 6306.
[60] M. Sovilj, G. Knezevic, *Collect. Czech. Chem. Commun.* **1994**, *59*, 2235 – 2243.
[61] P. V. Dankwerts, *Gas-Liquid Reactions*, McGraw-Hill, New York, **1970**.
[62] A. M. Dehkordi, *Ind. Eng. Chem. Res.* **2001**, *40*, 681 – 684.
[63] A. M. Dehkordi, *Ind. Eng. Chem. Res.* **2002**, *41*, 2512 – 2520.
[64] C. R. Harris (E. I. Du Pont de Nemours and Company), US 2479111, **1949** [*Chem. Abstr.* **1949**, *44*, 5600].
[65] F. F. Rust (N. V. de Bataafsche Petroleum Maatschappij), DE 935303, **1955** [*Chem. Abstr.* **1955**, *53*, 3613].
[66] D. W. Leyshon, R. J. Jones, R. N. Cochran (ARCO Chemical Technology), US 5254326, **1993** [*Chem. Abstr.* **1993**, *120*, 11302].
[67] A. Padilla-Polo, PhD thesis, University of Alcala de Henares (Spain), **1997**.
[68] Y. Ishii, T. Nakano (Daicel Chemical Industries), WO 2000046145, **2000** [*Chem. Abstr.* **2000**, *133*, 152720].
[69] R. A. Sheldon, I. W. C. E. Arends, *Adv. Synth. Catal.* **2004**, *346*, 1051 – 1071.
[70] J. A. Delgado-Oyague, M. P. de Frutos, A. Padilla-Polo (Repsol Química S.A.), EP 0839760, **1998** [*Chem. Abstr.* **1998**, *128*, 296617].
[71] M. P. de Frutos, A. Padilla-Polo, J. M. Campos-Martin (Repsol Química S.A.), EP 1074548, **2001** [*Chem. Abstr.* **2001**, *134*, 147993].
[72] G. A. Russell, *J. Am. Chem. Soc.* **1956**, *78*, 1047 – 1054.
[73] D. G. Hendry, G. A. Russell, *J. Am. Chem. Soc.* **1964**, *86*, 2368 – 2371.
[74] C. Parlant, *Rev. Inst. Fr. Pet. Ann. Combust. Liq.* **1964**, *19*, 1 – 9.
[75] C. Chevriau, *Rev. Inst. Fr. Pet. Ann. Combust. Liq.* **1966**, *21*, 1488 – 1494.
[76] P. C. Foller, R. T. Bombard, *J. Appl. Electrochem.* **1995**, *25*, 613 – 627.
[77] P. C. Foller, R. J. Allen, R. T. Bombard, R. Vora, *Proceedings of the 5th International Forum on Electrolysis in the Chemical Industry*, Electrosynthesis Inc., Fort Lauderdale, FL, **1991**.
[78] K. Henricson (Ahlstroem Oy), WO 9321106, **1993** [*Chem. Abstr.* **1993**, *120*, 109762].
[79] R. Gopal (Electrosynthesis Co. Inc.), US 2003019758, **2003** [*Chem. Abstr.* **2003**, *138*, 114047].
[80] E. T. Guenter, Hydrogen Peroxide, in *Encyclopedia of Chemical Processing and Design*, *Vol 27* (Eds.: J. J. McKetta, W. A. Cunningham), Marcel Dekker, New York, **1988**, p. 27 – 43.
[81] M. G. Clerici, P. Ingallina, *Catal. Today* **1998**, *41*, 351 – 364.
[82] W. Hölderich, *Appl. Catal. A* **2000**, *194–195*, 487 – 496.
[83] H. Henkel, W. Weber (Henkel & CIE), US 1108752, **1914** [*Chem. Abstr.* **1914**, *8*, 23927].
[84] J. S. Campbell (ICI Ltd.), GB 1056123, **1967** [*Chem. Abstr.* **1967**, *66*, 67450].
[85] P. N. Dyer, F. Moseley (Air Products & Chemicals Inc.), DE 2710279, **1977** [*Chem. Abstr.* **1977**, *88*, 25030].
[86] Y. Izumi, H. Miyazaki, S. Kawahara (Tokuyama Soda KK), DE 2655920, **1977** [*Chem. Abstr.* **1977**, *87*, 186651].
[87] F. Moseley, P. N. Dyer (Air Products & Chemicals, Inc), US 4336240, **1982** [*Chem. Abstr.* **1982**, *97*, 111978].
[88] L. W. Gosser (E.I. Du Pont de Nemours and Company), EP 132294, **1985** [*Chem. Abstr.* **1985**, *102*, 134404].
[89] W. F. Brill (The Halcon SD Group, Inc.), US 4661337, **1987** [*Chem. Abstr.* **1987**, *107*, 42558].
[90] L. W. Gosser, J.-A. T. Schwartz (E.I. Du Pont de Nemours and Company), EP 342047, **1989** [*Chem. Abstr.* **1989**, *112*, 39260].
[91] L. W. Gosser, J.-A. T. Schwartz (E.I. Du Pont de Nemours and Company), US 4832938, **1989** [*Chem. Abstr.* **1989**, *111*, 117783].
[92] L. W. Gosser, J.-A. T. Schwartz (E.I. Du Pont de Nemours and Company), JP 63156005, **1988** [*Chem. Abstr.* **1988**, *109*, 193175].
[93] C. Pralus, J.-P. Schirmann (Atochem ELF SA), EP 364374, **1990** [*Chem. Abstr.* **1990**, *112*, 219903].

© 2006 Wiley-VCH Verlag GmbH & Co. KGaA, Weinheim

[94] K. T. Chuang (Atomic Energy of Canada, Ltd.), EP 366419, **1990** [*Chem. Abstr.* **1990**, *113*, 43438].
[95] L. W. Gosser, M. A. Paoli (E.I. DuPont de Nemours and Company), US 5135731, **1992** [*Chem. Abstr.* **1992**, *117*, 215646].
[96] M. J. Maraschino (Kerr-Mc.Gee Corporation), US 5169618, **1992** [*Chem. Abstr.* **1992**, *118*, 105878].
[97] H. Nagashima, Y. Ishiuchi, Y. Hiramatsu (Mitsubishi Gas Chemical Co), EP 504741, **1992** [*Chem. Abstr.* **1992**, *117*, 215651].
[98] H. Nagashima, M. Ishiuchi, Y. Hiramatsu, M. Kawakami (Mitsubishi Gas Chemical Co), JP 0570107, **1993** [*Chem. Abstr.* **1993**, *119*, 11587].
[99] M. A. Paoli (E.I. DuPont de Nemours & Co.), WO 9204277, **1992** [*Chem. Abstr.* **1992**, *116*, 217480].
[100] H. Nagashima, Y. Ishiuchi, Y. Hiramatsu, M. Kawakami (Mitsubishi Gas Chemical Co), JP 05270806, **1993** [*Chem. Abstr.* **1993**, *120*, 110872].
[101] K. T. Chuang, B. Zhou (EKA Nobel AB), WO 9314025, **1993** [*Chem. Abstr.* **1993**, *120*, 274643].
[102] H. Nagashima, M. Ishiuchi, M. Kawakami, Y. Hiramatsu (Mitsubishi Gas Chemical Co), JP 06191804, **1994** [*Chem. Abstr.* **1994**, *121*, 283113].
[103] J. Van Weynbergh, J.-P. Schoebrechts, J.-C. Colery (Solvay Interox), WO 9215520, **1992** [*Chem. Abstr.* **1992**, *117*, 215653].
[104] J.-C. Colery, J. Van Weynbergh (Solvay Interox), EP 537836, **1993** [*Chem. Abstr.* **1993**, *119*, 11583].
[105] H. Nagashima, T. Tomita, M. Ishiuchi, M. Kawakami (Mitsubishi Gas Chemical Co), JP 07069604, **1995** [*Chem. Abstr.* **1995**, *122*, 294725].
[106] T. Tomita, H. Nagashima, M. Ishiuchi, M. Kawakami (Mitsubishi Gas Chemical Co), JP 07069605, **1995** [*Chem. Abstr.* **1995**, *122*, 294726].
[107] M. Kawakami, M. Ishiuchi, H. Nagashima, T. Tomita, Y. Hiramatsu (Mitsubishi Gas Chemical Co), JP 08002904, **1996** [*Chem. Abstr.* **1996**, *124*, 264972].
[108] M. E. Thompson, J. L. Snover, V. Joshi, L. A. Vermuelen (Princeton University), US 5480629, **1996** [*Chem. Abstr.* **1996**, *124*, 121344].
[109] H. A. Huckins (Princeton Advanced Technologies), US 5641467, **1997** [*Chem. Abstr.* **1997**, *127*, 110968].
[110] S. P. Webb, J. A. McIntyre (Dow Chemical Co.), US 5800796, **1998** [*Chem. Abstr.* **1998**, *129*, 191152].
[111] J. Wanngard (EKA Chemicals AB), EP 0816286, **1998** [*Chem. Abstr.* **1998**, *128*, 129921].
[112] F. Goto, K. Tanaka, T. Sasaki (Sumitomo Chemical Co.), US 5965101, **1999** [*Chem. Abstr.* **1999**, *130*, 40582].
[113] M. E. Thompson, V. V. Krishnan, A. G. Dokoutchaev, F. Abdel-Razzaq, S. Rice (University of Southern California), WO 9949971, **1999** [*Chem. Abstr.* **1999**, *131*, 248853].
[114] M. Devic, L. Delais (Atofina), WO 9941190, **1999** [*Chem. Abstr.* **1999**, *131*, 159392].
[115] H. A. Huckins (Advanced Peroxide Technology, Inc.), US 6042804, **2000** [*Chem. Abstr.* **2000**, *132*, 224461].
[116] M. Devic (Atofina), WO 0105498, **2001** [*Chem. Abstr.* **2001**, *134*, 133655].
[117] M. Devic, D. Dang (Atofina), WO 0105501, **2001** [*Chem. Abstr.* **2001**, *134*, 106456].
[118] B. Zhou, L.-K. Lee (Hydrocarbon Technologies, Inc.), US 6168775, **2001** [*Chem. Abstr.* **2001**, *134*, 47481].
[119] R. Burch, P. R. Ellis, *Appl. Catal. B* **2003**, *42*, 203 – 211.
[120] V. R. Choudhary, S. D. Sansare, A. G. Gaikwad, *Catal. Lett.* **2002**, *84*, 81 – 87.
[121] S. Chinta, J. H. Lunsford, *J. Catal.* **2004**, *225*, 249 – 255.
[122] J. H. Lunsford, *J. Catal.* **2003**, *216*, 455 – 460.
[123] *Focus Catal.* **2004**, *11*, 3; *Focus Catal.* **2004**, *12*, 6; *Focus Catal.* **2005**, *5*, 5 – 6.
[124] G. Paparatto, R. d'Aloisio, G. De Alberti, P. Furlan, V. Arca, R. Buzón (Enichem S.p.A.), EP 0978316, **2000** [*Chem. Abstr.* **2000**, *132*, 142643].
[125] V. R. Choudhary, C. Samanta, *J. Catal.* **2006**, *238*, 28 – 38.
[126] Q. Liu, J. H. Lunsford, *J. Catal.* **2006**, *239*, 237 – 243.
[127] D. P. Dissanayake, J. H. Lunsford, *J. Catal.* **2002**, *206*, 173 – 176.
[128] D. P. Dissanayake, J. H. Lunsford, *J. Catal.* **2003**, *214*, 113 – 120.
[129] S. Melada, R. Rioda, F. Menegazzo, F. Pinna, G. Strukul, *J. Catal.* **2006**, *239*, 422 – 430.
[130] M. P. de Frutos, J. M. Campos-Martin, J. L. G. Fierro, E. Cano-Serrano, G. Blanco-Brieva (Repsol Química S.A.), EP 1344747, **2003** [*Chem. Abstr.* **2003**, *139*, 247564].
[131] M. P. de Frutos, A. Padilla, J. M. Riesco, J. M. Campos-Martin, G. Blanco-Brieva, E. Cano-Serrano, M. C. Capel-Sanchez, J. L. G. Fierro (Repsol Química S.A.), EP 1443020, **2004** [*Chem. Abstr.* **2004**, *141*, 158948].
[132] G. Blanco-Brieva, E. Cano-Serrano, J. M. Campos-Martin, J. L. G. Fierro, *Chem. Commun.* **2004**, 1184 – 1185.
[133] C. Burato, P. Centomo, M. Rizzoli, A. Biffis, S. Campestrini, B. Corain, *Adv. Synth. Catal.* **2006**, *348*, 255 – 259.
[134] B. Corain, M. Kralik, *J. Mol. Catal. A* **2001**, *173*, 99 – 115.
[135] P. Landon, P. J. Collier, A. F. Carley, D. Chadwick, A. J. Papworth, A. Burrows, C. J. Kiely, G. J. Hutchings, *Phys. Chem. Chem. Phys.* **2003**, *5*, 1917 – 1923.
[136] V. R. Choudhary, A. G. Gaikwad, S. D. Sansare, *Angew. Chem.* **2001**, *113*, 1826 – 1829; *Angew. Chem. Int. Ed.* **2001**, *40*, 1776 – 1779.
[137] V. R. Choudhary, S. D. Sansare, A. G. Gaikwad (Council of Scientific and Industrial Research), US 6346228, **2002** [*Chem. Abstr.* **2002**, *137*, 199594].
[138] G. Paparatto, G. De Alberti, R. D'Aloisio, R. Buzzoni (ENI S.p.A./Polimeri Europa S.p.A.), WO 031014014, **2003** [*Chem. Abstr.* **2003**, *138*, 172784].
[139] B. Zhou, M. Rueter (Hydrocarbon Technologies, Inc.) US 20040018143, **2004** [*Chem. Abstr.* **2004**, *140*, 96308].
[140] U. Lückoff, H. Paucksch, G. Luft (Solvay Interox) DE 4127918, **1992** [*Chem. Abstr.* **1992**, *117*, 215650].
[141] B. Bertsch-Frank, I. Hemme, L. Von Hippel, S. Katusic, J. Rollmann (Degussa-Huls AG), EP 1127839, **2001** [*Chem. Abstr.* **2001**, *135*, 182681].
[142] A. G. Gaikwad, S. D. Sansare, V. R. Choudhary, *J. Mol. Catal. A* **2002**, *181*, 143 – 149.
[143] T. V. Choudhary, D. W. Goodman, *Top. Catal.* **2002**, *21*, 25 – 34.
[144] M. Haruta, *Cattech* **2002**, *6*, 102 – 115.
[145] P. Paredes Olivera, E. M. Patrito, H. Sellers, *Surf. Sci.* **2004**, *313*, 25 – 40.
[146] P. Landon, P. J. Collier, A. J. Papworth, C. J. Kiely, G. J. Hutchings, *Chem. Commun.* **2002**, 2058 – 2058.
[147] M. Okumura, Y. Kitagawa, K. Yamagcuhi, T. Akita, S. Tsubota, M. Haruta, *Chem. Lett.* **2003**, *32*, 822 – 823.
[148] J. K. Edwards, B. E. Solsona, P. Landon, A. F. Carley, A. Herzing, C. J. Kiely, G. J. Hutchings, *J. Catal.* **2005**, *236*, 69 – 79.
[149] D. H. Wells, Jr., W. N. Delgass, K. T. Thomson, *J. Chem. Phys.* **2002**, *117*, 10597 – 10603.
[150] N. S. Phala, G. Klatt, E. van Steen, *Chem. Phys. Lett.* **2004**, *395*, 33 – 37.
[151] D. H. Wells, Jr., W. N. Delgass, K. T. Thomson, *J. Catal.* **2004**, *225*, 69 – 77.
[152] E. M. Fernández, P. Ordejón, L. C. Balbás, *Chem. Phys. Lett.* **2005**, *408*, 252 – 257.
[153] M. Okumura, Y. Kitagawa, M. Haruta, K. Yamaguchi, *Appl. Catal. A* **2005**, *291*, 37 – 44.
[154] T. Ishihara, Y. Ohura, S. Yoshida, Y. Hata, H. Nishiguchi, Y. Takita, *Appl. Catal. A* **2005**, *291*, 215 – 221.
[155] J. K. Edwards, B. E. Solsona, P. Landon, A. F. Carley, A. Herzing, M. Watanabe, C. J. Kiely, G. J. Hutchings, *J. Mater. Chem.* **2005**, *15*, 4595 – 4600.

 © 2006 Wiley-VCH Verlag GmbH & Co. KGaA, Weinheim

[156] M. Chen, D. Kumar, C.-W. Yi, D. W. Goodman, *Science* **2005**, *310*, 291 – 293.
[157] I. T. Horvath, *Acc. Chem. Res.* **1998**, *31*, 641 – 650.
[158] F. Moseley, P. N. Dyer (Air Products & Chemicals Inc), EP 38701, **1981** [*Chem. Abstr.* **1981**, *96*, 71283].
[159] M. Kawakami, Y. Ishiuchi, H. Nagashima, T. Tomita, Y. Hiramatsu (Mitsubishi Gas Chemical Co), EP 623552, **1994** [*Chem. Abstr.* **1994**, *122*, 13132].
[160] A. Baiker, *Chem. Rev.* **1999**, *99*, 453 – 473.
[161] F. Solymosi, A. Erdöhelyi, M. Lancz, *J. Catal.* **1985**, *95*, 567 – 577.
[162] A. Erdöhelyi, M. Pásztor, F. Solymosi, *J. Catal.* **1986**, *98*, 166 – 177.
[163] D. Hâncu, J. Green, E. J. Beckman, *Ind. Eng. Chem. Res.* **2001**, *41*, 4466 – 4474.
[164] D. Hâncu, E. J. Beckman, *Green Chem.* **2001**, *3*, 80 – 86.
[165] D. Hâncu, J. Green, E. J. Beckman, *Acc. Chem. Res.* **2002**, *35*, 757 – 764.
[166] N. C. Patel, V. Abovsky, S. Watanasiri, *Fluid Phase Equilib.* **2001**, *185*, 397 – 405.
[167] R. Fernandez-Prinia, J. L. Alvarez, A. H. Harvey, *J. Phys. Chem. Ref. Data* **2003**, *32*, 903 – 916.
[168] O. H. Graaf, H. J. Smit, E. J. Stamhuls, A. A. C. M. Beenackers, *J. Chem. Eng. Data* **1992**, *37*, 146 – 158.
[169] V. V. Krishnan, A. G. Dokoutchaev, M. E. Thompson, *J. Catal.* **2000**, *196*, 366 – 374.
[170] A. I. Dalton, Jr., R. W, Skinner (Air Products & Chemicals Inc), EP 0049806, **1982** [*Chem. Abstr.* **1982**, *97*, 25902].
[171] L. Kim, G. W. Schoenthal (Shell Oil Co.), DE 2615625, **1976** [*Chem. Abstr.* **1976**, *86*, 92663].
[172] B. Zhou, M. A. Rueter, L.-K. Lee, P. B. Pelrine (Hydrocarbon Technologies, Inc.), US 2003/0232004, **2003** [*Chem. Abstr.* **2003**, *137*, 142559].
[173] Y.-F. Han, J. H. Lunsford, *J. Catal.* **2005**, *230*, 313 – 316.
[174] Y.-F. Han, J. H. Lunsford, *Catal. Lett.* **2005**, *99*, 13 – 19.
[175] G. Centi, R. Dittmeyer, S. Perathoner, M. Reif, *Catal. Today* **2003**, *79–80*, 139 – 149.
[176] G. D. Vulpescu, M. Ruitenbeek, L. L. van Lieshout, L. A. Correia, D. Meyer, P. P. A. C. Pex, *Catal. Commun.* **2004**, *5*, 347 – 351.
[177] S. Abate, G. Centi, S. Melada, S. Perathoner, F. Pinna, G. Strukul, *Catal. Today* **2005**, *104*, 323 – 328.
[178] S. Melada, F. Pinna, G. Strukul, S. Perathoner, G. Centi, *J. Catal.* **2005**, *235*, 241 – 248.
[179] S. Melada, F. Pinna, G. Strukul, S. Perathoner, G. Centi, **2006**, *237*, 213 – 219.
[180] A. Fujishima, T. N. Rao, D. A. Tryk, *J. Photochem. Photobiol. C* **2000**, *1*, 1 – 21.
[181] R. Cai, K. Hashimoto, A. Fujishima, K. Kubota, *J. Electroanal. Chem.* **1992**, *326*, 345 – 350.
[182] C. Kormann, D. W. Bahnemann, M. R. Hoffmann, *Environ. Sci. Technol.* **1988**, *22*, 798 – 806.
[183] R. Cai, K. Kubota, A. Fujishima, *J. Catal.* **2003**, *219*, 214 – 218.
[184] H. Goto, Y. Hanada, T. Ohno, M. Matsumura, *J. Catal.* **2004**, *225*, 223 – 229.
[185] K. Makkino, M. M. Mossoba, P. Riesz, *J. Am. Chem. Soc.* **1982**, *104*, 3537 – 3539.
[186] C. Petrier, M. F. Lamy, A. Francony, A. Benahcene, B. David, V. Renaudin, N. Gondrexon *J. Phys. Chem.* **1994**, *98*, 10514 – 10520.
[187] N. S. Foster, D. N. Richard, A. K. Carl, *Environ. Sci. Technol.* **1993**, *27*, 350 – 356.
[188] M. L. Hair, J. R. Habour, *Adv. Chem. Ser.* **1980**, *184*, 173 – 183.
[189] R. Cai, R. Baba, K. Hashimoto, Y. Kubota, A. Fujishima, *J. Electroanal. Chem.* **1993**, *360*, 237 – 245.
[190] M. Fujihira, Y. Satoh, T. Osa, *Nature* **1981**, *293*, 206 – 208.
[191] C. Minero, G. Mariella, V. Maurino, E. Pellizetti, *Langmuir* **2000**, *16*, 2632 – 2642.
[192] H. Park, W. Choi, *J. Phys. Chem. B* **2004**, *108*, 4086 – 4093.
[193] V. Maurino, C. Minero, G. Mariella, E. Pellizetti, *Chem. Commun.* **2005**, 2027 – 2029.
[194] K. Elbs, O. Schönherr, *Z. Elektrochem.* **1895**, *1*, 468.
[195] C. Oloman, A. P. Watkinson, *J. Appl. Electrochem.* **1979**, *9*, 117 – 123.
[196] K. Otsuka, I. Yamanaka, *Electrochim. Acta* **1990**, *35*, 319 – 322.
[197] S. P. Webb, J. A. McIntyre, *Proceedings of The Power of Electrochemistry, 10th International Forum of Electrolysis in the Chemical Industry*, Electrosynthesis Inc., Clearwater Beach, Florida, **1996**.
[198] I. Yamanaka, T. Onizawa, S. Takenaka, K. Otsuka, *Angew. Chem.* **2003**, *115*, 3781 – 3783; *Angew. Chem. Int. Ed.* **2003**, *42*, 3653 – 3655.
[199] I. Yamanaka, T. Hashimoto, K. Otsuka, *Chem. Lett.* **2002**, 852 – 853.
[200] F. Alcaide, E. Brillas, P. L. Cabot, J. Casado *J. Electrochem. Soc.* **1998**, *45*, 3444 – 3449.
[201] E. Brillas, F. Alcaide, P. L. Cabot, *Electrochim. Acta* **2002**, *48*, 331 – 340.
[202] K. Vaik, A. Sarapuu, K Tammeveski, F. Mirkhalaf, D. J. Schiffrin, *J. Electroanal. Chem.* **2004**, *564*, 159 – 166.
[203] M. S. Hossain, D. Tryk, E. Yeager, *Electrochim. Acta* **1989**, *34*, 1733 – 1737.
[204] P. Chen, R. L. McCreery. *Anal. Chem.* **1996**, *68*, 3958 – 3965.
[205] K. Otsuka, K. Hosokawa, I. Yamanaka, Y. Wada, A. Morikawa, *Electrochim. Acta* **1989**, *34*, 1485 – 1488.
[206] I. Yamanaka, T. Akimoto, K. Otsuka, *Electrochim. Acta* **1994**, *39*, 2545 – 2549.
[207] V. L. Kornienko, G. A. Kolyagin, *Russ. J. Electrochem.* **2003**, *38*, 1308 – 1316.
[208] L. Carrette, K. A. Friedrich, U. Stimming, *ChemPhysChem* **2000**, *1*, 162 – 193.
[209] R. Cai, S. Song, B. Ji, W. Yang, G. Sun, Q. Xin, *Catal. Today* **2005**, *104*, 200 – 204.
[210] V. V. Zudin, V. A. Likholobov, Y. I. Yermakov, *Kinet. Katal.* **1979**, *20*, 1559 – 1600.
[211] F. E. Jacobson (BOC), US 4711772, **1987** [*Chem. Abstr.* **1987**, *108*, 40590].
[212] D. Bianchi, R. Bortolo, R. D'Aloisio, M. Ricci, *Angew. Chem.* **1999**, *111*, 734 – 736; *Angew. Chem. Int. Ed.* **1999**, *38*, 706 – 708.
[213] D. Bianchi, R. Bortolo, R. D'Aloisio, *J. Mol. Catal. A* **1999**, *150*, 87 – 94.
[214] C. Querci, R. D'Aloisio, R. Bortolo, M. Ricci, D. Bianchi, *J. Mol. Catal. A* **2001**, *176*, 95 – 100.
[215] A. Yamamoto, *Organotransition Metal Chemistry. Fundamental Concepts and Applications*, Wiley, New York, **1986**, p. 280, 343.
[216] G. Wilke, H. Schott, P. Heimbach, *Angew. Chem.* **1967**, *79*, 62; *Angew. Chem. Int. Ed. Engl.* **1967**, *6*, 92 – 93.
[217] W. R. Thiel, *Angew. Chem.* **1999**, *111*, 3349 – 3351; *Angew. Chem. Int. Ed.* **1999**, *38*, 3157 – 3158.
[218] J. P. Collman, *Acc. Chem. Res.* **1968**, *1*, 136 – 143.
[219] C. J. Nyman, C. E. Wymore, G. Wilkinson, *J. Chem. Soc. A* **1968**, 561 – 563.
[220] W. F. Brill (Halcon SD Group Inc.), DE 334466, **1984** [*Chem. Abstr.* **1984**, *101*, 93741].
[221] Z. I. Ma, R. L. Jia, C. L. Liu, Z. T. Mi, *Chem. Lett.* **2002**, *31*, 884 – 885.
[222] W. L. Feng, Y. Cao, N. Yi, W. L. Dai, K. N. Fan, *New J. Chem.* **2004**, *28*, 1431 – 1433.
[223] M. Okumura, Y. Kitagawa, K. Yamaguchi, T. Akita, S. Tsubota, M. Haruta, *Chem. Lett.* **2003**, *32*, 822 – 823.
[224] R. M. Navarro, M. A. Peña, J. L. G. Fierro in *Metal Oxides: Chemistry and Applications* (Ed.: J. L. G. Fierro), Taylor & Francis, New York, **2005**, Chapter 14, pp. 463 – 490.

 © 2006 Wiley-VCH Verlag GmbH & Co. KGaA, Weinheim

[225] P. G. T. Fogg, W. Gerrand, *Solubility of Gases in Liquids*, Wiley, New York, **1991**.
[226] P. Chauduri, M. Hess, U. Flörke, K. Wieghardt, *Angew. Chem.* **1998**, *110*, 2340 – 2343; *Angew. Chem. Int. Ed.* **1998**, *37*, 2217 – 2220.
[227] Y. Wang, J. L. Dubois, B. Hedman, K. O. Hodson, T. P. D. Stark, *Science* **1998**, *279*, 537 – 540.
[228] W. R. Sanderson, *Pure Appl. Chem.* **2000**, *72*, 1289 – 1304.
[229] M. D. Aitken, *Chem. Eng. J.* **1993**, *52*, B49 – B58.
[230] A. M. Klibanov, T. M. Tu, K. P. Scott, *Science* **1983**, *221*, 259 – 261.
[231] J. S. Cao, L. Wei, Q. Huang, L. Wang, S. Han, *Chemosphere* **1999**, *38*, 565 – 571.
[232] S. Nam, P. G. Tratnyek, *Water Res.* **2000**, *34*, 1837 – 1845.
[233] S. V. Mohan, K. K. Prasad, N. C. Rao, P. N. Sarma, *Chemosphere* **2005**, *58*, 1097 – 1105.
[234] F. van de Velde, N. D. Lourenco, M. Bakker, F. van Rantwijk, R. A. Sheldon, *Biotechnol. Bioeng.* **2000**, *69*, 286 – 291.
[235] B. Dunn, J. M. Miller, B. C. Dave, J. S. Valentine, J. I. Zink, *Acta Mater.* **1998**, *46*, 737 – 741.
[236] J. Li, L. S. Chia, N. K. Goh, S. N. Tan, H. Ge, *Sens. Actuators B* **1997**, *40*, 135 – 141.
[237] K. H. Tong, K. Y. Wong, T. H. Chang, *Tetrahedron* **2005**, *61*, 6009 – 6014.
[238] C. J. Liu, W. Y. Yu, S. G. Li, C. M. Che, *J. Org. Chem.* **1998**, *63*, 7364 – 7369.
[239] B. K. Morinaga, *Bull. Chem. Soc. Jpn.* **1962**, *35*, 345 – 348.
[240] M. Venugopalan, R. A. Jones, *Chem. Rev.* **1966**, *66*, 133 – 160.
[241] J. Zhou, H. Guo, X. Wang, M. Guo, J. Zhao, L. Chen, W. Gong, *Chem. Commun.* **2005**, 1631 – 1633.
[242] G. Pierpont, C. W. Lange, *Prog. Inorg. Chem.* **1994**, *41*, 331 – 341.
[243] G. J. Gerfen, B. F. Bellew, S. Un, J. M. Bollinger, J. Stubbe, R. G. Griffin, D. G. Singel, *J. Am. Chem. Soc.* **1993**, *115*, 6420 – 6421.
[244] M. M. Whittaker, J. W. Whittaker, *J. Biol. Chem.* **1988**, *263*, 6974 – 6980, and references therein.
[245] W. Ruttinger, C. G. Dismukes, *Chem. Rev.* **1997**, *97*, 1 – 24.
[246] J. R. Hartmann, B. M. Foxman, S. R. Cooper, *Inorg. Chem.* **1984**, *23*, 1381 – 1387.
[247] C. G. Pierpont, C. W. Lange, *Prog. Inorg. Chem.* **1994**, *41*, 358 – 442.
[248] T. S. Sheriff, P. Carr, B. Piggott, *Inorg. Chim. Acta* **2003**, *348*, 115 – 122.
[249] A. Gelasco, S. Bensiek, V. L. Pecoraro, *Inorg. Chem.* **1998**, *37*, 3301 – 3304.
[250] T. S. Sheriff, P. Carr, S. J. Coles, M. B. Hursthouse, J. Lesin, M. E. Light, *Inorg. Chim. Acta* **2004**, *357*, 2494 – 2502.

 © 2006 Wiley-VCH Verlag GmbH & Co. KGaA, Weinheim

VIP Molecular Recognition

DOI: 10.1002/anie.200601796

A Bifunctional Molecularly Imprinted Polymer (MIP): Analysis of Binding and Catalysis by a Thermistor**

*Kristian Lettau, Axel Warsinke, Martin Katterle, Bengt Danielsson, and Frieder W. Scheller**

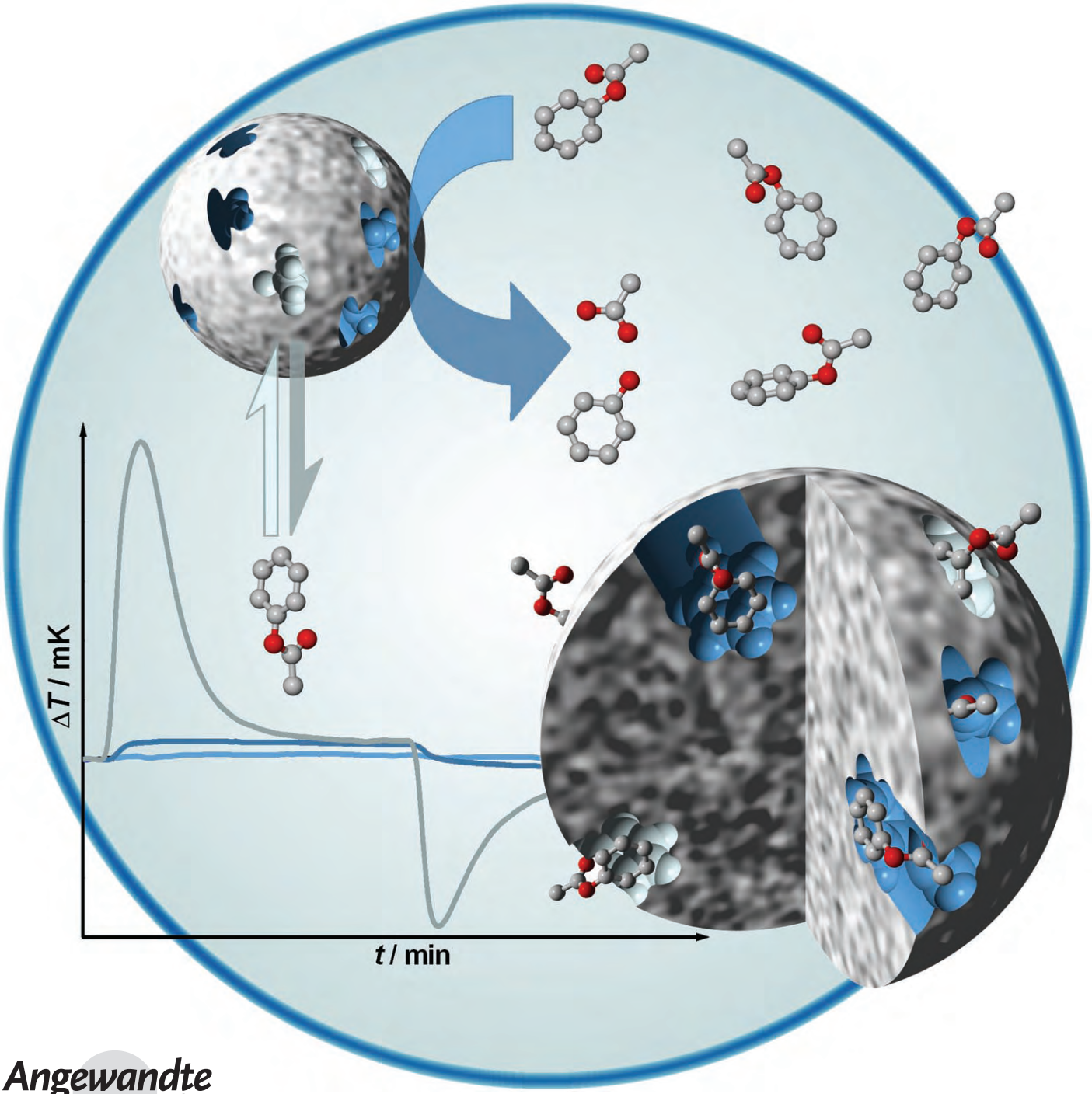

WILEY InterScience DISCOVER SOMETHING GREAT

© 2006 Wiley-VCH Verlag GmbH & Co. KGaA, Weinheim

Nature has created recognition elements based either on proteins or on nucleic acids, showing high chemical selectivity and catalytic power. As an alternative to the evolutionary generation of optimal binders and catalysts based amino acids and nucleotides, totally synthetic molecularly imprinted polymers (MIPs) have been proposed by the groups of Wulff, Shea, and Mosbach.[1–3]

Such bio-inspired molecularly imprinted polymers have the potential to substitute biological recognition elements in chemoselective affinity chromatography, biosensors, and biochips as a result of their high chemical and thermal stability and low cost. However, except for a few sensor configurations, widespread application has yet to come.[4,5] A barrier for routine applications is the signal generation when the analyte binds to the MIP. Although all marker types of immunoassays may be applied to the MIP–analyte interaction, direct (label free) transducers are particularly promising.[6–10] In this respect MIP-covered quartz crystal microbalances as well as surface plasmon resonance sensors have been successfully applied for the recognition of not only low-molecular substances, but also of proteins, viruses, and living cells.[11–13]

Another possibility for label-free detection is the use of calorimeters. In enzyme technology the enzyme thermistor is widely used for this purpose since most enzymatic reactions are accompanied by heat evolution in the range of 5–100 kJ mol^{-1}.[14–16] The first isothermal titration calorimetric studies with MIPs have been performed on the chiral recognition of phenyl-α-D/L-mannopyranoside, and Haupt et al. have already proposed that thermistor devices can measure adsorption and desorption processes with imprinted polymers.[17–19]

Herein we demonstrate for the first time the combination of a calorimetric transducer—the thermistor—with analyte recognition by a catalytically active MIP. Both effects, the binding/desorption and the catalytic conversion of the substrate, were reflected by concentration-dependant heat signals.

The catalytic polymer was prepared, as described elsewhere, with a phosphonic ester monoamide (template) as the transition-state analogue of the ester hydrolysis and 4-vinylimidazole.[20,21] The corresponding non-imprinted polymer (NIP) was prepared from the same monomer mixture but without template. The polymer particles had an average diameter of approximately 40 μm and catalyzed the solvolysis of non-activated phenolic esters (Scheme 1). The specific activity of this polymer towards 4-nitrophenylacetate (NPA) was 90 mU mg^{-1} polymer and the apparent Michaelis–Menten constant (K_M) 2.2 mM. The rate constants (Table 1) of nitrophenylacetate solvolysis are of the same order of magnitude as those reported for other esterolytic MIPs.[22–26]

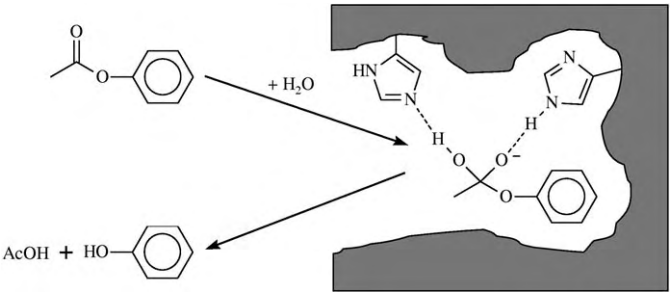

Scheme 1. Proposed mechanism for the MIP-catalyzed solvolysis of the non-activated substrate (phenylacetate) to phenol and acetic acid.

Table 1: Kinetic parameters for the MIP-catalyzed solvolysis of phenylacetate (PA) and nitrophenylacetate (NPA).

Reagent	Cat.[a]	k_{obs} [min^{-1}]	$k_{uncat.}$ [min^{-1}]	$k_{obs}/k_{uncat.}$	$(k_{obs}-k_{uncat.})/k_{uncat.}$
PA[b]	MIP	15.83×10^{-6}	5.92×10^{-6}	2.67	1.67
	NIP	7.01×10^{-6}		1.18	0.18
NPA[c]	MIP	3.83×10^{-3}	0.13×10^{-3}	28.69	27.69
	NIP	1.89×10^{-3}		14.2	13.12

[a] 100 μg mL^{-1} polymer catalyst. [b] 500 μM phenylacetate. [c] 5 mM nitrophenylacetate.

In general the rate constants for phenylacetate (PA) are lower than reported for NPA.[23] This result can be explained by the fact that our polymer was originally designed for the solvolysis of NPA, and also by the fact that NPA is more prone to hydrolysis than PA.[23] Phenylacetate was used as the substrate for the measurements with the thermistor. This substrate has a lower self-hydrolysis rate than the corresponding nitrophenyl ester; it is soluble in a buffer with 10% methanol in millimolar concentrations and shows, as reported for other substrates, no product inhibition in the expected product concentration range.[27]

For comparison of the esterolytic polymer with an enzyme, the catalytic cleavage of phenylacetate with esterase immobilized on amino-functionalized porous glass was investigated.[28] The measurements with the thermistor were performed in a flow-through reactor containing the immobilized enzyme. The signal/time response shows the typical form reported for enzyme reactions (Figure 1) and is a result of the steady-state heat generation by the catalytic reaction.[14] No peaks are found, either after substrate or buffer injection, which indicates that no measurable heating takes place on adsorption or desorption. This result is due to the hydrophilic surface of the particles which arises from functionalization with the esterase. A linear dependency of the steady-state

[*] Dipl.-Biochem. K. Lettau, Dr. habil. A. Warsinke, Dr. M. Katterle, Prof. Dr. F. W. Scheller
Institut für Biochemie und Biologie
Universität Potsdam
Karl-Liebknecht Strasse 24–25, 14476 Golm (Germany)
Fax: (+49) 331-977-5050
E-mail: fschell@uni-potsdam.de
Dr. B. Danielsson
Department of Pure and Applied Biochemistry
Lund University, P.O. Box 124, 22100 Lund (Sweden)

[**] The authors would like to thank Dr. E. Yilmaz for his ideas regarding the thermistor measurements and the IMPRS on Biomimetic Systems as well as the BMBF (BioHyTec InnoRegio 03i1314) for financial support.

 © 2006 Wiley-VCH Verlag GmbH & Co. KGaA, Weinheim

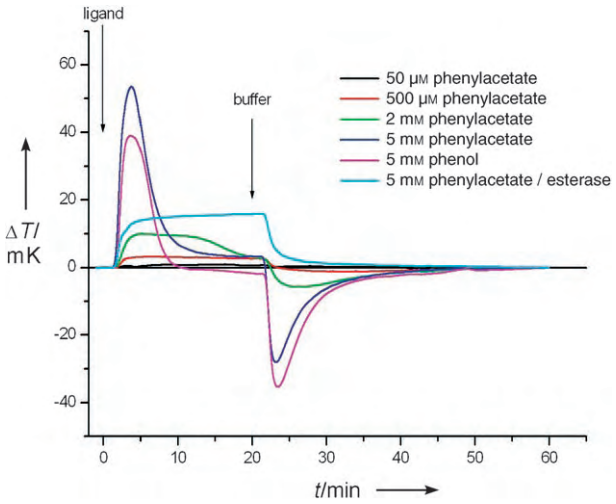

Figure 1. Thermistor response for MIP-catalyzed reactions with different phenylacetate concentrations or 5 mM phenol, and for immobilized esterase with 5 mM phenylacetate. Substrate flow at 0 min and start of washing at 20 min. 20 mM sodium phosphate buffer (pH 7.5)/10% methanol.

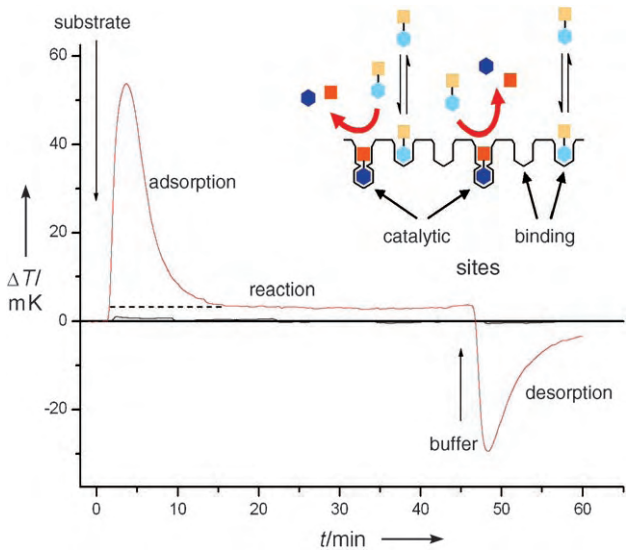

Figure 2. Heat signals of the reactions of the bifunctional MIP and NIP with 5 mM phenylacetate. Start of substrate flow at 0 min and start of washing with buffer at 45 min. The red curve represents the MIP and the black curve the NIP. Inset shows two different interactions between the polymer and the substrate inside the MIP at times between 25 and 45 min.

signal in the range of 0.5 to 5.0 mM phenylacetate was observed. Analysis of the phenol concentration of the effluent with a tyrosinase electrode indicated a conversion of almost 100%.

To test the polymers, a 500-μL reactor containing 150 mg of MIP or NIP was used. For low phenylacetate concentrations, in analogy to the esterase reactor, the imprinted polymer (Figure 1) shows a concentration-dependent plateau over more than 20 min, which indicates a steady state of catalytic reaction reaching saturation at 500 μM. The conversion rate at this substrate concentration was about 20%. After switching back to neat buffer, the signal decreases to the baseline. With higher concentrations of up to 5 mM of phenylacetate a peak can be observed in the first 10 min, followed by a decay of the signal to a saturation value. The subsequent buffer flow generates a negative peak which slowly comes back to baseline. The signal was recorded over a longer time for a concentration of 5.0 mM phenylacetate (Figure 2). After the initial peak, the signal remains at a steady state up to the switch to buffer. This switch again results in a negative peak.

To determine the cause of the initial peak at higher concentrations, measurements with the products of the reaction—phenol and acetic acid—were performed. For 5.0 mM phenol a much sharper initial peak is observed than for 5.0 mM phenylacetate, and the subsequent decrease to the baseline is fast (Figure 1). Solvolysis products are often described to interfere with the binding efficiency, therefore the influence of phenol on the PA solvolysis was investigated.[27] Experiments with running buffer containing 5 mM phenol and injections of different phenylacetate concentrations resulted in catalysis that was still detectable but decreased by 50%. Also the initial peak is still visible but less intense and broadened. This decrease is due to a prior occupation of binding sites with the high excess of product. However, since the product is only formed in a low concentration and in the flow system used is constantly washed out the inhibition effect should be negligible. For 5.0 mM acetic acid there was a spike for about 1 min which decreased very quickly back to the baseline. In contrast, with phenylacetate and phenol, the NIP shows less than 5% of the concentration-dependant heat signals of the MIP (Figure 2).

From this behavior we can conclude that as both polymers—the MIP and the NIP—are made from the same bulk monomer composition the signals from the MIP are due to an imprinting effect in the MIP. From the concentration dependence monitored with this method it seems that there are two different kinds of binding sites in the MIP. The steady state behavior at low substrate concentrations reflects the presence of a group of binding sites with higher affinity which are capable of hydrolyzing phenylacetate to phenol and acetic acid (Figure 2, inset). This catalysis gives rise to a concentration-dependant heat signal over the time when the substrate is pumped through the reactor. The peak formed at high concentrations is caused by a second group of binding sites which have a weaker affinity and are capable of reversibly binding both phenylacetate and phenol (Figure 2, inset). The signals arising from these binding sites are a result of the adsorption and desorption of these aromatic species. After a certain time of substrate supply, equilibrium of binding is reached and the signal drops to the catalytically generated heat level until the purging phase begins. A negative signal is then observed which can be attributed to the endothermic desorption process of the substrate.

Phenylacetate is converted by the catalytic sites with saturation above 500 μM. With higher concentrations, a signal caused by adsorption to the noncatalytic binding sites is superimposed, which corresponds to the desorption during washing and is also visible at concentrations higher than

 © 2006 Wiley-VCH Verlag GmbH & Co. KGaA, Weinheim

500 μM. Kirchner et al. mentioned a similar effect, where the most perfect cavities were preferably filled at low analyte concentrations, and less perfect cavities at higher concentrations, resulting in two different binding enthalpies.[19]

With this knowledge, we can now determine apparent kinetic data for both functional sites. For the catalytic site the heat signal at 20 min prior to washing and for the binding site the signal at 4 min is plotted against the substrate concentration used (Figure 3). The calculated apparent kinetic data are shown in Table 2.

In conclusion, enzyme-like catalysis and antibody-like binding of a bifunctional MIP can be simultaneously resolved by this method for the first time. The bifunctionality is based on two different types of recognition sets in the MIP, which can be distinguished by the differences in heat generation using a flow-through thermistor. Thus, the MIP thermistor allows measurements of two events: substrate conversion in the catalytic sites and its adsorption at the binding sites. With this method it will be possible to construct label-free multianalyte detectors and gain a closer insight into the interactions between the polymer catalyst and the substrate which is necessary to optimize the polymer synthesis for an efficient tailor-made catalyst.

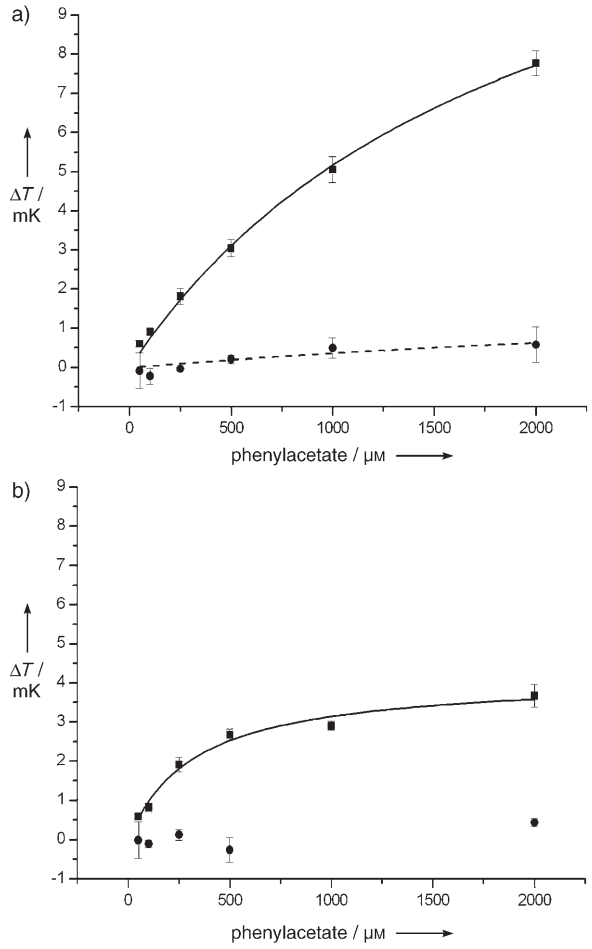

Figure 3. Michaelis–Menten plots of signals taken at a) 4 min and b) 20 min. Squares and circles are the mean values of three measurements for the MIP and the NIP, respectively, and error bars indicate the standard deviations.

Table 2: Apparent kinetic data in the flow.

Signal	Cat.	ΔT_{max}	$K^{[a]}$
Steady-state	MIP	4.16 ± 0.25 mK	322.17 ± 57.88 μM
	NIP	n.d.[b]	n.d.[b]
Peak	MIP	15.72 ± 0.94 mK	1836.28 ± 187.76 μM
	NIP	n.d.[b]	n.d.[b]

[a] K_M for steady-state signal; K_D for peak signal. [b] Not determinable.

Experimental Section

Polymers were prepared as described in Lettau et al.[20] Samples were dissolved in 20 mM sodium phosphate buffer (pH 7.5)/10% methanol immediately before use. Flow and physical conditions for the thermistor measurements: 1.0 mL min^{-1} 20 mM sodium phosphate buffer (pH 7.5)/10% methanol and a constant T of 303.15 K. Rate constants were determined in 20 mM sodium phosphate buffer (pH 7.5)/10% methanol.

Received: May 8, 2006
Revised: June 15, 2006

Keywords: biosensors · calorimetry · enzyme models · molecular recognition · solvolysis

[1] G. Wulff, W. Vesper, R. Grobe-Einsler, A. Sarhan, *Macromol. Chem. Phys.* **1977**, *178*, 2799–2816.
[2] K. J. Shea, E. A. Thompson, S. D. Pandey, P. S. Beauchamp, *J. Am. Chem. Soc.* **1980**, *102*, 3149–3155.
[3] R. Arshady, K. Mosbach, *Macromol. Chem. Phys.* **1981**, *182*, 687–692.
[4] S. A. Piletsky, A. P. F. Turner, *Electroanalysis* **2002**, *14*, 317–323.
[5] F. L. Dickert, O. Hayden, P. Lieberzeit, C. Haderspoeck, R. Bindeus, C. Palfinger, B. Wirl, *Synth. Met.* **2003**, *138*, 65–69.
[6] I. Surugiu, L. Ye, E. Yilmaz, A. Dzgoev, B. Danielsson, K. Mosbach, K. Haupt, *Analyst* **2000**, *125*, 13–16.
[7] B. Sellergren, L. I. Andersson, *Methods* **2000**, *22*, 92–106.
[8] K. Haupt, A. G. Mayes, K. Mosbach, *Anal. Chem.* **1998**, *70*, 3936–3939.
[9] R. J. Ansell, K. Mosbach, *Analyst* **1998**, *123*, 1611–1616.
[10] E. P. C. Lai, A. Fafara, V. A. VanderNoot, M. Kono, B. Polsky, *Can. J. Chem.* **1998**, *76*, 265–273.
[11] T. Kobayashi, Y. Murawaki, P. S. Reddy, M. Abe, N. Fujii, *Anal. Chim. Acta* **2001**, *435*, 141–149.
[12] F. L. Dickert, P. Lieberzeit, O. Hayden, *Anal. Bioanal. Chem.* **2003**, *377*, 540–549.
[13] A. Kugimiya, T. Takeuchi, *Biosens. Bioelectron.* **2001**, *16*, 1059–1062.
[14] K. Mosbach, B. Danielsson, *Anal. Chem.* **1981**, *53*, A83.
[15] B. Danielsson, L. Buelow, C. R. Lowe, I. Satoh, K. Mosbach, *Anal. Biochem.* **1981**, *117*, 84–93.
[16] I. Satoh in *Chemical Sensor Technology, Vol. 2* (Ed.: T. Seiyama), Elsevier, Amsterdam, **1989**.
[17] K. Haupt in *Ultrathin Electrochemical Chemo- and Biosensors, Vol. 2* (Ed.: V. M. Mirsky), Springer, Berlin, **2004**, pp. 23–37.
[18] A. Weber, M. Dettling, H. Brunner, G. E. M. Tovar, *Macromol. Rapid Commun.* **2002**, *23*, 824–828.
[19] R. Kirchner, J. Seidel, G. Wolf, G. Wulff, *J. Inclusion Phenom. Macrocyclic Chem.* **2002**, *43*, 279–283.
[20] K. Lettau, A. Warsinke, A. Laschewsky, K. Mosbach, E. Yilmaz, F. W. Scheller, *Chem. Mater.* **2004**, *16*, 2745–2749.

 © 2006 Wiley-VCH Verlag GmbH & Co. KGaA, Weinheim

[21] E. Yilmaz, K. Haupt, K. Mosbach, *Angew. Chem.* **2000**, *112*, 2178 – 2181; *Angew. Chem. Int. Ed.* **2000**, *39*, 2115 – 2118.
[22] C. G. Overberger, J. C. Salamone, *Acc. Chem. Res.* **1969**, *2*, 217 – 224.
[23] K. Ohkubo, Y. Urata, S. Hirota, Y. Honda, Y. Fujishita, T. Sagawa, *J. Mol. Catal.* **1994**, *93*, 189 – 193.
[24] K. Ohkubo, Y. Urata, S. Hirota, Y. Honda, T. Sagawa, *J. Mol. Catal.* **1994**, *87*, L21 – L24.
[25] J. M. Kim, K. D. Ahn, G. Wulff, *Macromol. Chem. Phys.* **2001**, *202*, 1105 – 1108.
[26] J. Q. Liu, G. Wulff, *Angew. Chem.* **2004**, *116*, 1307 – 1311; *Angew. Chem. Int. Ed.* **2004**, *43*, 1287 – 1290.
[27] G. Wulff, T. Gross, R. Schönfeld, *Angew. Chem.* **1997**, *109*, 2050 – 2052; *Angew. Chem. Int. Ed. Engl.* **1997**, *36*, 1962 – 1964.
[28] G. T. Hermanson, *Bioconjugate Techniques*, Academic Press, San Diego, **1996**.

 © 2006 Wiley-VCH Verlag GmbH & Co. KGaA, Weinheim

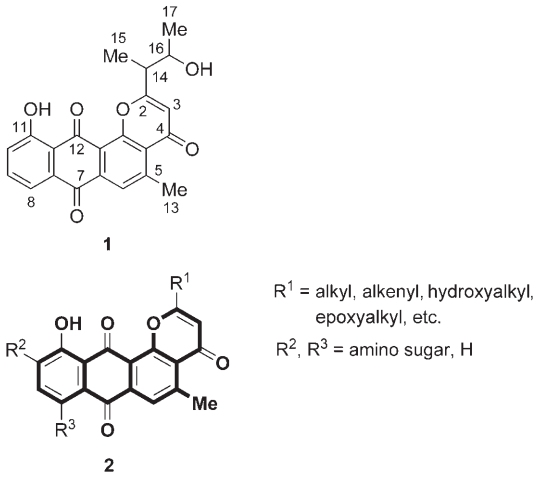

Figure 1. Proposed structure of AH-1763 IIa (**1**) and the structural core **2** of 4*H*-anthra[1,2-*b*]pyran-4,7,12-trione natural products.

Anthrapyran Natural Products

DOI: 10.1002/anie.200601992

Enantioselective Total Synthesis and Structure Determination of the Antiherpetic Anthrapyran Antibiotic AH-1763 IIa**

Lutz F. Tietze, Kersten M. Gericke, and Ramakrishna Reddy Singidi*

Dedicated to Professor Siegfried Blechert on the occasion of his 60th birthday

The anthrapyran antibiotic AH-1763 IIa (**1**) was isolated in 1997 by Uyeda et al.[1] from a culture broth of *Streptomyces cyaneus*. Compound **1** contains the 4*H*-anthra[1,2-*b*]pyran-4,7,12-trione nucleus **2** found in the pluramycin antibiotics (Figure 1).[2] These antibiotics, first described in 1956 by Umezawa et al.,[3] are most commonly isolated from terrestrial *Streptomyces* sp. and are known for their potent anticancer activity arising from the specific alkylation at N7 of the guanine base in DNA. Pluramycin antibiotics[2] have amino sugars typically attached at the C8 and C10 positions, which, however, are not found in AH-1763 IIa (**1**). This compound exhibits a remarkable inhibitory activity against Gram-positive bacteria like *Bacillus subtilis* and *Staphylococcus aureus*.[1] Moreover, it has a very strong antiherpetic activity ($EC_{50} = 2.1\ \mu g\,mL^{-1}$ against HSV-1), which has so far not been observed for any other compound of the anthrapyran natural products.[1,4]

Despite the excellent work from the research groups led by Hauser,[5a,b] Uno,[5c,d] Krohn,[5e] and McDonald,[5f] there is still no general approach to the anthrapyran antibiotics, especially those with stereogenic centers in the side chain.

Here we describe the enantioselective total syntheses of (14*S*,16*R*)- and (14*R*,16*R*)-AH-1763 IIa (**1** and **28**, respectively). Our work allowed us to determine the previously unknown relative and absolute configuration of the natural product and also provides a general synthetic entry to the anthrapyran antibiotics. The retrosynthetic analysis of (14*S*,16*R*)-AH-1763 IIa (**1**) is outlined in Scheme 1. The first

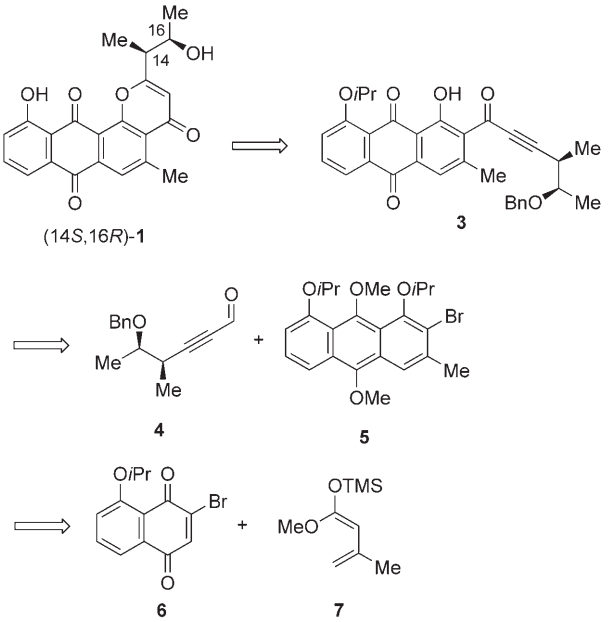

Scheme 1. Retrosynthetic analysis of (14*S*,16*R*)-AH-1763 IIa (**1**). Bn = benzyl, TMS = trimethylsilyl.

[*] Prof. Dr. L. F. Tietze, Dr. K. M. Gericke, Dr. R. R. Singidi
Institut für Organische und Biomolekulare Chemie
Georg-August-Universität
Tammannstrasse 2, 37077 Göttingen (Germany)
Fax: (+49) 551-399-476
E-mail: ltietze@gwdg.de

[**] The authors are grateful to the Fonds der Chemischen Industrie for supporting this work. R.R.S. thanks the Alexander von Humboldt Foundation for a postdoctoral grant.

Supporting information for this article (experimental procedure for the synthesis of **1** and its diastereomer **28**) is available on the WWW under http://www.angewandte.org or from the author.

WILEY InterScience DISCOVER SOMETHING GREAT
© 2006 Wiley-VCH Verlag GmbH & Co. KGaA, Weinheim

disconnection in the pyrone ring moiety envisions an intramolecular 6-*endo*-digonal cyclization of the ynone **3**, which in turn should result from a nucleophilic attack of an aryl lithium species generated from the bromodimethoxyanthracene derivative **5** on the propargylic aldehyde **4**. The stereogenic centers of the propargylic aldehyde **4** could be constructed using the well-established Evans aldol methodology,[6] and **5** should be accessible from a Diels–Alder reaction of fragments **6** and **7**.

The Diels–Alder reaction of **6**[7] and **7**[8] in benzene yielded the primary cycloadduct **8**, which was converted without further isolation into the thermodynamically more stable anthraquinone derivative **9** by treatment with silica gel as a mild acid (Scheme 2). The bromine atom acts as a

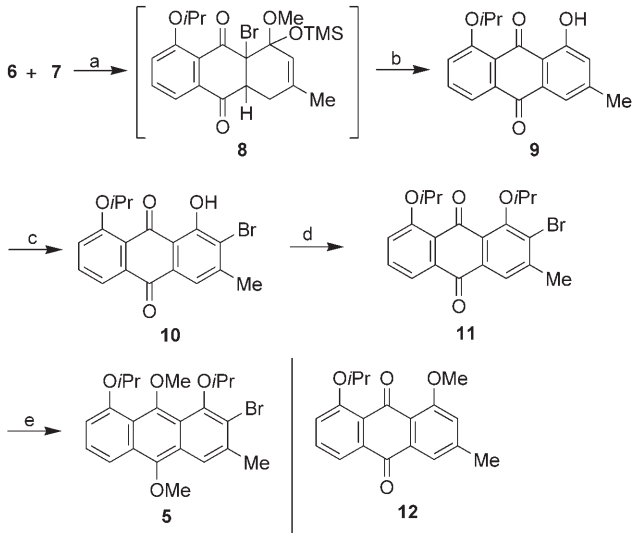

Scheme 2. Reagents and conditions: a) Benzene, RT, 6 h; b) SiO_2, CH_2Cl_2, RT, 24 h, 94% overall yield for two steps; c) NBS, cat. iPr_2NH, CH_2Cl_2, RT, 12 h, 97%; d) Cs_2CO_3, *i*PrI, acetone/DMF (3:1), reflux, 12 h, 94%; e) $Na_2S_2O_4$, TBABr, KOH, H_2O, $DMSO_4$, THF, RT, 4 h, 98%. DMF = *N*,*N*-dimethylformamide, $DMSO_4$ = dimethyl sulfate, NBS = *N*-bromosuccinimide, TBABr = tetrabutylammonium bromide.

regiochemical control element in the Diels–Alder reaction.[9] This method is operationally simpler and gives higher yields (94%) than the procedure developed by Brassard and Savard[8] for the preparation of the anthraquinone building block **9**, which is a common precursor also of other naturally occurring anthraquinone antibiotics. The *O*-methyl ether **12**, which was a major side product in the synthesis by Brassard[8] and has been proven to be worthless for further transformations (see also Reference [5e]), did not form. The subsequent regioselective bromination of anthraquinone **9** was feasible owing to the strong *ortho*-directing effect of the hydroxy group. Thus, treatment of **9** with NBS in dichloromethane in the presence of a catalytic amount of a secondary amine[10] gave after purification by column chromatography the monobromoanthraquinone **10** in nearly quantitative yield (97%). The regioselectivity of both the bromination and the Diels–Alder reaction was unambiguously deduced from HMBC ^{1}H NMR experiments. To complete the synthesis of the building block **5**, both the hydroxy group and the quinone moiety had to be protected. Following an orthogonal protecting-group strategy, the hydroxy group of bromoanthraquinone **10** was protected by treatment with *i*PrI and Cs_2CO_3 in a mixture of acetone and *N*,*N*-dimethylformamide to give its isopropyl ether **11** (94% yield).[11] Finally, reductive methylation[12] of the quinone moiety in **11** was realized by using aqueous sodium dithionite to furnish the corresponding air-sensitive hydroquinone, which underwent methylation upon treatment with KOH and dimethylsulfate to provide the bromodimethoxyanthracene **5** in an excellent overall yield of 98%.

The synthesis of the side-chain unit started from the known aldol product **14**,[13] which was obtained from **13**[14] and protected as its benzyl ether **15** using benzyltrichloroacetimidate (Scheme 3).[15] Reductive removal of the chiral auxiliary

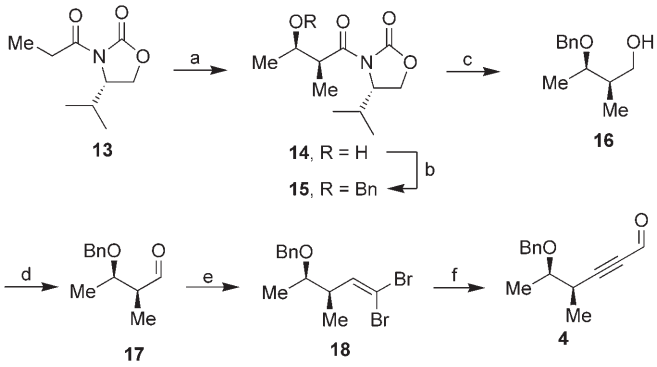

Scheme 3. Reagents and conditions: a) 1. nBu_2BOTf, Et_3N, CH_2Cl_2, −3°C, 1 h; 2. acetaldehyde, −78°C→0°C, 4.5 h, 3. phosphate buffer, MeOH, H_2O_2 (30%), 0°C, 45 min, 87%; b) benzyltrichloroacetimidate, cat. TfOH, cyclohexane/CH_2Cl_2 (2:1), RT, 1 h, 85%; c) $LiBH_4$, Et_2O, 0°C, 4 h, 92%; d) IBX, CH_2Cl_2, DMSO, RT, 2 h, 95%; e) PPh_3, CBr_4, Zn, CH_2Cl_2, RT, 12 h, 90%; f) *n*BuLi, THF, DMF, −78°C→0°C, 4 h, 90%. IBX = 2-iodoxybenzoic acid, DMSO = dimethyl sulfoxide, TfOH = trifluoromethanesulfonic acid.

with $LiBH_4$ in wet Et_2O[16] gave the primary alcohol **16** in 92% yield. Subsequent oxidation utilizing the very mild IBX[17] reagent furnished aldehyde **17** in very good yield (95%). Corey–Fuchs homologation[18] of **17** afforded the vinyl dibromide **18** in 90% yield. Subsequent treatment of **18** with *n*BuLi followed by formylation with *N*,*N*-dimethylformamide[19] furnished the desired propargylic aldehyde **4** in 90% yield with 99% *ee* and d.r. > 99:1.

Having successfully synthesized both the building blocks **4** and **5** in a convenient and highly efficient manner, we focused on coupling these intermediates. After conversion of **5** into the corresponding lithium derivative by bromine–lithium exchange using *n*BuLi at low temperature, the subsequent reaction with the propargylic aldehyde **4** proceeded smoothly to give alcohol **19** in 75% yield as a 1:1 mixture of the two possible diastereomers (Scheme 4). The yields were best when the aldehyde was added immediately after generation of the organolithium compound. Oxidative demethylation of the anthracene derivative **19** using $Ag^{II}O/HNO_3$[20] gave anthraquinone **20** in 90% yield. Compound **20** was subsequently subjected to IBX oxidation[17] to afford the ynone

 © 2006 Wiley-VCH Verlag GmbH & Co. KGaA, Weinheim

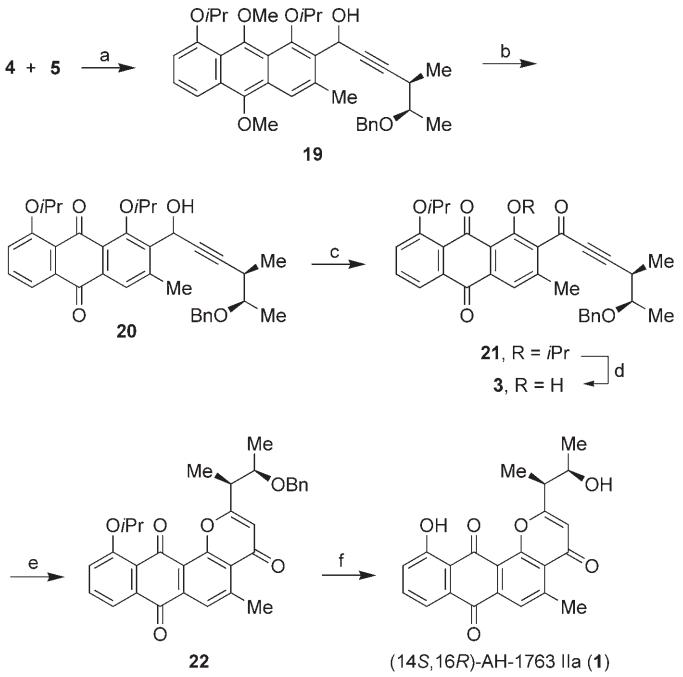

Scheme 4. Reagents and conditions: a) *n*BuLi, THF, −78 °C, 10 min, 75 %; b) $Ag^{II}O$, dioxane, 4 N HNO_3, RT, 30 min, 90 %; c) IBX, CH_2Cl_2, DMSO, RT, 5 h, 97 %; d) AcOH, cat. H_2SO_4, 60 °C, 10 min, 88 %; e) Cs_2CO_3, acetone, RT, 30 min, 71 %; f) $TiCl_4$, CH_2Cl_2, −78 °C→0 °C, 4 h, 90 %.

derivative **21** in 97 % yield. It was expected that the deprotection of phenolic hydroxy group at C12b and the proposed intramolecular 6-*endo*-dig cyclization could be done in one step under acidic conditions. However, treatment of **21** in acetic acid at 50 °C with a catalytic amount of sulfuric acid only led to cleavage of the isopropyl ether at C12b probably because of activation by the adjacent carbonyl groups.[21] Neither raising the temperature nor increasing the reaction time resulted in cyclization but resulted in an undesired elimination of the benzyloxy group in the side chain. The pyron ring was finally achieved under basic conditions. Thus, treatment of **3** in acetone with Cs_2CO_3 yielded the tetracycle **22** in 71 % yield.[5c,d,22] In the final steps in the synthesis of (14*S*,16*R*)-AH-1763 IIa (**1**) the isopropyl and benzyl protecting groups were removed by treating **22** with $TiCl_4$ in CH_2Cl_2 at −78 °C and then allowing the reaction mixture to warm slowly to 0 °C (yield of **1**: 90 %).[10d]

The published ^{1}H NMR spectrum of the compound isolated by Uyeda et al.[1] and that of our synthetic (14*S*,16*R*)-AH-1763 IIa (**1**) were identical in all respects, including chemical shifts and coupling constants. In addition, the ^{13}C NMR spectra deviated by at most 0.1 ppm. However, the optical rotation of the synthetic compound was measured to be $[\alpha]_D = -28.6$ ($c = 0.1$, $CHCl_3$), in contrast to the reported value of $[\alpha]_D = +6.6$ ($c = 0.1$, $CHCl_3$)[1] for the natural product. For that reason we also synthesized the (14*R*,16*R*)-AH-1763 IIa diastereomer **28** in order to compare the analytical data. Compound **28** was prepared from bromodimethoxyanthracene **5** and the propargylic aldehyde **27** following the synthetic route established for the synthesis of **1** (Scheme 5). For the synthesis of the aldehyde **27** the commercially available ester **23** was transformed into the primary alcohol **24** by a known procedure.[23] Oxidation of **24** using IBX[17] followed by treatment with the Corey–Fuchs

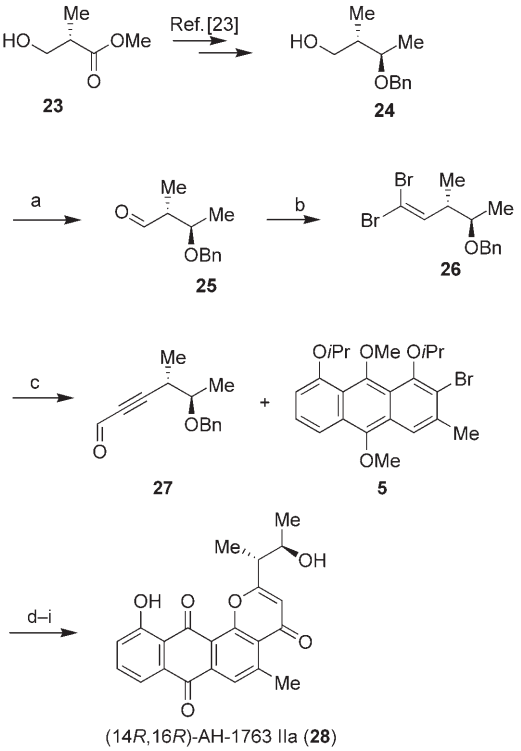

Scheme 5. Reagents and conditions: a) IBX, CH_2Cl_2, DMSO, RT, 2 h, 93 %; b) PPh_3, CBr_4, Zn, CH_2Cl_2, RT, 12 h, 92 %; c) *n*BuLi, THF, DMF, −78 °C→0 °C, 4 h, 88 %; d) *n*BuLi, THF, −78 °C, 10 min, 72 %; e) $Ag^{II}O$, dioxane, 4 N HNO_3, RT, 30 min, 90 %; f) IBX, CH_2Cl_2, DMSO, RT, 5 h, 97 %; g) AcOH, cat. H_2SO_4, 60 °C, 10 min, 86 %; h) Cs_2CO_3, acetone, RT, 30 min, 70 %; i) $TiCl_4$, CH_2Cl_2, −78 °C→0 °C, 4 h, 90 %.

reagent produced dibromoalkene **26**,[18] which was converted into the desired propargylic aldehyde **27** by successive treatment with *n*BuLi and *N*,*N*-dimethylformamide.[19] Finally reaction of **27** and **5** under the conditions optimized in the synthesis of **1** gave (14*R*,16*R*)- AH-1763 IIa (**28**).

Comparison of the ^{1}H and ^{13}C NMR spectroscopic data of synthetic **28** with those reported for isolated AH-1763 IIa (**1**) clearly indicate that the two compounds are not enantiomers but diastereomers. Thus, 14H and 16H in **28** give rise to signals at $\delta = 2.78$ and $\delta = 4.17$ ppm, respectively, with the coupling constant $J_{H14,H16} = 8.3$ Hz. In contrast, the signals for 14H and 16H in the isolated AH-1763 IIa (**1**) are found at $\delta = 2.88$ and $\delta = 4.32$ ppm, respectively, with $J_{H14,H16} = 3.3$ Hz. From these data we conclude that the relative stereochemistry of natural AH-1763 IIa (**1**) is identical to that of the synthetic material (14*S*,16*R*)-**1**. However, the sign of the $[\alpha]_D$ value of the two compounds is opposite. We therefore assume the absolute stereochemisty of the isolated natural product is 14*R*,16*S* even though the value of the optical rotation of (14*S*,16*R*)-AH-1763 IIa (**1**) is higher than that reported for the natural product. Unfortunately, direct comparison of the two com-

 © 2006 Wiley-VCH Verlag GmbH & Co. KGaA, Weinheim

pounds was not possible since we did not have a sample of the natural material.

In conclusion, we have developed a new general strategy for the synthesis of anthrapyran antiobotics which resulted in the first enantioselective total synthesis of (14*S*,16*R*)-AH-1763 IIa (**1**) and in addition the determination of the relative and absolute stereochemistry of the natural product **1**.

Received: May 19, 2006
Published online: September 29, 2006

Keywords: alkynes · antibiotics · cycloaddition · natural products · total synthesis

[1] M. Uyeda, K. Yokomizo, A. Ito, K. Nakayama, H. Watanabe, Y. Kido, *J. Antibiot.* **1997**, *50*, 828 – 832.
[2] a) K. Eckardt in *Quinones and Other Carbocyclic Antitumor Antibiotics in Antitumor Compounds of Natural Origin: Chemistry and Biology, Vol. II* (Ed.: A. Aszalos), CRC, Boca Raoton, **1981**; b) "The Antibiotics of the Pluramycin Group (4*H*-Anthra-[1,2-*b*]pyran Antibiotics)": U. Séquin in *Prog. Chem. Org. Nat. Prod.*, *Vol. 50* (Ed.: L. Zechmeister), Springer, Vienna, **1986**, pp. 58 – 122.
[3] T. Maeda, T. Takeuchi, K. Nitta, K. Yagishita, R. Utahara, T. Osato, M. Ueda, S. Kondo, Y. Okami, H. Umezawa, *J. Antibiot. Ser. A* **1956**, *9*, 75 – 81.
[4] a) T. Takeuchi, K. Nitta, H. Umezawa, *J. Antibiot.* **1956**, *9*, 22 – 30; b) N. Abe, Y. Nakatika, T. Nakamura, N. Enoki, H. Uchida, M. Munekata, *J. Antibiot.* **1993**, *46*, 1530 – 1535.
[5] a) F. M. Hauser, R. P. Rhee, *J. Am. Chem. Soc.* **1979**, *101*, 1628 – 1629; b) F. M. Hauser, R. P. Rhee, *J. Org. Chem.* **1980**, *45*, 3061 – 3068; c) H. Uno, K. Sakamoto, E. Honda, N. Ono, *Chem. Commun.* **1999**, 1005 – 1006; d) H. Uno, K. Sakamoto, E. Honda, K. Fukuhara, N. Ono, J. Tanaka, M. Sakanaka, *J. Chem. Soc. Perkin Trans. 1* **2001**, 229 – 238; e) K. Krohn, J. Vitz, *Eur. J. Org. Chem.* **2004**, 209 – 219; f) Z. Fei, F. E. McDonald, *Org. Lett.* **2005**, *7*, 3617 – 3620.
[6] D. A. Evans, J. Bartroli, T. L. Shi, *J. Am. Chem. Soc.* **1981**, *103*, 2127 – 2129.
[7] We could improve the synthesis of juglone to 55 % yield by using a new batch of 1,5-dihydroxynaphthaline and freshly recrystallized copper(I)chloride. a) T. Takeya, M. Kajiyama, C. Nakumara, S. Tobinaga, *Chem. Pharm. Bull.* **1999**, *47*, 209 – 219; b) A. S. Wheeler, B. Naiman, *J. Am. Chem. Soc.* **1922**, *44*, 2331 – 2334; c) R. H. Thomson, *J. Org. Chem.* **1948**, *13*, 377 – 383; d) R. L. Hannan, R. B. Barber, H. Rapoport, *J. Org. Chem.* **1979**, *44*, 2153 – 2158; e) L. F. Tietze, C. Güntner, K. M. Gericke, I. Schuberth, G. Bunkoczi, *Eur. J. Org. Chem.* **2005**, 2459 – 2467.
[8] J. Savard, P. Brassard, *Tetrahedron* **1984**, *40*, 3455 – 3464.
[9] J. R. Grunwell, A. Karipides, C. T. Wigal, S. W. Heinzman, J. Parlow, J. A. Surso, L. Clayton, F. J. Fleitz, M. Daffner, J. E. Stevens, *J. Org. Chem.* **1991**, *56*, 91 – 95.
[10] a) S. Fujisaki, H. Eguchi, A. Omura, A. Okamoto, A. Nishida, *Bull. Chem. Soc. Jpn.* **1993**, *66*, 1576 – 1579; b) K. Krohn, S. Bernhard, U. Floerke, N. Hayat, *J. Org. Chem.* **2000**, *65*, 3218 – 3222; c) K. C. Nicolaou, D. Gray, J. Tae, *Angew. Chem.* **2001**, *113*, 3791 – 3795; *Angew. Chem. Int. Ed.* **2001**, *40*, 3679 – 3683; d) G. Bringmann, D. Menche, J. Kraus, J. Mühlbacher, K. Peters, E.-M. Peters, R. Brun, M. Bezabih, B. M. Abegaz, *J. Org. Chem.* **2002**, *67*, 5595 – 5610.
[11] R. T. Winters, A. D. Sercel, H. D. Showalter, *Synthesis* **1988**, 712 – 714.
[12] P. Allevi, M. Anastasia, S. Bingham, P. Ciuffreda, A. Pierangela, *J. Chem. Soc. Perkin Trans. 1* **1998**, *3*, 575 – 582.
[13] a) D. A. Evans, M. D. Ennis, T. Le, N. Mandel, G. Mandel, *J. Am. Chem. Soc.* **1984**, *106*, 1154 – 1156; b) T. Nakata, S. Nagao, T. Oishi, *Tetrahedron Lett.* **1985**, *26*, 6465 – 6468; c) T. Berkenbusch, R. Brückner, *Chem. Eur. J.* **2004**, *10*, 1545 – 1557.
[14] D. A Entwistle, S. I. Jordan, J. Montgomery, G. Pattenden, *Synthesis* **1998**, 603 – 612.
[15] a) U. Widmer, *Synthesis* **1987**, 568 – 570; b) W. R. Roush, T. G. Marron, L. A. Pfeifer, *J. Org. Chem.* **1997**, *62*, 474 – 478.
[16] T. D. Penning, S. W. Djuric, R. A. Haack, V. J. Kalish, J. M. Miyashiro, B. W. Rowell, S. S. Yu, *Synth. Commun.* **1990**, *20*, 307 – 312.
[17] M. Frigerio, M. Santagostino, S. Sputore, *J. Org. Chem.* **1999**, *64*, 4537 – 4538.
[18] E. J. Corey, P. L. Fuchs, *Tetrahedron Lett.* **1972**, *36*, 3769 – 3772.
[19] H. Ohno, M. Anzai, A. Toda, S. Ohishi, N. Fujii, T. Tetsuaki, Y. Takemoto, T. Ibuka, *J. Org. Chem.* **2001**, *66*, 4904 – 4914.
[20] a) C. D. Snyder, H. Rapoport, *J. Am. Chem. Soc.* **1972**, *94*, 227 – 231; b) F. M. Hauser, R. P. Rhee, *J. Org. Chem.* **1980**, *45*, 3061 – 3068.
[21] M. Iwasaki, T. Watanabe, T. Ishiwaka, S. Chansakaow, Y. Higuchi, S. Tahara, *Heterocycles* **2004**, *63*, 1375 – 1392.
[22] M. A. Mzhel'skaya, A. A. Moroz, M. S. Shvartsberg, *Ser. Khim.* **1991**, *7*, 1469 – 1472.
[23] a) R. Baker, R. H. Boyes, D. M. Broom, M. J. Mahony, C. J. Swain, *J. Chem. Soc. Perkin Trans. 1* **1987**, 1613 – 1621; b) T. Hamada, Y. Kobayashi, *Tetrahedron Lett.* **2003**, *44*, 4347 – 4350.

 © 2006 Wiley-VCH Verlag GmbH & Co. KGaA, Weinheim

Tailored Nanorods

DOI: 10.1002/anie.200601957

TiO_2–Nb_2O_5 Nanotubes with Electrochemically Tunable Morphologies**

*Andrei Ghicov, Saule Aldabergenova, Hiroaki Tsuchyia, and Patrik Schmuki**

Recently, reports on the synthesis of TiO_2 nanotubes have generated considerable scientific interest,[1–5] owing to the broad range of applications of the oxide. TiO_2 can be used in solar cells,[6] photocatalytic devices,[8] and lithium-ion batteries,[9]and exhibits highly variable and tunable wetting behavior.[7] A particularly attractive method for the production of TiO_2 nanotubes is the controlled anodization of Ti in a fluoride-containing electrolyte, as self-organized and highly ordered layers of nanotubes can be generated.[10] A range of

[*] A. Ghicov, Dr. S. Aldabergenova, Dr. H. Tsuchyia, Prof. Dr. P. Schmuki
Department of Materials Science, WW4-LKO
University of Erlangen-Nuremberg
Martensstrasse 7, 91058 Erlangen (Germany)
Fax: (+49) 9131-852-7582
E-mail: schmuki@ww.uni-erlangen.de

[**] The authors would like to acknowledge Anja Friedrich and Helga Hildebrand for the SEM and XPS investigations, as well as Ulrike Marten for the XRD measurements. The DFG is acknowledged for financial support, and Robert Houser from ATI Wah Chang is thanked for providing the Ti45Nb alloy.

© 2006 Wiley-VCH Verlag GmbH & Co. KGaA, Weinheim

unusual properties have recently been described for these nanotubes, including wettability control (from superhydrophilic to superhydrophobic),[11] photo-electrochemical properties,[12] and pronounced electrochromic behavior.[13]

The electrochemical conditions under which the nanotubes are produced, such as the anodization time and potential, and the pH and viscosity of the electrolyte, have a large influence on the resulting tube morphology. High-aspect-ratio TiO_2 nanotubes were only recently obtained by using optimized reaction conditions.[4] Exceptionally homogeneous, smooth nanotubes with diameters of 40 nm and lengths of 7 μm were produced under very specific conditions.[5] However, such tube dimensions can only be obtained within a limited range of experimental parameters.

Herein, we show that the range of achievable diameters and lengths of TiO_2-based nanotubes can be significantly expanded, if a binary Ti–Nb alloy, rather than pure Ti, is used as a substrate for nanotube growth in an aqueous electrolyte. The length of the resulting mixed oxide nanotubes can be adjusted from 0.5–8 μm, and the diameter from 30–120 nm. The morphology of the tubes differs significantly from that of the nanostructures grown under the same conditions on pure Ti or Nb substrates: only considerably shorter tubes grow on Ti, whereas irregular porous structures grow on Nb.

In the past few years, it has been possible to grow ordered oxide nanoporous structures not only for Ti, but also for other transition metals, such as Zr,[14] Hf,[15] Nb,[16] Ta[17], and W[18] through anodization in fluoride-containing electrolytes. In this process, it is important to achieve an equilibrium between anodic oxide growth and local oxide dissolution. The equilibrium is particularly sensitive to the concentration of F^- ions, as the oxide dissolves chemically with the formation of soluble $[TiF_6]^{2-}$ complexes.

The various transition-metal oxides have very different dissolution kinetics in fluoride-containing solutions.[19] In particular, Nb_2O_5 produced at the anode is significantly more resistant to F^- ions than TiO_2: in a 1 M solution of NaH_2PO_4 with 0.5 wt% HF (pH 4.5), the dissolution rate of Nb_2O_5 is 1 nm min^{-1}, whereas that of TiO_2 is 20 nm min^{-1}.[20] Given that the dissolution rate of TiO_2 in a fluoride-containing electrolyte is of central importance to the length of the nanotubes formed,[4] it was anticipated that the growth behavior of anodic oxides on Ti–Nb alloys would deviate significantly from that on pure Ti.

For our investigation of the growth behavior of oxide nanotubes, the commercially available single-phase alloy β-Ti45Nb (45 wt% (30 at%) Nb) was compared with pure Ti and Nb. Figure 1 shows scanning electron microscope (SEM) images of the structures formed upon anodization of Nb, Ti, and the Ti45Nb alloy in a 1 M solution of NaH_2PO_4 with 0.5 wt% HF. After 2 h of polarization, an approximately 1-μm-thick layer of upright TiO_2 nanotubes with diameters of approximately 100 nm is formed on pure Ti (Figure 1b), whereas an approximately 0.6-μm-thick Nb_2O_5 layer perforated by irregular pores with diameters of approximately 15 nm is formed on pure Nb (Figure 1a). In contrast, on the Ti45Nb alloy, an approximately 3-μm-thick layer of nanotubes with diameters of approximately 60 nm is obtained. The difference in the oxide growth behavior on the alloy and the

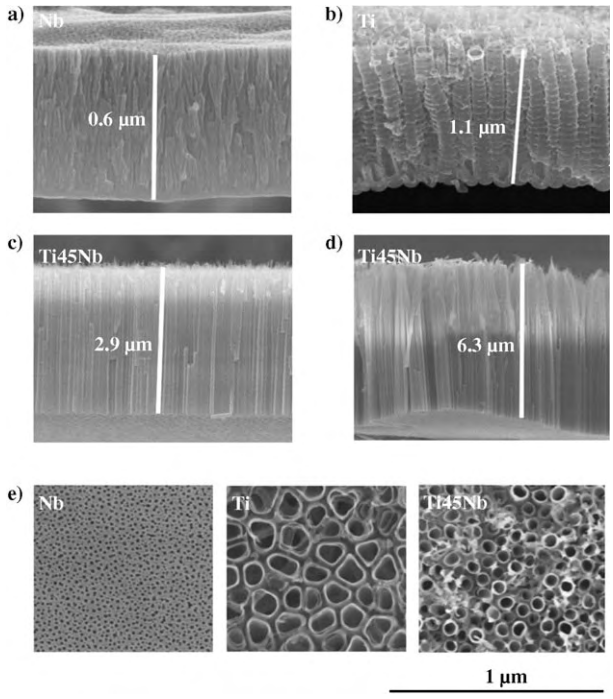

Figure 1. Cross-section SEM images of a) Nb, b) Ti, and c) Ti45Nb substrates after anodization at 20 V for 2 h in a 1 M solution of NaH_2PO_4 with 0.5 wt% HF, and of d) the Ti45Nb substrate after anodization at 20 V for 20 h. e) Top-view SEM images of the substrates in (a)–(c).

elements becomes even more evident when the polarization time is extended. On Ti and Nb, the thickness of the TiO_2 or Nb_2O_5 layer does not increase any further, but on the Ti45Nb alloy, the thickness of the oxide layer increases to 6.3 μm after polarization for 20 h (Figure 1d), while the diameter of the nanotubes remains constant.

Although the diameter of the nanotubes grown on the Ti45Nb alloy approaches a weighted average of those of nanotubes grown on Ti or Nb, the significantly greater length of the nanotubes grown on the alloy indicates that strong synergistic effects occur. Additionally, it is remarkable that the mixed oxide nanotubes on the alloy have very smooth walls, whereas the walls of the TiO_2 tubes and Nb_2O_5 pores are relatively irregular. In fact, TiO_2 nanotubes with a similar level of smoothness can only be obtained under very specific conditions.[5]

Figure 2 shows transmission electron microscope (TEM) images of nanotubes grown on the Ti45Nb alloy. As shown in the high-resolution (HR) image (Figure 2, right), the bottom walls of the tubes are approximately 30 nm thick, and the side walls are approximately 20 nm thick over the whole tube length. A selected area electron diffraction (SAED) pattern reveals that the as-formed oxide nanotubes are amorphous (Figure 2, left inset).

High-resolution X-ray photoelectron spectroscopy (XPS) showed that the nanotubes formed on Ti45Nb consist of a mixture of TiO_2 and Nb_2O_5, rather than a mixed Ti–Nb oxide. From the Ti 2p peak at 458.7 eV and the Nb 3d peak at 207.2 eV, the Ti/Nb/O atomic ratio of the nanotubes was determined as 26:13:61. The Ti/Nb ratio of the oxide reflects

 © 2006 Wiley-VCH Verlag GmbH & Co. KGaA, Weinheim

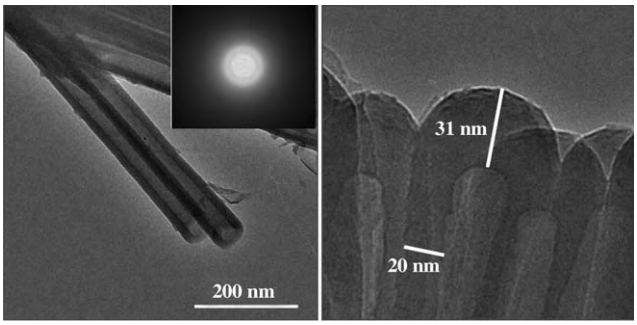

Figure 2. TEM (left; inset: corresponding SAED pattern) and HRTEM (right) images of TiO_2–Nb_2O_5 nanotubes formed after anodization of Ti45Nb at 20 V for 2 h in a 1 M solution of NaH_2PO_4 with 0.5 wt% HF.

the 2:1 atomic ratio of the Ti45Nb substrate. This ratio is also consistent with energy-dispersive X-ray (EDX) analysis (which has a larger analysis area and a much higher penetration depth than XPS), indicating that the composition remains approximately constant over the entire tube length.

Another feature of the tubes produced on the Ti45Nb alloy is that they can be formed in ordered arrays over a wide range of applied potentials. In Figure 3, the diameters and lengths of the nanotubes formed on Nb, Ti, and Ti45Nb are plotted against the anodization potential. On Nb, only irregular nanoporous structures with lengths of less than 1 μm can be grown at potentials of 5–30 V. On Ti, regular nanotubes with maximum lengths of slightly greater than 1 μm are grown at 10–20 V. In contrast, the Ti45Nb alloy allows the controlled synthesis of nanotubes with diameters of 30–120 nm and lengths of 0.5–8 μm at 5–60 V. A linear

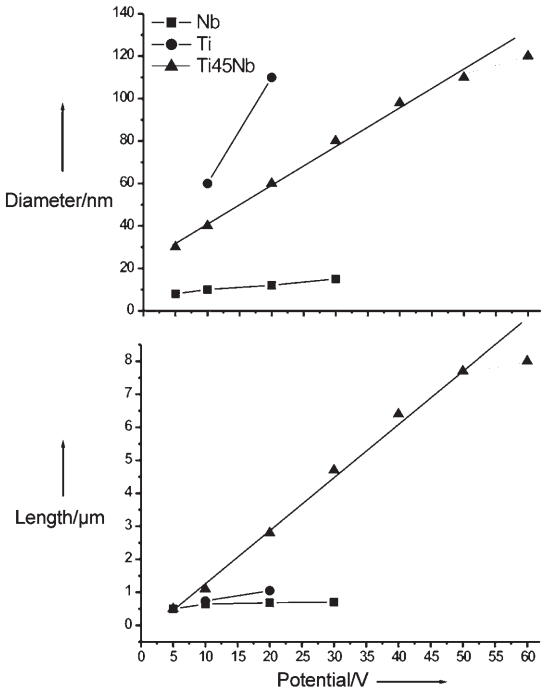

Figure 3. Dependence of the diameters (top) and lengths (bottom) of the Nb_2O_5, TiO_2, and TiO_2–Nb_2O_5 nanotubes on the anodization potential. The Nb, Ti, and Ti45Nb substrates were anodized for 2 h in a 1 M solution of NaH_2PO_4 with 0.5 wt% HF.

dependence on potential is observed for both the length and the diameter of the tubes up to 50 V. At higher potentials, the tube length does not increase significantly, and the nanostructures begin to exhibit irregular features.

Many applications of TiO_2 nanotubes require a crystalline substrate. Therefore, the amorphous tubes formed on the Ti45Nb anode must crystallized through annealing. Figure 4

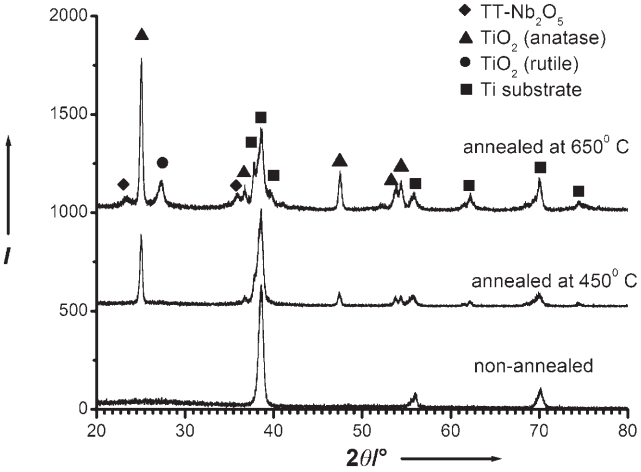

Figure 4. XRD patterns for the TiO_2–Nb_2O_5 nanotubes grown on Ti45Nb, directly after preparation (bottom), and after thermal treatment at 450 °C (middle) or 650 °C (top) for 1 h in air.

shows X-ray diffraction (XRD) patterns for the as-formed tubes and for the tubes after annealing at 450 or 650 °C for 1 h in air. In the pattern of the as-formed tubes, only reflections assigned to the substrate occur, confirming the amorphous nature of the nanotubes suggested by TEM. After annealing at 450 °C, a strong reflection assigned to anatase-type TiO_2 appears at $2\theta = 25°$. After annealing at 650 °C, an additional peak assigned to rutile appears, but the major TiO_2 phase remains anatase. This result indicates that the anatase–rutile transition takes place at a higher temperature in the polycrystalline mixed oxide nanotubes than in pure TiO_2. Similar behavior was observed in studies of the sintering behavior of TiO_2–Nb_2O_5 mixtures.[21] According to the Scherrer equation,[22] a size of 25 nm is calculated for the anatase crystallites obtained after annealing at 450 or 650 °C. Weak reflections assigned to pseudo-hexagonal TT-Nb_2O_5 ($2\theta = 22.6$ and 36.8°) were only detected after annealing at 650 °C. Apart from the retardation of the anatase–rutile transition by Nb_2O_5, it is also remarkable that the mixed oxide nanotubes are stable to annealing at 650 °C. For pure TiO_2 nanotubes treated at this temperature, a substantial collapse of the tubular morphology has been reported.[23]

In summary, the form and dimensions of TiO_2 nanotubes reinforced with Nb_2O_5 can be controlled within a broad parameter range. As Nb_2O_5 has a much lower chemical dissolution rate than TiO_2 in fluoride-containing electrolytes, it strongly retards the "corrosion" of the tubes once they are formed, permitting the formation of longer nanotubes. This "oxide stabilization" allows TiO_2-based nanotubes to be tailored for specific applications with defined length (for

 © 2006 Wiley-VCH Verlag GmbH & Co. KGaA, Weinheim

example, photon absorption) or diameter (for example, the insertion of microbiological species) requirements. Another significant finding is that the TiO_2–Nb_2O_5 nanotubes have a higher resistance to thermal degradation than pure TiO_2 nanotubes, which allows heat treatment at much higher temperatures.

In addition to allowing tube morphology to be controlled, the use of an alloy substrate provides the basis for introducing functionality associated with the TiO_2–Nb_2O_5 system. For example, Cui et al. reported that a TiO_2–Nb_2O_5 mixture exhibits a higher photocatalytic activity than TiO_2 alone (in the degradation of 1,4-dichlorobenzene);[24] Da Costa et al. reported improved electrochromic properties.[25] Furthermore, it was recently reported that TiO_2–Nb_2O_5 layers can display metallic behavior,[26] making them potential conducting transparent materials. Finally, the Ti45Nb alloy used herein is under investigation for biomedical applications, as it combines a low elastic modulus with excellent corrosion resistance.[27]

Experimental Section

The substrates for tube growth were Ti (99.6%, Advent Research Materials), Nb (99.9%), and β-Ti45Nb (ATI Wah Chang). Samples of 2×2 cm^2 were polished, the final polishing step was with a suspension of 0.06-μm colloidal SiO_2. The samples were subsequently sonicated in acetone, isopropyl alcohol, and methanol, rinsed with deionized water, and dried in an N_2 stream.

For the electrochemical experiments, samples were contacted with a Cu backplate and then pressed against an O-ring-sealed opening in the wall of the electrochemical cell, leaving 1 cm^2 exposed to the electrolyte. The experimental setup consisted of a conventional three-electrode arrangement, with Pt gauze as the counter electrode and a Haber–Luggin capillary with an Ag/AgCl (1M KCl) reference electrode. The anodization was carried out at room temperature with a high-voltage potentiostat (Jaissle IMP 88 PC) connected to a digital multimeter (Keithley 2000) and interfaced to a computer.

A 1M solution of NaH_2PO_4 in deionized water with 0.5 wt% HF (pH 4.5) was used as the electrolyte. For anodization, the potential was ramped from the open circuit potential (OCP) to the desired final voltage at a rate of 10 mV s^{-1} and then held at this voltage for the desired length of time. After anodization, the samples were rinsed with deionized water and dried in an N_2 stream. Thermal treatments at 450 and 650 °C were carried out using a rapid thermal annealer (Jipelec JetFirst 100). A heating/cooling rate of 30 °C min^{-1} was used, and the samples were annealed at the final temperature for 1 h in air.

A field-emission SEM (Hitachi S4800) was used for the morphological characterization of the samples. The length of the nanotubes was determined from cross-section images. XRD patterns were collected on an X'pert Philips PMD diffractometer with a Panalytical X'celerator detector, using graphite-monochromatized $Cu_{K\alpha}$ radiation ($\lambda = 1.54056$ Å). Further morphological and structural characterization of the TiO_2–Nb_2O_5 nanostructures was carried out with a TEM (Philips CM 30 TEM/STEM) and an HRTEM (Philips CM 300 UT).

Received: May 17, 2006
Published online: September 29, 2006

[1] G. R. Patzke, F. Krumeich, R. Nesper, *Angew. Chem.* **2002**, *114*, 2554 – 2571; *Angew. Chem. Int. Ed.* **2002**, *41*, 2446 – 2461.
[2] B. D. Yao, Y. F. Chan, X. Y. Zhang, W. F. Zhang, Z. Y. Yang, N. Wang, *Appl. Phys. Lett.* **2003**, *82*, 281 – 283.
[3] M. S. Sander, M. J. Côté, W. Gu, B. M. Kile, C. P. Tripp, *Adv. Mater.* **2004**, *16*, 2052 – 2057.
[4] J. M. Macak, H. Tsuchiya, P. Schmuki, *Angew. Chem.* **2005**, *117*, 2136 – 2139; *Angew. Chem. Int. Ed.* **2005**, *44*, 2100 – 2102.
[5] J. M. Macak, H. Tsuchiya, L. Taveira, S. Aldabergerova, P. Schmuki, *Angew. Chem.* **2005**, *117*, 7629 – 7632; *Angew. Chem. Int. Ed.* **2005**, *44*, 7463 – 7465.
[6] B. O'Regan, M. Grätzel, *Nature* **1991**, *353*, 737 – 740.
[7] a) R. Wang, K. Hashimoto, A. Fujishima, M. Chikuni, E. Kojima, A. Kitamura, M. Shimohigoshi, T. Watanabe, *Nature* **1997**, *388*, 431 – 432; b) X. Feng, J. Zhai, L. Jiang, *Angew. Chem.* **2005**, *117*, 5245 – 5248; *Angew. Chem. Int. Ed.* **2005**, *44*, 5115 – 5118.
[8] A. Fujishima, K. Honda, *Nature* **1972**, *238*, 37 – 38.
[9] L. Kavan, M. Grätzel, S. E. Gilbert, C. Klemenz, H. J. Scheel, *J. Am. Chem. Soc.* **1996**, *118*, 6716 – 6723.
[10] a) V. Zwilling, E. Darque-Ceretti, A. Boutry-Forveille, D. David, M. Y. Perrin, M. Aucouturier, *Surf. Interface Anal.* **1999**, *27*, 629 – 637; b) D. Gong, C. A. Grimes, O. K. Varghese, W. Hu, R. S. Singh, Z. Chen, E. C. Dickey, *J. Mater. Res.* **2001**, *16*, 3331 – 3334; c) R. Beranek, H. Hildebrand, P. Schmuki, *Electrochem. Solid-State Lett.* **2003**, *6*, B12 – B14.
[11] E. Balaur, J. M. Macak, L. Taveira, P. Schmuki, *Electrochem. Commun.* **2005**, *7*, 1066 – 1070.
[12] a) J. M. Macak, H. Tsuchiya, A. Ghicov, P. Schmuki, *Electrochem. Commun.* **2005**, *7*, 1133 – 1137; b) A. Ghicov, J. M. Macak, H. Tsuchiya, J. Kunze, V. Haeublein, L. Frey, P. Schmuki, *Nano Lett.* **2006**, *6*, 1080 – 1082.
[13] A. Ghicov, H. Tsuchiya, R. Hahn, J. M. Macak, A. G. Munoz, P. Schmuki, *Electrochem. Commun.* **2006**, *8*, 528 – 532.
[14] H. Tsuchiya, J. M. Macak, L. Taveira, P. Schmuki, *Chem. Phys. Lett.* **2005**, *410*, 188 – 191.
[15] H. Tsuchiya, P. Schmuki, *Electrochem. Commun.* **2005**, *7*, 49 – 52.
[16] I. Sieber, H. Hildebrand, A. Friedrich, P. Schmuki, *Electrochem. Commun.* **2005**, *7*, 97 – 100.
[17] I. Sieber, B. Kannan, P. Schmuki, *Electrochem. Solid-State Lett.* **2005**, *8*, J10 – J12.
[18] H. Tsuchiya, J. M. Macak, I. Sieber, L. Taveira, A. Ghicov, K. Sirotna, P. Schmuki, *Electrochem. Commun.* **2005**, *7*, 295 – 298.
[19] H. Böhni, PhD thesis, ETH Zürich, 4020, **1967**.
[20] A. Ghicov, P. Schmuki, unpublished results.
[21] B. M. Reddy, I. Ganesh, V. R. Reddy, *J. Mater. Sci. Lett.* **1998**, *17*, 1913 – 1915.
[22] H. P. Klug, L. E. Alexander, *X-ray Diffraction Procedures for Polycrystalline and Amorphous Material*, Wiley-Interscience, New York, **1974**.
[23] O. K. Varghese, D. Gong, M. Paulose, C. A. Grimes, E. C. Dickey, *J. Mater. Res.* **2003**, *18*, 156 – 165.
[24] H. Cui, K. Dwight, S. Soled, A. Wold, *J. Solid State Chem.* **1995**, *115*, 187 – 191.
[25] E. Da Costa, C. O. Avellaneda, A. Pawlicka, *J. Mater. Sci.* **2001**, *36*, 1407 – 1410.
[26] a) Y. Furubayashi, T. Hitosugi, Y. Yamamoto, K. Inaba, G. Kinoda, Y. Hirose, T. Shimada, T. Hasegawa, *Appl. Phys. Lett.* **2005**, *86*, 252101; b) Y. Furubayashi, T. Hitosugi, Y. Yamamoto, Y. Hirose, G. Kinoda, K. Inaba, T. Shimada, T. Hasegawa, *Thin Solid Films* **2005**, *496*, 157 – 159.
[27] R. Godley, D. Starosvetsky, I. Gotman, *J. Mater. Sci. Mater. Med.* **2006**, *17*, 63 – 67.

Keywords: alloys · electrochemistry · nanomaterials · nanotubes · titanium dioxide

 © 2006 Wiley-VCH Verlag GmbH & Co. KGaA, Weinheim

Silver Alkoxides and Silyl Oxides

DOI: 10.1002/anie.200600805

$AgOC(CF_3)_3$ and $AgOSiiPr_3$—Synthesis and Characterization of a Donor-Free Silver(I) Alkoxide and Silyl Oxide**

*Andreas Reisinger, Daniel Himmel, and Ingo Krossing**

Transition-metal alkoxides and silyl oxides are important synthons in organometallic synthesis as well as precursors for electronic or ceramic materials.[1] However, information on the structures and properties of donor-free coinage metal(I) alkoxides and silyl oxides is still sparse and so far limited to Cu.[2–8] Several of these homoleptic Cu^I alkoxides and silyl oxides were successfully tested for chemical vapor deposition (CVD) processes.[6,9] Of the Cu^I alkoxides and silyl oxides, only $CuOCR_3$ and $CuOSiR_3$ ($R = CH_3$ and C_6H_5) have been structurally characterized.[4–8] In all cases, the compounds are tetranuclear species and form approximately square-planar eight-membered rings in the solid state. Such square-planar ring structures have also been observed for Cu and Ag silyl amides.[10] However, when donors such as CO, alkenes, or phosphanes were supplied, the ring structure was lost and, depending on the R group and the donor molecule, heterocubane-type aggregates[11,12] or dinuclear four-membered ring structures[7,12,13] were formed. Monomeric and dimeric phosphane-stabilized Au^I alkoxides[14] and silyl oxides[2] with aurophilic interactions are also known, but have not been structurally characterized.

Although donor-free copper(I) alkoxides and silyl oxides have been known for a long time,[3] no homologous compounds with silver or gold have been reported, with the exception of two phosphane adducts.[2,15] However, homoleptic Ag^I alkoxides and silyl oxides might, analogously to the copper compounds, be versatile reagents in organometallic synthesis. For example, such alkoxides and silyl oxides could be useful reagents for the synthesis of new weakly coordinating anions that complement the known alkoxy aluminates of the type $[Al(OR^F)_4]^-$ (R^F = fluorinated alkyl or aryl group).[16] In recent years, these compounds have been widely and very successfully used in our group.[17] Furthermore, they might be promising precursors for Ag CVD processes, since only few volatile Ag compounds are currently known.

Most Cu^I alkoxides and silyl oxides were synthesized by the reaction of mesitylcopper (CuMes) with the respective alcohol or silanol and elimination of MesH [Eq. (1)]. By

$$CuMes + HOR \rightarrow CuOR + MesH \quad (1)$$

contrast, the syntheses of the homologous silver compounds in this work were performed by metathesis of the respective alkaline metal alkoxide $LiOC(CF_3)_3$ or silyl oxide $NaOSiiPr_3$ and a suitable silver(I) salt. The solids were mixed in a glove box and suspended in CH_2Cl_2 with exclusion of light. Initially, the synthesis of the alkoxide was attempted using relatively inexpensive AgF. However, no reaction was observed at first, and only upon treatment in an ultrasonic bath at 50 °C overnight, the suspension turned dark brown. After filtration and removal of the solvent, three to five very small crystals remained. The crystals were identified as the desired product, but with a very poor yield of less than 1%. Therefore, insoluble AgF was replaced by the more soluble $AgBF_4$, and the desired products $AgOC(CF_3)_3$ (**1**)[18] and $AgOSiiPr_3$ (**2**)[19] were formed in good yields after stirring at room temperature [Eq. (2)].

$$MOR + AgBF_4 \xrightarrow{CH_2Cl_2} AgOR + MBF_4 \quad \begin{matrix} M = Li \text{ or } Na \\ R = C(CF_3)_3 \text{ or } SiiPr_3 \end{matrix} \quad (2)$$

After filtration and concentration of the filtrate, large amounts of colorless and light-sensitive **1**·0.5 CH_2Cl_2 and **2** crystallized in the cooled filtrate and were characterized by NMR, IR, Raman spectroscopy, and X-ray crystallography.[18,19] The alkoxide **1** crystallized from the CH_2Cl_2 solution as a weakly bound hemisolvate while the silyl oxide **2** crystallized solvent-free.[20] Solvent-free crystals of **1** were obtained by complete evaporation of the solvent and subsequent sublimation at 130 °C and 10^{-2} mbar. Under the same conditions, **2** decomposed with formation of a silver mirror.

The successful sublimation of **1** indicates that applications as precursors for CVD processes should be possible. A thermogravimetric analysis of **1** indicated that the alkoxides decompose upon heating with separation of the volatile epoxide C_4F_8O[21,22] and solid AgF.[23] The formation of C_4F_8O was verified by an independent decomposition experiment and gas-phase IR analysis of the volatiles formed. Since the solvent-free silver alkoxide is light-sensitive, it is best stored as its hemisolvate and wrapped in aluminum foil in a freezer at −20 °C. With these precautions the compound is stable over months. Without these precautions, compound **1** turns brown within 30 minutes and completely black over night. The silyl oxide is also light-sensitive, but can be stored in the dark for several hours at room temperature without decomposition. For longer storage, it should also be kept at −20 °C.

In the solid state,[24,25] the dominating structural element of **2** also consists of a square-planar centrosymmetric eight-membered $(AgO)_4$ ring with O-Ag-O angles close to 180° (av. 173.1°) and Ag-O-Ag angles close to 90° (av. 96.5°; Figure 1).

Unlike the Cu structures and the silyl oxide **2**,[4,7,8] the alkoxide **1** does not form isolated square-planar rings, rather a one-dimensional polymeric structure built from distorted eight-membered rings that are connected through rectangular four-membered rings (Figure 2).[24,26] Within the eight-membered rings the averaged Ag–O bonds (221.2 pm) are

[*] A. Reisinger, Dr. D. Himmel, Prof. I. Krossing
Institut für Anorganische und Analytische Chemie
Albert-Ludwigs-Universität
79104 Freiburg (Deutschland)
Fax: (+49) 761/203-6001
E-mail: krossing@uni-freiburg.de

[**] This work was supported by the Deutsche Forschungsgemeinschaft, the Schweizer Nationalfonds, the EPFL, and the University of Freiburg.

 © 2006 Wiley-VCH Verlag GmbH & Co. KGaA, Weinheim

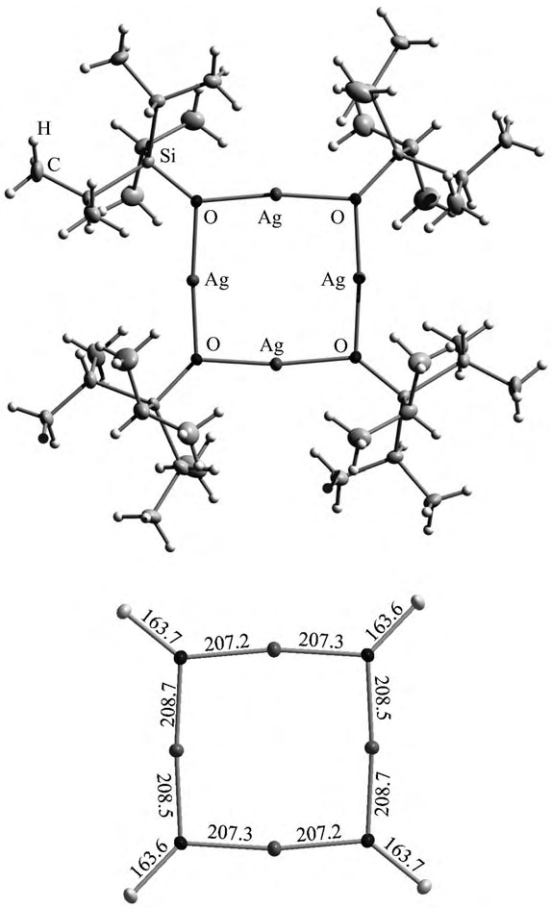

Figure 1. Sections of the solid-state structure of **2**. Thermal ellipsoids are drawn at the 50% probability level. Bond lengths are given in pm.

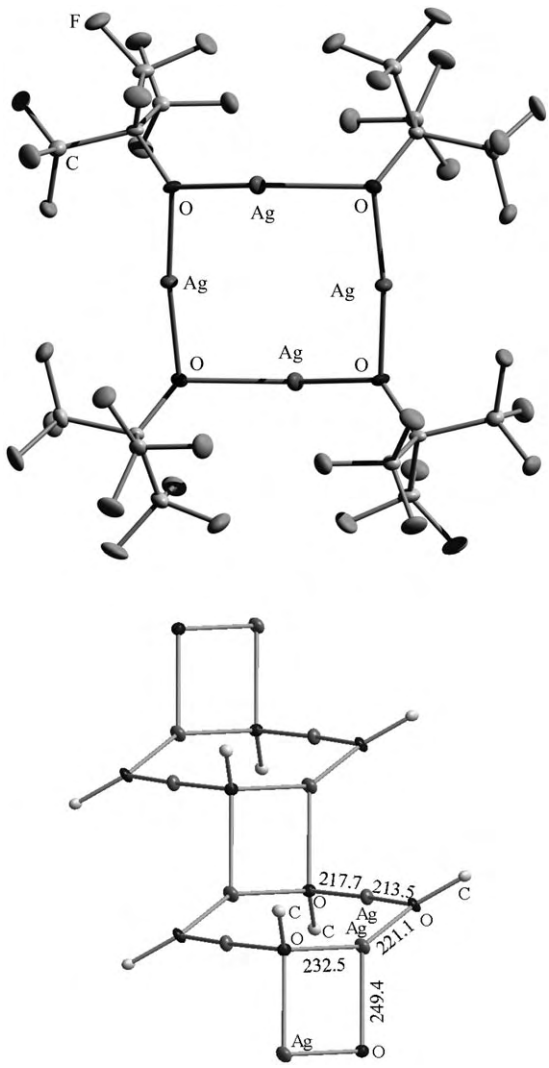

Figure 2. Sections of the solid-state structure of **1**: eight-membered ring (left) and polymeric ring structure (right, CF_3 groups omitted for clarity). Thermal ellipsoids are drawn at the 50% probability level. Bond lengths are given in pm.

elongated by 13.3 pm compared to those of the silyl oxide (207.9 pm). However, the elongation is more pronounced for the silver centers with T-shaped geometry (221.1 and 232.5 pm) than for the ones with linear geometry (213.5 and 217.7 pm; Figure 2). This difference is accompanied by longer ring-connecting Ag–O bonds (249.4 pm), which are shorter than the Cu–O bonds of the related CuO*t*Bu structure (251.5 pm). Accordingly, the O-Ag-O and Ag-O-Ag angles deviate from the ideal values of 180° and 90° (162.5° and 100.6°, Table 1).

The synthesis and full characterization of the silver alkoxide $AgOC(CF_3)_3$ and the silyl oxide $AgOSiiPr_3$ give the first structural information on these basic, but very interesting and potentially useful compounds. Because of their facile preparation, **1** and **2** are attractive reagents for CVD processes or syntheses including new alkoxy or siloxy metalates by reaction with Lewis acids $M(OR^F)_n$ or elemental halides such as $SbCl_5$. A more complete discussion of the spectroscopic data, additional quantum chemical calculations on the formation and stability of both compounds, as well as first applications are in progress.[20]

Table 1: Selected average bond lengths *d* [pm] and angles ∢ [°] of **1** and **2** compared to those in CuO*t*Bu[8] and $CuOSi(CH_3)_3$.[5]

	CuO*t*Bu	**1**	$CuOSi(CH_3)_3$	**2**
d_1(M-O)	181.2	221.2	184.4	207.9
d_2(M-O)	251.5	249.4	–	–
d_{cov}(M-O)[a]	183	200	183	200
d(O-(C/Si))	145.6	138.4	163.8	163.6
∢(O-M-O)	175.6	162.5	175.8	173.1
∢(M-O-M)	93.6	100.6	93.9	96.5

[a] d_{cov} = sum of covalent radii.

Experimental Section

All manipulations were performed using grease-free Schlenk or glove-box techniques and a dinitrogen atmosphere (H_2O and O_2 < 1 ppm). CH_2Cl_2 was rigorously dried by multiple additions of 20-g quantities of P_2O_5 and subsequent distillation and degassing prior to use. Solvents were added by condensation techniques. NMR spectra were recorded in CD_2Cl_2 at room temperature on a BRUKER AVANCE 400 spectrometer, and data are given in ppm relative to the solvent signals (^1H, ^{13}C), aqueous $AlCl_3$ (^{27}Al), and $CFCl_3$ (^{19}F). IR

 © 2006 Wiley-VCH Verlag GmbH & Co. KGaA, Weinheim

spectra were obtained as a nujol mull between CsI plates on a BRUKER VERTEX 70 IR spectrometer. Raman spectra were recorded on a BRUKER RAM II Raman module using a liquid-nitrogen-cooled, highly sensitive Ge detector. Single-crystal structure determinations were carried out on a BRUKER KAPPA APEX II diffractometer using graphite-monochromated $Mo_{K\alpha}$ radiation.

Received: March 1, 2006
Published online: September 22, 2006

Keywords: fluorinated ligands · silver · structure elucidation X-ray diffraction

[1] L. G. Hubert-Pfalzgraf, *Coord. Chem. Rev.* **1998**, *178–180*, 967; L. G. Hubert-Pfalzgraf, H. Guillon, *Appl. Organomet. Chem.* **1998**, *12*, 221; D. C. Bradley, *Chem. Rev.* **1989**, *89*, 1317; M. Veith, S. Weidner, K. Kunze, D. Kaefer, J. Hans, V. Huch, *Coord. Chem. Rev.* **1994**, *137*, 297.

[2] H. Schmidbaur, J. Adlkofer, A. Shiotani, *Chem. Ber.* **1972**, *105*, 3389.

[3] T. Tsuda, T. Hashimoto, T. Saegusa, *J. Am. Chem. Soc.* **1972**, *94*, 958.

[4] T. Greiser, E. Weiss, *Chem. Ber.* **1976**, *109*, 3142.

[5] M. J. McGeary, R. C. Wedlich, P. S. Coan, K. Folting, K. G. Caulton, *Polyhedron* **1992**, *11*, 2459.

[6] K. W. Terry, C. G. Lugmair, P. K. Gantzel, T. D. Tilley, *Chem. Mater.* **1996**, *8*, 274.

[7] C. Lopes, M. Hakansson, S. Jagner, *Inorg. Chem.* **1997**, *36*, 3232.

[8] M. Hakansson, C. Lopes, S. Jagner, *Inorg. Chim. Acta* **2000**, *304*, 178.

[9] I. J. Drake, K. L. Fujdala, S. Baxamusa, A. T. Bell, T. D. Tilley, *J. Phys. Chem. B* **2004**, *108*, 18421; K. L. Fujdala, I. J. Drake, A. T. Bell, T. D. Tilley, *J. Am. Chem. Soc.* **2004**, *126*, 10864; P. M. Jeffries, G. S. Girolami, *Chem. Mater.* **1989**, *1*, 8.

[10] M. Veith, K. L. Woll, *Chem. Ber.* **1993**, *126*, 2383.

[11] R. L. Geerts, J. C. Huffman, K. Folting, T. H. Lemmen, K. G. Caulton, *J. Am. Chem. Soc.* **1983**, *105*, 3503; M. Hakansson, C. Lopes, S. Jagner, *Organometallics* **1998**, *17*, 210.

[12] C. Lopes, M. Hakansson, S. Jagner, *Inorg. Chim. Acta* **1997**, *254*, 361.

[13] T. H. Lemmen, G. V. Goeden, J. C. Huffman, R. L. Geerts, K. G. Caulton, *Inorg. Chem.* **1990**, *29*, 3680.

[14] B. R. Sutherland, K. Folting, W. E. Streib, D. M. Ho, J. C. Huffman, K. G. Caulton, *J. Am. Chem. Soc.* **1987**, *109*, 3489; S. Komiya, M. Iwata, T. Sone, A. Fukuoka, *J. Chem. Soc. Chem. Commun.* **1992**, 1109.

[15] D. A. Edwards, R. M. Harker, M. F. Mahon, K. C. Molloy, *J. Chem. Soc. Dalton Trans.* **1997**, 3509.

[16] T. J. Barbarich, S. T. Handy, S. M. Miller, O. P. Anderson, P. A. Grieco, S. H. Strauss, *Organometallics* **1996**, *15*, 3776; S. M. Ivanova, B. G. Nolan, Y. Kobayashi, S. M. Miller, O. P. Anderson, S. H. Strauss, *Chem. Eur. J.* **2001**, *7*, 503; I. Krossing, H. Brands, R. Feuerhake, S. Koenig, *J. Fluorine Chem.* **2001**, *112*, 83; I. Krossing, *Chem. Eur. J.* **2001**, *7*, 490; I. Krossing, I. Raabe, *Angew. Chem.* **2004**, *116*, 2116; *Angew. Chem. Int. Ed.* **2004**, *43*, 2066.

[17] I. Krossing, A. Reisinger, *Inorg. Chem. Focus II* **2005**, 65; I. Krossing, *J. Am. Chem. Soc.* **2001**, *123*, 4603; I. Krossing, I. Raabe, *Angew. Chem.* **2001**, *113*, 4544; *Angew. Chem. Int. Ed.* **2001**, *40*, 4406; T. S. Cameron, A. Decken, I. Dionne, M. Fang, I. Krossing, J. Passmore, *Chem. Eur. J.* **2002**, *8*, 3386; I. Krossing, A. Bihlmeier, I. Raabe, N. Trapp, *Angew. Chem.* **2003**, *42*, 1569; *Angew. Chem. Int. Ed.* **2003**, *42*, 1531; I. Krossing, A. Reisinger, *Angew. Chem.* **2003**, *115*, 5725; *Angew. Chem. Int. Ed.* **2003**, *42*, 5725; M. Gonsior, I. Krossing, L. Müller, I. Raabe, M. Jansen, L. van Wüllen, *Chem. Eur. J.* **2002**, *8*, 4475.

[18] $LiOC(CF_3)_3$ (1.35 g, 5.136 mmol) and $AgBF_4$ (1.00 g, 5.137 mmol) were mixed in a glove box and weighed into one side of a two-bulb frit-plate flask with a glass stem that was closed with two greaseless YOUNG valves and wrapped in aluminum foil to exclude light. The mixture was suspended in CH_2Cl_2 (ca. 30 mL) and stirred overnight at room temperature. The next day, the solution was filtered, and all solvent was removed. The resulting white product was dried quickly (max. 15 min) in vacuo since drying over a longer period (1 h) already caused decomposition, most probably because of exposure to light. Single crystals were obtained by sublimation at about 130 °C and 10^{-2} mbar. Yield of isolated product: 1.71 g, 4.437 mmol (86 %). $^{13}C\{^1H\}$ NMR (63 MHz): $\delta = 82.0$ (dez, $^2J_{CF} = 26.9$ Hz), 122.9 ppm (q, $^1J_{CF} = 293.3$ Hz); ^{19}F NMR (376 MHz): $\delta = -75.94$ ppm (s); IR (CsI plates, nujol): $\tilde{\nu} = 405$ (w), 435 (vw), 493 (mw), 510 (vw), 537 (m), 573 (w), 726 (ms), 767 (m), 801 (mw), 966 (vs), 1135 (m), 1163 (ms), 1240 (vs), 1261 (s), 1303 (ms), 1377 (ms), 1460 (s), 2726 (w), 2850 (vs), 2900 (vs), 2947 cm^{-1} (vs); Raman: $\tilde{\nu} = 108$ (mw), 168 (w), 220 (mw), 300 (m), 329 (m), 361 (w), 506 (vw), 539 (m), 573 (vw), 680 (w), 726 (vw), 770 (ms), 806 (vw), 984 (w), 1008 (vw), 1114 (vw), 1165 (w), 1240 (vw), 1262 (vw), 1290 (vw), 1315 (m), 2757 (m), 2845 (vw), 2909 (m), 2937 cm^{-1} (m).

[19] $NaOSi\textit{i}Pr_3$ (392 mg, 2.00 mmol) and $AgBF_4$ (395 mg, 2.03 mmol) were mixed in a glove box and weighed into one side of a two-bulb frit-plate flask with a glass stem that was closed with two greaseless YOUNG valves and wrapped in aluminum foil to exclude light. The mixture was suspended in CH_2Cl_2 (20 mL) and stirred for 1 hour at room temperature in the dark. The solution was filtered, and all solvent was removed. Yield of isolated product: 368 mg, 1.31 mmol (65 %). ^1H NMR (400 MHz): $\delta =$ 0.97 (d, $^3J_{HH} = 7.2$ Hz), 0.81 ppm (sept, $^3J_{HH} = 7.2$ Hz); $^{13}C\{^1H\}$ NMR (63 MHz): $\delta = 19.8$ (s), 15.0 ppm (s); IR (CsI plates): $\tilde{\nu} = 409$ (w), 466 (w), 511 (m), 657 (vs), 878 (m), 952 (vs), 991 (m), 1070 (m), 1156 (vw), 1237 (s), 1361 (s), 1377 (s), 1462 (s), 2717 (vw), 2858 (vs), 2929 cm^{-1} (vs).

[20] A. Reisinger, I. Krossing, unpublished results; a detailed discussion of the solvent-containing structure will take place in an upcoming full paper.

[21] The silver alkoxide was decomposed, and the volatile fragments were characterized by IR spectroscopy. Comparison of the observed bands with those of C_4F_8O[22] shows a very good overall agreement: $\tilde{\nu} = 720$ (w), 799 (m), 984 (m), 1027 (s), 1092 (s), 1202 (mw), 1225 (w), 1262 (m), 1289 (w), 1316 (w), 1339 cm^{-1} (w).

[22] J. T. Hill, *J. Fluorine Chem.* **1977**, *9*, 97.

[23] The differential temperature analysis measurements were performed with a NETZSCH STA 429 DSC/DTA unit. About 20 mg of **1** was used for the experiment; preparation of the measurement and weighing were done in a glove box. The DTA curves were recorded at a heating rate of 5 K min^{-1}. During the heating period no distinct steps could be observed, but there was a continuous loss of mass between 110 and 240 °C. The dark brownish-black residue had approximately 39 % of its original weight. This weight fits best for the formation of the gaseous epoxide C_4F_8O (63 %) and solid AgF (37 %). Formation of either Ag_2O (33 %) or Ag (31 %) would be accompanied by a higher mass loss and, therefore, seems unlikely.

[24] CCDC-299939 and CCDC-299940 contain the supplementary crystallographic data for this paper. These data can be obtained free of charge from The Cambridge Crystallographic Data Centre via www.ccdc.cam.ac.uk/data_request/cif.

[25] Crystal-structure determination of $AgOSi\textit{i}Pr_3$: BRUKER KAPPA APEX II, graphite-monochromated $Mo_{K\alpha}$ radiation, $T = 100(2)$ K, 85655 reflections, Lorentz, polarization, and numerical absorption corrections, $\mu = 1.728$ mm^{-1}, direct methods with SHELXS-97 (G. M. Sheldrick, SHELXS-97, Program for the Solution of Crystal Structures, Universität Göttingen,

 © 2006 Wiley-VCH Verlag GmbH & Co. KGaA, Weinheim

1997), refinement against F^2 with SHELXL-97(G. M. Sheldrick, SHELXL-97, Program for the Refinement of Crystal Structures, Universität Göttingen, **1997**), orthorhombic, space group *Pbca*, $Z=8$, $a=1515.4(3)$, $b=1306.5(3)$, $c=2440.3(5)$ pm, $V=4.8314(17)$ nm^3, $\rho_{calcd}=1.546$ g cm^{-1}, $2\theta_{max}=55.06°$, reflections: 85655 collected, 5530 unique ($R_{int}=0.0206$), 18 restraints, 430 parameters, $R1=0.0190$, wR2 (all data) $=0.0404$, GOF $=1.275$.

[26] Crystal-structure determination of $AgOC(CF_3)_3$: BRUKER KAPPA APEX II, graphite-monochromated $Mo_{K\alpha}$ radiation, $T=100(2)$ K, 19041 reflections, Lorentz, polarization, and numerical absorption corrections, $\mu=2.825$ mm^{-1}, direct methods with SHELXS-97, refinement against F^2 with SHELXL-97, triclinic, space group $P\bar{1}$, $Z=2$, $a=681.08(14)$, $b=1012.2(2)$, $c=1092.0(2)$ pm, $\alpha=85.76(3)$, $\beta=89.62(3)$, $\gamma=88.93(3)°$, $V=3.9901(11)$ nm^3, $\rho_{calcd}=3.034$ g cm^{-1}, $2\theta_{max}=61.24°$, reflections: 19041 collected, 4000 unique ($R_{int}=0.0475$), 271 parameter, $R1=0.0352$, $wR2$ (all data) $=0.0493$, GOF $=1.133$.

 © 2006 Wiley-VCH Verlag GmbH & Co. KGaA, Weinheim

Microreactors

DOI: 10.1002/anie.200602167

Microreactor Synthesis of β-Peptides**

*Oliver Flögel, Jeroen D. C. Codée, Dieter Seebach, and Peter H. Seeberger**

β-Amino acid oligomers (β-peptides) are a unique class of peptides. In contrast to their natural α-amino acid counterparts, β-peptides require few residues to form secondary structures such as turns, helices, or sheets.[1] As a result of these structures and their metabolic stability, β-peptides have attracted considerable interest. However, the secondary structures can also severely hamper the synthesis of these oligomers.[2] Small- to medium-length β-peptides are generally synthesized in solution[1b] or on a solid support,[1c] whereas longer peptides can be prepared by chemical-ligation techniques.[1e] Microwave-assisted solid-phase-peptide-synthesis (SPPS) protocols have also been applied in the preparation of β-peptides.[2,3] Owing to the formation of β-peptidic secondary structures of short chains when synthesized on Merrifield beads, the solid-phase assembly of β-peptides may totally fail, especially when hair-pin turn structures can form. In this case, one has to resort to fragment coupling.[2b,c]

Microreactors (i.e. miniaturized chemical reactors) are attracting attention as an alternative to traditional synthesis in round-bottom flasks.[4] However, in contrast to widely used microanalysis systems, the development of microreactors as a tool for organic synthesis has been slow. A range of chemical transformations has been carried out by using microreactor technologies, whereby most of these reactions only served as a proof of principle.[5]

Herein we describe the first application of a silicon continuous flow microreactor (Figure 1) to the assembly of peptides. The microreactor not only allows for quick "scanning" of reaction conditions, but also for the procurement of synthetically useful amounts of peptides.[6] Our report is also the first demonstration of 1) peptide couplings with *tert*-butyloxycarbonyl (Boc)- and 9-fluorenylmethoxycarbonyl (Fmoc)-protected amino acids in 1–5 minutes at temperatures as high as 120 °C, 2) the use of β^2- and β^3-homoamino acid fluorides for β-peptide couplings, and 3) the advantageous application of a $C_{10}H_4F_{17}$-substituted benzylic ester protecting group in solution-phase peptide synthesis.[7–9]

Microstructured reaction devices hold several advantages for organic synthesis: only small amounts of valuable reagents are required, reaction parameters, such as reaction time and temperature, can be accurately controlled, and various reaction conditions can be scanned in a continuous, time-efficient fashion. The continuous-flow microreactor that we used for our studies is designed to be compatible with a wide range of organic solvents and can be operated over a broad temperature range (−80 °C to +150 °C) in a simple laboratory setting (Figure 1).[10] The reaction volume of the microreactor (78.3 μL) allows microscale reaction scanning (μmol of reagents) and the production of several grams of target material per day.

Initially, we explored the coupling of Fmoc-β^3-homophenylalanine fluoride (Fmoc-β^3hPhe-F, **1**) and H-β^3hPhe-OBn (**2**) in the microreactor (Scheme 1a). Acid fluorides were selected as activated forms of the amino acids as 1) they are readily available from the parent amino acids, 2) they are powerful acylating agents, and 3) the use of a tertiary amine base leads to an ammonium fluoride as the sole soluble by-product.[11] The reaction was monitored at different temperatures (25 °C, 60 °C, and 90 °C) and different reaction times (1, 2, 5, and 10 min) by using Fmoc-β^3hPhe-OBn (**5**) as the internal standard for liquid chromatography LC-MS analysis. Comparing the reaction progress at different temperatures revealed that the maximum yield was obtained after 3 minutes at 90 °C (Scheme 1b). Interestingly, when the coupling of **1** and **2** was conducted at a higher temperature and/or for a prolonged period of time, the amount of dipeptide diminished, as revealed in a second reaction scan (Scheme 1c).[12] Under these conditions, tripeptide **4** was also, not surprisingly, formed owing to Fmoc-cleavage and subsequent peptide coupling with excess acid fluoride.[13] Following reaction screening, dipeptide **3** was prepared on 0.5-mmol

[*] Dr. O. Flögel,[+] Dr. J. D. C. Codée,[+] Prof. Dr. D. Seebach, Prof. Dr. P. H. Seeberger
Laboratory of Organic Chemistry
Swiss Federal Institute of Technology (ETH) Zürich
Wolfgang-Pauli-Strasse 10, 8093 Zürich (Switzerland)
Fax: (+41) 44-633-1235
E-mail: seeberger@org.chem.ethz.ch

[+] Both authors contributed equally to this work

[**] We thank the ETH Zürich, the Deutsche Forschungsgemeinschaft, Swiss National Science Foundation, Novartis Pharma AG Basel, and the Netherlands Organization for Scientific Research (NWO) for financial support. Prof. Dr. K. F. Jensen and E. R. Murphy (Department of Chemical Engineering, Massachusetts Institute of Technology, Cambridge) are gratefully acknowledged for providing the microreactor used in this work.

Supporting information for this article is available on the WWW under http://www.angewandte.org or from the author.

InterScience
© 2006 Wiley-VCH Verlag GmbH & Co. KGaA, Weinheim

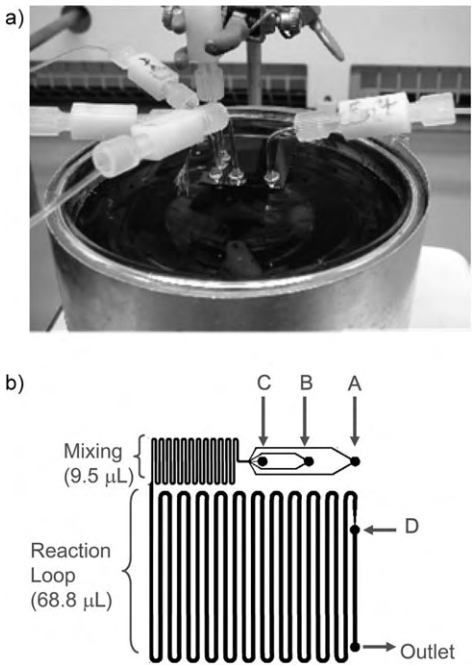

Figure 1. a) Microreactor setup. b) Schematic representation of the microreactor showing the three inlets (acid fluoride (A), amino acid benzyl ester (B) and *N*-methylmorpholine (NMM; C)), the quench port (TFA and the internal standard (D)), the outlet, and the dimensions of the channels (total prequench reactor volume = 78.3 μL).

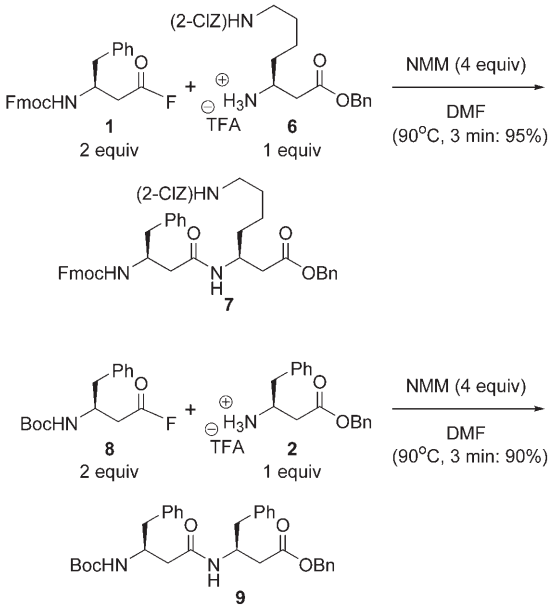

Scheme 2. Synthesis of the β^3-dipeptides **7** and **9**. 2-ClZ = 2-chlorobenzyloxycarbonyl.

scale (3 min reaction time at 90 °C, 92 % yield after column chromatography). Identical conditions were used for the construction of the β^3-dipeptides **7** (0.5-mmol scale) and **9** (0.3 mmol; Scheme 2).

After having established the utility of our microreactor system for the synthesis of β^3-dipeptides, we set out to assemble tetrapeptide **17** by using the Boc strategy (Scheme 3). The tetrapeptide contains all possible β-peptide bonds, (β^3–β^3)-, (β^3–β^2)-, and (β^2–β^3) as well as a β^3h(*R*)Ala-β^2h(*R*)Val turn-inducing segment.[1f,2b] A fluorous benzyl group was incorporated in the first amino acid to facilitate the purification procedure by fluorous solid-phase extraction (FSPE).[7,8,14] Thus, the assembly of the tetrapeptide **17** commenced with the construction of the first β^3–β^3 peptidic bond by applying the previously established conditions. A reaction time of 3 min at 90 °C provided the Boc-protected dipeptide **12b** in 91 % yield after FSPE. Notably, the product precipitated in the collection flask, which was kept at ambient temperature, indicating the poor solubility of this class of compound.[15]

The formation of the sterically more demanding β^3–β^2 peptide bond required higher temperatures and/or longer residence times as revealed by a reaction scan at 90 °C and 120 °C. Maximum conversion was obtained at 120 °C and 5 min reaction time[16] to give tripeptide **14b** in 93 % yield on a 0.4-mmol scale.[17] The final β^2–β^3 coupling was executed at

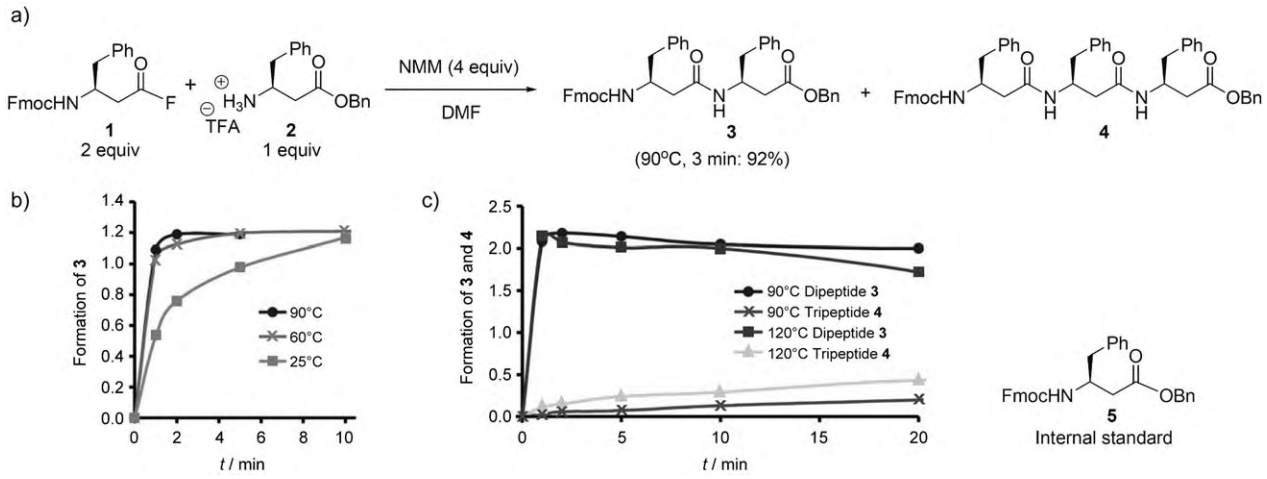

Scheme 1. a) Synthesis of dipeptide **3** in the microreactor. b) LC–MS analysis of the formation of **3** as a function of time and temperature. c) LC–MS analysis of the formation of **3** and **4** at higher temperatures and longer reaction times. Bn = benzyl, TFA^- = trifluoroacetate.

 © 2006 Wiley-VCH Verlag GmbH & Co. KGaA, Weinheim

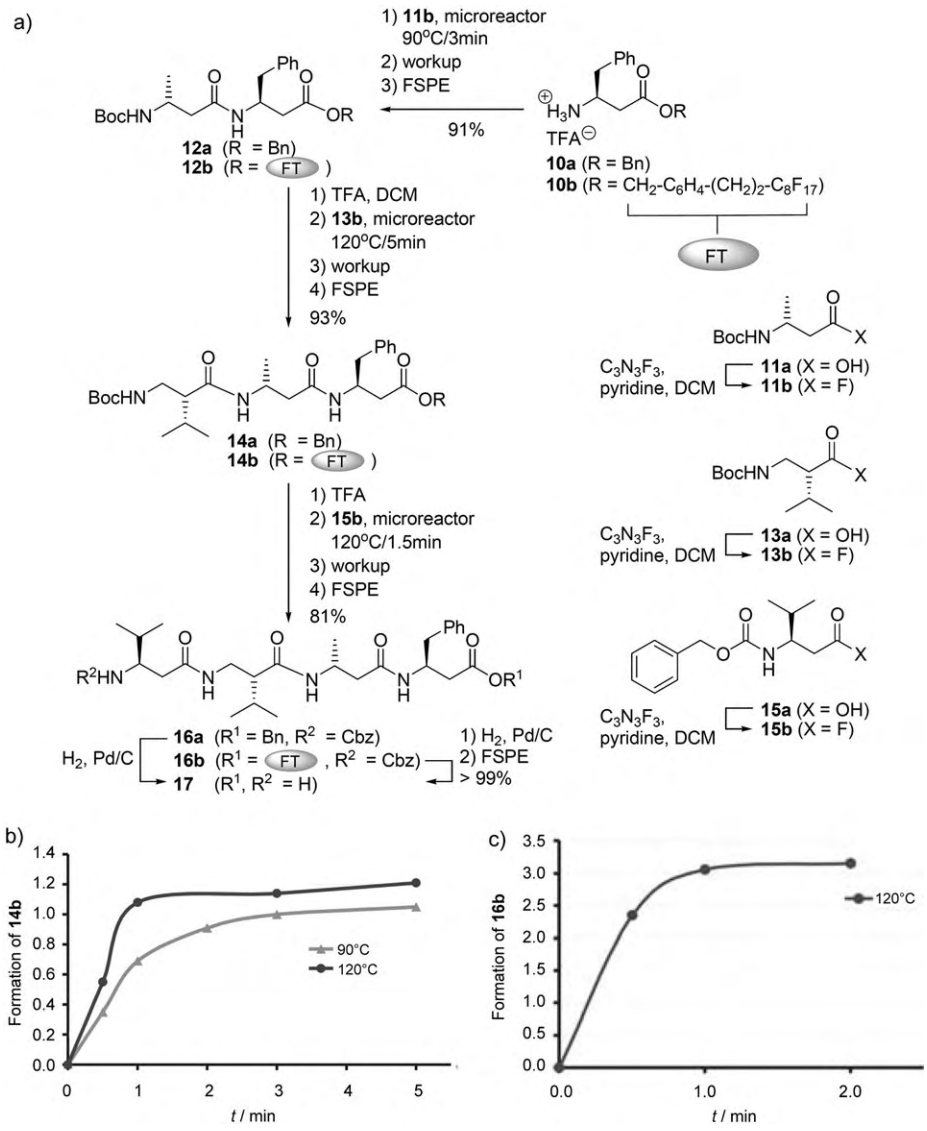

Scheme 3. a) Synthesis of the tetrapeptides **16** and **17**. b) Formation of **14b** at different temperatures. c) Formation of **16b** at 120 °C. Cbz = benzyloxycarbonyl, DCM = dichloromethane.

120 °C and a reaction scan revealed the coupling to be complete after 1.5 min. Tetramer **16b** was obtained in 81 % yield. Cleavage of the fluorous tag and removal of the benzyloxycarbonyl function provided the zwitterionic target compound **17**.

To compare the microreactor methodology with traditional assembly strategies, tetrapeptide **17** was also synthesized on a solid support by using the Fmoc strategy and HATU–DIPEA-mediated couplings,[18] as well as in solution by using conventional laboratory glassware. For the solution-phase assembly, two different strategies were investigated: in the first approach we used the above-mentioned fluorous tag in combination with acid fluorides, in the second approach we started from H-β^{3}hPhe-OBn and used HATU–DIPEA coupling conditions. The results of the four assembly methods are collected in Table 1. All procedures provided the tetramer in comparable overall yields. However, purification of the fluorous peptides was much easier when compared with the purification of the nonfluorous peptides. The nonfluorinated tetramer **16a** was particularly difficult to handle owing to its poor solubility. In addition, the microreactor system allowed for precise control over unconventionally high reaction temperatures. This control significantly reduces reaction times and prevents product precipitation during the reaction. Precipitation led to inhomogeneous gel-like reaction mixtures when using traditional laboratory glassware in the solution-phase synthesis.

Table 1: Synthesis of the tetrapeptides **16a/b** and **17** by microreactor technology, by solution-phase couplings, and by solid-phase assembly.[19]

Method	**12a/b** Conditions (Yield)	**14a/b** Conditions (Yield)	**16a/b** Conditions (Yield)	**17** Yield
microreactor	**11b** (2 equiv); NMM (4 equiv), 90 °C, 3 min (91 %)	**13b** (2 equiv); NMM (4 equiv), 120 °C, 5 min (93 %)	**15b** (2 equiv); NMM (4 equiv), 120 °C, 1.5 min (81 %)	> 99 %
solution phase, F tag	**11b** (2 equiv); NMM (4 equiv), RT, 3 h. (94 %)	**13b** (2 equiv); NMM (4 equiv), RT, overnight (93 %)	**15b** (2 equiv); NMM (4 equiv), RT, overnight (93 %)	> 99 %
solution phase[a]	**11a** (2 equiv); HATU (1.8 equiv), NMM (4 equiv), RT, overnight (85 %)	**13a** (2 equiv); HATU (1.8 equiv), NMM (4 equiv), RT, overnight (85 %)	**15a** (2 equiv); HATU (1.8 equiv), NMM (4 equiv) RT, overnight (87 %)	79 %
solid phase[b] (Wang Resin)	Fmoc-**11a** (3 equiv); HATU (2.8 equiv), DIPEA (6 equiv) RT, 1.5 h	Fmoc-**13a** (3 equiv); HATU (2.8 equiv), DIPEA (6 equiv) RT, 1 h	Fmoc-**15a** (3 equiv); HATU (2.8 equiv), DIPEA (6 equiv) RT, 1 h	55 % (after HPLC)[20]

[a] HATU = 2-(1*H*-7-azybenzotriazol-1-yl)-1,1,3,3-tetramethyluronium hexafluorophosphate. [b] DIPEA = diisopropylethylamine.

 © 2006 Wiley-VCH Verlag GmbH & Co. KGaA, Weinheim

In summary, we have demonstrated the use of a silicon-based microreactor for the effective synthesis of peptides. The microstructured reaction device allowed for the detailed investigation and optimization of reaction parameters by using minimal amounts of reagents. Furthermore, it opened the way for the use of unprecedented high reaction temperatures, leading to homogeneous reaction mixtures and of significantly reduced reaction times. Synthesis efficiency was further enhanced by the use of a fluorous benzyl tag that was applied for the first time in the assembly of β-peptides and proved to be particularly useful for the purification of poorly soluble products.[8] Not only will the synthetic strategy outlined herein find applications in the construction of challenging peptides, it will also be applied to the assembly of other biopolymers, including oligosaccharides and oligonucleotides. In general, the continuous-flow process opens many opportunities for multistep syntheses and automation.[21]

Received: May 31, 2006
Published online: September 29, 2006

Keywords: β-peptides · fluorous tags · microreactors · synthetic methods

[1] a) D. Seebach, A. K. Beck, D. J. Bierbaum, *Chem. Biodiversity* **2004**, *1*, 1111 – 1239; b) R. P. Cheng, S. H. Gellman, W. F. DeGrado, *Chem. Rev.* **2001**, *101*, 3219 – 3232; c) D. Seebach, M. Overhand, F. N. M. Kühnle, B. Martinoni, L. Oberer, U. Hommel, H. Widmer, *Helv. Chim. Acta* **1996**, *79*, 913 – 941; d) D. Seebach, J. V. Schreiber, P. I. Arvidsson, J. Frackenpohl, *Helv. Chim. Acta* **2001**, *84*, 271 – 279; e) T. Kimmerlin, D. Seebach, *J. Pept. Res.* **2005**, *65*, 229 – 260; f) D. Seebach, S. Abele, K. Gademan, B. Jaun, *Angew. Chem.* **1999**, *111*, 1700 – 1703; *Angew. Chem. Int. Ed.* **1999**, *38*, 1595 – 1597.

[2] a) J. K. Murray, S. H. Gellman, *Org. Lett.* **2005**, *7*, 1517 – 1520; b) G. Lelais, D. Seebach, B. Jaun, R. I. Mathad, O. Flögel, F. Rossi, M. Campo, A. Wortmann, *Helv. Chim. Acta* **2006**, *89*, 361 – 403; c) P. I. Arvidsson, J. Frackenpohl, D. Seebach, *Helv. Chim. Acta* **2003**, *86*, 1522 – 1553.

[3] M. Erdélyi, A. Gogoll, *Synthesis* **2002**, 1592 – 1596.

[4] a) W. Ehrfeld, V. Hessel, H. Löwe, *Microreactors: New Technology for Modern Chemistry*, Wiley-VCH, Weinheim, **2000**; b) K. F. Jensen, *Chem. Eng. Sci.* **2001**, *56*, 293 – 303; c) K. Jähnisch, V. Hessel, H. Löwe, M. Baerns, *Angew. Chem.* **2004**, *116*, 410 – 451; *Angew. Chem. Int. Ed.* **2004**, *43*, 406 – 446.

[5] a) P. D. I. Fletcher, S. J. Haswell, E. Pombo-Villar, B. H. Warrington, P. Watts, S. Y. F. Wong, X. L. Zhang, *Tetrahedron* **2002**, *58*, 4735 – 4757; b) P. Watts, S. J. Haswell, *Chem. Soc. Rev.* **2005**, *34*, 235 – 246; c) M. Brivio, W. Verboom, D. N. Reinhoudt, *Lab Chip* **2006**, *6*, 329 – 344; d) K. Geyer, J. D. C. Codée, P. H. Seeberger, *Chem. Eur. J.*, in press.

[6] For couplings of β-peptides in an electro-osmotic flow driven glass microreactor, see: a) P. Watts, C. Wiles, S. J. Haswell, E. Pombo-Villar, P. Styring, *Chem. Commun.* **2001**, 990 – 991; b) P. Watts, C. Wiles, S. J. Haswell, E. Pombo-Villar, *Lab Chip* **2002**, 141 – 144; c) P. Watts, C. Wiles, S. J. Haswell, E. Pombo-Villar, *Tetrahedron* **2002**, *58*, 5427 – 5439. Although these papers report on the formation of β-peptides, no synthetically useful amounts were procured.

[7] a) D. P. Curran, Z. Y. Luo, *J. Am. Chem. Soc.* **1999**, *121*, 9069 – 9072; b) W. Zhang, *Curr. Opin. Drug Discovery Dev.* **2004**, *7*, 784 – 797.

[8] For fluorous tagging in solid-phase α-peptide syntheses, see: a) D. V. Filippov, D. J. van Zoelen, S. P. Oldfield, G. A. van der Marel, H. S. Overkleeft, J. W. Drijfhout, J. H. van Boom, *Tetrahedron Lett.* **2002**, *43*, 7809 – 7812; b) P. C. de Visser, M. van Helden, D. V. Filippov, G. A. van der Marel, J. W. Drijfhout, J. H. van Boom, D. Noort, H. S. Overkleeft, *Tetrahedron Lett.* **2003**, *44*, 9013 – 9016.

[9] For α-peptide synthesis on a fluorous support, see: M. Mizuno, K. Goto, T. Miura, T. Matsuura, T. Inazu, *Tetrahedron Lett.* **2004**, *45*, 3425 – 3428.

[10] D. M. Ratner, E. R. Murphy, M. Jhunjhunwala, D. A. Snyder, K. F. Jensen, P. H. Seeberger, *Chem. Commun.* **2005**, *5*, 578 – 580.

[11] L. A. Carpino, M. Beyermann, H. Wenschuh, M. Bienert, *Acc. Chem. Res.* **1996**, *29*, 268 – 274.

[12] Longer reaction times (30 min) led to an irregular flow as judged from the large error margin in the relative LC–MS UV absorbances of the products and the internal standard.

[13] Tetramers were also observed (data not shown).

[14] a) D. P. Curran, *Synlett* **2001**, 1488 – 1496; b) W. Zhang, *Chem. Rev.* **2004**, *104*, 2531 – 2556.

[15] The poor solubility dictated the use of a relatively large amount of DMF (30 mg mL^{-1}) to apply it to the fluorous silica column (Fluorchrom, 20 g). The large amount of DMF did not adversely affect the purification. Also see the Supporting information.

[16] The low solubility of the product prohibited lower temperatures and longer reaction times in the microreactor.

[17] a) For this condensation, a ca. 93:7 mixture of enantiomers **(*R*)-13b**/**(*S*)-13b** was used, see [17b]. LC–MS analysis of the product revealed the same diastereomer ratio in the product, indicating that no epimerization had occurred under these reaction conditions. A more detailed epimerization study is currently underway. b) For the synthesis of amino acid fluoride **13**, a 93:7 diasteromeric mixture of Boc-β^2-homovaline ($R/S = 93:7$) was used: T. Hinterman; D. Seebach, *Helv. Chim. Acta* **1998**, *81*, 2093.

[18] *Synthesis of Peptides and Peptidomimetics (Houben-Weyl Methods of Organic Synthesis)*, *Vol. E22a* (Hrsg.: M. Goodman, A. Felix, L. Moroder, C. Toniolo), Georg Thieme, Stuttgart, **2002**, pp. 665 – 877.

[19] For detailed experimental conditions, see the Supporting Information.

[20] Only the major diastereomer was collected.

[21] I. R. Baxendale, J. Deeley, C. M. Griffiths-Jones, S. V. Ley, S. Saaby, G. K. Tranmer, *Chem. Commun.* **2006**, *24*, 2566.

 © 2006 Wiley-VCH Verlag GmbH & Co. KGaA, Weinheim

Enantioselective Reactions

DOI: 10.1002/anie.200602986

Kinetic Resolution of 4-Hydroxy-2-ketones Catalyzed by a Baeyer–Villiger Monooxygenase**

*Anett Kirschner and Uwe T. Bornscheuer**

Baeyer–Villiger monooxygenases (BVMOs) belong to the class of oxidoreductases and convert aliphatic, aryl aliphatic, and cyclic ketones into esters and lactones, respectively, using molecular oxygen.[1,2] Thus they mimic the chemical Baeyer–Villiger oxidation,[3] which is usually peracid catalyzed and proceeds through a two-step mechanism.[4] Additionally, BVMOs are capable of oxidizing heteroatom-containing functions (including S, N, and P groups).[5] In particular, for enantioselective Baeyer–Villiger oxidations,[6] BVMOs represent a valuable alternative to metal-based chiral catalysts.[7] While stereoselective Baeyer–Villiger oxidations using enzymes have been described for prochiral or racemic mono- and bicyclic ketones,[8] as well as for racemic aromatic ketones,[2,9] so far no example of an enantioselective BVMO-catalyzed conversion of racemic aliphatic acyclic ketones has been reported. Only the use of 3-chloro-2-butanone as the substrate for a 4-hydroxyacetophenone monooxygenase has been reported but the conversion was poor, and the potential enantioselectivity of the reaction was not addressed.[2] The chemical Baeyer–Villiger oxidation of β-hydroxyketones using peracids gave acylated diols, but the reactions were not enantioselective.[10]

Herein we report the first BMVO-catalyzed kinetic resolution of aliphatic acyclic ketones with racemic 4-hydroxy-2-ketones serving as model substrates. We were prompted to investigate these compounds as we recently discovered that a BVMO from *Pseudomonas fluorescens* DSM 50106, which we could recombinantly express in *E. coli*, converts aliphatic 2-ketones into the corresponding acetates but shows little activity towards cyclic ketones.[11] Indeed, we were pleased to find that the racemic 4-hydroxy-2-ketones **1a–c** (synthesized according to the method described by Smith and Levenberg)[12] gave hydroxyalkyl acetates **2a–c** with good enantioselectivity (Scheme 1, Figure 1, Table 1). The oxidation product was always obtained in greater than 90% *ee* and *S* configuration. *E* values[18] of around 50 should also enable the isolation of the optically active starting

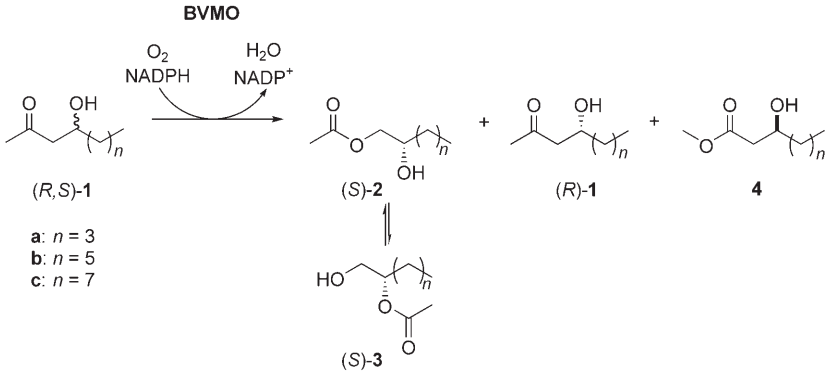

Scheme 1. Enzymatic Baeyer–Villiger oxidation of racemic 4-hydroxy-2-ketones by BVMO from *P. fluorescens* DSM 50106 expressed in *E. coli*. NAD = nicotinamide adenine dinucleotide.

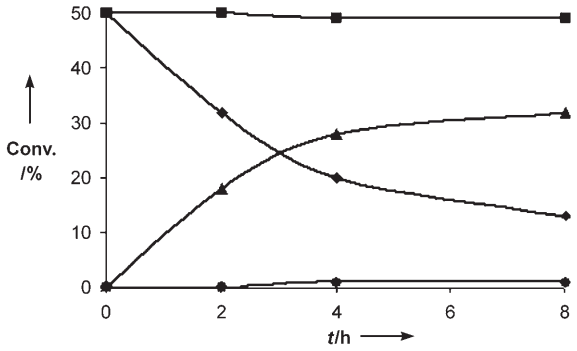

Figure 1. Time-dependent conversion of **1a** into **2a** at 30°C using resting cells of *E. coli*, which afforded the BVMO from *P. fluorescens* DSM 50106. ■: (*R*)-**1a**, ◆: (*S*)-**1a**, ▲: (*S*)-**2a**, ●: (*R*)-**2a**).

Table 1: Results of the kinetic resolution of **1a–c**.[a]

Substr.	*t* [h]	Conv. [%][b]	Enantiomeric excess[c] [% ee_S]	[% ee_P]	*E*[b]
1a	8	40	61	93	54
1b	4	48	84	91	55
1c	2	45	74	90	41

[a] Using resting cells of *E. coli* to produce the BVMO from *P. fluorescens* DSM 50106 at 30°C. [b] Calculated according to Chen et al.[18] [c] Determined by GC analysis on a chiral stationary phase.

hydroxyketones if the reaction proceeds with approximately 55% conversion. Although it is not relevant to the optical purity of the product, we observed migration of the acetyl group from the primary to the secondary hydroxy group, which gave a 4:1 mixture of the acetylated 1,2-diols **2a–c** and **3a–c** as determined by GC-MS analysis. A similar observation was reported by Park and Kozikowski, although their ratio of 7:3 possibly results from the different reaction conditions.[10]

[*] Dipl.-Biochem. A. Kirschner, Prof. Dr. U. T. Bornscheuer
Institute of Biochemistry
Dept. of Biotechnology & Enzyme Catalysis
Ernst Moritz Arndt University of Greifswald
Friedrich-Ludwig-Jahn-Strasse 18c, 17487 Greifswald (Germany)
Fax: (+49) 3834-86-80066
E-mail: uwe.bornscheuer@uni-greifswald.de
Homepage: www.chemie.uni-greifswald.de/~biotech

[**] The authors thank the Fonds der Chemischen Industrie (Germany) and the Studienstiftung des Deutschen Volkes (Germany) for stipends (A.K.). The assistance of A. Gollin for the chemical synthesis of β-hydroxyketones is acknowledged.

InterScience
© 2006 Wiley-VCH Verlag GmbH & Co. KGaA, Weinheim

Minor amounts ($\leq 5\%$) of the other possible product of a Baeyer–Villiger oxidation, hydroxy acid methyl esters **4a–c**, were also detected.

Although the BVMO from *P. fluorescens* DSM 50106 prefers short-chain aliphatic acyclic ketones, **1b** and **1c** were converted much faster than **1a**, with close to 50% conversion after 4 h when resting cells were used. Since BVMOs are flavin-dependent (mainly flavin adenine dinucleotide) and require NAD(P)H to catalyze the reaction, the biotransformations were performed using *E. coli* recombinant whole cells, either growing or resting, and thereby the Baeyer–Villiger monooxygenase was expressed from *P. fluorescens* DSM 50106.[11] Thus cofactor regeneration, and in our case also enzyme stability, were not limiting factors. When growing cells were used, the substrate was added at the same time as induction of BVMO expression, whereas for resting cells the enzyme was first expressed and then the harvested cells were resuspended in phosphate buffer prior to the biotransformations.[13] In the latter case, glucose was added along with the racemic substrate to facilitate efficient cofactor recycling.[14] The major advantage of using resting cells rather than growing cells was that reaction times were considerably shortened while higher conversions were observed. Additionally, these resting cells could be stored in the refrigerator for up to three weeks with only modest loss of activity (20–30%, data not shown). This is in contrast to the observations made using recombinant cyclohexanone monooxygenase, which is actively degraded during biocatalysis using *E. coli* resting cells.[15]

Interestingly, this kinetic resolution can be used to generate two different chemical species, which additionally differ in their configuration. Besides the residual optically active hydroxyketone (**1a–c**), an optically active acetate of a 1,2-diol is formed. This feature makes this biotransformation especially useful, as the regio- and enantioselective reduction of a 2,4-diketone to afford (*R*)-**1** would require a highly specific ketoreductase since four diastereomers may be formed.[16] The alternative kinetic resolution of a 1,2-diol using a lipase or esterase proceeds with low enantioselectivity,[17] as these hydrolases preferentially cleave (or acylate) the primary alcohol functionality. Thus, the reaction described here not only broadens the synthetic applicability of Baeyer–Villiger monooxygenases but also provides a synthetically useful alternative to established enzymes such as hydrolases and ketoreductases in organic synthesis.

Experimental Section

Unless otherwise specified, all chemicals were purchased from Sigma-Aldrich, Fisher Scientific, VWR, ABCR, and Roth GmbH and were used without further purification. All solvents were distilled prior to use. NMR spectra were recorded in $CDCl_3$ on a 300-MHz (Bruker) instrument.

The products from the BVMO-catalyzed reaction were synthesized separately for comparison purposes. Racemic 4-hydroxy-2-ketones **1a–c** were synthesized by aldol condensation according to the method described by Smith and Levenberg.[12] Corresponding hydroxyalkyl acetates **2a–c** were synthesized enzymatically using lipase B from *Candida antarctica*. Thus 5 mg of the immobilized enzyme (Chirazyme L-2, C-2, Roche) was mixed with 300 μL of isooctane and 300 μL of vinyl acetate in a 2-mL glass vial. The reaction was started by addition of the 1,2-diol (10 mg), and the mixture was incubated at 25°C in a thermoshaker (Eppendorf) for approximately 2 h until the conversion was complete. Samples were used directly for GC analysis. NMR data were consistent with previously published data.[19] Hydroxy acid methyl esters **4a–b** were synthesized from the corresponding β-ketoacid methyl esters through a reduction catalyzed by alcohol dehydrogenase, using the recombinant enzyme from *P. fluorescens* DSM 50106.[20] Thus, 5 mg of the enzyme lyophilisate was mixed with 800 μL of phosphate buffer (50 mM, pH 7.5), 200 μL of 2-propanol and 2 μL of β-ketoacid methyl ester. Reaction mixtures were incubated at 20°C for 24 h in a thermoshaker. The reaction mixture was then extracted twice with 500 μL ethyl acetate. The combined organic phases were dried over anhydrous sodium sulfate and concentrated by passing N_2 through the flask. The resulting products were analyzed by using GC. The β-ketoacid methyl esters that were not commercially available were synthesized according to the method described by Oikawa et al.[21]

Absolute configurations of the hydroxyalkyl acetates **2a–c** were determined by comparison with (*R*)-2-hydroxydecyl acetate ((*R*)-**2c**), which was synthesized from (*R*)-1,2-decanediol by using lipase-catalyzed transesterification. This result revealed a preferential oxidation of the *S* enantiomers of **1a–c** by the BVMO.

Biocatalysis using resting cells: The expression of the BVMO in *E. coli* JM109 pGro7 pJOE4072.6 + HT[11] was performed in 200 mL of LB_{cm+amp} containing 0.5 mg mL^{-1} L-arabinose at 30°C. Cells were grown up to an optical density of 0.5–0.6 at 600 nm, and BVMO expression was induced by the addition of L-rhamnose (0.2% (w/v) final concentration). After further growth for 4 h, cells were harvested by centrifugation and washed once with sterile phosphate buffer (50 mM, pH 7.5). For biocatalysis reactions in small volume, cells were resuspended in the same buffer to an OD of around 40, and 1-mL aliquots of this cell suspension were mixed in 2 mL Eppendorf reaction vials with 5 μmol of 4-hydroxy-2-ketone **1a–c** and 10 μL of a sterile 1M glucose solution. The vials were closed with air-permeable caps (Lid_{Bac}, Eppendorf) and incubated at 30°C in a thermoshaker (Eppendorf) at 1400 rpm. After set intervals, samples (300 μL) were taken, extracted twice with ethyl acetate, and dried over anhydrous sodium sulfate. Excess solvent was removed under nitrogen, and samples were analyzed by using GC.

GC analyses on a chiral stationary phase (Table 2) were carried out on a Shimadzu GC-14A gas chromatograph with a chiral β-cyclodextrin column (Hydrodex-β-3P, Macherey–Nagel). Injection and detection temperature were set at 220°C. GC-MS analysis was performed using a Shimadzu QP-2010 device equipped with the same chiral column.

Table 2: GC analyses on a chiral stationary phase of **1a–c** and **2a–c**.[a]

Cmpd.	Heating Program (Column)	t_R [min] S/R[b]
1a	20 min, 90°C//20°C min^{-1}//110°C, 15 min	17.8/18.6
1b	15 min,120°C//20°C min^{-1}//130°C, 15 min	12.7/13.3
1c	20 min, 135°C//20°C min^{-1}//145°C, 15 min	18.3/19.1
2a	20 min, 90°C//20°C min^{-1}//110°C, 15 min	23.3/24.1
2b	15 min,120°C//20°C min^{-1}//130°C, 15 min	23.3/24.1
2c	20 min, 135°C//20°C min^{-1}//145°C, 15 min	22.4/23.2

[a] Using a chiral β-cyclodextrin column (Hydrodex-β-3P). [b] Elution order of enantiomers is *S* before *R* as determined by using a standard of (*R*)-**2c**.

Received: July 25, 2006
Published online: October 2, 2006

Keywords: β-hydroxyketones · Baeyer–Villiger monooxygenases · enantioselectivity · enzyme catalysis · kinetic resolution

 © 2006 Wiley-VCH Verlag GmbH & Co. KGaA, Weinheim

[1] M. D. Mihovilovic, B. Müller, P. Stanetty, *Eur. J. Org. Chem.* **2002**, 3711.
[2] N. M. Kamerbeek, J. J. Olsthoorn, M. W. Fraaije, D. B. Janssen, *Appl. Environ. Microbiol.* **2003**, *69*, 419.
[3] a) C. Walsh, Y. C. J. Chen, *Angew. Chem.* **1988**, *100*, 342; *Angew. Chem. Int. Ed. Engl.* **1988**, *27*, 333; ; b) A. Baeyer, V. Villiger, *Ber. Dtsch. Chem.* **1899**, *32*, 3625.
[4] R. Criegee, *Justus Liebigs Ann. Chem.* **1948**, *560*, 127.
[5] a) G. Carrea, B. Redigolo, S. Riva, S. Colonna, N. Gaggero, E. Battistel, D. Bianchi, *Tetrahedron: Asymmetry* **1992**, *3*, 1063; b) G. de Gonzalo, D. E. Torres Pazmino, G. Ottolina, M. W. Fraaije, G. Carrea, *Tetrahedron: Asymmetry* **2006**, *17*, 130.
[6] M. D. Mihovilovic, F. Rudroff, B. Grötzl, *Curr. Org. Chem.* **2004**, *8*, 1057.
[7] G. Strukul, *Angew. Chem.* **1998**, *110*, 1256; *Angew. Chem. Int. Ed.* **1998**, *37*, 1199; .
[8] a) M. D. Mihovilovic, F. Rudroff, B. Grötzl, P. Kapitan, R. Snajdrova, J. Rydz, R. Mach, *Angew. Chem.* **2005**, *117*, 3675; *Angew. Chem. Int. Ed.* **2005**, *44*, 3609; ; b) M. J. Taschner, D. J. Black, Q. Z. Chen, *Tetrahedron: Asymmetry* **1993**, *4*, 1387; c) M. J. Taschner, L. Peddada, *J. Chem. Soc. Chem. Commun.* **1992**, 1384; d) M. J. Taschner, D. J. Black, *J. Am. Chem. Soc.* **1988**, *110*, 6892; e) A. J. Carnell, S. M. Roberts, V. Sik, A. J. Willetts, *J. Chem. Soc. Perkin Trans. 1* **1991**, 2385; f) V. Alphand, R. Furstoss, *J. Org. Chem.* **1992**, *57*, 1306; g) A. Carnell, A. Willets, *Biotechnol. Lett.* **1992**, *14*, 17; h) R. Gagnon, G. Grogan, M. S. Levitt, S. M. Robets, P. W. H. Wan, A. J. Willetts, *J. Chem. Soc. Perkin Trans. 1* **1994**, 2537; i) M. T. Bes, R. Villa, S. M. Roberts, P. W. H. Wan, A. Willets, *J. Mol. Catal. B* **1996**, *1*, 127; j) J. D. Stewart, K. W. Reed, C. A. Martinez, J. Zhu, G. Chen, M. M. Kayser, *J. Am. Chem. Soc.* **1998**, *120*, 3541; k) M. D. Mihovilovic, P. Kapitan, J. Rydz, F. Rudroff, F. H. Ogink, M. W. Fraaije, *J. Mol. Catal. B* **2005**, *32*, 135; l) M. D. Mihovilovic, F. Rudroff, B. Grötzl, P. Stanetty, *Eur. J. Org. Chem.* **2005**, 809.
[9] V. Alphand, R. Furstoss, *J. Mol. Catal. B* **2000**, *9*, 209.
[10] P. Park, A. P. Kozikowski, *Tetrahedron Lett.* **1988**, *29*, 6703.
[11] A. Kirschner, J. Altenbuchner, U. T. Bornscheuer, *Appl. Microbiol. Biotechnol.* **2006**, DOI: 10.1007/s00253-006-0556-6.
[12] A. B. Smith, P. A. Levenberg, *Synthesis* **1981**, 567.
[13] A. Z. Walton, J. D. Stewart, *Biotechnol. Prog.* **2002**, *18*, 262.
[14] T. Endo, S. Koizumi, *Adv. Synth. Catal.* **2001**, *343*, 521.
[15] A. Z. Walton, J. D. Stewart, *Biotechnol. Prog.* **2004**, *20*, 403.
[16] a) G.-J. Shen, Y.-F. Wang, C. Bradshaw, C.-H. Wong, *J. Chem. Soc. Chem. Commun.* **1990**, 677; b) A. Fauve, H. Veschambre, *Biocatalysis* **1990**, *3*, 95.
[17] a) F. Theil, J. Weidner, S. Ballschuh, A. Kunath, H. Schick, *Tetrahedron Lett.* **1993**, *34*, 305; b) F. Theil, S. Ballschuh, A. Kunath, H. Schick, *Tetrahedron: Asymmetry* **1991**, *2*, 1031; c) A. J. M. Janssen, A. J. H. Klunder, B. Zwanenburg, *Tetrahedron* **1991**, *47*, 7409.
[18] C.-S. Chen, Y. Fujimoto, G. Girdaukas, C. J. Sih, *J. Am. Chem. Soc.* **1982**, *104*, 7294.
[19] a) A. Lethbridge, R. O. C. Norman, C. B. Thomas, *J. Chem. Soc. Perkin Trans. 1* **1974**, 1929; b) S. Uemura, K. Ohe, S.-I. Fukuzawa, S. R. Patil, N. Sugita, *J. Organomet. Chem.* **1986**, *316*, 67.
[20] P. Hildebrandt, A. Musidlowska, U. T. Bornscheuer, *Appl. Microbiol. Biotechnol.* **2002**, *59*, 483.
[21] Y. Oikawa, K. Sugano, O. Yonemitsu, *J. Org. Chem.* **1978**, *43*, 2087.

 © 2006 Wiley-VCH Verlag GmbH & Co. KGaA, Weinheim

Iron

DOI: 10.1002/anie.200602100

The Two Odors of Iron when Touched or Pickled: (Skin) Carbonyl Compounds and Organophosphines**

Dietmar Glindemann, Andrea Dietrich, Hans-Joachim Staerk, and Peter Kuschk*

Humans are perplexed by the metallic odor from touching iron metal objects, such as tools, cutlery, railings, door handles, firearms, jewelry, and coins. Phosphorus-containing iron which is under acid attack gives rise to a different "carbide" or "garlic" odor which metallurgists have attributed to the gas phosphine (PH_3);[1–3] however, we found that purified PH_3 at breathable dilution has hardly any odor. The aim of our research is to understand the chemical causes of these two iron smells in our engineered metal environment.

1) Ironically, the iron odor on skin contact is a type of human body odor[4]

Seven human subjects sensed an immediate "musty" metallic odor when their palm skin touched a ferrous (Fe^{2+}) solution or metallic iron (ultra pure iron powder, steel, and cast iron plates) moistened with artificial sweat (pH 4.7 and 0.7 N chloride). The metallic odor was recognized on both the skin and on the metal plates. The test subjects agreed that this metallic odor was similar to that encountered in their life experience on smelling sweaty hands in contact with everyday iron objects. Ferric (Fe^{3+}) solution did not produce metallic odors.

Parallel chemical (SPME GC/MS) analysis (Figure 1, Supporting Information) of metallic-smelling gas samples from the skin of each human subject, after its contact with iron metal or aqueous ferrous ion, resulted in a reproducible distribution of highly abundant C_6 to C_{10} *n*-alkanals and at least five more minor peaks arising from unsaturated

[*] Dr. D. Glindemann, Prof. Dr. A. Dietrich
Department of Civil and Environmental Engineering
Virginia Polytechnic Institute and State University
418 Durham Hall, Blacksburg, VA 24061 (USA)
Fax: (+1) 540-231-7916
E-mail: dglindem@vt.edu
Homepage: www.glindemann.net/publications.htm

Dr. D. Glindemann
Institute of Animal Hygiene and Veterinary Public Health
Universität Leipzig
An den Tierkliniken 1, 04103 Leipzig (Germany)

Dr. H.-J. Staerk, Dr. P. Kuschk
UFZ Centre for Environmental Research Leipzig-Halle
Permoser Strasse 15, 04318 Leipzig (Germany)

[**] Financial support: NSF (USA), Directorate for Engineering, DMI#0329474 (part 1 of the article). UFZ Environmental Research Center (Germany), #UFZ-21/97 (part 2 of the article). Analysis of methylphosphinic acid by Eric Wils (TNO Prins Maurits Lab.).

Supporting information for this article is available on the WWW under http://www.angewandte.org or from the author.

 WILEY InterScience DISCOVER SOMETHING GREAT

© 2006 Wiley-VCH Verlag GmbH & Co. KGaA, Weinheim

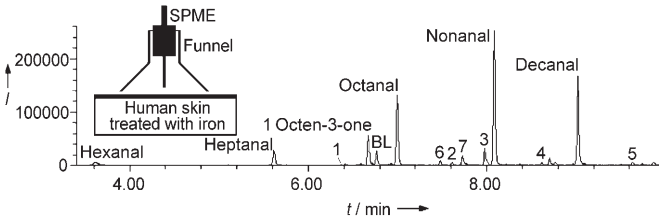

Figure 1. Typical chemical fingerprint of carbonyl hydrocarbons produced by human haired body skin on the addition of iron. Aqueous $FeCl_2$ solution, 150 μL, 10 mM, 0.3 dm^2 skin, solid-phase micro-extraction (SPME) GC/MS trace for ion mass 55. Inset illustrates sampling procedure for measuring the volatiles by SPME. **1**–**7** = unsaturated carbonyl compounds. BL = baseline peak (unsaturated ketone also present in control samples of skin without iron). See Supporting Information.

aldehydes and ketones. GC-olfactometry and classical dilution olfactometry revealed 1-octen-3-one (CAS no. 4312-99-6, mushroom-like metallic odor, odor threshold near 50 $ng\,m^{-3}$ [5]) as a key odorant that contributes about 1/3 of the total odor concentration (dilution factor to odor threshold ca. 300) of the complete gas sample above the skin under a glass funnel.

The quantity of the odorous carbonyl compounds (Figure 2) and the metallic odor increased with the quantity of Fe^{2+} (but not Fe^{3+}) ions in contact with the skin of one human subject, up to a relatively constant limit level near 300 $nmol\,dm^{-2}$ carbonyl compounds above 1000 $nmol\,dm^{-2}$ Fe^{2+} ions. The iron odor from UV-protected and unprotected haired skin (e.g., calf and thigh skin) and from palm skin was similar. Similar levels of carbonyl formation were found for the six other human subjects.

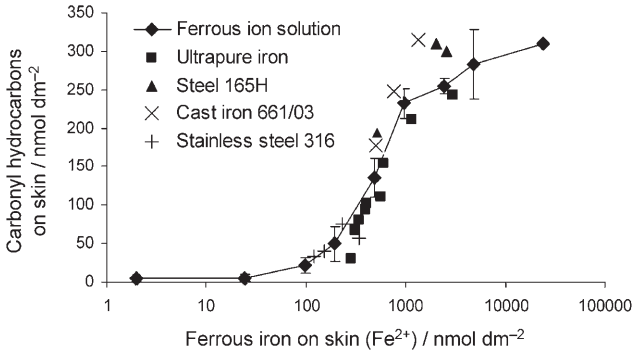

Figure 2. Molar amounts of carbonyl hydrocarbons formed by haired body skin of one human subject versus Fe^{2+} ion exposure. Fe^{2+} was either added as an aqueous solution or resulted from the corrosion of solid iron alloys in contact with skin and artificial sweat. For the impurity levels of the metals, see Table 1 and Supporting Information. Error bars indicate the low and high values of duplicate measurements. The corresponding concentration of the skin odor, measured as the dilution factor of the complete headspace gas (above the skin, under a glass funnel) to the odor threshold is approximately 300 (intensity rated moderate) at high Fe^{2+} ion exposure and approximately 10 without iron. Controls of iron alloys or an Fe^{2+} ion solution without skin, skin with artificial sweat but without iron, and skin with an Fe^{3+} ion solution produced diminishing levels of the hydrocarbon compounds, and the metallic odor was not detectable. Additional chemical reductants, such as ascorbic acid, regenerate Fe^{2+} from Fe^{3+} ions and increase the potency of small amounts of Fe^{2+}.

Odorant precursors: The molar quotient of Fe^{2+} ion reagent consumed and carbonyls (aldehydes) produced (Figure 2, below 1000 $nmol\,dm^{-2}$ Fe^{2+}) is on the order of five, similar to a reported[6] quotient of Fe^{3+} produced and lipidperoxide decomposed by Fe^{2+}. The Fe^{2+}/xylenol-orange test[6] produced orange coloration of the skin and a metallic odor, indicating the formation of Fe^{3+} from Fe^{2+} and the reductive decomposition of the preexisting skin lipidperoxides into odorants. Lipidperoxides can be formed from a plethora of skin lipids,[7,8] through lipoxygenases[9] or oxidative stress (e.g. UV light). The limited supply of skin lipidperoxides explains the leveling of odorants at higher amounts of Fe^{2+} addition (Figure 2). The specific "pure" metallic odor of live skin and Fe^{2+} is explained by a certain distinct mixture of skin lipidperoxides which are the precursors to the odorants, and this mixture is different to the peroxide composition of "dead" meat (food) and oxidized unsaturated fatty acids that smell more "fatty".

Blood iron: Blood of one of the authors rubbed onto his own skin resulted in similar metallic odor and the same odorants (78 ± 7 $nmol\,dm^{-2}$, 4 repetitions) as in the above experiments. Controls by addition of FerroZine which is a blood-iron chelator suppressed the reaction (4 ± 0.4). Aerated and homogenized blood also developed metallic odor on its own. There are reports that blood iron[10] can decompose blood lipidperoxides and that FerroZine inhibits this reaction.[11] This finding confirms that blood iron can trigger the metallic odor on skin or in blood itself.

Overall "skin–iron odor" mechanism: The metallic odor from iron contacting skin is surprisingly a type of human body odor. Sweaty skin corrodes iron metal to form reactive Fe^{2+} ions that are oxidized within seconds to Fe^{3+} ions while simultaneously reducing and decomposing existing skin lipidperoxides to odorous carbonyl hydrocarbons that are perceived as a metallic odor. This fast reaction creates the sensory illusion that it is the "metal in itself" that we smell right after touching it. Similar mechanisms underlie the skin–metal odors of iron, copper, and brass (Supporting Information) used as every-day objects.

Based on these findings, the medical community should consider developing this Fe^{2+} test of skin, blood, body tissues, to identify specific fingerprints of volatile carbonyls as indicators of individual body odor, oxidative stress, and diseases. Utility engineers could explain cases of customer complaints of metallic odor and flavor of drinking water by the production of carbonyls: We found that in a kitchen situation, ascorbic acid in foods and water promptly reduces Fe^{3+} ions ("red" rust) in water to the "green" Fe^{2+} form that triggers the intense metallic odor on the skin of hands used for food preparation. Biologists may interpret the distinctive and sensitive human smell for the (blood-)iron–skin odor as an evolutionary advantage that is much older than human use of metal tools: Early humans and their animal ancestors could probably like "blood-trailing" dogs track and locate wounded prey or tribal comrades by the metallic "blood scent" (of 1-octen-3-one etc.).

2) Pickled iron: carbon- and phosphorus-containing alloys of iron which are attacked by acid develop organophosphines with "garlic" metallic odor[4]

 © 2006 Wiley-VCH Verlag GmbH & Co. KGaA, Weinheim

Human subjects also noted that even without skin contact a faint but different "garlic" metallic odor came from cast iron standard plates after contact with only artificial sweat or with 0.01N HCl. Phosphine (100 ng m^{-3} in the headspace gas (above the metal plate, under a glass funnel)) did not cause this odor. Complete dissolution of carbon- and phosphorus-rich iron filings in hot oxygen-free 1N HCl resulted in sufficiently concentrated gas for olfactometry and for identification and quantification of a variety of organophosphines by GC/MS and GC/ICP-MS (ICP = inductively coupled plasma; Table 1, and Supporting Information).

The "garlic" metallic odor (see Supporting Information) of the gas product from acidic dissolution of cast iron is dominated by these organophosphines. We measured an extremely low odor threshold for two key odorants, methylphosphine and dimethylphosphine (6 and 3 ng P/m^3, respectively, garlic-metallic odor), which belong therefore to the most potent odorants known. Phosphine (PH_3) is not important for this odor because we found it has a much higher odor detection threshold ($>10^6$ ng m^{-3}). A "calcium carbide" (or "burned lime"/"cement") attribute of the general "garlic" odor is probably caused by unsaturated hydrocarbons (alkynes, alkadienes) that are linked to a high carbon content of iron (Table 1, see Supporting Information).

It is clear that these organophosphines arise for the high carbon and phosphorus contents in iron (Table 1). The carbon and phosphorus are chemically reduced and alloyed with the iron metal (iron–magnetite redox buffer), and react with hydrogen on dissolution of the iron in acid (similar to phosphine[3] (PH_3) formation from reduced phosphorus-containing iron). Specifically, solid phases of iron phosphide (Fe_3P), iron carbide (Fe_3C, cementite), or Fe–C–P alloys, could form hydrocarbons and PH_3 on iron dissolution that partially combine in the early stages to form organophosphines.

Alternatively, the iron metal could already contain C–P bonds that survive iron dissolution, and acquire hydrogen, such as hypothetical "iron–carbon–phosphide" (-Fe-P-C-) or "iron–phosphorus–carbide" (-Fe-C-P-) bonds. However, that would prove present materials-science knowledge wrong in that phosphorus (a substitutional solid solute) and carbon (an interstitial solid solution) in iron do not bind for energetic reasons (see exception in ref. [12]).

To test this hypothesis we verified the presence of methylphosphinic acid (CH_5PO_2, up to 3 μg g^{-1}) in rusted cast iron samples that do not form PH_3 and hydrocarbons as intermediates in the oxidation (rusting) process. Methylphosphinic acid (also a metastable oxidation product of methylphosphine) can oxidize further to methylphosphonic acid,[13] has no biological source, and is placed on the Schedule list of the Chemical Weapons Convention (CWC, Schedule 2.B.4). These C–P compounds could also influence the corrosion of iron.[14]

In conclusion: 1) The typical "musty" metallic odor of iron metal touching skin (epidermis) is caused by volatile carbonyl compounds (aldehydes, ketones) produced through the reaction of skin peroxides with ferrous ions (Fe^{2+}) that are formed in the sweat-mediated corrosion of iron. Fe^{2+} ion containing metal surfaces, rust, drinking water, blood etc., but also copper and brass, give rise to a similar odor on contact with the skin. The human ability to detect this odor is probably a result of the evolutionarily developed but largely dormant ability to smell blood ("blood scent").

2) The "garlic-carbide" metallic odor of phosphorus- and carbon-rich cast iron and steel under attack by acid, is dominated by volatile organophosphines. Corroding cast iron is an environmental source of C–P compounds that may lead to confusion in the verification and monitoring of the Chemical Weapons Convention (see also ref. [15]).

Received: May 25, 2006
Published online: September 28, 2006

Keywords: aldehydes · iron · ketones · peroxides · phosphines

Table 1: Production of volatile organophosphines and odors from dissolution of C–P-alloyed iron metal in hot oxygen-free HCl.

Metal standard	Metal impurity μg element/g metal		Odorants and odor from HCl dissolved metal μg volatilized element/g metal			m^3 air/g metal dissolved
	C	P	C as hydrocarbons[a]	P as PH_3	P as organophosphines[b]	Gas dilution to odor threshold[c]
Cast iron SCRM 665/3	32100	11100	1953	39	25	22300
Cast iron SCRM 661/3	26300	8300	5311	127	82	35700
Cast iron SCRM 664/3	29200	5500	3050	51	61	28600
Cast iron SCRM 662/3	30400	2500	5402	14	54	24100
Cast iron SCRM 663/3	34900	1030	4292	14	6	11600
Steel CKD 165 H	1500	890	747	6	0.24	800
Steel CKD 162 H	200	50	216	0.27	0.01	26
Iron, ultra pure	<10	<1	<10	0.02	n.d.	n.d.
Aluminum 122/03[d]	<10	75	<10	35	n.d.	24
Aluminum 124/03[d]	<10	1	<10	0.54	n.d.	31

[a] Hydrocarbons include C_1–C_6 alkenes and alkynes. [b] Organophosphines (GC/MS, GC/ICP-MS) in the same gas samples comprise methylphosphine > dimethylphosphine > trimethylphosphine (or methylethylphosphine) ≫ ethylphosphine > propylphosphine. Other volatile odorants found are H_2S, alkylsulfides, AsH_3, methylarsine, dimethylarsine, formed from sulfur and arsenic impurities in the iron alloys. [c] Dilution-olfactometry data mean that the complete gas product (hydrogen with odorants) of just one gram of iron 661/3 dissolved in HCl can be diluted with 35700 m^3 air before its odor becomes undetectable. One μg iron dissolved by the sweat of a human hand (instead of HCl) could explain a whiff of "garlic-carbide" metallic odor. The unit m^3 in the last column is akin to the odor unit (OU). [d] Aluminum is listed as a control (high PH_3, low odor). See Supporting Information.

 © 2006 Wiley-VCH Verlag GmbH & Co. KGaA, Weinheim

[1] B. F. Brown, *Foundry* **1951**, *79*, 174.
[2] F. Habashi, M. I. Ismail, *CIM Bull.* **1975**, *68*, 99.
[3] H. Bala, *Mater. Corros.* **1987**, *38*, 25.
[4] Supporting Information, Table S1–S4, Figure S1–S8.
[5] M. Rychlik, P. Schieberle, W. Grosch, *Compilation of odor thresholds, odor qualities and retention indices of key food odorants*, Deutsche Forschungsanstalt für Lebensmittelchemie, Garching, **1998**, p. 45.
[6] C. Gay, J. Collins, J. M. Gebicki, *Anal. Biochem.* **1999**, *273*, 149.
[7] S. C. Green, M. E. Stewart, D. T. Downing, *J. Invest. Dermatol.* **1984**, *83*, 114.
[8] C. Prottey, *Brit. J. Dermatol.* **1977**, *97*, 29.
[9] V. A. Ziboh, Y. H. Cho, I. Mani, S. D. Xi, *Arch. Pharmacal Res.* **2002**, *25*, 747.
[10] P. J. O'Brien, *Can. J. Biochem.* **1969**, *47*, 485.
[11] B. S. Berlett, R. L. Levine, P. B. Chock, M. Chevion, E. R. Stadtman, *Proc. Natl. Acad. Sci. USA* **2001**, *98*, 451.
[12] J. R. Cowan, H. E. Evans, R. B. Jones, P. Bowen, *Acta Mater.* **1998**, *46*, 6565.
[13] G. M. Kosolapov, *Organophosphorus Compounds*, Wiley, New York, **1950**, p. 24.
[14] G. Gunasekaran, R. Natarajan, V. S. Muralidharan, N. Palaniswamy, B. V. A. Rao, *Anti-Corros. Methods Mater.* **1997**, *44*, 248.
[15] A. Verweij, H. L. Boter, C. E. A. M. Degenhardt, *Science* **1979**, *204*, 616.

 © 2006 Wiley-VCH Verlag GmbH & Co. KGaA, Weinheim

Bioinformatics

DOI: 10.1002/anie.200602561

Structure–Activity Relationships in Chromatography: Retention Prediction of Oligonucleotides with Support Vector Regression**

*Oliver Kohlbacher, Sascha Quinten, Marc Sturm, Bettina M. Mayr, and Christian G. Huber**

The prediction of molecular properties for a given molecular structure is of considerable interest for many physicochemical and biochemical processes.[1] Efforts are particularly being made to theoretically predict retention times in the area of chromatographic separations that are based on molecular interactions between the molecules partitioning in separating systems comprised of two phases.[2,3]

Linear free-enthalpy relationships model chromatographic retention as a sum of individual energy contributions (dispersion, dipole–dipole, π–π, proton donor–acceptor interactions, etc.).[4] However, owing to their complex molecular structures, as in the case of biopolymers such as peptides or nucleic acids, use is frequently made of the addition of empirically calculated retention contributions of the individual amino acids or nucleotides that are then corrected by terms that take account of the total structure of the molecule.[5,6] However, for more complex molecules, this prediction model is imprecise and the relevant descriptors are very complex to determine. Sequence information (apart from the total composition) and information on secondary structures are not considered in these models.

Models have been developed for peptides that do not derive retention from the properties of the molecular building blocks, but learn them from data sets obtained with test analyses of known structures.[7] The retention data of approximately 7000 peptides have been used, for example, to train an artificial neural network (ANN) for the prediction of peptide retention times from peptide sequences with an accuracy of 3–10%.[8] Other methods from the field of statistical learning, for example, support vector machines (SVMs), may be used for regression problems. In addition to the advantage of leading exactly to a globally optimal solution (unlike ANNs), support vector approaches have also proved themselves for practical use with chemical problems.[9,10]

A model based on the determination and addition of the retention contributions of the nucleotides has been developed to predict the retention of oligonucleotides in ion-pair reversed-phase chromatography (IP-RPC).[11] This model provided satisfactory results at relatively high separating temperatures (60 °C) for cases in which secondary structures are less pronounced, whereas at lower temperatures, the influence of hairpin or partial double strands led to a poor correlation between the prediction and the experiment (own measurement results).

Our model for the retention of oligonucleotides in IP-RPC, even at low temperatures, is based on ν-support vector regression (SVR) as proposed by Schölkopf et al.[12] This method determines a model for a given data set that at the same time minimizes the model error and the model complexity. The training of this model is accomplished with a low number of 50–100 oligonucleotides. A test data set was created by the measurement of the retention times of 72 oligonucleotides. To record the influence of the sequence on the retention, 41 of the oligonucleotide sequences were generated by variation of a sequence of a 24 mer (GTA CTC AGT GTA GCC CAG GAT GCC). To take into account other possible secondary structures, four further sequences were selected that form stable hairpin structures even at higher temperatures. The remaining sequences were finally selected so that they covered a length range of 15–48 nucleotides.

Quantitative structure–property relationships (QSPR) code the input structures in the form of characteristic vectors. Relevant characteristics for the property to be predicted are,

[*] Dipl.-Chem. S. Quinten, Dr. B. M. Mayr, Prof. Dr. C. G. Huber
Fachbereich Chemie
Instrumentelle Analytik und Bioanalytik
Universität des Saarlandes
Gebäude B2.2, 66123 Saarbrücken (Germany)
Fax: (+49) 681-302-2433
E-mail: christian.huber@mx.uni-saarland.de
Prof. Dr. O. Kohlbacher, Dipl.-Inf. M. Sturm
Abteilung Simulation biologischer Systeme
Eberhard-Karls-Universität Tübingen
Sand 14, 72076 Tübingen (Germany)

[**] We thank LC Packings, Amsterdam, for the provision of the capillary HPLC system.

 © 2006 Wiley-VCH Verlag GmbH & Co. KGaA, Weinheim

for example, length, sequence, and secondary structure of the oligonucleotides under investigation. These characteristics are translated into numerical values that flow directly into the model. The sequence and structure of the oligonucleotide are described by a vector $\boldsymbol{x}_i$ at each measured retention time y_i. Characteristic-value pairs ($\boldsymbol{x}_i$, y_i) serve to determine an optimal function [Eq. (1)].

$$f(\boldsymbol{x}) = \boldsymbol{w} \cdot \boldsymbol{x} + b \text{ with } \boldsymbol{w}, \boldsymbol{x} \in \Re^n,\ b \in \Re \quad (1)$$

This function allows the prediction of retention times $y = f(\boldsymbol{x})$ for an arbitrary characteristic vector $\boldsymbol{x}$, that is, for an arbitrary sequence. We refer to comprehensive literature for mathematical details.[13,14]

In our model, the characteristic vector comprises eleven values that are derived from the sequence and secondary structure. Five of the values describe the sequence (length and relative proportion of the four bases), whereas the remaining six values represent the melting curve of the secondary structure. For this purpose, the secondary structure was predicted with Vienna RNA Package Version 1.4[15] for the temperatures 30, 40, 50, 60, 70, and 80 °C, and the percentage fraction of the bases in the paired regions was then calculated. The model showed the total length, the fraction of the different bases, and the fraction of paired bases to be the most important characteristics of an oligonucleotide. Other characteristic vectors that contained, for example, the base sequence, base stacking, or other codes containing secondary-structure information, did not produce better results.

Training of the SVR model was carried out by dividing the test data set into three parts (each of 24 data points). Two thirds of the test data were used for training the SVR model, and the remaining third was used for validation of the prediction. Triple cross-validation was carried out throughout. In each case, the values R^2 und Q^2 represent the correlation of the SVR model with the training data set and the correlation of the predicted retention times with the experimental times, respectively.

Figure 1 shows the results for the triple cross-validated model at 30 and 80 °C. The low scattering of the data points and the absence of significant outliers confirm the capabilities of the SVR model for the prediction of retention over a large temperature range and the total length region of 15–50 nucleotides. Unlike other models, the retention of hairpin structures was also predicted with the aid of SVR, with good agreement shown at both temperatures.

Examples of measured and simulated chromatograms are reproduced in Figure 2. In this case 61 of the 72 measured data points were used for training the model to simulate the retention times of the remaining eleven oligonucleotides. Table 1 confirms that all retention times were predicted with a maximum deviation of 4%, but with most less than 2%. The retention of hairpin structures that are stable at elevated temperature was also correctly reproduced by our model (Figure 2e). It is also interesting that the retention measured for the relatively long 39-mer oligonucleotide also agreed very well with the model even though there were few training data points for this length region (Figure 2d)

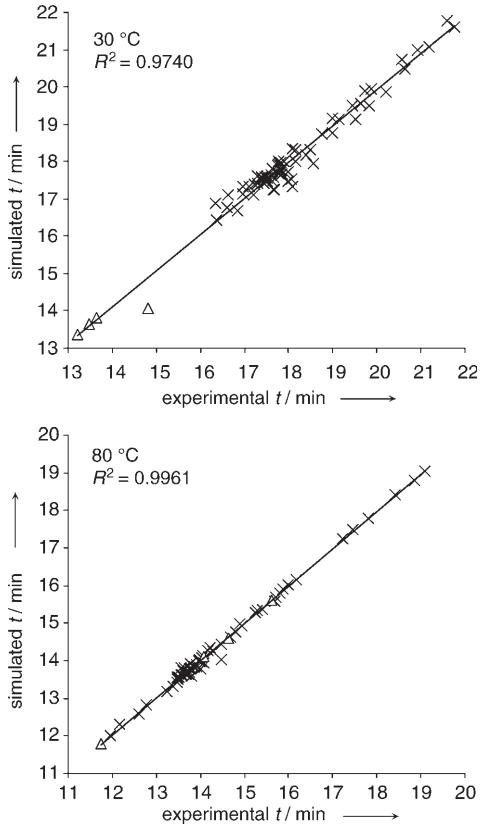

Figure 1. Retention prediction at 30 and 80 °C; R^2 values correspond to the squared correlation between the model and the experimental retention times. Hairpin structures are indicated by triangles.

The application of our method to a real oligonucleotide mixture is shown in Figure 3. It shows the mixture of

Table 1: Comparison of measured and predicted retention times of oligonucleotides at 30 and 80 °C.[a]

Sequence	Retention at 30 °C [min]			Retention at 80 °C [min]		
	measured	calcd	% error	measured	calcd	% error
GTG CTC AGT GTA ACC CAG GAT GCC	17.64	17.76	−0.64	13.99	13.93	0.42
GTG CTC AGT **A**TA **G**CC CAG GAT GCC	17.50	17.59	−0.51	14.00	13.78	1.59
ATG CTC AGT GTA **G**CC CAG GAT GCC	17.77	17.64	0.73	14.08	13.87	1.49
CTG CTC AGT GTA **G**CC CAG GAT GCC	17.23	17.49	−1.56	13.47	13.59	−0.83
GTG CTC AGT GTA **G**CC CAG GAT GC**G**	17.40	17.52	−0.69	13.67	13.58	0.64
GTG CTC AGT GTA **G**CC CAG GAT GC**A**	17.82	17.58	1.37	13.99	13.88	0.83
GTG CTC AGT GTA **G**CC CAG **A**AT GCC	17.29	17.65	−2.08	13.62	13.81	−1.39
GTG CTC AGT GTA **G**CC CAG GAT **A**CC	17.46	17.65	−1.06	13.85	13.81	0.34
GTG CTC AGT GTA **G**CC CAG GAT G**A**C	17.61	17.63	−0.12	13.88	13.82	0.46
GAG AGA GAG AGA TCT CTC TCT CTC	13.22	13.76	−4.11	14.08	14.26	−1.30
GTG CTC AGT GTA ACC CAG TTT TTT GAT GCC GTA GAT CAT	20.93	20.98	−0.28	17.80	17.76	0.24
	Q^2:	0.989			0.987	

[a] Bold letters represent modifications with respect to the first 24-mer sequence.

 © 2006 Wiley-VCH Verlag GmbH & Co. KGaA, Weinheim

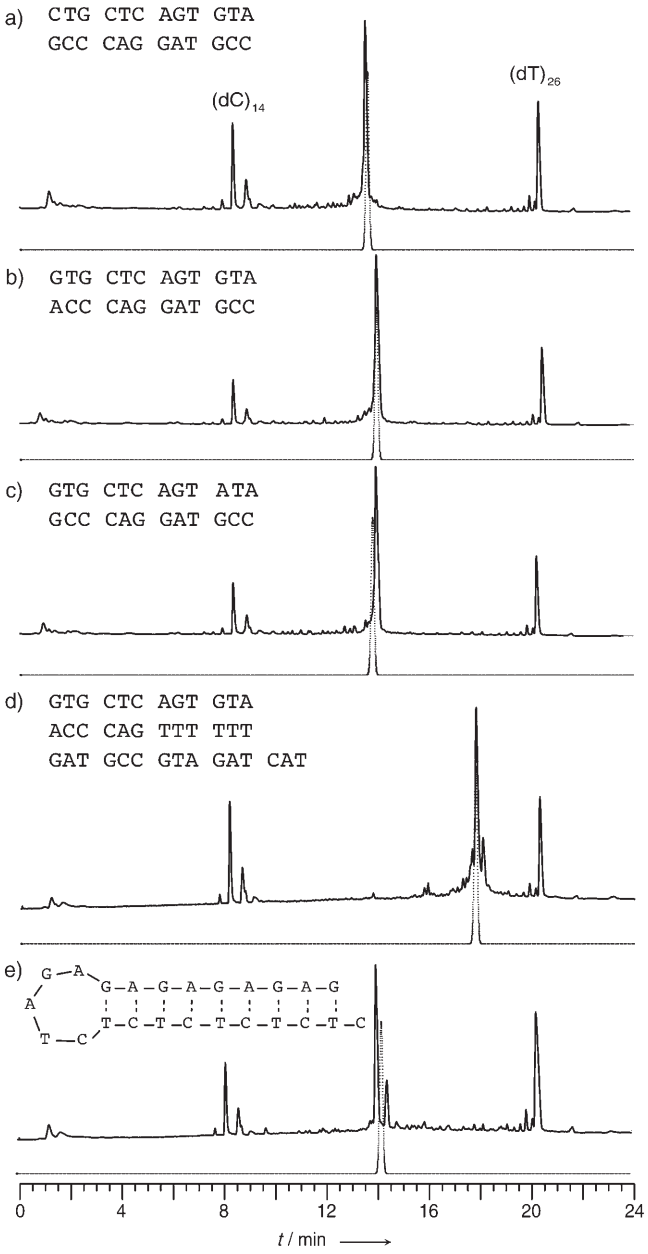

Figure 2. Comparison of the measured and simulated chromatograms of the oligonucleotides at 80 °C. The experimentally determined, mean peak standard deviation of 0.0575 min and a Gauss function were used for the peak profiles in the simulation.

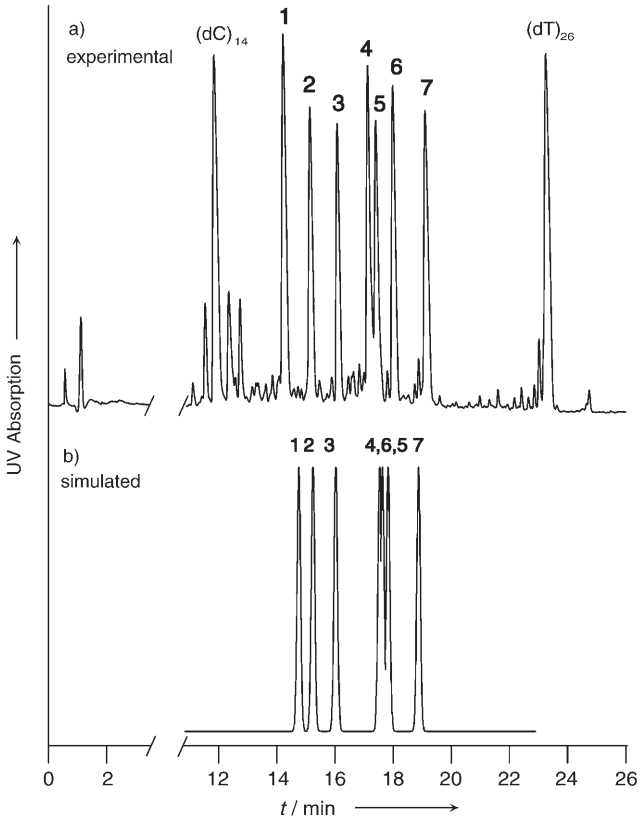

Figure 3. Prediction of a separation of seven oligonucleotide primers with lengths of 14 to 18 nucleotides at 50 °C. **1** = GTA GAG GTA GGT TGG, **2** = GAA GAG TTT TTG GA, **3** = GGG TTA ATT TGA GGT, **4** = TTT AGT TAG AAA AAG TT, **5** = GTT TAA ATA GGA AAT TT, **6** = GTT GGG ATT TTT GTA TTG, **7** = TAA GTT TTT TTT TGT TGT.

oligonucleotide primers that was used for a multiplex amplification by PCR. The strength of the model is demonstrated in that not only were the retention times of the relatively unusual A,T-rich sequences correctly predicted, but also, with the exception of the inversion of the sequence of oligonucleotides **5** and **6**, the retention sequence of the short oligonucleotides had an average and maximum deviation of 1.6% and 3.2%, respectively. The good agreement between the theory and experiment is an indication that the structural parameters integrated into the model describe the interactions between oligonucleotides and the stationary phase in IP-RPC very well.

In summary, a model has been developed that, for the first time, allows prediction of the retention of oligonucleotides with an accuracy of better than 3% over the whole temperature range of 30–80 °C. The method is characterized by training of the model by a restricted set of 50–100 oligonucleotides, and the influence of secondary structure on retention is taken into consideration. With the possibility of the inclusion and evaluation of many arbitrary structural parameters, it is possible to determine quickly and simply which structural properties are pivotal for the interactions of a molecule in a chromatographic separation system. In future work, we would like to exploit the method for the improved prediction of peptide retention times.

Experimental Section

The retention times of the oligonucleotides (in each case 2.5 ng was injected) were determined on a monolithic poly-(styrene/divinylbenzene) column ($60 \times 0.20\ mm^2$ diameter) with the aid of a 30 min (0–16%) gradient of acetonitrile in aqueous triethylamine acetate ($100\ mmol\,L^{-1}$)/ethylenediaminetetraacetic acid solution ($0.5\ mmol\,L^{-1}$), detection at 254 nm, and column temperature of 30–80 °C. The flow rate was held constant at $2.0\ \mu L\,min^{-1}$ with the aid of a HPLC system with an active split (U3000, LC Packings, Amsterdam). The standard deviation of the measured retention times for $(dT)_{18}$ from 20 repeat measurements lay between 1.3 s (0.097% relative standard deviation (RSD)) at 40 °C and 3.1 s (0.28%

 © 2006 Wiley-VCH Verlag GmbH & Co. KGaA, Weinheim

RSD) at 70 °C. The RSDs of the measured retention times fell to 0.028 % (40 °C) and 0.072 % (70 °C) by correction with internal standards (in each case 1 ng of $(dC)_{14}$ and $(dT)_{26}$). The standardized net retention time t' was calculated from Equation (2).

$$t' = (t - t_C)\frac{\bar{t}_T - \bar{t}_C}{t_T - t_C} + \bar{t}_C \quad (2)$$

t is the experimental retention time of the oligonucleotide, t_C and t_T are the retention times of $(dC)_{14}$ and $(dT)_{26}$, respectively, and $\bar{t}_C$ and $\bar{t}_T$ are the average retention times of $(dC)_{14}$ and $(dT)_{26}$, respectively, in all experiments. The SVR model was generated with the software package libSVM, Version 2.8[16].

Received: June 27, 2006
Published online: September 29, 2006

Keywords: bioinformatics · liquid chromatography · oligonucleotides · secondary structures · structure–activity relationships

[1] M. H. Abraham, J. Le, W. E. Acree, Jr., P. W. Carr, A. J. Dallas, *Chemosphere* **2001**, *44*, 855 – 863.
[2] R. M. Smith, *Retention and Selectivity in Chromatography*, Elsevier, Amsterdam, **1995**.
[3] P. Jandera, *Adv. Chromatogr.* **2005**, *43*, 1 – 108.
[4] L. C. Tan, P. W. Carr, M. H. Abraham, *J. Chromatogr. A* **1996**, *752*, 1 – 18.
[5] M. Palmblad, M. Ramstrom, K. E. Markides, P. Hakansson, J. Bergquist, *Anal. Chem.* **2002**, *74*, 5826 – 5830.
[6] T. Baczek, P. Wiczling, M. Marszall, Y. Vander Heyden, R. Kaliszan, *J. Proteome Res.* **2005**, *4*, 555 – 563.
[7] R. Kaliszan, T. Baczek, A. Bucinski, B. Buszewski, M. Sztupecka, *J. Sep. Sci.* **2003**, *26*, 271 – 282.
[8] K. Petritis, L. J. Kangas, P. L. Ferguson, G. A. Anderson, L. Pasa-Tolic, M. S. Lipton, K. J. Auberry, E. F. Strittmaier, Y. Shen, R. Zhao, R. D. Smith, *Anal. Chem.* **2003**, *75*, 1039 – 1048.
[9] K. R. Müller, G. Ratsch, S. Sonnenburg, S. Mika, M. Grimm, N. Heinrich, *J. Chem. Inf. Model.* **2005**, *45* 249 – 253.
[10] E. Byvatov, U. Fechner, J. Sadowski, G. Schneider, *J. Chem. Inf. Comput. Sci.* **2003**, *43*, 1882 – 1889.
[11] M. Gilar, K. J. Fountain, Y. Budman, U. D. Neue, K. R. Yardley, P. D. Rainville, R. J. Russell II, J. C. Gebler, *J. Chromatogr. A* **2002**, *958*, 167 – 182.
[12] B. Schölkopf, R. Bartlett, A. Smola, R. Williamson in *Proceedings of the 8th International Conference on Artificial Neural Networks* (Ed.: L. Niklasson, M. Boden, T. Ziemke), **1998**, p. 111 – 116.
[13] V. N. Vapnik, *The Nature of Statistical Learning Theory*, Wiley, New York, **1999**.
[14] T. Hastie, R. Tibshirani, J. Friedman, *The Elements of Statistical Learning*, Springer, New York, **2001**.
[15] I. Hofacker, *Vienna RNA Package, RNA Secondary Structure Prediction and Comparison*, http://www.tbi.univie.ac.at/~ivo/RNA (2006).
[16] C.-C. Chang, C.-J. Lin, *LIBSVM: a library for support vector machines*, http://www.csie.ntu.edu.tw/~cjlin/libsvm (2001).

 © 2006 Wiley-VCH Verlag GmbH & Co. KGaA, Weinheim

NMR Methods

DOI: 10.1002/anie.200602317

Charge-Induced Molecular Alignment of Intrinsically Disordered Proteins**

*Lukasz Skora, Min-Kyu Cho, Hai-Young Kim, Stefan Becker, Claudio O. Fernandez, Martin Blackledge, and Markus Zweckstetter**

Intrinsically disordered or unstructured proteins (IUPs) play a key role in normal and pathological biochemical processes. Despite their importance for function, this category of proteins remains beyond the reach of classical structural biology because of their inherent conformational heterogeneity. Measurements of global dimensions strongly suggested a random coil-like behavior of IUPs.[1] In contrast to these findings, NMR spectroscopy detected significant amounts of local structure in denatured and unfolded states. Recently, these two apparently contradicting behaviors were reconciled when it was shown that the local conformational behavior of IUPs can be described by a simple model based on residue-specific ϕ/φ propensities.[2,3] In particular, residual dipolar couplings (RDCs), which can be measured for proteins that are weakly aligned in dilute liquid-crystalline media, could be predicted from this model by assuming a steric interaction between the protein and the alignment medium. Furthermore, we showed that RDCs are also sensitive detectors of transient long-range interactions in IUPs.[4,5]

[*] L. Skora, M.-K. Cho, H.-Y. Kim, S. Becker, Dr. M. Zweckstetter
Department of NMR-based Structural Biology
Max Planck Institute for Biophysical Chemistry
Am Fassberg 11, 37077 Göttingen (Germany)
Fax: (+49) 551-201-2202
E-mail: mzwecks@gwdg.de
Homepage:
http://www.mpibpc.gwdg.de/abteilungen/030/zweckstetter
Dr. C. O. Fernandez
Instituto de Biología Molecular y Celular de Rosario
Consejo Nacional de Investigaciones Científicas y Tecnicas
Universidad Nacional de Rosario
Suipacha 531, S2002LRK Rosario (Argentina)
Dr. M. Blackledge
Institute de Biologie Structurale Jean-Pierre Ebel
CNRS-CEA-UJF, UMR 5085
41 rue Jules Horowitz
38027 Grenoble Cedex (France)

[**] L.S. acknowledges a Marie Curie fellowship (MEST-CT-2004-504193), M.-K.C. a DFG-Graduiertenkolleg (GRK782) scholarship, C.F. an institutional partnership supported by the Alexander von Humboldt Foundation, and M.Z. a DFG Emmy Noether grant (ZW 71/1-5). This work was supported by the CMPB Göttingen and by the European Union through UPMAN. We thank Christophe Fares for help with the CPCl medium and Prof. Dr. Christian Griesinger for stimulating discussions.

Supporting information for this article is available on the WWW under http://www.angewandte.org or from the author.

WILEY InterScience DISCOVER SOMETHING GREAT
© 2006 Wiley-VCH Verlag GmbH & Co. KGaA, Weinheim

Herein, we demonstrate that the assumption of a steric interaction between intrinsically disordered proteins and the alignment medium is only valid in the case of uncharged alignment media. Alignment of IUPs in charged media depends critically on electrostatic interactions, especially in charged regions of the protein, and is scaled with the ionic strength of the solution. In this case the RDCs can be predicted using a simplified electrostatic model.[6]

In our approach we investigated the molecular alignment of α-synuclein (αS), a natively unstructured protein of 140 amino acid residues that is implicated in the onset of Parkinson's disease, in two charged alignment media with different electrostatic properties: filamentous phage Pf1[7] and quasiternary surfactant cetylpyridinium chloride/hexanol/NaCl (CPCl).[8]

RDCs in αS that was weakly aligned in filamentous phage Pf1 are shown in Figure 1. At 300 and 500 mM NaCl the RDC profile resembles the one that was previously observed in an uncharged alignment medium.[4] All RDCs were positive, and regions with sizeable RDCs were separated by residues with RDC values close to zero. The C-terminal domain displayed the largest RDCs. At 100 mM NaCl, the RDCs of residues 23, 46, 50, 59, 86, and 103–104 turned from near-zero values to negative. Furthermore, the magnitude of RDCs for residues 15–21 increased, and for residues 124–131 it was nearly doubled. At even lower salt concentration, the RDCs in the N-terminal domain were further increased, thereby making several residues undetectable owing to strong $^{1}H,^{1}H$ dipolar couplings, and in the central part of αS nearly all RDCs became negative. This behavior is in agreement with the electrostatics of the system. The Pf1 alignment medium bears an overall negative charge on the outer, protein-accessible side[9] and therefore, at low salt concentrations, strongly attracts the positively charged N-terminal domain of αS (Figure 1a). At the same time, the negatively charged C-terminal domain of αS is repelled from the Pf1 surface.

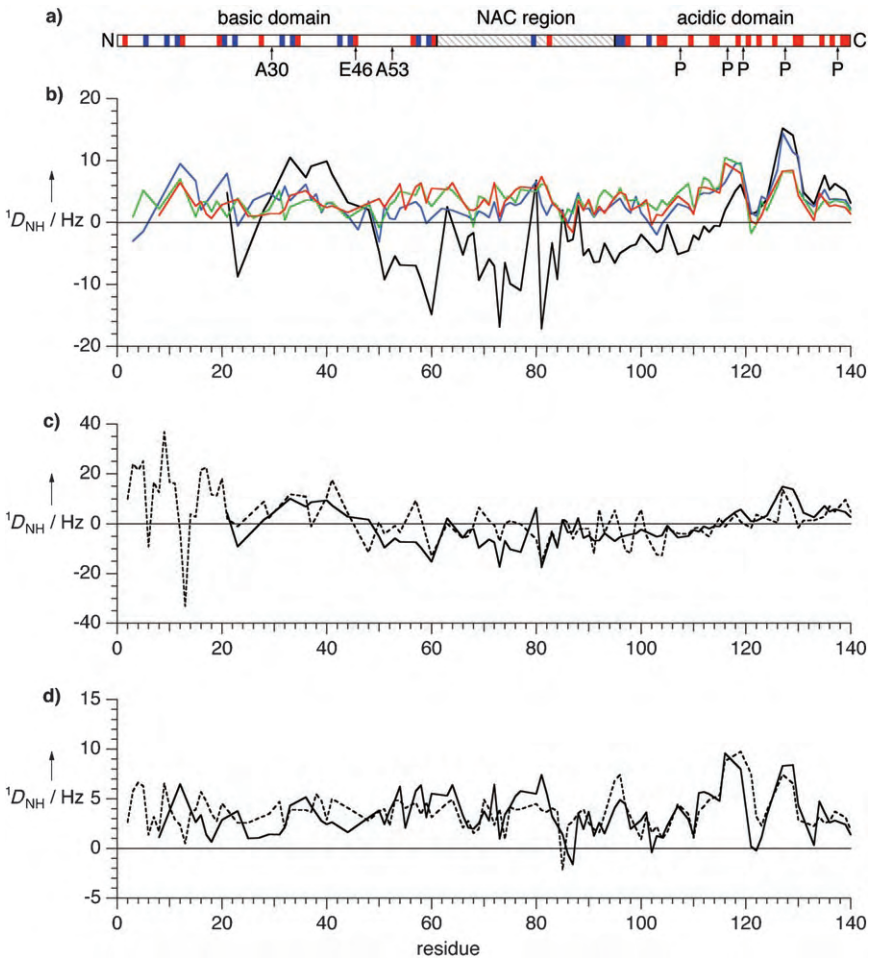

Figure 1. a) Surface charge distribution in αS. Positively and negatively charged residues are marked blue and red, respectively. Sites of mutations associated with Parkinson's disease and proline residues are indicated by arrows. b) $^{1}H,^{15}N$ RDCs in Pf1 phage at 50 mM (black), 100 mM (blue), 300 mM (green), and 500 mM (red) NaCl, scaled with respect to the splitting of the ^{2}H signal at 50 mM NaCl. All spectra were acquired on a Bruker DRX600 spectrometer with 0.2 mM αS in 20 mM Tris-HCl, pH 7.4, at 288 K. c,d) Comparison of experimental (solid line) and predicted (dashed line) $^{1}H,^{15}N$ RDCs in 15 mg mL^{-1} Pf1 bacteriophage at 50 mM NaCl (c) and 500 mM NaCl (d). Below 200 mM NaCl the predicted and experimental RDC magnitude strongly depend on the exact ionic-strength value and the Pf1 batch used.

Experimental RDCs were compared to values that were predicted from an ensemble of structures by using the software PALES. An ensemble comprising 50000 structures was generated using the flexible-meccano algorithm,[3] which sequentially builds peptide chains by random selection of ϕ/φ angles from a database of amino acid specific conformations found in loop regions of high-resolution X-ray structures. From these 50000 structures (30000–50000 structures were needed for convergence) RDCs were predicted on the basis of a highly simplified alignment model that approximates the electrostatic interaction between a solute and an ordered liquid-crystal particle as that between the solute side-chain charge and the electric field of the phage.[6] For Pf1 bacteriophage the following parameters were used: average surface charge density $-0.47\ e\,nm^{-2}$, order parameter 0.9, concentration 15 mg mL^{-1}. CPCl was modelled as a 26.8-Å thick, uniformly charged wall with a surface charge density of $+0.08\ e\,nm^{-2}$, order parameter of 0.8, and a concentration of 5% (w/v).[10]

Reasonably close agreement between experimental and charge-shape-predicted RDC patterns was found under all investigated conditions for Pf1 alignment medium (Figure 1c,d and the Supporting Information). The prediction of the magnitude of alignment is better at intermediate ionic strengths whereas at higher salt concentrations the RDC magnitude tends to be underestimated by PALES.[6]

© 2006 Wiley-VCH Verlag GmbH & Co. KGaA, Weinheim

Therefore, average RDC values predicted at 100 mM and 500 mM NaCl were scaled up by factors of 2.5 and 4, respectively, to maximize agreement with experimental values. At 50 mM NaCl no scaling was required.

CPCl is positively charged and interacts strongly with the acidic C-terminal region of αS, such that severe line broadening and disappearance of the corresponding signals was observed (Supporting Information). In agreement with the disappearance of signals, PALES predicted an up to eightfold increase in the RDC magnitude of residues 110–140. However, RDCs for residues 10–90 remained small, thus suggesting that the different domains of αS align independently. Experimental RDCs in this region fit reasonably well to predicted values. Moreover, a strong influence of the electrostatic interaction on the alignment properties of CPCl was observed. At 150 mM NaCl, the liquid-crystalline phase showed a ^{2}H splitting of 15 Hz, which dropped sixfold upon addition of αS. Thus, it cannot be excluded that the interaction with the CPCl medium changes the conformational ensemble of αS, although chemical shifts of observable residues were not significantly changed.

To further investigate the sign inversion of RDCs in the central region of αS at 50 mM NaCl (Figure 1b), we constructed a 30000-structure ensemble for a polyalanine fragment of 10 amino acid residues. Charges of $+5e$ and $-5e$ were placed on the N- and C-terminus, respectively, and RDCs were predicted using models of both steric[11] and electrostatic alignment[6] (Figure 2a). In the steric case, all RDCs were positive and showed the characteristic bell-shaped pattern.[12] In the electrostatic prediction, on the other hand, average RDC values turned negative, thus indicative of a preferential alignment perpendicular to the magnetic field and in agreement with a dipole-like behavior of the amino acid fragment. Furthermore, predictions at different salt concentrations demonstrated that shielding of charges leads to more steric alignment.

Previously, we showed that the large RDCs in the C-terminal region of αS are a result of long-range interactions involving the C- and N-terminal domains and the NAC region.[4] When steric alignment was assumed, enforcement of a long-range interaction between residues 1–20 and 120–140 in an ensemble of structures generated by flexible-meccano resulted in an increase in the RDC magnitude predicted for residues 2–30 and 110–140 and better agreement with RDCs measured in both sterically and electrostatically aligning media. The situation turns out to be more complicated when electrostatic alignment dominates (Figure 2b). Although RDCs for residues 116–121 were slightly increased upon enforcing the long-range contact, average RDCs that were predicted for the N-terminal region were strongly reduced. Thus, two opposing effects have to be taken into account. Owing to the long-range interaction the protein backbone becomes more rigid, potentially leading to larger RDCs, but at the same time the proximity of the negatively charged C-terminal region partially compensates the positive charges in the N-terminus, thus causing a decrease in the RDC magnitude.

This report demonstrates that molecular alignment of intrinsically unstructured and other disordered proteins in charged nematic media strongly depends on electrostatic interactions between the protein and the alignment medium. A simple electrostatic alignment model, however, reliably predicts RDCs under different sample conditions. Electrostatic effects have to be taken into account when using RDCs for the interpretation of residual structure in disordered proteins. At the same time, however, charge modulation of alignment provides an independent set of RDCs in disordered proteins, potentially improving the structural characterization of these systems. These findings have important consequences for the RDC-based interpretation of the structure and dynamics of the unfolded state.

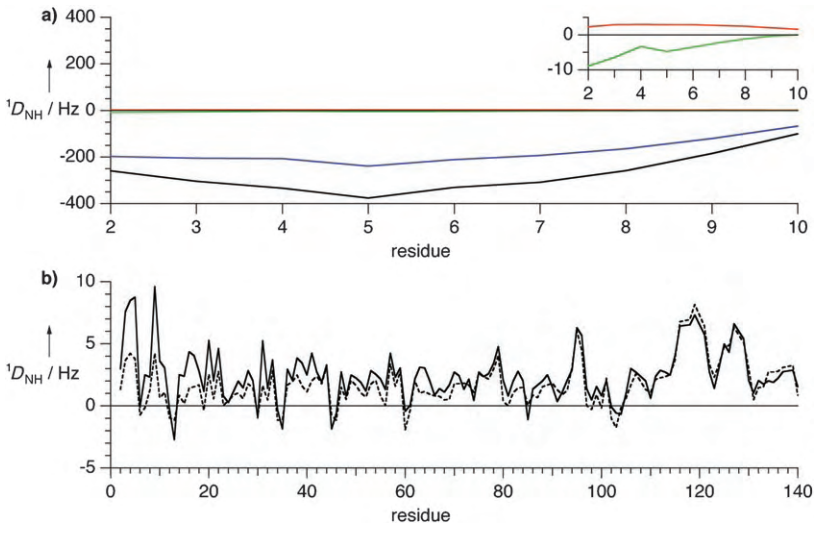

Figure 2. a) ^{1}H,^{15}N RDCs in a polyalanine fragment of 10 amino acid residues, predicted using a steric (red) and an electrostatic alignment model with salt concentrations of 50 mM (black), 100 mM (blue), and 500 mM (green) and charges of $+5e$ and $-5e$ at the N- and C-terminus, respectively. Inset: enlarged excerpt. b) ^{1}H,^{15}N RDCs in 15 mg mL^{-1} Pf1 phage at 100 mM NaCl, predicted with (dashed line) and without (solid line) enforcing a long-range interaction between residues 1–20 and 120–140.

Received: June 9, 2006
Published online: September 28, 2006

Keywords: molecular alignment · NMR spectroscopy · protein structures · residual dipolar couplings

[1] C. Tanford, K. Kawahara, S. Lapanje, *J. Biol. Chem.* **1966**, *241*, 1921–1923.
[2] A. K. Jha, A. Colubri, K. F. Freed, T. R. Sosnick, *Proc. Natl. Acad. Sci. USA* **2005**, *102*, 13099–13104.
[3] P. Bernado, L. Blanchard, P. Timmins, D. Marion, R. W. Ruigrok, M. Blackledge, *Proc. Natl. Acad. Sci. USA* **2005**, *102*, 17002–17007.
[4] C. W. Bertoncini, Y. S. Jung, C. O. Fernandez, W. Hoyer, C. Griesinger, T. M. Jovin, M. Zweckstetter, *Proc. Natl. Acad. Sci. USA* **2005**, *102*, 1430–1435.
[5] P. Bernado, C. W. Bertoncini, C. Griesinger, M. Zweckstetter, M. Blackledge, *J. Am. Chem. Soc.* **2005**, *127*, 17968–17969.
[6] M. Zweckstetter, G. Hummer, A. Bax, *Biophys. J.* **2004**, *86*, 3444–3460.

 © 2006 Wiley-VCH Verlag GmbH & Co. KGaA, Weinheim

[7] M. R. Hansen, L. Mueller, A. Pardi, *Nat. Struct. Biol.* **1998**, *5*, 1065 – 1074.
[8] R. S. Prosser, J. A. Losonczi, I. V. Shiyanovskaya, *J. Am. Chem. Soc.* **1998**, *120*, 11010 – 11011.
[9] K. Zimmermann, H. Hagedorn, C. C. Heuck, M. Hinrichsen, H. Ludwig, *J. Biol. Chem.* **1986**, *261*, 1653 – 1655.
[10] M. Zweckstetter, *Eur. Biophys. J.* **2006**, *35*, 170 – 180.
[11] M. Zweckstetter, A. Bax, *J. Am. Chem. Soc.* **2000**, *122*, 3791 – 3792.
[12] M. Louhivuori, K. Paakkonen, K. Fredriksson, P. Permi, J. Lounila, A. Annila, *J. Am. Chem. Soc.* **2003**, *125*, 15647 – 15650.

 © 2006 Wiley-VCH Verlag GmbH & Co. KGaA, Weinheim

Collagen

DOI: 10.1002/anie.200601432

Photocontrolled Folding and Unfolding of a Collagen Triple Helix**

Ulrike Kusebauch, Sergio A. Cadamuro, Hans-Jürgen Musiol, Martin O. Lenz, Josef Wachtveitl, Luis Moroder, and Christian Renner*

Collagens consist of three identical or different polypeptide chains which are arranged in a triple-helical supercoil of variable stability. Although the overall shape is that of a soft rod, collagens also contain stretches of low triple-helix stability and even disruptions of this structure. The local stability and recognition sites for interaction with other proteins of the extracellular matrix are defined and highly fine-tuned by the amino acids in the X and Y positions of the repeating Gly-Xaa-Yaa triplets with a Gly residue mandatory at every third position for the compact intertwining of three left-handed poly-Pro-II helices into the right-handed triple helix.[1] Extensive studies on synthetic model peptides have clearly identified the tripeptide unit Gly-Pro-Hyp as the most favorable triplet for stabilizing the triple helix,[1b,2] and crystal structures of collagen peptides allowed detailed insights into the hydrogen-bonding networks of this very repetitive and regular tertiary structure.[3]

From folding studies of natural collagens and related fragments a zipper-like folding mechanism was derived with the *cis*-to-*trans* isomerization of proline as the rate-limiting step.[1d,4] In absence of *cis*-proline isomers the folding is very fast and completed within time scales comparable to the folding rates of other repetitive structures, such as the α-helix.[5] However, to increase our understanding of the folding and stability of the collagen triple helix, a system should be available that is equipped with an ultrafast conformational trigger which allows the induced folding/unfolding events to be monitored by time-resolved spectroscopy. This challenging task was realized in the present study by using a purposely designed azobenzene derivative as a photoswitchable conformational clamp which, when incorporated into the single collagen chains as side-chain-to-side-chain crosslink, provides the required changes in the conformational space to trigger folding/unfolding of the collagen triple helix.

In preceding studies from our and other laboratories the concept of using azobenzene for ultrafast photomodulation of conformational states and thus of related biophysical properties has been validated.[6] The successful application of this principle for the photocontrol of α-helices[7] and recently of β-hairpins[8] as the most simple tertiary structure motifs, led us to exploit the favorable optical properties of azobenzene, together with the regular supramolecular structure of the collagen triple helix, for the design of a model system suited for time-resolved spectroscopic studies on collagen folding and unfolding. The strategy applied was to crosslink two side chains of a collagen $(Pro\text{-}Hyp\text{-}Gly)_n$ peptide by the azobenzene chromophore (Scheme 1). As the collagen peptide an N-acetylated and C-amidated $(Gly\text{-}Pro\text{-}Hyp)_7$-Gly-Gly was selected because of the relatively high thermal stability of its triple helix.[9] Molecular modeling served to identify suitable sequence positions in this peptide for grafting the azobenzene clamp intramolecularly so that the *trans*-azobenzene isomer should give a more stable triple helix than the *cis* isomer. Since 100% *trans*-azobenzene isomer can be obtained by thermal relaxation in the dark, a fully folded state would be accessible and unfolding can be induced by irradiation with light at an appropriate wavelength.

Moreover, to maximize the effect of chromophore isomerization on the triple-helix stability, a rather rigid acetylene-type linker between the peptide side chains and the azobenzene moiety was devised. Correspondingly, the bifunctional diiodo derivative **1** was used for reaction with the two thiols (Scheme 1). Taking into account the stabilizing role of imino acids in both the X and Y positions of collagen triplets, 4-mercaptoproline (Mpc) residues were selected to provide the required thiol functions for intramolecular crosslinking. While Cys residues in X and Y positions remarkably affect triple-helix stabilities,[10] a 4-mercapto or 4-thioether substituent in the pyrrolidine ring, as in compounds **2** and **3** (Scheme 1), respectively, was expected to affect, independent of its configuration, the triple-helix stability to a lesser extent than (4*R*)- and (4*S*)-hydroxyproline. Through stereoelectronic effects, the latter influence the *trans–cis* isomerization

[*] Dipl.-Ing. U. Kusebauch,[+] Dr. S. A. Cadamuro,[+] H.-J. Musiol, Prof. Dr. L. Moroder, Priv.-Doz. Dr. C. Renner[++]
Max-Planck-Institut für Biochemie
Am Klopferspitz 18, 82152 Martinsried (Germany)
Fax: (+49) 89-8578-2847
E-mail: moroder@biochem.mpg.de
Dr. M. O. Lenz, Prof. Dr. J. Wachtveitl
Institut für Physikalische und Theoretische Chemie
Johann Wolfgang Goethe-Universität
Max-von-Laue-Strasse 7, 60438 Frankfurt (Germany)
[+] Both authors contributed equally to this work.
[++] Current address: Deutsche Forschungsgemeinschaft
Kennedyallee 40, 53170 Bonn/Bad-Godesberg (Germany)
[**] This work was supported in part by the Deutsche Forschungsgemeinschaft (SFB 533, A8).
Supporting information for this article is available on the WWW under http://www.angewandte.org or from the author.

 © 2006 Wiley-VCH Verlag GmbH & Co. KGaA, Weinheim

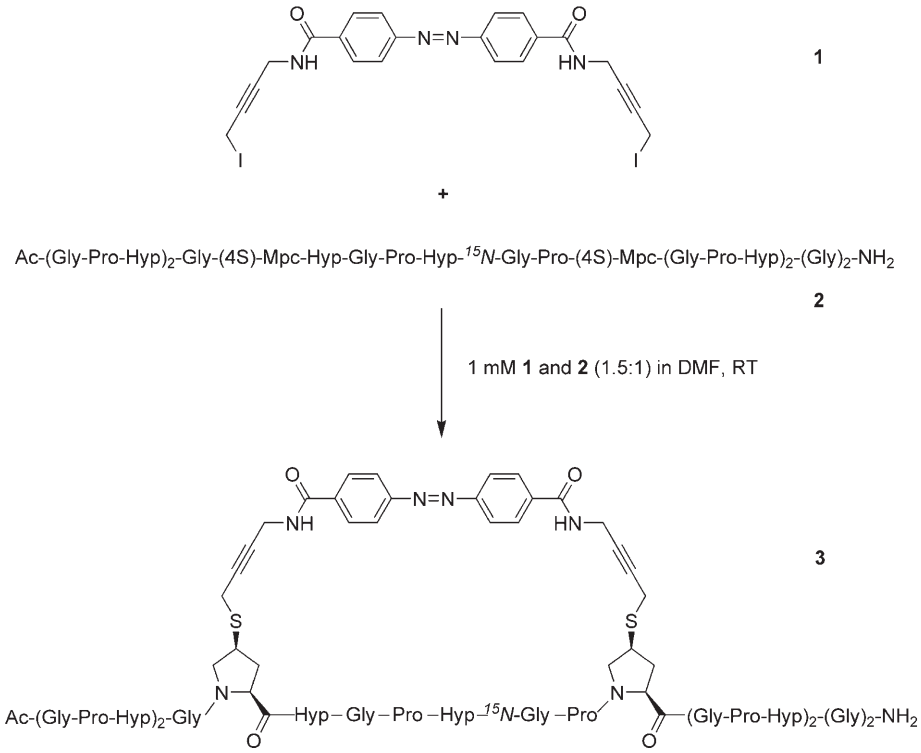

Scheme 1. Synthesis of a collagen peptide with an intramolecular side-chain-to-side-chain bridge containing the photoresponsive azobenzene moiety. For synthetic purposes, the collagen peptide was extended at the C-terminal with two Gly residues to avoid diketopiperazine formation;[10a] Mpc = (2*S*,4*S*)-mercaptopyrrolidine-2-carboxylic acid (4-mercaptoproline).

as well as the C^{γ}-*exo* and C^{γ}-*endo* pucker of the pyrrolidine rings to different extents.[2b,9a,11]

According to the peptide design a Pro residue in the X and a Hyp residue in the Y position should be replaced by Mpc. Despite the known triple-helix stabilizing effect of a C^{γ}-*endo* in X and C^{γ}-*exo* in Y position,[2c,3i,9a,11] the (2*S*,4*S*)-Mpc was used to replace these imino acids in preparing peptide **2** (Scheme 1). Correspondingly, the thermal stability of the triple-helix of **2** in aqueous solution ($T_m = 34.5\,^{\circ}C$) was found to be 8.5 °C lower than that of the reference peptide Ac-(Pro-Hyp-Gly)$_7$-Gly-Gly-NH_2 ($T_m = 43\,^{\circ}C$; this value fully agrees with those reported for similar peptides[9a,b]).

Reaction of peptide **2** with 4,4′-(diazene-1,2-diyl)bis(*N*-(4-iodobut-2-ynyl)benzamide (**1**) led to the azobenzene-peptide (**3**) as an analytically well characterized compound. This peptide derivative is not sufficiently soluble in aqueous media for spectroscopic characterization. Therefore [D_3]MeOH/0.1 M AcOH (4:1) was used as a solvent, since it is well-known that the triple-helical structure of collagen peptides is stabilized in aqueous/alcoholic mixtures.[2a,12] For CD, NMR, and IR spectroscopic measurements solutions of **3** at 1 mM concentration were prepared as required for fast self-association of the monomers into triple-helical homotrimers.[1d,13] Upon incubation at 4 °C, the CD spectrum of peptide **3** (Figure 1) as *trans*-azobenzene isomer is consistent with a triple-helical fold with an Rpn value of 0.190,[14] a value which is identical to that of peptide **2** (Rpn = 0.190) but higher than that of the reference peptide Ac-(Gly-Pro-Hyp)$_7$-Gly-Gly-NH_2 (Rpn = 0.161). However, CD spectral shapes, peak positions, and intensities are not fully conclusive, since the monomeric forms of these proline-rich peptides adopt a poly-Pro-II conformation that generates CD spectra very similar to those of triple helices. Compared to poly-Pro-II helices which unfold thermally without cooperativity, the thermal transitions of collagen triple helices are very cooperative.[1d] Because of the high stability of the collagen superhelix in aqueous MeOH and the limits imposed on heating by this alcoholic solution, a direct comparison of the thermal transitions of the reference peptide Ac-(Gly-Pro-Hyp)$_7$-Gly-Gly-NH_2 and the parent peptide **2** with the azobenzene-peptide **3** was not possible. However, by comparing the initial decrease of dichroic intensities at 225 nm in the temperature range 4 °C to 60 °C, a qualitative rank order of triple-helix stability can be derived: **3** > reference peptide > **2**. The conformation of the triple-stranded collagen structure of **3** was derived from NMR spectroscopic measurements. The chemical shifts of the ^{15}N-Gly amide protons around $\delta = 7.7$ ppm are indicative of the folded structure (unfolded and poly-Pro-II species exhibit shift values higher than $\delta = 8.0$ ppm) and the temperature shifts of the same amide protons are less negative than $-4.5\ \mathrm{ppb\,K^{-1}}$ indicating that hydrogen bonding is present in the triple helix, and diffusion measurements demonstrate the trimeric nature of the peptide under these conditions.[15] 2D ^{1}H–^{15}N correlation spectra (FHSQC) allowed the selective detection of the glycine residue preced-

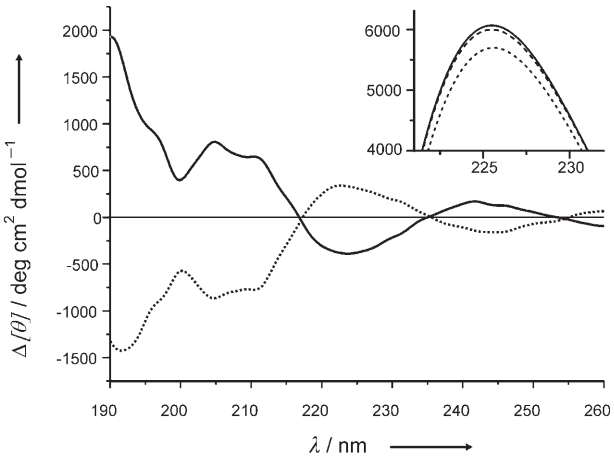

Figure 1. CD difference spectra of peptide **3** at 1 mM concentration in [D_3]MeOH/0.1 M AcOH (4:1) obtained by subtraction of the spectra upon irradiation at 330 nm for *trans*-to-*cis* isomerization (——) and at 420 nm from *cis*-to-*trans* isomerization (•••••). Inset: CD spectra of the thermally relaxed 100% *trans*-azobenzene peptide **3** (——), after irradiation at 330 nm to generate the maximum amount of the *cis* isomer (•••••), and again at 420 nm for conversion of the *cis* isomer back into the *trans* isomer (-----).

 © 2006 Wiley-VCH Verlag GmbH & Co. KGaA, Weinheim

ing the second Mpc residue in **3**. The left panel of Figure 2 shows that the ^{15}N-Gly residues of the three strands that form the triple helix are not equivalent, in line with the known stagger of one amino acid between the individual chains.[1]

Upon irradiation at 330 nm at 4 °C, photoisomerization of the azobenzene moiety was detected giving 27 % *cis* isomer,[16] but the changes in the 2D ^{1}H–^{15}N FHSQC spectra were not indicative of triple-helix unfolding. On increasing the temperature to 27 °C, photoisomerization leads to 45 % *cis* isomer and appearance of several new peaks in the NMR spectrum (Figure 2, right panel) corresponding to unfolded peptide and to "distorted" triple helical forms. By irradiation at 420 nm the triple helix is almost quantitatively restored and the content of *cis*-azobenzene isomer is $<8\,\%$. As the thermal relaxation of the *cis*-azobenzene to the *trans* isomer is slow even at 37 °C ($t_{1/2}=8.9$ h for **3**, $t_{1/2}=25.4$ h for **1** as dichloro derivative) the photostationary state of **3**, with a maximum *cis*-azobenzene content of approximately 45 % as obtained by irradiation at 330 nm can be investigated at 27 °C by NMR spectroscopy.

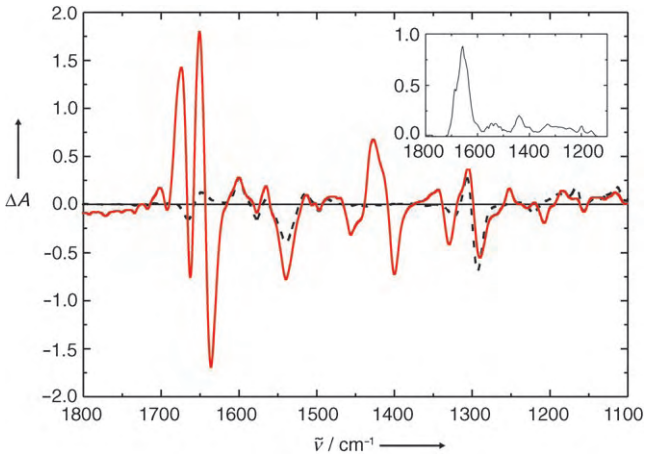

Figure 3. FTIR difference spectra ("*cis* minus *trans*") of peptide **3** (red) in comparison with chromophore **1** as the dichloro derivative (black dashed), both in [D$_6$]DMSO upon irradiation. For the peptide, additional bands can be identified in the regions 1650 cm^{-1} (amide I) and 1450 cm^{-1}. Inset: IR spectrum of peptide **3** in [D$_6$]DMSO.

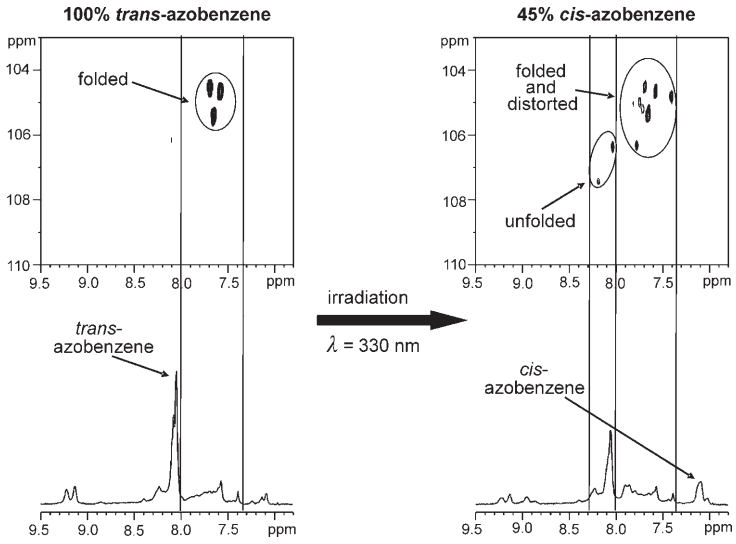

Figure 2. ^{1}H–^{15}N FHSQC (top) and ^{1}H NMR spectra (bottom) of 1 mM peptide **3** in [D$_3$]MeOH/0.1 M AcOH (4:1) recorded at 27 °C and 500 MHz before (left) and after (right) irradiation at 330 nm. After irradiation new signals are present which are assigned to "distorted" triple helices and unfolded monomers; the two signals seen for the unfolded monomer correspond to the *trans* and *cis* conformations of the (^{15}N-Gly)–Pro peptide bond.

The light-induced folding and unfolding of **3** can also be monitored with CD spectroscopy (Figure 1). The changes in CD intensity, however, are weak because of the small differences between the CD spectra of triple-helical and poly-Pro-II structured collagen peptides. Irradiation of **3** leads to significant changes in the IR spectrum (Figure 3). Comparison with the light-induced difference spectrum of **1** (as the stable dichloro derivative) allows the bands related to the *trans*-to-*cis* isomerization of the azobenzene moiety to be identified and also reveals strong additional peptide bands in the regions around 1650 (amide I) and 1450 cm^{-1}, indicative of conformational changes upon triple-helix unfolding.[20a] Photoswitching between the *trans*- and *cis*-azobenzene is fully reversible as shown by the CD spectra in the inset to Figure 1, and no signs of photobleaching or decomposition were observed even after extensive periods of irradiation. As, according to the NMR spectra, at lower temperatures (< 20 °C) even the *cis*-azobenzene isomer is folded into the triple helix, photomodulation of the folded fraction is possible only at temperatures where the difference in stability between the triple-helical and the monomeric form is comparatively small, with *trans*-azobenzene molecules more biased to the triple helix and *cis* isomers favoring the unfolded form.

Combined with the ultrafast isomerization of the chromophore,[17] the collagen peptide **3** should allow folding experiments to be performed with unprecedented time resolution, down to the picosecond time regime, by the use of ultrafast CD[18] and particularly, IR spectroscopy.[19] The IR spectra of triple-helical collagen peptides are characterized by well defined amide bands[20] and when recorded in time-resolved manner, could yield valuable information on the rate constants of formation for the periodic hydrogen-bonding network. Thus, comparison with molecular dynamics calculations that are limited to the nanosecond time scale would become feasible. Indeed, recently it was observed that the fastest folding/unfolding processes of the triple-helical structure are beyond the microsecond resolution of the stopped-flow techniques used.[5]

In summary, we have succeeded in constructing a collagen model peptide where the stability of the triple-helical structure is modulated by the isomeric state of an azobenzene-derived chromophore. At ambient temperatures folding or unfolding can be induced by photo-isomerization of the "light switch". The model peptide should allow ultrafast folding/unfolding experiments to be performed, thus provid-

 © 2006 Wiley-VCH Verlag GmbH & Co. KGaA, Weinheim

ing a link between experimental and theoretical studies on the triple-helical collagen structure.

Received: April 11, 2006
Revised: August 9, 2006
Published online: September 28, 2006

Keywords: collagen · folding/unfolding · peptides · photoswitches · triple helix

[1] a) R. D. B. Fraser, T. P. MacRay, E. Suzuki, *J. Mol. Biol.* **1979**, *129*, 463 – 481; b) P. L. Privalov, *Adv. Protein Chem.* **1982**, *35*, 1 – 104; c) K. Beck, B. Brodsky, *J. Struct. Biol.* **1998**, *122*, 17 – 29; d) H. P. Bächinger, J. Engel in *Protein Folding Handbook*, *Part I* (Eds.: J. Buchner, T. Kiefhaber), Wiley-VCH, Weinheim, **2005**, pp. 1059 – 1109.

[2] a) J. Engel, H. T. Chen, D. J. Prockop, H. Klump, *Biopolymers* **1977**, *16*, 601 – 622; b) E. S. Eberhardt, N. Panasik, R. T. Raines, *J. Am. Chem. Soc.* **1996**, *118*, 12261 – 12266; c) L. Vitagliano, R. Berisio, L. Mazzarella, A. Zagari, *Biopolymers* **2001**, *59*, 459 – 464.

[3] a) K. Okuyama, N. Tanaka, T. Ashida, M. Kakudo, S. Sakakibara, Y. Kishida, *J. Mol. Biol.* **1972**, *72*, 571 – 576; b) J. Bella, M. Eaton, B. Brodsky, H. M. Berman, *Science* **1994**, *266*, 75 – 81; c) R. Z. Kramer, L. Vitagliano, J. Bella, R. Berisio, L. Mazzarella, B. Brodsky, A. Zagari, H. M. Berman, *J. Mol. Biol.* **1998**, *280*, 623 – 638; d) K. Okuyama, V. Nagarajan, S. Kamitori, *Proc. Indian Acad. Sci. Chem. Sci.* **1999**, *111*, 19 – 34; e) C. Hongo, V. Nagarajan, K. Noguchi, S. Kamitori, K. Okuyama, Y. Tanaka, N. Nishino, *Polym. J.* **2001**, *33*, 812 – 818; f) R. Berisio, L. Vitagliano, L.; Mazzarella, A. Zagari, *Protein Sci.* **2002**, *11*, 262 – 270; g) J. Stetefeld, S. Frank, M. Jenny, T. Schulthess, R. A. Kammerer, S. Boudko, K. Landwehr, K. Okuyama, J. Engel, *Structure* **2003**, *11*, 339 – 346; h) J. Bella, B. Brodsky, H. M. Berman, *Structure* **1995**, *3*, 893 – 906; i) L. Vitagliano, R. Berisio, A. Mastrangelo, L. Mazzarella, A. Zagari, *Protein Sci.* **2001**, *10*, 2627 – 2632.

[4] a) H. P. Bächinger, P. Bruckner, R. Timpl, D. J. Prockop, J. Engel, *Eur. J. Biochem.* **1980**, *106*, 619 – 632; b) P. Bruckner, E. F. Eikenberry, D. J. Prockop, *Eur. J. Biochem.* **1981**, *118*, 607 – 613; c) J. Engel, D. J. Prockop, *Annu. Rev. Biophys. Biophys. Chem.* **1991**, *20*, 137 – 152.

[5] A. Bachmann, T. Kiefhaber, S. Boudko, J. Engel, H. P. Bächinger, *Proc. Natl. Acad. Sci. USA* **2005**, *102*, 13897 – 13902.

[6] a) C. Renner, U. Kusebauch, M. Löweneck, A. G. Milbradt, L. Moroder, *J. Pept. Res.* **2005**, *65*, 4 – 14; b) G. A. Woolley, *Acc. Chem. Res.* **2005**, *38*, 486 – 493; c) C. Renner, L. Moroder, *ChemBioChem* **2006**, *7*, 868 – 878.

[7] J. R. Kumita, O. S. Smart, G. A. Woolley, *Proc. Natl. Acad. Sci. USA* **2000**, *97*, 3803 – 3808.

[8] a) V. Kräutler, A. Aemissegger, P. H. Hünenberger, D. Hilvert, T. Hanson, W. F. van Gunsteren, *J. Am. Chem. Soc.* **2005**, *127*, 4935 – 4942; b) S.-L. Dong, M. Löweneck, T. Schrader, W. J. Schreier, W. Zinth, L. Moroder, C. Renner, *Chem. Eur. J.* **2006**, *12*, 1114 – 1120.

[9] a) L. E. Bretscher, C. L. Jenkins, K. M. Taylor, M. L. DeRider, R. T. Raines, *J. Am. Chem. Soc.* **2001**, *123*, 777 – 778; b) D. Barth, O. Kyrieleis, S. Franke, C. Renner, L. Moroder, *Chem. Eur. J.* **2003**, *9*, 3703 – 3714.

[10] a) A. V. Persikov, J. A. M. Ramshaw, A. Kirkpatrick, B. Brodsky, *Biochemistry* **2000**, *39*, 14960 – 14967; b) A. V. Persikov, J. A. M. Ramshaw, B. Brodsky, *J. Biol. Chem.* **2005**, *280*, 19343 – 19349.

[11] a) N. Panasik, E. S. Eberhardt, A. S. Edison, D. R. Powell, R. T. Raines, *Int. J. Pept. Protein Res.* **1994**, *44*, 262 – 269; b) M. L. DeRider, S. J. Wilkens, M. J. Waddell, L. E. Bretscher, F. Weinhold, R. T. Raines, J. L. Markley, *J. Am. Chem. Soc.* **2002**, *124*, 2497 – 2505; c) C. L. Jenkins, L. E. Bretscher, R. T. Raines, *Biochemistry* **2001**, *40*, 8658 – 8658.

[12] Y. Feng, G. Melacini, J. P. Taulane, M. Goodman, *J. Am. Chem. Soc.* **1996**, *118*, 10351 – 10358.

[13] S. P. Boudko, J. Engel, *J. Mol. Biol.* **2004**, *335*, 1289 – 1297.

[14] Rpn denotes the ratio of the positive maximum intensity over the negative maximum intensity and is used as index of triple-helical fold and stability (see also ref. [12]).

[15] The chemical shifts of the folded labeled glycine residues are $\delta =$ 7.691, 7.653, and 7.574 ppm at 27 °C and the temperature shifts relative to these values are −2.5, −3.8, and −4.1 ppb K^{-1}, respectively. The translational diffusion constants (given in 10^{-10} $m^2 s^{-1}$) at 4 °C for peptide **2** (1.09) and peptide **3** (0.90 before and 0.82, after irradiation) are indicative of trimeric species; at 27 °C the values for peptide **2** (1.34) and for peptide **3** before irradiation (1.15) correspond again to trimeric species, while after irradiation of **3** in addition to the trimeric species (0.61 and 1.07) a second species is formed, which shows a diffusion constant of 1.55 supporting the presence of an unfolded monomeric form.

[16] The relative amounts of *trans* and *cis* isomers were determined by integrating the signals of the amidic protons of the azobenzene moiety in the 1D ^{1}H NMR spectra at $\delta = 9.34$ and 9.08 ppm (4 °C), 9.21 and 8.94 ppm (22 °C), and 9.18 and 8.86 ppm (27 °C), respectively.

[17] a) R. Nägele, R. Hoche, W. Zinth, J. Wachtveitl, *Chem. Phys. Lett.* **1997**, *272*, 489 – 495; b) I. K. Lednev, T.-Q. Ye, P. Matousek, M. Towrie, P. Foggi, F. V. R. Neuwahl, S. Umapathy, R. E. Hester, J. N. Moore, *Chem. Phys. Lett.* **1998**, *290*, 68 – 74.

[18] T. Dartigalongue, F. Hache, *Chem. Phys. Lett.* **2005**, *415*, 313 – 316.

[19] a) J. Helbing, H. Bregy, J. Bredenbeck, R. Pfister, P. Hamm, R. Huber, J. Wachtveitl, L. De Vico, M. Olivucci, *J. Am. Chem. Soc.* **2004**, *126*, 8823 – 8834; b) J. Bredenbeck, J. Helbing, A. Sieg, T. Schrader, W. Zinth, J. Wachtveitl, C. Renner, R. Behrendt, L. Moroder, P. Hamm, *Proc. Natl. Acad. Sci. USA* **2003**, *100*, 6452 – 6457.

[20] a) Y. A. Lazarev, B. A. Grishkovsky, T. B. Khromova, *Biopolymers* **1985**, *24*, 1449 – 1478; b) K. J. Payne, A. Veis, *Biopolymers* **1988**, *27*, 1749 – 1760; c) Y. A. Lazarev, A. V. Lazareva, V. M. Komarov, *J. Biol. Phys.* **1999**, *24*, 217 – 221.

 © 2006 Wiley-VCH Verlag GmbH & Co. KGaA, Weinheim

Supramolecular Chemistry

DOI: 10.1002/anie.200601961

Cocrystallization and Encapsulation of a Fluorophore with Hexameric Pyrogallol[4]arene Nanocapsules: Structural and Fluorescence Studies**

Scott J. Dalgarno, Daniel B. Bassil, Sheryl A. Tucker, and Jerry L. Atwood**

The ability to encapsulate space is a concept that has attracted considerable attention in recent years. Significant advances have been made towards the formation of stable noncovalent assemblies that are voluminous and that show potential for molecular encapsulation.[1] We, amongst others, have been interested in the formation of large hydrogen-bonded nanocapsules based on *C*-methylresorcin[4]arene (CMRC, **1**; Figure 1) or the closely related *C*-alkylpyrogallol[4]arenes (general notation PgC*n*, **2**; Figure 1).[2–6] We have also shown that the latter form noncovalent nanotubes in the solid state under particular solvent conditions.[7] For CMRC, six calixarene building blocks assemble with eight structural water molecules into a near-spheroidal hexamer, which is stabilized by concerted hydrogen bonding.[2] Pyrogallol[4]arenes contain additional "upper-rim" hydroxy groups compared to CMRC which results in a larger number of hydrogen-bonding interactions per hexamer formed, preclusion of structural water molecules from the hydrogen-bonded capsule seam, and enhanced stability of the nanocapsule.[4–6] Alternative covalent approaches have been used to form pentameric "superbowls"[8a] or hexameric calixarene-based assemblies of relatively comparable size to those described above;[8b,c] however, inclusion of non-solvent guests is yet to be reported for such arrangements. Furthermore, metal-coordination approaches have also been used to form completely or partially sealed pyrogallol[4]arene-based hexamers.[9]

Some of our recent studies focused on the use of a fluorescent probe molecule (pyrene butyric acid, PBA) to report on the order of the inner phase of a PgC_6 hexamer (hexamer framework shown as $(\mathbf{2a})_6$ in Figure 1).[6e] This process involved the addition of a quenching agent (dimethylaniline, DMA) to a solution of the PBA-containing hexamers, the overall structures of which were found to be stable in the solution phase. Given this result, we sought to encapsulate a fluorescent probe molecule with a built-in

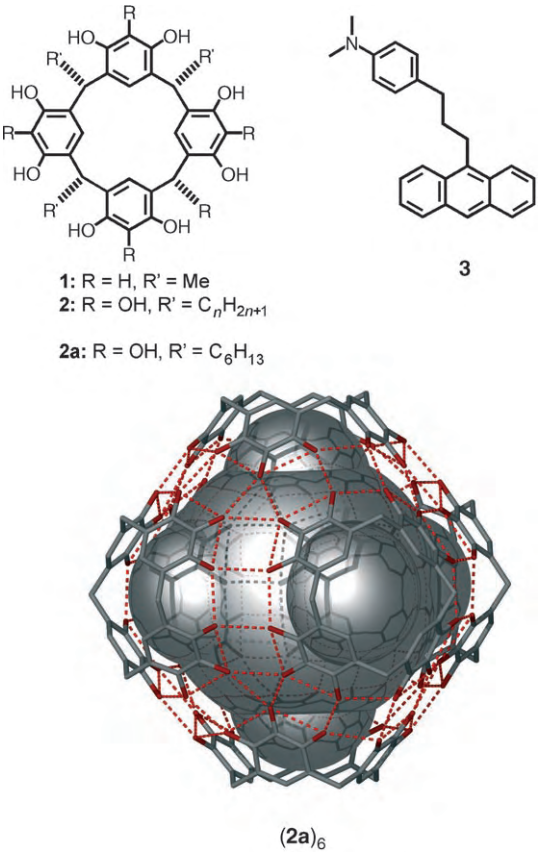

Figure 1. Structures of CMRC (**1**), PgC*n* (**2**), PgC_6 (**2a**), and ADMA (**3**), and a diagram of the PgC_6 hexamer framework $(\mathbf{2a})_6$ showing the possible space for molecular encapsulation (framework shown in stick representation: C gray, O red; internal volume shown in gray space-filling representation).

quencher to further examine the capsule microenvironment in terms of conformational restriction and probe movement. For this purpose, we selected 4-[3-(9-anthryl)propyl]-*N*,*N*-dimethylaniline (ADMA, **3**) as a probe for inclusion in the $(\mathbf{2a})_6$ nanocapsule. Following excitation of the anthryl moiety, the ADMA fluorophore can undergo charge transfer by accepting an electron from the DMA fragment. Furthermore, exciplex formation may be observed as the DMA portion folds to form a sandwich-like arrangement with the anthryl moiety.[10]

By using the same procedures employed for the inclusion of PBA, ADMA was found to crystallize either *exo* (occasionally) or *endo* (frequently) with respect to the $(\mathbf{2a})_6$ framework (see Supporting Information).[6e] For the *exo*-capsule ADMA array, small, colorless, cubic-shaped crystals occasionally grew during the slow evaporation step. Structural analysis showed the probe to be *exo* to the nanocapsule and to form an unexpected supramolecular array by intercalating between hexamers, forming channels in the solid state. For the *endo*-capsule ADMA array, the unit cell parameters of the crystals were identical to those of the pure acetonitrile (MeCN) solvate.[11] On examining the crystals under a UV lamp (365 nm), the observation of strong fluorescence confirmed the presence of the fluorophore within the nanocapsules. Herein, we report the single-crystal X-ray structure

[*] Dr. S. J. Dalgarno, D. B. Bassil, Dr. S. A. Tucker, Prof. J. L. Atwood
Department of Chemistry
University of Missouri-Columbia
601 South College Avenue, Columbia, MO 65211 (USA)
Fax: (+1) 573-882-2754
E-mail: tuckers@missouri.edu
atwoodj@missouri.edu

[**] We thank the NSF for financial support.
Supporting information for this article is available on the WWW under http://www.angewandte.org or from the author.

© 2006 Wiley-VCH Verlag GmbH & Co. KGaA, Weinheim

of the *exo*-capsule ADMA array, unit cell dimensions of crystals of the *endo*-capsule ADMA array, and solution-phase studies for both structural arrangements that show markedly different probe behavior.

Single-crystal X-ray diffraction studies of crystals of the *exo*-capsule ADMA array revealed them to be weakly diffracting.[12a] The crystals were in a triclinic system, and solution of the structure showed the asymmetric unit to contain half of a hexameric nanocapsule, a total of 1.5 molecules of ADMA disordered over four positions (stoichiometry confirmed by ^{1}H NMR spectroscopy; see Supporting Information), and a number of badly disordered acetonitrile molecules. The most noticeable feature of the asymmetric unit is that the probe is *exo* to the large internal cavity of the PgC_6 nanocapsule. Although there is significant disorder present within the structure, symmetry expansion of the asymmetric unit reveals a number of very interesting features in the extended array when compared with the simple PgC_6 MeCN solvate nanocapsule.[11] The structure is described in three parts: nanocapsule packing differences, interactions associated with full-occupancy ADMA, and the environment surrounding the badly disordered half-occupancy ADMA.

Examination of the packing of neighboring nanocapsules in the MeCN solvate structure revealed that the hexamers pack in a near-cubic-close-packed arrangement (Figure 2a).[11] The walls of neighboring nanocapsules (aligned along the *a* axis, Figure 2b) were found to interact through π stacking between aryl rings, thereby resulting in a short intercapsule distance of 19.573 Å (see Supporting Information for a full depiction of the intercapsule distances for both structures). The structure of the *exo*-capsule ADMA array revealed that the packing of adjacent hexamers is altered, as shown by the capsule spacings in Figure 2c (and the intercapsule distances listed in the Supporting Information, the shortest of which is 22.026 Å). When comparing the nanocapsules aligned along the *a* axes (Figure 2b and d), these appear to be slipped relative to the MeCN solvate and instead of π stacking, there is a crystallographically unique CH···π interaction from a neighboring PgC_6 hexyl chain to an aromatic ring with a CH···aryl centroid distance of 3.386 Å.

Upon examining the environment of the ADMA that is at full-occupancy over two closely disordered positions, numerous CH···π, CH···O, and π-stacking interactions are observed between the probe and neighboring molecules (observable to some extent in Figure 3). Perhaps the most influential of these interactions occurs between the faces of neighboring nanocapsules: two ADMA molecules (related by an inversion center) dimerize through N···aryl interactions from the nitro-

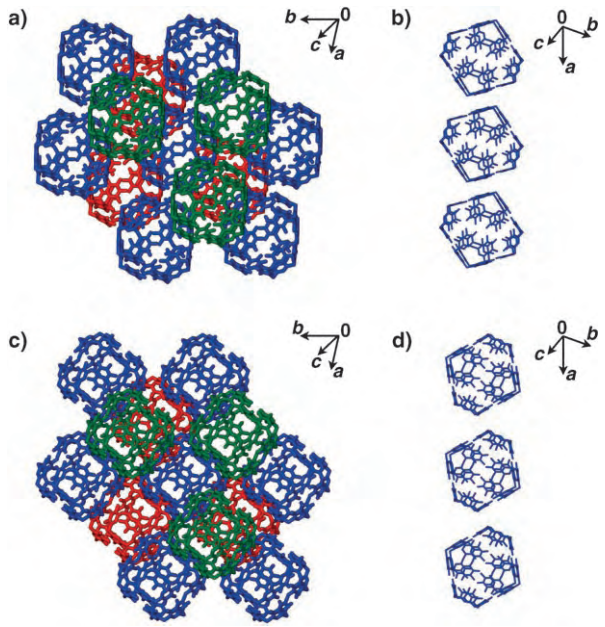

Figure 2. Comparison of the solid-state packing of PgC_6 hexamers in the MeCN solvate (a and b), and in the *exo*-capsule ADMA array (c and d). For the MeCN solvate, the hexameric nanocapsules form a near-cubic-close-packed arrangement (a) with π-stacking interactions between neighboring faces (b).[11] In the structure of the *exo*-capsule ADMA array, the nanocapsules pack with some larger intercapsule spacings (between centroids), as can be seen, for example, by the separation of blue nanocapsules along the *ab* diagonal (all separations are shown in the Supporting Information). For comparison with the MeCN solvate, the closest face-to-face interactions (b and d) show the hexamers in the *exo*-capsule ADMA array to be "slipped" in their alignment along the *a* axis.[11]

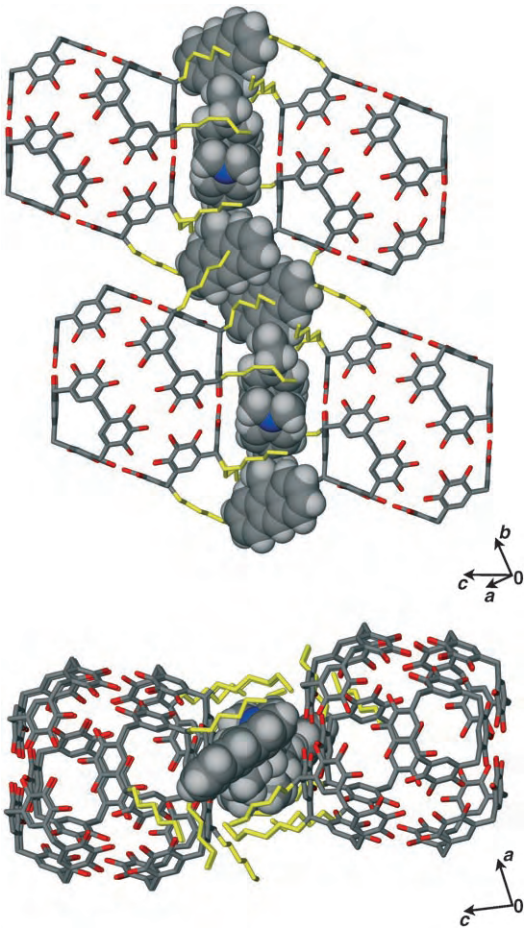

Figure 3. Two views of the ADMA channels (space-filling representation: C gray, N blue) formed by fluorophore intercalation between walls of neighboring nanocapsules (stick representation: C gray, O red). The PgC_6 hexyl chains proximate to the ADMA channels are shown in yellow, whilst all others are removed for clarity.

 © 2006 Wiley-VCH Verlag GmbH & Co. KGaA, Weinheim

gen atom of one DMA fragment to the aromatic ring of the symmetry-related DMA moiety (N···aryl centroid distance of 2.755 Å). Also, aryl hydrogen atoms of the DMA fragments form CH···π interactions to neighboring aryl rings of nanocapsule walls, with CH···aryl centroid distances of 2.818 and 3.361 Å. The proximate PgC_6 hexyl chains wrap around the probe molecules and interact through numerous CH···π interactions. The result of these concerted interactions is the formation of an ADMA channel within the extended structure (Figure 3).

The structure is badly disordered in the region containing the half-occupancy ADMA molecule, which is also disordered over two positions. This molecule occupies discrete interstitial sites between nanocapsules (completely surrounded by PgC_6 molecules/hexyl chains) that are also partially occupied by disordered *C*-hexyl chains. Given the extent of the disorder, it was not possible to precisely identify intermolecular interactions for discussion here.

To some extent, the solution-state results are consistent with the solid-state structure.[13] In THF, free ADMA shows clear exciplex emission at 550 nm as a result of charge transfer (CT, Figure 4a).[14] Crystals of the *exo*-capsule ADMA array were dissolved in dry THF and shaken for approximately 5 minutes prior to study of the fluorescence emission. The fluorescence emission intensity of the anthracene moiety of ADMA in the dissolved crystal solution increased by approximately 40% relative to free ADMA and is attributed to the intercalation of the probe between the nanocapsule assemblies. The exciplex emission intensity is reduced, which

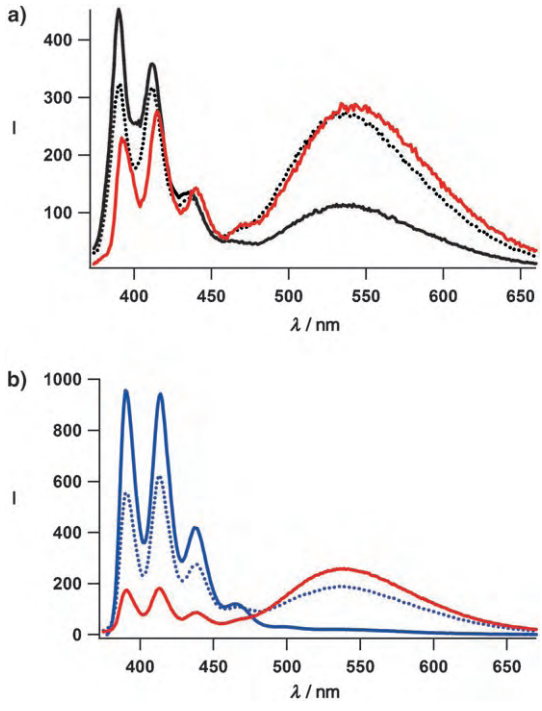

Figure 4. Spectral profiles (relative fluorescence intensities (I)): a) Free ADMA in THF (red), as well as the *exo*-capsule ADMA array in THF before (solid black line) and after sonication (dotted black line). b) Free ADMA in THF (red), as well as the *endo*-capsule ADMA array in THF at day zero (solid blue line) and after 14 days (dotted blue line).

is presumably due to enforced elongation of the ADMA molecules that are sandwiched in the channels between adjacent hexamers (black line, Figure 4a). To determine if this was the case, the solution was sonicated for 2 minutes and reexamined. Post sonication, the proposed structure/aggregate in solution appears to break apart, thereby releasing ADMA and allowing folding to occur; the emission spectrum resembles that of free ADMA in THF (Figure 4a). The spectral profile measured 12 h after sonication did not change, that is, the emission from ADMA in the sample remains similar to that of free ADMA in THF. This result indicates that at this concentration (10^{-6} M), ADMA does not reassociate with the nanocapsules to a significant extent, which would be identifiable by changes in the fluorescence emission spectrum.

For the *endo*-capsule ADMA array, unit cell dimensions of the single crystals closely matched those found for the PBA-containing nanocapsules and the MeCN solvate of $(\mathbf{2a})_6$.[6e,11,12b] Structural analysis showed the PgC_6 nanocapsule as expected, although the interior volume showed a complete lack of order. ^{1}H NMR spectroscopy revealed that the ADMA occupancy in the capsules was approximately 50%, assuming that each nanocapsule accommodates only one guest (see Supporting Information).[15]

Solution studies of crystals of the *endo*-capsule ADMA array dissolved in THF are consistent with the solid-state structure observed—they show that **3** *is* encapsulated in the MeCN-containing nanocapsule and does not reside exterior to the capsule in THF.[13] The fluorescence emission spectrum of the *endo*-capsule ADMA array (Figure 4b) shows little, if any, CT emission, which is consistent with the fact that the ADMA CT complex is not emissive in pure MeCN. Given that the crystals were grown from MeCN, **3** must be either encapsulated in a MeCN microenvironment or significantly constrained, as the presence of THF would cause prominent exciplex emission. Compared to free ADMA, the fluorescence emission intensity of the anthracene moiety of the *endo*-capsule ADMA array is dramatically increased (Figure 4b). This enhancement is attributed to the structural constraints imposed by the nanocapsule and to the protective nature of the host structure that most likely minimizes the possibility of non-radiative, excited-state deactivation, such as collisional quenching by solvent molecules.

In our previous studies concerning the encapsulation of PBA within $(\mathbf{2a})_6$, guest-to-wall binding was observed in both the solution and solid states, and was attributed to π-stacking and CH···π interactions between PBA and aryl rings of PgC_6 molecules.[6e] There is no spectral evidence to suggest that this type of interaction occurs with **3**. Moreover, the amount of PBA that leached from the capsules over 4 weeks, as measured by exciplex formation with DMA, was about 10%. The structural integrity of the the *endo*-capsule ADMA assembly is uncertain at this point. After 14 days, CT emission appears in the spectral profile, indicating either that around 40% of the encapsulated ADMA leaches from the capsules (Figure 4b) or that THF enters the capsule thereby facilitating CT emission.

To conclude, we have shown that relatively small molecules can dramatically change the extended packing of large

 © 2006 Wiley-VCH Verlag GmbH & Co. KGaA, Weinheim

robust supramolecular entities through a series of noncovalent interactions. Intercalated *exo*-capsule ADMA offers the opportunity to study the arrangement in the solution phase through fluorescence spectroscopy, and future studies will focus on both steady-state and dynamic fluorescence techniques with the possibility of elucidating nanocapsule dispersion times in the solution phase. Studies on encapsulated ADMA continue with a view to examining the stability of the assembly, as well as the fluorescence lifetime and conformational behavior of the guest.

Received: May 17, 2006
Published online: October 2, 2006

Keywords: calixarenes · charge transfer · fluorescence · structure elucidation · supramolecular chemistry

[1] J.-M. Lehn, *Supramolecular Chemistry: Concepts and Perspectives*, VCH, Weinheim, **1995**; J. W. Steed, J. L. Atwood, *Supramolecular Chemistry: A Concise Introduction*, Wiley, Chichester, **2000**.

[2] L. R. MacGillivray, J. L. Atwood, *Nature* **1997**, *389*, 469 – 472.

[3] A. Shivanyuk, J. Rebek, Jr., *Chem. Commun.* **2001**, *22*, 2374 – 2375; A. Shivanyuk, J. Rebek, Jr., *J. Am. Chem. Soc.* **2003**, *125*, 3432 – 3433; M. Yamanaka, A. Shivanyuk, J. Rebek, Jr., *J. Am. Chem. Soc.* **2004**, *126*, 2939 – 2943; J. Rebek, Jr., *Angew. Chem.* **2005**, *117*, 2104 – 2115; *Angew. Chem. Int. Ed.* **2005**, *44*, 2068 – 2078; L. C. Palmer, J. Rebek, Jr., *Org. Lett.* **2005**, *7*, 787 – 789.

[4] T. Gerkensmeier, W. Iwanek, C. Agena, R. Frölich, S. Kotila, C. Näther, J. Mattay, *Eur. J. Org. Chem.* **1999**, 2257 – 2262.

[5] L. Avram, Y. Cohen, *Org. Lett.* **2003**, *5*, 3329 – 3332; L. Avram, Y. Cohen, *J. Am. Chem. Soc.* **2003**, *125*, 16180 – 16181; L. Avram, Y. Cohen, *J. Am. Chem. Soc.* **2005**, *127*, 5714 – 5719; Y. Cohen, L. Avram, L. Frish, *Angew. Chem.* **2005**, *117*, 524 – 560; *Angew. Chem. Int. Ed.* **2005**, *44*, 520 – 554.

[6] a) J. L. Atwood, L. J. Barbour, A. Jerga, *Chem. Commun.* **2001**, *22*, 2376 – 2377; b) J. L. Atwood, L. J. Barbour, A. Jerga, *J. Supramol. Chem.* **2002**, *1*, 131 – 134; c) J. L. Atwood, L. J. Barbour, A. Jerga, *Proc. Natl. Acad. Sci. USA* **2002**, *99*, 4837 – 4841; d) G. W. V. Cave, J. Antesberger, L. J. Barbour, R. M. McKinlay, J. L. Atwood, *Angew. Chem.* **2004**, *116*, 5375 – 5378; *Angew. Chem. Int. Ed.* **2004**, *43*, 5263 – 5266; e) S. J. Dalgarno, S. A. Tucker, D. B. Bassil, J. L. Atwood, *Science* **2005**, *309*, 2037 – 2039.

[7] S. J. Dalgarno, G. W. V. Cave, J. L. Atwood, *Angew. Chem.* **2006**, *118*, 584 – 588; *Angew. Chem. Int. Ed.* **2006**, *45*, 570 – 574.

[8] a) E. S. Barrett, J. L. Irwin, A. J. Edwards, M. S. Sherburn, *J. Am. Chem. Soc.* **2004**, *126*, 16747 – 16749; b) D. A. Makeiff, J. C. Sherman, *J. Am. Chem. Soc.* **2005**, *127*, 12363 – 12367; c) X. Liu, Y. Liu, G. Li, R. Warmuth, *Angew. Chem.* **2006**, *118*, 915 – 918; *Angew. Chem. Int. Ed.* **2006**, *45*, 901 – 904.

[9] R. M. McKinlay, G. W. V. Cave, J. L. Atwood, *Proc. Natl. Acad. Sci. USA* **2005**, *102*, 5944 – 5948; R. M. McKinlay, P. K. Thallapally, G. W. V. Cave, J. L. Atwood, *Angew. Chem.* **2005**, *117*, 5879 – 5882; *Angew. Chem. Int. Ed.* **2005**, *44*, 5733 – 5736.

[10] T. J. Chuang, R. J. Cox, K. B. Eisenthal, *J. Am. Chem. Soc.* **1974**, *96*, 6828 – 6831.

[11] S. J. Dalgarno, R. M. McKinlay, J. Antesberger, J. L. Atwood, unpublished results.

[12] a) Crystal data for the *exo*-capsule ADMA array: $C_{209}H_{276.75}N_{9.25}O_{36}$, $M_r = 3494.65$, triclinic, $a = 22.026(3)$, $b = 22.631(3)$, $c = 24.430(3)$ Å, $\alpha = 73.184(3)$, $\beta = 65.777(3)$, $\gamma = 77.975(3)°$, $U = 10575(2)$ Å^3, $\mu = 1.098$ mm^{-1}, $T = 173(2)$ K, space group $P\bar{1}$, $Z = 2$, $Mo_{K\alpha}$ radiation ($\lambda = 0.71073$ Å), GOF = 1.066, agreement index $R_1 = 0.1657$, 59608 reflections measured, 44761 unique ($R_{int} = 0.0933$) which were used in all calculations. The final $\omega R(F^2)$ value was 0.4536 (all data). The crystals were weakly diffracting and the structure has a number of badly disordered regions. CCDC 603842 contains the supplementary crystallographic data for this paper. These data can be obtained free of charge from The Cambridge Crystallographic Data Centre via www.ccdc.cam.ac.uk/data_request/cif. b) Unit cell dimensions for the *endo*-capsule ADMA array (crystal structure): triclinic, $a = 19.5574(41)$, $b = 22.6032(47)$, $c = 23.4174(49)$ Å, $\alpha = 69.7844(34)$, $\beta = 70.0905(41)$, $\gamma = 71.9823(37)°$, $U = 8915(5)$ Å^3. This data was not submitted to the CCDC as no structural information relating to the interior volume of the nanocapsule could be reported as a result of the disorder and guest occupancy ($\approx 50\%$). These dimensions are consistent with those of the acetonitrile solvate for $(\mathbf{2a})_6$ and $(\mathbf{2a})_6 \cdot 1.5$ PBA.[6c,11]

[13] All measurements were performed at optically dilute concentrations (10^{-6} M) of ADMA (free, *exo*, or *endo*) in THF at room temperature. Fluorescence emission spectra were measured on a Varian Cary Eclipse Fluorometer with the following parameters: 15-W xenon arc lamp (pulsed at 80 Hz), excitation and emission step size of 2 nm, and a bandpass of 5 nm.

[14] M. Khajepour, J. F. Kauffman, *J. Phys. Chem. A* **2000**, *104*, 7151 – 7159.

[15] The occupancy is relatively low compared to that found for encapsulated PBA (1.5 molecules per hexamer), and given the fact that ADMA could be oriented over three equivalent axes within the crystal structure it is the likely reason for the irresolvable nature of the capsule interior.

 © 2006 Wiley-VCH Verlag GmbH & Co. KGaA, Weinheim

Metal Phosphate Clusters

DOI: 10.1002/anie.200601979

Octameric and Decameric Aluminophosphates**

Ramaswamy Murugavel and Subramaniam Kuppuswamy*

Dedicated to Professor C. N. R. Rao

Since the discovery of a novel class of microporous aluminophosphate materials ($AlPO_4$-*n*) nearly 25 years ago, the chemistry of AlPOs has seen a tremendous growth.[1] In particular, use of structurally diverse organic templates has yielded a wide variety of lower dimensional (0D, 1D, and 2D)

[*] Prof. R. Murugavel, S. Kuppuswamy
Department of Chemistry, IIT-Bombay
Powai, Mumbai-400076 (India)
Fax: (+91) 22-2572-3480
E-mail: rmv@chem.iitb.ac.in
Homepage: http://www.chem.iitb.ac.in/people/Faculty/prof/rmv.html

[**] This work was supported by DST, New Delhi, in the form of a Swarnajayanti Fellowship to R.M. We thank the National Single Crystal X-ray Diffractometer Facility and SAIF (IIT-Bombay) for the diffraction and spectroscopic data, respectively.

WILEY InterScience DISCOVER SOMETHING GREAT
© 2006 Wiley-VCH Verlag GmbH & Co. KGaA, Weinheim

and framework (3D) metal phosphates.[2,3] Parallel to the developments in the area of aluminophosphate materials, there has also been considerable interest in synthesizing discrete and soluble model compounds (and/or structural building units (SBUs) of zeolites) for a better understanding of the mechanism of the formation of zeolites.[4–6] The use of H_3PO_4 for this purpose has limited scope owing to its poor solubility in solvents other than water. Tilley and co-workers[5a,b] and our group[7] have partially overcome this problem by using a diester of H_3PO_4 (di-*tert*-butylphosphate; dtbpH) for the preparation of a wide range of molecular phosphates which could be decomposed at low temperatures to yield metal phosphate materials with exceptional surface area. Significant among these results are a) the facile synthesis of cyclic aluminophosphates with a "single 4-ring" (S4R) core, which serve as precursors for the low-temperature preparation of aluminophosphate (AlPO)[5a] and silicoaluminophosphate (SAPO)[5b] materials, and b) the conversion of one of these molecular phases into 2D framework solids.[3a]

Although dtbpH has been a great success in terms of the preparation of thermally labile metal phosphates, the presence of only one P-OH group means that dtbpH produces only cyclic or 1D polymeric phosphates and not cage-like molecules.[7] We have now overcome this problem by using a phosphoric acid mono-aryl ester[8] to synthesize two novel nanometric aluminophosphate clusters **1** and **2**.

$[Al_{10}\{\mu_3\text{-}O_3P(OR)\}_{12}(\mu_3\text{-}O)_2(O\mathit{i}Pr)_2(thf)_4]\cdot 6\,C_7H_8$ **1**

$[Al_8\{\mu_3\text{-}O_3P(OR)\}_8\{\mu_2\text{-}HO_3P(OR)\}_2(\mu_3\text{-}O)_2(\mu_2\text{-}OH)_2(thf)_4]\cdot 2\,C_7H_8$ **2**

$R = 2,6\text{-}\mathit{i}Pr_2C_6H_3$

The title clusters have been obtained by stirring an equimolar solution of $Al(O\mathit{i}Pr)_3$ and diisopropylphenylphosphate ($dippH_2$) at room temperature in tetrahydrofuran (THF) under dry dinitrogen atmosphere.[9] Cluster **1** is obtained when a THF solution of $Al(O\mathit{i}Pr)_3$ was added to a THF solution of $dippH_2$, while a reverse addition was necessary to obtain **2**. Compound **1** is soluble in common organic solvents despite its very high molecular weight. A single-crystal X-ray diffraction study confirms the molecular formula for **1** with six cocrystallized toluene solvate molecules,[10] whereas the vacuum-dried sample has lost five toluene solvate molecules.[11] In the ^{31}P NMR spectrum, six separate resonances of similar intensity were observed in the upfield range $\delta = -16.1$ to -26.5 ppm, suggesting the presence of six magnetically non-equivalent $\{(OR)PO_3\}^{2-}$ ligands (Figure 1).

The elemental analysis of **2** reveals the complete loss of solvent toluene molecules during the vacuum drying of the sample. The IR spectrum of **2** is essentially identical to **1** but for the presence of an additional weak absorption at $\tilde{\nu} = 2280\ cm^{-1}$ arising from the P-OH group. Unlike **1**, compound **2** is insoluble in all common NMR spectroscopy solvents. Both clusters are thermally stable and do not melt up to 275 °C. Thermolysis of these clusters at higher temperatures results in their conversion into dense-phase $AlPO_4$ materials.

Compound **1** crystallizes in $P\bar{1}$ space group with a large cell volume (5663 $Å^3$), corresponding to the volume of a single molecule of **1** that contains as many as 286 non-hydrogen atoms and has a molecular weight of 4336. The molecule, which displays several interesting structural features, is made up of two units which are connected together across the crystallographic inversion center (Figure 2). The molecular dimensions of **1** are similar to the unit cell dimensions. In fact the length of the molecule (ca. 25.0 Å) is longer than the largest unit cell dimension (*c* axis: ca. 21.05 Å). The size of the inorganic core excluding the organic substituents on the cluster is about 2 nm. A view of the cluster shown in Figure 2 demonstrates the spherical nature of the two $[Al_5(O_3P(OR))_6]$ units (which are built around a μ_3-O center which bridges Al3, Al4, Al5) as well as the presence of

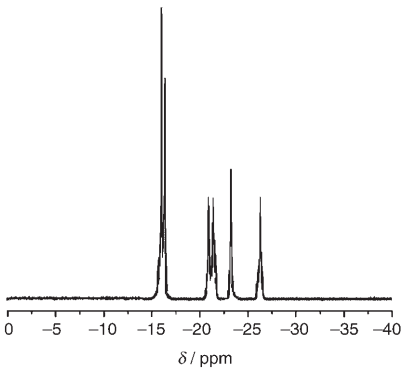

Figure 1. ^{31}P NMR spectrum of **1**.

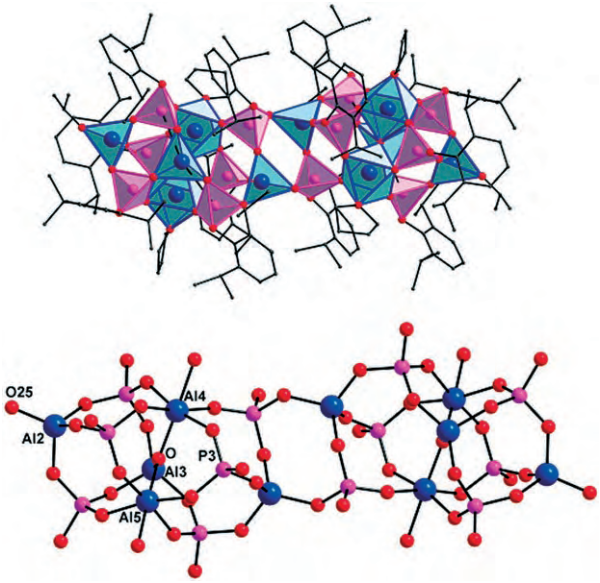

Figure 2. Molecular (top; Al and P coordination environments in polyhedral representation) and core (bottom) structure of **1** (C black, O red, Al blue, P pink). Selected bond lengths [Å] and angles [°]: Al–O(P) 1.723(2)–1.941(2) (av. 1.809), Al–O(*i*Pr) 1.656(2), Al–O(Al) 1.753(2), 1.917(2), 1.929(2), Al–O(thf) 1.966(2), 2.024(2), P–O(Al) 1.482(2)–1.538(2) (av. 1.514), P–O(Ar) 1.571(2)–1.587(2) (av. 1.577); O-Al1-O 107.9(1)–112.9(1), O-Al2-O 105.6(1)–113.2(1), O-Al3-O 102.2(1)–120.1(1), O-Al4-O (*cis*) 84.0(1)–95.5(1), (*trans*) 168.8(1), 172.6(1), 178.5(1), O-Al5-O (*cis*) 84.5(1)–96.5(1), (*trans*) 168.8(1), 175.6(1), 178.0(1), Al-O-P 118.4(1)–154.8(1), Al3-O-Al4 121.7(1), Al3-O-Al5 112.5(1), Al4-O-Al5 125.6(1); cluster dimensions [Å]: O25···O25′ 20.7, Al2···Al2′ 17.5.

 © 2006 Wiley-VCH Verlag GmbH & Co. KGaA, Weinheim

a central 4-ring that connects the two units. A closer inspection reveals that each of these $[Al_5(O_3P(OR))_6]$ units is made up of three 3-rings, five 4-rings, and a 6-ring. The cluster as a whole encloses six 3-rings, eleven 4-rings, and two 6-rings and has an architecture which has not been, to our knowledge, observed in any of the known SBUs of aluminophosphate frameworks. Interestingly, the five aluminum ions in each half of the molecule have four different coordination environments. While two of the aluminum ions are six-coordinated with an octahedral geometry, the three tetrahedral aluminum ions have three different coordination environments (one aluminum atom surrounded by four phosphate oxygen atoms, one aluminum atom surrounded by three phosphate oxygen atoms and one O^{2-} ion, and one aluminum surrounded by three phosphate oxygen atoms and one isopropoxide). This varied coordination environments around the aluminum also introduces chemical inequivalence among the six phosphorus atoms on each part of the molecule and hence the six different ^{31}P NMR resonances observed (Figure 1).

The molecule of **2** which crystallizes in $P2_1/n$ space group is also made up of two units, each of which occupying an asymmetric part in the unit cell. The two units are joined together across the crystallographic inversion center (Figure 3). Unlike **1**, the molecular dimensions of **2** are somewhat smaller; the size of the inorganic core is about 1.6 nm in its longest direction. Each of the two $[Al_4(O_3P(OR))_5]$ units is built around a μ_3-O bridge (linking Al3, Al4, Al5), which resides in the center of an $Al_3P_3O_6$ ring. Compound **2** differs from **1** by the absence of one aluminum center and one phosphate ligand per unit. This deficiency in this unsaturated cluster **2** is however compensated by the presence of Al-(μ-OH)-Al and P-O-(μ-H)-O-P bridges. The four aluminum centers in each sub-unit display four different coordination environments. While Al5 is octahedrally coordinated by four phosphate oxygen atoms, one O^{2-} ion, and one thf, the trigonal bipyramidal Al4 is surrounded by three phosphate oxygen atoms, one O^{2-} ion, and one thf. Although both Al1 and Al3 are nearly tetrahedral, Al1 is surrounded by three phosphate oxygen atoms and a hydroxy group while in Al3 the position of hydroxy group is taken up by the oxo ligand. Thus the aluminum cations in **1** and **2** display AlO_4, AlO_5, and AlO_6 coordination geometries with many different environments.

The formation of cluster **1** and **2** from an 1:1 mixture of the reactants is puzzling because of the observations that the equimolar reaction between RPO_3H_2 and AlR_3 normally leads to tetrameric cubanes $[RAlO_3PR']_4$,[12] although hexameric and decameric cages also have been isolated in a few instances.[6b,12c,13] Formation of **1** and **2** however can be understood by invoking the pathway suggested in Scheme 1.[14] It appears that the initial reaction between the

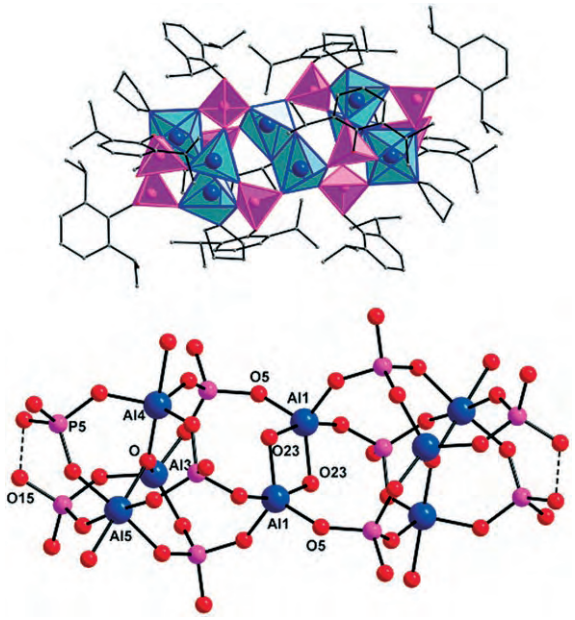

Figure 3. Molecular (top) and core (bottom) structure of **2** (color key as for Figure 2). Selected bond lengths [Å] and angles [°]: Al–O(P) 1.746(4)–1.888(4) (av. 1.807), Al–O(Al) 1.753(4), 1.858(4), 1.937(4), Al–O(thf) 1.959(2), 2.052(2), P–O(Al) 1.486(4)–1.536(4) (av. 1.509), P–O(Ar) 1.571(2)–1.598(2) (av. 1.586); O-Al1-O (tbp) 72.9(2)–97.8(2), 107.8(2)–127.2(2), 164.0(2), O-Al3-O (Td) 108.3(2)–111.0(2), O-Al4-O (tbp) 84.0(1)–96.9(2), 118.5(2)–123.1(2), 177.9(2), O-Al5-O (Oh) 87.1(2)–93.0(2), 174.9(2)–179.5(2), Al3-O-Al4 126.2(2), Al3-O-Al5 112.0(2), Al4-O-Al5 120.9(2), Al1-O23-Al′ 107.1(2); cluster dimensions [Å]: O15···O15′ 16.09, P5···P5′ 14.07. tbp = trigonal bipyramidal, Td = tetrahedral, Oh = octahedral.

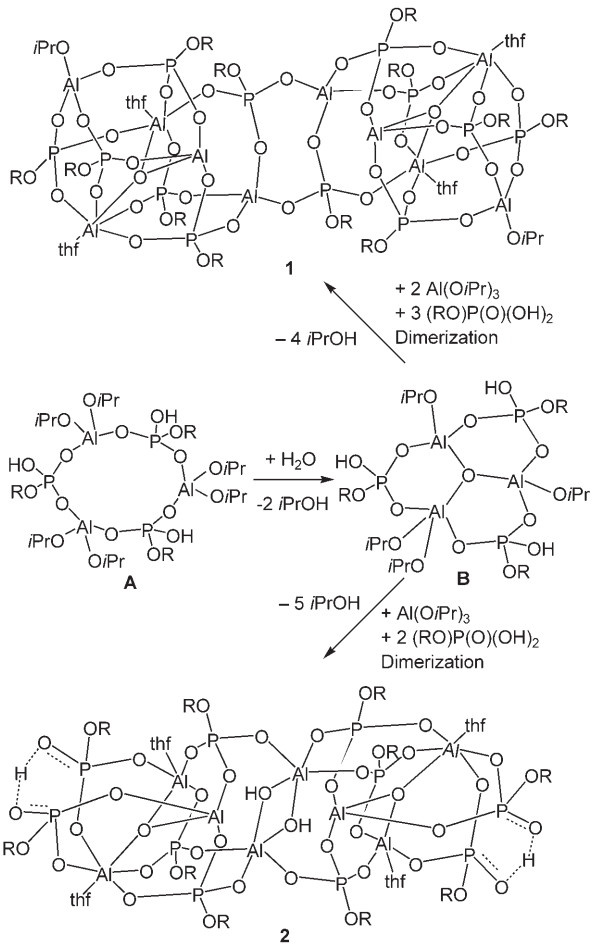

Scheme 1. Suggested pathway for the formation of **1** and **2**; see text for details.[14]

© 2006 Wiley-VCH Verlag GmbH & Co. KGaA, Weinheim

two starting materials proceeds via the formation of a "single 6-ring" (S6R) $[(OiPr)_2Al(O_3P(OR)]_3$ unit (**A**) which is attacked by adventitious water to produce the intermediate **B**. The formation of an S6R, capped by a μ-oxo group, and which is similar to **B**, has been observed in gallophosphonates.[15] Addition of two more equivalents of aluminum isopropoxide and three equivalents of $dippH_2$ to **B** followed by dimerization reaction between P–OH and Al–O*i*Pr terminals produces **1**. On the other hand, addition of only one equivalent of $Al(OiPr)_3$ and two equivalents of $dippH_2$ to **B** followed by dimerization and a slow Al–O*i*Pr hydrolysis yields **2**.

In summary, by introducing minor modifications in the choice of aluminum and phosphorus sources (AlR_3 versus $Al(OR)_3$; $(RO)_2P(O)(OH)$ versus $(RO)P(O)(OH)_2$) as well as the reaction conditions, we have assembled the largest molecular aluminophosphate. The cores of **1** and **2** represent new SBUs in zeolite chemistry. Further, the presence of a number of interconnected 3-, 4- and 6-rings (3R, 4R, and 6R) and residual functional groups, such as terminal Al–O*i*Pr, Al–thf, Al–OH, P–OH, and hydrolysable P–OR linkages, makes the nanometer sized **1** and **2** ideal building blocks for realizing newer framework structures. We are presently exploring these possibilities.

Experimental Section

Synthesis of **1**: $Al(OiPr)_3$ (408 mg, 2 mmol) in THF (30 mL) was added drop wise to $dippH_2$ (620 mg, 2 mmol) in THF (20 mL), and stirred for 12 h at 25 °C. The solvent was removed in vacuo and the residue was dissolved in toluene (10 mL) and left for crystallization on the bench top. Colorless crystals of **1** were obtained after one week. Yield: 62 %. M.p. > 275 °C. Elemental analysis (%) calcd for $Al_{10}(O_3P(OR))_{12}(O)(OiPr)_2(thf)_4]\cdot C_7H_8$ (3875.4): C 53.62, H 6.71; found: C 53.76, H 6.82. IR (KBr): $\tilde{\nu}$ = 2965(s), 2929(s), 2871(m), 1633(br), 1467(m), 1440(m), 1384(w), 1364(w), 1338(w), 1259(m), 1182(s), 1105(m), 1070(vs), 942(m), 775(m) cm^{-1}. ^1H NMR ([D_6]benzene, 300 MHz): δ = 6.89–7.11 (m, Ar), 4.85 (s, thf), 3.58–3.87 (m, *i*Pr-CH), 2.11(s, CH_3), 1.14–1.42 ppm (m, *i*Pr-CH_3). ^{31}P NMR ($CDCl_3$, 121 MHz): δ = −16.1, −16.4, −21.1, −21.5, −23.4, −26.4 ppm (all singlets).

Synthesis of **2**: The synthesis was similar to **1**. In the present case, $dippH_2$ was added to $Al(OiPr)_3$ (reverse addition). Yield: 53 %. M.p. > 275 °C. Elemental analysis (%) calcd for $[Al_8\{O_3P(OR)\}_8\{HO_3P(OR)\}_2(O)_2(OH)_2(thf)_4]$ (3110.6): C 51.74, H 6.68; found: C 52.53, H 6.45. IR (KBr): $\tilde{\nu}$ = 2967(s), 2930(s), 2870(m), 2280(w), 1630(br), 1467(m), 1443(m), 1385(w), 1364(w), 1338(w), 1259(m), 1172(s), 1160(s), 1051(vs), 939(m), 773(m) cm^{-1}.

Received: May 18, 2006
Revised: June 19, 2006
Published online: October 2, 2006

Keywords: aluminum · cluster compounds · phosphates · structure elucidation · zeolite analogues

[1] S. T. Wilson, B. M. Lok, C. A. Messina, T. R. Cannan, E. M. Flanigen, *J. Am. Chem. Soc.* **1982**, *104*, 1146–1147.

[2] a) J. Yu, R. Xu, *Acc. Chem. Res.* **2003**, *36*, 481–490; b) S. Oliver A. Kuperman, G. A. Ozin, *Angew. Chem.* **1998**, *110*, 48–64; *Angew. Chem. Int. Ed.* **1998**, *37*, 46–62.

[3] a) R. Murugavel, M. G. Walawalkar, M. Dan, H. W. Roesky, C. N. R. Rao, *Acc. Chem. Res.* **2004**, *37*, 763–774; b) C. N. R. Rao, S. Natarajan, A. Choudhury, S. Neeraj, A. A. Ayi, *Acc. Chem. Res.* **2001**, *34*, 80–87.

[4] J. E. Cassidy, J. A. J. Jarvis, R. N. Rothon, *J. Chem. Soc. Dalton Trans.* **1975**, 1497–1499.

[5] a) C. G. Lugmair, T. D. Tilley, A. L. Rheingold, *Chem. Mater.* **1999**, *11*, 1615–1620; b) K. L. Fujdala, T. D. Tilley, *J. Am. Chem. Soc.* **2001**, *123*, 10133–10134; c) M. R. Mason, R. M. Matthews, M. S. Mashuta, J. F. Richardson, *Inorg. Chem.* **1996**, *35*, 5756–5757; d) J. Pinkas, D. Chakraborty, Y. Yang, R. Murugavel, M. Noltemeyer, H. W. Roesky, *Organometallics* **1999**, *18*, 523–528; e) J. Pinkas, H. Wessel, Y. Yang, M. L. Montero, M. Noltemeyer, M. Fröba, H. W. Roesky, *Inorg. Chem.* **1998**, *37*, 2450–2457; f) J. Pinkas, J. Löbl, D. Dastych, M. Necas, H. W. Roesky, *Inorg. Chem.* **2002**, *41*, 6914–6918.

[6] a) M. G. Walawalkar, H. W. Roesky, R. Murugavel, *Acc. Chem. Res.* **1999**, *32*, 117–126; b) M. R. Mason, A. M. Perkins, V. V. Ponomarova, A. Vij, *Orgaometallics* **2001**, *20*, 4833–4839.

[7] a) R. Murugavel, M. Sathiyendiran, M. G. Walawalkar, *Inorg. Chem.* **2001**, *40*, 427–434; b) M. Sathiyendiran, R. Murugavel, *Inorg. Chem.* **2002**, *41*, 6404–6411; c) R. Murugavel, M. Sathiyendiran, R. Pothiraja, R. J. Butcher, *Chem. Commun.* **2003**, 2546–2547; d) R. Murugavel, M. Sathiyendiran, R. Pothiraja, M. G. Walawalkar, T. Mallah, E. Rivière, *Inorg. Chem.* **2004**, *43*, 945–953; e) R. Pothiraja, M. Sathiyendiran, R. J. Butcher, R. Murugavel, *Inorg. Chem.* **2004**, *43*, 7585–7587; f) R. Pothiraja, M. Sathiyendiran, R. J. Butcher, R. Murugavel, *Inorg. Chem.* **2005**, *44*, 6314–6323.

[8] R. Murugavel, S. Kuppuswamy, R. Boomishankar, A. Steiner, *Angew. Chem.* **2006**, *118*, 5662–5666; *Angew. Chem. Int. Ed.* **2006**, *45*, 5536–5540.

[9] Synthesis of $AlPO_4$ materials is carried out from $Al(OiPr)_3$ and H_3PO_4 in water, see, S. T. Wilson in *Introduction to Zeolite Science to Practice, Studies in Surface Science and Catalysis 58* (Eds.: H. van Bekkum, E. M. Flanigen, J. C. Jansen), Elsevier, Amsterdam, **1991**, p. 137.

[10] Crystal data for $[Al_{10}\{\mu_3\text{-}O_3P(OR)\}_{12}(\mu_3\text{-}O_2)(OiPr)_2(thf)_4]\cdot 6C_7H_8$ (**1**): $C_{208}H_{298}Al_{10}O_{56}P_{12}$, M_r = 4335.9, triclinic, $P\bar{1}$, Z = 1, a = 15.683(5), b = 18.663(2), c = 21.105(2) Å, α = 83.814(8), β = 70.497(17), γ = 76.689(14)°, V = 5663(2) Å^3, T = 150(2) K, λ = 0.71073 Å, ρ_{calcd} = 1.271 g cm^{-3}, $\mu(Mo_{K\alpha})$ = 0.205 mm^{-1}, F-(000) = 2304, θ = 3–25°, reflections = 19801, parameters = 1288, crystal size = 0.37 × 0.22 × 0.2 mm^3, $R1$ ($I > 2\sigma(I)$) = 0.0498, wR_2 = 0.1049, GOF = 0.892. Crystal data for $[Al_8\{\mu_3\text{-}O_3P(OR)\}_8\{\mu_2\text{-}HO_3P(OR)\}_2(\mu_3\text{-}O)(\mu_3\text{-}OH)_2(thf)_4]\cdot 2C_7H_8$ (**2**): $C_{150}H_{222}Al_8O_{48}P_{10}$, M_r = 3318.82, monoclinic, $P2_1/n$, Z = 2, a = 16.528(4), b = 31.470(6), c = 16.6746(7) Å, β = 98.495(2)°, V = 8578(3) Å^3, T = 150(2) K, λ = 0.71073 Å, ρ_{calcd} = 1.285 g cm^{-3}, $\mu(Mo_{K\alpha})$ = 0.218 mm^{-1}, $F(000)$ = 3520, θ = 3–25°, reflections = 14485, parameters = 973, crystal size = 0.33 × 0.26 × 0.21 mm^3, $R1$ ($I > 2\sigma(I)$) = 0.0708, wR_2 = 0.1599, GOF = 0.832. The diffraction data were obtained on an Oxford Diffraction XCalibur-S CCD system. The structure was solved by direct methods (SHELXS-96[16a]) and refined using SHELXL-97.[16b] All non-hydrogen atoms were subjected to anisotropic refinement. The hydrogen atoms were placed on calculated positions, but were allowed to ride on their parent atoms during subsequent cycles of refinement. CCDC-606933 (**1**) and CCDC-611387 (**2**) contain the supplementary crystallographic data for this paper. These data can be obtained free of charge from The Cambridge Crystallographic Data Centre via www.ccdc.cam.ac.uk/data_request/cif.

[11] Both elemental analysis and thermogravimetric analysis (TGA) indicate the loss of five toluene molecules during the vacuum drying of the crystals.

 © 2006 Wiley-VCH Verlag GmbH & Co. KGaA, Weinheim

[12] a) Y. Yang, H.-G. Schmidt, M. Noltemeyer, J. Pinkas, H. W. Roesky, *J. Chem. Soc. Dalton Trans.* **1996**, 3609 – 3610; b) M. G. Walawalkar, R. Murugavel, H. W. Roesky, H.-G. Schmidt, *Inorg. Chem.* **1997**, *36*, 4202 – 4207; c) Y. Yang, M. G. Walawalkar, J. Pinkas, H. W. Roesky, H.-G. Schmidt, *Angew. Chem.* **1998**, *110*, 101 – 103; *Angew. Chem. Int. Ed.* **1998**, *37*, 96 – 98; d) M. R. Mason, *J. Cluster Sci.* **1998**, *9*, 1 – 23.

[13] Although **1** has some structural resemblance to the decameric aluminum phosphonate $[t\mathrm{BuAlO_3PMe}]_{10}$ reported in ref. [6b], there are essential differences in the constitution of these two clusters.

[14] In the absence of spectroscopic characterization or identification of the intermediates, the suggested pathway should be considered tentative.

[15] In spite of drying the phosphate ester over anhydrous $MgSO_4$ and storing the recrystallized sample in a glove-box, small amounts of moisture are always present owing to the hydrophilicity of the phosphate ester. For the formation of a structural unit similar to **B** in the presence of traces of water, see: M. G. Walawalkar, R. Murugavel, A. Voigt, H.-G. Schmidt, H. W. Roesky, *J. Am. Chem. Soc.* **1997**, *119*, 4656 – 4661.

[16] a) G. M. Sheldrick, SHELXS-96, Program for Structure Solution, University of Göttingen, Germany, **1996**; b) G. M. Sheldrick, SHELXL-97, Program for Structure Refinement, University of Göttingen, Germany, **1997**.

 © 2006 Wiley-VCH Verlag GmbH & Co. KGaA, Weinheim

Supramolecular Chemistry

DOI: 10.1002/anie.200602286

Fluorescent H-Aggregates of Merocyanine Dyes**

Ulrich Rösch, Sheng Yao, Rüdiger Wortmann, and Frank Würthner**

Dedicated to Professor Hans-Georg Kuball on the occasion of his 75th birthday

Traditionally, dye aggregates are classified as H- and J-type on the basis of the observed spectral shift of the absorption maximum relative to the respective monomer absorption band (hypsochromic for H-type and bathochromic for J-type).[1–3] Many J-aggregates exhibit fluorescence, and their fluorescence quantum yield quite often surpasses that of the monomeric dyes.[4] In contrast, it is well documented that the fluorescence of H-aggregates is strongly quenched. This behavior was already observed a long time ago for a large number of dimer aggregates of classical fluorophores, including fluorescein, eosin, thionine, methylene blue, and certain cyanine dyes, and the non-emissive character of the excited state became commonly accepted as a general feature of H-aggregates.[5,6]

Theoretical interpretation by Förster (coupled oscillator model) and Kasha (exciton theory) could plausibly explain the nonfluorescent nature of dimeric as well as extended H-type aggregates.[2,7] Two exciton states arise in the case of face-to-face-stacked dimer aggregates, but only the transition to the higher energy exciton state is allowed, and can be observed in the UV/Vis absorption spectrum as a blue-shifted band. Subsequent rapid internal conversion of this excited state into the lower energy exciton state quenches the fluorescence as a result of the decreasing transition probability for a radiative process from this state to the ground state. Only a few exceptions to this rule have been reported, mostly either under special conditions such as at low temperature in frozen solution[8] or for dye aggregates embedded in Langmuir–Blodgett layers.[9] Other more recent examples include tethered mero- and hemicyanine chromophores which can fold into fluorescent H-type aggregates.[10] In these cases, however, the UV/Vis absorption spectra are typically quite different from those of conventional cyanine dye sandwich dimers.

Herein, we report an example of a fluorescent H-aggregate composed of two face-to-face-stacked merocyanine dyes. The observation of fluorescence for this dye aggregate is particularly remarkable because its absorption properties match perfectly those of classical H-type dimer aggregates,[6,8] that is, they show a pronounced hypsochromic shift. According to our earlier studies, dimerization of such strongly dipolar merocyanine dyes is driven by electrostatic interactions that can be related to the magnitude of their dipole moments, that is, the Gibbs binding energy ΔG° is proportional to the square of the ground-state dipole moment μ_g of the dye.[11] As a consequence, these dimer aggregates exhibit a high thermodynamic stability in solvents of low polarity and a well-defined centrosymmetric geometry (Scheme 1).[11,12] These two aspects are advantageous attributes for the current study; ionic cyanine dyes, in contrast, exhibit less predictable aggregate structures and aggregation free enthalpies. Although several of our merocyanine dyes, for example, dyes **1**–**3** were found to form fluorescent dimers,[13] we will focus our attention on merocyanine dye **2**, whose high solubility enabled concentration-dependent investigations even in low-polarity solvents.[14] Furthermore, as a result of the very high dipole moment of this chromophore, significant amounts of dimer aggregates are already formed under the dilute conditions required for fluorescence spectroscopy.

Figure 1 shows the concentration-dependent UV/Vis absorption spectra recorded in dioxane at concentrations between 0.8×10^{-6} and 5.5×10^{-6} mol L^{-1}. The observed

[*] Dr. U. Rösch, Prof. Dr. R. Wortmann[+]
Technische Universität Kaiserslautern
Physikalische Chemie
Erwin-Schrödinger-Strasse, 67663 Kaiserslautern (Germany)
Dr. S. Yao, Prof. Dr. F. Würthner
Universität Würzburg
Institut für Organische Chemie
Am Hubland, 97074 Würzburg (Germany)
Fax: (+49) 931-888-4756
E-mail: wuerthner@chemie.uni-wuerzburg.de
[+] deceased on March 13, 2005

[**] This work was supported by the Deutsche Forschungsgemeinschaft. We are grateful to Prof. Gereon Niedner-Schatteburg and Prof. Hans-Georg Kuball (both Physical Chemistry, Kaiserslautern) for helpful discussions and their ongoing support, and to the referees for valuable suggestions.

InterScience DISCOVER SOMETHING GREAT
© 2006 Wiley-VCH Verlag GmbH & Co. KGaA, Weinheim

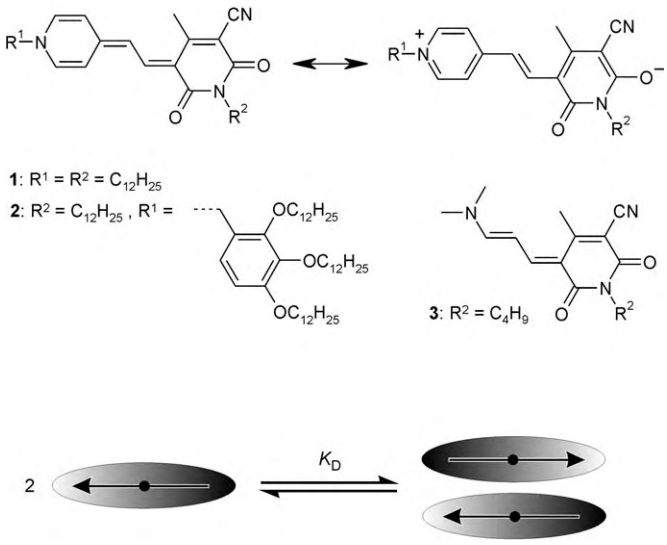

Scheme 1. Highly dipolar merocyanines **1**–**3** and formation of their dimer aggregates driven by dipole–dipole interactions.

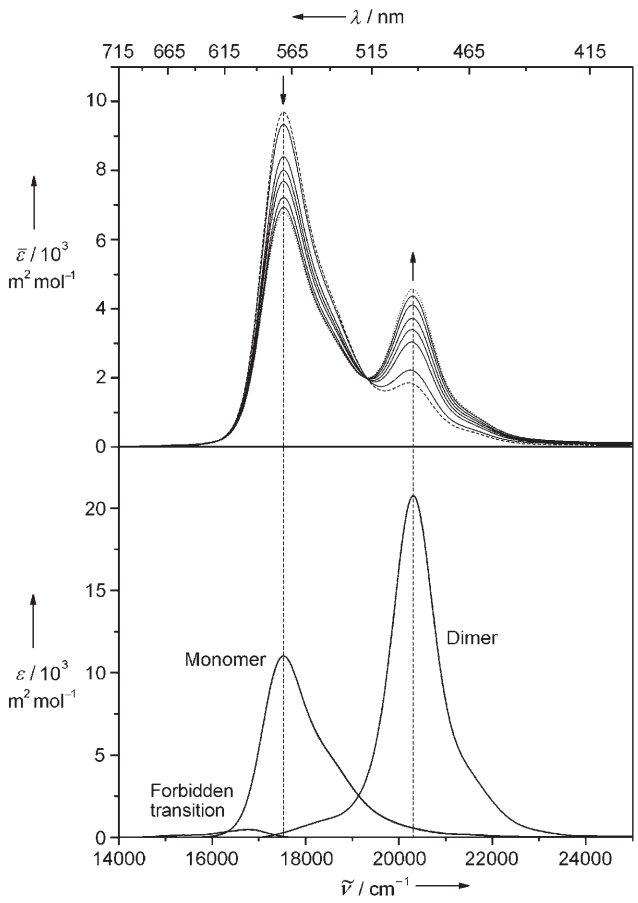

Figure 1. Top: UV/Vis absorption spectra of merocyanine **2** in dioxane at concentrations between 0.8×10^{-6} (dashed line) and 5.5×10^{-6} mol L^{-1} (dotted line) at 298 K. Arrows indicate the changes upon increasing the concentration. Bottom: UV/Vis absorption spectra for the monomer and dimer of merocyanine **2** calculated from the concentration-dependent spectra.

spectral changes and the well-defined isosbestic points at 19300 cm^{-1} and 16050 cm^{-1} provide good evidence for an equilibrium between monomeric and dimeric species (Scheme 1) and allow us to calculate the binding constant ($K_D^{298} = 108000$ L mol^{-1}) as well as the spectra for the pure monomer and dimer (Figure 1, bottom).[15] It is noteworthy that in addition to the very intense hypsochromically shifted absorption band ($\varepsilon_{max} = 20800$ m^2 mol^{-1}) for the dimer, a weak band ($\varepsilon_{max} = 480$ m^2 mol^{-1}) appears at longer wavelength which can be ascribed to the forbidden transition to the lower energy exciton state.

Much to our surprise, an increase in the fluorescence intensity could be observed for solutions of dye **2** upon increasing the concentration, thus suggesting the existence of fluorescent aggregates of the merocyanine dimer. Fluorescence spectra were recorded at excitation wavelengths between 400 and 650 nm in a matrix scan experiment. Figure 2 shows the recorded emission intensities which clearly

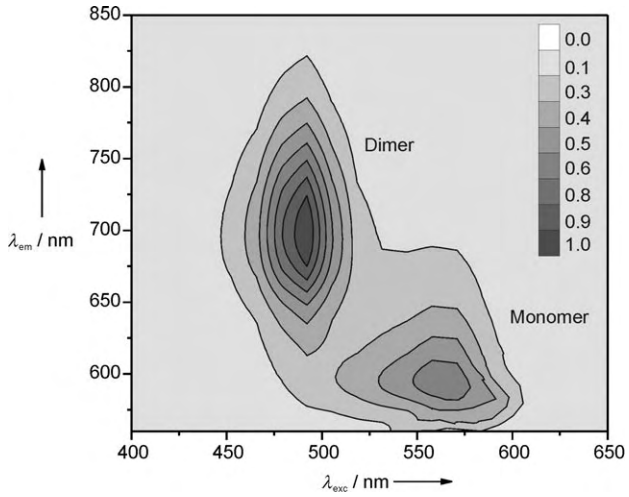

Figure 2. Contour map of the observed fluorescence intensity as a function of the fluorescence excitation λ_{exc} and emission wavelength λ_{em} ("matrix scan") for merocyanine **2** in dioxane at 298 K. Darker shades represent higher intensity.

confirm that the emission arises predominantly from the dimeric species. The strongest emission (black) is observed upon excitation of the dimer at about 480 nm. The pronounced hypsochromic shift of the UV/Vis absorption spectrum upon formation of the dimer aggregate enabled the monomeric and the dimeric species to be excited selectively and their fluorescence spectra to be recorded (Figure 3).

The absorption and fluorescence spectra of the monomeric dye exhibit no special features. Thus, they are close to mirror images, with a Stokes shift of 780 cm^{-1} between the absorption maximum at $\tilde{\nu}_{max,abs} = 17520$ cm^{-1} and the fluorescence maximum at $\tilde{\nu}_{max,fl} = 16740$ cm^{-1}. The full width at half maxima (FWHM) values for the absorption band and the fluorescence band were 1360 cm^{-1} and 1810 cm^{-1}, respectively.[16] The broader fluorescence band can be attributed to solvent-dependent influences on the vibronic progression. We have observed such a behavior for many betain-type mero-

 © 2006 Wiley-VCH Verlag GmbH & Co. KGaA, Weinheim

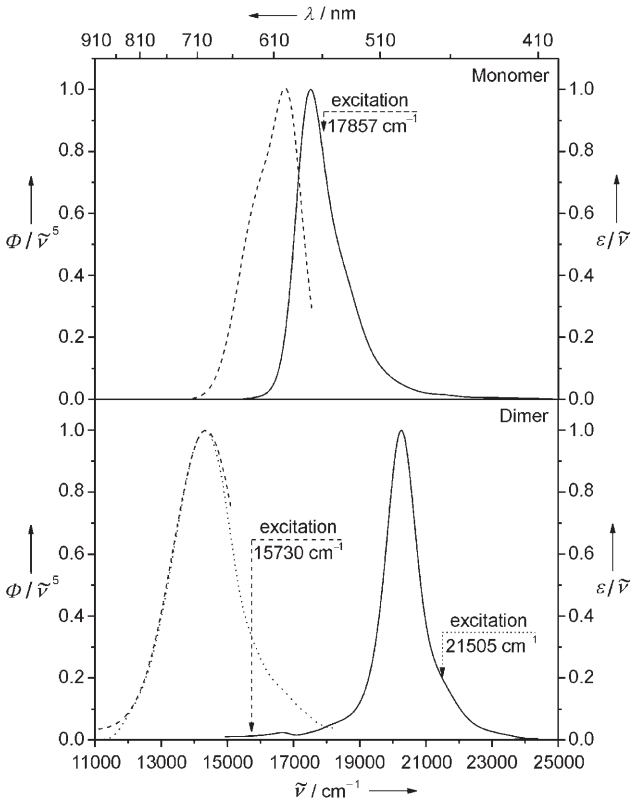

Figure 3. Top: Calculated UV/Vis absorption (solid line) and measured fluorescence (dashed line) spectra of monomeric dye **2** in dioxane at 298 K at a concentration of $c_0 = 8.32\times10^{-7}$ mol L^{-1} (leading to concentrations of the monomeric and dimeric species of $c_M = 7.20\times10^{-7}$ mol L^{-1} and $c_D = 5.59\times10^{-8}$ mol L^{-1}). Bottom: Calculated UV/Vis absorption spectrum (solid line) for dimer aggregates of **2** and the fluorescence spectra upon excitation at 21 505 cm^{-1} (dotted line) and 15 730 cm^{-1} (dashed line) in dioxane at 298 K at a concentration of $c_0 = 1.27\times10^{-6}$ mol L^{-1} (leading to $c_M = 5.70\times10^{-6}$ mol L^{-1} and $c_D = 3.50\times10^{-6}$ mol L^{-1}).

cyanine dyes such as **2** which exhibit a more polar ground state than excited state, as well as negative solvatochromism.

In contrast, the spectra of the dimer were more unusual. First, whilst the absorption spectra of dimer aggregates are typically much broader than those of their monomers, we note a narrowing of the dimer absorption band at $\tilde{\nu}_{max,abs} = 20330$ cm^{-1} for merocyanine dye **2** (FWHM = 1160 cm^{-1}). Second, the fluorescence band is observed at a rather long wavelength, that is, $\tilde{\nu}_{max,fl} = 14350$ cm^{-1} (FWHM = 2180 cm^{-1}). Most remarkably, the same fluorescence spectrum could be recorded upon excitation of the dimer aggregate at the tail of its weak low-energy absorption band (Figure 3). This observation provides unequivocal evidence that the dimer emission originates from the lower exciton state of the aggregated dimeric species. These observations by steady-state fluorescence spectroscopy were further substantiated by time-resolved fluorescence measurements, which showed two independent fluorescence lifetimes, a short one of 0.5 ns for the monomeric and a longer one of 4.4 ns for the dimeric species.[16]

These results confirm that a unique example of a fluorescent merocyanine H-type dimer aggregate is provided. Although our present observation seems to contradict the common perception that H-aggregates are not fluorescent, it complies with the exciton coupling theory.[2,3] Accordingly, the presence of the small but detectable absorption band at 16 780 cm^{-1} results in a nonvanishing transition probability between the ground and the lowest exciton state from which a weak fluorescence arises. This weak band may emanate from vibronic coupling or a small rotational twist between the two chromophores. Indeed, the latter interpretation is in accordance with our earlier electrooptical absorption (EOA) studies that revealed a small ground-state dipole moment for these dimer aggregates.[12,17] On the other hand, X-ray crystallographic data[11] as well as the optimized dimer geometry according to MP2/6-31G(d,p) calculations[18] show a perfectly centrosymmetric dimeric unit as the energetically preferred geometry (Figure 4).

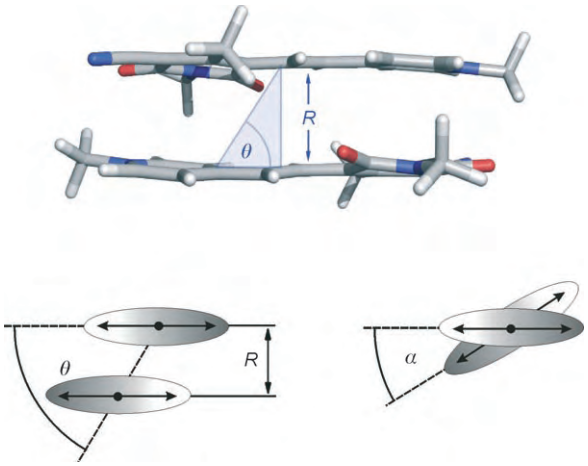

Figure 4. Top: MP2/6-31G(d,p)-optimized structure of the dimer aggregate of **2** with $\theta = 58.2°$ and $R = 3.25$ Å (all alkyl substituents have been replaced by methyl groups in the calculation). Bottom: Structural model (left: side view, right: top view) for the calculation of the exciton coupling between the transition dipole moments indicated as double arrows in the dimer aggregates arising from the distance R, the slipping angle θ, and the rotational angle α.

From the spectral deconvolution provided in Figure 3 we can calculate the transition dipole moments between the ground state and the allowed and forbidden exciton states $\mu_{ag}^{D} = 59.4\times10^{-30}$ C m and $\mu_{ag}^{D2} = 5.2\times10^{-30}$ C m. From these transition dipole moments, the transition dipole moment of the monomer $\mu_{M}^{ag} = 43.6\times10^{-30}$ C m, and the energy difference $V_{AB} = hc(\tilde{\nu}_{D}^{ag} - \tilde{\nu}_{D2}^{ag}) = hc\Delta\tilde{\nu}_{D-D2}^{ag}$ between the two exciton states we can now obtain the angles $\theta = 59.9°$ and $\alpha = 10.0°$ from Equations (1) and (2).[2,19]

$$\frac{\mu_{ag}^{D2}}{\mu_{ag}^{D}} = \frac{(1-\cos\alpha)}{(1+\cos\alpha)} = \tan^2\left(\frac{\alpha}{2}\right) \quad (1)$$

$$V_{AB} = \frac{2}{4\pi\varepsilon_0}\frac{(\mu_{ag}^{M})^2}{R^3}(\cos\alpha - 3\cos^2\theta)(\sin^3\theta) \quad (2)$$

If we consider the well-known deficiencies of the point dipole approximation,[3] the excellent agreement of these

 © 2006 Wiley-VCH Verlag GmbH & Co. KGaA, Weinheim

results with the geometry derived by XRD, NMR spectroscopy, and electrooptical absorption spectroscopy is remarkable.[11,12,17] The very small rotational twist of 10° is energetically only slightly disfavored according to our calculations[18] and is thus easily accessible in solution, either by a solvent effect or by the thermal energy provided at room temperature.

The fluorescence intensity of such a dimer should, however, be much weaker than the emission of the monomeric dye, which exhibits a strongly allowed $S_1 \leftarrow S_0$ transition. As a consequence, similar to other dimer aggregates, we might have expected that the fluorescence band corresponding to the dimer should be hidden beneath a more intense monomer band. The fact that nicely resolved fluorescence spectra of the dimer could be observed without any overlapping emission from the monomer in the given example can be attributed to the very weak fluorescence intensity (quantum yield $\Phi_f \approx 0.1\,\%$) of the monomeric dyes. The latter is a result of a rapid nonradiative deactivation pathway through a bond-twisting mechanism, as observed for most cyanine and merocyanine dyes,[20] which leads to fast rates of fluorescence decay. In accordance with this mechanistic picture, many polymethine dyes show increased fluorescence intensities after they have been rigidified by chemical or physical measures.[21] Thus, it is reasonable to assume that the major nonradiative decay channel for the excited monomeric dye **2** which causes the fast decay (0.5 ns) is suppressed upon formation of a tightly bound dimer aggregate that remains stable at least on the time scale of the observed fluorescence decay time of 4.4 ns.

In conclusion, we have presented a unique example of a merocyanine H-aggregate which exhibits a well-resolved fluorescence spectrum and a significantly longer fluorescence lifetime relative to its monomer.[22] These unexpected findings could be rationalized within the concept of exciton theory by taking into account the small transition probability caused by a slight rotation of the two coupled dyes in the excited state as well as the rigidification of the polymethine chain in the closely π-π-stacked sandwich aggregate.

Received: June 7, 2006
Revised: August 11, 2006
Published online: October 2, 2006

Keywords: chromophores · dye aggregates · dyes/pigments · fluorescence · supramolecular chemistry

[1] a) A. H. Herz, *Adv. Colloid Interface Sci.* **1977**, *8*, 237–298; b) F. Dietz, *J. Signalaufzeichnungsmater.* **1973**, *3*, 157–180 (Part 1) and F. Dietz, *J. Signalaufzeichnungsmater.* **1973**, *4*, 237–252 (Part 2).

[2] M. Kasha, H. R. Rawls, M. A. El-Bayoumi, *Pure Appl. Chem.* **1965**, *11*, 371–392. For good reasons, the expressions H- and J-aggregate have been avoided in this seminal paper on the theoretical description of dimer aggregate spectra by exciton theory. According to this theory as well as more elaborate ones (see Ref. [3]), for the majority of possible dimer geometries two absorption bands arise, one at higher ("H-band") and one at lower ("J-band") energy relative to the monomer band. Thus, spectra of perfect H- and J-aggregates (where the transition to one of the two exciton states is fully forbidden) will only occur for the special situation of a perfect parallel or antiparallel orientation of the two dyes in the dimer aggregate. Despite these facts, dye aggregates are most commonly classified as H- and J-type on the basis of their most intense absorption band. Accordingly, we regard aggregates of merocyanines **1–3** as typical representatives of H-type dimer aggregates.

[3] a) V. Czikklely, H. D. Försterling, H. Kuhn, *Chem. Phys. Lett.* **1970**, *6*, 207–210; b) H. Kuhn, C. Kuhn in *J-Aggregates* (Ed.: T. Kobayashi), World Scientific, Singapore **1996**, pp. 1–40; for a recent study by time-dependent quantum methodology with special emphasis on rotational displacements in perylenebisimide aggregates, see: c) J. Seibt, P. Marquetand, V. Engel, Z. Chen, V. Dehm, F. Würthner, *J. Chem. Phys.*, DOI:10.1016/j.chemphys.2006.07.023.

[4] a) G. Scheibe, *Z. Elektrochem.* **1948**, *52*, 283–292; b) D. Möbius, *Adv. Mater.* **1995**, *7*, 437–444; c) *J-Aggregates* (Ed.: T. Kobayashi), World Scientific, Singapore, **1996**.

[5] a) W. L. Lewschin, *Z. Phys.* **1927**, *43*, 230; b) E. Rabinowitch, L. Epstein, *J. Am. Chem. Soc.* **1941**, *63*, 69.

[6] a) T. Förster, E. König, *Z. Elektrochem.* **1957**, *61*, 344–348; b) K. Bergmann, C. T. O'Konski, *Z. Phys. Chem.* **1963**, *67*, 2169–2177; c) W. West, S. Pearce, *J. Phys. Chem.* **1965**, *69*, 1894–1903.

[7] T. Förster, *Naturwissenschaften* **1946**, *33*, 166–175.

[8] a) N. Cooper, N. B. Liebert, *Photogr. Sci. Eng.* **1972**, *16*, 25; b) R. W. Chambers, T. Kajiwara, D. R. Kearns, *J. Phys. Chem.* **1974**, *78*, 380–387; c) K. Teuchner, B. Bornowski, W. Becker, S. Dähne, *Z. Chem.* **1976**, *16*, 449–450; d) S. K. Rentsch, D. Fassler, P. Hampe, R. Danielius, R. Gadonas, *Chem. Phys. Lett.* **1982**, *89*, 249–253; e) V. Sundstöm, T. Gillbro, *J. Chem. Phys.* **1985**, *83*, 2733–2743; f) M. van der Auweraer, G. Biesmans, F. C. De Schryver, *Chem. Phys.* **1988**, *119*, 355–375.

[9] M. van der Auweraer, B. Verschuere, F. C. De Schryver, *Langmuir* **1988**, *4*, 583–588.

[10] a) L. Lu, R. J. Lachicotte, T. L. Penner, J. Perlstein, D. G. Whitten, *J. Am. Chem. Soc.* **1999**, *121*, 8146–8156; b) S. Zeena, K. G. Thomas, *J. Am. Chem. Soc.* **2001**, *123*, 7859–7865.

[11] F. Würthner, S. Yao, T. Debaerdemaeker, R. Wortmann, *J. Am. Chem. Soc.* **2002**, *124*, 9431–9447.

[12] R. Wortmann, U. Rösch, M. Redi-Abshiro, F. Würthner, *Angew. Chem.* **2003**, *115*, 2126–2129; *Angew. Chem. Int. Ed.* **2003**, *42*, 2080–2083.

[13] U. Rösch, PhD thesis, Technische Universität Kaiserslautern, **2006**.

[14] S. Yao, U. Beginn, T. Greß, M. Lysetska, F. Würthner, *J. Am. Chem. Soc.* **2004**, *126*, 8336–8348.

[15] In contrast to our earlier work,[11] in this study the nonlinear regression analysis was performed by taking into account the complete set of spectral data.

[16] The FWHM values have been calculated from Figure 3. If we plot the absorption data on a ε scale we obtain slightly different FWHM values of 1410 cm^{-1} for the monomer and 1160 cm^{-1} for the dimer band. If the fluorescence spectra are scaled against the measured intensity we obtain FWHM values of 1550 cm^{-1} for the monomer and 2260 cm^{-1} for the dimer band. All fluorescence measurements have been performed on a Jobin–Yvon Fluorolog 3–22 Tau instrument. The decay times were evaluated by applying single exponentials to the time-resolved measurements in the frequency domain.

[17] In our earlier study electooptical absorption (EOA) spectroscopy provided evidence for a non-disappearing ground-state dipole moment for the dimeric species and a value of 22×10^{-30} C m could be estimated (see Ref. [12], Table 1). If we now include the rotational angle of 10° obtained from this study into the formula for the evaluation of the EOA data, a more reliable value of 16×10^{-30} C m can be obtained for the dipole moment of the dimer aggregate. This value is in excellent agreement with the dipole

 © 2006 Wiley-VCH Verlag GmbH & Co. KGaA, Weinheim

moment of 14×10^{-30} C m at a torsion angle of $\alpha = 10°$ calculated at the MP2/6-31G(d,p) level of theory. However, we would like to point out that we are not yet sure if the small transition dipole moment for the lower energy excitonic transition that arises from such a small torsional twist of 10° is sufficient to explain the observed intensity of the dimer fluorescence. Alternatively, a relaxation of the Franck–Condon excited state could be taking place that affords an even more twisted excited state geometry which exhibits an increased radiative transition probability.

[18] All ab initio calculations were done with *Gaussian 03*, Revision C.02, Gaussian, Inc., Wallingford CT **2004**.

[19] K. K. Rohatgi-Muskerjee, *Indian J. Chem. Sect. A* **1992**, *31*, 500–511.

[20] a) H. Ephardt, P. Fromherz, *J. Phys. Chem.* **1989**, *93*, 7717; b) R. F. Khairutdinov, N. Serpone, *J. Phys. Chem. B* **1997**, *101*, 2602–2610; c) V. Karunakaran, J. L. P. Lustres, L. Zhao, N. Ernsting, O. Seitz, *J. Am. Chem. Soc.* **2006**, *128*, 2954–2962.

[21] Intense fluorescence has been reported for several merocyanine dyes upon rigidification in frozen solution, the solid state, or in an organogel; see, for example, a) F. Würthner, R. Sens, K.-H. Etzbach, G. Seybold, *Angew. Chem.* **1999**, *111*, 1753–1757; *Angew. Chem. Int. Ed.* **1999**, *38*, 1649–1652; b) S. Yagai, M. Higashi, T. Karatsu, A. Kitamura, *Chem. Commun.* **2006**, 1500–1502.

[22] An even longer fluorescence lifetime of 11.2 ns has been observed for dimers of dye **3**, see Ref. [13].

 © 2006 Wiley-VCH Verlag GmbH & Co. KGaA, Weinheim

Microporous Materials

DOI: 10.1002/anie.200602440

Hydrocarbon Uptake in the Alkylated Micropores of a Columnar Supramolecular Solid**

*Thomas J. Taylor, Vladimir I. Bakhmutov, and François P. Gabbaï**

Microporous self-assembled materials are attracting a great deal of interest for the storage of gases. The selective uptake and retention of small gaseous molecules, such as dihydrogen, are particularly attractive goals, which may lead to novel storage strategies.[1] In principle, similar strategies could be extended to gaseous alkanes, whose separation, transport, and storage continue to pose problems. Despite these important applications, limited effort has been devoted to the study of alkane sorption in microporous self-assembled materials. Available studies include the use of microporous metal–organic frameworks and van der Waals crystals for the storage,[2] size-selective encapsulation,[3] and gas-chromatographic separation of alkanes.[4] In all of these cases, the walls of the micropores are lined by aromatic groups, which interact with the guest hydrocarbon molecules through CH···π or van der Waals interactions.[2–4,5] Given that strong van der Waals attractions occur between saturated hydrocarbon molecules, microporous solids with alkylated cavity walls seem to be well-suited for the storage of alkanes. Despite the simplicity of this paradigm,[6] the synthesis of such microporous solids remains unprecedented.

We have shown that trimeric perfluoro-*ortho*-phenylene mercury (**1**)[7] interacts with benzene through secondary Hg···π interactions to form extended stacks that propagate in a direction perpendicular to the molecular planes.[8] Additionally, we have observed close contacts between **1** and unsaturated substrates in supramolecular adducts.[9] Herein, we describe how these assembly principles can be used for the construction of columns with alkylated exteriors. We also demonstrate that such columns can self-assemble to form a microporous solid that traps light alkanes in its alkylated cavities.

Reaction of **1** with 1,3,5-tris(trimethylsilylethynyl)benzene (1,3,5-$(Me_3SiC{\equiv}C)_3C_6H_3$) in THF led to the formation of a crystalline adduct, which after washing with CH_2Cl_2 and drying, was identified as [**1**-1,3,5-$(Me_3SiC{\equiv}C)_3C_6H_3$] (**2**), as indicated by X-ray diffraction and elemental analysis (Figure 1). This adduct dissolves in polar solvents, such as acetone and acetonitrile, through dissociation of the molecular components. ^{1}H NMR spectroscopy in [D_6]acetone indicates that **2** does not contain any THF or CH_2Cl_2 molecules. Crystals of **2** belong to the hexagonal space group $P6_3/mmc$.[10a] Examination of the structure reveals the formation of extended columns that run parallel to the *c* axis (Figure 1 a,b). These columns consist of binary stacks in which molecules of **1** and 1,3,5-$(Me_3SiC{\equiv}C)_3C_6H_3$ alternate. The molecules interact through secondary Hg···π and Hg···$C_{ethynyl}$ interactions (Hg1···C5 = 3.349(4) Å, Hg1···C6 = 3.363(5) Å), whose distances are within the sum of the van der Waals radii of mercury (1.7–2.0 Å)[11,12] and carbon (1.7 Å)[13] (Figure 1 a). The stacks are rather compact, as indicated by the distance of 3.28 Å separating the centroids of the two molecular components. This centroid distance can be compared to that of 3.24 Å found in [**1**-benzene], which adopts a similar stacked structure.[8] In **2**, neighboring columns are interdigitated and run parallel to one another to generate a three-dimensional honeycomb structure with large cylindrical channels parallel to the *c* axis (Figure 1 c). The trimethylsilyl groups of the 1,3,5-$(Me_3SiC{\equiv}C)_3C_6H_3$ molecules are oriented toward the centers of the channels and line the walls with nonpolar methyl groups. Probing the channels with a 1.2-Å sphere afforded a void volume of 200.0 Å^3 per unit cell, which corresponds to 8.9% of the total volume of the crystal.[14] Assuming that the channels are perfectly cylindrical, their internal effective diameter is 6.2 Å. The channels are essentially empty, as the as-prepared samples show negligible weight loss (< 0.1%) upon application of a vacuum. Further-

[*] T. J. Taylor, V. I. Bakhmutov, Prof. Dr. F. P. Gabbaï
Chemistry Department
Texas A&M University, 3255 TAMU
College Station, TX 77843-3255 (USA)
Fax: (+1) 979-845-4719
E-mail: gabbai@mail.chem.tamu.edu

[**] This work is supported by the Petroleum Research Fund (ACS PRF 38143-AC 3), the Welch Foundation (A-1423), and the National Science Foundation (CHE-0094264). We thank Raymond Schaak for the use of the DSC/TGA instrument.

Supporting information for this article is available on the WWW under http://www.angewandte.org or from the author.

InterScience DISCOVER SOMETHING GREAT
© 2006 Wiley-VCH Verlag GmbH & Co. KGaA, Weinheim

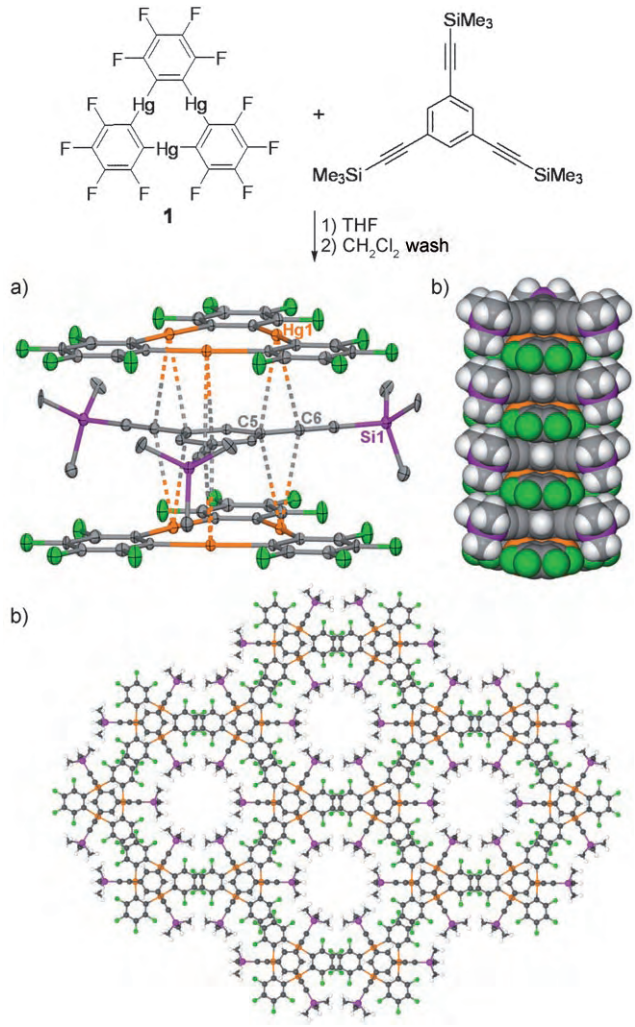

Figure 1. Synthesis and structure of **2**. a) View of part of a stack, showing the secondary Hg···π and Hg···$C_{ethynyl}$ interactions between **1** and 1,3,5-$(Me_3SiC{\equiv}C)_3C_6H_3$; thermal ellipsoids are set at 50% probability; H atoms are omitted. b) Space-filling view of a stack with four repeating units. c) View of the honeycomb structure of **2** along the *c* axis, showing the micropores. Hg orange, Si purple, C gray, F green, H white; only one conformation of the disordered Me_3Si groups is shown.

more, thermogravimetric measurements reveal that no weight change occurs up to a temperature of 190 °C, at which the adduct starts to decompose. As expected, the channels of **2** are hydrophobic and do not show any affinity for water.

To study the robustness of this microporous solid upon guest incorporation, a single crystal of **2** was indexed and subsequently immersed in neat bromoform. After 12 h, analysis of the crystal by X-ray diffraction indicated the encapsulation of bromoform and the formation of **2**⊃0.82 $CHBr_3$. Remarkably, this single-crystal-to-single-crystal transformation occurs with retention of the $P6_3/mmc$ space group and negligible changes to the unit-cell parameters.[10b] The structure of **2**⊃0.82 $CHBr_3$ only differs from that of **2** by the presence of bromoform molecules, which are located in the channels and have a refined occupancy of 82%. A similar occupancy was derived by integration of the ^{1}H NMR spectrum of **2**⊃0.82 $CHBr_3$ in $[D]_6$acetone. Encouraged by these results, which attest to the structural robustness of **2**, we decided to investigate its affinity for volatile alkanes.

Alkane uptake was investigated gravimetrically by exposure of solid **2** to an atmosphere of the corresponding alkane. Remarkably, uptake is observed not only for *n*-hexane and *n*-pentane vapor,[15] but also for *n*-butane, propane, and ethane, which are all gases under ambient conditions (Figure 2a). For

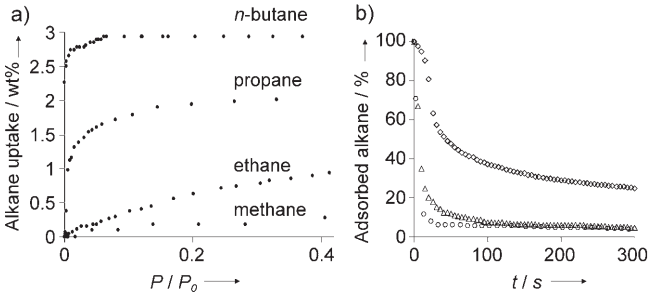

Figure 2. a) Alkane sorption isotherms for **2** at room temperature. b) Desorption of alkanes under vacuum as a function of time for **2**⊃0.57 C_2H_6 (○), **2**⊃0.67 C_3H_8 (△), and **2**⊃0.71 C_4H_{10} (◇).

methane, however, the maximum uptake was less than 0.5 wt%. Whereas ethane is still accumulating at a pressure of 1 bar, the sorption isotherms of propane and *n*-butane display plateaus indicating saturation of the pores. The total gas uptakes at $P/P_0 = 1$ are 1.2, 2.1, and 2.9 wt% for ethane, propane, and *n*-butane, respectively. For *n*-pentane and *n*-hexane, uptakes of 2.2 and 2.5 wt% are observed at $P/P_0 = 0.25$. For these two liquid alkanes, additional weight gain is observed at higher pressure, which is assigned to condensation on the external surface of the crystals.[16] Conversion of these gravimetric uptakes (wt%) into molar ratios leads to the formulations **2**⊃0.57 C_2H_6, **2**⊃0.67 C_3H_8, **2**⊃0.71 C_4H_{10}, **2**⊃0.45 C_5H_{12}, and **2**⊃0.41 C_6H_{14} for the adducts. Correlating the uptakes with the molecular volume of each alkane[17] indicates that ethane, propane, *n*-butane, *n*-pentane, and *n*-hexane occupy 38, 57, 74, 55, and 57% of the cavity space in **2**, respectively. The relatively low occupancies observed for ethane and propane can be explained by the weakness of the van der Waals attractions in which these small molecules can engage. It is not obvious why the uptake observed for *n*-butane is greater than that for *n*-pentane and *n*-hexane. However, given that two linear alkanes placed side by side necessitate more than 7.5 Å in width, the narrow channels of **2** probably force the longer alkanes to pack on top of one another, leading to a somewhat inefficient occupation of the space. Molecular mechanics simulations (MM2 force field) confirm this hypothesis: *n*-pentane and *n*-hexane are predicted to lay in the channels of **2** with their main molecular axes aligned with the *c* axis. In contrast, *n*-butane in the gauche conformation is small enough to lie sideways in the channels (Figure 3a), thus, leading to a more efficient occupation of the pores. This difference is probably at the origin of the higher uptake observed for *n*-butane.

To evaluate the stability of the adducts involving the gaseous alkanes, we studied guest release under vacuum

 © 2006 Wiley-VCH Verlag GmbH & Co. KGaA, Weinheim

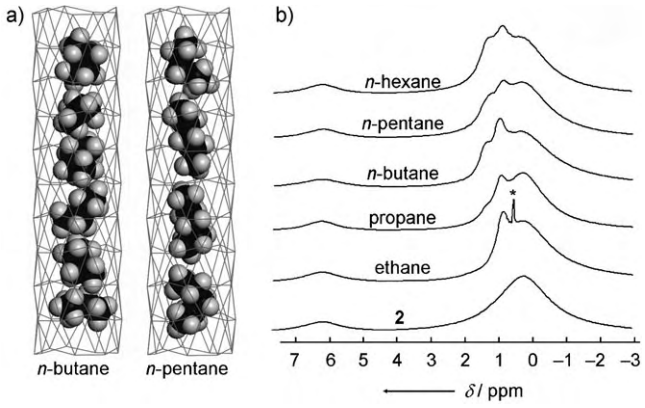

Figure 3. a) Arrangements and conformations of *n*-butane and *n*-pentane molecules in the channels of **2** determined by molecular mechanics simulations. The walls of the channels are approximated by the H atoms of the Me_3Si groups. b) ^{1}H MAS NMR spectra of **2** before and after alkane adsorption. The peak assigned to free ethane gas is indicated (*).

(Figure 2b). Although ethane is rapidly removed from the pores of **2** under vacuum, the propane and *n*-butane adducts show a more gradual weight loss as vacuum is applied. This behavior attests to the strength of the host–guest interactions in **2**⊃0.67 C_3H_8 and **2**⊃0.71 C_4H_{10}. X-ray powder diffraction patterns collected after uptake and guest release demonstrate that the original structure of **2** is retained, indicating permanent microporosity.

The microporous solid **2** does not immediately release the trapped alkanes. In fact, the samples are sufficiently stable to be analyzed by ^{1}H magic-angle spinning (MAS) NMR spectroscopy (Figure 3b).[18] Prior to exposure to an alkane, the spectrum of **2** consists of two resonances, corresponding to the methyl groups ($\delta = 0.18$ ppm) and the aromatic moiety ($\delta = 6.29$ ppm) of 1,3,5-$(Me_3SiC{\equiv}C)_3C_6H_3$. After exposure to ethane, an additional resonance assigned to adsorbed ethane molecules appears at $\delta = 0.90$ ppm. The spectrum also displays a sharp resonance at $\delta = 0.59$ ppm, which results from free ethane molecules caught in the rotor headspace. Note that the resonance due to the entrapped ethane molecules is only slightly shifted with respect to that of the free gas. This observation indicates that the walls of the channels do not generate significant magnetic anisotropy within the internal pore space. The ^{1}H MAS NMR spectrum of **2** after exposure to propane contains two new signals at $\delta =$ 1.15 and 0.75 ppm, which are assigned to the methylene and methyl groups of the entrapped hydrocarbon, respectively. In the spectra of the samples exposed to *n*-butane, *n*-pentane, and *n*-hexane, the intensity of the methylene signal increases with respect to that of the methyl signal. For *n*-pentane and *n*-hexane, the two different types of methylene groups are not resolved, but are detected as a single resonance.[19]

In conclusion, we have described how secondary Hg···π and Hg···$C_{ethynyl}$ interactions can be harnessed for the construction of supramolecular columns, allowing the formation of a microporous compound which can trap hydrocarbons in its alkylated interior.

Experimental Section

Owing to the toxicity of the mercury compounds in this study, extra care was taken at all times to avoid contact with the compounds in the solid state, in solution, or as airborne particulates.

2: **1** (30 mg, 0.029 mmol) and 1,3,5-$(Me_3SiC{\equiv}C)_3C_6H_3$ (10.6 mg, 0.029 mmol) were dissolved in THF (10 mL). Slow evaporation of the solvent led to the formation of colorless feathery crystals, which were washed twice with CH_2Cl_2 to afford **2** in 80% yield. Mp. 196 °C (decomp). Elemental analysis (%) calcd for $C_{39}H_{30}F_{12}Hg_3Si_3$: C 33.16, H 2.14; found: C 33.65, H 2.09. IR (KBr): $\tilde{\nu} = 2959$, 2164, 1252, 1162, 1046, 981, 880, 844, 760, 702, 692, 679, 653 cm^{-1}. ^{13}C MAS NMR (spinning at 7 kHz): for component **1**: $\delta = 156.0$ (t, $J_{Hg,C} = 743$ Hz, Hg-*C*), 144.1, 136.5 ppm (broad, F-*C*); for component 1,3,5-$(Me_3SiC{\equiv}C)_3C_6H_3$:[20] $\delta = \approx 135$ (obscured by peak from **1**), 122.2 (C_{aryl}), 100.2, 97.4 ($C_{ethynyl}$), −1.9 ppm (C_{silyl}).

Sorption isotherms were measured by monitoring the weight change of the sample as a function of pressure using a Cahn RG electrobalance connected to a manifold. A known weight of **2** (10–20 mg) was placed in the weighing pan. After evacuation of the system, the adsorbate was added incrementally through the manifold. Data points were recoded at equilibrium, when no further weight change was observed. Guest release was studied by monitoring the weight of the sample under vacuum every 5–10 s.

The room-temperature solid-state ^{1}H MAS NMR experiments were performed on an Avance-400 Solids NMR spectrometer with a 4-mm probe, at a spinning rate of 7 kHz. Saturated samples were packed in the rotor under ambient atmosphere. For the experiments with ethane and propane, the rotor was packed with **2**, exposed to an atmosphere of the gas, sealed, and transferred to the NMR spectrometer.

Received: June 17, 2006
Published online: August 29, 2006

Keywords: adsorption · alkanes · mercury · microporous materials · supramolecular chemistry

[1] For a general review: a) J. L. C. Rowsell, O. M. Yaghi, *Angew. Chem.* **2005**, *117*, 4748; *Angew. Chem. Int. Ed.* **2005**, *44*, 4670; for some recent examples: b) G. Férey, M. Latroche, C. Serre, F. Millange, T. Loiseau, A. Perceron-Guégan, *Chem. Commun.* **2003**, 2976; c) D. N. Dybtsev, A. L. Nuzhdin, H. Chun, K. P. Bryliakov, E. P. Talsi, V. P. Fedin, K. Kim, *Angew. Chem.* **2006**, *118*, 930; *Angew. Chem. Int. Ed.* **2006**, *45*, 916; d) P. M. Forster, J. Eckert, J.-S. Chang, S.-E. Park, G. Férey, A. K. Cheetham, *J. Am. Chem. Soc.* **2003**, *125*, 1309; e) L. Pan, M. B. Sander, X. Huang, J. Li, M. Smith, E. Bittner, B. Bockrath, J. K. Johnson, *J. Am. Chem. Soc.* **2004**, *126*, 1308; f) X. Zhao, B. Xiao, A. J. Fletcher, K. M. Thomas, D. Bradshaw, M. J. Rosseinsky, *Science* **2004**, *306*, 1012; g) Y. Kubota, M. Takata, R. Matsuda, R. Kitaura, S. Kitagawa, K. Kato, M. Sakata, T. C. Kobayashi, *Angew. Chem.* **2005**, *117*, 942; *Angew. Chem. Int. Ed.* **2005**, *44*, 920; h) B. Kesanli, Y. Cui, M. R. Smith, E. W. Bittner, B. C. Bockrath, W. Lin, *Angew. Chem.* **2005**, *117*, 74; *Angew. Chem. Int. Ed.* **2005**, *44*, 72; i) S. S. Kaye, J. R. Long, *J. Am. Chem. Soc.* **2005**, *127*, 6506.

[2] P. Sozzani, S. Bracco, A. Comotti, L. Ferretti, R. Simonutti, *Angew. Chem.* **2005**, *117*, 1850; *Angew. Chem. Int. Ed.* **2005**, *44*, 1816.

[3] L. Pan, D. H. Olson, L. R. Ciemnolonski, R. Heddy, J. Li, *Angew. Chem.* **2006**, *118*, 632; *Angew. Chem. Int. Ed.* **2006**, *45*, 616.

[4] B. Chen, C. Liang, J. Yang, D. S. Contreras, Y. L. Clancy, E. B. Lobkovsky, O. M. Yaghi, S. Dai, *Angew. Chem.* **2006**, *118*, 1418; *Angew. Chem. Int. Ed.* **2006**, *45*, 1390.

 © 2006 Wiley-VCH Verlag GmbH & Co. KGaA, Weinheim

[5] a) P. Sozzani, A. Comotti, S. Bracco, R. Simonutti, *Chem. Commun.* **2004**, 768; b) G. R. Desiraju, *Acc. Chem. Res.* **2002**, *35*, 565; c) E. A. Meyer, R. K. Castellano, F. Diederich, *Angew. Chem.* **2003**, *115*, 1244; *Angew. Chem. Int. Ed.* **2003**, *42*, 1210.

[6] J. L. Blin, B. L. Su, *Langmuir* **2002**, *18*, 5303.

[7] P. Sartori, A. Golloch, *Chem. Ber.* **1968**, *101*, 2004. V. B. Shur, I. A. Tikhonova, *Russ. Chem. Bull.* **2003**, *52*, 2539; M. R. Haneline, R. Taylor, F. P. Gabbaï, *Chem. Eur. J.* **2003**, *9*, 5188.

[8] M. Tsunoda, F. P. Gabbaï, *J. Am. Chem. Soc.* **2000**, *122*, 8335.

[9] T. J. Taylor, F. P. Gabbaï, *Organometallics* **2006**, *25*, 2143.

[10] a) Crystal data for **2**: $C_{39}H_{30}F_{12}Hg_3Si_3$, $M_r = 1412.67$, hexagonal, space group $P6_3/mmc$, $a = 19.852(3)$, $c = 6.5659(13)$ Å, $V = 2241.0(7)$ Å^3, $Z = 2$, $\rho_{calcd} = 2.093$ g cm^{-3}, $0.120 \times 0.030 \times 0.030$ mm^3, ω-scan mode, $\theta = 1.18$–$23.24°$, 656 unique reflections, 562 reflections with $I > 2\sigma(I)$, $\mu(Mo_{K\alpha}) = 10.407$ mm^{-1}, $R1 = 0.0455$, $wR2 = 0.1328$ (all data); b) Crystal data for **2**⊃0.82 $CHBr_3$: $C_{39.82}H_{30.82}Br_{2.46}F_{12}Hg_3Si_3$, $M_r = 1618.26$, hexagonal, space group $P6_3/mmc$, $a = 19.900(3)$, $c = 6.5529(13)$ Å, $V = 2247.3(6)$ Å^3, $Z = 2$, $\rho_{calcd} = 2.391$ g cm^{-3}, $0.095 \times 0.040 \times 0.040$ mm^3, ω-scan mode, $\theta = 1.18$–$23.27°$, 659 unique reflections, 603 reflections with $I > 2\sigma(I)$, $\mu(Mo_{K\alpha}) = 12.550$ mm^{-1}, $R1 = 0.0530$, $wR2 = 0.1433$ (all data); CCDC-611078 (**2**) and CCDC-611079 (**2**⊃0.82 $CHBr_3$) contain the supplementary crystallographic data for this paper. These data can be obtained free of charge from The Cambridge Crystallographic Data Centre via www.ccdc.cam.ac.uk/data_request/cif.

[11] P. Pyykkö, M. Straka, *Phys. Chem. Chem. Phys.* **2000**, *2*, 2489.

[12] A. J. Canty, G. B. Deacon, *Inorg. Chim. Acta* **1980**, *45*, L225.

[13] C. Caillet, P. Claverie, *Acta Crystallogr. Sect. A* **1975**, *31*, 448.

[14] A. L. Spek, Platon, A Multipurpose Crystallographic Tool, Utrecht, 2005.

[15] Subjecting the liquid adsorbates to freeze-pump-thaw cycles did not affect uptake values significantly. Degassing the headspace of the sample container multiple times was found to be sufficient for uptake experiments, as **2** does not have a high affinity for atmospheric gases.

[16] This phenomenon is not uncommon: a) M. Eddaoudi, H. L. Li, O. M. Yaghi, *J. Am. Chem. Soc.* **2000**, *122*, 1391; b) Q. Fang, G. Zhu, M. Xue, J. Sun, F. Sun, S. Qiu, *Inorg. Chem.* **2006**, *45*, 3582.

[17] J. Galvez, *J. Chem. Inf. Comput. Sci.* **2003**, *43*, 1231.

[18] For another recent ^{1}H NMR spectroscopy study on alkanes interacting with self-assembled microporous materials: F. Stallmach, S. Gröger, V. Künzel, J. Kärger, O. M. Yaghi, M. Hesse, U. Müller, *Angew. Chem.* **2006**, *118*, 2177; *Angew. Chem. Int. Ed.* **2006**, *45*, 2123.

[19] The linewidths of these peaks are similar to those in other ^{1}H MAS NMR spectra: a) K. P. Datema, C. J. J. den Ouden, W. D. Ylstra, H. P. C. E. Kuipers, M. F. M. Post, *J. Chem. Soc. Faraday Trans.* **1991**, *87*, 1935; b) S. S. Arzumanov, S. I. Reshetnikov, A. G. Stepanov, V. N. Parmon, D. Freude, *J. Phys. Chem. B* **2005**, *109*, 19748; c) V. E. Zorine, P. C. M. M. Magusin, R. A. van Santen, *J. Phys. Chem. B* **2004**, *108*, 5600; d) J. Roland, D. Michel, *Magn. Reson. Chem.* **2000**, *38*, 587.

[20] K. M. Gaab, A. L. Thompson, J. Xu, T. J. Martínez, C. J. Bardeen, *J. Am. Chem. Soc.* **2003**, *125*, 9288.

 © 2006 Wiley-VCH Verlag GmbH & Co. KGaA, Weinheim

RNA Structures

DOI: 10.1002/anie.200602583

Calculation of the Dependence of Homo- and Heteronuclear ^{3}J and ^{2}J Scalar Couplings for the Determination of the 2′-Hydroxy Conformation in RNA**

*Jörg Fohrer, Uwe Reinscheid, Mirko Hennig, and Teresa Carlomagno**

The presence or absence of the 2′-hydroxy group within the pentose sugar accounts for the major difference between RNA and DNA. In canonical environments, the pentose sugars of RNA and DNA adopt C3′-*endo* and C2′-*endo* conformations, respectively, leading to distinct differences in the hydration and structural stability.[1] In addition to the conformational preferences imposed by the 2′-OH group, its vital role in RNA catalysis has been studied extensively for self-splicing viral ribozymes, type II introns and spliceosomal RNAs.[2–4] Thus, conformational studies of 2′-hydroxy groups provide unique insights into the structural features of RNA and shed light on the structure–activity relationship of RNA catalytic processes.

Recently, we reported the assignments and conformational analysis of the 2′-hydroxy groups in the 30-mer HIV-2 transactivation response element (TAR) RNA[5] in solution at low temperature,[6,7] while another study from Ying and Bax focuses on the conformational analysis of the 2′-hydroxy groups in the RNA hairpin derived from the helix 35 of the 23S ribosomal RNA.[8] Molecular dynamics (MD) simulations of an RNA hairpin previously identified three preferred orientations for the 2′-hydroxy proton when the ribose sugar adopts the C3′-*endo* pucker:[9] a) toward O3′, stabilized by attractive electrostatic interaction with the phosphate backbone (O3′ domain), b) toward O4′, stabilized by intra-ribose electrostatic interactions (O4′ domain) and c) toward the base, stabilized by interactions with the N3 or O2 atom of the attached base (base domain). In our previous study we reported preferences for the 2′-OH groups of canonical A-

[*] Dipl.-Chem. J. Fohrer, Dr. U. Reinscheid, Dr. T. Carlomagno
Abteilung 030
Max-Planck-Institut für Biophysikalische Chemie
Am Fassberg 11, 37077 Göttingen (Germany)
Fax: (+49) 551-201-2202
E-mail: taco@nmr.mpibpc.mpg.de

Prof. M. Hennig
Department of Biochemistry and Molecular Biology
Medical University of South Carolina
173 Ashley Avenue, P.O. Box 250509
Charleston, SC 29425 (USA)

[**] J.F. thanks C. Boehme for help with the Gaussian program and C. Schwiegk for technical assistance. This work was supported by the MPG, the DFG (SFB416 to T.C.), and the National Institutes of Health (AI040187, to M.H.).

Supporting information for this article is available on the WWW under http://www.angewandte.org or from the author.

© 2006 Wiley-VCH Verlag GmbH & Co. KGaA, Weinheim

form helical regions to occupy the O3′ or base domains,[7] while the work of Ying and Bax places all 2′-OH groups of the hairpin RNA in the base domain.[8] Both findings support a stabilizing network of hydrogen bonds that spans the minor groove of the RNA helix and includes two water molecules in the base plane of nucleotides belonging to opposite strands in a base pair step. Such network of hydrogen bonds has been proposed in a high-resolution X-ray study of an RNA duplex.[10] Although ^3J(C1′,OH2) and ^3J(C3′,OH2) couplings could be obtained for several residues of the RNAs under investigation at low temperature, thus far the absence of a Karplus-like parametrization of the heteronuclear couplings impeded the quantitative analysis of the ^3J(C1′,OH2) and ^3J(C3′,OH2).

Here we present ab initio calculations, using density functional theory (DFT), to derive the Karplus-like relations for the heteronuclear and homonuclear ^3J(C1′/C3′/H2′,OH2) and ^2J(C2′,OH2) couplings involving the 2′-hydroxy group. Establishing the dependence of the ^3J(C1′/C3′/H2′,OH2) on the intervening dihedral angle H2′-C2′-O2′-OH is essential for a quantitative analysis of the measured scalar couplings and thus allows the accurate determination of the 2′-hydroxy group conformation.

The DFT calculations of the ^3J(C1′/C3′/H2′,OH2) and ^2J(C2′,OH2) couplings were performed using Gaussian 03 Revision C.02[11] on a ribose molecule bearing an amino group at C1′ along with a phosphodiester attached to the 3′-hydroxy group. A geometry optimization was carried out with the ribose in the C3′-*endo* conformation using a b3Lyp/6-31g(d) basis set as implemented in Gaussian.[12,13] The dihedral angles of the ribose ring remained within the typical ranges for the C3′-*endo* sugar pucker during the geometry optimization. The ^3J and ^2J couplings related to the orientation of the 2′-hydroxy group were calculated using a b3Lyp/6-311g(2df, 2pd) basis set. The dependence of the three vicinal ^3J(C1′/C3′/H2′,OH2) and the two-bond ^2J(C2′,OH2) scalar couplings on the intervening H2′-C2′-O2′-OH dihedral angle θ is shown in Figure 1 (see also Table S1 in the Supporting Information for the theoretical coupling values at each angle θ).

The calculated Karplus-like curve for the homonuclear ^3J(H2′,OH2) coupling compares well to the Karplus-like curve determined from experimental data on model compounds reported by Fraser et al.[14] and confirms the good quality of the model system used in the DFT calculations. The two curves for the heteronuclear ^3J(C1′/C3′,OH2) couplings are asymmetric and differ substantially from each other. In Figure 1 we compare the dependence of the ^3J(C1′/C3′,OH2) couplings on the H2′-C2′-O2′-OH dihedral angle calculated here (continuous lines) with a crude approximation of the Karplus-like curves used in our previous work.[7] This approximated dependence was obtained by scaling the coefficients of the ^3J(C,H) Karplus relation in alkenes to reflect the averaged value of the ^3J(C,OH) coupling in ethanol (dashed lines). In the theoretically calculated curve, the ^3J(C3′,OH2) coupling reaches a maximum of 6.5 Hz at $\theta =$ 302° (Figure 1b, green continuous line). The averaged coupling, assuming equal populations of the *gauche* +, *gauche* −, and *trans* conformations, is 2.3 Hz, in good qualitative agreement with the average coupling of 2.9 Hz

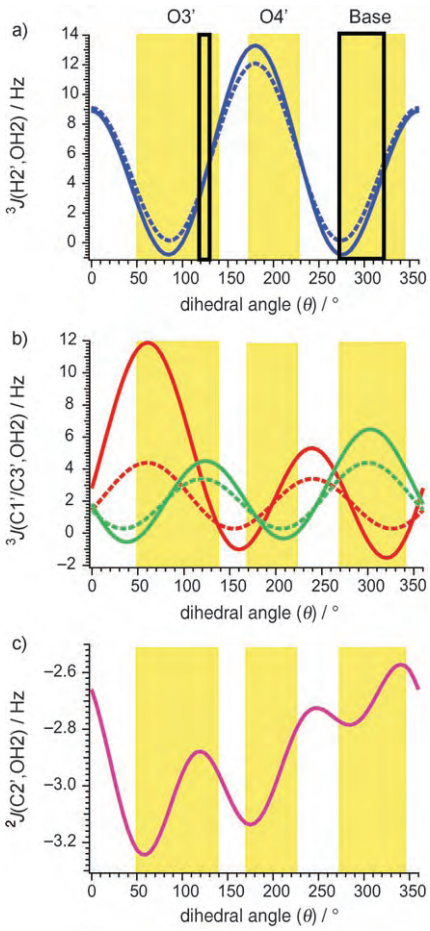

Figure 1. a) DFT-derived Karplus relations for the dependence of the ^3J(H2′,OH2) coupling on the dihedral angle H2′-C2′-O2′-OH, θ. The Karplus-like curve $^3J(H2',OH2) = 11.8\cos^2\theta - 2.2\cos\theta - 0.7$ derived by the DFT calculations is represented by the blue continuous line, while the Karplus-like curve determined by Fraser et al.[14] using two experimental values for 3β-acetoxy-5β,6β-oxidocholestan-19-ol, is shown by the dashed blue line for comparison. b) DFT-derived Karplus relations for the dependence of the ^3J(C1′,OH2) and ^3J(C3′,OH2) couplings on the dihedral angle H2′-C2′-O2′-OH. $^3J(C1',OH2) = 9.6\sin^2(\theta+30) + 3.3\sin(\theta+25.3) - 1.0$ (in red) and $^3J(C3',OH2) = 5.9\sin^2(\theta-33.2) - 1.0\sin(\theta-27.0) - 0.4$ (in green). The dashed lines represent the crude approximations derived in Reference [7] by scaling the coefficients of the ^3J(C,H) Karplus relation in alkenes to reflect the averaged value of the ^3J(C,OH) coupling in ethanol. c) DFT-derived relation for the dependence of the ^2J(C2′,OH2) coupling on the dihedral angle H2′-C2′-O2′-OH: $^2J(C2',OH2) = 0.6\cos^3(\theta+5.9) - 0.2\cos^2(\theta-46.1) - 0.4\cos(\theta-21.2) - 2.8$. Preferred conformational regions for the 2′-hydroxy proton identified by MD simulations are in yellow.[9] The black rectangles show the conformational regions in agreement with averaged and maximum scalar coupling values.

observed for the ^3J(C,OH) coupling in ethanol.[15] On the other hand, the ^3J(C1′,OH2) coupling adopts the maximum value of 11.6 Hz at $\theta = 62°$ (Figure 1b, red continuous line), which largely deviates from the crude approximation used previously (Figure 1b, red dashed line).[7] The ^2J(C2′,OH2) coupling assumes quite uniform values ranging from −3.3 to −2.6 Hz and shows only a moderate dependence on θ. These values are in very good agreement with those measured by Ying and Bax.[8]

 © 2006 Wiley-VCH Verlag GmbH & Co. KGaA, Weinheim

To understand the reasons for the strong asymmetry of the two ^3J(C1′/C3′,OH2) couplings, we performed DFT calculations to obtain the ^3J(C1′/C3′,OH) value for the linear 1-(dimethylamino)-2-hydroxy-1-methoxybutane-3-methylphosphate at dihedral angles θ(H-C-O-H) = 60° and 300° (Table S1 in the Supporting Information). The very similar values obtained for the ^3J(C1′,OH2) and the ^3J(C3′,OH2) couplings at $\theta = 60°$ and 300°, respectively, indicate that the strong asymmetry of the couplings in the ribose results from the cyclic structure of the sugar. Additionally, we verified the possibility that the high value observed at 62° for the ^3J(C1′,OH2) coupling could be significantly reduced by the involvement of the 2′-OH in a hydrogen bond either as a proton donor or acceptor. However, the presence of a water molecule that forms a hydrogen bond with the 2′-OH reduces the maximum value of the ^3J(C1′,OH2) coupling by 0.8 Hz only.

The effect of the ribose conformation on the Karplus-like relationship of the ^3J(C1′/C3′/H2′,OH2) couplings was verified by calculating the three couplings at the diagnostic θ angles of 60° and 300° for a ribose assuming the C2′-*endo* conformation. The values of the ^3J(C1′,OH2) and the ^3J(H2′,OH2) couplings are not significantly affected by the ribose conformation (< 0.5 Hz), while the ^3J(C3′,OH2) and the ^2J(C2′,OH2) couplings increase at $\theta = 300°$ by 1.6 Hz and −0.8 Hz, respectively.

The pronounced difference of both the ^3J(C1′,OH2) and the ^3J(H2′,OH2) couplings associated with the three distinct, preferred conformational regions (Figure 1) readily allows for distinguishing the conformational preferences around the dihedral angle H2′-C2′-O2′-OH when these couplings are available. In our previous work we found that the ^3J(H2′,OH2) and the ^3J(C1′,OH2) couplings did not exceed 5.5 and 4.0 Hz, respectively, for each RNA residue, while Ying and Bax measure uniform values of the ^3J(C1′,OH2) couplings of the order of 1.5 Hz.[8] Furthermore, in both studies the ^3J(C3′,OH2) coupling is found to be on average larger than the ^3J(C1′,OH2) coupling. These observations, in combination with the Karplus-like dependence calculated here, limit the conformational space accessible to the 2′-hydroxy group to a very small region of the O3′ domain ($\theta = 120$–$130°$) or to a large portion of the base domain ($\theta = 270$–$320°$; Figure 1). However, the observation that the H4′,OH2 NOE is always smaller than the H1′,OH2 NOE, as reported by Ying and Bax[8] for the RNA hairpin derived from the helix 35 of the 23S ribosomal RNA and measured by us for the G nucleotides in the helical regions of the TAR-RNA (Table S3 in the Supporting Information) seems to rule out population of the O3′ domain with $\theta > 90°$ (Figure S2 in the Supporting Information). In contrast, the approximated version of the Karplus dependence for the ^3J(C1′/C3′,OH2) couplings used in our previous work together with the measured heteronuclear couplings allowed for population of a large portion of the O3′ domain.

Thus far, the values of the ^3J(C1′/C3′/H2′,OH2) scalar couplings have been interpreted assuming one single conformation of the 2′-OH group. However, the ratio of the NOEs involving the 2′-OH reported by Ying and Bax[8] and measured here for the G nucleotides of the TAR-RNA (Table S3 in the Supporting Information) do not fully reconcile with the 2′-hydroxy groups occupying the base domain. While the H4′,OH2 NOE is always smaller than the H1′,OH2 NOE in the base domain, population of this domain exclusively would imply that the H4′,OH2:H1′,OH2 NOE ratio is approximately 0.1 while the H2′,OH2:H1′,OH2 NOE ratio is less than 2 or that the H4′,OH2:H1′,OH2 NOE ratio is greater than 0.1 while the H2′,OH2:H1′,OH2 NOE ratio is greater than 2 for a ribose molecule with $\tau_c = 5$ ns and in the presence of spin diffusion effects. The average ratios of 0.24 for the H4′,OH2:H1′,OH2 NOEs and of 1.25 for the H2′,OH2:H1′,OH2 NOEs suggest that conformational averaging is in effect. The absence of high values for all the measured couplings together with the mean values of each coupling and of the NOE ratios would reconcile with conformational averaging of the 2′-OH group between the O3′ domain with θ close to 120° and the base domain. This picture would still support the involvement of the 2′-OH in a network of hydrogen bonds spanning the minor groove.[7,10] The 2′-hydroxy group of one of the two nucleotides would switch between the O3′ domain, where it can accept a hydrogen bond from a water molecule, and the base domain, where it can function as a proton donor in a hydrogen bond with a water molecule, while the second nucleotide would remain in the base domain. Both situations, where the two 2′-hydroxy groups of opposite nucleotides in base pair steps are either alternatively in the O3′ and base domain or both in the base domain, support the hydration model of the minor groove proposed by Egli et al.[10] Conformational averaging between the O3′ domain and base domain for one of the two nucleotides would imply that one 2′-hydroxy and one water molecule concertedly switch their acceptor–donor roles.

The hypothesis of a two-state model for the conformation of the 2′-hydroxy group has to be verified by a quantitative interpretation of precisely measured ^3J(C1′/C3′/H2′,OH2) couplings together with diagnostic NOEs between the 2′-OH and the ribose protons. The Karplus parametrization reported here is an essential tool for this analysis and thus for an accurate understanding of the structural and functional role of the 2′-hydroxy group in RNA.

Experimental Section

The ^2J and the ^3J couplings involving the 2′-hydroxy groups were calculated using the DFT approach as implemented in Gaussian 03 Revision C.02.[11] The total nuclear spin–spin coupling was determined using the b3Lyp/6-311g(2df,2pd) basis set calculating the contributing Fermi contact (FC), spin dipolar (SD), paramagnetic spin orbit (PSO), and diamagnetic spin orbit (DSO) terms. The NOEs of the 2′-OH groups were measured in a ^{13}C-edited HSQC NOESY spectrum with a mixing time of 50 ms for a 1.5 mM sample of ^{13}C/^{15}N G-labeled TAR-RNA dissolved in H_2O/D_2O (90:10) at pH 6.4 (10 mM phosphate buffer, 50 mM sodium chloride).

Received: June 28, 2006
Published online: September 27, 2006

Keywords: ab initio calculations · Karplus relationship · NMR spectroscopy · RNA

 © 2006 Wiley-VCH Verlag GmbH & Co. KGaA, Weinheim

[1] J. I. Gyi, A. N. Lane, G. L. Conn, T. Brown, *Nucleic Acids Res.* **1998**, *26*, 3104 – 3110.
[2] R. F. Gesteland, T. Chech in *The RNA World* (Eds.: R. F. Gesteland, T. Chech, J. F. Atkins), Cold Spring Harbor, New York, **1998**.
[3] E. A. Doherty, J. A. Doudna, *Annu. Rev. Biochem.* **2000**, *69*, 597 – 615.
[4] F. Eckstein, D. M. J. Lilley in *Catalytic RNA* (Eds.: F. Eckstein, D. M. J. Lilley), Springer, Berlin, **1997**.
[5] A. S. Brodsky, J. R. Williamson, *J. Mol. Biol.* **1997**, *267*, 624 – 639.
[6] M. Hennig, J. Fohrer, T. Carlomagno, *J. Am. Chem. Soc.* **2005** *127*, 2028 – 2029.
[7] J. Fohrer, M. Hennig, T. Carlomagno, *J. Mol. Biol.* **2006**, *356*, 280 – 287.
[8] J. Ying, A. Bax, *J. Am. Chem. Soc.* **2006**, *128*, 8372 – 8373.
[9] P. Auffinger, E. Westhof, *J. Mol. Biol.* **1997**, *274*, 54 – 63.
[10] M. Egli, S. Portmann, N. Usman, *Biochemistry* **1996**, *35*, 8489 – 8494.
[11] M. J. Frisch et al. Gaussian Inc. Wallingford CT, **2004**.
[12] A. D. Becke, *Phys. Rev. A* **1988**, *38*, 3098 – 3100.
[13] A. D. Becke, *J. Chem. Phys.* **1993**, *98*, 5648 – 5652.
[14] R. R. Fraser, M. Kaufman, P. Morand, G. Govil, *Can. J. Chem.* **1969**, *47*, 403 – 409.
[15] H. O. Kalinowski, S. Berger, S. Braun in *Carbon ^{13}C NMR Spectroscopy*, Wiley, Chichester, **1984**.

 © 2006 Wiley-VCH Verlag GmbH & Co. KGaA, Weinheim

Persistent Radical Cations

DOI: 10.1002/anie.200603009

Formation and Structure of a Stable Monoradical Cation by Reduction of a Diphosphafulvenium Salt**

Frédéric Biaso, Thibault Cantat, Nicolas Mézailles, Louis Ricard, Pascal Le Floch, and Michel Geoffroy**

The attention paid by physical chemists to organic radical ions has never ceased to increase over the last 20 years,[1,2] mainly because these species often act as reaction intermediates and because their structure can determine the result of many chemical processes.[3] Considerable efforts have been devoted to gaining a better knowledge of their electronic structure; unfortunately their high reactivity make their identification difficult, and reports on their crystal structures remain sparse.[4] Renewed interest in the behavior of organic ion radicals has recently appeared owing to the practical applications predicted for some of these compounds in materials science and because of their potential use as electronic devices, organic magnets, and organic conductors.[5,6] Fulvene derivatives (**A**, Scheme 1) play an important role in this field;

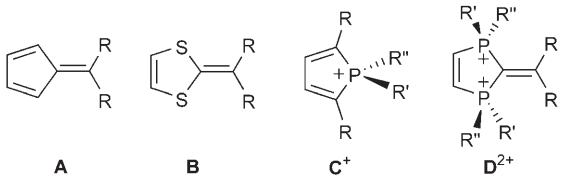

Scheme 1.

for example, dithiafulvene (**B**) constitutes one of the elementary units of conducting, semiconducting, and superconducting molecular solids. In this context, a crucial property of tetrathiafulvalene lies in its capacity to easily release one electron to give, reversibly, a rather persistent radical cation.[7] The discovery of novel fulvene-centered systems that are able to reversibly stabilize a radical cation is of considerable interest. The results herein contribute to this project, and as will be seen further, phosphorus chemistry can open new and very attractive perspectives in this area.

On the basis of early reports on the chemistry of 1,4-diphosphoniacyclohexa-2,5-dienes,[8] as well as our recent EPR study on the reduction processes of monophospholium cations $\mathbf{C}^+$,[9] we postulated that pentavalent phosphorus atoms could behave as strong electron acceptors and thus allow the synthesis and stabilization of persistent radical cations through reduction processes. We validate this hypothesis herein in the case of a diphosphafulvenium dication $\mathbf{D}^{2+}$ whose reduction leads to a stable radical cation. To the best of our knowledge, diphosphafulvenium cations have never been reported so far.[10]

The *trans*-tetraphenyldiphosphafulvene derivative **1**, whose synthesis was recently reported, was chosen as the starting precursor.[11] Reaction of **1** with excess methyl triflate (MeOTf) at 25 °C cleanly afforded dication $\mathbf{2}^{2+}$, which was isolated as a very stable white solid. The structure of $\mathbf{2}^{2+}$ was confirmed by NMR data and elemental analyses. Unfortunately, despite many attempts, $\mathbf{2}^{2+}$ proved to be reluctant towards crystallization, thus precluding the recording of an X-ray crystal structure. As expected, dication $\mathbf{2}^{2+}$ can be easily reduced, as indicated by cyclic voltammetry (CH_3CN, room temperature), which revealed four waves at −0.54 V (reversible), −1.10 V (irreversible), −1.37 (partially reversible), and −1.72 V (irreversible) versus SCE. Importantly, the first reduction process was found to be reversible even at low scan rates (50 $mV\,s^{-1}$), thereby suggesting that it would be possible to isolate a persistent radical cation. Reduction of $\mathbf{2}^{2+}$ was

[*] T. Cantat, Dr. N. Mézailles, Dr. L. Ricard, Prof. P. Le Floch
Département de Chimie
Laboratoire "Hétéroéléments et Coordination"
UMR CNRS 7653
Ecole Polytechnique
91128 Palaiseau Cédex (France)
Fax: (+33) 1-6933-3990
E-mail: lefloch@poly.polytechnique.fr
Dr. F. Biaso, Prof. M. Geoffroy
Département de Chimie Physique
Université de Genève
30 Quai Ernest Ansermet 1211, Genève 4 (Switzerland)
Fax: (+41) 22-379-6103
E-mail: michel.geoffroy@chiphy.unige.ch

[**] The authors thank the Swiss National Science Foundation, the CNRS, and the Ecole Polytechnique for the financial support and IDRIS for the allowance of computer time (project no. 51616).

Supporting information for this article is available on the WWW under http://www.angewandte.org or from the author.

InterScience
© 2006 Wiley-VCH Verlag GmbH & Co. KGaA, Weinheim

carried out at low temperature by adding 1,2-dimethoxyethane (DME) to a solid mixture of $\mathbf{2}^{2+}$ and $[CoCp_2]$. The solution immediately turned deep purple, and after warming to 25 °C, *n*-hexane was added to crystallize the radical monocation $\mathbf{2}^{\bullet+}$, which was then easily separated from cobaltocenium triflate (Scheme 2).

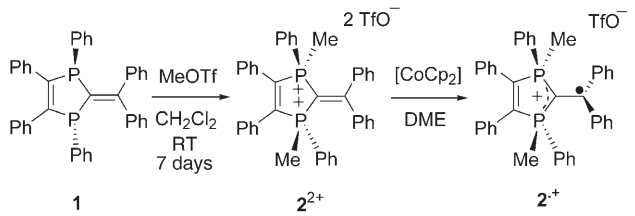

Scheme 2. Synthesis of compounds $\mathbf{2}^{2+}(TfO^-)_2$ and $\mathbf{2}^{\bullet+}TfO^-$.

The structure of $\mathbf{2}^{\bullet+}$ was confirmed by an X-ray crystallographic study.[12] A view of one molecule of $\mathbf{2}^{\bullet+}$ is presented in Figure 1. The most significant piece of data concerns the two

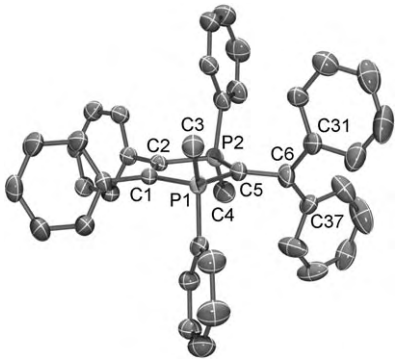

Figure 1. ORTEP plot of $\mathbf{2}^{\bullet+}$ (ellipsoids set at 50% probability). The cocrystallized triflate anion is omitted for clarity. Selected bond lengths [Å] and angles [°]: P1-C5 1.713(3), P2-C5 1.718(3), C5-C6 1.473(4); P2-C5-C6 123.2(2), P1-C5-P2 109.6(2), P1-C5-C6 127.0(3), C5-C6-C31 121.2(2), C5-C6-C37 118.4(3), C31-C6-C37 119.2(3).

P1–C5 (1.713(3) Å) and P2–C5 (1.718(3) Å) bond lengths, which are very short compared to the P1–C1 and P2–C2 bond lengths (1.809(3) Å). On the other hand, the C5–C6 bond (1.473(4) Å) is also very long and has clearly lost its double-bond character. The geometry at C6 is planar (Σangles = 358.8°). Furthermore, the CPh_2 group is twisted from the plane that is defined by the ring (ζ(P1-C5-C6-C31) = −70.5°) and participates in stabilizing the extra electron, as attested to by the short C6–C31 and C6–C37 bond lengths (av. 1.46 Å).[13] All these data suggest that reduction has taken place at the P1-P2-C5-C6 segment. This observation is confirmed by the fact that the C1–C2 bond length remains close to what is expected for a classical carbon–carbon double bond (1.34 Å).

EPR experiments and DFT calculations were carried out to determine the precise electronic structure of $\mathbf{2}^{\bullet+}$. Electrolysis in the EPR cavity at a potential corresponding to the first reduction wave leads to the spectrum shown in Figure 2a.

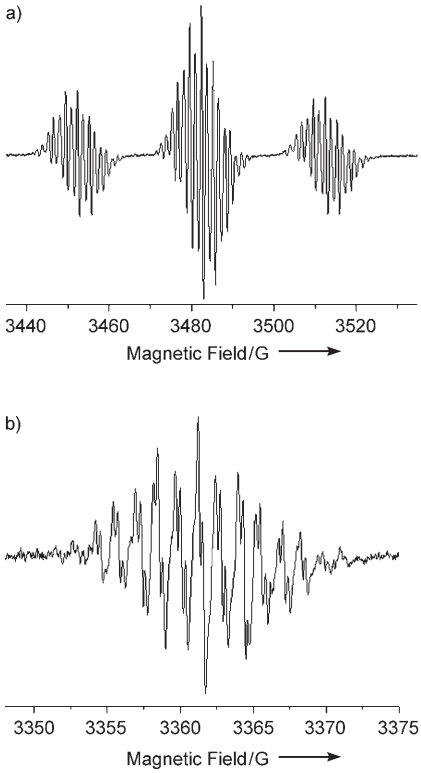

Figure 2. a) Liquid-solution EPR spectrum obtained at 300 K after reduction of a solution of $\mathbf{2}^{2+}(TfO^-)_2$ in THF. b) Expansion of the central part of the spectrum.

This spectrum, measured at 300 K, is characterized by a *g* value equal to 2.0029 and by a hyperfine interaction of about 30 G with two equivalent ^{31}P nuclei. Additional structure resulting from coupling with several protons of two phenyl rings is clearly visible (Figure 2b). It is interesting to note that these couplings are quite similar to those measured by ENDOR on $Ph_3C^{\bullet}$.[14] A simulation was performed by using the following coupling constants (expressed in Gauss): ^{31}P 30.1, H_a 3.00, H_b 2.83, H_c 2.82, H_d 1.35, H_e 1.11. Note that the spectrum of $\mathbf{2}^{\bullet+}$, which was also recorded at 100 K, clearly shows that the *g* and ^{31}P coupling tensors do not exhibit any anisotropy.[15] The reduced species is rather persistent, and its spectrum could be observed for several hours without voltage under a nitrogen atmosphere. The same spectrum was obtained by reducing a solution of $\mathbf{2}^{\bullet+}$ in THF with one equivalent of $C_{10}H_8Na$.

To get further insights into the electronic structure of $\mathbf{2}^{\bullet+}$, DFT calculations were carried out on the actual molecules $\mathbf{2}^{2+}$ and $\mathbf{2}^{\bullet+}$ at the quantum level.[15] A good agreement was found between the experimental and theoretical structures of $\mathbf{2}^{\bullet+}$. Only the dihedral angle of the CPh_2 group differs.[16] An examination of the molecular orbitals of the two species furnishes important information. In $\mathbf{2}^{2+}$ the LUMO is antibonding between C5 and C6 and bonding between the phosphorus atoms and C5 (Figure 3), thus explaining why the P–C5 bonds are shortened[17] upon reduction and why the C5–C6 bond is significantly elongated.[18] Upon reduction, one electron is added into the LUMO of $\mathbf{2}^{2+}$ as shown in the SOMO of $\mathbf{2}^{\bullet+}$ (Figure 3). Calculations of Wiberg bond indices

 © 2006 Wiley-VCH Verlag GmbH & Co. KGaA, Weinheim

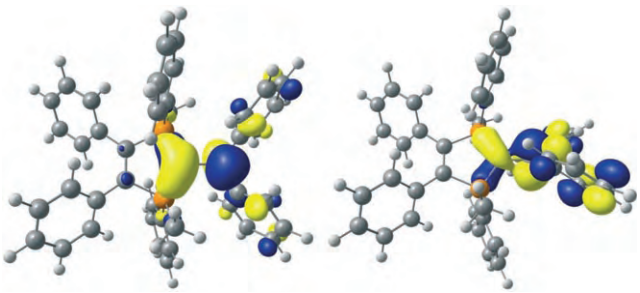

Figure 3. LUMO of $\mathbf{2}^{2+}$ (left) and SOMO of $\mathbf{2}^{\bullet+}$ (right) as given by DFT calculations (P orange, C dark gray, H light gray).

confirm that the order of the C5–C6 bond has been reduced on going from $\mathbf{2}^{2+}$ to $\mathbf{2}^{\bullet+}$ (1.58 to 1.11).

Isotropic and anisotropic hyperfine interactions with ^{1}H ($A_{iso} = -2.63$ and -2.84 G for H_{ortho}, 1.16 and 1.43 G for H_{meta}, and -3.05 G for H_{para}) and ^{31}P nuclei ($A_{iso} = 32.9$ and 33.2 G; $\tau_{aniso} = -4$, -3, and $+7$) were obtained from the DFT calculations and agree with the experimental values. In accord with frozen-solution spectra, the anisotropy of the ^{31}P coupling was also found to be rather small. All these data suggest that in diphosphafulvenium systems the two pentavalent phosphorus atoms behave as strong acceptors and prevent delocalization over the ring. Such systems are therefore different from their sulfur or carbon counterparts. The excess of electron density gained upon reduction mainly resides on the exocyclic double bond and is strongly stabilized by negative hyperconjugation with the two pentavalent phosphorus atoms. Therefore, two ylidic forms can be proposed to rationalize the electronic structure of $\mathbf{2}^{\bullet+}$ (Scheme 3).

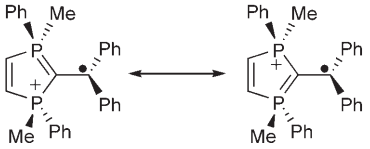

Scheme 3. Ylidic forms involved in $\mathbf{2}^{\bullet+}$.

From this study we can conclude that 1,1-bis(phosphonium) olefins can act as suitable precursors for the synthesis of persistent monoradical cations upon reduction at low potential. Further studies aimed at expanding this simple idea to the elaboration of highly conjugated paramagnetic structures are currently underway in our laboratories.

Experimental Section

All experiments were carried out in a dry argon or nitrogen atmosphere by using distilled and degassed solvents. For the synthesis of $\mathbf{2}^{2+}(TfO^{-})_2$, see the Supporting Information.

$\mathbf{2}^{\bullet+}TfO^{-}$: DME (25 mL) was condensed onto a mixture of $\mathbf{2}^{2+}(TfO^{-})_2$ (0.24 g, 0.27 mmol) and $[CoCp_2]$ (51 mg, 0.27 mmol) at $-78\,^{\circ}C$. The solution was warmed to room temperature and stirred for two hours. A mixture of hexanes was then condensed onto the crude mixture at $-78\,^{\circ}C$, which resulted in the formation of deep purple crystals of $\mathbf{2}^{\bullet+}TfO^{-}$ within 12 h. The resulting crystals were isolated and washed with diethyl ether (3×5 mL) to afford $\mathbf{2}^{\bullet+}TfO^{-}$ in 93% yield (0.19 g, 0.25 mmol). No NMR spectrum is available for this compound owing to its paramagnetic nature.

Received: July 26, 2006
Published online: October 2, 2006

Keywords: density functional calculations · EPR spectroscopy · phosphorus · radicals · reduction

[1] Z. V. Todres, *Organic Ion radicals*, Marcel Decker, New York, **2003**.
[2] M. Letzel, D. Kirchhoff, H.-F. Grützmacher, D. Stein, H. Grützmacher, *Dalton Trans.* **2006**, 2008–2016.
[3] R. L. Donkers, L. D. Stringle, M. S. Workentin, *Annu. Rep. Prog. Chem. Sect. B* **2001**, *97*, 345.
[4] C. Dutan, S. Choua, T. Berclaz, M. Geoffroy, N. Mézailles, A. Moores, L. Ricard, P. Le Floch, *J. Am. Chem. Soc.* **2003**, *125*, 4487–4494; P. B. Hitchcock, M. F. Lappert, A. V. Protchenko, *J. Am. Chem. Soc.* **2001**, *123*, 189–190.
[5] H. Wilhelm, D. Jaccard, R. Duprat, C. Bourbonnais, D. Jerome, J. Moser, C. Carcel, J. M. Fabre, *Eur. Phys. J.* **2001**, *21*, 175–183.
[6] V. Oison, C. Katan, C. Koenig, *J. Phys. Chem. A* **2001**, *105*, 4300–4307.
[7] F. Wudl, D. Wobsschall, E. J. Hufnagel, *J. Am. Chem. Soc.* **1972**, *94*, 670–672. M. Fourmigué, P. Batail, *Chem. Rev.* **2004**, *104*, 5379–5418; M. Mas-Torrent, C. Rovira, *J. Mater. Chem.* **2006**, *16*, 433–436; M. Herranz, L. Sanchez, N. Martin, *Phosphorus Sulfur Silicon* **2005**, *180*, 1133–1148; P. Frere, P. Skabara, *Chem. Soc. Rev.* **2005**, *34*, 69–98.
[8] R. D. Rieke, R. A. Copenhafer, A. M. Aguillar, M. S. Chattha, J. C. W. Jun, *J. Chem. Soc. Chem. Commun.* **1972**, 1130; R. D. Rieke, R. A. Copenhafer, C. K. White, A. Aguiar, J. C. Williams, M. S. Chattha, *J. Am. Chem. Soc.* **1977**, *99*, 6656–6662.
[9] P. Adkine, T. Cantat, E. Deschamps, L. Ricard, N. Mézailles, P. Le Floch, M. Geoffroy, *Phys. Chem. Chem. Phys.* **2006**, *8*, 862–868.
[10] For leading references concerning the chemistry of 1,3-diphosphafulvenes and their functional derivatives, see: N. Maigrot, L. Ricard, C. Charrier, F. Mathey, *Angew. Chem.* **1988**, *100*, 997–998; *Angew. Chem. Int. Ed. Engl.* **1988**, *27*, 950–951; N. Maigrot, L. Ricard, C. Charrier, F. Mathey, *Angew. Chem.* **1992**, *104*, 1082–1084; *Angew. Chem. Int. Ed. Engl.* **1992**, *31*, 1031–103; S. Ito, S. Sekiguchi, M. Yoshifuji, *J. Org. Chem.* **2004**, *69*, 4181–4184; A. Nakamura, K. Toyota, M. Yoshifuji, *Tetrahedron* **2005**, *61*, 5223–5228.
[11] T. Cantat, N. Mézailles, N. Maigrot, L. Ricard, P. Le Floch, *Chem. Commun.* **2004**, 1274–1275.
[12] Crystal data for $\mathbf{2}^{\bullet+}TfO^{-}$: $C_{42}H_{36}P_2/CF_3O_3S$, monoclinic, space group $P2_1/n$, $a = 10.5080(10)$, $b = 17.9590(10)$, $c = 19.5300(10)$ Å, $\beta = 90.3500(10)^{\circ}$, $V = 3685.5(4)$ Å^3, $Z = 4$, $\rho_{calcd} = 1.355$ g cm^{-3}, $F(000) = 1564$, $Mo_{K\alpha}$ radiation ($\lambda = 0.71069$ Å), $\mu = 0.230$ cm^{-1}, crystal dimensions $0.20 \times 0.20 \times 0.18$ mm. Data collection was performed on a Nonius Kappa CCD single-crystal diffractometer at $T = 150$ K; the crystal structure was solved with SIR97,[19a] refinement against F^2 (SHELXL-97[19b]) with anisotropic thermal parameters for all nonhydrogen atoms, calculated hydrogen positions with riding isotropic thermal parameters, *hkl* ranges: $-13/13$, $-20/22$, $-24/24$; 13478 data collected, 7774 unique data ($R_{int} = 0.0203$), 5796 data with $I > 2\sigma(I)$, 472 parameters refined, $GoF(F^2) = 1.022$, final R indices ($R1 = \Sigma\,||F_o| - |F_c||/\Sigma\,|F_o|$, $wR2 = [\Sigma w(F_o^2 - F_c^2)^2/\Sigma w(F_c^2)^2]^{1/2}$, $R1 = 0.0584$, $wR2 = 0.1643$, max/min residual electron density 0.664(0.055)/$-0.504(0.055)$ e Å^3. CCDC-612414 contains the supplementary crystallographic data for this paper. These data can be obtained

 © 2006 Wiley-VCH Verlag GmbH & Co. KGaA, Weinheim

free of charge from The Cambridge Crystallographic Data Centre via www.ccdc.cam.ac.uk/data_request/cif.
[13] A search of the Cambridge Structural Database afforded 15 structures of triarylmethyl radicals. We found an average C–C_{ipso} bond length of 1.46 Å. For comparison, an average corresponding bond length of 1.53 Å is found for Ar_3CH derivatives.
[14] B. Kirste, W. Harrer, H. Kurreck, *J. Am. Chem. Soc.* **1985**, *107*,20–28.
[15] See the Supporting Information for further details.
[16] ζ(P1-C5-C6-C31) = 53.3° for the optimized structure versus −70.5° for the X-ray structure.
[17] P–C5 bonds are shortened from 1.819 Å in $\mathbf{2}^{2+}$ to 1.756 Å in $\mathbf{2}^{\cdot+}$ (calculated values).
[18] C5–C6 bond is elongated from 1.397 Å in $\mathbf{2}^{2+}$ to 1.469 Å in $\mathbf{2}^{\cdot+}$ (calculated values).
[19] a) A. Altomare, M. C. Burla, M. Camalli, G. Cascarano, C. Giacovazzo, A. Guagliardi, A. G. G. Moliterni, G. Polidori, R. Spagna, SIR97, an integrated package of computer programs for the solution and refinement of crystal structures using single-crystal data, **1999**; b) M. Sheldrick, SHELXL-97; Universität Göttingen, Göttingen, Germany, **1998**.

 © 2006 Wiley-VCH Verlag GmbH & Co. KGaA, Weinheim

Lithium-Ion Batteries

DOI: 10.1002/anie.200602071

One-Step, Confined Growth of Bimetallic Tin–Antimony Nanorods in Carbon Nanotubes Grown In Situ for Reversible Li^+ Ion Storage

*Yong Wang and Jim Yang Lee**

The discovery of carbon nanotubes (CNTs)[1] has stimulated considerable interest in the synthesis and characterization of one-dimensional nanomaterials. A significant number of materials can now be produced in the form of nanorods or nanowires with diameters ranging from a few to several hundreds of nanometers.[2] One-dimensional electrochemically active materials, such as CNTs,[3,4] CNT-supported SnSb/Sn/SnO_2 particles,[5–8] SnO_2 nanowires, nanorods[9–11] and nanotubes,[12] and SnO_2–CNT duplex nanotubes[13] have been used as the anode of lithium-ion batteries and have delivered significant improvements in application performance over their bulk form. The enhancement effect of the one-dimensional topography should also be applicable to anode materials of a higher caliber. Intermetallic Sn–Sb compounds, which are known for their high specific capacities (relative to graphite) and good cyclability (relative to Sn) because of the reversibility in implementing the lithium insertion and extraction reactions in a stepwise manner,[14–21] spring to mind.

However, the synthesis of Sn–Sb nanorods has yet to be reported. Although Sn–Sb nanoparticles are usually prepared by the reductive co-precipitation of Sn and Sb with $NaBH_4$[14–16,19–21] or Zn,[17,18] the extreme reaction conditions are not conducive to the control of product morphology. The low melting points of Sn and SnSb alloys (ca. 230–240 °C) and the difficulty in composition control have also ruled out the use of a number of popular methods such as thermal evaporation and electrochemical co-deposition of the constituent metals into the pores of hard templates. Herein, we report that bimetallic Sn–Sb nanorods are produced in CNT templates formed in situ. The CNT-encapsulated Sn–Sb nanorods thus obtained show high specific capacities and good cyclability when tested as the anode of lithium-ion batteries.

The field-emission scanning electron microscopy (FESEM) and transmission electron microscopy (TEM) images of the commercial antimony tin oxide (ATO) nanoparticles that were used as the precursor for Sn–Sb nanorod growth can be found in Figure S1 of the Supporting Information. The products obtained from the decomposition of C_2H_2 over ATO are shown in Figure 1a, a large number of rod-like structures approximately 800 nm to 3.5 μm in length and with a uniform diameter are found. Under high magnification (see FESEM image in Figure 1b) the nanorods show a coaxially integrated core–shell structure that consists of a Sn–Sb core and a CNT shell, with no void space between the two. The tips of a few CNTs that have not been completely filled with Sn–Sb. The expanded view of a partially filled CNT tip and that of a completely filled CNT tip are shown in Figure 1c and Figure 1d, respectively. Powder X-ray diffraction (XRD)

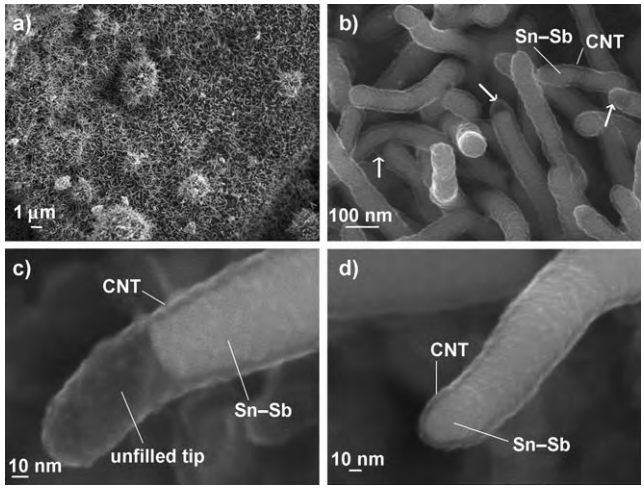

Figure 1. FESEM images of the CNT-encapsulated Sn–Sb nanorods showing a) a large number of rod-like products at low magnification, b) the thin CNT overlayer of filled nanorods at high magnification, the tips of a few CNTs that have not been completely filled with Sn–Sb are indicated by arrows, c) the unfilled tip of a filled CNT, and d) the completely filled tip of a filled CNT.

[*] Dr. Y. Wang, Prof. Dr. J. Y. Lee
Department of Chemical and Biomolecular Engineering
National University of Singapore
10 Kent Ridge Crescent, 119260 Singapore (Singapore)
Fax: (+65) 6779-1936
E-mail: cheleejy@nus.edu.sg
Homepage: http://www.chee.nus.edu.sg/staff/lee.html

Supporting Information for this article is available on the WWW under http://www.angewandte.org or from the author.

© 2006 Wiley-VCH Verlag GmbH & Co. KGaA, Weinheim

measurements (see Figure S2 in the Supporting Information) confirmed that the filling is a multiphase mixture of Sn and SnSb. inductively coupled plasma (ICP) spectroscopy and CHN elemental analysis of the core–shell nanorods gave the following composition: approximately 7.6 wt% of CNTs and approximately 92.4 wt% of Sn–Sb, with an overall stoichiometry of $SnSb_{0.11}$.

The TEM images in Figure 2a and Figure 2b show the tips of two free-standing CNTs one with and one without complete filling of their cores by Sn–Sb. The carbon shell is about 7–10 nm thick and the diameter of the Sn–Sb core is

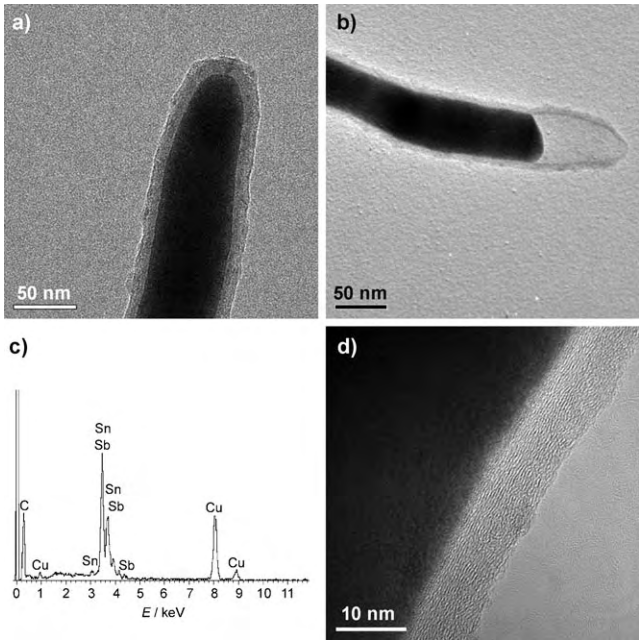

Figure 2. TEM images of a CNT-encapsulated Sn–Sb nanorod: a) a completely filled CNT tip, b) expanded view of a partially filled tip, c) EDS analysis of a CNT-encapsulated Sn–Sb nanorod, d) HRTEM image of a CNT encapsulated Sn–Sb nanorod showing the multiwalled structure of the CNT sheath.

about 70 nm. Energy-dispersive X-ray spectroscopy (EDS) of the core–shell structure in Figure 2c confirmed the presence of Sn and Sb. The measured Sn/Sb atomic ratio of about 8:1 is in good agreement with the ratio in the ATO nanoparticles and suggests no selective incorporation of either of the metals into the CNT interior. During the TEM examination of the core–shell structure (see Figure S3 in the Supporting Information) a number of Sn–Sb nanorods melted after a few minutes of electron-beam irradiation. This phenomenon, which is common for low-melting metals, such as Sn (232 °C),[22] In (157 °C),[23] and Bi (271 °C),[24] is the result of localized heating by the focused electron beam. The high resolution (HR)TEM image in Figure 2d shows that the carbon shell is made up of staggered, shortened graphene sheets. This less graphitic form of carbon could promote Li^+ ion diffusion into the Sn–Sb core through the "gaps" in the graphene sheets so that Li^+ ions need not enter only through the ends of the CNTs. There is some low level residual hydrogen in the CNTs (H/C weight ratio = 0.39%), although this should have only a minor effect on lithium-ion storage.[25]

Based on the experimental observations, a growth mechanism for the CNT-encapsulated Sn–Sb nanorods may be proposed: ATO is first reduced by C_2H_2 to form low-melting (ca. 230–240 °C) Sn–Sb intermetallic compounds which catalyze the growth of CNTs by C_2H_2 decomposition. Since no residual catalyst particles are found at the CNT tips (the closed end of the nanotube, see Figure 1b,c and 2b), the growth of CNTs is believed to occur by the "bottom-up" mechanism. At the high growth-temperature of 700 °C, the low-melting Sn–Sb intermetallic compounds are present as liquid droplets from which the CNTs grow. Capillary forces then draw the liquid droplets into the interior of the CNTs once the latter have grown to a sufficient length. In this way the CNTs formed in situ are the hard template[26,27] that shapes the molten Sn–Sb into nanorods (upon cooling) and prevents the coalescence of molten Sn–Sb into large spherical droplets. Figure 3 shows a schematic sketch of the perceived

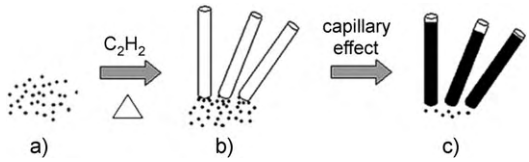

Figure 3. Schematic representation of the in situ growth of Sn–Sb nanorods inside carbon nanotubes. a) Antimony tin oxide nanoparticles. b) Growth of carbon nanotubes induced by molten Sn–Sb alloy. c) Capillary encapsulation of molten Sn–Sb into carbon nanotube interior.

growth process. It should be emphasized that the CNT shell is formed by the catalytic action of Sn–Sb rather than by the physical deposition of carbon onto fully developed Sn–Sb nanorods. This situation is evident from the presence of a considerable number of CNTs with unfilled Sn–Sb sections near their closed ends (Figure 1b). In addition, the low-melting Sn–Sb cannot be in the solid state at the high temperature of this process, let alone in a rod-like morphology that is energetically much less favorable than a spherical geometry.

The capillary encapsulation technique has been used previously to induct filler materials into prefabricated CNTs.[5,28,29] It requires the CNTs to be opened by chemical means. However, the filler material is often found on the CNT exterior because of the small pore and large aspect ratio of the CNTs, and most preparations require the "immersion" of CNTs in the filler material. The yield for the filling process is therefore often low.[5,29] The method presented herein, however, delivers a very high filling yield using CNTs that are grown in situ from an initial pool of the filler (Sn–Sb) material. Besides being the catalyst for the CNT growth, the liquid Sn–Sb droplets are also the source for sustaining the uninterrupted encapsulation of Sn–Sb through the collaborative action of the wicking effect (to draw in the molten liquid) and continuing CNT growth. This in situ process is highly efficient, as shown by the experimental findings that the process consumes most of the supplied Sn–Sb material,

 © 2006 Wiley-VCH Verlag GmbH & Co. KGaA, Weinheim

with practically no Sn–Sb remaining on the CNT exterior walls.

Sn–Sb was first identified as a promising anode material for lithium-ion batteries by the Besenhard group.[14] Lithium ions first insert into a more active (relative to Sn) Sn–Sb phase at around 0.7–0.8 V (vs. Li^+/Li), forming Li_3Sb and Sn phases in the process. Then Li ions insert into the Sn phase at 0.66 V or lower.[14–21] The inactive components (Sn during Li^+ insertion into Sn–Sb and Li_3Sb during Li^+ insertion into Sn) are used as the matrix to "buffer" the volume expansion in the alloying reaction, thereby improving the mechanical stability and consequently cyclability of the anode compared to a single Sn phase.[14–21] The above-mentioned stepwise insertion could be identified by the voltage plateaus in the first two cycles of the charge and discharge curves (see Figure S4 in the Supporting Information).

Figure 4 shows the cycling performance of a CNT-encapsulated Sn–Sb nanorod anode. Except for the first cycle, where coulombic efficiencies are 74.4% and 64.3% for the 5 mV–2 V and 0.1 V–1.2 V windows, respectively, the rest

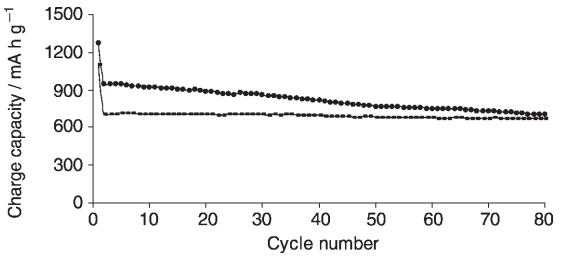

Figure 4. Cyclability of CNT-encapsulated Sn–Sb nanorods in the 5 mV–2 V (●, upper trace) and 0.1 V–1.2 V (vs. Li^+/Li) voltage windows (■, lower trace). Charge and discharge rate: ca. 0.2 C.

of the cycles are about 100% coulombic efficient. The CNT-encapsulated Sn–Sb nanorods are able to sustain high specific capacity in the neighborhood of 900 mA h g^{-1} for at least 30 cycles in the 5 mV–2 V range. This remarkably high capacity can be attributed to the rod-like morphology of Sn–Sb. It has been suggested that storage capacity is higher in one-dimensional nanomaterials because lithium-ion diffusion is facilitated.[30–32] Lithium ions could also be stored in the space between stacks of collapsed nanorods[30] and in the CNT shell. While the material still experiences discernible capacity fading after 80 cycles, this performance is nevertheless a significant improvement over previous efforts (a capacity reduction from 948 to 861 mA h g^{-1} in 30 cycles compared to a capacity reduction from 800 to about 200 mA h g^{-1} in 30 cycles[20]). The rate of capacity fading (ca. 0.3% loss per cycle) is substantially slower than those of SnO_2 nanowires[11] (ca. 3.9% loss per cycle) and SnO_2 nanorods[10] (ca. 1.2% loss per cycle). When tested in the narrower voltage window of 0.1–1.2 V,[16,19] the CNT-encapsulated Sn–Sb nanorods show an even more stable cycling performance. The specific capacity was found to be 672 mA h g^{-1} after 80 cycles, which corresponds to 94.9% retention of the initial capacity (708 mA h g^{-1}). The average fade rate of only 0.064% per cycle is excellent for this class of materials and has not been witnessed for Sn–Sb based anodes to date. The specific capacity (ca. 700 mA h g^{-1}) is lower in the 0.1–1.2 V voltage window, as expected, but it still greatly exceeds what is possible with Sn–Sb particles (500–600 mA h g^{-1}, 0.1–1.2 V).[16,19] Although the CNT shell only amounts to 7.6% of the composite weight, this thin skin of carbon is robust enough to keep the Sn–Sb in good electrical and mechanical contact. This feature has long been recognized as the key factor for prolonging the cyclability of alloy-based anodes.[33]

In summary, we report the confined growth of Sn–Sb nanorods with a previously unreported nanostructure—inside carbon nanotubes—starting from bulk antimony tin oxide particles. The CNT-encapsulated Sn–Sb nanorods contain 7.6 wt% of CNTs (ca. 90 nm in diameter and 7–10 nm in wall thickness) and 92.4 wt% of Sn–Sb nanorods (as $SnSb_{0.11}$; ca. 70 nm in diameter). The CNT skin is able to hinder the coalescence of molten Sn–Sb droplets at high temperatures and it also improves the electrical connectivity and mechanical integrity of the Sn–Sb nanorods. These CNT-encapsulated Sn–Sb nanorods, when tested as the anode material for lithium-ion batteries, display very high specific capacities and good cycling performance for this class of material. This method of fabrication should also be explored for other low-melting Li-alloying metals, such as Sn–Cu,[34] Sn–Fe,[35] and Sn–Ni.[36]

Experimental Section

Preparation of CNT-encapsulated Sn–Sb nanorods: Commercial antimony tin oxide nanoparticles (Aldrich, ATO, $Sb_3O_4{\cdot}SnO_2$, mean particle size: 19 nm; Sb_3O_4: 7–11 wt%; SnO_2: 89–93 wt%; 0.2 g) were uniformly distributed on an aluminum foil in a crucible. The crucible was heated in a tubular furnace under flowing C_2H_2 (10% C_2H_2 and 90% N_2; 200 sccm) at 700 °C for 4 h before the furnace was cooled naturally in the same gas mixture to room temperature. The recovered product was obtained as a black powder.

Characterization: The CNT-encapsulated Sn–Sb nanorods were characterized by FESEM (JEOL JSM-6700F), TEM and EDS (JEOL JEM-2010F), HRTEM (Philips FEG-CM300), and powder XRD (Shimadzu XRD-6000, $Cu_{K\alpha}$ radiation).

Electrochemical measurements: The working electrode was formulated from a mixture of 80 wt% of CNT-encapsulated Sn–Sb nanorods, 10 wt% of conductivity agent (carbon black, Super-P), and 10 wt% of binder (polyvinylidene difluoride (PVDF), Aldrich). Lithium foil was used as the counter electrode, and the electrolyte was 1M $LiPF_6$ in a 50:50 (w/w) mixture of ethylene carbonate (EC) and diethyl carbonate (DEC). More details on the electrode fabrication and cell assembly can be found elsewhere.[10,12] All cells were tested galvanostatically at a rate of about 0.2 C (ca. 0.2 mA cm^{-2} or 180 mA g^{-1}) and were charged (Li^+ insertion) and discharged (Li^+ extraction) between fixed voltage limits (5 mV–2 V or 0.1 V–1.2 V).

Received: May 24, 2006
Revised: August 23, 2006
Published online: September 29, 2006

Keywords: alloys · antimony · electrochemistry · lithium · tin

[1] S. Iijima, *Nature* **1991**, *354*, 56.
[2] C. N. R. Rao, F. L. Deepak, G. Gundiah, A. Govindaraj, *Prog. Solid State Chem.* **2003**, *31*, 5.

 © 2006 Wiley-VCH Verlag GmbH & Co. KGaA, Weinheim

[3] G. Che, B. B. Lakshmi, E. R. Fisher, C. R. Martin, *Nature* **1998**, *393*, 346.
[4] H. Shimoda, B. Gao, X. P. Tang, A. Kleinhammes, L. Fleming, Y. Wu, O. Zhou, *Phys. Rev. Lett.* **2002**, *88*, 015502.
[5] T. P. Kumar, R. Ramesh, Y. Y. Lin, G. T. K. Fey, *Electrochem. Commun.* **2004**, *6*, 520.
[6] W. X. Chen, J. Y. Lee, Z. L. Liu, *Electrochem. Commun.* **2002**, *4*, 260.
[7] Z. P. Guo, Z. W. Zhao, H. K. Liu, S. X. Dou, *Carbon* **2005**, *43*, 1392.
[8] J. Xie, V. K. Varadan, *Mater. Chem. Phys.* **2005**, *91*, 274.
[9] N. Li, C. R. Martin, *J. Electrochem. Soc.* **2001**, *148*, A164.
[10] Y. Wang, J. Y. Lee, *J. Phys. Chem. B* **2004**, *108*, 17832.
[11] Z. Ying, Q. Wan, H. Cao, Z. T. Song, S. L. Feng, *Appl. Phys. Lett.* **2005**, *87*, 113108.
[12] Y. Wang, J. Y. Lee, H. C. Zeng, *Chem. Mater.* **2005**, *17*, 3899.
[13] Y. Wang, H. C. Zeng, J. Y. Lee, *Adv. Mater.* **2006**, *18*, 645.
[14] J. Yang, M. Winter, J. O. Besenhard, *Solid State Ionics* **1996**, *90*, 281.
[15] J. Yang, M. Wachtler, M. Winter, J. O. Besenhard, *Electrochem. Solid-State Lett.* **1999**, *2*, 161.
[16] J. Yang, Y. Takeda, N. Imanishi, O. Yamamoto, *J. Electrochem. Soc.* **1999**, *146*, 4009.
[17] H. Li, G. Zhu, X. Huang, L. Chen, *J. Mater. Chem.* **2000**, *10*, 693.
[18] H. Li, L. Shi, W. Lu, X. Huang, L. Chen, *J. Electrochem. Soc.* **2001**, *148*, A915.
[19] M. Wachtler, J. O. Besenhard, M. Winter, *J. Power Sources* **2001**, *94*, 189.
[20] H. Mukaibo, T. Osaka, P. Reale, S. Panero, B. Scrosati, M. Wachtler, *J. Power Sources* **2004**, *132*, 225.
[21] S. A. Needham, G. X. Wang, H. K. Liu, *J. Alloys Compd.* **2005**, *400*, 234.
[22] J. Hu, Y. Bando, J. Zhan, D. Golberg, *Angew. Chem.* **2004**, *116*, 4706; *Angew. Chem. Int. Ed.* **2004**, *43*, 4606.
[23] Y. Li, Y. Bando, D. Golberg, *Adv. Mater.* **2003**, *15*, 581.
[24] Y. Li, J. Wang, Z. Deng, Y. Wu, X. Sun, D. Yu, P. Yang, *J. Am. Chem. Soc.* **2001**, *123*, 9904.
[25] T. Zheng, J. S. Xue, J. R. Dahn, *Chem. Mater.* **1996**, *8*, 389.
[26] X. R. Ye, Y. Lin, C. Wang, C. M. Wai, *Adv. Mater.* **2003**, *15*, 316.
[27] L. W. Yin, Y. Bando, Y. C. Zhu, M. S. Li, C. C. Tang, D. Golberg, *Adv. Mater.* **2005**, *17*, 213.
[28] P. M. Ajavan, S. Iijima, *Nature* **1993**, *361*, 333.
[29] L. Zhao, L. Gao, *Carbon* **2004**, *42*, 3251.
[30] R. Dominko, D. Arcon, A. Mrzel, A. Zorko, P. Cevc, P. Venturini, M. Gaberscek, M. Remskar, D. Mihailovic, *Adv. Mater.* **2002**, *14*, 1531.
[31] J. Chen, Z. L. Tao, S. L. Li, *Angew. Chem.* **2003**, *115*, 2197; *Angew. Chem. Int. Ed.* **2003**, *42*, 2147.
[32] J. Chen, L. Xu, W. Li, X. Gou, *Adv. Mater.* **2005**, *17*, 582.
[33] M. Winter, J. O. Besenhard, *Electrochim. Acta* **1999**, *45*, 31.
[34] H. C. Shin, M. Liu, *Adv. Funct. Mater.* **2005**, *15*, 582.
[35] O. Mao, J. R. Dahn, *J. Electrochem. Soc.* **1999**, *146*, 414.
[36] G. M. Ehrlich, C. Durand, X. Chen, T. A. Hugener, F. Spiess, S. L. Suib, *J. Electrochem. Soc.* **2000**, *147*, 886.

 © 2006 Wiley-VCH Verlag GmbH & Co. KGaA, Weinheim

Supramolecular Chemistry

DOI: 10.1002/anie.200602220

Electrochemical Switching and Size Selection in Cucurbit[8]uril-Mediated Dendrimer Self-Assembly**

*Wei Wang and Angel E. Kaifer**

Dendrimer self-assembly is an efficient approach to building sizable, soft-matter nanostructures without paying a large entropic cost, as the assembling units or building blocks are already macromolecules of considerable size. Several approaches have been described to assemble dendrimers which take advantage of π–π stacking,[1] fluorophobic,[2] solvophobic,[3] hydrogen-bonding,[4] ion–dipole,[5] metal coordination,[6] and other intermolecular interactions.[7] Recently, we reported a dendrimer self-assembly system under redox control,[8] in which dendronized 4,4′-bipyridinium (viologen) derivatives were efficiently dimerized by one-electron reduction in the presence of a cucurbit[8]uril (CB8) host.[9] This host greatly stabilizes the formation of viologen radical cation dimers[10] and, thus, its presence is crucial for the successful redox-driven dimerization or assembly of the dendrimers. CB8 is also an excellent host for charge-transfer complexes formed by the combination of an aromatic electron-deficient molecule (π acceptor) with a partner containing an aromatic electron-rich residue (π donor).[11] Here, we report on the preparation of a new series of dendrimers, **D1**–**D3**, which contain a *para*-dialkoxybenzene aromatic donor unit in their apical positions (Scheme 1). These dendrimers can form CB8-mediated, charge-transfer assemblies with the already reported dendronized viologens **A1**–**A3**.[12] Furthermore, one-electron reduction of the viologen unit disrupts the donor–acceptor complexes and leads to the dimerization of the viologen dendrimers as their radical cations.

The preparation of the π-donor dendrimers starts by reaction of **1** with each of the amine building blocks (Newkome dendrons) that we had already available.[13] This reaction was conducted in dry DMF with *N*-[(dimethylamino)-1*H*-1,2,3-triazole[4,5-*b*]-pyridin-1-ylmethylene]-*N*-methylmethanaminium hexfluorophosphate (*n*-HATU) and 1,8-bis(dimethylamino)naphthalene (proton sponge) to facil itate the coupling. The *tert*-butyl ester groups on the periphery of the resulting dendrimers were hydrolyzed with formic acid

[*] W. Wang, Prof. Dr. A. E. Kaifer
Center for Supramolecular Science and Department of Chemistry
University of Miami
Coral Gables, FL 33124-0431 (USA)
Fax: (+1) 305-284-4571
E-mail: akaifer@miami.edu

[**] We are grateful to the NSF (to A.E.K., CHE-0600795). W.W. acknowledges a Maytag graduate fellowship from the University of Miami.

Supporting information for this article is available on the WWW under http://www.angewandte.org or from the author.

WILEY InterScience DISCOVER SOMETHING GREAT
© 2006 Wiley-VCH Verlag GmbH & Co. KGaA, Weinheim

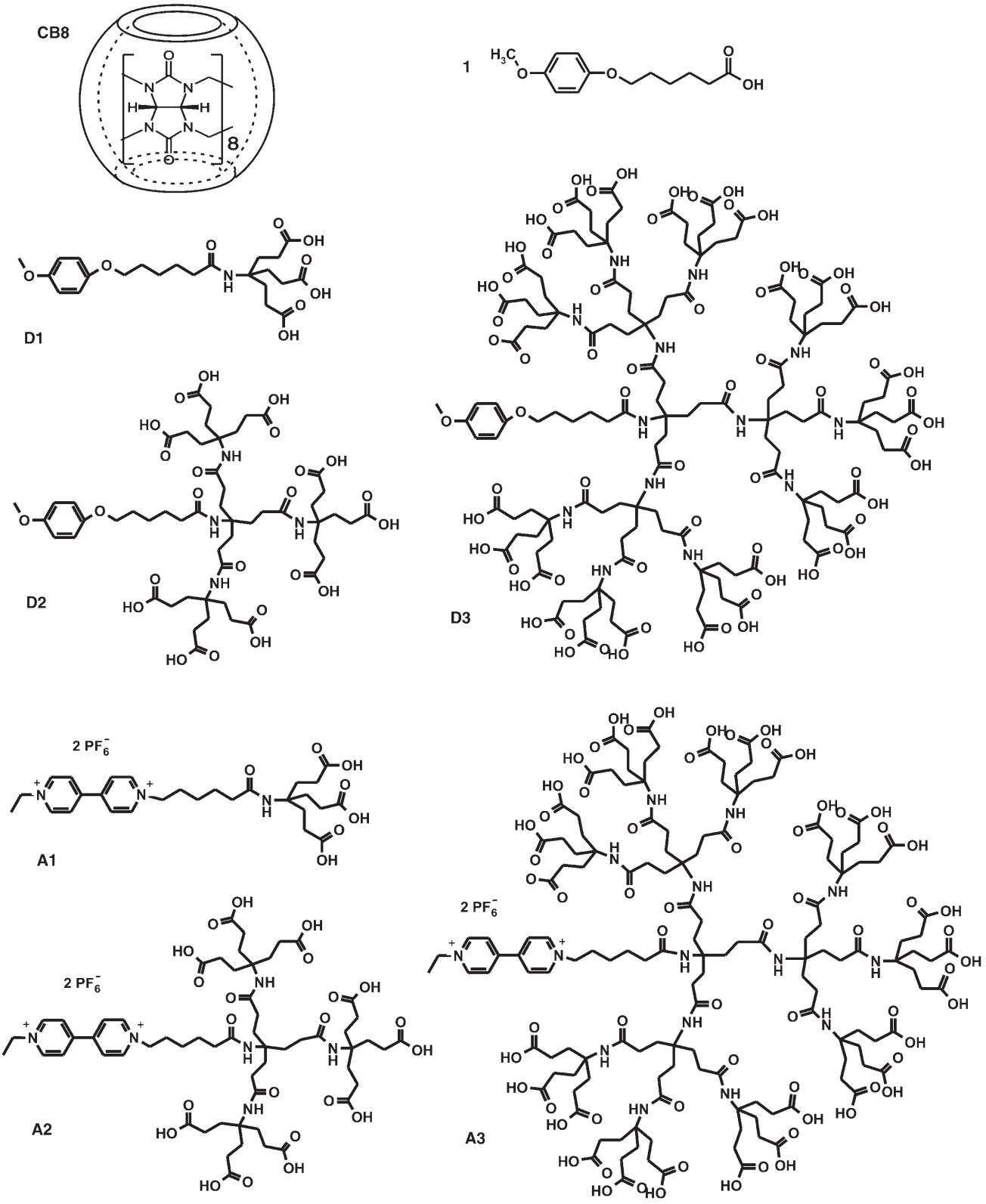

Scheme 1. Structures of precursor compound **1**, all the dendrimers studied, and the CB8 host.

to yield the water-soluble dendrimers **D1**–**D3**. All the new dendrimers were characterized by ^{1}H and ^{13}C NMR spectroscopy as well as by FAB and MALDI-TOF mass spectrometry.

Dendrimers **D1**–**D3** form stable charge-transfer complexes with the viologen-containing dendrimers in the presence of the CB8 host. This is clearly evidenced by the

 © 2006 Wiley-VCH Verlag GmbH & Co. KGaA, Weinheim

development of a charge-transfer band when a dendrimer from the **D1**–**D3** series and a dendrimer from the **A1**–**A3** series are mixed in the presence of CB8. Figure 1 shows the charge-transfer band at 490 nm that develops upon mixing **D2**

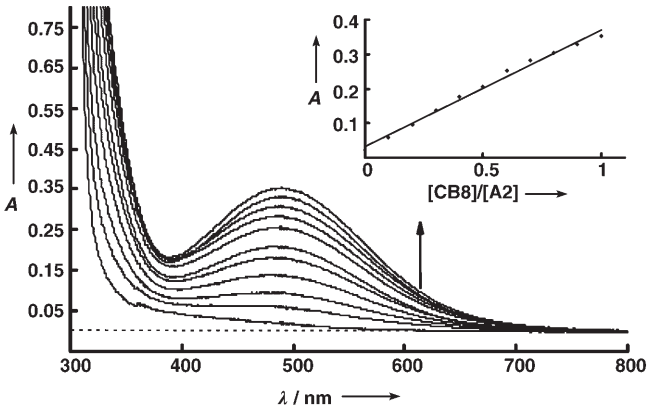

Figure 1. Charge-transfer absorption bands observed with a mixture of 2.0 mM **D2** and 2.0 mM **A2** in Na_3PO_4 buffered at pH 7.0 ($[Na^+] = 0.1$ M) in the presence of increasing concentrations of CB8 (from 0 to 2.0 mM in the direction of the arrow). The inset plots the dependence of the maximum absorbance on [CB8].

(2.0 mM), **A2** (2.0 mM), and CB8 (2.0 mM). The charge-transfer band is essentially undetectable unless CB8 is added to the solution and its intensity increases linearly with increasing concentration of CB8, at least until approaching 1.0 equivalents, at which point the solution turns turbid because of the low solubility of the host. Similar bands are observed when any two dendrimers (**A*n*–D*n***, ***n*** **= 1–3**), one from each series, are mixed in the presence of CB8. However, the band intensities tend to decrease as the sizes of the two assembling dendrimers increase, which probably reflects the increasing steric bulk and repulsive electrostatic interactions (from the peripheral carboxylate groups) in the formation of the complex.[8]

NMR spectroscopic data also confirm the formation of the **A*n*–D*n***–CB8 charge-transfer complexes. For example, Figure 2 shows the partial ^{1}H NMR spectra corresponding to a 1:1 mixture of dendrimers **A2** and **D2**. In the absence of CB8, the aromatic protons on the viologen residue of **A2** (at $\delta = 9.12$ and 8.56 ppm) and the aromatic benzyl protons of **D2** (at $\delta = 6.94$ ppm) resonate at essentially the same chemical shifts as observed in the spectra of each dendrimer before mixing, thus suggesting that the charge-transfer complex is not formed under these conditions. However, addition of the CB8 host shifts all these aromatic proton resonances to higher fields, with a CB8-induced shift that increases with the host concentration. This observation is also consistent with the formation of a charge-transfer complex in which the aromatic residues of dendrimers **A2** and **D2** share the cavity of CB8. Similar data were obtained with all other **A*n*–D*n*** combinations. We can thus conclude that CB8 mediates the formation of stable charge-transfer complexes between the viologen (π acceptor) and alkoxymethoxybenzene (π donor) residues of dendrimers **A*n*** and **D*n***, respectively, thus giving rise to the formation of well-defined **A*n*–D*n***–CB8 assemblies.

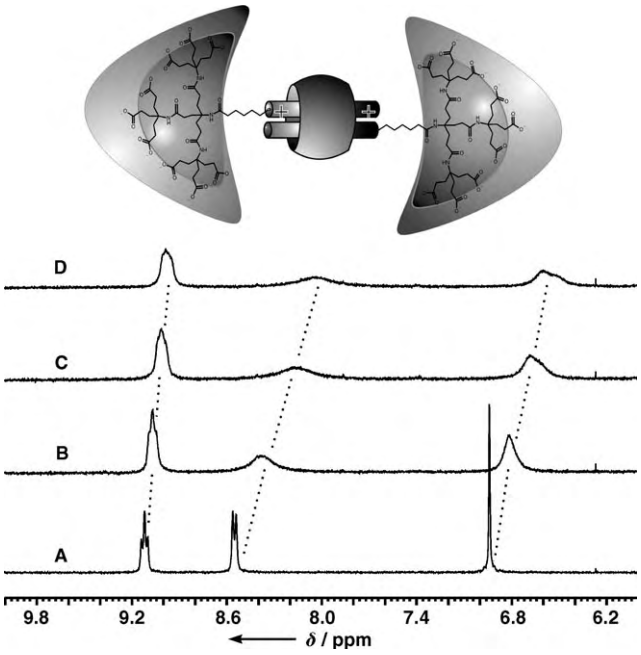

Figure 2. Partial ^{1}H NMR spectra (300 MHz, 0.1 M Na_3PO_4/D_2O, pD = 7.0) showing the effect of the CB8 host on the aromatic protons of dendrimers **A2** and **D2**: A) 0 equiv, B) 0.2 equiv, C) 0.4 equiv, and D) 0.6 equiv CB8.

The cyclic voltammetric behavior of the dendronized viologen derivatives **A1**–**A3** has already been described.[12] Viologen-containing dendrimers have the unique property of retaining relatively fast electrochemical kinetics through the first three generations of growth.[12,14] In the presence of CB8, one-electron reduction of the viologen units in **A1**–**A3** leads to the formation of highly stable viologen radical cation dimers inside the host cavity, while dimerization takes place to a very low extent in the absence of CB8. Figure 3 shows the cyclic voltammetric behavior recorded with an equimolar mixture of dendrimers **A1** and **D2** with and without added CB8. In the absence of CB8, the cathodic voltammetric behavior is dominated by the two consecutive one-electron

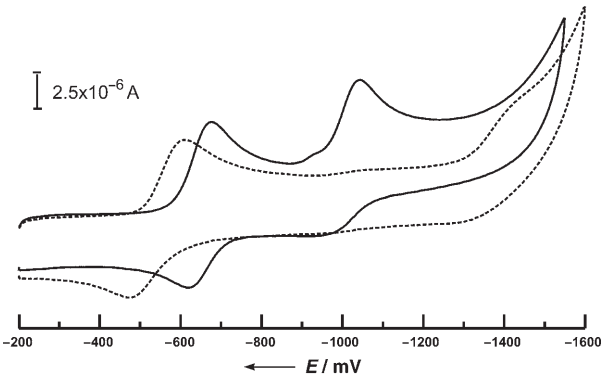

Figure 3. Cyclic voltammetric behavior on glassy carbon (0.07 cm^2) of a solution containing 0.5 mM **A1**, 0.5 mM **D2**, and Na_3PO_4 buffered at pH 7.0 ($[Na^+] = 0.1$ M) in the absence (solid line) and the presence (discontinuous line) of CB8. The potential is reported relative to an Ag/AgCl reference electrode. Scan rate: 0.10 $V s^{-1}$.

 © 2006 Wiley-VCH Verlag GmbH & Co. KGaA, Weinheim

reductions of the viologen unit on **A1**. The half-wave potentials are similar to those measured in the absence of **D2**, again suggesting that the charge-transfer complex is not stable in the absence of CB8. However, addition of the host alters the voltammetric behavior substantially. The first reduction wave shifts to less negative values and the second reduction wave shifts to more negative values, thereby revealing a considerable differential stabilization of the one-electron-reduced, radical cation form of the viologen dendrimer **A1**. In fact, when a suitable concentration (0.5 equiv or more) of host CB8 is present in the solution, the voltammetric behavior observed for **A1** in the presence of **D2** is essentially identical to that observed in the absence of the π-donor dendrimer, thus suggesting that dimerization of the viologen radical cation takes place in the presence of **D2** as long as CB8 is also present in the system. Similar voltammetric results were obtained with other dendrimer combinations.

The experimental data discussed here indicate that, in the presence of CB8, the dendronized viologens **A1**–**A3** form stable charge-transfer complexes with the π-donor dendrimers **D1**–**D3**, as long as the former are present in their oxidized (+2) electron-acceptor forms. However, one-electron reduction of the viologen units leads to the disruption of the charge-transfer complexes and the formation of stable viologen radical cation dimers. Recently, Kim and co-workers have taken advantage of similar interactions to control the behavior of a molecular loop.[11g] In our case, the redox-controlled selection of assembling partners for the dendronized viologens can be used to determine the size of the predominant dendrimer assembly. For example, assume that a mixture of **A1** and **D3** is prepared in the presence of CB8. From the data already presented here it should be clear that the **A1**–**D3**–CB8 charge-transfer complexes will self-assemble in this solution. Upon one-electron reduction of **A1**, however, we should expect the formation of homodimeric **A1**–**A1**–CB8 assemblies and this is indeed the case as shown by the electronic absorption spectra (see the Supporting Information). In fact, the extent of dimerization can be estimated from the ratio of absorbances at 364 and 390 nm, as shown by our research group almost 20 years ago.[15] From the electronic absorption data we estimate that 80% of the viologen radical cation undergoes dimerization. Therefore, one-electron reduction of the viologen units in **A1** leads to a substantial change in the effective size and molecular weight of the predominant assembly in the solution. Specifically, the molecular weight decreases from 5076 Da in **A1**–**D3**–CB8 to 2387 Da after reduction of **A1** to give the homodimeric assembly **A1**–**A1**–CB8. This conversion is fully reversible: exposure of the solution to oxygen regenerates the dicationic form of **A1** and leads again to the formation of the heavier **A1**–**D3**–CB8 assembly.

The results shown here are similar to those obtained with other combinations of dendrimers (**A*n*–D*n***), although in some cases the experiments are limited by the poor solubility of CB8. In general terms, dendrimer assembly becomes less efficient as the size of the dendritic components increase. Furthermore, one-electron reduction of the viologen subunit is kinetically hampered in large assemblies of the type **D3**–**A3**–CB8. Furthermore, in this case reduction would lead to the **A3**–**A3**–CB8 assembly (with a very similar molecular weight), thereby resulting in relatively trivial changes (and no size selection) upon electrochemical switching. The system composed of dendrimers **A1** and **D3** (Figure 4) is ideally suited for electrochemical switching and size selection, as it maximizes the change in molecular weight brought about by the one-electron reduction of the dendronized viologen.

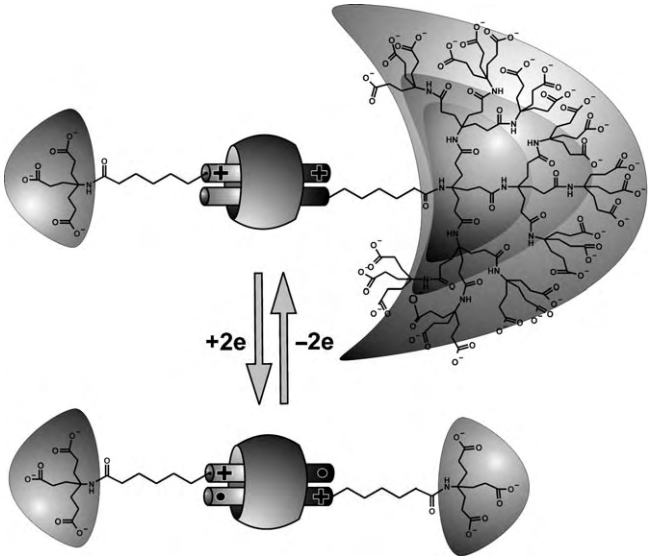

Figure 4. Pictorial representation of redox control on the size of the CB8-mediated dendrimer assemblies.

The study presented here takes advantage of the host properties of CB8 to mediate in a highly effective way the formation of charge-transfer complexes between dendrimers containing accessible π-donor and π-acceptor units. This dendrimer self-assembly system offers excellent possibilities for electrochemical switching and redox control over the type and size of the resulting macromolecular assemblies.

Experimental Section

Full synthetic and characterization details for dendrimers **D1**–**D3** are given in the Supporting Information. All other materials were prepared as previously described.[12] The cyclic voltammetric experiments were done in a single-compartment electrochemical cell fitted with glassy carbon working, auxiliary, and Ag/AgCl reference electrodes. All solutions were deoxygenated with purified nitrogen gas before cathodic voltammetric scans. Exhaustive one-electron reduction of the viologen dendrimers was carried out by exposure of the solution to Zn powder in an inert nitrogen atmosphere.

Received: June 2, 2006
Published online: October 2, 2006

Keywords: dendrimers · electrochemistry · host–guest systems · self-assembly · supramolecular chemistry

[1] V. Percec, M. Glodde, T. K. Bera, Y. Miura, I. Shiyanovskaya, K. D. Singer, V. S. K. Balagurusamy, P. A. Heiney, I. Schnell, A.

 © 2006 Wiley-VCH Verlag GmbH & Co. KGaA, Weinheim

Rapp, H.-W. Spiess, S. D. Hudson, H. Duan, *Nature* **2002**, *419*, 384.
[2] V. Percec, M. Glodde, G. Johansson, V. S. K. Balagurusamy, P. A. Heiney, *Angew. Chem.* **2003**, *115*, 4474; *Angew. Chem. Int. Ed.* **2003**, *42*, 4338.
[3] V. Percec, A. E. Dulcey, Y. Miura, U. Edlund, V. S. K. Balagurusamy, S. Hudson, H. Daurt, P. A. Heiney, *Polym. Prepr. Am. Chem. Soc. Div. Polym. Chem.* **2002**, *43*, 548.
[4] a) Y. Ma, S. V. Kolotuchin, S. C. Zimmerman, *J. Am. Chem. Soc.* **2002**, *124*, 13757; b) S. C. Zimmerman, F. Zeng, D. E. C. Reichert, S. V. Kolotuchin, *Science* **1996**, *271*, 1095; c) P. S. Corbin, L. J. Lawless, Z. Li, Y. Ma, M. J. Witmer, S. C. Zimmerman, *Proc. Natl. Acad. Sci. USA* **2002**, *99*, 5099; d) Y. Wang, F. Zeng, S. C. Zimmerman, *Tetrahedron Lett.* **1997**, *38*, 5459.
[5] a) V. Percec, W.-D. Cho, G. Ungar, D. J. P. Yeardley, *Chem. Eur. J.* **2002**, *8*, 2011; b) G. M. Dykes, D. K. Smith, *Tetrahedron* **2003**, *59*, 3999.
[6] a) W. T. S. Huck, F. C. J. M. van Veggel, B. L. Kropman, D. H. A. Blank, E. G. Keim, M. M. A. Smithers, D. N. Reinhoudt, *J. Am. Chem. Soc.* **1995**, *117*, 8293; b) M. Kawa, J. M. J. Fréchet, *Chem. Mater.* **1998**, *10*, 286.
[7] E. R. Zubarev, M. U. Pralle, E. D. Sone, S. I. Stupp, *J. Am. Chem. Soc.* **2001**, *123*, 4105.
[8] K. Moon, J. Grindstaff, D. Sobransingh, A. E. Kaifer, *Angew. Chem.* **2004**, *116*, 5612; *Angew. Chem. Int. Ed.* **2004**, *43*, 5496.
[9] a) J. W. Lee, S. Samal, N. Selvapalam, H.-J. Kim, K. Kim, *Acc. Chem. Res.* **2003**, *36*, 621; b) J. Lagona, P. Mukhopadhyay, S. Chakrabarti, L. Isaacs, *Angew. Chem.* **2005**, *117*, 4922; *Angew. Chem. Int. Ed.* **2005**, *44*, 4844.
[10] W. S. Jeon, H.-J. Kim, C. Lee, K. Kim, *Chem. Commun.* **2002**, 1828.
[11] a) W. S. Jeon, P. K. Bharadwaj, S. W. Choi, J. W. Lee, K. Kim, *Angew. Chem.* **2002**, *114*, 4654; *Angew. Chem. Int. Ed.* **2002**, *41*, 4474; b) J. W. Lee, K. Kim, S. W. Choi, Y. H. Ko, S. Sakamoto, K. Yamaguchi, K. Kim, *Chem. Commun.* **2002**, 2692; c) W. S. Jeon, A. Y. Ziganshina, Y. H. Ko, J.-K. Kang, J. W. Lee, C. Lee, K. Kim, *Angew. Chem.* **2003**, *115*, 4231; *Angew. Chem. Int. Ed.* **2003**, *42*, 4097; d) K. Kim, D. Kim, J. W. Lee, Y. H. Ko, K. Kim, *Chem. Commun.* **2004**, 848; e) H.-J. Kim, J. Heo, W. S. Jeon, E. Lee, J. Kim, S. Sakamoto, K. Yamaguchi, K. Kim, *Angew. Chem.* **2001**, *113*, 1574; *Angew. Chem. Int. Ed.* **2001**, *40*, 1526; f) Y. H. Ko, K. Kim, J.-K. Kang, H. Chun, J. W. Lee, S. Sakamoto, K. Yamaguchi, J. C. Fettinger, K. Kim, *J. Am. Chem. Soc.* **2004**, *126*, 1932; g) W. S. Jeon, E. Kim, Y. H. Ko, I. Hwang, J. W. Lee, S.-Y. Kim, H.-J. Kim, K. Kim, *Angew. Chem.* **2005**, *117*, 89; *Angew. Chem. Int. Ed.* **2005**, *44*, 87.
[12] W. Ong, J. Grindstaff, D. Sobransingh, R. Toba, J. M. Quintela, C. Peinador, A. E. Kaifer, *J. Am. Chem. Soc.* **2005**, *127*, 3353.
[13] C. M. Cardona, T. D. McCarley, A. E. Kaifer, *J. Org. Chem.* **2000**, *65*, 1857.
[14] C. S. Cameron, C. B. Gorman, *Adv. Funct. Mater.* **2001**, *11*, 60.
[15] P. A. Quintela, A. Diaz, A. E. Kaifer, *Langmuir* **1988**, *4*, 663.

 © 2006 Wiley-VCH Verlag GmbH & Co. KGaA, Weinheim

Diffusion

DOI: 10.1002/anie.200602223

A Simple Rule of Thumb for Diffusion on Transition-Metal Surfaces**

*Anand Udaykumar Nilekar, Jeff Greeley, and Manos Mavrikakis**

Diffusion of adsorbed species on solid surfaces involves the thermally activated lateral motion of these species. Among others, diffusion on surfaces plays an important role in many industrial heterogeneously catalyzed reactions and in crystal growth and aggregation processes.[1] Furthermore, an improved understanding of surface diffusion phenomena is relevant for characterizing the local deformation of metal surfaces,[2] and for analyzing the dynamics of metal corrosion.[3] Similarly, surface diffusion plays a key role in the transport of species in catalytic reactions,[4,5] as well as in the growth of surface nanostructures and the accumulation of subsurface/bulk species below metal surfaces.[6–9] Because of its importance in several areas, surface diffusion has been the focus of many experimental and theoretical studies involving a variety of adsorbates and surfaces, and there are many comprehensive reviews of the subject.[10–17] In spite of this widespread interest, however, very few general principles for diffusion on surfaces have been identified. Herein, we propose and provide quantitative evidence for two important principles: 1) that there is a simple correlation between the diffusion barrier and the binding energy of various species on transition-metal surfaces, and 2) that there is practically no compensation effect between the preexponential factor and the activation energy barrier for diffusion of adsorbed species on transition-metal surfaces.

Recent theoretical studies of surface-catalyzed bond-breaking reactions of diatomic molecules have elucidated some simple linear correlations between the transition-state (TS) energy and the final-state (FS) energy of the respective elementary steps. These Brønsted–Evans–Polanyi-type correlations span a wide range of energies and include several metal and alloy surfaces, which suggests the existence of a universality class for these simple catalytic reactions.[18–20] This universality reflects an inherent similarity between the TS and the FS structures. Such correlations are of great practical relevance to experimentalists, as they provide convenient

[*] A. U. Nilekar, J. Greeley, M. Mavrikakis
Department of Chemical and Biological Engineering
University of Wisconsin-Madison
Madison, WI 53706 (USA)
Fax: (+1) 608-262-5434
E-mail: manos@engr.wisc.edu
Homepage: http://www.engr.wisc.edu/che/faculty/mavrikakis_manos.html

[**] This work was supported by the DOE-BES, Division of Chemical Sciences. A.U.N. and M.M. thank S. C. Johnson for a distinguished fellowship. Supercomputing time at the NERSC, CI, PNNL, NCCS, and ORNL resources is gratefully appreciated.

WILEY InterScience DISCOVER SOMETHING GREAT
© 2006 Wiley-VCH Verlag GmbH & Co. KGaA, Weinheim

tools for predicting reaction activation energies on the basis of reaction thermochemistry, and therefore offer a useful platform for catalyst screening and design.[21]

Herein, we systematically demonstrate using periodic, self-consistent density functional theory (DFT) calculations (see Methods section for details) that a similar, universal relationship exists between the surface diffusion TS energy and the adsorption energy of the diffusing species. This relationship is established by analyzing the minimum-energy diffusion path for a large number of adsorbates on a variety of close-packed metal surfaces, including those modified by strain. More specifically, our study included 26 different adsorbate/surface pairs on seven different transition metals (Ru(0001), Re(0001), Cu(111), Pt(111), Pd(111), Ni(111), Ag(111)) with varying levels of surface strain, and seven different diffusing species, both atomic (O, N, H, C, S) and molecular (NO, CO). We deliberately chose many of the adsorbate/metal pairs so that our data would cover a wide range of adsorbate binding energies (−7 to 0 eV), and accordingly, the range of applicability of the final correlation derived from our studies would be quite broad.

A summary of our DFT results obtained for the diffusion barrier of various adsorbate/surface pairs, all at the low-coverage limit ($\theta = 1/8$ ML), is given in Table 1. Figures 1a and 1b show the relation between the binding energy of the adsorbate in the transition state (BE_{TS}) and that in the initial (BE_{IS}) and final states (BE_{FS}) of the diffusion path, respectively. Despite the very broad range of energies covered, both graphs suggest that there is an excellent correlation ($R^2 = 0.99$) between these values for atomic as well as molecular adsorbates on all the metal surfaces considered, including those surfaces with significant lateral strain (both compressive and expansive). The large variety of metal/adsorbate pairs, strain levels, and binding energies included in our study implies that a universal principle that governs the energetics of surface diffusion on metals may, in fact, exist.[22]

Having calculated the BE_{TS} and BE_{IS} values accurately, and by defining $E^* = BE_{TS} - BE_{IS}$ as the diffusion activation energy barrier, we then attempted to correlate E^* with the BE_{IS} for all systems studied (Figure 2). In view of the broad range of adsorbate binding energies covered (ca. 7 eV), the scatter around the best fit line is only modest. For most

Table 1: Experimentally estimated and calculated[a] diffusion barriers for adsorbate/metal pairs at various degrees of strain.[b]

Adsorbate/metal	% Strain	$\log_{10}(k)$[c]	E^*_{DFT}	E^*_{exptl}
C/Cu	−5.00	12.70	0.46	
C/Cu	0.00	12.71	0.56	
C/Pt	0.00	12.74	0.91	1.3[36]
C/Ru	0.00	12.72	0.60	
CO/Cu	0.00	13.09	0.06	0.10[37]
CO/Pd	0.00	12.72	0.27	0.52[38]
H/Cu	0.00	12.78	0.12	
H/Pt	0.00	12.72	0.18	0.30[39]
N/Ru	−5.11	12.72	0.60	
N/Ru	0.00	12.73	0.71	0.94[40]
N/Ru	5.11	12.73	0.79	
NO/Ru	−5.11	12.42	0.14	
NO/Ru	0.00	12.38	0.16	
NO/Ru	5.11	12.48	0.23	
O/Ag	0.00	12.61	0.33	
O/Pd	0.00	12.66	0.44	
O/Pt	0.00	12.67	0.46	
O/Pt	5.00	12.69	0.58	
O/Ru	−5.11	12.67	0.42	
O/Ru	0.00	12.69	0.49	0.70[4]
O/Ru	5.11	12.67	0.59	
S/Cu	0.00	12.45	0.23	0.25[41]
S/Ni	0.00	12.53	0.37	0.30[42]
S/Pt	0.00	12.59	0.54	0.57[43]
S/Re	0.00	12.56	0.46	0.80[44]
S/Ru	0.00	12.54	0.55	

[a] With zero-point energy corrections. [b] At a coverage of $\theta = 1/8$ ML and on static slabs. The diffusion coordinate proceeds from the most-stable to the second-most-stable site for the adsorbate on the metal surface. Model slabs represent the closest-packed surfaces of the respective metals (fcc(111) and hcp(0001)). [c] k = preexponential factor for diffusion.

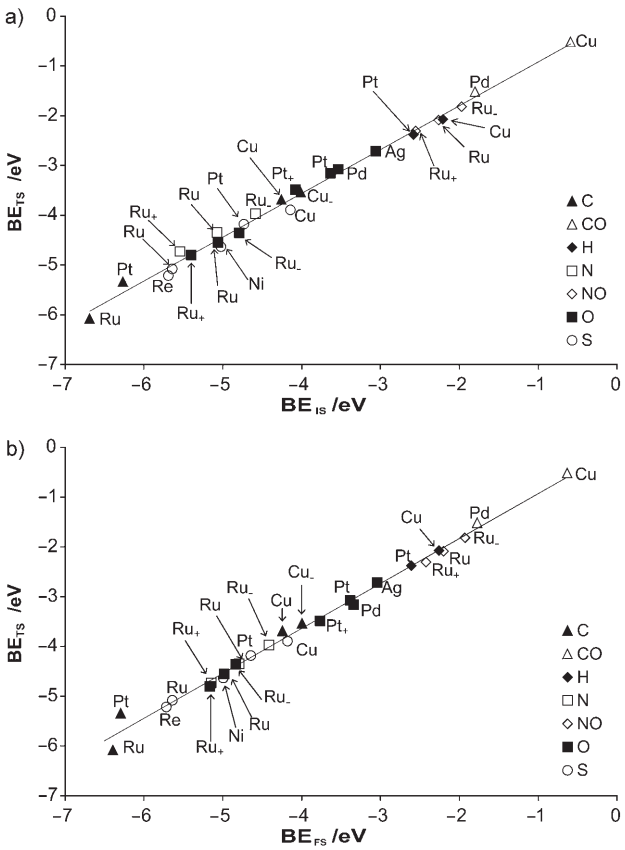

Figure 1. a) Binding energy of the transition state (BE_{TS}) for diffusion of the adsorbate from the most-stable site to the next-most-stable site on the metal surface plotted against the binding energy of the adsorbate in its initial state, that is, most favorable site (BE_{IS}). A + or − subscript on the metal label signifies expansive or compressive strain, respectively; the exact strain level is provided in Table 1. The absence of a + or − subscript indicates a surface with the equilibrium lattice constant. Linear regression gives the relation $BE_{TS} = 0.91\,BE_{IS} - 0.02$ with $R^2 = 0.99$. b) The binding energy of the transition state (BE_{TS}) for diffusion of the adsorbate plotted against the binding energy of the diffusion final state (BE_{FS}) on the metal surface. The derived linear-regression line is $BE_{TS} = 0.91\,BE_{FS} - 0.07$ with $R^2 = 0.99$.

 © 2006 Wiley-VCH Verlag GmbH & Co. KGaA, Weinheim

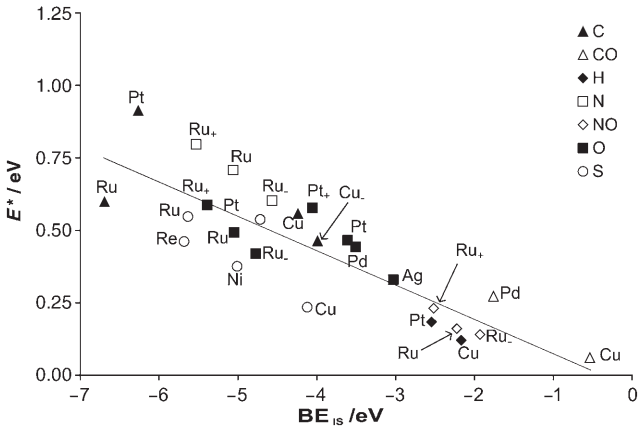

Figure 2. The diffusion barrier (E^*) plotted as a function of the binding energy of the adsorbate in its most-stable site on the metal surface (BE_{IS}). The linear-regression line obtained is $E^* = -0.12\,BE_{IS} - 0.02$ with $R^2 = 0.72$.

practical purposes, one can now correlate the diffusion activation energy barrier for common catalytic atoms and molecules with their binding energy on the respective surface. In particular, the line of best fit suggests that one can fairly accurately estimate the diffusion barrier of atomic and molecular species on transition-metal surfaces by simply taking 12% of the binding energy of the respective species. A rule of thumb for diffusion on metal surfaces has been established from experimental studies,[17] whereby the diffusion barrier is between 0.1 and 0.2 times the adsorbate binding energy. However, to our knowledge, this is the first example of such a relationship from rigorous quantitative studies of a broad range of catalytically relevant systems. Nevertheless, the considerable scatter found for some systems shown in Figure 2 shows that this correlation is only a rule of thumb, rather than a fundamental physical principle.

Table 1 shows a comparison of our calculated results with available experimental data. Estimates from experimental data were taken from the literature and rely on a variety of experimental techniques. Accordingly, the accuracy of the experimental estimates for diffusion barriers can vary significantly. We found that, in most cases, the calculated diffusion barriers are lower than the corresponding estimates drawn from experiments. The differences between experimental and theoretical results can be attributed to a number of factors, such as the use of static metal slabs in the calculations and the nonuniform accuracy of the experimental methods used.[23]

We now turn our attention to whether mutually compensatory changes exist for the activation energy barrier (E^*) and the preexponential factor for diffusion on metal surfaces, in general, and as a function of strain, in particular. The latter effect was studied for N, NO, and O on Ru(0001) (±5.11% strain), O on Pt(111) (5% strain), and C on Cu(111) (−5% strain). In general, and in good agreement with experimental results,[24] we found that compressive strain on the surface reduces the diffusion barrier, whereas expansive strain increases that barrier. The calculated preexponential factors, however, remain practically invariant with surface strain (Table 1). Furthermore, despite the fact that our studies were designed to cover a wide range of adsorbate binding energies, and in contrast to experimentally determined values, which often show large variation in estimates of the preexponential factor, the calculated preexponential factors for diffusion remain very close to $10^{13}\ s^{-1}$. As a result, the activation energy barrier alone should determine trends in diffusion on metal surfaces.

In summary, the following conclusions may be drawn: 1) that there is an excellent correlation between the binding energy of the adsorbed state and the binding energy of the respective transition state for diffusion; and 2) that the diffusion activation energy barrier can be estimated fairly accurately as approximately 12% of the binding energy of the adsorbed state. This rule-of-thumb estimate for the diffusion barrier could be of fundamental importance for metal-catalyzed surface reactions. Finally, through the detailed calculation of preexponential factors and activation energy barriers, we showed that there is no compensation effect for diffusion on close-packed transition-metal surfaces. To our knowledge, this is the first systematic first-principles study to elucidate these general principles of diffusion on transition-metal surfaces.

Methods Section

All calculations were performed by using DACAPO, a periodic, self-consistent, DFT-based total-energy code.[25,26] A static, three-layer (4×2) surface unit cell was used to model the adsorbate–metal systems. The effect of strain was simulated by implementing the specific lateral strain while keeping the metal interlayer distance fixed at the equilibrium value.[9,27] Adsorption was allowed on only one of the two metal surfaces exposed per slab, and the electrostatic potential was adjusted accordingly.[28] Ionic cores were described by ultrasoft pseudopotentials,[29] and the Kohn–Sham one-electron valence states were expanded in a basis of plane wave functions with kinetic energy below 25 Ry. The surface Brillouin zone was sampled by using a Monkhorst–Pack[30] grid of size $2\times4\times1$. The exchange correlation was described by the generalized gradient approximation (GGA-PW91).[31,32] The self-consistent PW91 density function was determined by iterative diagonalization of the Kohn–Sham Hamiltonian, Fermi population of the Kohn–Sham states ($k_B T = 0.1$ eV), and Pulay mixing of the resulting electronic density.[33] All total energies were extrapolated to $k_B T = 0$ eV. Binding energies (BEs) were calculated by Equation (1), in which E_{ads}, E_{clean}, and E_{gas} are the total energies of the slab with adsorbate, the slab without adsorbed species, and the adsorbate species in the gas phase, respectively.

$$BE = E_{ads} - E_{clean} - E_{gas} \quad (1)$$

BEs were found to be well-converged with respect to the calculation parameters. All binding-energy values were adjusted to reflect harmonic zero-point-energy corrections, but the slab chemical potentials were not corrected for finite temperature and pressure effects. Bollinger et al. estimated that such effects are much less significant than the corresponding gas-phase effects.[34] We used the climbing-image nudged elastic band (CI-NEB) method to estimate the diffusion barrier.[35] In all cases, the diffusion of the adsorbate from the most-stable site to the second-most-stable site on the metal surface was studied. The diffusion preexponential factor (A) was calculated by using Equation (2), in which $S^{\neq}_{vib}$ and S_{vib} represent the

 © 2006 Wiley-VCH Verlag GmbH & Co. KGaA, Weinheim

vibrational entropy of the transition state and the initial state for the diffusive jump, respectively.

$$A = \frac{k_B T}{h} \exp\left(\frac{S_{vib}^{\neq} - S_{vib}}{R}\right) \quad (2)$$

Both S_{vib} and $S_{vib}^{\neq}$ were calculated using Equation (3), in which x_i is defined as $\frac{h\nu_i}{k_B T}$ for each vibrational frequency ν_i.

$$R \sum_{i}^{\#\text{ of modes}} \left(\frac{x_i}{\exp(x_i)-1} - \ln(1-\exp(-x_i))\right) \quad (3)$$

Vibrational frequencies were calculated by numerical differentiation of the forces by using a second-order finite-difference approach with a step size of 0.015 Å. The Hessian matrix was mass-weighted and diagonalized to yield the frequencies and normal modes for each system.

Received: June 2, 2006
Published online: September 29, 2006

Keywords: density functional calculations · diffusion · heterogeneous catalysis · transition metals

[1] E. Penev, P. Kratzer, M. Scheffler, *Phys. Rev. B* **2001**, *64*, 085401.
[2] R. Gomer, *Rep. Prog. Phys.* **1990**, *53*, 917.
[3] F. U. Renner, A. Stierle, H. Dosch, D. M. Kolb, T. L. Lee, J. Zegenhagen, *Nature* **2006**, *439*, 707.
[4] J. Wintterlin, S. Volkening, T. V. W. Janssens, T. Zambelli, G. Ertl, *Science* **1997**, *278*, 1931.
[5] J. Wintterlin, T. Zambelli, J. Trost, J. Greeley, M. Mavrikakis, *Angew. Chem.* **2003**, *115*, 2956; *Angew. Chem. Int. Ed.* **2003**, *42*, 2850.
[6] P. Kamakoti, B. D. Morreale, M. V. Ciocco, B. H. Howard, R. P. Killmeyer, A. V. Cugini, D. S. Sholl, *Science* **2005**, *307*, 569.
[7] R. F. Sabiryanov, M. I. Larsson, K. J. Cho, W. D. Nix, B. M. Clemens, *Phys. Rev. B* **2003**, *67*.
[8] J. Tersoff, *Appl. Phys. Lett.* **2003**, *83*, 353.
[9] J. Greeley, W. P. Krekelberg, M. Mavrikakis, *Angew. Chem.* **2004**, *116*, 4396; *Angew. Chem. Int. Ed.* **2004**, *43*, 4296.
[10] G. Ehrlich, K. Stolt, *Annu. Rev. Phys. Chem.* **1980**, *31*, 603.
[11] T. T. Tsong, *Prog. Surf. Sci.* **1980**, *10*, 165.
[12] A. Kapoor, R. T. Yang, C. Wong, *Catal. Rev. Sci. Eng.* **1989**, *31*, 129.
[13] S. J. Lombardo, A. T. Bell, *Surf. Sci. Rep.* **1991**, *13*, 1.
[14] T. Alanissila, S. C. Ying, *Prog. Surf. Sci.* **1992**, *39*, 227.
[15] G. L. Kellogg, *Surf. Sci. Rep.* **1994**, *21*.
[16] E. G. Seebauer, C. E. Allen, *Prog. Surf. Sci.* **1995**, *49*, 265.
[17] J. V. Barth, *Surf. Sci. Rep.* **2000**, *40*, 75.
[18] J. Greeley, M. Mavrikakis, *Nat. Mater.* **2004**, *3*, 810.
[19] J. K. Nørskov, T. Bligaard, A. Logadottir, S. Bahn, L. B. Hansen, M. Bollinger, H. Bengaard, B. Hammer, Z. Sljivancanin, M. Mavrikakis, Y. Xu, S. Dahl, C. J. H. Jacobsen, *J. Catal.* **2002**, *209*, 275.
[20] Y. Xu, A. V. Ruban, M. Mavrikakis, *J. Am. Chem. Soc.* **2004**, *126*, 4717.
[21] T. Bligaard, J. K. Nørskov, S. Dahl, J. Matthiesen, C. H. Christensen, J. Sehested, *J. Catal.* **2004**, *224*, 206.
[22] Unlike the universality class revealed previously for simple bond-breaking elementary steps,[19,20] the diffusion TS energy correlates well with both the initial and the final state of the diffusion path, since both of these states and the TS itself are all similar to each other. In contrast, the correlation for the bond-breaking reaction on metals was far better between the TS and the FS, simply because the TS of the bond-breaking event was more like the final state (dissociation products) than the initial state.
[23] We estimated the effect of relaxation of the top metal layer in our slabs for the case of N and O diffusion on Ru(0001), both with the equilibrium lattice constant. We observed that the calculated diffusion barrier moves closer to the experimental value, thereby reducing the total error to less than 0.1 eV. We expect that the effect of surface relaxation would be similar for other adsorbate/surface pairs, thus indicating that the trends that we have determined on static surfaces are valid.
[24] S. Y. Ohno, K. Yagyuu, K. Nakatsuji, F. Komori, *Surf. Sci.* **2004**, *554*, 183.
[25] B. Hammer, L. B. Hansen, J. K. Nørskov, *Phys. Rev. B* **1999**, *59*, 7413.
[26] J. Greeley, J. K. Nørskov, M. Mavrikakis, *Annu. Rev. Phys. Chem.* **2002**, *53*, 319.
[27] M. Mavrikakis, B. Hammer, J. K. Nørskov, *Phys. Rev. Lett.* **1998**, *81*, 2819.
[28] J. Neugebauer, M. Scheffler, *Phys. Rev. B* **1992**, *46*, 16067.
[29] D. Vanderbilt, *Phys. Rev. B* **1990**, *41*, 7892.
[30] H. J. Monkhorst, J. D. Pack, *Phys. Rev. B* **1976**, *13*, 5188.
[31] J. P. Perdew, K. Burke, M. Ernzerhof, *Phys. Rev. Lett.* **1996**, *77*, 3865.
[32] J. A. White, D. M. Bird, *Phys. Rev. B* **1994**, *50*, 4954.
[33] G. Kresse, J. Furthmuller, *Comput. Mater. Sci.* **1996**, *6*, 15.
[34] M. V. Bollinger, K. W. Jacobsen, J. K. Nørskov, *Phys. Rev. B* **2003**, *67*, 085410.
[35] G. Henkelman, B. P. Uberuaga, H. Jónsson, *J. Chem. Phys.* **2000**, *113*, 9901.
[36] M. T. Martin, J. B. Hudson, *J. Vac. Sci. Technol.* **1978**, *15*, 474.
[37] A. P. Graham, F. Hofmann, J. P. Toennies, G. P. Williams, C. J. Hirschmugl, J. Ellis, *J. Chem. Phys.* **1998**, *108*, 7825.
[38] A. Vonoertzen, H. H. Rotermund, S. Nettesheim, *Chem. Phys. Lett.* **1992**, *199*, 131.
[39] E. G. Seebauer, L. D. Schmidt, *Chem. Phys. Lett.* **1986**, *123*, 129.
[40] T. Zambelli, J. Trost, J. Wintterlin, G. Ertl, *Phys. Rev. Lett.* **1996**, *76*, 795.
[41] B. J. Hinch, J. W. M. Frenken, G. Zhang, J. P. Toennies, *Surf. Sci.* **1991**, *259*, 288.
[42] G. L. Kellogg, *J. Chem. Phys.* **1985**, *83*, 852.
[43] S. Renisch, FU Berlin, **1999**.
[44] J. C. Dunphy, P. Sautet, D. F. Ogletree, O. Dabbousi, M. B. Salmeron, *Phys. Rev. B* **1993**, *47*, 2320.

 © 2006 Wiley-VCH Verlag GmbH & Co. KGaA, Weinheim

Catalyst Reactivation

DOI: 10.1002/anie.200602240

The Question of the Cr Oxidation State in the {Cr(SNS)} Catalyst for Selective Ethylene Trimerization: An Unanticipated Re-Oxidation Pathway**

Claire Temple, Amir Jabri, Patrick Crewdson, Sandro Gambarotta, Ilia Korobkov, and Robbert Duchateau**

The steady growth of interest in selective ethylene oligomerization[1] is easily understood in view of the importance of linear α-olefins for a wide range of applications. In particular, clarifying the reaction mechanism and identifying the redox couple utilized by the catalytically active species is clearly central to the rational design of new and better catalysts. Among all the metals that are known to catalyze the process, chromium is currently the most preferred since it produces the best activity as well as selectivity.[2] The metallacyclic mechanism[1,3] has become the most favored explanation for the selectivity of the process, yet important questions, including the metal oxidation state,[4] remain unanswered.

Previous work from our group has attempted to address this issue by examining one of the most versatile catalytic systems reported to date, one which is able to selectively tetramerize ethylene. For example, we found that when the trivalent catalyst precursor of the remarkable PNP system ($PNP = Ph_2PN(R)PPh_2$)[5] was exposed to $AlMe_3$, reduction to Cr^{II} and formation of a cationic complex ensued.[6] Along the same lines, a comparative testing of two σ,π-donating tripyrrolide Cr^{III} and Cr^{II} complexes indicated that the Cr^{II} species was more active while producing an identical product distribution to the Cr^{III} complex.[7] These results led us to believe that Cr^{III} is reduced by the alkyl aluminum activator in the early stages of catalyst formation.

A more recent investigation of the highly selective Sasol SNS trimerization system ($SNS = RSCH_2CH_2N(H)CH_2CH_2SR$)[8] initially indicated that even this system follows the same trend.[9] The main supporting evidence for this was the isolation of a divalent, cationic species resulting from the reaction of $[(SNS)CrCl_3]$ (**1**) with isobutylaluminoxane (*i*BAO). On the other hand, the identical reaction of **1** with either methylaluminoxane (MAO) or $AlMe_3$ did not lead to Cr^{II}, but instead gave a thermally robust cationic organochromium(III) species. This result indicates that the SNS ligand system has an unanticipated ability to stabilize some organochromium(III) functions. This observation led us to question whether the Cr^{II} oxidation state is effective in the SNS system. In other words, could the exceptional stability of the cationic Cr^{III}–R function be related to the selectivity? This idea was initially discounted because the Cr^{II} precursors of this ligand system display the same selectivity as the Cr^{III} precursors and that oxidation of Cr^{II} to the trivalent state cannot normally be foreseen in the presence of reducing alkyl aluminum activators. On the other hand, a cationic Cr^{III} species has been shown to perform the trimerization reaction even in the absence of activator.[10]

Herein we propose an intriguing alternative mechanistic possibility based on further results obtained while studying the effects of aluminum-based activators on the {Cr(SNS)} system.

When complex **1** was treated with 10 equivalents of $AlEt_2Cl$ in toluene, the dicationic dimer $[\{(SNS)Cr(\mu\text{-}Cl)Et\}_2][AlEtCl_3]_2$ (**2**) was obtained with an 83% yield of crystalline material (Scheme 1). Surprisingly, the crystal

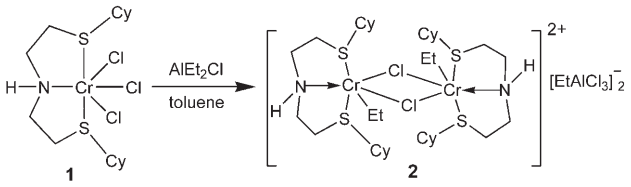

Scheme 1.

structure (Figure 1) clearly indicated that the trivalent state is preserved in this ethylchromium species.[11] The lack of metal reduction in this case and the isolation of a cationic ethylchromium(III) species in good yield was quite unexpected given the inclination of 1) trivalent organochromium towards reduction and 2) the M–Et function towards β-hydride elimination.[12]

The organochromium complex **2** displays a remarkable thermal stability in both the solid state and boiling toluene, where it slowly starts to degrade after one hour under reflux. On the other hand, if **2** is left in an excess of alkylating agent (e.g. MAO, $AlMe_3$, $AlEt_3$), intractable degradation products form rapidly. Since no well-defined/isolatable Cr^{II} complexes were obtained from any of the above reactions, we deliberately attempted the preparation of divalent species by treating $[CrCl_2(thf)_2]$ with either $AlEtCl_2$ or $AlMe_3$ in the presence of SNS (reaction with $AlEt_2Cl$ or NEt_3 led only to intractable materials). In the first case, the reaction did not directly ethylate the Cr center, but rather produced the cationic, monomeric, square-planar complex **3** (Figure 2).

[*] Dr. C. Temple, A. Jabri, P. Crewdson, Prof. Dr. S. Gambarotta, I. Korobkov
Department of Chemistry
University of Ottawa
10 Marie Curie, Ottawa ON K1N 6N5 (Canada)
Fax: (+1) 613-562-5170
E-mail: sgambaro@science.uottawa.ca
Prof. Dr. R. Duchateau
Department of Chemistry
Eindhoven University of Technology
P.O. Box 513, 5600 MB (The Netherlands)
Fax: (+31) 40-247-4918
E-mail: R.Duchateau@tue.nl

[**] This work was supported by the Natural Science and Engineering Council of Canada (NSERC) and by the Eindhoven University of Technology. $SNS = CySCH_2CH_2N(H)CH_2CH_2SCy$, Cy = cyclohexyl.

Supporting Information for this article is available on the WWW under http://www.angewandte.org or from the author.

© 2006 Wiley-VCH Verlag GmbH & Co. KGaA, Weinheim

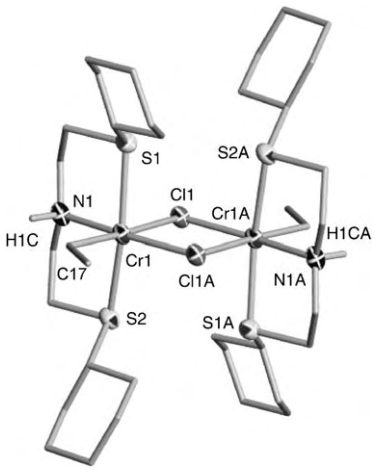

Figure 1. ORTEP view of **2** (thermal ellipsoids set at 30%); Al-containing counterions have been omitted for clarity. Relevant bond lengths [Å]: Cr1–S1 2.4654(14), Cr1–S2 2.4632(14), Cr1–N1 2.090(4), Cr1–Cl1 2.5529(13), Cr1–Cl1A 2.3574(13), Cr1–C17 2.108(5).

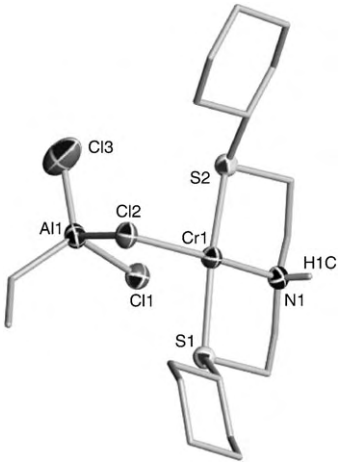

Figure 2. ORTEP view of complex **3** (thermal ellipsoids set at 30%); Al-containing counterions have been omitted for clarity. Relevant bond lengths [Å]: Cr1–S1 2.4828(18), Cr1–S2 2.4844(19), Cr1–N1 2.092(4), Cr1–Cl2 2.3974(17).

This Cr^{II} complex contains a chlorine atom bridging an $\{AlEtCl_2\}$ unit and is counter-balanced by an $[AlEtCl_3]^-$ ion. Thus, cationization also occurs in this case. When the same reaction was carried out with $AlMe_3$, the cationic Cr^{III} complex $[\{(SNS)Cr(\mu\text{-}Cl)Me\}_2][Al_2ClMe_6]_2$ (**4**)[9] was formed and subsequently isolated with a 32% yield of crystalline material. The oxidation of the metal center during the formation of **4** has no straightforward explanation given that an alkylating agent, such as $AlMe_3$, can hardly be regarded as an oxidizing agent. The only possibility of explaining this behavior is to propose that a disproportionation reaction may account for the re-oxidation of the metal center (Scheme 2). This proposal, in turn, implies that a species with a valence lower than two must be generated as a result of the formation of the trivalent **4**. The well-established stability of zero- and monovalent chromium–arene complexes[13] could well be a driving force for the disproportionation. However, we found no evidence for these species, although we did observe that a substantial amount of metallic chromium was invariably present in these reaction mixtures as a black, pyrophoric, and insoluble material. The X-ray fluorescence spectrum of this material confirmed the presence of Cr as the only heavy element while both the IR spectrum and combustion analysis showed the absence of organic functions. Furthermore, the EPR spectrum of the crude reaction mixture was found to be identical to that of an analytically pure sample of **4**,[9] thereby conclusively proving that **4** is the only EPR-active species formed during this unusual reaction.

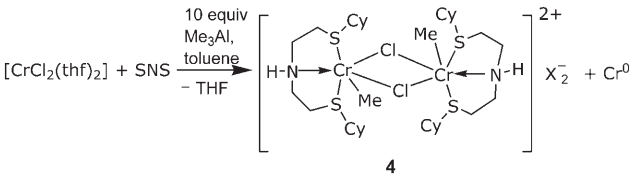

Scheme 2. X = $[Me_6Al_2Cl]$.

Results of the catalytic testing for ethylene trimerization (30 μmol of catalyst at 50 °C, 35 bar of ethylene, 1 h of reaction time, and 1000 equiv of MAO in 150 mL of toluene) are summarized in Table 1. Upon activation with MAO, the

Table 1: Oligomerization results.

Catalyst	PE [g]	Activity [g (g Cr)$^{-1}$ h^{-1}]	Product [mol%]		
			C_6	C_8	C_{10}
Cr^{III}					
$[(SNS)CrCl_3]$ (**1**)	0.08	5824	>98	trace	trace
$[\{(SNS)CrMeCl\}_2]^{2+}$ (**4**)	0.80	6903	>98	trace	trace
$[\{(SNS)CrEtCl\}_2]^{2+}$ (**2**)	0.80	9383	>98	trace	trace
Cr^{II}					
$[(SNS)Cr(ClAlEtCl_2)]^+$ (**3**)	0.64	2265	96.39	1.48	0.63

Cr^{III} precursors afford high selectivity. The increase in activity with no change in selectivity observed for complexes **1**, **2**, and **4** follows the order Cl < Me < Et. It is tempting to suggest that this sequence might be related to the different ability of the dinuclear structure of these complexes to dissociate and form coordinatively unsaturated catalytically active species.

These observations clearly indicate that, contrary to what we previously thought, the Cr^{III} oxidation state delivers a more active and selective catalyst in the case of cationic SNS complexes. On the other hand, our previous work[9] has also shown that this particular system is not immune from reduction to the divalent state. However, we have now discovered that the alkyl aluminum activator may indirectly induce re-oxidation of Cr^{II} towards the more active and selective Cr^{III} catalyst precursor. This oxidation by an alkyl aluminum species is unprecedented and, to our knowledge, has never even been considered. It is therefore tempting to conclude that, in the case of the SNS ligand, the selective trimerization might be performed by a trivalent catalyst. When reduction occurs, the activity of the catalyst decreases

 © 2006 Wiley-VCH Verlag GmbH & Co. KGaA, Weinheim

and it loses selectivity. Nonetheless, a disproportionation pathway promoted by the aluminum activator may restore the highly active and selective trivalent state, clearly at the expense of the overall concentration of chromium. Ultimately, the chromium complex is irreversibly decomposed to metallic chromium, which, incidentally, offers a reasonable explanation for why these thermally robust trivalent organochromium complexes decompose in the presence of an excess of activator. The possibility that a lower valent chromium species may be responsible for the high catalytic activity and selectivity cannot, in principle, be excluded at this stage. However, in the absence of evidence for stable mono- or zerovalent Cr complexes of this ligand system, this possibility remains, as yet, unsubstantiated. Finally, these results indicate that the N–H group of the ligand backbone is unaffected by the alkylating agents or the Cr–R function under the conditions studied so far for this system.

Experimental Section

2: A mixture of [{$CySCH_2CH_2N(H)CH_2CH_2SCy$}$CrCl_3$] (0.503 g, 1.1 mmol) and $AlEt_2Cl$ (1.32 g, 11 mmol) in toluene (15 mL) was stirred at 22 °C to give a dark green solution. After centrifugation and decantation, the resulting green solution was stored at −35 °C for one day. Green crystals of analytically pure **2** (0.570 g, 0.91 mmol, 83 %) were isolated from the solution. IR (nujol): $\nu_{N-H} = 3185\ cm^{-1}$. Elemental analysis (%) calcd for $C_{23.5}H_{45}AlCl_4CrNS_2$: C 45.05, H 7.24, N 2.24; found: C 45.41, H 7.63, N 2.01. $\mu_{eff} = 3.92\ \mu_B$.

3: A mixture of $[CrCl_2(thf)_2]$ (0.250 g, 0.93 mmol), $CySCH_2CH_2N(H)CH_2CH_2SCy$ (0.285 g, 0.95 mmol), and $[AlEtCl_2]$ (1.2 g, 9.5 mmol) in toluene (15 mL) was stirred at 22 °C to give a blue solution. Crystals of **3** (0.521 g, 7.7 mmol, 82 %) formed over the course of three days at −35 °C. IR (nujol): $\nu_{N-H} = 3174\ cm^{-1}$. Elemental analysis (%) calcd for $C_{20}H_{41}Al_2Cl_6CrNS_2$: C 35.41, H 6.09, N 2.06; found: C 35.61, H 6.33, N 2.01. $\mu_{eff} = 4.83\ \mu_B$.

Cr^{II} oxidation: Preparation of **4**: A mixture of $[CrCl_2(thf)_2]$ (0.122 g, 0.46 mmol) and $CySCH_2CH_2N(H)CH_2CH_2SCy$ (0.138 g, 0.46 mmol) in toluene (5 mL) was stirred at 22 °C to give a blue suspension. $AlMe_3$ (0.329 g, 4.57 mmol) was added and green crystals precipitated immediately. After filtration of the green suspension the solution was stored at −35 °C for 1 h. Complex **4** (0.100 g, 0.15 mmol, 32 %) was isolated as green crystals by removing the mother liquor, washing with hexanes (2 × 5 mL), and drying in vacuo. IR (nujol): $\nu_{N-H} = 3181\ cm^{-1}$. Elemental analysis (%) calcd for $C_{30}H_{60}Al_2Cl_2CrNS_2$: C 53.32, H 8.95, N 2.07; found: C 53.41, H 8.73, N 2.01. $\mu_{eff} = 3.94\mu_B$. Pyrophoric, black, and insoluble metallic chromium separated from the mother liquor when it was left to stand at room temperature for a few hours.

Crystal data for **2**: $C_{23.50}H_{45}AlCl_4CrNS_2$, $M_r = 626.51$, monoclinic, $C2/c$, $a = 27.329(4)$, $b = 13.296(2)$, $c = 28.167(6)$ Å, $\beta = 124.302(2)°$, $V = 6462.2(17)$ Å^3, $Z = 8$, $\rho_{calcd} = 1.288\ Mg\,m^{-3}$, $T = 202$ K, absorption coefficient $0.855\ mm^{-1}$, $F(000) = 2640$, 23795 reflections collected, 5486 independent reflections, GoF = 1.034, $R = 0.0605$ [$I > 2\sigma(I)$], $wR^2 = 0.1443$ [$I > 2\sigma(I)$].

Crystal data for **3**: $C_{20}H_{41}Al_2Cl_6CrNS_2$, $M = 678.32$, triclinic, $P\bar{1}$, $a = 11.836(3)$, $b = 12.263(5)$, $c = 12.733(3)$ Å, $\alpha = 75.302(7)°$, $\beta = 74.194(5)°$, $\gamma = 76.374(4)°$, $V = 1692.4(9)$ Å^3, $Z = 2$, $\rho_{calcd} = 1.331\ Mg\,m^{-3}$, $T = 200.2$ K, absorption coefficient $0.998\ mm^{-1}$, $F(000) = 704$, 12890 reflections collected, 4792 independent reflections, GoF = 1.025, $R = 0.0621$ [$I > 2\sigma(I)$], $wR^2 = 0.1594$ [$I > 2\sigma(I)$].

CCDC-608869 (**2**) and CCDC-608870 (**3**) contain the supplementary crystallographic data for this paper. These data can be obtained free of charge from The Cambridge Crystallographic Data Centre via www.ccdc.cam.ac.uk/data_request/cif.

Received: June 5, 2006
Revised: July 21, 2006
Published online: September 28, 2006

Keywords: alkylation · chromium · oligomerization · oxidation · trimerization

[1] J. T. Dixon, M. J. Green, F. M. Hess, D. H. Morgan, *J. Organomet. Chem.* **2004**, *689*, 3641 – 3668.
[2] See for example: A. K. Tomov, J. J. Chirinos, R. J. Long, V. C. Gibson, M. R. J. Elsegood, *J. Am. Chem. Soc.* **2006**, *128*, 7704 and references therein.
[3] a) P. J. W. Deckers, B. Hessen, J. H. Teuben, *Organometallics* **2002**, *21*, 5122 – 5135; b) P. J. W. Deckers, B. Hessen, J. H. Teuben, *Angew. Chem.* **2001**, *113*, 2584 – 2587; *Angew. Chem. Int. Ed.* **2001**, *40*, 2516 – 2519; c) C. Andes, S. B. Harkins, S. Murtuza, K. Oyler, A. Sen, *J. Am. Chem. Soc.* **2001**, *123*, 7423 – 7424; d) E. Y. Chen, W. J. Kruper, G. Roof, D. R. Wilson, *J. Am. Chem. Soc.* **2001**, *123*, 745 – 746; e) W. J. Van Rensburg, C. Grove, J. P. Steynberg, K. B. Stark, J. J. Huyser, P. J. Steynberg, *Organometallics* **2004**, *23*, 1207 – 1222.
[4] a) (Cr^{III}–Cr^{V}) N. Meijboom, C. J. Schaverien, A. G. Orpen, *Organometallics* **1990**, *9*, 774 – 782; b) (Cr^{II}–Cr^{IV}) K. H. Theopold, *Eur. J. Inorg. Chem.* **1998**, 15 – 24; c) D. H. Morgan, S. L. Schwikkard, J. T. Dixon, J. J. Nair, R. Hunter, *Adv. Synth. Catal.* **2003**, *345*, 939 – 942; d) W. J. Van Rensburg, C. Grove, J. P. Steynberg, K. B. Stark, J. J. Huyser, P. J. Steynberg, *Organometallics* **2004**, *23*, 1207 – 1222; e) (Cr^{I}–Cr^{III}) R. D. Kohn, M. Haufe, S. Mihan, D. Lilge, *Chem. Commun.* **2000**, 1927 – 1928; f) Y. Fang, Y. Liu, Y. Ke, C. Guo, N. Zhu, X. Mi, Z. Ma, Y. Hu, *Appl. Catal. A* **2002**, *235*, 33 – 38.
[5] a) M. J. Overett, K. Blann, A. Bollmann, J. T. Dixon, D. Haasbroek, E. Killian, H. Maumela, D. S. McGuinness, D. H. Morgan, *J. Am. Chem. Soc.* **2005**, *127*, 10723 – 10730; b) K. Blann, A. Bollmann, J. T. Dixon, F. M. Hess, E. Killian, H. Maumela, D. H. Morgan, A. Neveling, S. Otto, M. J. Overett, *Chem. Commun.* **2005**, 620 – 621; c) A. Carter, S. A. Cohen, N. A. Cooley, A. Murphy, J. Scutt, D. F. Wass, *Chem. Commun.* **2002**, 858 – 859; d) D. F. Wass (BP Chemicals Ltd), WO 02/04119, **2002**.
[6] A. Jabri, P. Crewdson, S. Gambarotta, I. Korobkov, R. Duchateau, *Organometallics* **2006**, *25*, 715 – 718.
[7] P. Crewdson, S. Gambarotta, M.-C. Djoman, I. Korobkov, R. Duchateau, *Organometallics* **2005**, *24*, 5214 – 5216.
[8] a) D. S. McGuinness, P. Wasserscheid, D. H. Morgan, J. T. Dixon, *Organometallics* **2005**, *24*, 552 – 556; b) D. S. McGuinness, P. Wasserscheid, W. Keim, D. Morgan, J. T. Dixon, A. Bollmann, H. Maumela, F. Hess, U. Englert, *J. Am. Chem. Soc.* **2003**, *125*, 5272 – 5273.
[9] A. Jabri, C. Temple, P. Crewdson, S. Gambarotta, I. Korobkov, R. Duchateau, *J. Am. Chem. Soc.* **2006**, *128*, 9238.
[10] a) T. Agapie, M. W. Day, L. M. Henling, J. A. Labringer, J. E. Bercaw, *Organometallics* **2006**, *25*, 2733 – 2742; b) S. J. Schofer, M. W. Day, L. M. Henling, J. A. Labinger, J. E. Bercaw, *Organometallics* **2006**, *25*, 2743 – 2749.
[11] Complexes containing the trivalent Cr–Et function are relatively rare: a) V. C. Gibson, C. Newton, C. Redshaw, G. A. Solan, A. J. P. White, D. J. Williams, *J. Chem. Soc. Dalton Trans.* **2002**, 4017 – 4023; b) V. C. Gibson, S. Mastroianni, C. Newton, C. Redshaw, G. A. Solan, A. J. P. White, D. J. Williams, *J. Chem. Soc. Dalton Trans.* **2000**, 1969 – 1971; c) O. Heinemann, P. W. Jolly, C. Kruger, G. P. J. Verhovnik, *J. Organomet. Chem.* **1998**, *553*, 477 – 479; d) B. J. Thomas, S. K. Noh, G. K. Schulte, S. C.

 © 2006 Wiley-VCH Verlag GmbH & Co. KGaA, Weinheim

Sendlinger, K. H. Theopold, *J. Am. Chem. Soc.* **1991**, *113*, 893 – 902; e) B. J. Thomas, K. H. Theopold, *J. Am. Chem. Soc.* **1988**, *110*, 5902 – 5903.

[12] a) H. Sugiyama, G. Aharonian, S. Gambarotta, G. P. A. Yap, P. H. M. Budzelaar, *J. Am. Chem. Soc.* **2002**, *124*, 12268 – 12274; b) D. Reardon, G. Aharonian, S. Gambarotta, G. P. A. Yap, O *rganometallics* **2002**, *21*, 786 – 788; c) M. Kooistra, Q. Knijnenburg, J. M. M. Smits, A. D. Horton, P. H. M. Budzelaar, A. W. Gal, *Angew. Chem.* **2001**, *113*, 4855 – 4858; *Angew. Chem. Int. Ed.* **2001**, *40*, 4719 – 4722; d) V. C. Gibson, M. J. Humphries, K. P. Tellmann, D. F. Wass, A. J. P. White, D. J. Williams, *Chem. Commun.* **2001**, 2252 – 2253.

[13] a) F. Calderazzo, U. Englert, G. Pampaloni, M. Volpe, *J. Organomet. Chem.* **2005**, *690*, 3321 – 3332; b) R. Kohn, D. Smith, M. F. Mahon, M. Prinz, S. Mihan, G. Kociok-Kohn, *J. Organomet. Chem.* **2003**, *683*, 200 – 208.

 © 2006 Wiley-VCH Verlag GmbH & Co. KGaA, Weinheim

Gas Separation

DOI: 10.1002/anie.200602308

Hierarchical Growth of Large-Scale Ordered Zeolite Silicalite-1 Membranes with High Permeability and Selectivity for Recycling CO_2**

Hailing Guo, Guangshan Zhu, Hua Li, Xiaoqin Zou, Xiaoju Yin, Weishen Yang, Shilun Qiu,* and Ruren Xu*

With growing consumption of fossil fuels, gigatons of carbon dioxide are emitted into the atmosphere every year. Carbon dioxide is the main component of greenhouse gases, and would trigger severe global climate change if it accumulated to a high level in the long run. To alleviate CO_2 accumulation it is important to separate and recycle carbon dioxide before it is released in to air.[1] In contrast to conventional techniques for CO_2 separation, membrane gas separation is more affordable and attractive. Recently, polymer membrane materials have been widely used for gas separation owing to their relatively low cost and ease of being processed into hollow fibers.[2–5] However, plasticization could significantly decrease the performance of the polymer membranes. A more promising choice is inorganic zeolite membranes.[6–9] Crystalline silica-based zeolites can bring their intrinsic properties, such as well-defined subnanometer channels, high thermal, chemical, and mechanical stabilities, and hydrophobicity/philicity, into the membrane.

Ideally, zeolite membranes should be large-scale ordered and defect-free, exhibiting high thermal stability, selectivity, and permeability. Zeolite FAU, DDR, T-type, and SAPO-34 membranes have been reported for CO_2/CH_4 and CO_2/N_2 separations. Although these membranes have demonstrated high selectivity for CO_2 over other gas molecules, they have low permeability owing to the thickness of the zeolite films, the random arrangement of zeolite crystals in the membrane,[10] and low thermal and mechanical stabilities because of their high Al contents.[11–13] High silica MFI or pure silica MFI zeolites with 5.3 Å intercross channels have higher thermal stabilities; as a result membranes of them have been considered for xylene isomer separation in the petrochemical industry.[14] Zeolite MFI membranes supported by, for example, porous ceramic, α-Al_2O_3, and stainless steel have many defects, such as pinholes or cracks, which are usually generated through different thermal-expansion coefficients and phase transitions between the membranes and matrices.[15–17] Some defect-free MFI films have been reported.[18] Considering the elasticity, tenacity, and low thermal-expansion coefficient of the stainless-steel-net, it is reasonable to expect that a stainless-steel-net-imbedded zeolite silicalite-1 membrane can resist cracking, temperature cycling, and possess high mechanical stability. Based on the preparation of a stainless-steel-net-supported zeolite NaA membrane,[19] the investigation of a large-scale ordered stainless-steel-net-imbedded zeolite silicalite-1 membrane was carried out. Mixed gas (N_2/CO_2, CH_4/CO_2, and H_2/CO_2) separation studies on the membrane revealed that the membrane has high permeability and selectivity for CO_2 over H_2, N_2,and CH_4.

The stainless-steel-net-imbedded zeolite silicalite-1 membrane was synthesized by the hydrothermal method. First, the silicalite-1 nanocrystal seeds were dispersed onto the pretreated stainless-steel net. The monolayer seeded net was then placed vertically in a Teflon-lined autoclave containing a reaction solution of 0.32 TPAOH/1.0 TEOS/165 H_2O (TPAOH = tetrapropylammonium hydroxide, TEOS = tetraethylorthosilicate) for secondary growth at 170 °C for 3 days.

Figure 1 shows the X-ray diffraction (XRD) patterns of the dispersed seeds on the substrate and as-synthesized zeolite silicalite-1 membranes after secondary growth for 1, 2, and 3 days. The pattern of the dispersed zeolite silicalite-1 seeds fits well with that of the simulated MFI structure, indicating that the sample was a pure phase. The XRD pattern in Figure 1b shows that after reaction for 1 day, the majorities of peaks were similar to those of a randomly oriented MFI structure, except that the intensities of the (*h*0*l*) peaks increased notably, implying the zeolite crystals are (*h*0*l*) oriented on the stainless steel net. When the reaction time was

[*] H. Guo, Prof. G. Zhu, H. Li, X. Zou, X. Yin, Prof. S. Qiu, R. Xu
State Key Laboratory of Inorganic Synthesis and Preparative Chemistry, College of Chemistry
Jilin University
Changchun 130012 (China)
Fax: (+86) 431-516-8331
E-mail: zhugs@mail.jlu.edu.cn
sqiu@mail.jlu.edu.cn
Prof. W. Yang
State Key Laboratory of Catalysis
Dalian Institute of Chemical Physics
Chinese Academy of Sciences
Dalian 116023 (China)

[**] We are grateful for the financial support of the State Basic Research Project (2006CB806100) and the National Natural Science Foundation of China (Grant nos. 20571030, 20531030, and 20371020).

Supporting information for this article is available on the WWW under http://www.angewandte.org or from the author.

 © 2006 Wiley-VCH Verlag GmbH & Co. KGaA, Weinheim

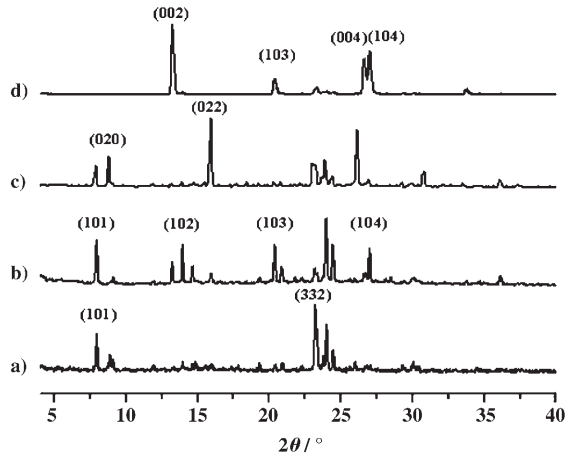

Figure 1. X-ray diffraction patterns of a) the zeolite silicalite-1 nanocrystal seeded substrate and the as-synthesized stainless-steel-net-supported zeolite silicalite-1 membrane after crystallization for b) 1, c) 2, or d) 3 days.

prolonged to 2 days, the intensities of the (020) peak located at a Bragg angle 2θ of 8.8° significantly increased, indicating that at this time the membrane was formed preferentially along the *b* axis (Figure 1c). After 3 days' crystallization, the peaks (101) and (020) (Figure 1d) disappear entirely while the (002), (004), (103), and (104) peaks dominate the XRD pattern, indicating that a *c*- and (*h*0*l*)-oriented zeolite silicalite-1 film has formed on the previously grown *b*-oriented zeolite layer.

To further understand the formation mechanism of the stainless-steel-net-imbedded zeolite silicalite-1 membrane, scanning electron microscopy (SEM) was used to monitor the surface morphology of the zeolite membrane during the synthesis process. As shown in Figure 2a,b, the zeolite silicalite-1 seeds around 150 nm in size were dispersed uniformly on the stainless steel net to form a compact monoseed layer. The lack of close-packed seeds on the net can lead to formation of dome-like defects,[20] which will further affect the gas separation performance of the membrane. The use of zeolite seeds will promote both the nucleation and growth of zeolite on the substrate.[21] The process of the secondary growth of the zeolite silicalite-1 membrane on the seeded substrate is shown in Figure 2c–h. It can be seen that after crystallization for 1 day (Figure 2c,d), most of the crystals grow along the stainless steel net wire to form a zeolite fiber net, consisting with the XRD results (Figure 1b). The formation of the zeolite fiber net with a preferred crystallographic orientation can be explained by a classic competitive growth model.[22–24] Figure 2e shows the image of the zeolite membrane grown after two days. At this stage, there are still many voids where zeolite crystals can not merge into a membrane. It can be seen that as crystallization progresses, the 40×50 μm rectangle pores constructed by zeolite fibers developed into 20×30 μm elliptic pores. The magnified SEM image of one elliptic pore (Figure 2f) clearly indicates that zeolite film is made up of two layers of zeolite crystal arrays. The prismatic crystals in the first layer are parallel to the plane of the net, with their *c*-axes pointing

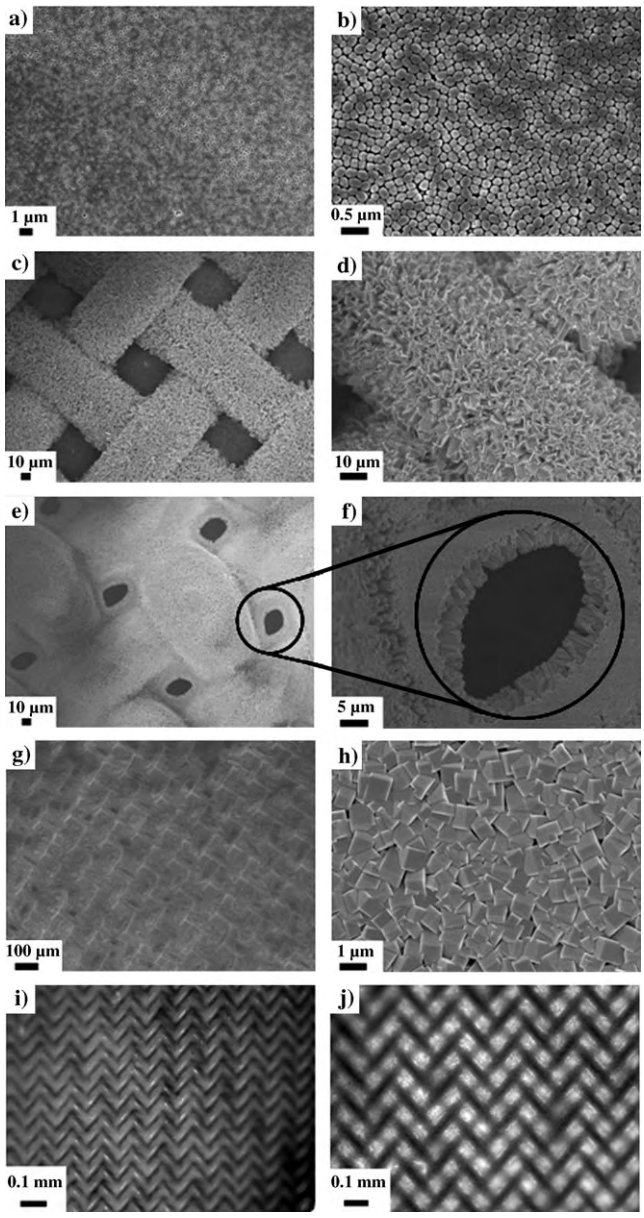

Figure 2. SEM images of a) the zeolite silicalite-1 nanocrystal seeds dispersed on the net wafer, and b) magnified image of the seed layer. Top-view SEM images of stainless-steel-net-supported zeolite silicalite-1 membrane after secondary growth with crystallization times of c,d) 1 day, e,f) 2 days, and g,h) 3 days, under low (left) and high (right) magnification. i,j) Optical microscope images of the membrane with reflected and transmitted light.

towards the center of the elliptic pores. Without space restriction, these crystals grew expitaxially and merged together.[25,26] The crystals in the second layer are grown over the first layer with their *c*-axes perpendicular to the plane of the net. Only those crystals with *c*-axes perpendicular to the substrate surface will survive, whereas those with other orientations are gradually suppressed.[27] Such an arrangement of zeolite crystals fits well with the XRD result (Figure 1c). After crystallization for 3 days, as shown in the Figure 2g, an entirely compact and continuous zeolite silicalite-1 membrane without any pinholes or cracks was synthe-

 © 2006 Wiley-VCH Verlag GmbH & Co. KGaA, Weinheim

sized successfully. The magnified SEM image (Figure 2h) indicates that almost all the crystals are in the *c* orientation with their *c* axis perpendicular to the plane of the membrane, which is consistent with the result of XRD pattern (Figure 1d) which shows that crystals prefer the (0*k*0) orientation. Optical microscope images of the membrane with reflected and transmitted light (Figure 2i,j) show that the zeolite net is uniform, ordered over a large area, and transparent. After calcination at 550 °C in air for 8 h, the membrane still retains its high crystallinity and pure phase, which is demonstrated by XRD and SEM analyses (see Supporting Information). It was noted that the thermal expansion coefficients of stainless steel ($15\times10^{-6}\,°C^{-1}$) and the zeolite crystals in the *c* direction ($0.5\times10^{-6}\,°C^{-1}$) are quite small, while the thermal expansion coefficients of zeolite crystals in the *a* and *b* directions are opposing (20×10^{-6} and $-22\times10^{-6}\,°C^{-1}$, respectively). It has been reported that the in-plane compressive stress may prevent crack formation.[28] Therefore, we speculate that it was the hierarchical (that is, layer-by-layer) structure of the zeolite membrane that enabled it to survive the high-temperature calcination process without cracking or formation of pinholes.

Following the encouraging characterization results, gas-separation studies were carried out on the high thermal stable and large-scale ordered silicalite-1 membrane. The calcined membrane was fixed in a gas-separation setup (see Supporting Information), and used for separation studies with different gas mixtures (CO_2/H_2, CO_2/N_2, and CO_2/CH_4). The determined permeation and separation factors are summarized in the Supporting Information. The permeation of CO_2 (around $7\times10^{-7}\,mol\,m^{-2}\,s^{-1}\,Pa^{-1}$) is much higher than that of the other gases in the mixtures, showing that the membrane provides highly selective separation of CO_2. Because CO_2 has a larger quadrapolar moment and higher boiling point (−44 °C) than the other test gas molecules, it can interact with the interior of the silicalite-1 micropore upon instant polarization, and was adsorbed into and diffused out of the silicalite-1 membrane much more easily than H_2, N_2, and CH_4. Furthermore, the stainless-steel-net has open voids and the first layer of the membrane is almost *b*-oriented which facilitates easy access to the straight-channels of zeolite silicalite-1, as a result the CO_2 permeation factors are much higher than those reported to date.[29–31] In the Supporting Information, it is also noted that the separation factors of mixture gas are much higher than the ideal separation factors. It can be deduced that the preferred adsorption of CO_2 blocks the flow of N_2, H_2, CH_4 molecules through the zeolite silicalite-1 channels of the membrane.[32,33]

To evaluate the mechanical stability of the zeolite membrane, the feed pressure was increased from 1.01×10^5 Pa to 3×10^5 Pa. It is found that the CO_2 permeability increased from 7.14×10^{-7} to $1.53\times10^{-6}\,mol\,m^{-2}\,s^{-1}\,Pa^{-1}$ and the separation factor of CO_2/N_2 still maintained a high value (Supporting Information). Interestingly, the CO_2/N_2 separation factor of the zeolite membrane increased noticeably from 68.7 to 75.0 when the permeation temperature decreased from 20 to 0 °C, suggesting that at lower temperature the adsorption of CO_2 on the zeolite silicalite-1 membrane is more selective than of N_2, H_2, and CH_4. The reproducibility and durability of the membranes were also examined. As shown in Figure 3, the separation factor and the permeation of the zeolite silicalite-1 membrane remains at high values. The membrane can be used repeatedly for at least six months, which shows that the stainless-steel-net-imbedded zeolite silicalite-1 membrane has significantly high stability.

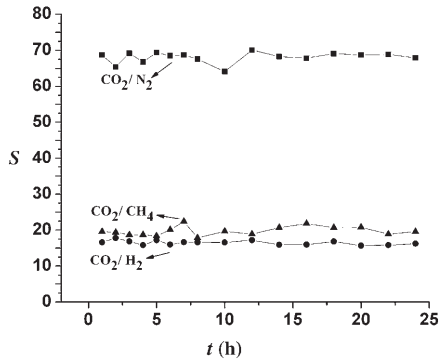

Figure 3. CO_2/N_2 (■), CO_2/H_2 (●), and CO_2/CH_4 (▲) separation factors (*S*) for the stainless-steel-net-supported zeolite silicalite-1 membrane over time; sweep rate = 50 ml min^{-1}, feed flow rate = 100 ml min^{-1}, feed pressure = 1.0×10^5 Pa, permeation temperature = 20 °C.

In summary, the stainless-steel-net-imbedded silicalite-1 zeolite membrane has been successfully synthesized by a hydrothermal approach. A hierarchical growth mechanism for the membrane formation can be deduced according to the XRD and SEM results. Compared with the conventional MFI membranes supported by other substrates, the stainless-steel-net-imbedded zeolite silicalite-1 membrane has high thermal and mechanical stabilities, large-scale order, and exhibits high permeation flux and excellent permeation selectivity for CO_2. Such highly efficient zeolite membranes could be used to separate, recycle, and reuse CO_2 exhaust gases from coal-fired power plants, chemical factories, and natural gas-sourced amine plants.

Experimental Section

Seeds dispersion and hierarchical growth: Silicalite-1 crystals of approximately 150 nm in size were prepared according to literature methods.[34] The seed solution (20 g L^{-1}) was prepared by adjusting the pH value to 10 using aqueous NH_3 to avoid the seed aggregation. Then the seed solution was dropped onto the net wafers which had been pretreated with a liquid detergent solution for 30 min under ultrasonic vibration condition.[16] The seeded net wafers were placed vertically in a Teflon-lined autoclave for secondary growth at 170 °C for 3 days, in which the composition of the reaction solution was 0.32 TPAOH/1.0 TEOS/165 H_2O.[35] To study the growth mechanism of membranes, autoclaves were taken out at 1, 2, and 3 days, respectively. The membranes were taken out, washed with distilled water, and dried at 80 °C. After being calcined at 550 °C for 8 h to remove the organic template, the membranes were characterized by XRD and SEM, and their gas-separation properties were determined.

The growth process of the membrane was monitored by X-ray diffraction (XRD, a Siemens D5005 diffractometer with $Cu_{K\alpha}$ radiation ($\lambda = 1.5418$ Å) and field-emission scanning electron microscope (FE-SEM: JEOS JSM 6700F). A soap-film flow meter was used

 © 2006 Wiley-VCH Verlag GmbH & Co. KGaA, Weinheim

to measure the flux of the gas, and the gas that penetrated through the membrane was analyzed by gas chromatograph (HP6890).

Received: June 9, 2006
Published online: October 2, 2006

Keywords: carbon dioxide · gas separation · hierarchical growth · membranes · zeolites

[1] R. F. Service, *Science* **2004**, *305*, 962.
[2] H. Lin, E. V. Wagner, R. Raharjo, B. D. Freeman, I. Roman, *Adv. Mater.* **2006**, *18*, 39.
[3] W. Xu, P. Blazkiewicz, S. Fleming, *Adv. Mater.* **2001**, *13*, 1014.
[4] L. Liu, A. Chakma, X. Feng, *Ind. Eng. Chem. Res.* **2005**, *44*, 6874.
[5] A. S. Kovvali, H. Chen, K. K. Sirkar, *J. Am. Chem. Soc.* **2000**, *122*, 7594.
[6] J. Caro, M. Noack, P. Kölsch, R. Schäfer, *Microporous Mesoporous Mater.* **2000**, *38*, 3.
[7] A. Tavolaro, E. Drioli, *Adv. Mater.* **1999**, *11*, 975.
[8] T. C. Bowenl, R. D. Noble, J. L. Falconer, *J. Membr. Sci.* **2004**, *245*, 1.
[9] M. C. Lovallo, A. Gouzinis, M. Tsapatsis, *AIChE J.* **1998**, *44*, 1903.
[10] T. Tomita, K. Nakayama, H. Sakai, *Microporous Mesoporous Mater.* **2004**, *68*, 71, and reference therein.
[11] Y. Cui, H. Kita, K. Okamoto, *J. Mater. Chem.* **2004**, *14*, 924.
[12] a) X. Gu, J. Dong, T. M. Nenoff, *Ind. Eng. Chem. Res.* **2005**, *44*, 937; b) K. Kusakabe, T. Kuroda, K. Uchino, Y. Hasegawa, S. Morooka, *AIChE J.* **1999**, *45*, 1220.
[13] a) S. Li, J. G. Martinek, J. L. Falconer, R. D. Noble, *Ind. Eng. Chem. Res.* **2005**, *44*, 3220; b) J. C. Poshusta, V. A. Tuan, J. L. Falconer, R. D. Noble, *Ind. Eng. Chem. Res.* **1998**, *37*, 3924.
[14] a) W. Yuan, Y. S. Lin, W. Yang, *J. Am. Chem. Soc.* **2004**, *126*, 4776, and reference therein; b) G. Xomeritakis, Z. Lai, M. Tsapatsis, *Ind. Eng. Chem. Res.* **2001**, *40*, 544.
[15] F. Z. Zhang, M. Fuji, M. Takahashi, *Chem. Mater.* **2005**, *17*, 1167.
[16] W. Dong, Y. Long, *Chem. Commun.* **2000**, 1067.
[17] J. Dong, Y. S. Lin, M. Z. C. Hu, R. A. Peascoe, E. A. Payzant, *Microporous Mesoporous Mater.* **2000**, *34*, 241.
[18] G. Xomeritakis, M. Tsapatsis, *Chem. Mater.* **1999**, *11*, 875, and reference therein.
[19] X. Yin, G. Zhu, W. Yang, Y. Li, G. Zhu, R. Xu, J. Sun, S. Qiu, R. Xu, *Adv. Mater.* **2005**, *17*, 2006.
[20] G. Xomeritakis, A. Gouzinis, S. Nair, T. Okubo, M. He, R. M. Overney, M. Tsapatsis, *Chem. Eng. Sci.* **1999**, *54*, 3521.
[21] J. Choi, S. Ghosh, Z. Lai, M. Tsapatsis, *Angew. Chem.* **2006**, *118*, 1172; *Angew. Chem. Int. Ed.* **2006**, *45*, 1154.
[22] A. J. Bons, P. D. Bons, *Microporous Mesoporous Mater.* **2003**, *62*, 9.
[23] A. Gouzinis, M. Tsapatsis, *Chem. Mater.* **1998**, *10*, 2497.
[24] R. Xu, G. Zhu, X. Yin, X. Wan, S. Qiu, *Microporous Mesoporous Mater.* **2006**, *90*, 39.
[25] J. Sun, G. Zhu, X. Yin, Y. Chen, Y. Cui, S. Qiu, *Chem. Commun.* **2005**, 1070.
[26] a) H.-K. Jeong, J. Krohn, K. Sujaoti, M. Tsapatsis, *J. Am. Chem. Soc.* **2002**, *124*, 12966; b) T. Okubo, T. Wakihara, J. Plévert, S. Nair, M. Tsapatsis, Y. Ogawa, H. Komiyama, M. Yoshimura, M. E. Davis, *Angew. Chem.* **2001**, *113*, 1103; *Angew. Chem. Int. Ed.* **2001**, *40*, 1069.
[27] G. Bonilla, D. G. Vlachos, M. Tsapatsis, *Microporous Mesoporous Mater.* **2001**, *42*,191.
[28] H. Jeong, Z. Lai, M. Tsapatsis, J. C. Hanson, *Microporous Mesoporous Mater.* **2005**, *84*, 332, and reference therein.
[29] W. Zhu, P. Hrabanek, L. Gora, F. Kapteijn, J. A. Moulijn, *Ind. Eng. Chem. Res.* **2006**, *45*, 767.
[30] D. W. Shin, S. H. Hyun, C. H. Cho, M. H. Han, *Microporous Mesoporous Mater.* **2005**, *85*, 313.
[31] S. Aguado, A. C. Polo, M. P. Bernal, J. Coronas, J. Santamaría, *J. Membr. Sci.* **2004**, *240*, 159.
[32] a) W. J. W. Bakker, F. Kapteijn, J. Poppe, J. A. Moulijn, *J. Membr. Sci.* **1996**, *117*, 57; b) Z. A. E. P. Vroon, K. Keizer, M. J. Gilde, H. Verweij, *J. Membr. Sci.* **1998**, *144*, 65.
[33] J. M. Graaf, E. Bijl, A. Stol, F. Kapteijn, J. A. Moulijn, *Ind. Eng. Chem. Res.* **1998**, *37*, 4071.
[34] G. Zhu, S. Qiu, F. Gao, D. Li, Y. Li, R. Wang, B. Gao, B. Li, Y. Guo, R. Xu, Z. Liu, O. Treasaki, *J. Mater. Chem.* **2001**, *11*, 1687.
[35] Z. B. Wamg, Y. Yan, *Chem. Mater.* **2001**, *13*, 1101.

 © 2006 Wiley-VCH Verlag GmbH & Co. KGaA, Weinheim

Dinuclear Complexes

DOI: 10.1002/anie.200602532

Efficient Phosphodiester Binding and Cleavage by a Zn^{II} Complex Combining Hydrogen-Bonding Interactions and Double Lewis Acid Activation**

Guoqiang Feng, Daniela Natale, Ravi Prabaharan, Juan C. Mareque-Rivas, and Nicholas H. Williams**

Considerable efforts have been invested in the development of small synthetic metallonucleases for the cleavage of RNA, or more ambitiously DNA, as a result of their potential application as therapeutic agents and robust, versatile replacements for nucleases as laboratory tools.[1] Currently, these complexes are still very inefficient relative to enzymes and this behavior limits their practical applications. More fundamentally, the development of artificial systems both tests and expands our understanding of how catalysis works under biological conditions. These compounds are also important for the development of artificial receptors for biologically important phosphates that are effective under

[*] D. Natale, Dr. R. Prabaharan, Dr. J. C. Mareque-Rivas
School of Chemistry
University of Edinburgh
Edinburgh EH9 3JJ (UK)
Fax: (+44) 131-6504743
E-mail: juan.mareque@ed.ac.uk
Homepage: http://www.chem.ed.ac.uk/staff/mareque.html
Dr. G. Feng, Dr. N. H. Williams
Centre for Chemical Biology
Department of Chemistry
University of Sheffield
Sheffield S3 7HF (UK)
Fax: (+44) 114-2229346
E-mail: N.H.Williams@Sheffield.ac.uk
Homepage: http://www.shef.ac.uk/chemistry/staff/profiles/nh_williams.html

[**] This work was supported by the BBSRC.

Supporting information for this article is available on the WWW under http://www.angewandte.org or from the author.

WILEY InterScience DISCOVER SOMETHING GREAT
© 2006 Wiley-VCH Verlag GmbH & Co. KGaA, Weinheim

these conditions.[2] Inspired by the structures of dinuclear metalloenzymes,[3] many studies have focused on the synthesis of dinuclear or polynuclear metal-ion complexes. Typically, these complexes bind phosphates more strongly and are significantly more reactive for the cleavage of phosphate esters than their corresponding mononuclear metal-ion complexes.[2,4] However, many metalloenzymes that catalyze the cleavage of phosphate esters also use amino acid side chains to stabilize the transition state directly as well as providing a scaffold for the metal-ion cofactor.[3] Recently, several ligands have been designed to enhance the properties of their corresponding mononuclear metal complexes through the second coordination sphere.[5–7] Generally, in artificial systems designed to efficiently bind and catalyze the cleavage of phosphate esters, these ligands have been functionalized by hydrogen-bond donors, such as ammonium, amino, or guanidine groups.[6,7] We have now combined both strategies to make a much more efficient dinuclear Zn^{II} complex and report our findings herein.

Specifically, the addition of 2-amino substituents to the pyridine units of metal-ion-binding ligands has been shown to be an effective modification for enhancing the binding and catalytic activity of mononuclear Cu^{II},[7c] Co^{III},[6a] and Zn^{II}[6c,7f,g] complexes. Interestingly, we showed that the introduction of aminopyridyl hydrogen-bond donors to a mononuclear Zn^{II} complex is as effective as the introduction of a second Zn^{II} ion for enhancing its activity towards the transesterification of phosphodiesters.[8] On the basis of these data, we designed the dinuclear Zn^{II} complex $[Zn_2(\mathbf{1})]$[9] (Scheme 1), which introduces four aminopyridyl hydrogen-bond donors positioned to interact with substrates bound to the metal-ion centers, to assess the effectiveness of this combination of strategies.

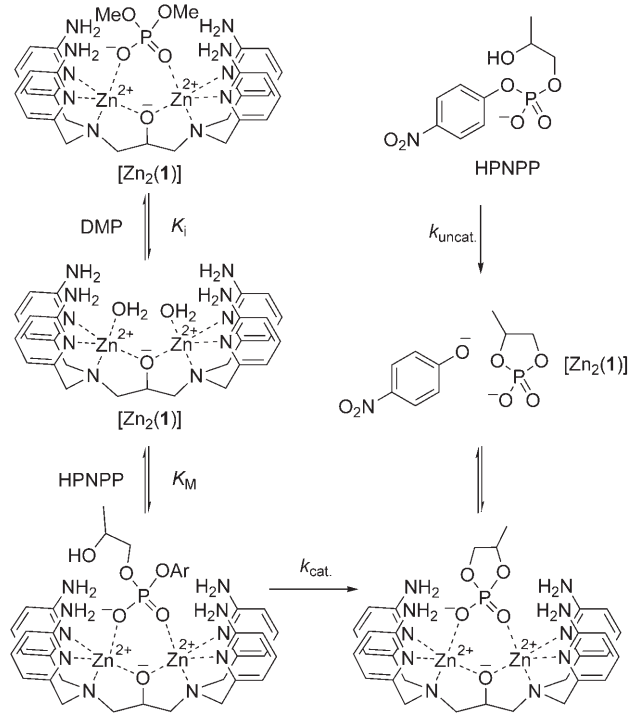

Scheme 1. Structures of complexes and substrates, and a proposed mechanistic scheme.

Crystallization of $[Zn_2(\mathbf{1})]$ in the presence of 4-nitrophenyl phosphate (PNPP) revealed that the phosphate binds to the complex by bridging the two Zn^{II} ions as required for

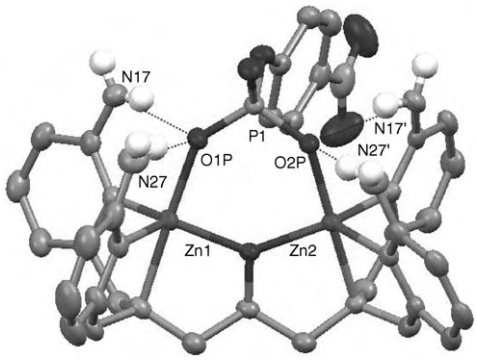

Figure 1. Structure of the $[Zn_2(\mathbf{1})]\cdot PNPP^+$ cation, with thermal ellipsoids drawn at 30% probability. Only N-bound hydrogen atoms (white) are shown for clarity; these were located in different maps and refined freely. Hydrogen-bonding interactions [Å]: N(17)···O(1P) 2.818(4), N(27)···O(1P) 2.884(4), N(17′)···O(2P) 2.882(4), N(27′)···O(2P) 2.872(4).

double Lewis acid activation (Figure 1). This structure is consistent with previous studies of Zn^{II} complexes containing the same core dinucleating ligand structure.[10] This behavior places the phosphoryl oxygen atoms in hydrogen-bonding distance of the amino groups so that they can assist the binding of phosphate substrates to the Zn^{II} ion centers and in stabilizing the transition state.

We started our studies with HPNPP (Scheme 1), which has been widely used as a convenient model for RNA-like phosphodiesters. Initial experiments confirmed that $[Zn_2(\mathbf{1})]$ was highly reactive, with a 0.2 mM solution decreasing the half-life of HPNPP (0.05 mM) to about a minute at pH 7.4 and 25 °C—thus corresponding to an observed fold-rate acceleration of approximately 10^6 and showing that this is the most effective artificial Zn^{II} complex for catalyzing this reaction reported to date.[1d,4b] ^{31}P NMR spectroscopic analysis showed that the catalyst cleanly converts HPNPP into propylene phosphate with a complete turnover of 5 mM of substrate by 1 mM of complex. To characterize this reactivity, the dependence of the initial rate of the reaction on HPNPP concentration was measured. As shown in Figure 2, higher concentrations led to saturation of the catalyst, and the data could be fitted to the Michaelis–Menten reaction scheme [Scheme 1; Eq. (1)], thus giving $k_{cat.} = 0.017 \pm 0.001\ s^{-1}$ and $K_M = 0.32 \pm 0.03$ mM at pH 7.4.

$$\text{Initial rate} = k_{cat.}[Zn_2(\mathbf{1})]\frac{[HPNPP]}{(K_M + [HPNPP])} \quad (1)$$

To further explore the catalytic turnover qualitatively observed by ^{31}P NMR spectroscopy, we gathered kinetic data by using UV/Vis spectroscopy (Figure 3). These data confirm that 5- and 10-fold excesses of substrate were rapidly turned over by the catalyst. These curves can be fit to a first-order curve; however, this analysis is only appropriate if the

 © 2006 Wiley-VCH Verlag GmbH & Co. KGaA, Weinheim

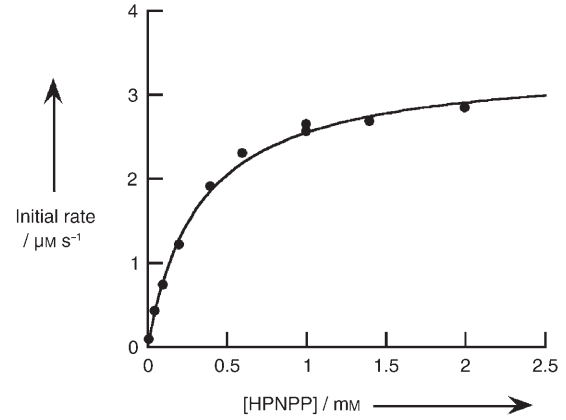

Figure 2. Saturation kinetic studies for the transesterification of HPNPP catalyzed by [Zn_2(**1**)] (0.2 mM) at pH 7.4 (50 mM HEPES buffer; HEPES = 2-[4-(2-hydroxyethyl)-1-piperazinyl]ethanesulfonic acid) and 25 °C. The solid line is the least-squares fit of Equation (1).

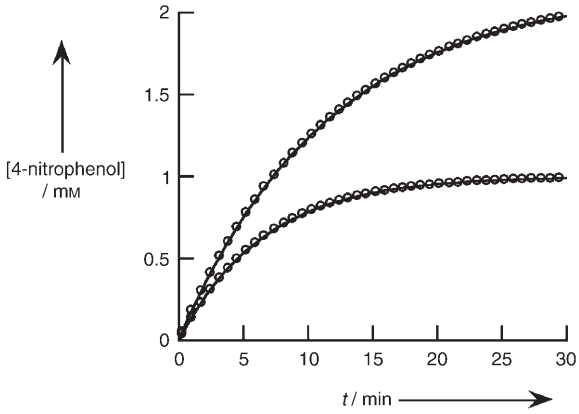

Figure 3. Turnover studies of the transesterification of 1 and 2 mM HPNPP catalyzed by [Zn_2(**1**)] (0.2 mM) at pH 7.4 (50 mM HEPES buffer) and 25 °C. Solid lines show the predicted reaction progress as described in the text.

substrate is at subsaturating concentrations—and in both cases, the initial substrate concentration is significantly greater than the value for K_M that we had determined. An alternative explanation is that the reaction is inhibited by product formation; if the K_i value is similar to the K_M value then apparent first-order behavior is also expected. This expectation is reasonable as the reaction generates a phosphate diester product that will have a similar affinity for the complex as the substrate. We tested this proposal by measuring how dimethyl phosphate (DMP) inhibited the transesterification of HPNPP. Figure 4 shows a plot of normalized first-order rate constant (k/k_0) for the transesterification of HPNPP at pH 7.4 with increasing concentration of DMP. The catalyzed reaction is clearly inhibited by DMP and is fit to Equation (2), which is derived for competitive inhibition (Scheme 1).

$$\frac{k}{k_0} = \frac{K_i}{(K_i + [\mathrm{DMP}])} \qquad (2)$$

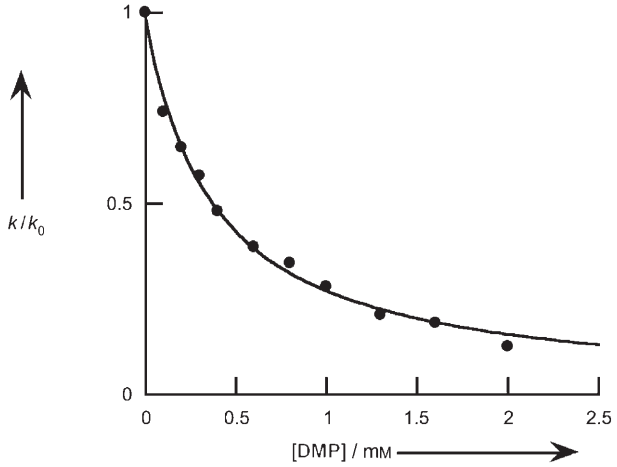

Figure 4. Variation in the ratio of the rate constants for transesterification of HPNPP catalyzed by 0.2 mM [Zn_2(**1**)] in the presence of DMP (k) to the rate in the absence of DMP (k_0) at pH 7.4 (50 mM HEPES). The solid line is the least-squares fit of Equation (2).

The value obtained for K_i (0.37 ± 0.07 mM) is in good agreement with the value for substrate binding to the complex. [Zn_2(**1**)] binds remarkably strongly to the diester monoanion in fully aqueous solution.[11] Using these parameters ($k_{cat.}$, K_M, and K_i) to simulate the expected progress curve for the complete reaction gives excellent agreement with the experimental data (solid lines in Figure 3).

Combining these parameters gives $k_{cat.}/K_M$, the apparent second-order rate constant for catalysis by [Zn_2(**1**)], as $53\,M^{-1}s^{-1}$. The value for the analogous dinuclear complex without 2-amino groups on the pyridine moieties is $0.073\,M^{-1}s^{-1}$,[8,12] so this modification enhances reactivity by almost three orders of magnitude. This increase is divided roughly equally between enhanced binding of the substrate and higher reactivity of the substrate–catalyst complex.

Although HPNPP transesterification has been widely used as a convenient model for RNA cleavage, it has a less effective intramolecular nucleophile and much better leaving group than RNA. These differences mean that a catalyst that can catalyze the hydrolysis of HPNPP may not be a good catalyst for RNA cleavage.[4b,13] Therefore, we investigated whether [Zn_2(**1**)] is also effective for catalyzing the cleavage of uridyl(3′-5′)uridine (UpU). At pH 7.3 and 25 °C, 1 mM [Zn_2(**1**)] does efficiently catalyze the hydrolysis of UpU (0.06 mM). The loss of UpU was monitored by reverse-phase HPLC and fitted to a first-order curve (Figure 5), thus giving an observed pseudo-first-order rate constant of $1.2 \pm 0.1 \times 10^{-4}\,s^{-1}$. This finding corresponds to a rate acceleration of approximately 10^6-fold,[14] which is similar to that observed for the catalysis of HPNPP cleavage—and so the high activity is not confined to the activated substrate.

A similar observation was reported by Richard and coworkers using a triazacyclononane-based dinuclear Zn^{II} complex that has the same bridging group but which under the same reaction conditions gives $k_{obs} = 0.7 \times 10^{-6}\,s^{-1}$.[14] This complex has similar reactivity to the pyridyl-based ligand with no 2-amino substituents, so the amino groups provide an additional rate acceleration of two orders of magnitude for

 © 2006 Wiley-VCH Verlag GmbH & Co. KGaA, Weinheim

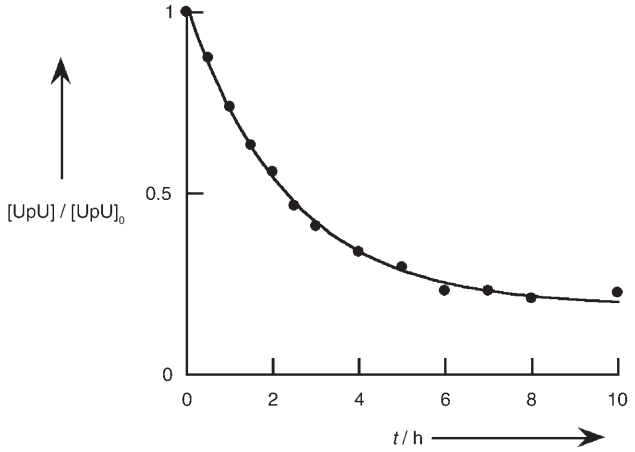

Figure 5. The hydrolysis of UpU (0.06 mM) catalyzed by [Zn_2(**1**)] (1 mM) in HEPES buffer (50 mM, pH 7.3) at 25 °C. The solid line is the least-squares fit to a first-order decay.

cleavage of unactivated substrates relative to double Lewis acid activation by the Zn^{II} ions alone.[15] As shown by the crystal structure in Figure 1, the phosphoryl moiety can bridge the two Zn^{II} ion centers to benefit from double Lewis acid activation, thus simultaneously placing the phosphoryl oxygen atoms in hydrogen-bonding distance of the amino groups. This enhances binding to the substrate, which is substantially tighter than in comparable complexes, and to the transition state, which leads to the high reactivity.

In summary, we have combined two strategies to achieve tight phosphate binding and high catalytic activity for phosphodiester transesterification with a synthetic Zn^{II} complex. Our kinetic studies show that this dinuclear complex shows remarkable rate enhancement both for the activated substrate HPNPP and UpU. This efficiency comes from the cooperation of double Lewis acid activation through two Zn^{II} ions and the hydrogen-bonding environment provided by the ligand. We are currently exploring whether these approaches can be used even more effectively to extend the limits of activity of small molecules to rival biological catalysts and to develop phosphate receptors with new practical applications.[16]

Received: June 23, 2006
Published online: September 29, 2006

Keywords: dinuclear complexes · enzyme models · hydrogen bonds · phosphate ester cleavage · receptors

[1] a) E. L. Hegg, J. N. Burstyn, *Coord. Chem. Rev.* **1998**, *173*, 133; b) M. Komiyama, J. Sumaoka, *Curr. Opin. Chem. Biol.* **1998**, *2*, 751; c) J. A. Cowan, *Curr. Opin. Chem. Biol.* **2001**, *5*, 634; d) J. R. Morrow, O. Iranzo, *Curr. Opin. Chem. Biol.* **2004**, *8*, 192; e) T. Lönnberg, H. Lönnberg, *Curr. Opin. Chem. Biol.* **2005**, *9*, 665; f) F. Mancin, P. Scrimin, P. Tecilla, U. Tonellato, *Chem. Commun.* **2005**, 2540.

[2] S. Aoki, E. Kimura, *Rev. Mol. Biotechnol.* **2002**, *90*, 129, and references therein.

[3] a) N. Sträter, W. N. Lipscomb, T. Klabunde, B. Krebs, *Angew. Chem.* **1996**, *108*, 2158; *Angew. Chem. Int. Ed. Engl.* **1996**, *35*, 2024; b) D. E. Wilcox, *Chem. Rev.* **1996**, *96*, 2435.

[4] a) N. H. Williams, B. Takasaki, M. Wall, J. Chin, *Acc. Chem. Res.* **1999**, *32*, 485; b) P. Molenveld, J. F. J. Engbersen, D. N. Reinhoudt, *Chem. Soc. Rev.* **2000**, *29*, 75; c) O. Iranzo, A. Y. Kovalevsky, J. R. Morrow, J. P. Richard, *J. Am. Chem. Soc.* **2003**, *125*, 1988; d) J. Chin, *Curr. Opin. Chem. Biol.* **1997**, *1*, 514.

[5] Recent examples: a) A. Wada, M. Harata, K. Hasegawa, K. Jitsukawa, H. Masuda, M. Mukai, T. Kitagawa, H. Einaga, *Angew. Chem.* **1998**, *110*, 2158; *Angew. Chem. Int. Ed.* **1998**, *37*, 798; b) C. E. MacBeth, A. P. Golombek, V. G. Young, Jr., C. Yang, K. Kuczera, M. P. Hendrich, A. S. Borovik, *Science* **2000**, *289*, 938; c) M. Matsu-ura, F. Tani, S. Nakayama, N. Nakamura, Y. Naruta, *Angew. Chem.* **2000**, *112*, 2083; *Angew. Chem. Int. Ed.* **2000**, *39*, 1989; d) D. B. Grotjahn, C. D. Incarvito, A. L. Rheingold, *Angew. Chem.* **2001**, *113*, 4002; *Angew. Chem. Int. Ed.* **2001**, *40*, 3884; e) D. K. Garner, S. B. Fitch, L. H. McAlexander, L. M. Bezold, A. M. Arif, L. M. Berreau, *J. Am. Chem. Soc.* **2002**, *124*, 9970; f) G. Rivera, R. H. Crabtree, *J. Mol. Catal. A* **2004**, *222*, 59; g) L. M. Berreau, *Eur. J. Inorg. Chem.* **2006**, 273; h) A. S. Borovik, *Acc. Chem. Res.* **2005**, *38*, 54.

[6] a) J. Chin, S. Chung, D. H. Kim, *J. Am. Chem. Soc.* **2002**, *124*, 10948; b) S. L. Tobey, B. D. Jones, E. V. Anslyn, *J. Am. Chem. Soc.* **2003**, *125*, 4026; c) J. Mareque-Rivas, R. Torres Martin de Rosales, S. Parsons, *Chem. Commun.* **2004**, 610.

[7] a) R. Krämer, *Coord. Chem. Rev.* **1999**, *182*, 243; b) E. Kövári, R. Krämer, *J. Am. Chem. Soc.* **1996**, *118*, 12704; c) M. Wall, B. Linkletter, D. Williams, A.-M. Lebuis, R. C. Hynes, J. Chin, *J. Am. Chem. Soc.* **1999**, *121*, 4710; d) H. Aït-Haddou, J. Sumaoka, S. L. Wiskur, J. F. Folmer-Andersen, E. V. Anslyn, *Angew. Chem.* **2002**, *114*, 4185; *Angew. Chem. Int. Ed.* **2002**, *41*, 4014; e) M. Forconi, N. H. Williams, *Angew. Chem.* **2002**, *114*, 877; *Angew. Chem. Int. Ed.* **2002**, *41*, 849; f) M. Livieri, F. Mancin, U. Tonellato, J. Chin, *Chem. Commun.* **2004**, 2862; g) G. Feng, J. C. Mareque-Rivas, R. Torres Martín de Rosales, N. H. Williams, *J. Am. Chem. Soc.* **2005**, *127*, 13470.

[8] G. Feng, J. C. Mareque-Rivas, N. H. Williams, *Chem. Commun.* **2006**, 1845.

[9] ESI mass-spectrometric analysis of an aqueous solution of the ligand **1** (1 mM; HCl salt), PNPP, and two equivalents of $Zn(NO_3)_2$ revealed peaks that correspond to the expected mass and isotope for [Zn_2(**1**)]·PNPP, thus suggesting that the complex persists in water as well as the solid phase.

[10] E. Kinoshita, M. Takahashi, H. Takada, M. Shiro, T. Koike, *Dalton Trans.* **2004**, *8*, 1189.

[11] Binding of monoanionic phosphate diesters to [Zn_2(**1**)] in water is even stronger than to Co^{III} complexes.[6a]

[12] This rate constant is slightly less than that measured by Richards and co-workers ($0.25\,M^{-1}s^{-1}$) for the catalysis of the transesterification of HPNPP by a triazacyclononane-based dinuclear Zn complex through double Lewis acid activation.[4c] [Zn_2(**1**)] is about 200-fold more effective under similar reaction conditions.

[13] K. Worm, F. Chu, K. Matsumoto, M. D. Best, V. Lynch, E. V. Anslyn, *Chem. Eur. J.* **2003**, *9*, 741.

[14] A. O'Donoghue, S. Y. Pyun, M.-Y. Yang, J. R. Morrow, J. P. Richard, *J. Am. Chem. Soc.* **2006**, *128*, 1615.

[15] Cleavage of ApA by the Zn^{II} complex of the pyridyl-based ligand with no 2-amino substituents has been reported at 50 °C and pH 7.0 with a concentration of 2.5 mM for the complex (M. Yashiro, A. Ishikubo, M. Komiyama, *Chem. Commun.* **1995**, 1793), thus giving $k_{obs} \approx 2 \times 10^{-5}\,s^{-1}$. Allowing for the different conditions, a similar value is estimated to that reported in reference [14] for our reaction conditions.

[16] Experimental details can be found in the Supporting Information.

 © 2006 Wiley-VCH Verlag GmbH & Co. KGaA, Weinheim

Superconductors

DOI: 10.1002/anie.200602614

Single-Step Synthesis and Surface-Assisted Growth of Superconducting TaS_2 Nanowires**

*Charles W. Dunnill, Hannah K. Edwards, Paul D. Brown, and Duncan H. Gregory**

The first nanostructures of layered chalcogenides observed were the scroll-like structures of WS_2 reported in 1979 as part of an investigation of dichalcogenide catalytic activity.[1] WS_2 nanotubes were subsequently characterized in 1992, generating considerable interest.[2] The nanostructured dichalcogenides of transition metals from Groups 5 and 6 have potential applications in solid-state lubricants,[3] nano-electronics,[4] hydrogen storage,[5] catalysis,[6] and as tips for scanning tunneling microscopes (STMs).[7] Tantalum disulfide (TaS_2), which has been known as a bulk compound for many decades,[8] exists in three principal polytype structures: trigonal 1T-TaS_2 ($P\bar{3}m1$), hexagonal 2H-TaS_2 ($P6_3/mmc$), and rhombohedral 3R-TaS_2 ($R3m$).[9] The 1T polytype is metastable below 550 K, but can be isolated by quenching a TaS_2 sample from above 1100 K.[10,11] In contrast, 2H-TaS_2 can be produced from 1T-TaS_2 by annealing at 823 K and is stable at room temperature.[12] The slow cooling of mixtures of the elements from high temperatures tends to yield 3R-TaS_2. The layered structures of the TaS_2 polytypes enable extensive intercalation chemistry, which combined with the inherent superconductivity of both the parent compound and its intercalated derivatives, has fuelled considerable research.[13,14] The prospect of reproducing these phenomena at the nanoscale is a tantalizing one.

Reports of TaS_2 nanostructures describe their formation by the reduction of bulk TaS_3 in an H_2 atmosphere[15] or by the pyrolysis of TaS_3 nanobelts under vacuum.[16] Both of these methods are two-step syntheses involving a trisulfide precursor. In the former report, the sensitivity of the nanomaterials to the electron beam prevented a determination of the crystal structure of the nanotubes and nanowires, whereas in the latter report, the TaS_2 nanobelts were found to adopt the rarely observed 6R polytype structure ($R\bar{3}m$). Superconductivity was observed in the 6R-TaS_2 nanobelts below 2.7 K. Herein, we report the synthesis of single-crystalline nanowires of TaS_2 by a facile one-step process, the direct heating of the elemental powders, for the first time. Our investigations aid the understanding of the polytypic nature of TaS_2 and the growth process of the material. They also indicate that the TaS_2 nanowires have enhanced superconducting properties compared to those of the bulk phase.

TaS_2 nanowires were synthesized from the elemental powders by chemical vapor transport (CVT) at elevated temperatures, in one step (see Experimental Section). Upon quenching the reaction mixture, a low-density fibrous material (LDFM) was observed on the inner surface of the reaction tube, which became free as the tube was manipulated. A black residual powder was observed at one end of the tube (**I**), and the LDFM at the opposite end (**II**; Figure 1a).

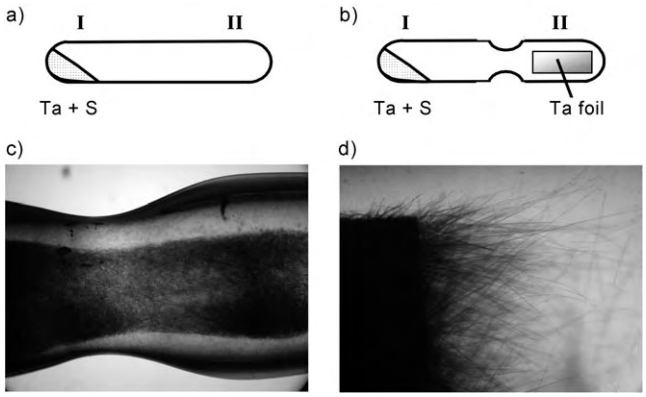

Figure 1. a) Normal and b) modified fused-silica tubes used in the synthesis of the TaS_2 nanowires. Optical microscope images showing the growth of LDFM c) within the neck of the modified tube and d) on the Ta foil.

The LDFM was easily removed after opening the ampoule, and the residual powder from region **I** was also retained. In a second series of experiments in which a Ta foil was inserted into a modified ampoule at region **II** (Figure 1b), a similar yield of LDFM was observed on the tube walls (Figure 1c), and another substantial mass of LDFM was observed on and around the Ta foil (Figure 1d). This observation suggests that the yield of nanowires may be increased through the addition of a Ta foil to the reaction ampoule. The LDFM consists of long needlelike structures growing perpendicular to the surfaces of the foil (Figure 1d).

In a control reaction with region **II** of a modified ampoule empty, we observed no nanostructure formation in this region. There was also a low yield of LDFM in, on, and around the residual powder in region **I**. A control reaction with an Fe foil in region **II** showed limited formation of LDFM in region **I** and no growth in region **II** on the Fe surface. There was, however, evidence of surface reaction on

[*] C. W. Dunnill, Prof. D. H. Gregory
Department of Chemistry
University of Glasgow
Joseph Black Building, Glasgow G12 8QQ (UK)
Fax: (+44) 141-330-4888
E-mail: d.gregory@chem.gla.ac.uk
Homepage: http://www.chem.gla.ac.uk/staff/duncang/
H. K. Edwards, Dr. P. D. Brown
School of Mechanical, Materials and Manufacturing Engineering
University of Nottingham
Nottingham NG7 2RD (UK)

[**] D.H.G. thanks the EPSRC for a DTA studentship for C.W.D. D.H.G and P.D.B thank the IDTC in Nanotechnology, University of Nottingham for a studentship for H.K.E. The authors would like to acknowledge use of the EPSRC's Chemical Database Service (ICSD) at the Daresbury Laboratory, Dr. G. S. Walker for discussions and support of H.K.E.'s work, and Mrs. N. Weston for assistance with the SEM.

Supporting information for this article is available on the WWW under http://www.angewandte.org or from the author.

WILEY InterScience DISCOVER SOMETHING GREAT
© 2006 Wiley-VCH Verlag GmbH & Co. KGaA, Weinheim

the Fe foil. The brittle, lustrous layer on the surface of the Fe foil was easily removed, and analysis by powder X-ray diffraction (PXRD) and scanning electron microscopy (SEM)/energy dispersive X-ray analysis (EDX) revealed the material to be crystalline platelets of FeS (ICDD PDF 00-051-0001; Fe/S 1:1.0(1) by EDX).

PXRD patterns for the black residual powder from both series of reactions were indexed to 3R-TaS_2 (ICDD PDF 04-001-0069; $a = 3.314(4)$, $c = 17.83(2)$ Å, $R3m$). Broad peaks in the PXRD patterns for the LDFM were matched to 2H-TaS_2 (ICDD PDF 04-003-2108) as the majority phase (see Supporting Information). SEM analysis of the LDFM showed bundles of filaments with aspect ratios up to 10000:1, and no evidence of crystallites. A low-magnification view of the bundles is shown in Figure 2a. A higher-magnification image (Figure 2b) reveals that the larger microwires are clustered

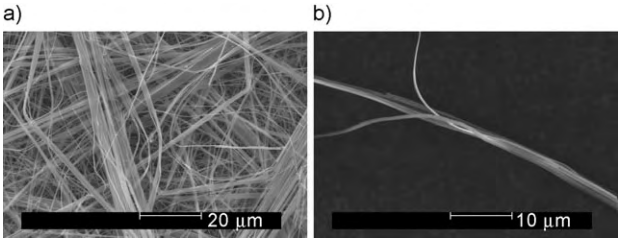

Figure 2. SEM images of TaS_2 nanowires showing a) the LDFM and b) a bundle of nanowires.

bundles of smaller individual nanofilaments. The diameters of the filaments are 100–600 nm, and their morphology is consistent for all reactions. Larger platelets of 3R-TaS_2 (identified by PXRD) were found in the residual powder in region **I**. EDX analysis of the bundles of fibers yielded a 1:1.8(3) Ta/S ratio (averaged over > 20 samples). This result is in reasonable agreement to the expected 1:2 ratio, given the porous nature of the sample (for EDX, uniform polished surfaces are optimal).

Transmission electron microscopy (TEM) showed nanowire bundles of up to 1 mm in length and up to 2.5 µm in diameter. The bundles consist of very straight individual nanowires with constant diameters along their length and aspect ratios of up to 50000:1 (1 mm:20 nm; Figure 3a). The nanowires displayed selected area electron diffraction (SAED) patterns consistent with a single-crystalline material (Figure 3a, inset).

The multifilamentary morphology of the nanowires suggests a cooperative growth mechanism, whereby a number of nanowires nucleate and simultaneously propagate along one crystallographic direction. This morphology is further illustrated by the large bundle shown in Figure 3b: the numerous crystalline TaS_2 filaments in the bundle lead to a varied contrast across the wire. The nanowire bundle appears to have fractured during sample preparation, hence, taking on an uneven terminal edge. The corresponding SAED pattern, shown in [0001] projection in Figure 3c, is characteristic of those produced by the nanowires, consisting of sharp spots in a hexagonal array.

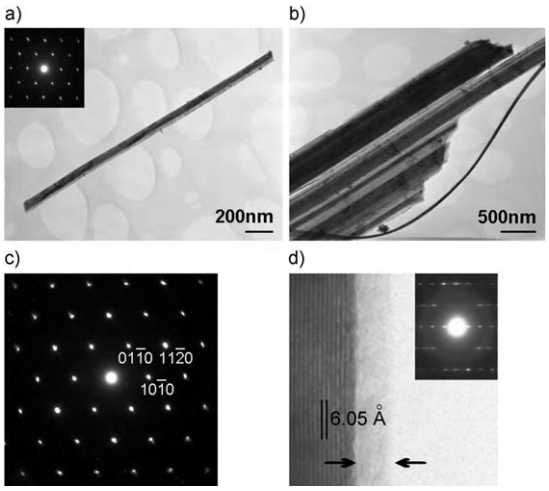

Figure 3. a) Bright-field TEM image of a single-crystalline TaS_2 nanowire and the corresponding SAED pattern in [0001] projection (inset). b) Bright-field TEM image of a bundle of nanowires and c) the corresponding SAED pattern in [0001] projection (indexed to the 2H-TaS_2 cell). d) Phase-contrast TEM image of a nanowire, showing lattice fringes with a spacing of 6.05 Å and an amorphous oxide layer (arrows), and the corresponding SAED pattern in approximately $[2\bar{1}\bar{1}0]$ projection (inset).

As the crystal structures of the 2H- and 1T-TaS_2 polytypes differ in the stacking of layers along the [0001] direction, leading to differences in the c parameters, the [0001] projections of the SAED patterns of the two polytypes are similar; hence, the diffraction pattern in Figure 3c could be indexed to either structure. However, careful analysis of this and further SAED patterns, such as that shown in the inset to Figure 3d, which approaches a $[2\bar{1}\bar{1}0]$ projection, yields a more precise match to 2H-TaS_2 than to 1T-TaS_2. The 3R and less-common 6R polytypes[9,17] were also considered, but neither provided an acceptable match to the SAED data. Therefore, the SAED data are consistent with the predominant phase of the nanowires being 2H-TaS_2.[9] This assignment concurs with previous work, where nanostructures produced through the reduction of TaS_3 with H_2 were tentatively identified as 2H-TaS_2, on the basis of PXRD data.[18] However, TaS_2 nanobelts prepared from the heating of TaS_3 under vacuum were reported to adopt the 6R structure.[16] Analysis of SAED patterns for the nanowires found that the $11\bar{2}0$ diffraction spots were coincident with the long axis of the nanowires, indicating that growth occurs along the $\langle 11\bar{2}0 \rangle$ directions.

Upon rotating the nanowires around their longitudinal axes, lattice fringes were observed parallel to the nanowire surface (Figure 3d). The fringe spacing is 6.05(8) Å, in good agreement with the (0002) plane spacing of 2H-TaS_2 (6.0485 Å), but in poor agreement with the equivalent (0001) spacing of the 1T polytype (5.8971 Å), again suggesting that the 2H-TaS_2 is the dominant phase of the nanowires. The measurement was calibrated for magnification and image resolution using the known $(10\bar{1}0)$ fringe spacing of Nb_3Te_4. The corresponding SAED pattern, which approaches a $[2\bar{1}\bar{1}0]$ projection, highlights the diffraction spacings corresponding to the (0002) planes (Figure 3d, inset). An amorphous film

 © 2006 Wiley-VCH Verlag GmbH & Co. KGaA, Weinheim

was also observed on the surface of the wires, which most likely originates from surface oxidation upon exposure to air, as has been observed in other systems.[19]

The nanowires exhibit superconductivity, with an onset temperature of 3.4 K (Figure 4). This behavior is in stark

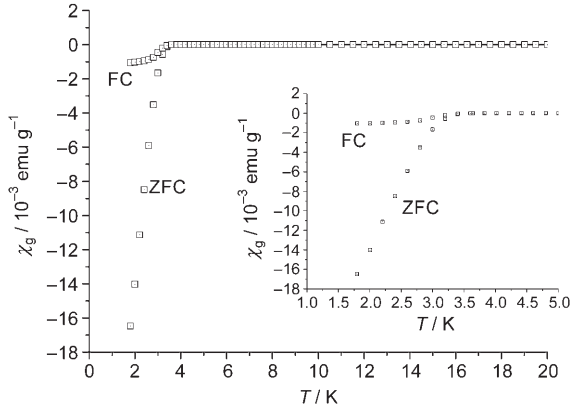

Figure 4. Temperature dependence of the magnetic susceptibility (χ_g) of the TaS_2 nanowires, under FC and ZFC conditions. The temperature region near the superconducting transition at $T_c = 3.4$ K is highlighted (inset).

contrast with that of bulk 2H-TaS_2, which exhibits superconductivity below 1 K ($T_c = 0.6$[14] or 0.8 K[20]). Further, the transition temperature of the 2H-TaS_2 nanowires is higher than that reported for the 6R-TaS_2 nanobelts ($T_c = 2.7$ K).[16] Bulk 6R-TaS_2 has been reported to exhibit superconductivity, with $T_c = 2.3$ K at ambient pressure and $T_c > 4$ K at 17.3 kbar.[21] As discussed with respect to 6R-TaS_2 nanobelts[16] based on the arguments of by Friend and Yoffe,[22] the increased transition temperatures of the nanomaterials, relative to that of the bulk material, could originate from a suppression of the periodic lattice distortion that drives charge density wave formation. A similar mechanism leads to an enhancement of the transition temperature of bulk 2H-TaS_2 following intercalation ($T_c = 2$–5.5 K) or the application of pressure. This effect may also be responsible for the observation of elevated transition temperatures in nanowires and nanotubes of $NbSe_2$,[23] for which electronic-structure calculations have predicted a high density of states (DOS) at the Fermi level (dominated by Nb 4d states).[24] Importantly, similar calculations have predicted broadly analogous effects for nanostructured 2H-TaS_2 and the likelihood of superconductivity.[25] Furthermore, when nanowires are arranged in bundles a "conductivity strengthening effect" occurs;[26] for example, semiconducting $B_xC_yN_z$ nanotubes become metallic,[27] and metallic single-walled C nanotubes become superconducting.[28] Thus, an increase in the superconducting transition temperature might occur when TaS_2 nanowires form bundles. This effect might also contribute to the increase in transition temperature from TaS_2 nanobelts to nanowire bundles.

In summary, we have exploited a simple one-step synthesis to produce superconducting TaS_2 nanowire bundles. These high-aspect-ratio wires, which adopt the 2H structure, exhibit superconductivity below $T_c = 3.4$ K. The nanowire bundles can be produced by using a surface-assisted growth process, which could find application in the selective synthesis of other dichalcogenide materials with enhanced electronic properties.

Experimental Section

In a typical reaction, elemental powders of Ta (99.9%, −325 mesh, Aldridge) and S (99.5%, Fisher) were ground together in a 1:2 Ta/S ratio and sealed in a 12-mm-diameter fused-silica tube under a vacuum of 4×10^{-5} Torr. The tube was placed horizontally in a box furnace and heated to 650–1000 °C for up to 70 h. It was then air quenched to room temperature and opened. The products were easily separated using tweezers.

In alternative reactions, 1:2 mixtures of the elemental powders were placed at one end (**I**) of a fused-silica tube with a width restriction (neck) halfway along its length (Figure 1a). A piece of Ta foil ($10 \times 30 \times 0.25$ mm^3, 99.9%, Aldridge) was placed at the opposite end (**II**) of the tube. The reactants were, thus, prevented from coming into direct physical contact with the foil as the tube was sealed or during the reaction. The tube was heated to 650 °C for up to 70 h, and the products were separated by mechanical methods. Two different control experiments were also run, in which region **II** either remained empty or contained Fe foil ($10 \times 30 \times 0.25$ mm^3, 99.9%, Aldridge). Fe is known to have catalytic effects on the formation of nanowires,[29–31] and was therefore a clear choice for comparison.

The products of the reactions were characterized by PXRD (Philips X'Pert diffractometer; θ–2θ; $Cu_{K\alpha}$ radiation), SEM (Philips XL30 SEM and XL30 ESEM-FEG, both with Oxford Instruments ISIS EDX systems; samples prepared by depositing powder on a C tab), TEM (JEOL 2000fx TEM and ISIS EDX system; samples prepared by sonicating powder in acetone and then pipetting drops of the suspension onto holey-C-film Cu grids), and magnetometry (Quantum Design MPMS 5T; field-cooled (FC) and zero-field-cooled (ZFC) measurements with an applied field of 10 Oe over 1.8–20 K; samples loaded into gelatin capsules).

Received: June 30, 2006
Published online: September 28, 2006

Keywords: chalcogenides · nanostructures · sulfur · superconductors · tantalum

[1] R. R. Chianelli, E. Prestridge, T. Pecorano, J. P. DeNeufville, *Science* **1979**, *203*, 1105.
[2] R. Tenne, L. Margulis, M. Genut, G. Hodes, *Nature* **1992**, *360*, 444.
[3] S. Prasad, J. Zabinski, *Nature* **1997**, *387*, 761.
[4] O. Tal, M. Remskar, R. Tenne, G. Haase, *Chem. Phys. Lett.* **2001**, *344*, 434.
[5] J. Chen, N. Kuriyama, H. Yuan, Hiroyuki T. Takeshita, T. Sakai, *J. Am. Chem. Soc.* **2001**, *123*, 11813.
[6] J. Chen, S.-L. Li, Q. Xu, K. Tanaka, *Chem. Commun.* **2002**, 1722.
[7] R. Tenne, *Chem. Eur. J.* **2002**, *8*, 5296.
[8] H. Biltz, C. Kircher, *Ber. Dtsch. Chem. Ges.* **1910**, *43*, 1636.
[9] F. Jellinek, *J. Less-Common Met.* **1962**, *4*, 9.
[10] J. A. Wilson, F. J. DiSalvo, S. Mahajan, *Adv. Phys.* **2001**, *50*, 1171.
[11] J. F. J. Revelli, W. A. Phillips, *J. Solid State Chem.* **1974**, *9*, 176.
[12] J. F. Revelli, *Inorg. Synth.* **1979**, *19*, 35.
[13] S. F. Meyer, R. E. Howard, G. R. Stewart, J. V. Acrivos, T. H. Gaballe, *J. Chem. Phys.* **1975**, *62*, 4411.

 © 2006 Wiley-VCH Verlag GmbH & Co. KGaA, Weinheim

[14] A. Schlicht, M. Schwenker, W. Biberacher, A. Lerf, *J. Phys. Chem. B* **2001**, *105*, 4867.
[15] M. Nath, C. N. R. Rao, *J. Am. Chem. Soc.* **2001**, *123*, 4841.
[16] X. Wu, Y. Tao, Y. Hu, Y. Song, Z. Hu, J. Zhu, L. Dong, *Nanotechnology* **2006**, *17*, 201.
[17] G. Hagg, N. Schonberg, *Ark. Kemi* **1954**, *7*, 371.
[18] M. Nath, C. N. R. Rao, *Pure Appl. Chem.* **2002**, *74*, 1545.
[19] a) Y. Z. Jin, W. K. Hsu, Y. L. Chueh, L. J. Chou, Y. Q. Zhu, K. Brigatti, H. R. Kroto, D. R. M. Walton, *Angew. Chem.* **2004**, *116*, 5788; *Angew. Chem. Int. Ed.* **2004**, *43*, 5670; b) H. K. Edwards, P. A. Salyer, M. J. Roe, G. S. Walker, P. D. Brown, D. H. Gregory, *Angew. Chem.* **2005**, *117*, 3621; *Angew. Chem. Int. Ed.* **2005**, *44*, 3555.
[20] F. J. DiSalvo, R. Schwall, T. H. Geballe, F. R. Gamble, J. H. Osiecki, *Phys. Rev. Lett.* **1971**, *27*, 310.
[21] E. Figueroa, Y.-K. Kuo, A. Olinger, M. A. Lloyd, L. D. Bastin, S. Petrotsatos, Q. Chen, B. Dobbs, S. Dev, J. P. Selegue, L. E. DeLong, C. P. Brock, J. W. Brill, *J. Solid State Chem.* **1995**, *114*, 486.
[22] R. H. Friend, A. D. Yoffe, *Adv. Phys.* **1987**, *36*, 1.
[23] a) M. Nath, S. Kar, A. K. Raychaudhuri, C. N. R. Rao, *Chem. Phys. Lett.* **2003**, *368*, 690; b) Y. S. Hor, U. Welp, Y. Ito, Z. L. Xiao, U. Patel, J. F. Mitchell, W. K. Kwok, G. W. Crabtree, *Appl. Phys. Lett.* **2005**, *87*, 142506.
[24] V. V. Ivanovskaya, A. N. Enyashin, N. I. Medvedeva, A. L. Ivanovskii, *Phys. Status Solidi B* **2003**, *238*, R1.
[25] A. N. Enyashin, I. R. Shein, N. I. Medvedeva, A. L. Ivanonskii, *Internet Electron. J. Mol. Des.* **2005**, *4*, 316, http://www.biochem-press.com.
[26] V. V. Pokropivnyi, *Powder Metall. Met. Ceram.* **2002**, *41*, 123.
[27] X. Blase, J.-C. Charlier, A. De Vita, R. Car, *Appl. Phys. Lett.* **1997**, *70*, 197.
[28] M. Kociak, A. Y. Kasumov, S. Gueron, *Phys. Rev. Lett.* **2001**, *86*, 2416.
[29] J.-Y. Raty, F. Gygi, G. Galli, *Phys. Rev. Lett.* **2005**, *95*, 096103.
[30] Y. Homma, Y. Kobayashi, T. Ogino, *J. Phys. Chem. B* **2003**, *107*, 12161.
[31] Z. P. Huang, D. Z. Wang, J. G. Wen, M. Sennett, H. Gibson, Z. F. Ren, *Appl. Phys. A* **2002**, *74*, 387.

 © 2006 Wiley-VCH Verlag GmbH & Co. KGaA, Weinheim

Encapsulated Catalysts

DOI: 10.1002/anie.200602700

Ligand-Free Platinum Nanoparticles Encapsulated in a Hollow Porous Carbon Shell as a Highly Active Heterogeneous Hydrogenation Catalyst**

Shigeru Ikeda, Satoru Ishino, Takashi Harada, Natsumi Okamoto, Takao Sakata, Hirotaro Mori, Susumu Kuwabata, Tsukasa Torimoto, and Michio Matsumura*

Studies on the synthesis of metal nanoparticles (MNPs) and their catalytic activity have become increasingly common because their specific properties, which are often distinct from those of bulk metals, lead to the induction of unique organic reactions.[1–7] These MNP-based catalysts are usually preserved by organic ligands, such as polymers,[2–4] surfactants,[5] and phosphines[6] to prevent coalescence and are used in homogeneous systems similar to those in which metal-complex catalysts are used. Current interest in the design of high-performance practical catalysts is directed towards the heterogenization of MNPs by fixing them on organic and inorganic solid surfaces. Thus, numerous supported MNPs have been studied as catalysts for a variety of reactions.[8] However, since these supported MNPs still have a propensity to coalesce, they are used in the presence of organic stabilizing and/or capping agents in most cases. Our research interest is therefore focused on the evaluation of the catalytic properties of ligand-free MNPs heterogenized on a solid support.

The creation of a core–shell structure is one technique to stabilize MNP cores in a solid shell without the use of organic

[*] Prof. Dr. S. Ikeda, S. Ishino, T. Harada, N. Okamoto, Prof. Dr. M. Matsumura
Research Center for Solar Energy Chemistry
Osaka University
1-3 Machikaneyama, Toyonaka 560-8531 (Japan)
Fax: (+81) 6-6850-6699
E-mail: sikeda@chem.es.osaka-u.ac.jp
Dr. T. Sakata, Prof. Dr. H. Mori
Research Center for Ultra-High Voltage Electron Microscopy
Osaka University, 7-1, Mihogaoka, Ibaraki 567-0047 (Japan)
Prof. Dr. S. Kuwabata
Division of Applied Chemistry
Graduate School of Engineering, Osaka University
2-1, Yamadaoka, Suita 565-0871 (Japan)
Prof. Dr. T. Torimoto
Department of Crystalline Materials Science
Graduate School of Engineering, Nagoya University
Furo-cho, Chikusa-ku, Nagoya, 464-8603 (Japan)

[**] This research was partially supported by a Grant-in-Aid for Young Scientists (A) (grant no. 16685020) from the Ministry of Education, Culture, Sports, Science and Technology, and the Iketani Science and Technology Foundation.

Supporting Information for this article is available on the WWW under http://www.angewandte.org or from the author.

© 2006 Wiley-VCH Verlag GmbH & Co. KGaA, Weinheim

ligands.[9] A promising structure for a catalyst in such a core–shell approach is a core MNP encapsulated by a hollow porous shell whose size is larger than that of the core particle. This "rattle-type" nanostructure enables stabilization of the core MNP without any ligands even under severe reaction conditions in a catalytic system. Although various examples of rattle-type nanostructures have been reported,[10] their catalytic properties have not been demonstrated owing to the difficulty of obtaining a core particle of sufficiently small size for use as a catalyst. Herein we fabricate a ligand-free platinum nanoparticle 2.2 nm in diameter as a typical catalyst which is encapsulated in a hollow porous carbon shell 30–40 nm in diameter (Pt@*hm*C). Since the carbon shell acts as a barrier that prevents the coalescence of Pt nanoparticles and also provides a void space where organic transformation occurs on the surface of the ligand-free Pt nanoparticle, the Pt@*hm*C particle was found to work as a robust and reusable heterogeneous catalyst for hydrogenation reactions.

Fabrication of Pt@*hm*C was performed using the procedure for fabrication of a hollow-core/mesoporous-shell carbon containing a gold nanoparticle about 20 nm in diameter.[10d] This procedure is based on the successive coating of a silica layer and a mesoporous silica layer on the surface of an MNP, subsequent growth of a carbon shell inside the mesoporous silica shell, and removal of the siliceous components by treatment with aqueous HF. When applying the procedure to much smaller Pt nanoparticles, we modified both the silica-coating and carbon-grafting steps of the above procedure (see Experimental Section). We employed Pt nanoparticles stabilized by poly(*N*-vinyl-2-pyrrolidone) (Pt–PVP) with an average particle size of 1.8 nm as a starting material (Figure 1a). As confirmed by the TEM image shown in Figure 1b, the Pt nanoparticles retain the size and size distribution of the original Pt–PVP after being covered with a double layer of silica and mesoporous silica (Pt@SiO_2–*m*SiO_2), while some Pt@SiO_2–*m*SiO_2 particles contain more than one Pt nanoparticle in each silica shell.

Figure 1c shows a TEM image of Pt@*hm*C obtained from the Pt@SiO_2–*m*SiO_2 and the size distribution of the Pt nanoparticles in this material. The Pt@*hm*C particle consists of a hollow carbon cage (30–40 nm in diameter with a shell thickness of 15 nm) and a central Pt nanoparticle with an average particle size of 2.2 nm. This value is consistent with the crystallite size determined by X-ray diffraction (XRD) analysis and implies the single crystalline nature of each Pt nanoparticle.[11] The increase (0.3 nm) of the Pt particle size relative to that in Pt@SiO_2–*m*SiO_2 is probably due to the coalescence of the Pt particles originally included in the same silica shell. The XP spectrum of Pt@*hm*C (Pt 4f region) is typical for Pt^0 with a small contribution from Pt^{2+}. The fact that almost no peak for expected impurities, such as Cl and F, is observed within the sensitivity of this measurement indicates that the surface of the Pt nanoparticle is free from any ligand but is partially oxidized.[11] The content of Pt in Pt@*hm*C, as measured by inductively coupled plasma (ICP) analysis, is 2.1 wt% under these reaction conditions.[11]

The N_2 adsorption–desorption isotherm of Pt@*hm*C measured at 77 K shows a significant hysteresis loop enclosed by a sudden drop in the adsorbed volume for the desorption

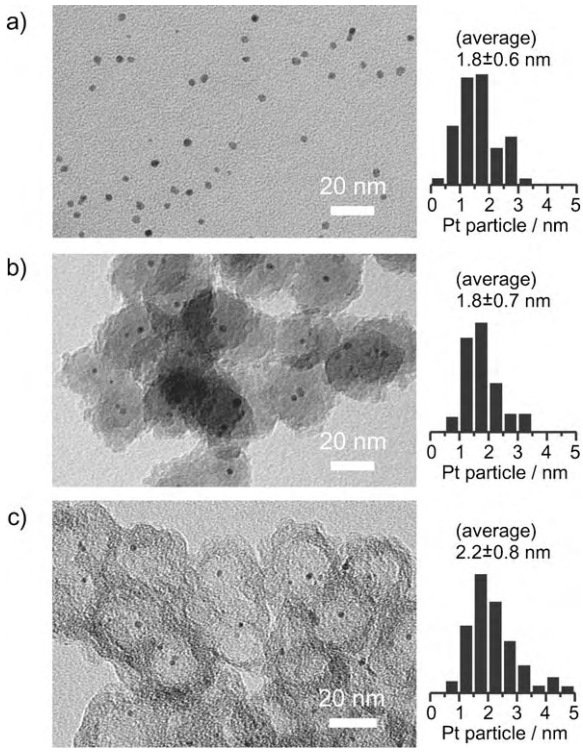

Figure 1. TEM images and Pt particle size distributions of a) Pt–PVP, b) Pt@SiO_2–*m*SiO_2, and c) Pt@*hm*C.

isotherm at a relative pressure (P/P_0) of 0.42–0.46. Since this phenomenon is typically observed in materials having a large mesopore encapsulated by a pore system of relatively small pore size,[12] the carbon shell of Pt@*hm*C is likely to consist of a porous wall structure. In practice, micropore and mesopore analyses of the adsorption branch by an α_s-plot and the BJH method revealed that the carbon shell has both micro- (< 0.9 nm) and nanosized (1–4 nm) pore systems.[11] It is also notable that the BET surface area calculated from the isotherm at a relative pressure of 0.05–0.09 reaches 1830 $m^2 g^{-1}$, which is an extremely high value that is comparable to representative activated carbons.

Figure 2 shows the catalytic performance of Pt@*hm*C for hydrogenation of nitrobenzene compared with that of the original Pt–PVP, a commercial Pt catalyst supported on activated carbon (Pt/AC),[13] and Pt@SiO_2–*m*SiO_2. It is clear that remarkable activity is achieved with Pt@*hm*C: all of the

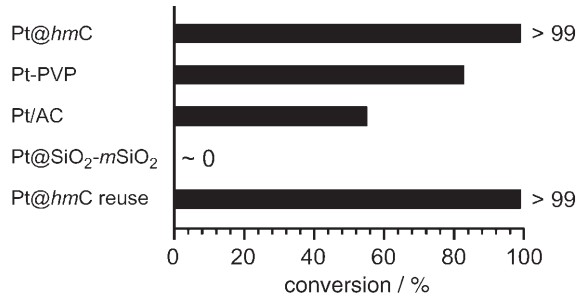

Figure 2. Liquid-phase hydrogenation of nitrobenzene into aniline by various Pt catalysts at 303 K.

 © 2006 Wiley-VCH Verlag GmbH & Co. KGaA, Weinheim

nitrobenzene is converted into aniline by Pt@*hm*C, whereas the reaction does not go to completion with Pt–PVP and Pt/AC.[14] The Pt@SiO_2–*m*SiO_2 particle shows no activity, thus indicating that the presence of voids in Pt@*hm*C is indispensable for induction of the reaction. Although the original Pt–PVP exhibits a higher level of activity than Pt/AC, it cannot be recovered and reused efficiently. However, the Pt@*hm*C catalyst can be recovered simply by centrifugation and recycled for further reaction. A TEM image of Pt@*hm*C taken after the reaction revealed that there is no change in the structure of the catalyst.[11]

As summarized in Table 1, Pt@*hm*C also shows a high level of catalytic activity for the hydrogenation of primary, secondary, and cyclic olefins in comparison with Pt–PVP and Pt/AC catalysts. The corresponding turnover frequency TOF (h^{-1}) for Pt was calculated to be more than 20000, which is much larger than that obtained with the platinum-nanoparticle-based system reported recently.[7] It is notable that the Pt@*hm*C catalyst also gives higher conversion for the hydrogenation of *trans*-stilbene (*trans*-1,2-diphenylethylene) into 1,2-diphenylethane than Pt–PVP or Pt/AC, which suggests that there is no significant effect of the porous carbon shell on the mass transfer of such a bulky substrate. Thus, we have demonstrated that Pt@*hm*C has high potential as a heterogeneous hydrogenation catalyst.

Table 1: Hydrogenation of various olefins by Pt@*hm*C, Pt/AC, and Pt-PVP catalysts.[a]

Substrate	Catalyst	Product	t [h][b]	Conv. [%][c]
	Pt@*hm*C		2	>99
	Pt–PVP		2	91
	Pt/AC		2	7
	Pt@*hm*C		2	96
	Pt–PVP		2	70
	Pt/AC		2	16
	Pt@*hm*C		1	91
	Pt–PVP		1	42
	Pt/AC		1	3
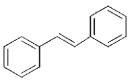	Pt@*hm*C	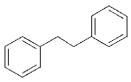	15	72
	Pt–PVP		15	46
	Pt/AC		15	16

[a] All reactions were carried out with 0.1 μmol of catalyst (Pt) and 0.5 mmol of substrate under H_2 (0.2 MPa in absolute pressure) at 348 K. [b] Reaction time. [c] Conversion of substrate.

All of the results described above are consistent with our prediction that a metal nanoparticle that is not bound to anything should be able to catalyze a chemical reaction efficiently. We have employed only Pt nanoparticles as hydrogenation catalysts in the present study. However, the basic concept of the system should be applicable to the selective oxidation of various organic compounds and C–C bond-formation reactions when other MNPs, such as Pd[1,2a,3b,c,8b,d,e] and Au,[2b] are used. Studies along these lines are now in progress.

Experimental Section

Poly(*N*-vinyl-2-pyrrolidone) (PVP)-stabilized Pt (Pt–PVP) was synthesized as reported elsewhere.[4b] Typically, PVP (66 mg) was added to a solution of hexachloroplatinic acid ($H_2PtCl_6{\cdot}6H_2O$; 0.03 mmol, 15.5 mg) in water (5 mL) and ethanol (45 mL) and the mixture was heated under reflux for 3 h. After adding acetone (160 mL) to 16 mL of the solution, the mixture was centrifuged (23000 g, 20 min) to collect the Pt–PVP precipitate. A mixture of ethanol (30.7 mL), aqueous NH_3 (0.28%, 1.28 mL), and tetraethylorthosilicate (TEOS, 0.1 mL, 0.45 mmol) was then added to the Pt–PVP precipitate and the mixture was stirred at room temperature for 16 h. The resulting precipitate of silica-covered Pt nanoparticles (Pt@SiO_2) was isolated by centrifugation (23000 g, 20 min). A mixture of ethanol (30.7 mL), aqueous NH_3 (0.28%, 1.38 mL), TEOS (0.1 mL, 0.45 mmol), and *n*-octadecyltrichlorosilane (ODTS, 0.04 mL, 0.09 mmol) was then added to this Pt@SiO_2 precipitate. After stirring the suspension at room temperature for 2 h, the precipitate was isolated by centrifugation (23000 g, 20 min), washed with ethanol, and calcined at 823 K for 6 h in air to produce Pt@SiO_2 coated with a mesoporous silica shell (Pt@SiO_2–*m*SiO_2).

The typical procedure for obtaining Pt@*hm*C: The carbon source used was resol-type phenol-formaldehyde resin (PF), which was prepared by the reaction of phenol (90 mmol, 8.46 g) and formaldehyde (110 mmol, 4 mL) in water (5.6 mL) in the presence of aqueous NH_3 (28%, 0.75 mL) at 363 K for 2 h. Pt@SiO_2–*m*SiO_2 (60 mg) was added to an ethanolic solution (2 mL) of PF (60 mg) and the solution was stirred overnight at room temperature to yield a PF–Pt@SiO_2–*m*SiO_2 composite. This composite was heated at 1173 K under vacuum for 2 h to carbonize the PF. Dissolution of the SiO_2–*m*SiO_2 shell with 10% aqueous HF generated Pt@*hm*C, which was characterized by TEM, XRD, XPS, N_2 adsorption–desorption measurements, and ICP analysis (see Supporting Information).

Catalytic hydrogenation of nitrobenzene was performed at 303 K whilst bubbling H_2 through the reaction vessel. Thus, 0.1 μmol of Pt catalyst (1.0 mg of Pt@*hm*C) and ethanol (5 mL) were placed in a cylindrical Schlenk flask (30 mL) and, after addition of substrate (0.5 mmol) under argon, the mixture was vigorously stirred (1200 rpm) at 303 K under H_2 bubbling (20 mL min^{-1}) for 1.5 h. For the hydrogenation of olefins, the reactions were conducted in a stainless-steel autoclave equipped with a glass reactor (50 mL). Typically, Pt@*hm*C (1.0 mg) and acetone (5 mL) were put into the glass vessel under N_2. After addition of substrate (0.5 mmol), the reactor was purged with H_2, pressurized with H_2 at 0.2 MPa (in absolute pressure), and heated to 348 K whilst stirring (1200 rpm). Catalytic activities were evaluated by determining the conversion of substrate with a Shimadzu GC-2010 gas chromatograph equipped with a flame ionization detector and a TC-FFAP capillary column.

Received: July 7, 2006
Published online: September 28, 2006

Keywords: heterogeneous catalysis · hydrogenation · materials science · nanostructures · platinum

[1] For recent reviews, see: a) N. Toshima, Y. Shiraishi, T. Teranishi, M. Miyake, T. Tominaga, H. Watanabe, W. Brijoux, H. Bönnemann, G. Schmid, *Appl. Organomet. Chem.* **2001**, *15*, 178–196; b) M. Moreno-Mañas, R. Pleixats, *Acc. Chem. Res.* **2003**, *36*, 638–643; c) D. Astruc, F. Lu, J. R. Aranzaes, *Angew. Chem.* **2005**, *117*, 8062–8083; *Angew. Chem. Int. Ed.* **2005**, *44*, 7852–7872.

[2] a) R. Narayanan, M. A. El-Sayed, *J. Am. Chem. Soc.* **2003**, *125*, 8340–8347; b) H. Tsunoyama, H. Sakurai, Y. Negishi, T. Tsukuda, *J. Am. Chem. Soc.* **2005**, *127*, 9374–9375.

 © 2006 Wiley-VCH Verlag GmbH & Co. KGaA, Weinheim

[3] a) R. M. Crooks, M. Zhao, L. Sun, V. Chechik, L. K. Yeung, *Acc. Chem. Res.* **2001**, *34*, 181 – 190; b) M. Ooe, M. Murata, T. Mizugaki, K. Ebitani, K. Kaneda, *J. Am. Chem. Soc.* **2004**, *126*, 1604 – 1605; c) J. C. Garcia-Martinez, R. Lezutekong, R. M. Crooks, *J. Am. Chem. Soc.* **2005**, *127*, 5097 – 5103.
[4] a) T. Teranishi, M. Miyake, *Chem. Matter.* **1998**, *10*, 595 – 600; b) T. Teranishi, M. Hosoe, T. Tanaka, M. Miyake, *J. Phys. Chem. B* **1999**, *103*, 3818 – 3827; c) C. Pan, F. Dassenoy, M.-J. Casanove, K. Philippot, C. Amiens, P. Lecante, A. Mosset, B. Chaudret, *J. Phys. Chem. B* **1999**, *103*, 10098 – 10101.
[5] a) J. Schulz, A. Roucoux, H. Patin, *Chem. Eur. J.* **2000**, *6*, 618 – 624; b) M. B. Thathagar, J. Beckers, G. Rothenberg, *J. Am. Chem. Soc.* **2002**, *124*, 11858 – 11859; c) M. T. Reetz, S. A. Quaiser, *Angew. Chem.* **1995**, *107*, 2461 – 2463; *Angew. Chem. Int. Ed. Engl.* **1995**, *34*, 2240 – 2241; d) J. S. Bradley, B. Tesche, W. Busser, M. Maase, M. T. Reetz, *J. Am. Chem. Soc.* **2000**, *122*, 4631 – 4636; e) N. R. Jana, X. Peng, *J. Am. Chem. Soc.* **2003**, *125*, 14280 – 14281.
[6] a) S. U. Son, Y. Jang, J. Park, H. B. Na, H. M. Park, H. J. Yun, J. Lee, T. Hyeon, *J. Am. Chem. Soc.* **2004**, *126*, 5026 – 5027; b) S. U. Son, Y. Jang, K. Y. Yoon, E. Kang, T. Hyeon, *Nano Lett.* **2004**, *4*, 1147 – 1151.
[7] C. W. Scheeren, G. Machado, J. Dupont, P. F. P. Fichtner, S. R. Texeira, *Inorg. Chem.* **2003**, *42*, 4738 – 4742.
[8] For example: a) G. Schmid, M. Harms, J.-O. Malm, J. O. Bovin, J. van Ruitenbeck, H. W. Zandbergen, W. T. Fu, *J. Am. Chem. Soc.* **1993**, *115*, 2046 – 2048; b) K. Ebitani, K.-M. Choi, T. Mizugaki, K. Kaneda, *Langmuir* **2002**, *18*, 1849 – 1855; c) H. Lang, R. A. May, B. L. Iversen, B. D. Chandler, *J. Am. Chem. Soc.* **2003**, *125*, 14832 – 14836; d) A. Biffis, E. Sperotto, *Langmuir* **2003**, *19*, 9548 – 9550; e) S. Mandal, D. Roy, R. V. Chaudhari, M. Sastry, *Chem. Mater.* **2004**, *16*, 3714 – 3724; f) R. Narayanan, M. A. El-Sayed, *J. Catal.* **2005**, *234*, 348 – 355.
[9] a) W. Schärtl, *Adv. Mater.* **2000**, *12*, 1899 – 1908; b) C. Graf, D. L. J. Vossen, A. Imhof, A. van Blaaderen, *Langmuir* **2003**, *19*, 6693 – 6700; c) X. Sun, Y. Li, *Angew. Chem.* **2004**, *116*, 607 – 611; *Angew. Chem. Int. Ed.* **2004**, *43*, 597 – 601.
[10] For some recent examples, see: a) Y. Yin, Y. Lu, B. Gates, Y. Xia, *Chem. Mater.* **2001**, *13*, 1146 – 1148; b) B. Rodríguez-González, V. Salgueiriño-Maceira, F. García-Santamaría, L. M. Liz-Marzán, *Nano Lett.* **2002**, *2*, 471 – 473; c) Y. Sun, B. T. Mayers, Y. Xia, *Nano Lett.* **2002**, *2*, 481 – 485; d) M. Kim, K. Sohn, H. B. Na, T. Hyeon, *Nano Lett.* **2002**, *2*, 1383 – 1387; e) K. Kamata, Y. Lu, Y. Xia, *J. Am. Chem. Soc.* **2003**, *125*, 2384 – 2385; f) K. T. Lee, Y. S. Jung, S. M. Oh, *J. Am. Chem. Soc.* **2003**, *125*, 5652 – 5653; g) Y. Sun, B. Wiley, Z.-Y. Li, Y. Xia, *J. Am. Chem. Soc.* **2004**, *126*, 9399 – 9406; h) D. Cheng, X. Zhou, H. Xia, H. S. O. Chan, *Chem. Mater.* **2005**, *17*, 3578 – 3581.
[11] Experimental data and a full discussion of these analyses are given in the Supporting Information.
[12] J. C. Groen, L. A. A. Peffer, J. Pérez-Ramírez, *Microporous Mesoporous Mater.* **2003**, *60*, 1 – 17.
[13] The Pt/AC sample was supplied by N. E. Chemcat Corporation.
[14] Since these catalysts gave aniline as the sole product, we used the conversion of nitrobenzene to evaluate their activities.

 © 2006 Wiley-VCH Verlag GmbH & Co. KGaA, Weinheim

Annulation

DOI: 10.1002/anie.200602782

The Use of Vinyl Sulfonium Salts in the Stereocontrolled Asymmetric Synthesis of Epoxide- and Aziridine-Fused Heterocycles: Application to the Synthesis of (−)-Balanol**

*Matthew G. Unthank, Nigel Hussain, and Varinder K. Aggarwal**

The asymmetric synthesis of epoxides fused to carbo- or heterocycles by epoxidation methods is inherently challenging because the two enantiotopic faces of the corresponding cyclic (*cis*) alkene are poorly differentiated. The use of chiral sulfur ylides offers a complementary method for preparing epoxides, but this method has essentially only been employed to make acyclic epoxides.[1] We considered the possibility of extending sulfur ylide reactions to make fused bicyclic epoxides, and in particular to the challenging substrates described above. We were particularly attracted by the possibility of designing a general asymmetric annulation process for the synthesis of N-heterocycles through the reaction of a bifunctional aminoaldehyde with a chiral vinyl sulfonium salt (Scheme 1). This type of reaction has been studied by Jimenez and co-workers in relation to the synthesis of mitomycins[2] but has not been explored beyond that.

If we could achieve such an annulation process, we envisaged that it could be employed in a short synthesis of the protein kinase C inhibitor balanol[3] from readily available

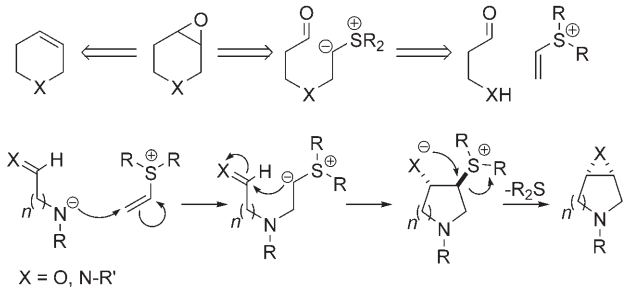

Scheme 1. An annulation reaction mediated by a vinyl sulfonium salt for the synthesis of fused bicyclic heterocycles.

[*] M. G. Unthank, Prof. Dr. V. K. Aggarwal
School of Chemistry
University of Bristol
Cantock's Close, Bristol, BS81TS (UK)
Fax: (+44) 117-929-8611
E-mail: v.aggarwal@bristol.ac.uk
N. Hussain
GlaxoSmithKline
Old Powder Mills, Tonbridge, Kent, TN119AN (UK)

[**] We thank GlaxoSmithKline and the EPSRC for financial support, and Dr. J.P.H. Charmant for X-ray analyses.

Supporting information for this article is available on the WWW under http://www.angewandte.org or from the author.

© 2006 Wiley-VCH Verlag GmbH & Co. KGaA, Weinheim

precursors (Scheme 2). We began our investigation with the diphenyl vinyl sulfonium salt[2b] **1** and α-,[4] β-,[5] and γ-[6] aminoaldehydes. Through extensive screening of solvents, bases and N-substituents, we found that the use of DBU in

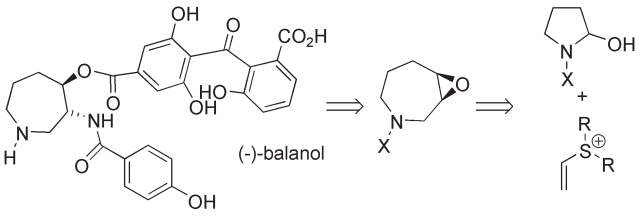

Scheme 2. Proposed retrosynthesis of balanol.

THF with sulfonamides was optimum, and the reaction gave the fused heterocyclic epoxides **2** and **3** in good yields (Scheme 3). The γ-aminoaldehyde substrate **4** proved to be a

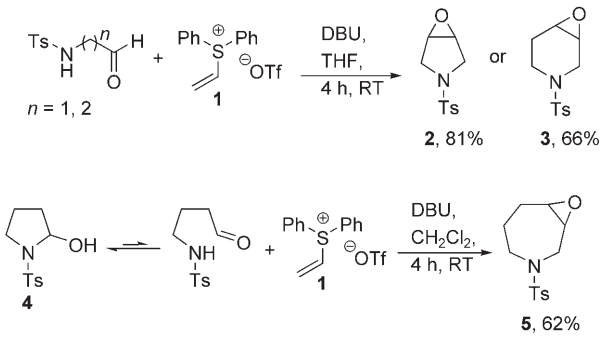

Scheme 3. The synthesis of five-, six-, and seven-membered heterocyclic epoxides through an annulation reaction mediated by **1**. DBU = 1,8-diazabicyclo[5.4.0]undec-7-ene, Ts = toluene-*p*-sulfonyl, Tf = triflate = trifluoromethanesulfonyl.

challenge, because: 1) the aldehyde exists predominantly in the ring-closed, hemiaminal form, which leads to a low concentration of the nucleophile, and 2) ring closure to form the seven-membered ring **5** is much more difficult. Nevertheless, after optimization, even this substrate participated in the annulation process, thus providing a new route to functionalized azepines from simple and readily available starting materials.

Having developed a new synthesis of fused heterocyclic epoxides, we sought to render the process asymmetric using the chiral vinyl sulfonium salt **6**. This was prepared in two steps from sulfide **7** (Scheme 4), which we had previously used in both our catalytic[7] and stoichiometric[8] epoxidations mediated by sulfur ylides.

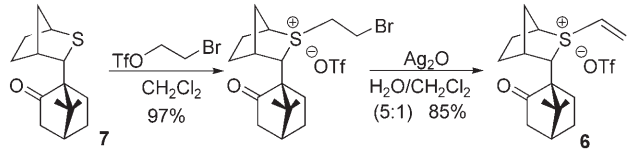

Scheme 4. The synthesis of the chiral vinyl sulfonium salt **6**.

We explored reactions with α-aminoketones, β-aminoaldehydes, and β-aminoketones (α-aminoaldehydes were not tested as they would give meso epoxides) (Table 1). Under optimized conditions (method B), the α-aminoketones **8a–c**[9,10] gave the desired epoxides **9a–c** in good yield and with very high enantioselectivity (Table 1, entries 1–3). Interestingly, we achieved even higher yields in the annulation process with the achiral, more robust diphenyl vinyl sulfonium salt **1** (Table 1, method A, entries 1–3). The β-aminoaldehydes[11] **10a**[5] and **10b**[12] were also effective and furnished the corresponding epoxides **3** and **11b**, again with high enantioselectivity (Table 1, entries 4 and 5). The absolute stereochemistry of epoxide **3** was determined by X-ray analysis[13] and is consistent with our established model for asymmetric induction; the remaining compounds are assigned by analogy (Scheme 5).[1b,14] The β-aminoketone **10c**[15] also provided good enantioselectivity, but yields were low because of a competing β elimination of the tosylamide[16] (Table 1, method B, entry 6). This elimination was not observed in the reaction with the achiral diphenyl vinyl sulfonium salt **1** (Table 1, method A, entry 6), which provided the epoxide **11c** in high yield. Interestingly, this methodology provides a class of enantiomerically pure epoxides (for example, **3**) that are very difficult to make by the well-established epoxidation methods, such as Jacobsen–Shi epoxidation of alkenes.[17] Although other methods exist for the synthesis of some of the other epoxides, for example, benzofused epoxides **11b**,[18] and trisubstituted epoxides **11c**,[19] our method offers a

Table 1: The reaction of chiral and achiral vinyl sulfonium salts with aminoaldehydes and -ketones.

Entry	Substrate	Product	Method	Yield [%]	*ee* [%]
1	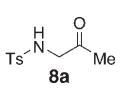 **8a**	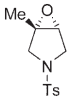 **9a**	A	90	–
			B	76	97
2	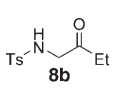 **8b**	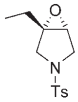 **9b**	A	90	–
			B	65	99
3	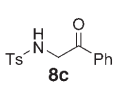 **8c**	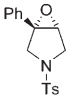 **9c**	A	96	–
			B	80	92
4	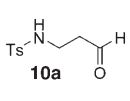 **10a**	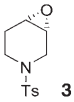 **3**	A	67	–
			B	67	98
5	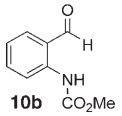 **10b**	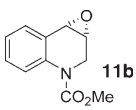 **11b**	A	50%	–
			B	50	88
6	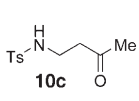 **10c**	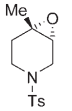 **11c**	A	77	–
			B	30	86

Method A: Diphenyl vinyl sulfonium salt **1** (1.2 equiv), DBU (2 equiv), CH_2Cl_2 (0.09 M), 2–4 h, 0 °C. Method B: Chiral vinyl sulfonium salt **6** (1.0 equiv), DBU (2 equiv), CH_2Cl_2 (0.015 M), 2–5 days, −20 °C.

 © 2006 Wiley-VCH Verlag GmbH & Co. KGaA, Weinheim

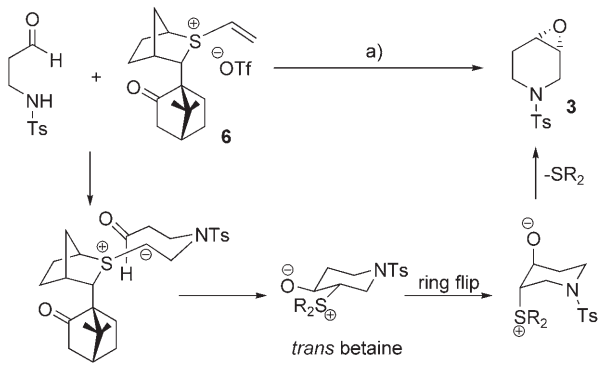

Scheme 5. Model for asymmetric induction in the epoxy-annulation reaction of β-aminoaldehyde **10a** with chiral vinyl sulfonium salt **6**. a) Chiral vinyl sulfonium salt **6** (1.0 equiv), DBU (2 equiv), CH_2Cl_2 (0.015 M), −20 °C, 3 days, 66% yield, 98% *ee*.

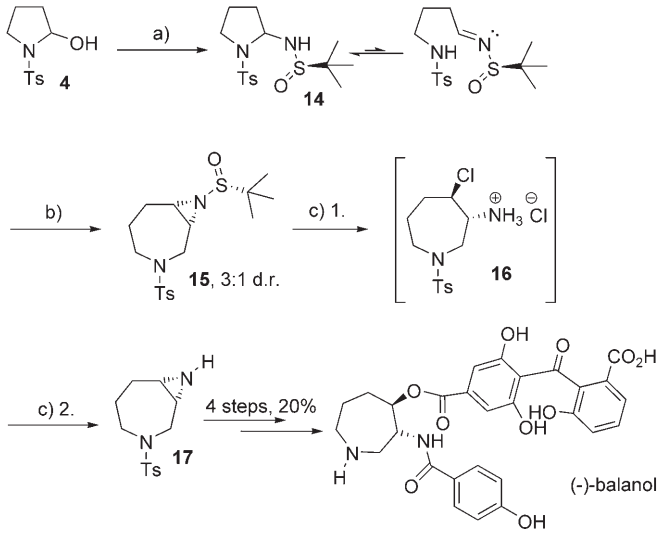

Scheme 7. Formal synthesis of (−)-balanol through an asymmetric aziridine-annulation reaction mediated by vinyl sulfonium salt. a) Ti(OEt)$_4$, *tert*-butylsulfinimine, CH_2Cl_2, 7 days, reflux, 95%; b) **1**, NaH (1.2 equiv), DMF (0.018 M), 4 h, 0 °C, 68%; c) 1. HCl (3 equiv) in dioxane, 20 min; 2. aq NH_3, 42 h, 80%.

completely different disconnection and requires very different starting materials, so is a complementary route.

Extension of this asymmetric process to the challenging seven-membered azepine ring **5**, the starting point of our proposed asymmetric synthesis of balanol, was unsuccessful. The hemiaminal was recovered, but the vinyl sulfonium salt **6** decomposed. Presumably the slower rate of addition of the amide nucleophile to the vinyl sulfonium salt allowed competing side reactions (decomposition pathways) of the more sensitive dialkyl vinyl sulfonium salt to dominate. However, even though the epoxide **5** has been used as an intermediate in the synthesis of balanol,[20a] it is not ideal, since the epoxide is opened regioselectively at the C4 position[19] (Scheme 6). Thus, the epoxide is first converted to the corresponding aziridine **12**, which undergoes selective ring opening, again at C4, to furnish the required 3-amino-4-hydroxyhexahydroazepine **13**.

We therefore considered the direct formation of the required aziridine, in which the identical annulation strategy would be used. For this we would need an aminal, and in order to induce asymmetry, we elected to use the Davis–Ellman *tert*-butyl sulfinimine.[21] Aminal **14** was prepared by condensation of the hemiaminal **4** with (*R*)-*tert*-butyl sulfinamide, and reaction with diphenyl vinyl sulfonium salt **1** under the optimized reaction conditions (NaH in DMF) furnished the desired hexahydroazepine **15** in 68% yield as a 3:1 mixture of diastereomers, which were separated by flash chromatography (Scheme 7).[22] The stereochemistry of the minor diastereomer was determined by X-ray analysis,[13] thus establishing the stereochemistry of the major isomer.

Deprotection of aziridine **15** was achieved on treatment with anhydrous HCl (3 equiv), which resulted in the unavoidable formation of the ring-opened product **16**. Monitoring of this reaction using LC-MS showed that the protected aziridine was very susceptible to ring opening under these conditions. In fact, it is likely that the protected aziridine **15** first underwent ring opening with HCl and the resulting 1,2-chlorosulfinamide was then deprotected to yield the intermediate **16**. Upon workup with saturated aqueous ammonia solution, the known chiral aziridine **17**[19] was obtained, thus completing a formal synthesis of balanol.

In conclusion, we have developed a new epoxy-annulation method for converting α-, β-, and γ-aminoaldehydes and -ketones into racemic five-, six-, and seven-membered epoxide-fused heterocycles. The reaction has been rendered asymmetric in the synthesis of five- and six-membered rings, using the chiral vinyl sulfonium salt **6**, and practical levels of asymmetric induction were achieved. The new process creates one new C–C bond and two C–X bonds with control over both relative and absolute stereochemistry. The methodology has been extended to an asymmetric aziridine-annulation process for the construction of the most challenging seven-membered hexahydroazepine ring **15**. This methodology now

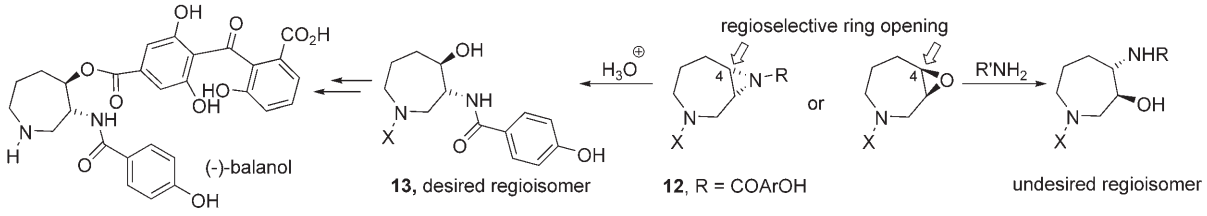

Scheme 6. The regioselective ring opening of the hexahydroazepine core of balanol.

 © 2006 Wiley-VCH Verlag GmbH & Co. KGaA, Weinheim

provides the shortest route (nine steps)[23] to the important protein kinase C inhibitor, balanol.

Received: July 13, 2006
Published online: September 29, 2006

Keywords: annulation · asymmetric synthesis · natural products · ring opening · sulfur ylides

[1] a) V. K. Aggarwal, C. L. Winn, *Acc. Chem. Res.* **2004**, *37*, 611 – 620; b) V. K. Aggarwal, J. Richardson, *Chem. Commun.* **2003**, 2644 – 2651.
[2] a) K. Kim, L. S. Jimenez, *Tetrahedron: Asymmetry* **2001**, *12*, 999 – 1005, and references therein; b) Y. Wang, W. Zhang, J. V. Colandrea, L. S. Jimenez, *Tetrahedron* **1999**, *55*, 10659 – 10672.
[3] a) P. Kulanthaivel, Y. F. Hallock, C. Boros, S. M. Hamilton, W. P. Janzen, L. M. Ballas, C. R. Loomis, J. B. Jiang, B. Katz, J. R. Steiner, J. Clardy, *J. Am. Chem. Soc.* **1993**, *115*, 6452 – 6453; b) J. M. Defauw, M. M. Murphy, G. E. Jagdmann, Jr., H. Hu, J. W. Lampe, S. P. Hollinshead, T. J. Mitchell, H. H. Crane, J. M. Heerding, J. S. Mendoza, J. E. Davis, J. W. Darges, F. R. Hubbard, S. E. Hall, *J. Med. Chem.* **1996**, *39*, 5215 – 5227.
[4] a) K. A. Tehrani, T. N. Van, M. Karikomi, M. Rottiers, N. De Kimpe, *Tetrahedron* **2002**, *58*, 7145 – 7152; b) S. Liu, R. P. Hanzlik, *J. Med. Chem.* **1992**, *35*, 1067 – 1075.
[5] H. Ohno, K. Miyamura, T. Tanaka, S. Oishi, A. Toda, Y. Takemoto, N. Fujii, T. Ibuka, *J. Org. Chem.* **2002**, *67*, 1359 – 1367.
[6] a) S. A. Harkin, O. Singh, E. J. Thomas, *J. Chem. Soc. Perkin Trans. 1* **1984**, 1489 – 1499; b) J. Ahman, P. Somfai, *Tetrahedron* **1992**, *48*, 9537 – 9544.
[7] V. K. Aggarwal, E. Alonso, I. Bae, G. Hynd, K. M. Lydon, M. J. Palmer, M. Patel, M. Porcelloni, J. Richardson, R. Stenson, J. R. Studley, J. L. Vasse, C. L. Winn, *J. Am. Chem. Soc.* **2003**, *125*, 10926 – 10940.
[8] a) V. K. Aggarwal, I. Bae, H.-Y. Lee, D. T. Williams, *Angew. Chem.* **2003**, *115*, 3396 – 3400; *Angew. Chem. Int. Ed.* **2003**, *42*, 3274 – 3278.
[9] a) T. R. Kasturi, L. Mathew, J. A. Sattigeri, *Indian J. Chem. Sect. B* **1990**, *29*, 1004 – 1006; b) W. R. McKay, G. R. Proctor, *J. Chem. Soc. Perkin Trans. 1* **1981**, 2435 – 2442.
[10] For reactions of α-aminoketones with vinyl phosphonium salts to give dihydropyrroles, see: a) I. Burley, A. T. Hewson, *Tetrahedron Lett.* **1994**, *35*, 7099 – 7102; b) C. M. Boynton, A. T. Hewson, M. Douglas, *J. Chem. Soc. Perkin Trans. 1* **2000**, 3599 – 3602.
[11] For reactions of β-aminoaldehydes with vinyl phosphonium salts, see: S. Kumarn, D. M. Shaw, D. A. Longbottom, S. V. Ley, *Org. Lett.* **2005**, *7*, 4189 – 4191.
[12] P. Y. Chong, S. Z. Janicki, P. A. Petillo, *J. Org. Chem.* **1998**, *63*, 8515 – 8521.
[13] CCDC 614698 and CCDC 614700 (**3** and **15b**) contain the supplementary crystallographic data for this paper. These data can be obtained free of charge from The Cambridge Crystallographic Data Centre via www.ccdc.cam.ac.uk/data_request/cif.
[14] a) V. K. Aggarwal, E. Alonso, G. Hynd, K. M. Lydon, M. J. Palmer, M. Porcelloni, J. R. Studley, *Angew. Chem.* **2001**, *113*, 1479 – 1482; *Angew. Chem. Int. Ed.* **2001**, *40*, 1430 – 1433; b) V. K. Aggarwal, J. Charmant, L. Dudin, M. Porcelloni, J. Richardson, *Proc. Natl. Acad. Sci. USA* **2004**, *101*, 5467 – 5471.
[15] A. B. Reitz, E. Sonveaux, R. P. Rosenkranz, M. S. Verlander, K. L. Melmon, B. B. Hoffman, Y. Akita, N. Castagnoli, M. Goodman, *J. Med. Chem.* **1985**, *28*, 634 – 642.
[16] Enolate formation and subsequent elimination results in the formation of *N*-tosylsulfonamide, which then underwent conjugate addition to the vinyl sulfonium salt. Following a 1,3-proton shift and subsequent ring closure, the tosyl aziridine was obtained in 45% yield.

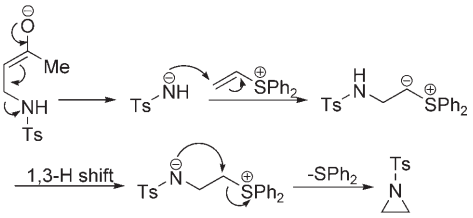

[17] For recent reviews, see: a) E. N. Jacobsen, M. H. Wu in *Comprehensive Asymmetric Catalysis*, *Vol. 2* (Eds.: E. N. Jacobsen, A. Pfaltz, H. Yamamoto), Springer, Berlin, **1999**, pp. 649 – 677; b) T. Katsuki in *Comprehensive Organic Catalysis*, *Vol. 2* (Eds.: E. N. Jacobsen, A. Pfaltz, H. Yamamoto), Springer, Berlin, **1999**, pp. 621 – 648.
[18] a) P. G. M. Wuts, R. L. Gu, J. M. Northuis, T. A. Kwan, D. M. Beck, M. J. White, *Pure Appl. Chem.* **2002**, *74*, 1359 – 1368; b) T. Katsuki, *Adv. Synth. Catal.* **2002**, *344*, 131 – 147.
[19] Y. Shi, *Acc. Chem. Res.* **2004**, *37*, 488 – 496.
[20] a) D. Tanner, A. Almario, T. Hogberg, *Tetrahedron* **1995**, *51*, 6061 – 6070; b) D. Tanner, L. Tedenborg, A. Almario, I. Pettersson, I. Csoregh, N. M. Kelly, P. G. Andersson, T. Hogberg, *Tetrahedron* **1997**, *53*, 4857 – 4868.
[21] J. A. Ellman, T. D. Owen, T. P. Tang, *Acc. Chem. Res.* **2002**, *35*, 984 – 995.
[22] Attempts to improve the diastereoselectivity through the reaction of aminal **14** with the chiral vinyl sulfonium salt **6** did not result in the formation of the desired aziridine **15**. Enolization α to the imine **14** and subsequent conjugate addition of the enolate to the chiral vinyl sulfonium salt **6** gave an ylide, which underwent 1,3-proton shift and ring closure to form the α-cyclopropylimine **18**.

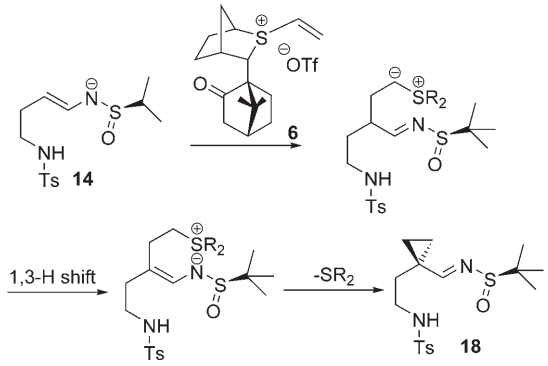

[23] For the shortest previously reported route to balanol (ten linear steps), see: a) A. Fürstner, O. R. Thiel, *J. Org. Chem.* **2000**, *65*, 1738 – 1742; Leading references to other total syntheses of balanol are contained therein.

 © 2006 Wiley-VCH Verlag GmbH & Co. KGaA, Weinheim

Multicomponent Reactions

DOI: 10.1002/anie.200602822

A Rearrangement to a Zirconium–Alkenylidene in the Insertion of Dihalocarbenoids and Acetylides into Zirconacycles**

*Emma Thomas, Sally Dixon, and Richard J Whitby**

We previously reported that addition of lithium diisopropylamide (LDA) to a mixture of zirconacycle **2**, formed by cocyclization of enyne **1**,[1] and (*E*)-β-bromostyrene leads to insertion of the carbenoid (*E*)-PhCH=CLiBr generated in situ, thus affording alkene **3** on protonolysis.[2] Recently, we attempted to insert the fluoro analogue (*E*)-PhCH=CLiF derived by deprotonation of β-fluorostyrene. Much to our surprise, the main product formed, apart from the protonation product of zirconacycle **2**, was compound **4** (30% yield; Scheme 1).

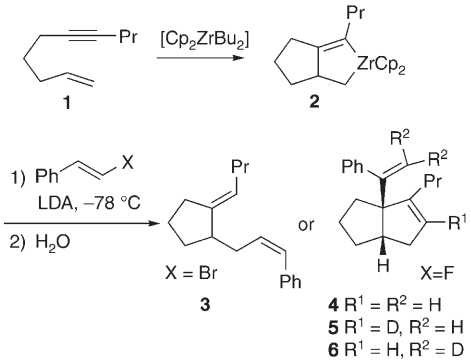

Scheme 1. An unexpected product from the attempted insertion of (*E*)-PhCH=CLiF into zirconacycle **2**. Cp = cyclopentadienyl.

The additional carbon atom present in **4** was traced to originate from dichloromethane present as an impurity (30 mol%) in the β-fluorostyrene. The use of pure β-fluorostyrene with added CD_2Cl_2 (30 mol%) gave the labeled compound **5** (Scheme 1). In the absence of dichloromethane, no insertion occurred at −78 °C, but **3** was produced by hydrolysis on warming to −20 °C, presumably through the known insertion of phenylacetylide (formed by elimination of HF from (*E*)-PhCH=CHF and deprotonation) into zirconacycle **2**.[3] Evidence that phenylacetylide is also the active species in the formation of **4** came from the failure to trap the carbenoid (*E*)-PhCH=CLiF when generated in the presence of Me_3SiCl—only $PhCCSiMe_3$ was formed. We previously demonstrated that Me_3SiCl is a faster trap for carbenoids than organozirconium species.[4] Evidence for the organometallic precursor of **4** came from workup of the reaction with D_2O to afford the bisdeuterated compound **6** predominantly (77% bisdeuterated; 23% monodeuterated), thus suggesting a zirconium–alkenylidene or 1-metallo-1-zircono–alkene (M = Zr or Li) intermediate. A reasonable mechanism for the formation of **4** is given in Scheme 2.

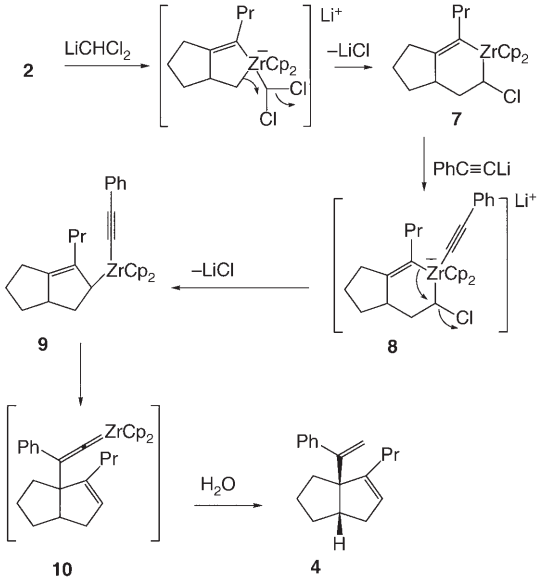

Scheme 2. Suggested mechanism for the formation of **4**.

The first proposed step is insertion of lithiated dichloromethane into **2** to form the intermediate **7**. After addition of lithiated phenylacetylide to afford the "ate" complex **8**, cyclization occurs to give **9**. We previously reported the insertion of 1-lithio-1,1-dihalocarbenoids into zirconacycles to give cyclized products, although dichloromethane gave rather low yields in this process.[5] We would expect the 1,2-rearrangement of the neutral intermediate **7** to be slow at −78 °C; hence, the requirement for the formation of **8** before rearrangement. There now follows a novel rearrangement to afford the alkenylidene complex **10**: Initially a [3,3] sigmatropic rearrangement was suspected, but successive 1,3-migration of the zirconium atom to the ring junction followed by a 1,3-alkyl shift from the metal center to the β-position of the alkyne unit is an alternative. There is a driving force for the initial 1,3-zirconium rearrangement in release of strain energy, as we have previously observed for a 1,3-amine rearrangement.[6] The only precedent for the second migration is the ring contraction of zirconacycle **11** to afford a zirconium–alkenylidene complex **12** that we recently proposed,[7] although similar transformations are known for mid-/late-transition-metal complexes (Scheme 3).[8]

Having suggested a reasonable mechanism for the formation of **4**, more appropriate conditions for its synthesis could be designed. Thus, the addition of lithium 2,2,6,6-tetramethylpiperidide (LiTMP; 1.1 equiv) to a mixture of

[*] Dr. E. Thomas, Dr. S. Dixon, Prof. R. J. Whitby
School of Chemistry
University of Southampton
Southampton, Hants, SO171BJ (UK)
Fax: (+44) 23-8059-3781
E-mail: rjw1@soton.ac.uk

[**] We thank the Engineering and Physical Sciences Research Council UK for funding this study.

InterScience
© 2006 Wiley-VCH Verlag GmbH & Co. KGaA, Weinheim

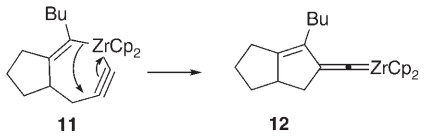

Scheme 3. Zirconocene–alkyne to zirconocene–alkylidene rearrangement.

zirconacycle **2** and dichloromethane (1.1 equiv) at −78 °C, followed by addition of lithium phenylacetylide (1.1 equiv) with warming to room temperature and quenching with water afforded product **4** in 52 % isolated yield (Table 1, entry 1).

Table 1: Zirconium-mediated multicomponent synthesis.

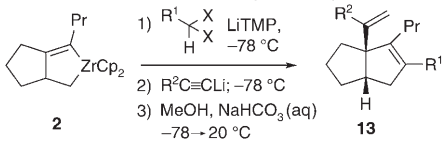

Entry	R^1	X	R^2	Yield of **13** [%][a]
1	H	Cl	Ph	72 (52[b])
2	Bu	Br	Ph	86 (42[b])
3	$(CH_2)_2Ph$	Br	Ph	72 (54[b])
4	$SiMe_3$	Cl	Ph	55[b]
5	H	Cl	Bu	47[b]
6	Bu	Br	Bu	76

[a] Yield of the isolated product **13** based on **1**, using 2.2 equivalents of the alkynyl lithium reagent. [b] Treatment with 1.1 equivalents of the alkynyl lithium reagent.

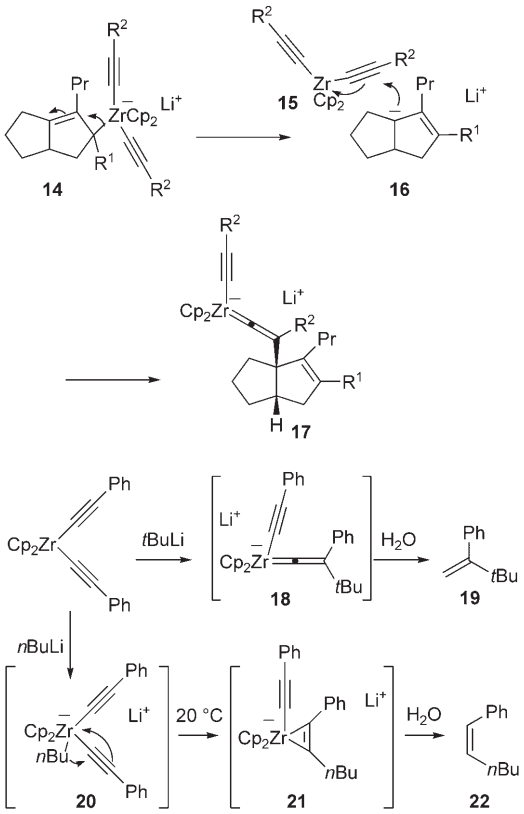

Scheme 4. Alternative route to zirconate–alkenylidene complexes.

We were able to extend the multicomponent reaction to the use of substituted dihalocarbenoids (Table 1, entries 2–4) and alkyl-substituted alkynes (Table 1, entry 5), but the yields of adducts **13** were only around 50 %. An important observation, with implications for the mechanism, was that the use of two equivalents of the acetylide substantially improved the yields of **13** (Table 1 entries 1–3 and 6), thus suggesting that the final zirconium product might be the "ate" complex **17** (Scheme 4). The formation of **17** also explained why we were unable to trap the supposed zirconium–alkenylidene complex **10** with reagents that might be expected to trap a carbene complex, such as alkynes, ethylene, and acetone.[9] The "ate" complex **17** lacks the empty orbital on the metal center required for normal "carbene"-type reactivity. The extra equivalent of alkynyl lithium reagent could just trap the suggested alkenylidene intermediate **10**, but we favor an alternative mechanism in which the "ate" complex **14**, formed by addition of the lithiated alkyne to **9** eliminates the allyl anion **16**.[10] Readdition of **16** to the β-carbon atom of the bis(alkynyl) zirconocene **15** would then afford **17**. Although such a β-addition to a metal alkyne is unknown for early transition metals, it is an established route for the formation of mid-/late-transition-metal–alkenylidene complexes.[8] An indication that the proposed mechanism is reasonable is the addition of *t*BuLi to bis(phenylethynyl)zirconocene at −78 °C with an immediate protic quench that affords alkene **19** (88 % yield of the isolated product), probably via the alkenylidene ate complex **18**. Addition of *n*BuLi to bis(phenylethynyl)zirconocene gave (*Z*)-1-phenylhexene **22** (73 %) only on warming to room temperature before protonolysis, presumably by initial addition to the metal to afford **20** followed by the type of 1,2-migration previously reported by Negishi and co-workers[11] to afford **21**. The result indicates that a bulky nucleophile is important for successful β-addition to the alkyne to inhibit direct attack on the metal.

Finally, reaction of zirconacyclopentane **23**, obtained by zirconium-induced cocyclization[12] of 4,4-bis(methoxymethyl)hepta-1,6-diene, with a dihalocarbenoid and two equivalents of lithium phenylacetylide with aqueous workup afforded the cyclized product **24** in good yield based on the diene (Scheme 5). Warming of the reaction mixture to −10 °C before quenching was required, thereby presumably reflecting the less stable, unconjugated tertiary anion, which needs to undergo the elimination/addition process. In this case, the yield of **24** when only 1.1 equivalents of lithiated phenylacetylene were used was very low.

Overall, we have demonstrated an efficient multicomponent assembly of bicyclo[3.3.0]oct-2-enes and bicyclo[3.3.0]octanes by using stoichiometric zirconium chemistry.

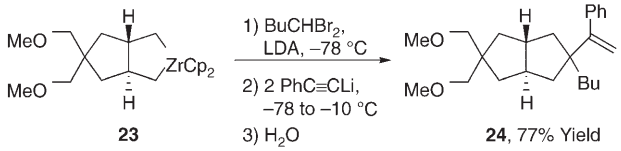

Scheme 5. Multicomponent assembly of bicyclo[3.3.0]octanes.

 © 2006 Wiley-VCH Verlag GmbH & Co. KGaA, Weinheim

These compounds will find use as cores for biologically active compounds and in natural product synthesis, for example, angular triquinanes.[13] The proposed mechanism includes facile loss of carbanions from zirconate species, and the first addition of a nucleophile to the β-carbon atom of a zirconium–alkyne complex to afford an alkenylidene–zirconate complex.

Experimental Section

4: *n*BuLi (0.8 mL of a 2.5 M solution in hexane, 2.0 mmol) was added to a stirred solution of [Cp_2ZrCl_2] (292 mg, 1.0 mmol) and dec-1-en-6-yne (136 mg, 1.0 mmol) in THF (5 mL) dropwise over 5 min at −78 °C. The solution was allowed to warm to room temperature after 25 min and was stirred for 2 h. After cooling the reaction mixture to −78 °C, a solution of CH_2Cl_2 (64.0 μL, 1.0 mmol) in THF (1 mL) was added, followed by dropwise addition of LiTMP (freshly prepared from 2,2,6,6-tetramethylpiperidine (0.17 mL, 1.0 mmol) and *n*BuLi (0.4 mL of a 2.5 M solution in hexanes, 1.0 mmol) in THF (2 mL) at 0 °C over 30 min) over 15 min. The reaction mixture was stirred at −78 °C for 30 min before dropwise addition of lithium phenylacetylide (freshly prepared from phenylacetylene (0.24 mL, 2.2 mmol) and *n*BuLi (0.88 mL of a 2.5 M solution in hexanes, 2.2 mmol) in THF (2 mL) at 0 °C over 15 min) over 15 min. The mixture was stirred at −78 °C for 20 min before addition of MeOH (5 mL) and aqueous $NaHCO_3$ (6 mL) and allowed to warm to room temperature overnight. The mixture was poured into H_2O (100 mL) and extracted with Et_2O (2 × 100 mL) before washing with aqueous $NaHCO_3$ (150 mL) and brine (150 mL), drying over $MgSO_4$, and concentration in vacuo. Purification by column chromatography on SiO_2 with hexane as the eluant gave **4** as a colorless oil (181.0 mg, 72 %). ^{1}H NMR (400 MHz, $CDCl_3$): $\delta = 7.19$–7.09 (5H, m), 5.33 (1H, apparent quintet, $J = 2.0$ Hz), 5.04 (1H, d, $J = 1.8$ Hz), 4.91 (1H, d, $J = 1.8$ Hz), 2.39 (1H, apparent tt, $J = 8.8$, 2.3 Hz), 2.20 (1H, m), 1.94–1.84 (1H, m), 1.83–1.73 (2H, m), 1.72–1.64 (3H, m), 1.54–1.42 (3H, m), 1.34 (1H, m), 1.24 (1H, m), 0.89 ppm (3H, t, $J = 7.3$ Hz); ^{13}C NMR (100.5 MHz, $CDCl_3$): $\delta = 155.39$ (C), 146.72 (C), 144.53 (C), 128.04 (CH), 127.63 (CH), 126.54 (CH), 124.76 (CH), 113.75 (CH_2), 69.14 (C), 46.50 (CH), 40.83 (CH_2), 36.62 (CH_2), 35.73 (CH_2), 29.48 (CH_2), 25.71 (CH_2), 21.48 (CH_2), 14.63 ppm (CH_3); IR (thin film): $\tilde{\nu} = 2949$ (m), 1620 (w), 1491 (m), 1449 (m), 900 cm^{-1} (s); LRMS (EI): *m*/*z*: 252 (M^+, 100 %), 237 (56 %), 223 (88 %), 181 (100 %), 149 (95 %); HRMS (EI): *m*/*z* calcd for $C_{19}H_{24}$: 252.1878; found: 252.1878; elemental analysis (%) calcd for $C_{19}H_{24}$: C 90.42, H 9.58; found C 90.83, H 9.47.

Received: July 14, 2006
Revised: August 2, 2006
Published online: September 29, 2006

Keywords: metalate complexes · multicomponent reactions · rearrangement · vinylidenes · zirconium

[1] E. Negishi, S. J. Holmes, J. M. Tour, J. A. Miller, F. E. Cederbaum, D. R. Swanson, T. Takahashi, *J. Am. Chem. Soc.* **1989**, *111*, 3336.
[2] S. Dixon, S. M. Fillery, A. Kasatkin, D. Norton, E. Thomas, R. J. Whitby, *Tetrahedron* **2004**, *60*, 1401.
[3] Y. Dumond, E. Negishi, *J. Am. Chem. Soc.* **1999**, *121*, 11223.
[4] A. Kasatkin, R. J. Whitby, *J. Am. Chem. Soc.* **1999**, *121*, 7039.
[5] N. Vicart, R. J. Whitby, *Chem. Commun.* **1999**, 1241.
[6] J. M. Davis, R. J. Whitby, A. Jaxa-Chamiec, *Synlett* **1994**, 110.
[7] D. Norton, R. J. Whitby, E. Griffen, *Chem. Commun.* **2004**, 1214.
[8] a) Y. Wakatsuki, *J. Organomet. Chem.* **2004**, *689*, 4092; b) M. I. Bruce, *Chem. Rev.* **1991**, *91*, 197.
[9] a) R. Beckhaus, *Angew. Chem.* **1997**, *109*, 694; *Angew. Chem. Int. Ed. Engl.* **1997**, *36*, 686; b) F. W. Hartner, J. Schwartz, S. M. Clift, *J. Am. Chem. Soc.* **1983**, *105*, 640; c) for a recent review on titanium carbenes, see: T. Takeda, *Bull. Chem. Soc. Jpn.* **2005**, *78*, 195.
[10] a) T. Takahashi, Y. Nitto, T. Seki, M. Saburi, E. Negishi, *Chem. Lett.* **1990**, 2259; b) D. Kondakov, E. Negishi, *Chem. Commun.* **1996**, 963; c) J.-P. Majoral, M. Zablocka, *New J. Chem.* **2005**, *29*, 32.
[11] K. Takagi, C. J. Rousset, E. Negishi, *J. Am. Chem. Soc.* **1991**, *113*, 1440.
[12] C. J. Rousset, D. R. Swanson, F. Lamaty, E. Negishi, *Tetrahedron Lett.* **1989**, *30*, 5105.
[13] G. Mehta, A. Srikrishna, *Chem. Rev.* **1997**, *97*, 671.

 © 2006 Wiley-VCH Verlag GmbH & Co. KGaA, Weinheim

Natural Products

DOI: 10.1002/anie.200602860

Total Synthesis of IKD-8344**

*Woo Han Kim, Sung Kil Hong, Sang Min Lim, Min-Ae Ju, Soon Kyu Jung, Yong Wook Kim, Jae Hoon Jung, Min Sang Kwon, and Eun Lee**

IKD-8344 (**1**, Scheme 1) is a novel 28-membered ring macrodiolide antibiotic from an unidentified alkalophilic Actinomycete, strain no. 8344,[1] which exhibits potent anthelmintic activity against *Trichinella spiralis* and strong cytotoxicity against L5178Y mouse leukemia cells with an IC_{50} value of 0.54 ng mL^{-1}.[1] More recently, it was also isolated from *Streptomyces* sp. A6792 and selective antifungal activities against the mycelial form of *Candida albicans* were noted.[2]

The unique bioactivities and stereochemical complexities of the molecule make it an attractive synthetic target. The monomeric *seco* acid **A** (Scheme 1) contains three methyl branches and three oxolane units: a *threo* (C2–C3)–*trans* (C3–C6) array is connected to a *threo* (C9–C10)–*cis* (C10–C13) arrangement, which is flanked by another *threo* (C16–C17)–*trans* (C17–C20) unit. Efficient and stereoselective construction and assemblage of these structural units is not trivial, and

[*] W. H. Kim, S. K. Hong, S. M. Lim, M.-A. Ju, S. K. Jung, Y. W. Kim, J. H. Jung, M. S. Kwon, Prof. E. Lee
Department of Chemistry
College of Natural Sciences
Seoul National University
Seoul 151-747 (Korea)
Fax: (+82) 2-889-1568
E-mail: eunlee@snu.ac.kr

[**] This work was supported by a grant from the Center for Bioactive Molecular Hybrids (Yonsei University and KOSEF), and a grant from MarineBio21, Ministry of Maritime Affairs and Fisheries, Korea. BK21 graduate fellowship grants to W.H.K., S.K.H., S.M.L., S.K.J., and Y.W.K. are gratefully acknowledged.

Supporting information for this article is available on the WWW under http://www.angewandte.org or from the author.

WILEY InterScience DISCOVER SOMETHING GREAT
© 2006 Wiley-VCH Verlag GmbH & Co. KGaA, Weinheim

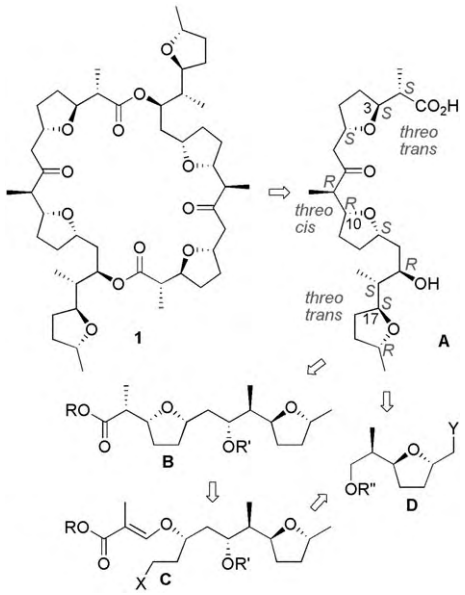

Scheme 1. Retrosynthetic analysis.

the difficulty therein is manifested by the absence of reports on the total synthesis of IKD-8344 (**1**) in the literature.[3] In the retrosynthetic analysis, synthesis of **1** would be accomplished through dimerization of the monomeric *seco* acid **A**, which may be prepared by coupling of fragments **B** and **D**. Fragment **B** may be obtained by radical cyclization of the β-alkoxymethacrylate derivative **C**, which should be accessible from fragment **D**. A reliable synthesis of fragment **D** is prerequisite for a successful total synthesis of this intriguing molecule, which is described in this communication.

Synthesis of the **B** fragment commenced with the aldol reaction of aldehyde **3**[4] with the boron enolate of the chiral imide **2** (Scheme 2).[5] Reduction of the product aldol imide and silyl protection of the primary hydroxy group afforded alcohol **4**. The *threo–trans* oxolane derivative **5** was obtained by mesylation of **4**, acetonide deprotection, and treatment with base. The corresponding mesylate **6** was converted into aldehyde **7** by silyl deprotection and PCC oxidation. Reaction of **7** with allyltrimethylsilane in the presence of titanium chloride led to a 4:1 mixture,[6] favoring **8**, of the homoallylic alcohols. At this point, the mesyloxy group was removed through $LiAlH_4$ reduction, and the aldehyde obtained by ozonolysis after benzyl protection was converted stereoselectively into the homoallylic alcohol **9** by reaction with allyltributylstannane in the presence of magnesium bromide etherate.[7] Iodide **11** was obtained from **9** by ozonolysis, sodium borohydride reduction, tosylation of the primary hydroxy group, reaction with the dimethyl acetal **10**,[8] and iodide substitution. Radical cyclization[9] of β-alkoxymethacrylate **11** proceeded smoothly to produce selectively (10:1) the *threo–cis* oxolane product **12** in good yield (Scheme 2).[10]

Coupling of fragments **B** and **D** was problematic. For example, the dithiane derivative prepared from ester **12** was not amenable to the reaction with mesylate **6**. After considerable exploration, it was found that efficient coupling was possible by employing a Wittig reaction. Aldehyde **13** was

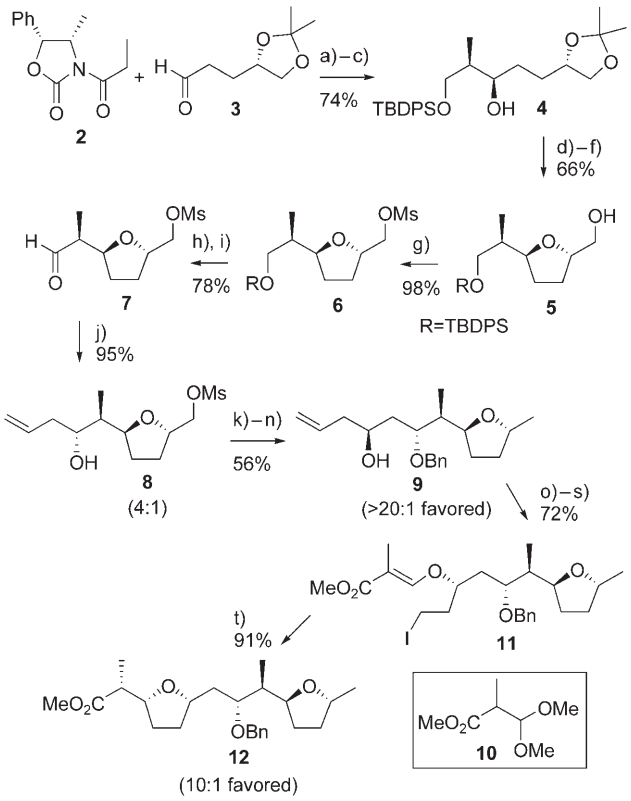

Scheme 2. Preparation of the **B** fragment. a) **2**, Bu_2BOTf, NEt_3, CH_2Cl_2, −40→0°C; **3**, −78°C; b) $LiBH_4$, diethyl ether, 0°C→RT; c) TBDPSCl, imidazole, CH_2Cl_2; d) MsCl, NEt_3, CH_2Cl_2, 0°C→RT; e) CSA, MeOH; f) NaHMDS, THF, 0°C→RT; g) MsCl, NEt_3, CH_2Cl_2, 0°C→RT; h) TBAF, THF; i) PCC, 4-Å MS, CH_2Cl_2; j) $CH_2CHCH_2SiMe_3$, $TiCl_4$, CH_2Cl_2, −78°C; k) $LiAlH_4$, diethyl ether, 0°C→RT; l) NaHMDS, BnBr, THF/DMF (5:1), 0°C→RT; m) O_3, CH_2Cl_2, −78°C; Ph_3P; n) $CH_2CHCH_2SnBu_3$, $MgBr_2{\cdot}Et_2O$, CH_2Cl_2; o) O_3, CH_2Cl_2, −78°C; Ph_3P; p) $NaBH_4$, MeOH, 0°C→RT; q) TsCl, NEt_3, CH_2Cl_2, 0°C; r) **10**, PPTS, benzene, reflux; s) NaI, acetone, reflux; t) Bu_3SnH, Et_3B, toluene, air, −78°C. Tf = trifluoromethanesulfonyl, TBDPS = *tert*-butyldiphenylsilyl, Ms = methanesulfonyl, CSA = (±)-camphorsulfonic acid, HMDS = 1,1,1,3,3,3-hexamethyldisilazane, TBAF = tetrabutylammonium fluoride, PCC = pyridinium chlorochromate, Bn = benzyl, Ts = toluene-4-sulfonyl, PPTS = pyridinium *p*-toluenesulfonate.

prepared from the primary alcohol **5** (Scheme 3). Ester **12** was converted into the corresponding phosphonium salt by lithium borohydride reduction, iodide substitution, and reaction with triphenylphosphine, and the ylide obtained from the phosphonium salt reacted with aldehyde **13** to produce olefin **14** in good yield. A mixture of epoxides was obtained from **14** by oxidation with *m*CPBA. Reaction of the mixture with excess lithium aluminum hydride, Dess–Martin oxidation of the diol produced, and chlorite oxidation of the aldehyde functionality provided regioselectively (12:1) the correct keto carboxylic acid **15**. Use of diisobutylaluminum hydride (DIBAH) as the reducing agent eventually produced the alternative ketone as the major product. The monomeric *seco* acid **16** was prepared by hydrogenolysis. The secondary alcohol **17** was obtained from **15** by TBDPS protection and hydrogenolysis (Scheme 3).

Direct macrodiolide formation of the monomeric *seco* acid **16** did not proceed. A relatively low yield of the

 © 2006 Wiley-VCH Verlag GmbH & Co. KGaA, Weinheim

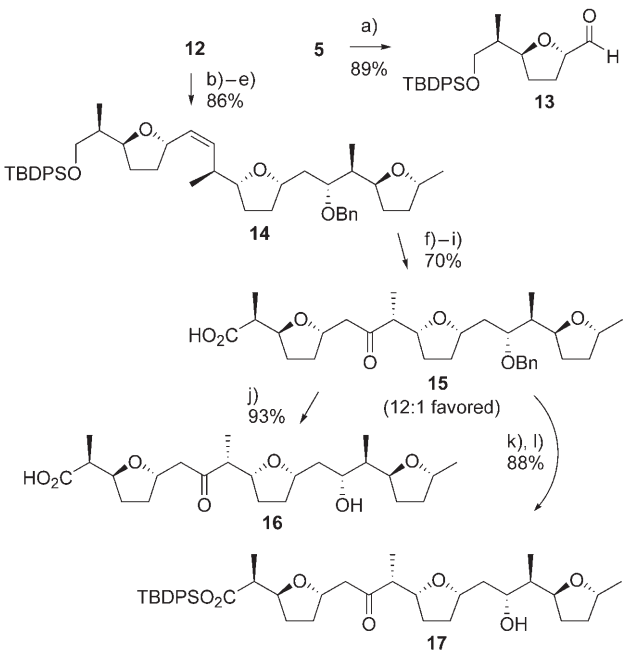

Scheme 3. Preparation of the **A** fragment. a) SO_3·pyridine, NEt_3, DMSO/CH_2Cl_2 (1:1); b) $LiBH_4$, diethyl ether, 0 °C→RT; c) I_2, Ph_3P, imidazole, THF, 0 °C→RT; d) Ph_3P, MeCN, reflux; e) BuLi, THF, −78 °C; **13**; f) *m*CPBA, CH_2Cl_2, 0 °C; g) $LiAlH_4$, diethyl ether, 0 °C; h) Dess–Martin periodinane (3.0 equiv), CH_2Cl_2; i) $NaClO_2$ (1.3 equiv), NaH_2PO_4 (1.3 equiv), *t*BuOH/2-methyl-2-butene/H_2O (10:5:1); j) H_2, Pd/C, MeOH; k) TBDPSCl (4.0 equiv), imidazole (7.0 equiv), DMAP (0.5 equiv), CH_2Cl_2; l) H_2, $Pd(OH)_2$/C, EtOAc. *m*CPBA = 3-chloroperoxybenzoic acid, DMAP = 4-dimethylaminopyridine.

macrolide product **18** was obtained under a variety of conditions (Scheme 4).[11] The coupling reaction of **15** and **17**, however, proceeded efficiently under standard Yamaguchi

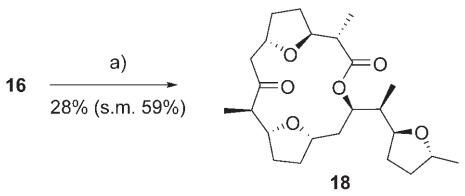

Scheme 4. Cyclization of the *seco* acid. a) CDIC (2.5 equiv), Cs_2CO_3 (1.0 equiv), CH_2Cl_2 (0.02 M), 0 °C; DMAP (20 equiv). CDIC = 2-chloro-1,3-dimethylimidazolinium chloride, s.m. = recovered starting material.

conditions to afford ester **19** (Scheme 5). The dimeric *seco* acid **20** was obtained efficiently through TBDPS deprotection and hydrogenolysis. IKD-8344 (**1**)[12] was finally obtained upon lactonization of **20** under modified Yamaguchi conditions (Scheme 5).[13]

The present synthesis is another example of the application of β-alkoxymethacrylate radical cyclization reactions[9] for the stereoselective construction of complex oxacyclic natural products.

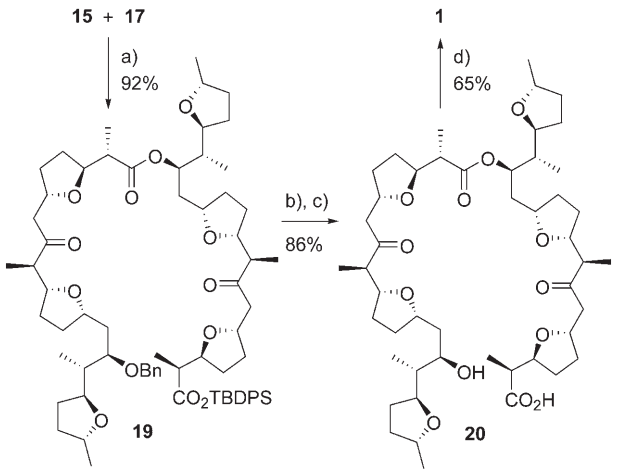

Scheme 5. Synthesis of IKD-8344. a) **15** (1.0 equiv), 2,4,6-Cl_3PhCOCl (1.7 equiv), NEt_3 (3.5 equiv), THF (0.025 M); **17** (1.3 equiv), DMAP (3.0 equiv), benzene (0.02 M); b) conc. HCl, MeOH; c) H_2, $Pd(OH)_2$/C, EtOAc; d) 2,4,6-Cl_3PhCOCl (40 equiv); NEt_3 (60 equiv), DMAP (20 equiv), toluene (0.15 μM), reflux.

Experimental Section

Ester **12:** nBu_3SnH (0.018 mL, 0.07 mmol) and Et_3B (1.0 M in hexane, 0.088 mL) were added to a solution of iodide **11** (31 mg, 0.058 mmol) in toluene (6 mL) at −78 °C. The resulting solution was stirred for 1 h under air at −78 °C. Concentration and purification of the residue by flash column chromatography (hexanes/EtOAc, 4:1) furnished ester **12** (21.5 mg, 91 %): $R_f = 0.31$ (hexanes/EtOAc, 4:1); ^{1}H NMR (300 MHz, $CDCl_3$): $\delta = 7.33$–7.24 (m, 5H), 4.53 and 4.47 (AB q, 2H, $J_{AB} = 11.3$ Hz), 4.08–3.99 (m, 3H), 3.86–3.78 (m, 2H), 3.69 (s, 3H), 2.60–2.55 (m, 1H), 2.05–1.90 (m, 6H), 1.70–1.39 (m, 5H), 1.19 (d, 3H, $J = 6.0$ Hz), 1.11 (d, 3H, $J = 7.0$ Hz), 0.82 ppm (d, 3H, $J = 6.9$ Hz); ^{13}C NMR (75 MHz, $CDCl_3$): $\delta = 175.5$, 139.2, 128.2, 127.7, 127.2, 80.0, 79.6, 77.9, 77.2, 74.6, 71.6, 51.6, 45.2, 40.6, 36.5, 33.9, 31.6, 30.7, 28.4, 21.4, 13.1, 10.0 ppm; IR (neat): $\nu_{max} = 3029$, 2967, 2877, 1739, 1455, 1376, 1197, 1068, 736, 698 cm^{-1}; MS (CI): *m*/*z* (relative intensity): 405 [$M^+ + 1$] (81), 297 (100), 295 (28), 279 (11), 213 (63), 183 (31), 157 (42), 91 (23); HRMS (CI): calcd for $C_{24}H_{37}O_5$ [$M^+ + 1$]: 405.2641; found: 405.2641; $[\alpha]_D^{27} = +14.0$ ($c = 1.16$, $CHCl_3$).

IKD-8344 (**1**): The dimeric *seco* acid **20** (15 mg, 0.017 mmol) was dissolved in toluene (113 mL). NEt_3 (0.15 mL, 1.04 mmol), 2,4,6-trichlorobenzoyl chloride (0.11 mL, 0.70 mmol), and DMAP (42 mg, 0.35 mmol) were added at room temperature, and then the solution was heated under reflux for 4 h. The reaction was quenched by addition of saturated NH_4Cl solution (100 mL) and the reaction mixture was extracted with CH_2Cl_2 (150 mL × 3). The organic extracts were dried over $MgSO_4$, filtered, and concentrated. Purification of the residue by flash column chromatography (hexanes/EtOAc, 2:1) gave IKD-8344 (**1**, 9.5 mg, 65 %): $R_f = 0.28$ (hexanes/EtOAc, 2:1); ^{1}H NMR (300 MHz, $CDCl_3$): $\delta = 5.32$–5.28 (m, 2H), 4.38–4.31 (m, 2H), 4.15–4.01 (m, 4H), 3.96–3.87 (m, 4H), 3.82–3.76 (m, 2H), 2.95–2.83 (m, 4H), 2.46–2.26 (m, 6H), 2.19–2.13 (m, 2H), 2.03–1.90 (m, 9H), 1.81–1.73 (m, 3H), 1.68–1.59 (m, 5H), 1.51–1.38 (m, 9H), 1.18 (d, 6H, $J = 6.0$ Hz), 1.09 (d, 6H, $J = 7.4$ Hz), 1.00 (d, 6H, $J = 7.3$ Hz), 0.83 ppm (d, 6H, $J = 7.5$ Hz); ^{13}C NMR (75 MHz, $CDCl_3$): $\delta = 212.0$, 175.1, 80.5, 80.0, 79.5, 75.2, 74.9, 74.8, 72.2, 53.4, 45.6, 45.6, 41.1, 36.2, 33.9, 32.1, 30.9, 30.7, 29.6, 29.4, 21.2, 14.4, 13.7, 10.9 ppm; MS (FAB): *m*/*z* (relative intensity): 867 [$M^+ + Na$] (58), 883 (45), 845 (14), 423 (12), 307 (22), 289 (11), 209 (43), 154 (83), 85 (100); HRMS (FAB): calcd for $C_{48}H_{76}O_{12}Na$ [$M^+ + Na$]: 867.5235; found: 867.5239; $[\alpha]_D^{15} = +39.7$ ($c = 0.25$, $CHCl_3$).

Received: July 18, 2006
Published online: October 2, 2006

 © 2006 Wiley-VCH Verlag GmbH & Co. KGaA, Weinheim

Keywords: anticancer agents · antifungal agents · macrodiolides · natural products · total synthesis

[1] a) Y. Minami, K. Yoshida, R. Azuma, M. Nishii, J. Inagaki, F. Nohara, *Tetrahedron Lett.* **1992**, *33*, 7373 – 7376; b) T. Ishida, Y. In, M. Nishii, Y. Minami, *Chem. Lett.* **1994**, 1321 – 1322.
[2] E. I. Hwang, B. S. Yun, W. H. Yeo, S. H. Lee, J. S. Moon, Y. K. Kim, S. J. Lim, S. U. Kim, *J. Microbiol. Biotechnol.* **2005**, *15*, 909 – 912.
[3] For a report on the synthesis of the fragments, see: W. Jiang, D. A. Lantrip, P. L. Fuchs, *Org. Lett.* **2000**, *2*, 2181 – 2184.
[4] For an example of the use of this known aldehyde, see: A. B. Smith III, D.-S. Kim, *J. Org. Chem.* **2006**, *71*, 2547 – 2557.
[5] For an example of asymmetric aldol reactions, see: D. A. Evans, S. W. Kaldor, T. K. Jones, J. Clardy, T. J. Stout, *J. Am. Chem. Soc.* **1990**, *112*, 7001 – 7031.
[6] Formation of the desired *anti–anti* product was problematic. For example, Roush allylation by using isopropyl (*S*,*S*)-tartrate yielded a mixture of the products favoring (1:2) the wrong isomer. For detailed discussions, see: D. A. Evans, B. D. Allison, M. G. Yang, C. E. Masse, *J. Am. Chem. Soc.* **2001**, *123*, 10840 – 10852.
[7] For the use of magnesium bromide etherate in an allylstannane reaction, see: E. Lee, E. J. Jeong, E. J. Kang, L. T. Sung, S. K. Hong, *J. Am. Chem. Soc.* **2001**, *123*, 10131 – 10132.
[8] R. D. Walkup, N. U. Obeyesekere, *Synthesis* **1987**, 607 – 611.
[9] For recent examples of β-alkoxyacrylate and β-alkoxymethacrylate radical cyclization, see: a) E. J. Kang, E. J. Cho, M. K. Ji, Y. E. Lee, D. M. Shin, S. Y. Choi, Y. K. Chung, J.-S. Kim, H.-J. Kim, S.-G. Lee, M. S. Lah, E. Lee, *J. Org. Chem.* **2005**, *70*, 6321 – 6329; b) H. Y. Song, J. M. Joo, J. W. Kang, D.-S. Kim, C.-K. Jung, H. S. Kwak, J. H. Park, E. Lee, C. Y. Hong, S. Jeong, K. Jeon, J. H. Park, *J. Org. Chem.* **2003**, *68*, 8080 – 8087; c) E. J. Jeong, E. J. Kang, L. T. Sung, S. K. Hong, E. Lee, *J. Am. Chem. Soc.* **2002**, *124*, 14655 – 14662; d) E. Lee, S. J. Choi, H. Kim, H. O. Han, Y. K. Kim, S. J. Min, S. H. Son, S. M. Lim, W. S. Jang, *Angew. Chem.* **2002**, *114*, 184 – 186; *Angew. Chem. Int. Ed.* **2002**, *41*, 176 – 178.
[10] E. Lee, S. J. Choi, *Org. Lett.* **1999**, *1*, 1127 – 1128.
[11] See, for example: A. Fürstner, J. Mlynarski, M. Albert, *J. Am. Chem. Soc.* **2002**, *124*, 10274 – 10275.
[12] $[\alpha]_D^{15} = +39.7$ ($c = 0.25$, $CHCl_3$; literature:[1a] $[\alpha]_D^{17} = +40.2$). The spectral data of the synthetic sample were identical with those of the natural product.
[13] For the use of the modified Yamaguchi conditions, see: D. A. Evans, H. P. Ng, D. L. Rieger, *J. Am. Chem. Soc.* **1993**, *115*, 11446 – 11459.

 © 2006 Wiley-VCH Verlag GmbH & Co. KGaA, Weinheim

Surface Chemistry

DOI: 10.1002/anie.200602876

A Pathway for NH Addition to Styrene Promoted by Gold**

*Xingyi Deng, Thomas A. Baker, and Cynthia M. Friend**

Gold-based heterogeneous catalysts have surprising potential for low-temperature oxidation processes,[1–4] including alcohol oxidation,[5–8] direct synthesis of hydrogen peroxide,[9,10] CO oxidation,[11,12] and olefin epoxidation.[11,13] These systems have potential for a substantial positive impact on the environment and economy because of their high selectivity and also the low temperature at which they operate.[14] Hence, a substantial amount of effort has been directed to further improve the performance of heterogeneous gold catalysts and to understand the origin of their catalytic activity.[15–18]

Herein, we investigate the addition of NH to styrene using heterogeneous Au because of the potential importance of these three-membered N-containing rings in organic synthesis as a building block for biologically active molecules and for use in antitumor and antibiotic applications.[19–21] Previously, we demonstrated that the Au(111) surface promotes oxidation reactions that also occur on catalysts with high surface areas at higher pressure, once oxygen has been adsorbed onto the surface,[22] thereby establishing that Au(111) is a good model for understanding the molecular-level detail of heterogeneous Au-based oxidation catalysis. Hence, reactions that occur on Au(111) provide a guide for the type of reactions that may be induced by heterogeneous gold catalysts.

Nitrene addition to styrene is promoted by a gold surface, which indicates that such reactions should be possible with heterogeneous Au catalysts. To our knowledge, this is the first report of gold-catalyzed functionalization of an olefin with NH in a heterogeneous system, which may have advantages and mechanistic differences when compared to aziridination in solution,[23,24] or in other methods of activating ammonia for amination.[25]

Aziridines are structurally analogous to epoxides and may be formed by addition of a nitrene group to the olefin. Recently, we showed that oxidized Au(111) promotes styrene epoxidation.[22] This observation motivated us to explore the

[*] X. Deng, T. A. Baker, Prof. C. M. Friend
Department of Chemistry and Chemical Biology
Harvard University
Cambridge, MA 02138 (USA)
Fax: (+1) 617-496-8410
E-mail: cfriend@deas.harvard.edu
Prof. C. M. Friend
Division of Engineering and Applied Sciences
Harvard University
Cambridge, MA 02138 (USA)

[**] This work was supported financially by the US Department of Energy, Basic Energy Sciences (grant no. FG02-84-ER13289) and the National Science Foundation Graduate Fellowship.

© 2006 Wiley-VCH Verlag GmbH & Co. KGaA, Weinheim

analogous aziridination of styrene on Au(111). Indeed, aziridination of styrene does occur on Au(111) covered with NH_x. By precovering the surface with NH, we are able to study the elementary steps important in catalytic processes. This is a well-established approach for studying other reactions important in catalysis using the tools of surface science.[26–28]

Reactive NH_x ($x = 1,2$) species are formed from the reaction of NH_3 with chemisorbed oxygen on Au(111) (Figure 1). By selecting the appropriate conditions, we are

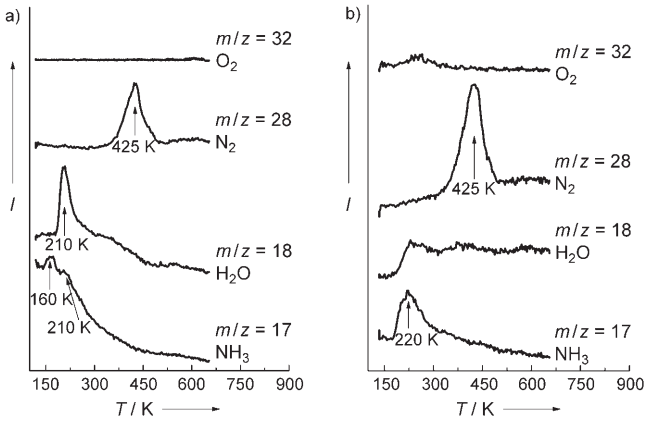

Figure 1. Temperature-programmed reaction spectra following the adsorption of NH_3 on O-covered Au(111) ($\theta_O = 0.2$ ML). When NH_3 is exposed to the O-covered surface at 110 K (a), all oxygen reacts with N–H bonds to form water on heating above 175 K. Exposure of NH_3 to the same surface at 190 K (b) leads to removal of all oxygen as water, so as to generate a surface which contains mainly adsorbed NH_x. The NH_x disproportionates to evolved gaseous NH_3 and adsorbed N upon heating to higher temperatures. The adsorbed nitrogen atoms combine to form N_2 at 425 K. The oxygen-covered surface was prepared by O_3 decomposition at 200 K. I = mass spectroscopy intensity.

able to remove all the oxygen through the evolution of water. In temperature-programmed reaction experiments, water is evolved at 210 K if NH_3 is exposed to O-covered Au(111) at 110 K; however, when dosed with an excess of ammonia and the surface maintained at 190 K, the oxygen is removed through water evolution (Figure 1 a,b). Notably, ammonia does not react on the clean Au(111) surface, but desorbs molecularly at 155 K (data not shown). The NH_x formed on the surface undergoes disproportionation upon heating (Figure 1). Molecular ammonia desorbs from the surface at 160 K. A second NH_3 peak at 210 K is ascribed to the reformation of NH_3 from disproportionation of NH_x species. Adsorbed nitrogen atoms are also formed, which ultimately lead to N_2 formation at 425 K. No H_2 is evolved; rather hydrogen is removed either as water during formation of NH_x or by reformation of NH_3. All these observations show that N–H bonds are activated by the reaction of ammonia with oxygen-covered Au(111), analogous to reactions reported previously on Ag and Cu surfaces,[29–31] and to recent reports for Au(111) oxidized using an oxygen plasma.[32]

All adsorbed oxygen is converted into water through the reaction with N–H bonds. Water is the only oxygen-containing species detected upon heating; NO, N_2O, and NO_2 are not detected (data not shown). Furthermore, there is no detectable formation of O_2, which would occur at around 550 K from oxygen-atom recombination if there were residual adsorbed oxygen present. The reactivity of the oxygen layer towards NH_3 and other species depends on the method used for oxidation.

To accumulate NH_x and remove OH and H_2O, as well as molecular NH_3 from the surface, we exposed the oxygen-covered Au(111) surface ($\theta_O = 0.2$ monolayer (ML)) to a larger dose of NH_3 at 190 K (a temperature that is high enough to prevent adsorption of molecular NH_3 and low enough to keep NH_x on the surface; Figure 1 b). After this treatment, NH_3 reformation from NH_x, was observed as a peak at 220 K and N_2 formation at 425 K. Water formed from the reaction of NH_3 with oxygen desorbs from the surface during the reaction and therefore there is no well-defined H_2O peak—only an increased water background was observed. This desorption is concomitant with ammonia desorption, possibly because of the displacement of water by ammonia from other surfaces. Since this method exclusively produces NH_x on the surface, it was used in all experiments described later.

Addition of NH to styrene was observed following the reaction of styrene on Au(111) covered with NH_x at 150 K (Figure 2). Specifically, a product with a parent ion at $m/z =$ 119 and the most intense peak at $m/z = 118$ was evolved at 390 K and tentatively identified as 2-phenylaziridine. A small amount of H_2O was also produced in the reaction, possibly because of the presence of some residual oxygen on the surface following exposure to ammonia. Notably, no oxygen-

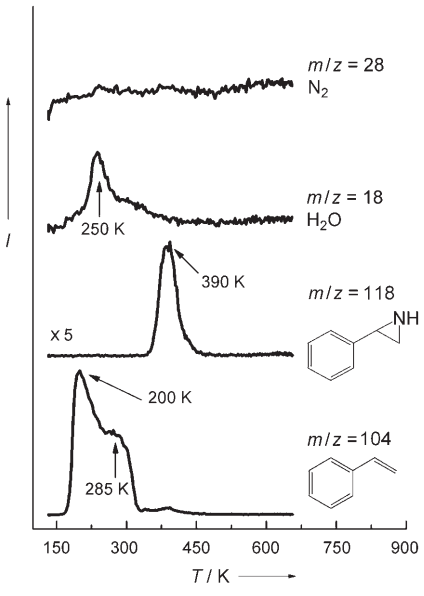

Figure 2. Temperature-programmed reaction spectra following the adsorption of styrene on NH_x-covered Au(111) at 150 K. The reaction yields 2-phenylaziridine (390 K), exclusively. Neither oxidation nor nitrilation products were observed. Some residual oxygen reacts with NH_x and forms H_2O at 250 K. No N_2 desorption was observed, which indicates a high overall activity since all the NH_x has been consumed in the reaction.

 © 2006 Wiley-VCH Verlag GmbH & Co. KGaA, Weinheim

addition products (CO, CO_2, epoxide, or organic acids) were detected. Remaining styrene desorbed from the surface at 200 K (multilayers) and 285 K (monolayer). A residue containing carbon and nitrogen remained on the surface after reaction of styrene and NH_x. NO and CO_2 were produced after exposing the residue on the surface to ozone and subsequent heating. The fact that NO was produced from post-oxidation of the residue, but no N_2 was observed after reaction of styrene with NH_x, indicates that the nitrogen is bound to carbon in the residue.

We unequivocally established that the product formed at 390 K contains nitrogen by using $^{15}NH_3$ as our starting reagent (Figure 3). The parent ion shifts from $m/z = 119$ to 120 when

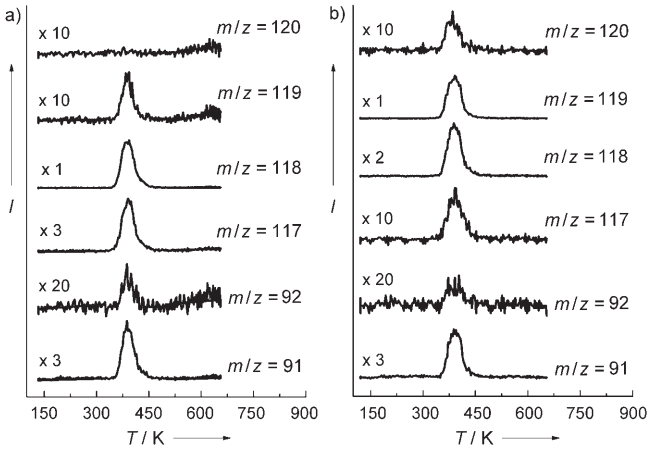

Figure 3. Mass spectrometer fragmentations of 2-phenylaziridine from the reaction of styrene on a Au(111) surface covered with a) $^{14}NH_x$ or b) $^{15}NH_x$. The shift of +1 for the parent ion (m/z 119 to 120), as well as the most intense peak (m/z 118 to 119) when using $^{15}NH_3$, is a strong indication that the product contains nitrogen.

the reaction of styrene on the surface covered with $^{15}NH_x$ was performed. Notably, a shift of the m/z signal by +1 is also observed for all the observed mass fragments which contain nitrogen; for example, the most intense fragmentation $[M-1]$ shifts from $m/z = 118$ to 119.

The stoichiometry (C_8H_9N) of the product was determined from the parent ion signal ($m/z = 119$) in conjunction with the shifts in the signals found in the experiments using $^{15}NH_3$. The intensities of the major fragmentation ions of the product from the experiment using our mass spectrometer were compared with the literature values of selected ion intensities of isomers with C_8H_9N stoichiometry (Table 1). The use of literature values to eliminate possible products based on the yields of the fragment ions is validated by the good agreement with the measured intensities of the fragment ions of indoline.

We assign the product formed in the reaction as 2-phenylaziridine based on analysis of its fragmentation pattern (Table 1). The fragments of the product we observed do not match any of those C_8H_9N isomers cited by the National Institute of Standards and Technology (NIST). In addition, the presence of the $m/z = 91$ fragment and the absence of a mass shift for this fragment when $^{15}NH_3$ was used as the

Table 1: Mass spectrometer fragmentation patterns of 2-phenylaziridine from the reaction of styrene on a Au(111) surface covered with NH_x and also reactions of isomers with C_8H_9N stoichiometry.

m/z	2-Phenylaziridine 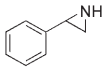	Indoline[a]	*N*-Phenylaziridine[b]	4-Aminostyrene[b] 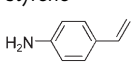
91	40	45 (30)	(100)	(24)
92	3	5 (3)	(10)	(5)
117	36	45 (29)	(0)	(15)
118	100	100 (100)	(9)	(58)
119	6	50 (63)	(40)	(100)
120	0	4 (6)	(4)	(8)

[a]These data rule out the possibility of the product being indoline, *N*-phenylaziridine, or 4-aminostyrene. [b] The numbers in the parentheses were obtained from the NIST database.

source of nitrogen is compelling evidence that the product has a benzyl group ($C_6H_5CH_2$-), which is consistent with the 2-phenylaziridine structure. Furthermore, this result rules out *N*-phenyl aziridines and the imine, $C_6H_5C(CH_3)$=NH as the product because the strong $m/z = 91$ signal contains nitrogen in this isomer. Although the mass spectrum for 2-phenylaziridine is not available from the NIST database for direct comparison, our observations all strongly point to it being the product. The other imine $C_6H_5CH_2C(H)$=NH cannot be completely ruled out.

We suggest that the formation of 2-phenylaziridine is the result of the transfer of NH to styrene on Au(111) by analogy with the corresponding epoxidation reaction on this surface.[22] Spectroscopic studies are underway to identify the NH_x species present on the surface during reaction. We will show in a subsequent report that styrene nitrilation (forming benzo- and benzyl nitrile) occurred only when nitrogen atoms were pre-adsorbed on Au(111).[33] This observation indicates that the presence of NH_x (NH and/or NH_2), not nitrogen atoms, is necessary for aziridination.

Our results indicate that 2-phenylaziridine is formed from the Au-promoted reaction of styrene and NH_x. In this reaction, oxygen is used to activate the NH_3 and to form NH_x species on the surface. By adjusting the preparation conditions, oxygen is consumed by the NH_3 and forms H_2O, which desorbs, and NH_x remains exclusively on the Au(111) surface.

The aziridination of organic molecules is generally a complex process usually promoted by a homogeneous catalyst.[24] Our study clearly shows the promise of the aziridination of a C=C bond by using a heterogeneous gold system, which may provide a convenient and more efficient route. The key features are the N–H bonds so as to form the desired nitrene and a C=C bond. Notably, the temperature needed for this process is low, which is significant for the selective synthesis of molecules important in the pharmaceutical industry. Nevertheless, there are still unanswered questions including the identification of the product by other means to completely rule out other products like imines, the generality of the process for more complex nitrenes and olefins, the degree of selectivity, whether these reactions can be carried

 © 2006 Wiley-VCH Verlag GmbH & Co. KGaA, Weinheim

out stereoselectively, and whether this process can be carried out catalytically. Although this study was carried out using a single crystal and under ultrahigh-vacuum conditions, it is reasonable that this pathway would also apply for high-pressure conditions using supported nanoscopic Au clusters, especially since the related oxidation reactions on gold occur under both low- and high-pressure conditions.

Experimental Section

All experiments were performed in a stainless-steel ultrahigh-vacuum chamber with a base pressure of $< 1 \times 10^{-10}$ Torr, as described previously.[34] The chamber was equipped with a quadrupole mass spectrometer (UTI model 100C) which was used for temperature-programmed reaction spectroscopy (TPRS), an Auger electron spectrometer (AES), and low-energy electron diffraction optics (LEED).

The Au(111) surface was prepared by cycles of sputtering of Ar^+ ions (1000 eV, 1.3 μA) at 300 K, followed by annealing at 900 K for 5 min, and then at 700 K for 30 min. This procedure was repeated until no impurities were detected using AES.

Ozone was produced by electrical discharge and was trapped in silica gel (3–8 mesh, Fisher Scientific Co.) at −78 °C using a mixture of dry ice and ethanol. The Au(111) surface at 200 K was exposed to O_3, with a pressure rise of 1×10^{-8} Torr over 20 s, which resulted in an approximate 0.2 ML. The resulting oxygen atom coverage was determined by comparing the integrated area of the O_2-desorption peak relative to a saturation coverage (ca. 1 ML) which had been determined previously.[35,36] Following the deposition of oxygen, the surface was exposed to NH_3 (Matheson, anhydrous grade) or $^{15}NH_3$ (Cambridge Isotope Laboratories, 98 %). The NH_3 was deposited at 190 K for 2 min with a pressure rise of 1×10^{-10} Torr. Finally, styrene (Alfa Aesar, 99.5 %) was deposited at 150 K for 30 s with a pressure rise of 1×10^{-10} Torr and was used after cycles of freeze-pump-thaw purification, with the purity checked by mass spectrometry.

All temperature-programmed reaction spectra (TPRS) were taken by a computer-controlled UTI 100c mass spectrometer, as described in detail previously.[37] The crystal was biased at −100 V during the collection of temperature-programmed reaction data, so as to avoid an electron-induced reaction from the mass-spectrometer filament. The temperature was measured with a K-type (Chromega/Alomega) thermocouple and radiative heating was used to achieve the temperature ramp to 650 K. The heating rate for TPRS was relatively linear, in the range 150–600 K with an average of about 6 $K\,s^{-1}$.

Received: July 19, 2006
Published online: October 2, 2006

Keywords: ammonia · aziridination · gold · heterogeneous catalysis · surface chemistry

[1] G. C. Bond, D. T. Thompson, *Catal. Rev. Sci. Eng.* **1999**, *41*, 319.
[2] Q. Fu, H. Saltsburg, M. Flytzani-Stephanopoulos, *Science* **2003**, *301*, 935.
[3] J. E. Bailie, G. J. Hutchings, *Chem. Commun.* **1999**, 2151.
[4] C. Mohr, H. Hofmeister, M. Lucas, P. Claus, *Chem. Ing. Tech.* **1999**, *71*, 869.
[5] S. Biella, L. Prati, M. Rossi, *Inorg. Chim. Acta* **2003**, *349*, 253.
[6] S. Biella, L. Prati, M. Rossi, *J. Catal.* **2002**, *206*, 242.
[7] S. Carrettin, P. McMorn, P. Johnston, K. Griffin, C. J. Kiely, G. J. Hutchings, *Phys. Chem. Chem. Phys.* **2003**, *5*, 1329.
[8] D. I. Enache, J. K. Edwards, P. Landon, B. Soslona-Espriu, A. F. Carley, A. A. Herzing, M. Watanabe, C. J. Kiely, D. W. Knight, G. J. Hutchings, *Science* **2006**, *311*, 362.
[9] P. Landon, P. J. Collier, A. J. Papworth, C. J. Kiely, G. J. Hutchings, *Chem. Commun.* **2002**, 2058.
[10] P. Landon, P. J. Collier, A. F. Carley, D. Chadwick, A. J. Papworth, A. Burrows, C. J. Kiely, G. J. Hutchings, *Phys. Chem. Chem. Phys.* **2003**, *5*, 1917.
[11] M. Haruta, *Catal. Today* **1997**, *36*, 153.
[12] G. C. Bond, D. T. Thompson, *Gold Bull.* **2000**, *33*, 41.
[13] T. Hayashi, K. Tanaka, M. Haruta, *J. Catal.* **1998**, *178*, 566.
[14] C. T. Campbell, *Science* **2004**, *306*, 234.
[15] M. Valden, X. Lai, D. W. Goodman, *Science* **1998**, *281*, 1647.
[16] M. S. Chen, D. W. Goodman, *Science* **2004**, *306*, 252.
[17] B. Yoon, H. Hakkinen, U. Landman, A. S. Worz, J. M. Antonietti, S. Abbet, K. Judai, U. Heiz, *Science* **2005**, *307*, 403.
[18] M. D. Hughes, Y. J. Xu, P. Jenkins, P. McMorn, P. Landon, D. I. Enache, A. F. Carley, G. A. Attard, G. J. Hutchings, F. King, E. H. Stitt, P. Johnston, K. Griffin, C. J. Kiely, *Nature* **2005**, *437*, 1132.
[19] K. Dvorakova, C. M. Payne, M. E. Tome, M. M. Briehl, T. McClure, R. T. Dorr, *Biochem. Pharmacol.* **2000**, *60*, 749.
[20] F. Brown, *Vaccine* **2001**, *20*, 322.
[21] T. B. Sim, S. H. Kang, K. S. Lee, W. K. Lee, H. Yun, Y. K. Dong, H. J. Ha, *J. Org. Chem.* **2003**, *68*, 104.
[22] X. Deng, C. M. Friend, *J. Am. Chem. Soc.* **2005**, *127*, 17178.
[23] D. A. Evans, M. M. Faul, M. T. Bilodeau, *J. Am. Chem. Soc.* **1994**, *116*, 2742.
[24] P. Müller, C. Fruit, *Chem. Rev.* **2003**, *103*, 2905.
[25] J. Zhao, A. S. Goldman, J. F. Hartwig, *Science* **2005**, *307*, 1080.
[26] J. M. Gottfried, K. Christmann, *Surf. Sci.* **2004**, *566*, 1112.
[27] J. T. Roberts, A. J. Capote, R. J. Madix, *Surf. Sci.* **1991**, *253*, 13.
[28] J. T. Roberts, R. J. Madix, *J. Am. Chem. Soc.* **1988**, *110*, 8540.
[29] B. Afsin, P. R. Davies, A. Pashuski, M. W. Roberts, *Surf. Sci.* **1991**, *259*, L724.
[30] X. C. Guo, R. J. Madix, *Surf. Sci.* **2002**, *501*, 37.
[31] B. Afsin, P. R. Davies, A. Pashusky, M. W. Roberts, D. Vincent, *Surf. Sci.* **1993**, *284*, 109.
[32] J. Gong, R. A. Ojifinni, T. S. Kim, J. M. White, C. B. Mullins, *J. Am. Chem. Soc.* **2006**, *128*, 9012.
[33] X. Deng, C. M. Friend, unpublished results.
[34] M. K. Weldon, C. M. Friend, *Surf. Sci.* **1994**, *310*, 95.
[35] N. Saliba, D. H. Parker, B. E. Koel, *Surf. Sci.* **1998**, *410*, 270.
[36] B. K. Min, A. R. Alemozafar, D. Pinnaduwage, X. Deng, C. M. Friend, *J. Phys. Chem. B* **2006**, ASAP DOI:10.1021/jp0616213.
[37] L. J. Deiner, J. G. Serafin, C. M. Friend, S. G. Weller, J. A. Levinson, R. E. Palmer, *J. Am. Chem. Soc.* **2003**, *125*, 13252.

 © 2006 Wiley-VCH Verlag GmbH & Co. KGaA, Weinheim

Heterogeneous Catalysis

DOI: 10.1002/anie.200602917

Domino Cu-Catalyzed C–N Coupling/Hydroamidation: A Highly Efficient Synthesis of Nitrogen Heterocycles**

*Rubén Martín, Marta Rodríguez Rivero, and Stephen L. Buchwald**

Heterocyclic compounds are of great chemical and biological significance.[1] In particular, nitrogen-containing heterocycles are structural constituents of many bioactive natural products, medicinally important compounds, and organic materials.[2] Recent strategies for the synthesis of heterocycles based on metal-catalyzed reactions nicely complement the classical synthetic approaches. Among their advantages is that harsh conditions are frequently avoided and readily available starting materials can be utilized.[3] Despite the advances realized, more flexible and general routes to a variety of heterocycles are needed. In particular, techniques that can readily give access to heterocyclic cores with a diverse and easily manipulated set of substituents are still of critical importance.

In the last decade, metal-catalyzed C–N bond-forming reactions[4] have become important methods for the preparation of nitrogen-containing compounds in both academic and pharmaceutical laboratories.[5] In recent years, Cu-promoted processes have evolved into viable alternatives to the more widely practiced Pd-catalyzed reactions.[6,7] The Cu-based methods are distinguished by their broad scope, high efficiency, and mild reaction conditions, thus making them attractive vehicles for further applications.[8]

The development of a method for generating multiple classes of nitrogen-containing heterocycles from common building blocks is a highly desirable goal. Previously, Ackermann showed that substrates for the Cacchi indole synthesis[9] can be prepared by Pd- or Cu-catalyzed amination of *o*-alkynyl aryl halides.[10] Under the conditions of these coupling processes, cyclization to the *N*-benzyl or *N*-aryl indoles takes place in an efficient manner.[11] We wondered whether it would be possible to effect a related transformation as a means to access other important nitrogen heterocycles, particularly pyrroles and pyrazoles. Herein, we describe our study of this approach, which combines an initial Cu-catalyzed amidation of a haloenyne followed by an intramolecular hydroamidation of the latent alkyne in situ[12,13] (Scheme 1). We also demonstrate that cyclization of the initially formed C–N coupling product **I**, which can be readily isolated, requires the presence of both a base and copper catalyst.

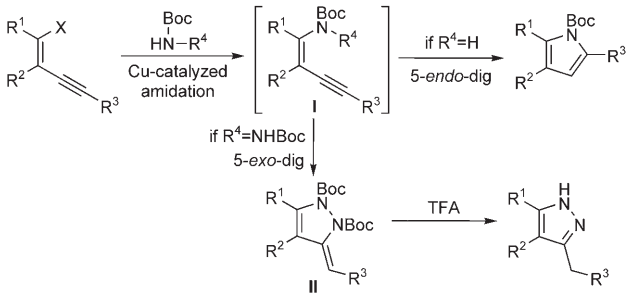

Scheme 1. Synthesis of heterocycles through a domino copper-catalyzed amidation/hydroamidation sequence. TFA = trifluoroacetic acid.

We envisioned that an array of heterocycles could be synthesized through 5-*exo*-dig and 5-*endo*-dig pathways involving intermediate **I**. This objective could be achieved both by varying the nature of the nucleophile as well as the substitution pattern on the haloenyne precursor. We focused our attention on the synthesis of pyrroles[14] and pyrazoles[15] as applications of the Cu-catalyzed vinylation methodology.[16] A series of ligands were examined for the reaction of the model substrate (*Z*)-4-iododec-4-en-6-yne (**1**) with *tert*-butyl carbamate and bis(*tert*-butyloxycarbonyl)hydrazine (bis(Boc)hydrazine; Figure 1). The reaction was carried out in THF with CuI as the precatalyst and Cs_2CO_3 as the base at 80 °C for 12 h. Among those examined, 1,2-diamine ligands show the highest activity, with 20 mol % *N,N′*-dimethylethylenediamine (ligand **g**) giving exclusively the desired cascade products in excellent overall yield. We note that the successful preparation of **2** represents, to the best of our knowledge, the first metal-catalyzed coupling of vinyl halides with a hydrazide.[17]

The transformation outlined above merits some further discussion: 1) two different heterocycles could be obtained from a common starting material; 2) no 6-*endo*-dig cyclization was observed using bis(Boc)hydrazine as the nucleophile; 3) although the *trans* arrangement of the hydrogen and iodide species in **1** suggests a potential for dehydrohalogenation, only traces of the undesired bisalkyne were detected.[18]

Encouraged by our initial results, we sought to examine the scope and the generality of the method. The domino Cu-catalyzed amidation/hydroamidation of haloenynes[19] with *tert*-butyl carbamate shows excellent chemoselectivity, and its wide scope is evident from the results compiled in Table 1. As summarized below, different combinations of substituents on the alkyne and alkene can be used to allow the synthesis of di- and trisubstituted pyrroles, including those bearing alkene, ester, silyl ether, and alkyl halide substituents.

[*] Dr. R. Martín, Dr. M. Rodríguez Rivero, Prof. Dr. S. L. Buchwald
Department of Chemistry, Room 18–490
Massachusetts Institute of Technology
Cambridge, MA 02139 (USA)
Fax: (+1) 617-253-3297
E-mail: sbuchwal@mit.edu

[**] Generous financial support from the National Institutes of Health (GM058160) is gratefully acknowledged. R.M. and M.R.R. thank the Spanish MEC for postdoctoral fellowships. The Bruker Advance 400 MHz NMR spectrometer used in this work was purchased with funding from the National Institutes of Health (GM 1S10RR13886-01).

Supporting information for this article is available on the WWW under http://www.angewandte.org or from the author.

 © 2006 Wiley-VCH Verlag GmbH & Co. KGaA, Weinheim

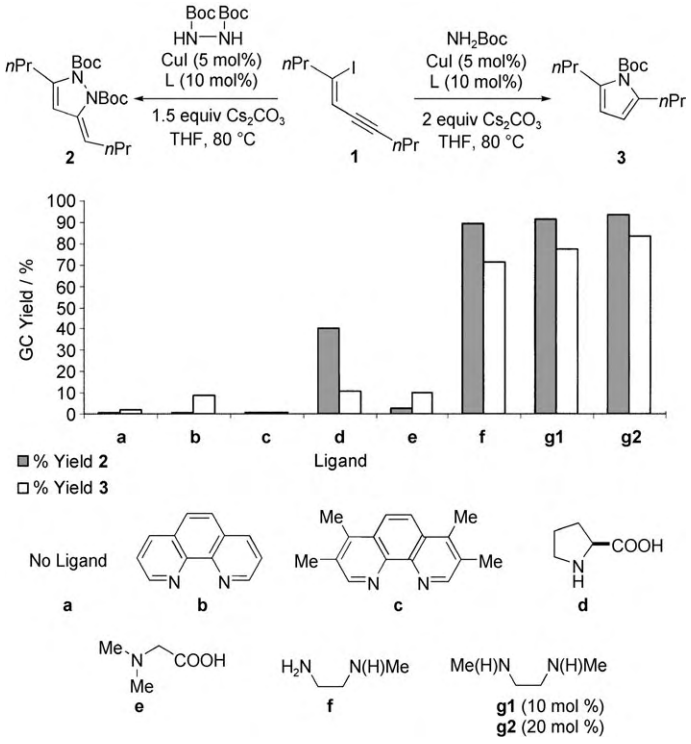

Figure 1. Ligand screening in the domino Cu-catalyzed amidation/hydroamidation of haloenyne **1**.

Although the reaction of a substrate bearing a terminal alkyne led to decomposition, the synthetic equivalent of this transformation can be accomplished by the use of a trimethylsilyl (TMS) group, which masks the terminal acetylene and is deprotected in situ (Table 1, entry 7).[20] Thus, not only 2,5- but also 2,3-disubstitution on the pyrrole core can be achieved, albeit in lower yield. Although the Cu-catalyzed coupling of primary amides with vinyl halides bearing an α-electron-withdrawing group has little precedent,[21] we were pleased to find that the cascade reaction took place, with cleavage of the carbamate group, thus providing the deprotected pyrroles in excellent overall yield (Table 1, entries 5 and 6). Although this study focused on the use of iodoenynes, we also demonstrated that bromoenynes could be used if the reaction was carried out in toluene at 110 °C (Table 1, entries 1, 5, 6, 13, and 14). Polyheterocylic compounds could also be prepared in high yields by introducing a heterocyclic moiety either in the alkene or alkyne counterpart (Table 1, entries 13–15).

To extend the scope of this methodology to the synthesis of pyrazoles, the reaction of several iodoenynes was evaluated under the optimized conditions using bis(Boc)hydrazine as the nucleophilic component (Table 2). In this case, simple treatment of the intermediate **II** with trifluoroacetic acid (Scheme 1), with no need for isolation, afforded the free pyrazoles (for simplicity, represented as one tautomer) in good-to-excellent overall yields. Although the hydroamidation reaction could theoretically proceed through two possible pathways, 5-*exo*-dig or 6-*endo*-dig, exclusive formation of the five-membered ring was observed in all cases. It is worth noting that mono-, di- and trisubstituted pyrazoles can be accessed through this route. As in the case of pyrroles, alkenes and alkynes with a wide variety of substituents are viable reaction components. Moreover, despite acidic treatment of **II**, many functional groups, such as alkyl halides, esters, benzyl ethers, and even silyl ethers, are well tolerated in the reaction. In this manner, this protocol provides rapid and modular access to a variety of nitrogen-containing heterocycles with different substitution patterns.

Table 1: Synthesis of pyrroles through Cu-catalyzed domino amidation/hydroamidation of haloenynes.[a]

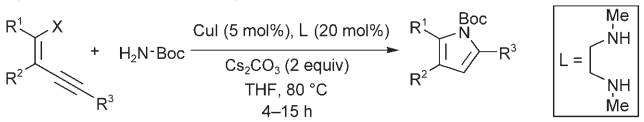

Entry	Product	X	Yield [%][b]
1[c]	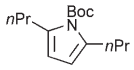	Br	70
2		I	74
3	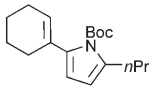	I	84
4	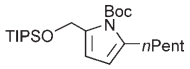	I	83
5[c]	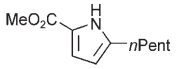	Br	82
6[c]	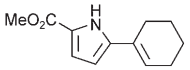	Br	81
7[d]		I	68
8	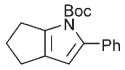	I	52
9	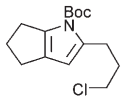	I	78
10	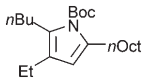	I	85
11	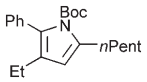	I	91
12	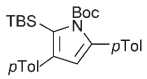	I	95
13[c]	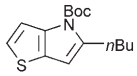	Br	83
14[c]	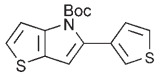	Br	74
15	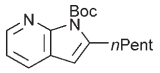	I	71

[a] Reaction conditions: haloenyne (1.0 equiv), NH_2Boc (1.2 equiv), CuI (5 mol%), *N*,*N*′-dimethylethylenediamine (20 mol%), Cs_2CO_3 (2.0 equiv), THF (0.5 M). [b] Yields of the isolated products are the average of two runs and are estimated to be over 95% pure by ^1H NMR spectroscopic and GC analysis. [c] Using K_2CO_3 (2.0 equiv) and toluene (0.5 M) at 110 °C. [d] R^3 = TMS. TBS = *tert*-butyldimethylsilyl, TIPS = triisopropylsilyl.

 © 2006 Wiley-VCH Verlag GmbH & Co. KGaA, Weinheim

Table 2: Synthesis of pyrazoles through Cu-catalyzed domino amidation-hydroamidation of iodoenynes.[a]

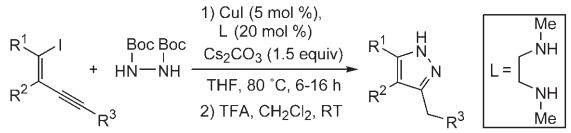

Entry	Product	Yield [%][b]
1	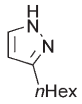	92
2	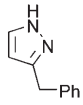	93
3	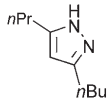	83
4	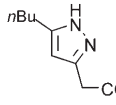	81
5	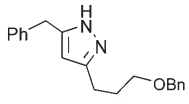	72
6	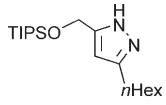	78
7	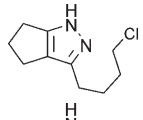	89
8	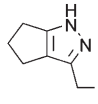	86
9[c]	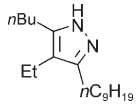	66
10	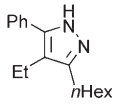	72

[a] Reaction conditions: iodoenyne (1.0 equiv), NHBoc–NHBoc (1.2 equiv), CuI (5 mol%), *N,N′*-dimethylethylenediamine (20 mol%), Cs_2CO_3 (1.5 equiv), THF (0.5 M). [b] Yields of the isolated products are the average of two runs and are estimated to be over 95% pure by ^{1}H NMR spectroscopic and GC analysis. [c] Ligand: *trans*-1,2-cyclohexanediamine (20 mol%).

In principle, two different mechanisms can be envisioned for these domino processes: 1) initial C–N coupling followed by intramolecular hydroamidation of the alkyne portion of **I** or 2) intermolecular hydroamidation and subsequent intramolecular amidation (Scheme 2). Experiments performed by Ackermann in his synthesis of indoles indicated that a mechanism consisting of an intermolecular hydroamination and a subsequent intramolecular metal-catalyzed C–N bond-forming process was predominantly operative, although no isolation of the proposed intermediate was reported.[10]

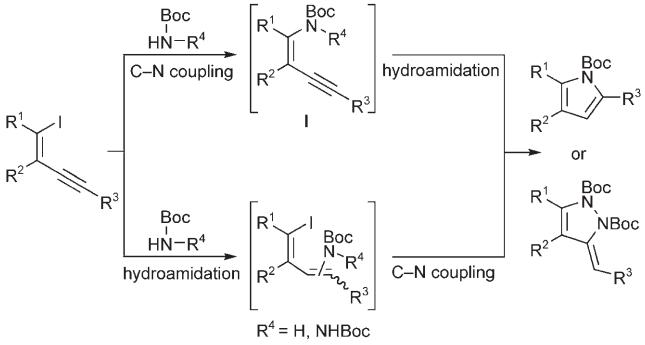

Scheme 2. Possible mechanisms for the domino reaction.

To probe the reaction mechanism of our method, the reaction of vinyl iodide **1** with *tert*-butyl carbamate and bis(Boc)hydrazine was stopped after 4 h at 80 °C (Scheme 3).

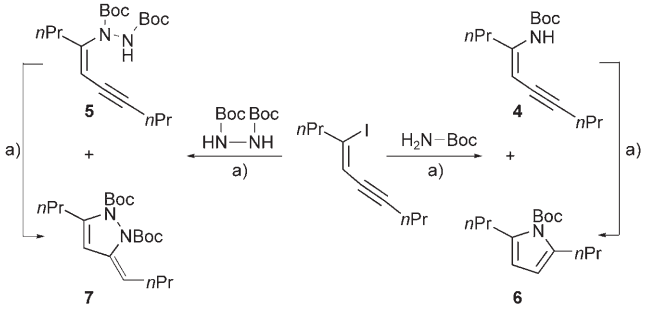

Scheme 3. Mechanistic insight by trapping the intermediates in the Cu-catalyzed domino process. a) CuI (5 mol%), *N,N′*-dimethylethylenediamine (20 mol%), Cs_2CO_3 (1.5 equiv), THF (0.5 M), 80 °C, 4 h.

As shown below, the only compounds detected by NMR spectroscopy of the crude reaction mixture were the corresponding C–N coupling intermediates **4** and **5** along with significant amounts of the final cascade product.[22] Remarkably, **4** and **5** could be obtained in analytically pure form by carrying out the reactions at room temperature and 40 °C in 59 and 48% yields of the isolated products, respectively. Full conversion into the desired cascade products was observed by resubjecting **4** and **5** to the reaction conditions for an additional 4 h. Interestingly, the treatment of **4** and **5** with either CuI (5 mol%) or Cs_2CO_3 (1.5 equiv) under otherwise identical conditions resulted in reisolated starting materials; not even traces of the final cascade products were observed. Only the combination of catalyst with base was effective, thus suggesting that the intramolecular hydroamidation is both a copper-catalyzed[23] and base-assisted process. These results strongly support a mechanism involving an initial C–N coupling followed by intramolecular hydroamidation of the latent alkyne (top pathway, Scheme 2).[24]

In conclusion, a general, highly flexible, and efficient Cu-catalyzed domino C–N coupling/hydroamidation reaction has been developed. The transformation constitutes a straightforward alternative to the existing methodology for the prepa-

 © 2006 Wiley-VCH Verlag GmbH & Co. KGaA, Weinheim

ration of pyrroles and pyrazoles. A mechanism in which the metal acts with dual roles, thus facilitating both amidation and hydroamidation reactions is proposed. Further studies on synthetic applications of these important and related transformations are currently in progress.

Received: July 21, 2006
Published online: September 29, 2006

Keywords: amidation · copper · domino reactions · heterocycles · hydroamidation

[1] T. Eicher, S. Hauptmann, *The Chemistry of Heterocycles—Structure, Reactions, Synthesis and Application* (translated by H. Suschitzky, J. Suschitzky), VCH, Weinheim, **2003**.
[2] a) M. S. Butler, *J. Nat. Prod.* **2004**, *67*, 2141; b) J. A. Joule, K. Mills, *Heterocyclic Chemistry*, Blackwell Science, Oxford, **2000**.
[3] For general reviews on the metal-catalyzed synthesis of heterocycles, see: a) I. Nakamura, Y. Yamamoto, *Chem. Rev.* **2004**, *104*, 2127; b) T. L. Gilchrist, *J. Chem. Soc. Perkin Trans. 1* **1999**, 2849.
[4] a) J. F. Hartwig, *Synlett* **2006**, 1283; b) L. Jiang, S. L. Buchwald in *Metal-Catalyzed Cross-Coupling Reactions*, 2nd ed. (Eds.: A. de Meijere, F. Diederich), Wiley-VCH, Weinheim, **2004**, p. 699.
[5] S. L. Buchwald, C. Mauger, G. Mignani, U. Scholz, *Adv. Synth. Catal.* **2006**, *348*, 23.
[6] For recent reviews on Cu-catalyzed cross-coupling reactions, see: a) I. P. Beletskaya, A. V. Cheprakov, *Coord. Chem. Rev.* **2004**, *248*, 2337; b) S. V. Ley, A. W. Thomas, *Angew. Chem.* **2003**, *115*, 5558; *Angew. Chem. Int. Ed.* **2003**, *42*, 5400.
[7] For leading references on copper-catalyzed C–N bond-forming reactions, see: a) D. Ma, Q. Cai, H. Zhang, *Org. Lett.* **2003**, *5*, 2453; b) F. Y. Kwong, S. L. Buchwald, *Org. Lett.* **2003**, *5*, 793; c) A. Klapars, X. Huang, S. L. Buchwald, *J. Am. Chem. Soc.* **2002**, *124*, 7421.
[8] Recent applications of Cu-promoted cross-coupling reactions: a) I. E. Wrona, A. E. Gabarda, G. Evano, J. S. Panek, *J. Am. Chem. Soc.* **2005**, *127*, 15026; b) X. Wang, E. J. Bowman, B. J. Bowman, J. A. Porco, *Angew. Chem.* **2004**, *116*, 3685; *Angew. Chem. Int. Ed.* **2004**, *43*, 3601.
[9] A. Arcadi, S. Cacchi, F. Marinelli, *Tetrahedron Lett.* **1989**, *30*, 2581.
[10] L. Ackermann, *Org. Lett.* **2005**, *7*, 439.
[11] For a recent report of a related transformation, see: Z.-Y. Tang, Q.-S. Hu, *Adv. Synth. Catal.* **2006**, *348*, 846.
[12] For a Cu-catalyzed intramolecular hydroamidation, see: a) Y. Yu, G. A. Stephenson, D. Mitchell, *Tetrahedron Lett.* **2006**, *47*, 3811; b) K. Hiroya, S. Itoh, T. Sakamoto, *J. Org. Chem.* **2004**, *69*, 1126; c) L. Xu, I. R. Lewis, S. K. Davidsen, J. B. Summers, *Tetrahedron Lett.* **1998**, *39*, 5159.
[13] For recent reviews on domino reactions, see: a) A. de Meijere, P. von Zezschwitz, S. Bräse, *Acc. Chem. Res.* **2005**, *38*, 413; b) L. F. Tietze, *Chem. Rev.* **1996**, *96*, 115.
[14] For recent reviews and selected syntheses of pyrroles, see: a) L. Lu, G. Chen, S. Ma, *Org. Lett.* **2006**, *8*, 835; b) J. T. Binder, S. F. Kirsch, *Org. Lett.* **2006**, *8*, 2151; c) T. J. Harrison, J. A. Kozak, M. Corbella-Pané, G. R. Dake, *J. Org. Chem.* **2006**, *71*, 4525; d) D. J. Gorin, N. R. Davis, F. D. Toste, *J. Am. Chem. Soc.* **2005**, *127*, 11260; e) S. Kamijo, C. Kanazawa, Y. Yamamoto, *J. Am. Chem. Soc.* **2005**, *127*, 9260; f) V. Larionov, A. de Meijere, *Angew. Chem.* **2005**, *117*, 5809; *Angew. Chem. Int. Ed.* **2005**, *44*, 5664; g) G. Balme, *Angew. Chem.* **2004**, *116*, 6396; *Angew. Chem. Int. Ed.* **2004**, *43*, 6238; h) V. F. Ferreira, M. C. B. V. de Souza, A. C. Cunha, L. O. R. Pereira, M. L. G. Ferreira, *Org. Prep. Proced. Int.* **2001**, *33*, 411; for the biological significance of pyrroles, see: i) A. Fürstner, *Angew. Chem.* **2003**, *115*, 3706; *Angew. Chem. Int. Ed.* **2003**, *42*, 3528; j) D. O'Hagan, *Nat. Prod. Rep.* **2000**, *17*, 435.
[15] For recent syntheses of pyrazoles, see: a) T. Persson, J. Nielsen, *Org. Lett.* **2006**, *8*, 3219; b) S. T. Heller, S. R. Natarajan, *Org. Lett.* **2006**, *8*, 2675; c) V. Nair, A. T. Biju, K. Mohanan, E. Suresh, *Org. Lett.* **2006**, *8*, 2213; d) A. Lévai, A. M. S. Silva, J. A. S. Cavaleiro, I. Alkorta, J. Elguero, J. Jekö, *Eur. J. Org. Chem.* **2006**, 2825; e) M. S. M. Ahmed, K. Kobayashi, A. Mori, *Org. Lett.* **2005**, *7*, 4487; for the biological significance of pyrazoles, see: f) "Pyrazoles as Drugs: Facts and Fantasies": J. Elguero, P. Goya, N. Jagerovic, A. M. S. Silva in *Targets in Heterocyclic Systems—Chemistry and Properties*, *Vol. 6* (Eds.: O. A. Attanasi, D. Spinelli), Italian Society of Chemistry, Rome, **2002**, p. 52.
[16] a) X. Pan, Q. Cai, D. Ma, *Org. Lett.* **2004**, *6*, 1809; b) L. Jiang, G. E. Job, A. Klapars, S. L. Buchwald, *Org. Lett.* **2003**, *5*, 3667; c) R. Shen, J. A. Porco, *Org. Lett.* **2000**, *2*, 1333.
[17] For the arylation of hydrazines, see: a) Y.-K. Lim, K.-S. Lee, C.-G. Cho, *Org. Lett.* **2003**, *5*, 979; b) M. Wolter, A. Klapars, S. L. Buchwald, *Org. Lett.* **2001**, *3*, 3803; c) J. B. Arterburn, K. V. Rao, R. Ramdas, B. R. Dible, *Org. Lett.* **2001**, *3*, 1351; d) Z. Wang, R. T. Skerlj, G. Bridger, *Tetrahedron Lett.* **1999**, *40*, 3543.
[18] G. Nordmann, S. L. Buchwald, *J. Am. Chem. Soc.* **2003**, *125*, 4978.
[19] Starting haloenynes were readily prepared, generally in one to three steps from commercially available starting materials. For details, see the supporting information.
[20] For examples of protodesilylation during a Cu-catalyzed hydroamination reaction, see: a) V. Kumar, J. A. Dority, E. R. Bacon, B. Singh, G. Y. Lesher, *J. Org. Chem.* **1992**, *57*, 6995; b) J. Fujiwara, Y. Fukutani, H. Sano, K. Maruoka, H. Yamamoto, *J. Am. Chem. Soc.* **1983**, *105*, 7177.
[21] D. J. Richard, B. Schiavi, M. M. Joullié, *Proc. Natl. Acad. Sci. USA* **2004**, *101*, 11971.
[22] a) Pyrrole cascade: 90% conversion after 4 h, 34% pyrrole and 41% C–N coupling product; b) pyrazole cascade: 80% conversion after 4 h, 25% cyclized product and 55% C–N coupling product.
[23] Isolation of a μ^2-alkyne Cu^I complex has been reported: D. W. Macomber, M. D. Rausch, *J. Am. Chem. Soc.* **1983**, *105*, 5325.
[24] Additionally, a control experiment was performed in which 1-(1-propynyl)cyclohexene was subjected to the reaction conditions; no traces of intermolecular hydroamidation products were detected after 24 h, thus indicating that intermolecular hydroamidation is unlikely using our protocol.

 © 2006 Wiley-VCH Verlag GmbH & Co. KGaA, Weinheim

Oxidative C–C Coupling

DOI: 10.1002/anie.200603024

Intermolecular Oxidative Enolate Heterocoupling**

Phil S. Baran and Michael P. DeMartino*

Oxidative dimerization of enolates has been known since 1935[1] and was studied further by Saegusa, Mislow, and others in the 1970s (Scheme 1 a).[2] Formally, this transformation

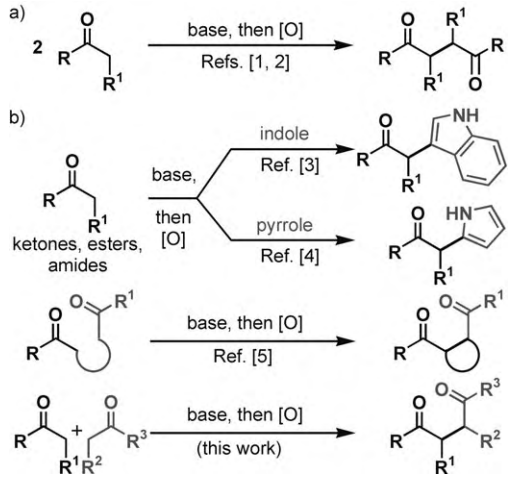

Scheme 1. Oxidative C–C bond formation via enolates.

accomplishes the direct union of two identical sp^3-hybridized carbon atoms with no substrate prefunctionalization by exploiting their innate oxidation state. The analogous process using two different types of coupling partners has remained unexplored.[2d,e] In 2004, we presented a method for the direct coupling of NH-containing heterocycles to various carbonyl compounds through enolate heterocoupling (Scheme 1 b).[3,4] It was later shown that two *different* types of carbonyl species can be coupled in an intramolecular sense (ester-amide).[5]

Herein, this approach is explored in an intermolecular setting with application to the enantioselective synthesis of medicinally relevant compounds[6] and the anticancer natural product (−)-bursehernin (**1**).

The intermolecular heterocoupling of two enolates is a particularly challenging chemical transformation given the potential background reactions that can occur. These include, but are not limited to, α-hydroxylation of each monomer, dehydrogenation of either the monomers or the newly forged C–C bond, intermolecular cross- and homo-Dieckmann/aldol condensations, and oxidative homodimerization of either coupling partner. In fact, if the intermolecular cross- and homocoupling processes alone were governed by only statistics, the heterocoupling of an equimolar mixture of two enolate species would take place with a maximum of 50 % conversion. Cross-coupling of two different ketones has been reported, but required a large excess of one partner (3–3.5 equiv, along with additional base and oxidant).[2d,e] In principle, intermolecular heterocoupling of enolates could be synthetically pragmatic if sufficient differences existed in their respective oxidation potentials and/or relative rates of homodimerization, such that equimolar ratios of the starting materials can be used. As depicted in Table 1, the cross-couplings of imides with ketones (entries 1–8), esters (entries 9–11), and lactones (entry 12) are now possible. Lactams such as oxindoles were also found to be amenable to cross-coupling (entries 13–17). In nearly all cases, equimolar ratios of the carbonyl species are employed and synthetically useful yields (greater than the 50 % statistical limit) were obtained, even when performed on a gram scale (entries 3 and 11, Table 1). In all cases, the remaining material was largely recovered monomer, although minor amounts of imide/oxindole homodimer were produced in entries 9–17. Notably, in entries 9–12 (Table 1), products with stereochemistry analogous to those of Evans' model for the diastereoselective alkylation of *N*-acyl oxazolidinones were produced,[7] whereas in entries 1–8, the adducts obtained were epimeric at this carbon center. This empirical observation is not fully understood at this time, and the mechanistic basis for this finding is under investigation. Although the diastereoselectivity is modest in most cases, this method offers a clear strategic benefit when forging such C–C bonds and thus provides molecules that would be difficult to access directly through use of current methods. Moreover, products may be amenable to thermodynamic equilibration, as in the following application to natural product synthesis.

(−)-Bursehernin (**1**) is a member of a large class of naturally occurring bioactive γ-butyrolactone lignans.[8] Inspection of **1** reveals that oxidative coupling of two dihydrocinnamic acid derivatives would be an intuitive and expedient route to construct these lignan lactones (Scheme 2 a). Indeed, symmetric dibenzyl lignan lactones ($R^1 = R^2$) have been synthesized in this manner.[9] Prior to this work, however, methodology necessary to accomplish intermolecular heterocoupling for the synthesis of unsymmetrical dibenzyl lignans was unavailable. Using the simple method described above, the oxidative union of oxazolidinone **2** and dihydrocinnamic ester **3** was accomplished (d.r. = 1.6:1). The crude mixture was submitted directly to chemoselective

[*] Prof. P. S. Baran, M. P. DeMartino
Department of Chemistry
The Scripps Research Institute
10650 North Torrey Pines Road, La Jolla, CA 92037 (USA)
Fax: (+1) 858-784-7375
E-mail: pbaran@scripps.edu

[**] We thank Dr. D. H. Huang and Dr. L. Pasternak for NMR spectroscopic assistance, and Dr. G. Suizdak and Dr. R. Chadha for mass spectrometric and X-ray crystallographic assistance, respectively. We are grateful to Professor M. G. Finn for the use of his cyclic voltammetry apparatus and Tomás Llamas for early contributions to the project. Financial support for this work was provided by The Scripps Research Institute, Amgen, Bristol-Myers Squibb, DuPont, Eli Lilly, GlaxoSmithKline, Roche, the Searle Scholarship Fund, and the NIH/NIGMS (GM071498).

Supporting information for this article is available on the WWW under http://www.angewandte.org or from the author.

 © 2006 Wiley-VCH Verlag GmbH & Co. KGaA, Weinheim

Table 1: Intermolecular oxidative enolate couplings.[a]

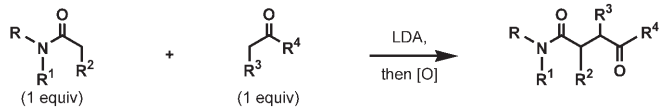

Entry	Carbonyl compound 1	Carbonyl compound 2	Oxidant	Product	Yield [%][b] (d.r.)[c]
1	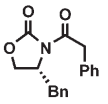	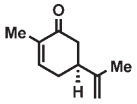	Fe^{III}	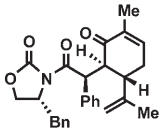	52 (2.7:1) (X-ray)
2	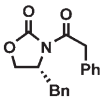	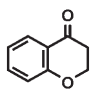	Fe^{III}	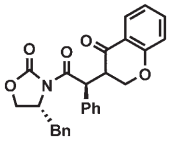	59 (2.8:1)
3					60 (2.6:1)[d]
	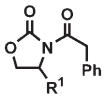	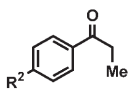	Fe^{III}	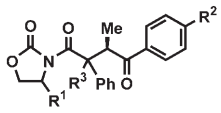	
4	R^1 = α-Bn	R^2 = H		R^3 = α-H	57 (2.8:1)
5	R^1 = α-Bn	R^2 = OMe		R^3 = α-H	67 (2.5:1)
6	R^1 = β-*i*Pr	R^2 = Br		R^3 = β-H (X-ray)	55 (2.5:1)
7	R^1 = β-*i*Pr	R^2 = H		R^3 = β-H	66 (2.1:1)
8	R^1 = β-*i*Pr	R^2 = OMe		R^3 = β-H	65 (2.3:1)
	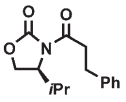	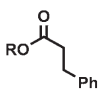	Cu^{II}	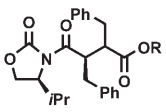	
9[e]		R = Me			51 (1.0:1)
10[e]		R = *t*Bu			51 (1.6:1)
11[e]		R = *t*Bu			53 (1.6:1)[f]
12[e]	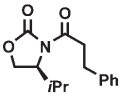	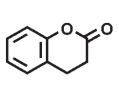	Cu^{II}	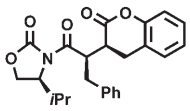	54 (2.4:1) (X-ray)
	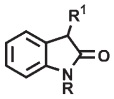	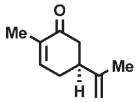	Fe^{III}	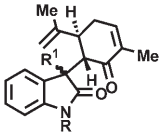	
13[g]	R = R^1 = Me				91 (1.2:1)
14	R = R^1 = Me				60 (1.2:1)
15	R = MOM, R^1 = prenyl				54 (1.0:1)
	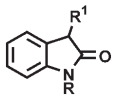		Fe^{III}	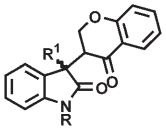	
16	R = R^1 = Me				72 (2.6:1)
17	R = MOM, R^1 = prenyl				73 (2.0:1)

[a] Stereochemistry of α-carbon (oxazolidinone) for entries 2–3 and 5–11 for the major diastereomers has been assigned by analogy to those confirmed by X-ray crystallographic analysis (entries 1, 6, and 12). [b] Isolated yields after chromatography. [c] Diastereomeric ratios refer to carbon β-carbon (oxazolidinone) for entries 1–12. [d] Gram scale (3.7 mmol). [e] 1.75 equiv ester/lactone used. [f] Gram scale (4.3 mmol). [g] 2 equiv ketone used. Fe^{III} = [Fe(acac)$_3$] (acac = acetylacetonate), Cu^{II} = copper(II) 2-ethylhexanoate, LDA = lithium diisopropylamide, Bn = benzyl, MOM = methoxymethyl.

reduction of the oxazolidinone using lithium borohydride, followed by treatment with DBU to furnish (−)-bursehernin (Scheme 2b). The NMR spectral data of synthetic **1** was identical to that reported for the natural substance.[10] Notably, the low diastereoselectivity (at C3) observed in the coupling step was inconsequential as this center was easily epimerized and driven to the *trans*-configured product. Strategic use of oxidative coupling facilitated the first, concise (three sequential synthetic operations with one purification), and enantioselective synthesis of **1**, accomplished in 41% overall isolated yield. By comparison, previous unsymmetrical lignan syntheses required a minimum of six steps proceeding overall in much lower yields.[11]

While α-aryl imides, oxindoles, and diketopiperizines[5] couple most effectively using Fe^{III}-based oxidants, simple imides, indoles,[3a] and pyrroles[4] require Cu^{II}-based oxidants. The precise role of the oxidants in enolate coupling has not been clearly determined and it was assumed[2] that they function as simple electron acceptors (possibly through an outer-sphere electron-transfer process).[12] To determine if the oxidative heterocoupling of enolates is amenable to reagent control, the coupling of oxindole **4** and carvone was studied (Table 2). In this case, homodimerization of the components is preferred over the desired heterocoupling using the standard copper- and iron-based oxidants, resulting in diminished yields. The absence of 3-substitution on oxindole coupling partner **4** is the apparent cause, as a steric bias disfavoring homodimerization is not present (compare with entry 15, Table 1). Notably, Fe(*t*BuCOCHCOCF$_3$)$_3$[10] furnished the heterocoupled product **5** in 83% isolated yield (entry 5, Table 2). In control reactions using either **4** or carvone alone, this oxidant was still competent in promoting homodimerization. Cyclic voltammetry revealed a unique oxidation potential for each oxi-

 © 2006 Wiley-VCH Verlag GmbH & Co. KGaA, Weinheim

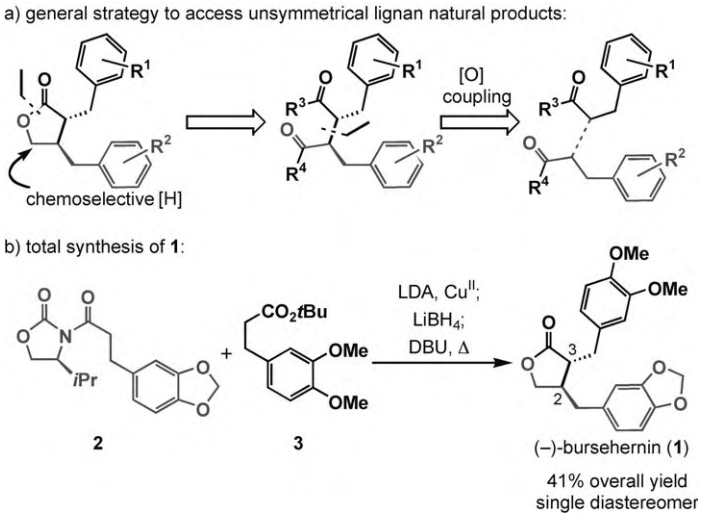

Scheme 2. Short, enantioselective synthesis of (−)-bursehernin (**1**). Reagents and conditions: **2**, LDA (THF, 1.15 equiv), LiCl (5.0 equiv), PhMe, −78→0→−78 °C (10 min each), **3** (1.75 equiv), PhMe, LDA (THF, 1.85 equiv), −78 °C, 30 min, then Cu^{II}, −78→23 °C, 20 min; $LiBH_4$ (10 equiv), MeOH (5.0 equiv), THF, −78→−10 °C, 1.5 h; DBU (10 equiv), PhMe, 110 °C, 24 h, 41% overall. DBU = 1,8-diazabicyclo[5.4.0]undec-7-ene.

Table 2: Oxidative coupling is amenable to reagent control.[a]

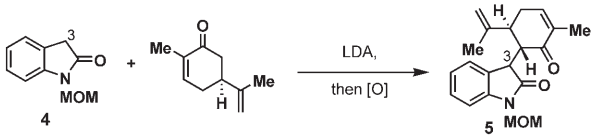

Entry	Oxidant	E_{ox} [eV][b]	Yield [%][c]
1	Cu(2-ethylhexanoate)$_2$	−1.65	15
2	PhI(OAc)$_2$	−1.53	≈10
3	[Fe(acac)$_3$]	−1.14	45
4	Fe(PhCOCHCOMe)$_3$	−1.07	30
5	**Fe(*t*BuCOCHCOCF$_3$)$_3$**	**−0.60**	**83**
6	Fe(MeCOCHCOCF$_3$)$_3$	−0.51	40
7	Fe(C$_{10}$H$_7$COCHCOCF$_3$)$_3$	−0.46	40

[a] 2 equiv carvone used. [b] Oxidation potentials measured using cyclic voltammetry, relative to ferrocene/ferrocenium standard. [c] Isolated yields after chromatography.

dant employed, suggesting that rationally controlled hetero-coupling of enolates is possible. This trend, as well as the success of reagent-controlled coupling, underscores great mechanistic complexity and is the subject of further study.[5c]

This work has demonstrated for the first time that oxidative C–C bond formation through the intermolecular union of two different types of enolates can be accomplished by exploiting the natural electronic or steric differences in coupling partners. Furthermore, undesirable homocoupling processes can sometimes be stifled by careful reagent control. As demonstrated in the total synthesis of **1**, conservation of the oxidation state of the starting material prior to the coupling event eliminates the need for prefunctionalization of the substrate (e.g. enol-silane formation or halogenation). It is anticipated that this conceptually unique method for merging sp^3-hybridized carbon atoms will continue to find useful applications in synthesis.[13]

Experimental Section

General procedure for Fe-based couplings (see Supporting Information). Oxazolidinone or oxindole (0.10 mmol, 1.0 equiv) and carbonyl compound (0.10 mmol, 1.0 equiv) were dissolved in benzene (1.0 mL), and the solvent was removed in vacuo. This process was repeated a second time (azeotropic water removal). The starting materials were then dissolved in THF (340 μL, 0.3 M), and the solution was cooled to −78 °C. A solution of LDA (0.50 M in THF, 428 μL, 2.1 equiv) was added dropwise by syringe over 30 s. The reaction was allowed to stir for 30 min at −78 °C and then warmed to ambient temperature. After 5 min of stirring at 23 °C, a solution of [Fe(acac)$_3$] (0.50 M, 408 μL, 2.0 equiv) was added all at once (less than 1 s addition time). The reaction mixture was stirred at ambient temperature for 20 min and then quenched by the addition of 1 N HCl (1 mL). The aqueous layer was partitioned with EtOAc (2 mL), separated, and then extracted twice with EtOAc (2 mL). The organic portions were combined, washed with brine (5 mL), dried over anhydrous $MgSO_4$, filtered, and concentrated in vacuo. Flash chromatography (silica gel) of the crude reaction afforded pure coupled product.

General procedure for Cu-based couplings (see Supporting Information). Oxazolidinone (0.33 mmol, 1.0 equiv) and powdered lithium chloride (1.64 mmol, 5.0 equiv) were taken up in benzene (1.0 mL), and the solvent was removed in vacuo. This process was repeated a second time (azeotropic water removal). Toluene (546 μL, 0.6 M) was added to this mixture, and the resulting solution was cooled to −78 °C. A solution of LDA (0.50 M in THF, 759 μL, 1.15 equiv) was added by syringe down the sides of the reaction vessel over 10 s. After stirring at −78 °C for 10 min, the solution was warmed to 0 °C for 10 min (color change from pale to bright yellow), and then cooled to −78 °C for 5 min. In a separate reaction vessel, the carbonyl compound (0.57 mmol, 1.75 equiv) was dissolved in benzene (1.0 mL) and the solvent was then removed in vacuo. This process was repeated a second time. Toluene (546 μL, 0.6 M) was added to the carbonyl compound, and the solution was cooled to −78 °C. A solution of LDA (0.50 M in THF, 1.2 mL, 1.85 equiv) was added by syringe down the sides of the reaction vessel over 10 s, and the resulting solution was stirred at −78 °C for 25 min. At this time, the carbonyl enolate solution was transferred by canula into the oxazolidinone enolate solution. The reaction mixture was stirred at −78 °C for an additional 5 min, at which time a solution of copper(II)-2-ethylhexanoate (0.3 M in toluene, 3.0 mL, 2.75 equiv) at −78 °C was transferred into the reaction vessel by canula. Immediately following addition, the vessel was quickly removed from the −78 °C bath and placed into a room-temperature water bath, which led to a color change from light blue to brown. The reaction mixture was stirred for 20 min and subsequently quenched by the addition of 5% aqueous NH_4OH (5 mL). The aqueous layer was partitioned with EtOAc (5 mL), separated, and then extracted twice with EtOAc (2 mL). The organic portions were combined, washed with brine (5 mL), dried over anhydrous $MgSO_4$, filtered, and concentrated in vacuo. Flash chromatography (silica gel) of the crude reaction afforded pure coupled product.

Received: July 27, 2006
Published online: September 29, 2006

Keywords: C–C coupling · enolates · lignans · synthetic methods · total synthesis

[1] D. Ivanoff, A. Spassoff, *Bull. Soc. Chim. Fr.* **1935**, *2*, 76.

 © 2006 Wiley-VCH Verlag GmbH & Co. KGaA, Weinheim

[2] a) M. W. Rathke, A. Lindert, *J. Am. Chem. Soc.* **1971**, *93*, 4605; b) C. A. Maryanoff, B. E. D. Maryanoff, R. Tang, K. Mislow, *J. Am. Chem. Soc.* **1973**, *95*, 5839; c) R. M. Dessau, E. I. Heiba, *J. Org. Chem.* **1974**, *39*, 3457; d) Y. Ito, T. Konoike, T. Saegusa, *J. Am. Chem. Soc.* **1975**, *97*, 2912; e) Y. Ito, T. Konoike, T. Harada, T. Saegusa, *J. Am. Chem. Soc.* **1977**, *99*, 1487; f) R. H. Frazier, R. L. Harlow, *J. Org. Chem.* **1980**, *45*, 5408; g) L. A. Paquette, E. I. Bzowej, B. M. Branan, K. J. Stanton, *J. Org. Chem.* **1995**, *60*, 7277.
[3] a) P. S. Baran, J. M. Richter, *J. Am. Chem. Soc.* **2004**, *126*, 7450; b) P. S. Baran, J. M. Richter, *J. Am. Chem. Soc.* **2005**, *127*, 15394.
[4] P. S. Baran, J. M. Richter, D. W. Lin, *Angew. Chem.* **2005**, *117*, 615; *Angew. Chem. Int. Ed.* **2005**, *44*, 609.
[5] a) P. S. Baran, C. A. Guerrero, N. Ambhaikar, B. Hafensteiner, *Angew. Chem.* **2005**, *117*, 612; *Angew. Chem. Int. Ed.* **2005**, *44*, 606; b) P. S. Baran, C. A. Guerrero, B. Hafensteiner, N. Ambhaikar, *Angew. Chem.* **2005**, *117*, 3960; *Angew. Chem. Int. Ed.* **2005**, *44*, 3892; c) for a detailed discussion of the mechanistic intricacies of intramolecular enolate hetereocoupling, see: P. S. Baran, B. D. Hafensteiner, N. B. Ambhaikar, C. A. Guerrero, J. D. Gallagher, *J. Am. Chem. Soc.* **2006**, *128*, 8678.
[6] a) J. M. Balkovec, G. Hammond, M. L. Greenlee, S. H. Olson, G. P. Rouen, J. H. Epstein-Toney, US Patent 29687, **2001**; b) R. E. Olson, US Patent 17865, **2001**; c) M. Whittaker, C. D. Floyd, P. Brown, A. J. H. Gearing, *Chem. Rev.* **1999**, *99*, 2735.
[7] D. A. Evans, M. D. Ennis, D. J. Mathre, *J. Am. Chem. Soc.* **1982**, *104*, 1737.
[8] P. B. McDoniel, J. R. Cole, *J. Pharm. Sci.* **1972**, *61*, 1992.
[9] a) J. L. Belletire, D. F. Fry, *J. Org. Chem.* **1987**, *52*, 2549; b) N. Kise, T. Ueda, K. Kumada, Y. Terao, N. Ueda, *J. Org. Chem.* **2000**, *65*, 464; c) T. Langer, M. Illich, G. Helmchen, *Synlett* **1974**, 1137.
[10] See Supporting Information for details.
[11] a) D. Enders, V. Lausberg, R. Tang, G. D. Signore, O. M. Berner, *Synthesis* **2002**, 515; b) M. P. Sibi, P. Liu, J. Ji, S. Hajra, J. Chen, *J. Org. Chem.* **2002**, *67*, 1738; c) T. Honda, N. Kimura, S. Sato, D. Kato, H. Tominaga, *J. Chem. Soc. Perkin Trans. 1* **1994**, *8*, 1043.
[12] P. Renaud, M. A. Fox, *J. Org. Chem.* **1988**, *53*, 3745.
[13] Detailed experimental procedures, copies of spectral data, and full characterization of compounds are contained in the Supporting Information. CCDC 617245–617247 (Table 1, entries 12, 1, and 6, respectively) contain the supplementary crystallographic data for this paper. These data can be obtained free of charge from The Cambridge Crystallographic Data Centre via www.ccdc.cam.ac.uk/data_request/cif.

 © 2006 Wiley-VCH Verlag GmbH & Co. KGaA, Weinheim

Antibiotics

DOI: 10.1002/anie.200603892

Total Synthesis of Platensimycin**

K. C. Nicolaou, Ang Li, and David J. Edmonds*

Infectious disease remains a menace to society despite the isolation of many new antibiotics over the last few decades. The drugs that are currently available to defend against such ailments are becoming progressively less effective because of the development of bacterial resistance, leading to an increase in potentially fatal, drug-resistant infections. The rather sporadic success in the development of antibiotics since the 1960s has led to a pressing need to discover new antibiotics to combat drug resistance.[1] Compounds that act through new mechanisms are particularly attractive as they offer the prospect of combating effectively infections resistant to all existing drugs. Platensimycin (**1**, Scheme 1) was isolated recently from a strain of *Streptomyces platensis* by a Merck research group as part of a high-throughput screening program of metabolites to identify inhibitors of bacterial fatty acid biosynthesis.[2] Platensimycin represents a new structural class of antibiotic, operating through a novel mechanism of action and, as such, presents a ray of hope for the development of a powerful new therapy. Specifically, the Merck research group showed that platensimycin inhibits the elongation–condensing enzymes β-ketoacyl-(acyl carrier protein) synthases I/II (FabF/B) in the type II bacterial fatty acid biosynthetic pathway by binding to the acyl–enzyme intermediate involved. These enzymes are essential for lipid biosynthesis and are found in many pathogenic species. Indeed, platensimycin was found to be the most potent inhibitor of these enzymes known to date and exhibited potent broad-spectrum antibacterial activity against Gram-positive bacterial strains, including methicillin-resistant *Staphylococcus aureus*, vancomycin-intermediate *Staphylococcus aureus*, and vancomycin-resistant *Enterococcus faecium*. In light of the gravity of the situation arising from drug-resistant bacteria and because of the activity and novelty

[*] Prof. Dr. K. C. Nicolaou, A. Li, Dr. D. J. Edmonds
Department of Chemistry
and The Skaggs Institute for Chemical Biology
The Scripps Research Institute
10550 North Torrey Pines Road, La Jolla, CA 92037 (USA)
Fax: (+1) 858-784-2469
E-mail: kcn@scripps.edu
and
Department of Chemistry and Biochemistry
University of California, San Diego
9500 Gilman Drive, La Jolla, CA 92093 (USA)

[**] We thank Dr. D. H. Huang and Dr. G. Siuzdak for assistance with NMR spectroscopy and mass spectrometry, respectively. We also gratefully acknowledge helpful discussions with Dr. P. G. Bulger and Dr. L. A. McAllister. Financial support for this work was provided by the National Institutes of Health (USA), the Skaggs Institute of Chemical Biology, and by Merck Sharp & Dohme (postdoctoral fellowship to D.J.E.).

WILEY InterScience DISCOVER SOMETHING GREAT
© 2006 Wiley-VCH Verlag GmbH & Co. KGaA, Weinheim

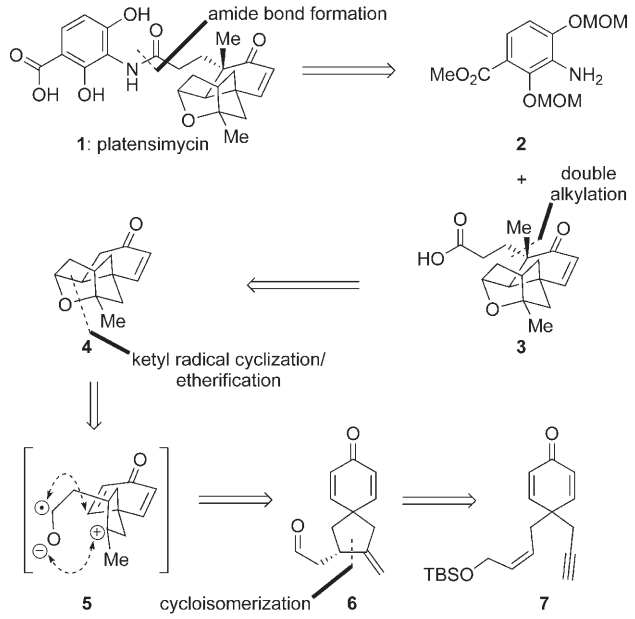

Scheme 1. Structure and retrosynthetic analysis of platensimycin (**1**). MOM = methoxymethyl, TBS = *tert*-butyldimethylsilyl.

of the structure of platensimycin, we undertook the total synthesis of this newly discovered antibiotic. Herein we report the first total synthesis of this potentially useful molecule in racemic form.

Platensimycin consists of an unusual 3-amino-2,4-dihydroxybenzoic acid polar domain linked through an amide bond to a relatively lipophilic, compact, pentacyclic ketolide structural motif, and thus presents an intriguing synthetic challenge. While the amide bond provides an apparent and reasonable site for coupling the two rather disparate fragments, the construction of the two domains is less predictable, despite the many possibilities that can be imagined. Scheme 1 shows the retrosynthetic analysis of one such possibility. Thus, disconnection of the amide bond reveals two subtargets: the aromatic amine **2** and the carboxylic acid **3**. The acid **3** can then be disconnected to remove the propionate and methyl substituents, leaving the cagelike core of the target molecule, compound **4**, as the next subtarget. Of the many disconnections possible for the further retrosynthesis of **4**, the one involving cleavage of the ether bond to leave a tertiary carbocation synthon, followed by rupture of the carbon–carbon bond adjacent to the generated secondary alcohol to reveal a spirocyclic cyclohexadienone (see structures **4** and **5**, Scheme 1) appealed to us because of its potential expediency. The proposed synthetic sequence at this juncture would involve selective generation of a ketyl radical from the corresponding aldehyde, stereoselective conjugate addition of the carbon-centered radical onto one side of the bis-enone, and regioselective ether formation between the hydroxy group of the resultant secondary alcohol and the proximal *exo*-methylene group to give the desired cagelike structure. The substrate for this key step, the spirocyclic cyclohexadiene **6**, can then be further disconnected to reveal the simple enyne **7** as a potential precursor.

The synthesis of the pentacyclic carboxylic acid **3** began with the preparation of enone **11** from **8**[3] in a manner analogous to that recently employed by Hayashi et al.,[4] and proceeded as shown in Scheme 2. Thus, sequential alkylation of **8** with allylic bromide **9**[5] (LDA, 92%) and propargyl

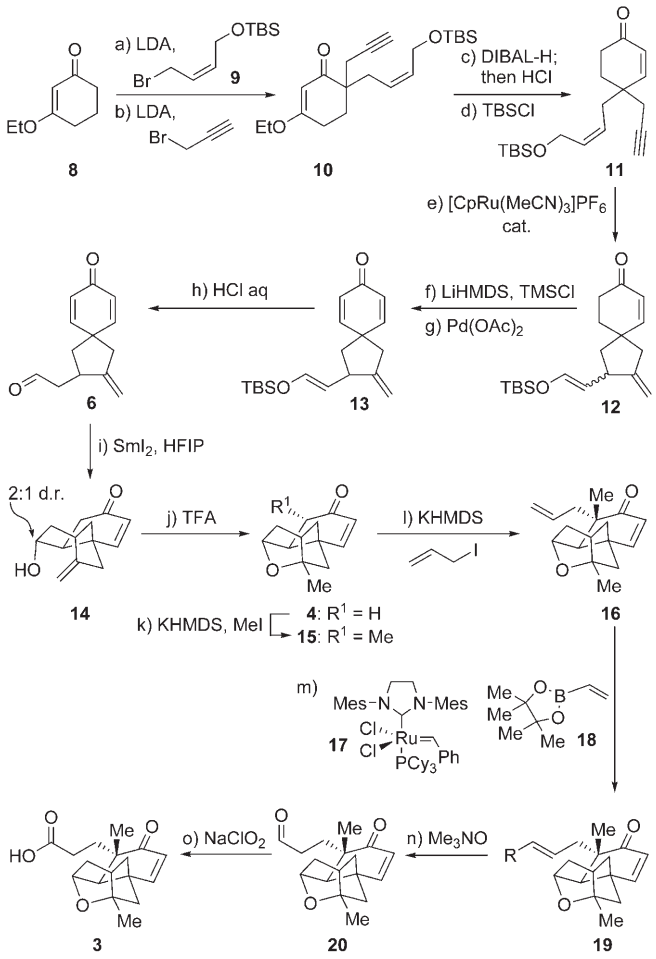

Scheme 2. Construction of the pentacyclic carboxylic acid **3**. Reagents and conditions: a) LDA (1.2 equiv), **9** (1.5 equiv), THF, −78→22 °C, 6 h, 92%; b) LDA (1.4 equiv), propargyl bromide (3.0 equiv), THF, −78→22 °C, 13 h, 97%; c) DIBAL-H (1.2 equiv), toluene, −78→−20 °C, 2 h; then MeOH, 2 N aq HCl, −20→22 °C, 2 h; d) TBSCl (1.2 equiv), imidazole (3.0 equiv), DMF, 22 °C, 20 min, 84% (two steps); e) $[CpRu(MeCN)_3]PF_6$ (0.02 equiv), acetone, 22 °C, 1.5 h, 92%, 1:1 diastereomeric mixture; f) LiHMDS (2.0 equiv), TMSCl (1.5 equiv), THF, −78 °C, 2 h; g) $Pd(OAc)_2$ (1.1 equiv), MeCN, 22 °C, 1.5 h, 68% (two steps); h) 1 N aq HCl/THF (1:1), 22 °C, 2 h, 85%; i) SmI_2 (0.1 M in THF, 2.2 equiv), HFIP (1.5 equiv), THF/HMPA (10:1), −78 °C, 1 min, 46%, ca. 2:1 d.r.; j) TFA/CH_2Cl_2 (1.8:1), 0 °C, 1.5 h, 87%; k) KHMDS (0.5 M in toluene, 1.5 equiv), MeI (8.0 equiv), THF/HMPA (5:1), −78→−10 °C, 2 h, 88%; l) KHMDS (0.5 M in toluene, 4.0 equiv), allyl iodide (8.0 equiv), THF/HMPA (5:1), −78→−10 °C, 2 h, 79%; m) **18** (6.0 equiv), **17** (0.25 equiv), CH_2Cl_2, 40 °C, 6 h, 85%, ca. 6:1 *E*/*Z*; n) Me_3NO (5.0 equiv), THF, 65 °C, 2 h, 95%; o) $NaClO_2$ (3.0 equiv), 2-methyl-2-butene (10 equiv), NaH_2PO_4 (5.0 equiv), *t*BuOH/H_2O (1:1), 22 °C, 15 min, 95%. Cp = cyclopentadienyl, Cy = cyclohexyl, DIBAL-H = diisobutylaluminum hydride, DMP = Dess–Martin periodinane, HFIP = 1,1,1,3,3,3-hexafluoropropan-2-ol, HMDS = hexamethyldisilazide, HMPA = hexamethylphosphoramide, LDA = lithium diisopropylamide, Mes = mesityl = 2,4,6-trimethylphenyl, TFA = trifluoroacetic acid, TMS = trimethylsilyl.

 © 2006 Wiley-VCH Verlag GmbH & Co. KGaA, Weinheim

bromide (LDA, 97%) afforded the bis-alkylated enone **10** as a single regioisomer. Reduction of **10** using DIBAL-H followed by acidic hydrolysis and reintroduction of the TBS ether gave enone **11** in 84% overall yield. Cycloisomerization of **11** was achieved by using the method of Trost et al., which involved exposure of the substrate to the catalyst $[CpRu(MeCN)_3]PF_6$ in an acetone solution[6] to give spirocycle **12** in 92% yield as an inconsequential 1:1 mixture of diastereoisomers. The bis-enone **13** was then generated from mono-enone **12** through the oxidation ($Pd(OAc)_2$) of the intermediate TMS enol ether (LiHMDS, THF, −78°C) in 68% overall yield.[7] Finally, the anticipated aldehyde **6** was unmasked by acidic hydrolysis of the TBS enol ether in 85% yield.

Rapid addition of a solution of the single-electron reductant samarium(II) iodide[8,9] to a dilute, solution of **6** and HFIP in THF/HMPA (10:1) at −78°C, followed by immediate quenching with saturated aqueous NH_4Cl solution, gave an approximately 2:1 mixture (as indicated by ^{1}H NMR spectroscopy) of secondary alcohol **14** and its diastereoisomer in 46% combined yield. Treatment of this inseparable mixture with TFA led to smooth etherification, thus reflecting the proximity of the hydroxy group of the desired diastereoisomer to the exocyclic olefin, and thereby gave the cagelike structure **4** in 87% yield based on the quantity of the correct isomer of **14** present. The undesired alcohol diastereoisomer was recovered unchanged from the etherification reaction. It was surmised from these experiments that the major isomer generated in the SmI_2-mediated cyclization reaction had the desired stereochemistry (**14**, Scheme 2). The conversion of **6** into **4** could also be achieved in a single reaction vessel by quenching the excess SmI_2 with oxygen at −78°C followed by addition of TFA to the resulting mixture and stirring at ambient temperature. This one-pot procedure allowed the isolation of **4** in around 25% overall yield, and streamlines to some extent this segment of the synthetic sequence. The required alkyl substituents adjacent to the carbonyl group were then stereoselectively and efficiently installed by treatment of **4** with KHMDS and MeI (88%) followed by KHMDS and allyl iodide (79%). In each case, the diastereomeric products were undetectable (<2%) in the crude reaction mixture by ^{1}H NMR spectroscopy. The use of allyl bromide in the second alkylation gave lower yields of **16**, accompanied by significant quantities of the O-alkylated isomer. The excellent stereocontrol observed in the alkylation sequence is rationalized by inspection of molecular models of ketones **4** and **15**, in which the rigid cage structure effectively shields the top face of the corresponding enolate. The conversion of terminal olefin **16** into the required carboxylic acid **3** was carried out through two different pathways, both involving aldehyde **20**. In the first case, hydroboration of **16** gave a diol (resulting from concomitant 1,2-reduction of the enone), which could be oxidized to give aldehyde **20** using excess Dess–Martin reagent[10] in CH_2Cl_2 (ca. 40% from **16**). The disappointing yield of this sequence and the low reactivity of the terminal olefin towards hydroboration led us to seek an alternative route for the conversion of **16** into **20**. The preferred method involved olefin cross-metathesis between **16** and vinyl pinacol boronate under the influence of the Grubbs second-generation catalyst **17**,[11] which furnished vinyl boronate **19** in 85% yield as a mixture of *E* and *Z* isomers (ca. 6:1).[12] This intermediate underwent smooth oxidation[13] upon treatment with trimethylamine *N*-oxide to give **20** in 95% yield, which was further oxidized to furnish the desired carboxylic acid **3** in excellent yield (95%) by using the Pinnick protocol.[14]

The synthesis of the aromatic amine, fragment **2**, proceeded smoothly from 2-nitroresorcinol (**21**) as outlined in Scheme 3. Protection of **21** as the bis-MOM ether (NaH, MOMCl, 82%) followed by catalytic hydrogenation (99%) of the resulting compound gave aniline **23**. Protection of the amino group of **23** with a Boc group was achieved by stirring the neat amine with Boc_2O at 40°C to furnish **24** in 99% yield. Interestingly, treatment of **23** with Boc_2O in CH_2Cl_2 in the presence of a catalytic amount of 4-dimethylaminopyridine led to formation of the corresponding isocyanate. Compound **24** was successfully carboxymethylated by using in situ silylation of the carbamate (*n*BuLi, TMSCl), followed by lithiation of the aromatic ring (*n*BuLi), and quenching with methyl cyanoformate (54% overall yield). Finally, thermolysis of the Boc group under microwave radiation (1,2-dichlorobenzene) promoted clean conversion into the required aniline **2** in 83% yield.

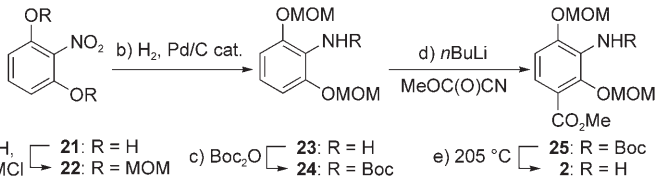

Scheme 3. Construction of the aromatic amine fragment **2**. Reagents and conditions: a) NaH (2.5 equiv), MOMCl (2.3 equiv), THF, 0→22°C, 1.5 h, 82%; b) H_2 (balloon), 10% Pd/C (0.1 equiv), MeOH/EtOAc (10:1), 22°C, 12 h, 99%; c) Boc_2O (3.0 equiv), 40°C, 4 h, 99%; d) *n*BuLi (2.2 M in pentane, 1.0 equiv), TMSCl (1.0 equiv), −78°C, 15 min; then *n*BuLi (2.2 M in pentane, 2.2 equiv), methyl cyanoformate (1.0 equiv), THF, −78°C, 30 min; then 1 N aq HCl, 22°C, 30 min, 54%; e) 1,2-dichlorobenzene, 205°C (microwave), 5 min, 83%. Boc = *tert*-butoxycarbonyl.

The total synthesis of platensimycin was completed as shown in Scheme 4. Coupling of carboxylic acid **3** with aniline **2** was achieved by treatment with HATU in 85% yield. The methyl ester of **26** was then hydrolyzed on exposure to aqueous LiOH. Following complete hydrolysis of the ester as determined by TLC analysis, 2N aqueous HCl was added to effect cleavage of the MOM ethers, thus furnishing (±)-platensimycin (±)-**1** in excellent overall yield (ca. 90%). The spectral data for (±)-**1** were consistent with the reported data[2a,b] and its structure (Table 1). The possibility of achieving an enantioselective synthesis of platensimycin exists at the cycloisomerization stage, where in principle a chiral, enantiomerically pure organometallic species, such as a rhodium catalyst,[15] could be employed to induce asymmetric induction. Alternatively, a resolution, either by classical means or by HPLC on a chiral stationary phase, at the carboxylic acid stage, may be used to provide the enantiomerically pure form

 © 2006 Wiley-VCH Verlag GmbH & Co. KGaA, Weinheim

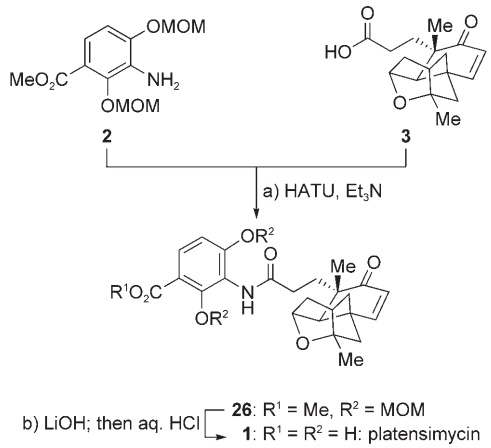

Scheme 4. Total synthesis of platensimycin. Reagents and conditions: a) **3** (1.0 equiv), **2** (2.0 equiv), HATU (4.0 equiv), Et_3N (5.9 equiv), DMF, 22 °C, 26 h, 85%; b) LiOH (55 equiv), THF:H_2O (4:1), 45 °C, 2 h; then 2 N aq HCl, THF:H_2O (3:1) 45 °C, 10 h, ca. 90% overall. HATU = *O*-(7-azabenzotriazol-1-yl)-*N*,*N*,*N*′,*N*′-tetramethyluronium hexafluorophosphate, HOAt = 1-hydroxy-7-azabenzotriazole.

of platensimycin. Further improvements of this route to platensimycin are envisaged.

The described chemistry renders platensimycin (**1**) readily available by chemical synthesis in its racemic form and sets the stage for the synthesis of designed analogues for structure-activity relationship (SAR) studies in search of new antibacterial agents. Certainly, numerous other synthetic sequences to this molecule can be imagined and no doubt many total syntheses will be reported following this one.

Received: September 21, 2006
Published online: September 29, 2006

Keywords: antibiotics · drug resistance · natural products · samarium diiodide · total synthesis

Table 1: Selected physical properties for compounds **1**, **3**, **4**, and **6**.

1: R_f = 0.11 (silica gel, acetone/hexane/AcOH 60:40:1); IR (film): $\tilde{\nu}$ = 3316br m, 2961m, 2921m, 2870w, 1664s, 1656s, 1605s, 1534m, 1448m, 1400m, 1380m, 1282m, 1218m, 1150m, 1102m, 1091m, 1072m, 953w, 831m, 786m cm^{-1}; ^1H NMR (500 MHz, C_5D_5N): δ = 8.12 (d, J = 8.7 Hz, 1H), 6.88 (d, J = 8.8 Hz, 1H), 6.37 (d, J = 10.0 Hz, 1H), 5.95 (d, J = 10.0 Hz, 1H), 4.50 (br s, 1H), 2.84 (ddd, J = 14.6, 11.7, 5.3, Hz, 1H), 2.76 (ddd, J = 14.3, 11.4, 4.6 Hz, 1H), 2.72–2.66 (m, 1H), 2.45 (s, 1H), 2.20 (t, J = 6.5 Hz, 1H), 2.08–2.02 (m, 1H), 1.94–1.90 (m, 1H), 1.82 (d, J = 11.6 Hz, 2H), 1.73 (dd, J = 11.2, 3.0 Hz, 1H), 1.58 (dd, J = 11.6, 6.9 Hz, 1H), 1.49 (d, J = 10.9 Hz, 1H), 1.40 (s, 3H), 1.15 ppm (s, 3H); ^{13}C NMR (150 MHz, C_5D_5N): δ = 203.7, 175.2, 174.9, 158.8, 158.5, 154.4, 129.9, 127.7, 115.7, 110.4, 107.5, 87.3, 76.9, 55.4, 47.2, 47.0, 46.6, 45.5, 43.5, 41.2, 32.6, 32.2, 24.9, 23.7 ppm; ^1H NMR (600 MHz, $CDCl_3$): δ = 8.14 (s, 1H), 7.61 (d, J = 8.9 Hz, 1H), 6.55 (d, J = 10.0 Hz, 1H), 6.51 (d, J = 8.9 Hz, 1H), 5.97 (d, J = 10.0 Hz, 1H), 4.64 (br s, 1H), 2.68–2.63 (m, 1H), 2.52–2.46 (m, 4H), 2.19–2.15 (m, 1H), 2.11 (dd, J = 12.0, 3.4 Hz, 1H), 2.07 (d, J = 11.7 Hz, 1H), 1.96 (dd, J = 11.4, 3.4 Hz, 1H), 1.88 (td, J = 11.4, 5.0 Hz, 1H), 1.84 (dd, J = 11.7, 7.2 Hz, 1H) 1.69 (d, J = 11.4 Hz, 1H), 1.57 (s, 3H), 1.31 (s, 3H); ^{13}C NMR (150 MHz, $CDCl_3$): δ = 203.8, 173.4, 172.2, 155.1, 154.2, 153.9, 128.2, 127.2, 114.3, 111.1, 103.7, 88.0, 76.4, 54.7, 46.5, 46.1, 45.9, 44.7, 42.9, 40.4, 31.5, 31.2, 24.4, 22.7; HR-MS (ESI TOF): m/z calcd for $C_{24}H_{28}NO_7$ $[M+H]^+$: 442.1860; found 442.1853.

3: R_f = 0.35 (silica gel, EtOAc); IR (film): $\tilde{\nu}$ = 2968br m, 1719s, 1657s, 1469w, 1445w, 1410w, 1297m, 1231m, 1183s, 1164m, 1151m, 1104m, 1095m, 953m, 831s, 758m cm^{-1}; ^1H NMR (600 MHz, $CDCl_3$): δ = 6.48 (d, J = 10.1 Hz, 1H), 6.90 (d, J = 10.1 Hz, 1H), 4.43 (br s, 1H), 2.41 (t, J = 6.5 Hz, 1H), 2.37 (br s, 1H), 2.35–2.24 (m, 3H), 2.10–2.07 (m, 1H), 2.04–2.00 (m, 2H), 1.88 (dd, J = 11.2, 3.5 Hz, 1H), 1.79–1.73 (m, 2H), 1.62 (d, J = 11.2 Hz, 1H), 1.45 (s, 3H), 1.24 ppm (s, 3H); ^{13}C NMR (150 MHz, $CDCl_3$): δ = 203.4, 178.5, 153.6, 127.3, 87.1, 76.5, 54.9, 46.5, 46.0, 45.9, 44.6, 43.2, 40.5, 30.6, 29.0, 24.5, 23.0 ppm; HR-MS (ESI TOF): m/z calcd for $C_{17}H_{23}O_4$ $[M+H]^+$: 291.1591; found 291.1581.

4: R_f = 0.20 (silica gel, EtOAc/hexane 3:7); IR (film): $\tilde{\nu}$ = 2951m, 1677s, 1448w, 1379w, 1327w, 1282w, 1248w, 1138w, 1082w, 1037w, 993w, 820w, 778w cm^{-1}; ^1H NMR (600 MHz, $CDCl_3$): δ = 6.62 (d, J = 10.0 Hz, 1H), 5.94 (d, J = 10.0 Hz, 1H), 4.17 (t, J = 3.4 Hz, 1H), 2.43–2.29 (m, 4H,), 1.97–1.94 (m, 2H), 1.90 (d, J = 11.6 Hz, 1H), 1.79–1.74 (m, 2H), 1.66 (d, J = 11.2 Hz, 1H), 1.45 ppm (s, 3H); ^{13}C NMR (150 MHz, $CDCl_3$): δ = 199.1, 155.2, 128.9, 87.2, 79.0, 51.7, 46.2, 44.2, 42.7, 42.2, 37.9, 37.5, 23.1 ppm; HR-MS (ESI TOF): m/z calcd for $C_{13}H_{17}O_3$ $[M+H]^+$: 205.1223; found 205.1216.

6: R_f = 0.31 (silica gel, EtOAc/hexane 1:1); IR (film): $\tilde{\nu}$ = 2831w, 2725w, 1718s, 1657s, 1621s, 1406m, 1284w, 1259m, 1180w, 1090w, 1059w, 1023w, 888w, 858s, 706w cm^{-1}; ^1H NMR (500 MHz, $CDCl_3$): δ = 9.83 (t, J = 1.3 Hz, 1H), 6.98–6.96 (m, 1H), 6.79–6.76 (m, 1H), 6.27–6.23 (m, 2H), 5.11–5.09 (m, 1H), 4.99–4.97 (m, 1H), 3.31–3.23 (m, 1H), 2.85 (ddd, J = 17.9, 4.9, 1.2 Hz, 1H), 2.68 (dq, 16.0, 2.4 Hz, 1H), 2.64 (ddd, J = 17.8, 8.3, 1.4 Hz, 1H), 2.47 (dd, J = 16.0, 1.6 Hz, 1H), 2.15 (ddd, J = 13.0, 8.0, 1.6 Hz, 1H), 1.69 ppm (dd, J = 13.0, 10.3 Hz, 1H); ^{13}C NMR (125 MHz, $CDCl_3$): δ = 200.5, 185.8, 154.2, 152.1, 151.2, 128.7, 127.7, 108.5, 49.2, 46.8, 44.4, 43.7, 36.2 ppm; HR-MS (ESI TOF): m/z calcd for $C_{13}H_{15}O_2$ $[M+H]^+$: 203.1067; found 203.1067.

[1] a) H. Pearson, *Nature* **2002**, *418*, 469; b) C. T. Walsh, *Nat. Rev. Microbiol.* **2003**, *1*, 65–70; c) S. B. Singh, J. Barrett, *Biochem. Pharmacol.* **2006**, *71*, 1006–1015.

[2] a) J. Wang, S. M. Soisson, K. Young, W. Shoop, S. Kodali, A. Galgoci, R. Painter, G. Parthasarathy, Y. S. Tang, R. Cummings, S. Ha, K. Dorso, M. Motyl, H. Jayasuriya, J. Ondeyka, K. Herath, C. Zhang, L. Hernandez, J. Allocco, A. Basilio, J. R. Tormo, O. Genilloud, F. Vicente, F. Pelaez, L. Colwell, S. H. Lee, B. Michael, T. Felcetto, C. Gill, L. L. Silver, J. D. Hermes, K. Bartizal, J. Barrett, D. Schmatz, J. W. Becker, D. Cully, S. B. Singh, *Nature* **2006**, *441*, 358–361; b) S. B. Singh, H. Jayasuriya, J. G. Ondeyka, K. B. Herath, C. Zhang, D. L. Zink, N. N. Tsou, R. G. Ball, A. Basilio, O. Genilloud, M. T. Diez, F. Vicente, F. Pelaez, K. Young, J. Wang, *J. Am. Chem. Soc.* **2006**, *128*, 11916–11920. For a discussion of the activity and possible origins of platensimycin, see: c) D. Häblich, F. von Nussbaum, *ChemMedChem* **2006**, *1*, 951–954.

[3] Compound **8** is commercially available from a number of sources. Alternatively, it can be prepared according to: W. F. Gannon, H. O. House, *Org. Synth.* **1960**, *40*, 41–42.

[4] Y. Hayashi, H. Gotoh, T. Tamura, H. Yamaguchi, R. Masui, M. Shoji, *J. Am. Chem. Soc.* **2005**, *127*, 16028–16029.

[5] M. Sun, Y. Deng, E. Batyreva, W. Sha, R. G. Salomon, *J. Org. Chem.* **2002**, *67*, 3575–3584.

[6] a) B. M. Trost, F. D. Toste, *J. Am. Chem. Soc.* **2000**, *122*, 714–715; b) B. M. Trost, J.-P. Surivet, F. D. Toste, *J. Am. Chem. Soc.* **2004**, *126*, 15592–15602. For a review of Ru-catalyzed reactions, see: B. M. Trost, M. U. Frederiksen, M. T. Rudd, *Angew. Chem.* **2005**, *117*, 6788–6825; *Angew. Chem. Int. Ed.* **2005**, *44*, 6630–6666.

[7] Y. Ito, T. Hirao, T. Saegusa, *J. Org. Chem.* **1978**, *43*, 1011–1013.

 © 2006 Wiley-VCH Verlag GmbH & Co. KGaA, Weinheim

[8] For similar conditions that have been used, see: H. Hagiwara, H. Sakai, T. Uchiyama, Y. Ito, N. Morita, T. Hoshi, T. Suzuki, M. Ando, *J. Chem. Soc. Perkin Trans. 1* **2002**, 583 – 591.

[9] For selected reviews of the use of SmI_2 in organic synthesis, see: a) G. A. Molander, *Chem. Rev.* **1992**, *92*, 29 – 68; b) G. A. Molander, *Org. React.* **1994**, *46*, 211 – 367; c) G. A. Molander, C. R. Harris, *Chem. Rev.* **1996**, *96*, 307 – 338; d) G. A. Molander, C. R. Harris, *Tetrahedron* **1998**, *54*, 3321 – 3354; e) H. B. Kagan, J.-L. Namy, *Lanthanides: Chemistry and Use in Organic Synthesis* (Ed.: S. Kobayashi), Springer, Berlin, **1999**, pp. 155 – 198; f) H. B. Kagan, *Tetrahedron* **2003**, *59*, 10351 – 10372; g) D. J. Edmonds, D. Johnston, D. J. Procter, *Chem. Rev.* **2004**, *104*, 3372 – 3404.

[10] D. B. Dess, J. C. Martin, *J. Org. Chem.* **1983**, *48*, 4155 – 4156.

[11] a) M. Scholl, S. Ding, C. W. Lee, R. H. Grubbs, *Org. Lett.* **1999**, *1*, 953 – 956; b) T. M. Trnka, J. P. Morgan, M. S. Sanford, T. E. Wilhelm, M. Scholl, T.-L. Choi, S. Ding, M. W. Day, R. H. Grubbs, *J. Am. Chem. Soc.* **2003**, *125*, 2546 – 2558.

[12] C. Morrill, R. H. Grubbs, *J. Org. Chem.* **2003**, *68*, 6031 – 6034.

[13] G. W. Kabalka, H. C. Hedgecock, Jr., *J. Org. Chem.* **1975**, *40*, 1776 – 1779.

[14] B. S. Bal, W. E. Childers, Jr., H. W. Pinnick, *Tetrahedron* **1981**, *37*, 2091 – 2096.

[15] A. Lei, M. He, X. Zhang, *J. Am. Chem. Soc.* **2002**, *124*, 8198 – 8199.

 © 2006 Wiley-VCH Verlag GmbH & Co. KGaA, Weinheim